MEDSI 2023

Beijing

Mechanical Engineering Design of Synchrotron Radiation Equipment and Instrumentation

The 12th International Conference on Mechanical Engineering Design of Synchrotron Radiation Equipment and Instrumentation

Nov. 6 - 10, 2023 · Beijing, China

PROCEEDINGS

Topics and Sessions

Photon Delivery and Process
Accelerators
New Facility Design and Upgrade
Simulation
Precision Mechanics
Core Technology Developments

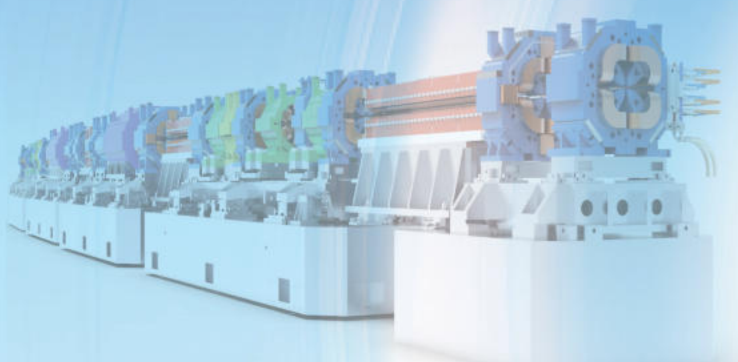

中国科学院高能物理研究所
Institute of High Energy Physics, Chinese Academy of Sciences

高能同步辐射光源
HEPS | High Energy Photon Source

The 12th International Conference on Mechanical Engineering Design of Synchrotron Radiation Equipment and Instrumentation

MEDSI2023

MEDSI 2023
Beijing
Mechanical Engineering Design of Synchrotron Radiation Equipment and Instrumentation

中国科学院高能物理研究所
Institute of High Energy Physics, Chinese Academy of Sciences

HEPS
高能同步辐射光源
High Energy Photon Source | HEPS

Beijing • China
Nov. 6-10, 2023

Preface

The 12th International Conference on Mechanical Engineering Design of Synchrotron Radiation Equipment and Instrumentation (MEDSI2023) took place from November 6 to 10, 2023, in Beijing, China. This important conference, hosted by the Institute of High Energy Physics, Chinese Academy of Sciences, gathers worldwide experts of the accelerator community and related technologies.

In the 5-day Conference, 370+ participants from 21 countries and regions registered. Speakers of 5 keynote talks, 37 contributed oral talks, and 150+ poster presenters presented their recent scientific achievements. We all have been inspired by the rapid advances in the field of synchrotron radiation and free-electron laser light sources worldwide, and deeply impressed by active academic exchanges between participants from different countries and regions. Your participation has made MEDSI2023 a great success.

It is worthwhile to mention the special support of JACoW team and our sponsors and exhibitors and the companies for their involvement in the academic activities of MEDSI2023 in different manners.

Finally, we want to take this opportunity to thank all the members of the Local Organizing Committee, the Scientific Program Committee, the International Organizing Committee, all session chairs, and volunteers. All of the people involved worked hard to make sure the conference ran smoothly.

Yuhui Dong
MEDSI2023 Conference Chair

Ping He
MEDSI2023 SPC Chair

International Organizing Committee

Brad Mountford (ANSTO)
Deming Shu (APS)
Carles Colldelram (ALBA)
June Rong Chen (NSRRC)
Will Hutcheson (LBL)
Keihan Tavakoli (SOLEIL)
Sunao Takahashi (SPRING 8)
Lixin Yin (SINAP)
Ping He (IHEP)
Martin Dommach (XFEL)
Ralph Doehrmann (DESY)
Yifei Jaski (APS)
Sarah Macdonell (DIAMOND)
Phillipe Marion (ESRF)
Lin Zhang (SLAC)
Sushil Sharma (BNL)

Scientific Program Committee

Chair: Ping He

Tiandou Hu
Weifan Sheng
Huamin Qu

Local Organizing Committee

Conference Chair: Yuhui Dong
Scientific Secretary: Lin Bian

Ye Tao
Ping He
Pei Zhang
Lijun Guo
Shaozhen Liu
Yin Li
Mengyao Yuan
Meijuan Yu
Xitong Sun

JACoW Editorial Team

Editor-in-Chief: Zhichu Chen (SARI)

Christine Petit-Jean-Genaz (CERN)
Volker RW Schaa (GSI)
Akihiro Shirakawa (KEK)
Thakonwat Chanwattana
Fangcong Zeng (IHEP)
Michaela Marx (DESY)

Contents

ISBN: 978-3-95450-250-9 ISSN: 2673-5520 doi:10.18429/JACoW-MEDSI2023-TUOAM02

UPDATE OF THE BM18 ESRF BEAMLINE DEVELOPMENT: PRESENTATION OF SELECTED EQUIPMENT AND THEIR COMMISSIONING

F. Cianciosi†, A.-L. Buisson, P. Carceller, P. Tafforeau, P. Van Vaerenbergh, ESRF, Grenoble, France

Abstract

This article highlights specific equipment that have not yet been described in previous publications, notably the in-vacuum cooled fast shutter for high-energy, the wide aluminium window and tailored high-precision slits (400 × 200 mm opening). 2022 and 2023 have seen the installation and commissioning of these new equipment. The ID18 beamline opened for user applications in September 2022 with limited capabilities and has been increasing its possibilities since then. It is expected to be fully equipped by the end of 2024.

INTRODUCTION AND BEAMLINE PERFORMANCES

The ESRF-EBS beamline BM18 has been tailored for hierarchical propagation phase-contrast tomography. The 220 m long beamline benefits from a high-coherence at high-energy beam from a 1.56 T triple short wiggler of the new 4th generation storage ring. The beamline combines a resolution range from 120 µm down to 0.65 µm with the possibility to scan samples up to 2.5 m high and 1.2 m in diameter. With a beam width up to 35 cm and energies ranging from 40 to 280 keV (polychromatic), the main applications are material sciences, cultural heritage, geology, biomedical imaging and industrial applications.

Due to the delays in the development and installation of the large sample stage previously described in [1], the beamline started user operation in September 2022 using a new version of a smaller sample stage initially developed by *LAB Motion Systems* in 2012 for palaeontology on the ID19 (2 stages) and ID17 (1 stage) beamlines and of which two more copies were installed later on BM05. The maximum dimensions of samples are therefore limited to 30cm in diameter, 30 kg in weight, and 50 cm vertically. Once the large sample stage is operational, the maximum dimensions will be 1.2 m diameter, 300 kg and 2.5 m vertically.

IN-VACUUM COOLED FAST SHUTTER

During the commissioning and the initial operation of the BM18 beamline, the quick obturation of the photon beam was made using the photon absorber placed at the end of the Optical Hutch. However, this instrument is not optimal for this purpose, because it is relatively slow (about 1s/cycle), it has a relatively short life (about 100k cycles) and it is part of the safety equipment of the beamline, therefore its use should be reserved to this function only.

For an impinging power of 300 W, and a beam size of 100 × 5 mm, it was decided to develop a specific beam shutter with the aim of shutting off the beam quickly (maximum opening/closing time: 0.1 s), the possibility of continuous operation (i.e. frequency: 1 Hz) and for a long-life (several millions of cycles).

The shutter itself is constituted by a tungsten blade, which rotates by 30° to either intercept the beam or let it pass. It is actioned by a cooled stepper motor. All the components are in vacuum. The blade is isolated from the shaft by a PEEK spacer. When the blade is in the upper position, it remains in contact with a water-cooled copper block which cools the tungsten blade. This block is mounted on springs to ensure good contact pressure with the blade and a perfect alignment between the contact surfaces. Figure 1 shows the blade in the open position (the blade in closed position is superimposed in transparency).

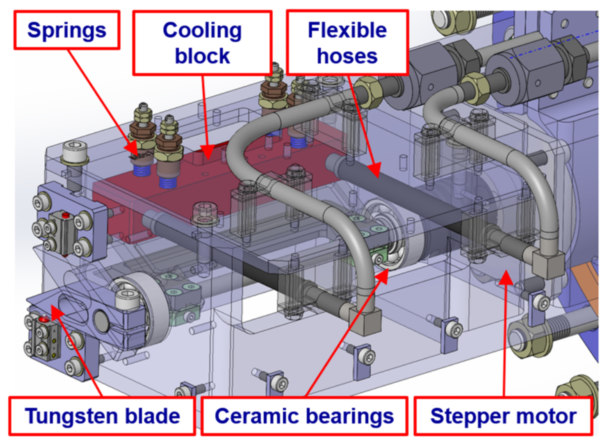

Figure 1: Design of the in-vacuum cooled fast shutter.

Calculated pressure contact between the blade and the cooling block is 0.85 bar. FEA calculations (Fig. 2) demonstrate that, for a thermal contact exchange coefficient of 800W/m²K [2], the blade would not exceed 214 degrees more than that of the cooling water temperature (20 ºC).

The control of the motor is done with an IcePAP controller [3] and the software is under development.

The foreseen closing movement will be done in two phases: a quick rotation to intercept the beam in the required time, followed by a slower movement to ensure contact with the cooling block.

The manufacturing drawings have been completed and the parts have been ordered. The assembly will be done at ESRF and the first test is scheduled before the end of 2023.

† cianciosi@esrf.fr

ISBN: 978-3-95450-250-9 ISSN: 2673-5520 doi:10.18429/JACoW-MEDSI2023-TUOAM02

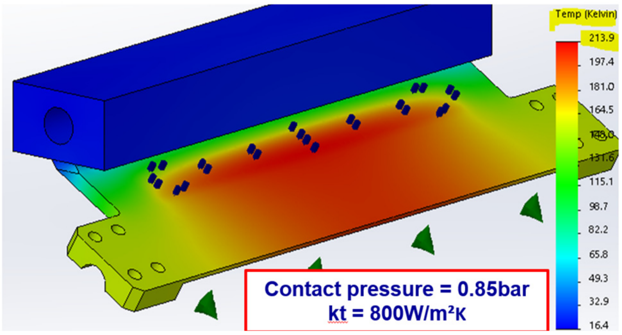

Figure 2: Temperature rise of the tungsten blade relative to the water temperature.

WIDE ALUMINIUM WINDOW

At the entrance of the Experimental Hutch (EH), the beam will go from vacuum to air. For that, a large vacuum-tight window is required, to allow a wide beam (i.e. 400 (h) × 200 (v) mm) to pass. The selection of the material, and the design of this component, was demanding. The window has to let the full wide beam pass (without reducing it), it has to sustain a 1bar pressure difference while heated by the beam and it has to be as transparent as possible to the radiation (up to 50 W would be absorbed by the window if using the full beam size without any filter in the optics hutch). In addition, the selected material has to be easy to polish close to an optical grade (i.e. Ra < 0.1) [1].

The selected design was a relatively simple membrane-type window made of aluminium (very low alloyed, "half-hard" state). The material has been sourced from *Goodfellow* (reference: AL00-FL-000300; purity of 99%).

The metallic membrane is clamped to a stainless-steel flange. The vacuum tightness is obtained by a Viton gasket (Fig. 3). Calculations show that, under pressure, a 1mm thick window would exceed the elastic limit with 2 % strain induced (Fig. 4).

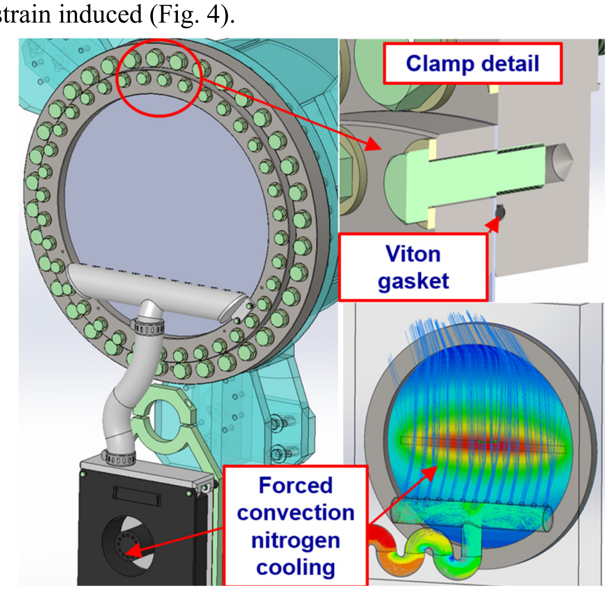

Figure 3: Design and thermal simulation of the membrane.

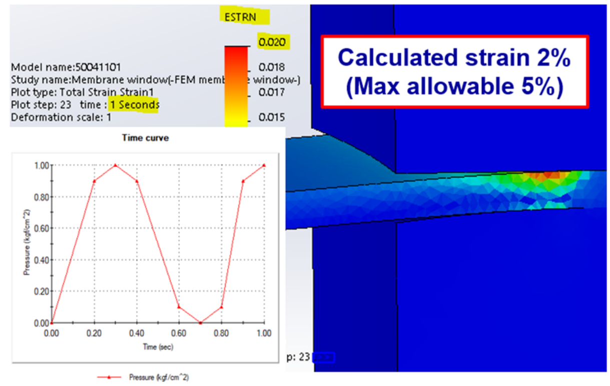

Figure 4: Strain calculation of the membrane showing a deformation of 2 % (5% is the failure deformation obtained during the collapsing tests).

It has to be pointed out that the relation between pressure and strain is not linear due to the geometrical shape. By increasing the pressure, the metallic membrane develops a dome shape which is more efficient in resisting the load.

ESRF has purchased several sheets of this material with thicknesses of 1, 1.2 and 2 mm (coming from the same production batch). This has permitted real-scale testing as well as making the final production of the window with exactly the same material. The mechanical characteristics, measured during the testing of this material is shown in Table 1.

Table 1: Mechanical Characteristics of the AL00-FL-000300 at 2 Temperatures

	20°C	100°C
Yield stress	115 MPa	97.5 MPa
Rupture stress	123 MPa	100 MPa
Max strain	5.2%	ND

The real-scale tests, performed by increasing pressure with water on the future air-side, has been repeated on the 3 available thicknesses. Tests have demonstrated a safety factor, regarding the load, always bigger than 3 even when using a 1mm thick membrane (Fig. 5). Therefore, the 1mm thickness has been selected for the production of the installed window.

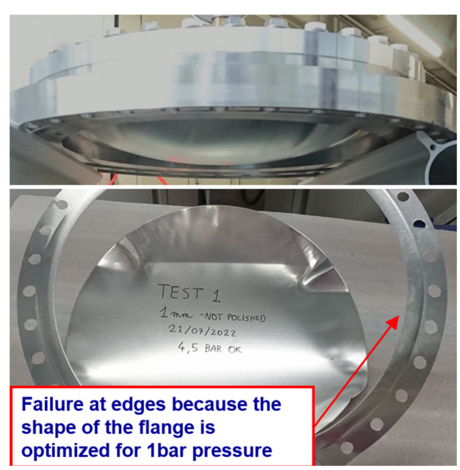

Figure 5: Aluminium window during water pressure test.

ISBN: 978-3-95450-250-9 ISSN: 2673-5520 doi:10.18429/JACoW-MEDSI2023-TUOAM02

The polishing was done by the BM18 scientist, who acquired good knowledge in this field thanks to his experience with fine polishing of filters and sample preparation.

QUINARY SLITS

Large aperture slits are settled downstream of the large window, inside a PETG chamber flushed by nitrogen (Fig. 6). They are composed of 4 tungsten blades of dimensions 400 (h) × 200 (v) mm height and 20 mm thick. They are equipped with an inner cooling loop and designed to accommodate the full beam (i.e. 400 × 20 mm in white beam mode and up to 350 × 200 mm with the current development to have an enlarged monochromatic beam). They are able to sustain the full impinging power of 300 W. The minimum vertical gap achievable is 20 µm with a measured parallelism error of 5 µrad. Their Minimum Incremental Motion (MIM) is 1µm, their repeatability is in the order of 1.5 µm as well as their stability over a week.

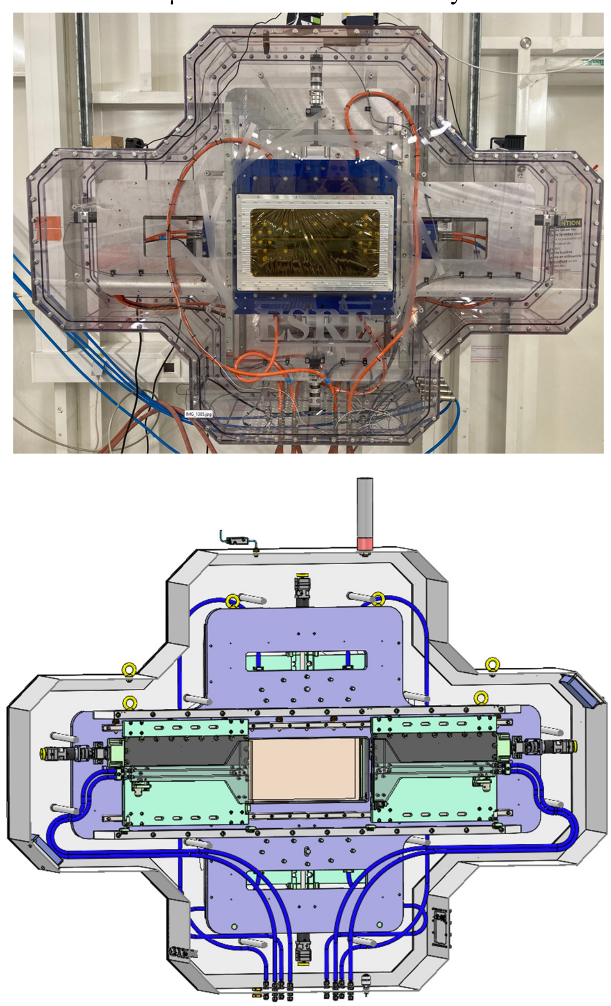

Figure 6: Picture and layout of the quinary slits inside the nitrogen box. A 25 µm Kapton window has been installed for 7 months now without failure.

DETECTOR GIRDER

The detector girder is the structure supporting the detectors and related equipment, for a total payload of about 3T. It has to move over 30 m along the hutch, and is compounded by a steel structure (2T) supporting a granite slab (3T). An additional trolley is used to carry controllers for the motorised stages and computers for the detectors (Fig. 7) [1].

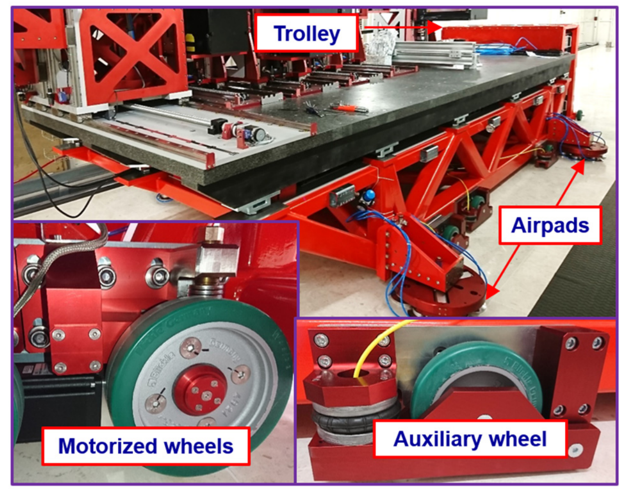

Figure 7: Detector girder on airpads. Details of motorized wheels and auxiliary wheels.

In the original design, the girder was placed on 4 groups of 6 precision airpads from *Positechnics* D160 mm, hovering above the marble floor of EH (140 m^2). Unfortunately, and despite the efforts of the supplier, this floor presented some local defects that made the motion of the airpads very difficult. The air gap for this type of pad is a function of the applied load and the feed pressure. For our application, this value is in the range of a few tenths of microns. Despite many polishing campaigns, the girder still did not move smoothly.

The solution that we have developed is based on wheels. It includes 7 auxiliary wheels (located over the periphery of the frame) and 4 main wheels (located at the 4 corners). The aim of the auxiliary wheels (already installed) is only to relieve the load. They are actuated pneumatically and they have no stroke limit. The 4 additional main wheels will replace the airpads. They will be actuated pneumatically too but their stroke is limited mechanically to lift the girder to the desired necessary value (i.e. around 1mm) as shown in Figs. 8 and 9. Four motorized wheels, instead of one, will be needed to overcome the greater friction of the wheels as compared to the former airpads. During the image acquisition, the air-pressure in the bellows will be removed in order that the girder may rest on aluminium pads for maximum stability and position repeatability.

ISBN: 978-3-95450-250-9 ISSN: 2673-5520 doi:10.18429/JACoW-MEDSI2023-TUOAM02

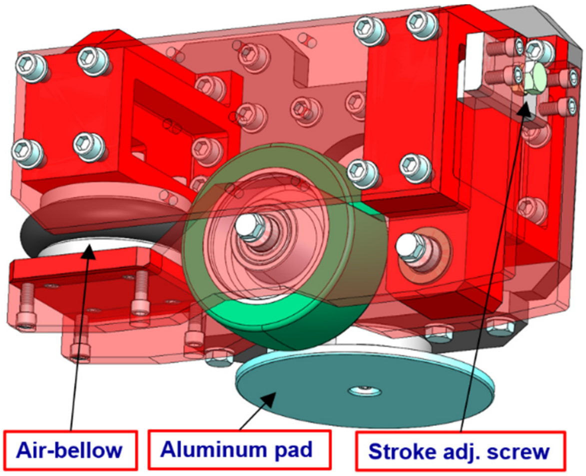

Figure 8: Main wheels to replace of the airpads.

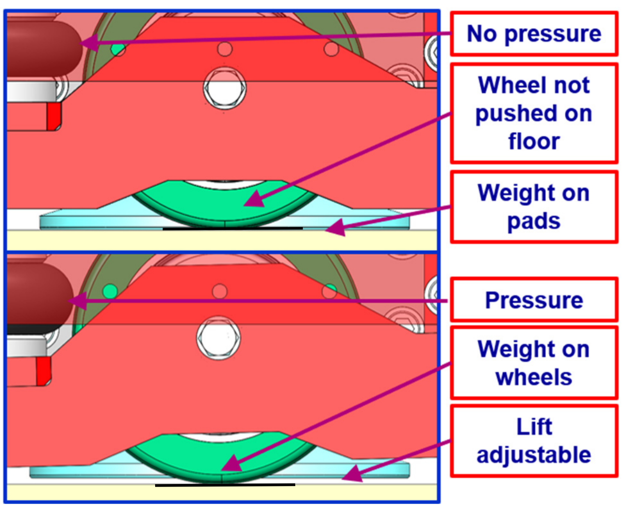

Figure 9: Main wheels in retracted position (top figure) and in contact with the floor (bottom figure).

DETECTOR STAGES

The detector girder is equipped with 9 combined stages (Fig. 10) with 600 mm stroke on the vertical and horizontal axes.

The beamline is currently equipped with 8 different detectors, covering pixel sizes from 0.65 µm to 120 µm. Additional optics are still in the development phase and will be implemented in 2024 and 2025. Each stage can host detectors from 50 kg to 200 kg. The maximal detector size is 700 × 900 × 500 mm. MIM of this equipment is 1 µm as well as the repeatability. Over 6 consecutive days of experiments, the stability was still within a single pixel size of the detector used for this experiment (i.e. 6 µm).

Figure 10: Two of the detector stages (in red), hosting detectors (in black).

CONCLUSIONS

After more than a year of commissioning and experiments, BM18 has largely fulfilled its goals. The main unfulfilled goal is evidently the use of the large sample stage for user experiments. This is expected to become a reality by mid-2024 based on the present state of the installation. The sample stage will be unique in the world in terms of sample size that can be accommodated for high-resolution imaging.

BM18 is already a highly subscribed beamline, both for academic research and for industrial applications. Most of the installed equipment are prototypes, based on cutting-edge technology and thus still require time and effort for final characterisation and optimization.

ACKNOWLEDGEMENTS

The BM18 project team wish to thank the *LAB Motion Systems* staff for their determination and diverse expertise. The BM18 project is partially funded by the German Federal Ministry of Education and Research (BMBF), in collaboration with the Fraunhofer Gesellschaft, the Julius-Maximilians-Universität Würzburg, and the Universität Passau.

REFERENCES

[1] F. Cianciosi *et al.*, “BM18, the new ESRF-EBS beamline for hierarchical phase-contrast tomography”, in *Proc. MEDSI’20,* Chicago, USA, Jul. 2021, pp. 1-5. doi:10.18429/JACoW-MEDSI2020-MOIO02

[2] B. Fell and K. Fayz, “Thermal contact resistance experimental investigation on the cooling of PHOENZ-UV mirror M1”, CLRC Daresbury Laboratory, UK, Rep. 107.51520, May 2020.

[3] N. Janvier *et al.*, “IcePAP: an advanced motor controller for scientific applications in large user facilities”, in *Proc. ICALEPS’13,* San Francisco, CA, USA, Oct. 2013, paper TUPPC081, pp. 766-769.

ISBN: 978-3-95450-250-9 ISSN: 2673-5520 doi:10.18429/JACoW-MEDSI2023-TUOAM04

NEW DEVELOPMENTS AND STATUS OF XAIRA, THE NEW MICROFOCUS MX BEAMLINE AT THE ALBA SYNCHROTRON

N. González†, J. Juanhuix, J. Nicolás, D. Garriga, M. Quispe, A. Crisol, I. Sics, C. Colldelram
ALBA Synchrotron Light Source, Cerdanyola del Vallés, Spain

Abstract

The new BL06-XAIRA microfocus macromolecular crystallography beamline at ALBA synchrotron is currently under commissioning and foreseen to enter into user operation in 2024. The aim of XAIRA is to provide a 4 − 14 keV, stable, high flux beam, focused to 3 × 1 μm² FWHM. The beamline includes a novel monochromator design combining a cryocooled Si(111) channel-cut and a double multilayer diffracting optics for high stability and high flux; and new mirror benders with dynamical thermal bump and figure error correctors. In order to reduce X-ray parasitic scattering with air and maximize the photon flux, the entire end station, including sample environment, cryostream and detector, is enclosed in a helium chamber. The sub-100 nm SoC diffractometer, based on a unique helium bearing goniometer also compatible with air, is designed to support fast oscillation experiments, raster scans and helical scans while allowing a tight sample to detector distance. The beamline is also equipped with a double on-axis visualization system for sample imaging at sub-micron resolutions. The general status of the beamline is presented here with particular detail on the in-house fully developed end station design.

INTRODUCTION

ALBA is a synchrotron light source located in the Barcelona area hosting ten operating beamlines, with four more beamlines in design or construction phases. Long-term plans include the upgrade of the facility to a 4th generation source together with major upgrades of the existing beamlines.

BL06-XAIRA is a new microfocus macromolecular crystallography (MX) beamline currently in commissioning, expecting first users along 2024. The beamline is designed to deliver high quality data from micron-sized and/or poorly diffracting crystals from oscillation and fixed-target MX experiments, as well as from experiments at low photon energies exploiting the anomalous signal of the metals naturally occurring in proteins (native phasing), which is enhanced in the case of small crystals. To this aim XAIRA is foreseen to provide a ~ 4 − 14 keV, 3 × 1 μm² FWHM (h × v), which can be slit down to 1 × 1 μm², with a flux of > 10^{13} ph/s/250 mA at 1 Å wavelength (12.4 keV).

The entire end station, that is detector, cryostream, diffractometer and sample conditioning elements, is enclosed in a helium chamber to provide optimal conditions for experiments at low energies as low as 3 keV. The system allows the recovery of the helium and is compatible with standard operation in air.

BEAMLINE DESCRIPTION

The optical design of the beamline was first described in the SRI2018 conference in Taiwan [1]. The beamline is fed by a permanent magnet in-vacuum undulator, IVU19, with a magnetic period of 19.9 mm and a minimum gap of 5.2 mm [2]. The high power produced by the undulator, up to 4.3 kW at 250 mA, and the absence of vacuum windows to maximize the flux at low photon energies impose severe constraints on the cooling systems of the optical elements up to the monochromator. To mitigate this, the aperture of the front-end moveable masks is set to limit the power delivered to the beamline optics to 1.3 kW.

The complete beamline layout is shown in Figure 1. The beam is focused by two horizontal focusing mirrors, the horizontally prefocusing (HPM) and focusing (HFM) mirrors, and a vertically focusing mirror (VFM), the two latter mounted as a KB mirror pair. The mirrors are elliptically bent in the meridional direction by ALBA mirror benders, which provide sub-nanometric resolution and stability and allow correcting the wavefront deformations caused by static or dynamic effects such as long-period figure errors and thermal bumps [3]. High-precision slits (HSS) are placed at the focal position of the HPM to reduce the horizontal beam size, so that it can be further focused by the HFM to 1 μm FWHM at the sample position.

The energy is selected using a cryogenically cooled monochromator that combines a narrow gap, 4.5 mm, channel-cut monochromator (CCM) and a double multilayer monochromator (DMM) mounted on the same Bragg axis. The geometry has been optimized to switch from one to another without the need of any translations. The beam diagnostics include one cooled and 4 non-cooled fluorescence screens (FS) [4] to monitor the beam profile and shape, and two 20 μm thickness CVD diamond XBPMs from Cividec to position and measure the incoming beam flux and two sets of slits to reduce the beam divergence.

The sample is located just 1 m downstream the last KB mirror, the HFM, in a vertically oriented goniometer. The entire end station, which includes the diffractometer, the detector, the cryostream and the sample visualization system, among others, is enclosed in a helium chamber, which can also be opened to air. In between the KB chamber and the helium chamber, the Beam Conditioning Elements (BCEM) enclose a fast shutter, a 4-blade slits set, an XBPM and a beam diagnostic unit with a YAG:Ce screen and a phodiode. The vacuum-helium or air interface between the BCEM chamber and the end station is maintained with a 10 μm thickness and 2 mm diameter diamond window. Besides, so as to monitor the beam stability at sample position, the two XBPMs include Q-Tools

† ngonzalez@cells.es

ISBN: 978-3-95450-250-9 ISSN: 2673-5520 doi:10.18429/JACoW-MEDSI2023-TUOAM04

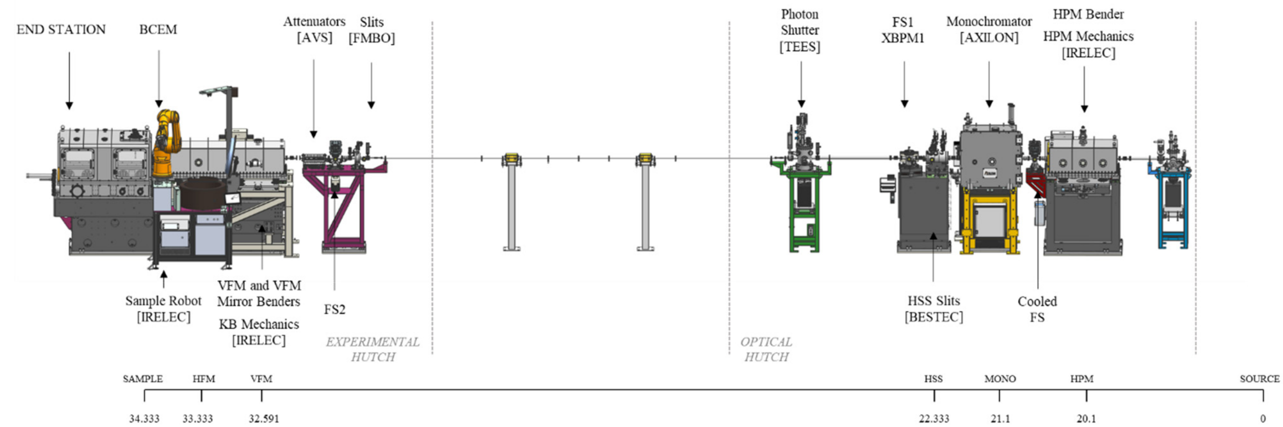

Figure 1: XAIRA beamline layout. Manufacturers are marked in brackets.

interferometers for vertical position feedback. Additionally, the HFM and VFM mirrors also include three interferometers each, pointing directly at the mirror surface and giving a direct reading of the mirror pitch and position. Three more interferometers will be used to monitor the sample position.

WHITE/PINK BEAM OPTICAL COMPONENTS

Horizontal Prefocusing Mirror (HPM)

The HPM consists on a silicon substrate of $40 \times 30 \times 670$ mm^3 (W × H × L) mounted on a horizontally deflecting ALBA mirror bender. The optical surface is limited to 450 mm length although the mirror acceptance is larger. The nominal applied forces, 438 N (upstream) and 623 N (downstream), allow to focus the beam at the HSS placed 2.233 m downstream. The power load on the HPM is limited vertically by the front-end aperture, and horizontally by the acceptance of the mirror and the cooled mask placed before the mirror. The resulting nominal absorbed power load is 154 W at 250 mA, which results in a moderate peak power density of ≤ 0.22 W/mm^2. These input conditions allow using a water-cooling system applied at the sides of the mirror. Still, the absorbed power induces a significant increase of the temperature and an expansion of the optical surface, thus, a cooling system to keep the mirror at a stable temperature while allowing the mirror bending was required.

The cooling system design is based on the method developed at SLAC [5], which uses a 100 µm eutectic InGa layer between the mirror and the silicon pads attached to the copper pads. Two independent stainless-steel tubes are brazed to these 500 mm copper pads. The pads are nickel plated in order to avoid Cu-InGa issues. The silicon pads, five on each side, are clamped to the copper pads with 50 µm Indium foils in between. The complete setup is shown at Figure 2. The difference of using Indium foils instead of InGa in this union was calculated by thermal FEA and no big impact was observed. The thermal conductivity of the system was validated at the optics lab before the installation at the beamline circulating hot water through the pipes and visualizing the temperature increase using a precision infrared camera (Optris PI640).

In-depth metrology measurements were done on the mirror bender, with and without the cooling, in order to evaluate its effect on the bender performance. The results show the performance was not affected by the shear forces of the 100 µm eutectic InGa layer, as shown at Table 1.

Table 1: Bender Performance

Parameter	Value
Bender Error	0.023 µrad rms
Radius repeatability ΔR/R	0.0076 %
Radius Stability (14h)	0.0054 % rms
Radius Resolution	≤ 0.0371 %
Slope Error	≤ 0.258 µrad rms
Height Error	1.56 nm rms

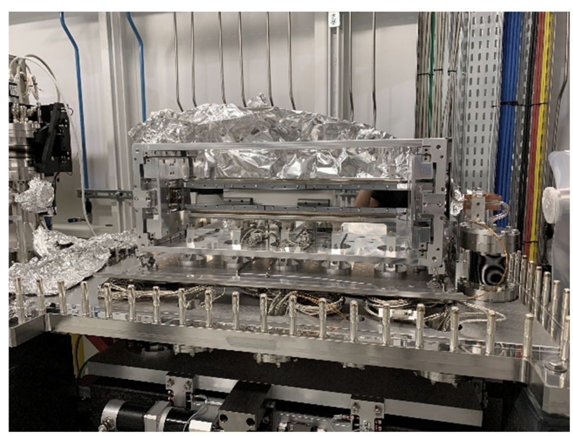

Figure 2: Picture of the HPM Bender at the beamline.

The cooling system was validated by illuminating the full optical length of the mirror at the maximum power delivered by the undulator. The mirror temperature increased with the front-end vertical aperture (Figure 3). At maximum tested aperture, beyond nominal conditions, the mirror absorbs 211 W power (incoming 604 W) while the mirror temperature rises to 30 ºC, as predicted by FEA. Mirror temperature can be seen in the next Figure 3.

ISBN: 978-3-95450-250-9 ISSN: 2673-5520 doi:10.18429/JACoW-MEDSI2023-TUOAM04

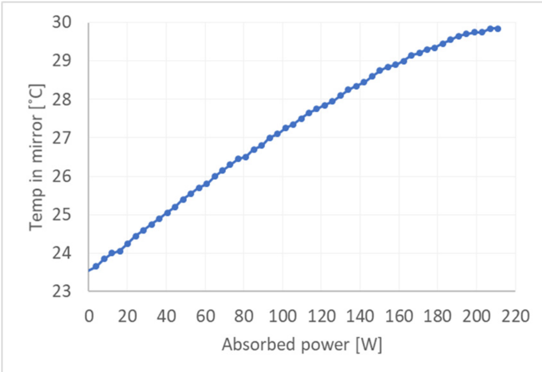

Figure 3: HPM Temperature vs. absorbed power.

Monochromator

The monochromator of XAIRA is based on a novel concept that combines a channel cut monochromator (CCM) and a double multilayer monochromator in a single mount. The Bragg axis is placed 2.3 mm underneath the first optical surface, both for the multilayer and the channel cut crystal, and intersects the beam axis. In this configuration, the center of the beam travels along the crystals surface depending only form the Bragg angle, θ. Due to the relatively small grazing incidence angle of the multilayers (ML) in the hard X-ray compared to the channel cut, the beam positions for the two diffracting surfaces do not overlap in the range of $4-14$ keV for the CC and $6-14$ keV for a ML with a d spacing of 26 Å. Therefore, it is feasible, from the geometrical point of view, to optimize the dimensions, so as to have the two surfaces in the same plane and change from one optics to another just changing the Bragg rotation angle without the need of any translations. The sketch is shown in Figure 4.

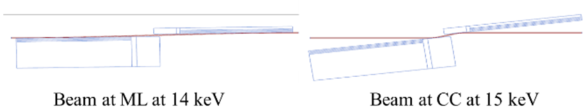

Figure 4: Conceptual Sketch of the CCM/DMM monochromator. Bragg angle 1 deg (left) and 7.6 deg (right).

The two optics, a Si(111) channel-cut crystal and a double Mo/B_4C multilayer are cryogenically cooled by a common pair of clamped cooling pads. The optimization of the cooling internal geometry was carefully done by CFD and thermal FEA simulations in order to make the LN2 flow as uniform as possible and minimize turbulences so as to maximize vibrational stability while maximizing the cooling capacity. Considering that the absorbed power is around 235 W at worst case, the cooling performance is especially important at low energies of the CC, with an incidence angle of around 29 deg and a peak power density of 20 W/mm^2. The influence of the LN2 cooling on the MM was also a main concern. Mo/B_4C was found to be the most suitable coating material for cryogenic temperatures and the cooling pads were also optimized so that the thermal cycling on the MM substrate was reduced to just a few kelvins in working conditions. Another critical aspect was the assembly of the optical substrates. While the clamping pressure is a key parameter in order to have a good thermal conductance, an overpressure induced surface deformations on the MM optical surface. The clamping procedure was carefully done measuring the optical surfaces with a Fizeau interferometer while increasing the pressure.

The design and construction of the monochromator mechanics was done by AXILON. First commissioning tests with beam have proven that the concept works fine, being able to change from one substrate to another just rotating the Bragg axis in less than 1.3 min (limited by the rotation speed) while keeping the horizontal beam position and energy. Beam images can be seen in Figure 5.

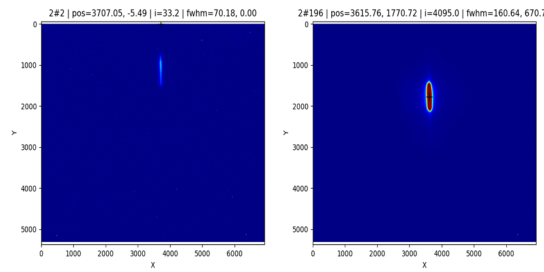

Figure 5: Beam at FS1, downstream the monochromator, for the CC (left) and ML (right), both at 7.3 keV.

END STATION

General Layout

The end station of XAIRA is composed by the following components which can be shown in Figure 6.

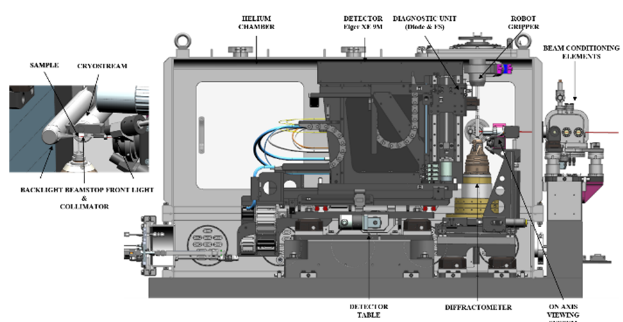

Figure 6: End Station Components.

- The Beam Conditioning Elements (BCEM), is the chamber located just downstream the KB and upstream the helium chamber. It contains a fast shutter, 4-blade slits, a XPBM and a diagnostic unit, all driven by SMARACT piezoguides, in a tight space of 150 mm. The chamber ends in a 10 µm 2 mm diamond window that separates the ultra-high vacuum section from the end station, at atmospheric pressure.
- The cryostream, Cryocool – G2b. Manufactured by Cryo Industries America, it provides continuous cold gas of helium or nitrogen in order to maintain the sample at cryogenic temperatures.
- The detector and detector table. The detector, a fast photon counting pixel Dectris EIGER2 XE 9M, is mounted over a longitudinal and transversal very stable translation table. The detector, which can also work both in helium and in air, can be located as close

ISBN: 978-3-95450-250-9 ISSN: 2673-5520 doi:10.18429/JACoW-MEDSI2023-TUOAM04

as 70 mm to the sample for high resolution experiments. In addition, the detector cover frame includes a fast in/out diagnostic unit to image the beam and measure flux at the detector position.

- The sample loading robot. The robot, manufactured by IRELEC, is capable of loading and unloading the samples at cryogenic temperatures. The double gripper has been customized with a sealing interface in order to minimize the helium leakage and make it compatible with the helium chamber, which has a valve on top to allow the gripper entrance.
- The sample illumination system and, beamstop and collimator assembly, from ARINAX. A front light, mounted on the on-axis sample viewing system and a removable backlight system illuminate the sample. A 500 µm-thick beamstop is mounted and pre-aligned with a 100 µm cleaning aperture capillary. The assembly is mounted on the on axis viewing (OAV) system so that they move together to follow the beam excursion but they can be retracted, for sample loading.

Helium Chamber

The Helium chamber is located and seals against the end station granite with Viton rings. The chamber is split in two parts, the bottom part, which will always remain installed, contains all the electrical feedthroughs and piping interfaces, manufactured as for UHV conditions to minimize helium leaks. The top part, removable, includes several doors to access for maintenance, the robot interface on the top with a get valve and the interfaces required by the helium recovery circuit [6].

Diffractometer

Due to the tight space constrains (only 70 mm from sample to detector) and the demanding performance requirements: Sphere of Confusion (SoC) ≤ 100 nm, resolution of 0.05 mdeg and maximum speed of 360 deg/s, together with the requirement of having to be compatible both with helium and air, it was decided to fully develop the diffractometer in house. The vertically oriented goniometer, Ω, is mounted on a high stability XY stage, that allows aligning the rotation axis and thus the sample with respect to the beam in a ± 5 mm with 50 nm resolution. The goniometer, consist of a slotless direct drive torque motor form Aerotech mounted on a customized helium/air bearing developed by Fluid Film Dynamics. The bearing can be fed by air or helium at 5.5 bar providing the same performance in terms of rigidity and runout.

On top of the goniometer, the sample centering stages (xyz) not only permit the sample centering with respect to the rotation axis but the creation of trayectories in combination with the Ω axis (i.e. helical scans or raster scans). The stages, actuated by SMARACT piezo guides, are mounted on a titanium frame to minimize the thermal expansion. A precision slip ring, attached to the goniometer axis by a flexible coupling, permits transmitting the electrical signals to the connectors bellow.

The goniometer runout measurements, with air and with helium can be shown in the next Figure 7.

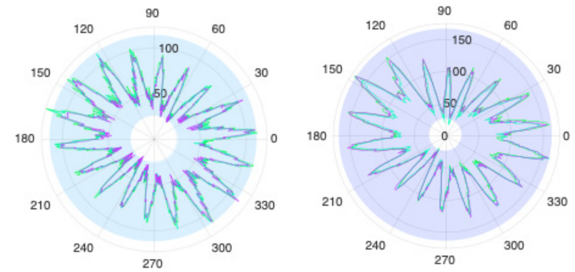

Figure 7: Run out measurements; 50 nm for goniometer with air (left) and 70 nm for the goniometer with He (right).

On Axis Viewing System

The sample visualization is based on two separate optics, namely a high magnification and a low/medium magnification microscope. The high magnification branch includes a high-resolution objective with a fixed resolution of 0.7 µm. The other branch, is a parallax-free commercial system (B-Zoom, ARINAX) composed of an objective with a 1mm diameter central hole and a splitter for 2 lens branches with 1.2 µm resolution and > 1.2 µm, respectively. The two systems are located in parallel and a fast motorized stage permits changing from one to another in less than 4 s. This stage is located over a high resolution and stability vertical stage, which is mounted over the same XY stage of the goniometer to allow the alignment with respect to the beam.

CONCLUSION

The design of the main white/pink beam optical elements and the end station have been presented, including the results that validate the performance of the cooling system of the HPM bender, the newly concept of the monochromator and the helium compatible diffractometer.

XAIRA beamline installation is foreseen to finished by the end of 2023. Further commissioning for optimization will be performed during this year.

ACKNOWLEDGEMENTS

The authors acknowledge the team involved in the design, construction and commissioning of the beamline: XAIRA Beamline Staff, Isidro Crespo and Alejandro Enrique; Alignment Group, Marta Llonch and Jon Ladrera; Mechanical Workshop, Jose Ferrer, David Calderón, Karim Maimouni, Lluis Ginés and Oscar Borrego; Engineering, Marcos Quispe, Liudmila Nikitina, Yuri Nikitin and Núria Martí; Electronics Section, Bernat Molas, Xavi Serra, Antonio Camps and Alberto Ruz; Controls Section, José Centeno Ganbadinho, Oriol Vallcorba and Alberto Rubio; Nanomotion group, Juan Luis Frieiro.

REFERENCES

[1] J. Juanhuix *et al.*, "Optical design of the new microfocus beamline BL06-XAIRA at ALBA", in *AIP Conference Proc.*, vol. 2054, p. 060032, Jan. 2019. doi:10.1063/1.5084663

[2] J. Campmany, J. Nicolás, J. Juanhuix, J. Marcos and V. Massana, "A general view of IDs to be installed at ALBA for

ISBN: 978-3-95450-250-9 ISSN: 2673-5520 doi:10.18429/JACoW-MEDSI2023-TUOAM04

second and third phase beam-lines," *in AIP Conference Proc.*, vol. 1741, p. 020021, Jul. 2016. doi:10.1063/1.4952800

[3] C. Colldelram, N. González, J. González, C. Ruget, J. Juanhuix and J. Nicolas, "Adaptive optics bender with sub-nanometer correction and stability", in *AIP Conference Proc.,* vol. 2054, p. 060013, Jan. 2019. doi:10.1063/1.5084644

[4] J. M. Alvarez, C. Colldelram, N. González, J. Juanhuix, J. Nicolas and I. Šics, "Design of monochromatic and white beam fluorescence screen monitors for XAIRA beamline at the Alba Synchrotron", in *Proc. MEDSI'20*, Chicago, USA, Jul. 2021, pp. 249-251. doi:10.18429/JACoW-MEDSI2020-WEPA11

[5] D. S. Morton, D. Cocco, N. M. Kelez, V. N. Srinivasan, P. M. Stefan and L. Zhang, "Design of a multipurpose mirror system for LCLS-2 photon transport studies (Conference Presentation)", in *Proc. SPIE 9965, Adaptive X-Ray Optics IV*, 996506, Nov. 2016. doi:10.1117/12.2238784

[6] M. Quispe *et al.*, "Design and fluid dynamics study of a recoverable helium sample environment system for optimal data quality in the new microfocus MX beamline at the Alba Synchrotron Light Source", presented at MEDSI'23, Beijing, China, Nov. 2023, paper WEPPP035, this conference.

ISBN: 978-3-95450-250-9 ISSN: 2673-5520 doi:10.18429/JACoW-MEDSI2023-TUOAM05

THERMAL-DEFORMATION-BASED X-RAY ACTIVE OPTICS DEVELOPMENT IN IHEP*

Dezhi Diao[1], Han Dong[1], Jun Han[1], Shaofeng Wang, Fugui Yang†[1], Ming Li[1], Weifan Sheng[1], Xiaowei Zhang, Institute of High Energy Physics, Beijing, China
Le Kang, Spallation Neutron Source Science Center, Dongguan, China
[1]also at University of Chinese Academy of Sciences, Beijing, China

Abstract

Active optics is a key technology for maintaining wavefront preservation during X-ray beam transport in fourth-generation light sources. In this paper, we propose a concept for surface thermal-driven active optics. In this scheme, the overlap between the position of driving source and the x-ray footprint can give strong modulation performance, including spatial resolution and modulation efficiency. Finite element analysis has experimentally verified the high modulation performance of this approach. To give the feedback of the modulation, we have established a vacuum in-situ surface profile measurement system. Preliminary experiments show that the measurement accuracy of the system's flat mirror can reach 80 nrad rms. The development of these technologies will provide new, low-cost solutions for fully exploiting the performance of fourth-generation light sources.

INTRODUCTION

The High Energy Photon Source (HEPS) currently under construction will be China's first fourth-generation X-ray light source with high energy and high brightness. Like other similar facilities, the quality of various optical instruments and equipment on the beamline seriously affects the X-ray beam transport performance of the beamline. On the one hand, it is important to choose high-quality optical components, such as ultra-precision X-ray mirrors and crystals. On the other hand, it is also necessary to consider the deformation errors of optical optics caused by clamping and thermal loads in the working environment. To solve these problems, the synchrotron radiation field has developed various active optics technologies over the past few decades, including bimorph mirrors [1, 2], bent mirrors [3, 4], phase plates [5-7], and REAL [8, 9] technology. To reduce the engineering risk of HEPS and the difficulties of budgeting, we propose and study a low-cost, low-technical-difficulty active optics technology scheme. By integrating the mirror surface with the driving element, the overlap between the footprint of x-ray beam and the driving modulation unit can be achieved, which is also conducive to improving the spatial frequency and driving efficiency of modulation. In conjunction with the surface shape modulation device, high-precision surface shape detection equipment is an important link in achieving feedback adjustment. To achieve in-situ measurement, extensive research has been done on various light sources, including measurement schemes using interferometers [10, 11] and long trace profilers [12-15]. However, due to the influence of scanning window errors, the measurement error of the system is relatively large. In this project, we have developed a vacuum-based surface profiler metrology system. Finally, a closed-loop active optics modulation system is formed.

DEFORMABLE MIRROR AND PERFORMANCE ANALYSIS

Surface Modulation Scheme

Thermal deformation has always been one of the challenges faced by synchrotron radiation beamlines. Studies have shown that thermal deformation can be effectively suppressed through various means, including notch structure design, advanced cooling schemes, and balanced design of cooling and heating areas. These methods have been developed to ensure that the optical instruments and equipment on the beamline maintain their shape and performance under heating load conditions.

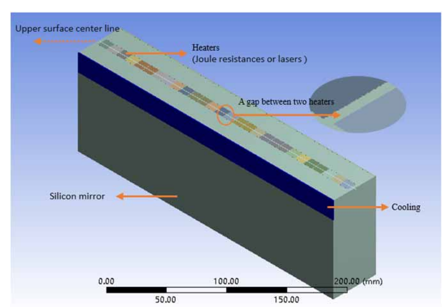

Figure 1: Multi-units surface heating-based shape modulation model.

In response to the demand for high spatial frequency modulation [16], a thermal-driven active optics mirror based on thermal deformation effects has been proposed, as shown in Fig. 1. The typical feature of this system is the overlap between the X-ray footprint and the heating driving area. Unlike traditional schemes, the fact that the position of the driving source is so close to the light-use area means that the transmission path is shorter, which is conducive to high spatial resolution. Each unit in the system is individually current-controlled, and the substrate material can be chosen as single crystal silicon, quartz, metal, etc., depending on the monochromatic and white light

*Work supported by National Natural Science Foundation of China
†yangfg@ihep.ac.cn

ISBN: 978-3-95450-250-9 ISSN: 2673-5520 doi:10.18429/JACoW-MEDSI2023-TUOAM05

conditions. The former has good thermal conductivity and can work under thermal load conditions. Quartz has a relatively high thermal expansion coefficient and can produce significant deformation under relatively low power drive in monochromatic light, reducing the demand for heat dissipation. The metal substrate is also attractive and suitable for thermal load conditions and extremely high thermal deformation capabilities. However, the processing technology of the metal substrate, especially the maintenance of roughness, is a major technical challenge. There are two methods for implementing the heating device: (1) forming a heating resistance channel on the substrate through modification or coating, and (2) laser irradiation of the mirror surface, which is absorbed and converted into heat. Both of these technologies have relatively mature processes. The size of the modulation unit is basically not limited by the process and can reach the millimetres level. The specific size depends on the performance requirements of the spatial resolution and the cost control of the entire system.

It is important to note that correcting the overall surface shape may not always be efficient. From the perspective of the entire beamline, high-order errors can be eliminated using thermal deformation mirrors, and the overall spherical curvature can be fine-tuned and compensated using pressure bending devices or tilted mirrors, as shown in Fig. 2.

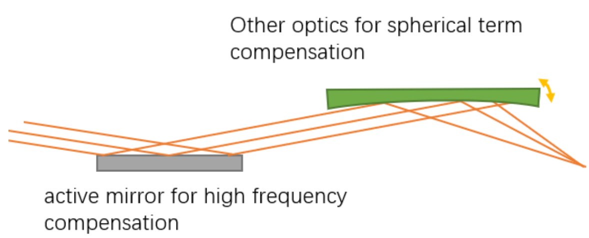

Figure 2: Beamline compensation strategy by combining with other optics devices.

Modulation Performance and Analysis

Due to the difficulty of solving thermal deformation using traditional analytical methods, we use the widely used finite element method (FEA) to simulate the thermal deformation of the mirror to verify the performance of the entire system, as shown in Fig. 1. In FEA, the thermal-structural coupling simulation scheme is designed as follows: the geometry dimension of mirror is 300 mm (L)*50 mm (W)*100 mm (H), single crystal silicon as substrate of the mirror. In the steady-state heat transfer module, the initial temperature of the mirror is 22 ℃. As shown in Fig. 3(a), assuming that the cooling surfaces on both sides of the mirror are ideal and maintained at a constant temperature of 20 ℃, a 10 mm × 10 mm area on the mirror's reflective surface is taken as a driving unit, with a gap of 0.5 mm between the units covering the entire mirror length. The constraint conditions in the steady-state structural module only suppress the rigid motion of the mirror, simulating the process of its free thermal expansion.

Considering the linear superposition characteristics of thermal deformation [17] and referring to the resolution analysis of optical imaging systems, we can use the single-point thermal deformation curve to characterize the spatial resolution of the system. Figure 3 shows the thermal deformation response curve of a single unit. To highlight the efficiency of surface excitation, the simulation results of lateral thermal excitation are also given, with the same unit size. The results show that the modulation half-width is increased by a factor of 5. At the same time, to achieve the same thermal deformation, the surface excitation method can reduce the power demand by a factor of 9.

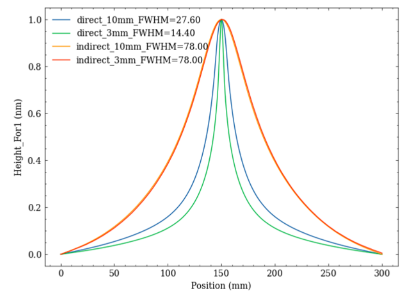

Figure 3: Deformation response for single driving unit.

Furthermore, we conducted simulation experiments to study the surface shape modulation performance of the deformation mirror. With 28 units covering the entire mirror length under the condition of equal thermal power loading, the response functions obtained for each unit are shown in Fig. 4(a). Taking the blue line shown in Fig. 4(b) as an example, the target function of surface shape modulation is a sine function with a period of 100 mm and an amplitude of 5 nm. The green line represents the surface shape obtained by least-squares optimization based on the theory of thermal deformation superposition effects, as well as the corresponding thermal power of each unit is calculated. By directly loading the corresponding thermal power in FEA, the mirror temperature field obtained is shown in Fig. 4(c), with a maximum/minimum value within a range of 1 degree Celsius. Within this temperature range, the thermal expansion coefficient of single crystal silicon is basically maintained at 2.46×10-6 C-1. The deformation result of the central line is shown as the red line in Fig. 4(b). It can be seen that the theoretical modulation residual curve is basically consistent with the residual curve obtained from finite element simulation (0.03 nm rms), which indicates that thermal deformation is a linear response under certain material properties. In the subsequent analysis and calculation, the theoretical value can be directly used for actual surface shape modulation.

ISBN: 978-3-95450-250-9 ISSN: 2673-5520 doi:10.18429/JACoW-MEDSI2023-TUOAM05

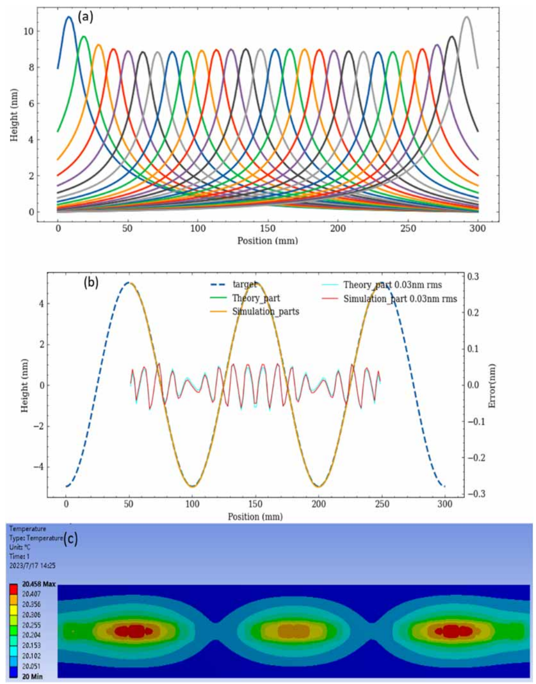

Figure 4: The response functions when each unit is loaded with 1 W heating power (a). Theoretical calculation results and their residuals for a spatial period of 100 mm target function Finite element simulation results and their residuals (b). Temperature distribution on the reflective mirror surface (c).

Compensation for Real Mirrors

Low- and medium- frequency errors are the challenges in mirror manufacturing. The use of active optical devices to compensate for these errors can significantly reduce the precision requirements and costs of the process. To verify the system's ability to correct various real surface shape errors, we calculated the correction for the mirrors in DABAM (Database for the Analysis of metrology of Beamline Mirrors) surface shape database. The response of each unit calculated in the previous section is used for modulating and compensating for these errors. For example, in Fig. 5, the surface shape modulation of a 200 mm length of one of the mirrors is performed, and its negative height value is taken as the modulation target function (blue dashed line). As can be seen, through this surface modulation method, theoretically, a relatively rough reflection mirror (26.51 nm rms, 86.21 nm pv) can be corrected to a surface with low residual error (0.23 nm rms, 1.23 nm pv), where the rms and pv values are reduced to 0.87% and 1.4% of the original values, respectively. The compensation results of the 28 mirrors in the database are shown in Fig. 6, which provides the compensation residuals and the required driving capabilities. The surface compensation accuracy can generally reach the sub-nanometer level, and the driving power depends on the choice of substrate material. Single crystal silicon requires higher power due to its low thermal expansion coefficient. From the perspective of the beamline, materials with a large thermal expansion coefficient can be chosen as the base of the active deformation mirror.

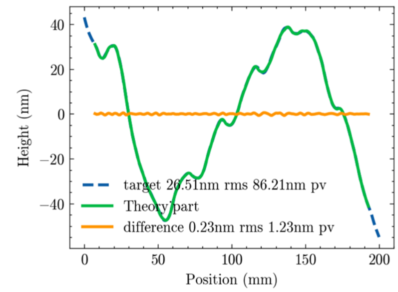

Figure 5: Shape compensation by the deformable mirror for No. 16 mirror in DABAM.

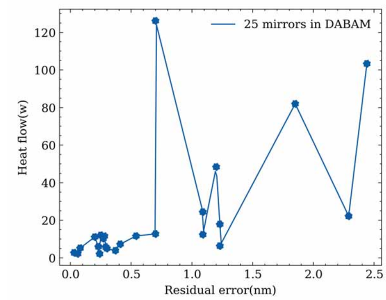

Figure 6: Power consumption in shape compensation by the deformable mirror for mirrors in DABAM.

VACUUM IN-SITU SURFACE PROFILE

Over the past two to three decades, various detection technologies have been developed, including long-range profilometers [18, 19], Hartmann screen lattice measurement methods [20] and stitching interferometers. To achieve surface shape detection of thermal load mirrors such as white light mirrors in a vacuum environment, measurement schemes based on long-range profilometers are the mainstream direction. In this project, a scanning pentaprism-based long-trace profiler (pp-LTP) was established.

The surface shape scanning device mainly includes a high-precision angle measurement device - optical head, pentaprism, and a low-motion error scanning device. When the collimated beam scanning the mirror, the slope of a certain point on the SUT surface is θ, the reflected light beam through this point will produce a 2θ angle change and will be detected by the optical head. To reduce the impact of the vacuum window, the optical head is placed outside the cavity, and the guide rail and pentaprism are inside the vacuum cavity. The maximum scanning length of the entire system is 500 mm.

The results of the angle calibration measurement of the optical head are shown in Fig. 7. By conducting a rotation test with a commercial autocollimator, within a range of 40 μrad, the angular measurement error is below 100 nrad, and the root mean square (rms) is below 10 nrad. In order to assess the practical measurement performance of PP-LTP, we conducted surface profile measurements on the same standard flat mirror using both PP-LTP and a clean-room-based FSP (Flag-type Surface Profiler). The comparative test is presented in Fig. 8. The blue curve represents the measurement results obtained with the FSP in the cleanroom, while the black curve represents the results obtained with the PP-LTP. After correcting for linear errors, the two instruments exhibited a similar trend in the change of their measured slopes. The root mean square (RMS) measurement error of the difference was 87 nrad rms.

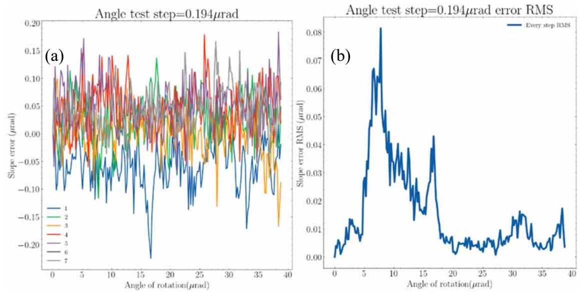

Figure 7: Performance of the optical head within 40 µrad.

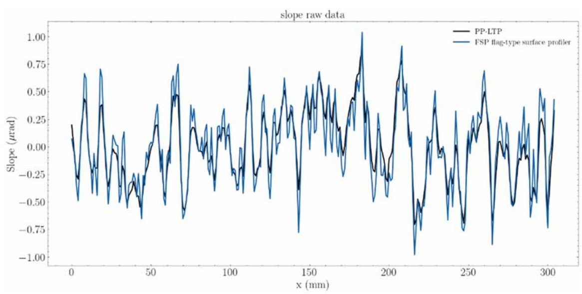

Figure 8: Performance of PP-LTP.

CONCLUSION

This paper reports on the development of a thermally-driven active optics mirror system. Analysis of the mirror's characteristics shows that surface heating-based modulation has the advantages of high spatial resolution, high precision, and high efficiency. Finite element analysis results show that using a high thermal expansion coefficient substrate can achieve high-precision deformation compensation at lower power, especially in the case of monochromatic light, which can alleviate the challenges of high-precision mirror fabrication. In terms of engineering, a vacuum in-situ surface shape detection device has been established, and comparison tests with FSP show that the measurement accuracy of the system can reach sub-100 nrad. To improve the measurement accuracy of the entire system, we plan to integrate the optical head into the vacuum chamber to eliminate the influence of window errors. Additionally, we plan to fabricate high-precision windows, considering the small size and low engineering difficulty of the pp-LTP scheme.

ACKNOWLEDGEMENTS

We appreciate the helpful discussions and helps from Dr. Hongxin Luo and Dr. Xiaohao Dong (Shanghai Synchrotron Radiation Facility, SSRF) during the commission of the metrology system.

REFERENCES

[1] L.E. Berman and J. Arthur, Eds., *Optics for high-brightness synchrotron radiation beamlines II"*, in *Proc. SPIE*, vol. 2856, 1996.

[2] H. Nakamori, S. Matsuyama, S. Imai, *et al.*, "Experimental and simulation study of undesirable short-period deformation in piezoelectric deformable x-ray mirrors", *Rev. Sci. Instrum.*, vol. 83, no. 5, p. 053701, 2012.

[3] J. Nicolas, C. Colldelram, C. Ruget, *et al.*, "Nanometer figure correction of x-ray mirrors using multiple spring actuators", in *Proc. SPIE,* vol. 9965, 2016. doi:10.1117/12.2239533

[4] I.T. Nistea, S.G. Alcock, P. Kristiansen, *et al.* "Long, elliptically bent, active X-ray mirrors with slope errors <200 nrad", *J. Synchrotron Rad.,* vol. 24, no. 3, pp. 615-621, 2017. doi:10.1107/S1600577517005422

[5] F. Seiboth, A. Schropp, M. Scholz, *et al.* "Perfect X-ray focusing via fitting corrective glasses to aberrated optics", *Nat. Commun.*, vol. 8, p. 14623, 2017. doi:10.1038/ncomms14623

[6] D. Laundy *et al.*, "Using refractive optics to broaden the focus of an X-ray mirror", *J. Synchrotron Rad.*, vol. 24, no. 4, pp. 744-749, 2017. doi:10.1107/S1600577517006038

[7] D. Laundy, V. Dhamgaye, T. Moxham, and K. Sawhney, "Adaptable refractive correctors for x-ray optics", *Optica,* vol. 6, no. 12, pp. 1484-1490, 2019. doi:10.1364/optica.6.001484

[8] L. Zhang, R. Barrett, K. Friedrich, *et al.* "Thermal distortion minimization by geometry optimization for water-cooled white beam mirror or multilayer optics", *J. Phys. Conference Series*, vol. 425, no. 5, p. 052029, 2013. doi:10.1088/1742-6596/425/5/052029

[9] C. Cocco, C. Hardin, D. Morton, *et al.* "Adaptive shape control of wavefront-preserving X-ray mirrors with active cooling and heating", *Opt. Express*, vol. 28, no. 13, pp. 19242-19254, 2020. doi:10.1364/OE.394310

[10] Y. Kayser, S. Rutishauser, *et al.*, "Wavefront metrology measurements at SACLA by means of X-ray grating interferometry", *Opt. Express*, vol. 22, no. 8, pp. 9004-9015, 2014.

[11] Y. Kayser, C. David, *et al.*, "X-ray grating interferometer for in situ and at-wavelength wavefront metrology*", J. Synchrotron Rad.*, vol. 2, no.1, pp. 150-162, 2017. doi:10.1107/S1600577516017562

[12] S. Qian *et al.*, "Advantages of in-situ LTP distortion profile test on high heat load mirrors and applications", in *Proc SPIE*, p. 2856, 1996. doi:10.1117/12.259870

[13] S. Qian *et al.*, "Precise measuring method for detecting the in situ distortion profile of a high-heat-load mirror for synchrotron radiation by use of a pentaprism long trace profiler", *Appl. Opt.,* vol. 36, no. 16, pp. 3769-75, 1997. doi:10.1364/ao.36.003769

[14] P.Z. Takacs *et al.* "Mirror distortion measurements with an in-situ LTP", in *Proc. SPIE,* San Diego, CA, USA, vol. 3447, 1998. doi:10.1117/12.33112

[15] S.W. Lin *et al,*. "Development of a long trace profiler in situ at National Synchrotron Radiation Research Center", *Rev. Sci. Instrum.*, vol. 90, no. 2, p. 021716, 2019. doi:10.1063/1.5055634

ISBN: 978-3-95450-250-9 ISSN: 2673-5520 doi:10.18429/JACoW-MEDSI2023-TUOAM05

[16] W. Hu, X. Cui, M. Li, W. Sheng, W. Zhang, Q. Jia, and F. Yang, "Study on the X-ray mirror quality specification in advanced light source", *Front. Phys.,* vol. 10, p. 915182, 2022. doi:10.3389/fphy.2022.915182

[17] F. Yang, M. Li, L. Gao, *et al.* "Laser-heating-based active optics for synchrotron radiation applications", *Opt. Lett.,* vol. 41, no. 12, pp. 2815-2818, 2016. doi:10.1364/ol.41.002815

[18] R.D. Geckele, "Error minimization in high-accuracy scanning deflectometry", in *Proc. SPIE*, vol. 6293, pp: 197-208, 2006. doi:10.1117/12.679339

[19] D. Ma, J. Sun, *et al*. "Investigation on testing the surface shape difference of high-precision large-aperture plane mirrors using the method of angle difference" *J. OAPE*, 2005 (z1): 121-126. doi:10.3321/j.issn:1004-924X.2005.z1.025.

[20] T. Mistsuhashi, "Measurement of Wavefront Distortion Caused by Thermal Deformation of Sr Extraction Mirror Based on Hartmann Screen Test and its Application for Calibration of SRI interferometer", in *Proc. APAC'01*, Beijing, China, Sep. 2001, paper TUP042, pp. 704-706.

ISBN: 978-3-95450-250-9 ISSN: 2673-5520 doi:10.18429/JACoW-MEDSI2023-TUOBM01

ForMAX: A BEAMLINE FOR MULTI-SCALE AND MULTI-MODAL STRUCTURAL CHARACTERISATION OF HIERARCHICAL MATERIALS

J. B. González*, V. Haghighat, S. A. McDonald, K. Nygård, L. Roslund
MAX IV Laboratory, Lund, Sweden

Abstract

ForMAX is an advanced beamline at MAX IV Laboratory, enabling multi-scale structural characterisation of hierarchical materials from nm to mm length scales with high temporal resolution. It combines full-field microtomography with small- and wide-angle x-ray scattering (SWAXS) techniques, operating at 8-25 keV and providing a variable beam size. The beamline supports SWAXS, scanning SWAXS imaging, absorption contrast tomography, propagation-based phase contrast tomography, and fast tomography. The experimental station is a versatile in-house design, tailored for various sample environments, allowing seamless integration of multiple techniques in the same experiment. The end station features a nine-meter-long evacuated flight tube with a motorized small-angle x-ray scattering (SAXS) detector trolley. Additionally, a granite gantry enables independent movement of the tomography microscope and custom-designed wide-angle x-ray (WAXS) detector. These features facilitate efficient switching and sequential combination of techniques. With commissioning completed in 2022, ForMAX End Station has demonstrated excellent performance and reliability in numerous high-quality experiments.

INTRODUCTION

Both natural and man-made materials often possess a hierarchical nature, with distinct structures evident across various length scales. Understanding the relationship between structure and function in these materials necessitates characterizing the structure across these scales, coupled with sufficient temporal resolution to observe in-situ processes. The ForMAX instrument efficiently addresses this challenge by combining two complementary techniques: full-field tomographic imaging covering µm to mm scales and SWAXS targeting nm scales.

The primary technical obstacle in integrating full-field tomography with SAXS arises from spatial limitations behind the sample. In full-field tomography, one observes the x-ray beam transmitted through the sample in a forward direction. In contrast, SAXS captures the x-ray beam scattered at small angles, $\leq 3^{\circ}$, essentially in a near-forward direction. At ForMAX, the innovative strategy is to conduct sequential tomography and SWAXS experiments. This is facilitated by a motorized detector gantry, enabling swift translation of the tomography microscope (and the WAXS detector) into and out of the x-ray beam. This design promotes a rapid and efficient transition between experimental modes.

* joaquin.gonzalez@maxiv.lu.se

In the following conference paper, we provide an in-depth overview of the ForMAX beamline's design. Table 1 list the main components of the beamline and their distance from source.

Table 1: Main ForMAX Components and Their Distance From Source

ForMAX Components	Distance from source (m)
Undulator	0
Front end movable mask	19.5
White-beam slits	23.9
Double multilayer monochromator	25.0
Double crystal monochromator	27.0
Vertically focusing mirror	30.2
Horizontally focusing mirror	31.0
Monochromatic slits	28.1, 32.3, 36.3, 41.5 - 41.8
Diamond window	35.8
Attenuator system	35.9
Fast shutter	36.1
X-ray prism lens	36.6
Compound refractive lenses	40.5
Experimental table	42.0
Full-field microscope	42.0 – 42.3
WAXS detector	42.1
SAXS detector	42.9-49.5

Throughout this article, we adhere to MAX IV's coordinate system: the lateral x-axis (outboard direction from the ring), the vertical y-axis (upward direction), and the longitudinal z-axis (downstream direction from the source). The direction of each rotation around the Cartesian axes (Rx, Ry, and Rz) adheres to the right-hand rule.

OPTICS

The primary optics of ForMAX comprises a double crystal monochromator (FMB Oxford), a double multilayer monochromator (Axilon), dynamically bendable vertical and horizontal focusing mirrors in Kirkpatrick-Baez (KB) geometry (IRELEC), a photon shutter (Axilon), and four diagnostic modules (FMB Oxford). These modules contain a fixed mask, a high-band-pass diamond filter for heat-load management, a white-beam stop, bremsstrahlung collimators, slits, beam viewers, and beam intensity monitors. This section explores the monochromators and mirrors. For an overview of the main components, see Fig. 1.

ISBN: 978-3-95450-250-9 ISSN: 2673-5520 doi:10.18429/JACoW-MEDSI2023-TUOBM01

ForMAX can operate using either a double crystal monochromator (DCM) or a double multilayer monochromator (MLM) based on experimental requirements.

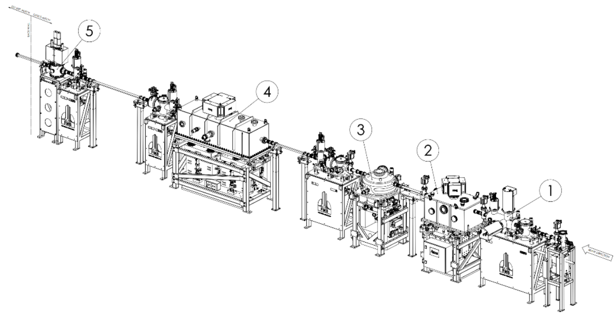

Figure 1: Main components of the optics: (1) white-beam slits, (2) MLM, (3) DCM, (4) mirrors, and (5) photon shutter.

The Si (111) DCM, which deflects horizontally, is situated 27 m from the source. Its compact and rigid design, assisted by a minor horizontal offset between the crystals, ensures superior stability [1]. The upstream crystal is anchored directly onto the Bragg goniometer (Ry) without additional motorized axes. However, the second crystal possesses motorized adjustments for pitch (Ry), roll (Rz), and perpendicular motion. The monochromator also features motorized lateral (x) and vertical (y) translations. Both crystals employ side cooling, achieved by clamping them to liquid-nitrogen-cooled Cu blocks.

The horizontally deflecting MLM is positioned 25 m from the source. Primarily intended for full-field imaging experiments demanding high temporal resolution, it may also be employed in select, photon-intensive scattering experiments. The multilayer mirrors on both units use flat Si (100) substrates, overlaid with 200 layers of W/B4C and 250 layers of Ru/B4C stripes. The monochromator's Bragg rotation (Ry), the upstream mirror's fine roll (Rz), and the downstream mirror's fine pitch (Ry) are all facilitated by linear actuators and unique flexure setups. Given the monochromator's extensive angular range, a longitudinal (z) translation of the downstream multilayer assembly is essential. Additional motorized motions incorporate the monochromator's lateral (x) and vertical (y) translations, as well as the perpendicular movement of the downstream multilayer assembly. Multilayer mirrors are adequately cooled using braids from water-cooled Galinstan baths.

The mirror system houses vertically (VFM) and horizontally (HFM) focusing mirrors in KB geometry within a singular vacuum chamber. Each operates at a consistent incidence angle of 3 mrad. These mirrors serve dual functions: providing harmonic rejection and focusing capabilities. To accommodate the beamline's broad energy range, each mirror possesses distinct stripes of Si, Rh, and Pt. Furthermore, each mirror can be adjusted to bend between approximately 5 and 100 km, enabling versatile focusing, collimation, or non-focusing operations. Each mirror is equipped with a few stiff, motorized axes, including lateral (x) and vertical (y) translation stages. Additionally, pitch rotation (Rx for VFM, Ry for HFM) employs a precision actuator and flexure components. The HFM further incorporates a motorized roll rotation (Rx) using a similar high-resolution actuator and flexure components.

EXPERIMENTAL STATION

As illustrated in Fig. 2, the primary components of the experimental station include two beam conditioning units (BCUs), an experimental table, a detector gantry, and a SAXS flight tube, all of which have been custom-designed at MAX IV [2]. Given the distinct—and at times conflicting—technical prerequisites of SWAXS and full-field tomography, we placed significant emphasis on seamlessly integrating these components into a singular instrument. The modular design of the experimental station, further detailed below, necessitated the integration of a dedicated PLC system to guarantee safe operation.

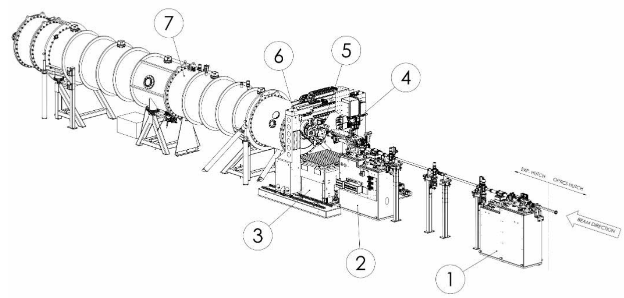

Figure 2: Main components of the experimental station: (1) BCU I, (2) BCU II, (3) experimental table, (4) tomography microscope, (5) WAXS detector, (6) detector gantry, and (7) flight tube.

Beam Conditioning Units

The experimental station features two beam conditioning units, BCU I and BCU II, positioned upstream of the experimental table. They adjust beam characteristics like size, microfocus, and attenuation based on the experiment.

BCU I, located 5 meters upstream of the sample table, has a diamond vacuum window, attenuator system, fast shutter, and slits. An upcoming addition is a motorized overfocusing x-ray prism lens for beam expansion during tomography.

BCU II, directly before the sample table, houses polymeric compound refractive lenses (CRLs) for SWAXS microfocusing, a beam diagnostic module with three intensity monitors, a YAG crystal screen, and slits. A telescopic vacuum tube minimizes the x-ray beam's air path.

Experimental Table

Located 42 meters from the source, the experimental table serves as a platform for equipment essential to SWAXS and tomography studies. With its 800 x 800 mm surface, it allows for adjustments in vertical (±105 mm), lateral (±100 mm), and pitch (±10 mrad) orientations of the sample environment. Its design, mirroring the “skin” concept from ALBA Synchrotron, ensures both stability and high-resolution performance [3].

Constructed with a granite base secured to the floor, the table features two movable lateral plates attached to the

ISBN: 978-3-95450-250-9 ISSN: 2673-5520 doi:10.18429/JACoW-MEDSI2023-TUOBM01

base. These plates, driven by ball screws and stepper motors, support a top plate connected by flexure hinges. An added lateral motion stage is positioned atop this structure. The table's carrying capacity is 200 kg.

Detector Gantry

Positioned 42 meters from the source, the granite detector gantry surrounds the sample location. Both the tomography microscope (Optique Peter) and the WAXS detector (X-Spectrum Lambda 3M), tailored specifically for the ForMAX beamline though commercially available, will be secured to the gantry. Two distinct linear stages, set on the gantry lintel, facilitate the lateral movement (≈670 mm) of both the microscope and detector, enabling them to easily enter or exit the beam's path. Additionally, two separate vertical stages allow for the vertical adjustment of both the microscope and the detector (±22.5 mm and ±7 mm, respectively). Each stage is constructed with ball screws and linear guides, driven by stepper motors. The entire assembly is mounted on motorized rails on the floor.

The motorized floor rails, extending from 41 to 42.5 meters from the source, enable phase-contrast imaging and accommodate large sample setups on the experimental table. The two lateral stages allow users to quickly switch between multiple techniques in a single experiment. Additionally, the design grants clear access to the sample table from the end-station's side.

Vibrations at the microscope's tip were measured using an LDV vibrometer, confirming rms amplitudes of less than 20 nm in both lateral and longitudinal directions [4].

Flight Tube

The flight tube links the sample to the SAXS detector (Dectris EIGER2 X 4M) and minimizes scattering and beam absorption. It's an eight-meter-long, one-meter-diameter stationary vacuum chamber divided into five sections. The SAXS detector is housed inside [5], on motorized rails, allowing for sample-to-detector distance adjustments between approximately 800 and 7600 mm.

The rail system, powered by an external servo motor, uses a belt drive. A girder, mechanically isolated from the vacuum chamber by bellows, supports the setup, ensuring stability from potential chamber vibrations during pumping. The SAXS detector has vertical and lateral adjustments, and a tungsten central beamstop with a GaAs diode is attached to its trolley, monitoring the x-ray beam's flux.

Safety measures include the MAX IV Personal Safety Systems, a rigorous search procedure, and emergency pull-wire switches to ensure no unintended personnel remain inside during operations.

Sample Manipulation

Given the diverse experimental techniques offered by ForMAX, each possessing unique sample manipulation requirements, ForMAX incorporates three distinct stage stacks for sample manipulation.

For standard SWAXS experiments, a high-load five-axis assembly (Huber). It comprises motorized pitch Rx (±13°), roll Rz (±12°), lateral x (±25 mm), longitudinal z (±25 mm), and vertical y (±20 mm) axes.

For scanning SWAXS, another assembly (Huber) is used. Its base has motorized lateral x (±25 mm), vertical y (variable ±10 or ±45 mm), and longitudinal z (±25 mm) axes. A yaw Ry axis and a wide-range pitch axis Rx (±45°) enable SWAXS tomographic imaging. A manual goniometer head assists in the precise alignment of the sample.

For tomography experiments, a five-axis assembly (Lab Motion) is employed. From the bottom up, this assembly consists of a motorized longitudinal z axis (with approximately 380 mm range) suitable for propagation-based phase-contrast imaging, a vertical y axis (±20 mm) designed for helical imaging, a tomographic yaw axis Ry paired with a rotary union that accommodates a fluid and an electrical slip ring, and horizontal xz axes (±5 mm each) for precise sample alignment. This electrical slip ring also features nine spare wires, allowing the integration of sample environments. The assembly's modular nature often leads to its operation without the vertical axis and the rotary union.

EXPERIMENTAL MODES

The versatile motions of the detector gantry facilitate a diverse range of experimental configurations. The design allows for the independent movement of the WAXS detector and the full-field microscope, providing a variety of experimental modes.

SAXS

In the SAXS setup (see Fig. 3), both the WAXS detector and the full-field microscope are moved out of the x-ray beam's path. An evacuated nose cone is also attached to the flight tube, reducing the air path downstream of the sample.

Figure 3: SAXS setup of the endstation.

SWAXS

For the SWAXS setup (as shown in Fig. 4), the x-ray beam is directed at the WAXS detector. Meanwhile, the SAXS signal (along with the unscattered beam) travels through the WAXS detector's central hole, eventually reaching the SAXS detector (and the central beam stop). During this mode, the full-field microscope is translated out of the x-ray beam's pathway.

Figure 4: SWAXS setup of the end station.

Full-Field Tomography

In this mode, the WAXS detector is moved out of the x-ray beam's trajectory (see Fig. 5). As a safety precaution, a gate valve at the entrance of the flight tube is closed, ensuring that the SAXS detector isn't exposed to x-rays.

Figure 5: Full-field tomography setup of the endstation.

Sequential SWAXS and Full-Field Tomography

For the combined SWAXS and full-field tomography setup, both the SAXS and WAXS detectors are aligned with the x-ray beam. The full-field microscope is then vertically moved in and out of the x-ray beam path for either full-field imaging or scattering modes, respectively (as depicted in Fig. 6). This vertical repositioning of the microscope takes no more than 15 seconds.

Figure 6: Sequential SWAXS and full-field tomography setup of the endstation.

Others

The spatial design of the ForMAX endstation, particularly in the areas surrounding the sample table and between the BCUs, can accommodate temporary configurations for unique experimental techniques. This includes niche methods like Ultra-fast Full-field Tomography and Multi-projection Imaging [6] among others.

Additionally, the beamline will provide dedicated sample environments, facilitating multiscale structural characterisation during complex rheological or mechanical tests, all under precisely controlled temperature and humidity conditions.

CONCLUSIONS

We have introduced the ForMAX beamline, highlighting its innovative design for multi-scale structural characterisation by combining full-field tomography and SWAXS. The adaptability of the experimental table and flight tube designs enables state-of-the-art SWAXS experiments across a variety of sample environments. The detector gantry's design supports multiple experimental modes, ranging from conventional SAXS to SWAXS and full-field tomography. The integration of full-field tomography and SWAXS experiments within the same experiment is facilitated by swift and fast transitions between setups. After completing its commissioning in 2022, the ForMAX End Station commenced regular user operations in 2023, consistently demonstrating outstanding performance and reliability in numerous high-quality experiments.

ACKNOWLEDGEMENTS

The construction of the ForMAX beamline was funded by the Knut and Alice Wallenberg Foundation, while its operational costs are supported by industry through Treesearch (www.treesearch.se), a national platform for research on new materials and specialty chemicals derived from forest raw material.

The authors extend their sincere gratitude to the staff at the MAX IV Laboratory for their invaluable support throughout the design, construction, and commissioning phases of the beamline.

REFERENCES

[1] Kristiansen *et al.*, "Vibrational stability of a cryocooled horizontal double-crystal monochromator", *J. Synchrotron Radiat.*, vol. 23, pp. 1076–1081, Sep. 2016. doi:10.1107/S1600577516009243

[2] J.B. González *et al.*, "ForMAX Endstation - a Novel Design Combining Full-Field Tomography with Small- and Wide-Angle X-Ray Scattering", in *Proc. MEDSI'20*, Chicago, IL, USA, Jul. 2021, paper WEPB12, pp. 289-291. doi:10.18429/JACoW-MEDSI2020-WEPB12

[3] C. Colldelram *et al.*, "ALBA XALOC Beamline diffractometer table skin concept", in *Proc. MEDSI'10*, Oxfordshire, UK, Jul. 2010, vol. 1, paper e44. doi:10.1017/S2044820110000754

[4] G. Felcsuti and J.B. González, "Structural Dynamic Testing and Design Evaluation of the Formax Detector Gantry", presented at MEDSI'23, Beijing, China, Nov. 2023, paper THOBM01, this conference.

[5] J. Léonardon *et al.*, "Design of a new detector tube for wide, small and ultra small-angle X-ray scattering", in *Proc. MEDSI'14*, Melbourne, Australia, Oct. 2014.

[6] P. Villanueva-Perez *et al.*, "Hard x-ray multi-projection imaging for single-shot approaches", *Optica*, vol. 5, pp. 1521-1524, Dec. 2018. doi:10.1364/OPTICA.5.001521

ISBN: 978-3-95450-250-9 ISSN: 2673-5520 doi:10.18429/JACoW-MEDSI2023-TUOBM02

SAPOTI - THE NEW CRYOGENIC NANOPROBE FOR THE CARNAÚBA BEAMLINE AT SIRIUS/LNLS

R.R. Geraldes†, F.R. Lena, G.G. Basilio, D.N.A. Cintra, V.B. Falchetto, D. Galante, R.C. Gomes, A.Y. Horita, L.M. Kofukuda, M.B. Machado, Y.A. Marino, E.O. Pereira, C.A. Pérez, P.P.R. Proença, M.H. Siqueira da Silva, A.P.S. Sotero, V.C. Teixeira, H.C.N. Tolentino
Brazilian Synchrotron Light Laboratory (LNLS), Campinas, São Paulo, Brazil

Abstract

SAPOTI will be the second nanoprobe to be installed at the CARNAÚBA (Coherent X-Ray Nanoprobe Beamline) beamline at the 4th-generation light source Sirius at the Brazilian Synchrotron Light Laboratory (LNLS). Working in the energy range from 2.05 to 15 keV, it has been designed for simultaneous multi-analytical X-ray techniques, including absorption, diffraction, spectroscopy, fluorescence and luminescence, and imaging in 2D and 3D. Highly-stable fully-coherent beam with monochromatic flux up to 10^{11} ph/s/100mA-/0.01%BW and size between 35 and 140 nm is expected with an achromatic KB (Kirkpatrick-Baez) focusing optics, whereas a new in-vacuum high-dynamic cryogenic sample stage has been developed aiming at single-nanometer-resolution images via high-performance 2D mapping and tomography. This work reviews and updates the entire high-performance mechatronic design and architecture of the station, as well as the integration results of some of its modules, including automation, thermal management, dynamic performance, and positioning and scanning capabilities. Commissioning at the beamline is expected in early 2024.

INTRODUCTION

Synchrotron scanning X-ray microscopy has been established as a mature technique and a key characterization tool for scientific, technological, and engineering fields, with several beamline X-ray microscopes with beams of nanometric sizes (a.k.a. nanoprobes) being developed during this decade [1-11]. In particular, complementing techniques such as ultra-high-resolution fluorescence, the use of ptychography as a coherent X-ray diffractive imaging technique enables single-digit nanometer level spatial resolution, ultimately limited only by the beam and the sample stability during the exposure time [5, 7, 8, 11-13].

SAPOTI will be the second nanoprobe to be installed at the CARNAÚBA (Coherent X-Ray Nanoprobe Beamline) beamline at the 4th-generation light source Sirius at the Brazilian Synchrotron Light Laboratory (LNLS) [14, 15]. It has been designed for simultaneous multi-modal state-of-the-art X-ray techniques, including absorption, diffraction, spectroscopy, fluorescence and luminescence, and imaging in 2D and 3D. At 142 m from the undulator source and with achromatic optics, full benefit can be taken from the brilliance of the new-generation storage ring to reach diffraction-limited beam sizes, from 140 to 35 nm in the energy range from 2.05 to 15 keV, while optimizing the photon flux up to 10^{11} ph/s/100 mA/0.01%BW at the sample.

As comprehensively described in [15] and depicted in Fig. 1, SAPOTI will be an all-in-vacuum station, with a Kirkpatrick-Baez (KB) set of mirrors and the sample stage sharing the same ultra-high vacuum chamber. This architectural decision was made for stability, metrology and alignment purposes, and for optimization of transmission in the low-energy end. Three photodiodes (PD) for flux and absorption measurements, as well as two silicon drift detectors (SDDs) for fluorescence, are also placed inside the chamber, whereas the area detector (PiMEGA) and a complementary optical arrangement, alternatively used for an optical or a luminescence (X-ray Excited Optical Luminescence – XEOL) microscope, are placed outside vacuum, accessing the sample signals via a large beryllium window and a small glass viewport, respectively. Above the main chamber, a loading chamber comprises a load-lock system for cryogenic sample transfer, a cryogenic parking station (carousel) for sample storage, and a cryogenic pick-and-place gripper mechanism for sample loading. Cryogenic cooling at both the sample stage in main chamber and the parking station in the loading chambers is achieved by means of efficient thermal management using two pulse tube (PT) coolers.

Since the beginning of the project, the main aspect driving its mechatronic architecture has been the extreme sensitivity of the focusing optics and the sample to mechanical stability, once ultimate mapping resolution is one of the key design targets in the station. Firstly, a granite bench following the concepts developed for Sirius systems provides a stand with high mechanical and thermal stability, while allowing for basic positioning of station with respect to the beam in all degrees of freedom (DoFs) [16, 17]. Next, both the KB module and the sample stage are quasi-directly fixed to the granite bench, i.e., stiffly mounted via the bottom flange of the main chamber. Although unusual for beamline in-vacuum systems, and significantly more challenging in terms of manufacturing, assembly and baking, this solution offers unique possibilities regarding dynamics, i.e., suspension frequencies and vibration amplitudes.

† renan.geraldes@lnls.br

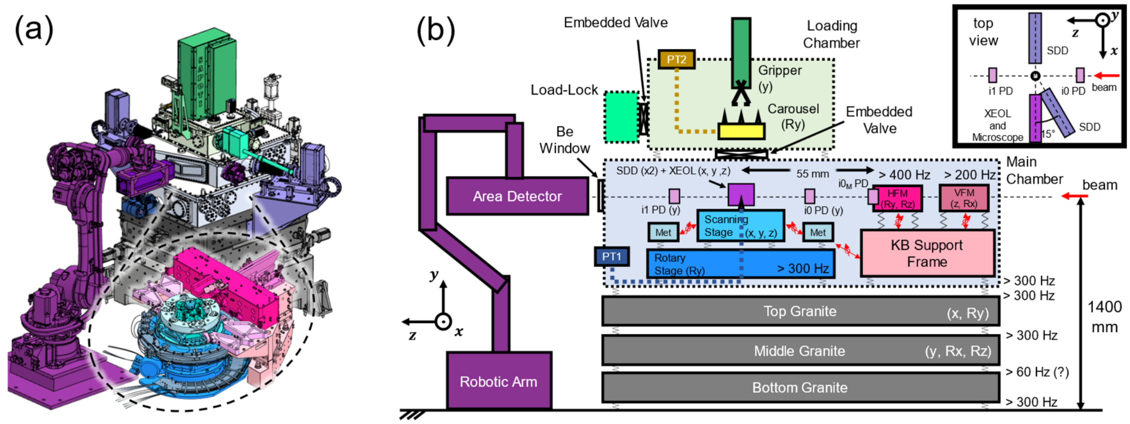

Figure 1: (a) Overview of the SAPOTI station, highlighting a few subsystems: granite bench, chambers, gripper and load-lock, detectors, sample stage and KB module. (b) Schematic overview of the main elements in the station, in color code. Distances, suspension frequencies, motion degrees of freedom and metrology links (red), are indicated for reference.

Indeed, this way these critical modules can benefit from the stiffness and inertia properties of the bench while preventing the use of long feedthrough structures via bellows. The KB design follows the exactly-constrained (isostatic) solution that has been recently developed for Sirius KB mirrors, in which flexural struts are combined with piezo actuators in optimized configurations [18]. The sample stage, in turn, follows a high-dynamic mechatronic concept, according to an isolated mechatronic architecture with high-bandwidth closed-loop control [19]. Using voice-coils actuators, laser interferometer feedback, a reaction mass working as a dynamic filter, and a set of folded-leafsprings acting as a parallel-kinematic arrangement, it allows for a relatively large stroke of 3 mm XYZ, while keeping positioning errors around 1 nm RMS (up to 10 kHz) and reaching scanning speeds up to hundreds of micrometers per second. Below the high-performance scanning stage, a rotary stage allows for tomography over 220º.

The following section is dedicated to the latest updates in design and experimental data (refer also to [15, 19]). Then, conclusions are summarized in the last section.

DESIGN AND INTEGRATION STATUS

Most of the design work for SAPOTI has been concluded. Thus, its modules are either in final manufacturing stage or already under assembly and integration in a cleanroom in the Metrology Building at the LNLS. The following sub-sections highlight the main updates for the system.

Pulse Tube Coolers

Given the low power extraction requirements for sample conditioning, together with their cost and/or operation advantages as compared to either open-circuit cryostats and closed-loop liquid nitrogen cryocoolers, helium gas closed-circuit pulse tube coolers are used as compact stand-alone systems both with the sample stage in the main chamber and the carousel in the loading chamber (see Fig. 1).

A potential issue, however, might be related to mechanical disturbances introduced by the systems compressors. In that sense, the first step was the selection of the low-vibration model LPT9310 by Thales Cryogenics. Relying on a pair of voice-coil actuators and flexural bearings, it provides an anti-vibration operation mode (AVR), in which a feedback loop with an accelerometer can be used to balance the magnitude and phase of the actuators and thus minimize vibrations [20]. A second action point was including in the design a decoupling solution at about 15 Hz for the mounting structure of the compressor, such that forces at higher frequencies can be passively filtered.

Figure 2 shows the mechanical assembly of one of the coolers and a vibration measurement plot. The AVR lowers the acceleration peaks of the first modes, which not only leads to lower amplitudes but also can be more efficiently filtered by the decoupling parallel flexures. One import remark is that the AVR is only effective once the heat pumping capacity is not saturated, i.e., the temperature setpoint of the cold finger can be achieved by the controller.

For the heat extraction needs for SAPOTI around 2 to 2.5 W, and temperatures around 20 to 35 °C in the reservoir and compressor (maintained via water cooling), the measurements resulted in 60 to 70 K as achievable targets. User interfaces and software layers for EPICS have been developed in house, and the units are ready for final integration.

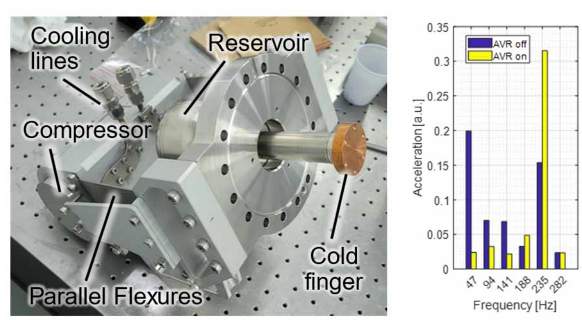

Figure 2: Pulse tube cooler LPT9310 mechanical assembly on a bench. Details drawn to its cold finger, reservoir and compressor, and the proposed mounting structure with decoupling flexures and cooling lines. The plot shows normalized acceleration levels at the multiple harmonics of the system, both with the anti-vibration system on and off.

ISBN: 978-3-95450-250-9 ISSN: 2673-5520 doi:10.18429/JACoW-MEDSI2023-TUOBM02

KB Module

A comprehensive description of the KB module global design and its specifications (with stability requirements as low as 4 nrad) can be found in [15]. Now, having finished its detailed design, the VFM (vertical-focusing mirror) is expected to achieve a motion range of 20 µrad and resolution of 20 nrad in pitch using a PIRest actuator, and a range of 250 µm and resolution of 10 nm in using a piezomike actuator. Modal analyses predict that its first suspension mode will be around 230 Hz, whereas first pitch mode above 650 Hz. As for the HFM (horizontal-focusing mirror), it is expected to achieve a motion range of 50 µrad and resolution of 50 nrad in pitch using a PIRest actuator, and 1.2 mrad of range and 80 nrad of resolution in using a piezomike actuator. Modal analyses predict that its first suspension mode will be around 400 Hz, whereas the first pitch mode above 600 Hz. Figure 3 depicts the structural simulation for these alignment DoFs.

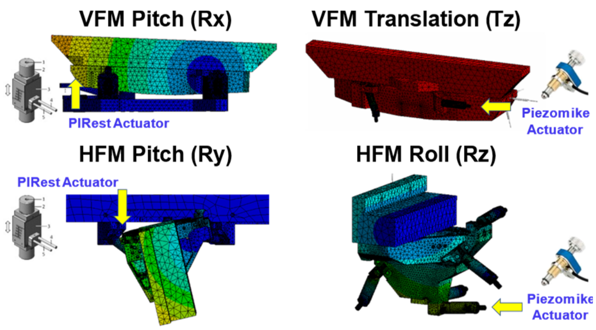

Figure 3: Structural simulations illustrating the fine-alignment degrees of freedom of the KB vertical- and horizontal-focusing mirror (VFM and HFM) mechanisms, designed for high suspension frequencies.

Regarding the main support frame (see Fig. 1), according to final simulations (including the masses of the VFM and HFM) the first suspension frequencies are expected around 300 to 400 Hz, which is sufficiently high for most environmental and operational disturbances, while limited by mass and mounting interface stiffnesses. The module parts are under manufacture and expected to be integrated and experimentally validated in the coming months.

Sample Stage

The design and preliminary results of the high-dynamic cryogenic sample stage developed for SAPOTI have been discussed in detail in [15, 19]. Regarding the reported limitations in thermal management, previously limiting the sample temperatures above 135 K, design upgrades have been proposed and partially validated in parallel setups, suggesting that 95 to 100 K shall be now practically achievable – which is critical for sample preservation against crystalline ice. More information on this, together with validation data, will be provided in a future publication. Here, more attention is dedicated to the updates in motion.

Figure 4 shows the open loop Bode plot of the three XYZ scanning DoFs according to the latest SISO (single-input-single-output) control proposal. As in [19], the characteristics of the system at different working points can be distinguished. And, now, by extending the working range from a sphere of 1.5 mm to 2 mm of radius, larger plant variations can be observed. They result from non-linearities in the system, such as changes in the stiffness of the folded-leaf-springs, in the inertia of short-stroke module and in the gains of the voice-coil actuators (see [19]). Hence, in addition to more or less impactful dynamics variations that must be considered in the controller for each DoF, this translates to bandwidth variations by as much as 100 Hz, between 100 and 300 Hz, for the different DoFs. These aspects can be taken into account by more sophisticated control strategies, but this has not proven necessary thus far, with sufficiently performing and robust operation.

Another instructive fact learned recently is related to the first bandwidth-limiting resonances in *x* and *z*, indicated by the arrows in Fig. 4. In [19], they had been misleadingly credited to limited stiffness in the bend of the folded leaf-springs, as compared to the original model. After some experimental evaluation, however, they proved to be related to previously unmodelled dynamics. In *x*, the root cause has been identified as internal modes in the folded leaf-springs, whereas in *z* it seems that internal dynamics in the flexural cooling core is to blame, which reinforces the importance of and the sensitivity to every design detail in advanced mechatronic systems. These remaining dynamics would require deeper design rework to be solved, which does not seem needed for the moment. Yet, this learning process has increased design awareness for possible future upgrades and future projects.

While its software migration to NI's cRIO final platform is ongoing, the sample stage continues to be operated with a Speedgoat's xPC prototyping platform at 20 kHz (see [19]). In the meantime, some work has been done on high-performance 2D scanning using feedforward control. Figure 5 summarizes a study contemplating 4 raster fly-scan scenarios, all of them taking 50 % overlap for ptychography and 1 kHz detection rate, namely: (i) 20×20 µm^2 out-of-focus (500 µm beam) scan for coarse mapping (maximum speed); (ii) standard 7.5×7.5 µm^2 high-resolution low-energy (120 nm beam) scan; (iii) short-range 1×1 µm^2 low-energy (120 nm beam) scan; and (iv) standard 1.5×1.5 µm^2 high-resolution high-energy (30 nm beam) scan. As an example, the main plot shows the XY reference and the metrology signals for (iv) (in a similar representation to that of [9]). The colors show the sections of each acquisition interval of 1 ms, which are used to the RMS errors statistics of the histogram in the inset. The full 2D map is extracted in only 6.4 s, with a mean RMS error of about 1.25 nm. Hence a full high-resolution tomogram might take less than one hour to be acquired, allowing for high throughput at beamline.

The embedded table outlines the parameters of all trajectories (with the RMS values taken over the full dataset). All scans can be performed within 10 s (with (iii) taking only 0.2 s) with average RMS errors always below 4 nm. The stage is still mounted to an optical table in the metrology room, so that final performances will be reached once the stage is mounted in vacuum and coupled to the bench.

ISBN: 978-3-95450-250-9 ISSN: 2673-5520 doi:10.18429/JACoW-MEDSI2023-TUOBM02

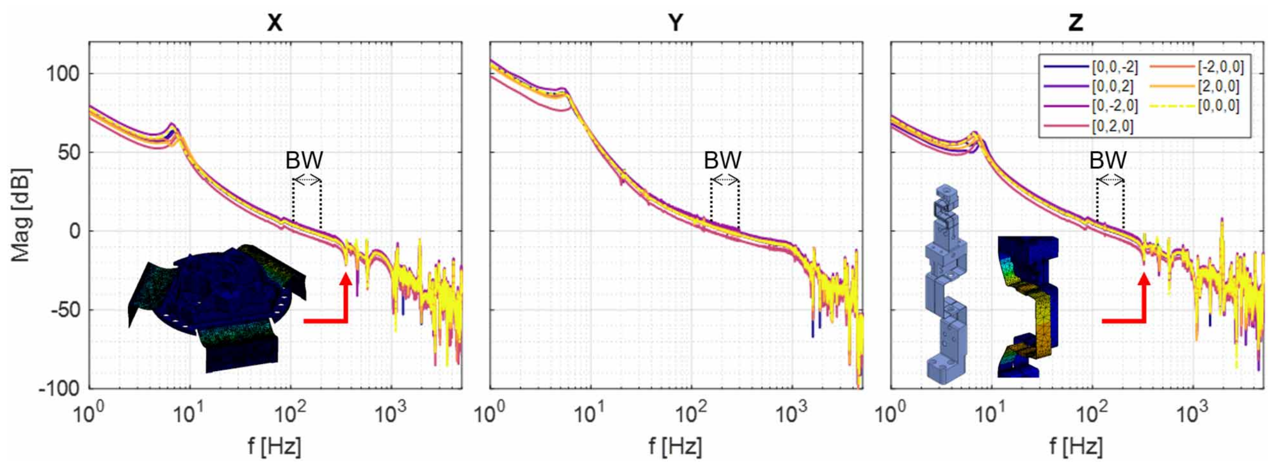

Figure 4: Open loop Bode plot for the *x*, *y* and *z* degrees of freedom of the SAPOTI sample stage for plants measured at an extended working range of ±2 mm in all directions (coordinates shown as [x,y,z]). Modal analysis simulations and experimental tests indicate unpredicted internal modes affecting achievable control bandwidth in *x* and *z*.

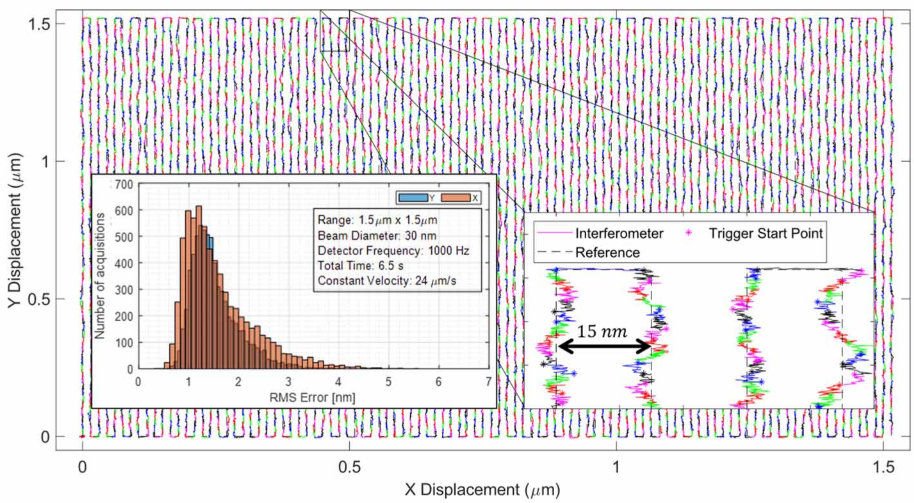

Trajectory	i	ii	iii	iv
Range [μm x μm]	20x20	7.5x7.5	1x1	1.5x1.5
Velocity [μm/s]	260	94	94	23.5
Total Time [s]	7.7	10	0.2	6.4
x_{RMS} [nm]	3.9	2.5	3.1	1.7
y_{RMS} [nm]	3.1	2.4	2.7	1.6
x_{p2p} [nm]	32.5	23.5	19.6	15.3
y_{p2p} [nm]	32.1	20.9	18.2	13.5

Figure 5: Trajectory performance analyses for SAPOTI's sample stage, including coarse mapping and low- and high-energy fly-scan scenarios (see text). The table shows range, velocity and scan time, as well as RMS and peak-to-peak (p2p) position errors. The plot depicts the high-energy high-performance raster scan (iv) with a histogram for statistics.

CONCLUSIONS

This work provides an updated overview and the status of the forthcoming SAPOTI cryogenic nanoprobe at the CARNAÚBA beamline at Sirius/LNLS. As the design work ends, and its modules are integrated, the multi-modal, high-throughput and high-resolution imaging requirements are gradually validated, thanks to a systematic design approach, based on high-performance mechatronics and systems engineering concepts and tools. The main next steps include: the conclusion of the software in cRIO; the definitive validation of the new cooling core with the sample stage; the assembly and validation of the KB module, and its integration with the sample stage in the main chamber; and the assembly, validation and integration of the carousel and gripper modules in the loading chamber. First commissioning experiments are expected in June 2024.

ACKNOWLEDGEMENTS

The authors would like to gratefully acknowledge the funding by the Brazilian Ministry of Science, Technology and Innovation, and the contributions of the LNLS and the MI-Partners teams to the instrument. This work is dedicated to the memory of the late team member and dear friend João Leandro de Brito Neto.

REFERENCES

[1] L. Mino *et al.*, "Materials Characterization by Synchrotron X-ray Microprobes and Nanoprobes", *Rev. Mod. Phys.*, vol. 90, pp. 25–30, 2018. doi:10.1103/revmodphys.90.025007

[2] R. Winarski *et al.*, "A Hard X-ray Nanoprobe Beamline for Nanoscale Microscopy", *J. Synchrotron Radiat.*, vol. 19, pp. 1056–1060, 2012. doi:10.1154/1.2951844

[3] S. Chen *et al.*, "The Bionanoprobe: Hard X-ray Fluorescence Nanoprobe with Cryogenic Capabilities", *J. Synchrotron Radiat.*, vol. 21, pp. 66–75, 2014. doi:10.1107/s1600577513029676

[4] G. Martínez-Criado *et al.*, "ID16B: a Hard X-ray Nanoprobe Beamline at the ESRF for Nano-Analysis", *J. Synchrotron Radiat.*, vol. 23, pp. 344–352, 2016. doi:10.1107/s1600577515019839

[5] E. Nazaretski *et al.*, "Design and Performance of an X-ray Scanning Microscope at the Hard X-ray Nanoprobe Beamline of NSLS-II", *J. Synchrotron Radiat.*, vol. 24, pp. 1113–1119, 2017. doi:10.1107/s1600577517011183

[6] R. S. Celestre *et al.*, "Nanosurveyor 2: A Compact Instrument for Nano-Tomography at the Advanced Light Source", *J. Phys. Conf. Ser.*, vol. 849, p. 012047, 2017. doi:10.1088/1742-6596/849/1/012047

[7] F. Villar *et al.*, "Nanopositioning for the ESRF ID16A Nano-Imaging Beamline", *Synchrotron Radiat. News*, vol. 31, pp. 9–14, 2018. doi:10.1080/08940886.2018.1506234

[8] M. Holler *et al.*, "OMNY – A tOMographic Nano crYo stage", *Rev. Sci. Instrum.*, vol. 89, p. 043706, 2018. doi:10.1063/1.5020247

[9] J. Deng *et al.*, "The Velociprobe: an Ultrafast Hard X-ray Nanoprobe for High-Resolution Ptychographic Imaging", *Rev. Sci. Instrum.*, vol. 90, p. 083701, 2019. doi:10.1063/1.5103173

[10] M. Osterhoff *et al.*, "Focus Characterization of the NanoMAX Kirkpatrick–Baez Mirror System", *J. Synchrotron Radiat.*, vol. 26, pp. 1173–1180, 2019. doi:10.1107/s1600577519003886

[11] A. Schropp *et al.*, "PtyNAMi: Ptychographic Nano-Analytical Microscope", *J. Appl. Cryst.*, vol. 53, pp. 957–971, 2020. doi:10.1063/1.5103173

[12] H. N. Chapman and K. A. Nugent, "Coherent Lensless X-ray Imaging", *Nat. Photonics*, vol. 4, p. 833, 2010. doi:10.1038/nphoton.2010.240

[13] A. M. Maiden *et al.*, "An Annealing Algorithm to Correct Positioning Errors in Ptychography", *Ultramicroscopy*, vol. 120, pp. 64–72, 2012. doi:10.1016/j.ultramic.2012.06.001

[14] H. C. N. Tolentino *et al.*, "The CARNAÚBA X-ray nanospectroscopy beamline at the Sirius-LNLS synchrotron light source: Developments, commissioning, and first science at the TARUM˜A station", *J. Electron. Spectrosc. Relat. Phenom.*, vol. 226, p. 147340, 2023. doi:10.1016/j.elspec.2023.147340

[15] R. R. Geraldes *et al.*, "The High-Dynamic Cryogenic Sample Stage for the SAPOTI Nanoprobe at the CARNAUBA Beamline at Sirius/LNLS", *AIP Conf. Proc.*, vol. 2990, p. 040017, 2023. doi:10.1063/5.0168438

[16] R. R.Geraldes *et al.*, "Granite Benches for Sirius X-ray Optical Systems", in *Proc. of MEDSI'18*, Paris, France, Jun. 2018, pp. 361-364. doi:10.18429/JACoW-MEDSI2018-THPH12

[17] R. R.Geraldes *et al.*, "Design and Commissioning of the TARUMÃ Station at the CARNAÚBA Beamline at Sirius/LNLS", in *Proc. MEDSI'20*, Chicago, USA, July 2021, pp. 292-295. doi:10.18429/JACoW-MEDSI2020-WEPB13

[18] G. B. Z. L. Moreno *et al.*, "Exactly-constrained KB Mirrors for Sirius/LNLS Beamlines: Design and Commissioning of the TARUMÃ Station Nanofocusing Optics at CARNAÚBA Beamline", in *Proc. of MEDSI'20*, Chicago, USA, July 2021, pp. 111-114. doi:10.18429/JACoW-MEDSI2020-TUOB01

[19] R. R.Geraldes *et al.*, "The Sample Positioning Stage for the SAPOTI Nanoprobe at the CARNAÚBA Beamline at Sirius/LNLS", in *Proc. of 37th ASPE Annual Meeting*, Bellevue, USA, Oct. 2022, pp. 91-97.

[20] D. L. Johnson *et al.*, "Characterization Testing of the Thales LPT9310 Pulse Tube Cooler", *Cryocoolers*, vol. 18, pp. 125-133, 2014.

ISBN: 978-3-95450-250-9 ISSN: 2673-5520 doi:10.18429/JACoW-MEDSI2023-TUOBM05

THE PROGRESS IN DESIGN, PREPARATION AND MEASUREMENT OF MLL FOR HEPS*

Shuaipeng Yue[1,2], Bin Ji[1], Ming Li[1], Qingyan Hou[1], Guangcai Chang[1,†]
[1] Institute of High Energy Physics, Chinese Academy of Sciences, 19B Yuquan Road, Beijing, China
[2] University of Chinese Academy of Sciences, 19A Yuquan Road, Beijing, China

Abstract

The multilayer Laue lens (MLL) is a promising optical element with large numerical aperture and aspect ratio in synchrotron radiation facility. The tilted MLLs are designed for the hard X-ray nano-probe beamline of HEPS. Two MLLs with 63(v)×43(h) μm^2 aperture and focal spot size of 8.1(v)×8.1(h) nm^2 at 10 keV are fabricated by a 7-meter-long Laue lens deposition machine. Ultrafast laser etching, dicing and focused ion beam are used to fabricate the multilayer into two-dimensional lenses meeting the requirement of diffraction dynamics. The multilayer grows flat without distortion. The smallest accumulated layer position error is below ±5 nm in the whole area and the root mean square (RMS) error is about 2.91 nm by SEM and image processing. The focusing performance of MLL with actual film thickness is calculated by a method based on the couple wave theory (CWT). The calculated full width at half maximum (FWHM) of focus spot is 8.4×8.2 nm^2 at 10 keV, which is close to the theoretical result.

INTRODUCTION

The smaller the spot of X-ray focus, the better the ability to distinguish the structure and composition of the material in a smaller spatial scale. The multilayer Laue lens has a large numerical aperture and depth-width ratio, and theoretically can focus x-rays below 1 nm [1], single-atom testing can be performed. Such high spatial resolution will enable the structure of materials to be studied at a new microscopic scale, effectively filling the gap between x-ray and electron microscopes in spatial resolution, it makes the exploration of the relationship between material structure and function more comprehensive and deepened, so it has been widely studied.

In order to improve the focusing resolution of MLL, a lot of research has been done by international researchers. In 2016, Sasa Bajt et al. carried out the fabrication and testing of wedged MLLs lens and obtained 8.4 nm × 6.8 nm at 16.3 keV [2]. In 2020, Xu et al. developed a MEMS template-based optical device for alignment of two linear MLLs, and realized a two-dimensional focusing spot of 14 nm × 13 nm at 13.6 keV photon energy [3]. In this study, we design and fabricate two MLLs with 63(v)×43(h) μm^2 aperture and calculate their focus performance at 10 keV.

DESIGN

The MLL consists of alternating regions made of two different materials. The thickness distribution is similar to that of a Fresnel zone plate (FZP). resulting in a focusing effect. The position of the nth layer of the film is determined by the zone plate formula:

$$x_n^2 = n\lambda f + n^2\lambda^2 / 4 \tag{1}$$

where x_n represents the position of the thin film, λ is the wavelength of the X-ray, and f is the focal length of the MLL. Additionally, the thickness of each layer dn can be expressed as follows:

$$d_n = x_n - x_{n-1} \approx \frac{\lambda f}{2x_n} \tag{2}$$

The MLL used within this study was designed at 10 keV using alternate target sputtering of WSi_2 and Si on a substrate. To achieve 8 nm focus spot for High Energy Photon Source (HEPS), the two-dimension focused MLLs are designed as follows (see Table 1).

Table 1: MLL Design Parameter

MLL@10KeV	Horizontal	Vertical
Aperture [μm]	43	63
Thickness [nm]	3.3-15	3-14
Layers	8030	13030
Optimum depth [μm]	3.5	3.3
Efficiency	8.4%	7.2%
Focal length [mm]	3	4
FWHM [nm]	8	8
Tilt angle [mrad]	7.4	8.3

The one-dimensional diffraction effect is calculated using the dynamics theory of X-ray diffraction. This was first used by Takagi and Taupin Diffraction (TTD) to describe the wavefront change of X-rays propagating when a crystal is distorted [4]. The MLLs' focusing property near focal plane is calculated using the Fresnel-Kirchhoff diffraction integral as shown in Figures 1 and 2. The intensity distribution of focal spot is shown in Figure 3.

* Work supported by by the National Natural Science Foundation of China Project 12005250
† changgc@ihep.ac.cn

12th Int. Conf. Mech. Eng. Design Synchrotron Radiat. Equip. Instrum. MEDSI2023, Beijing, China JACoW Publishing
ISBN: 978-3-95450-250-9 ISSN: 2673-5520 doi:10.18429/JACoW-MEDSI2023-TUOBM05

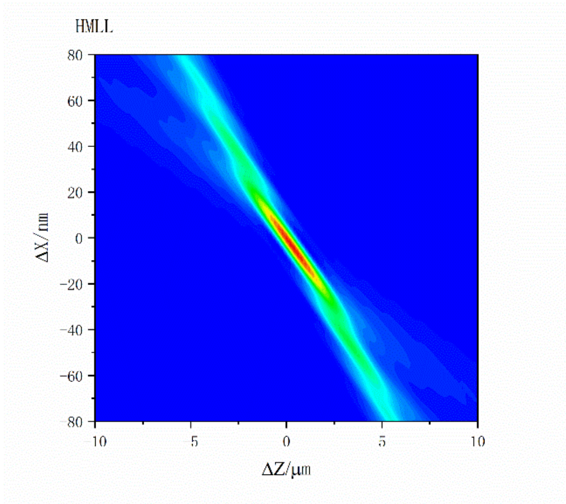

Figure 1: The intensity distribution of HMLL near focal plane.

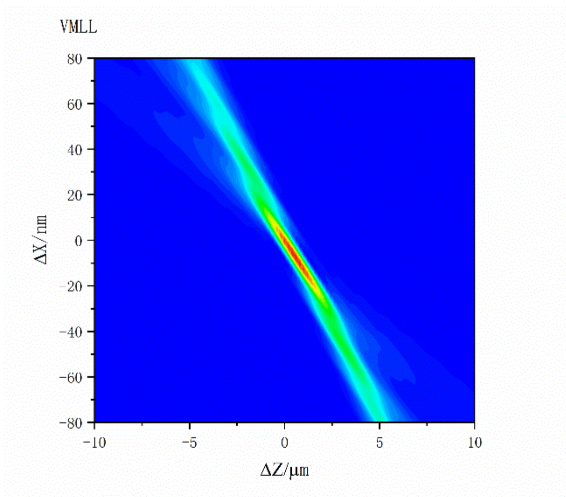

Figure 2: The intensity distribution of VMLL near focal plane.

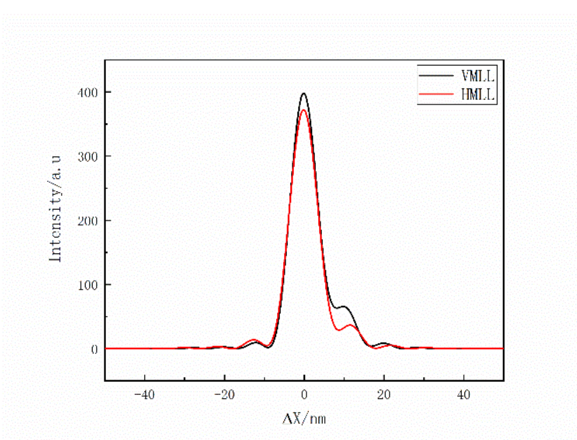

Figure 3: The intensity distribution of HMLL and VMLL at focal spot.

PREPARATION

Multilayer Preparation

The multilayer is deposited onto a super-polished silicon substrate using a 7-meter-long Laue lens deposition machine with 8 4-inch target. The coating system consists of three parts: (1) load-lock chamber, which can realize the transfer, loading and unloading of samples without destroying the high vacuum of the deposition chamber. (2) testing chamber, on-line measurement of film curvature and stress in the film deposition process. (3) deposition chamber, the target particles are sputtered and deposited on silicon wafer to form multilayer structure mainly by magnetron sputtering technology. The base pressure is below 8E-5 Pa before deposition, and Argon (99.99%) is used as the working gas with a pressure of 0.6 Pa, considering the factors of interface roughness and film stress. The power of the WSi_2 target is 40 W, while that of the Si target is 60 W.

The layer thicknesses range of the designed MLLs is varied from 3 nm to 15 nm. Several fixed individual thicknesses within the range are selected to process periodic multilayers to calculate the relationship between individual thickness and deposition time. The X-ray diffractometer (XRD) produced by Bruker D8 advance is used to perform the grazing incidence X-ray reflection (GIXRR) test of the periodic multilayer. The relationship between the thickness of WSi_2 and Si and deposition time iss obtained by data fitting as shown in Figure 4.

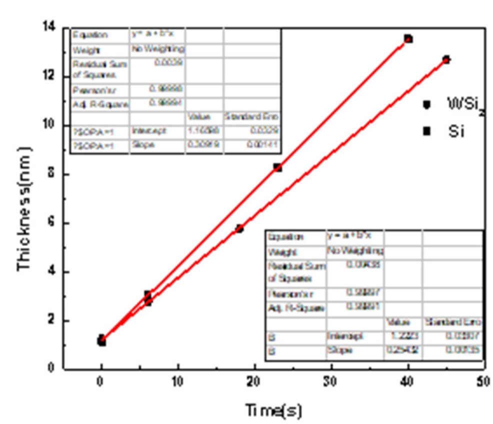

Figure 4: The relationship between the thickness of WSi_2 and Si and deposition time.

The linear fit equation of WSi_2 is $d = 0.25t+1.22$ while that of Si is $d = 0.31t+1.17$, where d represents the thickness, and t represents the time. In the linear equation, the slope represents the growing rate of individual material, while the intercept represents the thickness when the substrate is moved back and forth above each target. According to the above two equations, the 8030-layer and 13030-layer MLL multilayers are fabricated.

ISBN: 978-3-95450-250-9 ISSN: 2673-5520 doi:10.18429/JACoW-MEDSI2023-TUOBM05

Lenses Fabrication

The incident X-ray energy determines the lens depth along the optical axis to achieve the best efficiency of high numerical aperture focusing. For the MLL designed in Section 2, the optimal depths are determined to be 3.5 μm and 3.3 μm respectively at 10 keV. In order to precisely control the depth of the lenses and to achieve high-quality fine polishing of the entrance and exit surfaces, we use ultra-fast laser etching, dicing, and focused ion beam (FIB) polishing [5].

The multilayer surface is firstly etched by ultra-fast laser equipped with Trumpf ultraviolet femtosecond laser, SCANLAB two-dimensional mirror scanning system and six-axis positioning system produced by PI company. Adjust the sample stage so that the center of the laser focus is located on the surface of the sample. Single-layer etching is started by filling two rectangular patterns in the laser control software, and multiple etching cycles are carried out, so that the etching depth is greater than the total thickness of the MLL, as shown in Figure 5.

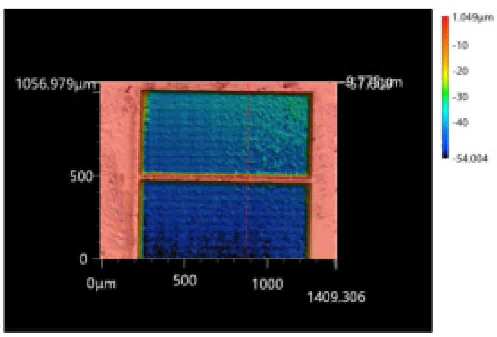

Figure 5: The etching morphology of MLL measured by confocal laser microscope with 10 × lens.

Because the focal length of the MLL is limited (3 ~ 4 mm), the multilayer after laser etching is cut and separated into small size samples (e. g. 2 mm × 1 mm) by a dicing machine. After that, FIB is carried out to further thin the lenses to the depth along the optical axis that satisfies the diffraction dynamics. It is simultaneously necessary to use FIB to finely polish the entrance and exit surfaces of the MLLs to improve the surface roughness and to reduce scattering of X-rays. The morphology of the final processed lenses under scanning electron microscope (SEM) test is shown in Figure 6.

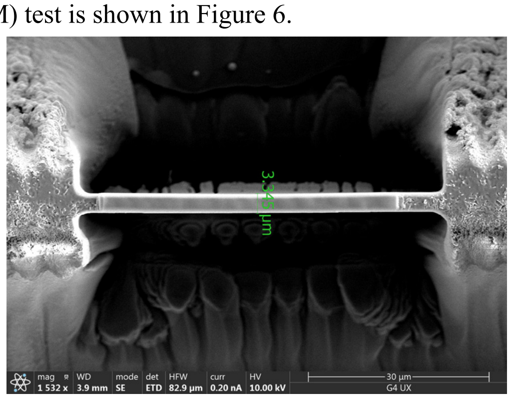

Figure 6: MLL top view measured by SEM.

CHARACTERIZATION

In order to characterize the processing quality of MLL, the cross-section of the multilayer was observed by Transmission electron microscope (TEM) before the lenses fabrication as shown in Figure 7. The material of dark layer is WSi_2, while the light layer represents the Si. It can be seen that multilayer structure is undamaged after deposition. All the layer interfaces stay smooth without distortion.

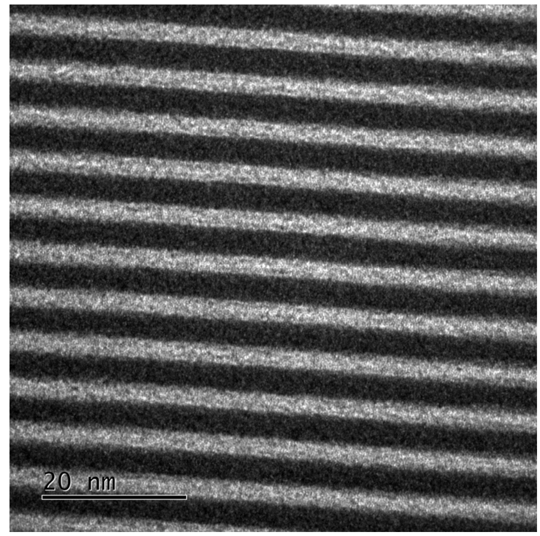

Figure 7: Cross-section of the multilayer observed by TEM.

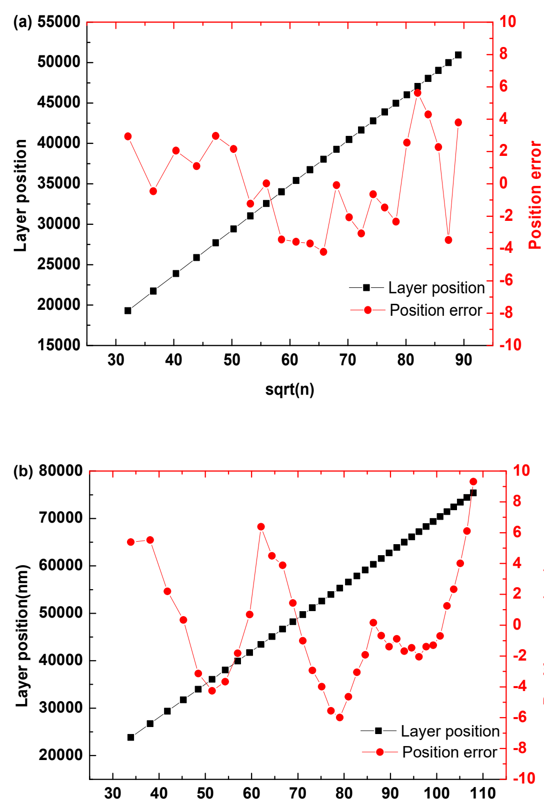

Figure 8: Layer position and position error of HMLL(a) and VMLL(b).

ISBN: 978-3-95450-250-9 ISSN: 2673-5520 doi:10.18429/JACoW-MEDSI2023-TUOBM05

During the preparation of the MLL multilayers, every 300th layer of Si was replaced by WS_{i2} as the marker. The location of each marker layer can be obtained by measuring the thickness of each marker region. In theory, the position of the zone is proportional to the arithmetic square root of the zone number, but the actual marker layer position has a small error that deviates from a linear distribution due to long-term drift of the deposition rate and rate stability, as shown in the Figure 8. The position error of HMLL and VMLL are listed in Table 2.

Table 2: Position Error of HMLL and VMLL

Position error	PV [nm]	RMS [nm]
HMLL	< ±4	2.91
VMLL	< ±8	3.70

Ideally, the positions of the layers should adhere to the zone plate law for optimal performance. However, due to a growth-rate error, an additional quadratic term is also present, as evidenced by the best fit to the experimental data. By substituting the actual layer positions measured by the SEM into the central equations for the CWT method for MLLs which are explained in detail elsewhere [6], we can derive a set of differential equations that can be solved numerically. This numerical solution allows us to calculate the wavefront of the diffracted wave on the exit surface of the MLL. Utilizing the Huygens-Fresnel principle, we can further determine the complex wavefront of the diffracted wave at any point beyond the MLL. The FWHM of the HMLL and VMLL is 8.4×8.2 nm^2, as shown in Figure 9.

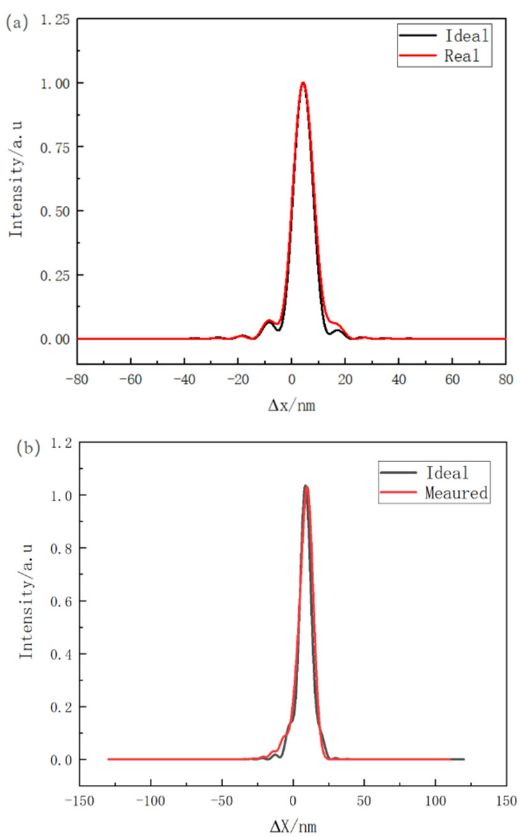

Figure 9: The intensity distribution of HMLL (a) and VMLL (b).

CONCLUSION

In this paper, two MLLs with 63(v)×43(h) μm^2 aperture and focal spot size of 8.1(v)×8.1(h) nm^2 at 10 keV are designed by diffraction dynamics and fabricated by a 7-meter-long Laue lens deposition machine. Ultrafast laser etching, dicing and focused ion beam are used to fabricate the multilayer into two-dimensional lenses meeting the requirement of diffraction dynamics. The accumulated layer position errors of HMLL and VMLL are 2.91 nm and 3.70 nm by SEM and image processing. The focusing performance of MLL with actual film thickness is calculated by a method based on CWT. The calculated FWHM of focus spot is 8.4×8.2 nm^2 at 10 keV, which is close to the theoretical result of 8.1×8.1 nm^2. The actual focusing performance of MLLs will be tested when the HEPS nano-probe beamline is mounted.

REFERENCES

[1] H. Yan, H. Kang, R. Conley, C. Liu, *et al.*, “Multilayer Laue Lens: A Path Toward One Nanometer”, *X-Ray Opt. Instr.*, vol. 2010, p. 401854, Dec. 2010.

[2] S. Bajt, M. Prasciolu, H. Fleckenstein, *et al.*, “X-ray focusing with efficient high-NA multilayer Laue lenses”, *Light Sci. Appl*. no. 7, p. 17162, 2018. doi:10.1038/lsa.2017.162

[3] W. Xu, W. Xu, N. Bouet, *et al.* “2D MEMS-based multilayer Laue lens nanofocusing optics for high-resolution hard x-ray microscopy”, *Opt. Express*, vol. 28, no. 12, pp. 17660-17771, 2020. doi:10.1364/OE.389555

[4] S. Takagi, “Dynamical Theory of Diffraction Applicable to Crystals with Any Kind of Small Distortion”, *Acta. Crystallogr.,* pp. 1311-1312, Dec. 1962.

[5] S. Yue, L. Zhou, Y. Yang, *et al.*, “Hard X-ray focusing resolution and efficiency test with a thickness correction multilayer Laue lens”, *Nucl. Sci. Tech.*, vol. 33, p. 118, 2022. doi:10.1007/s41365-022-01102-1

[6] S. Yue, L. Zhou, M. Li, *et al.*, “Calculated performance of multilayer Laue lens based on actual layer thickness and coupled wave theory”, *Opt. Eng*, vol. 60, no. 9, p. 094111, Sep. 2021. doi:10.1117/1.OE.60.9.094111

ISBN: 978-3-95450-250-9 ISSN: 2673-5520 doi:10.18429/JACoW-MEDSI2023-TUOBM06

MINERVA, A NEW X-RAY FACILITY FOR THE CHARACTERIZATION OF THE ATHENA MIRROR MODULES AT THE ALBA SYNCHROTRON

Antonio Carballedo†[1], Dominique Heinis[1], Carles Colldelram[1], Alejandro Crisol[1], Guifré Cuní[1], Núria Valls Vidal[1], Alejandro Sánchez[1], Joan Casas[1], Josep Nicolàs[1], Nicolas Barrière[2], Maximilien J. Collon[2], Giuseppe Vacanti[2], Dieter Skroblin[3], Michael Krumrey[3], Levent Cibik[3], Ivo Ferreira[4] and Marcos Bavdaz[4]
[1]ALBA Synchrotron, Cerdanyola del Vallès, Spain
[2]cosine measurement systems, Sassenheim, The Netherlands
[3]Physikalisch-Technische Bundesanstalt (PTB), Berlin, Germany
[4]European Space Agency, ESTEC, Noordwijk, The Netherlands

Abstract

In this paper we present the newly built beamline MINERVA, an X-ray facility recently under commissioning at the ALBA synchrotron. The beamline has been designed to support the development of the X-ray observatory newATHENA (Advanced Telescope for High Energy Astrophysics) mission. MINERVA will host the necessary metrology equipment to integrate the stacks produced by cosine in a mirror module and characterize their optical performances. The beamline optical and mechanical design is originally based on the X-ray Parallel Beam Facility (XPBF) 2.0 from the Physikalisch-Technische Bundesanstalt (PTB), at BESSY II already in use to this effect. The construction of MINERVA is meant to significantly augment the capability to produce mirror modules.

The development of MINERVA has addressed the need for improved technical specifications, overcome existing limitations and achieve enhanced mechanical performances.

We describe the design and implementation of MINERVA that lasted three years. Even though the beamline is still under a commissioning phase, we expose tests and analysis that have been recently performed, remarking the improvements accomplished and the challenges to overcome, in order to reach the operational readiness for the mirror modules mass production.

MINERVA is funded by the European Space Agency (ESA) and the Spanish Ministry of Science and Innovation.

INTRODUCTION

The newATHENA telescope [1] is a space observatory that will address fundamental questions about energetic objects (accretion disk around black holes, large-scale structure, etc...). One of the key elements of the telescope is the innovative modular architecture of its optics subdivided by 13 concentric rings and filed by about 600 sub-systems called mirror modules (MMs) as seen in Fig. 1. These allows to maximize the effective collection area for a given geometry reducing its weight, critical aspects to be considered in space missions. The technology used to manufacture the MM is based on the Silicon Pore Optics technology developed at cosine. Based on a modified Wolter-Schwarzschild geometry, photons in the energy range from 0.2 keV to 12 keV are reflected on two consecutive plates reaching the focal point located 12 meters further. At the focal plane, the telescope will be equipped with both imaging and spectroscopy instrumentation. Since the optics is based on the assembly of hundreds of individual and independent parts, the alignment operation is a crucial step to comply with the performance requested for the full assembled optics. At XPBF 2.0 [2], cosine is currently optimizing the method to produce MMs at large scale [3] and today MINERVA is built to strengthen and boost their production and characterization while preserving the interoperability between beamlines.

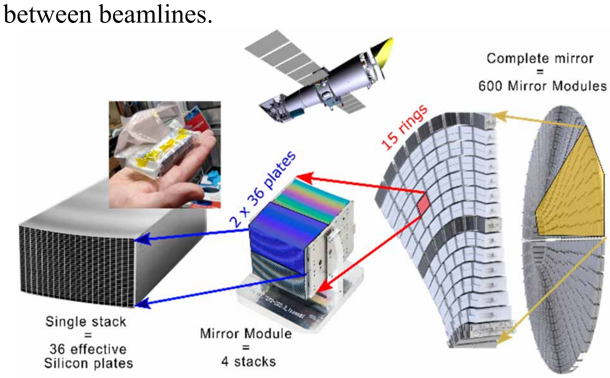

Figure 1: ATHENA Telescope Multiscale Optics Scheme

BEAMLINE OPERABILITY

MINERVA beamline works with samples consisting in a jig populated with 4 stacks composing a complete MM (Fig. 2). The relative position and orientation adjustment of an individual stack independently from the others is realized by using small hexapods. A 1 keV X-ray collimated beam impacts the optics at normal incidence. The jig is itself rigidly fixed on the top platform of a larger hexapod in order to control the 3D position of the MM respect to the incident X-ray beam. Light is then deflected and partially focused toward a 2D array detector about 12 meters further (close to the focal plane of the newATHENA optics). A complete characterization requires to repeat this operation over every single pore of the optics by mechanically moving the MM along a plane perpendicular to the input beam.

† acarballedo@cells.es

ISBN: 978-3-95450-250-9 ISSN: 2673-5520 doi:10.18429/JACoW-MEDSI2023-TUOBM06

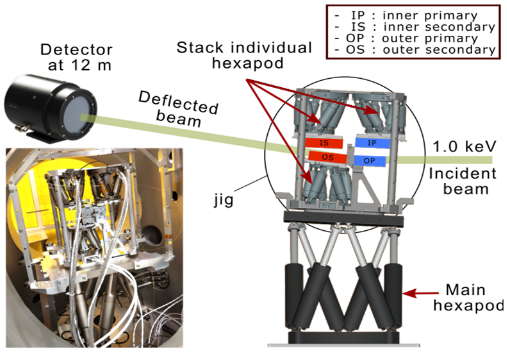

Figure 2: Mirror Module JIG and reflection scheme (from PTB).

The final angular resolution of newATHENA strongly depends on the alignment accuracy between the 4 stacks constituting a singular MM. It is why stability, accuracy and repeatability are crucial parameters for the optomechanical components specifications.

GENERAL BEAMLINE DESCRIPTION

MINERVA is located at the Front End 25 exit port of the ALBA experimental hall. The beamline X-ray source is a bending magnet that provides optimal spatial distribution to allow future upgrades of the components. The beamline will operate under Ultra High Vacuum (UHV) conditions from the source to the exit of the photon shutter, where a 1 µm thickness Silicon Nitride vacuum window will separate them from the rest of the beamline. Downstream the vacuum window, the beamline will operate under High Vacuum conditions (HV, 10^{-5} mbar). The beamline will provide a distance between the end detector and the MM origin with the required level of accuracy for data analysis. This measurement is performed by the combination of laser tracking technology and high positioning repeatability of the mechanics. MINERVA follows the optical layout sketched in Fig. 3 where the following components are presented:

- A bending magnet of the ALBA storage ring as the X-ray source and the front-end elements.
- A monochromator, consisting on a toroidal mirror (M1) with a multilayer coating which deflects the beam inboard, with a total deflection angle of 14 degrees. It collimates the beam in both the horizontal and vertical planes. Its reflective surface selects a narrow bandwidth at the nominal energy of 1.0 keV.
- A filter unit consisting of one Si_3N_4 membrane coated with a thin Al deposition which removes the visible light reflected by the M1 mirror.
- A set of pinholes ranging from 10 µm to 500 µm in diameter.
- A photon beam shutter which includes a fluorescent screen beam diagnostic unit.
- A Si_3N_4 window, which separates the upstream UHV
- A four-blade slit system that allow for apertures from fully closed to more than 10 mm in aperture.
- The sample station, which includes an in-vacuum hexapod and 2 linear stages for vertical and horizontal linear translations. The sample chamber and slits seats inside a temperature-controlled enclosure.
- A flight-tube, which links the sample station to the detector. It preserves the vacuum along the 12 meters long beam path between the MM and the detection system.
- The imaging detection is based on an indirect detection. The scintillator is coupled to the optical sensor by an optical fiber bundel. The camera proposed is based on sCMOS technology allowing fast readout.

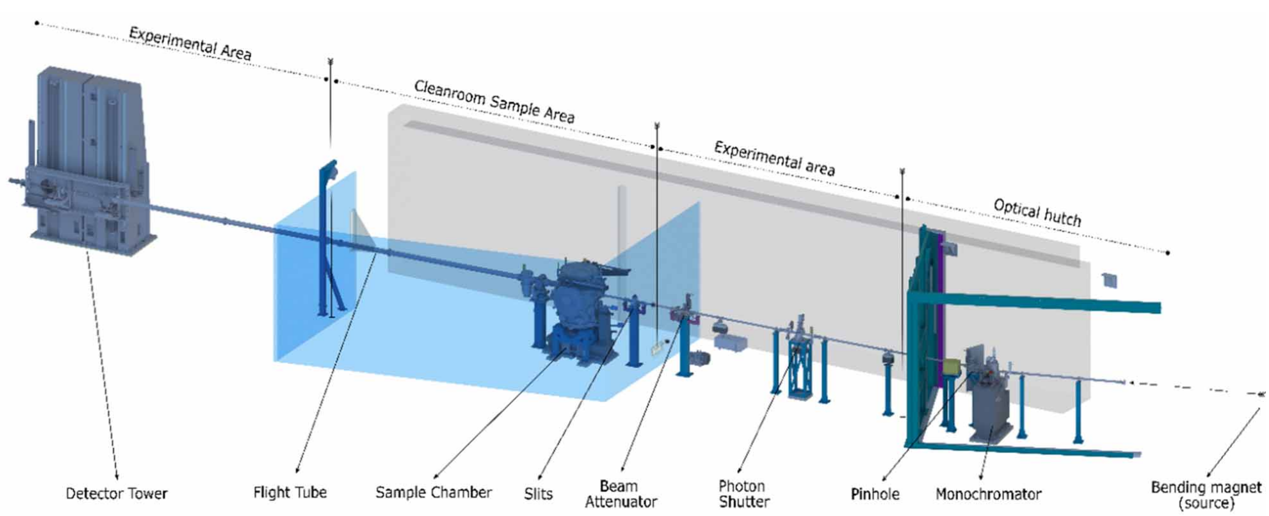

Figure 3: MINERVA layout presenting the main components of the beamline.

ISBN: 978-3-95450-250-9 ISSN: 2673-5520 doi:10.18429/JACoW-MEDSI2023-TUOBM06

BEAMLINE IMPLEMENTATION

As described above, MINERVA beamline consists of multiple equipment; however, there are three key components that play a central role and will be described in more detail, including their design, construction, installation and commissioning.

Monochromator

The first beamline optic is based toroidal mirror (M1) with a multilayer coating. The mirror substrate holder and surrounding elements are mounted on a single column as has been done before for MIRAS and LOREA beamline [4] with a proven outstanding resolution and stability reaching up to 192 Hz for the first resonance mode. The column is decoupled from the vacuum chamber thanks to a large bellow and acts as a standalone insert that constitutes the base for the mirror holder, the cooling pipes and electrical feedthroughs. The column motion mechanics are based on a high precision goniometer (Fig. 4) that adjusts the angular X-ray beam incidence angle with a sub-micro-radian angular resolution and a horizontal translation stage that move the substrate perpendicular to its surface. Everything is supported at beam height by a solid granite column, mounted on top of a flat plate grouted to the floor. The mirror holder itself is based on a kinematical mount preloaded with springs, which provides fine adjustment and repeatability. The mirror itself lies upon three balls (punctual contact) preloaded with springs and it is kept in position by clamps.

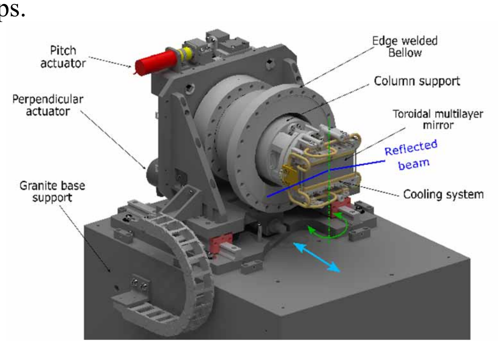

Figure 4: Monochromator.

Table 1: Monochromator Mechanical Specification

Parameter	Performance
Pitch rotation (Incidence angle variation)	
Stroke	≥(± 12 mrad)
Motion Resolution	≤0.5 µrad
Repeatability (open Loop)	≤1 µrad
Backlash (open Loop)	≤20 µrad
X-translation (Perpendicular mirror surface)	
Stroke	≥(± 5 mm)
Motion Resolution	≤0.4 µm
Repeatability (open Loop)	≤0.5 µm
Backlash (open Loop)	≤6.5 µm
Linearity (open Loop)	≤1.2 µm

In Table 1 are shown some values of the performance. The instrument's commissioning has met expectations; however, refinement tasks for alignment are still necessary to enhance the pencil beam in terms of divergence.

Sample Environment

For the characterization of each MM, the optical entrance is scanned both vertically and horizontally in front of the fixed incident beam. The main components used to fulfil those requirements are shown in Fig. 5. The jig is mounted on top of an in vacuum hexapod and two high precision linear stages. The vertical stage takes place in air and is particularly designed to keep constant the orientation of the MM during a vertical scan. It is based on the ALBA skin concept [5], where two precision synchronized vertical actuators are mounted at both sides of the granite for better mechanical and thermal stability. The combination of ball spindles and ball linear guides accurately move a thick horizontal platform with two flexures joints on its sides. The horizontal linear stage works under vacuum and consists in a ball spindle and cross roller linear bearings actuated by a stepper motor. Both vertical and horizontal stages are equipped with optical absolute encoders. The vacuum chamber is fully decoupled from the sample positioning stages by means welded bellows with robust columns holding the in-vacuum base plate.

Keeping the orientation of the MM the closest to 1.0 arcsec during the scan and the assembly is the target. To do that, a metrology system consisting of two autocollimators measuring the three orientation angles MM respect of the incident beam is provided. The signal then is reused to act on the main hexapod for orientation correction.

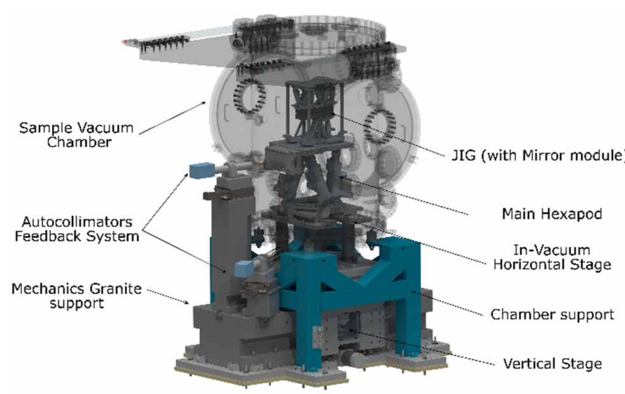

Figure 5: Sample environment.

Different motion tests measuring changes in orientation with autocollimators were done. Repeatability measurements within tolerance were observed; however, the orientation change across the entire range remained at 30 arcsec (Fig. 6). The implementation of the feedback control with autocollimators should allow to reach the required tolerances. Regarding the in-vacuum horizontal movement, some hysteresis issues and poor linearity have emerged and are currently under investigation.

ISBN: 978-3-95450-250-9 ISSN: 2673-5520 doi:10.18429/JACoW-MEDSI2023-TUOBM06

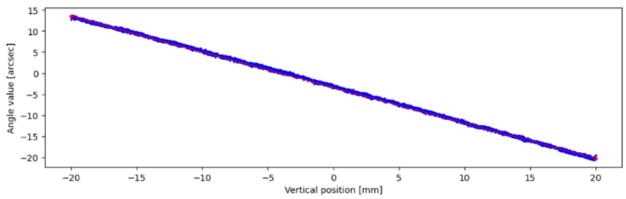

Figure 6: Orientation variation in 40 mm vertical range.

Another crucial aspect for the characterization of MM is stability. Measurements using both available autocollimators and the absolute encoders show almost constant values for a few hours, equivalent to the duration of one of the sample measurements (Fig. 7).

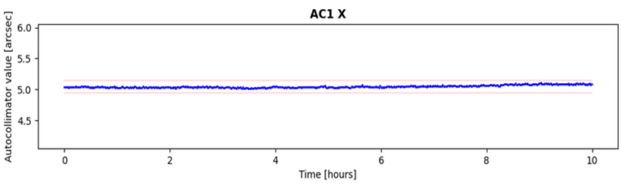

Figure 7: Orientation stability during 10 h scan.

Detector Tower

The beam deflected by the MM is then sent to a 2-dimensional array detector. To fully characterize a MM, the detector has to move on the portion of a cylinder surface with radius between 11.5 and 12.5 m. This trajectory is performed by using a 4-axis positioning combination as shown in Fig. 8. The height and the orientation of the detector are achieved by a pair of vertical linear stages placed side by side. The detector can also follow the line of sight of the deflected beam and be adjusted to find the focus of the optics. The mechanics of all the stages are based on precision ball spindles and ball linear guides, all actuated by stepper motors. Each stage position feedback is given by optical absolute encoders. The position of the detector is accurately measured and related with the MM position by a permanent laser tracker.

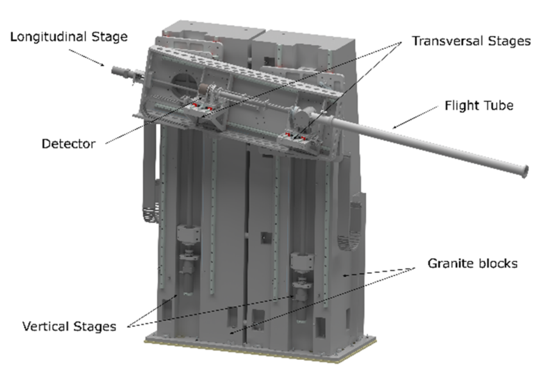

Figure 8: Detector tower.

Several stability measurements using the absolute encoders were performed. Cyclical position changes on the order of few microns were observed, closely associated with minor thermal variations on the experimental area throughout the day (Fig. 9).

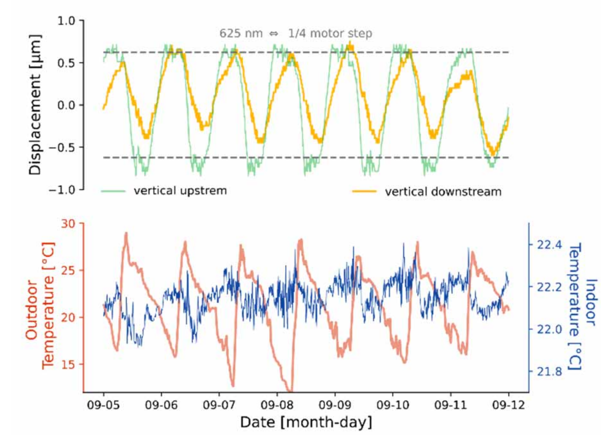

Figure 9: Position variation and temperature with time.

Nevertheless, as seen in Fig. 10 a proper configuration of the encoder closed-loop has allowed reducing those changes to almost negligible levels.

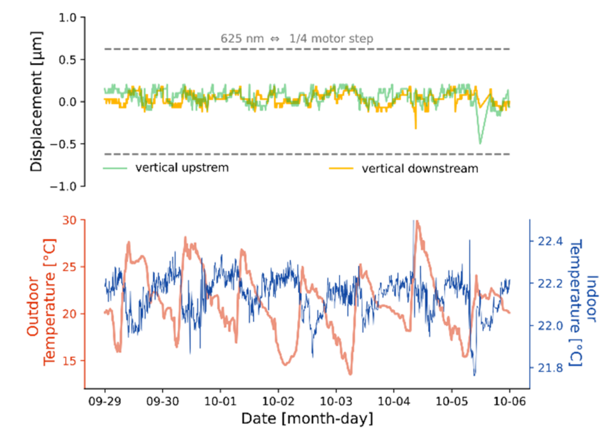

Figure 10: Position variation and temperature with time (fine close loop tunning).

CONCLUSIONS

A new X-ray beamline under commissioning at the ALBA synchrotron has been described. Although the optical layout is a replica of XPBF 2.0, MINERVA aims to reduce the MM characterization time by using, among other aspects, different approaches in the design of its mechanics. Various tests were performed, demonstrating favourable results in terms of repeatability and stability. However, there is a lot of commissioning work remaining from now until operational readiness for the mirror modules mass production by 2027.

ACKNOWLEDGEMENTS

The authors wish to acknowledge all the ALBA staff involved in several aspects of the construction and commissioning, in particular to Marc Sanchez, Marta Llonch, Jon Ladrera, Gabriel Peña, Núria Martí, Cristina Orozco, José Ferrer and workshop team, Borja Revuelta, Toni Camps, Bernat Molas, Jorge Villanueva, Albert Ollé, Oriol Vallcorba, Steven Wohl and Albert Van Eeckhout.

ISBN: 978-3-95450-250-9 ISSN: 2673-5520 doi:10.18429/JACoW-MEDSI2023-TUOBM06

REFERENCES

[1] D. Heinis *et al.*, "MINERVA installation status, an X-ray facility for the characterization of the ATHENA mirror modules at the ALBA synchrotron", in *Proc. SPIE Space Optics*, Dubrovnik, Croatia, Oct. 2022. doi:10.1117/12.2689958

[2] E. Handick *et al*., "Upgrade of the x-ray parallel beam facility XPBF 2.0 for characterization of silicon pore optics", in *Proc. SPIE Astronomical Telescopes + Instrumentation*, CA, USA, Dec. 2020. doi:10.1117/12.2561236

[3] N. M. Barrière *et al*., "Assembly of confocal silicon pore optic mirror modules for Athena", in *Proc. SPIE Optical Engineering + Applications*, San Diego, CA, USA, Aug. 2019. doi:10.1117/12.2530706

[4] L. R. M. Ribó *et al.*, "Mechanical Design of MIRAS, Infrared Microspectroscopy Beam Line at ALBA Synchrotron", in *Proc. MEDSI'16*, Barcelona, Spain, Sep. 2016, pp. 403-408. doi:10.18429/JACoW-MEDSI2016-FRAA03

[5] C. Colldelram *et al.*, "ALBA XALOC beamline diffractometer table skin concept design", in *Proc. Diamond Light Source 1 (MEDSI-6)*, Oct. 2011. doi:10.1017/S2044820110000754

ISBN: 978-3-95450-250-9 ISSN: 2673-5520 doi:10.18429/JACoW-MEDSI2023-TUOBM07

NEWLY DEVELOPED WAVEFRONT METROLOGY TECHNIQUE AND APPLYING IN CRYSTAL PROCESSING

Fang Liu†, Zhen Hong‡, Ming Li, Qianshun Diao, Junliang Yang, Hongkai Lian
Institute of High Energy Physics, CAS, Beijing, China

Abstract

In this work, we firstly propose an innovative wavefront metrology method at Beijing Synchrotron Radiation Facility (BSRF), named the double edges scan (DES) wavefront metrology technique. As the method resolved several vital problems of the first-generation synchrotron radiation source, including inferior lateral coherence, poor stability, and distortion of incident wavefront, it realized diffraction limit level wavefront metrology and has been successfully applied to crystal processing, which regarded as an important feedback of the fourth-generation synchrotron radiation source crystal fabrication process. The DES can achieve the precision better than 15 nrad (rms) with a 50 microns lateral resolution on crystal surface. The crystal we measured was processed by magnetically controlled small tool, which is also a creative processing technic. The technique gets rid of the limitation of the power system and transmission system, and realized the free machining of channel-cut crystal with narrow space. The results show that the channel-cut crystal can reach 101 nrad RMS with 5.5 mm dimension and the morphology was uniform, scratches and spot defects were eliminated completely. The roughness of inner surfaces reached 0.6 nm RMS. The Darwin widths of the channel-cut crystal processed by MC-CMP were consistent with the theoretical values, the two diffraction reflectivity rates of the crystal reached 85.1 %, very close to the theoretical limit of 88.3 %.

INTRODUCTION

The 4th synchrotron radiation sources are characterized by diffraction-limit emittance and extremely high average brilliance. For the diffraction-limit sources, based on the Maréchal criterion [1], the RMS wavefront error must be below λ/14, with λ being the X-ray wavelength. Crystal monochromators are indispensable optical components for the majority of beamlines at synchrotron radiation facilities, which can be applied in diffraction, imaging and spectroscopy experiments. In order to give full play to the diffraction-limited fourth-generation X-ray sources, crystals need to preserve wavefront in a much larger range, for the transverse coherence of such sources is theoretically two orders of magnitude larger than third-generation sources. Because of the diffraction geometry, a pure relative measurement comparing wavefront with and without the crystal is difficult owing to the beam flipping and the image blurring from the crystal extinction effect [1-2]. In this work, an innovative wavefront metrology method, named the double-edges scan (DES) wavefront metrology technique was developed at BSRF. Firstly, the Bragg diffraction wavefront error of a self-fabricated high-quality flat crystal and a self-fabricated high-quality channel-cut crystal were measured. Secondly, the measurement repeatability experiment was carried on with a commercial flat crystal. With the specially designed double-edge structure, high precision absolute Bragg diffraction wavefront measurements were realized. In addition, our self-developed magnetically controlled chemical – mechanical polishing (MC-CMP) approach [3] for fabricating channel-cut silicon crystals will also be introduced.

METHOD

Templates are provided for recommended software and authors are advised to use them. Please consult the individual conference help pages if questions arise.

The Wavefront Metrology Technique

The equivalent X-ray beam geometry is displayed in Figure 1. A beam passing through the double-edge structure (moveable edge & fixed edge) is diffracted by the crystal sample with an angle of Bragg diffraction angle θ_B, and received by the detector. Here, we name the beam passing through the fixed edge for beam 1 and passing through the movable edge for beam 2. The lateral distance between the two edges is D. Firstly, when the crystal is out of the optical path, using detector to record the projection positions of both moveable edge and fixed edge. The distance between the two edge projections is y_0 and the longitudinal distance between edges and detector is Z. The incident reference wavefront slope α_0 can be described as:

$$\alpha_1 = \frac{y_1 - h}{z_2} \qquad (1),$$

Secondly, when the crystal is in the optical path, because of diffraction wavefront error that introduced by crystal, beam 2 propagate in the direction of α_1 and detector records the distance y_1 between the two edge projections. Then α_1 can be described as:

$$\alpha_1 = \frac{y_1 - h}{z_2} \qquad (2),$$

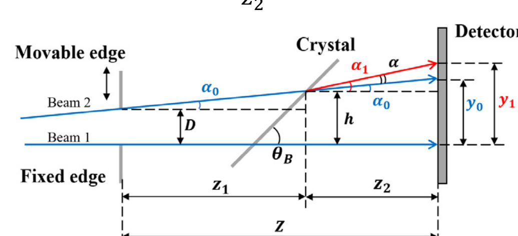

Figure 1: Geometry schematic for the DES method.

† fliu@ihep.ac.cn
‡ hongzhen@ihep.ac.cn

ISBN: 978-3-95450-250-9 ISSN: 2673-5520 doi:10.18429/JACoW-MEDSI2023-TUOBM07

The parameter h is the lateral distance between the two beams on the plane of beam 2 incident on crystal. The parameters z_1 and z_2 are the longitudinal distance from double-edge structure to the plane of beam 2 incident on crystal and from the plane of beam 2 incident on crystal to detector, respectively. The parameters h, z_1 and z_2 can be derived from simple geometric relationships. Thus, the diffraction wavefront slope α can be depicted as:

$$\alpha = \alpha_1 - \alpha_0 \quad (3),$$

The Crystal Processing

The high-quality channel-cut crystal can be processed by our self-developed magnetically controlled chemical – mechanical polishing (MC-CMP) approach [3].

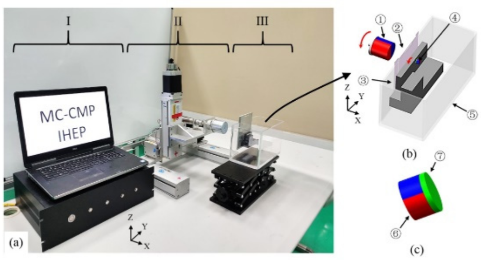

Figure 2. (a) photo of the MC-CMP system; (b) sketch of the vessel and a work piece of crystal and (c) Small polishing magnets. Major components are: ①large magnet ②the pad which can be inserted into the vessel; ③the channel-cut crystal; ④small polishing tool; ⑤vessel filled with slurry; ⑥mini magnet; ⑦covering layer.

The Magnetically-controlled chemical-mechanical polishing system (MC-CMP) as shown in Figure 2. consists of three major components: a) a mini cylinder magnet in the vessel filled with slurry or polishing solution; b) a gantry guide rail and rotating mechanics for driving magnet; and c) a control computer. The rotation of the large cylinder magnet is achieved by a DC motor while the three-dimensional translation movements X/Y/Z movements are implemented through a gantry guide rail. Both magnets are radially magnetized.

The processing procedure can be described as follows:

1) Rough mechanical polishing. nearly 120 µm-thick layer was removed.
2) Rough CMP polishing. a thickness ~55 µm were removed.
3) Wet chemical etching (WCE). The CC crystal was etched in HNO_3/HF (10:1) over 12 minutes. In this step, totally 35-µm thick layer was removed.
4) Final CMP polishing. Covering layer on the small tool was polyurethane, nearly 8 µm thickness was removed during polishing.

EXPERIMENT RESULTS

We performed the experiment at beamline 1B3B of BSRF. We have measured both flat and channel-cut crystals.

Firstly, a self-fabricated high-quality flat crystal was measured. Through scanning the movable edge along meridional direction, the one-dimension deflection angle can be directly measured and wavefront can be reconstructed by our own data analysis procedures. In the data processing, we picked out a suitable area that was free of any visible defects which was marked in Figure 3 (a) with red dashed frame. The measured equivalent Bragg diffraction surface slope error along meridional direction is shown in Figure 3 (b) with a sagittal spatial resolution of about 50 µm. The wavefront height error can be calculated through integration and the result is shown in Figure 3 (c).

The root mean square (RMS) value of equivalent Bragg diffraction surface slope error is 65.91 nrad and the RMS of wavefront height error is 3.78 pm (or 4.57%λ) which indicate that the crystal meets the wavefront preservation requirement of the diffraction-limited fourth-generation X-ray sources.

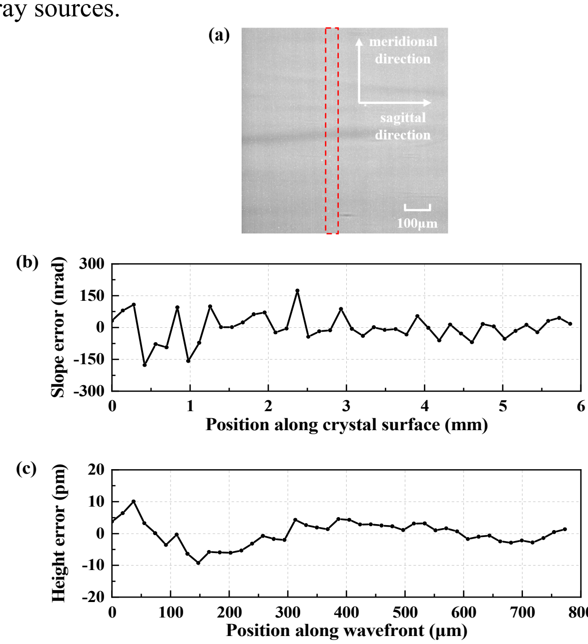

Figure 3: (a) X-ray diffraction image of the self-fabricated high-quality flat crystal. (b) Equivalent Bragg diffraction surface slope error profile of red dashed frame in Figure 3 (a). (c) Wavefront height error profile of red dashed frame in Figure 3 (a).

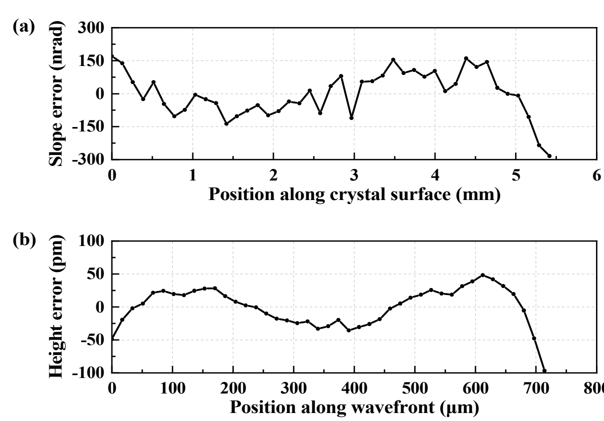

Figure 4: (a) Equivalent Bragg diffraction surface slope error profile of channel-cut crystal. (b) Wavefront height error profile of channel-cut crystal.

ISBN: 978-3-95450-250-9 ISSN: 2673-5520 doi:10.18429/JACoW-MEDSI2023-TUOBM07

Then, a self-fabricated high-quality channel-cut crystal (Si111, processed with the approach named magnetically controlled chemical–mechanical polishing [3]) was measured. The equivalent Bragg diffraction surface slope error profile and the wavefront height error profile is shown in Figure 4 (a) and Figure 4 (b), respectively. The RMS of the slope errors is 101.73 nrad and the RMS of wavefront height errors is 7.65 pm (or 9.25%λ). As the processing of channel-cut crystal is more difficult because of the narrow gap between the two crystal surfaces, the wavefront error is obviously larger than the flat crystal.

We also carried on repeatability test with a commercial flat crystal from a Japan company (EXCEED). The slope error measurement was conducted three times. Figure 5 (a) shows the measured equivalent Bragg diffraction surface slope error profile for each time as well as the average slope error profile and Figure 5 (b) shows the deviations of the measured slope errors from the average. The RMS of average slope errors is 82.08 nrad and the measurement-to-measurement reproducibility is 13.51 nrad. The wavefront height error profile and the deviations of the measured height errors from the average and the results are shown in Figure 5 (c) and Figure 5 (d), respectively. The average wavefront height error RMS is 6.71 pm (or 8.11%λ) and the reproducibility is 0.54 pm (or 0.65%λ). The results indicated that the DES method has excellent repeatability which meet the requirement of characterizing high-quality crystals Bragg diffraction wavefront.

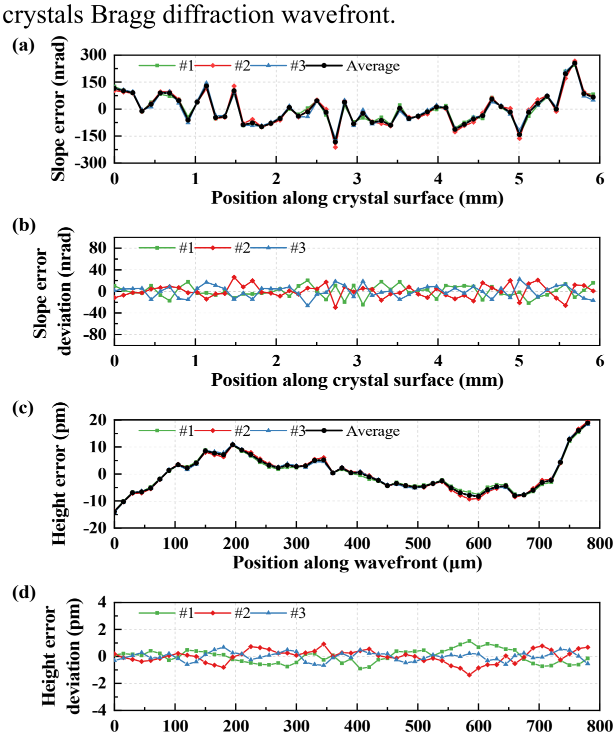

Figure 5: (a) Equivalent Bragg diffraction surface slope error profiles of three measurements and average profile. (b) The deviations from the average of the three measurements slope error profiles. (c) Wavefront height error profiles of three measurements and average profile. (d) The deviations from the average of the three measurements wavefront height error profiles.

We also characterize the channel-cut crystal with roughness, rocking-curve, topography and HRTEM photograph and EDX mapping [3].

For the channel-cut crystal with wet chemical etching (WCE), numerous and large-size speckles was found on the surface (Figure 6 (a)) and the roughness value of the etched one is 873.9nm rms (Figure 6 (b)). By contrast, for the MC-CMP channel-cut crystal, the obtained surface is homogeneous without any observable speckle and scratch (Figure 6 (c)) and a substantially high surface roughness was measured as 0.614 nm RMS (Figure 6 (d)).

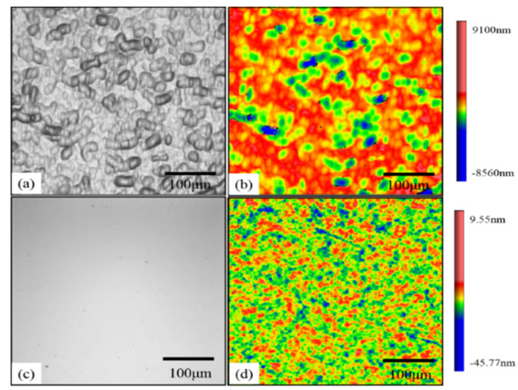

Figure 6: (a) Optical micrograph of WCE CC; (b) the corresponding roughness; (c) Optical micrograph of MC-CMP CC (d) the roughness.

The rocking curves at 15 keV was measured for both WCE CC and MC-CMP CC crystals (Figure 7). The Darwin width for both WCE and MC-CMP CC crystals agrees well with the theoretical calculations based on dynamical diffraction theory. Meanwhile, the peak reflectivity of MC-CMP CC and WCE CC are 85.1% and 84.8% respectively, which are close to theoretical value of 88.3%. Indicating that diffraction volume is perfect crystal and damaged layers are removed by both MC-CMP or WCE process. On the other hand, the diffraction surface is well preserved by using MC-CMP method for polishing the inner-face of channel-cut crystals.

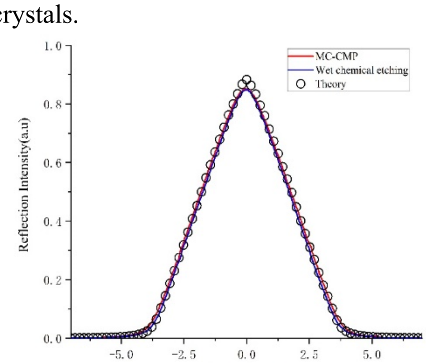

Figure 7: Comparison of experimental and theoretical rocking curves for MC-CMP and WCE processed channel-cut crystals.

Figure 8 shows the X-ray topography of crystal surface for the WCE-CC and MC-CMP-CC crystals. There are numerous scratches in the WCE-CC crystals, but the MC-

ISBN: 978-3-95450-250-9 ISSN: 2673-5520 doi:10.18429/JACoW-MEDSI2023-TUOBM07

CMP-CC crystal is quite homogeneous and free of scratch. a few dark points originate from the CCD.

According to the EDX mapping, a SiO2 layer with a uniform thickness of about 2.5 nm was found on the surface of the perfect crystalline matrix. There are no amorphous layers that often exist in the traditional CMP process, Using the MC-CMP method, the SiO2 layer (Figure 9) with nanometer scale thickness and uniform construction obtained on perfect crystalline matrix could be beneficial for preserving the wavefront and coherence of high quality photons from 4th generation synchrotron radiation or Free-electron lasers.

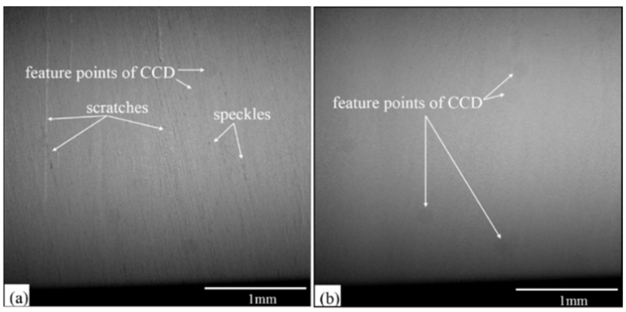

Figure 8: (a) Topography of etching surface (b) Topography of polishing surface.

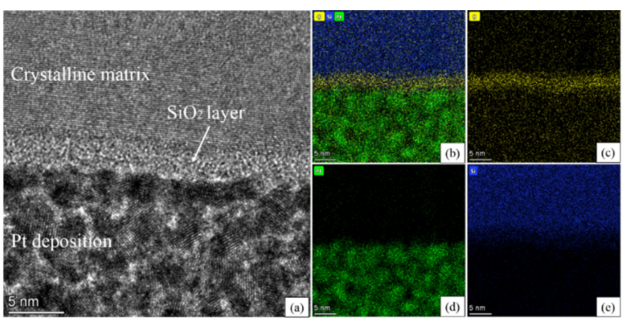

Figure 9: Cross section HRTEM photograph of polishing CC workpiece.

CONCLUSION

An innovative wavefront metrology method, named the double-edges scan (DES) wavefront metrology technique was developed at BSRF, and it realized diffraction limit level wavefront metrology. By means of the DES methods, the heigh precision absolute Bragg diffraction wavefront characterization of flat crystals and channel-cut crystals came into reality. Benefit from the double-edge structure design, the wavefront measurement precision below 15 nrad RMS can be achieved.Currently, the DES method has already been regarded as an important feedback in the next-generation crystal processing.

The magnetically controlled Chemical Mechanical polishing (MC-CMP) is a nice approach with high cost-effectiveness ratio for polishing Channel-cut crystals with small gap.This novel technique can be readily applied for almost every crystal optics lab to manufacture channel-cut monochromators for any hard X-ray beamline at either 4 th generation synchrotron radiation sources or Free-electron lasers.

REFERENCES

[1] X. Shi, Z. Qiao, P. Pradhan, P. Liu, L. Assoufid, K. Kim, Y. Shvyd'ko, "At-wavelength characterization of X-ray-wavefronts in Bragg diffraction from crystals", *J. Synchrotron Rad.* vol. 30, 1100-1107, 2023.

[2] D. Cocco, G. Cutler, M. S. D. Rio, L. Rebuffi, X. Shi, K. Yamauchi, "Wavefront preserving X-ray optics for Synchrotron and Free Electron Laser photon beam transport systems," *Phys. Rep.* 974, 1–40, 2022.

[3] Z. Hong, Q. Diao, W. Xu, Q. Yuan, J. Yang, Z. Li, Y. Jiang, C. Zhang, D. Zhang, F. Liu, X. Zhang, P. Liu, Y. Tao, W. Sheng, M. Li, Y. Zhao, "A magnetically controlled chemical – mechanical polishing (MC-CMP) approach for fabricating channel-cut silicon crystal optics for the High Energy Photon Source", *J. Synchrotron Rad.* 30, 84-89, 2023.

ISBN: 978-3-95450-250-9 ISSN: 2673-5520 doi:10.18429/JACoW-MEDSI2023-TUPYP001

SHINING LIGHT ON PRECISION: UNRAVELING XBPMs AT THE AUSTRALIAN SYNCHROTRON

B. Lin†, J. McKinlay, S. Porsa, Y. E. Tan, ANSTO, Australian Synchrotron, Melbourne, Australia

Abstract

At the Australian Synchrotron (AS), the need for non-destructive X-ray beam positioning monitors (XBPM) in the beamline front ends led to the development and installation of an in-house prototype using the photoelectric effect in 2021. This prototype served as a proof of concept and an initial step towards creating a customised solution for real time X-ray position monitoring. Of the new beamlines being installed at the AS, the High-Performance Macromolecular Crystallography (MX3) and Nanoprobe beamlines require XBPMs due to their small spot size and high stability requirements. However, a significant hurdle is the short distance from the source point to the XBPM location, resulting in an extremely restricted aperture to accurately monitor the beam position. Scaling down the photoelectric prototype to accommodate the available space has proven challenging, prompting us to explore alternative designs that utilize temperature-based methods to determine the beam position. This paper details insights made from investigating this alternative method and design.

INTRODUCTION

X-ray beam positioning monitoring technology plays an important role in synchrotron facilities, gaining increasing significance as light sources move towards smaller source sizes and nanoscale sample probing. The AS has been exploring this technology to develop an in-house, non-destructive white beam XBPM catered to its light source requirements. A photoemission XBPM was designed and installed by 2021 on the optical diagnostic beamline (ODB) as a proof of concept and prototype for future beamlines. The design was derived from LNLS and Soleil XBPM designs [1, 2]. However, there have been challenges with scaling this prototype to the new beamlines that need an XBPM due to their small spot size and high stability requirements, namely the Nanoprobe and MX3 beamline. Consequently, there has been a need to investigate alternative methods and designs that can cater for the requirements and specifications for the two beamlines.

PHOTOEMISSION XBPM

A photoemission prototype XBPM was fabricated and installed on the ODB with these requirements in consideration:

- Drain current from a single XBPM blade needs to be a minimum of 2 µA at 200 mA [3].
- Position resolution of < 1 µm for an undulator source at nominal beam current of 200 mA.
- Misalignment tolerance in the insertion device (ID) source point of ± 0.5 mrad in both planes.

† becky.lin@ansto.gov.au

XBPM Prototype Using Photoemission

The final design and assembly before the last flange was fastened can be seen below in Fig. 1 with the respective beam direction in red.

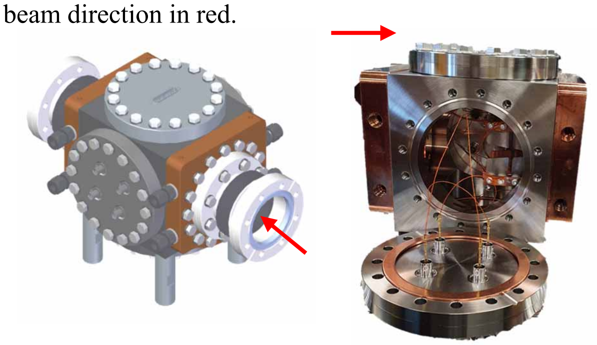

Figure 1: Final render and assembly of XBPM prototype.

The body is an ultra-high vacuum (UHV) stainless steel cube with flanged faces. Looking from upstream, the blades are mounted to the rear flange, the front flange has a pinhole mask for the beam fringes, the left and right flange both have four triaxial feedthroughs to pick up the drain current from the blades, and the top flange has a D-sub miniature (D-sub) port for temperature monitoring of the XBPM. The front and rear face of XBPM is shown in Fig. 2.

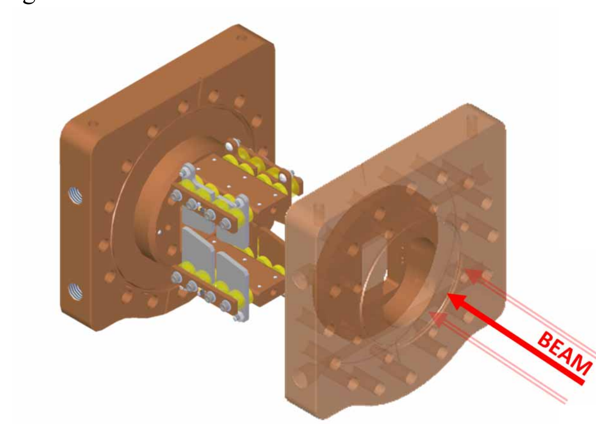

Figure 2: Front and rear flange of XBPM.

The pinholes in the mask have a diameter of 2 mm that allow the beam fringes to pass through. Theoretically, it samples the beam distribution more accurately as it strikes a more specific part of the blade, as this enables sampling of the beam at fixed points in space with a well-defined size. This allows a beam distribution to be fitted through the collected data more accurately and determine a verified centre point of the beam. Figure 3 exhibits the front view of the mask, where the pinholes are the four smaller holes adjacent to the centre window.

ISBN: 978-3-95450-250-9 ISSN: 2673-5520 doi:10.18429/JACoW-MEDSI2023-TUPYP001

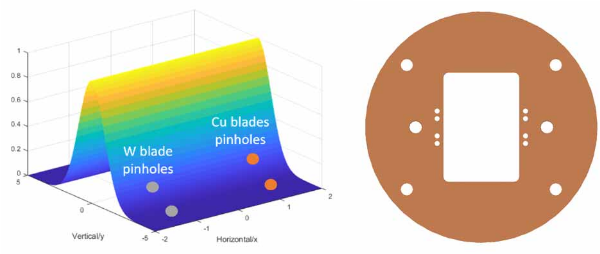

Figure 3: Beam distribution with pinhole samples and front view of XBPM mask.

Two blade materials were used, copper (Cu) and tungsten (W), to test any differences in sensitivity or accuracy. Figure 4 reveals the resolution of the prototype compared to the storage ring radio frequency (RF) BPM with fast orbit feedback disabled on the left side and after feedback is enabled on the right.

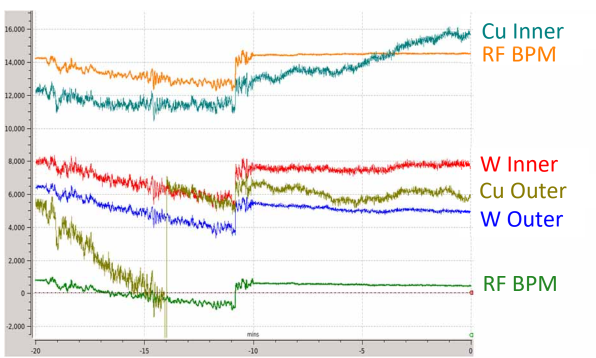

Figure 4: BPM signal level vs time.

The position resolution achieved is < 200 nm and short-term drifts appear to be < 2 µm over 10 minutes, whilst long term drifts were much larger, over a few hours, and were significantly dependent on beam current and temperature stability of low conductivity water (LCW) supply.

Limitations of XBPM Prototype

Even though, the results of the prototype seemed promising, given the aperture imposed by the first mask in the new beamlines, it has resulted in an extremely restricted orifice to accurately monitor beam position. Therefore, scaling down the photoemission prototype proved unrealistic due to space constraints. The beam fringes will be approximately 2.3 keV in the given area for the blade positions, which is around 8 x 6 mm and permitting the critical beam area of 2 x 1.5 mm in the centre. This prompted an investigation for different technologies to downscale.

Both photoemission and auger electron emission are surface layer processes therefore a thin film coating is sufficient and equivalent in signal intensity to a solid metal blade.

EXPERIMENTATION

Various trials were performed to determine if there was a viable method of creating "blades" from thin film coating. Laser cutting a diamond wafer was conducted to observe its feasibility to create unique shapes for assembly and design purposes.

Thin Film Coating

The first tests seen in Fig. 5 were two Cu blocks polished to 30 nm, coated in 500 nm of alumina (Al_2O_3) as an insulation layer, then a layer of 100 nm of gold (Au). The technique applied was electron beam (e-beam) deposition and differing Au widths were trialled to simulate varying "blade" thicknesses.

Secondly, in Fig. 5, a silicon wafer was similarly coated with 500 nm of Cu, then 500 nm of Al_2O_3 and 100 nm of Au, as prepared in the previous test. This was performed to assess the level of surface polishing required, as the silicon wafer emulates a near optimal polished Cu surface.

X-ray photoelectron spectroscopy (XPS) was used to analyse the sufficiency of thin film thickness and measure the drain current from Au.

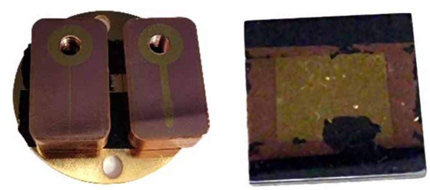

Figure 5: First and second test pieces.

The final coat test applied a strip of 100 nm thick Au on a diamond wafer to determine if there was an adequate drain current detected from the thin film.

Laser Cutting Diamond

A 2 mm hole was laser cut with a YAG laser type through an optical grade chemical vapour deposition (CVD) diamond wafer and the cut precision was observed.

RESULTS AND DISCUSSION

In Fig. 6, the first test result, with a photon energy level at 1.99 keV, produced a resolution of 200 µm with the drain current from Au, peaking at around 2 nA both at 400 sec and 700 sec for the two "blade" thicknesses. The insulating layer had an average of 0.7 nA and thus giving a differentiating factor of 2.86.

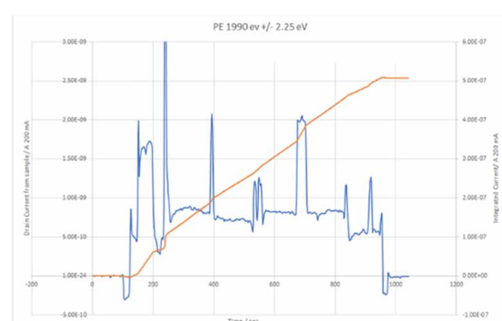

Figure 6: Drain and integrated current vs time.

The second test results proved better, with a photon energy level at 1.5 keV, as there was a drain current to insulator current ratio of 82.35, with Au peaking at 14 nA compared to the insulating layer of 0.17 nA.

This difference in the Au drain current to the insulating drain current ratio could be attributed to the polishing surface of the copper contrasted to the silicon surface.

ISBN: 978-3-95450-250-9 ISSN: 2673-5520 doi:10.18429/JACoW-MEDSI2023-TUPYP001

Additionally, the XPS indicated Cu was visible on the Al_2O_3 layer, which may suggest cavities in this layer.

Thirdly, the results in Fig. 7 revealed that the Au drain current average was 0.6 nA, opposed to the diamond drain current of 0.2 nA. The signal to noise ratio was suboptimal, and thus photoemission was discontinued as a viable option.

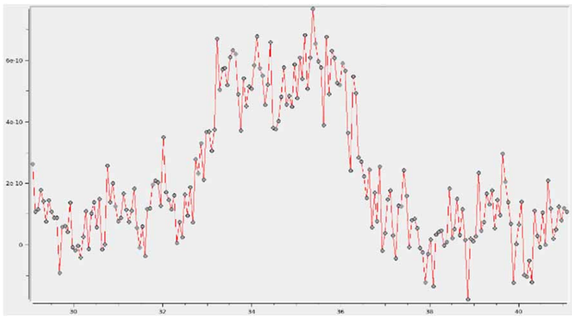

Figure 7: Drain current vs time.

Lastly, below in Fig. 8, it displays the uneven cut edge of the diamond and noticeable kerf after being laser cut.

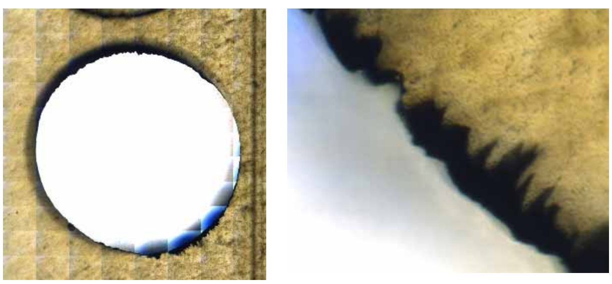

Figure 8: Laser cut diamond edges.

This result may increase stresses in the diamond when heated. It is intended that different laser cutting methods will continue to be investigated, such as newer laser cutting technology that utilises a waterjet stream simultaneously with the YAG laser which produces a cleaner edge [4].

TEMPERATURE-BASED APPROACH

The AS is in the early stages of developing an XBPM using a temperature-based approach. It is inspired by RTD technology where an increase in temperature will cause an increase in electrical resistance. A current is passed through the sensor and resistance is measured through the voltage drop across the track. Figure 9 shows a PT100 scanned by AS Micro-Computed Tomography (MCT) beamline and a render of a preliminary track design on a diamond wafer.

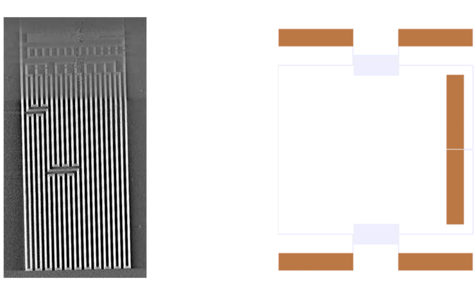

Figure 9: PT100 track and preliminary piece.

It is common for platinum (Pt) to be used as a track due to its wide temperature range, high melting point and stability over time. Diamond was selected as a substrate material as it had properties of high insulation and thermal conductivity. When the beam passes through the centre of the diamond, it will heat the middle while the sides of the wafer piece is being cooled by surrounding CuCrZr that is connected to LCW supply. The temperature sensor track will be coated on through photolithography. Early designs of this track for the XBPM is shown in Fig. 10.

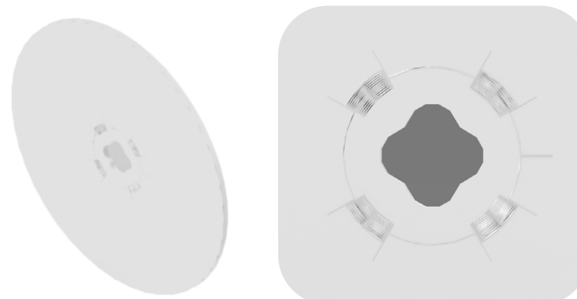

Figure 10: Early design of temperature-based approach.

The position of the beam will be determined by temperature, as there is a relatively linear relationship between thin film Pt resistivity and temperature [5].

Figure 11 shows both a finite element analysis (FEA) model of the diamond wafer and its temperature gradient in °C when the beam is going directly through the centre and when it is shifted 0.1 µm to the left.

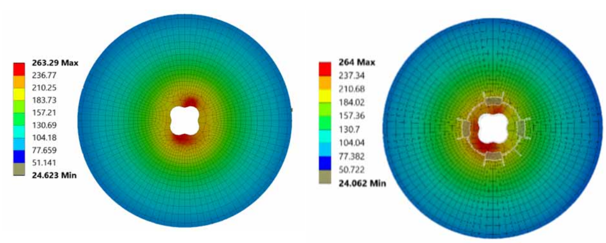

Figure 11: Beam travelling through the centre of piece (left) and beam with a 0.1 µm shift to the left (right).

This illustrates that there is a significant temperature change for a small movement in the beam as it is greater than 0.1 C change at the region of track placement. Some variables to also consider in the temperature-based approach are track material, size, and position for the best sensitivity.

CONCLUSION

After developing a prototype XBPM using the photoelectric effect, it has been shown that there are constraints of scaling the model and effect. Through experiments with thin film, valuable insight of its application has been gained, in addition to the limitations of certain laser cutting methods for diamond. Currently, the aim is to explore and establish an XBPM that utilises thermal properties to its advantage and further investigate the realm of XBPM possibilities.

ISBN: 978-3-95450-250-9 ISSN: 2673-5520 doi:10.18429/JACoW-MEDSI2023-TUPYP001

ACKNOWLEDGEMENTS

This work was performed in part at the Melbourne Centre for Nanofabrication (MCN) in Victorian Node of the Australian National Fabrication Facility, University of Melbourne School of Physics Advanced Materials Laboratory, and AS beamline scientists from MCT (Benedicta Arhatari, Andrew Stevenson), Soft X-ray (Bruce Cowie, Anton Tadich) and Infrared (IR) (Annaleise Klein).

Thank you to those who have helped in the XBPM projects - Brian Jensen, Trent Smith, Jason Wirthensohn, Andy Starritt, Adrian Hawley, Emily Griffin, Chris Ampt and Brad Mountford.

REFERENCES

[1] N. Hubert *et al.,* "Design of a new blade type X-BPM", in *Proc. IBIC'14*, Monterey, CA, USA, Sep. 2014, paper WEPD22, pp. 687-690.

[2] L.M. Volpe, "Blade XBPM optimizations for Sirius", presented at *MEDSI'16*, Barcelona, Spain, Sep 2016, paper not published.

[3] A. Kosicek and P. Leban, "Libera Brilliance and Libera Photon Working Together in Fast Orbit Feedback", in *Proc. ICALEPCS'09*, Kobe, Japan, Oct. 2009, paper THP070, pp. 797-799.

[4] Synova, `https://www.synova.ch/technology/synova-laser-microjet.html`

[5] J. Kim, J. Kim, Y. Shin, and Y. Yoon, "A study on the fabrication of an RTD (resistance temperature detector) by using PT thin film", *Korean J. Chem. Eng.,* vol. 18, no. 1, pp. 61–66, 2001. doi:10.1007/bf02707199

ISBN: 978-3-95450-250-9 ISSN: 2673-5520 doi:10.18429/JACoW-MEDSI2023-TUPYP004

A SETUP FOR THE EVALUATION OF THERMAL CONTACT RESISTANCE AT CRYOGENIC TEMPERATURES UNDER CONTROLLED PRESSURE RATES

B.A. Francisco†, W.H. Wilendorf, V.B. Zilli, G.S. de Albuquerque, D.Y. Kakizaki, V.C. Kuriyama, A.R. Ribeiro[1], J.H.R. dos Santos[2], M. Saveri Silva
Brazilian Synchrotron Light Laboratory, Campinas, Brazil.
[1] also at Federal University of Uberlândia, Uberlândia, Brazil
[2]also at Federal University of Rio Grande do Sul, Porto Alegre, Brazil

Abstract

The design of optical elements compasses different development areas, such as optics, structures, dynamics, thermal, and control. Thermal designs of mirrors aim to minimize deformations, whose usual requirements are around 5 nm RMS and slope errors in the order of 150 nrad RMS.

One of the main sources of uncertainties in thermal designs is the inconsistency in values of thermal contact resistances (TCR) found on the literature. A device based on the ASTM D5470 standard test was proposed and designed to measure the TCR among materials commonly used in mirror systems. Precision engineering design tools were used to deal with the challenges related to the operation at cryogenic temperatures (145 K) and under several pressures rates (1~10 MPa) whilst ensuring the alignment between the specimens. We observed that using indium as Thermal Interface Material reduced the TCR in 10~42,2% for SS316/Cu contacts, and 31~81% for Al/Cu. Upon analyzing the measurements, we identified areas for improvements in the equipment, such as mitigating radiation and improving the heat flow on the cold part of the system that were implemented for an upgraded version.

INTRODUCTION

Thermal contact resistance (TCR) is a parameter that indicates the ratio between surfaces temperature gradients of two bodies in contact and the heat load and exchanged.

A heat exchange measurement setup was developed for improving our database about TCR, especially for cryogenic applications, in which uncertainties become critical for the performance of the instruments.

It is well-known that during mechanical contact between solid bodies, the surfaces typically touch each other from less than 1% to 2% of the nominal contact area [1]. This limited contact area plays an essential role in reducing the heat load exchange. The TCR is also influenced by several variables, encompassing thermal factors (material properties, interface temperature, and heat flow direction), morphological aspects (shape, roughness, finishing), as well as mechanical conditions (applied pressure between the surfaces and potential deformations) in addition to those related to the other heat transfer mechanisms: radiation (emissivity) and convection (fluid characteristics between the surfaces), which is minimized in a vacuum environment.

An experimental approach was chosen since the diversity of models for calculating TCR values are limited to specific configurations. Among the known methods, including T-type, Infrared Thermography, Laser-Flash Method, and 3ω, the one with the lowest uncertainties (2-10%) [2] was selected: the Standard Steady-State Method. This method is comprehensively described in ASTM standard D5470-06 [3], and based on this standard, we developed a setup version for measurements at cryogenic temperatures.

EXPERIMENTAL SETUP

The standard test primarily involves column samples equipped with sensors. These samples are insulated to prevent heat loss through radiation and convection. A heat gradient is generated between the samples by using a heater, which is installed at one end, and a cooling source at the other end. A force actuator can be introduced to vary the stress across the samples. A test schematic is presented in Fig. 1. The temperature acquisition takes place after the system achieves a stationary state, and from this information, the contact region is determined.

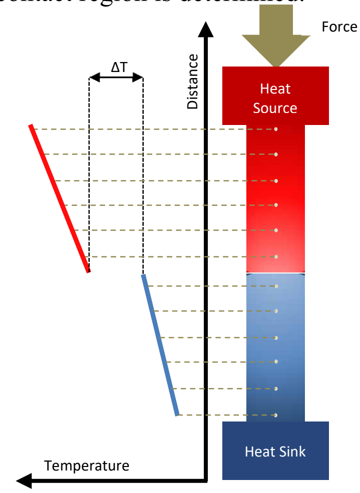

Figure 1: Diagram of how the data related to the standard steady-state method is obtained, from [4].

Thermal Management

Some adaptations were made in response to the cryogenic condition. The system was designed for operation within vacuum chambers, under a pressure level of $1 \cdot 10^{-7}$ mbar

†barbara.francisco@lnls.br

ISBN: 978-3-95450-250-9 ISSN: 2673-5520 doi:10.18429/JACoW-MEDSI2023-TUPYP004

produced by a turbo pump station. The cooling system employed was a Janis ST-100 open-cycle cryostat with relied on a liquid nitrogen flow and was maintained in contact with the system through copper braids. For a visual representation of the system, please refer Figs. 2 and 3.a).

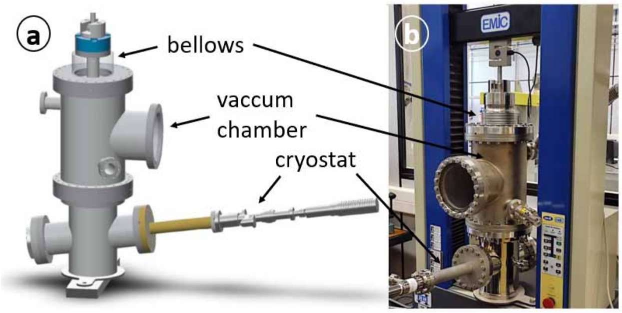

Figure 2. CAD representation (a) and photo (b) of the setup.

The support bases of the coldest temperature sample are depicted in Fig. 3.b). They were designed after a lumped-mass analysis to isolate the cold parts from the external environment, whose temperature remained above the dew point (~15 °C).

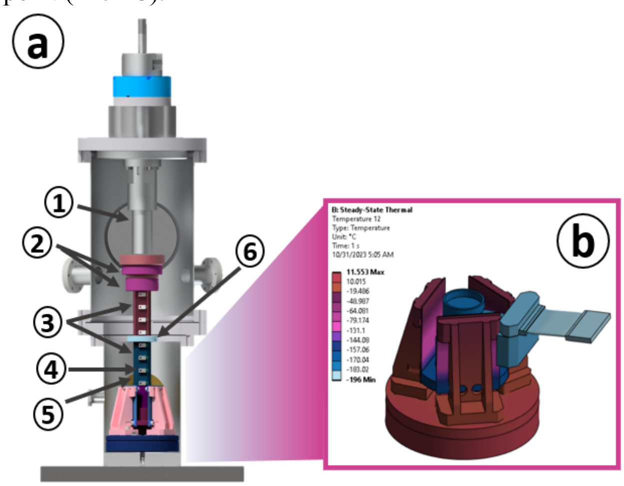

Figure 3: (a) CAD representation of internal view of the setup: 1. Piston; 2. Heaters Placement; 3. Samples; 4. Sensor; 5. Copper Braid; 6. Alignment Ring. (b) Thermal steady-state simulation of down part.

Testing Apparatus

The system was installed in an EMIC machine [5] (Fig. 2.b)). The force was transmitted unidirectionally to the samples in-vacuum through a specially designed bellows-piston feedthrough containing fittings to ensure the alignment and polymeric insulators to minimize heat leaks (Fig. 3.a)).

Samples with 35 mm diameter were selected to ensure that the range and resolution of forces provided by the EMIC actuator would result in pressures consistent with those applied in optical instruments at beamlines such as mirrors and monochromators. Additionally, this choice allowed for the accommodation of sensors with a significant temperature gradient between them.

Data Acquisition and Actuation

A CompactRio 9045 [6] device equipped with 9226 module was employed to monitor the temperatures from the Pt-2k thermal sensors whereas a 9403 module was used to regulate the 0~10 W heaters by sending the signal to an in-house designed amplifier [7]. Vacuum levels were read using a MKS cold cathode gauge [8] distinct from the pump station.

The heat load can be calculated from the heater current or from the slope of the curve using thermal conductivities from literature.

Force measurements were obtained via a script developed specifically for the EMIC machine, considering displacement inputs.

PRELIMINARY RESULTS

The prototype was applied for the determination of TCR of two contacts frequently present in thermal paths of optical instruments: Cu-SS and Cu-Al, both with and without indium as TIM (Thermal Interface Material).

Loads were incrementally applied, ranging from 0 to 12 kN, and subsequently returned to 0, with such cycle being repeated three times. The repetition aimed to ensure reproducibility of the data while also considering that, during the initial steps, under low loads, indium is not subject to plastic deformation.

The results for Cu-Al and Cu-In-Al when 1 kN (0.331 MPa) is applied are shown on in Fig. 4. The markers refer to the readings of the temperature sensors, which are interpolated to the contact region to calculate the temperature gradient and, consequently, the TCR.

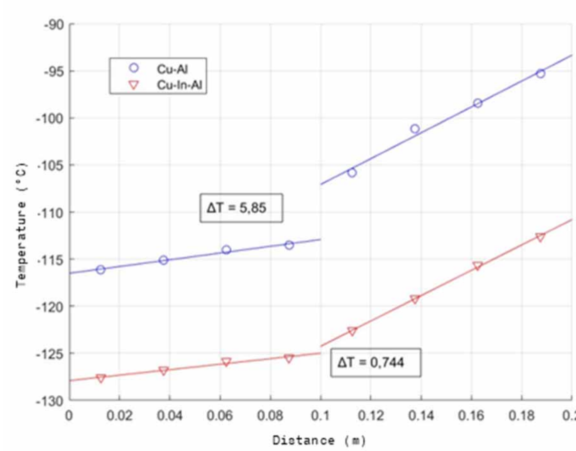

Figure 4. Temperature sensors positions vs temperatures for Cu-Al samples under 1 kN.

A summary of the TCR calculations at various pressures is presented in Fig. 5. The values range from 1.7E-5 m²K/W (Cu-In-Al @ 13.2 MPa) to 1.9E-3 m²K/W (Cu-SS @ 0 MPa). As expected, the inclusion of an indium layer results in a significant reduction in TCR, with the TCR decreasing as the applied pressure increases.

ISBN: 978-3-95450-250-9 ISSN: 2673-5520 doi:10.18429/JACoW-MEDSI2023-TUPYP004

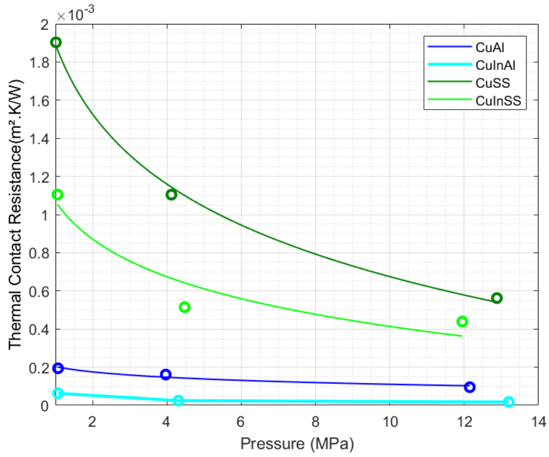

Figure 5: TCR for Cu-Al and Cu-SS pairs with and without indium as TIM as a function of the applied load.

Each point required a considerable amount of time to achieve the steady-state, particularly when dealing with low-diffusivity materials such as stainless steel and titanium. Conversely, due to the high thermal conductivity of copper, small temperature gradients emerged among the sensors, which compromised the data resolution. Besides that, the absence of radiation shielding also compromises the obtained values.

PERSPECTIVES

An upgraded setup is under design with the goal of improving the results accuracy and to shorten the test duration time. The upcoming version is incorporating a radiation shield and the heat exchange between cryostat and samples will be optimized, besides the exchange to a higher power heater.

Silicon samples have been machined for the evaluation of Cu-Si and SS-Si contacts. Moreover, we expect to extend the analysis by investigating varying levels of roughness on some pairs of material.

Finally, the addition of a mathematical analysis of errors and uncertainties associated with the measurements is required for a more accurate estimation of the final values.

CONCLUSION

A setup for the evaluation of thermal contact resistance (TCR) at cryogenic temperatures was proposed. Preliminary studies led to the conclusion that using indium as Thermal Interface Material reduced the TCR in 10~42% for SS316/Cu contacts, and 31~81% for Al/Cu.

We have ongoing plans for equipment enhancements, such as the introduction of a radiation shield, further investigations into contacts with varying surface roughness, and the application of mathematical analysis to refine result accuracy. Our work expects to advance the understanding of TCR and contribute to more effective thermal designs for optical instruments.

REFERENCES

[1] M. Bahrani, J. Culham, M. Yananovich, *et al.,* “Review of thermal joint resistance models for nonconforming rough surfaces”, *Appl. Mech. Rev.,* vol 59, no. 1, pp. 1-12, 2006. doi:10.1115/1.2110231

[2] Y. Xian, P. Zhang, S. Zhai, P. Yuan, *et al.,* “Experimental characterization methods for thermal contact resistance: A review”, *Appl. Therm. Eng.,* vol. 130, pp. 1530-1548, 2018. doi:10.1016/j.applthermaleng.2017.10.163

[3] ASTM International, “*Standard Test Method for Thermal Transmission Properties of Thermally Conductive Electrical Insulation Materials*”, ASTM D5470-06, 2006.

[4] Z. Bulinski *et al.,* “Determination of the thermal conductivity of solids based on the ASTM D 5470 standard”, *Steel Metals and New Technologies*, vol. 3-4, pp. 57-62, 2019.

[5] https://www.emic.com.br/

[6] https://www.ni.com/pt-br/shop/model/crio-9045.html

[7] M.M. Donatti, D.H.C. Araujo, F.H. Cardoso, G.B.Z.L. Moreno, L. Sanfelici, and G.T. Semissatto, “Multi-Channel Heaters Driver for Sirius Beamline’s Optical Devices”, in *Proc. ICALEPCS'21,* Shanghai, China, Oct. 2021, pp. 705-709. doi:10.18429/JACoW-ICALEPCS2021-WEPV026

[8] https://www.mks.com/p/104220008

ISBN: 978-3-95450-250-9 ISSN: 2673-5520 doi:10.18429/JACoW-MEDSI2023-TUPYP005

ON THE PERFORMANCE OF CRYOGENIC COOLING SYSTEMS FOR OPTICAL ELEMENTS AT SIRIUS/LNLS

B. A. Francisco†, M. P. Calcanha, L. M. Volpe, G. P. Lima, L. M. Kofukuda, R. R. Geraldes, M. Saveri Silva
Brazilian Synchrotron Light Laboratory, Campinas, Brazil

Abstract

Several of Sirius' beamlines employ cryogenically cooled optics to take advantage of the silicon properties at low temperatures. A series of improvements has been evaluated based on our early operational experience focusing on the prevention of thermal instabilities of the optics. This work discusses the performance of the systems after optimizing the pressure of the vessels and their control logics, the effectiveness of occasional purges, and the cooldown techniques, and presents the monitoring interface. Furthermore, we introduce solutions (commercial and in-house) for achieving better beam stability, featuring active control of liquid nitrogen flow. We also propose the approach for the future 350 mA operation, including different cooling mechanisms.

INTRODUCTION

Sirius light source demands high performance instruments for ensuring photon-beam quality, especially in terms of wavefront integrity and position stability. Effective cooling of numerous silicon optical elements is essential to precisely control temperatures and related parameters, ensuring acceptable thermal effects regarding figure distortions and drifts at various timescales. Achieving the necessary precision equipment standards relies on robust thermal design. An alternative for cooling optical instrumentation in CATERETÊ [1] and CARNAÚBA [2] beamlines was described by Saveri Silva, et al [3]. This solution used open-cycle cryostats and continuous 24/7 functioning according to the diagram in Fig. 1. This approach was selected as a cost-effective alternative to closed-cycle cryocoolers for handling low-to-medium thermal loads with low vibration. Some of the adopted strategies continue to be integrated into the ongoing operation. However, during the working phase, it became evident that various instabilities occurred, posing significant hurdles to the reliable performance of the system.

The current research delves into an analysis of these instabilities and the series of tests undertaken to develop effective strategies for their mitigation. Three instances of instability were observed: temperature drifts (I) at the optics initiated after gradual variations in the temperature of the cold fingers at the end of the cryostats, variations associated with changes in the pressure (II) of the liquid nitrogen (LN2) vessels, and significant temperature spikes (III) during their refilling, as illustrated in Fig. 2.

It is believed that the explanation for all cases is related to the formation of vapor films at the cold fingers, Fig. 1. In the first case, there may be a gradual growth of the vapor film until the cold finger reaches a critical temperature, beyond

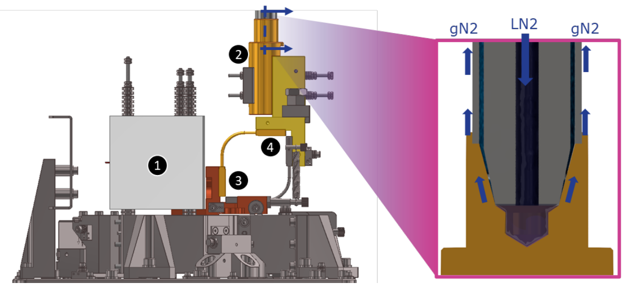

Figure 1: The second mirror (1) of CATERETE beamline is thermally connected to a cryostat (2) by a copper braid (3-4). In detail, the operation of the coupled open flow cryostat.

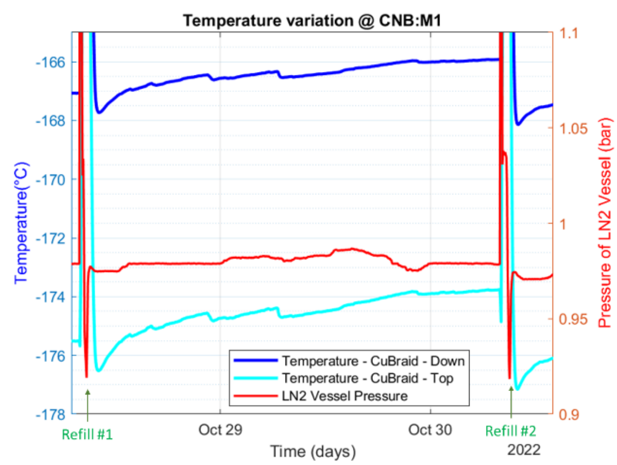

Figure 2: Temperature of a copper braid between first mirror and cold finger at CARNAÚBA beamline presenting drifts (case I), pressure-dependent variation (case II) and spikes (case III) during the refill.

which the current of the heaters that control the temperatures of the parts reaches zero and temperature variations in the optics start. In the other cases, the forced entry of vapor into the transfer line is the primary trigger for these variations [4].

It was noted that agitating the transfer line, whether through manual shaking or temporarily adjusting the flow (by a manual needle valve) and then returning it to its previous state, was sufficient to make temperatures decrease. However, this approach would require the operator to be systematically monitoring the graphs. Consequently, a general solution to these challenges could be achieved by implementing a closed-loop automatic control that adjusts the flow of liquid nitrogen based on the cold finger temperature, or, for the second and third cases, by implementing a solution that

12th Int. Conf. Mech. Eng. Design Synchrotron Radiat. Equip. Instrum. MEDSI2023, Beijing, China JACoW Publishing
ISBN: 978-3-95450-250-9 ISSN: 2673-5520 doi:10.18429/JACoW-MEDSI2023-TUPYP005

effectively prevents vapor from entering the transfer line, which motivated a test with a Phase Separator prototype.

INITIAL UPGRADES

The active pressure control approach for the primary vessels (that are connected directly to the cryostats) using solenoids induced mechanical impulses contributing to temperature fluctuations at the cryostat's end. Initially, passive relief valves were used as an alternative, resulting in clearance and non-repetitive oscillations, particularly during refilling. Subsequently, a passive control strategy was implemented by introducing nitrogen gas to a vent valve connected to a regulating valve, which exhibited periodic fluctuations.

In addition, the setpoint for this pressure control was decreased to enhance the system's flow adjustment sensitivity. Furthermore, the setpoint of maximum level was decreased to 90 % to prevent ice formation near the needle valve. The pressure of the secondary vessels (those located outside the hutch, which supply the primary ones.) was also reduced to minimize the pressure gradient during refilling.

Additionally, a purging process was standardized to eliminate water of the circuit. The purging process involved introducing heated N2 gas at 100 °C into the vessels and transfer lines until the gas emerged hot, followed by 12 additional hours of purging. After that, the transfer line needle valve is closed, and the transfer line is introduced into the cryostat. The dewar is then filled with liquid nitrogen, and the cooldown process is initiated with the cryostat being pumped by a vacuum pump. Finally, the vacuum pump is disconnected, and once the temperature stabilizes, the needle valve is adjusted.

An updated user-interface enables scheduling (date and time) for LN2 refills. Furthermore, the system incorporates a safety feature that, regardless of the time, triggers a forced filling if the level of the vessel falls below 30 %. A timeout ensures that no filling takes longer than 2h30 min, which prevents excessive interference of the process with the beamline time and contributes to operational safety. Additionally, if a timeout occurs during the filling process or if the system experiences faults, an email notification will be automatically sent to the individuals responsible for the subsystem, allowing for a quicker response to any potential issues. All variables are archived in EPICS [5] and shown by the human-machine interface (HMI) whereas a supervisory system centralizes information from all cryogenic systems in Sirius, allowing a quick check of levels, pressures, status, and alerts.

AUTOMATIC FLOW CONTROL

As mentioned in the previous section, at times, the needle valve needed to be manually adjusted. In order to make these sets at all times without the need to open the hutch and consequently shut down the beamline, the installation of a motorized bayonet was proposed. A transfer line between primary LN2 vessel and cryostat was replaced by a commer-

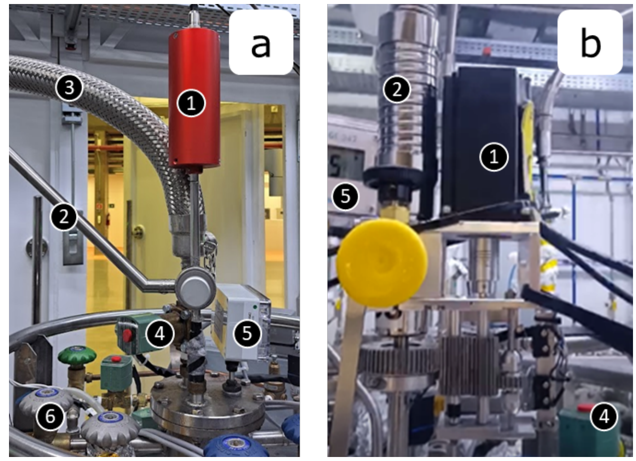

Figure 3: Commercial (a) and in-house (b) actuators (1). Also highlighted: transfer lines between primary vessel and cryostat (2), transfer line between vessels (3), valves for automatic filling (4), level gauge (5) and vent valve (6).

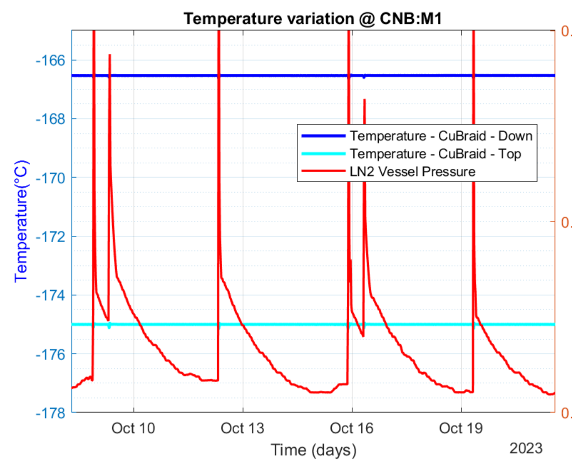

Figure 4: Temperature versus time for M1 Carnauba after introducing the commercial flow control valve. The red curve shows pressure fluctuation when operating with passive control.

cial transfer line with automatic needle valve (Fig. 3(a)), that receives a 0–10 V signal from the same CompactRio [6] that is already associated to the optics. The PID control loop is closed by reading the temperature of the mirror.

This approach resulted in a 95 % reduction in the amplitude of temperature variations over 10 days (Fig. 4) even during refills as well as an 80 % reduction in beam movement.

A prototype was developed to motorize the needle valves currently in use, as shown in Fig. 3(b). This prototype featured a stepper motor coupled to the needle valve through gears in a ratio of 2.8:1. The control loop uses signals from temperature and from a rotary encoder, whereas mechanical limit switches were applied for homing and safety. The result of the bench test confirmed that the solution can eliminate drifts. The temperature was controlled within ±0.9 °C during 16 hours (Fig. 5(a)), which is expected to be fur-

ISBN: 978-3-95450-250-9 ISSN: 2673-5520 doi:10.18429/JACoW-MEDSI2023-TUPYP005

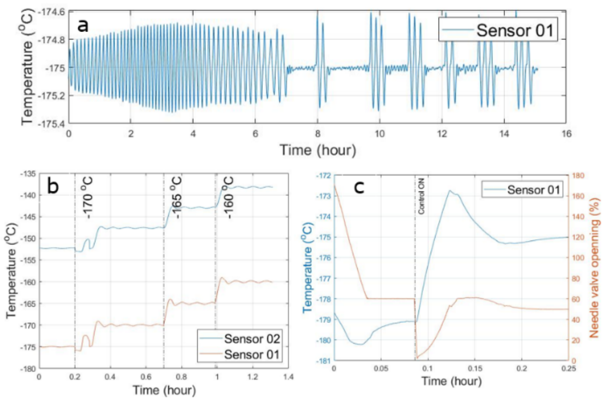

Figure 5: Temperature controlled for 16 hours during bench testing with unoptimized PID (a); setpoint selection for cryostat tip (b); activation of the PID control of the prototype when assembled at CARNAUBA 2nd Mirror.

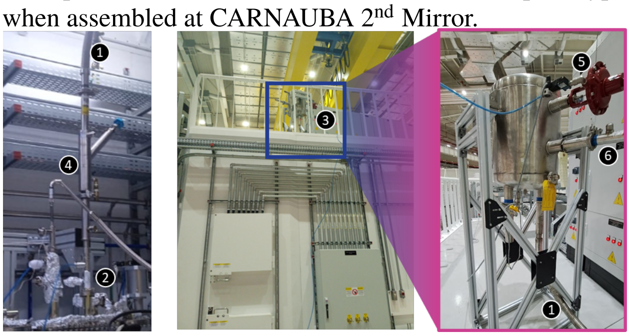

Figure 6: PS setup. A transfer line (1) connects the cryostat (2) to the PS (3) above the hutch. A manual valve (4) regulates the LN2 flow between them and an automatic valve (5) controls the LN2 level inside the PS, that is supplied by the secondary LN2 vessel by the 2nd transfer line (6).

ther improved after PID optimization. Other improvements aimed at field application are the replacement of the mechanical limit switch by inductive ones aiming to reduce backlash and improve the homing procedure. Figure 5(b) illustrates that the flow control mechanism prototype allows for setpoint adjustment. Figure 5(c) displays the moment when the flow control prototype is active in CARNAUBA second mirror.

PHASE SEPARATOR

A customized setup was assembled (Fig. 6) wherein a phase separator (PS) replaced the primary vessel. The PS was positioned atop of the optical hutch containing the first mirror of the CARNAÚBA beamline and fed the cryostat by gravity. A manual valve was introduced to regulate the flow between them. As this setup was a prototype using in-house equipment, its length was notably extended due to the need for adaptations among various vacuum-isolated connections.

Significant temperature fluctuations were observed in this setup, as seen in Fig. 7, which were not reduced by increasing the flow rate. Such oscillations were not related to variations

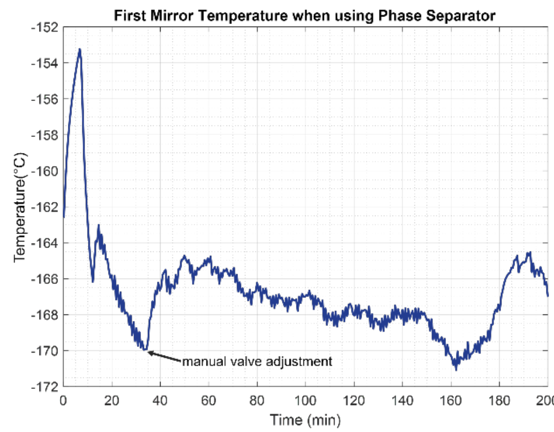

Figure 7: Temperature fluctuations of first mirror of CARNAUBA along 4 hours of cooling using the PS.

in the pressure of the LN2 vessel or to the opening of the PS valve. The working hypothesis is that the fluid undergoes a phase change along the path between PS and cryostat. For future applications, it would be beneficial to build a more compact circuit to ensure effective thermal insulation and stability of the transfer line.

In comparison to the motorized bayonet, the mirror supplied by PS exhibited more vibration at both high and low frequencies, suggesting that switching to the PS is not advisable for the current system.

NON-CRYOGENIC SOLUTIONS

The flow control approach presented good perspectives and the in-house actuator tends to be economically advantageous. Despite of this, sporadic instability events persist related to the cryogenic circuit or even mechanical vibration transmitted by the thermal path between large mirrors and cryostats.

Preliminary simulations assuming higher temperatures indicate the possibility of keeping acceptable deformation rates on the surfaces of some mirrors currently cryogenically cooled. Therefore, three new designs have been considered using Peltiers with 0.5–9 W range and ±0.01 °C resolution.

CONCLUSIONS

This study focused on the actions taken to improve the performance of open-circuit cryogenically cooled systems at Sirius/LNLS, addressing temperature drifts, pressure variations, and temperature spikes during refilling. We implemented automatic flow control, enhancing system stability. The use of a Phase Separator was explored, but further investigation is needed. Now, even looking ahead to 350 mA operation, non-cryogenic solutions like Peltiers have been contemplated as viable options for some mirrors. In the other hand, motorizing transfer lines emerge as a promising solution for the optical instruments that will remain cryogenic.

ISBN: 978-3-95450-250-9 ISSN: 2673-5520 doi:10.18429/JACoW-MEDSI2023-TUPYP005

REFERENCES

[1] F. Meneau, *et al.*, “Cateretê: the coherent X-ray scattering beamline at the fourth-generation synchrotron facility SIRIUS”, *Acta Crystallogr., Sect. A: Found.*, vol. A77, p. C283, 2021. doi:10.1107/S0108767321093995

[2] H. C. N. Tolentino, *et al.*, “Innovative instruments based on cryogenically cooled silicon crystals for the CARNAÚBA beamline at Sirius-LNLS”, *AIP Conf. Proc.*, vol. 2054, no. 1, p. 060026, Jan. 2019. doi:10.1063/1.5084657

[3] M. Saveri Silva *et al.*, “Cryogenic systems for optical elements cooling at Sirius/LNLS”, in *Proc. MEDSI'20*, Chicago, USA, Jul. 2021, pp. 21. doi:10.18429/JACoW-MEDSI2020-MOPB02

[4] M. Kida *et al.*, “Pool-Boiling Heat Transfer in Liquid Nitrogen”, *J. Nucl. Sci. Technol.*, vol. 18, no. 7, pp. 501–513, 1981. doi:10.1080/18811248.1981.9733284

[5] EPICS - Experimental Physics and Industrial Control System, https://epics-controls.org/

[6] CompactRIO Systems (22 August 2023), NI, https://www.ni.com/en/shop/compactrio.html

ISBN: 978-3-95450-250-9 ISSN: 2673-5520 doi:10.18429/JACoW-MEDSI2023-TUPYP008

EXACTLY CONSTRAINED, HIGH HEAT LOAD DESIGN FOR SABIA'S FIRST MIRROR*

V. B. Zilli†, B. A. Francisco, G.G. Basilio, J.C. Cezar, A.C. Pinto, V. S. Ynamassu, R.G. Oliveira, G.R.B. Ferreira, F. A. Del Nero, G. L. M. P. Rodrigues, R.R. Geraldes, M.E.O.A Gardingo, C. Ambrosio, L. M. Volpe
Brazilian Synchrotron Light Laboratory, Campinas, Brazil

Abstract

The SABIA beamline (Soft x-ray ABsorption spectroscopy and ImAging) will operate in a range of 100 to 2000 eV and will perform XPS, PEEM and XMCD techniques at SIRIUS/LNLS. Thermal management on these soft x-ray beamlines is particularly challenging due to the high heat loads. SABIA's first mirror (M1) absorbs about 360 W, with a maximum power density of 0.52 W/mm², and a water-cooled mirror was designed to handle this substantial heat load. To prolong the mirror operation lifetime, often shortened on soft X-ray beamlines due to carbon deposition on the mirror optical surface, a procedure was adopted using high partial pressure of O_2 into the vacuum chamber during the commissioning phase. The internal mechanism was designed to be exactly constrained using folded leaf springs. It presents one degree of freedom for control and alignment: a rotation around the vertical axis with a motion range of about ±0.6 mrad, provided by a piezoelectric actuator and measured using vacuum compatible linear encoders. This work describes the SABIA's M1 exactly constrained, high heat absorbent design, its safety particularities compared to SIRIUS typical mirrors, and validation tests results.

INTRODUCTION

Unique challenges emerged with the introduction of innovative optics instruments such as DCML [1] and the exactly constrained mirrors for the Sirius facility. The solution for SABIA's first mirror consists of an exactly constrained side bounce mirror [2] with direct internal cooling. The technical commission of SABIA Beamline (SAB) started on the early 2023. The beamline optical layout is shown on Figure 1.

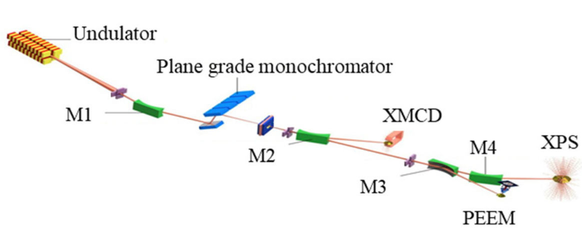

Figure 1: SABIA's optical layout.

Internal water cooling is not new for the synchrotron community, it has been proposed as a solution for previous generation sources heat management [3] but it still been used by some of the major manufacturers [4] as it can manage high heat load. Hose connections pose electronic and vacuum safety challenges, demanding meticulous mechanical isolation and leak protection. We looked at this with special attention to ensure both safety in case of coolant leakage, and mechanical decoupling on important degrees of freedoms.

THERMO-MECHANICAL DESIGN

The SAB M1 mechanism is comprised of two main parts. The first one is the granite bench, responsible for rough alignment and mechanical support for the ultra-high-vacuum vessel [5]. The other is the multifunctional internal mechanism, as it is the mirror support, short stroke for fine alignment, thermal insulator, and thermo-mechanical deformation accommodator. The main requirements for this system's internal mechanism can be found on Table 1.

Table 1: System Summarized Specs

Description	Spec
Ry range:	> 1 mrad
Ry resolution:	< 150 nrad
Resonances:	> 100 Hz
Max beam distortion	<10% nominal size
Power load @ 300mA:	~ 360 W
Cooling scheme:	Internal water flow

Figure 2 shows the complete in-vacuum parts for this system: A) the mirror with internal water channels; B) photo-collector used as indirect beam illumination over the optical face; C) the mirror support and metrology assembly, including the frame (often called *"Patrick")*, responsible for the fine mechanical motion and metrology and thermal deformation accommodator and Folded Leaf Springs (FLS); D) optical encoders RL26BVS001C30V [6], for fine metrology; E) fine rotation motion stiff actuator N-470.U PiezoMike [7]; F) water hose and vacuum guard assembly; G) water and safety vacuum inlet/outlet.

* Work supported by Brazilian Ministry of Science, Technology, and Innovation
† vinicius.zilli@lnls.br

ISBN: 978-3-95450-250-9 ISSN: 2673-5520 doi:10.18429/JACoW-MEDSI2023-TUPYP008

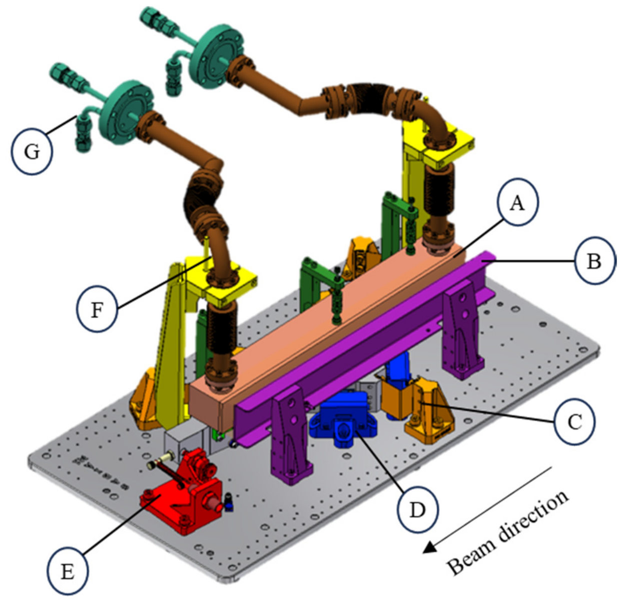

Figure 2: Complete internal mechanism of SAB M1.

Mechanical Design and Results

An optimization-based design process was adopted to improve the design, employing analytical models for a first adequate system layout, and the Finite Element Analysis method using both mechanical and thermal simulations on Ansys. By using Ansys DesignXplorer, we identified potential design enhancements, achieving greater stiffness without sacrificing motion range, despite a great computational expense. The result was an exactly constrained rotation mechanism with range of ± 0.6 mrad about the vertical axis (Y axis) with a 1° natural frequency of 136 Hz.

By utilizing a flexible water hose allowed us to maintain continuous mirror rotation around the vertical axis. The hose is safeguarded by a vacuum enclosure. This dedicated low vacuum system features pressure monitoring to detect leaks, ensuring electronics and vacuum protection. Parasitic forces are minimized by anchoring the hose vacuum guard on the frame, eliminating direct forces on the water nozzle brazed to the substrate. Hose placement directs parasitic forces along the beam axis, the mirror's least sensitive direction. An upstream mask was implemented to prevent beam illumination on the side face, to protect the mirror's brazed optical face interface. Figure 3 shows the motion range scan test using the systems encoders, the motion shows little influence of the hoses on the motion range and linearity.

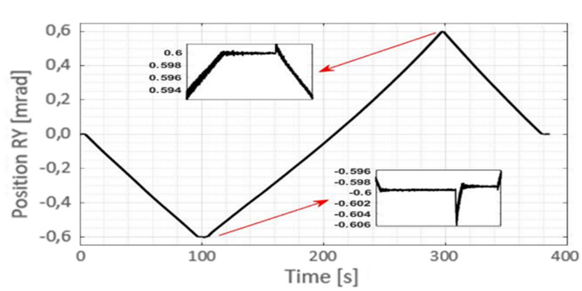

Figure 3: Mechanism motion scan.

Thermal Management

The mirror substrate was designed to incorporate internal channels allowing the cooling liquid to flow through the system. To ensure the minimal deformation possible, simulations were conducted at various flow rates, considering the manufacturer-provided pressure limits within the mirror. The smallest thermal deformation achieved was 176 nm PV, with a flow rate of 5.2 lpm at 24°C. For comparison, gravity deformations account for only 3 nm. Despite efforts to enhance the heat exchange within the system, the reduction of the cross section on the transition between the inlet and the channels resulted on the relaminarization of the flow. While larger water flux promises improved thermal performance, the elevation of internal water pressure over the optical face increases the deformations. Figure 4 shows Computational Fluid Dynamics results on the water flow and the mirror thermal gradient, besides the thermal deformation profile on caparison to gravity deformations.

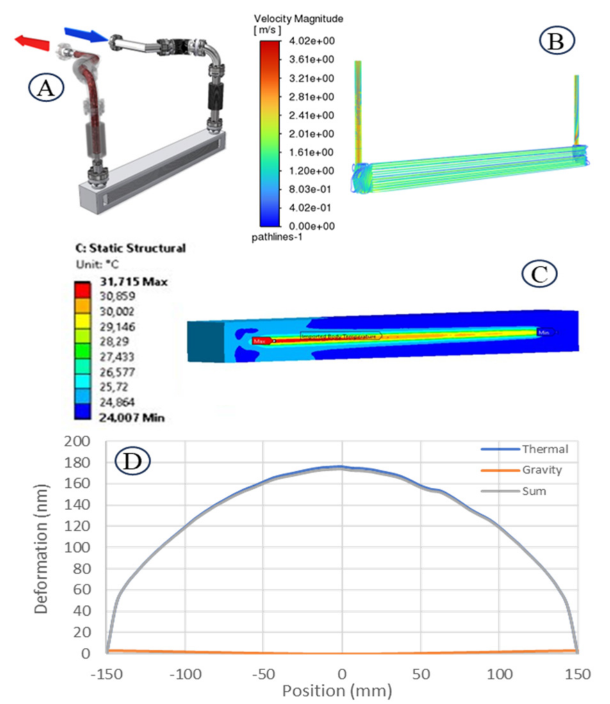

Figure 4: A) Mirror internal channels and the water hose assembly; B) Flow relaminarization due to the cross section abrupt change; C) Thermal gradient on the mirror; D) deformation profile on the optical face.

Assembly and Validation Results

The assembly and installation of this mechanisms followed the standardized procedure described on [8, 9], except for the clamping process. The mirror was glued to the mirror frame using MasterBond 42HT-2LO epoxy adhesive [10] and micro silica spheres of 53 µm to ensure a uniform glue layer using the method described on [11]. The optical surface was measured before and after the gluing to characterize the deformation induced by the glue shrinkage, since it is very complicated to be simulated. The

12th Int. Conf. Mech. Eng. Design Synchrotron Radiat. Equip. Instrum. MEDSI2023, Beijing, China JACoW Publishing
ISBN: 978-3-95450-250-9 ISSN: 2673-5520 doi:10.18429/JACoW-MEDSI2023-TUPYP008

comparison of the mirror deformation before and after the glue shrank down, measured in-house by a Fizeau interferometer as well as the supplier measurements, are shown on the Figure 5.

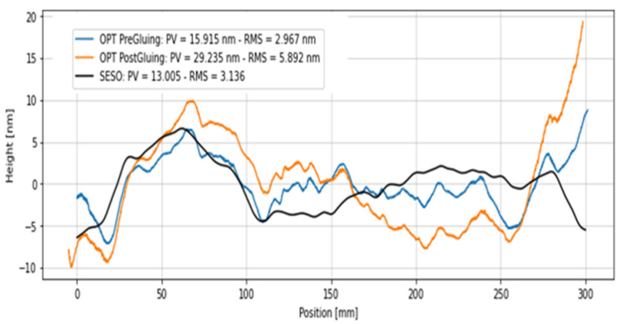

Figure 5: Heigh-error before and after the cured of the glue.

Some tests were executed to validate the mechanical performance. Modal testing was conducted before and after gluing using 3D axial 8762A5 accelerometer and PDV-100 vibrometer. By comparing test results and simulations we could identify assembly unconformities, FLS manufacturing irregularities and the effects of the glue on the dynamical performance.

The encoders were used to characterize the system stability after installation on its granite bench, in vacuum, shown on Figure 6. These tests were conducted both with the cooling system activated and deactivated, to distinguish the impact of water flow-induced vibrations. The results indicated that the cooling system increased over 35% of the mechanical instability. The system's designed and achieved performances are summarized on Table 2.

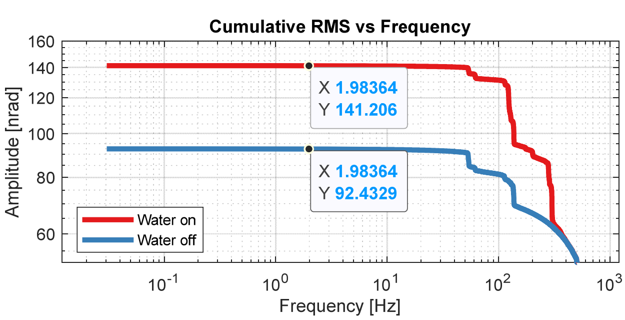

Figure 6: Cumulative amplitude spectrum of the random vibrations on the mechanism.

Table 2: Mechanism Performance

Description	Designed	Tested
Motion range [mrad]	0.604	0.6
Motion resolution [nrad]	135	129
1° Natural Frequency [Hz]	135,57	136
Stability [nrad]	--	141
Vacuum guard pressure [mbar]	1e-3	1e-8
Thermo-Mechanical deformation [nm]	173	--

Commissioning Results

During the early stages of technical commissioning, the M1 system was set under 1e-7 mbar of partial pressure of oxygen gas, as a test to slow down or prevent carbon deposition on the optical surface. Figure 7 shows a RGA monitoring of the vacuum chamber. It is possible to observe the changing on partial pressures when the system is illuminated by the photon beam, indicating that hydrocarbons and/or other carbon-based structures are reacting with the oxygen. More studies and testing are necessary to certify that this method works and how long can it prolong the mirror lifetime.

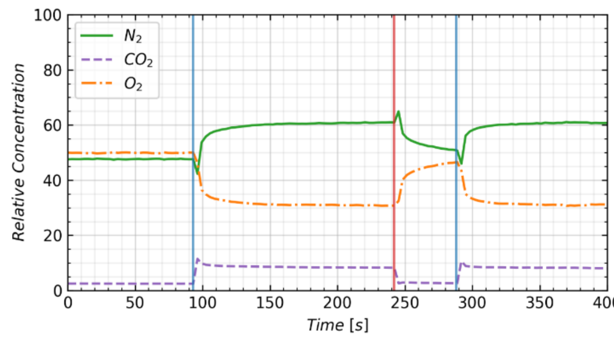

Figure 7: RGA monitoring during the M1 commissioning phase. The blue lines indicate the shutter opening, the red its closure. N_2 was monitored as it has the same atomic mass of carbon monoxide, changes on its concentration indicates that we were indeed monitoring CO on our experiment.

CONCLUSION

The SABIA M1 exactly constrained, high heat absorbent mirror was designed, assembled, and commissioned in 2023. The challenge on this design was to combine an internal water-cooled mirror with precision engineering concepts. Using a combination stiff actuator and FLS we developed a highly linear and stable mechanism. To protect both vacuum levels and electronics used, a vacuum guard was designed to encapsulate the water hoses used to cool the mirror down during operation.

As it is complex to determine the water flow induced vibration contribution on stability on the water hoses, tests were performed. It shows that water flow is responsible on over 35% of the instabilities. Yet this represent only 2nm increase on linear instabilities, when converted to rotation it is about 49nrad.

By using a partial pressure of oxygen gas onto the vacuum chamber we observed possible reactions with carbon-based structures on an attempt to prolong the mirror lifetime, but we need more testing to be certain. In the forthcoming months the SABIA beamline shall end its technical commissioning and entered the scientific commissioning.

ACKNOWLEDGEMENTS

The authors would like to gratefully acknowledge the funding by the Brazilian Ministry of Science, Technology and Innovation, the contributions of the LNLS team and partners.

ISBN: 978-3-95450-250-9 ISSN: 2673-5520 doi:10.18429/JACoW-MEDSI2023-TUPYP008

REFERENCES

[1] A. V. Perna *et al*. "The HD-DCM-Lite: A High-Dynamic DCM with Extended Scanning Capabilities for Sirius/LNLS Beamlines", in *Proc. MEDSI'20,* Chicago, USA, Jul. 2021, pp. 203-206. doi:10.18429/JACoW-MEDSI2020-TUPC11

[2] R. R. Geraldes *et al*., "THE DESIGN OF EXACTLY-CONSTRAINED X-RAY MIRROR SYSTEMS FOR SIRIUS" in *Proc. MEDSI'18*, Paris, France, Jun. 2018, pp. 173-178. doi:10.18429/JACoW-MEDSI2018-WEOAMA04

[3] R. DiGennaro *et al*., "A water-cooled mirror system for synchrotron radiation", *Nucl. Instrum. Methods Phys. Res. Sect. A, Accelerators, Spectrometers, Detectors and Associated Equipment*, vol. 266, issues 1–3, pp. 498-506, 1988, ISSN 0168-9002. doi:10.1016/0168-9002(88)90437-8

[4] P468 – MIRROR UNIT IPE LNLS, https://www.bestec-berlin.de/2019/optics/product-category/mirror-unit/p468-mirror-unit-ipe-lnls/

[5] R. R. Geraldes *et al.* "Granite benches for sirius x-ray optical systems", in *Proc. MEDSI'18*, Paris, France, Jun. 2018, pp. 361-364. doi:10.18429/JACoW-MEDSI2018-THPH12

[6] Plc, R. (n.d.). Renishaw: RESOLUTETM UHV com escala linear RTLA30, https://www.renishaw.com.br/pt/sistema-de-encoder-absoluto-resolute-uhv-com-escala-linear-rtla30--18333

[7] GmbH, P. I. (n.d.), N-470 PiezoMike Linear Actuator, Physikinstrumente, https://www.physikinstrumente.com/en/products/linear-actuators/piezomike-for-long-term-stability/n-470-piezomike-linear-actuator-1000140

[8] G. Rovigatti, H. Geraissate, R. Leao. "Alignment strategies and first results on Sirius beamlines", in *Proc. MEDSI'20*, Chicago, USA, Jul. 2021, pp. 349-352. doi:10.18429/JACoW-MEDSI2020-THOA03

[9] V.B. Zilli *et al*., "Installation and Commissioning of the Exactly-Constrained X-Ray Mirror Systems for Sirius/LNLS", in *Proc. MEDSI'20*, Chicago, USA, Jul. 2021, pp. 33-36. doi:10.18429/JACoW-MEDSI2020-MOPB06

[10] EP42HT-2LO Product Information, MasterBond.com (n.d.), https://www.masterbond.com/tds/ep42ht-2lo

[11] F. R. Lena. "Determinação de métodos de colagem com resinas epóxi para fixação de espelhos para raios X em linhas de luz da fonte de radiação síncrotron Sirius". doi:10.13140/RG.2.2.28802.66248

ISBN: 978-3-95450-250-9 ISSN: 2673-5520 doi:10.18429/JACoW-MEDSI2023-TUPYP015

INVESTIGATION OF VIBRATIONS ATTENUATION WITH DIFFERENT FREQUENCY ALONG HEPS GROUND

Yuning Yang[1], Fang Yan†, Zihao Wang, Xiangyu Tan
The Institute of High Energy Physics of the Chinese Academy of Sciences, Beijing, China
Xiangrong Fu, Wenjie Wu, Lan Yan, China Agricultural University, Beijing, China
Jun Lei, Peking University, Beijing, China
[1]also at China Agricultural University Beijing, China

Abstract

High Energy Photon Source (HEPS) has a strict restriction on vibration instabilities. To fulfil the stability specification, vibration levels on HEPS site must be controlled. The control standards are highly related with the vibration amplitude of the sources and the distance between sources and the critical positions. To establish reasonable regulations for new-built vibration sources, the decay patterns are investigated on HEPS site for different frequency noises. A series of experiments were conducted using shaker to generate vibrations with frequency from 1 Hz up to 100 Hz. The vibration attenuation on ground and slab were measured using seismometers and the attenuation law were analysed. Details will be presented in this paper.

INTRODUCTION

With the usage and development of high precision equipment, the impact of vibrations on large scientific facility is becoming increasingly prominent. Depending on source of the vibrations, the noises can be classified into artificial vibrations and natural vibrations [1]. Natural vibration include ground motions, wind-induced vibrations, water wave vibrations et al., while artificial vibration include vibrations generated by vehicles, light rail, building facilities, large machinery et al.. The random noise generated by these vibration sources can have a significant impact on the resolution and sampling efficiency of equipment. In severe cases, it can even cause expensive equipment or system unworkable. Therefore, controlling the internal and outside vibrations are necessary [2].

Due to the non-uniformity of the ground medium and the uncontrollability of random noise (frequency, amplitude), it is difficult to accurately predict the vibrations generated by external vibration sources using widely used Bornitz model [3]. Therefore, it is necessary to propose more reasonable prediction formulas based on the measured attenuation data on HEPS.

To ensure the validity of the measurement data, the self-noise measurement of the employed instrumentation was conducted, and compared with the environmental noise level on the foundation of HEPS storage ring and the vibration amplitude transmitted over a distance of 170 m from the shaker. Subsequently, vibrations with frequency of 1 Hz up to 100 Hz were generated using the shaker, and the ground and floor vibrations along the propagation line were measured using a seismometer. The attenuation of these vibrations was analysed and presented in this paper.

Instrumentation

The seismometers and velocimeters used in this experiment include five Gaia Code Alpha and three Guralp 3espcde all-in-one seismometers and the detailed parameters of these equipment are listed in Table 1:

Table 1: Margin Specifications

Seismometer	Frequency Ranges	Sensitivity
Alpha	0.0083~150 Hz	6000 V/m/s
3espcde	0.017~100 Hz	2000 V/m/s

ANALYSIS AND CALCULATION OF DEVICE SELF-NOISE

Seismometer Self-noise Measurement

The three-sensor coherence analysis method is a seismic instrument self-noise analysis method based on correlation analysis. Its basic principle is that when three seismometers observe the same input signal, the correlated parts of the signal are removed, and the remaining parts are considered as the device's self-noise. This analysis method requires two assumptions [4]:

1. The internal noise of the data acquisition channels is uncorrelated.
2. The internal noise of the seismometer and the environmental noise signal are uncorrelated.

The basic model is shown in Fig. 1. The calculation formula is shown in Eq. (1):

$$N_{ii} = P_{ii} - P_{ji} \cdot \frac{P_{ik}}{P_{jk}} \tag{1}$$

The experimental site for the self-noise testing of the 8 devices used in this study was located in an observation cave at the Beijing National Seismic Observatory. Each device was shielded using a simple shielding cover as shown in Fig. 2.

All the seismometers have low self-noise levels. Due to limited space, the result of one Guralp's 3espcde plotted in Fig. 3.

†yanfang@ihep.ac.cn

ISBN: 978-3-95450-250-9 ISSN: 2673-5520 doi:10.18429/JACoW-MEDSI2023-TUPYP015

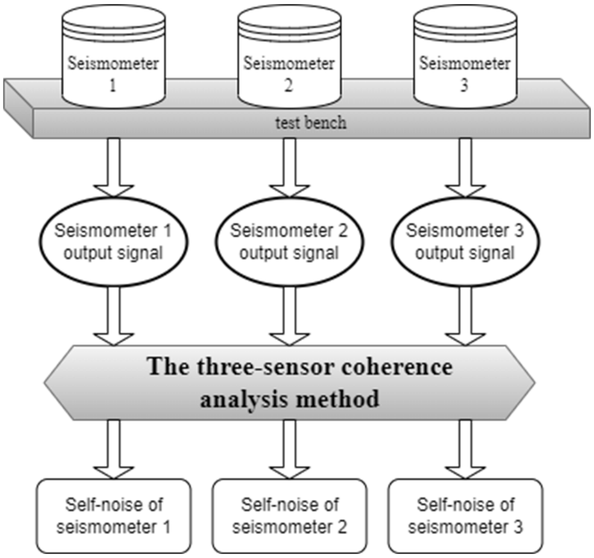

Figure 1: The three-sensor coherence analysis method.

Figure 2: Self-noise test site.

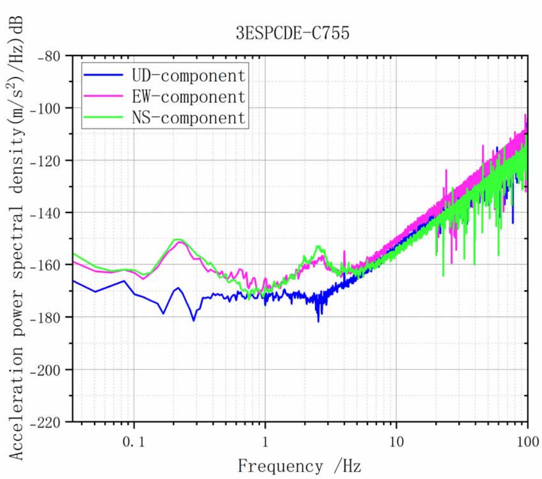

Figure 3: Self-noise curve of C755.

ATTENUATION EXPERIMENTS AND ANALYSIS OF EXPERIMENTAL DATA

Experimental Arrangement

HEPS has implemented special treatment for the foundations of storage ring and experimental hall. Four meters underground layer has been dug out and refilled with 3 m of plain concrete and 1 m of reinforced concrete. The measurement point for the decay experiment is located in the experimental hall of HEPS (6 points on the floor of the experimental hall and 1 point outside the raft: Fig. 4). The shaker was positioned approximately 170 m away from the experimental hall, on a paved road as shown in Fig. 5.

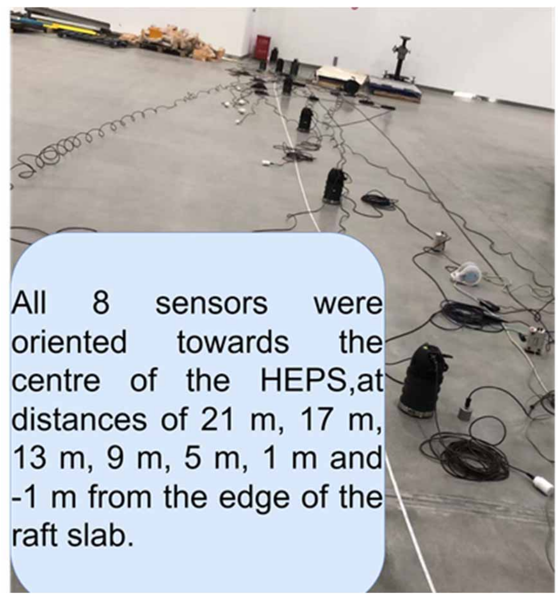

Figure 4: Attenuation test site.

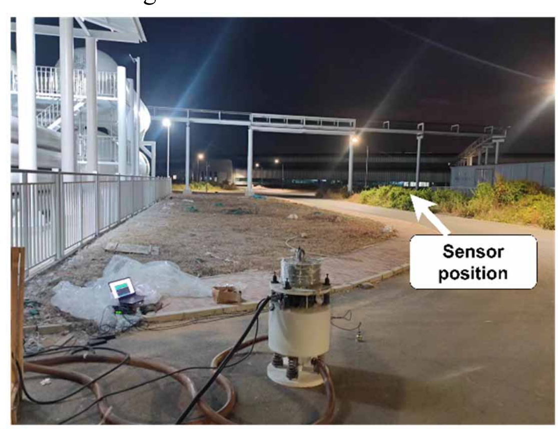

Figure 5: Shaker position.

To investigate the attenuation characteristics of external vibrations on a raft foundation, a vertical sinusoidal wave with frequency of 1 Hz up to 100 Hz was applied to the shaker. The excitation of each frequency lasted for 40 s, and the first 5 s and last 5 s of data were discarded to eliminate the frequency changing part. The remaining 30 s

ISBN: 978-3-95450-250-9 ISSN: 2673-5520 doi:10.18429/JACoW-MEDSI2023-TUPYP015

data were used to calculate the root mean square (RMS) displacement of the vibration for each frequency.

Experimental Data and Analysis

To ensure accurately and reliablely observation of the excitation signal and the tunnel ambient noise, the self-noise of the equipment farthest away from the shaker is compared to the vibration amplitude and ambient tunnel noise generated by the shaker propagating through 170 m distance, and the displacement power spectral density (PSD) on the ground in the vicinity of the shaker. (see Fig. 6). It was found that the self-noise of the C755 device is significantly lower than the noise from the excitation signal and tunnel environment, this indicates that the signals observed by this device are valid, and the vibrations generated by the shaker are at the same level within the frequency range of 10 Hz to 70 Hz.

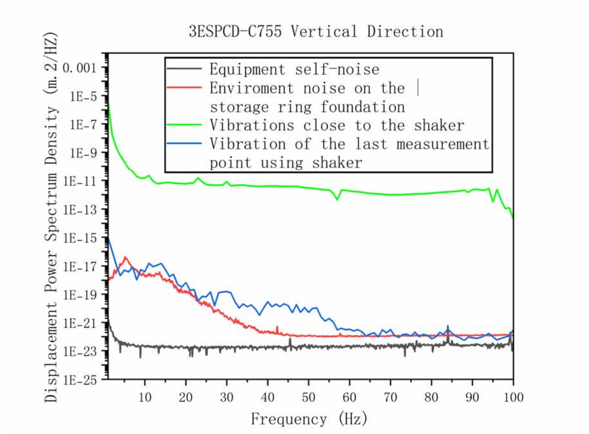

Figure 6: Displacement PSD comparison.

A comparison was made using the displacement responses at frequencies of 10 Hz, 20 Hz, 30 Hz, 40 Hz, 50 Hz, 60 Hz, and 70 Hz (see Fig. 7). In Fig. 7, the x-axis represents the distance from the edge of the raft foundation in the experimental hall, the shaker was located 170 m away from the foundation raft edge in the other direction.

The result shows that:

1. When the frequency exceeds 70 Hz, the vibration generated by the shaker has already overlapped with the ambient noise of the tunnel itself, indicating that vibrations above 70 Hz have become equivalent to the environmental noise after attenuation by the ground at a distance 170 m.
2. High-frequency vibrations decay faster than low-frequency vibrations, vibrations with frequency of 10-30 Hz still exhibiting high amplitudes after propagating 170 m, while the decay curve for vibrations above 40 Hz is relatively flat.
3. Some frequency points may experience amplification of vibrations when entering or propagating through a raft foundation, possibly due to the phenomenon of reflection superposition occurring during the process of wave propagation between different materials.

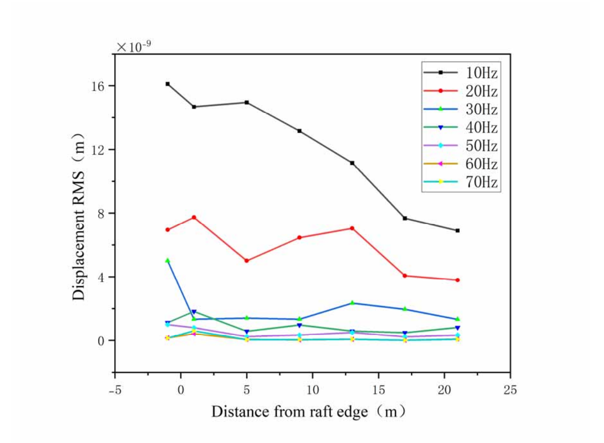

Figure 7: Attenuation of displacement response at different frequencies.

CONCLUSION

The test was conducted on the foundation of HEPS experimental hallusing a shaker for generating vibrations with frequency of 1 Hz to 100 Hz. The attenuation pattern of vibrations in the tunnel and the experimental hall was summarized.

In this test, measurement points were arranged radially within one period. Subsequent plans involve conducting the same experiment in multiple periods of the tunnel to analyze the attenuation pattern of different frequencies at different locations. This analysis will be used to develop a predictive formula for vibration attenuation, which will be validated by applying traffic loads on the road close by. The aim is to provide engineering strategies for controlling vibrations.

REFERENCES

[1] Fan Chen, "Experimental study of site vibration attenuation patterns under environmental excitation", Ph.D. thesis, Geol. Dept., Beijing University of Architecture, Beijing, China, 2019.

[2] Xianjian Yang, *Earth-foundation vibration and vibration isolation*. Beijing, CHN: China Construction Industry Press, 2013.

[3] Gerhard Bornitz, *Über die Ausbreitung der von Großkolbenmaschinen erzeugten Bodenschwingungen in die Tiefe*. Berlin Heidelberg, GER:Springer-Verlag, 2013.

[4] Caihuai Li, "Research on seismometer self-noise test technique", Ph.D. thesis, GP. Dept., Institute of Geophysics, China Earthquake Administration, Beijing, China, 2014.

ISBN: 978-3-95450-250-9 ISSN: 2673-5520 doi:10.18429/JACoW-MEDSI2023-TUPYP017

DESIGN AND TEST OF PRECISION MECHANICS FOR HIGH ENERGY RESOLUTION MONOCHROMATOR AT THE HEPS

Lu Zhang, Hao Liang[†,1], Wei Xu[1], Zekuan Liu, Yang Yang, Yunsheng Zhang
Institute of High Energy Physics, Beijing, China,
[1]also at University of Chinese Academy of Sciences, School of Physics, Beijing, China

Abstract

A monochromator stands as a typical representative of optical component within synchrotron radiation light sources. High resolution monochromators (HRMs), which incorporate precision positioning, stability control, and various other technologies, are a crucial subclass within this category. The next generation of photon sources imposes higher performance standards upon these HRMs. In this new design framework, the primary focus is on innovating precision motion components. Rigorous analysis and experimentation have confirmed the effectiveness of this design. This structural model provides valuable reference for developing other precision adjustment mechanisms within the realm of synchrotron radiation.

INTRODUCTION

The Nuclear Resonance Scattering (NRS) spectroscopy at High Energy Photon Source (HEPS) demands extremely high energy-resolving power better than 10^{-7}. As an optical element upstream of focusing mirror, the HRM shall maintain a high stability in terms of positioning, which could influence the energy precision as well as the beam stability at sample position, at fourth generation sources like HEPS. In the proposed monochromator configuration [1, 2], the range for fine pitch adjustment mechanism is relatively small. There also lacks an integrated angular sensing measurement device, thus real time precise tracking of fine pitch position is not possible. These factors impose constraints on the operation and performance of the monochromator. By referring to the previous design from APS and PETRA III [3-6], we have designed a new compact HRM mechanism with an *in-situ* metrology framework. This newly designed flexure mechanism is promising in increasing the stroke while minimizing errors of measurement system through highly rigid metrology devices. The developed mechanism successfully balances requirements between large travel range and high stability. In this paper, we will present the concept, simulation and offline measurements of the new HRM.

MECHANICAL DESIGN

According to the optical design, the HRM comprises two pairs of pseudo channel-cut crystals, with each pair being secured and adjusted by a pose adjustment mechanism. Consequently, the HRM is equipped with two pose adjustment mechanisms for each pair of pseudo channel-cut crystals.

As shown in Fig. 1, in response to the crystal pose adjustment requirements, each set of pose adjustment mechanisms comprises of six motion axes. These include x-axis coarse adjustment, z-axis coarse adjustment, Bragg axis adjustment, lattice matching axis tilting adjustment, and precision adjustment for crystal pitch angle and roll angle. While the first four motion axes are directly actuated by precision stages from KOHZU, the design of the last two precision adjustment mechanism is intricately linked to the ultimate performance of the monochromator and forms the core of the monochromator's structural design.

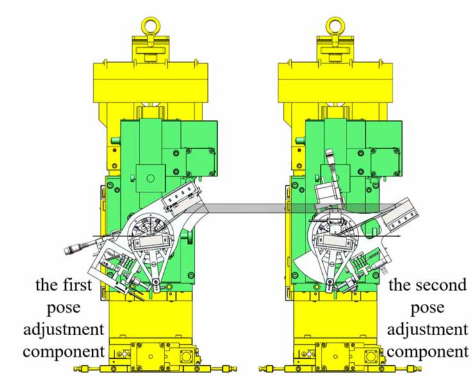

Figure 1: Mechanical design of the HRM.

In Fig. 2, we present the design of the first pose adjustment component. Due to the relatively lower resolution requirement for roll angle adjustment compared to pitch, we have directly employed a Newport 8321 picomotor as the actuator and an industrial flexible pivot as the rotational bearing. This configuration allows for the precise adjustment of the crystal's roll angle. In the design process, we carefully considered the impact of the driver's travel distance on the final angular resolution. As a result, we maximized the driver's travel distance while ensured high stability.

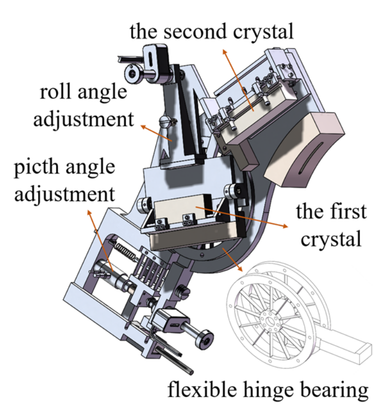

Figure 2: The first pose adjustment component.

† lianghao@ihep.ac.cn

ISBN: 978-3-95450-250-9 ISSN: 2673-5520 doi:10.18429/JACoW-MEDSI2023-TUPYP017

Given the stringent requirements for pitch angle adjustment precision and the need for a broad adjustment range, the mechanism necessitates a delicate balance between high flexibility to ensure a large range of motion up to 2 degrees and high stiffness to guarantee resolution of 25 nrad and stability of 50 nrad in motion. The original designs found in the literature struggled to meet these criteria, prompting the redesign of the core precision rotating component – the flexible hinge bearing.

The flexible hinge bearing is, illustrated in Fig. 2, composed of twelve sets of leaf spring hinges radially connected. The outer ring remains fixed, while the inner ring serves to drive the upper roll angle adjustment mechanism and facilitate precise angle rotation for the crystal within the series drive system. Flexible bearings built on leaf spring hinges can achieve substantial motion strokes within compact dimensions while upholding axial and radial stiffness, thus ensuring the mechanism's reliable load-bearing capacity.

The series drive system incorporates a picomotor and a piezoelectric actuator. The coarse motion is enabled by picomotor which can travel by tens of millimeters with position resolutions in the tens of nanometers., Fine tuning with sub-nanometer resolution can be attained with the piezoelectric actuator. However, the latter is limited to a stroke in the micrometer range. To effectively meet both stroke and resolution requirements, these two types can be connected in series. The connection between the piezoelectric actuator and the inner ring of the flexible hinge bearing is established via a straight rod. Simultaneously, the piezoelectric actuator and the outer ring of the flexible hinge bearing are affixed to the same flat plate, and a flexible guide mechanism is integrated between them. The leaf spring hinges are arranged in parallel, with one end anchored while the other consistently delivers precise displacement with outstanding linearity, powered by the force generated by the piezoelectric actuator. This arrangement guarantees the high-quality input displacement for the monochromator mechanism.

FINITE ELEMENT ANALYSIS

Finite element analysis (FEA) of the designed mechanism was conducted to validate the design.

As illustrated in Fig. 3, the analysis of the flexible hinge bearing revealed that with the utilization of aluminum alloy materials, the optimized configuration provides a ±2° stroke with a stress value of 196 MPa. Additionally, the radial stiffness is 26802 N/mm, while the axial stiffness reaches 886 N/mm. In the free state with an arm, the natural frequency achieves 58 Hz.

Similarly, the simulation analysis results for the flexible guide mechanism, as depicted in Fig. 4, demonstrate a significantly larger total stroke compared to the piezoelectric actuator, excellent output linearity across its stroke range, a maximum stress of 21 MPa, and a natural frequency of 414 Hz.

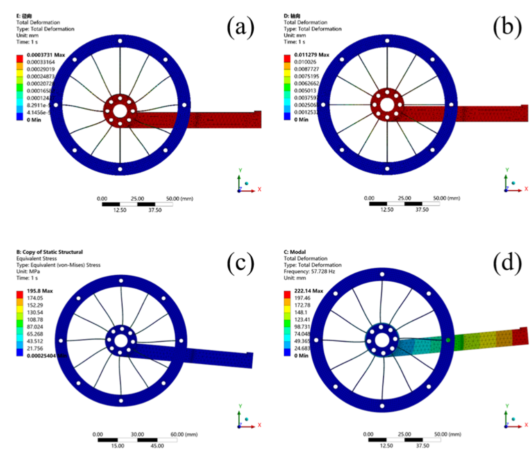

Figure 3: FEA of the flexible hinge bearing. (a) Radial stiffness, (b) axial stiffness, (c) stress and (d) modal FEA.

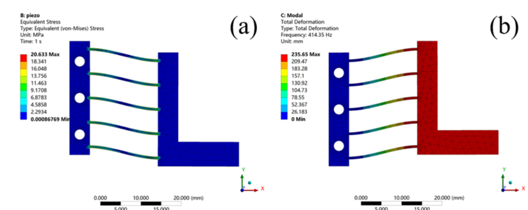

Figure 4: FEA of the flexible guide mechanism. (a) Stress and (b) modal FEA.

The precision pose adjustment mechanism incorporates a grating ruler measurement device, enabling real-time detection. In the structural design, the emphasis lies on maximizing the solid structure while ensuring that the sensor can be adjusted with multiple degrees of freedom. The representative simulation analysis results in Fig. 5 indicate a mode with a frequency of 331 Hz and a stable foundation for measurement.

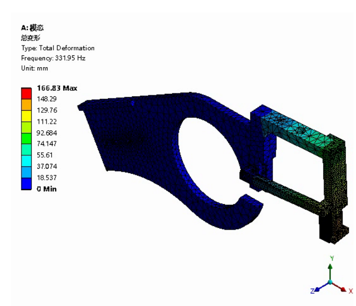

Figure 5: Modal FEA of the measurement structure.

A comprehensive dynamic simulation analysis was performed on the entire precision pose adjustment mechanism with crystals included. In accordance with Fig. 6, the findings reveal a first natural frequency of 155 Hz, which greatly contributes to achieving high stability. Specifically, the first-order vibration modal aligns with the roll angle direction of crystal, the second-order vibration shape corresponds to the yaw direction, and the third-order modal of 249 Hz is in pitch angle direction, all in accordance with the design expectations.

ISBN: 978-3-95450-250-9 ISSN: 2673-5520 doi:10.18429/JACoW-MEDSI2023-TUPYP017

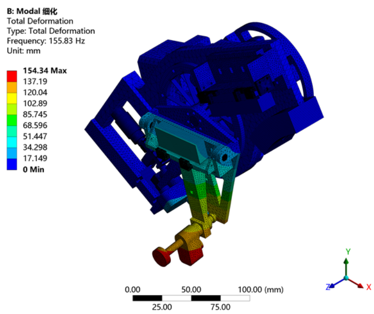

Figure 6: Modal FEA of the pose adjustment component.

OFFLINE TEST

Preliminary testing of the precision pose adjustment mechanism has been conducted. The two sets of pose adjustment mechanisms have been individually affixed to KOHZU's three-axis motorized stages, KTG and KHI. The motor's base is bolted to a granite table via an adapter. The granite table is positioned on the ground supported by 4 wedge blocks, as shown in Fig. 7.

Figure 7: Experimental device.

Regarding kinematic testing, the precision pose adjustment mechanism's stroke and resolution were measured.

As depicted in the Fig. 8, the mechanism attains a motion stroke of ±1.3°, fully aligning with the design specifications.

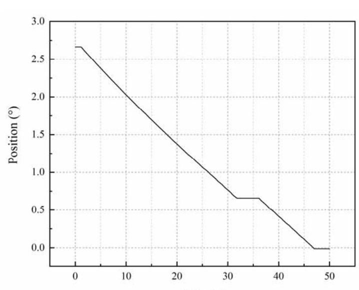

Figure 8: Stroke test of coarse pitch.

Figure 9 illustrates the coarse adjustment resolution of the picomotor and the fine adjustment resolution of the piezoelectric actuator, respectively. The experimental results were obtained using the encoder integrated into the design. With a sample rate of 2000 Hz and no filtering by an ACS controller, distinct step signals are visible at the coarse adjustment resolution of 250 nrad, and similarly, clear step signals are observed at the fine adjustment resolution of 8.3 nrad. These results not only align with the design specifications but also surpass the related test outcomes of known HRMs.

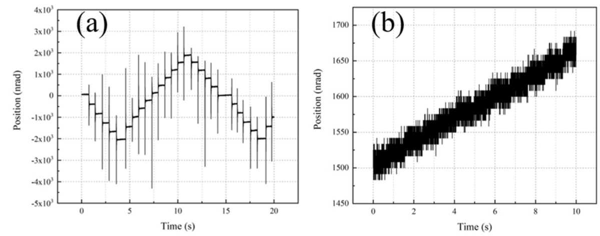

Figure 9: Resolution test. (a) Coarse adjustment resolution and (b) fine adjustment resolution.

In stability testing, evaluations were conducted for the stability between the first and second crystals, and the stability between the first and second pose adjustment mechanisms. Experimental data were collected using laser interferometers. As shown in Fig. 10, the results reveal that the stability between the first and second crystals is 12.5 nrad RMS (0.5-500Hz), while the stability between the first and second mechanisms is 55.0 nrad RMS (0.5-500Hz). The off-line angular stability is sufficient to meet the experimental requirements; however, it is still promising for further improvement through environmental control and other measures.

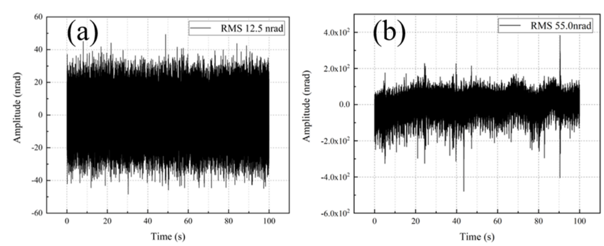

Figure 10: Stability test. (a) The stability between the first and second crystals and (b) the stability between the first and second mechanisms.

CONCLUSION

The precision adjustment mechanism incorporated within the HRM has been designed to address the demands for large stroke and high accuracy. FEA results confirm the viability of this solution, and experimental testing validates the efficiency of the design. In the future, the designed HRM will be tested under conditions more similar to its final locations. The current results demonstrate that the newly developed HRM can offer dependable optical modulation capabilities for the high energy resolution beamline of HEPS.

ACKNOWLEDGEMENTS

The authors would like to thank Weifan Sheng, Ming Li and Shanzhi Tang for the guidance on mechanical design, Yuanshu Lu, Shan Zhang, Dashan Shen and Gang Wang for the support in system testing. This work was supported by the High Energy Photon Source (HEPS), a major national science and technology infrastructure in China.

ISBN: 978-3-95450-250-9 ISSN: 2673-5520 doi:10.18429/JACoW-MEDSI2023-TUPYP017

REFERENCES

[1] S.G. Alcock, A. Bugnar, I. Nistea, *et al.,* "A novel instrument for generating angular increments of 1 nanoradian", *Rev. Sci. Instrum.,* vol. 86, p. 125108, 2015. doi:10.1063/1.4937352

[2] T.S. Toellner, J. Collins, K. Goetze, *et al.,* "Ultra-stable sub-meV monochromator for hard X-rays", *J. Synchrotron Radiat.,* vol. 22, no. 5, pp. 1155-1162, 2015. doi:10.1107/S1600577515012230

[3] S. Narayanan, A. Sandy, D. Shu, *et al.* "Design and performance of an ultra-high-vacuum-compatible artificial channel-cut monochromator", *J. Synchrotron Radiat.,* vol. 15, no. 1, pp. 12-18, 2008. doi:10.1107/s090904950705340x

[4] T.S. Toellner, A. Alatas, and A.H. Said, "Six-reflection meV-monochromator for synchrotron radiation", *J. Synchrotron Radiat.,* vol. 18, no. 4, pp. 605-611, 2011. doi:10.1107/s0909049511017535

[5] S.P. Kearney, C. Preissner, and D. Shu, "Progress of mechanical design of nanopositioning stages at the Advanced Photon Source", *Synchrotron Radiat. News*, vol. 31, no. 5, pp. 38-44, 2018. doi:10.1080/08940886.2018.1506242

[6] D. Shu, T.S. Toellner, and E.E. Alp, "Modular overconstrained weak-link mechanism for ultraprecision motion control", *Nucl. Instrum. Methods Phys. Res. A*, vol. 467, pp. 771-774, 2001. doi:10.1016/S0168-9002(01)00499-5

ISBN: 978-3-95450-250-9 ISSN: 2673-5520 doi:10.18429/JACoW-MEDSI2023-TUPYP018

DESIGN AND IMPROVEMENTS OF A CRYO-COOLED HORIZONTAL DIFFRACTING DOUBLE CRYSTAL MONOCHROMATOR FOR HEPS

Yunsheng Zhang†, Hao Liang, Lu Zhang, Yuanshu Lu, Dashan Shen
Institute of High Energy Physics Beijing Synchrotron Radiation Laboratory, Beijing, China

Abstract

Horizontal diffracting double crystal monochromator (HDCM) are usually used in a 4th generation light source beamline due to the larger source size in the horizontal direction. This paper introduces the mechanical design and optimization of a HDCM for Low-dimension Structure Probe Beamline of HEPS. In order to achieve the high stability requirement of 50 nrad RMS, the structural design is optimized and modal improved through FEA. In order to meet the requirement of a total crystal slope error below 0.3 μrad, FEA optimizations of the clamping for first and second crystal are carried out. The vacuum chamber is optimized to become more compact, improving the maintainability. Fabrication of the HDCM is under way. The results show that the design is capable of guarantee the required surface slope error, stability, and adjustment requirements.

INTRODUCTION

HEPS is the first high energy beamline and the first 4^{th} generation beamline in China. Thanks to the low emittance of the source, the beam source size could be as small as 10 microns. The low-dimension structure probe beamline (LODiSP) of HEPS is beamline dedicated on x-ray surface diffraction technique. The energy range of this beamline is the beamsize is in vertical and in horizontal. When a monochromator is used in horizontal diffraction mode, the tolerance of vibration in pitch direction for a double crystal monochromator could be as low as 50 nrad.

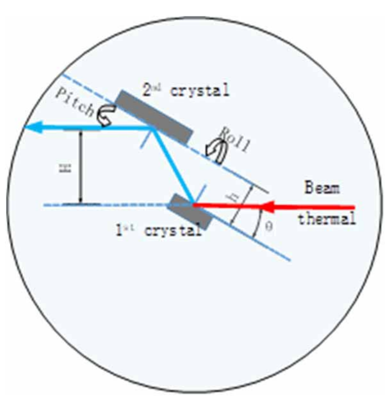

Figure 1: Beam path in a DCM.

The energy of the exit beam is a function of the Bragg angle θ (Fig. 1), and the resulting angular. and the resulting angular range with silicon crystals Si(111) is about 2.52°～24.32° (4.8～45 keV).

† zhangys97@ihep.ac.cn

According to Fig. 1, the spacing between reflected beam and Incident beam can be expressed as Eq. (1) [1]:

$$H = h \times 2cos\theta \quad (1)$$

A linear slide table under the second crystal enables high requirements to be fixed. Through the bellows (Fig. 2), the vibration of the cavity and the internal components is decoupled to achieve the purpose of improving stability.

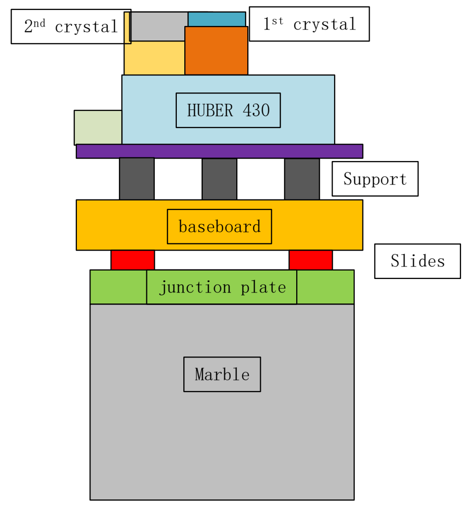

Figure 2: Monochromator construction.

DESIGN OF THE MONOCHROMATOR

The crystal slope error is an important parameter affecting the beam quality. The design of this monochromator (Fig. 3) uses a scheme in which copper blocks are clamped on both sides of the crystal [2, 3].

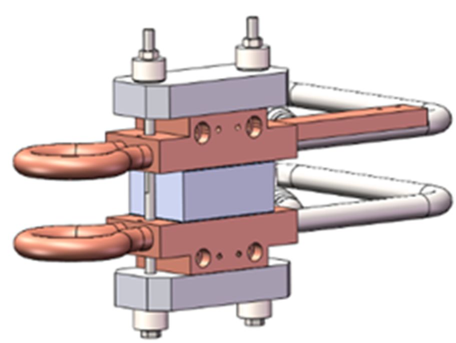

Figure 3: 1st crystal holder.

The FEA method was used to analyze the influence of different clamping positions and different thicknesses of pressure plate on it. Through multiple iterative optimizations, the clamping structure that meets the requirements of slope error is obtained, and the strain cloud diagram is shown (Fig. 4).

ISBN: 978-3-95450-250-9 ISSN: 2673-5520 doi:10.18429/JACoW-MEDSI2023-TUPYP018

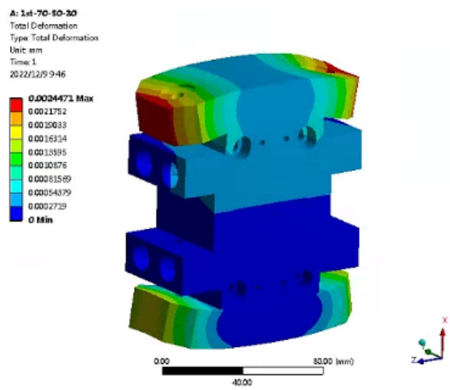

Figure 4: 1st crystal component strain analysis results.

The slope error affects the beam quality [4], Fig. 4 shows the FEA deformation analysis result as a contour map. The curve reflects the change in slope of the centerline of the crystal surface when stressed. The slope error is calculated as 0.1 μrad RMS (Fig. 5).

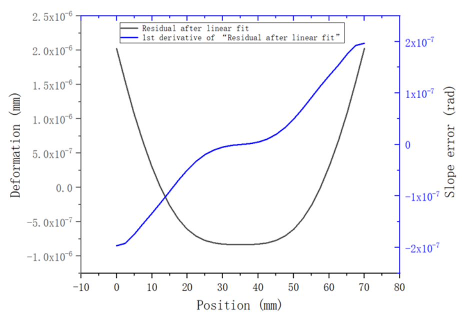

Figure 5: 1st crystal slope error

From the information given above, the device works by the position of the spot on the surface of a crystal is immovable. For this reason, in order to obtain more accurate results, it is more appropriate to use the data within a central range as the research object.

The result of 30 mm area in the center of the crystal plate was calculated as 0.006 μrad RMS with the slope error of removing the quadratic term (Fig. 6).

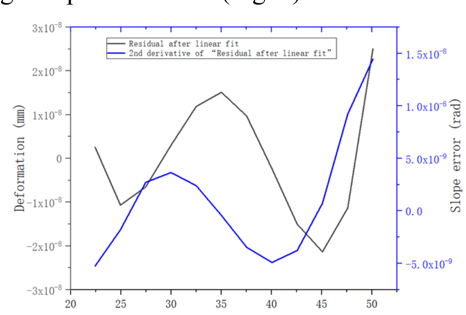

Figure 6: 1st crystal slope error (30 mm area).

Due to the long crystal, the position of the support point has a significant impact on the overall slope error result under the action of gravity.

The second crystal adopts the Bessel points clamping scheme, which is conducive to controlling the slope error of the crystal surface. Figure 7 shows the FEA deformation analysis result as a contour map.

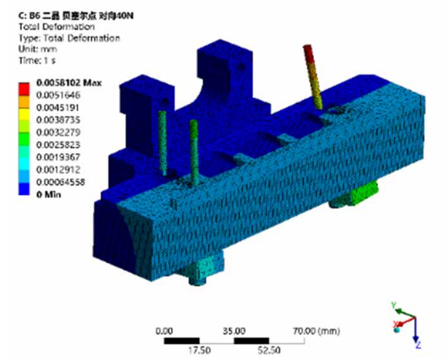

Figure 7: 2nd crystal component strain analysis results.

The overall surface shape of the two crystals in the arc vector direction of the photonic surface is 0.175 μrad (Fig. 8) after deducting quadratic term, the overall surface shape of the crystal in the full length range is 0.066 μrad (Fig. 9).

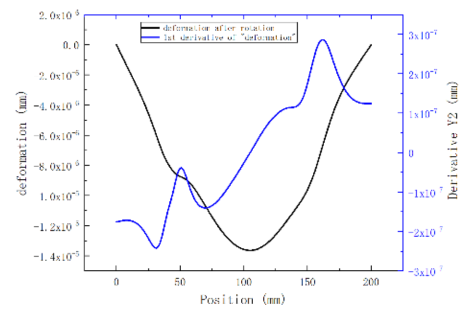

Figure 8: 2nd crystal slope error.

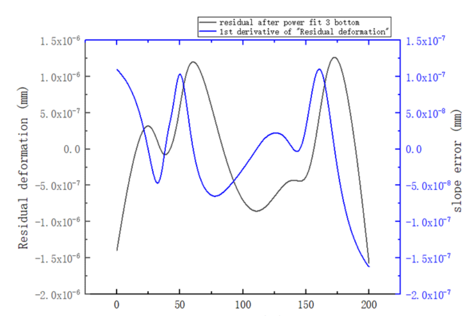

Figure 9: 2nd crystal slope error (deducting quadratic term).

VACUUM CHAMBER

The vacuum chamber was partially replaced with a square chamber. Improved compactness. The total weight of the cavity is about 645 kg. The FEA results show that the maximum stress is 55 MPa (Fig. 10) and the maximum strain of the chamber is 0.1 mm (Fig. 11). According to the yield strength, safety is calculated as 3.7.

The chamber is designed to be divided into two layers for easy access and maintenance. A cool-conducting copper column is added at the bottom plate. Reduce motor heat generation and temperature drift. The monochromator is equipped with 2 pneumatic insert valves along the inlet and outlet flanges in the direction of the beamline to isolate the vacuum and participate in the safety interlock; The

ISBN: 978-3-95450-250-9 ISSN: 2673-5520 doi:10.18429/JACoW-MEDSI2023-TUPYP018

molecular pump and ion pump port are equipped with manual insert valve, which is used to isolate the vacuum of the vacuum pump and the monochromator cavity; Equipped with metal angle valve, it can be used for pre-evacuation (Fig. 12).

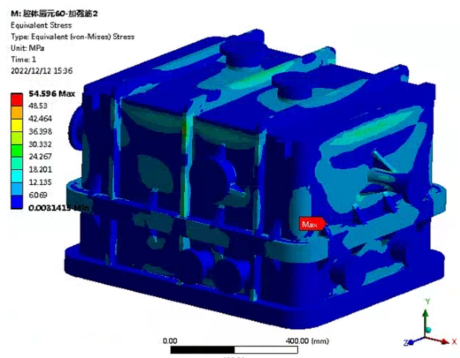

Figure 10: Crystal component strain analysis results.

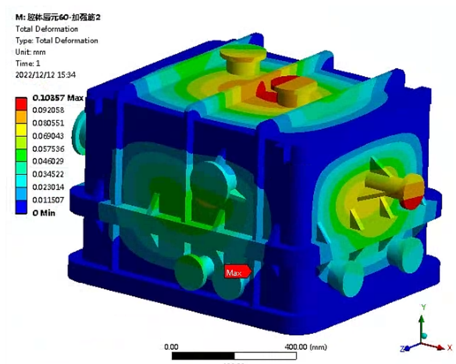

Figure 11: Crystal component strain analysis results.

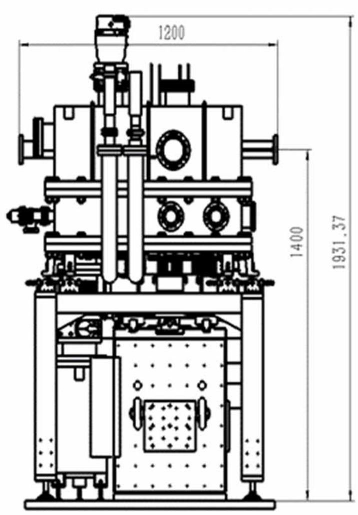

Figure 12: Crystal component strain analysis results.

CONCLUSION

The results show that the above analysis and calculation theoretically prove that the design can guarantee the required surface slope error, stability and adjustment requirements. The Fabrication of the equipment is underway.

ACKNOWLEDGEMENTS

Many thanks to the members of our group (including Yuanshu Lu, Yang Yang, Shan Zhang, Zekuan Liu, Dashan Shen, Zheng Sun) for their discussion during the monochromator design process, thank you to staff of the beamline station and review experts (including Huanhua Wang, Weifan Sheng, Ming Li, Xiaodong Li, Shanzhi Tang and more) for their valuable advice in the development of the monochromator. This work was supported by the High Energy Photon Source (HEPS), a major national science and technology infrastructure in China.

REFERENCES

[1] A. Gambitta, "A double crystal monochromator with self-compensation mechanism for ELETTRA XRD2 beamline," *Diamond Light Source Proceedings*, MEDSI-6, p. e23, Oct. 2010. doi:10.1017/S2044820110000377

[2] T. Mochizuki *et al.*, "Cryogenic cooling monochromators for the SPring-8 undualtor beamlines," *Nucl. Instrum. Methods Phys. Res., Sect. A*, vol. 467, pp. 647-649, Jul. 2001. doi:10.1016/S0168-9002(01)00436-3

[3] K. Tamasaku *et al.*, "Performance of cryogenically cooled monochromators at SPring-8," *SPIE Optics + Photonics*, Dec. 2002. doi:10.1117/12.450980

[4] R. Follath, "The versatility of collimated plane grating monochromators," *Nucl. Instrum. Methods Phys. Res., Sect. A*, vol. 467, pp. 418-425, Jul. 2001. doi:10.1016/S0168-9002(01)00338-2

ISBN: 978-3-95450-250-9 ISSN: 2673-5520 doi:10.18429/JACoW-MEDSI2023-TUPYP021

DEVELOPMENT AND IMPROVEMENT OF HEPS MOVER*

Shu Yang†, Lei Wu, Chunhua Li, Zihao Wang, Siyu Chen, Yuandi Xu
Institute of High Energy Physics, Beijing, China

Abstract

High Energy Photon Source (HEPS) has been constructed after decade of research. As the first diffraction-limited storage ring light source, many advanced devices are applied in this project, including the Beam Based Alignment Mover (Mover), which support and adjust the position of the Sextupole Magnet. It undertakes to remotely online adjust the position of Sextupole to meet the Physical requirement to correct the optics coefficient of Electron beam current. The positioning accuracy, attitude angle, and coupled error of Mover with 450 kg load strictly proposed and tested during the development of Mover. There are three main types of Mover, including Four-layer with sliding guide, Three-layer with rolling guide, and Three-layer with sliding guide. This paper introduces the development and improvement of Mover.

INTRODUCTION

The High Energy Photon Source (HEPS) has been designed and constructed to be the first high energy diffraction-limited storage ring (DLSR) light source whose electron beam energy reach to 6GeV and emittance is less than 60pm·rad [1].

Movers are designed to accurately adjust the position of Sextupoles to eliminate a strong feed-down effect and so formed dominating contribution to the optics distortion [1-2]. In LCLS, EXFEL, SXFEL, and DCLS, Mover is applied to carry relative lightweight quadrupoles [3-5]. HEPS firstly apply Mover to accurately adjust the position of 450kg Sextupoles.The specific requirements are shown in Table 1.

Table 1: The physical Requirements for Mover

Content	Requirement
Positioning Accuracy	± 5 μm
Yaw	3″
Roll	3″
Pitch	2″
Coupled Error	15 μm
Natural Frequency of support system	54 Hz

Three kinds of of prototype, including four-layer with sliding guide, three-layer with rolling guide, and three-layer prototype with sliding guide are studied.

The method and result of measuring process of motion performance of batch production of Mover is described in this paper.

STRUCTURE & MANUFACTURE

The structure of Mover should be elaborately designed to possess the properties such as high precision, low velocity, good stability, resistance to radiation, long service life, and compact size.

The model of four-layer with sliding guide is firstly designed based on previous research [6]. It is basically consisted of five parts (see Fig. 1), including horizontal plate, lateral constraint guide, upper wedge plate, lower wedge plate and base plate. Three-layer with rolling guide which is driven by piezoelectric ceramic motor is designed then (see Fig. 2). It mainly consists of upper wedge plate, lower plate, base plate, and high rigidity linear guide. The structure is further simplified to three-layer prototype with sliding guide (see Fig. 3). It mainly consists of upper wedge plate, lower plate, and base plate.

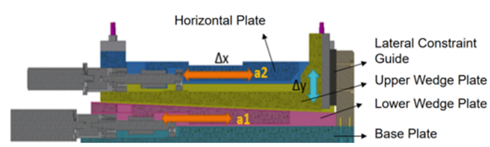

Figure 1: Four-layer with sliding guide Mover.

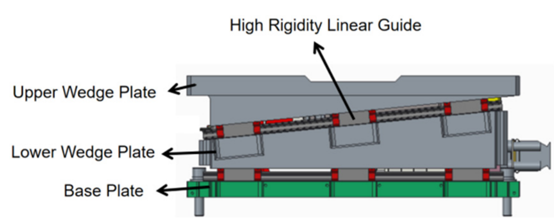

Figure 2: Three-layer with rolling guide Mover.

Figure 3: Three-layer with sliding guide Mover.

Cast iron is chose to be the material of Mover body since its properties of good resistance to vibration, stable performance and good accuracy retention, and easy to shape.

One of an important manufacture process should be scraping and grinding of sliding guide (see Fig. 4). It is helpful to decrease the residual stress in the plate so that accuracy and rigidity are enhanced. The lubricant could be reserved at series of uniform pit after scraping and grinding to form an oil film to improve friction performance and service life as a result.

* Work supported by the National Natural Science Foundation of China (No.12105295)
† yangshu@ihep.ac.cn

ISBN: 978-3-95450-250-9 ISSN: 2673-5520 doi:10.18429/JACoW-MEDSI2023-TUPYP021

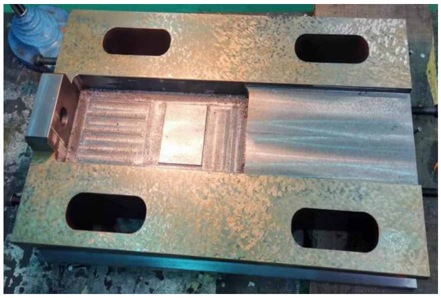

Figure 4: Surface after scraping and grinding.

At the end of processing, the upper layer of Mover would be ground after assembling (see Fig. 5) to improve the flatness and parallelism. This process can eliminate error both in machining and assembling. It is pivotal for alignment of magnet during the installation of HEPS.

Figure 5: Assemble grinding.

MOTION PERFORMANCE

Each Mover will be tested before its applied installing, including Attitude Angle, Positioning Accuracy and Coupled Error. And the Attitude angle includes Roll, Yaw, and Pitch. Figure 6 shows the coordinate system of Mover.

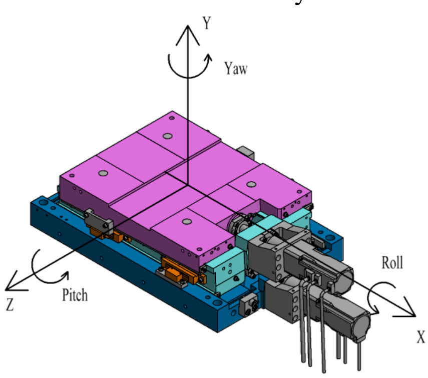

Figure 6: Coordinate system of Mover.

Attitude Angle

Three attitude angles, including pitch, roll and yaw, are measured by the CCD dual-axis autocollimator and the electronic level meter (see Fig. 7). During pratical moving range of $\pm$ 0.3 mm, yaw and roll should be less than 3″ while pitch should be less than 2″. This index mainly represents the quality of manufacturing.

Figure 7: Measurement of attitude angle.

Positioning Accuracy

The position of Mover is determined by two absolute grating rulers. The installed position of grating ruler is crucial to ensure the positioning accuracy. The basic position is fixed by the machining process.

Positioning accuracy both in horizontal and vertical direction is measured by Renishaw XL-80 laser interferometer (see Fig. 8). The measured point is higher than the center of sextupole magnet where the magnified positioning error that amplified more by the attitude angle than the error at the center.

Figure 8: Measurement of positioning accuracy.

Coupled Error

The vertical motion of Mover should be finished by co-operating axis A1 and axis A2 to eliminate the horizontal shift. This horizontal shift is called coupled error, which should be less than 15 µm.

Coupled error is measured by Attocube laser interferometer at the starting moment (See Fig. 9). It monitors the horizontal shift during the whole moving process. Mover is set to vertically moves and stop for 5 seconds at each 0.3 mm. Then the coupled error can be obtained at the starting moment.

Table 2: Comparison of Three Kinds of Mover

Margin		**Four-layer with sliding guide**		**Three-layer with rolling guide**		**Three-layer with sliding guide**	
		Horizontal	Vertical	Horizontal	Vertical	Horizontal	Vertical
Positioning Accuracy		1.9 µm	1.3 µm	0.5 µm	2.7 µm	1.8 µm	1.5 µm
Attitude Angle	Yaw	2″	3″	0.4″	3″	0.4″	1.7″
	Roll	1.2″	2.6″	0.2″	1.5″	1.2″	0.9″
	Pitch	1.8″	1.2″	0.4″	1.8″	0.3″	2″
Coupled Error		13 µm		1.5 µm		15 µm	
Natural Frequency of support system		58 Hz		25 Hz		74 Hz	

Figure 9: Measurement of coupled error.

Natural Frequency

The process of natural frequency measurement has been studied in previous work [6-7]. Vibration sensors are attached to the support system model (See Fig. 10). The natural frequency of mover is mainly decided by its material and structure. This test proves the rationality of design and machining craft.

Figure 10: Measurement of natural frequency of support system model.

RESULT

Table 2 shows the detailed information of three kinds of Mover. All of them satisfy the requirements of positioning accuracy and attitude angle. However, the coupled error of the four-layer prototype with sliding guide cannot be easily maintained. The efficiency of production is low. The natural frequency of support system which three-layer prototype with rolling guide is installed is just 25 Hz. The three-layer prototype with sliding guide can both satisfy the moving requirement and the stability of support system.

CONCLUSION

Three layer Mover with sliding guide is successful to satisfy the requirement. This batch of Mover is qualified to be applied in HEPS. There is still room for improvement. The coupled error could be decrease more by enhancing the quality of contact surface. This research will be continued.

REFERENCES

[1] Yi Jiao *et al.*, “The HEPS project”, *J. Synchrotron Radiat.*, vol. 25, pp. 1611-1618, 2018. doi:10.1107/S1600577518012110

[2] Yi Jiao, Weimin Pan, *et al.*, “High Energy Photon Source”, *High Power Laser and Particle Beams*, vol. 34, p. 104002, 2022. doi:10.11884/HPLPB202234.220080

[3] M. White, J. Collins, M. Jaski, G. Pile, *et al.*, “Magnets, Supports, and Controls for the Linac Coherent Light Source (LCLS) Undulator System”, in *Proc. FEL'08*, Gyeongju, Korea, Aug. 2008, paper TUPPH088, pp. 452-454.

[4] J. Munilla, J. Calero, A. Guirao, *et al.*, “Design, Manufacturing and Tests of Closed-loop Quadrupole Mover Prototypes for European XFEL”, in *Proc. IPAC'11*, San Sebastian, Spain, Sep. 2011, paper MOPO026, pp. 535-537.

[5] Yongmei Wen, Li Wang, *et al.*, “Mechanical design and experimental test of a remote controlled quadrupole mover for SINAPFEL projects”, *Nucl. Tech.*, 2016. doi:10.11889/j.0253-3219.2016.hjs.39.040101.

[6] Lei Wu *et al.*, “Design and Test of the Beam-Based Alignment Sextupole Experimental Mover Prototype for HEPS.” *Radiat. Detect. Technol. Methods*, vol. 5, no. 4, pp. 570–575, 2021. doi:10.1007/s41605-021-00287-0

[7] Chunhua Li *et al.*, “Design and Test of Support for HEPS Magnets”, *Radiat. Detect. Technol. Methods*, vol. 5, no. 1 pp. 95–101, 2021. doi:10.1007/s41605-020-00223-8

12th Int. Conf. Mech. Eng. Design Synchrotron Radiat. Equip. Instrum. MEDSI2023, Beijing, China JACoW Publishing
ISBN: 978-3-95450-250-9 ISSN: 2673-5520 doi:10.18429/JACoW-MEDSI2023-TUPYP022

THE DEVELOPMENT AND APPLICATION OF MOTION CONTROL SYSTEM FOR HEPS BEAMLINE

Gang Li, Yu Liu, Xiaobao Deng, Dianshuai Zhang,
Aiyu Zhou, Chunxia Yin, Qun Zhang, Zhenhua Gao, Zongyang Yue*
Institute of High Energy Physics, Chinese Academy of Sciences, Beijing, Peoples Republic of China

Abstract

In synchrotron radiation facilities such as the High Energy Photon Source (HEPS) beamline, thousands of motorized actuators are equipped on different optical devices, such as K-B mirrors, monochromator and transfocators, in order to acquire the specified properties of X-ray. The motion control system, as a part of the ultra-precision mechatronics devices, is used to precision positioning control, which not only has ability to realize basic motion functions but also can handle complex motion control requirements. HEPS has developed a standardized motion control system (MCS) for synchrotron radiation applications. In this paper, the structure of hardware and software of MCS will be presented, and some applications are demonstrated in detail.

INTRODUCTION

In the 15 beamlines of HEPS Phase I [1], there are thousands of actuators that required to control, including of PMSM, VCM, piezo and stepper motors. The number of stepper motors accounts for approximately 90 percent due to its high resolution ability, including two phase stepper and five phase stepper.

In order to satisfy the torque and size requirements of the optical devices, different motors must be employed, which demand that the MCS has the flexibility in configuring the driver current and micro-step. The position encoders were utilized in some motion axes for the application of close-loop to achieve the high repeatability. Therefore the MCS must be capable of supporting the different sensors, such as AqB, Biss-C and Endat2.2. Meanwhile, MCS should support the various types of limit switches, brakers and so on, to protect the mechanics devices. It is necessary to establish a uniform electrical standard, such as the connection between controller and devices (e.g. motor, encoder), the interface between controller and driver. In the aspect of field deployment, the large distances between controller and motors should be guaranteed. Besides the fundamental motion control requirements mentioned above, the complex devices in the end station of beamline especially, introduces more demanding performance criteria for MCS, include of synchronisation of multiple axis motions, complex trajectory planning, and real-time position event trigger.

Considering of the personnel resources and development costs, it's a significant challenge to satisfy all the control requirements of motion axes through a unified motion control system. It is very popular to use the VME controller in the majority of synchrotron labs worldwide, such as CLS [2], BESSY [3], and SSRF [4]. But the VxWork OS is so expensive, HEPS give up this scheme. From the perspective of HEPS and with reference to the other synchrotron labs, we have developed a novel motion control system utilizing commercial products.

In this paper, we will introduce the hardware structure of motion control system in detail. The software was developed under the Experimental Physics and Industrial Control System (EPICS) control framework [5]. Finally, several applications of MCS were demonstrated.

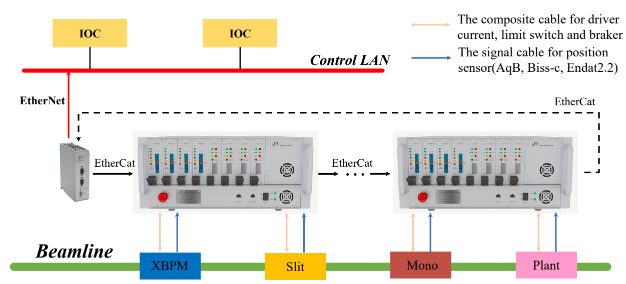

Figure 1: The overall hardware architecture of HEPS MCS.

THE ARCHITECTURE OF MOTION CONTROL SYSTEM

System Overview

The MCS is built of three main hardware components: master controller, control rack and driver board, the hardware architecture as shown in Fig. 1. A single MCS can support up to 64 axis, according to the EtherCAT fieldbus.

Figure 2: The control rack of MCS.

The MCS as the distributed system separates the control unit and driver unit. The master controller and control rack belong to the control unit. The controllers of ACS products (SPiiPlusEC and PDIcl) are the core of control unit where

* yuezy@ihep.ac.cn

ISBN: 978-3-95450-250-9 ISSN: 2673-5520 doi:10.18429/JACoW-MEDSI2023-TUPYP022

SPiiPlusEC is the master controller and PDIcl is the slave module, which are connected through EtherCAT fieldbus. The driver unit includes two-phase driver and five-phase driver, both of which are composed of core driver module (e.g. Phytron, Melec and oriental motor) and interface board. And the interface boards have been developed for different driver module, which make the driver unit have uniform electrical interface.

The Structure of Control Rack

The size of control rack is 3.5U 19-inch as shown in Fig. 2. In the front panel,there are two RJ45 interfaces for EtherCAT fieldbus, a emergency stop switch, several power supply leds and a drvier supply button. The eight slots of rack are used to install the driver board. To ensure system reliability, the back panel is equipped with standard connectors for motors, encoders and digital I/O.

Figure 3: The internal structure of control rack

A control rack contains PDIcl (slave module of EtherCAT), motherboard, the power supply for controller and driver. The detail of inside structure of control rack is demonstrated in Fig. 3. PDIcl as slave controller was used to acquire the I/O signal and send control signals to motherboard. The motherboard is a core component of control rack, which transforms the signal level and distributes signals to corresponding channels. The different types of driver units are compatible with all motherboard channels.

The way of processing of signal inside the control rack is displayed in the Fig. 4. Except of the encoder, digital I/O and braker devices be directly controlled by PDIcl, all of signals have been processed though the motherboard. All of input and output signals between the motherboard with the driver unit and PDIcl are optically isolated.

The Driver Unit

As is mentioned above, the driver unit consist of driver module and interface board. For convenience, we have already developed different interface boards to suit for different driver modules, all of which have same functions. The characteristics of driver module are shown in Table 1.

The driver current and micro-step can be configured though the DIP switch in the driver module. The interface

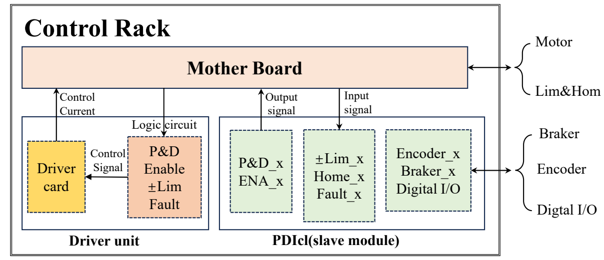

Figure 4: The way of processing of signal inside the control rack.

Table 1: The Type of Driver Module of MCS

Driver unit	SMD2	SMD514	SMD524
Driver type	Two phase	Five phase	Five phase
Core module	ZMX+	GDB-5F40	CVD524BK
Motor current	0.12-6 A	0.3-1.35 A	0.6-2.4 A
Micro-step	1-512	1-800	1-250

board provides flexible configuration capabilities for adjusting the effectiveness of limit switch, direction signal and remote enable signal. The true control signals that are finally sent to driver module have been processed by the logic protected circuits based on the state of limit, error and enable signals. In the front panel of driver board, several leds are utilized to indicate the status of axis.

THE APPLICATION

In practice, we make use of the EPICS control system as the highest level applications to provide process variable (PV) interface. The IOC of MCS [6] has been developed based on the the asynMotor (Model3) framework [7]. All of properties of motion axis have been realized by standard motor record, which provides the user with basic motion control functions. In the experiment, users of beamline are accustomed to controlling the properties of x-ray directly, instead of the motion axis, such as adjusting the hole of slit to change the size of X-ray beam and manipulating the Bragg angle to modify the energy of monochromatic light. Combing the motor record and other EPICS record can realize the complex control function by the channel access (CA) protocol of EPICS.

The white beam mirror (WBM) of BE has five degrees of freedom needed to be adjusted, which not directly driven by the motor. The motion of yaw is achieved though the motor driving the compliant mechanism, and the adjustment of height and pitch of WBM are accomplished by synchronized motion of two axes. In this situation, the combination the soft channel of motor record and the transform record not only can realize the conversion of coordinates, but also can decouple the relationship of motion axis. The control logic of the freedom of height and pitch is illustrated in the Fig. 5.

Firstly, the height and pitch are defined as pseudo motors though soft channel of motor record, whose command will be processed into the true motion command of motion axes by the transform record. The readback of motion axes are also handled by the other transform record, and the calcula-

ISBN: 978-3-95450-250-9 ISSN: 2673-5520 doi:10.18429/JACoW-MEDSI2023-TUPYP022

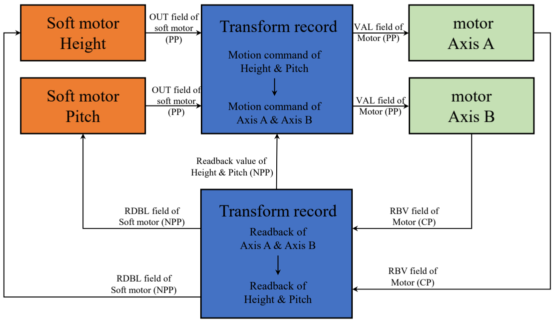

Figure 5: The control logic of whit beam mirror

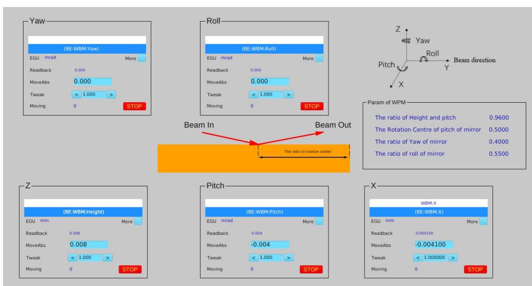

Figure 6: The OPI of white beam mirror

tion results will be respectively transmitted to pseudo-motor record and transform record in different ways. The WBM GUI is developed by CSS (Pheobus), as shown in Fig. 6. By this method, users not only can directly control the DOF of the WBM to deflect the X-ray, but also can independently control the position of motion axes, thus achieving the decoupling between pseudo motor and true motion axes.

CONCLUSION

The paper proposes a novel motion control system for HEPS beamline. The hardware structure of MCS has been described in detail. The design of the modular structure and the unification of standard interface allows to provide the best solution for each mechatronics device during the design and installation. The application of MCS for the white beam mirror demonstrate its feasibility and effectiveness. In the future, we will gradually complete the installation of MCS in HEPS, and novel EtherCAT-based systems will be developed to support the servo motor and piezo-actuators.

REFERENCES

[1] Yi Jiao *et al.*, "The HEPS project", *J. Synchrotron Radiat.*, vol. 25, no. 6, pp. 1611-1618, 2018. doi:10.1107/S1600577518012110

[2] D. Bertwistle, E. Matias, and M. McKibben, "Experience with Motion Control Systems at the Canadian Light Source", in *Proc. ICALEPCS'09*, Kobe, Japan, Oct. 2009, paper WEP052, pp. 501–503.

[3] A. Balzer, R. Follath, D. Herrendörfer, G. Reichardt, and P. Stange, "Diagnostics and Optimization Procedures for Beamline Control at BESSY", in *Proc. ICALEPCS'05*, Geneva, Switzerland, Oct. 2005, paper O1_014.

[4] Xuying Lan *et al.*, "The design of control and data acquisition system for IXS experiment in SSRF", *Nucl. Elec. Detect. Technol.*, vol. 36, no. 5, pp. 475-478, 2016.

[5] EPICS home page, https://epics.anl.gov/about.php

[6] IOC software, https://gitee.com/ihep-yzy/epics-motorSPiiPlus

[7] B.J. Nutter, T.M. Cobb, M.R. Pearson, N.P. Rees, and F. Yuan, "Recent Developments in Synchronised Motion Control at Diamond Light Source", in *Proc. ICALEPCS'11*, Grenoble, France, Oct. 2011, paper WEPMN013, pp. 901–904.

ISBN: 978-3-95450-250-9 ISSN: 2673-5520 doi:10.18429/JACoW-MEDSI2023-TUPYP023

DESIGN OF A LONG VERSATILE DETECTOR TUBE SYSTEM FOR PINK BEAM SMALL-ANGLE X-RAY SCATTERING (SAXS) BEAMLINE AT HEPS

Zhaoqiang Cui†, Shanzhi Tang, Jiuchang Zhang, Zina Ou, Guang Mo, Xueqing Xing
Institute or High Energy Physics Chinese Academy of Sciences, Beijing, China

Abstract

The X-ray scattering experiment vacuum camera device is the first piping system of high-energy synchrotron radiation light source applied to pink small-angle scattering experiments, which has a variety of functions and can be used for WAXS, SAXS and USAXS experiments. This paper introduces the size, vacuum parameters, motion parameters and part of the radiation protection of the equipment, briefly summarizes how to solve the problem of the influence of uneven ground in the light source hall on the installation of the equipment, outlines how to solve the problem of maintaining good straightness of the track in a very long case, theoretically briefly analysis the influence of ground vibration on the stability of the detector, and outlines the radiation protection scheme of some vacuum cavities.

INTRODUCTION

This equipment is a small angle scattering experimental device applied to Huairou BB line station, which can perform SAXS/WAXS/USAXS, SAXS-CT and ASAXS combination experiments.

A 23m long versatile detector tube system is shown as Figure 1. Three Eiger2 detectors will be installed along the deciVe. The WAXS detector is suspended diagonally above the sample to collect about -5°~50° scattering signals. The SAXS detector, which is used to collect 0. 04°~6°, is installed in the front large tube with a diameter of 1.5 m and a length of 14 m. The detector can move freely within the tube according to experimental requirements. The distances between sample and SAXS [1] detector can be altered freely. The USAXS detector, which is used to collect 0.001°~0.1° signals, is placed at the end of tube. The vacuum degree of the tube is less than 1 Pa. The three detectors can work simultaneously to collect the whole larger angle range from 0.001°~50°. Two kinds of beamstop used for transmission mode and grazing incidence mode respectively, are installed in front of the SAXS and USAXS detectors.

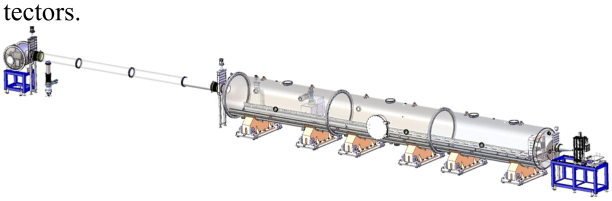

Figure 1: X-ray scattering experiment vacuum camera device.

STRCTURAL DESIGN

Figure 2 shows the overall overview of the equipment. The X-ray small-angle scattering experiment vacuum camera device consists of four parts: the device for WAXS experiment, the device for SAXS experiment, the device for WAXS experiment and the vacuum chamber.

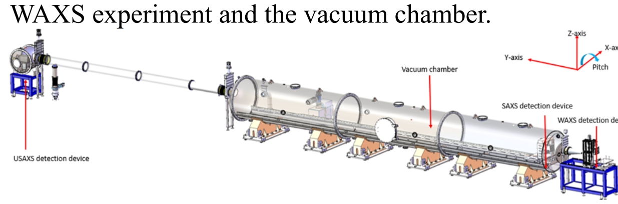

Figure 2: Overall device composition.

As shown as Figure 3, the WAXS device is located in the atmosphere and moves in a straight line in three directions of the detector. The probe's projection angle motion range is 55°. The lifting displacement table and the horizontal displacement table are spliced by processed aluminum alloy steel plates, and this structural design effectively reduces the weight of the device and effectively helps to improve the stability of the equipment structure. The base of the device is composed of square steel pipes. After the welding of the base is completed, it is treated with stress relief process, and then finished to effectively reduce the influence of welding deformation on the motion accuracy of the detector. In addition, the base is welded from Q235 square steel, which reduces the manufacturing cost. Similarly, the shelves used for the hoisting of the detectors are made of welded steel plates, which are subjected to a strain relief process of heat treatment after welding. Then drill the holes, which can ensure the concentricity of the two holes, and effectively reduce the error of detector installation.

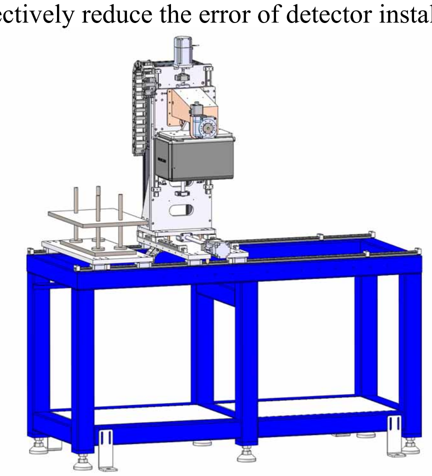

Figure 3: The device for WAXS experiment.

ISBN: 978-3-95450-250-9 ISSN: 2673-5520 doi:10.18429/JACoW-MEDSI2023-TUPYP023

Figure 4 shows that SAXS device is located in a vacuum environment, and although the cavity of the device is a low-vacuum environment, it has a lot of space. In order to reduce the pumping time and quickly achieve the vacuum specifications we require. Therefore, most of the parts are selected as special materials for vacuum. The SAXS device is composed of a track, a board for track support, a structure for track swing angle adjustment, a structure for track lifting adjustment, a trolley for the detector moving in the Y-axis direction, an electric slide table for the detector's displacement in the X-axis direction, an electric slide table for the detector to lift in the X-axis direction, and a support base. The SAXS device is capable of continuously moving the detector in the Y-axis direction for a travel of 12.5 meters. The motion straightness of the trolley in the direction of the beam line is guaranteed by the track of V-section and the track of rectangular section, and the adjustment mechanism of the lifting and swing angle of the track is increased, and the straightness error is less than 1mm by splicing. The device used for the lifting movement of the detector adopts a gantry-type steel plate splicing structure to ensure the stability of the detector's movement in the up and down and front and rear directions. In addition, the detector's lifting slide uses a single motor to drive two ball screws, which realizes the synchronization of the detector's lifting and lowering movements. The detector has a long distance of movement in the direction of the beam line, so the cable length of the motor, feedback element, BEAMSTOP and limit element will be very long, and its regularity will be very poor.

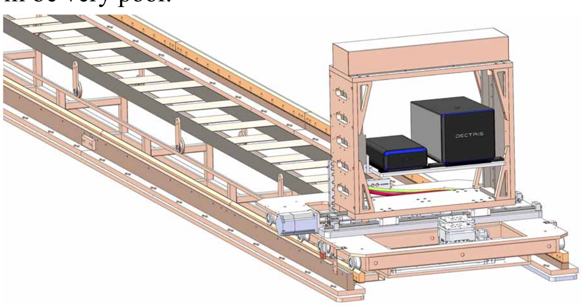

Figure 4: The device for SAXS experiment.

Figure 5 shows the structure of USAXS device. It only has two functions: lifting and lateral displacement. Its structure is relatively simple. Again, it is located in a vacuum and is used to do USAXS experiments.

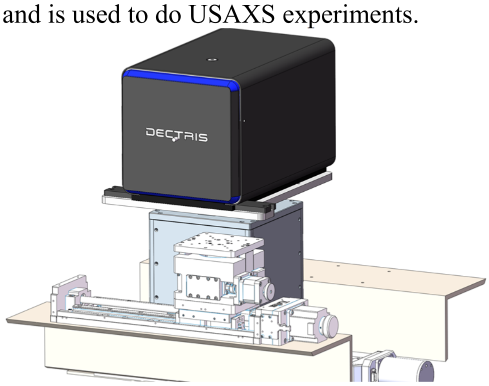

Figure 5: The device for USAXS experiment.

The vacuum chamber is the most basic component of the X-ray scattering experimental setup. Figure 6 shows an overview of its structure. Both the coarse and thin pipes are on the outside of the shed for radiation protection. In order to save the design cost, there are three types of radiation protection design for the cavity, namely the design of radiation protection shed, the design of thick pipe wall thickness, and the design of the lead layer wrapping structure of thin pipe. According to the calculations of the teachers of the relevant majors, the wall thickness of the thick pipe should not be less than 20 mm. The thick pipe consists of three sections, which allows the trolley of the SAXS unit to move in it according to the design specifications.

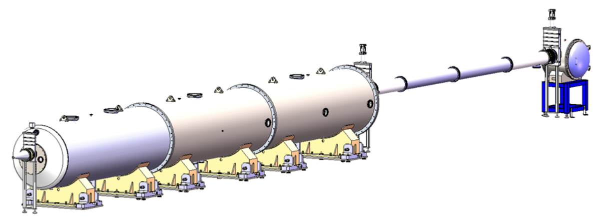

Figure 6: Vacuum chamber.

Figure 7 shows the support base of three thick pipes. The thick pipe has the characteristics of large mass and high center of the pipeline. There is a moving mechanism inside the pipeline, so the stability of the three-section thick pipe is required by higher requirements. Combining the above characteristics, the base of the pipe is designed as a saddle type.

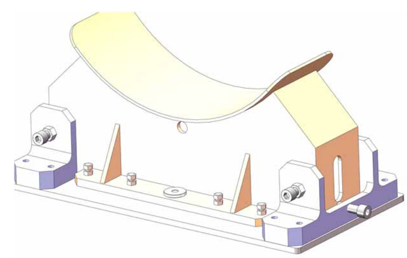

Figure 7: Support base of three thick pipes

Stability

When using this device for experiments, the stability [2] requirements for the detector are not very high, which is 30 % of the resolution, which belongs to the micron level. The ground vibration is about 10nm, and when the actual natural frequency of the system is 50 Hz, the amplification factor of the system is about 1.2 times, so when designing the structure, there is no need to simulate the natural frequency of the structure to more than 120 Hz.

PARAMETRIC INDICATORS

Detector Motion Parameters

As can be seen from Table 1, the Y-axis travel is very long, so it is very important to ensure the straightness of the track.

ISBN: 978-3-95450-250-9 ISSN: 2673-5520 doi:10.18429/JACoW-MEDSI2023-TUPYP023

Table 1: Detector Motion Parameters

	Resolution [µm]	Repeatability accuracy [µm]	Itinerary [mm]
WAXS-X	5	10	150
WAXS-Y	1000	1000	1210
WAXS-Z	2	5	230
WAXS-pitch	0.06°	0.06°	55°
SAXS-X	5	10	320
SAXS-Y	1000	1000	12500
SAXS-Z	5	10	260
USAXS-X	5	10	160
USAXS-Z	5	10	100

CONCLUSION

The X-ray scattering experiment vacuum camera device is a device that takes into account vacuum, radiation protection, ground profile, structural stability and functional design at the same time. If the requirements allow, more structural designs can be added for experiments. The design presented in this article leaves something to be desired in many areas and needs to be improved in the future.

REFERENCES

[1] https://www.xenocs.com/knowledge-base/saxs/

[2] W. F. Sheng, H. Liang, Y. S. Lu, and Z. Zhang, "Investigations on Stability Performance of Beamline Optics Supports at BSRF", in *Proc. MEDSI'20*, Chicago, USA, Jul. 2021, pp. 125. doi:10.18429/JACoW-MEDSI2020-TUPA04

ISBN: 978-3-95450-250-9 ISSN: 2673-5520 doi:10.18429/JACoW-MEDSI2023-TUPYP026

INFLUENCE OF THE GROOVE CURVATURE ON THE SPECTRAL RESOLUTION IN A VARIED-LINE-SPACING PLANE GRATING MONOCHROMATOR (VLS-PGM)*

Jingjing Du†, Zimeng Wang, Xuewei Du, Qiuping Wang
National Synchrotron Radiation Laboratory,
University of Science and Technology of China, Hefei, China

Abstract

Diffraction-limited synchrotron radiation (DLSR) light source with smaller source size and emittance makes ultra-high spectral resolution beamline possible. Here, we report an undulator-based beamline optical design with ultra-high spectral resolution using a varied-line-spacing plane grating monochromator (VLS-PGM), which is a well-proven design for achieving ultra-high resolution in the soft X-ray band. A VLS plane grating with a central groove density of 2400 l/mm is utilized to cover the photon energy region of 250 ~ 2000eV. VLS gratings are generally fabricated using the holographic method, but the resulting grating grooves are two-dimensionally curved curves, which can affect the resolution of the monochromator. To analyse this effect, we first use a spherical wavefront and an aspherical wavefront to generate the fringes and optimized the recording parameters. We also present a method for calculating the grooves curvature of holographic plane VLS grating grooves. Furthermore, the influence of grating grooves curvature on beamline resolution is theoretically analysed based on the aberration theory of concave grating.

INTORDUCTION

Diffraction limited synchrotron radiation (DLSR) has higher brightness and coherence. How to transmit the light from the storage ring to the experimental station with high quality is a challenge faced by beamline technology. Ultra-high spectral resolution beamlines are possible due to the smaller source size and emittance. The BL10 test beamline of Hefei Advanced Light Facility (HALF) proposed a design specification to achieve 100,000 resolving power at 400eV photon energy. In this paper, a beamline optical design based on varied-line-spacing plane grating monochromator [1, 2] (VLS-PGM) is given, which uses a VLS plane grating with a central groove density of 2400 l/mm to cover the soft X-ray photon energy region of 250~ 2000 eV。 And this beamline can achieve 100,000 resolving power at 1000 eV photon energy.

There are two methods for making varied-line-spacing plane gratings, mechanically ruling method and holographic exposure method. Compared with mechanically ruled gratings, holographic gratings are simple to fabricate, easy to change the shape of the grooves, and have the advantages of no ghost lines. However, the grating grooves fabricated by the holographic method are two-dimensionally curved curves. When calculating the beamline resolving power, it is not only necessary to analyse the effects of aberration, entrance slit width, exit slit width, the slope error of optical elements, and diffraction limit of the grating on the monochromator spectrum broadening, but also to analyse the influence of grating grooves curvature on beamline resolution. We established a calculation model for the curvature of holographic VLS plane grating grooves. The curvature of the grating grooves is used as an important evaluation criterion when optimizing the parameters of the holographic recording system [3]. How to make the curvature of the optimized holographic grating grooves smaller is also a new challenge.

OPTICAL DESIGN

The period length of the undulator is 40mm and the total length is 3920 mm. Figure 1 shows the layout of the optical system. The total length of the beamline is 72.41 m. The first mirror is a water-side-cooled plane mirror, coated with Au, deflecting the beam horizontally by 1.6°. The monochromator consists of a varied-line-spacing plane grating and a plane mirror, which is used to change the included angle of the grating while wavelength scanning. The nominal groove density of the grating is 2400 l/mm, covering the energy range of 250 ~ 2000 eV. The toroidal mirror downstream the exit slit has a grazing incidence angle of 0.8° and is used to focus vertically and horizontally to the experimental station.

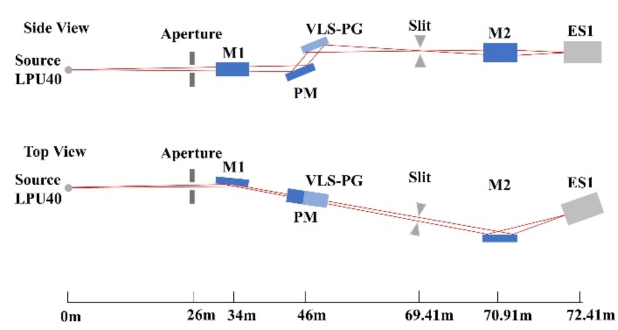

Figure 1: Layout of the optical system.

Due to the focusing characteristics of the VLS grating, a focusing mirror can be omitted upstream the exit slit, thereby improving the transmission efficiency of the beamline. The VLS grating parameters is expressed by equation $n(w)=n0(1+a_1w+a_2w^2+a_3w^3\ldots)$, where w is the position on the grating along the light propagation direction, n(w) is the grooves density, n0 is the grooves density at the center of the grating, a_i is the space variation parameters.

According to the concave grating aberration theory, the VLS coefficient a2 can be obtained by F20 = 0. Then,

† jjdu@mail.ustc.edu.cn

ISBN: 978-3-95450-250-9 ISSN: 2673-5520 doi:10.18429/JACoW-MEDSI2023-TUPYP026

according to the grating including angle 2K changes from 174.904° at 250 eV to 178.223° at 2000 eV, and eliminating coma and spherical aberration at 1000 eV photon energy, the grating parameters can be calculated. Table 1 shows the parameters of grating.

Table 1: Parameters of Grating

Optical elements	PG
Shape	Plane
Total surface size [mm]	350 × 30
Material	Au
N0(l/mm)	2400
a1(l/mm^{-2})	-8.75357×10^{-5}
a2(l/mm^{-3})	5.51853×10^{-9}
a3(l/mm^{-4})	-3.14971×10^{-13}

RESOLUTION

The main contributions to beamline spectral broadening are source width, exit slit width, optical system aberration, the slope error of optical elements, and grating diffraction limit. The tangential slope error of the grating is 0.1 µrad, the tangential slope error of the plane mirror is 0.2 µrad, and the sagittal slope error of the plane mirror M1 is 3 µrad. Figure 2 shows the influence of various factors on the beamline resolution. It can be seen from the figure that the slope error of the grating, source width and the width of the exit slit are the main influencing factors.

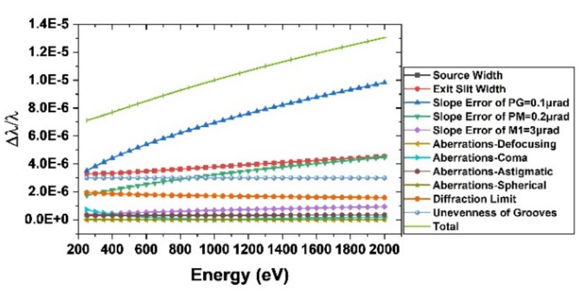

Figure 2: Contributions to the spectral broadening from different factors.

Figure 3 shows the ray tracing results of the beamline at the exit slit by SHODOW software. This beamline can achieve 100,000 resolving power at 1000 eV photon energy.

HOLOGRAPHIC GRATING

A spherical wavefront and an aspherical wavefront to generate the fringes and optimized the recording parameters. According to the VLS grating coefficients given in the design, the parameters of each component in the holographic grating recording system were optimized. The multiple sets of data obtained from the optimization were screened based on factors such as actual experimental conditions and the degree of curvature of the grating grooves. A more reasonable set of recording systems parameters was finally selected for grating fabrication. Figure 4 shows the dN error diagram between the optimized holographic grating and the target VLS grating along the W (grating Length) axis under different L (grating Width) widths.

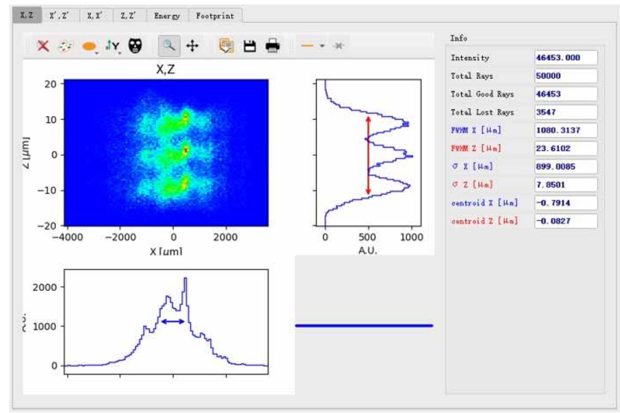

Figure 3: Ray-tracing result.

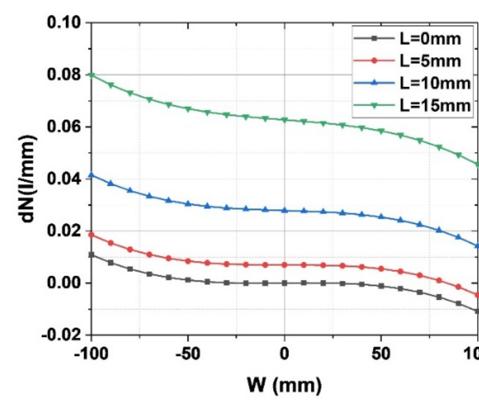

Figure 4: The dN error diagram between the optimized holographic grating and the target VLS grating.

GRATING GROOVE CURVATURE

The calculation method for the maximum curvature of the grooves at the edge of the holographic varied-line-spacing is: Under the same number of grooves, the focal positions of grating carving and W axis $w_{l=0}$ and $w_{l=L}$ are calculated by $nh(w_{l=0},0)=nh(W,0)$ and $nh(w_{l=L},0)=nh(W,0)$ at $l=0$ and $l=L$, respectively. Then $(w_{l=0}-w_{l=L})/L$ is the maximum curvature of the grooves at the edge of the grating, where W and L are the half length and half width of the grating respectively. It is calculated that the maximum curvature of the optimized holographic VLS grating grooves is 2.73 mrad, as shown in Fig. 5.

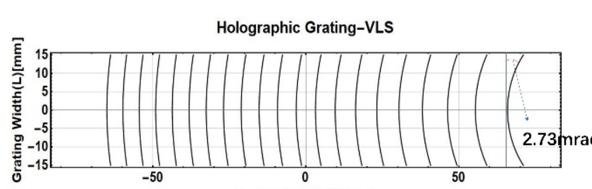

Figure 5: Grating grooves curvature diagram.

ISBN: 978-3-95450-250-9 ISSN: 2673-5520 doi:10.18429/JACoW-MEDSI2023-TUPYP026

According to the concave grating aberration theory [4], the two-dimensional curvature of the grating grooves will increase the aberration term related to the L direction of the grating grooves, thereby reducing the resolution of the beamline. Figure 6 shows the variation of the beamline resolving power with photon energy using the varied-line-spacing grating fabricated by holographic method and using the target straight grooves grating.

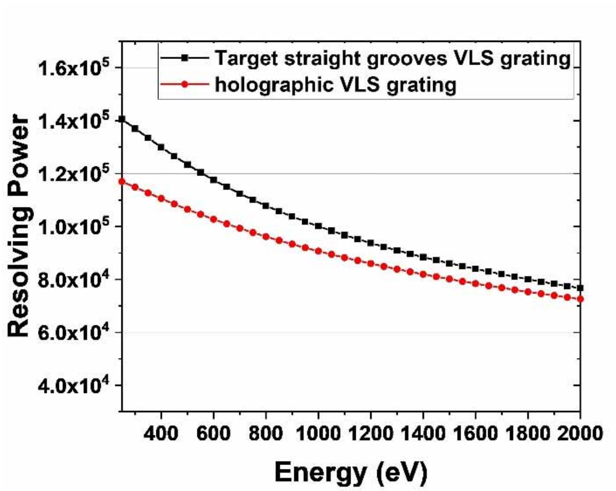

Figure 6: Variation of the beamline resolving power with photon energy.

It can be seen from the figure that the beamline resolving power of the grating fabricated by the holographic method is slightly lower than that of the target straight-line grating. Due to the current holographic VLS grating recording system parameter optimization range is limited to the actual use of the optical element surface accuracy, the size of the optical platform and other factors. In order to further reduce the curvature of the holographic VLS grating, it is necessary to upgrade the various components used in the recording system and further optimize the calculation program of the recording system parameters.

CONCLUSION

In this work, we introduce an ultra-high resolution beamline optical design and the optimized design of the VLS grating holographic recording system. We calculated the curvature of the grating grooves and the influence of holographic grating grooves curvature on the beamline resolving power through concave grating aberration theory. And theoretically analysed the factors that contribute to the spectral broadening of the grating monochromator from the perspective of grating fabrication process.

REFERENCES

[1] W. R. McKinney, “Varied line-space gratings and applications”, *Rev. Sci. Instrum,*, vol. 63, no. 1, pp. 1410-1414, 1992. doi:10.1063/1.1143030

[2] Jarrige, Ignace *et al*., “Paving the way to ultra-high-resolution resonant inelastic x-ray scattering with the SIX beamline at NSLS-II”, *Synchrotron Radiat. News*, vol. 31, no. 2, pp. 7-13, 2018. doi:10.1080/08940886.2018.1435949

[3] T. Namioka, and M. Koike, “Aspheric wave-front recording optics for holographic gratings”, *Appl. Opt.*, vol. 34, no. 13 pp. 2180-2186, 1995. doi:10.1364/AO.34.002180

[4] H. G. Beutler, “The theory of the concave grating”, *J. Opt. Soc. Am.*, vol. 35, no. 5, pp. 311-350, 1945. doi:10.1364/JOSA.35.000311

ISBN: 978-3-95450-250-9 ISSN: 2673-5520 doi:10.18429/JACoW-MEDSI2023-TUPYP027

A SUBNANOMETER LINEAR DISPLACEMENT ACTUATOR

Shuaikang Jiang†, Xuewei Du, Qiuping Wang
USTC/NSRL, Hefei, Anhui

Abstract

With the development of synchrotron radiation technology, an actuator with sub-nanometer resolution, 100 N driving force, and compatible with ultra-high vacuum environment is required. To achieve synchrotron radiation micro-nano focusing with adjustment resolution of sub-nanometer and high-precision rotation at the nano-arc level, most of the commercial piezoelectric actuators are difficult to meet the requirements of resolution and driving force at the same time. The flexure-based compound bridge-type hinge has the characteristic of amplifying or reducing the input displacement by a certain multiple, and can be used in an ultra-high vacuum environment. According to this characteristic, the bridge-type composite flexible hinge can be combined with commercial piezoelectric actuators, to design a new actuator with sub-nanometer resolution and a driving force of 100 N. This poster mainly presents the principle of the new actuator, the design of the prototype and the preliminary test results of its resolution, stroke.

INTRODUCTION

Flexure-based compliant mechanisms are wildly used due to their positive merits including free of backlash and friction, vacuum compatibility, and can achieve high-resolution motion. But the final resolution the mechanism can achieved is limited not only by flexure-based structure but also limited by the actuators.

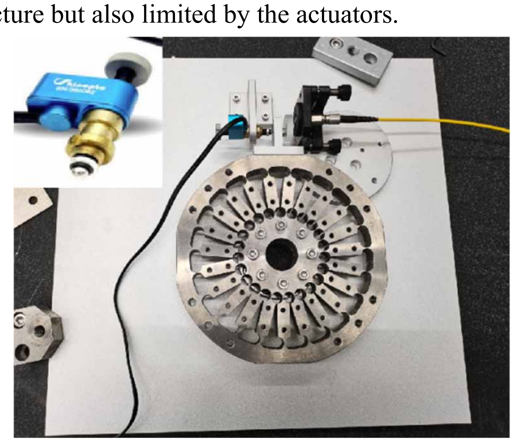

Figure 1: Preliminary resolution test of a weak-link mechanism.

As shown in Fig. 1, for example. When we use a domestic piezoelectric actuator to driven a weak-link mechanism [1] to measure the minimum angular resolution of the weak-link mechanism. The radius of the wheel-shaped flexible hinge is 200 mm. And the angular resolution we got finally is about 120 nrad, the result is limited by the minimum step size of the piezoelectric actuator (about 15 nm). So we need an actuator with smaller minimum step size if we want to achieve a higher angular resolution.

SOLUTION AND CALCULATION

To achieve higher resolution at lower cost, a compound bridge-type hinge [2] is chosen as a pantograph mechanism to achieve smaller minimum step size by scaling down the step size of the piezoelectric actuator we have. Figure 2 shows the schematic diagram of the compound bridge type hinge, as can be seen from the figure, the bridge-type composite flexible hinge has four ends A, B, C, and D. When we fix end C and apply opposite thrust to ends B and D, end A will move along the x direction relative to end C. direction displacement.

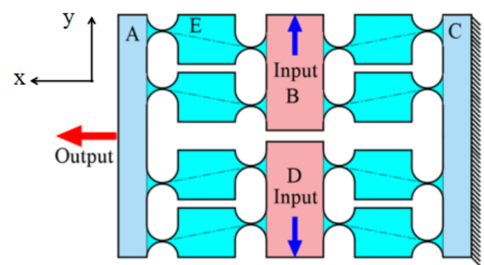

Figure 2: The schematic diagram of the compound bridge- type hinge.

In order to more accurately analyze the relationship between the relative displacement of ends B and D and the relative displacement of ends A and D, One-quarter of the model shown in Fig. 2 is taken for theoretical analysis, as shown in Fig. 3.

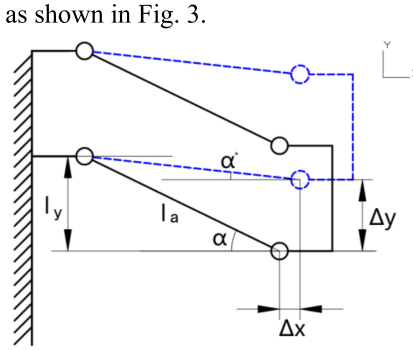

Figure 3: Simplified analysis of bridge-type composite hinge model.

In Fig. 3, l_y represents the distance (eccentricity) between the two ends of the hinge structure E in the y direction, l_a represents the arm length of the hinge structure (the length of the dotted line in Fig. 2), and α represents the angle between the arm length and the horizontal direction.

†jiangshuaikang@mail.ustc.edu.cn

ISBN: 978-3-95450-250-9 ISSN: 2673-5520 doi:10.18429/JACoW-MEDSI2023-TUPYP027

Refer to Figs. 2 and 3, when a certain force is applied to ends B and D to cause a certain displacement Δy along the y direction, according to the geometric relationship in Fig. 3, ends B and D will produce a certain parasitic displacement Δx in y direction. We can establish the relationship between the parameters l_y, l_a, α and Δx, Δy :

$$\begin{aligned} l_a cos\alpha + \Delta x = l_a cos\alpha^* \\ l_a \ sin\alpha - \Delta y = l_a sin\alpha^* \end{aligned} , \quad (1)$$

where:

$$\alpha = \text{arcs}\left(\frac{l_y}{l_a}\right) . \quad (2)$$

Eliminate parameter α^*:

$$\Delta y = l_a sin\alpha - \sqrt{l_a{}^2 sin^2\alpha - \Delta x^2 - 2 l_a cos\alpha \Delta x} . (3)$$

Then we can get the relationship between the multiples of the input displacement Δy and the output displacement Δx:

$$A = \frac{\Delta y}{\Delta x} = l_a sin\alpha - \sqrt{\frac{l_a{}^2 sin^2\alpha - \Delta x^2 - 2 l_a \Delta x cos\alpha}{\Delta x}} . \quad (4)$$

That is, through the bridge-type composite flexible hinge structure shown in Fig. 2, with terminals B and D as input terminals and A as the output terminal, the displacement of the input terminal can be reduced by A times and output from terminal A.

It can be seen from the formula that the displacement scaling factor A is ultimately related to l_y and l_a, so the displacement scaling factor of the bridge composite flexible hinge can be adjusted by changing the value of l_y, as shown in Fig. 4.

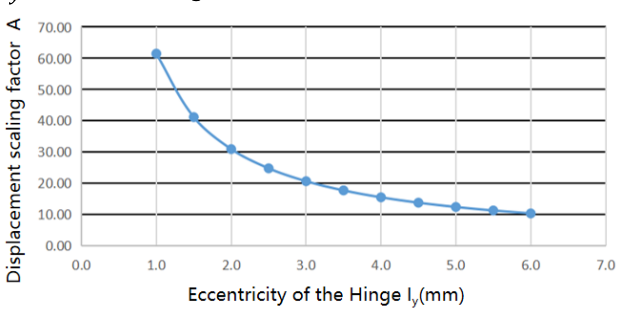

Figure 4: The relationship between l_y and A.

MECHANICAL DESIGN OF THE ACTUATOR

Figure 5(a) shows a sub-nanometer displacement actuator based on a compound bridge-type hinge design. The piezoelectric actuator is fixed on the D end of the bridge-type composite flexible hinge, so that it can push the B end. Due to the interaction of forces, the piezoelectric actuator exerts equal magnitude and direction on the B and D ends of the bridge-type composite flexible hinge. Opposite driving force, resulting in input displacement. In order to enhance the lateral stiffness of the bridge-type composite flexible hinge, a lateral hinge is designed at its output end to support and constrain the degrees of freedom except the driving direction. Figure 5(b) shows a hierarchical composite actuator with a piezoelectric actuator as a coarse adjustment stage and a sub-nanometer displacement actuator as a fine adjustment stage.

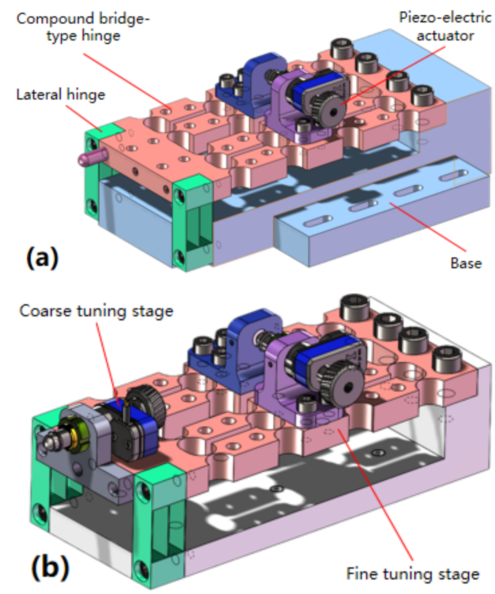

Figure 5: The mechanical design of the actuator.

EXPERIMENT AND RESULT

A prototype machine was produced for testing based on the design in Fig. 5. As shown in Fig. 6, a laser interferometer was used to measure the displacement of the input end and the output end to calculate the actual displacement scaling factor of the prototype machine.

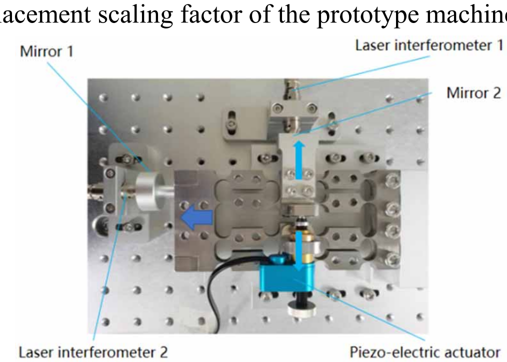

Figure 6: Minimum resolution test for the prototype.

We also drove the piezoelectric actuator with a step value of 1 to test the minimum resolution that can be achieved at the output end of the prototype machine in this case. The measured minimum resolution result at the output end is shown in Fig. 7. The experimentally measured displacement scaling factor of the prototype is about 40. Combined with the measured minimum resolution of the prototype of 0.35 nm, it can be calculated backwards that the step displacement of the piezoelectric actuator in 1 step is about 14 nm, which is the same as the measurement in Fig. 1. The step

ISBN: 978-3-95450-250-9 ISSN: 2673-5520 doi:10.18429/JACoW-MEDSI2023-TUPYP027

displacement of the piezoelectric actuator is consistent with 1 step.

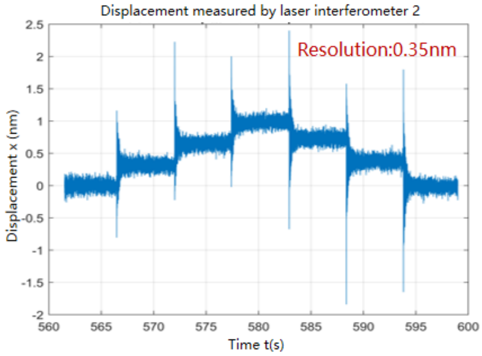

Figure 7: Minimum resolution test results.

On the basis of the prototype machine in Fig. 5(a), a piezoelectric actuator is added as a coarse adjustment stage to form the composite actuator shown in Fig. 5(b), which is used to drive the weak-link mechanism, as shown in Fig. 8. We place three different types of laser interferometers on the weak-link mechanism to measure the minimum angular resolution that the mechanism can achieve.

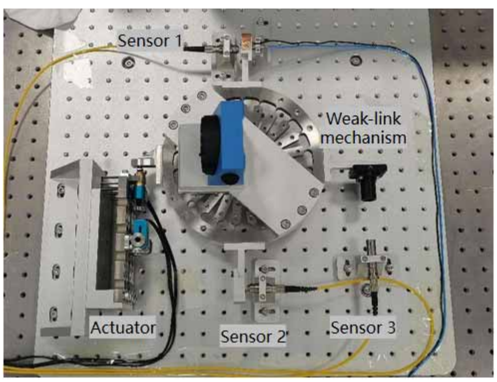

Figure 8: Angular resolution test device.

Figure 9 shows the measurement results of one of the laser interferometers. The measured minimum angular resolution of the weak-link mechanism is about 3.5 nrad. Combined with the magnification of the driver (40 times), it is exactly the same as the direct piezoelectric actuator in Fig. 1. The angular resolution measured by the sensor driver is consistent, further proving the reliability of the prototype.

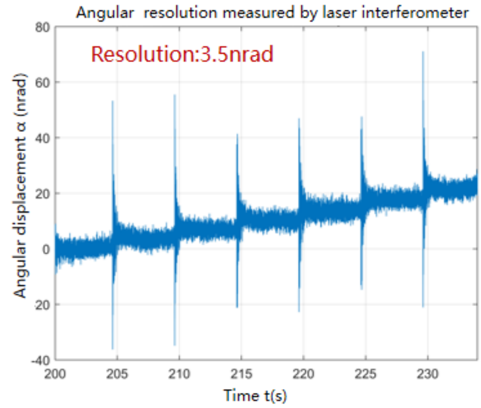

Figure 9: Measurement results from one of the laser interferometers.

CONCLUSION

This poster briefly proposes a method to achieve sub-nanometer displacement actuation at a lower cost and shows preliminary experimental results of the prototype produced. Due to time constraints, relevant tests on the driving force and stability of the driver will be carried out later.

REFERENCES

[1] D. Shu *et al.*, “Applications of Laminar Weak-Link Mechanisms for Ultraprecision Synchrotron Radiation Instruments”, in *AIP Conf. Proc. 879,* pp. 1073-10-76, 2007. doi:10.1063/1.2436249

[2] Q. Xu and Y. Li, “Analytical modeling, optimization and testing of a compound bridge-type compliant displacement amplifier”, *Mech. and Mach. Theory*, vol. 46, no. 2, pp. 183-200, 2011. doi:10.1016/j.mechmachtheory.2010.09.007

ISBN: 978-3-95450-250-9 ISSN: 2673-5520 doi:10.18429/JACoW-MEDSI2023-TUPYP028

THERMAL ANALYSIS SOFTWARE FOR OPTICAL ELEMENTS OF HEFEI ADVANCED LIGHT FACILITY*

Minghao Lin#, Jie Chen, Zimeng Wang, Shuaikang Jiang, Qiuping Wang, NSRL, University of Science and Technology of China, Hefei, Anhui, P. R. China

Abstract

Thermal deformation is a key influencing factor in the surface shape of optical elements for beamline. In the process of beamline design, it is necessary not only to select different cooling schemes based on thermal loading conditions but also to extensively optimize the parameters of these cooling schemes. The traditional approach for optimizing cooling scheme design often requires significant manual effort. By integrating existing experience in optimizing cooling scheme designs, this study transforms the parameterized design tasks that are originally performed manually into automated processes using software. This paper presents the latest advancements in the automated design software for cooling schemes of beamline optical components, and the results indicate that the optimization outcomes of the existing automated design software are close to those achieved through manual optimization.

INTRODUCTION

ANSYS-based thermal analysis methodologies have found extensive application in the design of cooling strategies for optical elements employed in synchrotron radiation light sources worldwide. As the development of synchrotron radiation light sources progresses, the thermal analysis of optical elements faces two key challenges: (1) A notable increase in the quantity of high heat load optical elements, imposing a substantial burden on the engineering optimization phase of cooling system design, often demanding significant efforts from designers. (2) The need for optical elements to conform to exacting standards regarding the non-destructive transmission of radiation from the light source to the end-station, which significantly complicates the engineering optimization of cooling schemes, often necessitating iterative refinement.

Cooling methods for synchrotron optics are generally well-established, encompassing techniques such as direct cooling, indirect side cooling, and indirect liquid metal cooling [1-3]. At the Hefei Advanced Light Facility (HALF), the predominant cooling methods include direct cooling, indirect side cooling, and indirect liquid metal cooling. Within HALF, principal cooling mechanisms involve side water cooling, liquid metal bath water cooling, and side liquid nitrogen cooling. While these cooling schemes possess relatively fixed spatial structures, variations in parameters, such as the positioning and depth of Smart cut, can substantially impact the geometry of optical elements. Consequently, the optimization of structural parameters assumes paramount importance in cooling scheme design.

To address this challenge, we have leveraged ANSYS secondary development technology [4-5] with the aim of crafting software tailored for the thermal analysis of synchrotron optics, thereby enhancing the efficiency of cooling scheme design.

* This work is supported by the Chinese Academy of Science (CAS) and the Anhui province government for key techniques R&D of Hefei Advanced Light Facility.
# mhlin@mail.ustc.edu.cn

SOFTWARE DESIGN

Solving Process

There are two routes for secondary development based on ANSYS: one is based on the secondary development of UPF inside ANSYS; the other is through MATLAB or python software, calling the command flow and ANSYS to solve the problem, and then return the results of the solution to MATLAB and python for further processing. We finally chose the second route for two reasons: firstly, we need to calculate the residual surface shape error and other information after obtaining the surface shape data, which is more conducive to data processing and visualization in MATLAB or python; secondly, we hope that in the future, the software can communicate with the optical calculation software, so as to obtain a more comprehensive beamline design software.

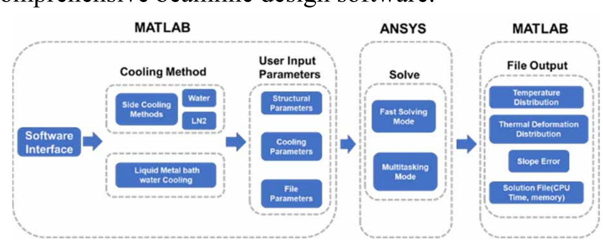

Figure 1: Computational route of the software.

The software gives priority to the service of Hefei Advanced Light Source, so the functions developed for the time being include: side cooling method (water cooling, liquid nitrogen) and liquid metal bath water cooling method. Software operation process is as follows: first of all, in the MATLAB interface to select the cooling program, and input structural parameters, cooling parameters and file location information; the parameters are processed and then written into the command flow file, and then call ANSYS to read the command flow file for the solution, after the completion of the solution, the output of the results of the file, such as the distribution of the surface type, the temperature distribution, as well as the solution of the information (such as solving time, consume memory, etc.), and finally MATLAB is used for data processing and

ISBN: 978-3-95450-250-9 ISSN: 2673-5520 doi:10.18429/JACoW-MEDSI2023-TUPYP028

visualization for easy reading. The computational route is shown in Fig. 1.

SOFTERWARE EXAMPLE

In this section, the focus is on the side cooling method in the software and its optimization example for plane mirror in test beamline in the Hefei Advanced Light Facility.

Model

For side cooling model, the optics are held on both sides by perforated copper blocks with an indium film sandwiched between the optics and the blocks to increase heat transfer. The model is shown in Fig. 2.

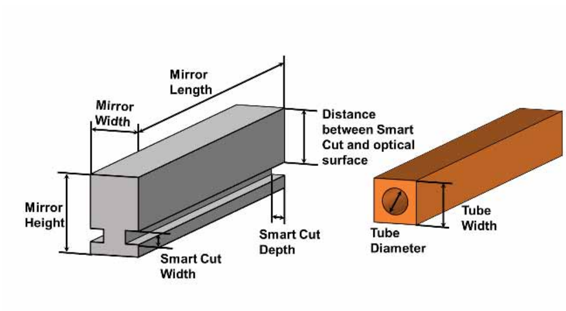

Figure 2: Model of side cooling method.

The factors affecting thermal deformation in the side cooling scheme are also all listed in Fig. 2. These parameters need to be set by the user in the software.

In the simulation, the indium film model is not established, but contact thermal conductivity of 12000 W/m^2/K is used to replace it [6].

Software Interface

In the software, in addition to the parameters in the previous section, it is also possible to set the footprint size to be used, which corresponds to the realistic situation of setting the slit downstream of the beamline as shown in Fig. 3. If the spot size used is too small, it will reduce the slope error but will also reduce the flux.

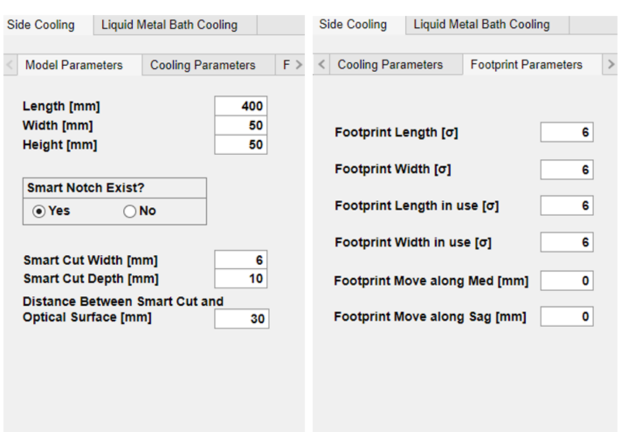

Figure 3: Model parameters interface.

The shift in the footprint meridional direction corresponds to the spot shift due to the off-axis rotation of the optics. The shift in the sagittal direction, on the other hand, is used to calculate whether the thermal deformation meets the design requirements when the optics are in service for a certain period of time by moving the optics to avoid areas of possible damage.

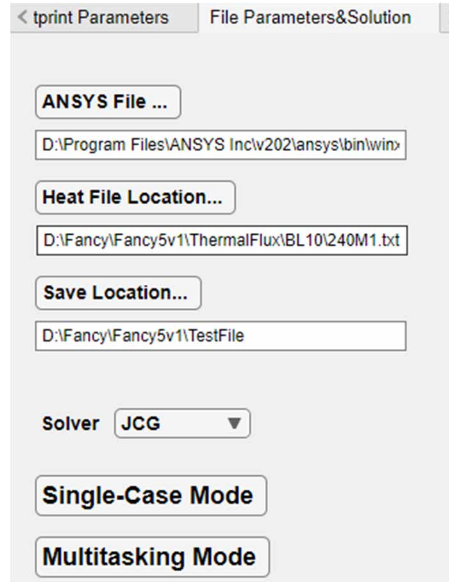

Figure 4: File information interface.

Designers can use the multitasking mode in the software to analysis the effect of a parameter on thermal deformation by traversing it, and also to find the optimal solution as shown in Fig. 4. The multitasking mode allows traversing several parameters at the same time, which saves the designer's time.

The designer needs to select the location of the ANSYS .exe, the location of the heat load file, and the path to save the file in order to run the program correctly.

Designers can view the thermal deformation calculation results through the interface, in which the blue line represents the original thermal deformation and the red line represents the fitted circle as shown in Fig. 5. In the Slope Error curve, the blue line represents the original slope error and the red line represents the residual slope error.

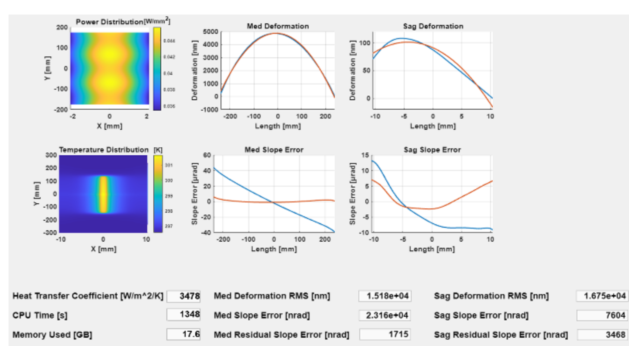

Figure 5: Result interface.

Optimized Example

PM is the second mirror in test beamline with an absorbed total power of 64 W and power density of 0.2 W/m^2.

ISBN: 978-3-95450-250-9 ISSN: 2673-5520 doi:10.18429/JACoW-MEDSI2023-TUPYP028

The optimization process allows us to study the effect of a particular parameter on thermal deformation as shown in Fig. 6. Figure 6(a) demonstrates the thermal deformation in the case of different smart cut depths, and Fig. 6(b) shows the relationship between the residual slope error in the meridional direction at the Smart cut depth.

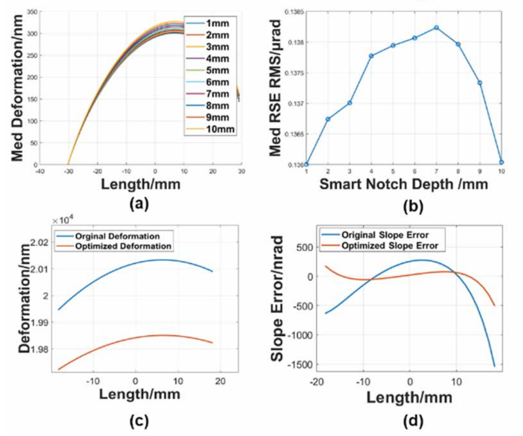

Figure 6: Optimized result.

After optimization of all parameters, Fig. 6(c) demonstrates the thermal deformation of PM before and after optimization, and Fig. 6(d) demonstrates the Slope Error of PM before and after optimization. Further information is shown in Table 1.

Table 1: Optimized Result

	Before	After
Sag Slope Error (μrad)	7.63	8.41
Sag Residual Slope Error (μrad)	0.09	0.08
Med Slope Error (μrad)	9.11	5.23
Med Residual Slope Error (μrad)	0.47	0.13

From Table 1, it can be seen that for the sagittal direction, the optimization effect is not obvious, while for the meridian direction the residual slope error is reduced from 0.47 μrad (rms) to 0.13 μrad (rms), which reaches the engineering requirement of 0.2 μrad (rms).

CONCLUSION

A thermal analysis software has been designed to optimize the design of the cooling structure and method of the optical components. The PM of the test beamline is used as an example to illustrate the cooling structure of the optical element. In the future, we will further optimize the design interface and improve the human-machine interaction.

REFERENCES

[1] L. Zhang *et al.*, "Thermal distortion minimization by geometry optimization for water-cooled white beam mirror or multilayer optics". *J. Phys. Conf. Ser.*, vol. 425, no. 5, p. 052029, 2013. doi:10.1088/1742-6596/425/5/052029

[2] L. Zhang *et al.*, "The performance of a cryogenically cooled monochromator for an in-vacuum undulator beamline", *J. Synchrotron Radiat.*, vol. 10, no. 4, pp. 313-319, 2003. doi:10.1107/S0909049503012135

[3] C. Cocco *et al.*, "Adaptive shape control of wavefront-preserving X-ray mirrors with active cooling and heating", *Opt. Express*, vol. 28, no. 13, pp. 19242-19254, 2020. doi:10.1364/OE.394310

[4] *ANSYS® ANSYS Mechanical APDL Command Reference*, ANSYS, Release 2020R2.

[5] *ANSYS® ANSYS Mechanical APDL Element Reference*, ANSYS, Release 2020R2.

[6] A.M. Khounsary *et al.*, "Measurement of thermal contact conductance of SPring-8 beamline components", in *Proc. SPIE*, vol. 6705, 2007. doi:10.1117/12.735397

ISBN: 978-3-95450-250-9 ISSN: 2673-5520 doi:10.18429/JACoW-MEDSI2023-TUPYP030

THE DESIGN OF HIGH STABILITY DOUBLE CRYSTAL MONOCHROMATOR FOR HALF

Zhanglang Xu, Jie Chen, Yang Peng, Xuewei Du, Qiuping Wang, National Synchrotron Radiation Laboratory (NSRL), University of Science and Technology of China (USTC), Hefei 230026, China

Abstract

The monochromator is known to be one of the most critical optical elements of a synchrotron beamline, since it directly affects the beam quality with respect to energy and position. Naturally, the new 4th generation machines, with emittances in the range of order of 100 pm rad, require even higher stability performances. A high stability DCM (Double Crystal Monochromator) is under development at the HALF, the new 4th generation synchrotron. In order to achieve high stability of tens of nano radians, as well as to prevent unpredicted mounting and clamping distortions, simulation are proposed for crystal angular vibration and thermal management. This paper gives an overview of the DCM prototype project including specifications, Mechanical design, heat load management and stability consideration.

INTRODUCTION

In the recent years it has become clear to the Diffraction Limit Storage Rings (DLSR) that the stability performance of DCMs would turn out to be one of the main bottlenecks in the overall performance of many X-rays beamlines. With the arrival of the diffraction-limited ring, This is because the instabilities in the DCM affect the position and the size of the virtual source, and, consequently, the spot size and the position of the beam at the sample. The angular instability between the two crystals is the most critical one because its effects on the virtual source scales with the lever-arm between the monochromator and the source [1].

Of the ten lines in the HAFL pre-construction, two of them use crystal monochromators. One of them has an energy range of 2-8 keV, and they both have high requirements for stability. In order to ensure that the stability required to meet the target requirements, this paper briefly describes the design of the DCM from the convenience of mechanical structure design, thermal stability analysis (1st crystal slope and temperature distribution of the core module) and vibration analysis. Detailed finite element analysis ensures that stability requirements and optical requirements (energy range, resolution and luminous flux) can be met. This prototype is designed to meet basic engineering needs.

SPECIFICATIONS

Depending on the energy, stability and coherence requirements of the beamline, an prototype of a high stability vertical DCM (Double Crystal Monochromator) with angular range between 14 and 81 degrees (equivalent to 2 to 8 keV with Si(111)) has been developed at the National Synchrotron Radiation Laboratory. Table 1 summarizes the main functional specifications of this DCM.

Table 1: Main Specifications for the DCM Prototype

Parameter	Description
type	Vertical DCM
Beam offset	20 mm
Angular range	14° - 81°
Angular resolution	0.5 μrad
Crystal	Si (111): 2 to 8 keV
Crystal Cooling	1st crystal: Indirect LN2
	2nd crystal: Copper straps
Beam size	4×3.3 mm^2
Input power	38.9 W

STRUCTURE DESIGN

The DCM can be divided in the following parts: support, vacuum vessel, rotary system and core (Fig. 1). The DCM is divided into the following parts: support, vacuum chamber, rotation system and core mechanism. The main axis mainly realises the crystal Bragg angle adjustment for energy selection and regulation. The crystal assembly contains the clamping, cooling, and adjustment of the first and second crystals, which directly affects the face shape, stability, and adjustment accuracy of the crystals. The granite support pedestal mainly realises attitude adjustment, provides support, ensures high stability, and at the same time carries out the exchange of crystals to achieve energy expansion. The cooling pipeline mainly provides liquid nitrogen delivery, and the reasonable design can control the vibration problem caused by the fluid. Cavity components mainly contain vacuum chamber, providing various types of vacuum interfaces and monitoring role.

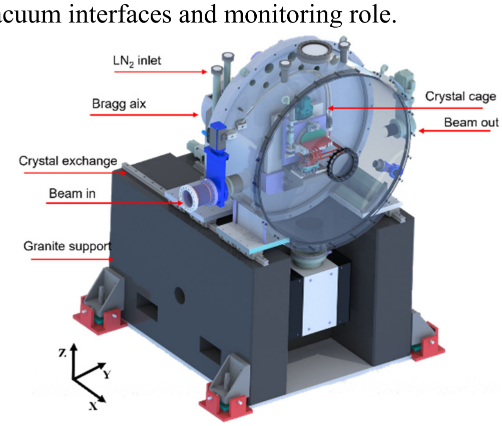

Figure 1: DCM assembly.

ISBN: 978-3-95450-250-9 ISSN: 2673-5520 doi:10.18429/JACoW-MEDSI2023-TUPYP030

Crystal Cage

All motorized movements of the optics (common horizontal, crystal gap translation, roll2, and pitch2) are integrated to the vacuum vessel. Those mechanics are mounted onto a shaft rigidly fixed to the monochromator support assembly (Fig. 2).

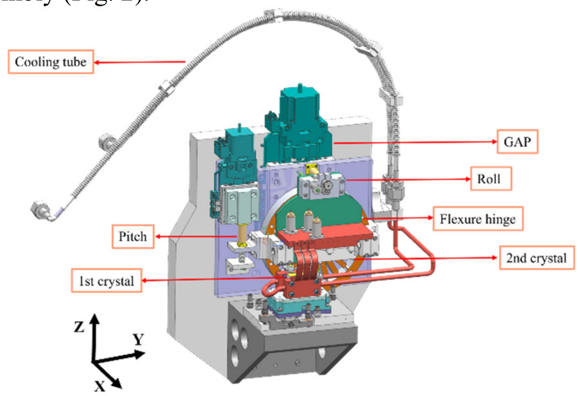

Figure 2: Schematic view of crystal cage.

In order to keep the fixed exit condition whilst changing the energy a gap translation varying the distance between 1st and 2nd crystal is used for the 2nd crystal assembly. The stage design uses two slides based on cross roller bearings driven by a stepper actuated recirculating ball screw assembly. The entire stage is preloaded. During assembly the stage is pre-characterized and optimized to reduce the parasitic movements of the axis down to a minimum in order to achieve high parallelism between 1st and 2nd crystal when scanning the energy (combined motion of Bragg and gap). For high stiffness of the stage the width between the rails as well as their length is enlarged as much as reasonably possible.

For parallelizing the reflecting surfaces of 1st and 2nd crystal a fine adjustment is placed on top of the 2nd optics gap translation. This stage rotates the 2nd crystal surface around an axis parallel to the Bragg axis. A preloaded flexure hinge stage is integrated and actuated with a stepper and piezo via a sine bar. The flexure hinge mechanism for the pitch consists of a number of bars connected to an outer (movable) ring on which the piezo actuates and an inner (fixed) ring by means of flexures on both ends (cartwheel design). All bars are directed to the center of the two rings which is the center of rotation for the pitch, coinciding with the 2nd optics surface. The entire flexure mechanism is made from one single part by means of precision EDM wire erosion. For the pitch stage a combination of stepper motor (gear reduced) driven spindle and piezo is used to allow for coarse adjustment over a wide range and for high-resolution fine adjustment over a limited range facilitating RC scans and the possibility to integrate the pitch stage into a position or intensity feedback system.

The in-vacuum mechanics contains a roll movement parallelizing 1st and 2nd optics around the beam direction. The rotation in roll is realized by means of a cradle with two cross flexure bearings providing a stiff and backlash free mechanical connection. This cradle is actuated by means of a stepper motor (gear reduced) driven spindle and a piezo as well. The actuation mechanism is again a sine bar with an additional reversing element changing the direction of actuation by 90°. This is done to allow for integration of the roll actuator in horizontal. Both piezos for pitch and roll can be operated in closed loop feeding back on the real angular position of the pitch and roll stage monitored by an external encoder. For that the piezo driver is equipped with an encoder input on which the feedback loop of the piezo driver works on. The resolution of the piezo actuator being < 2E-6 of the full stroke is sufficiently large to provide increments of < 0.01 µrad. The used piezo actuators are strongly pre-loaded to provide high stiffness in the actuation mechanism.

Thermal Management

From long term experience as well as the results of the preliminary FEA indicate, a heat load of up to 300 Watts and power densities of ~3 Watts / mm² (projected, worst case consideration) can still be coped with an indirect cooling of the 1st crystal mount assuming sufficiently large cooling surface. In order to provide sufficient cooling for the 1st crystal the substrate is clamped between two copper heat exchangers [2, 3]. Cu tubing is brazed to those heat exchangers to let the LN2 flow through for cooling. The thermal contact is enhanced using a layer of thin Indium foil between Si substrate and the Cu heat exchanger. The FEA, referring to the heat leakage from thermal conduction and radiation, was performed, so that the structure of the cryo-area was optimized. The result shows that under the clamping cooling method, the residual slope error has reduced down to 0.01µrad whose thermal deformation is shown (Fig. 3).

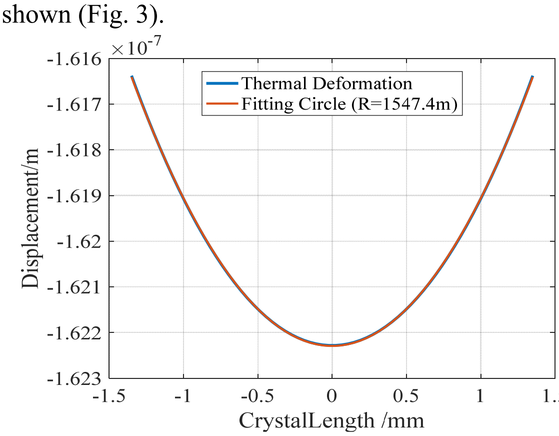

Figure 3: Surface height of 1st crystal.

In order to stabilize the main mechanics also in temperature providing a high thermal stability of the system heaters are integrated to the mechanics. This thermal stabilization avoids long term thermal variations due to (a) drifts introduced by the cryogenically cooled parts mounted close to the mechanics. In particular for the parts and adjustment units positioned very close to the cryogenically cooled crystal assemblies the stabilization system supports the thermal isolation between cooled parts and the mechanics at ambient temperature. (b) changing thermal conditions in the crystal assemblies and their shields due to changing heat loads (varying ID gap, changing the energy)

ISBN: 978-3-95450-250-9 ISSN: 2673-5520 doi:10.18429/JACoW-MEDSI2023-TUPYP030

(c) temperature fluctuations of the environment. After finite element thermal analysis, The temperature distribution of the core area of the DCM is as Fig. 4. Thermal isolation is achieved between the crystal, the core mechanism and the environment.

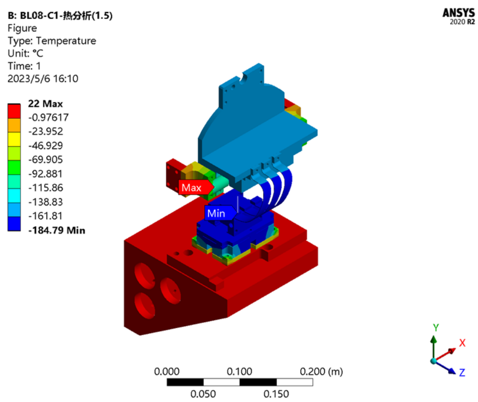

Figure 4: Temperature distribution of the core area.

Vibration Analysis

After vibration simulation analysis, the vibration data from the HALF ground was used as input to obtain the absolute angular vibration. in the pitch direction of the first crystal as 17.8 nrad, the absolute angular vibration of the second crystal as 11.5 nrad, and the relative angular vibration of the crystal as 10.2 nrad (Fig. 5).

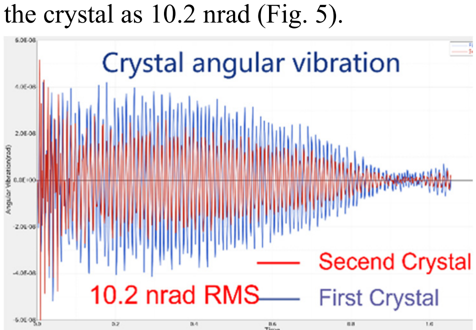

Figure 5: Crystal angular vibration.

CONCLUSIONS

This paper briefly described the DCM design and thermal management for the DCM for HALF. Several analytical and numerical tools have been used in order to design them with specific targets regarding slope errors, thermal response, and crystal vibration.

ACKNOWLEDGEMENT

This work is supported by the Chinese Academy of Science (CAS) and the Anhui province government for key techniques R&D of Hefei Advanced Light Facility.

REFERENCES

[1] P. Kristiansen, J. Horbach, R. Doehrmann, J. Heuer, *et al.*, “Vibration measurements of high-heat-load monochromators for DESY PETRA III extension”, *Synchrotron Rad*, vol. 22, pp. 879-885, Jul. 2015.

[2] M. Saveri Silva *et al.*, “Thermal Management and Crystal Clamping Concepts for the New High-Dynamics DCM for Sirius”, in *Proc. MEDSI’16*, Barcelona, Spain, Sep. 2016, pp. 44-47. doi:10.18429/JACoW-MEDSI2016-MOPE19.

[3] P. Carpentier, M. Rossat, P. Charrault, *et al.*, “Synchrotron monochromator heating problem, cryogenic cooling solution”, *Nucl. Instrum. Methods A*, vol. 456, issue 3, Jan. 2001, pp. 163–176.

ISBN: 978-3-95450-250-9 ISSN: 2673-5520 doi:10.18429/JACoW-MEDSI2023-TUPYP032

AN ARGON-OXYGEN OR ARGON-HYDROGEN RADIO-FREQUENCY PLASMA CLEANING DEVICE FOR REMOVING CARBON CONTAMINATION FROM OPTICAL SURFACES

Hongjun Yuan†, Xuewei Du, Qiuping Wang, National Synchrotron Radiation Laboratory, University of Science and Technology of China, 230026 Hefei, China

Abstract

Due to synchrotron radiation, carbon contamination on the surfaces of optical elements inside the beamlines, such as mirrors and gratings, remains an issue. Future beamline designs will select more optical element surface coating materials according to the specific needs, including gold, platinum, chromium, nickel, and aluminum, and a single cleaning method will not be able to adequately address the demands. We have studied the radio-frequency (RF) plasma cleaning of optical elements. After the Ar/O_2 or Ar/H_2 gas mixture was injected into the chamber, glow discharge was carried out, and the carbon on the surface of the inert metal-coated optical element and oxidation-prone metal-coated optical element was removed by the oxidation or reduction reaction of radicals. In order to optimize the discharge parameters, it utilizes a differential mass spectrometry system and an optical emission spectrometer to monitor the cleaning process. This poster introduces the principles of the two cleaning methods as well as our existing cleaning device.

INTRODUCTION

Carbon contamination is a typical issue for high flux optical elements in synchrotron radiation beamlines. Short-wave light irradiation cracks the hydrocarbons, which then deposit a layer of carbon deposition on the surface of the optical element. This causes a decrease in reflectivity in the vacuum ultraviolet and soft X-ray regions as well as a loss of photon flux.

More varieties of coated mirrors and gratings will be chosen for the Hefei Advanced Light Facility (HALF) beamline in order to attain high performance. When the mirror coating is made of inert metal, such as Au or Pt, the carbon contamination could be removed using Ar/O_2 RF plasma cleaning. However, the reflectivity in the soft X-ray area may be decreased due to oxidation of the metal surface when the coating material is readily oxidized metal, such as Ni, Cr, or Al. The RF plasma cleaning approach using Ar/H_2 was suggested to clean optical elements in order to prevent the loss of reflectance by the oxidation of coating materials [1-3].

Based on the aforementioned reasons, Ar/O_2 and Ar/H_2 RF plasma cleaning system is constructed, equipped with cleaning parameter optimization system, which can achieve the optimal cleaning rate under varied operating conditions.

EXPERIMENTAL SETUP

Figure 1 shows the principle of cleaning carbon contamination with RF plasma. Under the influence of RF discharge, the mixed gas produces active free radicals that oxidize or reduce the carbon on the surface of the optical element to produce the volatile gas, such as CO_2, or CxHy, which could be removed by the vacuum pump.

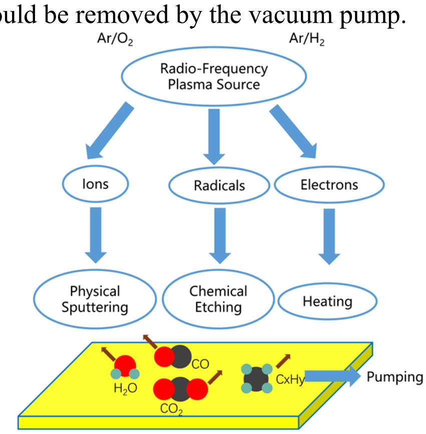

Figure 1: Schematic diagram of cleaning carbon contamination with RF plasma.

As seen in Fig. 2, the experimental device utilizes the laboratory's current RF plasma cleaning technology. The experimental equipment includes: cleaning chamber, gas mixing chamber, RF power supply and RF matching device, vacuum pumping system, etc. Ar/O_2 or Ar/H_2 enter the gas mixing chamber with a certain ratio through the mass flow meter. The mixed gas enters the cleaning chamber through the needle valve. By adjusting the needle valve and the pumping speed of the molecular pump unit, the cleaning chamber is maintained at a certain pressure. Turn on the RF power supply, adjust the RF matcher to find the appropriate discharge power, and perform glow discharge.

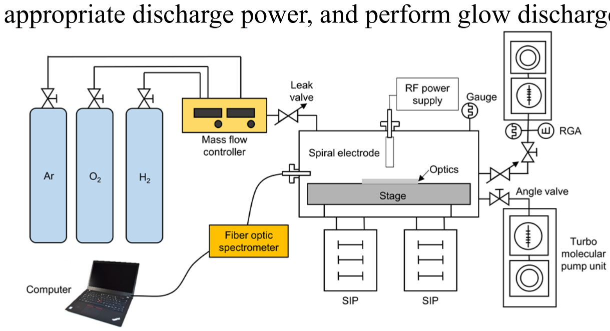

Figure 2: Setup for carbon contamination cleaning with RF plasma.

† yuanhj@mail.ustc.edu.cn

ISBN: 978-3-95450-250-9 ISSN: 2673-5520 doi:10.18429/JACoW-MEDSI2023-TUPYP032

OPTIMIZATION OF CLEANING PARAMETERS

A cleaning parameter optimization system based on a fiber optic spectrometer and quadrupole mass spectrometer was constructed, as shown in Fig. 2, in order to study the optimization of cleaning parameters for cleaning synchrotron radiation optical elements using RF plasma.

Previous research has demonstrated that chemical etching of active O or H atoms rather than physical sputtering of active Ar atoms plays a more significant role in the cleaning process. Indirectly, the rate of cleaning of the carbon contamination is seen with the concentration of O or H atoms. A CF35 fiber feeding flange is installed on the side of the cleaning chamber, connect the optical fiber to couple the spectral signal into the fiber spectrometer, and then detect the RF electrode discharge to see how the intensity of the O I (777.2 nm), H I (656.2 nm), and Ar I (750.3 nm) light emission spectral lines changes.

Ar/O2 Plasma Cleaning Parameter Optimization

The gas mixing ratio has a greater influence on the cleaning rate, and is first controlled as a variable. The reading of the vacuum gauge is 5 Pa, the integration time of the spectrometer is 200 ms, and the flow indicator is changed. The gas mixing ratio is controlled by the Ar/O_2 flow. Spectral detection of the glow discharges generated under different gas ratios was carried out, and the curve of change rule of O atom intensity at 777.2 nm was obtained. The collected spectral information is shown in the Fig. 3.

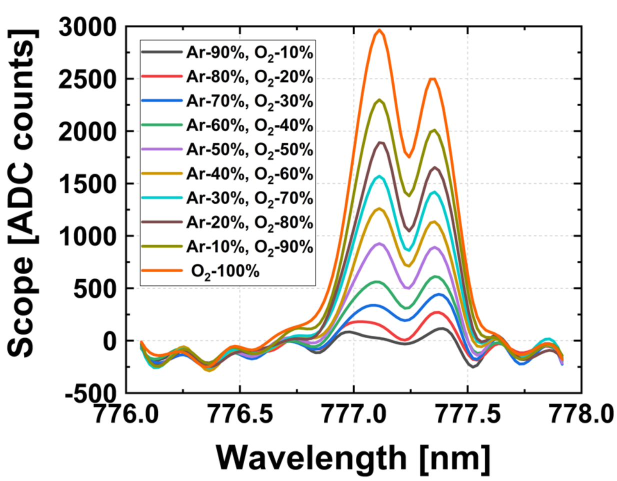

Figure 3: O atom intensity (@777.2 nm) at 5 Pa with different Ar/O_2 ratio.

In Ar/O_2 plasma cleaning, although 100 % oxygen produces more reactive oxygen species, the total number of ions in the chamber will be less, as shown in the Fig. 4. Considering the physical sputtering effect during cleaning, the argon-oxygen cleaning ratio will be adjusted to 30 %-70 %.

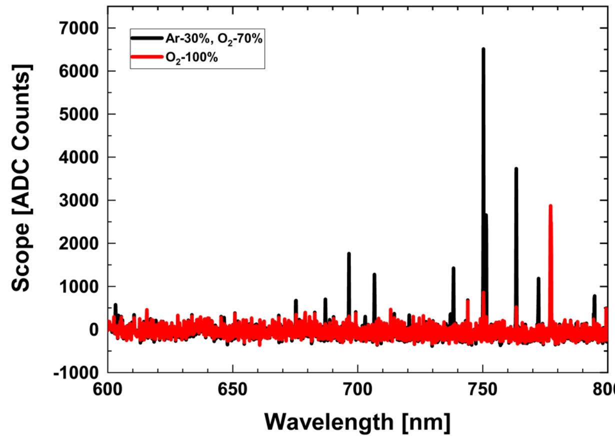

Figure 4: Optical spectrum when Ar/O_2 is 30 %:70 % and 100 % oxygen.

The working pressure also has a great influence on the cleaning rate, which is controlled as a variable. The Ar/O_2 flow ratio of the flow indicator is 30 %-70 %, the integration time of the spectrometer is 200 ms. Changed the indication of the vacuum gauge from 0.2 Pa to 10 Pa. Spectral detection of the glow discharges generated under different pressures was carried out, and the curve of change rule of the oxygen atom intensity at 777.2 nm was obtained, as shown in the Fig. 5.

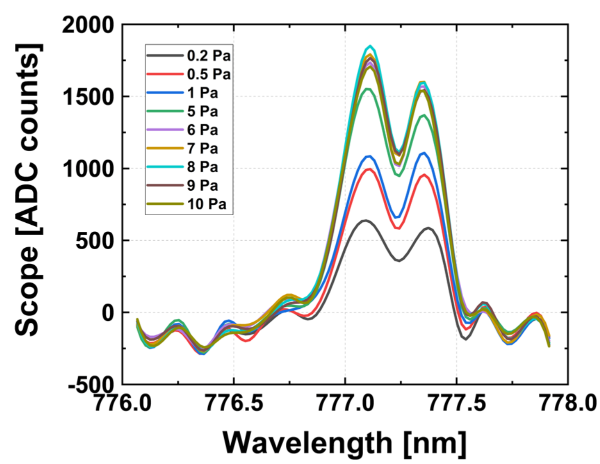

Figure 5: O atom intensity (@777.2 nm) at 5 Pa with different working pressure.

Ar/H2 Plasma Cleaning Parameter Optimization

The same technique was applied to optimize the Ar/H_2 plasma cleaning parameters, and the spectral intensity at the H atom (656.2 nm) was observed. Figures 6 and 7 show the results of tests on the mixing ratio and working pressure, respectively.

ISBN: 978-3-95450-250-9 ISSN: 2673-5520 doi:10.18429/JACoW-MEDSI2023-TUPYP032

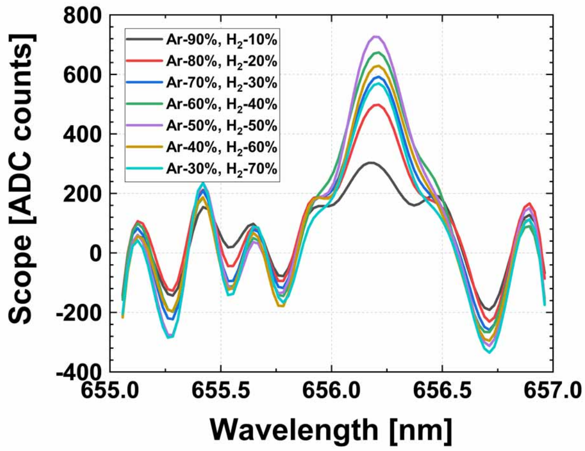

Figure 6: Hydrogen atom concentration (@656.2 nm) at 5 Pa with different Ar/H_2 ratio.

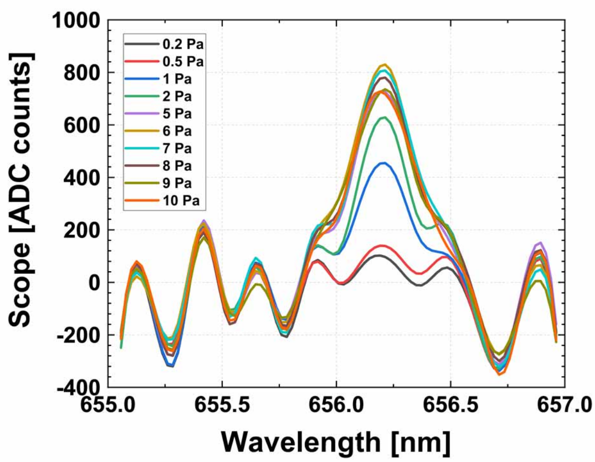

Figure 7: H atom concentration (@656.2 nm) at 50 %:50 % with different working pressure.

Results

The results of cleaning parameter optimization are shown in Table 1.

Table 1: Results of Cleaning Parameter Optimization

Plasma Type	Ar/O_2	Ar/H_2
Mixing Ratio	30 %:70 %	50 %:50 %
Working Pressure	8 Pa	6 Pa

EXPERIMENT

The carbon-contaminated Au-coated grating was cleaned with Ar/O_2 plasma for 6 h, the cleaning pressure was 8 Pa, and the Ar/O_2 mixing ratio was 30 %-70 %. The cleaning effect was shown as Fig. 8.

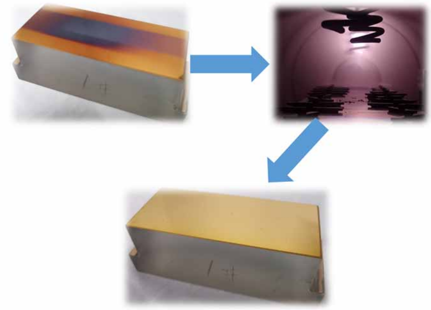

Figure 8: Cleaning of Au-coated grating with Ar/O_2.

The carbon-contaminated Al-coated mirror was cleaned with Ar/H_2 plasma for 4 h and 9 h, the cleaning pressure was 6 Pa, and the Ar/H_2 mixing ratio was 50%-50%. The cleaning effect was shown as Fig. 9.

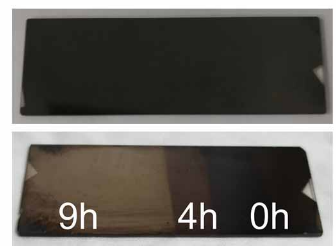

Figure 9: Cleaning of Al-coated mirror with Ar/H_2.

CONCLUSION

A system for RF plasma cleaning with Ar/O_2 and Ar/H_2 was constructed, and optical and mass spectrometers were used to optimize the discharge parameters and determine the cleaning cutoff point. The system can be used to remove carbon contamination from the surface of optical elements coated with easily oxidized or inert metal in the beamlines, enhance reflectivity, and boost photon flux. To create an ultra-clean, ultra-high vacuum environment, the method can also be used to clean superconducting RF cavities and storage rings.

REFERENCES

[1] Y. Wang *et al.*, "Enhanced removal of X-ray-induced carbon contamination using RF Ar/H_2 plasma", *Nucl. Sci. Tech.*, vol. 30, no. 2, p. 26, Jan. 2019. doi:10.1007/s41365-019-0547-9

[2] E. Pellegrin *et al.*, "Characterization, optimization and surface physics aspects of in situ plasma mirror cleaning", *J. Synchrotron Radiat.*, vol. 21, no. 2, pp. 300-314, Mar. 2014. doi:10.1107/S1600577513032402

[3] H. Moreno Fernández *et al.*, "Characterization of carbon-contaminated B_4C-coated optics after chemically selective cleaning with low-pressure RF plasma", *Sci. Rep.*, vol. 8, no. 1, p. 1293, Jan. 2018. doi:10.1038/s41598-018-19273-6

ISBN: 978-3-95450-250-9 ISSN: 2673-5520 doi:10.18429/JACoW-MEDSI2023-TUPYP037

MECHANICAL DESIGN OF MULTILAYER KIRKPATRICK-BAEZ (KB) MIRROR SYSTEM FOR STRUCTURAL DYNAMICS BEAMLINE (SDB) AT HIGH ENERGY PHOTON SOURCE (HEPS)

Ruiying Liao †, Haihan Yu, Lidan Gao, Zina Ou, Bingbing Zhang, Shanzhi Tang
Institute of High Energy Physics, Chinese Academy of Sciences, Beijing, China

Abstract

SDB aims in-situ real-time diagnosis in dynamic compression science and additive manufacturing. Nano-experimental environment requires highly multilayer KB mirror system in thermal deformation and stability of mechanism. This paper illustrates the KB cooling scheme and mechanical design. Only using variable-length water cooling to control the temperature and thermal deformation of mirror has limitations here. First, the installation of cooling system should be non-contact so that the surface shape can be sophisticatedly controlled without deformation of chucking power. Second, the distance between the HKB and the sample stage is too small to arrange the cooling pipe. Third, the KB mirror has multi-dimensional attitude adjustment. Cu water cooling pipe would be dragged with adjustment thus it has to be bent for motion decoupling, which occupies considerable space. Thus, the Cu cooling block and water cooling pipe are connected by copper braid. Eutectic Gallium-Indium fills a 100 µm gap between the cooling block and KB mirror to avoid chunking power deformation. Finally, the structural stability and chamber sealability are analyzed.

INTRODUCTION

Structural Dynamic Beamline (SDB) at High Energy Photon Source (HEPS) [1] intends to realize in-situ real-time diagnosis of dynamic and non-reversible processes in dynamic compression science and additive manufacturing fields [2]. The beamline station includes a micro-beam hutch, a large-spot hutch, and a nano-beam hutch. The multilayer Kirkpatrick-Baez (KB) mirror system is located at the last nano-beam hutch, which focuses the secondary source at 95.5 m on 210 m to form a 60 nm light spot. The nano experimental environment requires multilayer KB mirror system highly since any chunking power or thermal source would deform the KB mirror surface shape. The mechanical structure of multilayer KB mirror system was meticulously designed, especially the cooling scheme. Water or liquid nitrogen [3] cooling with oxygen-free high-conductivity (OFHC) copper braid [4] or copper stripe [5] is a common method for beamline station equipment, such as Fresnel zone plates (ZP) microscope modules [6] and monochromators [7]. Considering the installation space limitations and the surface shape requirement of the KB mirror, a water cooling scheme combining copper braids and eutectic GaIn [8] was utilized to remove thermal load. Deep calculation and finite element analysis (FEA) have been operated.

† email address : liaory@ihep.ac.cn

The remaining parts of this paper are organized as follows: Section 2 gives the overview of mechanical structure design. Section 3 depicts the cooling scheme and thermal ansys results. The conclusions are reported in Section 4.

MECHANICAL STRUCTURE DESIGN

The overview of mechanical structure design is shown in Fig. 1. The length, width, and height of the whole KB mirror system are 1430 mm, 740 mm, and 1150 mm respectively. The size of horizontal Kirkpatrick-Baez (HKB) is 70 mm×40 mm×50 mm and of vertical Kirkpatrick-Baez (VKB) is 120 mm×40 mm×40 mm. Except for the KB mirror, the multilayer KB mirror system includes pose adjustment mechanism, a gantry, and cooling system. The fishbone flexure hinge and U-frame flexure hinge mechanism are used for position and attitude adjustment respectively, which fulfill the movement requirement in Table 1. The granite air-bearing table outside the chamber controls the whole KB mirror system moving in X and Z-axis directions.

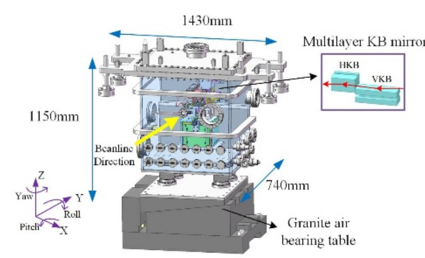

Figure 1: The mechanical structure.

Table 1: Adjustment Parameter Index for HKB, VKB, and Whole KB Mirror System

	Movement	Resolution	Range
HKB	X-axis	1µm	±0.5mm
	Yaw	1µrad	±10mrad
VKB	Z-axis	1µm	±0.5mm
	Y-axis	1µm	±0.5mm
	Pitch	1µrad	±10mrad
	Roll	10µrad	±20mrad
Whole System	X-axis	1µm	±5mm
	Z-axis	1µm	±5mm

A stable invar gantry shown in Fig. 2(a) is designed for metrology and to solve the problem of the limited installation space for HKB. By lightweight design, the gantry mass is only 188.3 kg. The granite stage is sufficiently stiff to not amplify vibrations. In FEA modal simulation, the resonance frequency is over 140 Hz. The first modal analysis and the direction of rigid motion are performed in Fig. 2(b). To avoid interference with the sample stage, the

ISBN: 978-3-95450-250-9 ISSN: 2673-5520 doi:10.18429/JACoW-MEDSI2023-TUPYP037

design of a special-shaped KB vacuum chamber is shown in Fig. 2(c). The max deformation of sealing surface is less than 0.05 mm in Fig. 2(d). The mechanical design is considered feasible.

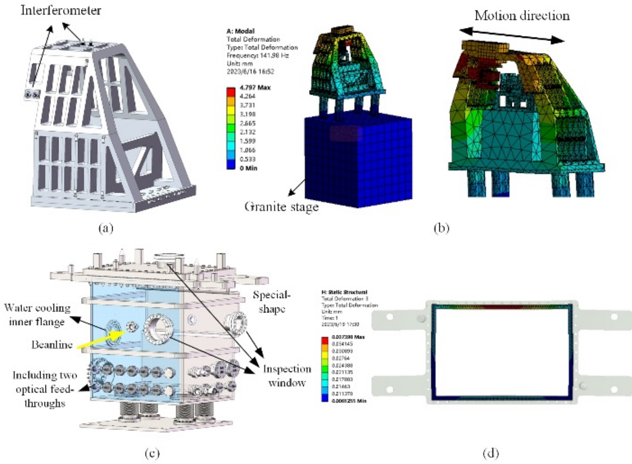

Figure 2: (a) The structure of the gantry. (b) FEA simulaiton result of gantry. (c) Mechanical structure of KB vacuum chamber. (d) Deformation of the sealing face.

COOLING SCHEME

By efficient thermal deformation optimization iteration analysis, a variable-length water cooling scheme was adopted [9]. The distribution of Cu cooling block of HKB and VKB is shown in Fig. 3.

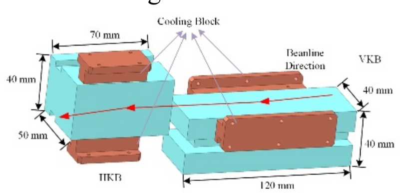

Figure 3: The distribution of Cu cooling block of HKB and VKB.

There are two things to note. First, the Cu cooling block design of HKB is very close to the sample stage. The distance between the HKB mirror and the sample stage is too small to arrange copper pipe and window flange. Besides, the VKB has a four-dimensional attitude adjustment. The copper pipe would be dragged with adjustment thus it has to bend for motion decoupling, which occupies considerable space in the chamber. To solve the two issues above, the Cu cooling block and cooling copper pipe are connected by copper braids. Second, the Cu cooling block should be in non-contact with KB mirror so that the surface shape would not be deformed by chucking power. Hence, a 100 µm gap between the cooling block and KB mirror is reserved, which is filled with eutectic Gallium-Indium (eGaIn). The eGaIn has a good thermal conductivity, whose thermal conductance is larger than 10^5 W/(m^{2}K). Therefore, a cooling scheme of copper braid & eGaIn is proposed. The mechanical structure of cooling part is shown in Fig. 4, which consists of HKB and VKB Cu cooling block, cooling pipe, copper braids, and a mask. The mask protects the mirror from the X-ray source.

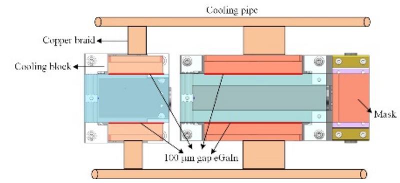

Figure 4: The mechanical structure of the cooling part.

Thermal Deformation Simulation

The cooling effect of copper braids with different thicknesses was analyzed. Four groups of simulations are conducted, including three groups with 2 mm, 5 mm, and 10 mm copper braids, and one group without. Through the same thermal power density distribution, the steady-state thermal simulation results are summarized in Table 2.

Table 2: The Simulation Temperature Results of Different Cooling Designs

Copper braids	HKB (°)		VKB (°)	
	Max	Difference*	Max	Difference
Without	25.160	0.114	25.662	0.501
10 mm	25.337	0.122	26.054	0.511
5 mm	25.435	0.124	26.426	0.521
2 mm	25.714	0.126	27.503	0.530

*The surface max difference temperature.

The max and max surface difference temperature of HKB and VKB is increased with decreasing thickness of copper braid, while too thick copper braids will put a burden on the mechanical structure. Hence, the cooling scheme of the copper braids with 5 mm thickness is utilized, and the thermal transient analysis of this scheme is given. The period of the heat source is 100 ms and the duty ratio is 0.2. In the simulation, the max temperature variation with time is shown in Fig. 5.

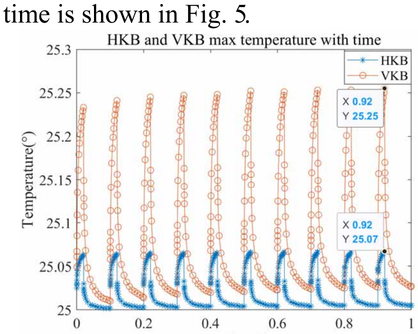

Figure 5: The variation of the max temperature in HKB and VKB surfaces with time.

In a period cycle, the max temperature values of HKB and VKB are about 25.07° and 25.25° respectively. Considering the mirror fix method, the thermal deformation difference on HKB and VKB mirror surface between the peak and valley (PV) situations is given in Fig. 6(a) and (b). According to Fig. 6, the thermal deformation pv difference on the meridional plane is shown in Fig. 7. The PV value of HKB is 0.11 nm and of VKB is 0.60 nm, which fulfills the experimental requirement.

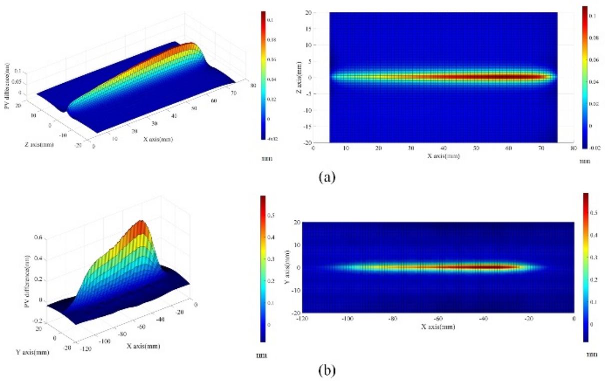

Figure 6: The thermal deformation PV difference on the mirror surface of HKB (a) and VKB (b).

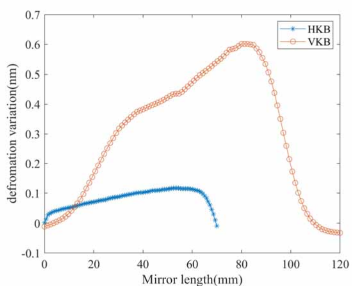

Figure 7: The thermal deformation PV difference at the meridional plane

Stress Analysis of Copper Pipe

Though the copper braids can decouple the motion of KB mirrors, the copper pipe still has to be bent for the two-dimensional movement of the whole equipment system. The cooling system is installed on the gantry. The water cooling outlet is connected to the outer chamber by a flange. When the whole KB equipment is adjusted, the gantry moves relative to the chamber. The X-axis and Z-axis movement range are both -5 to 5 mm. Therefore, the shape of the copper pipe is designed in Fig. 8(a). The maximum compound displacement of the X-axis and Z-axis is load in simulation and the static structural analysis is shown in Fig. 8(b). The max equivalent stress is 57 MPa, whose position is at a clamping point. Therefore, this bend design of copper pipe is optimized. The cooling design is not complex and space-occupying.

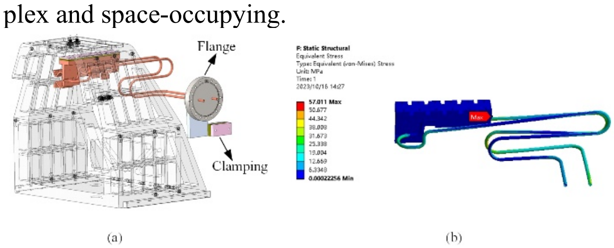

Figure 8: (a) The mechanical design of the cooling system. (b) The static structural analysis.

Mask Design

The mask is installed before the VKB in Fig. 9(a). In the simulation, a five times heat flux is loaded on the mask bevel. The result shows that the thickness of copper braids connected with the mask should reach 5 mm so that the max temperature of the mask surface, 257° in Fig. 9(b), does not exceed the melting point of OFHC.

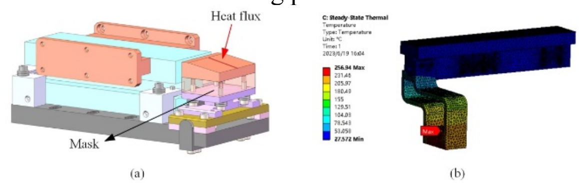

Figure 9: (a) The installation of the mask. (b) The steady-state thermal simulation result of the mask.

CONCLUSION

In this paper, the mechanical structure of multilayer KB mirror system for SDB at HEPS is designed. According to practical engineering cases, the water cooling system is adjusted. The structure and thermal FEA simulation is given. The analysis results fulfill the requirement. The KB mirror system will soon be in process and go into service.

REFERENCES

[1] Y. Jiao, G. Xu, X. H. Cui, *et al.,* "The HEPS project*", J. Synchrotron. Radiat.,* vol. 25, pp. 1611-1618, 2018. doi:10.1107/ S1600577518012110

[2 D. Zhang, C. Yu, M. Wang, *et al.,* "In situ transient Laue x-ray diffraction during high strain-rate tension", *Rev. Sci. Instrum.*, vol. 93, no. 3, p. 033902, 2022. doi:10.1063/5.0079582

[3] T. Mochizuki, Y. Kohmura, A. Awaji, *et al.,* "Cryogenic cooling monochromators for the SPring-8 undualtor beamlines", *Nucl. Instrum. Methods A.,* (467-468, Part 1), pp. 647-649, 2001.doi:10.1016/S0168-9002(01)00436-3

[4] F. R. Lena, G. V. Claudiano, J. C. Corsaletti, *et al,* "Copper braid heat conductors for sirius cryogenic x-ray optics", in *Proc. MEDSI'20*, Chicago, IL, USA, July 2021, pp. 207-210. doi:10.18429/JACoW-MEDSI2020-TUPC14

[5] T. Takeuchi, M. Tanaka, Y. Senba, *et al.,* "Thermal-contact-conductance measurement for high-heat-load optics components at SPring-8", in *Proc. SPIE 8139*, Advances in X-Ray/EUV Optics and Components VI, vol. 813911, Sep. 2011. doi:10.1117/12.894612

[6] E. Nazaretski, H. Yan, K. Lauer, *et al,* "Design and performance of an X-ray scanning microscope at the Hard X-ray Nanoprobe beamline of NSLS-II", *J. Synchrotron Radiat.*, vol. 24, pp. 1113-1119, 2017. doi:10.1107/S1600577517011183

[7] J. Horbach, M. Degenhardt, A. Donat, *et al.,* "PETRA III special optics", *J. Phys. Conf. Ser, 2013*, vol. 425, p. 052012. doi: 10.1088/1742-6596/425/5/052012

[8] A. Crisol, F. Bisti, C. Colldelram, *et al.,* "ALBA BL20 new monochromator design", in *Proc. MEDSI'20*, Chicago, IL, USA, July, 2021, pp. 14-16. doi:10.18429/JACoW-MEDSI2020-MOOB02

[9] S. Wang, D. Zhang, and M. Li, "Highly efficient thermal deformation optimization method for smart-cut mirrors over the entire photon energy range", *J. Synchrotron Radiat.*, vol. 29, pp. 1152-1156, 2022. doi:10.1107/S1600577522007160

ISBN: 978-3-95450-250-9 ISSN: 2673-5520 doi:10.18429/JACoW-MEDSI2023-TUPYP038

A DESIGN OF AN X-RAY PINK BEAM INTEGRATED SHUTTER FOR HEPS*

Sai Liu, Guang Mo†, Qingfu Han, Aiyu Zhou
Institute of High Energy Physics, Chinese Academy of Sciences, Beijing, China

Abstract

The main function of the shutter is to accurately control the exposure time of the sample so that the sample as well as the detector can be protected. In order to cover the high thermal load and high energy working environment, we designed an integrated shutter device. The device includes a thermal absorber shutter, a piezoelectric ceramic fast shutter, a vacuum chamber and an adjustable height base. Firstly, SPECTRA and ANSYS were used to verify the device's institutional temperature reliability at a thermal power density of 64 W/mm^2. In addition, the device is suitable for both monochromatic and pink light operation with a horizontal pitch of 15 mm. The device is also compatible with both vacuum and atmospheric working environments, and the recollimation of the device is not necessary when switching modes. Finally, the thermal absorber shutter is also able to function as a beam profile monitor, and the position of the spot can be monitored through a viewing window on the cavity.

INTRODUCTION

The high energy photon source (HEPS) is a fourth-generation synchrotron radiation facility and has characteristics of high brightness, high flux, and high coherence [1].

The integrated shutter is designed for the small angle X-ray scattering station, which is under construction at HEPS and characterized by a pink beam with enormous high photon flux. In order to solve the problem of the vacuum heat dissipation and at the same time ensure a fast response, we proposed the following schematic design. Firstly, as shown in Fig. 1, the integrated shutter is comprised of a thermal absorber shutter in series with a piezoelectric ceramic fast shutter. It works as follows: in the off-work state, the thermal absorber shutter is responsible for taking away the heat from the pink beam to protect the piezoelectric ceramics. When working, the thermal shutter is opened first, and then the piezoelectric ceramic shutter turns on, at the same time the detector starts sampling. After the exposure time, the detector and the piezo shutter turn off first, after that the thermal shutter is closed and continues to absorb the heat. By coordinating their different opening and closing times, the exposure time of the sample can be controlled.

The monochromatic beam and pink beam in SAXS can be switched through moving in and out of the monochromator and there is 15 mm in the horizontal direction between the two beams. In order to ensure that the position of the integrated shutter does not need to be adjusted after switching modes, we designed two pass-through holes in the piezo shutter, which can meet the passing of pink beam as well as monochrome beam.

In addition, after being coated with fluorescent powder, the thermal absorber shutter is also able to function as a beam profile monitor and the position of the spot can be monitored through a viewing window on the cavity.

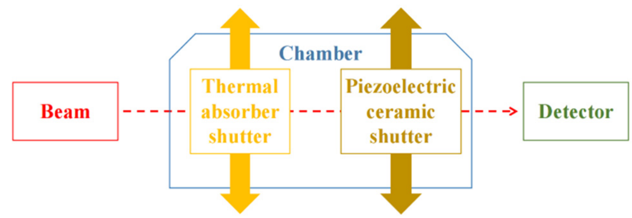

Figure 1: Schematic diagram of integrated shutter.

DESIGN

Overall Description

The integrated shutter consists of three parts: a thermal absorber shutter, a piezoelectric ceramic fast shutter and a stainless-steel vacuum chamber. The assembly drawing is sketched in Fig. 2.

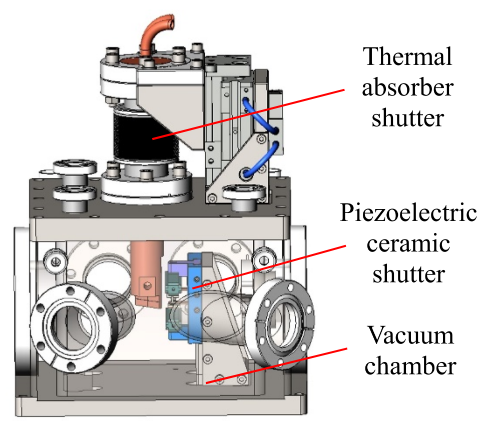

Figure 2: Schematic diagram of integrated shutter.

Thermal Absorber Shutter

At this position the spot size of pink beam is 500 µm and the thermal power density is 64 W/mm^2. It will be a burden for the thermostat system if the heat is emitted directly into the experimental hutch. For this reason, we decided to use water cooling instead of natural cooling. The thermal absorber shutter is driven by an LCG cylinder slide with a stroke of 5 mm, as shown in Fig. 3 and the response time of the cylinder slide is less than 0.1 seconds. The material of water-cooled absorber is OFHC, and the light-receiving surface of the absorber is angled at 45° to the optical axis.

* Work supported by HEPS project.
† Email address: mog@ihep.ac.cn

12th Int. Conf. Mech. Eng. Design Synchrotron Radiat. Equip. Instrum. MEDSI2023, Beijing, China JACoW Publishing
ISBN: 978-3-95450-250-9 ISSN: 2673-5520 doi:10.18429/JACoW-MEDSI2023-TUPYP038

This can reduce the power density and also facilitate the observation of the spot position. According to these boundary conditions, we performed simulation of the absorber using ANSYS, and the results are shown in Fig. 4. The steady-state temperature of the absorber is about 67 °C, which is much lower than the safe temperature of OFHC [2], indicating that the structural design is reasonable.

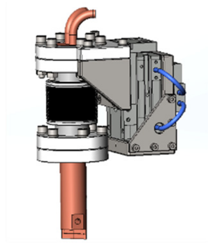

Figure 3: Thermal absorber shutter.

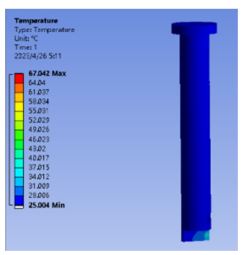

Figure 4: Simulation results.

Piezoelectric Ceramic Shutter

Due to the water-cooled absorber, the response time of the thermal shutter is hardly to the millisecond level, so we need a faster shutter to block x-rays. Piezoelectric ceramic actuators have very fast response, compact structure and small stroke, so they are very suitable as a driving part of the fast shutter.

The fast shutter structure is shown in Fig. 5, which is composed of two piezoelectric ceramic actuators. The stroke of each actuator is 0.6 mm, so an opening range of 1 mm can be achieved through two matching and the response time is less than 1 millisecond. The material for blocking photons of the piezoelectric ceramic shutter is tungsten alloy. There is a horizontally distance of 15 mm between the monochromatic beam and the pink beam in the SAXS station. Considering this, two through-holes with the same distance are designed on the fast shutter, which ensure that both kinds of beams can pass through.

Although most of the heat can be taken away by the upstream absorber shutter, there will still be heat accumulation after a long period of operation in a vacuum environment. This will seriously affect the working life of piezoelectric ceramics. For this reason, a copper braid connected to the tungsten alloy is added, which can transfer the heat to the environment through the cavity. Under the condition that the pink beam continuously irradiated the tungsten alloy for 60 seconds, both structure designs are simulated

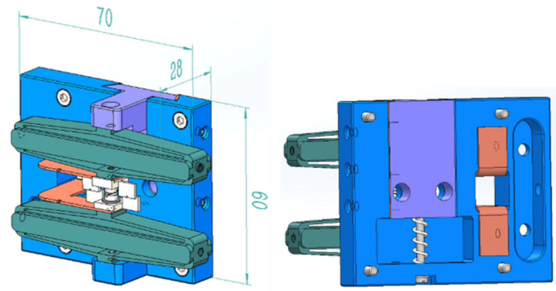

Figure 5: Design of piezoelectric ceramic fast shutter.

and the results are shown in Fig. 6. The maximum temperature of the structure with copper braid is 388 °C, which is much lower than the maximum temperature of 850 °C for the structure without copper braid. After that, natural cooling is carried out and the simulation results are shown in Fig. 7. Obviously, the structure with copper braid has a faster cooling rate and is also closer to the ambient temperature with time.

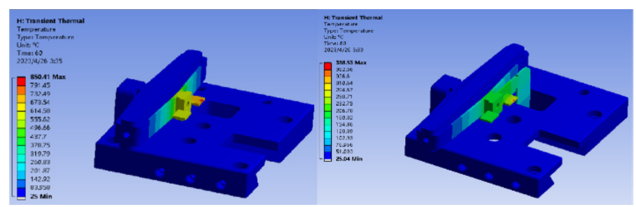

Figure 6: Simulation results of shutter with and without copper braid after heating for 60 s.

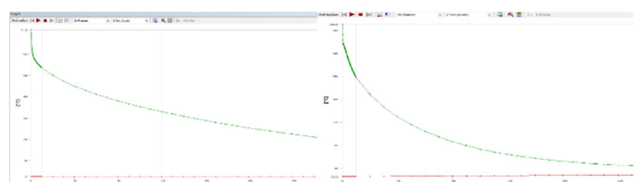

Figure 7: Simulation results of naturally cooling.

Vacuum Chamber

The working environment of the integrated shutter is mainly low vacuum. The design of the vacuum chamber is shown in Fig. 8. The cavity is not only for integration of the thermal absorber shutter and the piezoelectric ceramic shutter, but also can be compatible with the working environment of the atmosphere. When working in atmosphere, an Uniblitz shutter can be used as shown in the Fig. 9. The upstream of the integrated shutter is a beryllium window, while the downstream can be isolated from vacuum by installing a mylar window in the cavity with a quick release flange.

Two observation windows are designed on the cavity. One of them is used to observe the position of the spot on the absorber as well as the functioning state of the piezoelectric ceramic shutter. The other is primarily for observing the functioning state of the shutter UNIBLITZ. After being coated with fluorescent powder, the absorber can be used as a beam monitor. The field of view through both windows is shown in Fig. 10.

ISBN: 978-3-95450-250-9 ISSN: 2673-5520 doi:10.18429/JACoW-MEDSI2023-TUPYP038

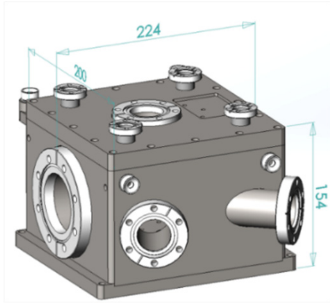

Figure 8: Vacuum chamber.

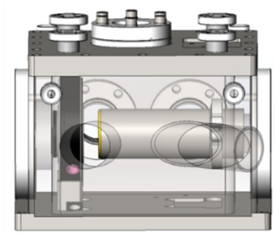
Figure 9: Uniblitz and mylar window.

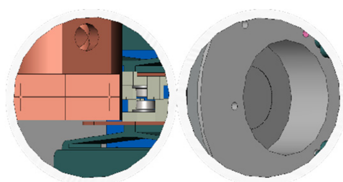
Figure 10: Field of view through the windows.

Main Specifications

The main specifications of integrated shutter are shown in Table 1.

Table 1: Main Specifications

Integrated shutter	
Beam size	500*500 μm^2
Thermal power	16 W
Response time	Less than 2 ms
Function module integration	Thermal absorber shutter, Piezoelectric ceramic fast shutter, Beam profile monitor

CONCLUSION

The integrated shutter incorporates many functional modules, which means that the corresponding control system and collimation calibration work will be challenging. At present, the machining of shutter parts is in progress, and we will carry out further work on the collimation calibration, motion control and accurate response time test of equipment in the future.

REFERENCES

[1] IHEP, `http://english.ihep.cas.cn/doc/2639.html`

[2] Bernard Kosciuk, “Final Design Review of X-Ray Flag”, Rep. BNL NSLS-II Final Design Review, August 5th, 2014.

ISBN: 978-3-95450-250-9 ISSN: 2673-5520 doi:10.18429/JACoW-MEDSI2023-TUPYP039

A DESIGN OF AN X-RAY MONOCHROMATIC ADJUSTABLE SLIT FOR HEPS BEAMLINES*

Sai Liu[1], Qingfu Han[†], Zhe Li, Junliang Yang, Qihui Duan,
Zongyang Yue, Zebin Zhang, Qun Zhang
Institute of High Energy Physics, Chinese Academy of Sciences, Beijing, China

Abstract

The monochromatic slit is a commonly used device in HEPS beamlines. It can limit the synchrotron beam-spot within a desired size required by the downstream optical equipment. In addition, the four-blade structure is the most widely used form of slit. The slit with this form usually consists of a pair or two parallel tungsten carbide blades. With their edges close to each other, a slit can be formed, and the size of which can be controlled by micromechanical guides. This structure is very suitable for the case of large beam size. In this work, we have designed a monochromatic slit based on the four-blade form for BF beamline in HEPS. It can be used in ultra-high vacuum, high luminous flux working environment. The maximum opening range is up to 30*10 mm^2 (H*V), while it can allow a white beam of 136*24 mm^2 (H*V) to pass through. Furthermore, we adopted a point to surface contact design, which can effectively avoid the over-constraint problem between two guide rails.

INTRODUCTION

The test beamline (ID42) is under construction at HEPS. Its main function is to perform comprehensive testing and evaluation of some high-performance optical elements and detectors before they go online [1]. That means it can provide various modes of beam, including white, pink, monochromatic, and focused beam [2]. Therefore, the design of general optical equipment on this beam is usually very challenging: we have to consider the compatibility between different modes.

This monochromatic slit is designed for the test beamline. Its major functional requirements are that the maximum opening range is up to 30*10 mm^2 (H*V), while it can allow a white beam of 136*24 mm^2 (H*V) to pass through. The working environment is ultra-high vacuum, and the energy range is 5-45 keV.

DESIGN

Overall Description

The monochromatic slit consists of three parts: horizontal tungsten blade module, vertical tungsten blade module, vacuum chamber and a height-adjustable granite base. The assembly drawing is sketched in Fig. 1. It is well known that one of the most important technical parameters of an adjustable slit is the parallelism between the blades, which directly affects the spot quality. For this reason, drive and guide components with good precision are essential [3]. At present, there are many technologically mature products with integrated drive and guide on the market, and their motion accuracy can even reach the manometer level [4]. Considering practicality and economy, we mainly choose these standard products as driving and guiding components.

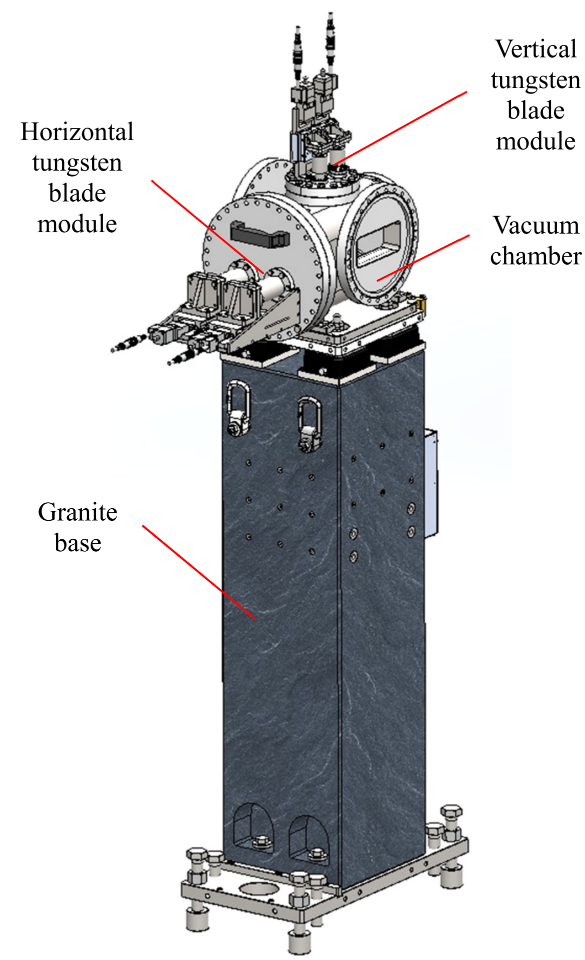

Figure 1: Overview of the monochromatic adjustable slit.

Horizontal Tungsten Blade Module

The design of the horizontal tungsten blade module is shown in Fig. 2, which consists of two KOHZU slide models (SXA0575-R01) as drive components to move the tungsten blades in the vacuum chamber by a connecting rod. The blade holder is located on an AML slide. In this way, the parallelism between the two tungsten blades depends on the parallelism between the two slide guides. However, the motion guidance of the slide itself can be over-constrained with the guide rails inside the vacuum. For this reason, a flexible connection is proposed. As shown in Fig. 3, the end side of the connecting rod is machined into

ISBN: 978-3-95450-250-9 ISSN: 2673-5520 doi:10.18429/JACoW-MEDSI2023-TUPYP039

a spherical surface, which is in point surface contact with the tungsten blade holder and by applying a certain preload force through the two springs, it can be ensured that the connecting rod is always in contact with the holder, but not hindering the relative swing between them. This way is simple and effective to solve the problem of over-constraint and guarantee the motion accuracy [4].

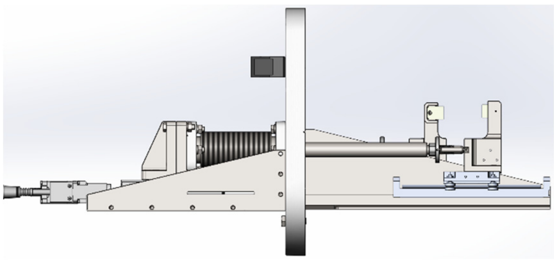

Figure 2: Horizontal tungsten blade module.

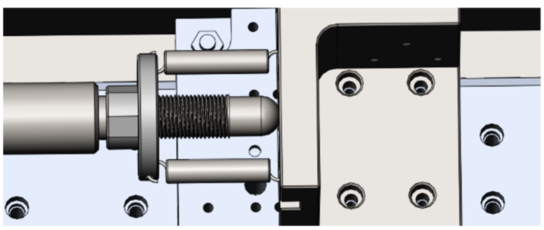

Figure 3: Flexible connection method.

Vertical Tungsten Blade Module

The basic idea of design, sketched in Fig. 4, the vertical tungsten blade module also consists of two KOHZU slides (SXA0530) as drive components to move the tungsten blades in the vacuum chamber by a connecting rod. The structure adopts modular design and has an interchangeability with other monochromatic slits on the beamline. In the vertical direction, the moving range of the blade is ±15 mm and when both blades are in the -15 mm position, it can give way to the white beam path. We used a standard block to calibrate the tungsten blade edge, after which it was measured and the parallelism of blade edge is better than 0.5 mrad.

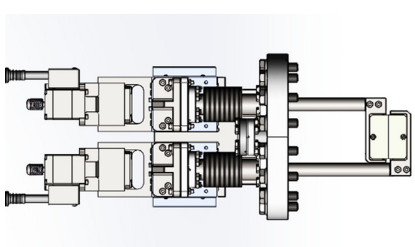

Figure 4: The vertical tungsten blade module.

The Height-Adjustable Granite Base

In order to ensure the stability of the equipment and considering the actual installation space, we adopt the granite base design with the cross-section size of 300*300 mm^2, as shown in Fig. 5. The granite base is poured together with the ground and according to the simulation results, the first order natural frequency of the granite base is higher than 86 Hz. The height of the base is adjusted by four M24 bolts at the bottom, and the level of the equipment is adjusted by four AIRLOC. There are two relatively movable stainless-steel plates at the top, one of which is connected to the cavity and the other to the base. The entire chamber can be adjusted horizontally by adjusting the screws on the side with a travel of ±15mm.

Figure 5: The height-adjustable granite base.

CONCLUSION

The integrated shutter incorporates many functional modules, which means that the corresponding control system and collimation calibration work will be challenging. At present, the machining of shutter parts is in progress, and we will carry out further work on the collimation calibration, motion control and accurate response time test of equipment in the future.

REFERENCES

[1] Hirokatsu Yumoto *et al.*, “A test bench of X-ray optics for next generation high-energy high-flux X-ray beam lines”, *Proc. SPIE*, vol. 11492, 2020. doi:10.1117/12.2570154

[2] Zhongliang Li *et al.*, “The design of the test beamline at SSRF”, *AIP Conf. Proc.*, vol. 2054, no. 1, p. 060040, 15 January, 2019. doi:10.1063/1.5084671

[3] Songwen Xiao, Tao Zhu, Qingfu Han, *et al.*, “Slit device and four-knife slit”, Tech. Report, 2013.

[4] KOHZU products, https://www.kohzuprecision.com/products

ISBN: 978-3-95450-250-9 ISSN: 2673-5520 doi:10.18429/JACoW-MEDSI2023-TUPYP043

THE DESIGN OF TEST BEAMLINE AT HEPS

Junliang Yang†, Quanjie Jia, Ming Li, Peng Liu, Ye Tao
Institute of High Energy Physics, Chinese Academy of Science, Beijing, China

Abstract

This paper describes the design of a test beamline for a new generation of high-energy, high-flux, and high-coherence synchrotron radiation beamlines. The beamline will be built at ID42 of HEPS. The beamline includes two sources, a wiggler and an undulator, to provide high-energy, high thermal power, large size, and high-coherence, high-brightness X-ray beams, respectively. In the current design, the beamline mainly has optical components such as monochromators, CRLs, and filters. With different combinations of sources and optical components, the beamline can provide various modes, including white, monochromatic, and focused beam. Using a Si(111) double-crystal monochromator (DCM), the beamline covers a wide photon energy range from 5 to 45 keV. In the future, the beamline will be capable of providing monochromatic beam with photon energy higher than 300 keV. And the wiggler's white beam can provide high thermal load test conditions over 1 kW. The beamline offers high flexibility and versatility in terms of available beam size (from 1 μm to over 100 mm), energy resolution, and photon flux range. Various experimental techniques including diffraction, spectroscopy, imaging, and at-wavelength measurement can be performed on this beamline. At present, the construction of the radiation shielding hutch for the beamline has been completed.

INTRODUCTION

For the fourth-generation synchrotron source (SR), high brightness, high flux, and high coherence are its main characteristics. To match the advanced performance of the fourth-generation SR, the use of the highest performance optical elements and detectors is necessary. However, these optical elements and detectors are not widely used, and their quality and performance cannot be fully guaranteed. To ensure successfully operate the beamline, comprehensive testing and evaluation before the equipment goes online is essential. Furthermore, even with the highest performance optical elements and detectors in current state of the art, it is difficult to achieve certain extreme performance limits of the fourth-generation SR. Therefore, continue research and development (R&D) are needed to improve the performance of various optical elements and detectors. Testing is a necessary step in the R&D of new equipment [1, 2]. To achieve these goals, a test beamline has been designed at high energy photon source (HEPS). This paper mainly introduces the sources, beamline layout, and expected performance of the beamline.

SOURCE OF THE BEAMLINE

The HEPS design has an electron operating energy of 6 GeV, a beam current of 200 mA, and a natural horizontal emittance of smaller than 60 pm·rad, which can accommodate up to 48 straight sections [3]. The test beamline occupies a straight section with a total length of approximately 6 m, located at ID42. From upstream to downstream, arrange two sources, an undulator source with a length of 1.94 m and a wiggler source with a length of 1.05 m, as well as a reserved space of approximately 1.5 m that can be used for future light source performance upgrades. The main parameters of the HEPS storage ring and the straight section where the test beamline are summarized in Table 1. The design of the test beamline's sources considers the requirements of HEPS engineering tests and various experimental methods as much as possible. The undulator source is designed to provide conditions such as high brightness, high coherence, and micro-focusing. The wiggler sources are used to provide conditions such as continuous spectrum, large spot size, and high thermal load.

The undulator source is cryogenic permanent magnet undulator (CPMU), with a gap range of 7.2-16.0 mm, a magnetic period of 22.8 mm, a number of periods of 85, and a maximum peak magnetic field $B_0 = 1.18$ T. Table 2 provides the basic parameters of the CPMU22.8 source. Figure 1 shows the brightness and coherent flux spectrum of the CPMU22.8 source, and the results show that its brightness can reach 2.5×1021 phs/s/mr2/mm2/0.1%BW, with a maximum coherent flux of 0.9×1014 phs/s/ 0.1%BW.

Table 1: The Main Parameters of the HEPS Storage Ring and the Straight Section where the Test Beamline

Parameter		Value
Electron energy		6 GeV
Beam current		200 mA
Circumference of the storage ring		1360.4 m
Natural horizontal emittance		＜60 pm·rad
Parameters of straight sections	βx	10.12 m
	βy	9.64 m
	σx	17.74 μm
	$\sigma x'$	1.753 μrad
	σy	5.48 μm
	$\sigma y'$	0.568 μrad

The wiggler source is permanent magnet wiggler (PMW), with a gap range of 11−46.5 mm, a magnetic period of 73 mm, a number of periods of 14, and a peak magnetic field of 1.64 T. Table 3 provides the basic parameters of the PMW73 source. Figure 2 shows the energy spectrum of the PMW73 source at different gaps and the angular distribution of flux density at different energy values at the minimum gap. The results show that it can provide photons with energy above 300 keV. The light source size of

ISBN: 978-3-95450-250-9 ISSN: 2673-5520 doi:10.18429/JACoW-MEDSI2023-TUPYP043

Table 2: The Main Parameters of the CPMU22.8

Parameter	Value	Parameter	Value
Number of periods	85	Phase error	3: gap≤12.3 mm 6: gap>12.3 mm
Period length	22.8 mm	Fundamental energy range	3.622−10.892 keV
Total length	1.94 m	Brightness	2.5×10^{21} phs/s/mr^2/mm^2/0.1%BW @10.8 keV
Maximum magnetic field	1.18 T	Flux	5.1×10^{14} phs/s/ 0.1%BW@10.8 keV
Minimum magnetic gap	7.2 mm	Maximum central power density	277.7 W/mrad^2
K-value range	0.8679-2.5061	Divergence angle	11 μrad×11 μrad @10.8 keV
Maximum harmonic number	11	Source size (FWHM)	34 μm×11 μm@10.8 keV

Table 3: The Main Parameters of the PMW73

Parameter	Value	Parameter	Value
Number of periods	14	Maximum power	12.52 kW
Period length	73 mm	Maximum central power density	64.43 kW/mrad2
Total length	1.05 m	Brightness	4.45×10^{18} phs/s/mm^2/mr^2/0.1%BW@15 keV
Magnetic field range	0.22~1.64 T	Flux	5.96×10^{14} phs/s/ 0.1%BW@15 keV
Minimum magnetic gap	11~42.5 mm	Divergence angle	1.8 mrad×0.18 mrad @15 keV
K-value range	1.5~11.186	Source size (FWHM)	42 μm×11 μm
Maximum critical energy	39.26 keV		

CPMU22.8 and PMW73 simulated by Shadow, with a full width at half maximum (FWHM) of 34 μm × 11 μm and 42 μm × 11 μm (H×V), respectively.

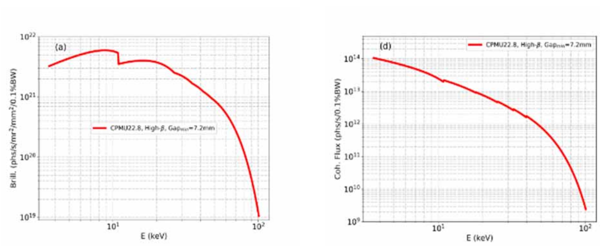

Figure 1: Brightness and coherent flux spectrum of CPMU22.8 Source.

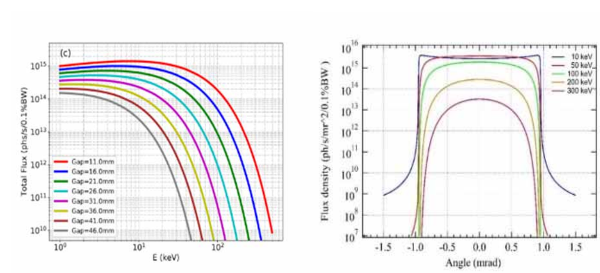

Figure 2: Energy spectrum of PMW73 source at different gaps and angular distribution of flux density at different energy values at minimum gap.

DESCRIPTION OF THE BEAMLINE

The test beamline includes two testing hutches, hutch1 and hutch2. Hutch1 is mainly used for testing sources, front-end (FE), and beam equipment in vacuum. Hutch2 is mainly used for testing optical elements, detectors, R&D, and conducting various experimental methods. The FE of the beamline ends at 32.8 m. The maximum acceptance of the beamline is 1.8 mrad × 0.2 mrad with PMW, and 50 μrad × 50 μrad with CPMU. In hutch1, the X-ray beam passes through XBPM, attenuator, and white beam slit, followed by the diagnostic area of the source and FE. At 46m is the Si(111) double crystal monochromator (DCM), followed by the testing area for monochromators, mirrors, and other equipment, as well as the reserved area for future beamline upgrades. hutch 1 ends at 61.2 m. In hutch2, there is also a section of equipment testing area. A set of CRLs suitable for a wide energy range is located at 69.5 m, and X-ray is focused at 73 m after passing through the CRL. The X-ray enters the air through a Be window at 72 m, and then there is an optical platform that can be used for various tests. The beam ends at 81 m. Figure 3 is the configuration diagram of the test beamline.

To meet the requirements of various experiments for high stability, high energy resolution, and spectral scanning of monochromatic beam, the test beamline uses a fixed-exit type liquid nitrogen-cooled Si(111) DCM with a height difference of 15 mm. The photon energy range covered is 5−45 keV. In addition, considering the imaging

12th Int. Conf. Mech. Eng. Design Synchrotron Radiat. Equip. Instrum. MEDSI2023, Beijing, China JACoW Publishing
ISBN: 978-3-95450-250-9 ISSN: 2673-5520 doi:10.18429/JACoW-MEDSI2023-TUPYP043

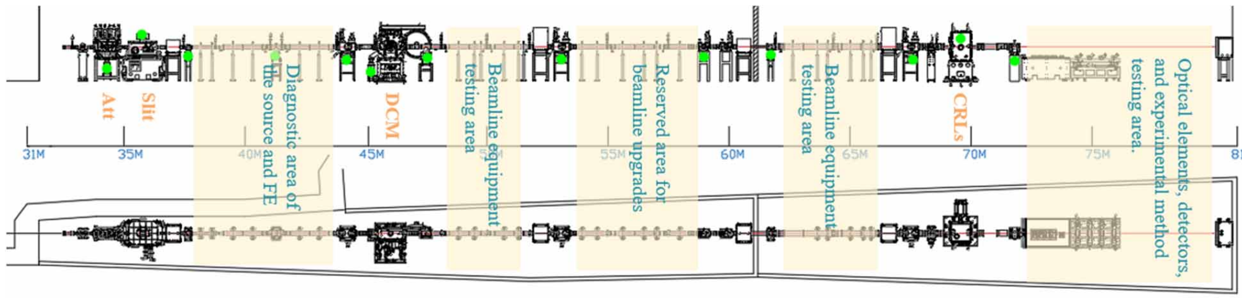

Figure 3: Configuration diagram of test beamline.

experiments require a larger spot size, the maximum acceptance angle of the DCM is set to 0.3 mrad × 0.05 mrad.

The transfocator, consisting of 11 arms, is located after the DCM, and each arm can accommodate up to 10 Compound Refractive Lenses (CRLs). By combining multiple CRLs with different curvature radii, the transfocator can operate in the energy range of 5−45 keV, achieving a focal spot size smaller than 1 μm at a distance of 73 m. This transfocator can be operated under water-cooling conditions, allowing the CRLs to be used for focusing the beam emitted from the CPMU source, thereby obtaining pink beam.

The attenuator (ATT) is installed at 34.2 m and consists of graphite, aluminium, and copper plates of different thicknesses. It can attenuate the X-ray beam emitted from the PMW, which has a power exceeding 10 kW, with a step size of approximately 15% in $\Delta P/P$, down to 1 kW. Additionally, there are vacant slots on the attenuator, allowing for the installation of attenuator plates made of different materials to modulate the energy spectrum according to specific experimental needs. Furthermore, the use of attenuator plates can also generate pink X-ray beams.

Using different combinations of sources and optical elements, the test beamline offers several operational modes including white, pink, monochromatic, focused and unfocused beam (Table 4). Table 5 provides the main expected performance parameters of the test beamline.

Table 4: Operational Modes of the Test Beamline

Mode	CPMU	PMW	ATT	DCM	CRL
White beam		√			
Monochromatic beam	√			√	
		√		√	
Pink beam	√		√		
		√	√		
Monochromatic focused beam	√			√	√
		√		√	√
Pink focused beam	√		√		√
		√	√		√

SUMMARY

The HEPS test beamline is a flexible and versatile beamline with excellent optical performance. It can provide

Table 5: Main Parameters of Expected Performance of the Test Beamline

Parameter	Value
Energy range	5 – 45 keV
Energy resolution	2×10^{-4}
Photon flux @ 73 m	3.31×10^{12} phs/s@15 keV, W 6.32×10^{13} phs/s@10.8 keV, U
Beam size range	<1 μm–100 mm
Thermal load range	<10 kW
Energy upper limit	>300 keV

various modes of beam, including white, pink, monochromatic, and focused beam. It is the only test beamline in the world that includes both a wiggler and an undulator as sources. Currently, the final design has been completed, and the radiation shielding hutch has been constructed. It is expected to start operation in 2025. By then, this beamline will cover a wide energy range and exhibit high flexibility in terms of available beam size and energy resolution. Various experimental techniques, including diffraction, spectroscopy, imaging, and wavelength measurements, can be realized on this beamline. It will meet the testing needs of HEPS projects and various advanced performance optical elements and detectors. In conclusion, it will be a flexible and multifunctional beamline.

ACKNOWLEDGMENT

The authors would like to acknowledge the hard work of all the staff members at HEPS, especially the optical group, general mechanical group, and optical mechanical group.

REFERENCE

[1] K. J. S. Sawhney *et al.*, “A Test Beamline on Diamond Light Source”, *AIP Conf. Proc.*, June 2010, vol. 1234, pp. 387–390. doi:10.1063/1.3463220

[2] Zhongliang Li *et al.*, “The design of the test beamline at SSRF”, *AIP Conf. Proc.*, 2019, vol. 2054, p. 060040. doi:10.1063/1.5084671

[3] Y. Jiao *et al.*, “The HEPS project”, *J. Synchrotron Radiat.*, vol. 25, pp. 1611-1618, 2018. doi:10.1107/s1600577518012110

12th Int. Conf. Mech. Eng. Design Synchrotron Radiat. Equip. Instrum. MEDSI2023, Beijing, China JACoW Publishing
ISBN: 978-3-95450-250-9 ISSN: 2673-5520 doi:10.18429/JACoW-MEDSI2023-TUPYP045

USABILITY STUDY TO QUALIFY A MAINTENANCE ROBOTIC SYSTEM FOR LARGE SCALE EXPERIMENTAL FACILITY

J. Y. Zhang†,[1,3], J. X. Chen[2], L. Kang[1], R. H. Liu[2], J. B. Yu[2]
[1]Institute of High Energy Physics, Chinese Academy of Sciences, Beijing, China
[2]Spallation Neutron Source Science Center, Dongguan, China
[3]University of Chinese Academy of Sciences, Beijing, China

Abstract

The primary stripper foil device is one of the most critical devices of The China Spallation Neutron Source Project Phase-II (CSNS-II), which requires regular foil replacement maintenance to ensure its stable operation. To mitigate the potential hazards posed to workers by prolonged exposure to high levels of radiation, a maintenance robotic system has been developed to perform repetitive and precise foil changing task. The proposed framework encompasses various aspects of the robotic system, including hardware structure, target detection, manipulator kinematics design, and system construction. The correctness and efficiency of the system are demonstrated through simulations carried out using ROS Moveit! and GAZEBO.

INTRODUCTION

Nowadays, the role of robotics in industrial and scientific applications is growing exponentially, one of which is the usage of maintenance robotic systems in large experimental facilities such as Synchrotron Radiation Equipment and Instrumentation [1].

The China Spallation Neutron Source Project Phase-II (CSNS-II) poses ongoing challenges in terms of both its upgrade and remodelling. The primary stripper foil device is one of the most critical devices of CSNS-II, which undergoes significant changes due to the increased beam injection energy from 80 MeV to 300 MeV, as well as the radiation dose in the injection zone is expected to be further amplified (see Table 1). During the maintenance process, the foil components that are being exchanged need to be placed in radiation shielding containers until the radiation dose has decayed to a safe level before new foils can be installed.

Table 1: Downtime Dose Statistics

Shut-down Time	Proton-Induced Dose Rate	Dose Rate in 1 W/m Mode	Total Dose Rate
0 s	0.5 mSv/h	2.2 mSv/h	2.7 mSv/h
1 h	0.3 mSv/h	1.3 mSv/h	1.6 mSv/h
1 day	0.23 mSv/h	1.0 mSv/h	1.23 mSv/h
1 week	0.18 mSv/h	0.77 mSv/h	0.95 mSv/h
1 month	0.13 mSv/h	0.55 mSv/h	0.68 mSv/h

From the maintenance work described above, this paper presents a usability study that aims to evaluate a maintenance robotic system for large-scale experimental facilities.

The findings of this study will contribute to the development of robust and reliable robotic system, which would emerge as viable industrial solutions to replace humans in executing construction tasks that are safe, efficient, and precise.

SYSTEM FRAMEWORK

The overall framework of the robotic system is depicted in Fig. 1, which consists of a vision and image processing system, a ROS operating system, a hardware system, and a host computer system.

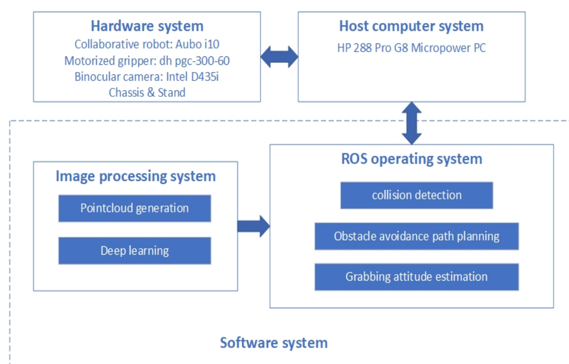

Figure 1: Robotic system framework.

Leveraging the Robot Operating System (ROS) platform, the proposed robotic system exhibits the capability to successfully execute target recognition and motion planning tasks for a 6-degree-of-freedom tandem robotic arm, as well as the ability to transition to a solid robot configuration. The system workflow diagram is illustrated in Fig. 2.

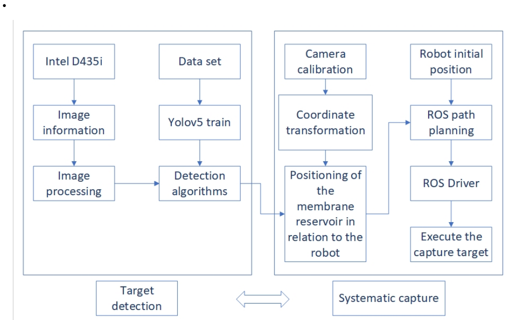

Figure 2: System workflow diagram.

Hardware Component Design

The entire system is installed in the CSNS Experiment II Testbed (see Fig. 3). Considering the workspace and

† zhangjingyu@ihep.ac.cn

ISBN: 978-3-95450-250-9 ISSN: 2673-5520 doi:10.18429/JACoW-MEDSI2023-TUPYP045

payload requirements, the AUBO-i10 arm with a customized fingertip end effector DH-PGC-300-60 was selected. Furthermore, the robot base, which was designed according to the beam height specifications, underwent static and modal analyses conducted using ANSYS Workbench to ensure stability and reliability. In the design of the robot grasping system, the depth camera is fixed in the world coordinate system, thereby ensuring that image acquisition is independent of the motion of the robotic arm.

Figure 3: Hardware components.

SOFTWARE SYSTEM

The main control tasks of the robotic system involve motion planning for grasping and placing the target objects. ROS Moveit! is an integrated development platform that includes various functionalities such as motion planning, kinematic solving, 3D perception, and perception configuration. Consequently, both motion control and planning of the robotic system are carried out within the ROS framework.

Machine Visualization

YOLOv5 is presently one of the most extensively employed algorithms for object detection, which primary objective is to accurately and efficiently detect objects in both images and videos [2].

As shown in Fig. 4, the structure of the YOLOv5 model consists of four main parts. During training, the algorithm divides the input image into N×N grids and predicts the bounding boxes and classes of objects in each grid, while optimizing network parameters to improve detection accuracy and speed.

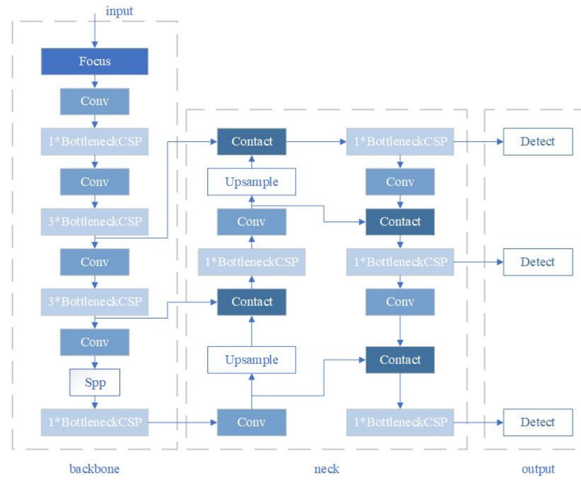

Figure 4: YOLOv5 network.

Coordinate Conversion

When predicting the grasp parameters of the target in the image, it is also necessary to perform coordinate transformations. Assuming the camera focal length is f, the image coordinate position is $P(x,y)$, and the camera position coordinate is $L_c(x_c,y_c,z_c)$. According to the camera imaging principle, Eq. (1) converts a two-dimensional pixel into a point in camera coordinate system.

$$\begin{bmatrix} x_c \\ y_c \\ z_c \\ 1 \end{bmatrix} = \begin{bmatrix} \frac{Z_c}{f} & 0 & 0 \\ 0 & \frac{Z_c}{f} & 0 \\ 0 & 0 & Z_c \\ 0 & 0 & 1 \end{bmatrix} \begin{bmatrix} x \\ y \\ 1 \end{bmatrix}. \quad (1)$$

By further applying the pose transformation relationship between the camera coordinate system and the robot base coordinate system, based on Eq. (2), we can determine the optimal grasping point in the robot coordinate space $L_r(x_r,y_r,z_r)$.

$$\begin{bmatrix} u \\ v \\ 1 \end{bmatrix} = k \begin{bmatrix} R & T \\ 0 & 1 \end{bmatrix} \begin{bmatrix} x_r \\ y_r \\ z_r \end{bmatrix}. \quad (2)$$

Campaign Planning

The campaign planning mainly involves solving inverse kinematics and trajectory planning, as shown the workflow depicted in Fig. 5.

ISBN: 978-3-95450-250-9 ISSN: 2673-5520 doi:10.18429/JACoW-MEDSI2023-TUPYP045

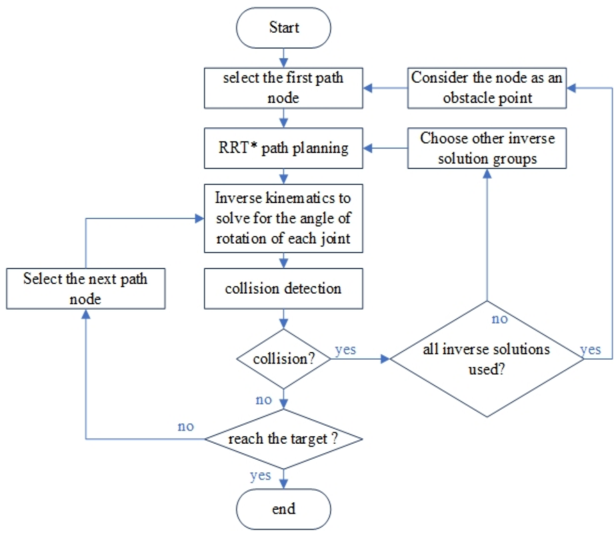

Figure 5: Trajectory planning.

The Bi-RRT* combines the benefits of RRT* in terms of finding optimal paths with the inherent efficiency and simplicity of RRT-Connect [3]. It is particularly useful in scenarios where an optimal and feasible path is desired in complex environments. The algorithm explores the configuration space from both the start and goal nodes simultaneously, aiming to find a feasible path connecting them.

Random 3D Scene Construction with Path Search Results, as shown in Fig. 6, the improved algorithm reduces search time and explored states (see Table 2).

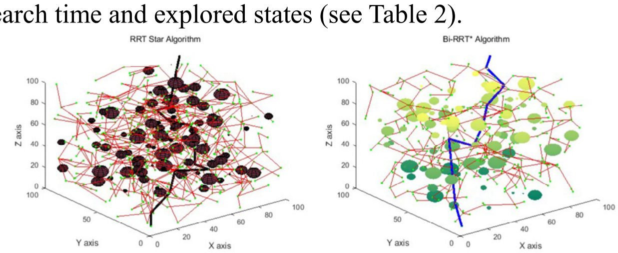

Figure 6: RRT* search result (right) and Bi-RRT* search result (left).

Table 2: Algorithm Comparison

Algorithm	Average Running Time	Average Explored States	Average State in Path
Bi-RRT*	1.91 s	4000	12.5
RRT*	0.12 s	159.5	10.5

EXPERIMENTS

Machine Visualization

The original dataset was created by capturing RGB images at different tilt angles and heights. To improve the generalization capability, the dataset of 300 samples was randomly divided into a training set (80 %) and a test set (20 %), using data augmentation techniques such as random rotation and brightness adjustment. In addition, the LabelImg annotation tool has been applied to annotate the outer bounding rectangle and assign class labels.

The training and testing of the model were conducted on a system with Windows 11 operating system, utilizing the PyTorch 2.0.1 deep learning framework, implemented in Python 3.9.

During the model training process, a batch size of 4 samples was used, with an initial learning rate of 0.01. After 100 iterations, The training and testing sample results are shown in Fig. 7, demonstrating successful target localization and recognition of the foil components.

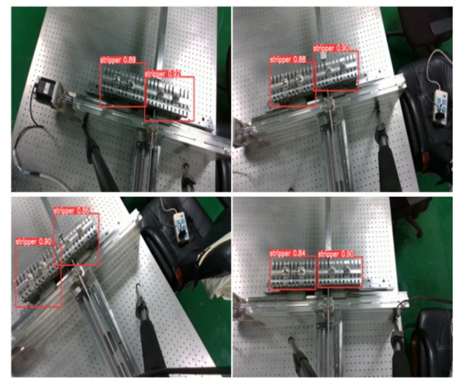

Figure 7: Testing set detection results.

Gazebo

Finally, the MoveIt! module is used to import the robot system and configure the grasp environment. The Move_group core node is then employed to establish communication between various software modules, enabling the simulation of arm grasping in the Gazebo environment (see Fig. 8).

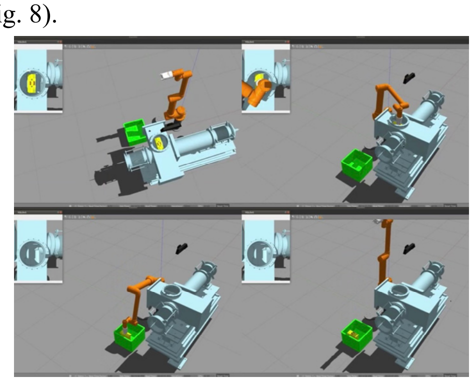

Figure 8: Simulation grasping results.

CONCLUSION

In conclusion, we have developed a grasping robotic system based on YOLOv5, which experiments in the simulated environment have demonstrated the effectiveness and feasibility of the system. This system holds great potential for a wide range of applications, as well as performs various maintenance tasks by equipping different end effectors.

Further improvements can be made to enhance the system's performance and adaptability, such as integrating more advanced object detection algorithms and optimizing the grasping mechanism. The next step will involve conducting real-world experiments based on the results obtained from object detection.

Overall, our work presents a new solution for the routine maintenance of gas pedal installations.

ISBN: 978-3-95450-250-9 ISSN: 2673-5520 doi:10.18429/JACoW-MEDSI2023-TUPYP045

REFERENCES

[1] M. Di Castro, M. Ferre, and A. Masi, "CERNTAURO: A Modular Architecture for Robotic Inspection and Telemanipulation in Harsh and Semi-Structured Environments," *IEEE Access,* vol. 6, pp. 37506-37522, 2018. doi:10.1109/access.2018.2849572

[2] Y. Shao, D. Zhang, H. Chu, X. Zhang, and Y. Rao, "A Review of YOLO Object Detection Based on Deep Learning," *Journal of Electronics & Information Technology,* vol. 44, no. 10, pp. 3697-3708, Oct 2022. doi:10.11999/jeit210790

[3] S. Karaman and E. Frazzoli, "Sampling-based algorithms for optimal motion planning," *Int. J. Rob. Res.,* vol. 30, no. 7, pp. 846-894, Jun 2011. doi:10.1177/0278364911406761

ISBN: 978-3-95450-250-9 ISSN: 2673-5520 doi:10.18429/JACoW-MEDSI2023-TUPYP047

DESIGN OF LIQUID INJECTION DEVICE FOR THE HARD X-RAY ULTRAFAST SPECTROSCOPY EXPERIMENT STATION*

Linghao Li, Bing Li, Xing Liu, Jianwei Meng, Ruixue Zhu, Kaiyu Zhang, Tsu-Chien Weng†
Center for Transformative Science, ShanghaiTech University, Shanghai, China

Abstract

The Hard X-ray Ultrafast Spectroscopy Experiment Station (HXS) of the Shanghai high repetition rate XFEL and extreme light facility (SHINE) requires the design and manufacture of a specialized liquid sample injection device when studying the liquid phase state of matter. Due to the damage caused by high-repetition-rate XFEL pulses on the sample, it is necessary to ensure that the liquid sample is refreshed before the next pulse arrives. In order to reduce the impact of liquid film thickness on pump-probe ultrafast spectroscopy experiments, it is required that the liquid film thickness be less than 20 μm. This article describes the use of oblique collision of two jets, from simulation calculation to the construction of experimental device, and the use of absorption spectroscopy principle to construct a thickness characterization system. This system can stably produce ultrathin liquid films with thickness ranging from 3-20 μm. The article proposes views on the limitations and future improvements of this device.

INTRODUCTION

The Shanghai high repetition rate XFEL and Extreme light facility (SHINE) is equipped with a high-quality electron beam continuous wave superconducting linear accelerator with an energy of 8 GeV. The energy wavelength coverage of this device is 0.4-25 keV, and the pulse repetition rate can reach up to 1 MHz. The device has the characteristics of high brightness, short pulse, high repetition rate, and high coherence [1]. The main experimental platform of the Hard X-ray Ultrafast Spectroscopy Experiment Station (HXS) located in FEL-III is the high-energy resolution X-ray photo-in-photo-out (PIPO) spectrometer, which can achieve femtosecond time resolution by combining pump-probe technology. The reactions involved in the liquid phase state of matter are currently an important research area in the fields of chemistry and biology [2], and are also an important research direction of HXS. Therefore, it is necessary to build a liquid sample injection device that meets the requirements of the experiment station.

After in-depth analysis of the characteristics of X-ray free-electron lasers and samples, we propose the following requirements for the in-situ environment of liquid samples: Firstly, due to the high repetition rate and radiation damage characteristics of X-ray free-electron lasers, sample replacement is necessary. Therefore, we need to establish a system that can continuously deliver samples to ensure that the pulse of the X-ray free-electron laser is not wasted. Secondly, in order to control the impact of liquid film thickness on the pump-probe time resolution within 66 fs, the liquid film thickness must be less than 20 μm. At the same time, the outline of the liquid sample should be much larger than the light spot of the X-ray beam to ensure that the detector receives the signal after passing through the liquid sample.

This article designs and implements a super-thin liquid film generation device, and verifies the stability and thickness of the generated liquid film through the construction of a test optical path, which meets the experimental requirements. This research provides an important experimental foundation for subsequent research in related fields.

EXPERIMENTAL METHODS

Liquid Film Generation Device

In recent years, the principles of generating flowing liquid films suitable for X-ray spectroscopy research mainly include the following three types:

Slit jetting [3]. This method involves spraying liquid through a slit to overcome the surface tension of the liquid and form a liquid film. However, this method is limited by the size of the tube wall, and the production of microfluidic tubes with dimensions of a few microns can easily encounter problems such as clogging during use.

Liquid flow collision [4-6]. This method utilizes two liquid flows that collide with each other to form a liquid film through interaction, and has high stability. This method has broad application prospects in pump-probe ultrafast spectroscopy experiments.

Gas focusing [7-9]. This approach is similar to gas-dynamic focusing virtual nozzle (GDVN), which requires gas pressure to change the cross-sectional shape or size of the liquid flow, typically serving the needs of lower dimensions. This approach is not further discussed in this article.

Based on the principle of liquid flow collision, this study built an experimental platform as shown in Figure 1. Using an HPLC pump to provide power for liquid transport and control the liquid flow rate, a liquid pipeline was constructed at the output end of the pump, using PEEK tubes, liquid-phase connectors, T-shaped tees, stainless-steel tubes, and other parts.

* This work supported by the National Natural Science Foundation of China (Grant NO.21727801), the Shanghai Sailing Program (No.22YF1454600)
† wengzq@shanghaitech.edu.cn.

ISBN: 978-3-95450-250-9 ISSN: 2673-5520 doi:10.18429/JACoW-MEDSI2023-TUPYP047

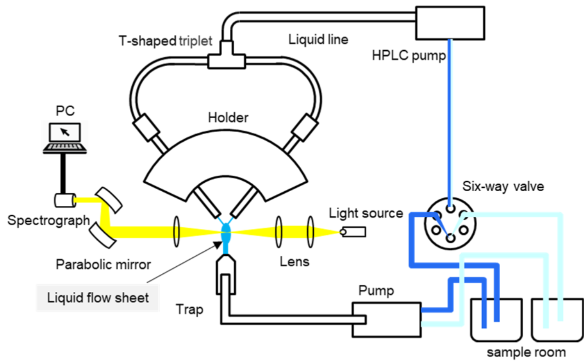

Figure 1: Liquid film generation device and characterization system.

Liquid Film Characterization System

For the generated liquid film, its size and thickness need to be tested to ensure compliance with the requirements of the experimental station. A 3×10^{-5} mol/L methylene blue solution [10] was selected as the sample liquid for the experiment. A colorimetric cuvette was used for the molar absorptivity test. It was found that the visible light absorption peak of the methylene blue solution at this concentration was at 664 nm, with a molar absorptivity of 6.78×10^{4} L/(mol·cm).

The thickness of the liquid film is characterized by reference to the Lambert-Beer law, which calculates the film thickness based on the intensity absorption of light by the liquid film. Using HL-2000 as the light source, the light beam is emitted from a fiber with an inner diameter of 600 μm, and a monochromatic light source with a desired wavelength band is obtained through an optical filter. Since the light source is a point light source, it needs to be focused and aligned, and an experimental optical path as shown in the figure is constructed. After the converged light is received by the fiber probe, a PG-2000 fiber spectrometer and its supporting spectral testing software Morpho are used for spectral analysis.

RESULTS

Flow Rate Testing

In the experiment, due to the influence of factors such as the sealing performance of the liquid pipeline and the viscous resistance of the pipe wall, there is a difference between the actual flow rate of the liquid emitted from the stainless-steel pipe and the flow rate set by the pump [11]. Therefore, before measuring the thickness of the liquid film, it is necessary to test the actual flow rate of the jet. The test results are shown in Figure 2. The higher flow rate set by the pump is denoted as A, and the lower flow rate is denoted as B. The liquid flow rate for subsequent thickness characterization experiments is also tested and calculated according to these two gears.

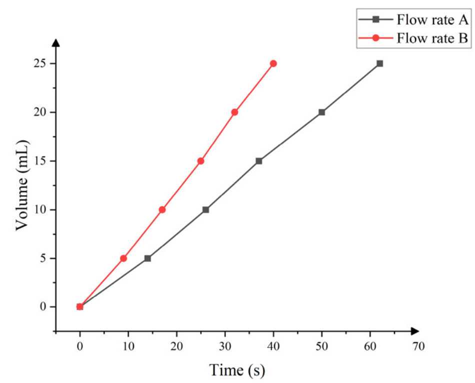

Figure 2: Flow rate test.

It can be seen that the actual volumetric flow rate of the liquid at flow rate A is 0.406 mL/s, and the volumetric flow rate at flow rate B is 0.629 mL/s. The inner diameter of the pipeline is 125 μm, which is converted to a length flow rate of 33.084 mm/s and 51.256 mm/s, respectively.

Calculation of Liquid Film Thickness

In order to have a estimate of the size and thickness of the liquid film, the liquid film generated by the collision of two jets can be simulated and calculated based on the Hasson-peck formula [12, 13]:

$$\frac{hr}{R^2} = \frac{sin^3\theta}{(1-\cos\phi\cos\theta)^2} \tag{1}$$

$$\frac{r_e}{R\,We} = \frac{sin^3\theta sin^2\psi}{4(1-\cos\phi\cos\theta)^2} \tag{2}$$

Equation (1) is the thickness distribution formula, and equation (2) is the liquid film shape formula. According to these two equations, the thickness of the liquid film is mainly affected by the collision angle and the pipe diameter, while the jet velocity will affect the size of the liquid film. Figures 3 and 4 show the radial variation of the thickness of the liquid film formed under different collision angles and different pipe diameters under limited conditions. By summarizing the results of the simulation calculations, this experiment finally chose to use 125 μm stainless-steel pipe for the collision experiment. At the same time, in order to simplify the calculation and statistics, the collision angle of the two jets was designed to be 90° and 120°.

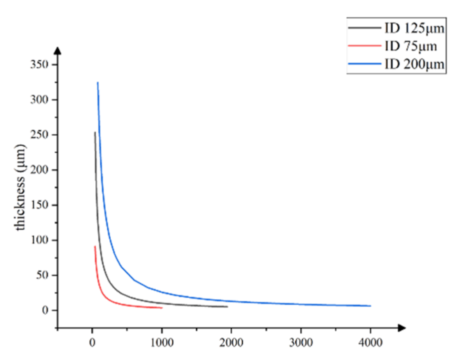

Figure 3: Simulation curve of liquid film thickness: jet diameter factor.

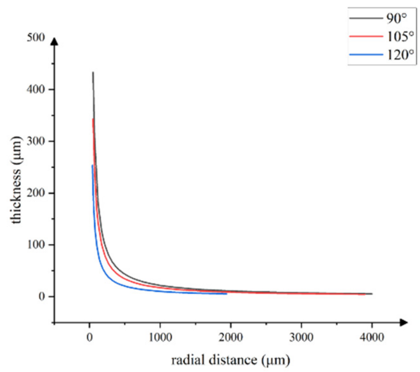

Figure 4: Simulation curve of liquid film thickness: collision angle factor.

Characterization of Liquid Film Thickness

The ultra-thin liquid film generation device can eventually form a liquid film as shown in Figure 5. We conducted quantitative measurements of the liquid film size, and the results showed that the width of the liquid film was between 1-2 mm, with a maximum length of 3-6 mm, which was much larger than the size of the focused spot, meeting the requirements for conducting the experiment. In addition, within this range, as the flow rate increases, the size of the liquid film also increases, while as the collision angle increases, the size of the liquid film decreases.

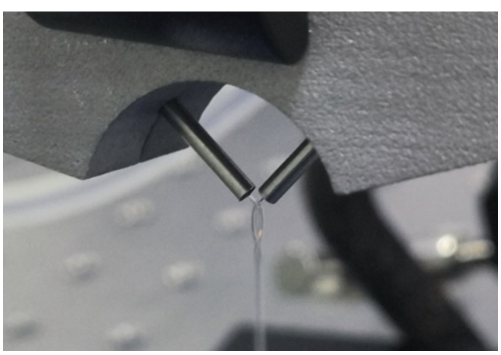

Figure 5: Schematic diagram of liquid film.

The focused light passes through the liquid film and is received by the spectrometer's fiber probe. By comparing the intensity changes at the 664 nm absorption peak of the methylene blue solution before and after passing through the liquid film, the absorption data is converted into thickness data according to the Lambert-Beer law, and the final result is shown in Figure 6. From the figure, it can be seen that although the size of the liquid film decreases after increasing the angle, the thickness of the liquid film can be reduced to a certain extent. The reason is speculated to be that the increase in collision angle increases the radial momentum, making it easier for the liquid to overcome surface tension and become a flat liquid film. The increase in liquid flow rate increases the thickness of the liquid film, and the range of measured data also increases. The reason is speculated to be that after the collision of higher flow rate liquid, the stability of the liquid film itself is impacted to some extent, resulting in large changes in measured data. However, in the experiment with a collision angle of 120°, the liquid film thickness meets the requirements of the experimental station.

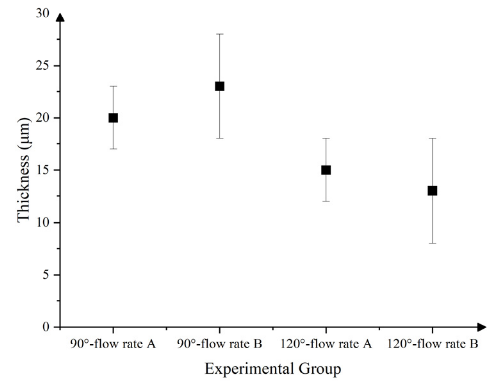

Figure 6: Liquid film thickness data chart.

SUMMARY

The article studies a liquid sample injection device applied to the hard X-ray ultrafast spectroscopy experiment station of the Shanghai high repetition rate XFEL and extreme light facility. The device is based on the principle of liquid flow collision, which can form a liquid film that meets the experimental requirements, and is equipped with a thickness measurement device for the liquid film. By designing a specific optical path, the precise measurement of the liquid film is achieved. In the experiment, methylene blue solution is used as the sample solution to test the device. The results show that the size and thickness range of the liquid film are consistent with the theoretical calculation results, meeting the needs of the hard X-ray ultrafast spectroscopy experiment station for liquid sample testing.

At the same time, there are some areas for improvement in this device: Firstly, the mechanical fixing method used for all liquid pipelines and clamping devices has the problem that if the angle needs to be changed or the stainless-steel tube needs to be replaced, it needs to be disassembled and replaced with the corresponding components, and then reinstalled. The whole process is very cumbersome. The follow-up improvement plan is to automatically adjust the collision angle through motor control, and change the installation method of the stainless-steel tube to make it easier to disassemble and replace. Secondly, for the thickness detection device, currently the spectrometer can only measure the thickness of liquid samples with absorption peaks from visible light to near-infrared bands. If the testing range needs to be expanded, it is necessary to use a light source with a wider wavelength range and use equipments such as FTIR.

REFERENCES

[1] N. Huang, H. Deng, B. Liu, D. Wang, Z. Zhao, "Features and futures of X-ray free-electron lasers", *The Innovation*, vol. 2, issue 2, 100097, May 2021, New York, NY, USA. doi:10.1016/j.xinn.2021.100097

ISBN: 978-3-95450-250-9 ISSN: 2673-5520 doi:10.18429/JACoW-MEDSI2023-TUPYP047

[2] L. Chen, X. Zhang and M. Shelby, "Recent advances on ultrafast X-ray spectroscopy in the chemical sciences", *Chem. Sci.*, vol. 5, issue 11, pp. 4136-4152, 2014.

[3] J. Barnard, J. Lee, O. Alexander, S. Jarosch, *et al.*, "Delivery of stable ultra-thin liquid sheets in vacuum for biochemical spectroscopy", *Front. Mol. Biosci.*, vol. 9, 1044610, Nov. 2022. doi:10.3389/fmolb.2022.1044610

[4] S. Menzi, G. Knopp, A. Al Haddad, S. Augustin, *et al.*, "Generation and simple characterization of flat, liquid jets", *Rev. Sci. Instrum.*, vol. 91, issue 10, 105109, Oct. 2020. doi:10.1063/5.0007228

[5] M. Kondoh, M. Tsubouchi, "Liquid-sheet jets for terahertz spectroscopy", *Opt. Express*, vol. 22, issue 12, pp. 14135-14147, Jun. 2014.

[6] G. Galinis, J. Strucka, J. Barnard, A. Braun, R. Smith, J. Marangos, "Micrometer-thickness liquid sheet jets flowing in vacuum", *Rev. Sci. Instrum.*, vol. 88, issue 8, 083117, Aug. 2017. doi:10.1063/1.4990130

[7] J. Koralek, J. Kim, P. Brůža, *et al.*, "Generation and characterization of ultrathin free-flowing liquid sheets", *Nat. Commun.*, 9, 1353, pp. 1353-1358, Apr. 2018.

[8] C. Crissman, M. Mo, *et al.*, "Sub-micron thick liquid sheets produced by isotropically etched glass nozzles", *Lab on a Chip*, vol. 22, issue 7, pp. 1365-1373, 2022.

[9] D. DePonte, U. Weierstall, K. Schmidt, J. Warner, *et al.*, "Gas dynamic virtual nozzle for generation of microscopic droplet streams", *J. Phys. D, Appl. Phys.*, vol 41, no. 19, 195505-195505, Sep. 2008.

[10] A. Fernández-Pérez, T. Valdés-Solís, G. Marbán, "Visible light spectroscopic analysis of Methylene Blue in water; the resonance virtual equilibrium hypothesis", *Dyes and Pigments*, vol. 161, pp. 448-456, Feb. 2019. doi:10.1016/j.dyepig.2018.09.083

[11] X. Nie, S. Chen, W. E and M. Robbins, "A continuum and molecular dynamics hybrid method for micro- and nano-fluid flow", *J. Fluid Mech.*, vol. 500, pp. 55-64, Feb. 2004.

[12] D. Hasson, R. Peck, "Thickness distribution in a sheet formed by impinging jets", *AIChE J.*, 10, 5, pp. 752-754, Sep. 1964.

[13] R. Li and N. Ashgriz, "Characteristics of liquid sheets formed by two impinging jets", *Phys. Fluids*, vol. 18, issue 8, 087104-087104-13, Aug. 2006.

ISBN: 978-3-95450-250-9 ISSN: 2673-5520 doi:10.18429/JACoW-MEDSI2023-TUPYP048

A HIGH REPETITION RATE FREE-ELECTRON LASER SHUTTER SYSTEM

Jiacheng Gu, Yajun Tong†, Zhen Wang, Huaidong Jiang
School of Physical Science and Technology, ShanghaiTech University, Shanghai, China

Abstract

The Shanghai High repetition rate XFEL and Extreme light facility (SHINE) is the first high repetition rate XFEL in China. It is a powerful tool for scientific research. The high repetition rate XFEL has not only high peak power but also high average power. The high average power will cause the distortion of optics and make the diagnostics failure. To measure the distortion of optics, the diagnostics, such as wavefront sensor, imager, should be working properly. A fast shutter system is designed to protect the diagnostics and to make the diagnostics working properly. It can control the number of pulses and average power on the diagnostics. The time window of shutter can be as small as 10 milliseconds. It can absorb most of FEL power.

INTRODUCTION

X-ray free electron laser (XFEL) is a new generation of advanced light source based on particle accelerators, with excellent characteristics such as ultra-short pulses, ultra-high brightness, high coherence, and continuously adjustable output wavelength. It has made significant progress in the past decade [1], and the XFEL facility has also become a powerful tool for cutting-edge research in life sciences, materials science, physics, and other fields [2]. The Shanghai High repetition rate XFEL and Extreme light facility (SHINE) is the first hard X-ray free electron laser facility in China, with a maximum electron energy of 8 GeV and a maximum repetition rate of 1 MHz. In the phase-I, it offers a photon energy range of 0.4-25 keV. SHINE's accelerator parameters are listed in Table 1 [3].

However, high repetition rate XFEL has both peak power and average power, and its high peak power can cause damage to the devices in the optical path. High average power can bring thermal load on the devices and cause thermal distortion to the optics, affect the beam transportation and focusing, and cause diagnostics failure. Therefore, how to diagnostics the distorting beam under high repetition rate is particularly important.

M. Renier and colleagues previously designed an X-ray shutter for the European Synchrotron Radiation Facility (ESRF) [4]. It can control the shortest exposure time achieved 3 milliseconds. However, it was not suitable for operation under high vacuum conditions. In a different endeavour, Chang Yong Park and collaborators designed a shutter tailored for high vacuum environments [5]. Their shutter realized the use of vacuum environment but their stopper cannot withstand 100W laser's heat load for a long time. To address this critical need, we have designed a shutter system based on M. Renier's design, but it can work in vacuum. The shutter's aperture is 4mm which is suitable for the small beam size of hard X-ray beamline, with a minimum time window of 10 milliseconds. To ensure efficient heat conduction within the stoppers and free falling, liquid metal is employed for cooling purposes.

Table 1: The Main Parameters of SHINE

Parameters	Nominal	Objective
Beam energy [GeV]	8	4~8.5
Bunch charge [pC]	100	10~300
Peak current [kA]	1.5	0.5~3
Slice emittance [µm·rad]	0.4	0.2~0.7
Max repetition rate [MHz]	1	1
Beam power [MW]	0.8	0~2.4
Photon energy [keV]	0.4~25	0.2~25
Pulse length [fs]	66	3~600

SHUTTER DESIGN

Basic Principle of the Device

The shutter consists of two sandwiched stoppers, as illustrated in Fig. 1. Each stopper is guided to move linearly along a track and is driven by a combination of an electromagnet and its own gravity. The system operates in the following states:

(a) State 1: In this configuration, both stoppers are positioned at their lowest point, and they are actively cooled. Notably, stopper 1 is responsible for absorbing the thermal load.

(b) State 2: When the need arises to create an time window, both stoppers are raised to their highest position, and at this point, neither receives cooling. This state typically lasts for less than 1 second.

(c) State 3: The electromagnets of the two stoppers begin to fall at different time, forming a defined time window. Eventually, both stoppers return to their lowest position, effectively reverting to the configuration of State 1.

The stopper is designed as a sandwich structure, comprised of three key components: a radiation damage resistant block (diamond), a burn-through detector, and a tungsten block, as depicted in Fig. 2. The burn-through detector serves the purpose of identifying whether the radiation damage resistant block has experienced burn-through. Its fundamental operational principle relies on the interaction of incident light with a YAG crystal, resulting in the generation of visible fluorescence. A photodiode is employed to detect this optical signal, which is subsequently transmitted as an interlocking signal through the connecting lead wire. Meanwhile, the tungsten block is deployed

† tongyj@shanghaitech.eud.cn

ISBN: 978-3-95450-250-9 ISSN: 2673-5520 doi:10.18429/JACoW-MEDSI2023-TUPYP048

to ensure that no photons can pass through the shutter, thus reinforcing its protective function. radiation damage resistant block should be designed to be removable, allowing for replacement once it has been burned through.

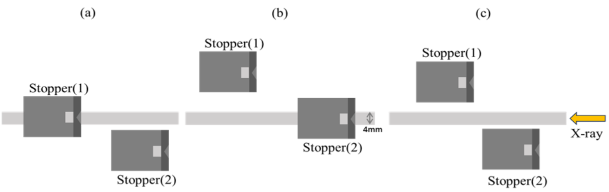

Figure 1: Principle of operation.

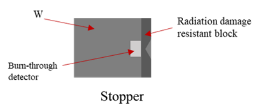

Figure 2: The composition and structure of the stopper

As illustrated in Figs. 3(a) and 3(b), the actuation of the stopper is achieved through a combination of a solenoid-type electromagnet, and gravity. Stoppers rise by electromagnetic force and fall by gravity. A guide rail ensures the linear motion of the device, while the spring serves to impact forces at the end of the stopper's stroke. As the stopper enters the water-cooled tank, its lower surface makes initial contact with a reservoir of liquid In-Ga. A section of the stopper is submerged in this liquid, thereby enhancing the heat exchange efficiency between the stopper and the water-cooled tank. Ultimately, heat is conducted out of the vacuum environment through the cooling water within the vacuum water pipe. The welding flange of each individual stop device is connected to the chamber flange. A heat sink is deployed to enhance the heat dissipation efficiency of the outer solenoid coil. The upper edge of the heat sink is welded to the stationary iron core, while the lower edge is welded to the welding flange, preserving the vacuum integrity of the chamber environment.

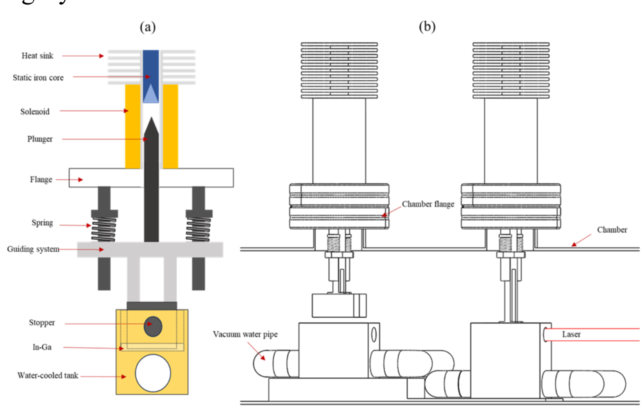

Figure 3: Shutter structure. (a) schematic diagram of key driving principles (b) actual drive plan structure assembly drawing.

SHUTTER SIMULATION

Finite Element Analysis of Thermal Load

Given the substantial thermal load absorbed by the stopper, a crucial element in its reliable operation is the use of high thermal conductivity liquid indium gallium for effective heat dissipation. In this system, heat is efficiently transferred from the stopper to a copper tank by means of the liquid In-Ga. Subsequently, the heat is exchanged with the copper tank through a water-cooled tube, facilitating the transfer of heat to the exterior of the chamber. This designed process enables vacuum cooling, ensuring the maintenance of ideal operating conditions.

Theory And Model

In our analysis of the key component, the stopper, we employed simulation software. Initially, we chose diamond as the damage-resistant block and B_4C was used as a comparison. As depicted in Fig. 4b, the fundamental model structure involved a laser beam with a total power of 100 W and a half-height width of 1.41 mm, adhering to a standard Gaussian distribution. The heat generated was deposited on the surface of the diamond and subsequently diffused into the heavy metal tungsten block. Concurrently, heat was transferred into the copper water-cooled channel, which exhibits high thermal conductivity, through the liquid In-Ga. Ultimately, the heat within the copper was conveyed out of the vacuum environment through water flow, enabling efficient heat dissipation. The final mesh division results are showcased in Figs. 4(c) and 4(d).

In this model, we set the centre of the beam at the surface as the beam origin O(0,0,0), the beam direction e(0,0,-1), and refer to Fig. 4c for the coordinate system. The light source follows a Gaussian distribution:

$$f(O,e) = \frac{1}{2\pi\sigma^2}\exp\left(-\frac{d^2}{2\sigma^2}\right), d = \frac{\|e \times (x - O)\|}{\|e\|} \quad ,$$

where, $\sigma = 0.6$ mm.

When a high repetition frequency free electron laser irradiates a material, the energy absorbed by the material is deposited inside the material, and the final energy diffuses in the form of thermal energy inside the material, following the thermal conduction law. In the three-dimensional coordinate system of the HT module, the classical Fourier heat transfer equation expression is:

$$\begin{aligned}\rho(T)C_P(T)\cdot\partial T(x,y,z,t)/\partial t \\ &= \partial/\partial x\,(k(T)\cdot\partial T(x,y,z,t)/\partial x) \\ &+ \partial/\partial y\,(k(T)\cdot\partial T(x,y,z,t)/\partial y) \\ &+ \partial/\partial z\,(k(T)\cdot\ \partial T(x,y,z,t)/\partial z) \\ &+ Q(x,y,z,t),\end{aligned}$$

where $T(x,y,z,t)$ is the variation of temperature over time and space, $\rho(T), C_P(T), k(T)$ are functions of material density, constant pressure heat capacity, and thermal conductivity. $Q(x,y,z,t)$ is the heat source converted from laser to the material. The detailed parameters are shown in Table 2.

ISBN: 978-3-95450-250-9 ISSN: 2673-5520 doi:10.18429/JACoW-MEDSI2023-TUPYP048

Table 2: The Main Parameters of Material

Material	ρ (kg/m^3)	C_P $(J/kg \cdot K)$	k $(W/m \cdot K)$
Diamond	3515	516	2500
Copper	8960	385	400
In-Ga	6440	420	28
B_4C	2520	20-2000	14-32

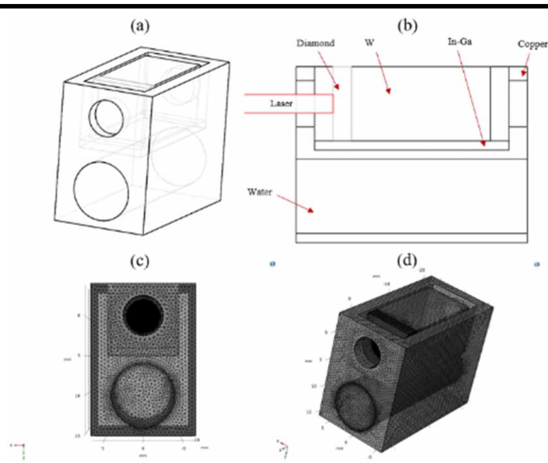

Figure 4: Block structure. (a) structure diagram, (b) half sectional detailed structure, (c) front view, (d) side view.

Result

Under steady-state conditions with a water flow rate of 0.33 litters per minute, the highest temperature observed on the diamond surface is 114 °C, the highest temperature on the tungsten surface is 97 °C, and the highest temperature on the liquid In-Ga surface is 91 °C (Fig. 5). These temperatures fall within the reasonable range for these materials. Taking into account cost considerations, a comparative analysis was conducted to assess the impact of different radiation damage resistant materials on the overall equipment performance. Specifically, 2 mm thick B_4C and 2 mm thick diamond were compared. Notably, B_4C exhibits significantly lower thermal conductivity than diamond. Under steady-state conditions with a water flow rate of 0.33 litters per minute, the highest surface temperature reached 1800 °C when B_4C was use (Fig. 6). This result indicates that B_4C's heat dissipation performance is less effective than that achieved with diamond.

CONCLUSION

To ensure the proper operation of diagnostic equipment for the high repetition rate FEL, we have designed a spiral tube-driven shutter. All materials used in the shutter are compatible with high vacuum conditions. Through careful design of the stopper, the heat dissipation system, and the driving mechanism, it is expected to meet the requirements for long-term usage and with a minimum 10-millisecond window.

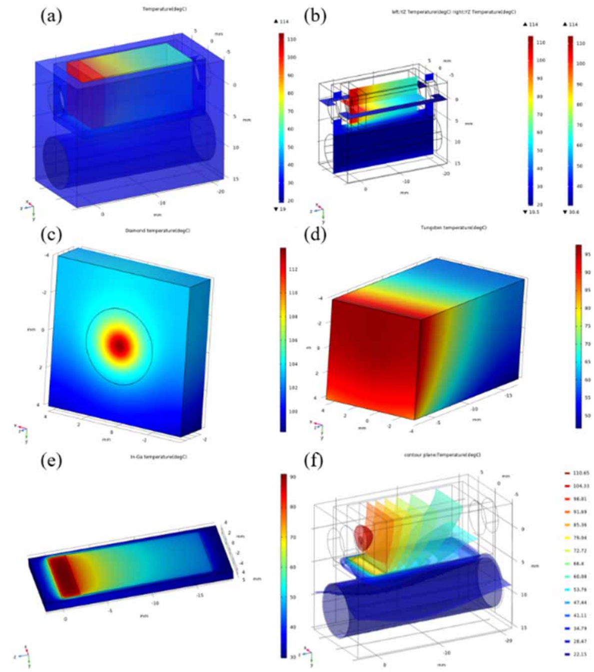

Figure 5: 2 mm thick Diamond with steady state temperature at a water flow rate of 0.33 L/min. (a) surface temperature distribution, (b) profile temperature distribution map, (c) diamond temperature distribution, (d) tungsten temperature distribution, (e) liquid indium gallium temperature distribution, (f) temperature contour map.

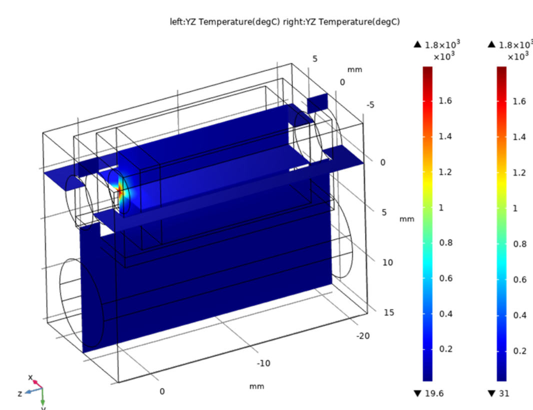

Figure 6: 2 mm thick B_4C with steady-state temperature at a water flow rate of 0.33 L/min.

REFERENCES

[1] P. Emma *et al.*, “First lasing and operation of an angstrom-wavelength free-electron laser”, *Nat. Photonics*, vol. 4, p. 641-647, 2010. doi:10.1038/Nphoton.2010.176

[2] H. N. Chapman, “X-Ray Free-Electron Lasers for the Structure and Dynamics of Macromolecules”, *Annu. Rev. Biochem.*, vol. 88, p. 35-58, 2019. doi:10.1146/annurev-biochem-013118-110744

[3] Z. Zhu, Z. T. Zhao, D. Wang, Z. H. Yang, and L. Yin, “SCLF: An 8-GeV CW SCRF Linac-Based X-Ray FEL Facility in Shanghai”, in *Proc. FEL'17*, Santa Fe, NM, USA, Aug. 2017, pp. 182-184. doi:10.18429/JACoW-FEL2017-MOP055

ISBN: 978-3-95450-250-9 ISSN: 2673-5520 doi:10.18429/JACoW-MEDSI2023-TUPYP048

[4] M. Renier *et al.*, "A white-beam fast-shutter for microbeam radiation therapy at the ESRF", *Nucl. Instrum. Methods Phys. Res., Sect. A,* vol. 479, no. 2-3, pp. 656-660, 2002. doi:10.1016/S0168-9002(01)00905-6

[5] C. Y. Park *et al.*, "Ultra-high vacuum compatible full metal atom beam shutter for optical lattice clocks", *Rev. Sci. Instrum.,* vol. 94, p. 013201, 2023. doi:10.1063/5.0123971

ISBN: 978-3-95450-250-9 ISSN: 2673-5520 doi:10.18429/JACoW-MEDSI2023-TUPYP050

DESIGN AND CALCULATION OF VACUUM SYSTEM FOR WALS STORAGE RING*

Chengyin Liu, Jian Li†, Geng Wei, Jianhua He, Haohu Li, Yuan Chen, Jike Wang, Yuancun Nie, Ye Zou, Xuerui Hao, Yuxin Zhang, Jingmin Zhang, Pai Xiang, Hui Li, Yong Wang, Yuhai Xu
Wuhan Advanced Light Source Research Center, Wuhan University, Wuhan, China

Abstract

Wuhan Advanced Light Source (WALS) is a fourth-generation synchrotron radiation facility with 1.5 GeV designed energy and 500 mA beam current. The storage ring vacuum system has to be designed in such a way which is compatible with a multi-bend achromat (MBA) compact lattice. the new technology of non-evaporable getter (NEG) coating was used, which is more and more popular in accelerator equipment.

The design of the whole vacuum chamber and the necessary calculations were posted in the paper. The results indicated that the design of the vacuum system can meet the design requirement.

INTRODUCTION

Wuhan Advanced Light Source (WALS) is a fourth-generation synchrotron radiation facility with 1.5 GeV designed energy and 500 mA beam current. The storage ring vacuum system has to be designed in such way which is compatible with a multi-bend achromat (MBA) compact lattice. The emittance of WALS is less than 230 pm·rad, which can provide high brilliance lights to experimental stations. To achieve these objectives, the aperture of the various types of the vacuum chambers to be much smaller and more compact than that of the 3rd generation light source, which is complexity of the design of vacuum chamber [1].

The general requirements for vacuum chamber have to be considered for the cost, performance, and required maintenance, these factors will lead to a design by which the details of the chamber construction various according to local spatial constraints and synchrotron radiation (SR) loading [2].

In this paper, the design of the whole vacuum chamber is introduced, the vacuum distribution results calculated by PTMC and the SR heat loads calculated by FEM indicated that the design of the vacuum system is reasonable.

THE OBJECTIVES AND THE LAYOUT OF THE WALS VACUUM SYSTEM

The parameters of the storage ring in WALS are show in Table 1. The Ring circumference is 180 m with 8 cells. Thus, the length of each cell is 22.5 m, contains 6.8 meters of insertion devices. The internal aperture of vacuum chamber is 32 mm (except Super-bend combination magnet section). Each cell contains 12 BPMs, including 7 BPM with bellows in each side, connected with vacuum chamber through knife flanges, and other 5 BPMs directly soldered to the vacuum vessels. The layout of the cell is show in Fig. 1.

Table 1: Parameters of the Storage Ring

Parameter	Value
Beam energy [GeV]	1.5
Current [A]	0.5
Ring circumference [m]	180
Max. magnet field strength [T]	3.5
Total synchronous radiation power [kW]	54.35
Photon desorption coefficient [molecules/photon]	2×10^{-6}
Linear photon airborne [Pa×L/s×m]	2.66×10^{-5}
Static pressure [Pa]	$<5\times10^{-8}$
Dynamic pressure [Pa]	$<2\times10^{-7}$
Vacuum box beam aperture [mm×mm][H×V]	Ø 32 (standard vacuum box) 12×30 (SuperBend combination magnet vacuum box)

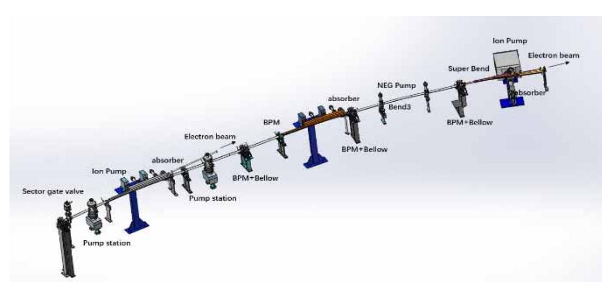

Figure 1: Layout of the 1/2 cell of WALS vacuum system.

According to the overall design requirements, the vacuum system should meet the requirements of static vacuum less than 5×10^{-8} Pa and dynamic vacuum less than 2×10^{-7} Pa. Due to the small aperture of the vacuum chamber, traditional methods with lumped pumping station can

* Work supported by the Key R&D Project of Hubei Provincial Department of Science and Technology, No. 2021AFB001.
† lijian901020@whu.edu.cn.

12th Int. Conf. Mech. Eng. Design Synchrotron Radiat. Equip. Instrum. MEDSI2023, Beijing, China JACoW Publishing
ISBN: 978-3-95450-250-9 ISSN: 2673-5520 doi:10.18429/JACoW-MEDSI2023-TUPYP050

hardly meet the ultra-high vacuum (UHV) requirements [3].

To achieve the UHV requirement, the new technology of non-evaporable getter (NEG) coating was used, which is more and more popular in accelerator equipment [4].

NEG coating acts as a diffusion barrier between vacuum chamber material and vacuum resulting in a reduction of the electron, photon and ion stimulated desorption yields. It also provides distributed pumping along vacuum chamber. Thus, the specified UHV pressure level could be met with a reduced number and a size of external pumps.

CALCULATION RESULTS OF THE VACUUM LOADS

Synrad and Moflow code were used to simulate the vacuum behaviour of a whole storage ring cell. The Synrad was used to calculated the desorbed of the gas load of the chamber walls. And the data were exported into Moflow to calculated the vacuum distribution. The reflection of the walls were considered. The photon stimulated desorption yields of the material varies according to the dose of the beam, shown in Fig.2.

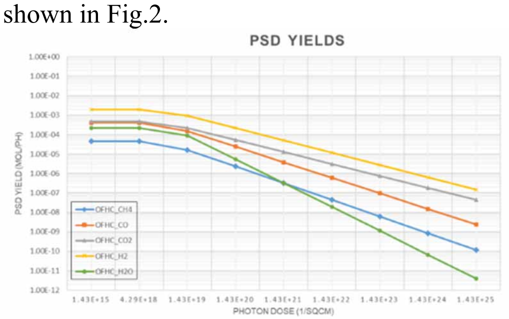

Figure 2: PSD yield with Beam dose.

The pumping speeds of the discrete pumps and the sticking probability of the NEG coating should be provided for each different gas.

Figure 3 shows the individual gas partial pressure vs. distance along the beam after 100 Ah beam dose with both active and saturated NEG coating. It can be seen that the target pressure of 5×10^{-7} Pa at 500 mA is achieved after a beam dose of 100 Ah in the case of fully active NEG coating.

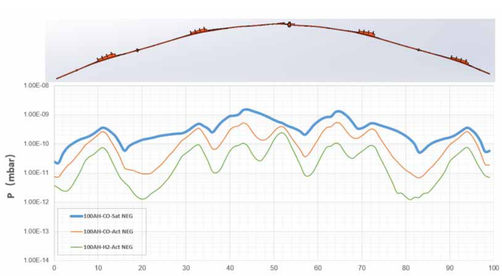

Figure 3: The individual gas partial pressure vs. distance along the beam after 100 Ah beam dose with different NEG condition.

SR LOADS AND PHOTON ABSORBERS

Considering the distribution of synchrotron radiation power, the form of centralized absorption and distributed absorption were adopted in WALS. The high-heat-load absorbers were used in the place where the radiation power is large. And in the place where the radiation power is small, the pipe wall welding water pipe is used for cooling. Shown in Fig. 4.

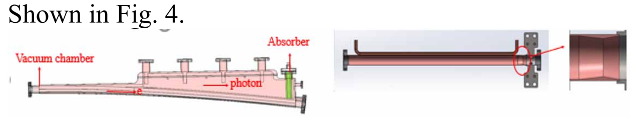

Figure 4: Assembly relationship of absorber and welded tube.

For the high-heat-load absorbers, we compared 3different materials: OFHC, Gild-cop Al-15, and Cu-Cr-Zr alloys, the results show in Table 2. Cu-Cr-Zr has good thermal conductivity, high softening temperature, good weldability, and high mechanical strength and is considerably less expensive which is widely available in all sizes form many suppliers.

Table 2: Properties Comparison of Several Copper Alloys

Properties	OFHC	Gildcop Al-15	Cu-Cr-Zr alloys
Thermal conductivity (W/m/K)	391	365	335
Density (g/cm^3)	8.9	8.9	8.9
Coefficient of Thermal Expansion (µm/m/K)	17.7	16.6	17.0
Melting point (°C)	1083	1083	1083
Poisson's ratio	0.323	0.326	0.32
Elastic Modulus (GPa)	115	130	123
Yield Strength (MPa)	344~381	470~580	350~550

Synrad was used to predict photon heat loading onto the vessel walls caused by the bending magnets for the current lattice, assuming a beam current of 500 mA + 10% margin. Dipole field strengths and arc positions were created using data provided by Accelerator Physics. Fully sticking surfaces were used with no reflection. Synrad used a nominal cell size of 100 cells/cm for the calculation of absorbed power. The calculated photon distribution is shown in Fig. 5. Heat loads were exported into ANSYS for thermal calculations, the results are show in Figs. 6-8.

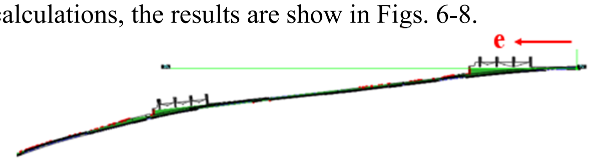

Figure 5: Photon distribution calculated via Synrad software.

ISBN: 978-3-95450-250-9 ISSN: 2673-5520 doi:10.18429/JACoW-MEDSI2023-TUPYP050

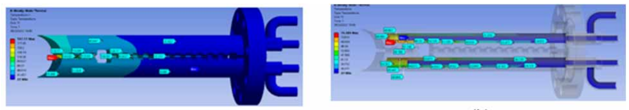

(a) (b)

Figure 6: Temperature distribution: (a) absorber body (b) flow path.

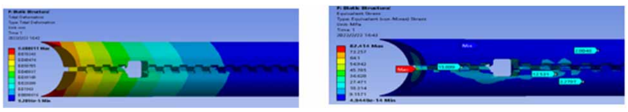

Figure 7: Strain and stress caused by temperature.

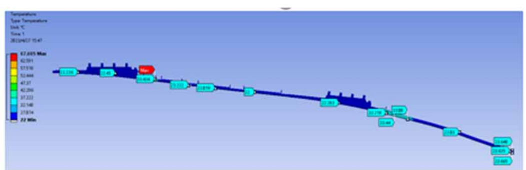

Figure 8: Temperature distribution of vacuum chambers.

The synchrotron radiation load calculated by Synrad was imported into Ansys. The maximum temperature of the absorber body is 197 °C which is far from the melting point of the material. The maximum temperature of the flow path is 79 °C, below the boiling point of the water. The maximum strain is below 0.1mm, and the maximum stress is about 82.4 MPa, far from the yield strength of the Cu-Cr-Zr alloys.

CONCLUSION

The status of the vacuum systems for the WALS vacuum system has been reviewed. The vacuum and SR absorber calculation has been posted in this paper. The results indicated that the design of the chamber and the absorber can meet the design requirement.

REFERENCES

[1] P. He *et al.*, “Progress in the Design and Related Studies on the High Energy Photon Source”, *Physics Procedia*, vol. 84, pp. 40-46, 2016. doi:10.1016/j.phpro.2016.11.008

[2] P. F. Tavares *et al.*, “The MAX IV storage ring project”, *J. Synchrotron Radiat.*, vol. 21, pp. 862-77, 2014. doi:10.1107/S1600577514011503

[3] M. Grabski and E. Al-Dmour, “Commissioning and operation status of the MAX IV 3 GeV storage ring vacuum system”, *J. Synchrotron Radiat.*, vol. 28, pp. 718–731, 2021. doi:10.1107/S1600577521002599

[4] O. Seify *et al.*, “Optimisation of the RGA location in the evaluation of NEG coating pumping properties”, *Vacuum*, vol. 165, pp. 207-214, 2019. doi:10.1016/j.vacuum.2019.04.006

ISBN: 978-3-95450-250-9 ISSN: 2673-5520 doi:10.18429/JACoW-MEDSI2023-TUPYP051

PROGRESS OF WALS NEG COATING EQUIPMENT AND TECHNOLOGY*

Geng Wei, Yuan Chen, Jian Li, Chengyin Liu, Jianhua He, Haohu Li, Jike Wang, Yuancun Nie, Ye Zou, Xuerui Hao, Yuxin Zhang, Jingmin Zhang, Pai Xiang, Hui Li, Yong Wang, Yuhai Xu
Wuhan Advanced Light Source Research Center, Wuhan University, Wuhan, P. R. China

Abstract

The objective of WALS (Wuhan Advanced Light Source) is to establish a world-class radiating light source. For the entire storage ring vacuum vessels, chromium-zirconium-copper has been selected as the primary material. Additionally, the magnetron sputtering (PVD) process has been employed to apply NEG (Non-Evaporable Getter) coatings to the inner surfaces of the copper vacuum chambers. This coating process enhances the vacuum performance.

Currently, the coating laboratory has taken shape and includes various components such as a standard cleaning platform, a coating platform, an ultimate vacuum test platform, an extraction rate test platform, and a coating microstructure test process. In terms of coating equipment, a bias power supply and customized ceramic components have been integrated to provide additional functionality. Multiple electrode control is utilized to manage different target materials, and experiments are conducted to deter-mine the composition of multilayers for various deposition ratios. Furthermore, sample tube bias control access is maintained during the coating process, and diverse combinations of target materials and bias parameters have been thoroughly investigated. Coating is presently in progress, and specific test results are underway.

INTRODUCTION

Process Difficulty Introduction

The 1.5 GeV storage ring vacuum system designed by WALS has a circumference of 180 m. According to the characteristics of physical design, the storage ring vacuum system was divided into 8~cells (standard segment) and 8 straight segments of 6.8 m. Chromium-zirconium-copper was chosen as the primary material for the entire ring vacuum vessel [1, 2]. At the same time, 316L was selected as the material for the pumping, bellows unit, and BPM mechanical shell.

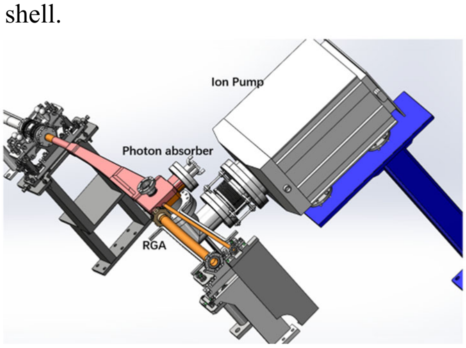

Figure 1: Model of vacuum chamber (Super Bend composite magnet).

One of the major challenges of WALS vacuum system design is magnet clearance small aperture (14 mm). The vacuum chamber (Super Bend composite magnet) has an oval profile with an inner diameter of 30×12 mm, a wall thickness of 1 mm, and a front chamber structure, which is a vacuum chamber about 1.8 m long, where the bending angle at the bipolar magnet is 10.8°, and the reverse bending is 1°, as shown in Fig. 1. The corresponding sample tube with the NEG coating [3] deposited on the inner wall is shown in the *Technical Status* section.

COATING MACHINE EQUIPMENT

Currently, the coating laboratory has taken shape and includes various components such as a standard cleaning platform, a coating platform, an ultimate vacuum test platform, an extraction rate test platform, and a coating microstructure test process, as shown in Fig. 2.

Figure 2: The coating laboratory.

Figure 3 shows the schematic diagram of the vacuum coating system [4]. The copper alloy pipe to be plated reaches vacuum through the flange and the auxiliary vacuum box at the lower end, and an appropriate amount of high-purity krypton gas is injected into the pipe as the discharge gas. The sputtering cathode target is made of a wire wound with a diameter of 1 mm. The end of the sputtering cathode target is fitted with a ceramic sheet to ensure insulation from the inner wall of the pipe. The magnetic field is provided by an external solenoid coil, which generates an adjustable magnetic field of $0.03 - 0.08$ T at the central axis.

Three feasible research directions for NEG coating have been pursued:

1. Different target materials were controlled by means of multi-electrode control, while experiments were performed on deposited compositions of different ratios of multilayers,

ISBN: 978-3-95450-250-9 ISSN: 2673-5520 doi:10.18429/JACoW-MEDSI2023-TUPYP051

2. Sample tube bias control access during the coating process, additional control parameters, and different crystal types of multilayers have been completed,
3. Multiple combinations of target materials and bias parameters have been investigated for this technique.. Research on the different components of the multilayer NEG coatings is currently underway, and specific test results are in progress.

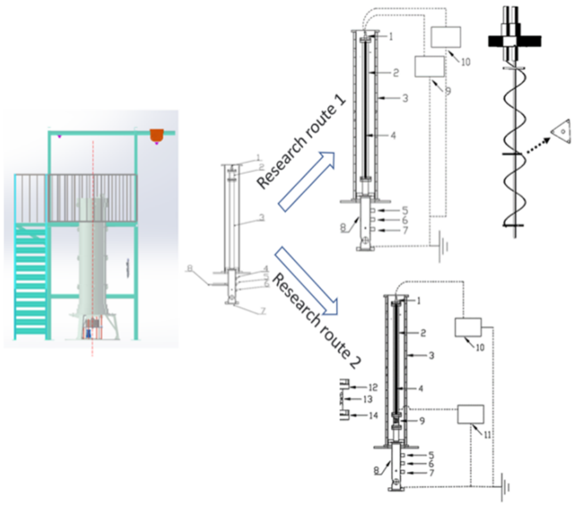

Figure 3: Te schematic diagram of the vacuum coating system.

TECHNICAL STATUS

Generally, the thickness of the plated pipe coating was controlled within 800~1500 nm, and the ratio of Ti:Zr:V atoms was maintained at 1:1:1.

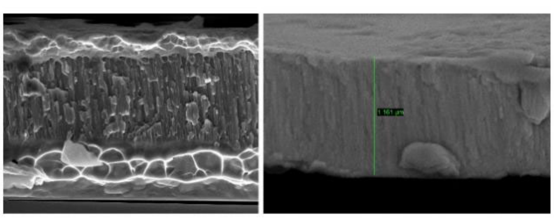

Figure 4: The section structure of NEG coating.

At an early stage, experimental work was carried out for the study of pipeline coating technology. By controlling relevant coating parameters, NEG coating [5] with a stable structure and good extraction performance was obtained. The morphology and mechanical characteristics of NEG coatings were tested using utilizing scanning electron microscope and nano-indentation. As can be seen from Fig. 4, the surface of the NEG coating obtained is smooth, the lattice distribution is uniform, and the thickness is about 1.1 μm.

Figure 5: Measured number of limiting vacuum.

The NEG coating has a smooth surface, a fairly uniform lattice distribution, and a thickness of around 1 μm. Nanoindentation test coating adhesion was 17 N. With 180 °C high temperature roasting activation, in the case of no external pump maintained for half a year, NEG ultimate vacuum coating of pipe was 7.43 x10^{-9} Pa, as shown in Fig. 5.

Table 1: Current NEG Coating Pumping Rate

	α(H2)	α (CO)	Q (CO)
180 °C 24 h	0.0041	0.1125	0.0201 mL

A 32 mm straight round tube with an inner diameter of 700 mm (**C** in Fig. 6) was baked and activated by 24 h at 180 ℃ standard vacuum. The viscosity coefficient of the NEG coatings after the first activation are shown in Table 1.

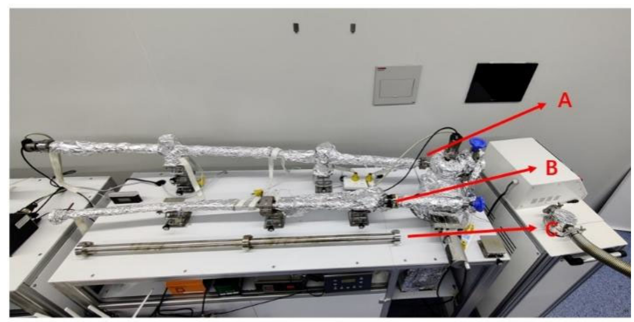

Figure 6: Typical sample tube.

Custom ceramics were used to ensure shielding and securing of the target wires in the chamber of the Super Bend composite magnet, and similar sample coatings were carried out, as shown in **B** in Fig. 6, **A** is a 1.9 m long circular tube vacuum chamber with a bending angle of about 6° and an inner diameter of 32 mm, which is characterized by two small pump ports with grilles and a 1° reverse twist.

Currently, the three typical vacuum chamber structures in Fig. 6 have been coated.

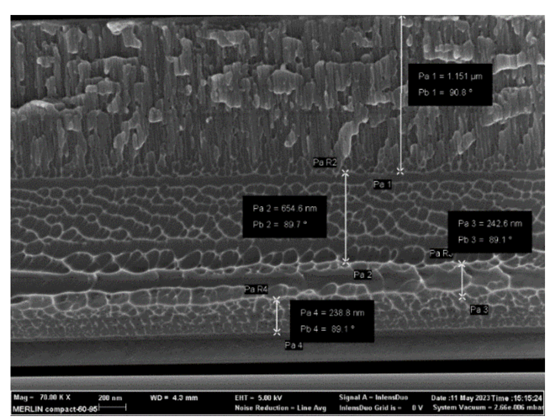

Figure 7: The section structure of NEG coating.

In the course of investigating the NEG coating process, WALS introduced a minor modification to the coating equipment. This entailed the addition of a small ceramic component to insulate the sample tube, isolating it from both the bottom transition vacuum chamber and the target

ISBN: 978-3-95450-250-9 ISSN: 2673-5520 doi:10.18429/JACoW-MEDSI2023-TUPYP051

point. This adjustment was made to create a suitable vacuum environment for the sample tube. Concurrently, an additional bias power supply was integrated to establish an electrical connection with the sample tube.

During the coating process, an additional bias control was introduced for the sample tube, supplementing the conventional coating power supply that provides the target wire. As depicted in Fig. 7, the SEM (Scanning Electron Microscope) image of the NEG coating section on the silicon wafer can be broadly categorized into three layers: the binding layer, the dense structure layer, and the columnar structure layer.

A noteworthy observation is that, under the same coating DC power supply parameters applied to the compact layer, elevating the bias voltage of the sample tube by 101V induces a notable transition from a dense structure to a distinct columnar structure. This phenomenon can be attributed to the additional bias effects, where electron bombardment of the inner wall leads to heating of the sample tube. Simultaneously, positive ions in the filtered plasma bombard the inner wall, reducing the energy of the metal particles within the coating, thus resulting in the transformation into a columnar structure.

CONCLUSION

WALS has established an experimental platform for NEG coatings, successfully conducting experiments on sample tubes of different sizes within the storage ring.

These experiments have resulted in improved NEG coating properties, with viscosity coefficients of H_2 0.0041 and CO 0.1125. A single activation process yields a CO volume of 0.02016 mL. Notably, the coating machine has been enhanced to introduce additional bias control, enabling the creation of a unique columnar structure.

REFERENCES

[1] G. Cattenoz *et al.*, "Vacuum Acceptance Tests for the UHV Room Temperature Vacuum System of the LHC during LS1", in *Proc. IPAC'14*, Dresden, Germany, Jun. 2014, pp. 2357-2359. doi:10.18429/JACoW-IPAC2014-WEPME041

[2] O. B. Malyshev and R. Valizadeh, "Further Optimisation of NEG Coatings for Accelerator Beam Chamber", in *Proc. IPAC'14*, Dresden, Germany, Jun. 2014, pp. 2399-2402. doi:10.18429/JACoW-IPAC2014-WEPME056

[3] P. H. Nallin *et al.*, "The Sirius Heating System for the In-situ NEG Activation", in *Proc. IPAC'19*, Melbourne, Australia, May 2019, pp. 4109-4111. doi:10.18429/JACoW-IPAC2019-THPTS004.

[4] M. M. Dehler et al., "Characterization of NEG Coatings for SLS 2.0", in *Proc. IPAC'19*, Melbourne, Australia, May 2019, pp.1662-1665. doi:10.18429/JACoW-IPAC2019-TUPGW108

[5] R. Sirvinskaite, M. D. Cropper, A.N. Hannah, O.B. Malyshev, R. Valizadeh, and S. Wang, "Electron Stimulated Desorption from Cryogenic NEG-Coated Surfaces", in *Proc. IPAC'19*, Melbourne, Australia, May 2019, pp. 2193-2196. doi:10.18429/JACoW-IPAC2019-TUPTS114

ISBN: 978-3-95450-250-9 ISSN: 2673-5520 doi:10.18429/JACoW-MEDSI2023-TUPYP053

CURRENT STATUS OF VIBRATION MONITORING SYSTEM AT SOLARIS

M. Piszak*, SOLARIS National Synchrotron Radiation Centre, Cracow, Poland

Abstract

Solaris synchrotron radiation centre, despite being relatively new facility, began enlargement of its experimental hall in 2022 in order to accommodate new beamlines. The construction works were carried out along with regular accelerators and beamlines operation and generated high levels of vibration. To better understand the influence of vibrations on electron and x-ray beams' stability, an accelerometer-based monitoring system was designed and implemented. The system consists of a triaxial measurement point equipped with seismic accelerometers located on bending magnet inside storage ring and a central signal conditioning and acquisition point. The results of long-term vibration data collection and analysis will be presented along with plans for the future system development.

INTRODUCTION

Low vibration environment is crucial for an optimal operation of storage rings and beamlines at synchrotron light sources. Evaluation of background vibrations in synchrotron facilities is typically carried out using accelerometers in short-term survey measurement campaigns [1]. Some facilities decide on permanent monitoring systems installation [2]. The Vibration Monitoring System (VMS) at SOLARIS synchrotron radiation centre has been developed in order to provide continuous diagnostic data of vibration conditions in the storage ring.

The VMS started operation in the beginning of 2023 and the commissioning period ended in September 2023 (due to long component delivery schedules). Along with the development of the system, the enlargement of the experimental hall and related construction works were carried out. The VMS has played an important role during accelerators and beamlines operation coinciding with heavy construction equipment works that generated high levels of vibrations. When established vibration limits were exceeded, actions were taken: the problematic construction methods were changed to lower the impact of vibrations; the activities were rescheduled to take place during less-critical time periods.

SYSTEM DESIGN

Hardware

Currently, the VMS consists of a single Measurement Point (MP) located inside the storage ring on Double-Bend Achromat (DBA) cell in section 01. Measurement point consists of three PCB Piezotronics Model 393B31 seismic accelerometers (nominal sensitivity: $1\ \mathrm{V\,m^{-1}\,s^2}$, frequency range: 0.1 Hz to 200 Hz). Transducers are fixed to a custom-build, triaxial adapter that allows for axial alignment with respect to the DBA cell. The MP's orientation was chosen accordingly: the x-axis of the MP is normal to the electron beam at the DBA center, the y-axis is tangential to the beam and the z-axis is oriented vertically (Fig. 1).

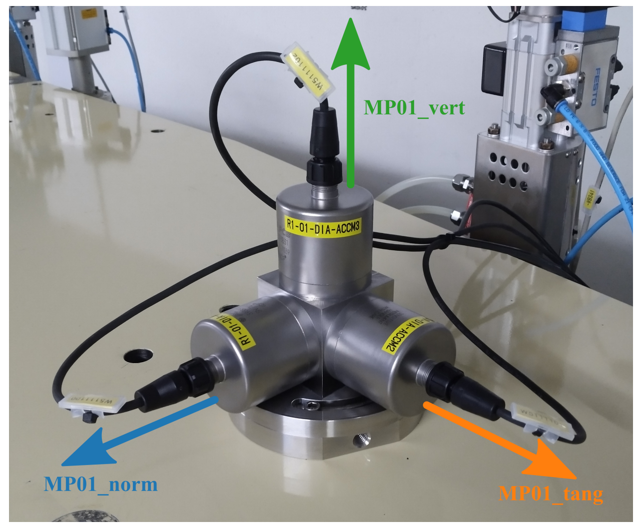

Figure 1: Triaxial measurement point with custom adapter mounted on the top surface of a DBA cell.

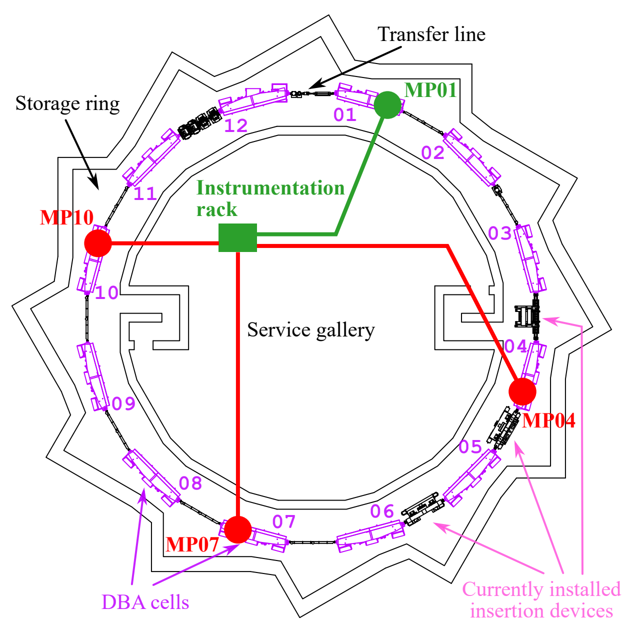

Figure 2: VMS arrangement view over the storage ring area (green color indicates existing infrastructure; red color indicates planned measurement points).

* marcel.piszak@uj.edu.pl

ISBN: 978-3-95450-250-9 ISSN: 2673-5520 doi:10.18429/JACoW-MEDSI2023-TUPYP053

Analog IEPE signals from accelerometers run to the central acquisition point of the system located in a rack cabinet in the service gallery area (Fig. 2).

The central point consists of PCB Piezotronics Model 483C50 signal conditioner (8-channel, gain: ×0.1 to ×200), NI cDAQ-9185 chassis and a single NI 9239 CompactDAQ voltage input module (4-channel, 24-bit, input range: ±10 V). Network data streaming is provided by the Chassis via Ethernet LAN connection. Conditioner is also connected to the same network, providing remote configuration and control possibilities. The system has a dedicated server for data acquisition, processing and logging. The VMS has a modular design, allowing for expansion of up to 16 channels with a single chassis configuration (Fig. 3).

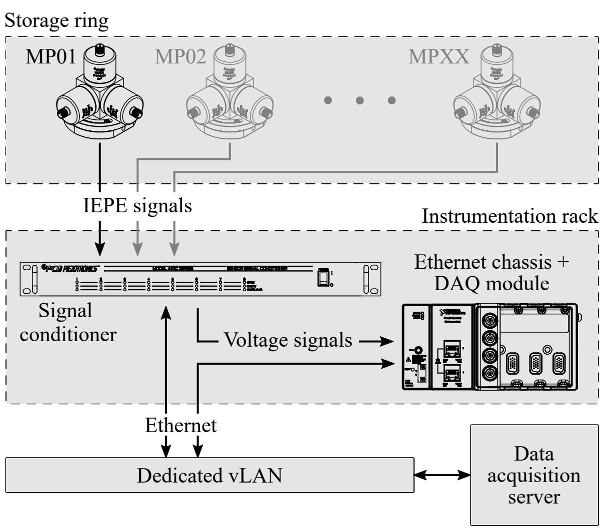

Figure 3: VMS schematic view.

Software

Data streamed by the DAQ hardware is routed to the server running a Windows virtual machine. Control software was developed in-house using LabVIEW programming environment. The software provides data acquisition, preprocessing and logging as well as system configuration and basic real-time analysis capabilities. In order to fully utilize the input range of the DAQ module, a programmable gain on the signal conditioner was set to ×100. The system's sampling frequency was set to 2 kHz. The software performs bandpass filtering (1 Hz to 300 Hz) and single integration to obtain velocity from acceleration. Then, the root-mean-square value is calculated and averaged over 10 s windows. Processed data is being continuously logged using TDMS file format. Other available real-time analysis options are: displacement PSD and third-octave spectra views (Fig. 4). Software has the ability to log complete data waveforms on-demand or using preset time schedule.

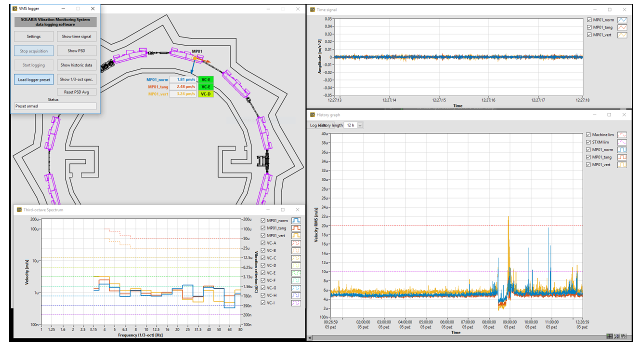

Figure 4: Control software GUI.

MEASUREMENTS AND ANALYSIS

Time Domain Analysis

The final installation of MP01 was completed in July 2023 and the process of data acquisition and archiving started. The construction works related to experimental hall enlargement were ongoing and involved heavy equipment operation. The accelerators' shutdown period finished in the end of August 2023 and some construction works overlapped with the operation of accelerators. Sample time history presenting RMS vibration velocity (10 s averaged) can be seen in Fig. 5. During normal storage ring operation, a stable level of 4 $\mu m\,s^{-1}$ to 6 $\mu m\,s^{-1}$ is observed in all three axes. During shutdown, levels as low as 1.2 $\mu m\,s^{-1}$ can be observed (in vertical direction). Contributions from construction works were as high as 80 $\mu m\,s^{-1}$. The maximum allowed value for storage ring operation in any direction was set to 20 $\mu m\,s^{-1}$. Construction works were either rescheduled or modified when vibrations exceeded limit for a prolonged time.

Frequency Domain Analysis

Short-term time series of acceleration signals during various operating conditions were recorded for further frequency analysis. Power spectral densities were calculated and resulting spectra were integrated to obtain displacement information. Figure 6a represents PSD averaged using Welch's method [3] from 1-hour long waveform obtained during normal operation of the storage ring. Visible peak at approx. 26 Hz is corresponding to 1st mode of DBA cell on concrete supports. Results of finite element modal analysis (Fig. 7) indicates that the biggest directional magnitude of 1st DBA cell mode is corresponding to the MP01 normal axis.

The difference of RMS velocity levels between shutdown and operation was further investigated. The influence of DBA cell's magnet cooling system is believed to be the main cause of increased vibrations. Water flowing through ducts in magnet coils generate broadband vibrations that propagate throughout DBA body. Increased energy in frequency band up to 45 Hz can be seen in Fig. 6b.

CONCLUSION

The VMS system at SOLARIS was build and commissioned with success. Despite relatively short operation time,

ISBN: 978-3-95450-250-9 ISSN: 2673-5520 doi:10.18429/JACoW-MEDSI2023-TUPYP053

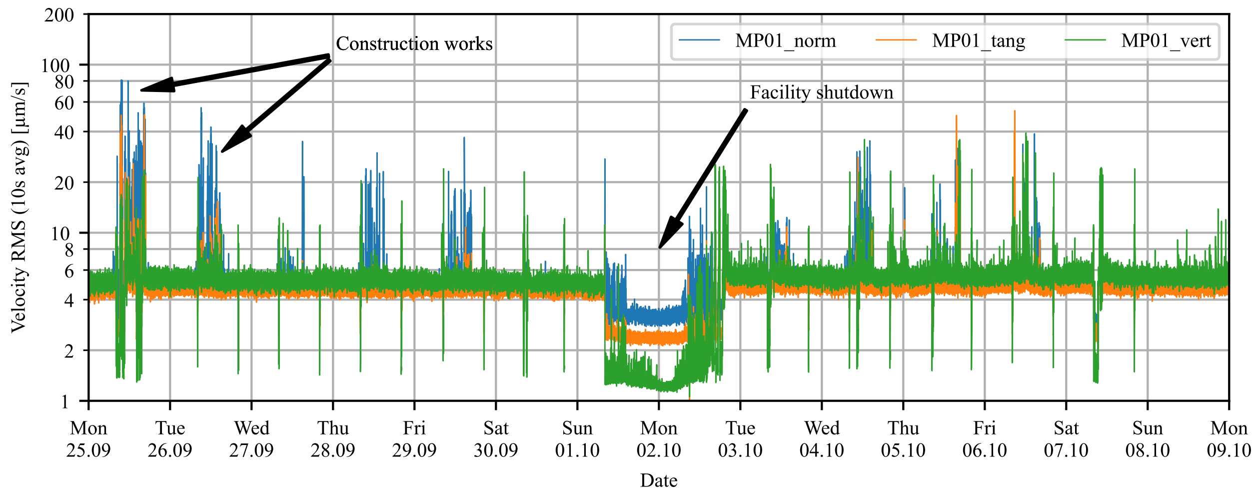

Figure 5: RMS vibration velocity time history spanning 2 week period.

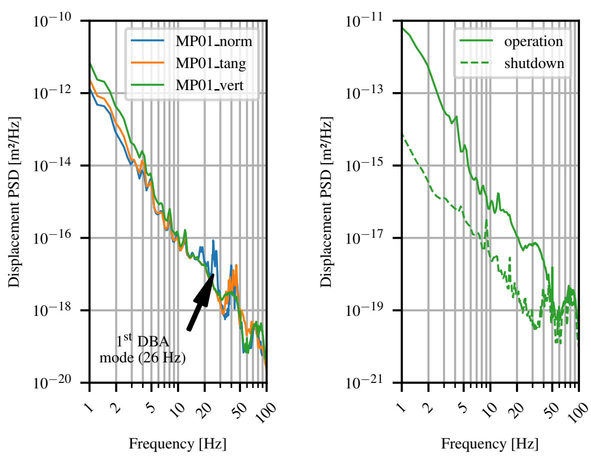

(a) (b)

Figure 6: Displacement PSD of (a) all axes during operation and (b) vertical direction during shutdown vs. operation.

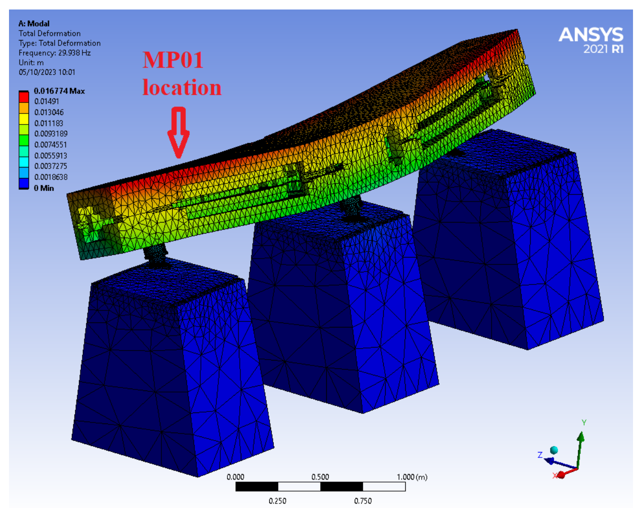

Figure 7: Results of modal FEA showing 1st mode (30 Hz) of DBA cell on supporting structures.

data gathered by the system proved to be useful during construction works.

The system is planned to be expanded with two or three additional measurement points distributed across remaining DBA cells in order to provide more information about the mechanical dynamics of the storage ring. Obtained data is planned to be correlated with electron beam parameters as a part of a greater study on beam stability at SOLARIS. Plans for the future also include new software development with integration to the Tango control system of the synchrotron facility.

ACKNOWLEDGEMENTS

The work is supported under the Polish Ministry and Higher Education project: "Support for research and development with the use of research infrastructure of the National Synchrotron Radiation Centre SOLARIS" under contract nr 1/SOL/2021/2.

REFERENCES

[1] K. Haga *et al.*, "The Vibration Measurements at the Photon Factory Storage Ring Building," in *Proc. EPAC'00*, Vienna, Austria, Aug. 2000, pp. 2388–2390. https://jacow.org/e00/papers/TUP4A11.pdf

[2] K. H. Hsu, C. K. Kuan, W. Y. Lai, and H. S. Wang, "Vibration Monitoring at TPS Storage Ring," in *Proc. MEDSI'18*, Paris, France, Jun. 2018, pp. 227–230. doi:10.18429/JACoW-MEDSI2018-WEPH13

[3] P. Welch, "The use of fast fourier transform for the estimation of power spectra: A method based on time averaging over short, modified periodograms," *IEEE Trans. Audio Electroacoust.*, vol. 15, no. 2, pp. 70–73, 1967. doi:10.1109/TAU.1967.1161901

ISBN: 978-3-95450-250-9 ISSN: 2673-5520 doi:10.18429/JACoW-MEDSI2023-TUPYP054

MECHANICAL DESIGN OF THE BEAM GAS IONISATION (BGI) BEAM PROFILE MONITOR FOR CERN SUPER PROTON SYNCHROTON

M. T. Ramos†, W. Andreazza, P. Bestmann, H. Bursali, N. S. Chritin, W. Devauchelle, A. Harrison, G. Khatri, M. McLean, C. Pasquino, F. Sanda, P. Schwarz, J. W. Storey, R. Veness, W. Vollenberg, C. Vollinger
CERN, Meyrin, Switzerland

Abstract

The Beam Gas Ionisation (BGI) instrument of the Proton Synchrotron (PS), presently installed and operational, has been re-designed for the Super Proton Synchrotron (SPS), the following machine along the Large Hadron Collider (LHC) injector chain at CERN accelerator complex. Using the same detection technology, Timepix3, the SPS-BGI infers the beam profile from the electrons created by the ionisation of rest gas molecules and accelerated onto an imaging detector. This measurement method will allow for continuous, non-destructive beam size measurement in the SPS. In view of the upgrade, the design has been simplified and validated for integration, radio-frequency & impedance, high-voltage, and ultra-high vacuum compatibility.

INTRODUCTION

Accurate time-resolved measurements of the transverse beam profile are required to identify the causes of emittance growth. A new generation of Ionisation Profile Monitors (IPM) based on the detection of ionisation electrons with Hybrid Pixel Detectors (HPD's) installed directly inside the accelerator beam pipe, are currently being designed, produced, installed, and commissioned along the LHC injector chain [1]. Furthermore, in the scope of the High-Luminosity Large Hadron Collider (HL-LHC) upgrade, IPM's based on this technology are under development. Henceforth, the present proceeding will focus on the design phase of the new IPM's for the Super Proton Synchrotron accelerator – which at CERN are called Beam Gas Ionisation (BGI) profile monitors.

The working principle of the BGI for SPS is presented in Fig. 1. Electrons (and ions) are released by the interaction of the beam with residual gas. An electric field of 357 kV/m, formed by a cathode at -30 kV and a grounded anode, accelerates electrons onto an imaging device. The density of detected electrons is a direct measure of the transverse beam profile. The corresponding ions are transported through a hole – called the ion trap – to prevent the production of background electrons. A 0.26 T magnetic field, parallel to the electric field, ensures that the transverse position of the electrons is maintained, mitigating the effects of electron drift caused by electric field imperfections, the ionisation process, and the beam space-charge [1].

† teresa.ramos@cern.ch

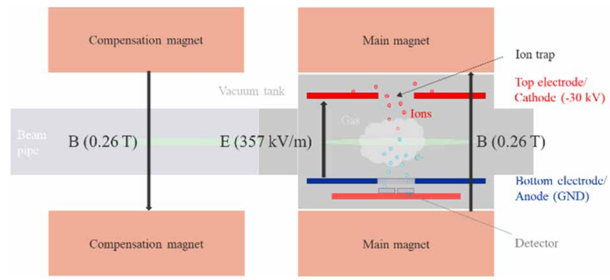

Figure 1: SPS-BGI working principle.

INSTRUMENT OVERVIEW

In the following section, a general overview of the instrument installed inside the vacuum tank will be described. The explanation will focus on the main function of the components listed in Fig. 2. The particular design features that have been implemented to address issues of radio-frequency (RF) & impedance, high-voltage (HV) and ultra-high vacuum (UHV) compatibility requirements will be described in the corresponding sections.

Structural Components

The BGI structural components are those that shape and give rigidity to the arrangement. Among them, these parts stand out: the support arms, the front reinforcement, and the Ultra-High Vacuum ConFlat (UHV CF) rectangular flange, a technology developed at CERN in 2015 for the first prototype of the BGI instrument [2].

Field Cage Design

The BGI field cage is required to provide a homogeneous electric field, protect the hybrid pixel detectors from background electrons, and shield the readout electronics from electromagnetic interference from the beam [3].

As illustrated in Fig. 2B, two parallel electrodes hold a potential difference of 30 kV. The top electrode or cathode, at -30 kV, is mechanically connected and electrically insulated from the support arm with ceramic spacers. To supress the formation of background electrons, a slit – called the ion trap – allows the corresponding ions to pass through and be directed onto the back of the cathode, where secondary (background) electrons will find no path back to the pixel detector. The bottom electrode or anode is grounded by means of fingerstock gaskets. A square pattern provides an opening in the faraday cage to allow the electrons to reach the surface of the chips, while protecting the electron detection system from electromagnetic interference.

ISBN: 978-3-95450-250-9 ISSN: 2673-5520 doi:10.18429/JACoW-MEDSI2023-TUPYP054

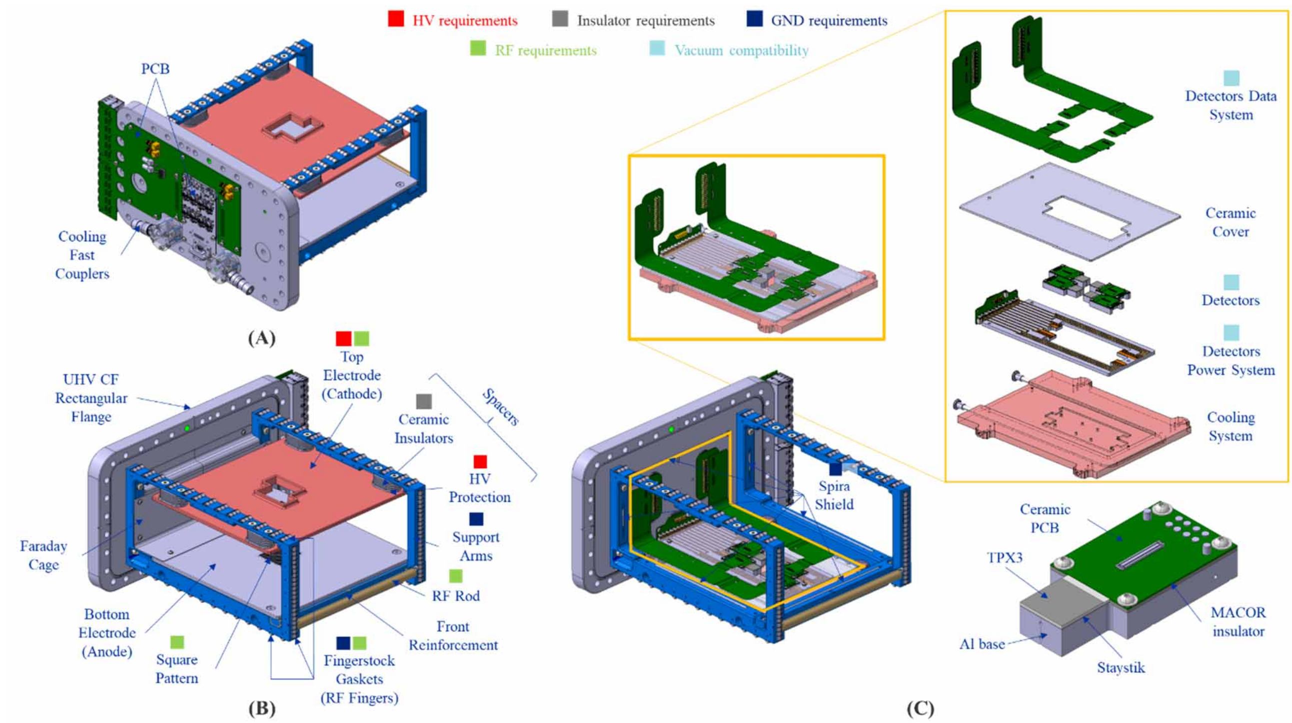

Figure 2: Instrument overview. Component classification based on HV, RF and UHV compatibility requirements.

Detection System

The detection system consists of a set of in-vacuum (Fig. 2C) and air side (Fig. 2A) components.

Detector Modules The ionisation electron detector module consists of a Timepix3 hybrid pixel detector (TPX3) attached to a metal base using a "Staystik 672" thermoplastic adhesive. The aluminium base is the thermal interface between the TPX3 chip and the cooling system. The TPX3 chip is also wire-bonded to a ceramic PCB, which provides the interface for the electrical and power connections. The ceramic PCB itself is directly secured onto the metal base through an electrical insulator. A total of four modules are used to cover a detection width of 54 mm and oriented to optimise the data readout [4].

In-Vacuum Electronics Flexible cables, made with a Liquid Crystal Polymer (LCP) substrate, connect the ceramic PCB to electrical feedthroughs on the vacuum flange. Power is distributed to the detector modules by means of micro-copper bus bars embedded in ceramic insulators.

Air Side Electronics Front-end readout electronics located beneath the instrument are used to transmit the data outputs from the TPX3 chips via radiation hard optical transceivers to back-end readout electronics based on COTS components [3]. The front-end is connected by ethernet cables to a PCB mounted on the air side of the vacuum flange, which connects to the electrical vacuum feedthroughs and hosts the DC/DC voltage regulators for the TPX3 chips.

Cooling System Each TPX3 chip produces ~2 W of heat that must be removed by conduction. The cooling system is based on the circulation of ambient temperature demineralised water in a continuous stainless-steel pipe that is brazed into a copper plate. Each detector module is fixed to the copper plate, which provides the thermal path for the heat, but also defines the positions of the detector modules.

INTEGRATION REQUIREMENTS

In Fig. 3, a section of the instrument in the vacuum tank inside the magnet reveals the narrow margin between the assemblies. The main constraint comes from the aperture of the dipole magnets, which are being reused from an old design.

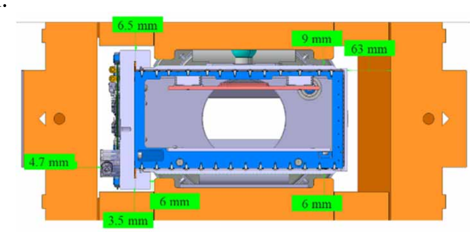

Figure 3: Section view of the final assembly.

The installation procedure has been designed to allow a straightforward maintenance of the equipment, whereby the instrument needs to be accessible and easily disassembled. Only three steps will be required during the installation process. First, the instrument will be integrated inside the vacuum tank with yoke handles. Second, the electrical feedthrough, air side vacuum electronics and cooling system will be connected. Finally, the magnet will be slid into the nominal position and aligned (Fig. 4).

ISBN: 978-3-95450-250-9 ISSN: 2673-5520 doi:10.18429/JACoW-MEDSI2023-TUPYP054

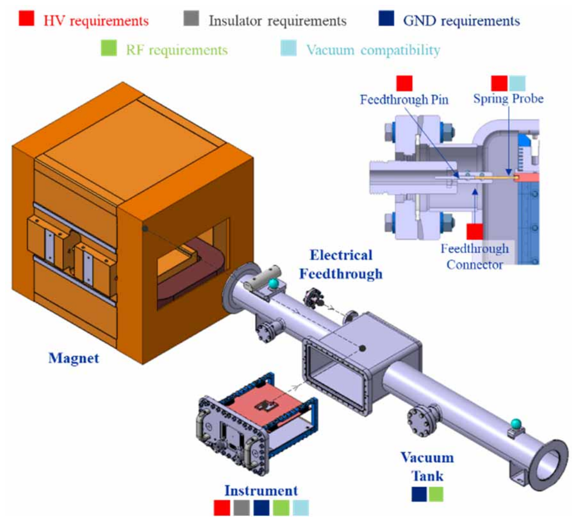

Figure 4: Integration overview. Component classification based on RF, HV and UHV compatibility requirements.

RADIO-FREQUENCY & IMPEDANCE REQUIREMENTS

An impedance study has investigated possible resonances which may occur inside the instrument causing beam induced heating and instabilities during the operation. The longitudinal impedance optimisation of the SPS-BGI has been done by Wakefield and Eigen solvers of CST Particle and Microwave Studios, respectively [5]. Among the implemented design changes:

- The support arms are fully covered by fingerstock gaskets (RF fingers) to provide good RF contact.
- A highly resistively metal coated ceramic cathode has been selected instead of a stainless-steel electrode. In consequence, the cathode is “transparent” to the beam and possible resonances are mitigated.
- A low resistivity coated ceramic rod is placed between the support arms and hidden from the beam to help minimise resonances below 1.5 GHz.

Figure 5 shows the longitudinal impedance reduction after the study, together with SPS 26 GeV and 450 GeV beam spectrums. Pending the final resistivity values after coating, some simulations will have to be repeated to verify these results. To check the simulations outcome, RF tests (wire and probe measurements) will be performed before the installation of the vacuum tank and instrument assemblies [6].

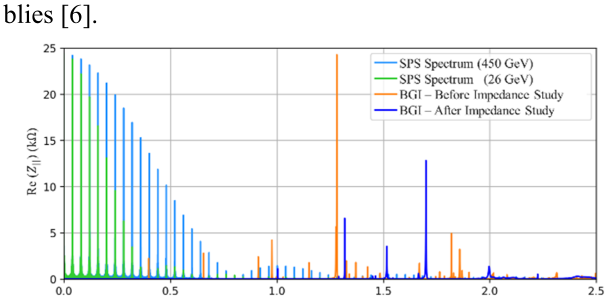

Figure 5: Longitudinal impedance after the optimisation study compared to SPS 26 GeV and 450 GeV beam spectrums.

HIGH-VOLTAGE REQUIREMENTS

All the components of the instrument and vacuum tank assembly can be classified into three groups detailed in Fig. 6. A section view illustrating these categories for the different parts of the assembly is shown in Fig. 7. Components operating at HV (-30 kV) have required particularly careful design to avoid breakdown, for example, by mitigating triple junction effects (HV protection), and ensuring a minimum vacuum gap between HV and GND [7].

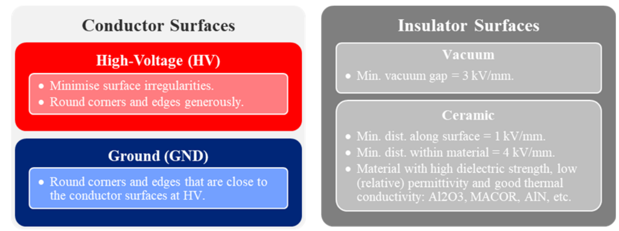

Figure 6: Schematic of HV, Insulator and GND design requirements [7].

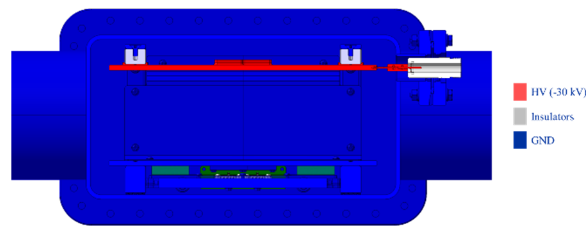

Figure 7: Section view of all the components of the instrument plus vacuum tank assembly classified into HV, Insulator and GND parts.

VACUUM COMPATIBILITY

To provide CERN accelerators and experiments with the required residual gas pressure, vacuum acceptance tests are essential. They include the measurement of leak tightness, level of contamination, and outgassing and inleakage (or virtual leak) rates [8].

The quality of a vacuum system is firstly based on the choice of materials and its mechanical design. For example, metals and ceramics are preferred over polymers, and vented screws are used to avoid virtual leaks. Secondly, the fabrication processes of assemblies or subassemblies exposed to beam vacuum are subjected to different criteria to prevent the above-mentioned problems [9].

CONCLUSION

The design of the BGI profile monitor for the SPS has been successfully adapted from the PS design and integrated within the constraints of an existing dipole magnet. It has also been optimised to simplify assembly & long-term maintenance, and particular focus has been put on minimising longitudinal impedance.

Two instruments (horizontal and vertical) are planned to be installed during 2023/24 winter shutdown. The successful installation and commissioning of these instruments will allow operators and beam physicists to obtain continuous non-destructive measurements of the transverse beam profile in the SPS.

ISBN: 978-3-95450-250-9 ISSN: 2673-5520 doi:10.18429/JACoW-MEDSI2023-TUPYP054

REFERENCES

[1] S. Levasseur *et al.*, "Time-Resolved Transverse Beam Profile Measurements with a Rest Gas Ionisation Profile Monitor Based on Hybrid Pixel Detectors", in *Proc. IPAC'18*, Vancouver, Canada, Apr.-May 2018, pp. 2361-2364. doi:10.18429/JACoW-IPAC2018-WEPAL075

[2] A. Miarnau, G. Schneider and R. Veness, "Developtment and test of a rectaungular CERN ConFlat-type flange", *Vacuum,* vol. 121, pp. 202-206, 2015. doi:10.1016/j.vacuum.2015.08.018

[3] J. W. Storey *et al.*, "Development of an Ionization Profile Monitor Based on a Pixel Detector for the CERN Proton Synchrotron", in *Proc. IBIC'15*, Melbourne, Australia, Sep. 2015, pp. 470-473. doi:10.18429/JACoW-IBIC2015-TUPB059

[4] H. Sandberg, "Development of a Novel Transverse Beam Profile and Emittance Monitor for the CERN Proton Synchrotron", Ph.D. Thesis, Manchester University, 2020.

[5] Dassault Systemes, "CST Studio Suite", 2023. https://www.3ds.com/products-services/simulia/products/cst-studio-suite/.

[6] T. Kroyer, F. Caspers and E. Gaxiola, "Longitudinal and Transverse Wire Measurements for the Evaluation of Impedance Reduction Measures on the MKE Extraction Kickers", CERN, Geneva, Switzerland, Rep. CERN-AB-Note-2007-028, Jul. 2007.

[7] D. Faircloth, "Technological Aspects: High Voltage", CERN, Geneva, Switzerland, pp. 381-419, Apr. 2013. doi:10.5170/CERN-2013-007.381

[8] P. Chiggiato, J. Ferreira and G. Bregliozzi, "Criteria for Vacuum Acceptance Tests", CERN, Geneva, Switzerland, Rep. ACC-V-ES-0001, Aug. 2018.

[9] J. Hansen and G. Vandoni, "Specification for Mechanical Assemblies or Sub-Assemblies Exposed to Beam Vacuum", CERN, Geneva, Switzerland, 2019.

ISBN: 978-3-95450-250-9 ISSN: 2673-5520 doi:10.18429/JACoW-MEDSI2023-TUPYP055

APPLICATION OF QXAFS IN THE MEDIUM-ENERGY X-RAY ABSORPTION SPECTROSCOPY

Y.H. Xia†, G.K. Zhang, F.F. Yang, J.F. Chang, H.Y. Zhang, S.H. Liu, L. Zheng, S.Q. Chu, J. Zhang
|Institute of High Energy Physics, Chinese Academy of Sciences, Beijing, China

Abstract

A quick scanning X-ray absorption fine structure spectroscopy (QXAFS) system has just been installed in 4B7A, a general medium-energy X-ray beamline at Beijing Synchrotron Radiation Facility (BSRF). This system is independent so that the QXAFS system can be employed by other beamlines equipped with a double-crystal monochromator (DCM) to achieve quick scanning and data acquisition. Continuous scanning is available in this system to satisfy the time scale from a few seconds to several minutes, depending on the energy range to be scanned. In this case, our QXAFS system applied to medium-energy X-ray beamlines will broaden the application of time-resolved measurement to a greater range of elements, thereby benefiting a wider user community.

INTRODUCTION

Time-resolved X-ray absorption fine structure (XAFS) measurements play a crucial role in studying in situ dynamic processes. Numerous techniques have already been applied to many synchrotron radiation beamlines to shorten the acquisition time of a XAFS spectrum down to a few seconds or even milliseconds. Among these, quick scanning XAFS is one of the successful modes.

QXAFS maintains a full compatibility with the step-by-step mode, based on the double-crystal monochromator, that is commonly used for general XAFS experiments. In QXAFS, one key difference from traditional XAFS methods is that the crystal monochromator continuously and rapidly rotates, significantly reducing the collection time of the spectrum. More importantly, it is easily compatible with various sample conditions. Therefore, with the development of photon sources and mechanization, QXAFS has the potential to become a primary method in the future.

Up to now, QXAFS has mainly been applied to hard X-ray beamlines, with limited applications in the lower energy range. However, in the medium-energy X-ray regime, there is a pressing need for a time-resolved XAFS experimental technique to investigate dynamic processes occurring within short time frames, especially elements like sulfur that are active in the field of electrochemistry.

In this paper, we will introduce the QXAFS system built at 4B7A, where can conduct medium-energy XAFS experiments at BSRF. The newly equipped QXAFS will be applied in the total electron yield experimental mode, providing a new and reliable experimental platform for various in-situ experiments in the future [1].

BEAMLINE OVERVIEW

The 4B7A beamline, completed in 2005 at BSRF, is dedicated to experiments in the medium-energy X-ray range [2]. BSRF is the first-generation synchrotron radiation facility of China, with its storage ring supporting high-energy physics experiments (Beijing Electron Positron Collider) and synchrotron radiation research. After an upgrade project in 2008, BSRF now operates in 2.5 GeV full-energy injection and top-up mode with 250 mA beam current in dedicated synchrotron radiation mode. Beamline's source is the No. 7 bending magnet in region 4 of storage ring. The bending magnet generates a magnetic field of 0.808 T and has a critical energy of 3358.6 eV. The source size is approximately 1.5 mm (H) × 0.4 mm (V). At the critical energy, the vertical divergence of the source is around 0.28 mrad. The maximum horizontal acceptance angle is 5 mrad, defined by the apertures in the front-end section.

As shown in Fig. 1, this beamline is equipped with a fixed-exit DCM, and usually used crystals are Si(111) and InSb(111). The corresponding energy range is from 1.75 to 3.5 keV while using InSb(111), and from 2.1 to 6.0 keV for Si(111), the useful Bragg angle is about from 19° to 71°, only one pair of crystals can be used at the same time. The energy resolution power (E/ΔE) was higher than 5000 at 3206 eV and 1800 at 5465 eV. The measured flux at the sample is higher than 3×10^{10} photons/s/250 mA in the energy region of 1.75–6.0 keV. The measured beam size at the sample position is about 5 mm (H) × 1.5 mm (V). Finally, due to diffraction forbiddance, Si(111) cannot emit even-order harmonics of X-rays. This will allow the experimental station to obtain high-purity monochromatic light.

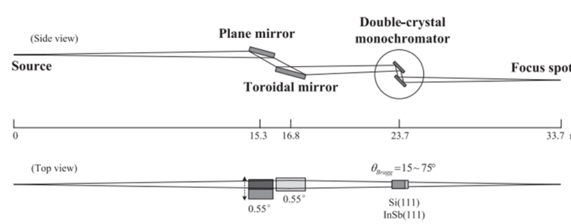

Figure 1: Schematic layout of beamline 4B7A.

QXAFS SYSTEM AND PERFORMANCE

For time-resolved XAFS experiments, QXAFS converts the motion mechanism of the monochromator and improves the data acquisition system. The 4B7A beamline has been equipped with a fixed-exit Si(111) DCM. The angle position is rotated through a stepper motor and recorded by

† xiayh@ihep.ac.cn

ISBN: 978-3-95450-250-9 ISSN: 2673-5520 doi:10.18429/JACoW-MEDSI2023-TUPYP055

an encoder. Ionization chamber (IC) is used to measure the incident X-ray intensity while an ammeter measures the photocurrent signal generated by the incident light excitation in total electron yield mode. By utilizing these two detectors, we aim to determine how fast does the QXAFS system can operate.

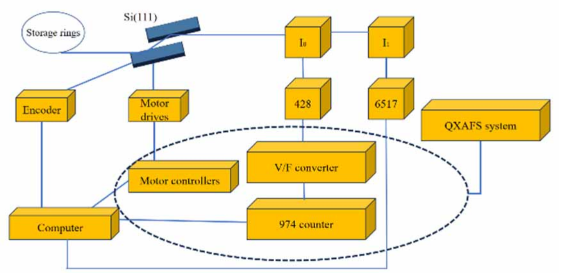

Figure 2: Schematic diagram of QXAFS.

Figure 2 is a schematic diagram of the QXAFS data acquisition process. QXAFS system is an independent system that uses a field programmable gate array (FPGA) module as a key logic unit to control the movement of the Bragg motor and data acquisition, thus it is more convenient and portable compared with previous complex acquisition systems for QXAFS [3]. The original data acquisition process for 4B7A is, the weak current detected by the IC is amplified by a 428 current amplifier to convert it into voltage. Then, the voltage signal is input into the compute through voltage-to-frequency converter (VFC) and analog-to-digital converter (ADC). The electronic signal from I_1 is directly read by a 6517B picoammeter and input into the computer. The computer controls the monochromator rotation and collects the signals from both channels, it then calculates the absorption coefficient. In the QXAFS system, integrating FPGA programming functionality does bring some advantages. By using FPGA programming, fast communication between hardware components and perfect time synchronization can be achieved without waiting for responses from other devices. This can save time and improve system efficiency. Additionally, FPGA offers flexibility and customization, allowing programming and configuration based on specific requirements to meet different application scenarios and experimental needs. In summary, integrating FPGA programming into the QXAFS system can provide better performance and faster data acquisition speed. Considering the signal-to-noise ratio (SNR) of the data and the finite response time of the detectors, the collection time for each data point is set to be greater than 1 ms.

By continuously scanning the motor at maximum speed, the acquisition time can be reduced greatly. The XANES spectrum can be obtained in approximately ten seconds, while the EXAFS spectrum requires about one minute. In practice, the speed limitation of QXAFS mainly comes from the inability of the monochromator to rotate too quickly, as it cannot exceed 0.28 degrees per second.

After setting up the apparatus, we first compared the differences between QXAFS and the conventional step-scan mode by using a potassium sulfate standard sample to ensure the reliability of the system.

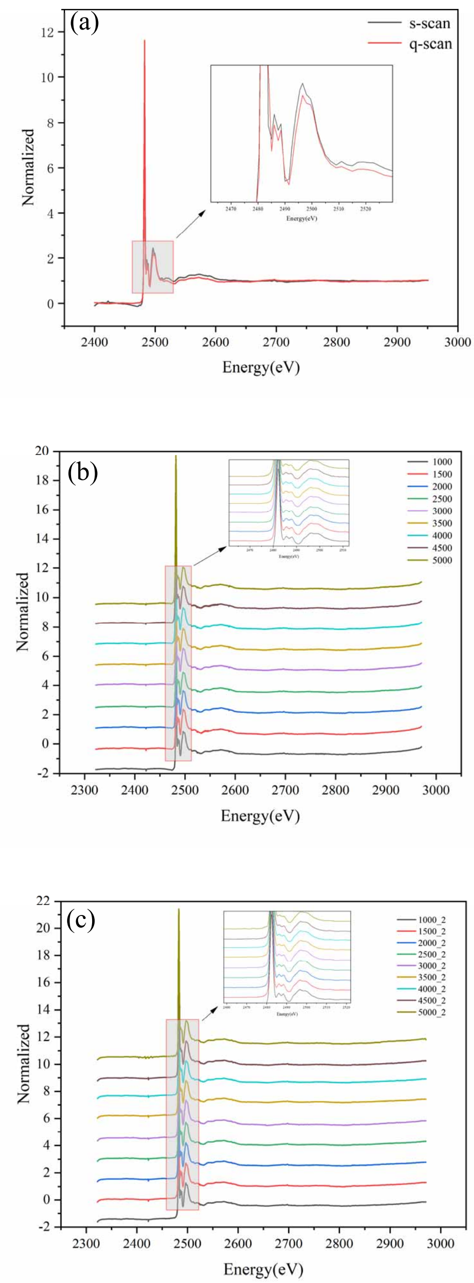

Figure 3: (a) Comparison of s-scan and q-scan for potassium sulfate; absorption spectra obtained from monochromator (b) forward rotation and (c) reverse rotation.

For the potassium sulfate standard sample, the data collection range was 2322~2972 eV at the monochromator speed was 0.17 degrees per second, here the step-scan took over half an hour, while the quick-scan only took 100 seconds. Figure 3 (a) shows that both QXAFS and the conventional mode exhibit similar oscillation features in the near-edge region. Additionally, we analyzed the effect of monochromator speed on spectrum quality. As shown in Fig. 3 (b) and (c), we tested spectra under different pulse speeds

ISBN: 978-3-95450-250-9 ISSN: 2673-5520 doi:10.18429/JACoW-MEDSI2023-TUPYP055

ranging from 1000 pulses per second (pps) to 5000 pulses per second (the monochromator rotates one degree every 18000 pulses) [4]. The obtained spectra represent the positive and negative spectra during one complete rotation of the monochromator. It can be observed that for spectra in the same direction, the near-edge oscillation parts are similar for different speeds, and the amplitude of the oscillations decreases as the speed increases, which means we can adjust the testing speed according to experimental needs with minimal sacrifice.

CONCLUSION

We have developed a QXAFS system at medium-energy X-ray absorption spectroscopy beamline and conducted preliminary performance testing, which can improve the function of XAFS beamlines and extend their capabilities to a wider user community. The results indicate that the spectra obtained from QXAFS are essentially consistent with those from conventional step-scanning, while significantly reducing the acquisition time. This provides a viable approach for elements in the medium-energy range that require time-resolved XAFS experiments. Furthermore, we will continue to develop QXAFS methods related to fluorescence yield mode and transmission mode to expand the application range of this system.

REFERENCES

[1] L. Zheng *et al.*, "Total electron yield mode for XANES measurements in the energy region of 2.1–6.0 keV," *Chin. Phys. C*, vol. 35, no. 2, p. 199, 2011. doi:10.1088/1674-1137/35/2/018

[2] L. Zheng *et al.*, "A new experiment station on beamline 4B7A at Beijing Synchrotron Radiation Facility," *Spectrochim. Acta, Part B*, vol. 101, pp. 1-5, Nov. 2014. doi:10.1016/j.sab.2014.07.006

[3] S. Q. Chu *et al.*, "Time-resolved XAFS measurement using quick-scanning techniques at BSRF," *J. Synchrotron Radiat.*, vol. 24, no. 3, pp. 674-678, May 2017. doi:10.1107/S1600577517005276

[4] B. Ravel and M. Newville, "ATHENA, ARTEMIS, HEPHAESTUS: data analysis for X-ray absorption spectroscopy using IFEFFIT," *J. Synchrotron Radiat.*, vol. 12, pp. 537–541, Jul. 2005. doi:10.1107/S0909049505012719

ISBN: 978-3-95450-250-9 ISSN: 2673-5520 doi:10.18429/JACoW-MEDSI2023-WEOAM02

A VACUUM ASPIRATED CRYO COOLING SYSTEM (VACCS)

G. Duller, B. Olafsson, M. Nagy, Diamond Light Source, Didcot, United Kingdom
D. Magrath*, Brompton Bicycles, Greenford, United Kingdom

Abstract

The use of liquid nitrogen for cooling of synchrotron equipment is widespread. The cryogenic sub-coolers commonly employed come with some significant drawbacks such as cost, complexity, stiffness of distribution lines, and vibration induced by pressure variations. The typical sub-cooler is capable of handling 2 to 3 kW of absorbed power whilst many optics require no more than 50 to 150 W of cooling. We present a Vacuum Aspirated Cryo-cooling System (VACCS) which overcomes many of these disadvantages and which allows cryo-cooling to be implemented more widely. The VACCS system uses a vacuum, generated with no moving parts, to draw LN2 through a heat exchanger. Thus the system does not have to be pressure rated. We describe our designs for highly flexible distribution lines. A simple control system offers variable temperature at the heat exchanger by varying the flow rate of LN2. A system is installed at Diamond which allows the independent control of three zones. A test rig has demonstrated cooling capacity in excess of 100 W for a monochromator crystal assembly and controlled temperatures −194 to −120 °C.

INTRODUCTION

Many synchrotron optics require some sort of cooling. Cryogenic cooling is often an attractive choice due to, for instance, the enhanced properties of silicon and copper which can be accessed. Equally, scientific goals commonly demand that sample environments are held at cryogenic temperatures (77 K and above).

As a result closed-cycle cryogenic cooling systems are frequently employed where the high cost of implementation can be warranted. Unfortunately these systems come with some significant drawbacks, including high capital and running costs, take up a substantial footprint, have a tendency to excite vibrations due to pressure fluctuations, and require high stiffness distribution lines. These sub-coolers circulate liquid nitrogen (LN2) at elevated pressures to increase the boiling point of the fluid, thus allowing the coolant to extract power from the heat exchanger without inducing local boiling. Commonly rated at 5 to 10 bar, these pressures demand that all distribution lines are constructed to withstand these pressures whilst having minimal thermal losses, and vacuum vessels equipped with these systems require safety assessment and protection (burst disc or similar). These sub-cooler systems are typically rated at 2 to 3 kW cooling power, significantly in excess of the requirements of a typical beamline. In our tests the majority of monochromators require cooling of less than 100 W.

* daniel.magrath@brompton.co.uk

We have developed a novel cryocooling system, the Vacuum Aspirated Cryo-Cooling System (VACCS), with the goal of addressing many of the issues associated with sub-cooler systems and have demonstrated its cooling ability up to 100 W. This has been implemented at the Diamond Light Source (DLS) beamline, VMXm, to control three independent end-station zones and will shortly be implemented in a monochromator.

DESIGN

Principles of Operation

The VACCS system is designed with a focus on simplicity and cost-effectiveness, aiming to cool assemblies down to cryogenic temperatures using basic components. As the name implies, flow of LN2 is induced by generating partial vacuum at the exhaust. This is achieved by using an ejector pump and the basic function of it is shown in Fig. 1, where suction is generated by a motive fluid (pressurised air in our case), entering from the left side. The converging/diverging nozzle increases the velocity of the motive fluid and the kinetic energy is balanced by a drop in pressure, thereby generating suction at the bottom inlet [1].

A schematic of the VACCS system is shown in Fig. 2 which illustrates its principle components. The dewar supplying the LN2 to the system is vented to atmosphere. By placing a temperature sensor on the heat exchanger (device to be cooled), flow of LN2 can be adjusted via a PID controller by varying the pressure of the compressed air entering the ejector pump to achieve a desired temperature. Alternatively, the flowmeter in front if the ejector pump can used as a set point for control.

Taking advantage of the latent heat of vaporisation to cool the device, most of the LN2 is expected to have transformed to gaseous form (GN2) as it exits the heat exchanger. The purpose of having an exhaust heater after the heat exchanger is to heat the nitrogen to ambient temperature, allowing for uninsulated pipework to be used beyond this point, and thereby increasing the system's flexibility and ease of installation. Additionally, a standard calibrated flowmeter for air can be used, making it more cost-effective.

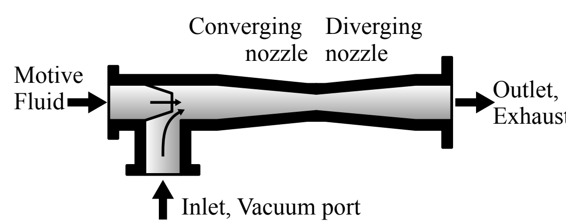

Figure 1: An illustration of an ejector pump (Figure based on a diagram from the product sheet in [2]).

ISBN: 978-3-95450-250-9 ISSN: 2673-5520 doi:10.18429/JACoW-MEDSI2023-WEOAM02

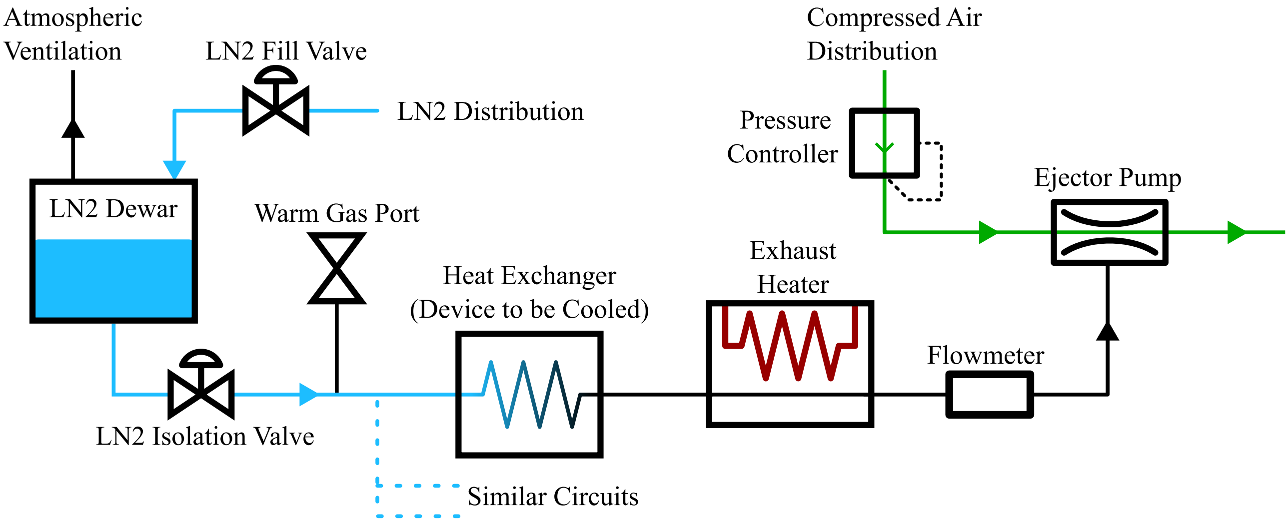

Figure 2: A diagram of the VACCS system. Liquid nitrogen is represented with blue lines, gaseous nitrogen with black lines, and air with green lines.

Flexible LN2 Distribution Lines

Having the dewar vented is one of the system's standout advantages. No specific pressure rating downstream of the LN2 fill valve is required. Rigid lines with flexible joints have been designed for this system and are shown in Fig. 3. In this design, edge-welded bellows are used as joints for both internal and external pipework, resulting in a highly flexible joint. A gimbal with limits was designed to prevent the joints from exceeding their maximum bending angle, which can also be used to restrict the motion of the joint if needed.

VACCS ON VMXM

As previously mentioned, VACCS has already been successfully implemented on VMXm, a beamline at DLS, on three individually controlled zones, all interconnected to in vacuo sample cooling. The three zones are as follows:

- **Sample hotel** A closed vessel above the goniometer that stores up to 5 samples.
- **Anti-contaminator** Aimed to be the coldest object inside the sample environment.
- **Sample gripper** A vertical arm that transfers a selected sample from the hotel and places it on the goniometer.

The control system for the three zones are depicted in Fig. 4. The compressed air distribution enters through the blue pneumatic tubes on the left side of the figure and is then subdivided into three distinct paths to three separate pressure controllers, one for each zone [3]. Each of these paths corresponds to a specific zone and is indicated by varying colors of pneumatic tubing: yellow for the sample hotel, green for the anti-contaminator, and red for the sample gripper. Gaseous nitrogen, emerging from the heater, enters from the right side of the diagram, passing through a flowmeter before continuing on to the ejector pump [2,4].

The cool down process from room temperature for the sample gripper is illustrated in Fig. 5, where the gripper's temperature is depicted in blue on the left y-axis and the nitrogen flow rate is shown in orange on the right y-axis. It

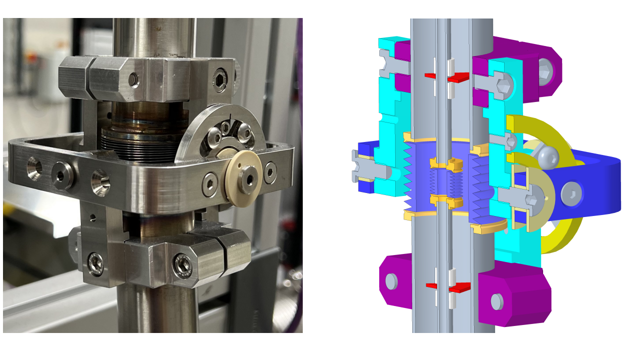

(a) (b)

Figure 3: Joint of a flexible LN2 distribution line. (a) a picture of a joint on VMXm, (b) a section view of the CAD model.

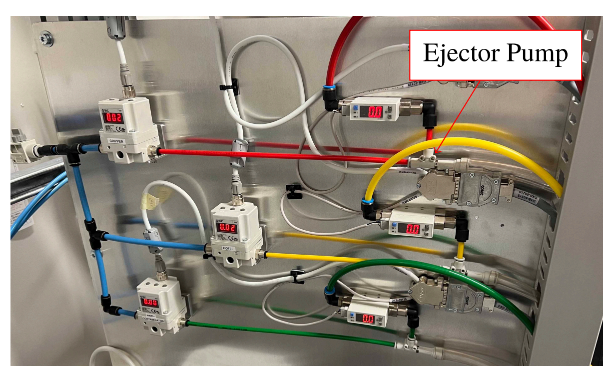

Figure 4: The pneumatic control system for the three zones on VMXm. Sample gripper zone (red tubing) on top, the sample hotel zone (yellow tubing) in the middle, and the anti-contaminator zone (green tubing) at the bottom.

ISBN: 978-3-95450-250-9 ISSN: 2673-5520 doi:10.18429/JACoW-MEDSI2023-WEOAM02

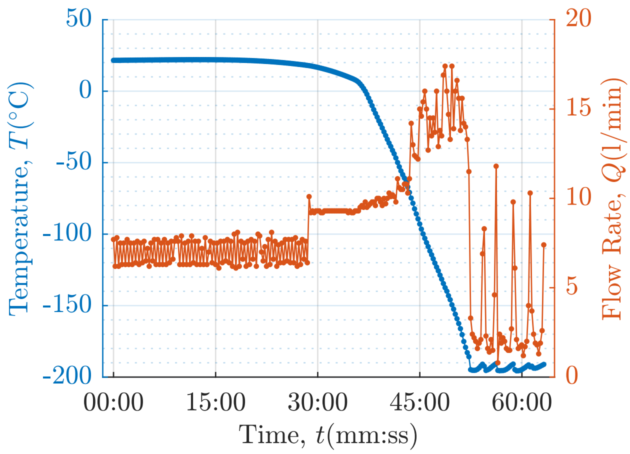

Figure 5: Cool down of the sample gripper. The left axis depicts the temperature of the gripper, while the right axis depicts the flow rate of GN2.

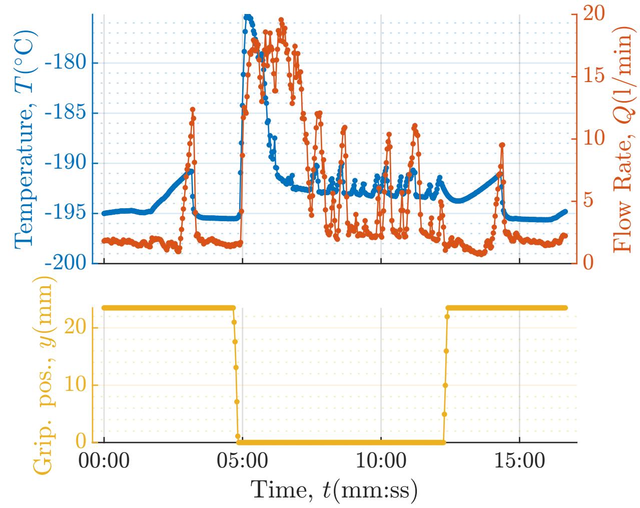

Figure 6: Cooling performance of the sample gripper. The upper plot depicts sample gripper and flow rate of GN2, on the left and right axis respectively, while the lower plot depicts the vertical position of the sample gripper.

takes the gripper approximately 50 min to reach cryogenic temperatures and the flow rate of GN2 peaks at 17 l/min. It should be noted that liquid-to-gas expansion ratio of nitrogen is approximately 1:700 at 20 °C, making the LN2 usage only about 25 ml/min [5]. As it stabilises, the flow rate of GN2 oscillates between 2 to 10 l/min keeping an average temperature of −193.6 °C with a standard deviation of 1.3 °C.

The Sample Gripper is intermittently used to re-cool samples, and hence experiences variations in heat loads. The moment the sample is positioned on the goniometer, it starts warming up due to conduction. Typically, within 7 min the temperature of the sample rises to approximately −140 °C and needs to be re-cooled. Figure 6 depicts results from the sample gripper's interaction with a sample as it is lowered to cool the sample back to cryogenic temperatures. The lower plot on Fig. 6 shows the gripper's position, starting 23.5 mm above the sample and then lowered to 0 mm when it engages with the sample on the goniometer, and then subsequently released and raised back to 23.5 mm. Meanwhile, the upper plot displays the gripper's temperature and flow rate, mirroring the format seen in Fig. 5. These plots effectively illustrate the system's rapid response to temperature changes in the gripper. As a result, prior to lowering the gripper, it maintains a temperature of −195 °C and as it grips the sample it increases to −175 °C and the control system increases the flow to reduce the temperature of the sample and within a mere 3 min it has descended to −193 °C at which point it reduces the flow again.

MONOCHROMATOR TEST RIG

The previous section demonstrated the applicability of the system for sample environments. To assess the potential extension of the VACCS system to cool monochromators with relatively modest heat loads, an offline monochromator test rig was designed and manufactured. The designed test rig is illustrated in Fig. 7.

The crystal assembly is presented in Fig. 8a, it consisting of a single dummy crystal block (made from aluminium), dimensions 30 (W) × 100 (L) × 70 (T) mm and two heat exchangers mounted on each side of the block with a 0.5 mm indium sheet in between. A more comprehensive depiction of the assembly is illustrated in Fig. 8b which shows an exploded view of the CAD model.

In order to replicate the heat absorbed from the beam, two Lake Shore cartridge heaters (HTR-50) [6] were mounted inside the dummy crystal. These heaters are both compatible with UHV and cryogenic conditions. To minimize the thermal resistance between the components, thermal grease, Apiezon N, was applied between the dummy crystal and the heaters [7]. Two PT100 temperature sensors were placed on the dummy crystal. Both of them were attached on the end of the crystal, where one was clamped and the other glued. Based on our experience, the glued sensor provides more

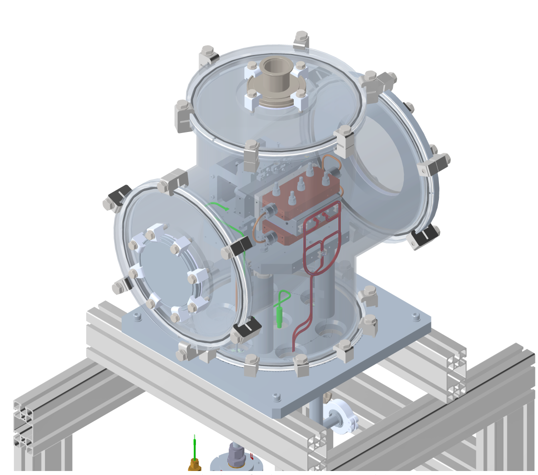

Figure 7: A CAD model of the monochromator test rig for validating the application of the VACCS system.

ISBN: 978-3-95450-250-9 ISSN: 2673-5520 doi:10.18429/JACoW-MEDSI2023-WEOAM02

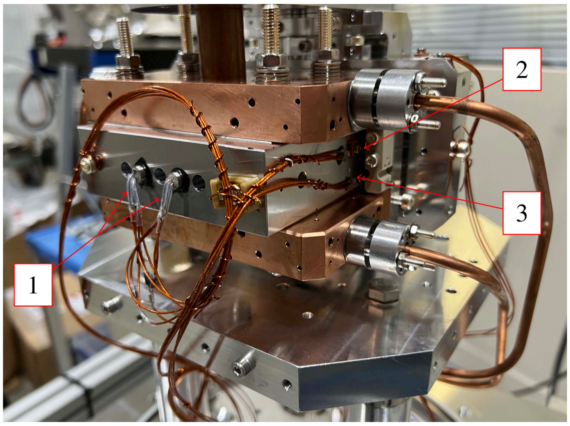

(a)

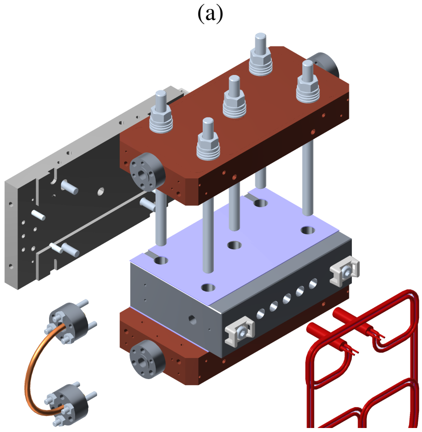

(b)

Figure 8: Dummy crystal assembly on the monochromator test rig. (a) A picture of the assembly (1) heaters, (2) clamped PT100, (3) glued PT100, and (b) an exploded view of the CAD model.

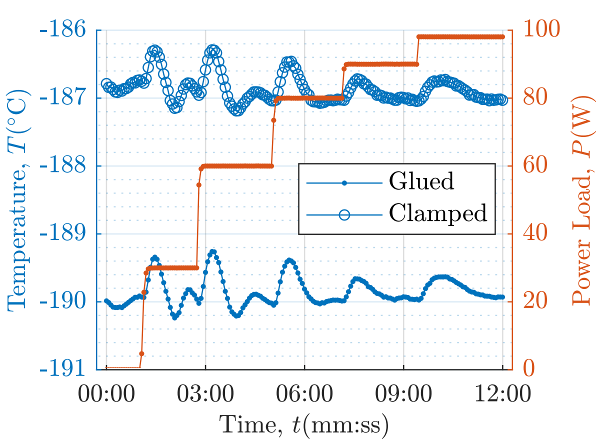

Figure 9: Power load variation on the test rig. The glued PT100 is depicted with pointed markers and the clamped PT100 circle markers.

precise results, but the clamped one has been included as a reference. To measure the power applied to the dummy crystal, the voltage and current were data-logged.

Figure 9 shows the results of varying the power load on the dummy crystal. The figure shows the temperature measured on the dummy crystal represented on the left y-axis and the power load applied to the heaters on the right y-axis. In this case, the temperature was set to −190 °C and the power load on the heaters was incrementally increased to 100 W.

As anticipated, a minor discrepancy is evident between the two PT100 readings, but both readings exhibit remarkable stability. Throughout this test, the glued PT100 yielded an average temperature of −189.9 °C with a standard deviation of 0.2 °C, while the clamped yielded an average of −186.9 °C with a corresponding standard deviation of 0.2 °C.

CONCLUSION

This paper has introduced an innovative and cost-effective approach to cryogenic cooling by using basic components and does not require pressure rated distribution lines. The system has been successfully implemented on an existing beamline at DLS to facilitate sample environment cooling. A thorough performance evaluation of the system has been carried out.

Moreover, the potential suitability for cooling a monochromator has been investigated on a dedicated test rig. Notably, the results were highly promising demonstrating to consistently maintain the target temperature, exhibiting merely 0.2 °C of standard deviation when subjected to a varying heat load of up to 100 W.

REFERENCES

[1] Wikipedia, `https://en.wikipedia.org/wiki/Venturi_effect`

[2] SMC Pneumatics, `https://www.smc.eu/en-gb/products/zh-a~138195~nav?productId=138197`

[3] SMC Pneumatics, `https://www.smcpneumatics.com/ITV1030-31F1N3.html`

[4] SMC Pneumatics, `https://www.smcpneumatics.com/PFM725-F01-F.html`

[5] Wikipedia, `https://en.wikipedia.org/wiki/Liquid_nitrogen`

[6] Lake Shore Cryotronics, `https://www.lakeshore.com/products/categories/specification/temperature-products/cryogenic-accessories/miscellaneous-cryogenic-accessories`

[7] Apiezon, `https://apiezon.com/products/vacuum-greases/apiezon-n-grease/`

ISBN: 978-3-95450-250-9 ISSN: 2673-5520 doi:10.18429/JACoW-MEDSI2023-WEOAM03

MAGNETIC LEVITATION ON A BUDGET: A STUDENT DISCOUNT

J. H. Kelly, M. Hurlstone, S. Farrelly, D. Crivelli
Diamond Light Source, Harwell Science & Innovation Campus, Harwell, UK

Abstract

The successful mechatronics development i. e. modelling, simulation, design, build and test of a magnetic levitation stage at the Diamond Light Source is presented. The concept was to use a low control bandwidth across the 6 degree of freedom MIMO system, to provide both an alignment stage and vibration isolation. The project simultaneously upskilled staff and developed a proof-of-concept system demonstrator at a low cost. The final motion stage was constructed for a component cost of less than £15,000.

INTRODUCTION

The Diamond Light Source (DLS) is the UK national synchrotron facility. Numerous beamlines focus X-ray beams to less than 100 nm and hence require relative sample & optics stability to be a fraction of this. The new flagship beamline I17 to be built as part of the Diamond II upgrade has extreme stability requirements yet to be achieved on existing beamlines. The sample position jitter specification is ± 0.5 nm Peak – Peak, 1-1000 Hz relative to the beam. To even come close to this performance significant mechatronics modelling, simulation, testing will be required. A component of this research and development has been performed by Year-in-Industry engineering students. The primary goal of their project was to deliver the knowledge & processes required to design a magnetically levitating motion stage (maglev), as this had never been done before at DLS. This paper details the significant achievements of two students to model, simulate, design, build and test a magnetic levitation stage suitable for synchrotron endstation vibration isolation.

The benefit of an active maglev solution as compared to a passive isolator is that the amplification at resonance can be eliminated, the system stiffness and damping adjusted in software and the isolation also provides a compact parallel kinematic 6 degree of freedom (DOF) system which may be stepped or rotated about any arbitrary co-ordinate system. The downside is the inherent mechanical system instability and complexity.

REQUIREMENTS

The top-level requirements defined for the project were:

- Load capacity > 10 kg
- Low profile ~ 0.5 × 0.5 × 0.2 m maximum envelope
- Vibration transmission < 10% from 10 – 500 Hz
- Provide 6 DOF motorised alignment
- Position Stability ± 500 nm, 1-1000 Hz Peak-Peak
- Angular Stability ± 500 nrad, 1-1000 Hz Peak-Peak
- Travel Range XYZ ± 1 mm, Pitch/Roll/Yaw ± 1 mrad

PROJECT PROCESS

A clear Mechatronics workflow was followed; requirements specification, hand calculations, literature review, concept simulation, design iteration, final system simulation including the motion control software and hardware, Dynamic Error Budget, build, commission, test, validate & update the original model to improve the process.

SYSTEM DESIGN

It was decided to use commercial voice coils (Motion Control Products AVA2-20-0.5) with sufficient clearance to meet the desired motion requirements rather than manufacturing custom coils to save resources. The flat rather than cylindrical design enabled the co-location of the position sensor. The design is deliberately symmetric with the centre of mass located at the geometric centre. The nominal required control bandwidth was calculated to be ~10 Hz via hand calculations [1]. The bracketry was designed to have a 1st mode above 100 Hz i.e. 10 times the fundamental rather than the usual 3-5 time rule-of-thumb so a higher bandwidth could be tested.

GRAVITY COMPENSATOR

Most magnetically levitating motion stages employ a gravity compensator to minimise the power required to resist gravity [2–4].

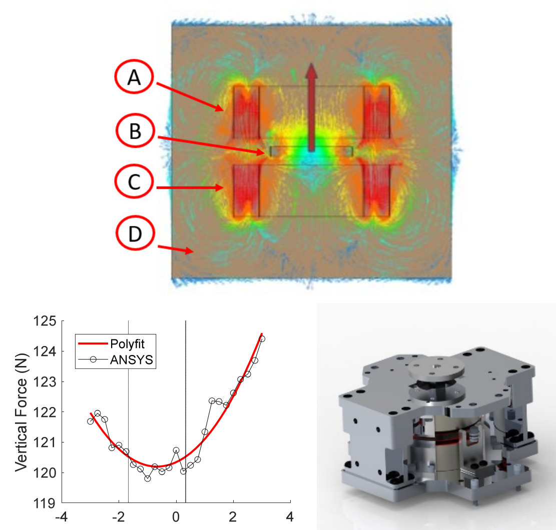

Figure 1: ANSYS Magnetostatic simulation of permanent magnet gravity compensator magnetic field vectors (Top) A) Upper fixed ring magnet, B) Floating magnet, C) Lower fixed magnet, D) Simulation space. Predicted vertical force variation with vertical translation (bottom left) and gravity compensator 3D design (bottom right).

ISBN: 978-3-95450-250-9 ISSN: 2673-5520 doi:10.18429/JACoW-MEDSI2023-WEOAM03

This is critical for vacuum applications to prevent overheating in the absence of convection. The ideal gravity compensator provides a constant force equal to the floating weight independent of position i.e. not a spring following Hook's Law. A negative stiffness spring could be used but as the main goal was to physically isolate vibration a non-contact permanent magnet compensator was designed. Although the magnetic attractive force is non-linear it is possible to optimise the geometry of fixed and moving magnets to provide an approximately constant force region with minimal off axis parasitic forces. Figure 1 gives a section view through a magnetostatic simulation from ANSYS. The large red ring magnets were fixed to the base and the smaller central ring magnet was connected to the levitating plate.

SENSOR & ELECTRONICS

One of the challenges with a parallel kinematic closed-loop system is sensor selection. The ideal sensors only measure a single DOF with no cross coupling with the other 5. Conventional linear encoders would not operate over the motion range. Capacitance sensors, Eddy current sensors and interferometers were all too expensive, in fact almost any commercial sensor was too expensive, so the decision was made to build sensors in-house. A retro-reflective phototransistor (OSRAM SFH 9206) had been used previously for a very similar application[5]. The sensor exhibits 2 approximately linear regions. The shallower gradient and hence lower resolution negative slope was used due to the desired motion range. A significant benefit of this sensor was its compact size. The whole unit was approximately 4 × 3 × 2 mm. This enabled the sensor to be integrated within the voice coil to give truly co-located feedback. In theory this makes the single axis control inherently stable [1].

A mount within the voice coil, amplification and low pass filter printed circuit boards were designed using Cadence®. The sensor was fully characterised during the early stages of the project to measure the current vs. distance output relative to different target surfaces. The voltage to distance curve was approximated as a straight line for simplicity. The axis cross-coupling was measured to be nil in the translation axes and 0.001 mm/mrad in the 2 non-normal rotations. It was decided that this was decoupled enough to not affect the performance.

DYNAMIC ERROR BUDGET

One of the fundamental tenets of Mechatronics is the optimisation of the system via simulation prior to manufacture. This significantly reduces project risk, reduces design iteration time and system commissioning time along with potentially delivering a superior product. The process followed was; to create a 3D model using the CREO® design software, perform a modal analysis in ANSYS, extract a reduced order model (ROM) state space matrix and import the ROM into MathWorks® Simulink®. The Simulink® model was then used for time domain simulations using measured disturbances. A dynamic error budget [6] was performed by extracting the frequency dependent disturbance transfer functions from Simulink®. The square of the transfer functions were multiplied by the disturbance power spectral density (PSD). The dynamic error budget (DEB) given in Figure 2 not only shows the relative effects of disturbances on the system it also predicts the RMS stability via the square-root of the total Cumulative PSD.

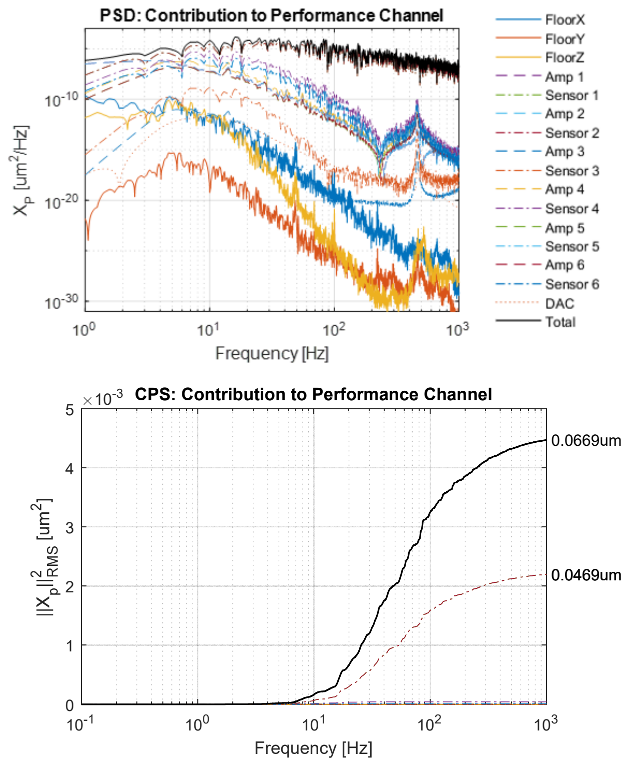

Figure 2: Maglev stage x direction PSD disturbance vs. frequency (top) and Cumulative PSD with RMS stability prediction (bottom).

It may be observed from the DEB that the sensor noise is by many orders of magnitude the dominant predicted disturbance limiting the position stability, which is not surprising when they cost about a Euro. The key data was that the predicted position jitter/error in the x direction was 70 nm RMS which is well within the required specification.

CO-ORDINATE TRANSFORMATIONS

A parallel kinematic system such as a 6 DOF maglev stage has intrinsically coupled actuators i.e. an open loop step applied to one actuator will be observed by the others. This means that classical single input single output (SISO) control can't be applied individually to each actuator. The method employed on this multiple input multiple output (MIMO) system was to create decoupling co-ordinate transformation matrices from the 6 actuator frames to the global reference frame located at the centre of mass. Once in the global reference frame, the 6 DOF decoupled axes used SISO PID control. The demand signals were then transformed back into the actuator frames to be fed to the power amplifiers.

MOTION CONTROL & SYSTEM IDENTIFICATION

The dSPACE control platform was used to perform the motion control. This has the significant benefit that the simulated control functions could be directly compiled into C code and uploaded to the dSPACE. This coupled with accurate system modelling meant that no commissioning of the stage control parameters was required to make the system fly. The simulated plant was close enough to the real plant that the simulated control was functional and stable with the actual system. Once the system was operational system identification was performed in order to compare simulation with reality. The diagonal direct terms e.g. x demand to x position were quite similar however there was far more axis cross-coupling in reality than the perfect simulation. This is likely due to geometric position and alignment errors, sensor non-linearities, imperfect actuators and model imperfections. Figure 3 shows the final system with the motion control hardware and the test accelerometers mounted.

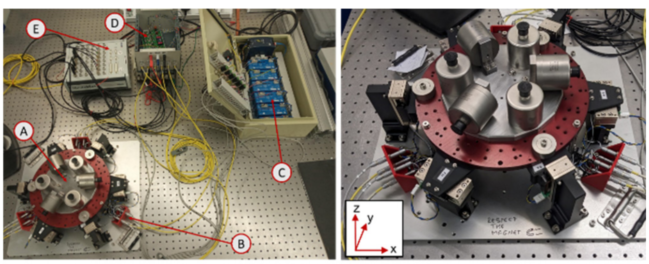

Figure 3: Operational maglev system, A) Maglev stage, B) Cable Interface, C) Trust Automation Amplifiers, D) Sensor Signal Conditioning, E) dSPACE Controller.

TEST RESULTS

The predicted x direction position jitter was 70 nm RMS Figure 4 shows the measured jitter was 40 nm RMS.

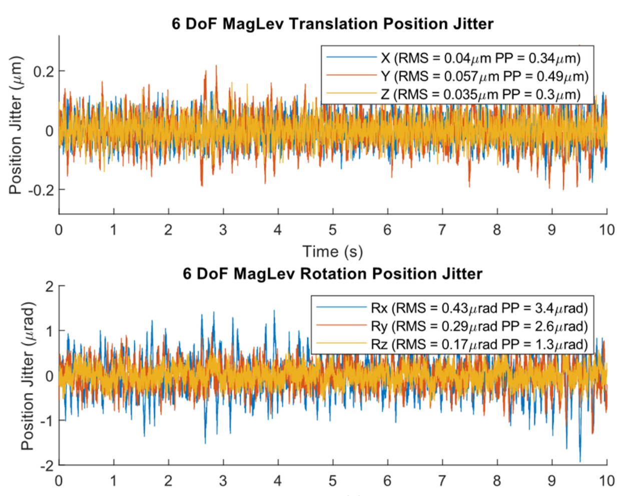

Figure 4: Position jitter measured by the internal stage sensors in translation (top) and in rotations (bottom).

Both the linear and angular measured stability data are close to the simulated values however only the translation data meet the project requirements. The best angular stability was Rz at 170 nrad RMS.

The system was tested on an optical table with a strong fundamental resonance at 12 Hz which is clear in the measured accelerometer data given in Figure 5 . The closed loop stage is effectively tracking the table motion but decouples above 15 Hz to provide vibration isolation above this. The upper plot is for the maglev stage floating on the table with the background disturbances. In this case the sensor noise can be seen to set a lower signal limit. The lower plot is for the same configuration as the first but with the table impacted to increase the vibration signal to make it the dominant disturbance. The vibration is isolated by 4 orders of magnitude at 250 Hz. This clearly demonstrates the potential performance if the sensors were upgraded.

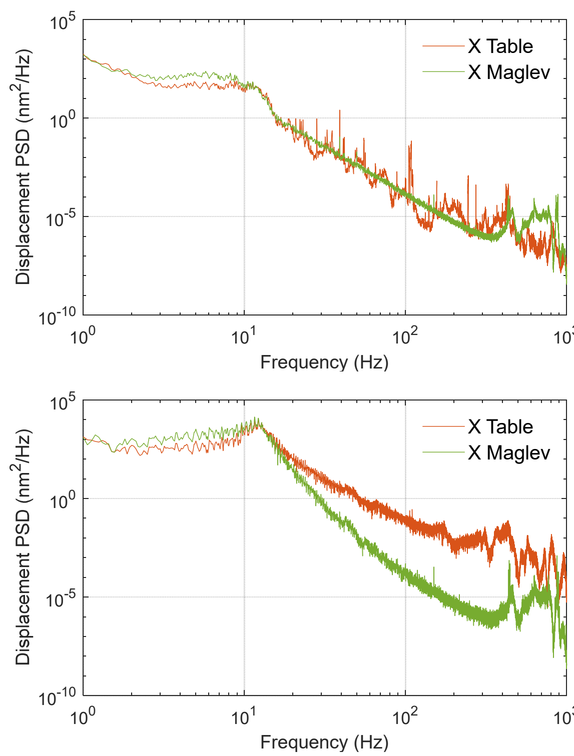

Figure 5: Integrated accelerometer signal to give horizontal stage and table displacement PSD, with background vibration (top), with table impact to improve signal to noise ratio (bottom).

CONCLUSION

A magnetically levitating stage was successfully designed, simulated, built and tested. The motion control parameters may be adjusted to balance position stability, tracking error and vibration isolation. The performance limiting factor was the in-house built position sensors which gave a position jitter around ± 60 nm RMS with a control bandwidth of 10 Hz. It would be easy to upgrade the sensors to interferometers to give even better performance suitable for new beamline applications.

ISBN: 978-3-95450-250-9 ISSN: 2673-5520 doi:10.18429/JACoW-MEDSI2023-WEOAM03

REFERENCES

[1] R. Munnig Schmidt, G. Schitter, A. Rankers, J. Van Eijk, *The Design of High Performance Mechatronics - 3rd Revised Edition*, IOS Press, Feb. 2020.

[2] S. A. J. Hol, "Design and optimization of a magnetic gravity compensator", Phd Thesis 1, Technische Universiteit Eindhoven. doi:10.6100/IR574485

[3] R. Deng, "Integrated 6-DoF Lorentz Actuator with Gravity Compensation for Vibration Isolation in In-Line Surface Metrology", doctorial thesis, TU Delft, Sep. 2017. doi:10.4233/uuid:e8590c25-5cfc-43a9-989e-e98b1ea9a8d8

[4] A. C. P. De Klerk, G. Z. Angelis, and J. Van Eijk, "Design of a next generation 6 DoF stage for scanning application in vacuum with nanometer accuracy and mGauss magnetic stray field", https://www.researchgate.net/publication/240624066

[5] A. M. Mulder, "Department of Precision and Microsystems Engineering Design of a 6-DoF Miniature Maglev Positioning Stage for Application in Haptic Micromanipulation", master thesis, TU Delft, Jul. 2011.

[6] L. Jabben, "Mechatronic design of a magnetically suspended rotating platform", doctorial thesis, TU Delft, Dec. 2007.

12th Int. Conf. Mech. Eng. Design Synchrotron Radiat. Equip. Instrum. MEDSI2023, Beijing, China JACoW Publishing
ISBN: 978-3-95450-250-9 ISSN: 2673-5520 doi:10.18429/JACoW-MEDSI2023-WEOAM04

DEVELOPMENT OF LOW-FREQUENCY SUPERCONDUCTING CAVITIES FOR HIGH ENERGY PHOTON SOURCE

X.Y. Zhang[1]*, J. Dai, L. Guo[1], Q. Ma[1], F.B. Meng, P. Zhang[1], H.J. Zheng[1]
Institute of High Energy Physics (IHEP), Chinese Academy of Sciences (CAS), Beijing, China
[1]also at University of Chinese Academy of Sciences, Beijing, China

Abstract

A low-frequency superconducting cavity is one of the most critical devices in the High Energy Photon Source (HEPS), a 6 GeV diffraction-limited synchrotron light source under construction in Beijing. A higher-order-mode (HOM) damped 166.6 MHz β=1 quarter-wave superconducting cavity, first of its kind in the world, has been designed by the Institute of High Energy Physics. Compact structure, excellent electromagnetic and mechanical properties and manufacturability were realized. An enlarged beam pipe was proposed allowing HOMs to propagate out of the cavity and be subsequently damped by a toroidal beamline HOM absorber at room temperature. Mounted with a forward power coupler, a tuner, two thermal break beam tubes, a collimating taper transition, two gate valves and some shielded bellows, the jacketed cavity was then assembled into a cryomodule. Two cryomodules were later required to fit into HEPS straight sections with a length limitation of 6 meters, which posed a significant challenge for the design of the cavity string. The success of the horizontal test also verifies the design of the cavity string. This article presents the design, fabrication, post-processing, system integration, and cryogenic tests of the first HOM-damped compact 166.6 MHz superconducting cavity module.

INTRODUCTION

High energy photon source (HEPS) is a diffraction-limited synchrotron light source designed by the Institute of High Energy Physics [1]. It is a 6 GeV kilometer-scale light source. The construction of HEPS began at Beijing in Jun 2019 and is expected to be completed in 2025. Five 166.6 MHz superconducting rf (srf) cavities will be installed in the storage ring as main accelerating cavities. The frequency of 166 MHz was chosen to implement a novel beam injection scheme proposed by physics [2], while compromising with the kicker technology [3]. The main parameters of HEPS are listed in Table 1.

Table 1: Main Parameters of the HEPS [4]

Parameter	Value	Unit
Circumference	1360.4	m
Beam energy	6	GeV
Beam current	200	mA
Total energy loss per turn	4.14	MeV
Total power loss to radiation	828	kW
Forward RF frequency	166.6	MHz
Total RF voltage (main)	5.16	MV
3^{rd} harmonic RF frequency	499.8	MHz
Total RF voltage (HC)	0.91	MV
Transmitter power per rf station	260	kW

A proof-of-principle (PoP) cavity has been successfully developed in HEPS-Test Facility (HEPS-TF) project [5, 6]. A HOM-damped 166.6 MHz β=1 quarter-wave superconducting cavity was proposed for HEPS storage ring [4, 7]. Mounted with a forward power coupler (FPC), a tuner, two thermal break beam tubes, a HOM absorber, a collimating taper transition, two gate valves and some shielded bellows, the jacketed cavity was then assembled into a cryomodule. In this paper, the design, fabrication, post-processing, system integration, and cryogenic tests of the first HOM-damped 166.6 MHz cavity module were introduced in detail.

* Email: zhangxinying@ihep.ac.cn

DESIGN OF THE CAVITY STRING

Layout of the Cavity String

A total of four layouts for the cavity string were analyzed and finally layout1 was chosen as the baseline scheme [8], as shown in Fig. 1. The total loss factor of this setup was calculated to be 5.2 V/pC. Synchrotron light can be nicely collimated, producing sufficient shadow for downstream components.

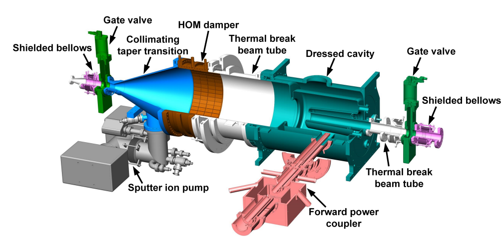

Figure 1: The 166 MHz cavity string.

Component Design of Cavity String

The Jacketed Cavity The jacketed 166 MHz cavity was fabricated by Beijing HE-Racing Technology Co., Ltd. There are 44 individual components. Grade-2 titanium was chosen to join the jacket and the NbTi flanges by using electron beam welding. The inlet flange was located at the bottom of the vessel and the feed pipe with a diameter of 8 mm guides the liquid helium into the LHe vessel. The outlet of the gas helium with a diameter of 160 mm was traditionally located on the top of the vessel. The welded cavity with helium jacket dressed are shown in Fig. 2.

ISBN: 978-3-95450-250-9 ISSN: 2673-5520 doi:10.18429/JACoW-MEDSI2023-WEOAM04

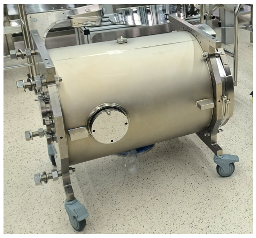

Figure 2: The jacketed 166.6 MHz srf cavity.

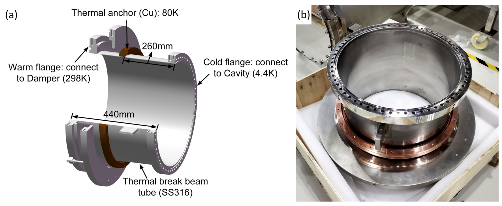

Figure 3: (a) Model and (b) fabricated thermal break beam tube.

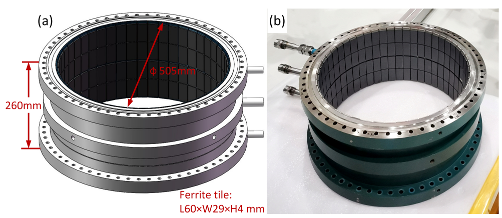

Figure 4: (a) Model and (b) fabricated HOM absorber.

Thermal Break Beam Tube The thermal break beam tube is a transition from 4 K at the cavity beam pipe to the room temperature outside the cryomodule. A thermal anchor at 80 K was added to reduce the cryogenic heat load. To minimize the heat load of 4.2 K, the thermal anchor position and tube thickness were optimized to be 260 mm and 2.5 mm, respectively. The total length of the thermal break tube was determined to be 440 mm to increase the temperature of warm flange higher than the dew point of 14°C (287 K). And the static heat load of 4.2 K and 80 K was reduced to 6.2 W and 87 W, respectively. The thermal break tube were shown in Fig. 3.

HOM Absorber The HOM absorber was made of 200 ferrite tiles, as shown in Fig. 4. Each ferrite tile was brazed to the copper base and water cooling channels were designed with a cooling capability of 10 kW rf power. The impedance of M2 was calculated to be $1.29 \times 10^4\ \Omega$, marginally exceeding the most stringent damping requirement of $1.14 \times 10^4\ \Omega$. The impedances of all other HOMs are below the threshold. The mechanical and thermal performances were also examined and acceptable for operation.

Collimating Taper Transition The transition from the cavity aperture of 505 mm to 63 mm of the interconnecting section is realized by a taper structure. After the beam comes out of the last bending magnet, it transverses a drift distance and then enters the cavity. Therefore, collimating is required

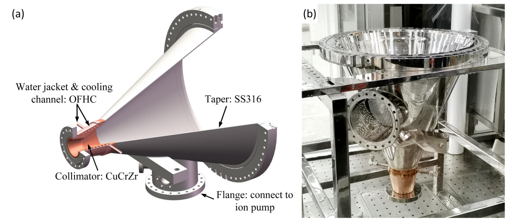

Figure 5: (a) Model and (b) fabricated collimating taper transition.

to create shadows for the downstream components like cavities, gate valves and shielded bellows. The well designed collimators were simple, compact, sufficiently cooled, and with large tolerances, as shown in Fig. 5. The higher temperature of 64°C observed on the spot of the direct light incidence, meeting the HEPS requirement.

Shielded bellows A rf-shielded bellows was designed to compensate for the longitudinal length variations from manufacturing, installation, cavity shrinkage during cooldown, tuner movement and so on. The maximum compression displacement is ±15 mm with a total length of 66 mm of the bellows.

ASSEMBLY AND HORIZONTAL TEST

Assembly

The assembly of the 166 MHz cavity string and the cryomodule was performed at the Platform of Advanced Photon Source Technology (PAPS), as shown in Fig. 6. The jacketed cavity, two thermal break beam tubes and a collimating taper transition were high-pressure rinsed by ultrapure water. The HOM absorber was cleaned with alcohol while the gate valves were purged by nitrogen until the particle count was reduced to 0. Next, the cavity string without ion pump were assembled in a class 10 clean room. After a slow pumping, a leak check of the cavity string was performed. Then, the cavity string was transferred outside the clean room. The HOM absorber was 150 °C baked for 86 h, and the cavity was subsequently 120 °C baked for 48 h while the other components were kept below 110 °C in experiment hall. Next, the position of the string was collimated, after which the temperature sensors and cables were placed. After that, the cavity string was pushed into the cryomodule for cryogenic pipeline connection and magnetic shield installation. Then, the cavity string and cryomodule were integrated successfully. Because the sputter ion pump was too large, it couldn't be integrated with the cavity string until the cryomodule endplates were installed. A movable clean room was built, and the assembly of the ion pump and cavity string was completed in the class 100 movable clean room. Next, the cryomodule was pushed out and the tuner was equipped on the cryomodule endplate in the experiment hall. At last, the cryomodule was transported to a horizontal test stand and connected to a distribution valve box, high-power transmission line, FPC, rf cables, etc.

ISBN: 978-3-95450-250-9 ISSN: 2673-5520 doi:10.18429/JACoW-MEDSI2023-WEOAM04

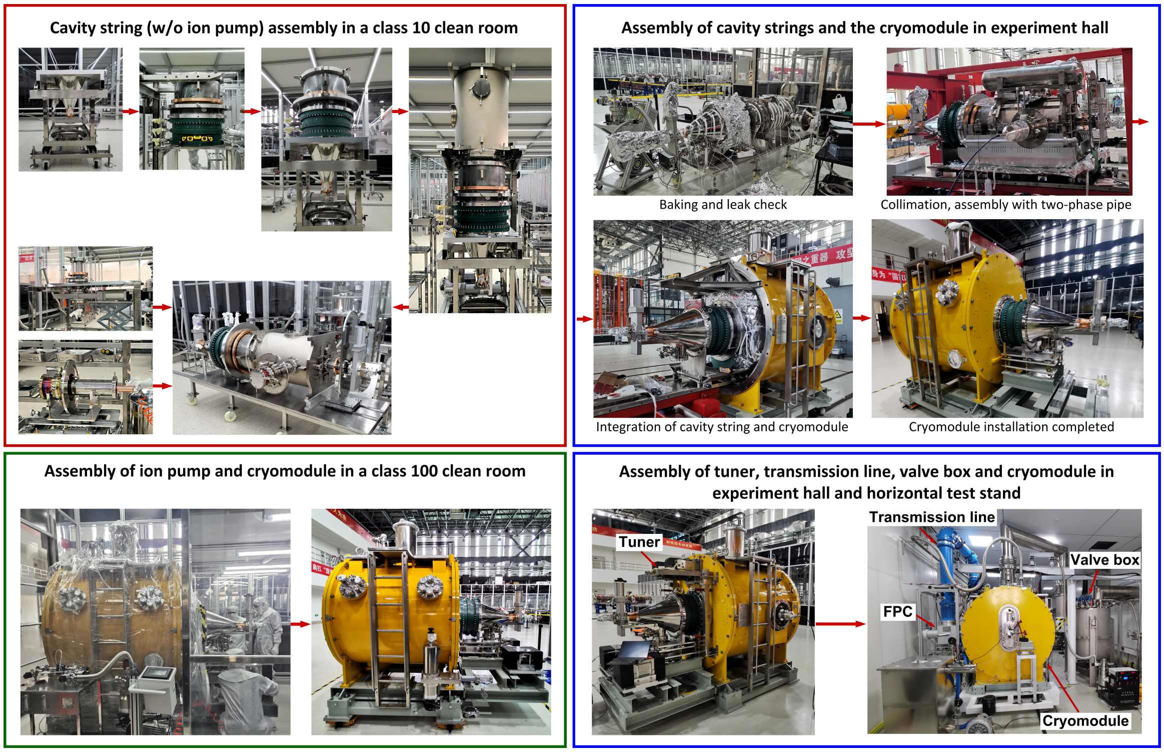

Figure 6: Assembly of the 166 MHz cavity string and the cryomodule.

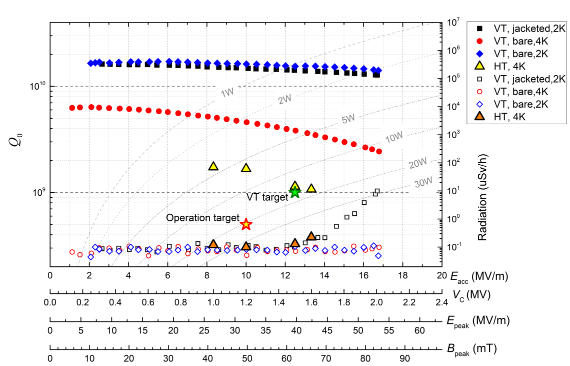

Figure 7: Quality factor and radiation level of the jacketed cavity during horizontal tests.

Horizontal Test

The cooldown process from room temperature to 4.2 K was conducted in two stages: a slow cooldown to ~40 K and a fast cooldown to 4.4 K. The former required a maximum temperature difference of less than 10 K on the cavity to reduce the risk of vacuum leak in particular on large beam pipe with a diameter of 505 mm caused by excessive stress from thermal contraction. The frequency of the cavity cooled down to 4.4 K in the cryomodule was measured to be 166.596 MHz, which was highly consistent with the design frequency. Then, the frequency was easily pulled up 4 kHz by the tuners and the target frequency of 166 MHz was achieved. This excellent consistency and accurate frequency demonstrated a successful frequency control and reliable manufacturing and post-processing methods.

The unloaded quality factor (Q_0) of the jacketed cavity was measured as a function of accelerating voltage (V_c) at 4.4 K, as shown in Fig. 7. The Q_0 at designed V_c of 1.2 MV was measured to be 1.7×10^9, greatly exceeding the operation target of 5×10^8. The dynamic heat loss at designed V_c was calculated to be 6.2 W based on the liquid level gauge. The corresponding radiation readouts are also displayed on the same plot, and no early field emission was observed.

FINAL REMARKS

The first dressed 166.6 MHz HOM-damped cavity has been designed for HEPS. The cavity string, including the jacketed cavity, a collimating taper transition, two thermal break beam tubes, a HOM absorber, a forward power coupler and a tuner were designed, fabricated, processed and assembled in a cryomodule. Horizontal tests at 4.4 K were subsequently conducted and the Q_0 greatly exceeded the long-term operation goal. After a slow cooldown process, the cavity was tuned to the operating frequency of 166.6 MHz, indicating an excellent frequency control and reliable development capabilities. The entire cavity system has been successfully verified by the horizontal test.

ACKNOWLEDGEMENTS

This work was supported in part by High Energy Photon Source, and in part by the National Natural Science Foundation of China under Grant 12005241.

ISBN: 978-3-95450-250-9 ISSN: 2673-5520 doi:10.18429/JACoW-MEDSI2023-WEOAM04

REFERENCES

[1] Y. Jiao *et al.*, "Progress of physics studies and commissioning preparations for the High Energy Photon Source", in *Proc. IPAC'23*, Venice, Italy, May 2023, pp. 980–983. doi:10.18429/JACoW-IPAC2023-MOPM002

[2] Z. Duan *et al.*, "Top-up Injection Schemes for HEPS", in *Proc. eeFACT'16*, Daresbury, UK, Oct. 2016, pp. 85–89. doi:10.18429/JACoW-eeFACT2016-TUT2H4

[3] L. Wang *et al.*, "A novel 5-cell strip-line kicker prototype for the HEPS on-axis injection system", *Nucl. Instrum. Methods Phys. Res. A*, vol. 992, p. 165040, 2021. doi:10.1016/j.nima.2021.165040

[4] P. Zhang *et al.*, "Radio-frequency system of the high energy photon source", *Radiat. Detect. Technol. Methods.*, vol. 7, pp. 159–170, 2023. doi:10.1007/s41605-022-00366-w

[5] P. Zhang *et al.*, "Development and vertical tests of a 166.6 MHz proof-of-principle superconducting quarter-wave beta = 1 cavity", *Rev. Sci. Instrum.*, vol. 90, p. 084705, 2019. doi:10.1063/1.5119093

[6] X. Y. Zhang *et al.*, "Design and Mechanical Performance of a Dressed 166.6 MHz β=1 Proof-of-Principle Superconducting Cavity in Horizontal Tests", *IEEE Trans. Appl. Supercond.*, vol. 30, no. 8, p. 3500208, 2020. doi:10.1109/TASC.2020.2999541

[7] L. Guo *et al.*, "Multipacting suppression of the HOM-damped 166.6 MHz β=1 quarter-wave superconducting cavities at HEPS", *J. Instrum.*, vol. 11, p. P11003, 2021. doi:10.1088/1748-0221/16/11/p11003

[8] X. Y. Zhang, Z. Q. Li, Q. Ma, and P. Zhang, "Synchrotron Light Shielding for the 166 MHz Superconducting RF Section at High Energy Photon Source", in *Proc. IPAC'21*, Campinas, Brazil, May 2021, pp. 1169–1172. doi:10.18429/JACoW-IPAC2021-MOPAB382

ISBN: 978-3-95450-250-9 ISSN: 2673-5520 doi:10.18429/JACoW-MEDSI2023-WEOBM01

CHALLENGES AND SOLUTIONS FOR THE MECHANICAL DESIGN OF SOLEIL-II

K. Tavakoli†, F. Alves, G. Baranton, Y. Benyakhlef, A. Berlioux, J. Dasilvacastro, M-E. Couprie, S. Ducourtieux, Z. Fan, C. Herbeaux, C. Kitegi, F. Lepage, A. Loulergue, V. Leroux, A. Mary, F. Marteau, A. Nadji, V. Pinty, M. Ribbens, A. Carcy, S. Pautatd, S. Thoraud, A. Lejollec
SOLEIL-II TDR team, Synchrotron SOLEIL, L'Orme des Merisiers, Saint-Aubin, France

Abstract

The Synchrotron SOLEIL is a large-scale research facility in France that provides synchrotron radiation from terahertz to hard X-rays for various scientific applications. To meet the evolving needs of the scientific community and to remain competitive with other European facilities, SOLEIL has planned an upgrade project called SOLEIL-II. The project aims to reconstruct the storage ring as a Diffraction Limited Storage Ring (DLSR) with a record low emittance which will enable nanometric resolution.

The mechanical design of the upgrade project involves several challenges such as the integration of new magnets, vacuum chambers, insertion devices and beamlines in the existing infrastructure, the optimization of the alignment and stability of the components, and the minimization of the downtime during the transition from SOLEIL to SOLEIL-II. The mechanical design is mainly based on extensive simulations, prototyping, and testing to ensure the feasibility, reliability, and performance of several key elements.

INTRODUCTION

SOLEIL is the French third generation light source operated for users since 2008 with an electron beam emittance of 4 nm·rad at an energy of 2.75 GeV in high intensity (500 mA, multibunch) [1].

The current lattice of the SOLEIL storage ring is composed of 16 modified two-bend achromat cells, 8 of which have short straight sections between the dipoles, altogether giving a total of 24 straight sections. After years of successful operation, a series of feasibility studies were initiated for a possible upgrade of the storage ring with a significantly lower emittance.

The SOLEIL Upgrade project, known as SOLEIL-II aims to design and build a 2.75 GeV diffraction-limited synchrotron light source preserving the actual infrastructure, 29 beamlines (far-IR to hard X-rays) and the 500 mA uniform filling pattern. The lattice of the new storage ring presented in CDR report [1] is built over a non-standard combination of twelve 7BA cells and eight 4BA cells [2, 3]. The main comparison parameters are listed in Table 1.

Table 1: Main SOLEIL-II Lattice Parameters

	Actual	Upgrade
Emittance (2.75 GeV)	4 nm·rad	84 pm·rad
Circumference	354.1 m	353.5 m
Straight section number	24	20
Long straight length	12 m	8.0/8.3 m
Medium straight length	7 m	4.25 m
Short straight length	3.8 m	3.0 m

Figure 1 shows the arrangement of the magnets in the 7BA cell and the 4BA cell of SOLEIL-II lattice. The length of the 7BA cell is rather short (~16 m) containing 52 magnets, depending on the lattice version, and including 7 dipoles. This very high density of multipoles increases the problem of compactness and creates implementation difficulties.

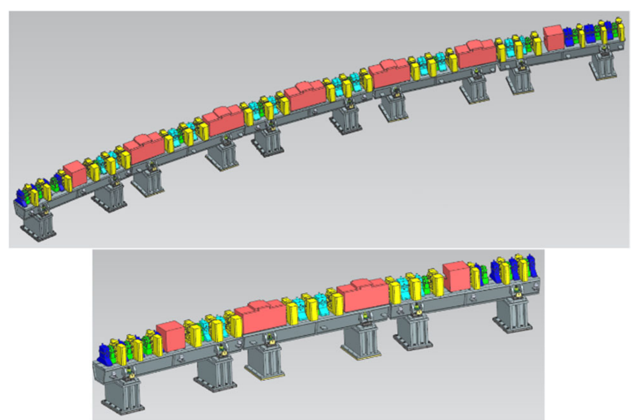

Figure 1: Engineering layout of the 7BA cell type of the new MBA-ARC (top) and the 4BA cell (bottom).

GIRDER DESIGN

The design of the girders is the result of a compromise between the vibration and thermal stability, adjustment precision and overall fabrication costs. After few iterations, SOLEIL mechanical engineers came up with a design based on four girder length families. Each girder family can be assembled in different configurations carrying single or double dipole [4].

The specification defined by accelerator physicists for the first modal frequency is around 40 Hz under load. Figure 2 shows the FE simulations on one of girder families in two different configurations.

† Keihan.tavakoli@synchrotron-soleil.fr

ISBN: 978-3-95450-250-9 ISSN: 2673-5520 doi:10.18429/JACoW-MEDSI2023-WEOBM01

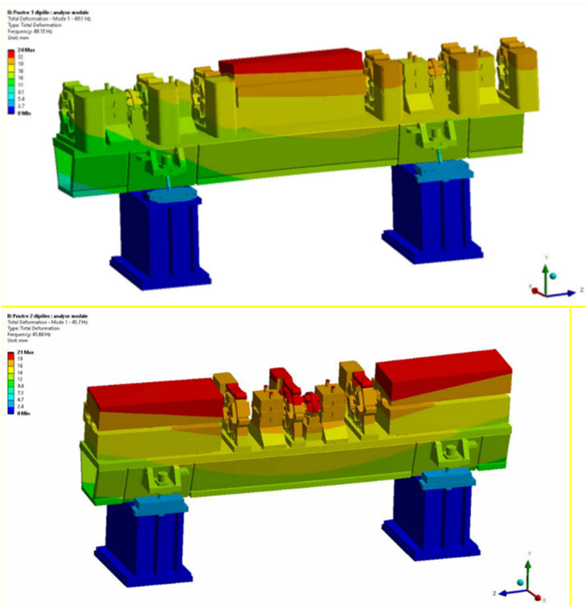

Figure 2: 1st modal frequency at 49 Hz in single dipole configuration (top) and 45 Hz in double dipole configuration (bottom).

Special toolings have been developed to extract dipoles from the girder without touching the vacuum chamber. Figure 3 shows the operation sequences: dipole at its initial position on the girder (Fig. 3 top-left), assembly of the tooling (Fig. 3 top-right), sliding parts assembly on the dipole (Fig. 3 bottom-left), lifting the dipole and slide it aside (Fig. 3 bottom-right) [5].

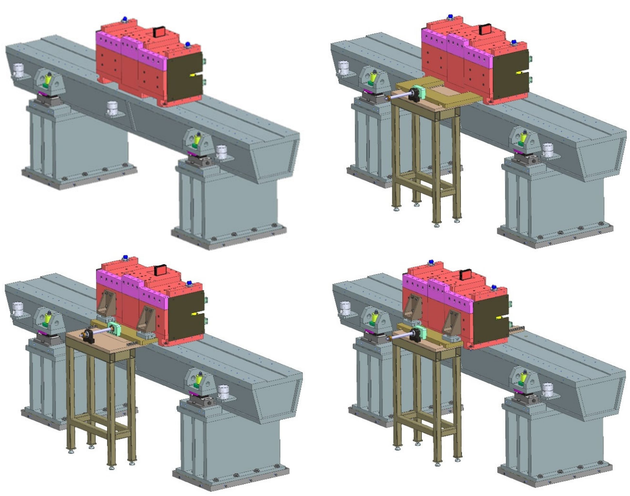

Figure 3: Retracting scenario of a dipole from the girder (from top-left to bottom right).

VACUUM SYSTEM

The main challenge designing SOLEIL-II vacuum system is the extreme compactness of the layout. In most cases, there is less than 60 mm between multipoles. The standard vcuum chamber diameter is 12 mm in achromat cells. The goal is to have a full distributed Ti-Zr-V NEG coating of 0.5 µm average thickness covering almost 100% of the internal surface. The NEG pumping system will be activated by ex-situ bake-out.

In addition to the NEG coating, one standard ion pump will be foreseen after each dipole near to the crotch absorber (see Fig. 4).

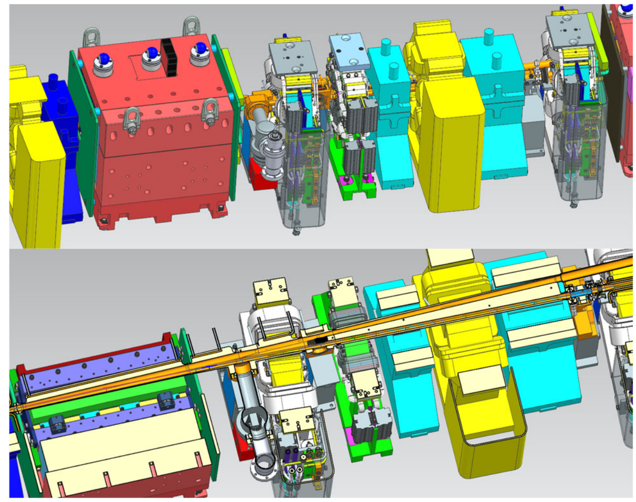

Figure 4: DNC short dipole vacuum chamber implementation in the restraint environment.

The vacuum system will be mainly fabricated in CuCr1Zr or OFHC copper. All parts in stainless steel will be coated by 10 µm copper or silver to reduce the impedance. In order to guarantee the RF continuity, two different kinds of gaskets will be used: MO type [6] for smaller diameter (12-16 mm) and CF-RF for larger diameters (see Fig. 5).

Figure 5: MO-type copper gasket (left) and CF-RF gasket (right).

The same philosophy has been used for RF bellows. In the achromat, a comb-type bellows is under prototyping. This kind of bellows has a limited stroke (few mm) and small lateral flexibility but an excellent RF contact. A classic RF finger bellows will be used in straight sections where more flexibility is needed (see Fig. 6).

In downstream of each dipole, an absorber bloc in CuCr1Zr is inserted containing two crotch absorbers (upper and lower crotch) and a sputtering ion pump. The deviation angle of the short dipoles on SOLEIL-II lattice is only around 2°. Thus, the distance between the photon beam and the electron beam does not exceed ~30 mm. small crotch absorbers based on additive manufacturing (AM) procedure have been designed at this location. The cooling channels have been optimized to reduces maximum temperature, comparing to a crotch fabricated in a classical way, by more than 30 °C (see Fig. 7).

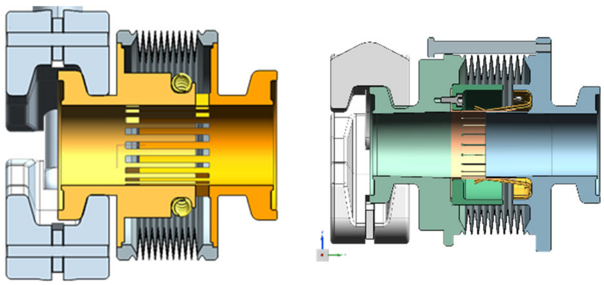

Figure 6: Comb-type bellows (left) and RF-finger based bellows design (right).

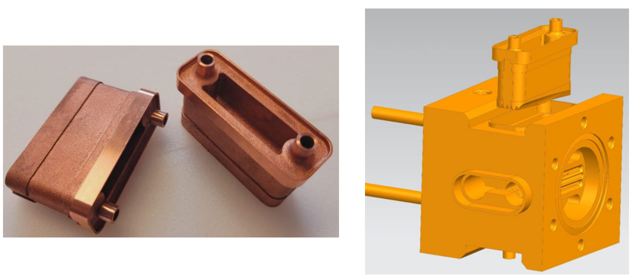

Figure 7: CuCr1Zr Additive manufacturing crotch (left) inserted and welded on the absorber bloc (right).

CONCLUSION

SOLEIL II is an ambitious project, promising very high performance, but is not without its challenges. A Machine Advisory Committee (MAC) has been established with a mandate lasting for three years 2022–2024. The project could get the 'green light' in autumn 2023, which could provide some preliminary funding in 2024, and allow the placing of some orders with payments due in 2025 and beyond.

The extreme compactness of the layout pushes the mechanical engineers to use innovative solutions and emerging technologies like copper alloys powder metallurgy additive fabrication. Many prototypes are under study, fabrication or already under qualification.

REFERENCES

[1] Synchrotron SOLEIL
https://www.synchrotronsoleil.fr

[2] O.R. Blanco-García, D. Amorim, M. A. Deniaud, A. Loulergue, L. S. Nadolski, and R. Nagaoka, "Status of the Soleil Upgrade Lattice Robustness Studies", in *Proc. IPAC'22*, Bangkok, Thailand, Jun. 2022, pp. 433-436.
doi:10.18429/JACoW-IPAC2022-MOPOTK004

[3] A. Loulergue *et al.*, "TDR Baseline Lattice for the Upgrade of SOLEIL", in *Proc. IPAC'22*, Bangkok, Thailand, Jun. 2022, pp. 1393-1396.
doi:10.18429/JACoW-IPAC2022-TUPOMS004

[4] J. Da Silva Castro *et al.*, "Girders on storage ring in SOLEIL II", presented at MEDSI'23, Beijing, China, Nov. 2023, paper THPPP038, this conference.

[5] A. Berlioux *et al.*, "Permanent Magnets in SOLEIL II", presented at MEDSI'23, Beijing, China, Nov 2023, paper WEPPP058, this conference.

[6] Y. Suetsugu, M. Shirai, and M. Ohtsuka "Application of a Matsumoto-Ohtsuka-type vacuum flange to beam ducts for future accelerators", *J. Vac. Sci. Technol. A*, vol 23, no. 6, pp. 1721–1727, 2005. doi:10.1116/1.2101808

ISBN: 978-3-95450-250-9 ISSN: 2673-5520 doi:10.18429/JACoW-MEDSI2023-WEOBM02

DEVELOPMENT OF THE BENT FOCUSING MIRROR IN HEPS FROM DESIGN TO TEST

Minwei Chen†, Ming Li, Fugui Yang, Shanzhi Tang
Institute of High Energy Physics, CAS, Beijing, China

Abstract

The focusing mirrors are important for each beamline in the 4th generation photon source. One bent focusing face-down mirror in HEPS is taken for an example to be introduced from the design to the test. The effect of the gravity of the mirror is considered in the design. Moreover, for the sake of the compromise between the processing and the precision, the polygonal structure is adopted. Also, the iteration of the solution is improved to increase the design efficiency. The results reveal that the theoretical precision of the mirror after bending can reach less than 100 nrad RMS. In the aspect of the mechanics, the scheme of four roller bender comes out to avoid the parasitic moment, and the movable component in the bender are all coated with the MoS_2. As the type of the measurement is facing side which is different from the type of the actual condition, the effect of the gravity must be included in the metrology results. In the meantime, the stability and the repeatability are also measured. The result can be converged to around 200 nrad RMS, which is less than the required error. The stability, ΔR/R, can be constrained under the 0.6%, showing the outstanding performance.

INTRODUCTION

Since the small spot and the high brightness, people around the world engage in pursuing the 4th synchrotron radiation facility (SRF). Bent mirror is one of the most significant optical element in the SRF, which can not focus the light but also decrease the error induced by other elements in the beamline. High energy photon source (HEPS) is one of the establishing 4th SRF, of which the circumference is about 1360 m and the emittance is 34 pm·rad [1].

This paper is dedicated to illustrating one focusing bent mirror in the HEPS beamline from design to test, which is seldom explained in other articles. The method used in the design is one kind of new iteration algorithm to increase the efficiency [2]. And the outstanding performance of the whole system is shown in the off-line testing.

DESIGN METHOD

Since the bent mirror is vertical reflection, the influence of the gravity is nonnegligible in this design. In order to decrease the cost of the bent mirror, the gravity compensation is also considered, thus the polygonal profile is adopted. The width of the mirror can be described as

$$b(x)=\frac{M(x)+M_g(x)}{EI_0C(x)}b_0 \ , \tag{1}$$

where $b(x)$ is the width varying with the position of the mirror, $M(x)$ is the moment of the mirror, $M_g(x)$ is the moment caused by gravity, E is the elastic module, $C(x)$ is the curvature of the mirror shape, b_0 and I_0 are the width and the inertia moment at the mirror center, respectively.

The solution on mirror width is utilized by the method in this article [2], which can improve the efficiency of the calculation.

DESIGN RESULTS

The active area of the bent focusing mirror used in HEPS is 605×20 mm^2. The requirement for the total slope error is less than 0.3 µrad. The final width can be solved by the theory above, and the results of the performance of the mirror are also shown as following.

The mirror width is plotted in Fig. 1. For sake of the processing convenience, the mirror edge is divided into 5 segments. Due to its direction of reflection, the distribution of the width shows a concave polygon. This width shape can effectively reduce the influence of the gravity.

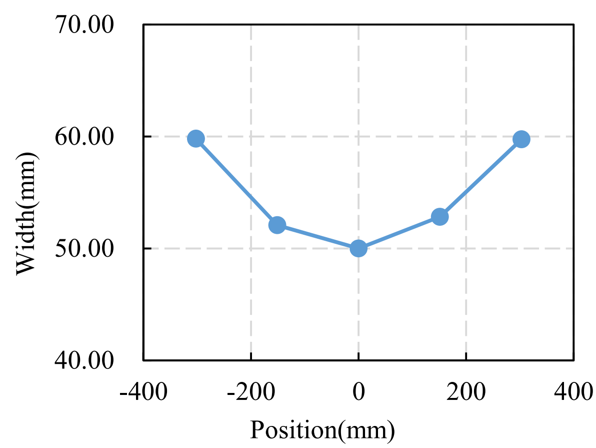

Figure 1: Mirror width along the position.

The design result of the slope error is shown in Fig. 2. The curve fluctuates between -0.03 µrad and 0.03 µrad, indicating the excellent performance of the mirror. The RMS (root mean square) of the slope error is about 14 nrad that is a very low value. Besides the design error, the material error, fabrication error and mechanical error are all included in this stage. The total error can be controlled around the 140 nrad RMS, which meets the requirement for less than 300 nrad RMS.

† chenmw@ihep.ac.cn

ISBN: 978-3-95450-250-9   ISSN: 2673-5520   doi:10.18429/JACoW-MEDSI2023-WEOBM02

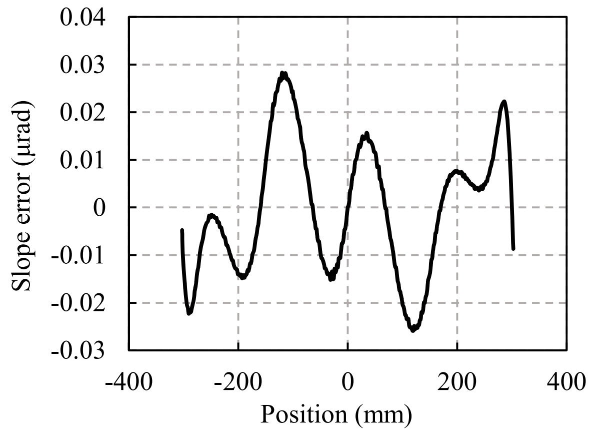

Figure 2: Slope error of the mirror in the design.

OFF-LINE TEST

Test Preparation

The inspection instrument we use in the off-line test is horizontal LTP (long trace profiler), while the direction of the reflection is face-down in the working condition. Therefore, the inspection result we obtain should be extra considered the influence of the gravity.

The drive force adjusting the shape of the bent focusing mirror comes from the four-cylinder benders that can avoid the parasitic moment. The most significant parts of the mechanism, even determine the performance of the adjustment, is the sleeve system which is shown in Fig. 3. The component is located in the front of the rotating motor, which is utilized to transfer the rotation to translation. Thus, all the sleeve systems are all coated with MoS_2 to improve the lubrication. In order to rotate the whole mirror system, the clamping is also fabricated.

Figure 3: Sleeve system with MoS_2 coating.

Test Results

The variation of the height error and the slope error with each iteration are presented in the Figs. 4 and 5, respectively. Because the error in the first iteration is too large, the curve in this step is eliminated. From the figure, one can find that the height error and the slope error both decrease as the iteration number increasing. Moreover, 4 or 5 iterations are enough to almost meet the requirement. The final slope error is converged to about 200 nrad RMS, which is also shown in Table 1. In the near future work, we intend to explore the limitation of the iteration or search for the better method on iteration to reduce the height error or the slope error.

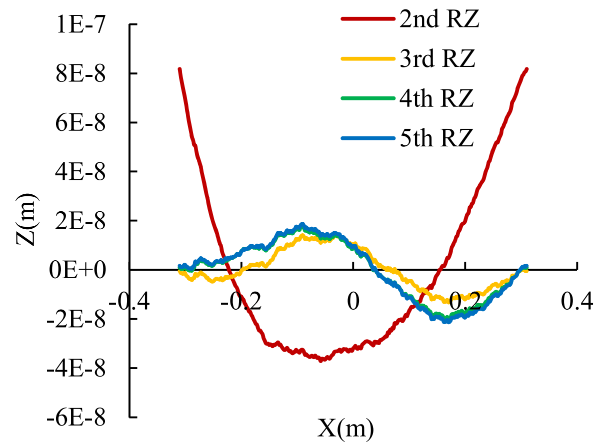

Figure 4: Height error curve for each iteration.

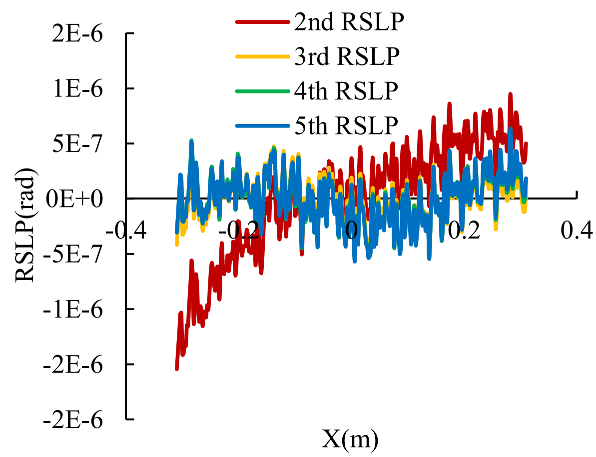

Figure 5: Slope error curve for each iteration.

Table 1: RMS of Residual Error for Each Iteration

Iteration number	Height error RMS [m]	Slope error RMS [rad]
1	3.31E-06	2.70E-05
2	4.77E-08	6.33E-07
3	1.32E-08	2.80E-07
4	1.44E-08	2.53E-07
5	1.21E-08	2.25E-07

After the adjustment of the mirror shape is accomplished, the stability of the system also should be cared about. The stable test is conducted. The period lasts about 3 days, and the evaluation index we used is the curvature radius that is shown in Fig. 6. The stable interval of the radius locate in about 5,320 m and the parameter $\triangle R/R$ corresponds to the 0.5%.

ISBN: 978-3-95450-250-9 ISSN: 2673-5520 doi:10.18429/JACoW-MEDSI2023-WEOBM02

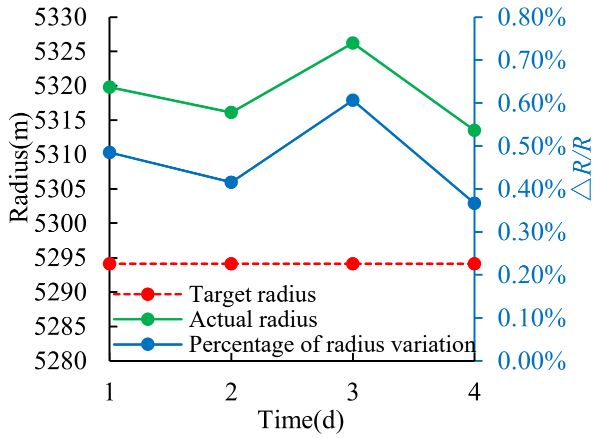

Figure 6: Variation of the curvature radius as the time.

CONCLUSION

This article states the development of one bent focusing mirror in HEPS from design to off-line test. The main topic is based on the performance of the mirror system. The results reveal that the theoretical precision of the mirror after bending can reach less than 100 nrad RMS. In the off-line test stage, the whole mirror system can be converged to around 200 nrad RMS, which is less than the required error. The stability, ΔR/R, can be constrained under the 0.6%, showing the outstanding performance.

REFERENCES

[1] M. Chen, L. Gao, W. Sheng, S. Wang, and F. Yang, "Numerical iteration method to reduce the surface shape error of a bendable mirror in synchrotron radiation," *Appl. Opt.*, vol. 61, pp. 2096-2102. 2022. doi.org/10.1364/AO.451088

[2] M. Chen *et al.*, "Efficient method on the determination of optimized width of bendable mirrors with gravity compensation", Results Opt., vol. 5, p. 100141, 2021. doi.org/10.1016/j.rio.2021.100141

ISBN: 978-3-95450-250-9 ISSN: 2673-5520 doi:10.18429/JACoW-MEDSI2023-WEOBM03

THE DESIGN AND PROGRESS OF THE NETWORK AND COMPUTING SYSTEM FOR HEPS

H. Hu, F. Qi, X. Wang, Y. Cheng, Q. Hu, H. Zhang, Y. Hu, S. Zeng
Institute of High Energy of Physics, Beijing, China

Abstract

China's High Energy Photon Source (HEPS) is the first national high-energy synchrotron radiation light source. The 14 beamlines for the phase I of HEPS will produces about 300 PB/year raw data, it represents significant challenges in data storage, data access, data analysis and data exchange. HEPS Computing and Communication System (HEPSCC), is an essential work group responsible for the IT R&D and services for the facility, including IT infrastructure, network, computing, analysis software, data preservation and management, public services etc. This paper mainly introduces the design and progress of HEPSCC's work in addressing the data challenges faced by HEPS from various aspects, including machine room, network, storage, computing, and scientific software of data management and data analysis.

MANUSCRIPTS

HEPS is the first national high-energy synchrotron radiation light source and soon one of the world's brightest fourth-generation synchrotron radiation facilities [1], has been constructed from 2019 in Beijing's Huairou District, and will be completed in 2025. The 14 beamlines for the phase I of HEPS will produces about 300 PB/year raw data (see Table 1). Efficiently storing, analyzing, and sharing this huge amount of data presents a significant challenge for HEPS.

Table 1: Estimated Data Volume of HEPS at Phase I

Beamlines	Burst output(Byte/day)	Average output(Byte/day)
B1 Engineering Materials Beamline	600TB	200TB
B2 Hard X-ray Multi-analytical Nanoprobe (HXMAN) Beamline	500TB	200TB
B3 Structural Dynamics Beamline (SDB)	8TB	3TB
B4 Hard X-ray Coherent Scattering Beamline	10TB	3TB
B5 Hard X-ray High Energy Resolution Spectroscopy Beamline	10TB	1TB
B6 High Pressure Beamline	2TB	1TB
B7 Hard X-Ray Imaging Beamline	1000TB	250TB
B8 X-ray Absorption Spectroscopy Beamline	80TB	10TB
B9 Low-Dimension Structure Probe (LODISP) Beamline	20TB	5TB
BA Biological Macromolecule Microfocus Beamline	35TB	10TB
BB pink SAXS	400TB	50TB
BC High Res. Nanoscale Electronic Structure Spectroscopy Beamline	1TB	0.2TB
BD Tender X-ray beamline	10TB	1TB
BE Transmission X-ray Microscope Beamline	25TB	11.2TB
BF Test beamline	1000TB	60TB
Total average:		**805.4TB/day, 24.16PB/month**

HEPS Computing and Communication System (HEPSCC), also called HEPS Computing Center, is an essential work group responsible for the IT R&D and services for the facility, including IT infrastructure, network, computing, analysis software, data preservation and management, public services etc. Aimed at addressing the significant challenge of large data volume, HEPSCC has designed and established a network and computing system, making great progress over the past two years.

As the most fundamental part of the IT infrastructure, a deliciated and high-standard machine room, with about 900 m^2 floor space for more than 120 high-density racks in total, has been prepared for production since this August. The power system has two transformers for dual power supply and has a total capacity of 2,500KVA, with the UPS providing 800KVA of power capacity and offering a half-hour backup during emergencies. Row-Air conditioning with natural cooling is used for the refrigeration of the machine room, which can greatly reduce the energy consumption.

For the data center network, we designed it as a spine-leaf architecture which makes it very easy to scale out. The backbone bandwidth of the data center network can support speeds up to 4*400 Gb/s, which can fully meet the demands of high-speed data exchange. Meanwhile, we also support RoCE [2] (RDMA over Converged Ethernet) to provide a lossless and high-performance network environment for scientific workload in HEPS data center. Previous test evaluations showed that RoCE can reach the same performance as InfiniBand (IB) in both point-to-point and collective tests.

In order to balance the cost-effectiveness of storage devices and realize the high reliability of data storage, a three-tier storage is designed for storing experimental data, including beamline storage, central storage, and tape. There is a storage policy for data preservation (see Fig. 1), the raw data and processed data are stored on the beamline storage for a maximum of 7 days, on the central storage for a maximum of 90 days, and only the raw data are archived to tape for long-term storage with two copies. Of course, this data storage policy could be adjusted according to the actual data volume and funding situation of HEPS. The beamline storage utilizes distributed all-flash SSD arrays to achieve high data input/output speeds, while offering a total storage capacity of 800 TB. The central storage leverages distributed high-density HDD arrays to get medium-high speed data IO, providing a total capacity of 30 PB. The tape storage is compliant with the LTO9 [3] standard, and provides 2 PB at the first stage although we have no budget for tape.

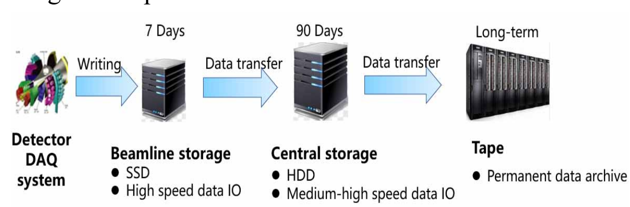

Figure 1: Storage policy for HEPS data.

To meet the requirements of data analysis scenarios for HEPS, a computing architecture has been designed and deployed in three types (see Fig. 2), including Openstack [4], Kubernetes, and Slurm. Openstack integrates the virtual cloud desktop protocol to provide users with remote

ISBN: 978-3-95450-250-9 ISSN: 2673-5520 doi:10.18429/JACoW-MEDSI2023-WEOBM03

desktop access services, and supports users to use browsers to access windows/Linux desktop, running commercial visualization data analysis software. Kubernetes manages container clusters, and starts container images with multiple methodological software according to user analysis requirements [5]. Slurm is used to support HPC computing services and meet users' offline data analysis needs.

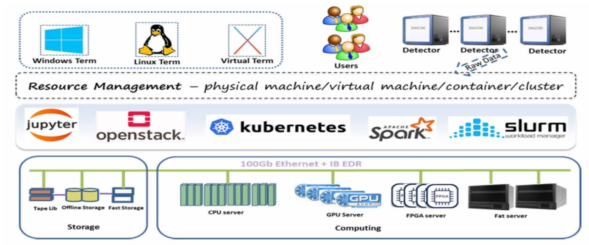

Figure 2: the computing architecture.

In addition to providing the IT infrastructure, HEPSCC also designed and developed the software for the data management and analysis, DOMAS and DAISY.

DOMAS (Data Organization, Management and Accessing Software stack), which is aimed for automating the organization, transfer, storage, distribution and sharing of the scientific data for HEPS experiments, provides the features and functions for metadata catalogue, metadata acquisition, data transfer, data web portal. The metadata catalogue module is responsible for storing metadata into database and providing RESTful APIs to access metadata. The data transfer module facilitates the automatic migration of data between different levels of storage media. The metadata acquisition and processing module is responsible for obtaining metadata from different stages and systems involved in data management and integrating them into the database. The data service module provides users with a web portal for data access, viewing, downloading, and offline analysis.

The core functional module of DOMAS has been completed, and we are progressively open-sourcing each module. Combined with the specific scientific data policy of HEPS [6], standardized data file formats, and data storage directory designs, we have completed the development of the scientific data management system for HEPS. Meanwhile, the system implemented the fully automated movement and management of data among three-tiered storage (beamline storage, central storage, and tape).

The Daisy (Data Analysis Integrated Software System) [7,8] has been designed for the data analysis and visualization of X-ray experiments. Daisy framework consists of a highly modular C++/Python architecture composed of four pillars (see Fig. 3): algorithm, workflow, workflow engine and data store. The algorithm defines the scientific domain model and support the integration of third-party library. The workflow is a sequence of algorithms and defines the scientific domain architecture. The workflow engine manages the runtime environment of workflow. The data store manages the data objects. The architecture supporting customized plug-in functions can easily access visualization tools and the Python-based scientific computing ecosystem.

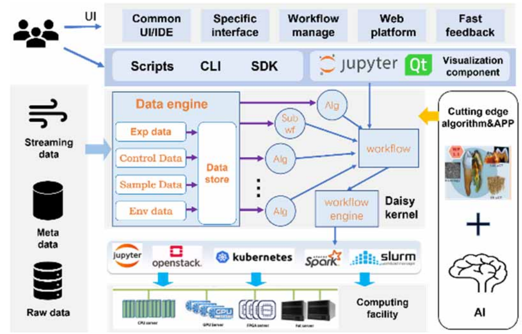

Figure 3: The architecture of DAISY.

Based on the Daisy framework, several specific scientific applications have been developed. For example, HEPSCT integrated an in-house developed 3D tomographic reconstruction package, cumopy, into the framework. It can conduct real-time computing to remove the background, control the white balance, carry motion correction, detect the position of rotation axis according to the parameters setting, then the reconstruction algorithms are executed on GPUs. Daisy-BMX is an AI-based biological macromolecular data-processing application. It implemented a data processing pipeline from diffraction to structure, including the real-time data processing, AI-based structure prediction, and model refinement. The Pair Distribution Function (PDF) implemented a pipeline from diffraction to PDF, include the pre-processing, azimuth integration, PDF transition and post-process. In addition, DAISY implemented and integrated several X-ray absorption spectrum analysis applications, include spectrum matching application and PCA/LCF spectrum component analysis application. Other data analysis algorithms/software will be continuously integrated to the framework in the future.

In 2021, A testbed was set up at beamline 3W1 of BSRF, which is a running synchrotron radiation facility and provides the technology R&D and test platforms for HEPS. The 3W1 beamline, which is dedicated to test high-throughput instruments for HEPS. It is an ideal candidate to set up the testbed where we can deploy the system and verify the functions and the whole process of data acquisition, data processing, data transfer, data storage and data access. The integration and the verification of the whole HEPSCC system at 3W1 beamline achieved great success. It strongly proved the rationality of the design scheme and the feasibility of the technologies. After the optimization and upgrade of the functionality, in July 2022, the HEPSCC system were deployed at 4W1B, which is a running beamline at BSRF, can provide full process service for beamline users.

Now HEPSCC entered the stage of equipment installation and system debugging. The machine room is prepared and provides the operation environment for another IT equipment. The campus network and data center network have been ready since this September, awaiting access from other devices. The software for data management and analysis are deploying and testing.

ISBN: 978-3-95450-250-9 ISSN: 2673-5520 doi:10.18429/JACoW-MEDSI2023-WEOBM03

REFERENCES

[1] Y. Jiao *et al.*, "The HEPS project", *J. Synchrotron Radiat.*, vol. 25, pp. 1611-1618, Nov. 2018. doi:10.1107/S1600577518012110

[2] S. Zeng *et al.*, "Research and Evaluation of RoCE in IHEP Data Center", *EPJ Web Conf.*, vol. 251, p. 02018, 2021. doi:10.1051/epjconf/202125102018

[3] LTO9, https://www.lto.org/lto-9/

[4] A. Celesti *et al.*, "Improving desktop as a Service in OpenStack", in *Proc. 2016 IEEE Symposium on Computers and Communication (ISCC)*, Messina, Italy, Jun. 2016. doi:10.1109/ISCC.2016.7543755

[5] J. Stubbs *et al.*, "Integrating jupyter into research computing ecosystems: Challenges and successes in architecting jupyterhub for collaborative research computing ecosystems", *Practice and Experience in Advanced Research Computing*, pp. 91-98. Jul. 2020. doi:10.1145/3311790.3396648

[6] H. Hu, F. Qi, H. Zhang, H. Tian, and Q. Luo, "The design of a data management system at HEPS", *J. Synchrotron Radiat.*, vol. 28, pp. 169-175, Jan. 2021. doi:10.1107/S1600577520015167

[7] Y. Hu *et al.*, "Daisy: Data analysis integrated software system for X-ray experiments", *EPJ Web Conf.*, vol. 251, p. 04020, Aug. 2021. doi:10.1051/epjconf/202125104020

[8] Y. Hu and H. Tian, "Data Analysis Integrated Software System in IHEP, design and implementation", in *Proc. International Symposium on Grids & Clouds 2022 (ISGC2022),* Taipei, Taiwan, March 2022. doi:10.22323/1.415.0028

ISBN: 978-3-95450-250-9 ISSN: 2673-5520 doi:10.18429/JACoW-MEDSI2023-WEOBM04

ADVANCING SIMULATION CAPABILITIES AT EUROPEAN XFEL: A MULTIDISCIPLINARY APPROACH

F. Yang*, D. La Civita, M. Di Felice, B. Friedrich, N. Kohlstrunk, M. Planas, M. Wuenschel, L. Samoylova, H. Sinn, European XFEL, Schenefeld, Germany
T. Stoye, DESY, Hamburg, Germany

Abstract

At European XFEL, computational techniques such as finite element analysis (FEA) and computational fluid dynamics (CFD) are widely applied in various scientific and engineering fields, such as damage simulation due to heat load, bleaching effect study of gas attenuator, optimization of fluid cooling system for detectors and characterization of liquid sheet jets for sample delivery system. Without being constrained by experimental conditions, the multiphysics and multiscale models in simulation could virtually replicate the interaction process of XFEL beam with different materials, taking into consideration heat transfer, structural deformation and phase transition. In this contribution, to gain comprehensive insights into the fluid behaviors of the detector cooling system, as well as the performance of reduced order modelling solvers, parametric studies are conducted using CFD simulation code. Furthermore, a realistic simulation requires a secured process of Verification and Validation (V&V) of the computational model. Specific guides and standards need to be followed to ensure the credibility and accuracy of the simulation results. Besides following the FAIR principle (Findable, Accessible, Interoperable, and Reusable), a smart simulation data management system using machine learning algorithm is under construction. Moreover, the large amount of data from the simulations in the past can be utilized to train the machine learning model, which can be used for simulation results prediction without running further simulations. Further AI and machine learning tools are going to be employed to set up generative design workflow and digital twin scheme for the beamline components, serving as a new safety constraint for monitoring and optimizing of the facility operation.

VERIFICATION, VALIDATION AND UNCERTAINTY QUANTIFICATION

The goal of setting up a systematic verification, validation and uncertainty quantification (VVUQ) for all simulations is to build a common agreement based on corresponding ISO standard [1–3] regarding the reliability of simulation results. This topic is increasingly important when many models could be reused for new applications. As an example, to characterize the thickness change of the CVD diamond of the spectrometer, simulation results using various numerical methods are compared in Fig. 1. It shows that the divergence between these methods is obvious. Without having possibility to validate with experimental results, it is important to execute a VVUQ process. The comparison shows that the element using convective coordinates which include the 2nd order bending moment is the most precise and efficient computational model. But since the elements in commercial code are only based on Cartesian coordinates, finer meshing is needed for a precise results [4]. Therefore, a standard workflow is essential, to ensure the credibility of the simulation models and results as following: (a) Purpose and Scope (b) Model Development (c) Verification and

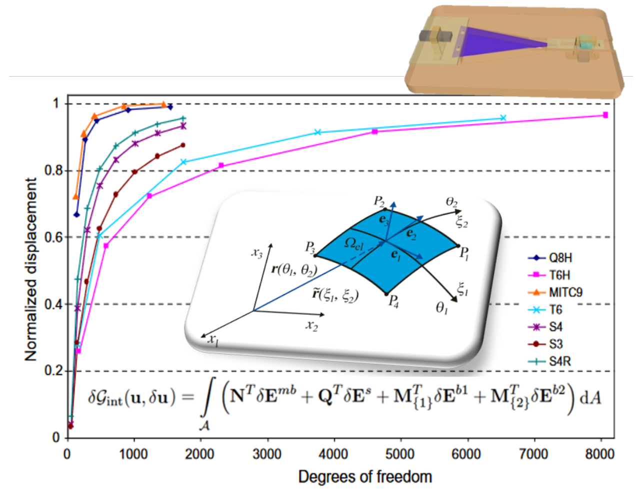

Shell element to avoid shear locking phenomena

Figure 1: Characterization of thickness change of bending crystal.

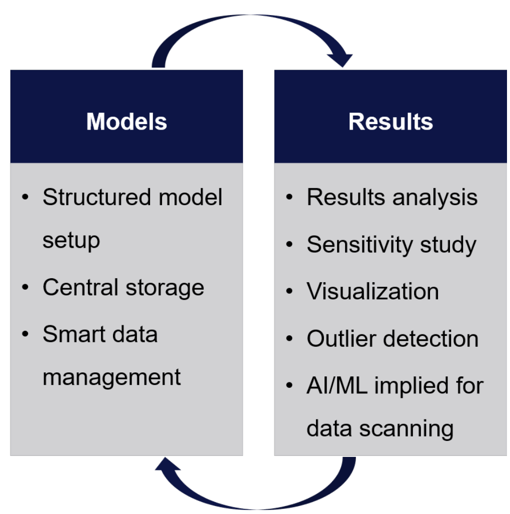

Figure 2: Simulation data management Scheme.

* fan.yang@xfel.eu

12th Int. Conf. Mech. Eng. Design Synchrotron Radiat. Equip. Instrum. MEDSI2023, Beijing, China JACoW Publishing
ISBN: 978-3-95450-250-9 ISSN: 2673-5520 doi:10.18429/JACoW-MEDSI2023-WEOBM04

Pulse energy [mJ]	Photon Energy [keV]	power [W]	FWHM [mm]	simulation results [°C]	AI predicted [°C]
1.87	10	5.05	0.2	29.34	30.77
1.56	12	4.21	0.19	26.23	27.94
1.34	14	3.61	0.18	24.90	24.99
1.17	16	3.16	0.17	24.13	23.46
1.04	18	2.81	0.17	23.60	23.04
0.94	20	2.53	0.16	23.41	22.63

Figure 3: Simulation results prediction.

Validation (d) Uncertainty Quantification (e) Credibility Assessment. For each term there are key points that need to be clarified, communicated and documented.

APPLICATION OF AI AND MACHINE LEARNING IN SIMULATION

Accompanied with the development of artificial intelligence and machine learning algorithm, as well as the interaction of natural language with machine language, the mode of simulation is being revolutionized. In the following subsections, some first applications of AI and ML tools in the field of simulation at European XFEL are briefly introduced.

Simulation Data Management (SDM) System

A systematic data management for the large amount of simulation data has been for long time a crucial subject in the research facilities [5]. To improve the current situation, two main categories are being reconstructed in SDM, see Fig. 2. Using ML algorithm, it is possible to scan the models and results in very short time on the central storage, automatically accomplish the sensitivity analysis, outlier detection and visualization functions.

Simulation Results Prediction

AI/ML tools could be used in simulation for the results prediction based on the input data [6]. As an example, the interaction of X-ray laser beam with B4C component for shutters at European XFEL are show in Fig. 3. Hundreds of input data, such as photon energy, pulse energy, beam size, penetration depth are used to train the model. Using layer wise neural network of machine learning code, the temperature profile could be precisely predicted without running further simulations.

Generative Design

AI and ML could be implied not only in the data management system, but also during the complete life cycle of engineering design. In the conventional design workflow, simulation is used to be a bottle neck in the design iteration loop, see Fig. 4. Using AI driven generative design, it is possible to get an optimized solution in relative short time, see Fig. 5. Different from topology optimization, generative design doesn't start from an existing design. Based on the defined targets that need to be fulfilled, e.g. minimize the temperature gradient, set the maximum allowed flow velocity below 1 m s^{-1}, etc., the ML algorithm will generate several hundreds of conceptual design and layer wise find the optimized solution based on simulation with reduced order models.

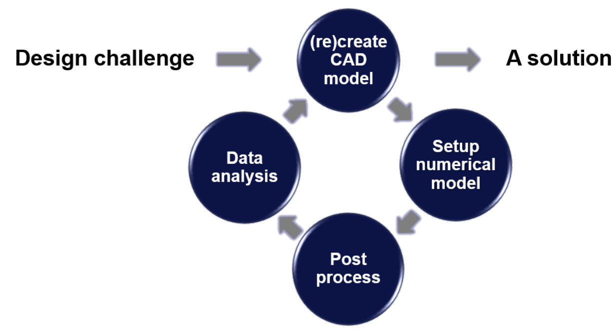

Figure 4: Conventional design workflow.

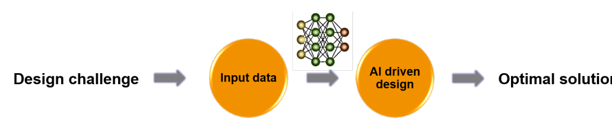

Figure 5: Generative design workflow.

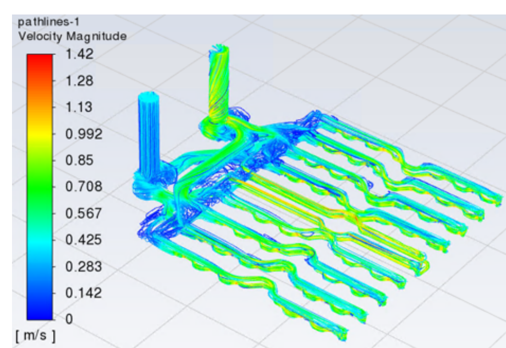

Figure 6: CFD simulation of detector cooling component using ANSYS Fluent.

ISBN: 978-3-95450-250-9 ISSN: 2673-5520 doi:10.18429/JACoW-MEDSI2023-WEOBM04

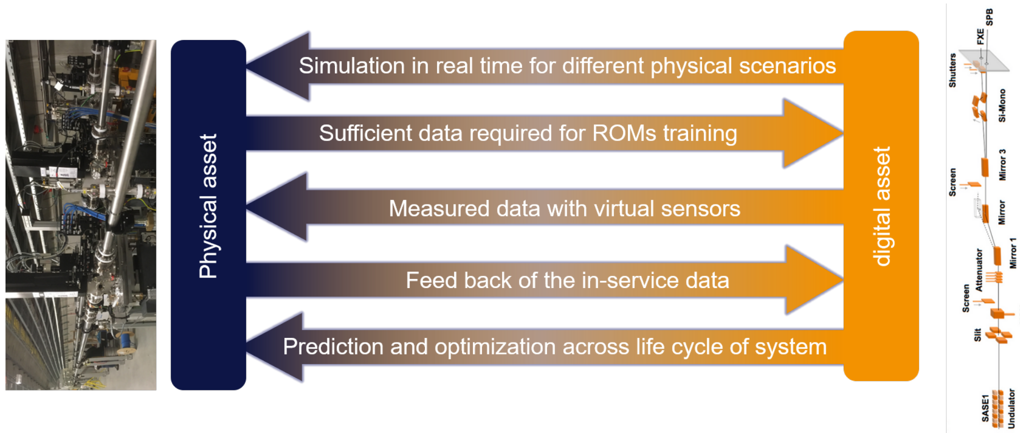

Figure 7: Diagram of digital twin.

Reduced Order Modelling (ROM) and Digital Twin

Reduced order modelling [7] offers opportunity for an efficient, in real time simulation, by reducing the number of equations that need to be solved significantly without losing main features of the system. ML algorithm enhanced the ROM by data driven optimization in reducing the model orders. It is specifically used for CFD simulations and complex system, in which millions of variables need to be solved. Figure 6 presents a cooling element for detectors. Using ROM with ML algorithm integrated in the solver, the computing time reduced from 4 hours to 5 seconds, without losing accuracy of the results.

The real time simulation capability of ROM enables the implementation of digital twin for either single device or assembly of the beamline, see Fig. 7. In a digital twin system, parametric study with hundreds of scenarios could be simulated in real time, and the optimized setup will be transferred to the physical asset, vice versa the measured data from physical sensors will feedback the performance of the device to the virtual system. Through communicating with each other synchronously, the digital replica will accompany the physical asset during the whole life cycle of the components.

CONCLUSION

In this contribution, a multidisciplinary approach of simulation at the European XFEL [8, 9] has been presented . Verification and validation workflow ensure the credibility of simulation results. With the aid of AI/ML tools, data management and simulation results prediction is under developing gradually. Looking forward, generative design and digital twin with implied generative AI model will reshape the world of simulation [10].

REFERENCES

[1] B. L. Boyce *et al.*, “The Sandia Fracture Challenge: blind round robin predictions of ductile tearing”, *Int. J. Fract.*, vol. 186, pp. 5-–68, 2014. doi:10.1007/s10704-013-9904-6

[2] ASME VVUQ 1-2022, https://webstore.ansi.org/standards/asme/asmevvuq2022

[3] ISO 23247-1, https://www.ap238.org/iso23247/

[4] J. Scheidl, Y. Vetyukov, *et al.*, “Mixed Eulerian–Lagrangian shell model for lateral run-off in a steel belt drive and its experimental validation”, *Int. J. Mech. Sci.*, vol. 204, p. 106572, 2021. doi:10.1016/j.ijmecsci.2021.106572

[5] R. L. Clay, E. J. Friedman-Hill, *et al.*, “Simulation Data Management - Requirements and Design Specification”, Sandia National Lab., Albuquerque, NM, United States, Rep. SAND2017-12477. doi:10.2172/1410169

[6] https://www.daive.de/

[7] C. Touzé, A. Vizzaccaro, and O. Thomas, “Model order reduction methods for geometrically nonlinear structures: a review of nonlinear techniques”, 2021. doi:10.48550/arXiv.2107.05077

[8] H. Sinn *et al.*, “The SASE1 X-ray beam transport system”, *J. Synchrotron Rad.*, vol. 26, pp. 692–699, 2019. 10.1107/S1600577519003461

[9] F. Yang, D. La Civita, H. Sinn, and M. Vannoni, “Heat Load Simulation of Optic Materials at European XFEL”, in *Proc. MEDSI’20*, Chicago, IL, USA, Jul. 2021, pp. 357–359. doi:10.18429/JACoW-MEDSI2020-THOB02

[10] https://leam.ai/

ISBN: 978-3-95450-250-9 ISSN: 2673-5520 doi:10.18429/JACoW-MEDSI2023-WEOBM05

THERMAL CALCULATION AND TESTING OF SLS 2.0 CROTCH ABSORBERS

Xinyu Wang†, Colette Rosenberg, Romain Ganter, André Weber, Markus Maehr, Samuel Bugmann
Paul Scherrer Institut, Villigen, Switzerland

Abstract

After 22 years of operation, the Swiss Light Source (SLS) was recently shut down on September 30, 2023, and the construction of SLS 2.0 has commenced. The storage ring of SLS2.0 based on a multibend achromat lattice will have the maximum electron energy of 2.7 GeV. SLS 2.0 crotch absorbers are designed to have two water-cooled, toothed jaws made of Glidcop to dissipate a maximum heat power of 6 kW. Finite element analysis has been conducted to validate the thermal and mechanical strength of the absorber's mechanical design. A conjugate heat transfer (CHT) simulation was performed to verify the water cooling concept. Furthermore, a prototype absorber underwent testing in an e-beam welding chamber. This paper describes numerical simulation and thermal testing of SLS 2.0 absorber.

INTRODUCTION

The storage ring of SLS 2.0 will feature a 40-fold increase in hard X-Ray brilliance, achieved through a low-emittance magnet lattice and a beam pipe with smaller aperture [1, 2]. The majority of over 100 pieces of absorbers is designated to dissipate synchrotron radiation power from normal bend dipoles [3]. The normal incidence power density is at a maximum of 600 W/mm^2 for a total power up to 3.5 kW. This absorber was initially designed using the age-hardenable CuCrZr alloy with two individually water-cooled upper and lower parts with saw-tooth surfaces. The idea was to produce the absorbers by wire erosion with a directly machined Conflat type knife edge in the absorber body. As no welding or brazing procedure would be necessary, this was expected to reduce material and fabrication costs [4-6]. From the 5 T superconducting magnets, a total power of about 7 kW is generated with the normal incidence power reaching as high as 1100W/mm^2. A different design and material is required, and Glidcop® AL-15 alloy was chosen due to its higher thermal conductivity and better resistance to thermal stress. The jaw has an inclination of 1° with a number of flat teeth and intermediate grooves. The teeth of upper and lower jaws interleave without contacting each other. In this way, the power was distributed to the upper and lower jaws, so that the power density is reduced to less than 30 W/mm^2. The two jaws are water-cooled and brazed into a stainless-steel flange.

WATER COOLING MODELLING

The cooling concept of SLS1 absorber has been adapted: the inlet water is guided by a stainless steel tube to the end of the pin hole and flows back through the helical channel on outer surface of the tube. Each jaw has three 10 mm pinholes, and the tube has a diameter of 6 mm (inner) and 8 mm (outer). The average water velocity is limited to 1.5 m/s due to corrosion concerns, which corresponds to a flow rate of 15.3 l/min for an absorber with 6 channels.

In thermal calculations, water cooling can be simulated as forced convection using a heat transfer coefficient with a constant water temperature. Alternatively, water flow can be modeled using 1D thermal fluid elements, taking into account temperature changes in the water. For most common pipe geometries and flow conditions, the heat transfer coefficient can be estimated from correlations, such as Dittus-Boelter, Sieder-Tate, etc. Ultimately, the Computational Fluid Dynamics (CFD) analysis can be employed to investigate heat transfer between the solid and fluid.

A conjugate heat transfer simulation of a full absorber body including six stainless steel water pipes in parallel and with fluid water, would be very complex and time-consuming. Therefore a sub-model contains one water pipe with the lower-left part of the absorber, which removes more than ¼ of total heat power, has been analysed [7]. The Fluent model contains 3.7 million zones and 9.5 million nodes for the fluid, and 197’000 zones and 847’000 nodes for the solid. The turbulence model used was SST k-omega.

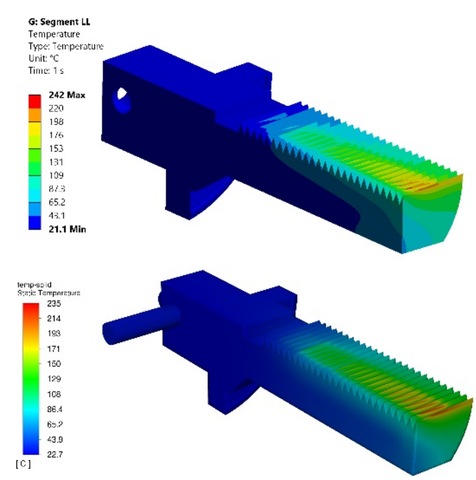

Figure 1: Temperature distribution in °C, from a): mechanical thermal model (top) and b): CFD model (bottom).

The adiabatic boundary condition was applied on the horizontal cutting face, as heat transfer between the upper and lower parts of the absorber is negligible. On the vertical section face, a convective boundary condition was applied to simulate the heat transfer to the colder, cut portion of the absorber jaw. Further simplification includes uniform distribution of heat flux on the surfaces. The thermal

† Xinyu.wang@psi.ch

ISBN: 978-3-95450-250-9 ISSN: 2673-5520 doi:10.18429/JACoW-MEDSI2023-WEOBM05

calculation with the sub-model closely represents the temperature distribution in the global model.

Figure 1a) shows the temperature distribution on the absorber body, calculated from thermal analysis with a heat transfer coefficient of 15 kW/(m^{2}K) and a constant water temperature of 25 °C. Fig. 1b) is calculated from CFD analysis with an inlet water temperature of 25 °C and a velocity of 1.5 m/s. The outlet water temperature is calculated to be 30.3 °C. The maximum temperature from mechanical thermal analysis is slightly higher than that from CFD calculation by 3%. This verifies the accuracy of cooling parameter in the thermal model.

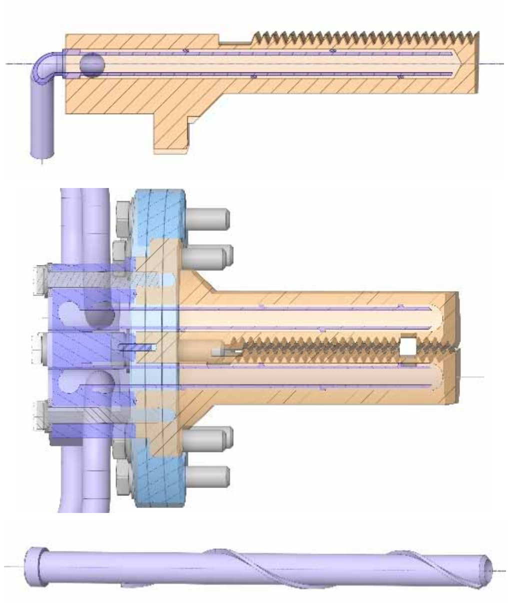

Figure 2: Cooling water channel, a) CFD model water returns at conical end (top), b) Cross section of prototype absorber, water channel with spherical end (middle), c) water pipe with integrated guide (bottom).

The pressure drop in one channel from CFD calculation is 11.5 kPa, primarily due to flow direction reversal at the end of the channel. The maximum velocity reached 3.5 m/s after flow direction reversal. The swirl flow was recognized immediately after flow returned and crossed helical coil on the outside of water tube, which guides the water flow and fix the cooling pipe to the surface of absorber's water channel. The conical shape at the end of water channel is then modified to spherical shape, as shown in Fig. 2b). In addition, the helical coil is replaced by machining the channel guide into stainless steel tube (Fig. 2c)). These design modifications will enable a smooth and stable attachment of water tube and reduce vibrations caused by water flow.

PROTOTYPE ABSORBER

Thermal Test

The prototype absorber made of CuCrZr, was tested in an e-beam welding chamber at PSI mechanical workshop. The absorber was turned vertically, with e-beam coming from the top (Fig. 3). The upper jaw was facing the front and could be observed via a view window of the vacuum chamber. The absorber was fixed by clamping the two inlet stainless steel water pipes. A precisely angle alignment of welding beam to the absorber was difficult. Power was applied on the top surface of the front jaw in the picture (Fig. 3). Rather than distributing the power across the teeth of both jaws, it was concentrated on the side wall of a single jaw. In addition, the water velocity was low due to restrictions from the chiller. While we did not replicate the exact conditions with synchrotron radiation, this test provided valuable information about the cooling effect and was used for comparison with simulations.

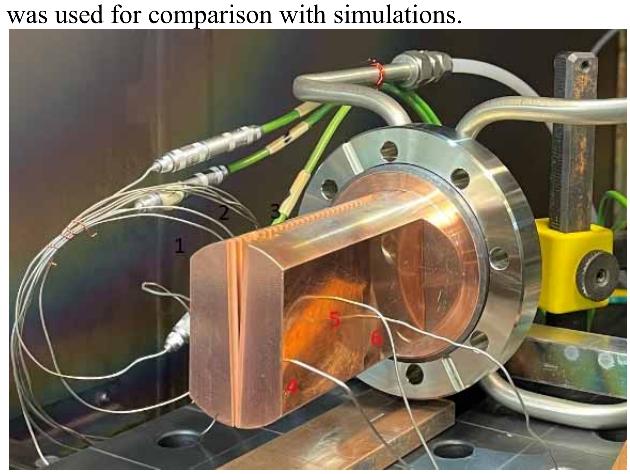

Figure 3: Thermal test in e-beam welding chamber on a prototype absorber.

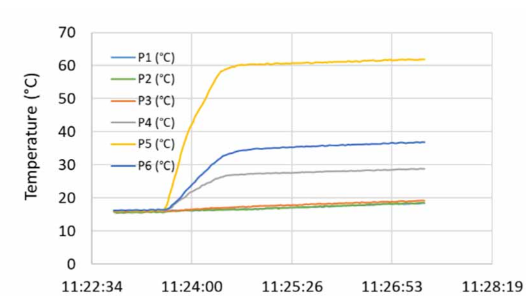

Figure 4: Temperature at absorber body with heat power 2790 W and flow rate 6.2 l/min.

From a calibration measurement, 75% of incident e-beam power was transmitted to heat power. The inlet and outlet water temperatures and temperatures on the absorber body at six locations were measured.

The measurement was started by shifting the e-beam position at a constant flow rate of 5.2 l/min. At each position, the heating process took several minutes until the temperature stabilized and steady-state heat transfer was achieved (Fig. 4). After reaching the final position, the total flow rate was switched to 6.2 l/min. After reached to the maximum flow rate of 6.7 l/min at the test site, it was reduced to 4.1 l/min. The inlet water pressure was 3.6 bar. The maximum heat power during the test reached 3 kW on the half of absorber, corresponding to 6 kW on a full absorber. No damage was observed in the visual inspection after the test.

ISBN: 978-3-95450-250-9 ISSN: 2673-5520 doi:10.18429/JACoW-MEDSI2023-WEOBM05

Thermal Simulation of the Test

The observed e-beam spot diameter was 10 mm. As the exact power density distribution of electron beam is unknown, calculations with different beam sizes have been performed to investigate their influence on the temperature measurement. It was found that by reducing the beam size from 10 mm to 6 mm, which corresponds to a reduction of projection area from 82 mm^2 to 31 mm^2, the maximum temperature on the absorber body increased significantly from 710 °C to 1080 °C. The hotspot temperature at the beam footprint was resulted from the test conditions in the welding chamber, where concentrated power was applied, and it did not match the real conditions in the storage ring. Thermal sensors were inserted through holes to surfaces very close to water channel. From thermal calculations, temperatures at these positons were independent of beam spot size (ΔT<0.1 °C). Therefore, the uncertainty in the power density of the e-beam has no impact on the temperature measurement. In the thermal calculation, the heat power of 2790 W was applied with a 6 mm beam, corresponding to 90.6 W/mm^2 on the projection area.

Figure 5 shows the thermal model. 1D fluid elements were used to simulate the water flow, which was simplified as straight flow. With a total flow rate at 6.7 l/min for example, the cooling water from the heated jaw was heated up by 11 °C from the measurement, close to the estimated value of 12 °C. The water temperature increase, however, was not equal for each channel. While the water temperature in the lowest channel away from the beam spot increased only slightly, it was heated up by 27 °C in the channel closest to the beam spot, as suggested in the calculation. Increased water temperature is able to be considered with 1D fluid elements in the convective heat transfer modeling, enables the temperature calculation with improved accuracy. Where the outlet water temperature increase is high, for example, more than 10 °C, it is advantageous to consider the use of fluid elements.

With a heat transfer coefficient of 15.5 kW/(m^{2}K) for flow rate 6.7 l/min, good correlation between calculation and measurement temperatures was achieved. According to Dittus-Boelter correlation, the heat transfer coefficient h is related to fluid speed v by: $h \sim v^{0.8}$ for turbulence water flow. The heat transfer coefficients for other flow rates were calculated with this relationship, as displayed in Fig. 6.

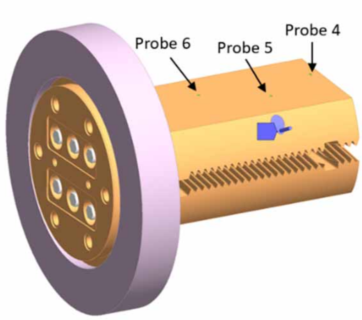

Figure 5: Thermal model, water flow is modelled as straight 1D fluid element.

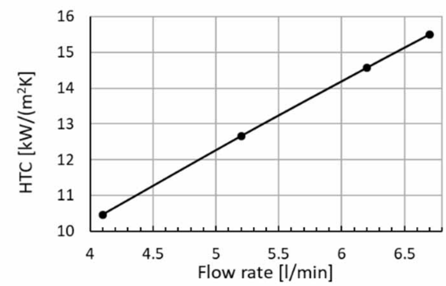

Figure 6: Teat transfer coefficient (HTC) versus flow rate.

Figure 7 displays the measured and calculated temperatures at thermal sensors 4, 5 and 6 on the heated jaw. Temperatures measured by sensors 1 to 3 was only slightly higher than the inlet water temperature. Probe 5 was the closest one to the beam spot, and the highest temperature was measured there. Probe 6 was closer to the beam spot than probe 4 and had a higher temperature.

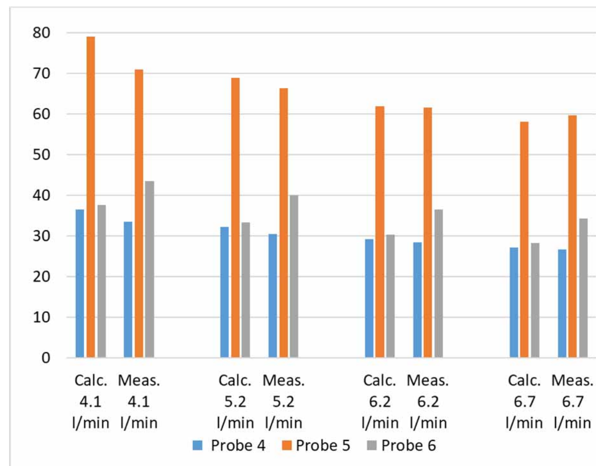

Figure 7: Temperature [°C] of thermal sensors 4, 5 and 6, from calculation and measurement and with different flow rates.

Because a very high power density was assumed in the simulation, the temperature on the water channel surface was calculated to be above 280 °C. This significantly exceeds the water saturation temperature of 140 °C at 3.6 bar [8], and phase transition to vapor is expected. Once phase transition is initiated, the mechanical thermal model is no longer valid for predicting local temperature. Thermal modelling in this calculation, however, is found to be useful for predicting temperature distribution on absorber body in correlation with flow rate in the range of this test. The water velocity in the thermal test reached up to 0.6 m/s, which was well below the designated water velocity for operation at 1.5 m/s. Nonetheless, a significant amount of heat transfer was achieved with flow boiling. The measurement shows that the prototype absorber is capable of withstanding a heat load of 3 kW on the half of absorber in a stable steady-state thermal condition.

ISBN: 978-3-95450-250-9 ISSN: 2673-5520 doi:10.18429/JACoW-MEDSI2023-WEOBM05

ABSORBER SIMULATIONS

Absorber Design

For a total power of 7 kW from the 5 T superconducting magnets Glidcop® AL-15 alloy, due to its high thermal conductivity and material strength, must be used. To sufficiently spread the SR power, the absorber has two jaws with interleaved flat teeth and intermediate grooves. As a consequence of the small opening angle of only 2 degrees, the vertical electron beam orbit offset is limited within +/-250 µm. The first absorber has a window opening and absorbs 5.9 kW of power. The rest of the initial 7 kW was sent to a second absorber a few meters downstream, which can be transversally aligned for fine adjustment of pointing direction.

In the manufacturing process, all components, including the jaws, flange, water distributor, and water pipes, are assembled and brazed together in a single operation. After the manufacturing process, quality assurance tests are conducted. Since the cost of the CuCrZr and Glidcop absorber versions were comparable, it was decided to choose Glidcop for all absorbers.

Thermal-Mechanical Models

Power density distributions on absorber surfaces has been calculated from SYNRAD simulation [3]. In thermal mechanical calculations with ANSYS Workbench, spatial heat power density distribution was defined as surface heat flux using APDL script. Due to the large number of faces, a MATLAB program was used to generate APDL script from SYNRAD output power data. It also converted the data into the desired format for ANSYS solver. This approach enabled fast and efficient data transfer from SYNRAD to ANSYS.

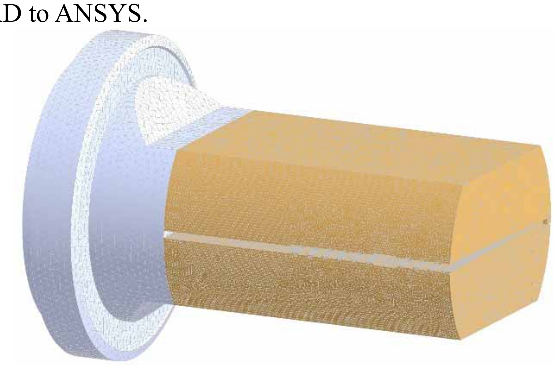

Figure 8: Finite element model of absorber.

To minimize the mapping error on surfaces with high power density, a mesh seed size of 0.2 mm was chosen, which was smaller than the SYNRAD mesh size.

For the remaining irradiated surfaces, the mesh seed size was 0.8 mm, while the general mesh size of the model was 2 mm. The finite element model consisted of a total of 3 million nodes and 2 million elements (Fig. 8).

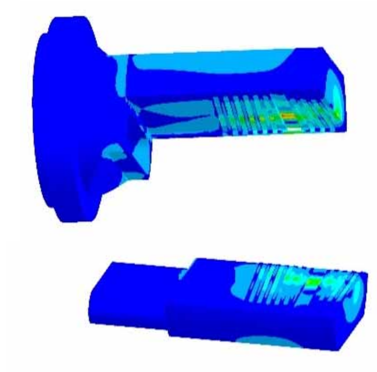

Figure 9: Thermal stress of absorber.

In the finite element analysis, stress, thermal deformation and temperature of absorber were calculated and verified against design criteria (Fig. 9). The maximal temperature on absorber surface was below 300°C and maximal thermal stress was about 200 N/mm^2. The maximum strain was 0.16% and below 0.2% for 10^5 heat loading cycles. The maximal cooling water temperature was limited to 160°C, below the water boiling temperature at 6 bar.

CONCLUSIONS

Comparison of the mechanical thermal calculation with a Fluent CFD simulation shows that the thermal model is capable of simulating the water-cooled absorber under specified heat load. When the heat load is high and water temperature increases significantly, 1D fluid elements may be used to account for heat transfer from the solid with increased water temperatures. For extreme heat loads involving phase transition, CFD simulation is necessary.

In a prototype thermal test, the temperatures of the absorber and cooling water were measured and compared against calculated values. The heat power in the test was much more concentrated, and the water flower was lower than in the real situation with synchrotron radiation. The absorber withstood the 3 kW power on a single jaw without visible damage. The test results validate the absorber's ability to dissipate the specified heat load and the cooling water's capacity to remove the heat. Furthermore, the final calculation verifies that the absorber temperature and stress meet the design requirements.

ACKNOWLEDGEMENTS

The authors kindly acknowledge Demian Lauper from CADFEM for his consultancy in CFD modelling.

REFERENCES

[1] H. Braun *et al.*, "SLS 2.0 storage ring. Technical design report", Paul Scherrer Institut, Villigen, Switzerland (PSI Bericht, Rep. No.: 21-02).

[2] R. Ganter *et al.*, "SLS 2.0 Vacuum components design", in *Proc. IPAC'23*, Venice, Italy, 2023, pp. 2726-2729. doi:10.18429/JACoW-IPAC-23-THPA147

[3] C. Rosenberg *et al.,* "SLS 2.0 Crotch absorbers design", in *Proc. IPAC'23,* Venice, Italy, 2023, pp. 2730-2733. doi:10.18429/JACoW-IPAC-23-THPA148

ISBN: 978-3-95450-250-9 ISSN: 2673-5520 doi:10.18429/JACoW-MEDSI2023-WEOBM05

[4] F. Thomas *et al.*, “X-Ray Absorber Design and Calculations for the EBS Storage Ring”, in *Proc. MEDSI'16*, Barcelona, Spain, Sep. 2016, pp. 257-261. doi:10.18429/JACoW-MEDSI2016-WEAA02

[5] M. Quispe, “Development of the Crotch Absorbers for ALBA Storage Ring” in *Proc. MEDSI’08*, Canada.

[6] F. A. DePaola, C. Amundsen, and S. K. Sharma, “Manufacturing of Photon Beam-Intercepting Components from Cu-CrZr”, in *Proc. MEDSI'16*, Barcelona, Spain, Sep. 2016, pp. 233-235. doi:10.18429/JACoW-MEDSI2016-TUPE31

[7] D. Lauper, “CHT Simulation eines Kühlkanals”, CADFEM Technical Report CON-20-PAU-001_TB1, 2000.

[8] W. Wagner *et al.,* “D2.1 Properties of water and steam”, in *VDI Heat Atlas,* Springer, Berlin, Heidelberg, Apr. 2016. doi:10.1007/978-3-540-77877-6_11

ISBN: 978-3-95450-250-9 ISSN: 2673-5520 doi:10.18429/JACoW-MEDSI2023-WEOBM07

DESIGN, MODELING AND ANALYSIS OF A NOVEL PIEZOACTUATED XY NANOPOSITIONER SUPPORTING BEAMLINE OPTICAL SCANNING

Lingfei Wang*, Guangcai Chang, Zongyang Yue, Lu Zhang, Shanzhi Tang
Institute of High Energy Physics, Beijing, P. R. China

Abstract

In recent years, with the advancement of X-ray optics technology, the spot size of synchrotron beamlines has been reduced to 10nm or even smaller. The reduction in spot size and the emergence of ultra-bright synchrotron sources necessitate higher stability, resolution, and faster scanning speeds for positioning systems. This paper presents the design, analysis, and simulation of an XY piezoelectric driven nanopositioning platform that supports high-precision optical scanning systems. To achieve fast and highly precise motion under the load of an optical system, a design scheme based on a hollow structure with flexible amplification and guiding mechanisms is proposed. This scheme increases displacement output while minimizing coupling displacement to ensure a high natural frequency. The rationality of this platform design is verified through modeling and finite element simulation.

INTRODUCTION

The High Energy Photon Source (HEPS) is a new generation light source that offers enhanced brightness and performance capabilities. The hard x nanoprobe beamline is primarily utilized for nanoscale scientific research. The minimum spot size can be less than 10 nm. Owing to the limitations inherent in conventional stepper motors, piezoelectric actuators have emerged as the preferred choice in this field, offering advantages such as exceptional positioning accuracy, rapid response times, compact dimensions, and lightweight construction.

The piezoelectric actuators utilized in synchrotron radiation light sources can be broadly categorized into two groups. One category encompasses the piezoelectric stick-slip actuators, which operate based on the principle of frictional inertia [1, 2]. These actuators are predominantly employed for large-scale position adjustments. One is the direct drive piezoelectric scanning platform [3–5], which is mostly used for sample scanning. This paper introduces an XY scanning platform specifically designed for nano-scanning experiments conducted at light sources. Subsequent chapters will provide detailed explanations on the structural design, static modeling, and simulation analysis of the XY scanning platform.

DESIGN OF THE MECHANICAL STRUCTURE

The schematic diagram of the nano-positioning platform driven by a piezoelectric stack is illustrated in Fig. 1. The nano-positioning platform features a symmetrical structure, comprising a bridge amplifying mechanism, two sets of guiding mechanisms, a piezoelectric stack, and a central moving stage. The piezoelectric stack is integrated into the bridge amplifying mechanism through a preload bolt, while the end of the bridge mechanism is connected to both the base and central moving stage via two sets of guiding mechanisms, ensuring optimal platform stiffness. The central moving stage adopts a hollow structure design with screw holes at the four corners, which facilitates scanning experiments and the installation of position feedback lenses.

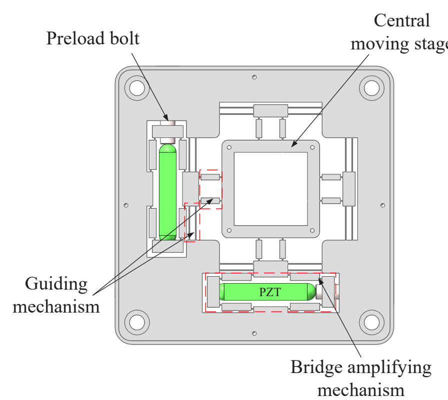

Figure 1: Schematic diagram of the XY positioning platform.

MODELING AND ANALYSIS

The amplifying mechanism analyzed in this paper is a planar mechanism, thus only the deformation of flexible hinges within the plane needs to be considered. The model diagram of the prismatic beam hinge is illustrated in Fig. 2. The thickness, width and length of the hinge are expressed by h, t_b and l_b, the loads on the prismatic beam flexure hinge are F_{xi}, F_{yi} and M_{zi}. and the flexibility matrix of the prismatic beam hinge can be obtained by considering it as a cantilever beam.

The expression of the flexibility matrix of the prismatic beam hinge [6] is as follows:

$$\begin{bmatrix}\delta x\\ \delta y\\ \delta\theta\end{bmatrix}=\begin{bmatrix}c_{11}&c_{12}&c_{13}\\ c_{21}&c_{22}&c_{23}\\ c_{31}&c_{32}&c_{33}\end{bmatrix}\begin{bmatrix}F_{xi}\\ F_{yi}\\ M_{zi}\end{bmatrix} \tag{1}$$

$$\begin{bmatrix}c_{11}&c_{12}&c_{13}\\ c_{21}&c_{22}&c_{23}\\ c_{31}&c_{32}&c_{33}\end{bmatrix}=\begin{bmatrix}\frac{l_b}{Eht_b}&0&0\\ 0&\frac{4l_b^3}{3Eht_b^3}+\frac{l_b}{Ght_b}&\frac{6l_b^2}{Eht_b^3}\\ 0&\frac{6l_b^2}{Eht_b^3}&\frac{12l_b}{Eht_b^3}\end{bmatrix} \tag{2}$$

* wanglf@ihep.ac.cn

ISBN: 978-3-95450-250-9 ISSN: 2673-5520 doi:10.18429/JACoW-MEDSI2023-WEOBM07

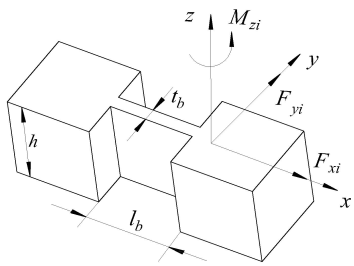

Figure 2: Prismatic beam hinge.

The static analysis of the bridge amplifier mechanism is further conducted. Due to the inherent symmetry and identical parameter sizes of each prismatic beam hinge in the bridge mechanism, only one-quarter of its structure needs to be modeled and analyzed.

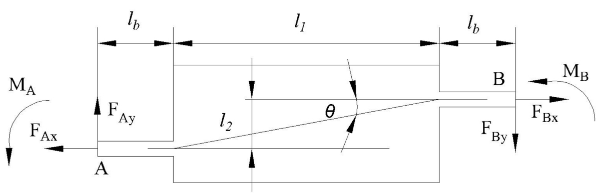

Figure 3: Force condition.

According to the Euler-Bernoulli theory, the torque acting at point A or point B is equivalent, and the stress of the bridge mechanism can be determined based on the stress equilibrium conditions.

$$F_{Ax} = F_{Bx} = F_x = \frac{F_{pzt}}{2} \tag{3}$$

$$F_{Ay} = F_{By} = F_y = \frac{F_s}{2} \tag{4}$$

$$M_A = M_B = M = \frac{F_x l_2 - F_y l_1}{2} \tag{5}$$

In the above equations, F_{pzt} and F_s are respectively the input force and the reaction force of the end load of the bridge mechanism.

The prismatic beam hinge shares identical force conditions and dimensions, experiencing equivalent deformation. By substituting Eqs. (3)-(5) into Eq. (2), its deformation can be calculated.

$$\Delta x = c_{11} F_x w \tag{6}$$

$$\Delta y = c_{22} F_y + c_{23} M \tag{7}$$

$$\Delta \theta = c_{32} F_y + c_{33} M \tag{8}$$

The stress analysis diagram of the bridge mechanism in Fig. 3 reveals that the deformation of a single bridge arm is attributed to the flexible hinge's deformation and the rotation of the bridge arm. The expressions for its input displacement ΔX and output displacement ΔY are as follows:

$$\Delta X = 2\Delta x + l_2 \Delta \theta \tag{9}$$

$$\Delta Y = 2\Delta y + l_1 \Delta \theta \tag{10}$$

The input and output displacements of the bridge mechanism are determined by substituting Eqs. (8)-(10) into the aforementioned equations.

$$\Delta X = (c_{11} + \frac{l_2^2 c_{33}}{4}) F_{pzt} + (\frac{l_2 c_{32}}{2} - \frac{l_2 l_1 c_{33}}{4}) F_s \tag{11}$$

$$\begin{aligned}\Delta Y =& (\frac{l_2 c_{23}}{2} + \frac{l_1 l_2 c_{33}}{4}) F_{pzt} + (c_{22} + \frac{l_1 c_{32}}{2} - \\ & \frac{l_1 c_{23}}{2} - \frac{l_1^2 c_{33}}{4}) F_s\end{aligned} \tag{12}$$

Reformulate the flexibility matrix of the prismatic beam hinge in Eq. (3) and incorporate it into the aforementioned equation, thereby deriving the displacement amplification ratio of the bridge amplifier mechanism.

$$R_a = \frac{9 l_2 (l_b + l_1) F_{pzt} + (4 l_b^2 + 6 t_b^2 (1 + u) - 9 l_1^2) F_s}{3 (t_b^2 + 3 l_2^2) F_{pzt} + 9 l_2 (l_b - l_1) F_s}, \tag{13}$$

where u is the Poisson ratio of the material. And when there is no external load or the external load is very small, the displacement amplification ratio of the bridge mechanism can be regarded as a constant R_{a0}:

$$R_{a0} = \frac{3 l_2 (l_b + l_1)}{t_b^2 + 3 l_2^2}. \tag{14}$$

SIMULATED ANALYSIS

The design platform's performance will be further analyzed and the modeling accuracy verified through finite element analysis in this section. The platform structure model and AL7075 material parameters are imported into Workbench.

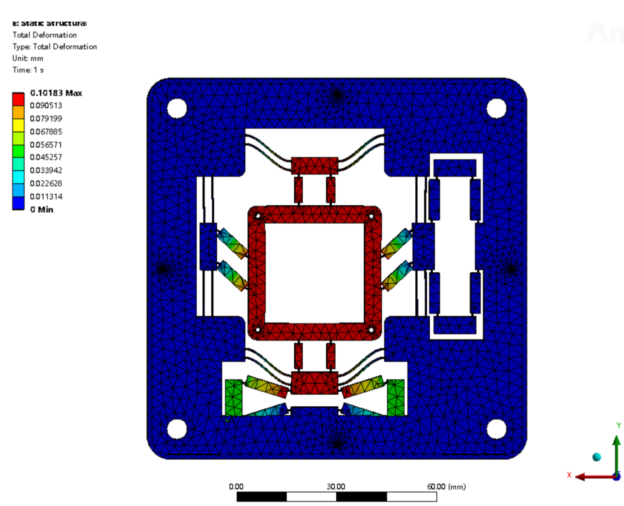

Figure 4: Simulation of displacement amplification ratio.

ISBN: 978-3-95450-250-9 ISSN: 2673-5520 doi:10.18429/JACoW-MEDSI2023-WEOBM07

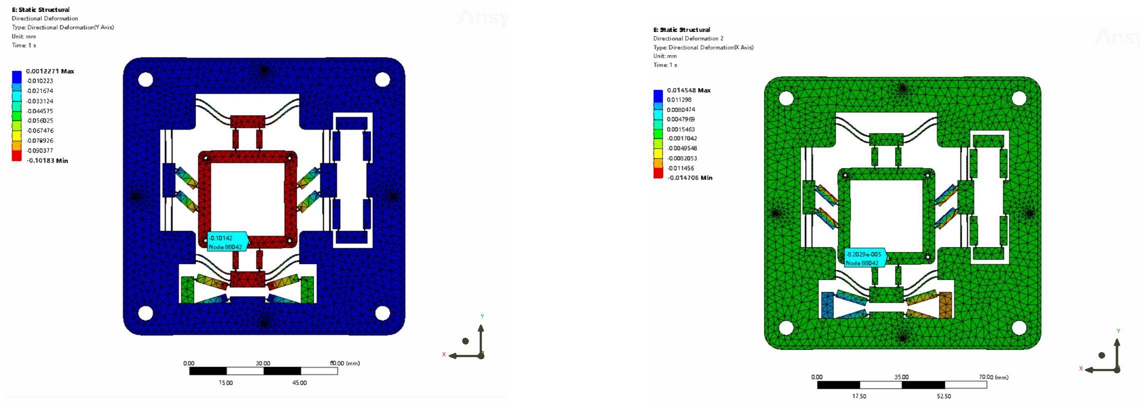

(a) Y-direction displacement (b) X-direction displacement

Figure 5: Simulation of platform decoupling characteristics.

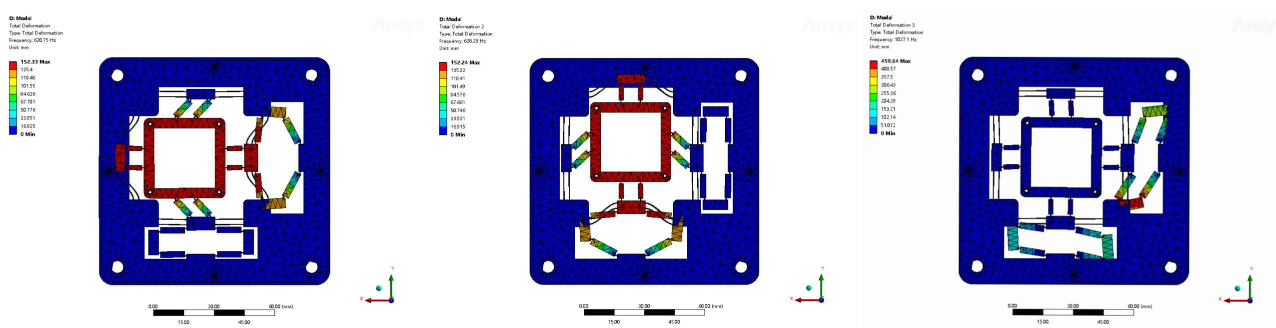

(a) (b) (c)

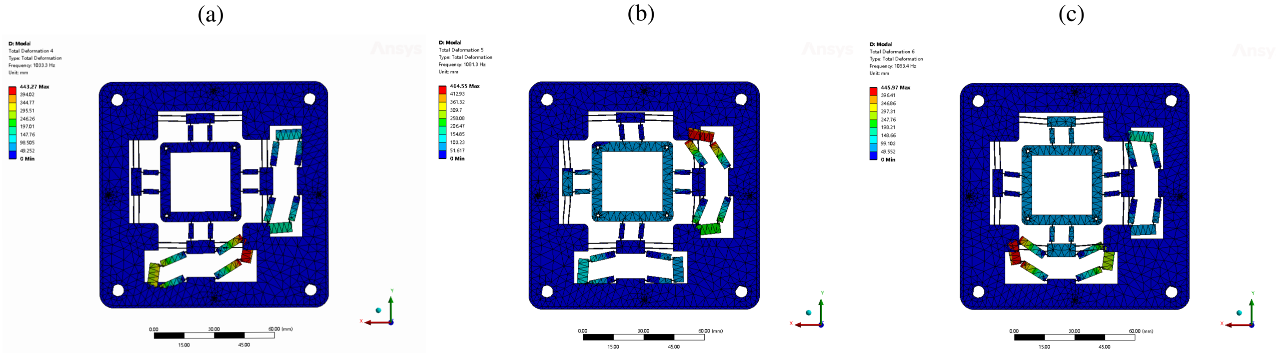

(d) (e) (f)

Figure 6: The first six mode shapes of the platform. (a) The first mode, (b) the second mode, (c) the third mode, (d) the fourth mode, (e) the fifth mode, (f) the sixth mode.

Static Simulation

In the static simulation, a fixed constraint is applied to the fixed hole positions at the four corners of the platform. The input displacements of 10 µm are separately applied to both inputs of the bridge amplification mechanism in order to obtain the output displacement of the platform, as depicted in Fig. 4. The simulation results demonstrate that the terminal output displacement of the platform measures 101.42 µm, with a corresponding displacement amplification ratio reaching up to 10.142.

Furthermore, it is imperative to conduct an analysis on the decoupling characteristics of the platform and separately compare its output displacements in the y-direction and x-direction under the aforementioned conditions, as depicted in Fig. 5. The results reveal that the platform exhibits an output displacement of 101.42 µm in the y-direction, while only 0.08 µm in the x-direction. Consequently, a coupling error of merely 0.07 % is observed, indicating a remarkable decoupling capability possessed by this platform.

Modal Analysis

The modal characteristics of the flexible mechanism significantly influence the dynamic behavior of the entire system and impact the tracking control performance. Therefore, a modal analysis of the platform is conducted in this section. As illustrated in Fig. 6, the first six modes of the platform are presented. Due to the symmetrical structure of the platform,

ISBN: 978-3-95450-250-9 ISSN: 2673-5520 doi:10.18429/JACoW-MEDSI2023-WEOBM07

the modes manifest in pairs. The first six modes correspond to 620.7 Hz, 628.2 Hz, 1027.1 Hz, 1033.3 Hz, 1081.3 Hz, and 1083.4 Hz. Consequently, the platform exhibits remarkable dynamic characteristics.

Stress Analysis

Ensuring a large output displacement while maintaining the stress condition of the platform is crucial. In this section, the maximum stress of the platform is simulated. As illustrated from the simulation results presented in Fig. 7, the maximum stress occurs at the connecting flexible hinge of the inner guiding mechanism of the platform. The maximum stress of the platform is 108.66 MPa, which is significantly lower than the material's yield strength of 455 MPa.

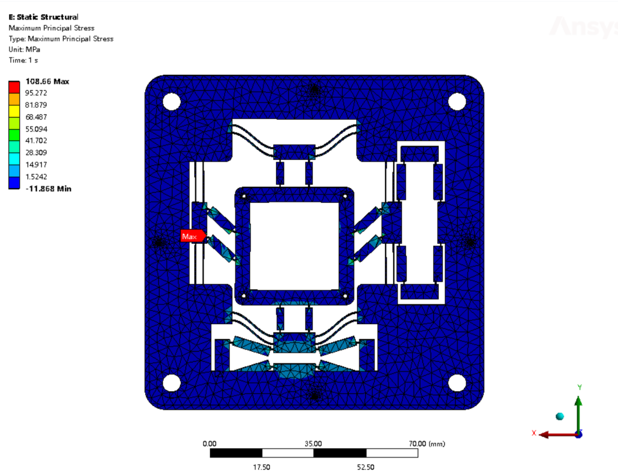

Figure 7: Maximum stress of the platform.

FUTURE WORK

After executing the mechanical design, modeling, and ANSYS simulation of the XY scanning platform, we shall proceed to fabricate the platform, construct a real-time control system with a voltage amplifier and an NI controller, and implement a high-precision, high-dynamic rapid closed-loop control of the platform using a laser interferometer as a sensor.

CONCLUSION

In this paper, we propose an XY piezoelectric scanning platform for synchrotron radiation light source, introduce the structure and composition of the platform, and clarify its working principle. The amplification ratio of the bridge amplifier mechanism is analyzed via the static model, and further validated by finite element simulation.The results indicate that the platform exhibits an amplification ratio surpassing 10. The implementation of two sets of guiding mechanisms enables the platform to exhibit a high degree of decoupling. The overall symmetry and compact structure design of the platform also ensure its excellent dynamic characteristics, with the first-order natural frequency reaching up to 620 Hz.

REFERENCES

[1] E. Nazaretski *et al.*, "Design and performance of an X-ray scanning microscope at the Hard X-ray Nanoprobe beamline of NSLS-II", *J. Synchrotron Radiat.*, vol. 24, no. 6, pp. 1113-1119, 2017. doi:10.1107/S1600577517011183

[2] X. Chen *et al.*, "Quantitative microstructural imaging by scanning Laue x-ray micro-and nanodiffraction", *MRS Bulletin*, vol. 41, no. 6, pp. 445-453, 2016. doi:10.1557/mrs.2016.97

[3] C.G. Schroer *et al.*, "Hard X-ray nanoprobe at beamline P06 at PETRA III", *Nucl. Instrum. Methods Phys. Res., Sect. A*, vol. 616, no. 2-3, pp. 93-97, 2010. doi:10.1016/j.nima.2009.10.094

[4] J.J. Deng *et al.*, "The velociprobe: An ultrafast hard x-ray nanoprobe for high-resolution ptychographic imaging", *Rev. Sci. Instrum.*, vol. 90, no. 8, p. 083701, 2019. doi:10.1063/1.5103173

[5] G. Martínez-Criado *et al.*, "ID16B: a hard X-ray nanoprobe beamline at the ESRF for nano-analysis", *J. Synchrotron Radiat.*, vol. 23, no. 1, pp. 344-352, 2016. doi:10.1107/S1600577515019839

[6] Y. Koseki *et al.*, "Kinematic analysis of a translational 3-d.o.f. micro-parallel mechanism using the matrix method", *Adv. Rob.*, vol. 16, no. 3, pp. 251-264, 2002. doi:10.1163/156855302760121927

ISBN: 978-3-95450-250-9 ISSN: 2673-5520 doi:10.18429/JACoW-MEDSI2023-WEPPP002

THE STATUS OF THE HIGH-DYNAMIC DCM-Lite FOR SIRIUS/LNLS

G. S. de Albuquerque*, T. R. S. Soares, J.P. S. Furtado, N. P. Hara, M. Saveri Silva
Brazilian Synchrotron Light Laboratory, LNLS, Campinas, Brazil

Abstract

Two new High-Dynamic Double Crystal Monochromators (HD-DCM-Lite) are under installation for QUATI (superbend) and SAPUCAIA (undulator) beamlines at Sirius. The HD-DCM-Lite portrays an updated version of Sirius LNLS HD-DCMs not only in terms of being a lighter equipment for sinusoidal scans speeds with even higher stability goals, but also bringing forward greater robustness for Sirius monochromators projects. It takes advantage of the experience gained from assembly and operation of the previous versions during the last years considering several work fronts, from the mechanics of the bench and cooling systems to FMEA, alignment procedures and control upgrades. In this work, those challenges are depicted, and first offline results regarding thermal and dynamical aspects are presented.

INTRODUCTION

In recent years, LNLS has successfully developed and operated a cutting-edge high dynamic double crystal monochromator (HD-DCM) tailored for 4th generation light sources, representing a significant leap forward in terms of mechanical design and control. This innovation has yielded a state-of-the-art product, distinguished by its stability, both for fixed-energy and scan work [1–3]. The success of the first units in MANACA and EMA beamlines has driven the design of two new units, containing improvements designed [4] and assembled entirely by the LNLS team. Such enhancements focused on enabling high-speed sinusoidal scans capabilities [5] as required by QUATI [6], adapting to the energy range of the new beamlines (QUATI and SAPUCAIA), increasing stiffness, implementing control and FPGA optimizations [7], and applying Design for Manufacturing and assembly (DFMA) techniques to minimize the efforts required during mounting and offline commissioning phases.

Figure 1 shows the complete system's in-vacuum parts, highlighting its subcomponents, namely: the granite bench (GRA) (1); the goniometers rotary stages (ROT) (2) with their cooling systems; the goniometer frame (GOF) (3) for the crystal module mounting; the first crystals (CR1) (6), Si(311) and Si(111), which are fixed on the Metrology Frame 1 (MF1) (5), where the interferometer mirrors (IFM) are placed; the Auxiliar Frame 1 (AF1) (4), supporting the MF1; and the ShortStroke (SHS) (8), for mounting the second crystals (CR2) (7), elastically connected to the Short Stroke Frame (SSF) (9). The lower image offers an upstream view of the monochromator, showcasing the Upstream Mask (10) and the Cryogenic Pump (11). For a more detailed and functional explanation, please refer to [4].

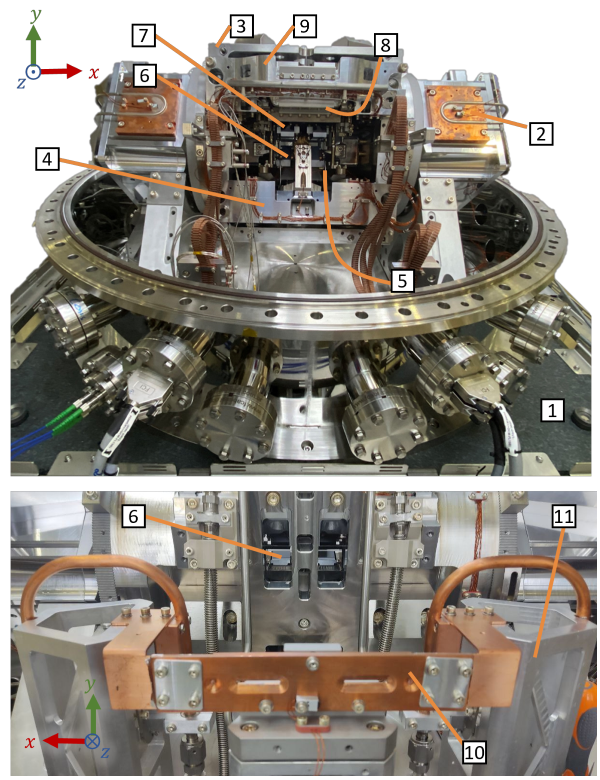

Figure 1: Overview of the assembled SAPUCAIA's HD-DCM-Lite with annotated subparts.

KEY DESIGN MODIFICATIONS

Drawing upon the insights gleaned from the design, assembly, and commissioning of previous HD-DCMs, we have implemented several design updates with the goals of enhancing performance, streamlining the production process, and facilitating the assembly phase. For example, we attest that improvements in the granite base, such as new routing parts, equipment protection components, and features designed to facilitate the placement of feet during assembly, played pivotal roles in the the assembly phase. Specific details regarding some updates will be elaborated upon in the subsequent subsections.

Rotary Stages

To meet the requirements of the QUATI (quick-EXAFS) beamline, a redesign of the rotary stage system was necessary. In addition to doubling the number of actuators to achieve extended scanning speeds, scans of longer duration required the implementation of a specialized thermal solution. This solution took the form of a water cooling system using machined copper components, as illustrated in Figure 1 under item (2).

The use of two mechanically coupled rotary stages intro-

* guilherme.sobral@lnls.br

ISBN: 978-3-95450-250-9 ISSN: 2673-5520 doi:10.18429/JACoW-MEDSI2023-WEPPP002

duces a synchronization challenge. To address this issue, we separately identified each goniometer plant and implemented a closed-loop gantry system to control both. For more comprehensive information, refer to [7].

Furthermore, goniometers are intricate systems that may contain contaminants capable of impeding ultra-high vacuum (UHV) processes. A straightforward method to optimize the overall baking time for the monochromator system involves baking the goniometers separately in a dedicated vacuum chamber while the core components of the system are still in the assembly phase. This approach also helps prevent the rotary stages from contaminating the DCM's vacuum chamber.

Alignment

We replaced the C01 interferometer with the F04 model from SmarAct [8], extending the operating range, simplifying alignment, and enabling in-house self-testing. Previously, this test required specialized equipment and was only feasible during initial assembly. It involves rotating the SHS to its angular End of Stroke (EoS), ensuring clearance in the voice coil's axial direction. Figure 2 displays test results, with ranges up to 15 mrad measured by the interferometer.

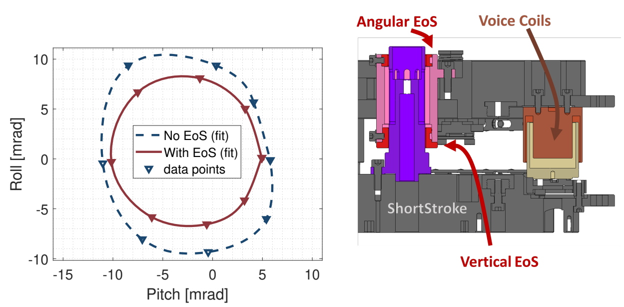

Figure 2: Angular limits on pitch and roll with and without the EoS (left), along with a CAD image (right) illustrating the physical components involved.

However, these new interferometers have uncollimated beams, causing signal quality variations with head-to-mirror distance. System self-adjustment is required at a specific position for optimized readings across the entire vertical range.

Interferometers also presented challenges in crystalline plane alignment. Even from reputable suppliers, silicon crystals often exhibited miscut errors around 2 mrad. Our goal was to achieve total parallelism below 250 µrad to maximize displacement ranges and streamline commissioning. XRD measurements and machining of mounting pads determined the expected parallelism, detailed in Table 1.

LN2 Cooling Circuit

The liquid nitrogen cooling circuit comprises the following subsystems: the cryocooler and its hoses, and, inside the vacuum chamber: the cryogenic pump, the manifold with cooling blocks, and the hoses connecting them. The design of the cryogenic pump remained as originally planned, with

Table 1: Expected Relative Alignment to Correct Mismatch μ Between Inter-Crystalline Planes Before and After Corrections

Crystal pair		**Before** [µrad]		**After** [µrad]	
Beamline	**Orientation**	μ_{pitch}	μ_{roll}	μ_{pitch}	μ_{roll}
SPU	Si(111)	-1185	374	-43	-207
SPU	Si(311)	1849	-875	99	93
QUA	Si(111)	-171	1032	-210	58
QUA	Si(311)	456	56	-206	2

a geometric difference from previous units to facilitate access to other components while retaining the use of a copper tube brazed to standard VCR fittings. The flexible hoses from previous units were retained after fatigue testing and as their torque within a 40° range remained well below actuator limits. The manufacturing process for the manifold, detailed in [9], stands out as the most labor-intensive. The order of certain processes was altered due to the risks associated with concurrent brazing in multiple regions as the final step, including potential leaks or channel blockages. Therefore, it was decided to make the laser welding between capillary tubes and stainless steel inserts the final step in the process.

IN-POSITION AND SCANNING PRELIMINARY RESULTS

The system's identified plant closely mirrors the model, also exhibiting minimal cross-talk, which simplifies the task of developing an appropriate controller [7]. The offline stability results (RMS) are as follows: the gap below 1 nm; pitch and roll around 7 and 8 nrad, respectively; while Bragg is within the encoder count of 191 nrad. Notably, all results meet the designed specifications [5]. The pitch performance, while not consistently reaching the expected 5 nrad yet, still outperforms previous state-of-the-art HD-DCM units. Figure 3 compares HD-DCM-Lite's experimental validation with the HD-DCM, and their respective models for pitch parallelism.

Introducing new challenges in fly-scan perspectives, synchronization is crucial. Doubling the number of Bragg actuators, while simultaneously reducing inertia by a factor of 6, presents a promising outlook for rapid scanning. Figure 3 (b) illustrates an example scan with its respective error in synchronism between rotary stages. While fly-scan results remain preliminary, high amplitude in mid-frequencies and high frequencies with low amplitudes have been reached. Further studies on current control are now in place, in order to optimize the rotary stages torque output, further extending the scanning capabilities.

THERMAL MANAGEMENT

In addition to maintaining components within their respective operating temperature ranges, the primary goal of HD-DCM-Lite's thermal management is to ensure that CR2 maintains the same d-spacing as CR1 (see [4, 10]).

ISBN: 978-3-95450-250-9 ISSN: 2673-5520 doi:10.18429/JACoW-MEDSI2023-WEPPP002

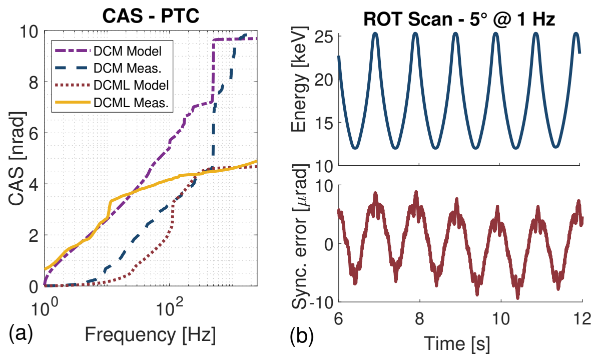

Figure 3: Performance results: (a) Pitch stability Cumulative Amplitude Spectrum (courtesy data from [3]), and (b) Fly-scan example: 5° amplitude at 1 Hz frequency.

Given the HD-DCM's design principle of decoupling the crystal pair's movement, it's crucial to maintain a thermo-mechanical balance. The dynamical model assumes negligible braid stiffness. However, the initial thermal design incorporated smaller copper braids as a safety margin, introducing unwanted stiffness between the first and second crystal modules.

This issue prompted the exploration of two primary approaches for resolution. First, with the physical braids in hand, we sought to experimentally characterize their effective thermal conductivity, enabling more precise estimates of the ideal braid length. Second, by analyzing the dependence of stiffness on the mounting geometry, we aimed to optimize the braid configuration. Figure 4 illustrates a comparison between an 'S' and a 'C' braid configuration.

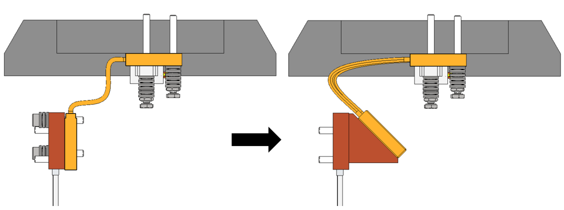

Figure 4: Braid configurations: in 'S', on the left and, 'C', on the right.

As illustrated in the figure, an intermediate triangular copper component was necessary to enable the assembly of the braid's end at the desired angle.

By adopting the 'C' configuration with a 55 mm braid, we achieved both high mechanical decoupling and the ideal temperature for the second crystal. It's crucial to highlight, however, that achieving the desired dynamic outcome heavily relies on the assembly process. This process requires meticulous attention to create specific braid conformations that optimize decoupling while ensuring no components obstruct the beam path. The final temperatures and expected values are detailed in Figure 5.

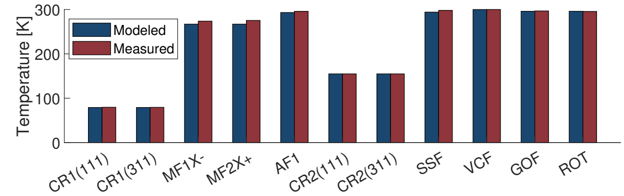

Figure 5: Final temperatures of the system and comparison with expected values.

FMEA

The DCM is pivotal for beamline instrumentation, impacting efficiency and research accuracy. Calibration, alignment, dynamics, and internal conditions must be precise. We employ Failure and Effects Mode Analysis (FMEA) for systematic design fitness evaluation.

Adopting FMEA enhances project quality and reliability via a '7-Step' approach, deepening system understanding, and prioritizing actions based on failure severity, prediction, and detectability. Optimizing this process entails integrating risk assessment with early-stage design. A Baseline FMEA is intended for future projects. Consistent information flow is crucial as complexity increases.

Preventive and detective controls were introduced, including reviews during design, manufacturing, and assembly. Enhanced monitoring and interlocking signals mitigate motion and chamber environment issues.

After multidisciplinary meetings, teams were assigned to implement improvements. The control team safeguards system integrity, while the automation team uses transducer data for environmental monitoring. Optics and Design teams develop tests based on previous experiences to meet specifications. Overall, this initiative fosters better knowledge sharing across teams, enhancing design, documentation, and support.

NEXT STEPS

The SAPUCAIA's unit is currently undergoing offline commissioning and is being prepared for vacuum procedures and it's expected to undergo online commissioning in the start of 2024. Meanwhile, QUATI's HD-DCM-Lite is still finishing in the assembly phase, with offline commissioning expected to start also at the start of 2024.

CONCLUSION

Key design modifications have streamlined assembly and boosted performance. In-position and scanning results meet specifications, showing great promise for fly-scan capabilities. Effective thermal management has been achieved, and FMEA has enhanced system reliability. These advancements demonstrate LNLS's commitment to advancing synchrotron technology.

ISBN: 978-3-95450-250-9 ISSN: 2673-5520 doi:10.18429/JACoW-MEDSI2023-WEPPP002

REFERENCES

[1] R. R. Geraldes *et al.*, "A review on the High-Dynamic Double-Crystal Monochromator for Sirius/LNLS", *J. Phys.: Conf. Ser.*, vol. 2380, no. 1, p. 012 050, 2022. doi:10.1088/1742-6596/2380/1/012050

[2] R. R. Geraldes *et al.*, "Fly-scan-oriented motion analyses and upgraded beamline integration architecture for the High-Dynamic Double-Crystal Monochromator at Sirius/LNLS", *J. Synchrotron Radiat.*, vol. 30, no. 1, pp. 90–110, 2023. doi:10.1107/S1600577522010724

[3] R. R. Geraldes, "The High-Dynamic Double-Crystal Monochromator: a Mechatronic Paradigm Shift in Synchrotron Beamline Instrumentation", Ph.D. thesis, Eindhoven University of Technology, 2023.

[4] A. V. Perna *et al.*, "The HD-DCM-Lite: A High-Dynamic DCM with Extended Scanning Capabilities for Sirius/LNLS Beamlines", in *Proc. MEDSI'20*, Chicago, USA, Jul. 2021, pp. 203–206. doi:10.18429/JACoW-MEDSI2020-TUPC11

[5] G. S. de Albuquerque *et al.*, "The Dynamic Modeling and the Control Architecture of the New High-Dynamic Double-Crystal Monochromator (HD-DCM-Lite) for Sirius/LNLS", in *Proc. ICALEPCS'21*, Shanghai, China, 2022, pp. 619–624. doi:10.18429/JACoW-ICALEPCS2021-WEPV003

[6] S. J. Figueroa *et al.*, "QUATI beamline: QUick x-ray Absorption spectroscopy for TIme and space-resolved experiments at the Brazilian Synchrotron Light Laboratory", *Radiat. Phys. Chem.*, vol. 212, p. 111 198, 2023. doi:10.1016/j.radphyschem.2023.111198

[7] T. R. Silva Soares, J. L. Brito Neto, J. P. S. Furtado, and R. Geraldes, "Dynamical modelling validation and control development for the new High-Dynamic Double-Crystal Monochromator (HD-DCM-Lite) for Sirius/LNLS", presented at ICALEPCS'23, Cape Town, South Africa, 2023, paper TUPDP006, unpublished.

[8] Sensor Heads & Options, https://www.smaract.com/en/picoscale-sensor-heads

[9] M. Saveri Silva, R. L. Parise, and R. Geraldes, "Challenges in the manufacturing of a cryogenic cooling manifold for an X-ray monochromator at Sirius Light Source", in *Proc. 26th Int. Congr. Mech. Eng.*, 2021. doi:10.26678/abcm.cobem2021.cob2021-0370

[10] R. M. Caliari *et al.*, "Studies on Flow-Induced Vibrations for the New High-Dynamics DCM for Sirius", in *Proc. MEDSI'16*, Barcelona, Spain, 2016, pp. 8–11. doi:10.18429/JACoW-MEDSI2016-MOPE02

ISBN: 978-3-95450-250-9 ISSN: 2673-5520 doi:10.18429/JACoW-MEDSI2023-WEPPP004

HIGH HEAT LOAD TRANSFOCATOR FOR THE NEW ID14 ESRF BEAMLINE

Laurent Eybert, Philipp Brumund, Juan Reyes Herrera, Noel Leve
ESRF, Grenoble, France
Miguel Lino Diogo dos Santos, CERN, Geneva, Switzerland

Abstract

X ray refractive lenses (CRL) are powerful in line optics for focusing/collimating x-rays. They offer many advantages such as compactness, a comfortable working distance, robustness, and are suitable for use in a wide range of energy. In the scope of the new nuclear resonance ID14 beamline at ESRF, a new **white beam transfocator** (WBT) was developed. This transfocator benefits from the previous experience of ESRF's transfocator to withstand the high heat load power densities (645 W/mm^2) and total power (405 W) generated by the future CPMU18. A thermal load analysis was carried out to optimize the cooling design. The tight alignment specifications within the same CRL (Compound Refractive Lenses) stack assembly and between different assemblies was achieved thanks a good machining of both lenses unit mechanical assembly and reference V shaped rail. High positioning repeatability of CRLs actuator is assured thanks to an optimized flexor and a good alignment procedure. The transfocator vessel is installed on a granite and on a 4-DOF alignment table.

INTRODUCTION

The mission of new ID14 beamline at ESRF is to carry out nuclear resonance scattering experiments. ID14 have 2 optic hutch (OH1) and (OH2). OH1 is a white beam hutch used for pre-conditioning of the X-ray beam for downstream high resolution optics as high resolution monochromators and a Synchrotron Mossbauer Source installed in OH2.

OH1 LAYOUT

In OH1 a high-heat-load monochromator (HHLM), a **white-beam transfocator** (WBT) and a monochromatic-beam transfocator are installed (see Fig. 1).

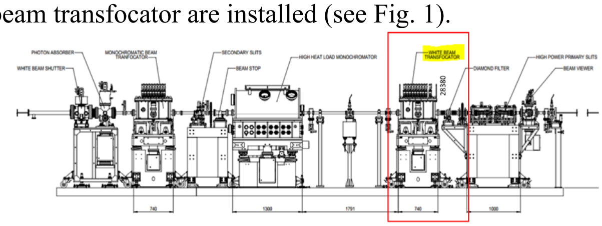

Figure 1: The white beam transfocator is installed in OH1 at 28.5 m from source.

WHITE BEAM TRANSFOCATOR OVERVIEW

The only purpose of the white beam transfocator installed on ID14 is to avoid flux loss by matching the divergence of the collimated beam into the acceptance of the Si(111) reflections used in HHLM. Figure 2 shows the collimation of the beam with 1D lenses.

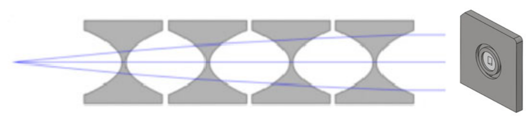

Figure 2: Use of Be CRL to collimate the beam.

Only a moderate, not an ultimate collimation is required to keep effective focusing. Focusing will be done downstream, in experimental hutches using KB mirrors. HHLM works in horizontal scattering plane so WBT collimates beam in horizontal plane only with 1D Beryllium lenses. Exceptions are 2D lenses for very high energies, where 1D lenses with very small radius (0.05) are not available. For the EBS machine, horizontal and vertical divergences are both about 14 µrad.

Table 1: Ω Angular Acceptance of HHLM - ΔΘ Divergence after Collimation [1] (Courtesy A. Chumakov)

Energy [keV]	type	R_A [mm]	N_{CRL}	T [%]	A [mm]	A_{eff} [mm]	$\Delta\theta$ [μrad]	Ω [μrad]	X
14.412	1D	0.50	3	93.6	1.39	1.35	6.8	17.5	0.45
21.541	1D	0.30	5	93.3	1.08	1.05	4.5	11.8	0.32
22.494	1D	0.20	4	94.7	0.88	0.86	3.5	11.3	0.25
23.879	1D	0.20	4	94.8	0.88	0.86	4.7	10.7	0.33
25.614	1D	0.20	5	93.8	0.88	0.86	3.9	10.0	0.28
27.78	1D	0.20	5	96.5	0.88	0.86	5.4	9.2	0.38
35.46	1D	0.20	12	88.0	0.88	0.83	3.6	7.2	0.10
37.13	1D	0.20	12	88.1	0.88	0.83	3.6	6.9	0.17
39.58	1D	0.20	12	88.4	0.88	0.83	3.6	6.5	0.27
67.408	2D	0.05	12	85.0	0.44	0.42	3.6	3.8	0
89.571	2D	0.05	21	76.9	0.44	0.41	3.6	2.9	0

As the Table 1 above shows, the type and number of lenses must be changed as the energy varies. This is the role of the transfocator (see Fig. 3). A maximum of 3 lenses casings are used simultaneously. They are installed next to each other.

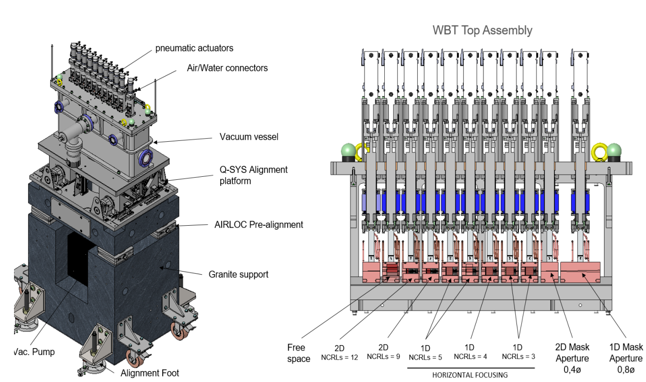

Figure 3: 11 axis water cooled transfocator.

12th Int. Conf. Mech. Eng. Design Synchrotron Radiat. Equip. Instrum. MEDSI2023, Beijing, China JACoW Publishing
ISBN: 978-3-95450-250-9 ISSN: 2673-5520 doi:10.18429/JACoW-MEDSI2023-WEPPP004

HEAT LOAD ANALYSIS

ID14 started operation with the former ID18 source, composed by three ex-vacuum U20/U27 revolver undulators but in future an **EBS-dedicated** single in vacuum Cryogenic Permanent Magnet Undulator (CPMU-18) will be installed. Heat load analysis (see Fig. 4) has been done with the most demanding configuration = CPMU18 undulator.

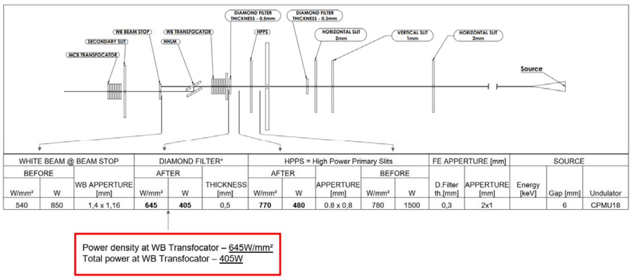

Figure 4: Front End and optical hutch heat loads configuration.

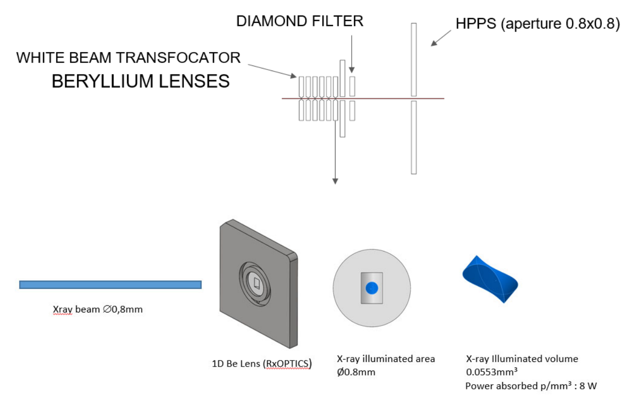

Figure 5: Power absorption at ID14 – Be lens = 8*0.0553= 0.45 W.

Figure 5 illustrates the beam absorption in 1D lens.

To have a reasonable safety margin we decided to add a water cooled 0.5 mm diamond window before the WBT in addition to the one (0.3 mm thick) already installed in the FE (Front End). Then the mechanical stress induced by thermal absorbed power is well below the yield limit of Beryllium (see Fig. 6).

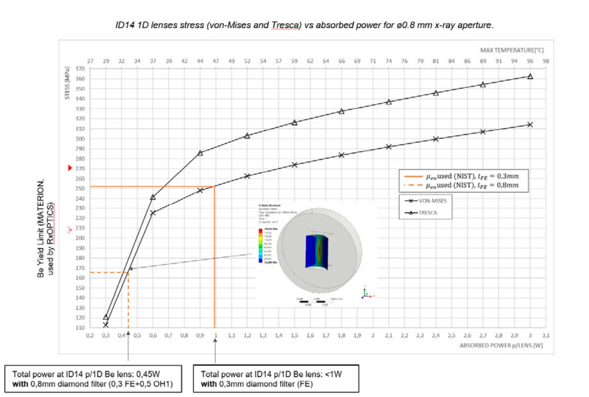

Figure 6: Thermal stress before/after 0.5 mm thick diamond window.

In this configuration and with appropriate thermal interfaces (we use a 0.2 mm thick graphite layer on 3 sides of the lenses to keep one reference side free for positioning and a copper foam layer on the front side of stack assembly) and a good mechanical pressure (we use spring washers to apply 0.85 MPa pressure), the temperatures of the lenses and masks are well below the critical temperature with good safety margins. Unfortunately, Kovar's poor thermal conductivity (17 W·m^{-1}·K^{-1}) limits the thermal cooling performance. Figure 7 shows the mechanical assemby of 1D lens.

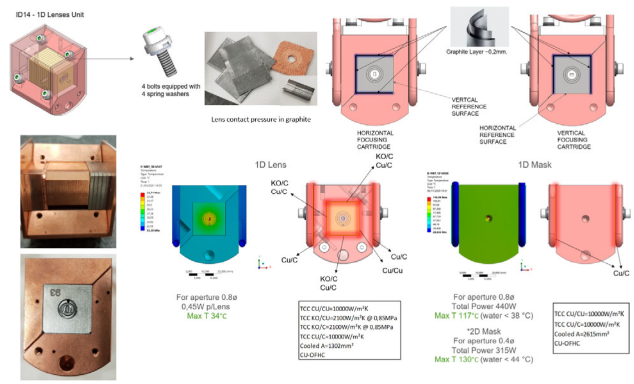

Figure 7: Lenses unit cooling optimization with spacer and thermal interfaces.

ALIGNMENT

In order to achieve optimum performance for focusing/collimating it is necessary to align the optical axes of individual lenses in a stack and between stack assemblies with micro-meter precision. We provide high precision lens casings and pneumatic actuator are used to push these casings on reference V shaped rail.

For 1D lenses, one side is used as reference (vertical or horizontal depending on the direction of the collimation), for 2D lenses the cylinder is pressed on two perpendicular flat surfaces – only half of the cylinder is used as thermal contact.

The copper lens casings are manufactured by wire erosion to a precision of better than 10 µm while straightness and accuracy of the 600 mm long v-rail is better than 3 µm in Y and Z after grinding. All parts have been carefully controlled with high precision three-dimensional measuring machine (see Fig. 8).

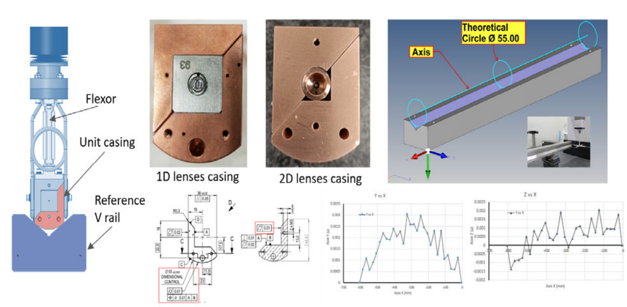

Figure 8: Manufacturing accuracy of 1D/2D casings and reference V rail.

12th Int. Conf. Mech. Eng. Design Synchrotron Radiat. Equip. Instrum. MEDSI2023, Beijing, China JACoW Publishing
ISBN: 978-3-95450-250-9 ISSN: 2673-5520 doi:10.18429/JACoW-MEDSI2023-WEPPP004

The transfocator needs to be aligned in four axes with respect to the X-ray beam : (2 translations Y,Z and 2 rotations ΘY, ΘZ). The motion platform designed by Q-SYS is based on two wedges driven by means of ballscrews with stepper motors and Harmonic drive gear. The platform has to carry 400 kg load and additionally 200 N external force (with offset) – 120 mm due to vacuum bellows. Figure 9 shows the alignment specification of the whole WBT in respect to the beam.

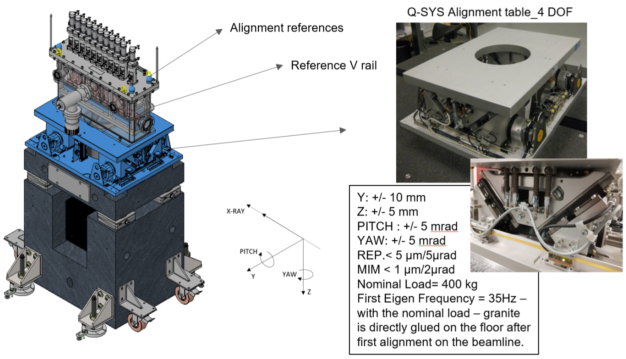

Figure 9: Alignment specifications for WBT (Reference V rail alignment/lenses units) with X-ray.

FLEXOR DESIGN AND REPEATABILITY

A flexor is used to move the lens casing cylinder (∅ 55 mm) in line with the reference V-rail to ensure that the casings are correctly positioned in relation to each other. After a manual pre alignment when the casing is in the operating position (in V rail) the flexor strokes can be limited to ±1 mm in Y (lateral) and ±10 mrad in pitch and yaw. The flexor design (see Fig. 10) below gives a good safety margin (>2).

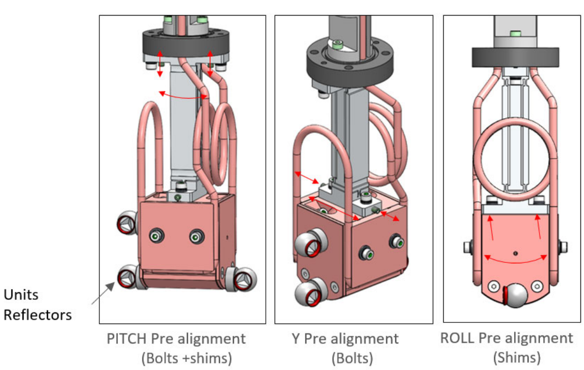

Figure 10: Pre-alignment to limit flexor strokes.

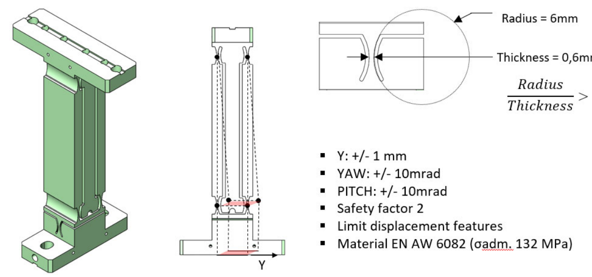

Figure 11: Flexor optimization.

Repeatability of lensing casing has been measured with both laser tracker (thanks to reflectors – see Fig. 11) and micrometers as shown in Fig. 12. Repeatability is better than 1 µm in Y, Z.

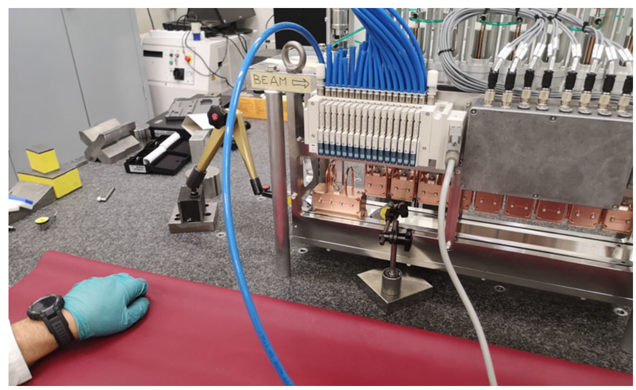

Figure 12: Repeatability measurement.

CONCLUSION

Despite an optimized cooling design of the Be CR lenses we had to insert a 0.5 mm thick diamond window to withstand the high thermal power (generated by the future Cryogenic Permanent Magnet Undulator (CPMU-18). Thanks to high precision machining of mechanical parts (lenses casing, reference positioning rail and flexor) – a compact design – we achieved a high accuracy positioning (<10 µm in one single casing and <20 µm between casings relative to X-ray beam) of cooled CR lenses.

REFERENCES

[1] "Technical Design Report for the Nuclear Resonance Beamline ID14 at the ESRF", ESRF, Grenoble, France, December 18, 2020.

ISBN: 978-3-95450-250-9 ISSN: 2673-5520 doi:10.18429/JACoW-MEDSI2023-WEPPP009

POLAR SYNCROTRON DIFFRACTOMETER

G. Olea, N. Huber, J. Zeeb
HUBER Diffraction GmbH & Co.KG, Rimsting, Germany

Abstract

A new product for research purposes aiming to work in a 4th generation synchrotron facility (APS-U) after its upgradation has been recently developed. POLAR-Dm was conceived on a traditional 6C (C-circles) geometry, maintaining the common kinematic structural principle of the family. With the addition of several interchangeable devices, the multipurpose system is expanding the spectrum of possible investigations, maintaining the precision of setups. Mainly, it consists of two customized sample (S) modules for high-precision versatile sample manipulation and a dovetail detector arm (D) module for manipulating the detector, optics (polar analyzer), slits, etc. An alignment base (Ab) module stable supports the above modules and roughly adjusts the motions towards the incoming X-ray beam. In addition, a planar non actuated manipulator is facilitating the cable management during the work. The kinematic, design and precision concepts applied, together with the obtained test results are all in detail presented.

INTRODUCTION

The advanced synchrotron investigations require not only improved beam characteristics and/or new modern techniques, but dedicated instruments adapted to the specificity of the applications.

Advanced Photon Source (APS) research facility is currently under an upgradation process (APS-U) [1]. Apart from several improved characteristics e.g., emittance, coherence, etc for new / enhanced beam lines, an appreciable number of experimental stations (hutches) are to be developed and/or improved, as well. Several beamlines will be allocated to magnetic materials (MM) group from X-ray Science Division (XRS). After its completion, the 4-ID (POLAR) beam line will investigate the emergent electronic properties (e.g., inhomogeneity) of advanced magnetic and ferroelectric functional materials, relevant to quantum and energy technologies, using spectroscopy and/or X-ray magnetic scattering techniques [2].

A request to develop a dedicated diffractometer has been issued for one of the end stations (G) [3]. The intention was to use a common fife-circle (5C) diffractometer architecture adapted with the geometry for horizontal scattering (Q-range access) for a superconducting magnet (2T) and low vibration for thin films, under extreme conditions - low temperature (cryo) and high pressure (HV) investigations. In addition, adequate support for a vacuum polarizer analyzer and area detector has to be included. The new Dm has to offer not only heavy load/small manipulation capabilities, but (high) precision features, as well [4].

The main features of the final product (prototype) are described below, including most important aspects related to kinematics, design and precision concepts.

POLAR DM

Dm should accommodate with the use of x-ray techniques based on spectroscopic (absorption, polarized dependent resonant) and magnetic (XRMS) scattering principles. A 2T magnet sample (120 kg), sample cells (30 kg) and (15 kg), together with small (200 g) one must be manipulated by the two sample positioning systems. 1D/point (5 kg) detector and the polarized analyzing optics (100 kg) are to be manipulated, as well. The manipulation errors must be inside of the Sphere of Confusion (SoC < 50µm).

Kinematics

Basically, from a kinematic point of view, the chosen Dm (POLAR) architecture belongs to 5C (2D + 3S) class – two (C_i, i = 1,2) for detector(D) and three (C_i, i = 3…5) for the sample (S) actuated circles, respectively [5]. However, as (S) comes with two independent setups called manipulators (S_1, S_2), each of them is composed from another actuated circle $(C_6)_i$, i = 1...2. Thus, the structure became a 6C (2D + 4S). However, there are also another three (3) circles inside of the polar analyzer (C_7 - C_9), so the entire system falls into a multi-circles Dm class.

Mainly, it has two distinct (kinematics) chains (K_D, K_S) supported by another (K_B), Fig. 1. The experimental investigations are based on the corelated motions (positioning) of the two (K_D, K_S) relative to X-ray (incident/scattered) fixed beam, respecting the diffraction law (Bragg).

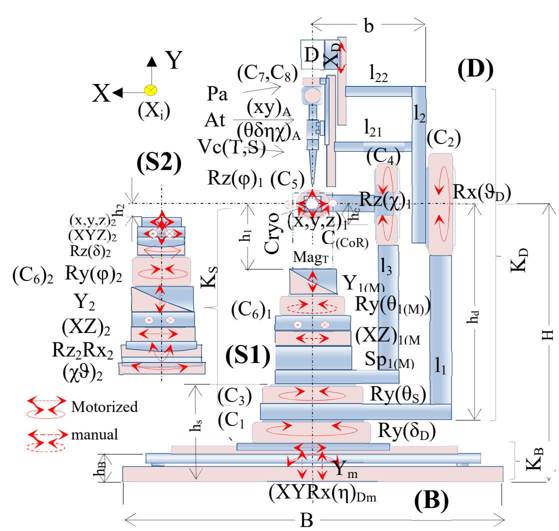

Figure 1: POLAR-Dm kinematics.

The detector (D) manipulator kinematic chain (K_D) mechanism consists of two active rotational joints C_1 (δ_D) and C_2 (ϑ_D) linked together through (l_1). In addition, a dove

ISBN: 978-3-95450-250-9 ISSN: 2673-5520 doi:10.18429/JACoW-MEDSI2023-WEPPP009

tail arm (l_2) supports two linear sliding guides (L_{21}, L_{22}) to accommodate with the use of different detectors and polar analyzer (An) instrument, catching the scattered X-rays. In addition, the polar analyzer mechanism is based on a combination of three orthogonal motions $C_7(\theta_X = \pm 5°)$ / C_8 $(\delta_X = \pm 10°)$, C_9 $(\eta_Z = +30° - 110°)$ and C_{10} $(\chi_Y = \pm 5°)$.

The sample manipulator (S) is composed of two configurations (S1, S2) corresponding to two distinct serial kinematic chain (Ks = 1,2) mechanisms.

In its first configuration (S1) two orthogonal circles $C_4(\theta_M)$ and $C_5(\chi)$ supported by $C_3(\theta_S)$ are forming an opened Euler cradle mechanism ($\chi = \pm 100°$), holding an instrument (cryostat) to move in (XZ = ±2 mm, Y = ±3 mm). The access to the sample (setup, maintenance) is almost entirely free, opening the way for large (and, heavy) load sample manipulations (magnet). In addition, on a strong support (Sp) translational & rotational (manually) driven devices $(X, Y, Z, \theta)_M$ are included. Note: The cryostat tip performs spherical motions around the fixed point (C), called center of rotation (CoR).

In the second configuration (S2), the kinematics consists of several precision positioning devices which are stacked one on the another starting with two (2)-partial rotations $(\chi\vartheta)_2$, following a displacement for all three axis $(XYZ)_2$. On top of them, a high precision device performing full–$Ry(\varphi)_2$ / $(C_6)_2$ and partial - $Rz(\delta)_2$ rotations are carrying a course $(XYZ)_2$ and precision translational devices $(xyz)_2$.

Note: C_3 is a common actuated joint (circle) for both configurations (S1, S2).

An alignment base (B) has to support the above structures, providing stiff and short motions - Y, X = ± 20 mm and $Rx(\eta_{Dm}) = \pm 5°$ for roughly alignment against X-ray. The main Dm motions, together with their range and precision parameters are included in Table 1.

Table 1: POLAR-Dm Basic Motion Parameters

Circles 5C (6C)	Range (°)	Rep.* (″/ µm)	Res.* (″/ µm)	SoC* (µm)
C_1	$(\delta_D = \pm 180)$	8	3.6	15
C_2	$\vartheta_D = -30+180$	0.5	3.6	15
C_3	$\theta_S = \pm 180$	0.5	0.36	0.1
C_4	$(\chi_S)_1 = \pm 100$	8		5
C_5	$(\varphi_S)_1 = \pm 180$	8	3.6	50
$(C_6)_{1/2}$	$(\theta)_1/(\varphi)_2 = \pm 180$	8	0.5/3.6	5/15

* At least (<)

An overview of the most important motorized motions performed is shown in a short simulation video [5].

Note: O-XYZ, is a right-handed set of orthogonal axes with Z (+) along the X-ray beam and Y (+) vertically upwards; O ≡ C (CoR).

Design

A modular approach has been applied in the design process [6], adopting the detector, sample and base manipulation subsystems, as main positioning modules (Pm_i, i = 1,2,3), Fig. 2. Each of them built from a (stacked) combination of several linear/rotational Positioning units $(Pu)_i$.

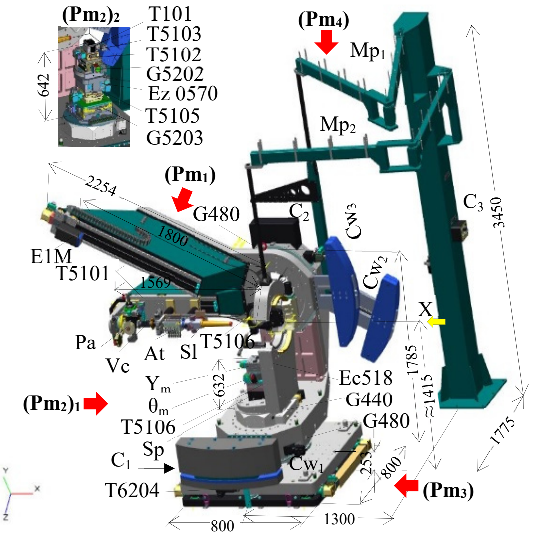

Figure 2: POLAR-Dm CAD layout (3D).

Due to the long arm carrying the necessary detection and auxiliar devices, the detector (D) positioning module (Pm_1) was built (first time) on two similar heavy load precision gonio(s) - G480 with vertical(V) and horizontal(H) axis. They provide the necessary actuation forces (moments) to manipulate: a) detector (Eiger1M/5kg), b) ancillary devices - polar analyzer (Pa/15kg), attenuator (At/3002) and vacuum tube (Vc/12kg) & slit (JJ-Xray/IB-C30-HV) together with their supports (linear stages, etc). The (Pa) has been built on a combination of two gonio - G410A/G409 (XEW2), one linear (T5101/XE) and head (H1005) Pu(s).

Note: Solutions have been applied for the static balance, using counterweight (Cw_i, i = 1…3).

In the first configuration of the sample (S1) the module $(Pm_2)_1$ a dedicated open Euler cradle device (Ec518) based on a combination of two active positioning units (Pu_i, i = 1,2) called Goniometers (Gm) or simply gonio (G) linked together, as described before, is used. The device is completed with a linear translation stage – XYZ (5106/XE), carrying the cryostat (ARS DE-202G/ARS).

Note: The value of reproducibility following the interchanged operation for Ec module must be inside of 50 µm.

In the second configuration (S2) = $(Pm_2)_2$, a high precision goniometer system is built on two gonio segments (G5203/XE), supporting a XYZ translational stage (5105 XE) on which a high speed (and, high precision) air bearing stage (EZ0570) is located. On top of it a (segment) stage (S5202/XE) is supporting a combination of two translational stages (5102&5103/XE) on which the nano positioning(piezo) stage (Tritor101 CAP /JENA) was fixed.

All above Pu(s) for both configurations are moved in rotational motion by a precision gonio (G440/XEW2).

The alignment base (B) module $(Pm)_3$ was designed upon a standard table type (T6204), providing stiff and stabile support (> 1000 kg) for all necessary operations.

An overview of the main features (type and precision) of Pu used is included in Table 2.

ISBN: 978-3-95450-250-9 ISSN: 2673-5520 doi:10.18429/JACoW-MEDSI2023-WEPPP009

Table 2: POLAR-Dm Basic Motion Axis

Axis	Pu	Prec.	Note
$A_1(\delta_D)$	G480	XEW2V	Pm_1
$A_2(\vartheta_D)$	G480	XEW2H	Pm_1
A_3 (θ_S)	G440	XEW2V	$(Pm_2)_{1,2}$
$A_4(\chi_{S1})/A_5$ (φ_{S1})	G518	-	$(Pm_2)_1$(Ec)
$A_6(\theta)_{1M}/A_6(\varphi)_2$	G409/EZ0570	XEW2/-	$(Pm_2)_{1,2}$

As precision was one of the requirements, *modelling and simulations* using Finite Element Analysis (FEA) have been performed iteratively to estimate the deflections and stresses (von Misses), reducing/eliminating them, e.g., (D), (Ec), slides, etc., improving by this their stiffness. (Ec) being one of the critical components, the specific simulations performed are shown below (Fig. 3).

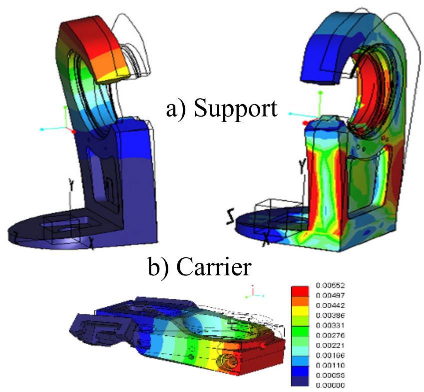

Figure 3: Euler cradle deformation and stresses (FEA).

The control of the actual multi-axis system (Ai, i = 30) has been generally realized, using closed loop – stepping motors (Vexta/ORIENTAL/PK(P)), gears (HUBER) and incremental encoders (Vionics/RENISHAW/RKLC (RES M)). In this respect four power drive (PowerPack) and two driving (SMC9300) boxes have been provided. *Cable management* for a machine with multiple axes is always a challenge. In addition, as in this case, the cables must be directed to the roof electronics, a dedicated module (Pm_4) consisting of two planar manipulators (Mp_1-D, Mp_2-Ec) has been designed. Motor cables are routed to RJ45 jacks and encoders to a DB9 connectors, both at APS-U standard pinned. The connections between wires have been performed through three main (connection) boxes - Cb_i, i = 1…3 (1 = (B) + (S2), 2 = (D) + (Pa) + (At)+(Sl), 3 = Ec). To prevent the crushing hazard, warning stickers have been included, as well. Note: Most of the wires have been chosen to go through (central) holes and/or slip rings.

Prototype

Based on the above design considerations and related documents, the components have been carefully manufactured. The product (prototype) is now in the final step of its assembly, Fig. 4. Attention was given in the machining process for obtaining high quality functional surfaces, respecting the geometrical tolerances, as those in contact with sensitive components e. g., circular/linear guides or measurements bases for instruments. Fine adjustments in the assembly process have been performed mounting the precision components, from the beginning to the end.

After its completion, the prototype will be tested at the factory site from a functional and precision point of view. A factory acceptance test (FAT) report will be issued, before the installation on the indicated premises will be done. All the values of motion and precision required parameters must totally fulfill with the specifications.

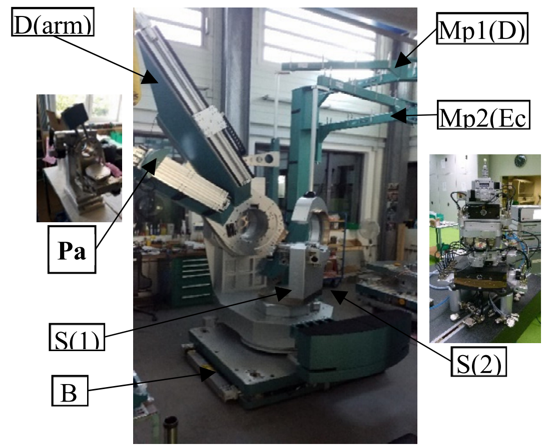

Figure 4: POLAR-Dm Prototype.

CONCLUSION

A new dedicated diffractometer (POLAR-Dm) with flexible capabilities for various X-ray diffraction investigations (XRD) of different magnetic materials able to work in a 4th generation synchrotron facility has been developed. POLAR-Dm has resulted from a successful combination of standard/customized precision components and instruments to use the specific X-ray (magnetic) techniques, under extreme conditions (pressure and temperature), maintaining a high precision manipulation level of both, the heavy and small samples. Mainly, it offers an adequate solution to selective manipulate: a) magnet (2 T) with appreciable load inside of (SoC = 50 µm) and b) smaller loads (30 / 15 / 0.2 kg) inside of (SoC = 15 µm). In this respect, two types of interchangeable devices (Euler, gonio) have been provided with a high rate of reproducibility (< 50 µm). It is expected that due to its specific features, the final product will enhance the investigation capabilities to a new level.

REFERENCES

[1] T. E. Fornek, "Advanced Photon Source Upgrade Project Final Design Report", ANL, USA, APSU-2.01-RPT-003, May 2019.

[2] R. Hettel, "Status of the APS-U Project", in *Proc. IPAC'21*, Campinas, Brazil, May 2021, pp. 7-12. doi:10.18429/JACoW-IPAC2021-MOXA02

[3] J. Strempfer, "4-ID-G Diffractometer", *Statement of Work / APS Upgrade*, ANL, USA, 2020.

[4] J. Strempfer *et al.*, "Possibilities at Polar beamline with APS-U", *J. Physics*, *SRI2021,* 2380, 012038, 2022, pp. 1-7.

[5] HUBER Diffraktionstechnik GmbH, https:// www.xhuber.com

[6] CREO9, Design Package, 2023, https:// www.ptc.com/en/products/creo/package

ISBN: 978-3-95450-250-9 ISSN: 2673-5520 doi:10.18429/JACoW-MEDSI2023-WEPPP010

THE MID INSTRUMENT OF EUROPEAN XFEL: UPGRADES AND EXPERIMENTAL SETUPS

G. Ansaldi†, A. Schmidt, U. Boesenberg, J. Hallmann, J. Möller, J.-E. Pudell, K. Sukharnikov, T. Andersen, J. Wonhyuk, R. Shayduk, A. Bartmann, A. Rodriguez-Fernandez, A. Zozulya, A. Madsen
European X-Ray Free-Electron Laser Facility, Schenefeld, Germany

Abstract

This article provides examples of setups and upgrades currently under development at the Materials Imaging and Dynamics (MID) instrument of the European X-Ray Free-Electron Laser (Eu. XFEL) concerning the X-ray Scattering and Imaging Setup (XSIS):

- The Multi-environmental multi-Detector Setup (MDS_2) is a set of setups designed to integrate in the MID Instrument an additional detector chamber (the Multi Detector Stage, MDS) to be used in parallel with the AGIPD detector, allowing simultaneous coverage of the wide- (WAXS) and small-angle X-ray scattering (SAXS) regions by use of several area detectors. It can also be used in Large Field-of-View (LFOV) configuration.
- The Multi-Purpose Chamber 2 (MPC-2) is an evolution of the current MPC and includes design upgrades of both the exterior of the vessel as well as some internal improvements concerning simultaneous use of optical laser excitation of the sample and Nano-focusing X-ray optics.

Both upgrades will improve the capabilities of MID and enable new types of experiments.

- We also show examples of recent developments of dedicated setups for experiments at MID, as well going in the simultaneous multi-detector-use direction.

THE MULTI-ENVIRONMENTAL MULTI-DETECTOR SETUP (MDS_2)

Environment

The MDS_2 at (Eu. XFEL) [1,2] is an important addition to the instrumentation at MID. The integration is currently in progress allowing to use and move an additional detector chamber (MDS) simultaneous the common detector AGIPD [3] in several positions of MID high-quality floor. It has been designed to be compatible with the current XSIS [1,2], but expands the capabilities of the instrument in three areas:

- AGIPD in WAXS geometry: in this case the MDS is situated on the Support Structure Girder Assembly (SSG) (see Figs. 1 and 2) with its own sliding carts and rails and movable using air pads along the beam axis for SAXS applications or direct beam imaging. The AGIPD detector on the XSIS arm can be freely positioned in the usual WAXS geometry.
- AGIPD in SAXS geometry: in this case the MDS will be mounted onto the XSIS arm using the SSG interchangeable rails, behind the AGIPD detector in SAXS position, see Fig. 3.
- LFOV: in this configuration the MDS will also be mounted onto the XSIS Arm behind the AGIPD detector, but in LFOV configuration (see Fig. 4).

For further information about the MDS, see also the paper of A. Schmidt in this conference.

Design

The MDS_2 Setup, designed and partly realized for the aforementioned three Environments consists of the following assemblies (see the **Poster** of this Paper: Nr. **WEPPP010** and Figs. 1-4):

MDS_2 SSG has been designed, simulated by FEA (see Poster WEPPP010, Fig. 1), and manufactured to withstand the expected static and dynamic loads. The motion concept has been successfully tested by moving it on its air pads.

MDS_2 Upstream Adapter Flange (UAF) has been designed, simulated by FEA (see Poster WEPPP010, Fig. 1), and manufactured to withstand foreseen vacuum load. It has been successfully tested sealing the vacuum of the MDS. It is connected to the other MPC_2 assemblies via a central DN250CF rotatable flange and features 4x DN160ISO-K viewports for visual inspection of the the detectors inside.

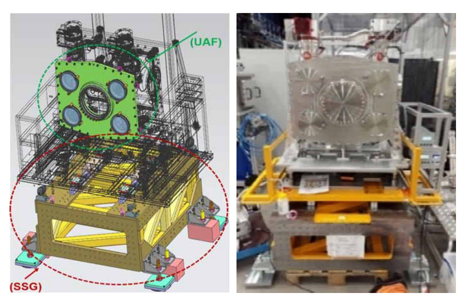

Figure 1: left) design of the Support Structure Girder Assembly moved on airpads (SSG) and Upstream Adapter Flange (UAF), in green. right): manufactured MDS_2 installation during air pads motion and vacuum tests.

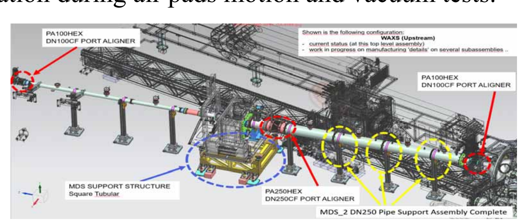

Figure 2: MDS_2 Environment in WAXS Configuration.

† gabriele.ansaldi@xfel.eu , www.xfel.eu

ISBN: 978-3-95450-250-9 ISSN: 2673-5520 doi:10.18429/JACoW-MEDSI2023-WEPPP010

MDS_2 Port Aligners (PA): new connecting elements specifically custom designed to allow for maximum possible lateral displacement and to withstand foreseen vacuum forces. They constitute the connecting elements to the Flight Tube Assemblies before and after the AGIPD detector. Therefore, they are realized in 2 versions: DN200 and DN100.

MDS_2 Movable Chamber (MC) in principle a new small vacuum chamber carrying the new MDS_2 Beam Stop Assembly (BS), that can be vertically inserted into/removed from the beam via the MDS_2 Manipulator (see Fig. 4).

MDS_2 Zero Length Adapter (ZLA) design allows the transition from PA DN250 to DN100 components upstream of the AGIPD, while at the same time featuring 2x DN40ISO-K viewports for direct visual inspection of the interaction point and components inside the MDS (see Fig. 4).

The MDS_2 is completed with several different sets of connecting elements to accommodate the various setups, for instance DN100 and DN250 flight tube assemblies with matching pipe support structures.

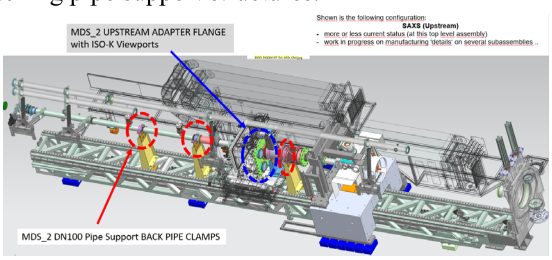

Figure 3: MDS_2 Environment in SAXS Configuration.

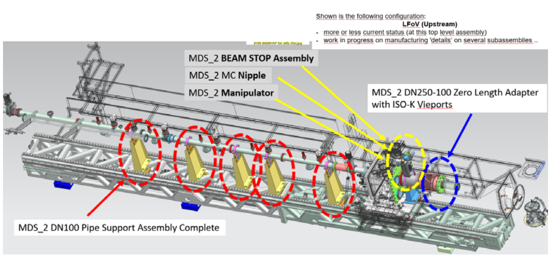

Figure 4: MDS_2 Environment in LFOV Configuration.

THE MULTI PURPOSE CHAMBER 2 (MPC-2)

The MPC-2 project represents another upgrade of MID's instrumentation which is currently being developed. It is an evolution of the current multi-purpose chamber which has been used at MID since the first experiments in 2019. The aim is to enable new types of scientific experiments to expand the current capabilities of MID. Another aim is to make operation of experiments easier with better access to the sample environment and possibilities to install ancillary equipment (see Figs. 5-7).

Design

A recurrent request, beyond the capabilities of the current MPC setup, is to use an optical pump laser beam in

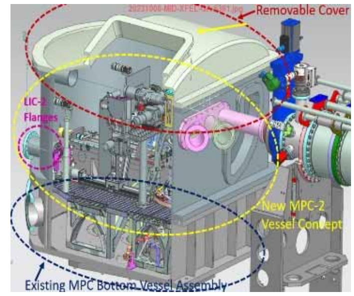

Figure 5: MPC-2 design (VESSEL SEGMENTED) and interior assembly with BA and LIC-2 (section).

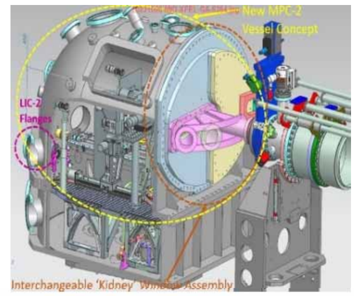

Figure 6: MPC-2 design (VESSEL SUCCESSOR) and interior assembly with BA and LIC-2 (section).

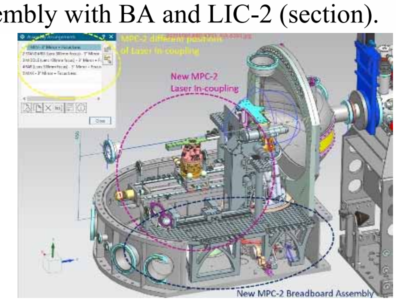

Figure 7: MPC_2 Interior Assembly Upgrade: design in progress with examples of different LIC-2 positions on the BA.

vacuum in combination with the existing nano-focusing (NaFo) setup using beryllium lenses. The new MPC-2 will accommodate this possibility by adding additional windows and flanges, hence allowing the optical laser beam to enter the chamber parallel to the X-ray beam (Figs. 5-7) and with sideboards mounted inside the vessel to accommodate optical components for the laser beam path (see also Fig.7).

Two scenarios of the MPC-2 Vessel are currently under development. Both must fulfil the following requirements:

- Compatibility with the current MPC bottom part onto which MPC-2 will be mounted;
- Compatibility with the current infrastructure and ancillary sample environment setups, including developments in progress (e.g. the Interior Assembly Upgrade (MPC-2_IAU) and laser in-coupling (LIC2)) and other additional future upgrades (e.g. the Interferometer Project).
- Easy access to the sample and internal setups via larger side ports.

The two different MPC designs explored are:

MPC-2 VESSEL UPGRADE SEGMENTED is a possible design scenario featuring a completely removable top

ISBN: 978-3-95450-250-9 ISSN: 2673-5520 doi:10.18429/JACoW-MEDSI2023-WEPPP010

cover, wide apertures, interchangeable flight-tubes at distinct scattering angles and new laser in-coupling flanges (see Fig. 5).

MPC-2 VESSEL UPGRADE SUCCESSOR is another possible design scenario featuring a kidney-shaped window compatible with current WAXS window, wide apertures and interchangeable flight-tubes at distinct scattering angles and new laser in-coupling flanges (see Fig. 6).

The MPC-2 Project also comprises the Interior Assembly Upgrade (MPC-2_IAU), featuring (see Fig. 7):

- A new Laser In-Coupling (LIC-2) device, positioned downstream of the NaFo Setup and movable along the beam direction. It is designed to make the X-rays and optical laser beam to hit the sample co-linearly;
- Upgraded Breadboard Assembly (BA), a suitable support structure designed to ensure a secure mounting of the future LIC-2, as well as mounting and aligning lenses, mirrors and cameras. It will be fixed to the existing threads at the bottom part of the current MPC.

EXPERIMENTAL SETUP FOR WIDE-ANGLE SCATTERING XPCS ON LIQUID JETS

In these experiments speckle patterns need to be detected with high precision in space and time and in WAXS geometry.

Design

The setup consists of (see Figs. 8 and 9):

- XSIS installed in SAXS Configuration
- Multi-purpose chamber (MPC) in vacuum

- DN200ISO-K Flight Tube Setup (FTS) at 25 deg from the beam, installed on XSIS Arm (2 scenarios: @1.2m and @1.8m from the interaction point)

- 2x or 4x EPIX detector [4] Setup installed on FTS

- Liquid Injector setup (LIS)
- Cold Trap installed on MPC

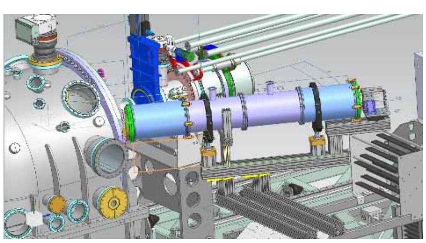

Figure 8: Design of WA-XPCS setup - Scenario: @1.8m from the interaction point and 2x Epix Detectors.

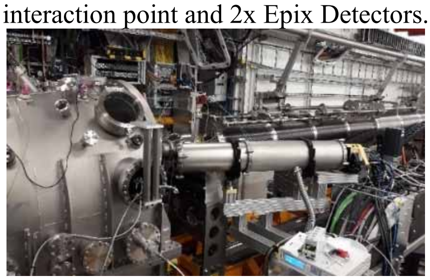

Figure 9: Implementation of Design.

EXPERIMENTAL SETUP FOR SMALL-AND WIDE-ANGLE SCATTERING XPCS ON SOLID SAMPLES

In these experiments speckle patterns need to be detected with high precision in space and time in SAXS and WAXS geometry.

Design

The setup for this kind of experiment consists of (see Figs. 10 and 11):

- XSIS Instrument installed in SAXS Configuration;
- DN40KF Flight Tube Assembly connecting the MID Laser In-coupling (LIC) to MID XSIS
- R+K Assembly Setup installed on bottom of MPC;
- DN200ISO-K FTS;
- a sample chamber (cryostat) integrated into MID FTS;
- Jungfrau [5] detector Setup installed on FTS.

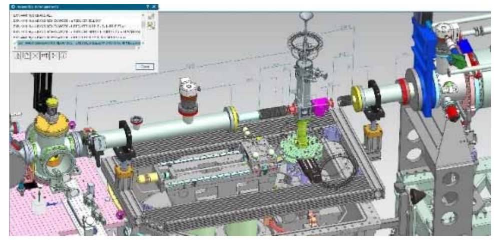

Figure 10: Design of Exp. Setup - Scenario: reducer bellow.

Figure 11: Implementation of Design.

CONCLUSION

Several upgrades are currently underway at the MID instrument of EuXFEL. The MDS_2 manufacturing and assembly is in progress but not yet in operation. MPC-2 is in the design phase, allowing for improved operation of MID and simultaneous use of nano focused X-ray beams and optical laser excitation of the sample. The flexibility of the MID instrument is illustrated by examples of experimental setups and the MDS_2 and MPC-2 projects aim at standardizing some of these configurations.

REFERENCES

[1] A. Madsen, J. Hallmann, T. Roth, and G. Ansaldi, “Technical Design Report: Scientific Instrument MID”, DESY, Rep. TR-2013-005, 2013. doi:10.3204/XFEL/EU/TR-2013-005

[2] A. Madsen *et al.*, “Materials Imaging and Dynamics (MID) instrument at the European X-ray Free-Electron Laser Facility”, *J. Synchrotron Radiat.*, vol. 28, pp. 637, 2021. doi:10.1107/S1600577521001302

ISBN: 978-3-95450-250-9 ISSN: 2673-5520 doi:10.18429/JACoW-MEDSI2023-WEPPP010

[3] A. Allahgholi *et al.*, "Megapixels @ Megahertz – The AGIPD high-speed cameras for the European XFEL", *Nucl. Instrum. Methods Phys. Res. Sect. A*, vol. 942, p. 162324, 2019. doi:10.1016/j.nima.2019.06.065

[4] G. A. Carini *et al.*, "ePix100 camera: Use and applications at LCLS", *AIP Conf. Proc.*, vol. 1741, p. 040008, 2016. doi:10.1063/1.4952880

[5] A. Mozzanica *et al.*, "Characterization results of the JUNGFRAU full scale readout ASIC", *JINST*, vol. 11, p. C02047, 2016. doi:10.1088/1748-0221/11/02/C02047

ISBN: 978-3-95450-250-9 ISSN: 2673-5520 doi:10.18429/JACoW-MEDSI2023-WEPPP012

MULTIPLE DETECTOR STAGE AT THE MID INSTRUMENT OF EUROPEAN XFEL

A. Schmidt, G. Ansaldi, A. Bartmann, U. Boesenberg, T. Falk, J. Hallmann, J. Möller, K. Sukharnikov, A. Madsen
European X-Ray Free-Electron Laser Facility, Schenefeld, Germany

Abstract

The Multiple Detector Stage (MDS) is an ancillary detector setup for the Materials Imaging and Dynamics (MID) instrument at the European X-Ray Free-Electron Laser Facility (EuXFEL). It is developed to improve the current capabilities concerning X-ray detection and make entirely new experiments possible.

A unique feature of the MID instrument is the large flexibility in positioning of the AGIPD detector relative to the sample. This enables a large variety of instrument configurations ranging from small-angle (SAXS) to wide-angle (WAXS) X-ray scattering setups. A recurrent request from the users, which is currently not enabled, is the option of simultaneously recording both wide- and the small angle scattering by using two area detectors.

The aim of developing MDS is to provide this missing capability at MID so that SAXS and WAXS experiments can be performed in parallel. The MDS will not be installed permanently at the instrument but only on request to provide as much flexibility as possible.

In this article, the background and status of the MDS project is described in detail.

INTRODUCTION

The basis for the MDS is a vacuum chamber which can host two small area detectors simultaneously. The detectors inside the vacuum chamber can be arranged differently with the help of two translation stages. The full chamber is assembled on a platform which includes a vertical motion. The platform also carries electronics required for the X-ray detectors, motors, and the vacuum system.

An important feature of MDS is that it can be positioned either on the existing arm of the XSIS instrumentation at MID [1], together with the AGIPD detector [2], or as a standalone device on a separate girder (Figs. 1 and 2). The girder stands on air pads, suitable for the floor in the MID experimental hutch. With this the MDS can be positioned inside the hutch and operated in parallel with the AGIPD detector. Space constrains and cable routing are limiting factors for the positioning. As day-1 configuration the MDS is used only in SAXS geometry, either mounted behind AGIPD on the XSIS arm, or on its own girder if AGIPD is positioned in WAXS.

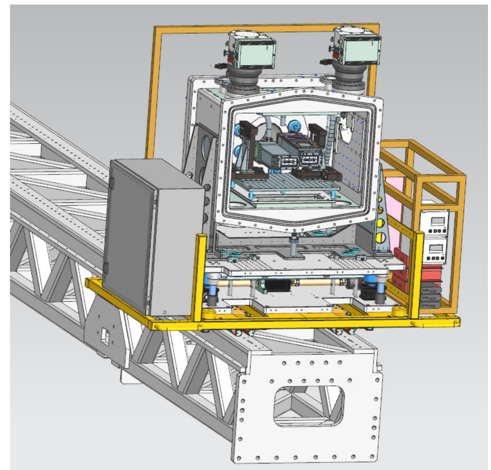

Figure 1: Vacuum chamber with detectors and platform with electronics of the MDS on the arm of the AGIPD at the MID instrument (CAD model).

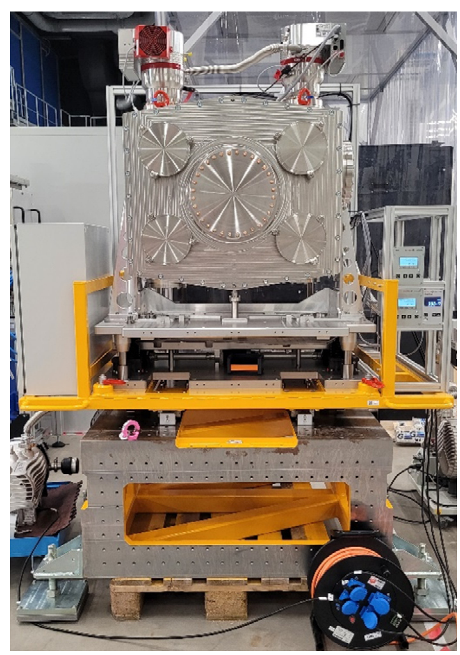

Figure 2: Assembled mechanics of the MDS on separate girder with air pads.

CONFIGURATIONS

The recurrent request of the user community for simultaneous wide- and small-angle scattering capabilities is the motivation behind the MDS project.

Experiments, where information about the scattering sample is required in-situ on both atomic (nm and sub-nm)

ISBN: 978-3-95450-250-9 ISSN: 2673-5520 doi:10.18429/JACoW-MEDSI2023-WEPPP012

and larger length scales (µm and sub-µm) would benefit enormously from such a setup. Another frequent request is to move a detector into the direct beam, for example for beam characterization, X-ray holography, or other X-ray imaging applications.

By positioning of the MDS on the XSIS arm behind AGIPD, such measurements are feasible (Fig. 3).

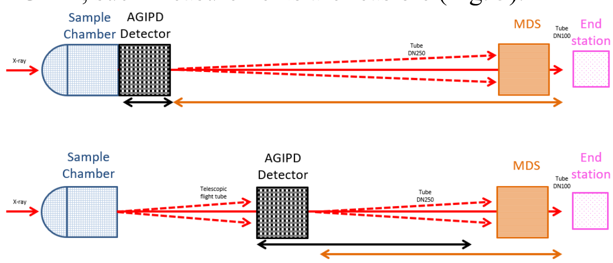

Figure 3: Sketch of the geometry with MDS positioned behind AGIPD on a common detector arm.

Another option provided by the MDS is its individual positioning independent of the AGIPD detector arm. For this purpose, a support girder was built were the MDS can reside on. The girder sits on air pads and can be moved freely on the high-quality floor of MID. Figure 4 shows that when the AGIPD detector is moved to WAXS, the MDS can cover the SAXS configuration. For further information about the girder see also the poster and paper [3] presented at this conference..

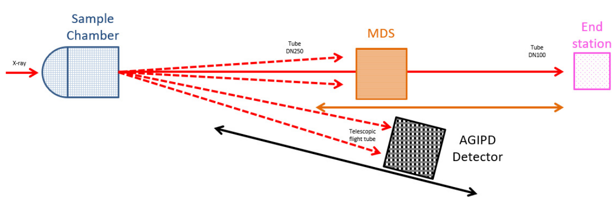

Figure 4: Sketch of the geometry with AGIPD in WAXS while MDS covers the SAXS region mounted on its own girder.

Detectors / Orientation

The MDS contains a high vacuum chamber with two detectors mounted on individual horizontal and vertical stages. The chamber can host versatile configurations and different types of small detectors. For instance, two ePix [4] or two Jungfrau [5] detectors can be operated in parallel and positioned in "elongated" and "square" arrangements (Figs. 5 and 6).

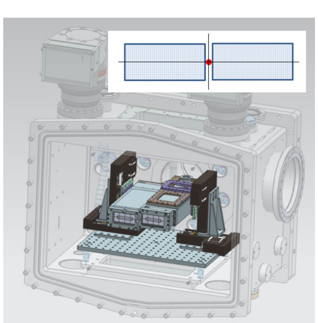

Figure 1: Elongated setup of two Jungfrau detectors.

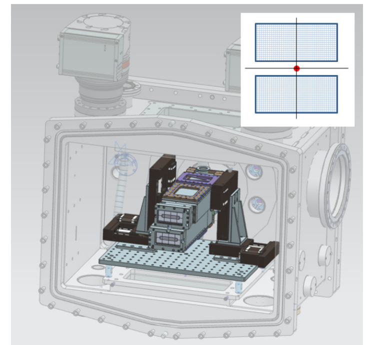

Figure 6: Square setup of two Jungfrau detectors.

Jungfrau Detector

The Jungfrau detector [4] must operate in air which means that for vacuum integration special precautions must be taken. For this purpose, an air housing was developed by the HED instrument of EuXFEL and also used at the MDS of MID (Fig. 7). The cables of the Jungfrau detector are guided out of the chamber from the air housing through a bellow mounted with an "inside-out" ISO-KF flange.

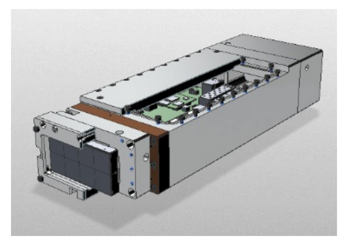

Figure 7: Jungfrau detector in air housing.

ePix

The ePix100 detector [5] can be operated in vacuum without any further measures and is hence installed in the MDS directly (Fig. 8).

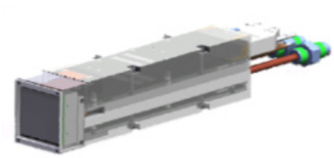

Figure 8: ePix100 detector.

Both detectors require cooling water which will be provided via the platform.

Relevant pixel and sensor parameters of the Jungfrau and ePix detector can be seen in Table 1.

Table 1: Compatible Detectors in Use for the MDS

Parameters	ePix (SLAC)	Jungfrau (PSI)
Sensor	300 µm Si	320 µm Si
Sensor size	704×768	512×1024
Pixel size	50 µm	75 µm
Repetition	120	2000 (200 tested)

12th Int. Conf. Mech. Eng. Design Synchrotron Radiat. Equip. Instrum. MEDSI2023, Beijing, China JACoW Publishing
ISBN: 978-3-95450-250-9 ISSN: 2673-5520 doi:10.18429/JACoW-MEDSI2023-WEPPP012

ENVIRONMENT

The MID instrument is designed with a "window less" option were all components in the beam are under vacuum. Therefore, vacuum beam pipes can be installed upstream and downstream of the MDS assuring vacuum conditions along the beam. Segmented flight tubes provide feasibility that the MDS can be installed at several positions along the beam direction (Fig. 9).

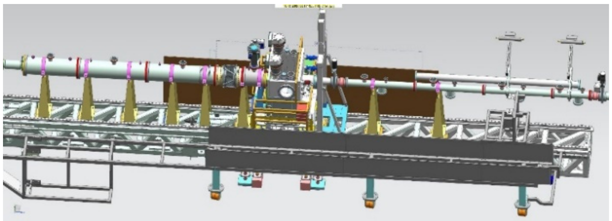

Figure 9: MDS integrated into MID beam line.

The front flange of the MDS detector chamber hosts four ISO-K window flanges were cameras can be installed but the flanges can also be used for quick access to the inner mechanics. A motorized beam stop is positioned in front of the MDS, directly attached to the front flange. It consists of a tungsten piece and can be placed to block the direct beam, if required. A small X correction is integrated in the Y Stage of the beam stop (Fig. 10).

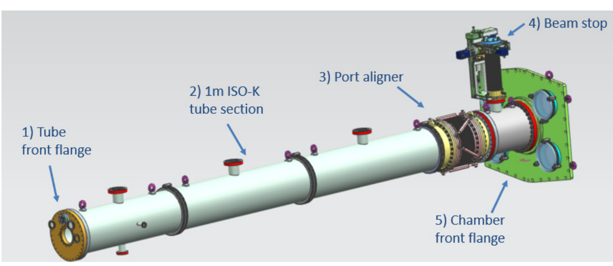

Figure 10: 1) Tube front flange, 2) Flight tubes, 3) port aligner, 4) beam stop, and 5) front flange.

For more details of the Front assembly please see [3].

ELECTRICAL COMPONENTS

All the relevant electronical components are located on the sides of the platform. A local crate on the left side will host the power supply and Beckhoff modules for driving the motors (Fig. 11). On the right-hand wing, IT patch panels, detector electronics, and the vacuum pump controller are located.

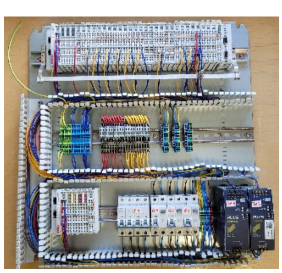

Figure 11: Electronics of the local crate with Beckhoff PLC for the motors.

VACUUM SYSTEM

Two turbo pumps (Pfeiffer, HiPace 300M) connected at the top of the chamber will assure the requested vacuum level of < 5×10^{-6} mbar. They are backed by a scroll pump (Edwards, nXDS20i). A venting unit with particle filter, pressure relief valve, and an angle valve for rough pumping (if requested) are attached at the back of the chamber at DN40 ports (Fig. 12). All this is provided by VAT. All components can be controlled remotely with the EuXFEL control system KARABO [6].

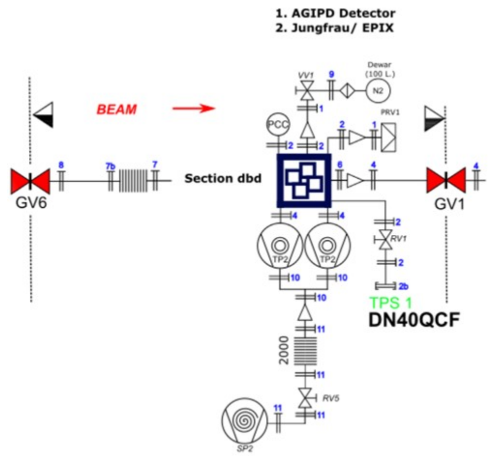

Figure 12: Vacuum scheme of MDS.

STATUS AND OUTLOOK

The MDS is not in operation so far. Most of the mechanical parts are available or under procurement and manufacturing of the electronics is at an advanced stage. A first vacuum test has been performed of the chamber in a realistic configuration and 5×10^{-7} mbar was reached. The detectors are in use at the instrument and will be integrated into the MDS soon.

Once the requirements of the day-1 configuration are fulfilled by the setup, a day-2 configuration will be studied. The aim of day-2 is to employ the MDS in WAXS position, independent of AGIPD.

REFERENCES

[1] A. Madsen *et al.*, "Materials Imaging and Dynamics (MID) instrument at the European X-ray Free-Electron Laser Facility", *J. Synchrotron Radiat.* vol. 28, pp. 637-649, 2021. doi:10.1107/S1600577521001302

[2] A. Allahgholi *et al.*, "Megapixels @ Megahertz – The AGIPD high-speed cameras for the European XFEL", *Nucl. Instrum. Methods Phys. Res. A,* vol. 942, p. 162324, 2019. doi:10.1016/j.nima.2019.06.065

[3] G. Ansaldi *et al.*, "The MID Instrument of European XFEL: Upgrades and Experimental Setups", presented at MEDSI'23, Beijing, China, Nov. 2023, paperWEPPP010, this conference.

[4] A. Mozzanica *et al.*, "Characterization results of the JUNGFRAU full scale readout ASIC", *J. Instrum.*, vol 11, no. C02047, 2016. doi:10.1088/1748-0221/11/02/C02047

ISBN: 978-3-95450-250-9 ISSN: 2673-5520 doi:10.18429/JACoW-MEDSI2023-WEPPP012

[5] G. A. Carini *et al.*, "ePix100 camera: Use and applications at LCLS", *AIP Conf. Proc.*, vol. 1741, p. 040008, 2016. doi:10.1063/1.4952880

[6] S. Hauf *et al.*, "The Karabo distributed control system", *J. Synchrotron Radiat.*, vol. 26, p. 1448, 2019. doi:10.1107/S1600577519006696

ISBN: 978-3-95450-250-9 ISSN: 2673-5520 doi:10.18429/JACoW-MEDSI2023-WEPPP013

MECHANICAL DESIGN AND INTEGRATION OF THE SXP SCIENTIFIC INSTRUMENT AT THE EUROPEAN XFEL

V. Vardanyan†, P. Grychtol[1], E. Tikhodeeva[1], D. Doblas-Jimenez[1], J. Ohnesorge[1], N. Kohlstrunk[1], J. Buck[2,3], S. Thiess[3], M. Dommach[1], D. La Civita[1], M. Vannoni[1], K. Rossnagel[2,3], G. Schönhense[4], S. Molodtsov[1,5,6], M. Izquierdo[1]

[1]European XFEL, Schenefeld, Germany
[2]Ruprecht Hänsel Laboratory, Deutsches Elektronen-Synchrotron DESY, Hamburg, Germany
[3]Institut für Experimentelle und Angewandte Physik, Christian-Albrechts-Universität Kiel, Kiel, Germany
[4]Institut für Physik, Johannes Gutenberg Universität Mainz, Mainz, Germany
[5]Institute of Experimental Physics, TU Bergakademie Freiberg, Freiberg, Germany
[6]Center for Efficient High Temperature Processes and Materials Conversion (ZeHS), TU Bergakademie Freiberg, Freiberg, Germany

Abstract

The European XFEL provides femtosecond X-ray pulses with a MHz repetition rate in an extended photon energy range from 0.3 to 30 keV. Soft X-rays between 0.3 and 3 keV are produced in the SASE3 undulator system, enabling both spectroscopy and coherent diffraction imaging of atoms, molecules, clusters, ions and solids. The high repetition rate opens the possibility to perform femtosecond time-resolved photoelectron spectroscopy (TR-XPES) on solids. This technique allows the simultaneous understanding of the evolution of the electronic, chemical and atomic structure of solids upon an ultrafast excitation. The realization with soft X-rays requires the use of MHz FELs. In this contribution, we present the mechanical design and experimental realization of the SXP instrument.

The main technical developments of the instrument components and the TR-XPES experimental setup are described.

INTRODUCTION

The SXP Scientific Instrument is designed as an open port were users' provided stations can be integrated [1, 2].

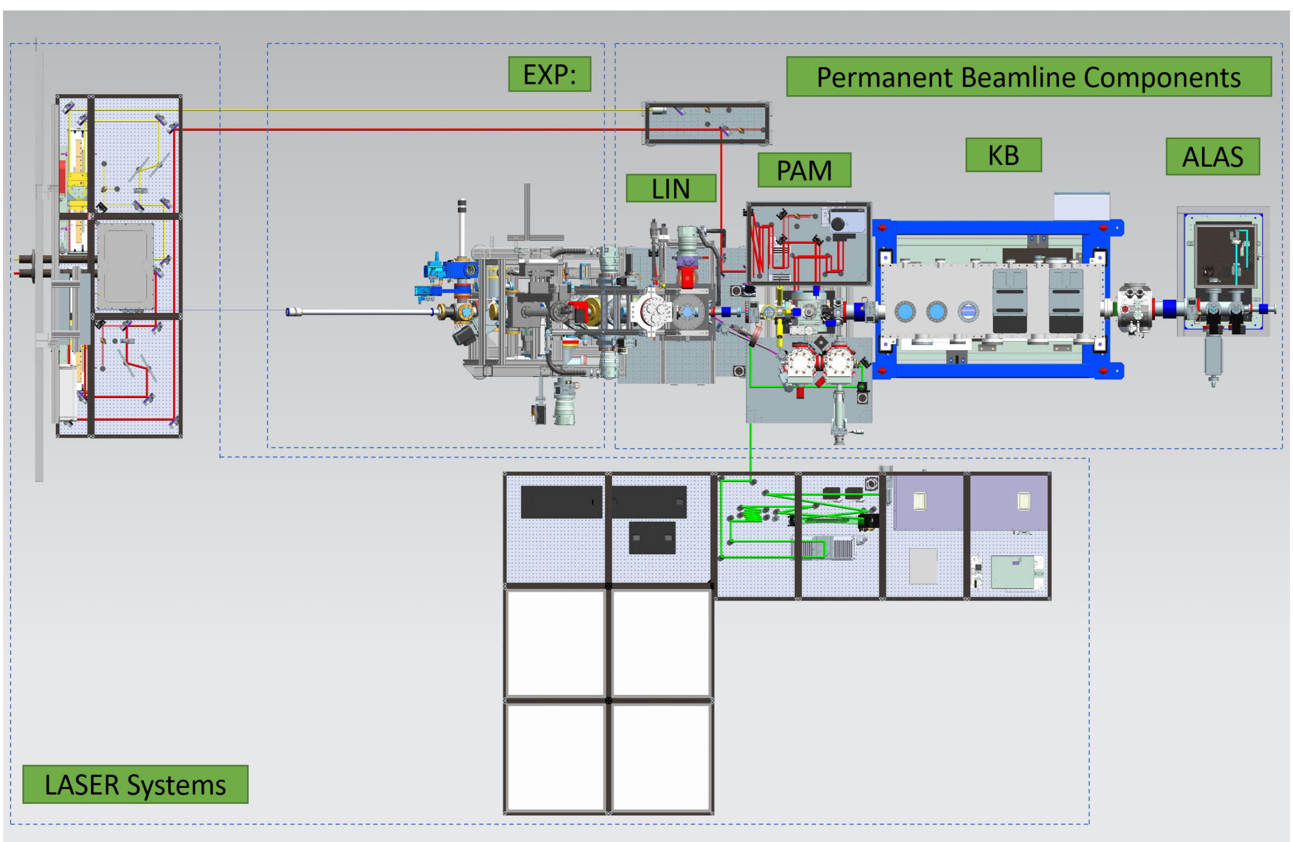

Figure 1: Layout of the SXP Scientific Instrument.

ISBN: 978-3-95450-250-9 ISSN: 2673-5520 doi:10.18429/JACoW-MEDSI2023-WEPPP013

Figure 1 shows the layout of the SXP Scientific Instrument is presented. It is divided in three distinct areas: the permanent beamline components (BLC), the laser system (LAS) and the experimental station (EXP).

- BLC: It consists of the alignment laser system (ALAS) and it is designed to pre-align all components prior to FEL experiments The Kirkpatrick–Baez (KB) X-ray mirror focusing system currently provides a FEL beam of 2 x 35 µm^2 (horizontal x vertical) using directionally fixed focus mirrors. The photon arrival time monitor (PAM) uses the spectral encoding technique on thin membranes to measure the relative arrival time and jitter between the FEL and optical pulses [3]. The membranes also serve as X-ray beam attenuators. The laser in-coupling unit (LIN), couples the optical pulses into the experimental station. At the end of the main experimental station an instrument beam stop (IBS) based on B4C and diamond is installed.
- LAS: Integrates the EuXFEL pump-probe laser with 800 and 1030 nm outputs and a 60 W, 1030 nm, 200 fs, 20 MHz AFS laser. The latter has been compressed to 40 fs using multi-pass Herriot cells. Several frequency conversion schemes, including an optical parameter amplifier allow pulses to cover the wavelength range from ~200 nm to ~15 µm [4].
- EXP is the experiment station area. The first realization will allow femtosecond time-resolved photoelectron spectroscopy on solids (TR-XPES).

In the following, the LIN and TR-XPES experiment station are described.

LIN – LASER IN-COUPLING SYSTEM

Figure 2 displays a section of the LIN model in the central plane of the FEL propagation.

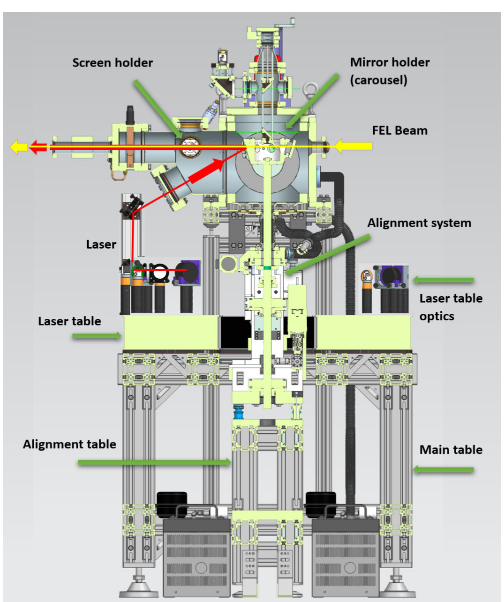

Figure 2: Central section of the LIN system.

It consists of two optical tables: one holds the vacuum chamber and the in-air optical mirrors. It has the laser beam height of 900 mm. The optical pulses are transported and focused by optics on the optical table.

A periscope mirror couples the in-vacuum beam through a flange with an optical viewport in a 15° orientation. The beam is reflected in the in-vacuum mirrors, which are installed in kinematic mounts with piezo motors at 15° with respect to the incident beam to produce a reflection along the FEL beam path. They are installed in a carousel that can accommodate up to 5 mirrors to cover the full range of laser wavelengths available on the instrument. The mirrors have a center hole that allows the FEL to propagate collinearly with the optical pulse.

The carousel is installed in a second breadboard decoupled from the main one to allow independent alignment and also to decouple the in-vacuum mirrors from the vacuum chamber. The latter is equipped with a vacuum system with a turbo molecular pump and a getter ion pump, viewports and electrical feedthroughs to control the in-vacuum kinematic mounts.

TR-XPES – TIME-RESOLVED X-RAY PHOTOELECTRON SPECTROSCOPY

TR-XPES is the first experimental station at the SXP instrument. It designed to perform femtosecond time-resolved photoelectron spectroscopy on solids. Figure 3 shows a central section of the entire station.

The system is divided into several chambers with different functionalities. The main chamber is made of mu-metal to avoid stray and earth magnetic fields. It houses a homemade momentum microscope-type photoelectron spectrometer [5] installed in a vertical configuration at 22° with respect to the FEL beam. The unconventional vertical mechanical configuration has required the definition of a specific support structure. It is made of Al and PEEK parts. The latter parts were required to ensure that all the electrostatic lenses of the momentum microscope were electrically-isolated from each other and from the chamber. The instrument beam stop (IBS) is installed in the back of the main chamber. The momentum microscope allows both spatially resolved photoemission electron microscopy (PEEM) and momentum resolved (angle-resolved photoelectron spectroscopy ARPES, X-ray photoelectron diffraction XPD) experiments. The electrons are detected by microchannel plate based delay-line (MCP-DLD) detectors. The samples are mounted on a homemade hexapod system equipped with a cryostat. The motors allow the sample to be aligned with micrometer precision over a range of up to 20 mm. The six degrees of freedom are organized in three sets: three motors are installed in the flange supporting the sample receiver. When they are moved in the same direction by the same amount, the sample is displaced vertically towards the axis of the momentum microscope. Moving them differently allows the sample to be tilted in two different directions. The second set of two motors is installed along the FEL beam direction. Moving them simultaneously by the same amount translates the sample linearly along the FEL beam. Moving them asymmetrically allows an azimuthal rotation up to about 3°. The sixth motor allows translation orthogonal to the FEL beam direction.

ISBN: 978-3-95450-250-9 ISSN: 2673-5520 doi:10.18429/JACoW-MEDSI2023-WEPPP013

The main chamber is connected to a chamber equipped with a low energy electron diffraction (LEED) system and a transfer bar with a one-meter arm. It is used to load samples into the main chamber and the preparation chamber. Samples can be loaded through a dedicated load lock or from a vacuum suitcase. The load lock is a DN63 cube equipped with a transfer bar and a sample loading stage that allows the installation of up to five samples in omicron type sample holders. The latter allows users to bring their own prepared samples. A preparation chamber is installed on top of the LEED chamber. It has a spherical shape to ensure that all flanges are facing its center. It is equipped with basic equipment to prepare samples by sputtering and annealing. It has a series of DN40 viewports prepared to install different types of evaporators. The samples are hosted on a manipulator with four degrees of freedom: X, Y, Z and azimuthal rotation. A cryostat allows samples to be cooled down to 20 K. The sample receiver is equipped with an e-beam heating station reaching temperatures up to 1600 K.

The entire system is installed on an Al support that can be aligned manually. In a second step. the system will be installed on an automated alignment system.

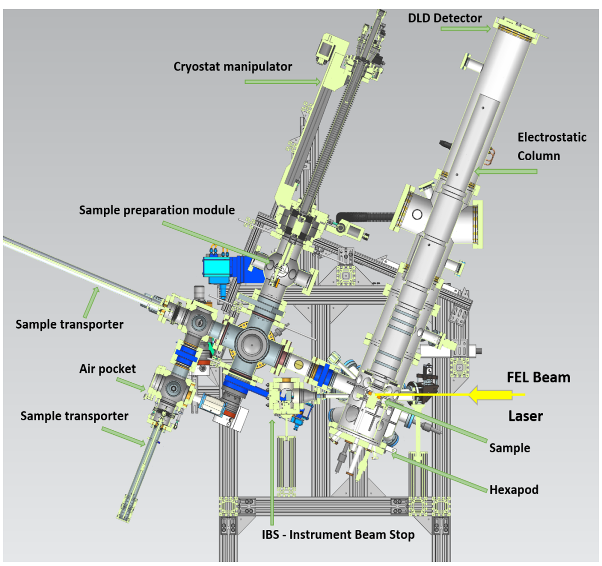

Figure 3: Central section of the TR-XPES experiment.

CONCLUSION

This contribution presents the mechanical design and experimental realization of the SXP instrument. The instrument is organized in a series of permanent components along the FEL beamline, an optical laser system that uses both the central EuXFEL pump probe laser and the experimental station area. The laser in-coupling system and the first experimental station, TR-XPES, developed to perform femtosecond time-resolved photoemission experiments, have been described.

ACKNOWLEDGEMENTS

We thank the data department and instrumentation departments, the X-ray operations, safety and the administration groups of the EuXFEL for their support to the SXP project.

REFERENCES

[1] M. Izquierdo, "Technical Design Report: Scientific Instrument Soft X-Ray Port (SXP): Part A - Scientific cases", European XFEL, Schenefeld, Germany, January 4, 2022.

[2] P. Grychtol, N. Kohlstrunk, J. Buck, S. Thiess, V. Vardanyan, D. Doblas-Jimenez, M. Izquierdo, *et al.,* "The SXP instrument at the European XFEL", *J. Phys.: Conf. Ser.*, vol. 2380, p. 012043, 2022. doi:10.1088/1742-6596/2380/1/012043

[3] P. Grychtol *et al.*, "Timing and X-ray pulse characterization at the Small Quantum Systems instrument of the European X-ray Free Electron Laser", *Opt. Express*, vol. 29, p. 37435, 2021. doi:10.1364/OE.440718

[4] P. Grychtol, , V. Vardanyan, D. Doblas-Jimenez, and M. Izquierdo, "The Laser Infrastructure at the SXP instrument of the European XFEL", *J. Phys.: Conf. Ser.*, vol. 2380, no 1, p. 012114, 2022. doi:10.1088/1742-6596/2380/1/012114

[5] D. Kutnyakhov *et al.*, "Time- and momentum-resolved photoemission studies using time-of-flight momentum microscopy at a free-electron laser", *Rev. Sci. Instrum.*, vol. 91, p. 013109, 2020. doi:10.1063/1.5118777

ISBN: 978-3-95450-250-9 ISSN: 2673-5520 doi:10.18429/JACoW-MEDSI2023-WEPPP015

PROGRESS OF FRONT ENDS AT HEPS

Hong Shi†, Ping Luo, Yaxin Ma, Heying Wang, Yinglei Tan
Institute of High Energy Physics (IHEP), Chinese Academy of Sciences, Beijing, China

Abstract

High Energy Photon Source (HEPS) is a 6 GeV synchrotron radiation facility building in Huairou, with a storage ring perimeter of 1390.6 m and 41 straight sections. In phase I, 15 front ends will be installed, including 14 insertion device front ends and 1 bending magnet front end. These front ends are divided into three types: the Undulator front end, the Wiggler front end, and the BM front end. The U-type front end will receive 766 W/mrad^2 of peak power density and 25 kW of the total power. The design of the W-type front end is based on compatibility with various insertion devices, including undulators and wigglers. In this paper, the designs and the progress of HEPS front ends are presented.

INTRODUCTION

HEPS is a 6 GeV synchrotron radiation facility building in Huairou, storage ring has 48 straight sections, and 41 of them that are 6 m long can extract user beams, as 7 are required for injection and RF straights. Therefore, there is a capacity for 41 Insertion Device (ID) Front Ends and 41 Bending Magnet Front Ends to be installed. Fifteen beamlines are being built in Phase I of HEPS project. One of them is BM beamline, others use ID as light source. These front ends are divided into three types: the Undulator front end (UFE), the Wiggler front end (WFE), and the BM front end (BFE). The UFE will receive 766 W/mrad^2 of peak power density and 25 kW of the total power. The design of the WFE is based on compatibility with various insertion devices, including undulators and wigglers.

GENERAL LAYOUT

Front ends at HEPS are divided into three types: Undulator Front End (UFE), Wiggler Front End (WFE), and Bending Magnet Front End (BFE). There are 12 UFEs, 2 WFEs, and 1 BFE. Due to the implementation of a unified standardized design, the layout of the three types of front ends is similar. The main components of front ends are: (1) Pre-Mask, (2) Low Power Photon Shutter, (3) All-metal Fast Valve, (4) 1st Fixed Mask, (5) XBPM, (6) Photon Shutter, (7) Slits, (8) Filters, (9) Safety Shutter, (10) Ratchet Wall, (11) 2nd Fixed Mask, (12) Be Window. Figure 1 shows the layout of UFE. Table 1 summarizes the front end parameters.

COMPONENTS

Pre-Mask

The isolation valve on the crotch leg of the storage ring is followed by the Pre-Mask which is to reduce dipole radiation to downstream 1st Fixed Mask. The absorber of the Pre-Mask is made of OFHC and cooled by water. The mechanical module of the Pre-Mask is shown in Fig. 2.

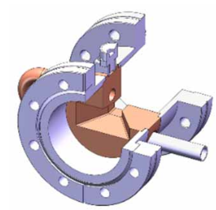

Figure 2: Mechanical module of the Pre-Mask.

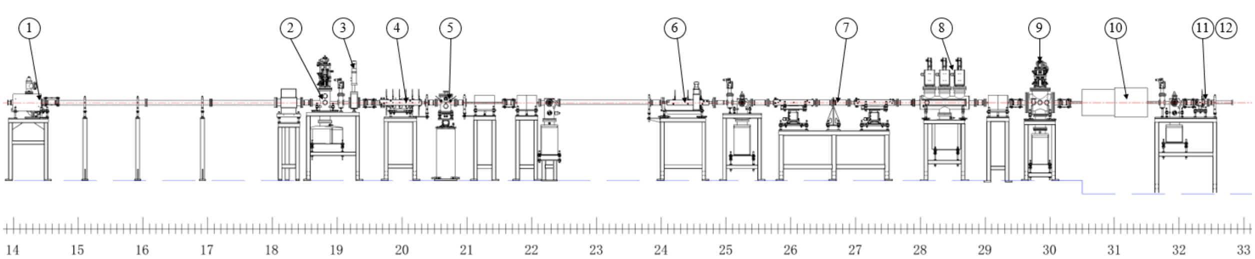

Figure 1: Layout of the UFE.

Table 1: The Parameters of Front Ends at HEPS

	UFE	WFE	BFE
Length [m]	18.9	18.9	22.2
Beam Size at Entrance [mrad]	3.1×1.3	3.1×1.3@ID19, 3.2×1.5@ID42	3.3×1.5
Beam Size at Exit [mrad]	0.2×0.2	1.0×0.9@ID19, 2.0×0.3@ID42	2.0×0.4
Peak Power Density [kW/mrad^2]	766	414	0.18 kW/mrad
Total Power [kW]	25	9	

† shihong@ihep.ac.cn

ISBN: 978-3-95450-250-9 ISSN: 2673-5520 doi:10.18429/JACoW-MEDSI2023-WEPPP015

Fixed Mask

The Fixed Mask defines the angle of departure of the beam which pass into the front end, and prevents downstream components from irradiated by misteered beam. In the case of normal incidence, the Fixed Mask will be subjected to a power density of 2.0 kW/mm^2. Therefore, the form of aperture presents an hourglass, which provide grazing incidence to the beam in order to reduce the power density on the footprint. The grazing incidence is 0.689˚. The Fixed Mask absorber is made of dispersed copper alloy, which has high thermal conductivity, high yield strength, and high softening temperature, making it very suitable for the manufacturing of absorbers under high heat load. In order to take away the heat load as quickly as possible and reduce the maximum temperature, copper wire-coils are placed in the uniformly distributed water-cooled pipes near the internal surface for enhanced heat transfer [1]. After testing, the convective heat transfer coefficient of the pipe wall can reach 25000 W/m^2·K at 4.4 kgf/cm^2[2]. The Fixed Mask module is shown in Fig. 3.

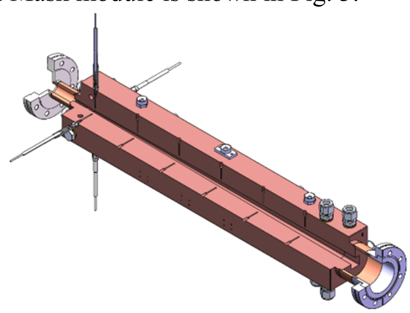

Figure 3: Section view of Fixed Mask.

Photon Shutter

The front ends at HEPS have two types of the Photon Shutter (PS). One of them is a Low Power Photon Shutter (LPPS) (Fig. 4) which is subject to the heat load from upstream and downstream bending magnet of an insertion device. It can be combined with the downstream vacuum isolation valve to ensure that the operation of the storage ring and other beam lines are not affected when the current front end malfunctions. The LPPS absorber is made of OFHC and cooled by water. Another is a white beam Photon Shutter (PS) (Fig. 5), which can close the synchrotron radiation to downstream components. Due to suffering from the peak power density up to 1.3 kW/mm^2, it has a grazing incidence surface with 1.3˚ angle that will intercept the beam. There are four water-cooled channels near the surface, and copper wire-coil inside the channels enhance heat transfer.

Safety Shutter

The function of the Safety Shutter is to block bremsstrahlung radiation. The absorber which is made of Tungsten has two parts, movable block and fixed block, the material thickness is 200 mm. To close the Safety Shutter, the movable block moved down. The size from the edge of the block to the bremsstrahlung radiation spot is larger than three times the Moliere radius. The Safety Shutter is shown in Fig. 6.

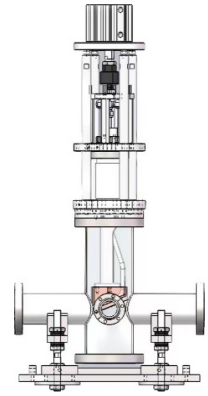

Figure 4: The Low Power Photon Shutter module.

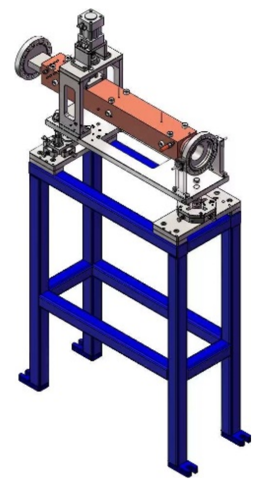

Figure 5: Mechanical module of the Photon Shutter.

Figure 6: Safety Shutter.

Slits

A set of Slits is to define the beam size exiting the front end, the upstream and downstream absorber both are L-shaped components can independently move in the vertical and horizontal directions. The stages below the absorbers have an accuracy of 1 µm with an equivalent angular accuracy of approximately 0.04 µrad. The mechanical module of slits is shown in Fig. 7.

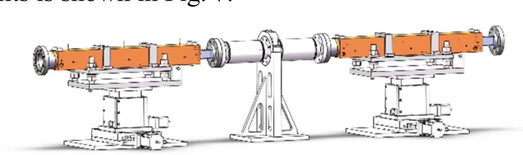

Figure 7: Slits module.

ISBN: 978-3-95450-250-9 ISSN: 2673-5520 doi:10.18429/JACoW-MEDSI2023-WEPPP015

Filters

A set of Filters is used to reduce the heat load on the downstream components in the First Optical Enclosure. It is composed of three sets of 3-position carbon foils which have different thicknesses installed according to various requirements. A water-cooled copper frame is used to clamp the graphite foils.

Fast Valve

An all metal Fast Valve is installed downstream of LPPS, with a maximum aperture of 60 (H) mm × 20 (V) mm and can be closed within 8 ms. The leakage rate is less than 0.4 Torr·L/s, and the service life is greater than 1000 times. The all metal Fast Valve is shown in Fig. 8.

Figure 8: All Metal Fast Valve.

PROJECT CHALLENGES

Fatigue Life

As a fourth-generation synchrotron radiation facility, HEPS can generate a peak power density of 766 kW/mrad^2 from its insertion devices, which means that the absorbers in the front ends will withstand very high heat loads. In order to reduce the power density on the surface, a grazing incidence design scheme is usually adopted. Previous design and criteria did not allow the maximum stress of the absorber to exceed the yield limit. According to these criteria, if the front end at HEPS is designed with a fixed mask, the total length of the absorber will exceed 2 m. In a storage ring tunnel with limited space, this design is clearly not the optimal choice. According to the research and the practical experience of ESRF [3], APS [4], and SPring-8 [5], the low cycle fatigue life design method within the elastic-plastic range allows for a certain degree of plastic deformation, effectively solving the contradiction between high heat load and absorber length. The design of the HEPS front end absorber is based on a strain based low cycle fatigue life analysis method. The length of the absorber for UFE 1st fixed mask can be restricted within 700mm, and its service life can meet the 30 year usage requirement under twice the safety factor.

Mechanical Manufacturing

The length of the absorber of the UFE components is nearly 700 mm, shown in Fig. 9, and the maximum processing length of the high-precision slow wire-cut machine is only 300 mm. Therefore, the processing technology of the absorber internal surface and optical aperture is a major challenge for the manufacturing of the front ends at HEPS. The current processing technology is to first use a deep hole drill to make a small hole in the centre of the absorber, then use a medium wire-cut machine to process the optical aperture, then cut out the hourglass shape of the grazing incidence surface, and finally manually polish the inner surface through customized tooling. After testing, the internal surfaces and apertures of the 12 UFE 1st Fixed Masks meet the requirements of geometric tolerances, and the surface roughness is less than Ra0.8.

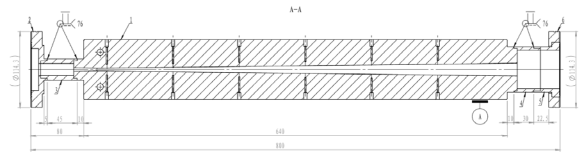

Figure 9: Section view of Fixed Mask.

CONCLUSION AND DISCUSSIONS

The 15 front ends constructed in the phase I of HEPS adopt standardized design, and most of the materials of the absorber are made of dispersed copper alloy. The challenge of High heat loads are well solved by using grazing incidence and enhanced heat transfer, and the design criteria are based on the strain based low cycle fatigue life analysis method. The project has overcome the impact of the COVID-19. At present, 13 of the 15 front ends have completed factory acceptance, and some of the 12 front ends are installed in the tunnel of the storage ring, which is expected to be formally installed in January 2024.

ACKNOWLEDGEMENTS

Thanks to the engineers of HEPS related system for their support and cooperation. Thank you to Sunao Takahashi (SPring-8), Liu Xia (DLS), Zhang Min (SSRF), Li Yongjun (SSRF), Chen Haibo (China University of Science and Technology), and Xiao Weiling (Jiangxi Institute of Technology) for their strong assistance in front end design, fatigue life calculation, and other aspects.

REFERENCES

[1] J. T. Collins, C. M. Conley, J. N. Attig, and M. M. Baehl. "Enhanced Heat Transfer Using Wire-Coil Inserts for High-Heat-Load Applications", in *Proc. MEDSI'02*, Argonne, IL, USA, Sep. 2002.

[2] S. Wang *et al.*, "Test report of enhanced transfer pressure drop of Front End absorber at HEPS", IHEP, Beijing, China, Aug. 2022.

[3] L. Zhang, J. C. Biasci, and B. Plan, "ESRF Thermal Absorbers: Temperature, Stress and Material Criteria", in *Proc. MEDSI'02*, Argonne, IL, USA, Sep. 2002.

[4] J. Collins *et al.*, "Establishment of new design criteria for GlidCop® X-ray absorbers", *J. Synchrotron Radiat.*, vol. 24, pp. 402–412, 2017. doi:10.1107/S1600577517001734

[5] S. Takahashi *et al.*, "Fatigue life prediction for high-heat-load components made of GlidCop by elastic-plastic analysis", *J. Synchrotron Radiat.*, vol. 15, pp. 144–150, 2008. doi:10.1107/S0909049507065

ISBN: 978-3-95450-250-9 ISSN: 2673-5520 doi:10.18429/JACoW-MEDSI2023-WEPPP016

MECHANICAL DESIGN OF XRS AND RIXS MULTI-FUNCTIONAL SPECTROMETER AT THE HIGH ENERGY PHOTON SOURCE

Jiuchang Zhang, Yujun Zhang, Zina Ou, Ruzhen Xu, Zhiying Guo, Shuoxue Jin, Xun Jia, Shanzhi Tang, Weifan Sheng, Wei Xu
Beijing Synchrotron Radiation Facility and High Energy Photon Source, Institute of High Energy Physics (IHEP), Chinese Academy of Sciences, Beijing, China

Abstract

The integration of an X-ray Raman spectroscopy (XRS) spectrometer and a Resonant Inelastic X-ray scattering (RIXS) spectrometer at HEPS is described. The XRS has 6 regular modular groups and 1 high resolution modular group. In total 90 pieces of spherically bent analyzer crystals are mounted in low vacuum chambers with pressure lower than 100 Pa. On the other hand, the RIXS spectrometer possesses one spherically bent analyzer crystal configured in Rowland geometry whose diameter is changeable from 1 m to 2 m. The scattering X-ray photons transport mostly in helium chamber to reduce absorption by air. The RIXS and the high resolution module can be exchanged when needed. Six air feet are set under the granite plate to unload the weight when the heavy spectrometer is aligned. The natural frequency and statics of the main granite rack were analyzed and optimized to maintain high stability for the HEPS-ID33 beamline at the 4th generation source. A type of compact and cost-effective adjustment gadget for the crystals was designed and fabricated. Economic solutions in selection of motors and sensors and other aspects were adopted for building the large spectrometer like this.

INTRODUCTION

The inelastic X-ray scattering spectroscopy in the hard X-ray(>6 keV) regime is an indispensable tool for studying electronic excitations in condensed matter physics. The incident energy can either be in resonance with the binding energy of core-levels, or near the backscattering energy of crystal optics. The former is called resonant inelastic X-ray scattering (RIXS) and the latter is non-resonant inelastic X-ray scattering (NRIXS), also known as X-ray Raman scattering (XRS). To perform RIXS [1] and XRS [2], an energy-analysis spectrometer should be employed. More strictly, the RIXS also requires momentum-analysis, e.g. for studying the dispersion of magnons. Instrumentally, the spectrometers for both techniques are in common, based on the principles of Rowland circle, on which the sample, crystal analyzers and detectors are strictly aligned. Nevertheless, the RIXS spectrometer should sweep over the region of interest in the energy spectrum of scattered energy; while the XRS spectrometer can be static during data acquisition, in so-called “inverse scanning geometry” mode.

The ID33 beamline at High Energy Photon Source is the first beamline dedicated to inelastic X-ray scattering at HEPS. As is designed, the XRS and RIXS techniques will be operated in the same experimental hutch. To be cost-effective, it is reasonable to share the same focusing mirrors and sample stages. In this contribution, we will describe the mechanical design of the spectrometers and the concept for integrated spectrometer for beamlines targeting RIXS and XRS techniques together.

Integration of XRS and RIXS

This spectrometer integrates two functions, an X-ray Raman spectroscopy (XRS) spectrometer and a Resonant Inelastic X-ray scattering (RIXS) spectrometer, on one site, running separately at different time periods as needed.

The XRS has 6 regular modules and 1 high resolution module as planned. Each of them has a low vacuum chamber with pressure lower than 100Pa. A total of 90 pieces of spherical bent analyzer crystals evenly distributed across six chambers. Three modules rotate around sample point in vertical sliding on an arch bridge with a range -35°～163°. Other modules rotate around sample point in horizontal sliding on a base board and are separated by the vertical group on the bridge. The base board has two semicircles with different radii. The larger radius half supports the high-resolution module as well as regular. The XRS is showed in Fig. 1 below.

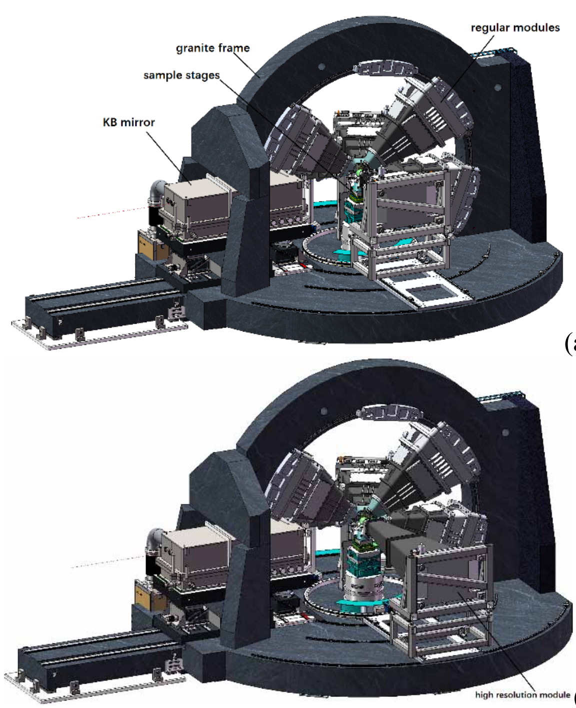

Figure 1: a) XRS with a regular resolution module; b) XRS with a high energy resolution module.

ISBN: 978-3-95450-250-9 ISSN: 2673-5520 doi:10.18429/JACoW-MEDSI2023-WEPPP016

The RIXS is also on the larger half side. It can be exchanged by the high-resolution module. It possesses one spherically bent analyzer crystal configured in Rowland geometry whose diameter is changeable from 1m to 2m. The scattering X-ray photons transport mostly in helium chamber to reduce absorption by air. The RIXS is showed in Fig. 2 below.

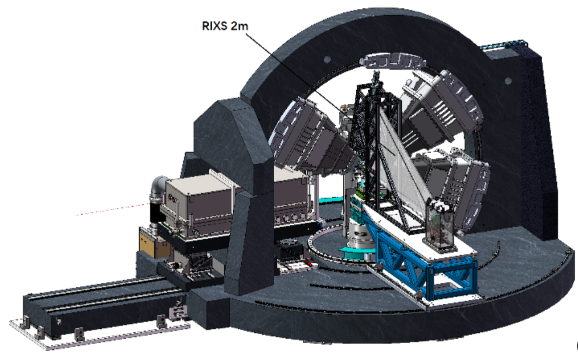

(a)

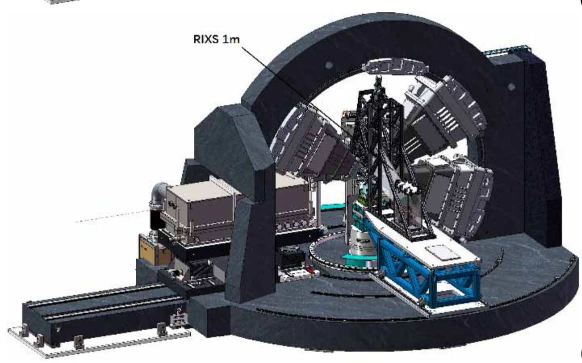

(b)

Figure 2: a) RIXS with 2 m Rowland circle; b): RIXS with 1 m Rowland circle.

Module chambers are made of aluminium. Fifteen analyzer crystals are mounted as a 3×5 array in every chamber. As shown in Fig. 3.

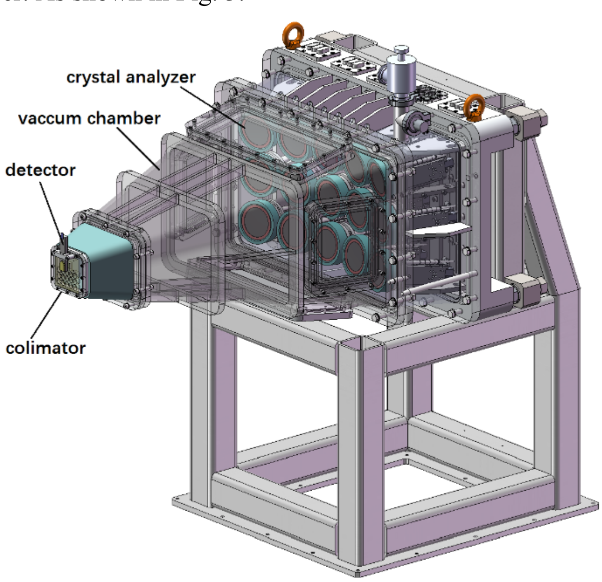

Figure 3: Regular module.

Main Frame

The main frame of the spectrometer is made of granite. The natural frequency and statics of the main granite frame were analyzed and optimized to maintain high stability. According to the measurement of ground vibration, it needed to Increase natural frequency of the frame as highly as possible. The final result is about 44 Hz, as shown in Fig. 4., a) and b) below.

(a)

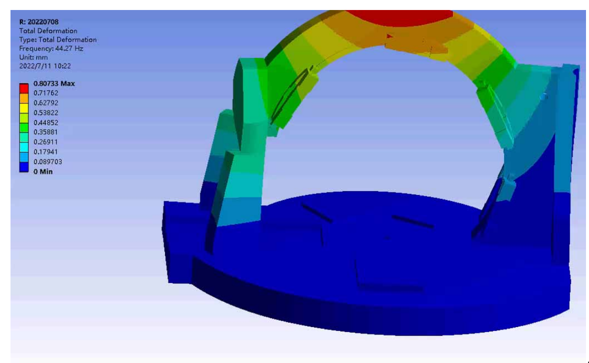

(b)

Figure 4: a) Final frame; b): Natural frequency analysis.

Its total weight is up to 20 tons. Six air feet are set under the granite plate to unload the weight when the heavy spectrometer is aligned finely. Other than these feet, there are several ordinary wedge pad under the base board to support the spectrometer.

Compact and Cost-effective Adjustment Gadget

Analyzer crystals need to adjust at three dimensions, two angles and one translation (Θ, c and a translation along the incident beam direction, tx). Every crystal is in a circular box with a aperture facing the sample and detector. The box can be mounted or removed easily and quickly shown as Fig. 5.

ISBN: 978-3-95450-250-9 ISSN: 2673-5520 doi:10.18429/JACoW-MEDSI2023-WEPPP016

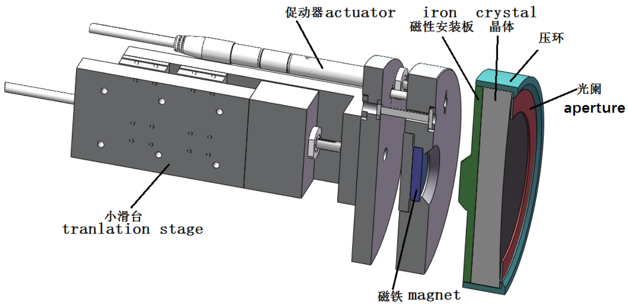

Figure 5: Compact and cost-effective adjustment gadget.

Status and Outlook

The granite frame has been made and is being assembled, as shown in Fig. 6.a). Fifteen analyzer crystal gadgets and one module chamber have been made and tested on one end station in BSRF. Results are satisfied, as shown in Fig. 6 below.


(a)
(b)

Figure 6: a) The granite frame picture; b): Module picture.

CONCLUSION

The multi-functional spectrometer for RIXS and XRS techniques at High Energy Photon Source (HEPS) are described. The granite structure is optimized both to reach a reasonably high natural frequency and to be manufacturable for practical reasons.

There are several advantages for this new design. Firstly, the flexibility of the modular design allows transformer-like combination of spectrometers for different scientific objectives. Secondly, this design is highly cost-effective; hence most of the concept also allows for testing or commissioning new-concept spectrometers at a reasonably low cost in the future. The project is still ongoing, the performance of the spectrometer will be tested at the beamline ID33 once HEPS is running.

ACKNOWLEDGEMENTS

The This work was supported by the High Energy Photon Source (HEPS), a major national science and technology infrastructure in China. We are inspired by various spectrometers in the world, like ESRF ID20, PETRA III P01, APS ID20, SPring-8 BL12XU, etc. We are indebted to fruitful discussions with S. Huotari, M. Sundermann, G.T. Seidler, C. Sahle, J. Ablett, Y. Cai, E. Alp, A. Baron, T.C.Weng, S. Zhang, Y. Ding, etc.

REFERENCES

[1] M. Moretti Sala *et al.*, “A high-energy-resolution resonant inelastic X-ray scattering spectrometer at ID20 of the European Synchrotron Radiation Facility”, *J. Synchrotron Radiat.*, vol. 25, pp. 580-591, 2018. doi:10.1107/S1600577518001200

[2] S. Huotari *et al.*, “A large-solid-angle X-ray Raman scattering spectrometer at ID20 of the European Synchrotron Radiation Facility”, *J. Synchrotron Radiat.*, vol. 24, pp. 521-530, 2017. doi:10.1107/S1600577516020579

ISBN: 978-3-95450-250-9 ISSN: 2673-5520 doi:10.18429/JACoW-MEDSI2023-WEPPP019

COATING REMOVAL OF SILICON-BASED MIRROR IN SYNCHROTRON RADIATION BY SOLUBLE UNDERLAYER

Q. Y. Hou†, S. P. Yue, G. C. Chang, B. Ji, M. Li
Institute of High Energy Physics, Chinese Academy of Sciences, Beijing, China

Abstract

Multilayer optics is widely used for the x-ray beam monochromatization, focusing, and collimation in synchrotron light source. However, the multilayer coatings might be damaged by the high heat loads, the poor film adhesion, the high internal stress, or the inadequate vacuum conditions. As a result, it is essential to develop a method to make the optical substrate reusable without compromising its quality. In our published work, we successfully prepared a W/B_4C multilayer coating with a 2 nm Cr buffer layer on a small-sized Si wafer. The coating was stripped from the Si substrate by dissolving the Cr buffer layer using an etchant. After the etching process, the sample's roughness was comparable to that of a brand-new substrate. We have since utilized this method to clean the multilayers on the surface of a 20 cm × 5 cm silicon-based mirror for High Energy Photon Source (HEPS). The surface roughness and shape were measured, and they reached the level of a brand-new mirror.

INTRODUCTION

The surface of the mirror is coated with a single or multilayer coating of different materials, so that the mirror has high reflectivity or spectral selectivity. Monocrystalline silicon is an ideal substrate for synchrotron radiation optics due to its low density, high mechanical strength, and good thermal stability. Silicon substrates are typically polished to a roughness of only a few angstroms and have an excellent surface shape before being coated with a single or multilayer coating. After long-term service, the coating will deteriorate or even fail due to contamination, mishandling, instantaneous temperature changes, poor adhesion between the coating and the substrate, and high internal stress of the film. The optics need to be updated after a period of service. Therefore, there is a need to study ways to remove optical films to make the expensive high-precision Si substrates reusable.

There are many ways to remove films, such as liquid etching, vapor etching, laser etching, and soluble underlayers [1]. In the preparation of optics with coating in synchrotron radiation, researchers usually prepare a Cr buffer layer on the substrate, and then prepare various optical thin films to reduce the stress of the film and enhance the adhesion force. Therefore, for synchrotron radiation optics, there is an inherent advantage to using the method of soluble underlayers to remove the film. In our published work in Optics Express [2], we successfully prepared a W/B_4C multilayer coating with a 2 nm Cr buffer layer on a small-sized (2 cm × 1 cm) Si wafer. As is shown in Fig. 1, the coating was stripped from the Si substrate by dissolving the Cr buffer layer using an etchant. After the etching process, the sample's roughness was comparable to that of a brand-new substrate. The W/B_4C multilayer coatings with a Cr buffer layer were recoated on the etched samples, and the results of X-ray reflection (XRR) show that the interface roughness was not damaged by the etching process.

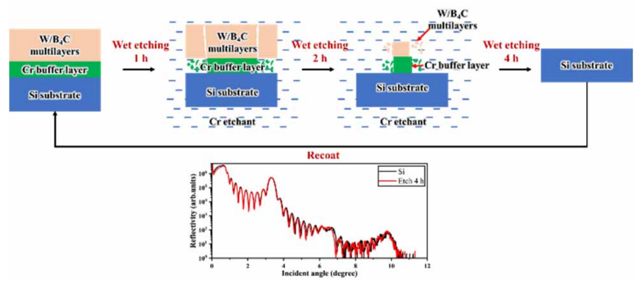

Figure 1: Schematic diagram and XRR results of a refurbished coated silicon wafer with a Cr buffer layer.

The optics used in synchrotron radiation are usually large-size silicon stripes, it is necessary to investigate the applicability of the method of soluble underlayers for refurbishing large-size silicon strips. We have since utilized this method to clean the multilayers on the surface of a 20 cm × 5 cm silicon-based mirror for High Energy Photon Source (HEPS), and the surface roughness and shape at different stages were measured.

EXPERIMENTAL

Films were deposited on the surface of a 20 cm × 5 cm silicon-based mirror by magnetron sputtering at the Platform of Advanced Photon Source Technology R&D (PAPS) in Huairou, Beijing. The deposition parameters of the Cr buffer layer and W/B_4C multilayer film and the etching process were the same as those previously applied on small-sized wafers. To compare the effects of the etching process on different coatings, Pt/ B_4C multilayer film with a Cr buffer layer were also deposited in different areas of the same silicon strip. A mask was used to allow the film to be deposited in a designated area of the silicon stripe. The deposition parameters of the Cr buffer layer in both coatings are the same. The surface roughness was investigated using a non-contact 3D optical surface profiler. The optical figure was measured by Long Trace Profiler (LTP).

RESULTS AND DISCUSSION

Figure 2 is the image of the coated silicon stripe. The W/B_4C multilayer coating was intact, while the surface of the Pt/B_4C multilayer coating was crazing, which might be caused by the high internal stress in the film. Figure 3 shows the etching process. Figure 3(a) shows that the

† Email address: houqy@ihep.ac.cn

ISBN: 978-3-95450-250-9 ISSN: 2673-5520 doi:10.18429/JACoW-MEDSI2023-WEPPP019

middle area of Pt/B_4C multilayer coating, which originally had many cracks, quickly fell off after two minutes etching, while at the same time, the W/B_4C multilayer coating was still intact. After 16 h static etching (Fig. 3(b)), the W/B_4C multilayer coating peeled off completely, while the Pt/B_4C multilayer coating changed little compared to that in Fig. 3(a). After wiping with absorbent cotton for two minutes, the Pt/B_4C multilayer coating peeled off completely quickly. This indicates that different coatings require different etching conditions, static etching is sufficient for the W/B_4C multilayer coating, and for Pt/B_4C multilayer coatings, the etchant diffused from the edge is not enough to complete the etching, it is difficult for the etchant to pass through the Pt//B_4C multilayer coating, and it is necessary to add stirring to create a dynamic etching environment to accelerate the diffusion of etchant.

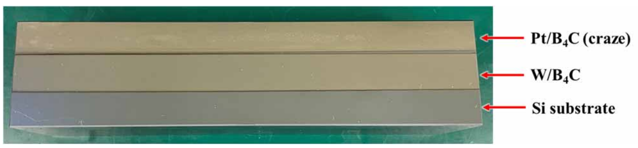

Figure 2: Si stripe after coating.

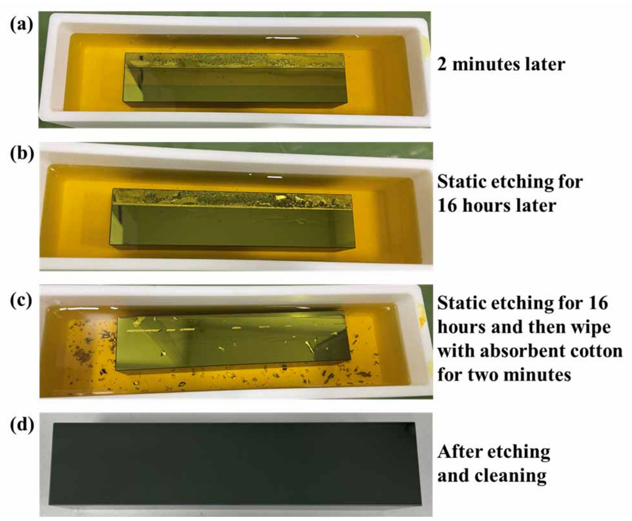

Figure 3: The etching process.

Figures 4 and 5 show the results of the area of W/B_4C multilayer coating measured by 3D optical surface profiler and LTP, respectively. The roughness of eight points was randomly taken to take the average value, and the results are shown in Fig. 6. The standard deviation (SD) of roughness at each stage is also plotted in Fig. 6. Figure 4 (c) shows that the etched surface is homogeneous and free of obvious defects. This is also indicated by the SD in Fig. 6. The specific values of roughness and figure of different stages obtained by 3D optical surface profiler and LTP are listed in Table 1. The roughness and figure of the etched surface do not change much compared to the original surface. Dissolving the buffer layer under static condition can well remove the W/B_4C multilayer coating on the surface of large-size silicon strips.

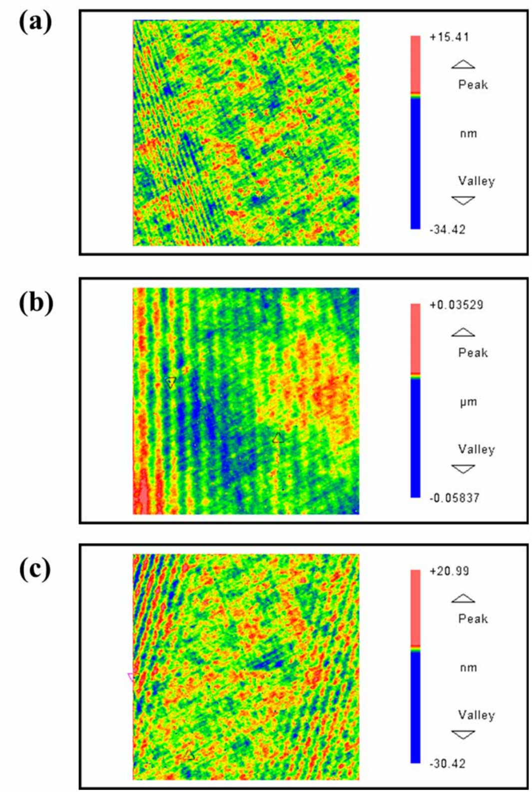

Figure 4: Surface morphology of samples measured by 3D optical surface profiler: (a) Si stripe, (b) after coating and (c) after etching.

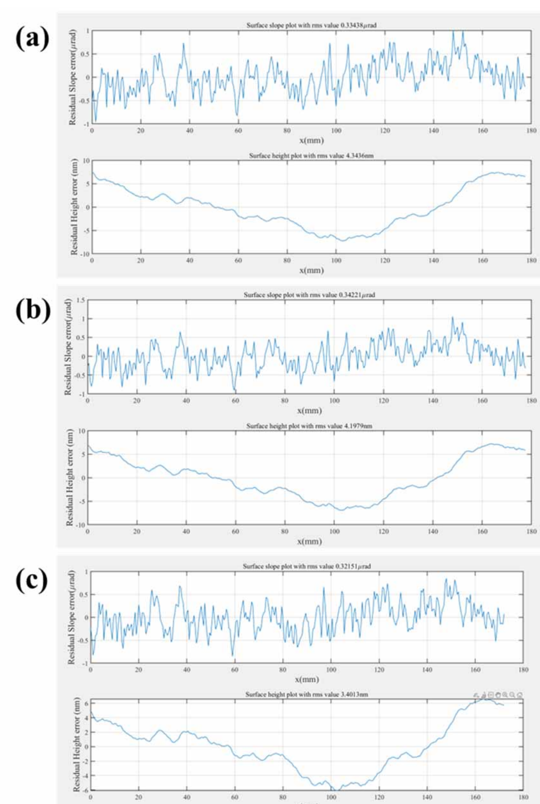

Figure 5: Results measured by LTP: (a) Si stripe, (b) after coating and (c) after etching.

ISBN: 978-3-95450-250-9 ISSN: 2673-5520 doi:10.18429/JACoW-MEDSI2023-WEPPP019

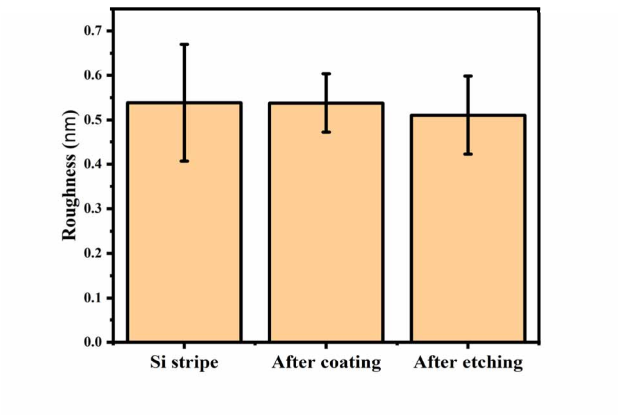

Figure 6: The surface roughness of the Si stripe at different stages.

Table 1: Results Obtained by 3D Optical Surface Profiler and LTP

Silicon-based mirror	Roughness (nm)		Surface slope rms (μrad)
	Average	SD	
Silicon stripe	0.54	0.13	0.33
After coating	0.54	0.07	0.34
After etching	0.51	0.09	0.32

CONCLUSION

Multilayer coatings on large-size Si mirror could be removed by dissolving the Cr buffer layer. Different multilayer coatings need different etching condition. For Pt/B_4C multilayer coatings, it is necessary to add stirring to create a dynamic etching environment to accelerate the diffusion of etchant. Static etching is sufficient for W/B_4C multilayer coatings, and the surface roughness and shape could reach the level of a brand-new mirror by dissolving the Cr buffer layer using an etchant.

ACKNOWLEDGEMENT

A special thanks goes to Rongli Cui at IHEP for sharing their measurement technology.

REFERENCES

[1] A. Khounsary *et al.*, “Recoating mirrors having a chromium underlayer”, in *Proc. SPIE 5193*, San Diego, California, USA, Aug. 2003. doi:10.1117/12.512779

[2] Q. Y. Hou *et al.*, “Refurbishment of W/B4C multilayers on Si substrate by etching a chromium buffer layer”, *Opt. Express*, vol. 30, no. 26, pp. 48042-48050, 2022. doi: 10.1364/OE.477147

ISBN: 978-3-95450-250-9 ISSN: 2673-5520 doi:10.18429/JACoW-MEDSI2023-WEPPP024

DESIGN OF A HARD X-RAY NANOPROBE BASED ON FZP*

Keliang Liao, Maohua Song, Panyun Li
Jinan Hanjiang Opto-Electronics Technology Company Ltd., Jinan, China
Ping Zhou, Wenqiang Hua†
Shanghai Advanced Research Institute, Chinese Academy of Sciences, Shanghai, China
Qili He, Peiping Zhu†
Institute of High Energy Physics, Chinese Academy of Sciences, Beijing, China
Liang Luo, Tsinghua University, Beijing, China

Abstract

A high-resolution hard X-ray nanoprobe (HXNP) based on Fresnel Zone plate (FZP) was designed. The HXNP relies on a compact, high stiffness, low heat dissipation and low vibration design philosophy and utilizes FZP as nanofocusing optics. The optical layout and overall mechanical design of the HXNP were introduced. Several important modules, such as probe module, sample module, interferometer module and vacuum chambers were discussed in detail.

INTRODUCTION

In recent years, X-ray nanoprobe operating in the hard X-ray regime has achieved rapid improvements based on the development of a lot of advanced X-ray optics, such as Fresnel zone plate (FZP) [1], multilayer Laue lens (MLL) [2], nanofocuisng K-B mirror. With outstanding quantitative non-destructive three-dimensional (3D) imaging capabilities, the hard X-ray nanoprobe (HXNP) has attracted significant interest across many different disciplines. In previous work, a prototype of HXNP with about 70 nm spacial resolution was constructed and tested at Shanghai Synchrotron Radiation Facility (SSRF) [3]. Driven by the needs of observing and analyzing the internal fabrication defects of the chips with feature size smaller than 28 nm, this paper introduced the recent development of a new HXNP based on FZP.

INSTRUMENT DESIGN

Optical Layout

As depicted in Fig. 1(a), the FZP was chosen as the nanofocusing optics. In order to select the -1st diffraction order of the FZP, a central beamstop (BS) and an order sorting aperture (OSA) were also utilized. The BS, FZP, OSA and their corresponding adjustment components together constituted the probe module. The coherent X-ray from the upstream of the beamline could be focused by the above probe module to form an X-ray nanoprobe, which was also the illumination probe for the ptychographic imaging.

The sample was located near the focus of the FZP. With XY two-dimensional (2D) scan of the sample, a series of diffraction patterns could be acquired by the far-field detector. As the over-sampling condition is satisfied, the 2D electron density distribution of the sample over the fully scanning area could be reconstructed. Moreover, by combining with the CT technology, the 3D sample information could be revealed. An in-line visible light microscope (VLM) was placed behind the sample for coarse adjustment of the FZP and fast calibration of the sample.

According to the functional requirements of the instrument, the freedom of motion required by the HXNP was also shown in Fig. 1(b).

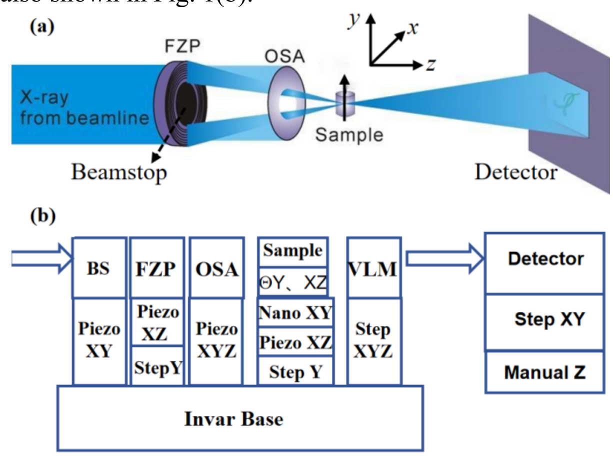

Figure 1: The optical layout of the HXNP.

Overall Scheme of the HXNP

The 3D mechanical design of the HXNP optimized for ptychographic imaging was shown in Fig. 2. The HXNP mainly consists of several important modules, including the welding supporting frame, the marble supporting base, the imaging module, the vacuum chamber and the detector module, which have been marked clearly in Fig. 2. The following was a further introduction.

First, a set of welding frame with high-rigidity was designed as the supporting base for the vacuum chamber. In order to decouple the vibration of the optical vacuum chamber from that of the imaging module, a more stable marble base was utilized for the supporting of the imaging module.

Second, the imaging module is composed of the probe module, the sample module, the interferometer module and

*Work supported by Jinan Haiyou Industry Leading Talent Project (2022), the National Natural Science Foundation of China (No.11505278, 11875315), the National Key R&D Program of China (2020YFA0405802), Innovation Promotion Project of SME in Shandong Province (No.2023TSGC0093).
† huawenqiang@zjlab.org.cn and zhupp@ihep.ac.cn

ISBN: 978-3-95450-250-9 ISSN: 2673-5520 doi:10.18429/JACoW-MEDSI2023-WEPPP024

the VLM module, which were depicted in Fig. 3. The imaging module was designed in a compact style. As for the selection of motion stages, a combination of piezo stages with low heat dissipation and stepper stages with large stroke and high load capability was balanced.

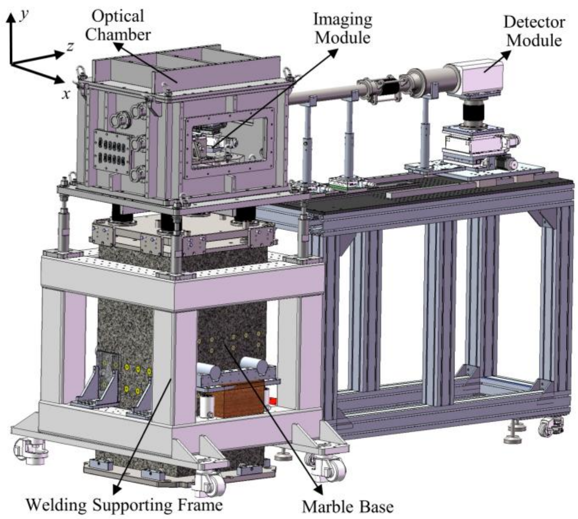

Figure 2: The overall scheme of the HXNP.

Third, the imaging module of the HXNP was installed on the Invar supporting base with a kinematic mounting design.

The design of all modules, including the selection of motion stages, the corresponding structural design and assembly design, was optimized by means of engineering analysis.

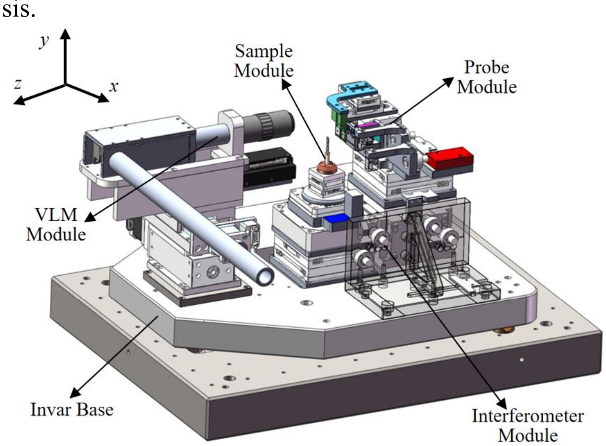

Figure 3: Mechanical model of the imaging module.

Probe Module

The probe module consists of FZP, OSA, BS and their adjustment components. As presented in Fig. 4, this module is quite compact with all components mounted on a high-load vertical stage ES10-Z12, which could handle up to a 5 kg load over 12 mm stroke. Two CLS9292 piezo stages were utilized for the movement of FZP in X and Z directions. The XY piezo stages for beamstop were mounted near the central part of the FZP assembly. As a comparison, the XYZ piezo stages for OSA was mounted on one side. The balancing of weight was also carefully considered.

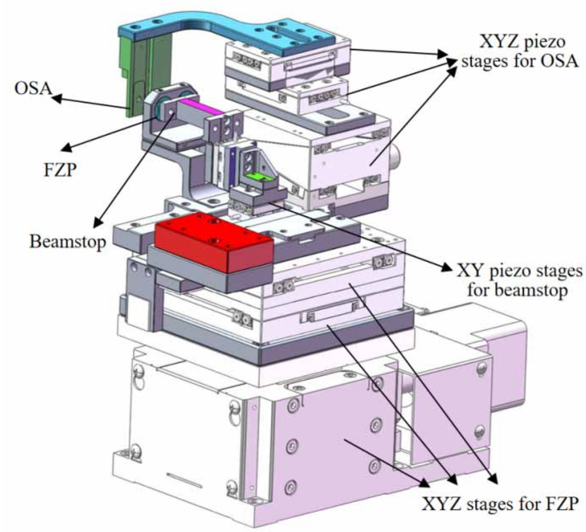

Figure 4: Details of the probe module.

Sample Module

A useful sample module was designed as shown in Fig. 5. The bottom was one stepper stage with high load capability in Y axis. Two piezo stages CLS9292 were used for the adjustment of sample in X and Z direction. The 2D ptychographic scan of the sample was realized through the flexure nano stage P-733.3DD. A piezo rotation stage SRM7012 was selected for the CT scan. Two piezo stages CLS3232 were used for the calibration of the rotation axis.

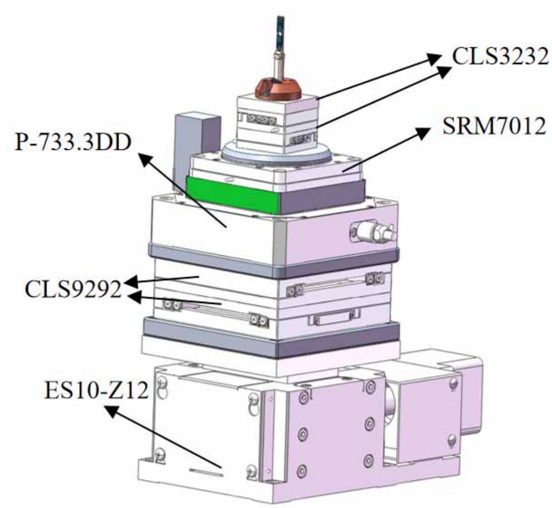

Figure 5: Details of the sample module.

Interferometer Module

The interferometer module is crucial for the HXNP especially when CT imaging is required. Two sets of IDS3010 interferometer with sub-nm accuracy from Attocube were utilized for the closed-loop control of both the probe module and the sample module. Totally 6-Axes closed-loop control were available by the above two sets of IDS3010. Figure 6 shows all the six optical paths of the interferometer, among which two absolute position loops

ISBN: 978-3-95450-250-9 ISSN: 2673-5520 doi:10.18429/JACoW-MEDSI2023-WEPPP024

were designed for FZP, another two absolute position loops were designed for sample, and the last two loops were prepared for the relative position control between FZP and sample. In Fig. 6, the red arrow and the yellow arrow represent the horizontal loop (X direction) and the vertical loop (Y direction) respectively.

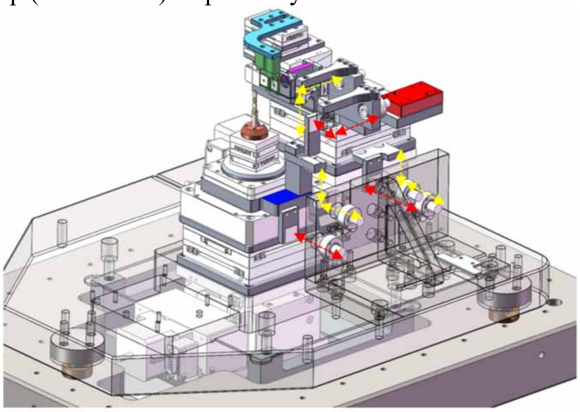

Figure 6: Schematic of the interferometer module.

Vacuum Chamber

A vacuum chamber was designed for the optical elements, shown in Fig. 7. The imaging module was mounted inside the optical chamber with the decoupling mechanism. This chamber could operate with HV pressures and at atmospheric pressure. The length of the vacuum pipe between the chamber and the detector was adjustable for different applications. A 3D manual adjustment assembly for the vacuum pipe was designed.

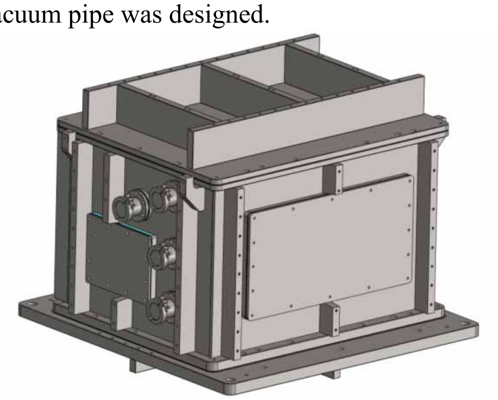

Figure 7: Schematic of the vacuum chamber.

The vacuum chamber was designed with various ports for SDD fluorescence detector, laser interferometers, and windows, which can be seen in Fig 7. The SDD fluorescence detector was mounted parallel to the horizontal X axis. A vacuum door was designed for the convenience of sample exchanging.

Control System

The control system for this HXNP is called HDC-Instrument, which is a distributed control system developed by C# programming language and based on the .NET 6 platform. The HDC-Instrument is configured with powerful functions, including motion control, environment parameter monitor, process control, log system, and imaging process.

CONCLUSION

Based on the prototype of HXNP, which has been constructed and verified at the beamline of SSRF [3], a new high-resolution HXNP utilizing FZP as nanofocusing optics was designed. In future work, further optimization and upgrade for this HXNP will be conducted.

REFERENCES

[1] Z. Qin *et al.*, “Initial probe function construction in ptychography based on zone-plate optics”, *Appl. Opt.*, vol. 62, pp. 3542-3550, May 2023. doi:10.1364/AO.487694

[2] E. Nazaretski *et al.*, “Design and performance of an X-ray scanning microscope at the Hard X-ray Nanoprobe beamline of NSLS-II”, *J. Synchrotron Radiat.*, vol. 24, pp. 1113-1119, Nov. 2017. doi:10.1107/S1600577517011183

[3] G. Zhou *et al.*, “Preliminary exploration of hard X-ray coherent diffraction imaging method at SSRF”, *Acta Phys. Sin.*, vol. 69, no. 3, p. 034102, Feb. 2020. doi:10.7498/aps.69.20191586

ISBN: 978-3-95450-250-9 ISSN: 2673-5520 doi:10.18429/JACoW-MEDSI2023-WEPPP025

APPLICATION OF CuCrZr IN THE FRONT-END OF SHANGHAI SYNCHROTRON RADIATION FACILITY

Shuai Wu, Jun-Nan Liu, Jin-Wei Wang, Yong-Jun Li
Shanghai Advanced Research Institute, Chinese Academy of Sciences, Shanghai, China

Abstract

At present, Glidcop® Al-15, oxygen-free high thermal conductivity（OFHC）copper and other materials are mainly used in the front-end of the Shanghai Synchrotron Radiation Facility (SSRF). CuCrZr has high heat load capacity, high yield strength and tensile strength, good thermal conductivity, and low vacuum outgassing rate. At present, it has been used as the heat sink material in the heat exchanger of nuclear reactors. Due to the above characteristics, CuCrZr has the basic ability to be an excellent substitute material for synchrotron radiation heat load. However, there are also some problems in the application of CuCrZr materials. The softening temperature is not high enough. Because the brazing process is needed in the processing engineering of the heat load absorber, the brazing process needs more than 500 °C, so the brazing process cannot be used in the processing of the absorber. In this paper, based on the previous process exploration, the front-end absorber is made of CuCrZr material, and the technical scheme of integral processing of flange and absorber is adopted. The thermal stress and deformation of CuCrZr absorber are analyzed by finite element method, and the processing of CuCrZr absorber is completed, and it is applied to the SSRF BL04U&04W canted front-end. After a period of electron beam cleaning, vacuum and temperature tests were carried out under high thermal load power, and the characteristics of the material in practical use were analyzed, which proved that CuCrZr material can be used for the high heat load at SSRF font end.

INTRODUCTION

The main materials used for thermal radiation absorption in the front end of synchrotron radiation light source are Glidcop® Al-15, oxygen-free high thermal conductivity（OFHC）copper and other materials. OFHC is usually used as a material for synchrotron radiation absorbers, especially in the first and second-generation synchrotron radiation light sources. However, the third-generation synchrotron radiation light source uses more insert devices, and the power density of the synchrotron radiation light source is improved. OFHC cannot handle the higher power and higher power density thermal power. Glidcop® Al-15 material has high tensile strength and is used as the material of high heat load absorber. At present, Glidcop® Al-15 material is used as the fixed mask (FM) at the front end of most beamline in SSRF. Glidcop® Al-15 material is an Al_2O_3 dispersed copper oxide material developed by Hoganas, USA. Generally, it is provided in standard size, non-standard size can only be customized, and the cost of customization is so high. CuCrZr material has high heat load capacity, high yield strength and tensile strength, good thermal conductivity and low vacuum outgassing rate. At present, it has been used as a heat sink material in the heat exchanger of nuclear reactors. Due to the above characteristics, CuCrZr has the basic ability to be an excellent substitute material for synchrotron radiation heat load. The mechanical properties, photo desorption properties and vacuum properties of CuCrZr have been tested [1–3]. It is proved that the material can be used for absorption of synchrotron radiation light source.

However, there are also some problems in the application of CuCrZr materials. The softening temperature is not high enough. Because the brazing process is needed in the processing engineering of the heat load absorber, the brazing process needs more than 500 °C, so the brazing process cannot be used in the processing of the absorber. SSRF is the first third-generation synchrotron radiation light source in China. Most of the absorbers at the front end of the beamline use Glidcop®AL15 material as the main heat absorption material. At present, CuCrZr is a good alternative material to meet the needs of high heat load in the front-end. The main beamlines of SSRF are divided into three types, bending magnet beamline, insert device beamline and Canted beamline. The Canted beamline is generally composed of two insertion beamlines. The general insert device is the undulator, and the angle between the two beamline stations is 6 mrad.

DESIGN OF BL04U&04W FRONT-END

Physical Parameters of Insert Devices

The BL04U and BL04W beamline stations are Canted beamline. BL04U uses a vacuum undulator (IVU20), which is located upstream of the insert device center, and BL04W uses a wiggler, which is located downstream of the insert device center. The angle between the beamlines and the center line of insert device is 4 mrad, and the angle between beamlines is 8 mrad. Incident angle BL04U, BL04W are shown is Table 1.

Table 1: Incident Angle of BL04U&BL04W

Beamline	Insert device	Output angle (mrad²)	Input angle (mrad²)	Power (kW)
BL04W	Wiggler	1.8×0.18	4×1	9.287
BL04U	IVU	0.3×0.15	2×1	2.62

Design of PreM

Generally, the PreM only bears the light source from bending magnet, and the main body adopts OFHC material. However, the horizontal tracing of the BL04U & 04W front-end, the PreM bears the appropriate beam source

ISBN: 978-3-95450-250-9 ISSN: 2673-5520 doi:10.18429/JACoW-MEDSI2023-WEPPP025

from the insert device can reduce the photon beam size, thereby reducing the component size after the PreM.

The inlet flange of PreM adopts CuCrZr, the cover plate of the cooling pipe adopts OFHC, and the outlet adopts stainless steel flange to weld with the main part of CuCrZr. After brazing the stainless-steel cooling pipe and OFHC cover plate, the electron beam welding is carried out with the main part. It can be seen in Fig.1.

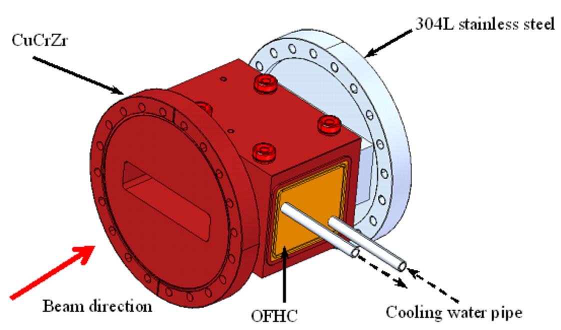

Figure 1: Design of Pre-M (CuCrZr).

Design of BS

CuCrZr is made as the main body of BS. There are two cavities in the body. The middle part is made for absorption of the beam from beading magnet. The mask adopts a double V-shaped. The cover plate adopts OFHC material. The stainless-steel cooling pipe and the OFHC cover plate are brazed and then using electron beam welding into one with the CuCrZr part. The structure of the BS is shown in Fig. 2.

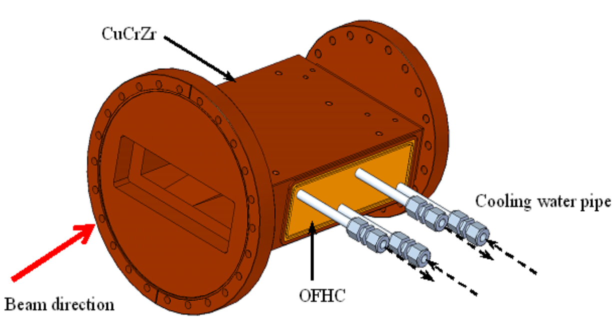

Figure 2: Structure of BS (CuCrZr).

THERMAL ANALYSIS

The PreM is 8048 mm away from the wiggler light source, the incident angle is 4.4 × 1 mrad^2, the distance from the downstream bending magnet is 3203 mm, the incident angle is 16.3 × 2.75 mrad^2, the water cooling is adopted, the water volume is 8 L/min, the thermal convection coefficient is 20000 W/m^2°C, temperature of cooling water = 30 °C, and the water pressure is 8 bar. CuCrZr materials were selected for thermal analysis both. The parameters of OFHC and CuCrZr are shown in Table 2.

Table 2: Parameters of CuCrZr

Materials	CuCrZr
Density (kg/m^3)	8900
Thermal Conductivity (W/m°C)	330
CTE (l/°C)	1.7e-5
Young's modulus(GPa)	128
Poisson's Ratio	0.33

The design criteria of materials CuCrZr are shown in Table 3 [1, 4].

Table 3: Design Criteria of CuCrZr

Maximum equivalent stress (MPa)	Overall maximum temperature (°C)	Maximum temperature of the cooling wall (°C) at 8bar
350	250	160

RESULTS AND DISCUSSION

Thermal Analysis Results

PreM needs to withstand the heat load from undulator, CuCrZr materials is used for thermal analysis.

The FEA results are shown in Fig. 3, all of which meet the design criteria listed in Table 3.

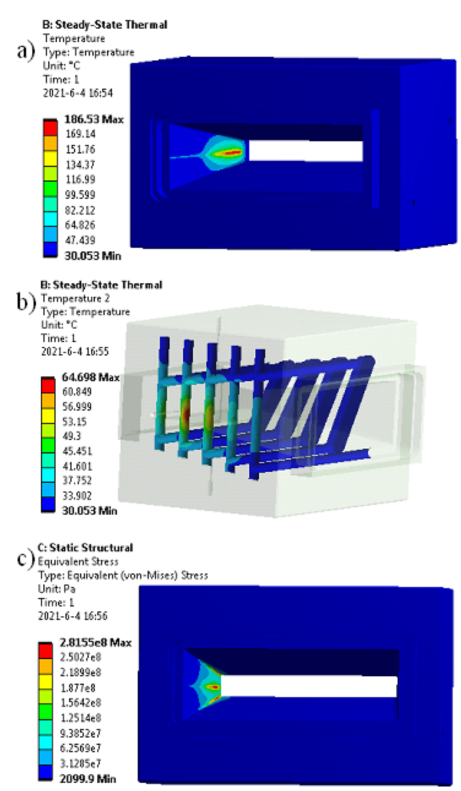

Figure 3: FEA results of PreM (CuCrZr). a) Overall temperature distribution b) Cooling tube wall temperature distribution c) Equivalent stress distribution.

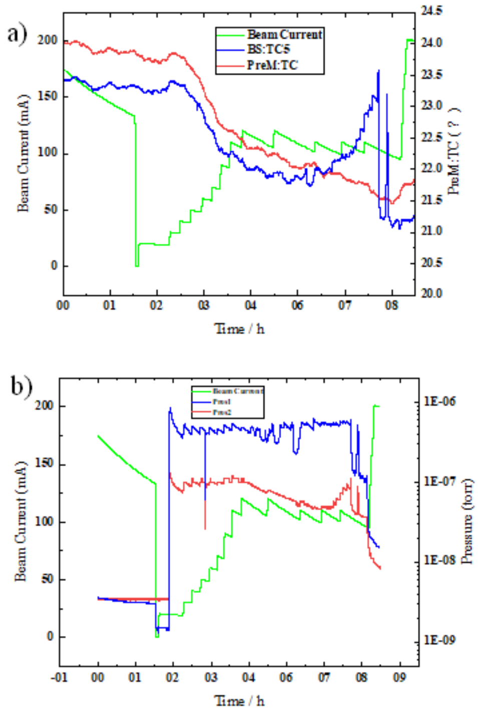

Figure 4: Online results of BL04U&04W front-end. a) Temperature of Prem and BS; b) Vacuum of front-end.

Application Results

On April 26, 2023, the PreM (CuCrZr) and BS (CuCrZr) was tested. Firstly, under the beam current of 20 mA to 120 mA, the temperature of the PreM and the vacuum of the front-end are recorded. Then, under the beam current of 120 mA, the BL04U undulator gap is gradually closed from 20 mm to 6 mm, and the BL04W wiggler gap is closed from 100 mm to 15 mm. From the results of Fig. 4a), the temperature of BS and PreM does not change much, and the temperature rises when the insert device adjusted the gap. From the results of Fig. 4b), the vacuum of front-end changes from 10^{-9} torr to 10^{-6} torr, the vacuum is difficult to maintain, but the vacuum gradually decreases. It shows that the light-induced desorption gasrelease rate of CuCrZr is still large, and it more hours to handle the gas release. The results show that the BS(CuCrZr) and PreM (CuCrZr) of BL04U & BL04W front-end meet the requirements.

CONCLUSION

Glidcop® Al-15 and OFHC are the main materials of high heat load absorbers now. However, Glidcop® Al-15 is expensive and OFHC cannot withstand high heat load. CuCrZr has good mechanical properties and is very suitable for the high heat load absorber in the front-end. This paper introduces the application of CuCrZr in BL04U and BL04W front-end at SSRF. In the design of PreM and BS, CuCrZr is used as main body. Some stainless-steel flanges are used, and the water-cooled cover plate is separately brazed and electron beam welded with the main part. This not only avoids the disadvantage that CuCrZr cannot be brazed, but also CuCrZr is applied to the absorption of high heat load. Then, the FEA of the PreM with CuCrZr the PreM with CuCrZr the BS with CuCrZr are carried out. The results show that the PreM and BS with CuCrZr can meet the demands. Finally, the front-end has been successfully installed and tested.

REFERENCES

[1] Chen Ming, “Study on Vacuum Properties of CuCrZr based on Synchrotron Radiation High Heat Load”, Ph.D. thesis, University of Chinese Academy of Sciences, 2021.

[2] C. Shueh *et al.*, “Investigation of vacuum properties of CuCrZr alloy for high-heat-load absorber”, *Nucl. Instrum. Methods Phys. Res. Sect. A*, vol. 841, pp. 1—4, 2017. doi:10.1016/j.nima.2016.10.025

[3] Yongjun Li, Limin Jin, Wanqian Zhu, Song Xue, Min Zhang, and Shuai Wu, “Vacuum joints of CuCrZr alloy for high-heat-load photon absorber”, *J. Synchrotron Radiat.*, vol. 29, pp. 363–368, 2022. doi:10.1107/S160057752101273X

[4] Yongjun Li, “Design and Study of High Heat Load Front-end at SSRF”, Ph.D. thesis, University of Chinese Academy of Sciences, 2016.

ISBN: 978-3-95450-250-9 ISSN: 2673-5520 doi:10.18429/JACoW-MEDSI2023-WEPPP029

A NOVEL FLEXIBLE DESIGN OF THE FaXToR END STATION AT ALBA

L. Ribó†, A. Patera, N. Gonzalez, L. Nikitina
ALBA Synchrotron Light Source, Cerdanyola del Valles, Spain
A. Mittone, Argonne National Laboratory, Illinois, US

Abstract

FaXToR is one of the beamlines currently in construction and commissioning phase at ALBA, dedicated to fast hard X-ray imaging. It will offer absorption and phase contrast imaging to users. Possible applications of the beamline include 3D static and dynamic inspections in a wide range of applications. FaXToR aims to provide both white and monochromatic beam of maximum 36x14 mm (HxV) at sample position with a photon energy up to 70 keV. The optical layout of the beamline will tune the beam depending on the specific experimental conditions. Among the required optical elements, there is a multilayer monochromator, the cooled slits, the filtering elements, the intensity monitor and the beam absorption elements. The end station will be equipped with a rotary sample stage and a detector system table to accommodate a dual detection thus simultaneously scanning the samples with high spatial and temporal resolutions. On top of it, a motorized auxiliary table dedicated to complex sample environment or future upgrades will translate along the total table length, independently from the two detector system bridges. The design and construction process of the beamline will be presented.

INTRODUCTION

The FaXToR - Fast X-ray Tomography and Radioscopy beamline at ALBA will operate a micro-tomography station working in the hard x-ray regime. The beamline will provide users with sub-second computed tomography capabilities in both absorption and phase-contrast imaging regimes [1]. FaXToR will give service for material science and engineering, health, biology, food science, archaeology, cultural heritage, geology, paleoethology, environment. The capability of performing simultaneous fast 3D acquisition with a multi-resolution approach and the presence of a versatile detector environment will make the beamline unique thus providing the opportunity to users to access a novel data package, which can be reconstructed and analysed directly at the facility site or remotely.

FaXToR LAYOUT

FaXToR source is an in-vacuum multipole wiggler. The front-end angular opening is set to 1×0.4 mrad^2 (H×V). The main optical element of the beamline is a Double Multilayer crystal Monochromator (DMM). No other optics elements besides attenuators, slits and diagnostics are included in the design.

The experimental hutch includes a beam conditioning elements table holding the sample slits, a second CVD diamond window and a fast shutter. It follows a fly tube equipped with Kapton foil windows to minimize the air absorption at lower x-ray energies and the exhaust ozone in white beam conditions. Such a pipe will be directly link to the tomography stage, located at 36.5 m from the source. Samples of different dimensions up to 5 cm in diameter and 30 cm in height will be located on top of the rotary stage, reaching a maximum speed of 750 rpm depending on the sample weight. The detector table is 4 meters long and is supporting two detection systems: a triple magnification microscope and a low resolution macroscope, together with a dedicated positioning stage and an auxiliary table. All those mentioned elements are able to be displaced along the beam direction. FaXToR foresees two detectors and four cameras to be positioned at a short distance from the sample (for scanning in absorption mode) or at a longer distance (to implement the free space propagation modality in the case of low absorbing matters). Such a configuration is easily interchangeable according to the user experimental requirements. Figure 1 represents the previously mentioned elements.

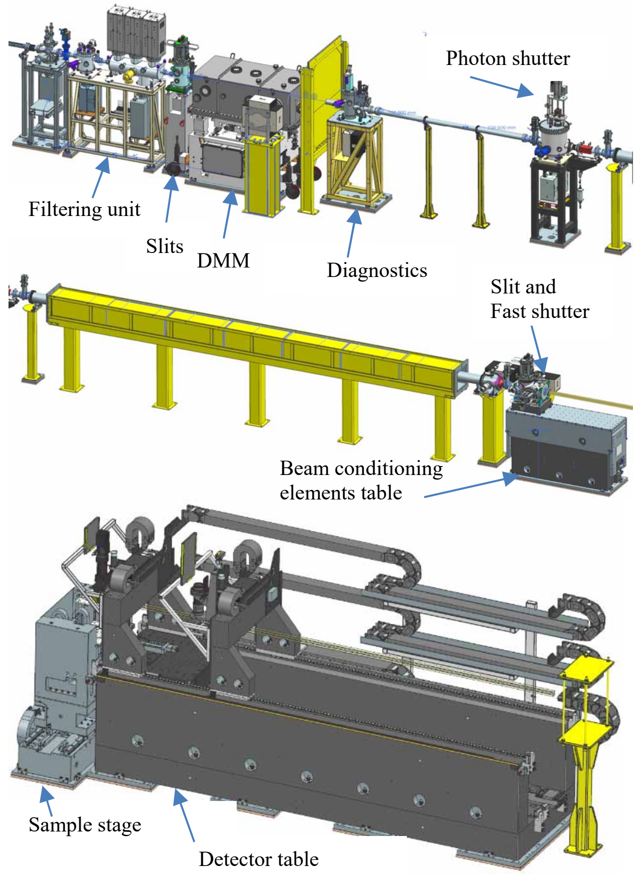

Figure 1: Layout of FaXToR: optics (top), shielded transfer pipe (middle) and end station (Bottom).

† lribo@cells.es

12th Int. Conf. Mech. Eng. Design Synchrotron Radiat. Equip. Instrum. MEDSI2023, Beijing, China JACoW Publishing
ISBN: 978-3-95450-250-9 ISSN: 2673-5520 doi:10.18429/JACoW-MEDSI2023-WEPPP029

DETECTOR TABLE SPECIFICATION

The detector table consists of two detector positioners and an auxiliary table. The detector positioners are bridge shaped and are designed to accommodate the two microscopes equipped with scintillators and CMOS cameras on top. Furthermore, an auxiliary table is integrated in the design to be positioned along the full detector longitudinal range and to be aligned in height accordingly to the beam position.

A schematic view of the detector table and its main parts are represented at Fig. 2. A front view of the design is included, showing the auxiliary table embedded into the detector table which can move independently from the bridges.

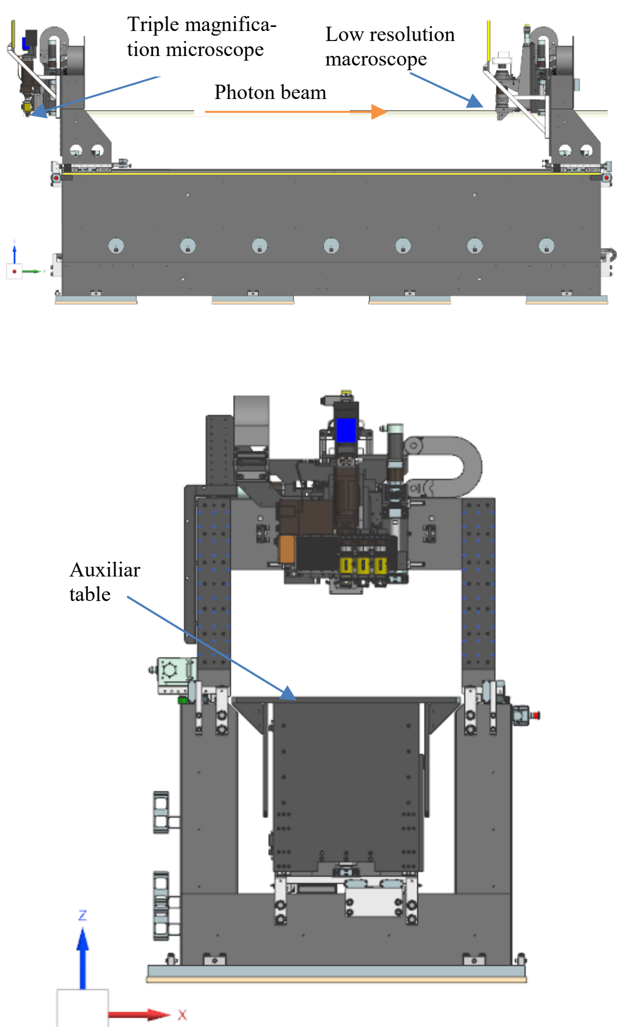

Figure 2: Top: side view of the detector table, bottom: front view.

The specification for full equipment is summarized in Table 1.

Table 1: Specification

parameter	value	comments
Detectors positioning in Y	3225 mm	
Detector positioning in X	+/-50 mm	
Detector positioning in Z	0/+100 mm	To position depending on beam height and to put detector fully apart from beam path
Resolution Y	100 µm	Along the beam
Accuracy Y	50 µm	Guiding accuracy in full length
Resolution X, Z	2 µm	Transversal to the beam,
Auxiliary table Y range	3500 mm	
Auxiliary table Z range	350 mm	Height of top surface from 1000 to 1350 mm
Auxiliary table max. supported weight	95 kg	

DETECTOR BRIDGES

The detector bridge design is identical for both detectors, as the positioning specifications are the same. The guiding in Z and X has solved with recirculating ball linear guides, and force transmission for their movements are by ball spindles. In order to maximize vibration stability, matched pairs of roller linear guide assemblies are chosen for guiding the detector bridge along the photon beam direction. In the case of the force transmission, a rack and pinion system were considered optimal, due to its long stroke and because the resolution requested for this axis is not as high as needed in the transversal plane.

The detector plane perpendicular to the beam can be aligned in yaw with the use of a goniometer designed to be guided by circular guides and driven by a linear movement actuated by spindle. The transmission of the force is given by a flexure.

All those mentioned movements are foreseen to be moved by stepper motors while their position is known by the read of an absolute encoder. Limit switch between detector bridges has been implemented in order to avoid collisions during operation.

The bridge is composed by three granite pieces assembly similar to the base table which presents a U shape and has been designed to support the two bridges and the auxiliary table on the floor. In Fig. 3, an overview of the bridges elements is shown.

ISBN: 978-3-95450-250-9 ISSN: 2673-5520 doi:10.18429/JACoW-MEDSI2023-WEPPP029

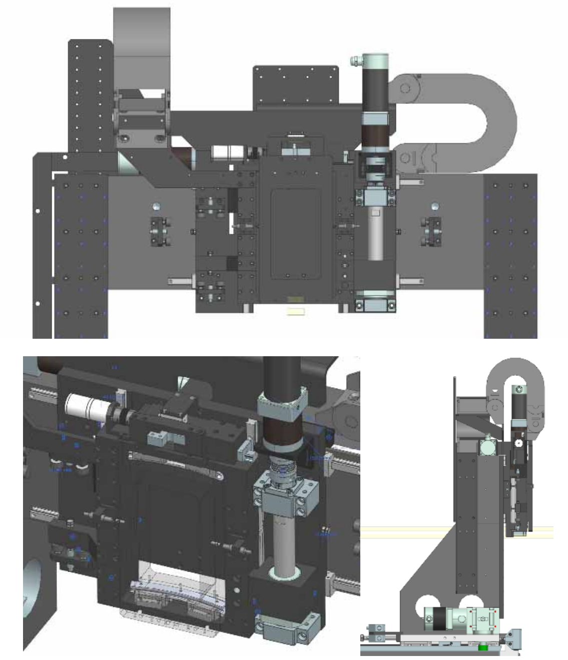

Figure 3: XY stage of the detector positioning bridge. transversal and longitudinal guiding, and spindle for vertical movement can be appreciated. Bottom left: Detail of the integrated goniometer for yaw adjustment, the circular guides are represented in top view. Bottom right: left side view of the detector positioning bridge where the rack and pinion are located.

THE AUXILIARY TABLE

The auxiliary table, which is integrated into the main detector table, as it can be seen in Fig. 2, is able to be displaced along the beam direction independently of the position of the two detectors. This makes the design very flexible in terms of the its capability for user operation.

The auxiliary table has been designed to be stable enough to support in-situ sample devices, or other setups that require high stability. The top interface of the table is 800 mm^2 with a standard hole pattern to provide flexibility on the preparation of different setups.

The height is variable from 1000 to 1350 mm and is driven by a double actuator driven by ball linear guides and spindles. Both actuators are driven with a single motor and a gear box. The system is designed to be irreversible when no power is holding the torque of the motor.

Same as the detector bridges, the auxiliary table is driven along beam direction by roller linear guides and a rack and pinion system for transmission. All the mentioned elements can be seen in Fig. 4.

FEA CALCULATION

Final geometry has been optimized after several runs of FEA. The results are shown in Fig. 5.

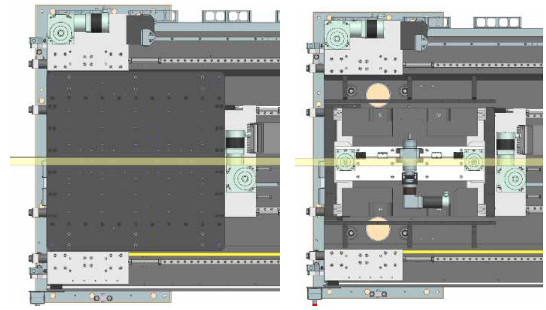

Figure 4: left: the top surface of the auxiliary table. Right: same view without top plate where the driving mechanism are shown.

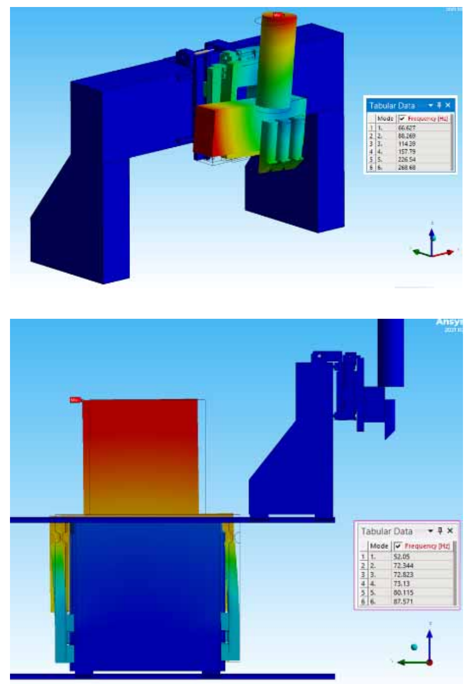

Figure 5: First eigenmodes on the detector bridge (top). eigenmodes on top of auxiliary table, with a mass of 100 kg on top (bottom).

CONCLUSION AND NEXT STEPS

A flexible design for the tomography end station has been conceived, as the detector position can be independent on the position of the auxiliary table. Both detectors can be moved in three linear axis and can rotate on the vertical axis. The triple magnification microscope and the macroscope can be interchangeable, same for the four cameras. The detector table will be assembled and commissioned on the first half of 2024, when all the motorized axis is going to be tested in terms of guiding accuracy and repeatability. FaXToR will provide light to the users on the second half of 2024.

REFERENCES

[1] A. Mittone, L. Ribo, A. Patera, J. Campmany, C. Colldelram, and J. Nicolas, “A new beamline for hard X-ray tomographic microscopy at the Spanish Synchrotron ALBA”, *J. Phys. Conf. Ser.*, vol. 2380, p.012035, 2022. doi:10.1088/1742-6596/2380/1/012035

ISBN: 978-3-95450-250-9 ISSN: 2673-5520 doi:10.18429/JACoW-MEDSI2023-WEPPP030

MAX IV – MicroMAX DETECTOR STAGE*

S. Benedictsson†, M. Al-Najdawi[1], O. Aurelius, G. Felcsuti, J. Lidon-Simon, M. Milas, T. Ursby
MAX IV Laboratory, Lund, Sweden
[1]also at SESAME, Allan, Jordan

Abstract

The MicroMAX beamline at MAX IV Laboratory will employ two detectors to be used independently and move along the beam depending on the diffraction target resolution, starting close to the sample hanging partially over the sample table. The X-ray beam can be deflected by Kirkpatrick-Baez (KB) mirrors in the horizontal and vertical directions or pass undeflected.

The MAX IV Design office designed a detector stage as an in-house project based on the ALBA table skin concept to switch between the two detectors and accurately position the selected detector, either with or without the KB mirrors.

To achieve stability and precision during translations, a large granite block is used, as well as preloaded linear and radial guides, and preloaded ball screws with stepper motors and, in most cases, a gear box. Flexures are used to allow linear motion's pitch and yaw angles. The various motions are layered so that alignment to the beam axis can be done first, and then sample-to-detector distance can be adjusted independently.

A Finite Element Analysis (FEA) were performed to achieve a stable design and measurements of resonance frequencies on the finalized stage were done to verify it.

INTRODUCTION

The MicroMAX beamline at MAX IV Laboratory is designed for macromolecular crystallography and will employ two detectors: the DECTRIS Eiger 2 X CDTe 9M and the Paul Scherrer Institute (PSI) developed Jungfrau 4M. The X-ray beam can be deflected by Kirkpatrick–Baez (KB) mirrors in the horizontal and vertical directions by 6 mrad, or it can pass undeflected. Beam Conditioning Unit (BCU), Diffractometer and the detector stage are designed to align with the beam. The individual detector should have a variable positioning along the beam path, depending on the target resolution of the diffraction data collection.

SPECIFICATION

The stage shall align the active detector to match either the deflected or undeflected beam following in line with the sample. Translations needs to be performed at a fast enough speed to avoid unnecessary waiting times, this is mainly important for the longitudinal translation that is long and can vary within one experimental setup. The detector stage is designed to accomplish the specifications (Table 1). All motion needs to be motorized. The table shall allow for a passthrough vacuum pipe to be manually placed between the detectors to allow the beam to pass to a second experimental hutch.

Table 1: Specifications

	Vert-ictal	Horiz-ontal	Longi-tudinal	Pitch	Yaw
Range	10 mm	382.5 mm	940 mm	±0.5°	±0.5°
Resolution	10 µm	10 µm	100 µm	10 µrad	10 µrad
Repeatability	50 µm	50 µm	100 µm	50 µrad	50 µrad
Resonance frequency f_0	>55 Hz				
RMS displacement	<7.5 µm (<10 % of pixel size)				

DESIGN

Inspired by the ALBA table skin concept design [1] a stage was designed around a grouted granite block. Two opposing steel plates are attached with linear guides for vertical translation. On the top part of the plates a thin neck is milled to create a flexure, allowing pitch by moving the two sides by different amounts. The sides are connected by a horizontal plate stiffened by two longitudinal side plates and a centre beam, together forming the vertical/pitch table. On top the other translations are worked out step by step, first horizontal translation for sideways adjustment and to switch between detectors and passthrough pipe. The horizontal is followed by yaw, using radial linear guides motorized by a linear translation translated into an angle by a flexure and then compensating the offset rotation centre with the horizontal axis (Fig. 1). Finally, the two longitudinal stages move each detector independently (Fig. 2) to find the correct focus and keep the unused detector out of the way in the centre of the table where it has less impact on the resonance frequencies. All translations are done with preloaded linear and radial guides and preloaded ball screws with stepper motors and all except for the motion of the detector along the X-ray beam also use a gear box to increase the resolution.

*Funded by Novo Nordisk Fonden for the MicroMAX project, grant number NNF17CC0030666
† staffan.benedictsson@maxiv.lu.se

ISBN: 978-3-95450-250-9 ISSN: 2673-5520 doi:10.18429/JACoW-MEDSI2023-WEPPP030

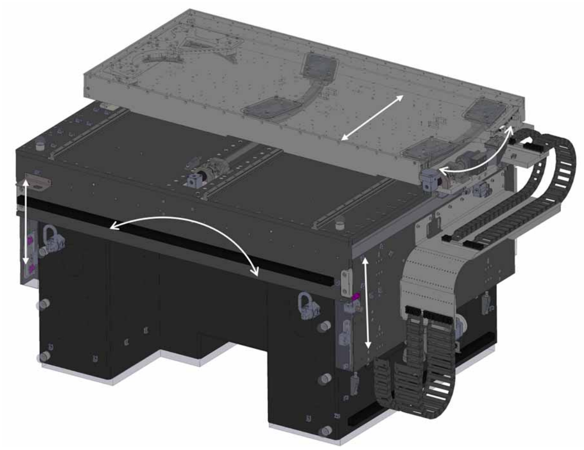

Figure 1: Translations.

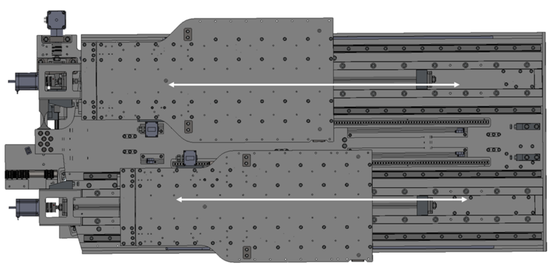

Figure 2: Translations along the beam.

Each flexure neck is specified to handle ±0.5° without having too much negative impact on the resonance frequency. 0.5° pitch causes stress at 192 MPa, giving a comforting safety factor before plastic deformation for the chosen steel (1.2738 / DIN 40CrMnNiMo7) and allowing for some over travel if necessary.

Much effort was put into overall stability of the detector stage, where the overhang of the detectors and the large size of the horizontal plate were the biggest initial concerns. The latter resulting in a stiffening centre beam and the overhang by finding a stiff but weight conservative design of the girders connecting the detector with the linear guides.

The worst cases for stability (Table 2) that can occur during operations is the heaviest detector in the back with the lighter being close to the sample hanging outside the table (Fig. 3) and both detectors sitting together in the detector stage´s centre, acting together (Fig. 4). The complete assembly is shown in Fig. 5.

Table 2: Eigenfrequencies

	Mode 1	Mode 2
Detector by sample	60.1 Hz	65. Hz
Detectors centred	63.2 Hz	64.6 Hz

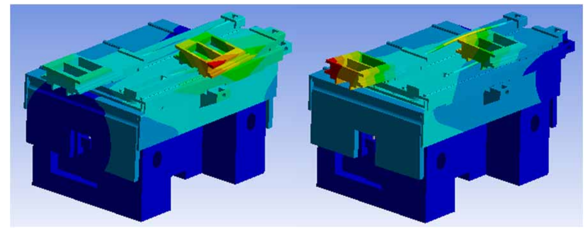

Figure 3: Lighter detector close to sample.

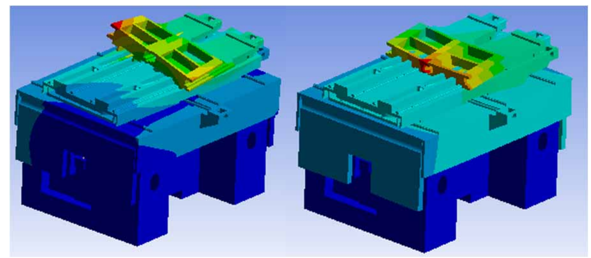

Figure 4: Detectors centred.

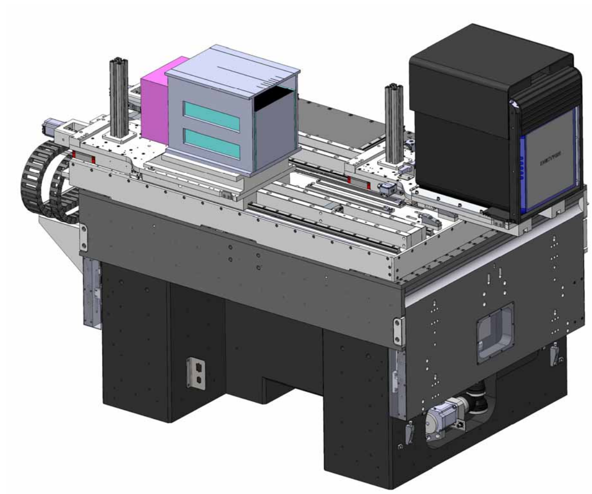

Figure 5: Complete detector stage.

PRODUCTION AND INSTALLATION

The production of mechanical parts was outsourced to a local company and the manufacturing of the granite block together with the assembly of the crucial parts were outsourced to the granite manufacturer that possessed the capability to assemble the main components with precision. Parts not crucial to the main function were later assembled at MAX IV. The stage is temporarily placed on adjustable feet in the experimental hutch, to be grouted later. The final installation, also illustrating some of the electrical routing is shown in Fig. 6.

ISBN: 978-3-95450-250-9 ISSN: 2673-5520 doi:10.18429/JACoW-MEDSI2023-WEPPP030

Figure 6: Installed in the hutch.

MOTION CONTROL

Tests to verify the resolution and repeatability were performed by comparing intended translation with the motor compared to the value shown by the absolute encoders, in open loop and closed loop (Table 3).

Table 3: Motion Tests

	Vert-ictal	**Hori-zontal**	**Longit-udinal**	**Pitch**	**Yaw**
Resolution	0.1 µm	1 µm	1µm	<1 µrad	<1 µrad
Repeatability Closed loop	<1 µm	<3 µm	<3 µm	<3 µrad	<1 µrad
Repeatability Open loop	<5 µm	<7 µm	<7 µm	<5 µrad	<4 µrad
Translations	All axis cover the specified range				

FINAL RESULTS / METEROLOGY TESTS

Measurements of the Root mean square (RMS) displacements on the Eiger2 detector has been performed by the MAX IV Survey, Alignment and Mechanical Stability team. During this test, the detector stage was installed on alignment feet but not grouted and the Jungfrau detector was not installed. The goal was to find the maximum RMS displacements on the Eiger detector and any eigenfrequencies <55 Hz.

The measured RMS displacement at the detector position was below the specified limit of 7.5 µm as shown in Table 4.

Table 4: RMS Displacement

Direction		**Floor**	**Detector**
Horizontal	RMS	3.9 nm	36.8 nm
Vertical	RMS	2.2 nm	60.4 nm

The mode indicator function, sum of squared Frequency Response Functions (FRF), indicates vibration modes between 24 and 40 Hz (Fig. 7). According to previous experience, these are likely to be related to rigid body rocking of the entire unit on the alignment feet and will be mitigated once the unit is grouted to the floor. Comparison with the integrated RMS function between detector and floor indicates significant contribution to the total RMS at 48.6 Hz originating from the floor that will prevail even after grouting. This can be accepted if the RMS displacements are below the specified limit as in this case.

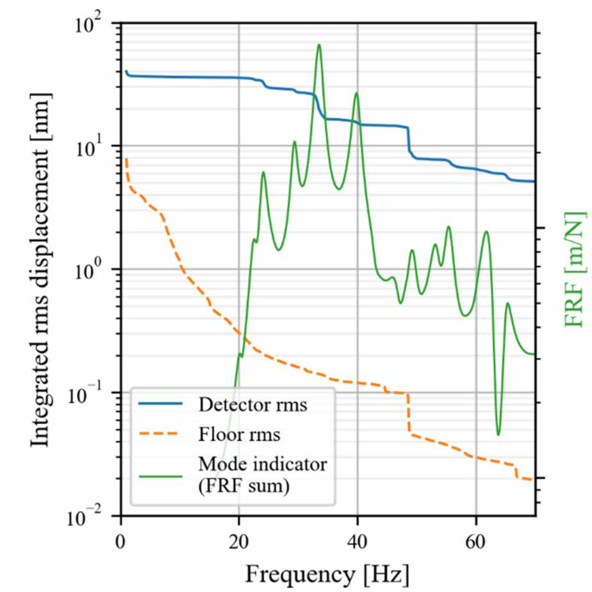

Figure 7: Integrated RMS of horizontal displacement (left y-axis) and mode indicator (right y-axis).

CONCLUSIONS

The Detector Stage has designed, installed, and tested. Results have overall been satisfying and fulfil the specifications.

REFERENCES

[1] C. Colldelram, C. Rudget, and L. Nikitina, "ALBA XALOC beamline diffractometer table skin concept design", *Diamond Light Source Proceedings 1(MEDSI-6)*, Oct. 2011. doi:10.1017/S2044820110000754

ISBN: 978-3-95450-250-9 ISSN: 2673-5520 doi:10.18429/JACoW-MEDSI2023-WEPPP032

PHOTON SLITS PROTOTYPE FOR HIGH BEAM POWER USING ROTATIONAL MOTIONS

X. Liu †, W. Cheng, A. Walters, L. Hudson, H. Patel, Diamond Light Source, Didcot, UK

Abstract

A new slits prototype utilising a rotatable oxygen-free high thermal conductivity (OFHC) copper block to absorb high heat load is developed for the Diamond-II upgrade. The slits will be used at front end of Diamond I13 X-ray Imaging and Coherence beamline which has two canted beamline branches. Required by the beamline optics, the front end slits function as virtual sources for the 250 meters long beamline. Working for the dual beam geometry, these specialised slits can vary the size of one x-ray beam with rotational motions while allowing the second beam to pass through unaffected. The rotational operations of the slits are achieved by an innovative commercial flex pivot and a unique in-house designed pivoting flexure.

INTRODUCTION

This paper describes the prototype design of a new slits utilising a rotatable OFHC copper block to absorb high heat load. The prototype is part of Diamond-II upgrade pre-development for three front end applications. The design case picked is to prototype for Diamond I13 X-ray Imaging beamline.

The I13 X-ray Imaging and Coherence beamline has two canted beamline branches. The front end slits function as virtual sources which is required by the I13 beamline optics in the long insertion straight of I13. It is essential to place the opposite beam defining blades at close proximity to collimate the x-ray beam. Diamond traditional white beam slits are not suitable for this function. In the traditional layout, the virtual focal point required by the beamline optics cannot be formed because the opposite slit blades are placed at a great distance due to one 'L' shaped blade being fixed onto an upstream copper assembly and another 'L' shaped blade being fixed onto a downstream copper assembly.

The newly developed slits prototype utilises a rotatable copper block assembly with the integration of a pair of 'L' shaped slits blades in one brazed copper block. The pair of 'L' shaped blades are placed at close proximity which is the perfect solution for creating the needed virtual source at the front end. The design concept is inspired by Schmidt's design of "Variable aperture photon mask (slits) for canted undulator beamlines at the Advanced Photon Source" [1]. Working for the dual beam geometry, these specialised slits can vary the size of one x-ray beam with rotational motions while allowing the second beam to pass through unaffected. The rotational operations of the slits are achieved by innovatively designed pivoting flexure and commercial flex pivots. Since the slits are used in the front end, the rotatable slits block is required to handle high beam power from the undulator insertion device of I13 beamline. To consider other Diamond-II applications, we developed the slits to be capable of carrying out raster scanning.

DESIGN

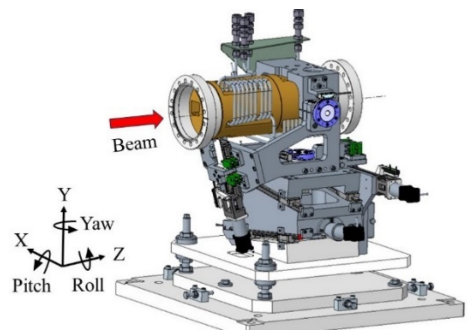

Figure 1: Slit assembly and the coordinate systems.

The overview of the slit assembly is shown in Fig. 1. The slits are installed at 18.4 meters from the source. The dual beam geometry is shown in Fig. 2. At the location, the photon beam size of the I13 Imaging branch is 4.1 × 4.1 mm, and the beam size is 3.7 × 3.7 mm for the Coherence branch. The separation distance of the two canted photon beams is 64.7 mm. The slits vary the size of Imaging beam while allowing the Coherence beam to pass through unaffected. The slit is also required to scan the beam. When carrying out the scanning, the slits are opened a set amount and then driven across the beam in a vertical or horizontal motion.

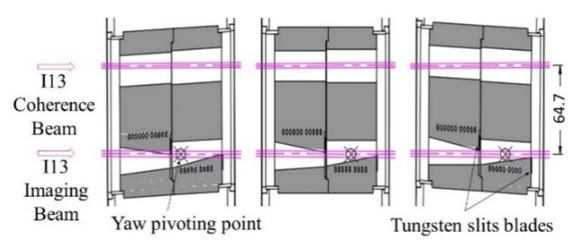

Figure 2: Anamorphic view of sections in X-Z plane showing yaw rotations of the slits. Left: closed position; Middle: neutral position; Right: open position.

Slits Rotary Motions

In normal operation mode, slits are only required for varying opening apertures. Using the concept from Schmidt [1], the variation of slit aperture is achieved by rotating the slit block horizontally (yaw rotation) and vertically (pitch rotation). Two unique pitch and yaw rotary stages (Figs. 3 and 4) are designed to control the slit width in the vertical and horizontal direction. The rotary stages are driven by a linear drive with the rotary motion produced by a flexure link between linear and rotary motion. The

† xia.liu@diamond.ac.uk

ISBN: 978-3-95450-250-9 ISSN: 2673-5520 doi:10.18429/JACoW-MEDSI2023-WEPPP032

distance of this drive from the centre of rotation will determine the linear to rotation ratio of the drive.

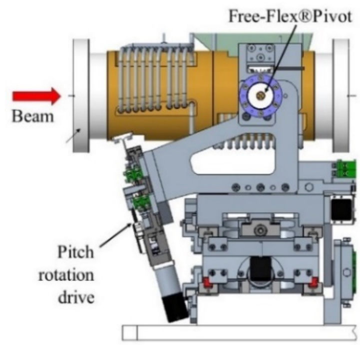

Figure 3: Design of the pitch rotary stage.

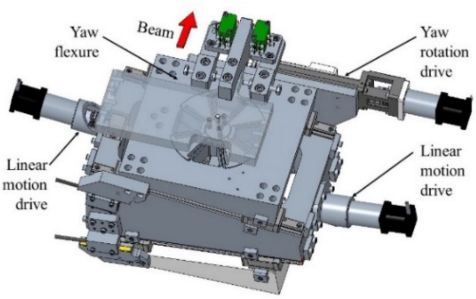

Figure 4: Design of the yaw rotary stage.

In both pitch and yaw rotation, the neutral position of the pivoting axis is set to align the centre of the slit to the beam centre. By rotating ± 1° from the neutral position, the slit is fully closed or fully opened (Fig. 5). Motion limits are set at ± 1° rotation angle. To safely handle the overtravel of the rotary stage, there are additional backup switches and hard stops. Hard stops are set at ± 1.6° rotation from the neutral position.

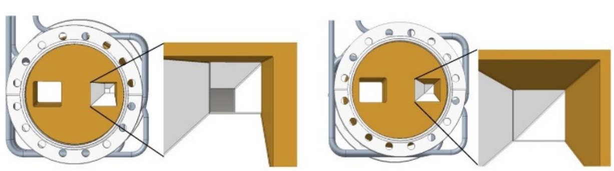

Fully opened slits
Yaw = -1°, Pitch = -1°

Fully closed slits
Yaw = +1°, Pitch = +1°

Figure 5: Details of fully opened and closed slits.

We were concerned with the performances of rolling element bearings for small intermittent angle rotations involved in this design application, because frictional hysteresis typically found in rolling element bearings would prevent very accurate control of small rotational positions. For the pitch axis we choose to use a pair of Free-Flex® pivots where we have many successful designs with using them in other Diamond instruments. Stiction-free and lubrication-free Free-Flex® pivots [2] are uniquely suited for the pitch rotary stages that have limited angular travel and use in a radioactive environment such as a front end. For yaw axis, we attempted a unique rotary flexure design as it was not feasible to support the yaw axis from both ends.

The Design of Yaw Rotary Flexure

The rotary flexure uses similar symmetrical leaf flexure design as the concept published by S. Wan and Q. Xu for a rotational micro positioning stage [3]. The design of the yaw flexure is shown in Fig. 6.

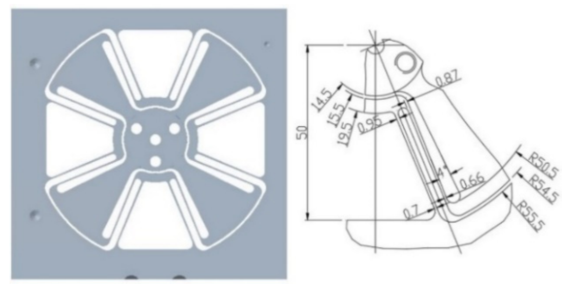

Figure 6: Details of yaw rotary flexure.

We chose to use a martensitic stainless steel BS 970 420S45 heat treated to QT800 condition. This gives a good combination of high strength, tough and corrosion resistant material.

Finite Element Analysis (FEA) was employed to optimise the thickness of the cross sections of the leaf flexure as the thicker the rib section, the higher the stresses on the rib but also the stiffer the rib in the pitch and roll direction. The thickens of the rib varies along its length to give equal stresses along the length of the rib (Fig. 7).

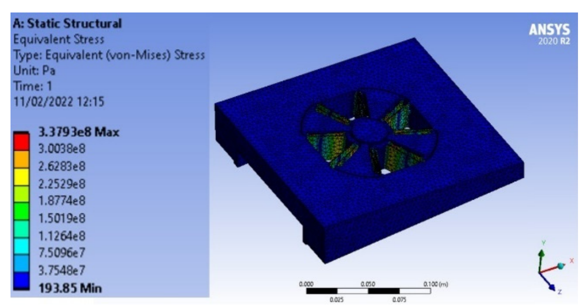

Figure 7: Stress distribution in the flexure.

Based on the FEA analysis, the designed rib configuration gave a maximum stress of 338 MPa at an equivalent deflection of 2° rotational movement. This compares with the material yield stress of 650 MPa at QT800 condition.

Slits Linear Motions

Placed underneath the pitch and yaw rotary stages, the X-Y stages are used to align the slit aperture to the centre of the photon beam, and to allow slits scanning in horizontal and vertical directions (Fig. 4). Due to space restrictions from existing installations, the linear motion components are on a wedge configuration which means that a compound motion is needed to produce a purely horizontal or vertical motion. The scan distance is +/− 2.5 mm horizontal and vertical from the slits neutral position. The scan distance is +/− 4.5 mm at motion hard stops.

Slit Block Design

The Slits block is constructed from an OFHC copper body with cooling channels placed close to the surface

ISBN: 978-3-95450-250-9 ISSN: 2673-5520 doi:10.18429/JACoW-MEDSI2023-WEPPP032

struck by photon beam. The cooling channels are machined within the body and connected by vacuum brazed stainless steel pipes. The body is constructed in two sections and is brazed to stainless steel flanges. 'L' shaped tungsten blades are fixed to the downstream end of each copper block (Fig. 8).

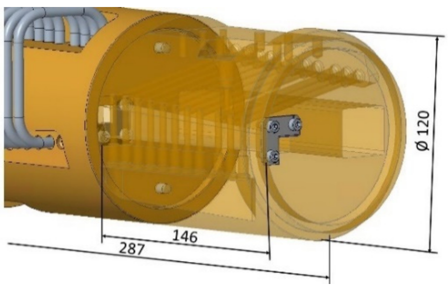

Figure 8: Slit block (downstream cooling pipe hidden).

VIBRATION MEASUREMENT

The initial vibration measurement was caried out with laser vibrometer. The prototype was measured under vacuum and connected to water services with pressure and flow close to operational conditions. Measurements evidenced that was no clear correlation or significant contribution to the power spectral density when adjusting the flow rate or changing the slit position to strain bellows. Cumulative power spectral density (CPSD) for each setup were similar (Fig. 9). We will use accelerometer to measure the slits vibration and further compare the results.

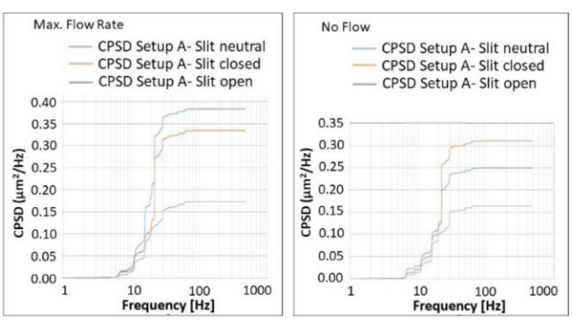

Figure 9: Vibrometer vertical measurement.

THERMAL AND STRESS ANALYSIS

The thermal loading on the copper body is greatly affected by the photon beam grazing angles as the slits rotate and the slits scanning position with a fixed grazing angle. The FEA was carried out for different combinations of grazing angles and liner travels for sensitivity study. The result described here is the worst case condition of the prototyping design case with maximum beam grazing angle of 5.6˚, and the maximum linear travel of X +4.5 mm and Y -4.5 mm. In actual application, the FEA condition is better than the above mentioned worst case. The beam power data is in Table 1. The highest temperature is 125.2 °C (Fig. 10) which is well below Diamond design criteria of 400 °C [4]. However, the peak thermal stress at the corner of the aper-ture is 269 MPa which is slightly higher than the limit (250 MPa) [4] for the elastic analysis. Further elastic-plastic analysis will be carried out.

Table 1: Beam Power Data

Beam energy & current	3.5 GeV, 330 mA
Undulator U22	K: 1.8899
Total power at copper body	2.86 kW
Peak power density at 18.4 m	127.9 W/mm^2

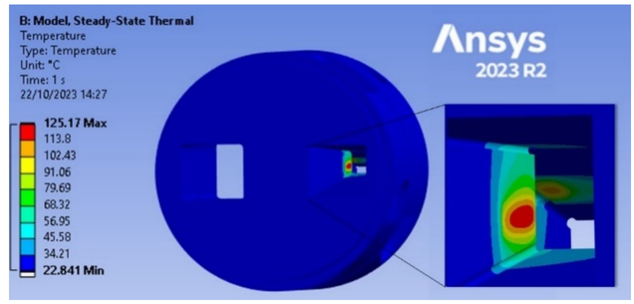

Figure 10: Temperature distribution.

CONCLUSION

This prototype has validated the idea of using rotatable slits as a space saving solution for front ends. The initial vibration measurement confirms that the slits could be used as the beamline virtual source. It is promising that through geometry optimisation, rotatable slits using OFHC copper is feasible for high beam power applications. In our further endeavour, we will measure the slits in close to operational conditions with collimated light to explore the performance of the in-house designed rotary flexure.

ACKNOWLEDGEMENTS

Our sincere gratitude to Oliver Schmidt from APS for his warm support and updating the latest development of the rotatable slits at APS without reservation. Our special thanks to Lucia Alianelli for her invaluable knowledge with the I13 beamline optics, to John Margerum, Richard Howard, Paul Amos, Jason Giles, Tony Lundyates for their expertise in the assembly, vacuum, wiring and alignment of the prototype, and Carlos Tilbury for the procurement.

REFERENCES

[1] O. Schmidt *et al.*, "Variable aperture photon mask (slits) for canted undulator beamlines at the Advanced Photon Source", in *Proc. MEDSI 2014*, Melbourne, Australia, Oct. 2014.

[2] Free-Flex® Pivots, `http://www.flexpivots.com`

[3] S. Wan and Q. Xu, "Design of a new rotational micropositioning mechanism driven by limited-angle torque motor", in *Proc. 10th IEEE Int. Conf. on Nano/Micro Engineered and Molecular Systems*, Xi'an, China, Apr. 2015, pp 209-213. `doi:10.1109/NEMS.2015.7147412`

[4] H. Huang *et al.*, "Elasto-plastic analysis of heat absorbers in Diamond Light Source", presented at the NWC Salzburg, Austria, June 2013.

ISBN: 978-3-95450-250-9 ISSN: 2673-5520 doi:10.18429/JACoW-MEDSI2023-WEPPP034

ALBA EXPERIMENTAL SET UP FOR THE EVALUATION OF THERMAL CONTACT CONDUCTANCE UNDER CRYOGENIC AND VACUUM CONDITIONS

O. Traver†, J.J. Casas, C. Colldelram, J. L. Frieiro, B. Molas, M. Quispe, M. Sanchez
ALBA-CELLS Synchrotron, Cerdanyola del Vallès,

Abstract

The Thermal Contact Conductance (TCC) between two surfaces plays a very important role in the design of components in particle accelerators. The TCC depends on many variables such as surface finish, type of material, pressure, temperature, etc. As a general rule, the TCC comes from experimental results reported in the specialized literature. However, it is not always possible to find this information, especially if components are designed to operate in cryogenic and vacuum conditions, for this reason, assumptions are made that render results with high uncertainty. In this context, ALBA has designed an experimental set up to carry out axial heat flow steady state experiments for the evaluation of TCC under vacuum and cryogenic conditions. The minimum pressure achievable in the set up will be 1e-5 mbar while the temperature may vary between 80 and 300 K. The results will provide inputs to further optimize ALBA designs, including ALBA II, our ongoing fourth-generation synchrotron upgrade project. This paper describes the experimental setup, the thermal and mechanical design considerations and experimental validation tests.

INTRODUCTION

Real engineering surfaces exhibit a complex three-dimensional landscape, characterized by peaks and valleys of diverse sizes and shapes. A “flat surface” contains microscopic irregularities which compose its roughness and macroscopic irregularities such as waviness and deviation from flatness [1, 2, 3]. Consequently, when two surfaces are pressed together, they touch each other at only limited discrete points separated by large gaps. Thus, the *real* contact area is found to be much smaller than the *geometrical* contact area (1-2% for metallic contact) [2]. The remaining space between the contact points can be filled with an interstitial medium, such as air or a vacuum.

Thermal contact conductance (*hj*), also known by the acronym TCC, can happen through conductance along three primary pathways: the real contact spots (h_c), conduction through the interstitial fluid (h_g) and thermal radiation (h_r).

$$h_j = h_c + h_g + h_r \ . \tag{1}$$

Conceptually, *hj* is defined as the ratio of the heat power (Q) per unit area (A) flowing across the interface and the temperature drop (ΔT) at the interface.

$$h_j = \frac{Q/A}{\Delta T} \, . \tag{2}$$

If the heat transfer takes place in vacuum conditions, the conduction through the interstitial fluid can be neglected. Radiative heat transfer can also be disregarded in the current context, as it becomes significant only above 400 ºC [3].

$$h_j \approx h_c = \frac{\frac{Q}{A}}{\Delta T} \ . \tag{3}$$

According to [4], *hj* increases proportionally to the applied load at the interface since the real contact area is proportional to the load. When the load increases the average contact spot size remains relatively stable. However, the quantity of contact spots changes.

The *hj* dependence on temperature varies over different temperature ranges. From 30 K to 200 K, *hj* approaches a linear dependence with T, above this range it tends to a temperature-independent conductance value.

To determine *hj*, experimental research is fundamental, as it can provide realistic results compare to theoretical studies. Obtaining information on *hj* under cryogenic and vacuum conditions is often challenging. In this context, at ALBA an experimental setup has been built to evaluate *hj* values in these special conditions. This work describes relevant aspects of its design, its operating principle and the first validation tests.

EXPERIMENTAL SET-UP

Description

The experimental setup (Figs. 1 and 2). consists of a heating block (1), a cold finger (2), an insulating block (3) an insulating ring (4), a load cell (5), a mechanical loading system (6), a vacuum system (7) and two specimens (8).

The heating block is a cylindrical copper block of Ø25 mm with its cylindrical surface covered by two 45 W kapton heaters foils, which are powered by a current source. The cold finger is a cylindrical copper block of Ø25 mm x 150 mm with a hole of Ø8 mm x 110 mm where liquid nitrogen circulates. In order to avoid losses and ensure one dimensional heat flow, an insulating block made of PEEK has been provided at the top of the heating block and an insulating ring has been provided at the bottom of the cold finger. Between the heating block and the cold finger, the two specimens, with a cylindrical shape (Ø25 mm x 48 mm high) and which can be fabricated from any material of interest for the experiment are brought in contact. One of the specimens is heated, the other one is cooled, allowing the generation of a downward axial heating flow. The experimental set-up aims at measuring the TCC

† otraver@cells.es

ISBN: 978-3-95450-250-9 ISSN: 2673-5520 doi:10.18429/JACoW-MEDSI2023-WEPPP034

between the two specimens when different contact pressures and temperatures at the interface are applied.

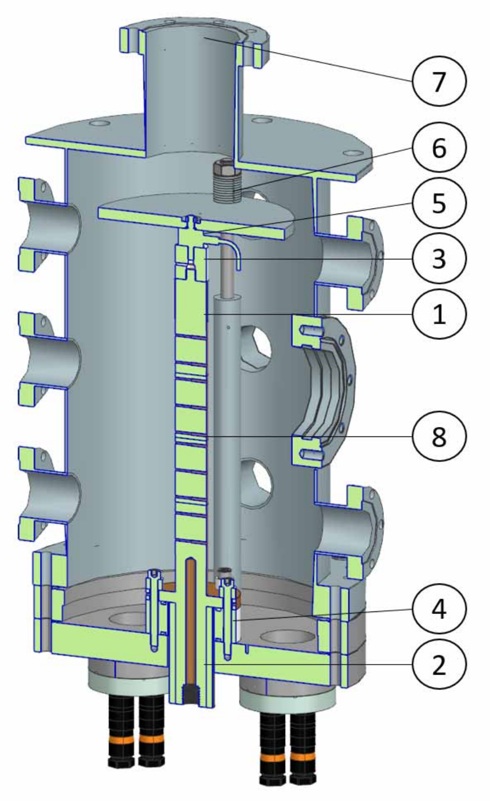

Figure 1: Cross section of the experimental set-up for the evaluation of TCC.

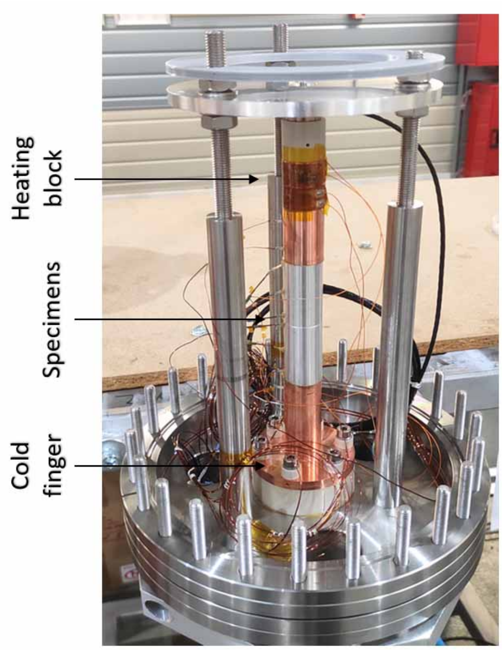

Figure 2: Image of the experimental setup manufactured in ALBA. Note that the specimens are made of aluminium instead of copper for our upcoming tests.

The interfaces between the heating block and the upper specimen, as well as between the lower specimen and the cold finger, have been filled with highly conductive paste Apiezon N, to reduce the contact resistance and to maximize the heat flow.

Platinum Resistance Temperature Detectors (RTDs) of Ø1,8 x 5 mm. have been precisely inserted up to the centre line of the column, utilizing small holes of Ø2 mm in diameter for precise placement. Apiezon N paste has been applied to fill the holes, ensuring optimal thermal contact between the temperature sensor and the column.

To conduct the experiment across a variety of contact pressures, a mechanical loading system composed of 3 screws with bellevile washers has been mounted at the top of the column in conjunction with a miniature diaphragm loadcell.

The experimental set-up can operate under vacuum by enclosing the set-up within a vacuum chamber, and using a special cryogenic Astraseal O-rings for ensuring the sealing between the cold finger and the chamber. A vacuum level of 1·10-5 mbar has been achieved by using a turbomolecular vacuum pump.

Working Procedure

The preparation of the experiment starts by cleaning all the surface of the specimen with isopropanol alcohol and then all the surface, except the test interface, are filled with highly conductive Apiezon N paste. The temperature sensors are inserted in the specimen with their holes pre-filled with paste. Before closing the vacuum chamber, the loading system is adjusted to the pressure of interest. When the pressure inside the vacuum chamber reaches 1·10-4 mbar, liquid nitrogen is allowed to circulate inside the cold finger. The heaters are operated at a fixed power reaching up to 90 W. The higher the thermal contact conductance of the specimen, higher heating power should be applied to create a measurable temperature in the interface.

The flow of the liquid nitrogen is regulated to attain a precise temperature in the cold finger. The system is left running until the temperature gradient along the heat flow column remains stable, meaning that an axial heat flow steady state has been achieved, Then the temperatures at each location of the column are written down.

EVALUATION TEST

The experimental setup has been validated through the experimental study of a pair of specimens made of copper, at a vacuum level of $1\cdot10^{-5}$ mbar, as described below.

Specimens

A pair of specimens has been fabricated in copper. Three holes have been drilled into each specimen at 20 mm intervals, but 4 mm away from the specimen ends (Fig. 3).

12th Int. Conf. Mech. Eng. Design Synchrotron Radiat. Equip. Instrum. MEDSI2023, Beijing, China JACoW Publishing
ISBN: 978-3-95450-250-9 ISSN: 2673-5520 doi:10.18429/JACoW-MEDSI2023-WEPPP034

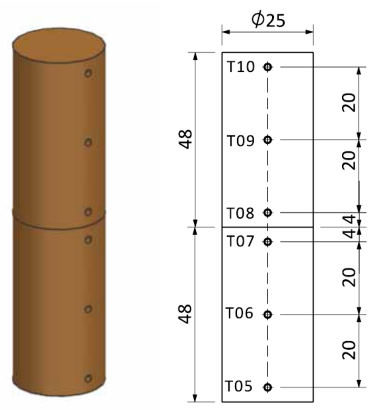

Figure 3: Isometric and front view of the specimens with the location of the temperature sensors.

Data Acquisition

The temperature distribution along the length of the specimens is observed to follow a linear dependence, while at the interface a temperature drop appears, denoted as (ΔT), which is calculated through linear extrapolation based on the temperatures in close proximity to the interface of the two specimens (Fig. 4). The heat flow across the interface (Q) is equal to the heating power supplied by the heaters at the top of the column.

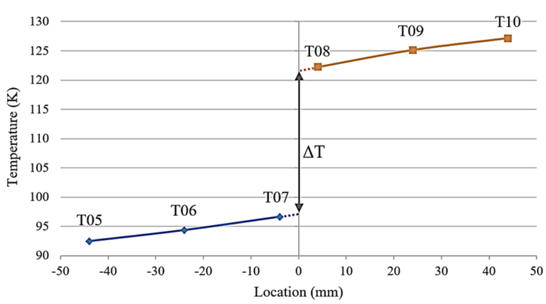

Figure 4: Plot of the temperature at different axial location in both specimens, pressure 0.4 bar.

By knowing the temperature drop at the interface (ΔT), along with the heat flow across it (Q) and the interface area (A), the thermal contact conductance (h_j) can be calculated using the Eq. (3).

Results: Effect of Pressure

Test with specimen pairs under a pressure of 0.2 and 0.4 bar and stable cryogenic temperature of 157 K have been carried out. It is observed that TCC increases when the pressure increases (see Table 1).

Table 1: TTC Values of Cu Specimens at Different Contact Pressure and Fixed Temperature

Pressure [bar]	Cu-Cu TCC [W/m²·K]
0.2	1582
0.4	2618

Results: Effect of Temperature

Experiments were conducted with interface temperatures between 110 to 170 K at a stable interface pressure of 0.4 bar. It is observed that TCC increases with increasing temperature (see Table 2).

Table 2: TTC Values of Cu Specimens at Different Temperature and Fixed Contact Pressure

Temperature [K]	Cu-Cu TCC [W/m²·K]
110	2422
147	2576
170	2674

Set-up Evaluation

With the setup we successfully generated a temperature gradient in the column and observed a temperature drop at the specimen interface enabling us to calculate their TCC.

Steady-state heat flow was reached after 45 minutes of machine running. It was at this stage that the temperature variation in the sensors remained below 0.5 K every 10 minutes while a vacuum level of $1 \cdot 10^{-5}$ mbar was reached after 15 minutes of operation and remained stable throughout the entire experiment.

Further Development

The cold finger and heating block are expected to function as a heat flowmeter by measuring its temperature gradient along its axial. This capability will be established after calibration. The liquid nitrogen flow is controlled using a manual valve, leading to challenges in achieving and maintaining precise temperatures in the cold finger. To address this, a PDI-controlled liquid nitrogen flow system is planned to be installed. To identify and measure heat losses, we plan to install temperature sensors on the inner surface of the vacuum chamber to monitor temperature variations. Currently, data recording is done manually every 10 minutes during operation. We aim to automate this process; recording more data will enable us to assess uncertainties effectively.

CONCLUSION

An experimental set up for the evaluation of thermal contact conductance under cryogenic and vacuum conditions have been fabricated at ALBA. Test with pairs of copper specimens under different interface pressure and temperature had been carried out. The TCC at the interface of the specimens has been estimated by measuring the temperature across the specimen and the heat flux.

The experimental setup is prepared to evaluate the contact of new material interfaces of interest for our current designs, and especially for the new components of the ALBA II upgrade project.

ISBN: 978-3-95450-250-9 ISSN: 2673-5520 doi:10.18429/JACoW-MEDSI2023-WEPPP034

REFERENCES

[1] Y.A. Cengel and R.H. Turner, "Steady heat conduction", *Fundamentals of Thermal-Fluid Sciences*, Ed. 5, McGraw-Hill Education, 2016.

[2] C.V. Madhusudana, "Solid Spot Thermal Conductance of a Joint" and "Gas Gap Conductance", *Thermal contact conductance*, Ed. 2, Springer-Verlag, New York Inc, USA, 1996, pp. 23-61.

[3] J.H. Lienhard, "Heat conduction concepts, thermal resistance, and the overall heat transfer coefficient", *A heat transfer textbook,* Ed.3, Cambridge, MA, USA. J.H. Lienhard 2000, pp. 64-66.

[4] E.Gmelin *et al.,* "Thermal boundary resistance of mechanical conctacts between solids at sub-ambient temperatures", *J. Phys. D*, vol. 32, no. 6, R19-R43, 1999. doi:10.1088/0022-3727/32/6/004

ISBN: 978-3-95450-250-9 ISSN: 2673-5520 doi:10.18429/JACoW-MEDSI2023-WEPPP035

DESIGN AND FLUID DYNAMICS STUDY OF A RECOVERABLE HELIUM SAMPLE ENVIRONMENT SYSTEM FOR OPTIMAL DATA QUALITY IN THE NEW MICROFOCUS MX BEAMLINE AT THE ALBA SYNCHROTRON LIGHT SOURCE

M. Quispe†, J.J. Casas, C. Colldelram, D. Garriga, N. González, J. Juanhuix, J. Nicolàs, Y. Nikitin
ALBA-CELLS, Cerdanyola del Vallès, Spain
M. Rabasa, ESEIAAT, Terrassa, Spain

Abstract

XAIRA is the new microfocus MX beamline under construction at the ALBA Synchrotron Light Source. For its experiments, data quality will be optimized by enclosing all the end station elements, including the diffractometer, in a helium chamber, so that the background due to air scattering is minimized and the beam is not attenuated in the low photon energy range, down to 4 keV. This novel type of chamber comes with new challenges from the point of view of stability control and operation in low pressure conditions while enabling the recovery of the consumed helium at the ALBA Helium Liquefaction Plant. Besides, the circuit includes a dedicated branch to recirculate the helium used by the goniometer bearing at the diffractometer. This paper describes the fluid dynamic conceptual design of the Helium chamber and its gas circuit, as well as numerical results based on one-dimensional studies and Computational Fluid Dynamics (CFD).

INTRODUCTION

The new microfocus beamline BL06-XAIRA at ALBA, in commissioning phase, will have a chamber enclosing the goniometer that holds the sample, the detector, a cryostream, and other sample environment elements. The setup allows the experiments to be performed either in air or in helium atmosphere, and both at room temperature or under cryogenic conditions. The helium atmosphere not only reduces the background noise, thus increasing data quality for the whole energy range, but also prevents flux loss at low energies, providing the optimal conditions for anomalous phasing and elemental analysis experiments [1].

From the point of view of fluid dynamic engineering, a description of the design of this special chamber, as well as its adjacent gas circuit, is presented in the following sections. This design includes the possibility to recycle the helium, directing it to the ALBA Helium Liquefaction Plant.

PIPING AND INSTRUMENTATION DIAGRAM (PID)

Figure 1 shows the PID of the gas distribution. The design has been based on the requirement to operate in three modes: sample in helium atmosphere at a nominal cryogenic temperature of 95 K (mode 1), sample in helium atmosphere at room temperature (23 ºC, mode 2); and sample surrounded by nitrogen gas at a nominal cryogenic temperature of 100 K (mode 3) [2]. For modes 1 and 2, a helium purity of 95% is required (experimental criterion).

The elements of the circuit are distributed inside and outside the experimental hutch (marked in green in Fig. 1) and regulate the different beamline components that blow helium into the helium chamber (bold black line). In the Fig. 1 the circuit for helium gas is highlighted with black lines (mode 1), while the distribution lines for air and nitrogen gas are marked in grey.

Under steady state regime, the balance of helium gas inside the chamber is conserved according to the following input and output conditions: (1) Gas input to the chamber from the detector. This component, has to be connected to a dry air (or nitrogen, or helium) source to avoid humidity and condensation damage. The gas first enters the detector (0.167 l/min, 296 K and 2.5 bar ABS), then is distributed inside the chamber; (2) Injection of pure helium gas from the cryostream to the sample, under nominal conditions 2.74 l/min, 95 K and 1.2 bar ABS; (3) Helium gas input from the goniometer. The rotation movement of this component requires helium gas under the conditions 5.61 l/min, 296 K and 5.5 bar ABS. During its operation, the goniometer "loses" approximately 5% of gas, which becomes a gas supply to the chamber; and (4) A single output is fixed, represented in the PID with an output arrow on the left side of the chamber.

For the circulation of helium gas, two compressors are required. One of them is dedicated exclusively to supplying helium to the goniometer under its working conditions; the other compressor, located on the exit branch of the chamber, takes the exit gas and then distributes the helium in three branches: one towards the detector, another towards the aspiration of the other compressor (to recover the 5% of "lost" gas inside of the chamber), and the last one towards the Helium Liquefaction Plant, for recovery. Under ideal fluid balance conditions, the recovery line should recover the same amount of gas injected by the cryostream into the chamber.

The system has 12 bottles of pure helium gas, each of 50 litres at 200 bars of pressure. This assembly will feed gas directly to the cryostream during experimentation. An individual bottle of helium gas, connected to the chamber (He pressure control unit), has been added to inject helium in case of gas losses during the operation.

† mquispe@cells.es.

ISBN: 978-3-95450-250-9 ISSN: 2673-5520 doi:10.18429/JACoW-MEDSI2023-WEPPP035

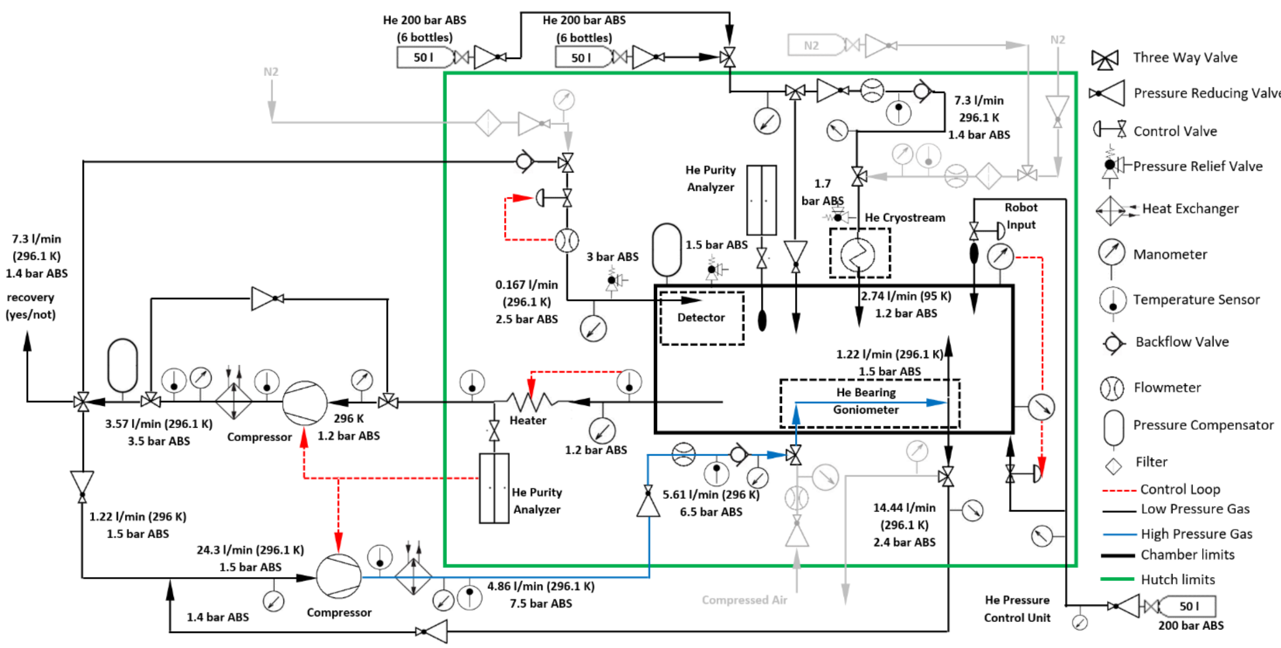

Figure 1: XAIRA PID operational mode 1: Helium gas with Cryostream on.

The operation of the beamline includes a sample mounting system (marked as robot in the PID diagram) to mount and unmount the samples on the goniometer head. This is one of the critical points where the purity of the helium in the chamber can be affected, because the access valve must be opened and there will be direct contact with the outside air. The chamber is sealed when the robot is inside the chamber (typically for ~ 4 sec) by the gripper itself, which has a diameter that matches the aperture of the gate valve. The effect on purity of the helium will be assessed during the commissioning of the He circuit in 2024.

One-Dimensional Modelling

All pipes with their components have been simulated with the one-dimensional software PIPEFLOWEXPERT [3] to determine the pressure drops. In all cases the pressure drops are very low and fluid dynamics is guaranteed. There is a branch where fluid dynamics has a high dependence on the nominal operating points. This is the branch that connects the outlet of the chamber with the suction area of its respective compressor. On the one hand, the design pressure of the chamber must be maintained below 1.2 bar ABS, which is a requirement of the detector manufacturer to protect its membrane. On the other hand, the nominal working pressure of the compressor suction is 1.2 bar ABS, however, it can be operated up to the limit of 1.1 bar ABS. In a better scenario we would have a gradient of 100 mbar between the chamber and the compressor. In this branch the pressure drop is 4 mbar, calculated with PIPEFLOWEXPERT. During commissioning we must ensure the appropriate working points to always have a gradient > 4 mbar.

HELIUM GAS DISTRIBUTION IN THE CHAMBER: CFD STUDIES

CFD Simplified Geometry

Figure 2 shows the simplified model of the stainless-steel chamber, located on a granite base, and some of its main components. Its dimensions are 1345 x 1010 x 844 mm. The gas outlet, a 12 mm inner diameter tube, is located on the same wall of the chamber where the cryostream is fixed.

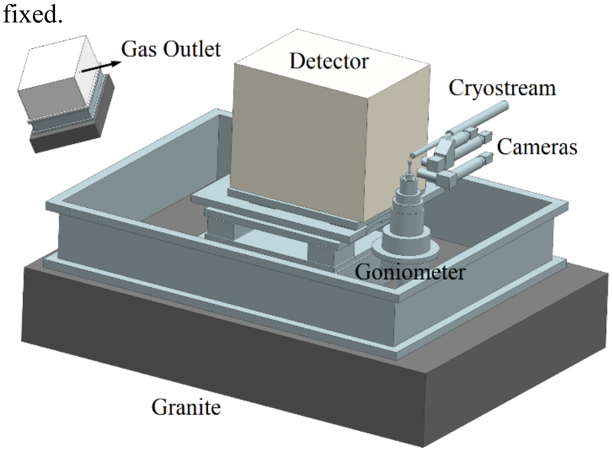

Figure 2: Simplified model of the chamber, showing some of its internal components.

CFD Model

The helium gas has been simulated under conditions of forced convection, assuming 100% purity and imposing three inlet flowrates as detailed in the previous section. The gas injected by the cryostream has been simulated at 80 and 95 K. The gravitational effect has also been introduced. In this case, the effect of gravity is relevant due to the high sensitivity of the density of helium gas with respect to

ISBN: 978-3-95450-250-9 ISSN: 2673-5520 doi:10.18429/JACoW-MEDSI2023-WEPPP035

temperature, especially under cryogenic conditions. The properties of helium gas as a function of temperature have been introduced. A laminar regime has been assumed for the fluid dynamics and the incompressibility approximation for the gas. The internal heat input has also been implemented: 3.66 Watts in each of the three cameras. For external heat transfer to the chamber, air in natural convection at 23ºC has been applied, with a convective heat transfer coefficient equals 5 W/m^{2}K. The optimal mesh generated has been around 8 million elements, which ensures the asymptotic result of the simulations. The ANSYS WORKBENCH software has been used for the calculations [4].

CFD Results

The temperature distribution around the sample is shown in Fig. 3. The sample is completely immersed in helium gas at 95 K. In the same figure, in the upper part, the temperature distribution in a vertical plane at the position of the sample is presented. In this plane it is observed that the cold zone of the gas has an influence on a small space around the sample, and close to the wall of the chamber the temperature is around 294 K.

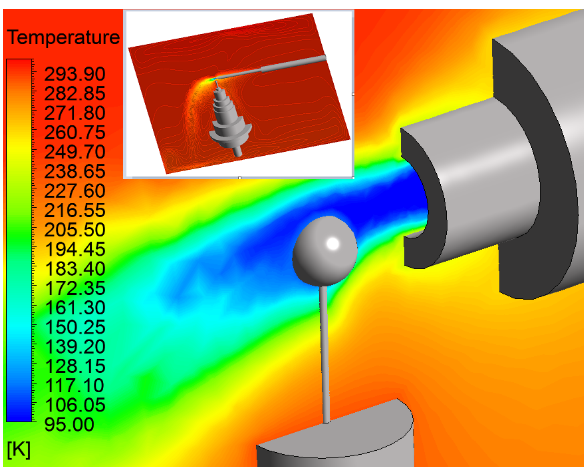

Figure 3: Temperature distribution around the sample and in a vertical plane at the position of the sample.

Figure 4 shows the distribution of the velocity vectors around the sample. A maximum velocity of the gas on the sample equals 2.53 m/s is obtained.

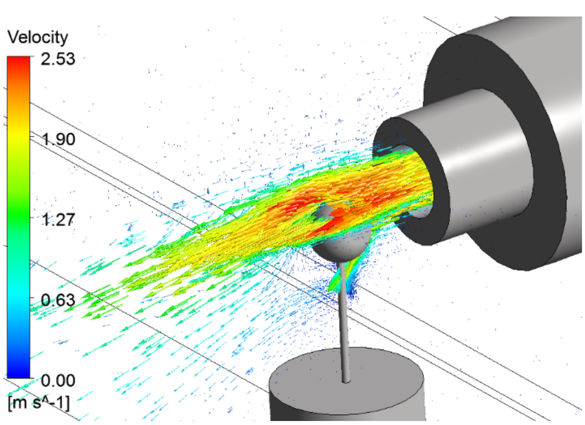

Figure 4: Velocity vectors around the sample.

The temperature value of the helium gas at the exit of the chamber has been evaluated under the conditions presented in Table 1. It can be concluded that the temperature values are close to the external air. This behaviour is due to the significant influence of heat transfer from the outside air to the chamber. It is also observed that the influence of the heat generated in the cameras on the gas outlet temperature is negligible.

Table 1: Average Helium Gas Temperature at the Exit of the Chamber, for Different Conditions

Temp. Cryostream (K)	Cameras	Temp. Outlet (K)
95	On	296.81
95	Off	295.86
80	On	296.74
80	Off	295.79

The CFD results also show high temperature values in the three cameras, around 350.7 K. This temperature peak enhances the movement of the fluid in a vertical direction due to the high difference in densities in this region, as can be seen in Fig. 5.

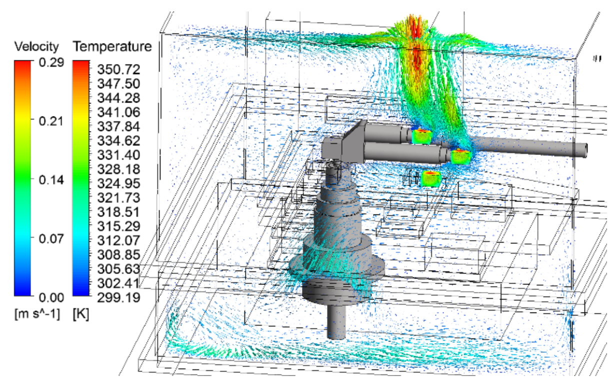

Figure 5: Distribution of the velocity vectors towards the upper zone, due to the thermal load of the three cameras.

Another significant result is that for the cryostream injection conditions, at 80 and 95 K, the values of the temperature distribution on the external wall of the chamber remain in the range of 295 to 300 K, for both cases.

CONCLUSIONS

This work describes the design details and results of the fluid-dynamic simulations obtained for the experimental helium gas chamber and its adjacent piping of the new microfocus beamline BL06-XAIRA at ALBA. The results of the one-dimensional and CFD simulations confirm an optimal fluid dynamic behaviour of the proposed design.

The piping and instrumentation configuration and the chamber have been designed to recover the helium gas used in the experimentation, which, under ideal conditions, should be equal to the gas injected by the cryostream. The purity of the recovery gas will depend on many factors, such as the action of the automated robot and the tightness of the piping and attached components.

ISBN: 978-3-95450-250-9 ISSN: 2673-5520 doi:10.18429/JACoW-MEDSI2023-WEPPP035

REFERENCES

[1] D. Garriga, "XAIRA End Station: Conceptual Design Report", unpublished.

[2] M. Quispe, "Detailed Design Report: XAIRA Helium Gas Circuit", unpublished.

[3] PIPEFLOWEXPERT, https://www.pipeflow.com/

[4] ANSYS, https://www.ansys.com/products/fluids

ISBN: 978-3-95450-250-9 ISSN: 2673-5520 doi:10.18429/JACoW-MEDSI2023-WEPPP039

DATA PREPROCESSING METHOD OF HIGH-FREQUENCY SAMPLING XAFS SPECTRA COLLECTED IN A NOVEL COMBINED SAXS/XRD/XAFS TECHNIQUE*

Yunpeng Liu [1,†], Zhongjun Chen [1], Guang Mo [1], Zhonghua Wu [1,2]
[1] Beijing Synchrotron Radiation Facility, Institute of High Energy Physics, Chinese Academy of Sciences, Beijing 100049, China
[2] University of Chinese Academy of Sciences, Beijing 100049, China

Abstract

High-frequency (HF) sampling X-ray absorption fine structure (XAFS) spectra with a time-resolution of ~8 s were collected in our newly developed synchrotron radiation small-angle X-ray scattering (SAXS)/X-ray diffraction (XRD)/XAFS combined technique. Restoring the HF XAFS spectrum which contains hundreds of thousands to millions of data points to a normal XAFS spectrum consisting of hundreds of data points is a critical step for the subsequent neighbor structure analysis. Herein, the data preprocessing method and procedure of HF XAFS spectra were proposed according to the absorption edge of the standard sample and the rotation angular velocity of the monochromator. This work is expected to facilitate the potential applications of HF XAFS spectra in a time-resolved SAXS/XRD/XAFS experiment.

INTRODUCTION

To achieve the goals of controllable synthesis and performance optimization [1, 2], the knowledge of the structural evolution of materials in the processes of synthesis or service is a prerequisite. During the material synthesis and some dynamic changes, the synthesized material structures often be hierarchical. Tracking the entire material synthesis process and capturing useful information on all possible metastable precursors and intermediates will facilitate the controllable synthesis of materials. However, it is difficult for a single technique to meet all the detection requirements of hierarchical structure. It is very necessary to develop in-situ combined techniques to obtain simultaneously time-resolved hierarchical structural information on a dynamic reaction process.

Recently, we developed a novel SAXS/XRD/XAFS combined setup [3], where an area detector, a curved detector, and a point detector are, respectively, used for the detections of SAXS, XRD, and XAFS signals. This kind of combining technique can be used to track the changes [4] ranging from the molecular (local coordination state) to nanoscale (primary units) to microscale (crystallite formation) dimension during the crystallization process of samples. It should be noted here that, an ion chamber (IC) is often used detector to collect XAFS signals due to its good linear response to the X-ray intensity. However, for this compact combined setup, it is a failure to collect the XAFS spectra using IC as a result of its large volume. Intelligently, silicon PIN photodiodes [5] (SPPD) and diamond detectors[6] (DD) were used to substitute for IC due to their small size and good performance. Furthermore, to meet the time-resolved dynamic detection requirements, a high frequency (HF) sampling transmission scheme based on the high-speed counting cards (HSCC) was adopted to collect quick XAFS (QXAFS). However, the HF sampling XAFS data are very different from the conventional XAFS data in terms of abscissa and data points. Thus, the abscissa conversion and data reduction must be properly performed for the raw HF sampling scheme XAFS data.

Herein, the data preprocessing method of HF XAFS spectra will be proposed in detail according to the absorption edge of the standard sample and the rotation angular velocity of the monochromator. The data batch preprocessing program based on MATLAB code will also be introduced.

COLLECTION AND PREPROCESSING OF HF SAMPLING XAFS DATA

Data Collection

All the data was collected at beamline 1W2B of Beijing Synchrotron Radiation Facility (BSRF). The X-ray photon flux is about 1.0×10^{12} photons/s at Cu K-edge (8979 eV) with an X-ray spot size of about 0.8 (H) × 0.5 (V) mm^2 at the sample position. In HF sampling XAFS transmission mode, DD is used to monitor the X-ray intensity (I_0) in front of the sample, and DD or SPPD is used to monitor the X-ray intensity (I) behind the sample. For a sample with a thickness of d, the absorption coefficient (μ) can be written as:

$$\mu(\mathrm{E}) = \ln(I_0/I)/d \qquad (1)$$

The high-speed counting module [5] (NI 9223) instead of the 974 counter was used for the Cu K-edge XAFS measurements of Cu foil at a sampling frequency of 10 kHz. Here, the sampling frequency represents the number of times that an experimental signal (here it is the X-ray intensity) was repeatedly read out in one second. A higher sampling rate can greatly improve data quality by raising statistics. Figure 1 clearly shows the raw data of an HF sampling XAFS spectrum for standard Cu foil at the sampling frequency of 10 kHz. Figures 1a and 1b clearly show the dependences of I_0, I, and μ on counting (0~80,000). Based on the data acquisition frequency, the abscissa can also be expressed in terms of time t:

* Work supported by the National Natural Science Foundation of China (Project No. 12305372), and the National Key R&D Program of China (Grant No. 2017YFA0403000).
† liuyunpeng@ihep.ac.cn

ISBN: 978-3-95450-250-9 ISSN: 2673-5520 doi:10.18429/JACoW-MEDSI2023-WEPPP039

$$t = N/F \tag{2}$$

Here, N is the total number of data, and F is the data acquisition frequency. There are large amplitude fluctuations in raw spectra before 872 numbers and after 70,231 numbers (Figs. 1c and 1d), which corresponds to the position of 200 eV before the absorption edge and 800 eV after the absorption edge, respectively. This is due to the uneven speed of the monochromator during the start and stop phases. Anyway, the HF sampling XAFS is very different than that of the conventional XAFS in appearance. It is very necessary to make a data preprocessing so that one can determine the data qualities and features from the raw HF sampling XAFS data.

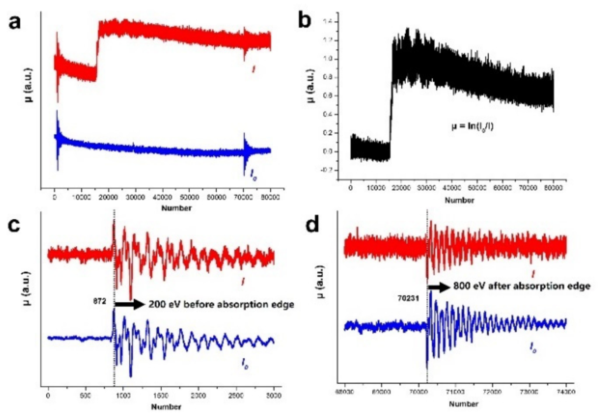

Figure 1: Raw HF sampling XAFS spectra of Cu-foil at 10 kHz. (a) I_0, I; (b) absorption coefficient μ; and the enlarged images of before (c) and after (d) absorption edge.

Abscissa Conversion

Firstly, the XAFS data should be converted from time-domain into energy-space. To do this, the absorption-edge position was first determined and marked as E_0, which corresponds to the first derivative maximum of the XAFS spectrum. For a typical double-crystal monochromator, its rotation in the Bragg-angle (θ) space is usually uniform. It means that the Bragg angle of Si (111) monochromator was linearly changed and followed the formula:

$$\theta - \theta_0 = \omega\,(t - t_0) \tag{3}$$

Here, θ_0 is the Bragg angle corresponding to the absorption edge of the element to be measured, t_0 is the required time for the monochromator to rotate to the absorption edge of the element, and ω is the rotation angular velocity of the monochromator. Based on the linear relation between the Bragg angle (θ) and the rotation time (t), the data-point distribution of HF sampling XAFS spectrum is also uniform in the Bragg-angle space. As an example, Fig. 2 clearly shows the abscissa conversion process from t-space to angular-space. After conversion, each of these data points (80,000 points) has its angle value. Meanwhile, the abscissa of the HF sampling XAFS spectra can be further converted from the Bragg angle (θ) to the incident X-ray energy (E) by the following formula:

$$E(eV) = hc/2d_{(111)}\sin\theta = 1977/\sin\theta \tag{4}$$

Here, h is the Planck constant (6.626×10^{-34} J·s); c is the velocity of light (2.998×10^{8} m·s^{-1}); $d_{(111)}$ is the interplanar spacing of Si(111) crystal plane (3.1357 Å). For the Cu-foil sample, the absorption-edge energy of Cu K-edge (E_0) is 8979 eV. Finally, the 80,000-absorption coefficient (μ) and energy (E) data points can be obtained.

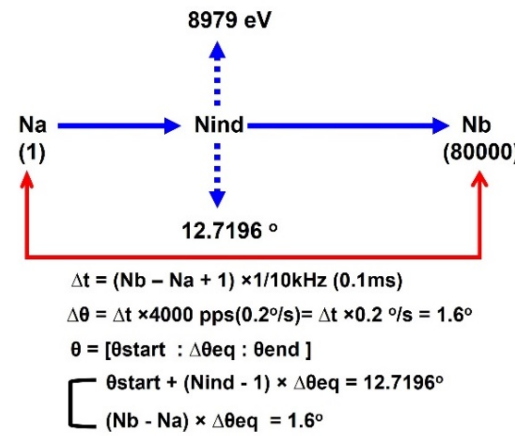

Figure 2: Abscissa conversion process from t-space to angular-space.

Data Reduction

The second step is data reduction. The simple and convenient way to reduce the number of data points is to divide the XAFS spectrum of high-frequency sampling into hundreds of segments. Each segment consists of hundreds of data points, being required to have an energy span equal to or better than the energy resolution of the monochromator. By averaging statistically all data points in each segment into one data point, the energy span between two adjacent data points was enlarged. Finally, the high-frequency sampling XAFS spectrum is restored to a normal XAFS spectrum consisting of hundreds of data points (reduced from 80,000 points to 800 points). The raw (black) and reduced (red) HF XAFS spectra are shown in Fig. 3.

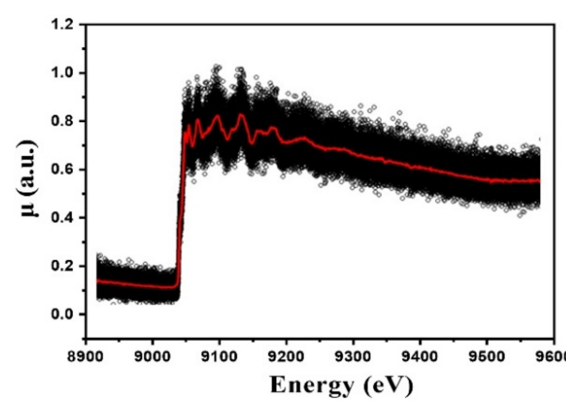

Figure 3: Raw and preprocessing (abscissa conversion and data reduction) HF sampling XAFS spectra of the standard Cu foil at 10 kHz.

Data Batch Processing Program

Even on the first-generation synchrotron source (BSRF), the repeated acquisition of HF sampling XAFS spectra can achieve a time resolution of the order of seconds [3]. It is clear that, when conducting in situ time resolution experiments in the reaction process of materials, a huge amount of data will be obtained. Therefore, developing a data batch processing program is very necessary. According to the above theory and procedure, a data batch processing program based on MATLAB code was written by Y. Liu.

It should be mentioned that, except for the data preprocessing of HF sampling XAFS data, the obtained SAXS and XRD data also need to be energy-normalized when the follow-up analysis. Therefore, the first thing is to obtain an energy file (two columns including time and energy, and the two correspond one-to-one). Figure 4 shows the MATLAB program interface of energy file acquisition for a standard sample. The parameter values of scanning speed, periodic time, acquisition frequency, and absorption edge energy are needed to be input. To shorten the repetition interval of XAFS, we adopt a novel bidirectional (two-way) energy scanning strategy. Meanwhile, to exactly obtain the energy coordinates, the deadtime (eliminate the return difference) should also be calculated in the forward and backward scanning. The energy coordinates of these data points are considered to be the same since the monochromator has no mechanical motion.

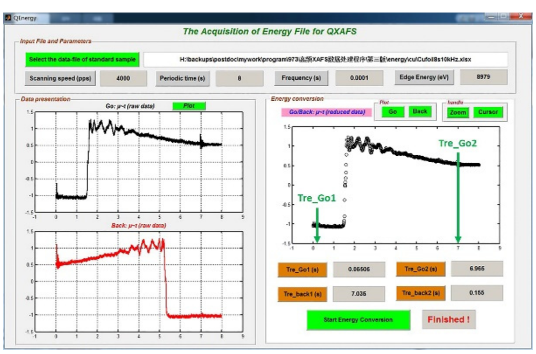

Figure 4: The MATLAB program interface of energy file acquisition for a standard sample Cu-foil.

Since the data acquisition adopts the two-way energy-scanning strategy, two conversion files (here, that is called Ego data and Eback data) from the acquisition time (t) to the diffraction angle (θ) of the monochromator or the incident X-ray energy (E) should be prepared in advance, which are used for the forward scanning process with the incident X-ray energy changing from low to high and for the backward scanning process with the X-ray energy changing from high to low, respectively. As an example, the energy calibration process using the XAFS spectra of Cu foil acquired by the two-way energy scanning strategy is shown in Fig. 4.

In the subsequent batch processing of HF sampling XAFS collected by the two-way energy-scanning strategy for the real sample, one only needs the two energy files (Ego data and Eback) of the standard sample obtained from the MATLAB program shown in Fig. 4. The batch data processing program for the HF sampling XAFS and the preprocessing result are shown in Fig. 5, which makes it easy for users to process data in batches.

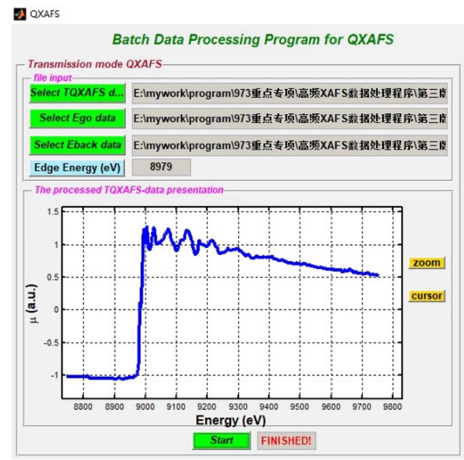

Figure 5: The batch data processing MATLAB program interface for HF sampling XAFS data.

CONCLUSION

This paper presented a simple and practical data preprocessing method for the novel HF sampling XAFS data, which facilitates the potential applications of HF XAFS spectra in a time-resolved SAXS/XRD/XAFS experiment.

ACKNOWLEDGEMENTS

This work was supported by the National Natural Science Foundation of China (Project No. 12305372), and the National Key R&D Program of China (Grant No. 2017YFA0403000).

REFERENCES

[1] N. Kumar *et al.*, “Achieving controllable MoS_2 nanostructures with increased interlayer spacing for efficient removal of Pb (II) from aquatic systems”, *ACS Appl. Mater. Interfaces*, vol. 11, pp. 19141-19155, 2019. doi:10.1021/acsami.9b03853

[2] Y. P. Liu *et al.*, “Bismuth-iron-based precursor: preparation, phase composition, and two methods of thermal treatment”, *RSC Adv.*, vol. 10, pp. 20713-20723, 2020. doi:10.1039/d0ra00177e

[3] Z. Wu *et al.*, “A novel SAXS/XRD/XAFS combined technique for in-situ time-resolved simultaneous measurements”, *Nano Res.*, vol. 16, pp. 1123-1131, 2023. doi:10.1007/s12274-022-4742-3

[4] A. M. Beale *et al.*, “Probing ZnAPO-34 self-assembly using simultaneous multiple in situ techniques”, *J. Phys. Chem. C*, vol. 115, pp. 6331-6340, 2011. doi:10.1021/jp200043b

[5] Y. Liu *et al.*, “Silicon PIN photodiode applied to acquire high-frequency sampling XAFS spectra”, *Nucl. Sci. Tech.*, vol. 33, p. 91, 2022. doi:10.1007/s41365-022-01066-2

[6] L. Yao *et al.*, “A polycrystalline diamond micro-detector for X-ray absorption fine-structure measurements”, *J. Synchrotron Radiat.*, vol. 29, pp. 424-430, Mar. 2022. doi:10.1107/S1600577521013011

ISBN: 978-3-95450-250-9 ISSN: 2673-5520 doi:10.18429/JACoW-MEDSI2023-WEPPP040

EXPERIMENTAL METHODS BASED ON GRAZING INCIDENCE AT THE 1W1A BEAMLINE OF THE BEIJING SYNCHROTRON RADIATION FACILITY AND ITS APPLICATION IN CHARACTERIZING THE CONDENSED STATE STRUCTURE OF CONJUGATED POLYMERS

Yu Chen[1]*, Hongxiang Li[2†], Pei Cheng[2‡], Yanchun Han[3§]
[1] Institute of High Energy Physics, Chinese Academy of Sciences, Beijing, China
[2] School of Polymer Science and Engineering, Sichuan University, Sichuan Province, China
[3] Changchun Institute of Applied Chemistry, Chinese Academy of Sciences, Jilin Province, China

Abstract

The Beijing Synchrotron Radiation Facility (BSRF) 1W1A Diffuse X-Ray Scattering Station can conduct grazing incidence wide/small angle scattering (GIWAXS/GISAXS) experimental method characterization, which is an important method for characterizing the condensed structure of conjugated polymers. To this end, we have upgraded and optimized the experimental method of grazing incidence. After updating the EIGER 1M area detector and reducing stray light interference, the exposure time of a single sample was reduced from 300 seconds to 30 seconds. And we have developed a remote rapid sample change platform, which can achieve remote testing operations outside of the hutch, greatly reducing testing time, and enabling users to remotely conduct online testing operations in their own labs. Subsequently, we further established in-situ steam treatment, in-situ thermal annealing, in-situ drip coating, in-situ spin coating, in-situ scraping coating, and GISAXS testing platforms, enriching the beamline’s grazing incidence methods. In the future, relying on the 1W1A diffuse X-ray scattering station, more in-depth research can be conducted on the crystallization behavior, film formation process, crystallization and phase separation size, and film structure of solution processed conjugated polymers.

INTRODUCTION

The Wiggler insert 1W1 in the storage ring I area of the Beijing Synchrotron Radiation Facility has led out two stations: 1W1A diffuse scattering and 1W1B-XAFS experimental stations (Fig. 1(a)). The 1W1A station utilizes the dual focusing monochromatic X-ray provided by the beam line to conduct structural research on crystals and thin film materials. This station can be operated in both dedicated and parasitic modes. The main optical components of the 1W1A beam line include an asymmetric cut crystal monochromator and a vertical bent reflector. The asymmetric cut crystal monochromator is 19 meters away from the light source, achieve monochromatization and horizontal focusing of the beam, and splitting with the 1W1B beam. The vertical bent reflector is located 1.6 meters behind the monochromator, used to realize vertical focusing of the beam and effectively suppress high-order harmonics. This beamline can conduct experiments such as high-resolution diffraction (XRD), low angle reflection (XRR), grazing incidence diffraction (GIXRD), GIWAXS, and GISAXS.

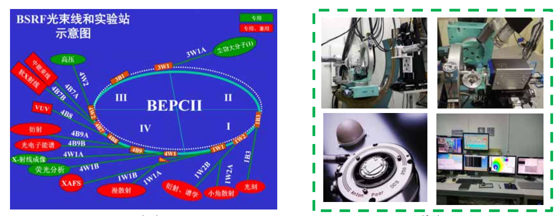

(a) (b)

Figure 1: (a) Schematic diagram of BSRF Beamline Station; (b) Multiple experimental platforms of the 1W1A.

Recently, we optimized the detectors, flight channels, attenuators, beamstop, etc., and reduced the exposure time of a single sample from 300 seconds to about 30 seconds. And we have developed a remote rapid sample change platform for grazing incidence experiments. Subsequently, we further established a series of in-situ steam treatment, in-situ thermal annealing, in-situ drip coating, in-situ spin coating, in-situ scraping coating, and GISAXS testing platforms, enriching the grazing incidence experimental methods (Fig. 1(b)).

REMOTE OPERATION GRAZING INCIDENCE EXPERIMENTAL PLATFORM

This experimental platform is equipped with a fast sample change device, which saves time for calibration of the sample in grazing incidence mode. Paired with E63 intelligent lightweight 6-degree of freedom modular collaborative robot, it can achieve continuous sampling without entering the hutch, and can achieve continuous testing of hundreds of samples (Fig. 2). Utilization of remote control software, users can realize remote operation of the experiment, greatly reducing the testing time for conventional thin film samples and simplifying the testing steps. (`http://202.122.38.138/docs/1w1aremote.mp4`).

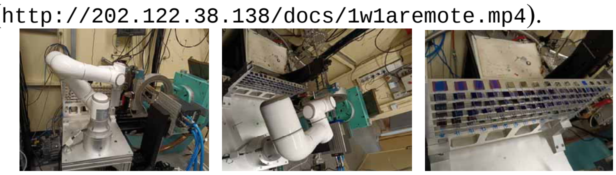

Figure 2: Remote operation GIWAXS platform.

* chen_yu@ihep.ac.cn, † lihongxiang@scu.edu.cn,
‡ chengpei@scu.edu.cn, § ychan@ciac.ac.cn

ISBN: 978-3-95450-250-9 ISSN: 2673-5520 doi:10.18429/JACoW-MEDSI2023-WEPPP040

The crystallization behaviour of solution processing conjugated polymers is a key factor determining their condensed state structure and device performance. To meet user's needs, 1W1A station has established in-situ steam treatment, in-situ thermal annealing, in-situ drip coating, in-situ spin coating, and in-situ scraping coating experimental platforms, which can conduct in-depth research on the crystallization behaviour and film formation process of solution processing conjugated polymers (Fig. 3).

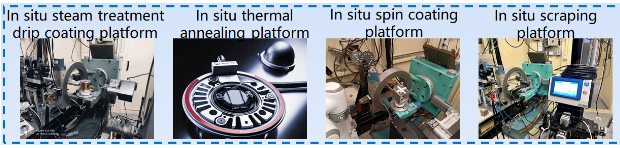

Figure 3: In-situ platform based on conjugate polymerization crystallization behavior and film formation process.

RECENT EXPERIMENTAL RESULTS

Prof. Yanchun Han (Changchun Institute of Applied Chemistry, Chinese Academy of Sciences) and Dr. Hongxiang Li (Sichuan University), have systematically studied the condensed structure and crystallization behavior of conjugated polymers and published related papers (Fig. 4) [1-5]. The in-situ GIWAXS mode of the experimental station serves as the core characterization method, providing rich data support for the overall experiment (Fig. 5) [6-8].

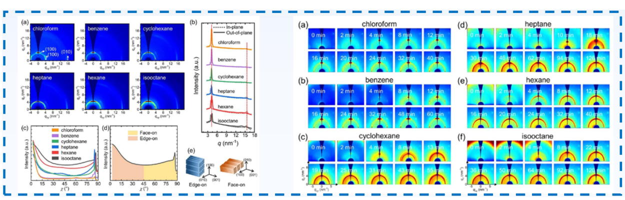

Figure 4: Solubility parameter regulation of D-A conjugated polymer condensed state structure.

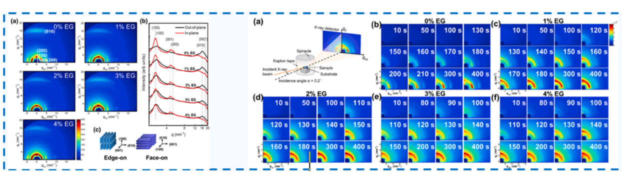

Figure 5: Additives regulate the crystallization behavior of D-A conjugated polymers.

ACKNOWLEDGEMENTS

National Natural Science Foundation of China, Sichuan Provincial Department of Science and Technology, State Key Laboratory of Polymer Physics and Chemistry, State Key Laboratory of Polymer Material Engineering, Beijing Synchrotron Radiation Facility, Shanghai Light Source, China Spallation Neutron Source.

REFERENCES

[1] L. Wan *et al.,* "Sensitive near-infrared circularly polarized light detection via non-fullerene acceptor blends", *Nat. Photonics*, vol. 17, no. 649, 2023. doi:10.1038/s41566-023-01230-z

[2] H.R. Zhang *et al.,* "Mitigating Exciton Recombination Losses in Organic Solar Cells by Engineering Nonfullerene Molecular Crystallization Behavior", *Adv. Energy Mater.*, p. 2302063, 2023. doi:10.1002/aenm.202302063

[3] X. Ma, G. Ran, H. Li, Y. Liu, *et al.,* "Modulating the Growth of Nonfullerene Acceptors Toward Efficient and Stable Organic Solar Cells Processed by High-Boiling-Point Solvents", *Adv. Energy Mater.*, p. 2302554, 2023. doi: 10.1002/aenm.202302554

[4] J.J. Zhao *et al.,* "Impact of Intermolecular Interactions between Halogenated Volatile Solid Additives and the Nonfullerene Acceptor in Organic Solar Cells", *Adv. Funct. Mater.*, p. 2307355, 2023. doi:10.1002/adfm.202307355

[5] X. Cao *et al.,* "An Amorphous n-Type Conjugated Polymer with an Ultra-Rigid Planar Backbone", *Angew. Chem., Int. Ed.*, vol. 62, no. 2, p. e2022129, 2023. doi:10.1002/anie.202212979

[6] R. Chen *et al.,* "Improving Carrier Mobility of Near-Amorphous Donor-Acceptor Conjugated Polymer Thin Films via Promoting Intensive and Continuous Polymer Aggregations", *Macromolecules.*, vol. 56, pp. 5356-5368, 2023. doi:10.1021/acs.macromol.3c00316

[7] Z. Zhou, Y. Xu, J. Yang, *et al.,* "New Medium-Bandgap Non-fused Ring Guest Acceptor with a Higher-Lying LUMO Level Enables High-Performance Ternary Organic Solar Cells", *ACS Appl. Mater. Interfaces*, vol. 15, pp. 42792-42801, 2023. doi:10.1021/acsami.3c06529

[8] S.Y. Hou, H.Q. Chen, D. Lv, *et al.,* "Highly Conductive Inkjet-Printed PEDOT:PSS Film under Cyclic Stretching", *ACS Appl. Mater. Interfaces,* vol. 15, pp. 28503-28515, 2023. doi: 10.1021/acsami.3c03378

ISBN: 978-3-95450-250-9 ISSN: 2673-5520 doi:10.18429/JACoW-MEDSI2023-WEPPP041

THE JOY OF VIBRATION MITIGATION

J. H. Kelly, D. Crivelli, S. Beamish, S.G. Alcock
Diamond Light Source, Harwell Science & Innovation Campus, UK

Abstract

As part of the Diamond-II facility upgrade, a new Optics Metrology Lab has been built at Diamond Light Source. This replaced the old lab which will be demolished to make space for a “flagship” beamline. However, the location for the new lab has intermittent 100 times higher floor velocity in the range 50-150 Hz compared to the original. This paper describes the engineering developments to successfully mitigate vibrations within the new lab. The raft of measures includes: ‘skyhook’ damping (i.e. active damping using geophone velocity feedback) and novel 2-stage passive vibration isolation. New vibration isolation & damping systems have been installed and will enable ultra-sensitive metrology tests to continue in the new lab.

INTRODUCTION

Diamond Light Source is the UK’s national synchrotron light facility. Each beamline uses a range of optics to focus and monochromate the ultra-intense X-ray beams created by the synchrotron. Prior to beamline installation, all X-ray optics are assembled and characterised in the Optics Metrology Laboratory (OML1). This cleanroom lab contains a suite of state-of-the-art metrology instruments to measure X-ray optics with sub-nanometre precision. These sensitive instruments require a mechanically and thermally stable environment. After > 15 years of operation, OML1 is to be demolished to make space for a new flagship beamline. To continue optical metrology operations and prepare for the improved-quality X-ray optical systems required for Diamond-II beamlines, a new lab (OML2) has been built. However, due to space limitations within the Experimental Hall, the location for OML2 has an intermittent 100 times higher floor velocity in the range 50-150 Hz compared the original. Such vibrations are caused by nearby plant, including a large, motorised dewar store. The engineers were given the task of finding isolation solutions to mitigate these increased levels of disturbances and provide an ultra-stable environment for the optical metrology instruments. Commercial passive vibration isolated tables only provide transmission data over a limited frequency range (e.g., Newport™ S-2000A from 0.8 to 30 Hz) and the supplied plots look like simple 1D lump mass models. Active damping options were also investigated, but they were not considered to be cost-effective, or provide the required damping bandwidth. Therefore, in-house damping solutions were designed and built.

PASSIVE VIBRATION ISOLATION

To replace existing air-isolation optical benches, a concept using spring isolators (from Farrat) was developed. The design re-used unwanted optical breadboards, which were supported via an intermediate granite block with two isolation stages i.e. floor to granite, and granite to table. This provided an attachment method that did not over-constrain the breadboard as well as providing a steeper isolation slope with frequency, as shown in Fig. 1. The performance of the vibration isolation system is significantly different from a simple 1D lump mass model since the higher-order vibration modes cross-couple. Rotation modes are measured as translations with amplitudes that depend upon the modal lever [1]. A 3D modal analysis of the proposed design was performed using ANSYS software to both visualise the mode shapes and to generate a reduced order model (ROM) for input into Simulink®. The sensor location was close to, but not exactly at, the centre of the table, as with the measured data. This prevents symmetry from making modes unobservable. The simulated vibration transfer function depends upon the point of measurement and the variation of spring rate across isolators. A random distribution of a realistic ± 10% spring rate causes higher-order modes to become more significant.

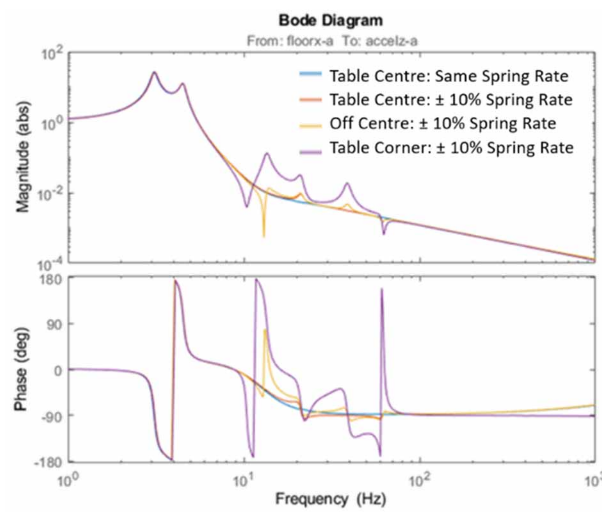

Figure 1: Simulated floor to tabletop transfer functions showing the effect of varying the spring stiffness and sensor location.

Passive Vibration Test Results

A measured transmissibility plot of the installed table, to compare with Fig. 1, is given in Fig. 2. The very low coherence is caused by the acoustic disturbance which is comparable to the floor vibration. Significant energy is passing through the air which is not measured by the floor accelerometer corrupting the transmissibility ratio. That said the measured data does show the simulated 2 resonant peaks below 10 Hz which amplify the floor acceleration and vibration isolation above 6-8 Hz.

ISBN: 978-3-95450-250-9 ISSN: 2673-5520 doi:10.18429/JACoW-MEDSI2023-WEPPP041

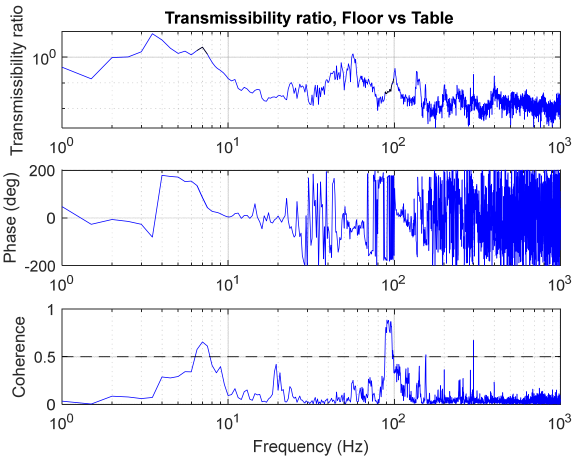

Figure 2: Measured accelerometer transmissibility plot from the floor to the table top. The low coherence indicates that there is no correlation between floor and table motion at those frequencies

To give a clearer view of the isolation performance an integrated displacement plot which runs from high to low frequency is presented in Fig. 3. The data plotted in blue above with the dewar store running is the same colour below.

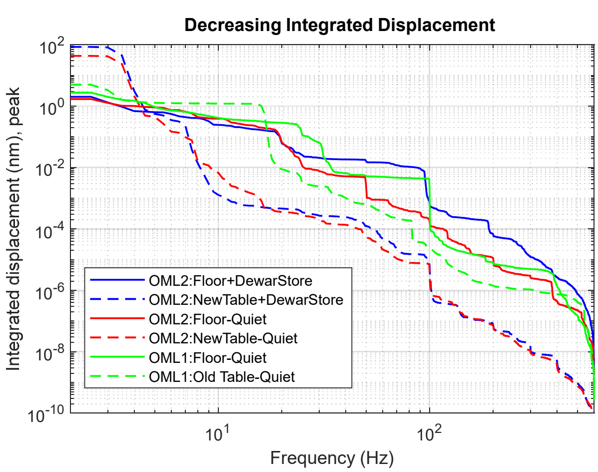

Figure 3: Measured accelerometer data plotted as an integrated displacement running from high to low frequency to compare the new table performance with the old commercial solution

The ratio of floor to table spectra does not make sense when significant energy is also passing through the air. The effect of the turning off the lab air-conditioning was clearly demonstrated in preliminary tests in OML1, when the peak sound level was reduced from 60 dB to 55 dB, causing the table peak acceleration to reduce by an order of magnitude.

The region of interest i.e., the typical equipment resonant frequency range coincides with the increased floor vibration over the 50-150 Hz range. The new table with dewar store disturbance, exhibits an isolation factor of over 200 at frequencies above 10 Hz. The new table design is significantly more stable above 10 Hz than the old commercial air isolation table in OML1.

ACTIVE DAMPING

The Diamond-NOM (Nano Optical Metrology) is a non-contact, slope profiler capable of characterizing optical surfaces with sub-nm repeatability. Air-bearing stages are used to translate the autocollimator beams across the surface under test [2]. As supplied by the manufacturer (Q-Sys), the granite base was supported on steel wedges with an elastomer layer. The original installation did not exhibit any significant vibration isolation, and so was replaced with Farrat spring mount isolators. The new passive vibration isolation was effective above 6 Hz. However, an undesirable effect was that the acceleration reaction forces from the scanning stage caused the granite system to resonate. Oscillation at ~2 Hz created secondary reaction forces back to the scanning stage, corrupting the dynamic, measurement of X-ray optics.

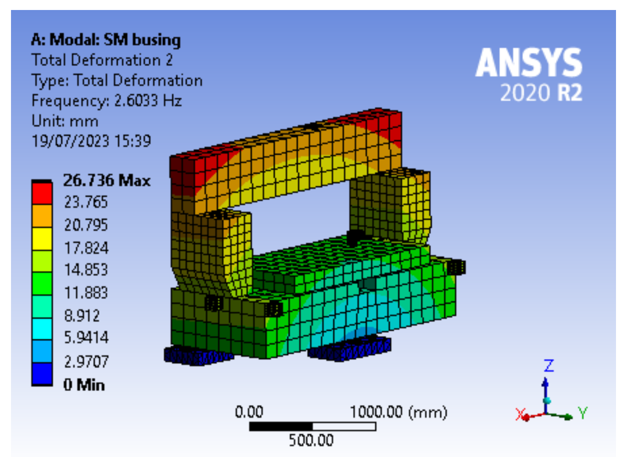

Figure 4: ANSYS modal analysis showing the dominant resonant mode driven by the scanning stage reaction forces.

Options considered to mitigate the resonance were: reduce the stage acceleration (at the expense of measurement throughput); modify the system by adding a balancing mass (but this would be a complex task for a commercial system with a granite structure); add additional passive dampers (which would corrupt the vibration isolation); or the chosen solution of developing an active damping system.

A ROM was exported from ANSYS see Fig. 4. The ROM was used as the plant block in a Simulink model to capture the 6 DOF (Degree of Freedom) complexity of the lowest 20 mode shapes. A simple 'skyhook' damping (i.e., active damping using geophone velocity feedback) was simulated [1]. Disturbance to position transfer functions were exported to create a dynamic error budget (DEB) [3]. It may be seen from Fig. 5 that neither amplifier current noise (Trust Automation TA105), 16-bit DAC quantisation noise, nor the geophone noise, limit the system stability. It was critical that the active system did not worsen the stability. The floor motion trace is hidden under the total trace.

ISBN: 978-3-95450-250-9 ISSN: 2673-5520 doi:10.18429/JACoW-MEDSI2023-WEPPP041

Above 100 Hz, a first order low pass filter was added as the sensor noise became dominant.

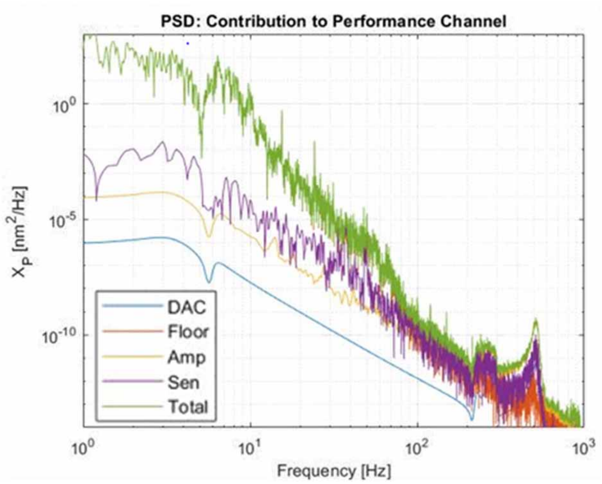

Figure 5: Dynamic error budget showing that the amplifier, sensor, and DAC noise would not degrade the position stability

Active Damping Test Results

The apparatus for the active damping system is shown in Fig. 6. The system implemented was a single axis, however it effectively damps multiple modes. The contact point with the granite was carefully chosen to maximise the number of modes which could be controlled. The measurement and actuator systems were closely located to enable closed-loop stability.

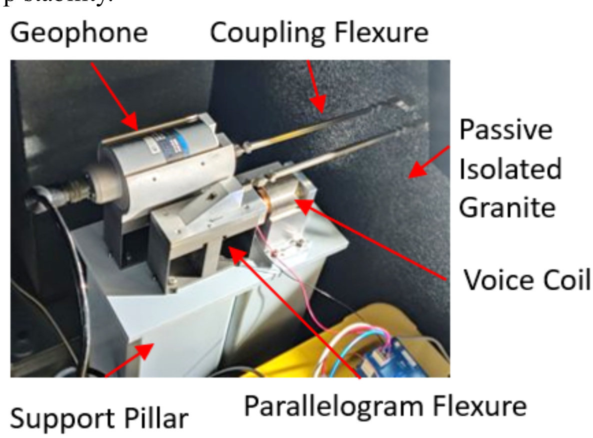

Figure 6: The main apparatus of the active damping system for the Diamond-NOM slope profiler.

The measured performance was in good agreement with the simulation, i.e., the resonant frequencies and vibration decay times were very similar. Representative active damping results are shown in Fig. 7. The damping ratio has improved by an order of magnitude, from 0.009 to 0.24, and settling time (to within 5%) are reduced from 47 s to 2.4 s.

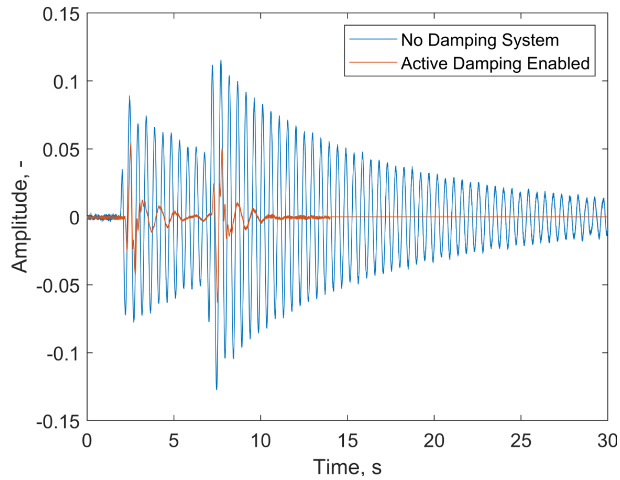

Figure 7: Accelerometer scans (velocity versus time) to show the effect of moving the scanning stage of the Diamond-NOM, with and without the active damping system.

CONCLUSION

The active and passive isolation systems were successful in reducing vibrations transmitted to the metrology instruments in the new Optics Metrology Lab (OML2).

- The passive system successfully isolated the floor vibrations, leaving acoustics as the dominant disturbance force.
- The active damping system applied to the Diamond-NOM reduced the settle time between steps by an order of magnitude. This enables scanning to be performed more quickly, increasing measurement throughput while maintaining the passive vibration isolation.

REFERENCES

[1] R. Munnig Schmidt, G. Schitter, and A. Rankers, *The Design of High Performance Mechatronics - 3rd Revised Edition*, Amsterdam, the Netherlands: IOS Press, 2020.

[2] S. G. Alcock, I. Nistea, and K. Sawhney, "Nano-metrology: The art of measuring X-ray mirrors with slope errors <100 nrad", *Rev. Sci. Instrum.*, vol. 87, no. 5, May 2016. doi:10.1063/1.4949272

[3] L. Jabben, "Mechatronic design of a magnetically suspended rotating platform", Ph.D. thesis, Delft University of Technology, Delft, the Netherlands, 2007.

ISBN: 978-3-95450-250-9 ISSN: 2673-5520 doi:10.18429/JACoW-MEDSI2023-WEPPP044

DEVELOPMENT OF HIGH POWER DENSITY PHOTON ABSORBER FOR SUPER-B SECTIONS IN SSRF*

Qisheng Tang[†, 1], Changyu Jin[2], Qinglei Zhang[1], Yeliang Zhao[1], Yiyong Liu[1]
[1]Shanghai Advanced Research Institute, CAS, Shanghai, China
[2]SKY Technology Development Co., Ltd., CAS, Shenyang, China

Abstract

There are two symmetrical standard bend (standard-B) sections been upgraded to super-B sections in the storage of Shanghai Synchrotron Radiation Facility (SSRF). Photon absorbers made up of CuCrZr were used for absorbing radiation with very high power density in the super-B sections. Meanwhile, CuCrZr absorbers were also used as beam chamber and pump port for the lattice of super-B section is very compacted. The absorbing surface was designed as serrate structure in order to diminish the power density. CuCrZr was cold-forged before machining to enhance its strength, thermal conductivity and hardness. Friction welding is adopted for absorber fabrication to avoid material properties deterioration. Rectangle flanges of absorbers were designed as step rather than knifer for vacuum seal. These high power density photon absorbers have been installed on the storage ring, both pressure and temperature being in accordance with design anticipation under the condition of 240 mA beam.

INTRODUCTION

The purpose of upgrading 2 symmetric standard-B sections to super-B sections is to provide hard X-ray with the energy of 18.7 keV for users in SSRF [1], as shown in Fig. 1. Moreover, short straight sections in which insert devices can be installed to provide photon for beamline laboratories were added in super-B sections of which the total length is same with that of standard-B sections. Compare to standard-B, much stronger magnetic field can be generated by super-B, the power of synchrotron radiation being much higher. Furthermore, the majority of synchrotron radiation has to be absorbed in much compact space.

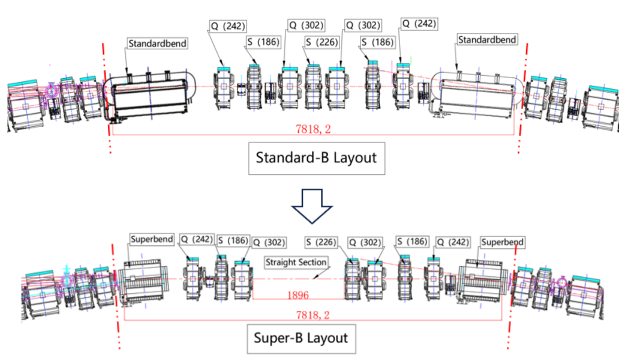

Figure 1: Standard-B section upgrade to super-B section in SSRF.

* Work supported by "SSRF Phase-II Beamline Project" (1173SRCZ01), "Ultra-high Vacuum, Precision Machinery and Collimation Technology Development for Diffraction-limited Storage Ring" (2016YFA0402004)
† email address: tangqs@sari.ac.cn

The density of photon power is much higher because of limited absorbing space and much stronger magnetic field. CuCrZr photon absorbers were developed to absorb photon with high power density in super-B sections. Friction welding was adopted to fabricate these absorbers with complex structure. The comparison of main specification between standard-B and super-B is shown in Table 1.

Table 1: Main Specification of Standard-B and Super-B

	Standard-B	Super-B
Arc length (mm)	1440	832.5
Magnetic field (T)	1.27	2.29
Magnet gap (mm)	50	30
Bending angle (°)	9	9
Radiation Power (kW)@300mA	10.9	18.8

ABSORBERS DISTRIBUTION AND MATERIAL

There are just five absorbers distributed in each super-B section and downstream because of very limited available installing space. The lattice of super bend magnet 2 downstream haven't been changed. However, original absorbers have been replaced by two new absorbers (absorber 4 and absorber 5) to absorb high power density radiation from super bend magnet 2, vacuum chambers also being redesigned, as shown in Fig. 2.

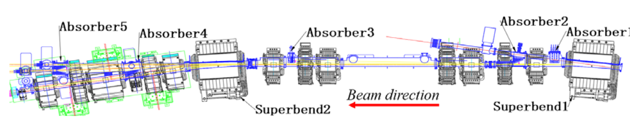

Figure 2: Absorbers distribution on super-B section.

All absorbers were installed at clearance of each couple of magnets. Ion pumps were installed next to these absorbers to enhance pumping efficiency. The maximum heat flux density on absorber 2 is yet up to 43 W/mm^2 @300 mA after structure optimization, as shown in Table 2.

Oxygen free copper (OFHC) is widely adopted to fabricate absorbers on storage rings because of its high thermal conductivity. However, it can't endure so high power density. Glidcop is another kind of absorber material for absorbing photon with high power density in some light source [2, 3]. However, Glidcop imported is very expensive. CuCrZr is attractive material for fabricating high power density photon absorbers because of its high thermal conductivity [4], high softening temperature and good mechanical properties [5-8]. Domestic CuCrZr was chosen as material for these absorbers finally. Properties of the

ISBN: 978-3-95450-250-9 ISSN: 2673-5520 doi:10.18429/JACoW-MEDSI2023-WEPPP044

CuCrZr are improved apparently after cold forging, as shown in Table 3.

Table 2: Radiation Power on Absorbers

	Absorbing power (kW)	Maximum power density (W/mm^2)
Absorber 1	4.3	16
Absorber 2	11.7	43
Absorber 3	1.1	8
Absorber 4	9.5	34
Absorber 5	5.4	15

Table 3: Properties of Domestic CuCrZr by Test

	Before cold forging	After cold forging
Young Modulus (GPa)	85.3	119
Yield Strength (MPa)	111.6	400.6
Ultimate Limit (MPa)	239.3	434.7
Hardness (HB)	61	151.7
Expansion at 100 ℃ （10^{-6}/K）	15.9	16.6
Conductivity at 100 ℃ (W/(m·K))	283.5	358.5

ABSORBERS STRUCTURE AND FABRICATION

The absorbing face of absorbers were designed as slope with comb shape to dilute heat flux density, as shown in Fig. 3. The typical structure of absorbers was made up of up-absorbing body and down-absorbing body, both of which having comb shaped absorbing face. Up-body and down-body were assembled by friction-welding, their comb teeth engaging together to complete absorbing face.

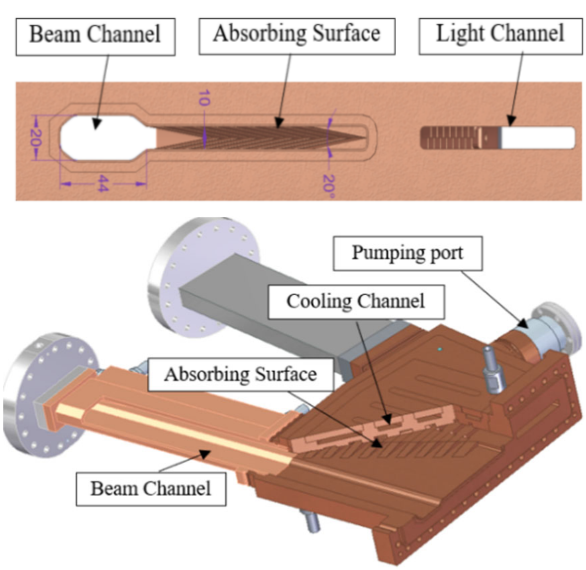

Figure 3: 3D model of the structure of absorber 2.

Knife can be directly machined on CuCrZr circular flange like that of absorbers in ESRF [9] and in TSP [10] for vacuum seal by the advantage of its hardness. Instead, step flange directly machined on CuCrZr absorbers in SSRF is used for vacuum seal because the surface of rectangle flange is very large. Flange sample was test for several times before formal fabrication, the result showing this type of flange is suitable for ultra-high vacuum seal. The sample of CuCrZr step flange and seal test are shown in Fig. 4.

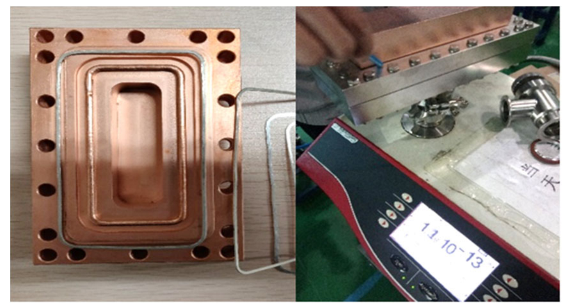

Figure 4: The sample of CuCrZr step flange and seal test.

Cooling channels were formed by grooves on the back of absorbing bodies welding with CuCrZr cover plates. The maximum temperature on absorbing face is about 270 °C under the situation of beam of 300 mA by simulation. The nephogram of temperature and equivalent stress of absorber 2 by simulation are shown in Fig. 5.

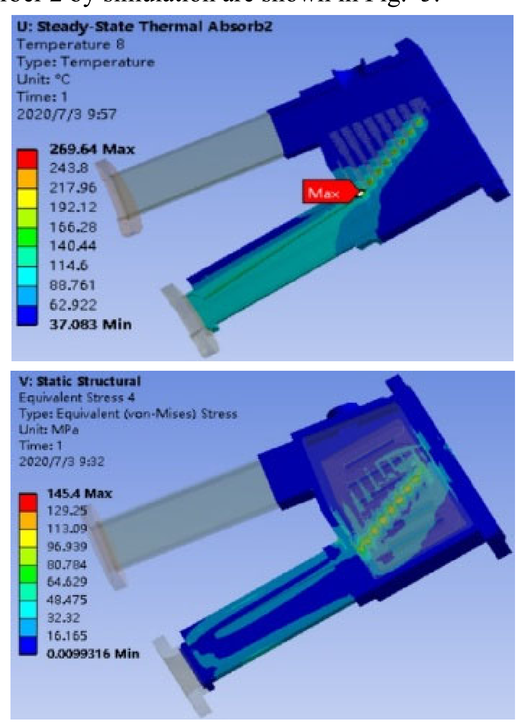

Figure 5: Nephogram of temperature and equivalent stress of absorber 2.

Braze could not be adopted to welding CuCrZr absorbers for properties of the material will be deteriorated at the temperature higher than 500 °C [8]. However, welding can not be avoided for these absorbers in super-B sections because of their complex structure. Several welding

ISBN: 978-3-95450-250-9 ISSN: 2673-5520 doi:10.18429/JACoW-MEDSI2023-WEPPP044

process were carried out to complete photon absorber 2 fabrication. It can be shown from the reference [11] that the temperature outside the welding seam is already lower than 500 ℃ in welding process. Therefore, friction welding was mainly adopted for absorbers, avoiding material properties deteriorate. Fabrication process for absorber 2 is shown in Fig. 6.

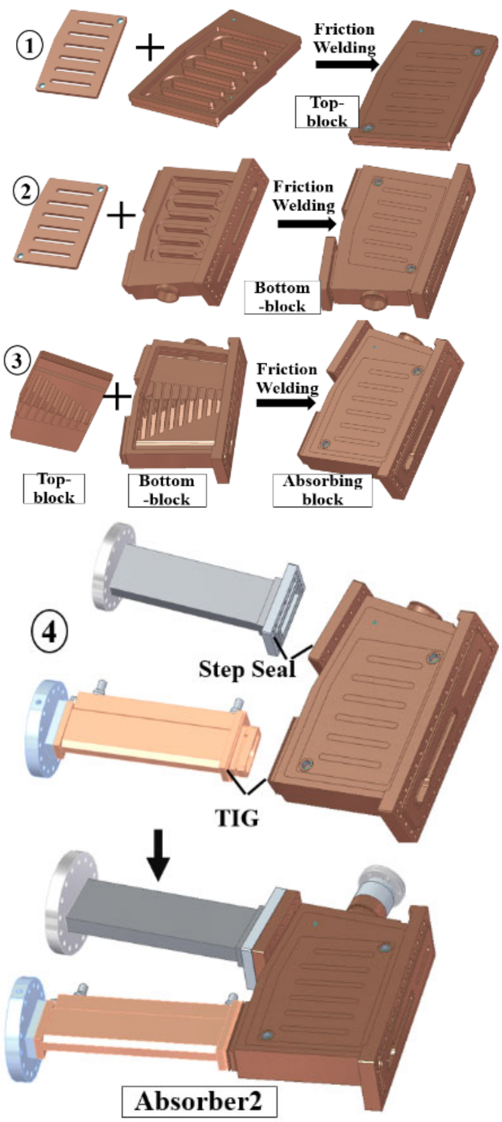

Figure 6: Main fabrication process for absorber 2.

VACUUM PERFORMANCE

CuCrZr absorbers have been installed on the storage ring in August 2019, as shown in Fig. 7. Static average pressure of super-B sections was about 3.3×10^{-8} Pa after vacuum baking in site. Dynamic average pressure has reduced from 1×10^{-6} Pa at the beginning of beam operation to 1.5×10^{-7} Pa @260 mA after 100 Ah of integral current. The curves of per-pressure versus integrate current in the early stage of startup after super-B sections installing completely is shown in Fig. 8. These CuCrZr absorbers have been on the storage ring for several years, Dynamic average pressure being lower than 6×10^{-8} Pa @200 mA now.

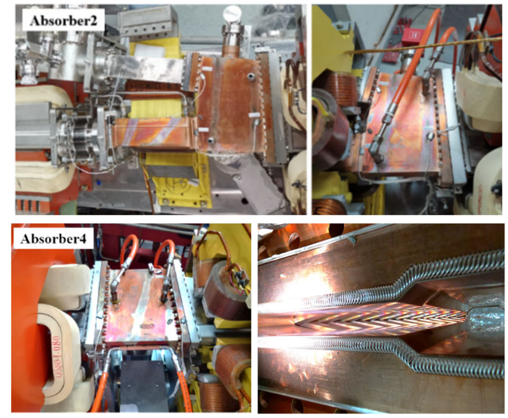

Figure 7: CuCrZr absorbers installed on the storage ring.

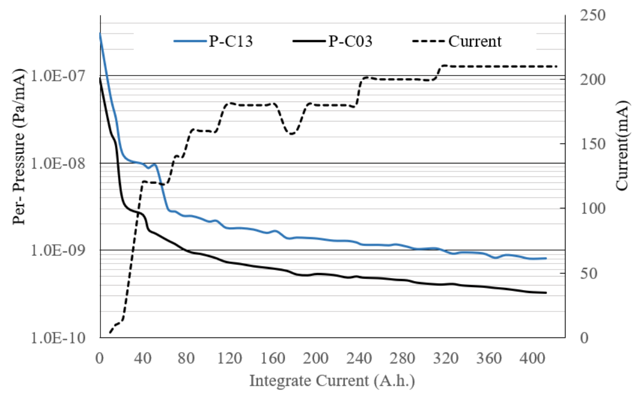

Figure 8: Curves of per-pressure versus integrate current in the early stage of startup.

The temperature on these CuCrZr absorbers rise proportionally to the beam current. The highest temperature measured on outer surface of absorber 2 is about 80 °C @240 mA, which is accordance with the result of simulation, as shown in Fig. 9.

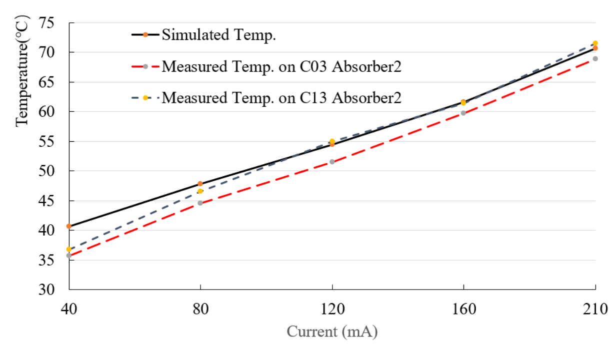

Figure 9: Temperature comparison between simulation and measurement on absorber 2.

CONCLUSION

Friction welded CuCrZr absorbers have been successfully developed and used for absorbing high power density synchrotron radiation at super-B sections in SSRF. It is concluded that the structure of the face of oblique teeth engaged on CuCrZr body for diluting power density and step flange on the body for vacuum seal is feasible from the result of operation in site for several years.

ISBN: 978-3-95450-250-9 ISSN: 2673-5520 doi:10.18429/JACoW-MEDSI2023-WEPPP044

REFERENCES

[1] M. Qian, Q. Zhou, *et al.*, "The Design and Magnetic Measurement of a Superbend Dipole Magnet at SSRF", *IEEE Trans. Appl. Supercond.*, vol. 28, p. 4002403, 2018. doi:10.1109/TASC.2017.2786224

[2] T. Takahashi, T. Honda, *et al.*, "Development of a movable synchrotron-radiation mask for the Photon Factory Advanced Ring (PF-AR)", *Nucl. Instrum. Methods Phys. Res., Sect. A*, vol. 607, pp. 334–339, 2009. doi: 10.1016/j.nima.2009.05.132

[3] E. Al-Dmour, D. Einfeld, *et al.*, "The conceptual design and thermal analysis of ALBA crotch absorbers", in *Proc. PAC'07*, Albuquerque, NM, USA, Jun. 2007, p. 299-301. https://jacow.org/p07/PAPERS/MOPAN065.PDF

[4] P. Hanzelka, V. Musilova, *et al.*, "Thermal conductivity of a CuCrZr alloy from 5 K to room temperatures", *Cryog.*, vol. 50, pp. 737-7 42, 2010. doi:10.1016/j.cryogenics.2010.08.001

[5] U. Holzwarth *et al.*, "On the recovery of the physical and mechanical properties of a CuCrZr alloy subjected to heat treatments simulating the thermal cycle of hot isostatic pressing", *J. Nucl. Mater.*, vol. 279, pp. 19–30, 2000. doi:10.1016/S0022-3115(99)00278-0

[6] M. Li and J.F. Stubbins. "Evaluation of irradiation effect on fatigue performance of copper alloys for high heat flux applications", *Fusion Sci. Technol.*, vol. 44, pp. 186–190, 2003. doi:10.13182/FST03-A331

[7] A. Hernández-Pérez, M. Eddahbi, *et al.*, "Microstructure and mechanical properties of an ITER-grade Cu–Cr–Zr alloy processed by equal channel angular pressing", *Fusion Eng. Des,*, vol. 98-99, pp. 1978–1981, 2015. doi:10.1016/j.fusengdes.2015.06.180

[8] J.Y. Parka, J.S. Lee, *et al.*, "Effect of cooling rate on mechanical properties of aged ITER-grade CuCrZr", *Fusion Eng. Des,*, vol. 83, pp. 1503–1507, 2008. doi:10.1016/j.fusengdes.2008.07.006.

[9] F. Thomas, J.C. Biasci, *et al.*, "X-ray Absorber Design and Calculations for the EBS Storage Ring", in *Proc. MEDSI'16*, Barcelona, Spain, Sep. 2016, pp. 257–61. doi:10.18429/JACoW-MEDSI2016-WEAA02

[10] C. Shueh, C.K. Chan, *et al.*, "Investigation of vacuum properties of CuCrZr alloy for high-heat-load absorber", *Nucl. Instrum. Methods Phys. Res., Sect. A*, vol. 841, pp. 1–4, 2017. doi:10.1016/j.nima.2016.10.025

[11] R.L. Lai, X.Q. Li, *et al.*, "Microstructures evolution and localized properties variation of a thick friction stir welded CuCrZr alloy plate", *J. Nucl. Mater.*, vol. 510, pp. 70–79, 2018. doi:10.1016/j.jnucmat.2018.07.055

ISBN: 978-3-95450-250-9 ISSN: 2673-5520 doi:10.18429/JACoW-MEDSI2023-WEPPP045

PARTICLE-FREE ENGINEERING IN SHINE SUPERCONDUCTING LINAC VACUUM SYSTEM

Y.L. Zhao†, Y.Y. Liu, Y.F. Liu, Q.S. Tang, L.X. Yin
Shanghai Advanced Research Institute, CAS, Shanghai, China

Abstract

The Shanghai high-repetition-rate XFEL and extreme light facility (SHINE) is under design and construction. The linac of SHINE facility is superconducting accelerating structures of high gradients, whose performance is closely related to the cleanliness of superconducting cavities. Therefore, the beam line vacuum system has extremely high requirement for particle free to avoid particles down to submicrometric scale. To control particle contamination, particle-free environment has been built for cavity string assembly and other beam line vacuum components installation, clean assembly criterion has been established. Furthermore, the particle generation of vacuum components (valve, pump, etc.) has been studied. Moreover, dedicated equipment and component (slow pumping & slow venting system, non-contact RF shielding bellow) have been developed for particle-free vacuum system.

INTRODUCTION

SHINE is a new hard-XFEL facility under construction in China, which is designed to accelerate electron beams to 8 GeV by 600 1.3 GHz 9-cell cavities working in continuous wave mode, and the cavities is installed in 75 cryomodules [1]. Cleanliness is essential in the preparation of field emission free, high gradient, low loss superconducting cavities [2], therefore, not only the cavities but also the beamline vacuum components adjacent to cryomodules has extremely high cleanness requirement. The design, fabrication, cleaning, assembly, testing process of these components must be followed the cleanliness requirement.

In SHINE linac, the total length of particle-free zone is 1.2 km, including cryomodules and room temperature (RT) beamline. For cryomodules, the vertical test of single cavity, cavity string assembly and cryomodule horizontal test are all carried out in SHINE. For RT beamline vacuum components, most pre-cleaning is performed at supplies. For integrated equipment like collimators, profile monitors wire scanners, e.g., the particle-free assembly is carried out at supplies. For standard components like vacuum gauges, valves, pumps, the cleaning before final assembly is carried out in SHINE.

INFRASTRUCTURES, EQUIPMENTS AND TECHNOLOGIES

A 400 m^2 cleanroom have been built in 2019 for SHINE superconducting cavity string assembly, which has 300 m^2 ISO 4 class area and 100 m^2 ISO 5 class area.(Fig. 1 top).

The cleanroom includes ultrasonic cleaning, high press rinsing (HPR), cavity drying areas, and the cavity string assembly area is capable for up to 8 persons to assembly 2 cavity strings at the same time (Fig. 1 bottom).

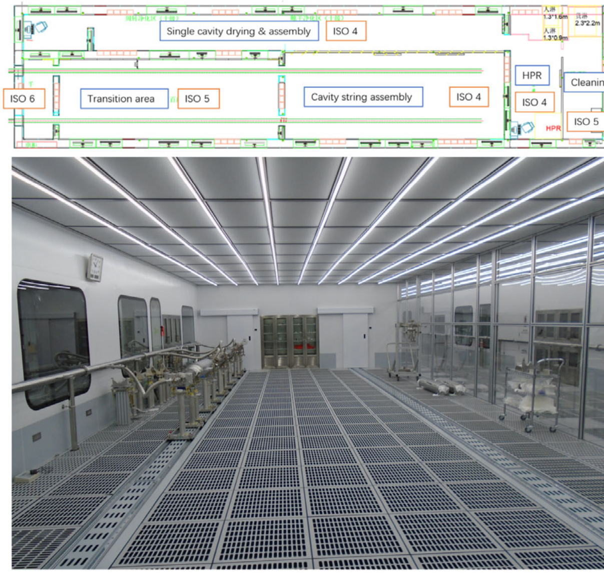

Figure 1: ISO 4 class cleanroom for cavity string assembly.

Various moveable laminar flow booths have been used for particle-free operation at cryomodule horizontal test, cavity vertical test, beam line vacuum components, e.g. High Efficiency Particulate Air (HEPA) filter was used in all of these booths, so as to obtain a local cleanness higher than

Figure 2: Moveable laminar flow booths for local particle-free assembly.

ISBN: 978-3-95450-250-9 ISSN: 2673-5520 doi:10.18429/JACoW-MEDSI2023-WEPPP045

than ISO 5 class, while the direction of laminar flow of each booth is various according on specific working conditions (Fig. 2).

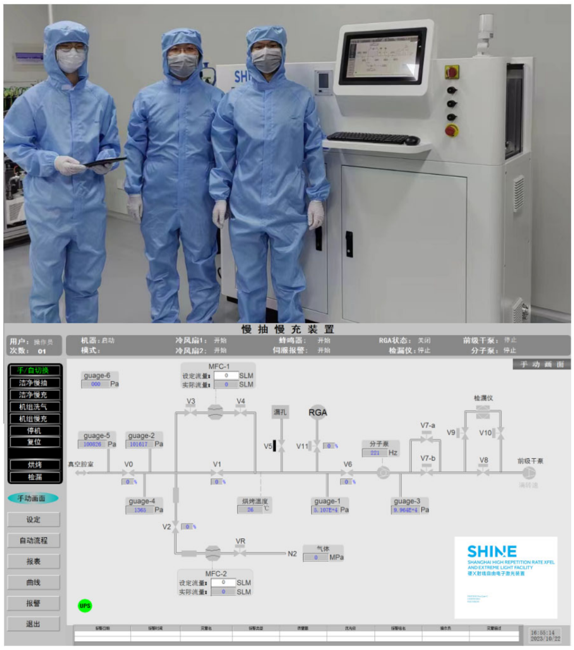

Figure 3: Dedicated slow pumping, slow venting system.

Several kinds of full-automatic slow pumping and slow venting (SPSV) systems have been developed for particle-free vacuum system (Fig. 3). The mass flow rate in pumping and venting procedures could be set down to 0.2 SLM, so as to avoid turbulent flow and reduce the probability of contamination and particulates transporting in vacuum system.


Figure 4: Ion pump assembled in ISO 4 clean room.

More than 200 ion pumps will be installed onto the particle-free vacuum system, which were cleaned and assembled follow the particle-free criterion, the body of pump was rinsed in flowing super purified water, and baked out in ISO 6 class cleanroom, after that purified nitrogen gas blowing cleaning were carried out before final assembly in ISO 4 class cleanroom (Fig. 4).

Non-evaporable getter pumps are used at the RT section adjacent to cryomodule, hence the cleanness of getter pump after activation is much concerned. Cleanness tests of getter pump was performed in two ways, one is in-vacuum monitoring, and the other is nitrogen gas blowing at atmosphere.

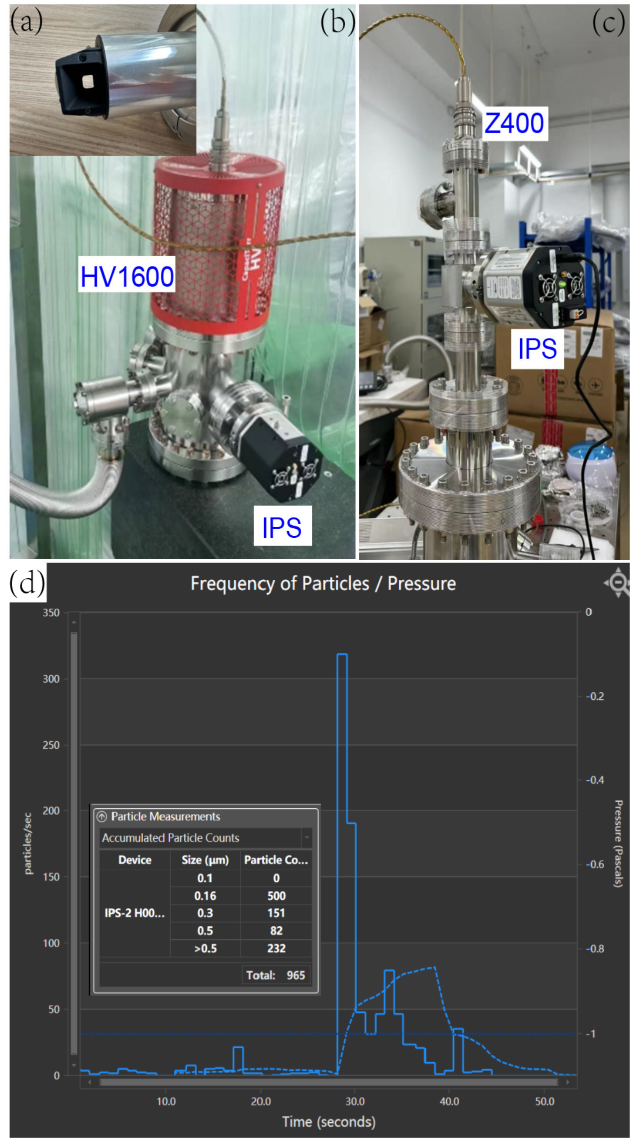

Figure 5: (a) In-vacuum sensor of IPS, (b) Saes HV 1600 getter pump particle test, (c) Saes Z400 getter pump particle test, (d) particle count of IPS.

To monitor the particle generated in the process of getter pump activation, a in-vacuum particle counter (In-line particle sensor, IPS, CyberOptics) was used, which can measure particles greater than 0.16 μm size, with less than 5 false counts per hour. However, the inlet of the measuring area of IPS is smaller than 1 cm^2, showed in Fig. 5a, the possibility of particle in vacuum transport to measuring area is quite low, to monitoring the particles, IPS has been installed right under a getter pump (Saes Z400), the setup is showed in Fig. 5c. During the process of degas of Z400, the voltage range is 0 to 5 V, 1×10^{-3} Pa, no particle was detected. Afterwards, the voltage was raised to 15 V gradually, while the pressure was 5×10^{-4} Pa, few particle was detected until the voltage and current of Z400 reached 14.9 V and 3.9 A, respectively. The count of particle (size 0.16, 0.3, 0.5, >0.5 μm) is several hundred per minute, showed in Fig. 5d. The number of counts lasted for 5 minutes, and dropped to 300 pc/minute.

ISBN: 978-3-95450-250-9 ISSN: 2673-5520 doi:10.18429/JACoW-MEDSI2023-WEPPP045

In another in-vacuum test of Saes HV1600 getter pump, the measuring area of IPS is not right under the pump, therefore nearly no particle was detected.

Another HV1600 getter pump have been installed in a pump station for the cavity string vacuum at the cryomodule horizontal test stand. After 3 times activation and 2 months operation at 200 °C, the NEG pump was dismounted from the pump station and blowed using purified nitrogen gas at 4 bar, the particle was monitored by airborne particle counter (28.3 L/min), nearly 700 pc/10 s of 0.3 µm and 200 pc/10 s of 0.5 µm was detected, no more particle was detected after 5 minute blowing.

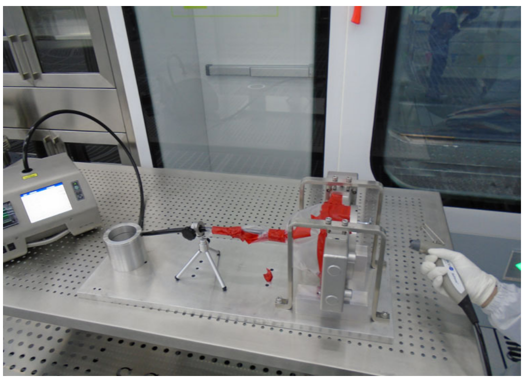

Figure 6: Particle test of valve open/close action.

The valves used in SHINE beamline vacuum is all-metal, therefore, valve open/close action always generate particles. Tests have been carried out for angle valves and gate valves (Fig. 6), the results show that every single open/close action could generate dozens of particles at 0.3 and 0.5 µm size.

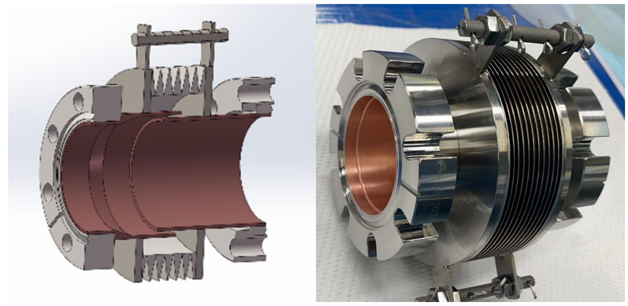

Figure 7: Non-contact RF shielding bellow.

To avoid friction between metals which could generate the large number of particles, a non-contact type RF shielding bellow design is adopted in room temperature beamline vacuum (Fig. 7). This RF bellow has 2 copper tube nested inside and out, with a radial direction offset 2 mm.

CONCLUSION

Due to the adoption of superconducting RF technology the SHINE project is facing with new challenges in UHV engineering. Infrastructures, technologies and procedures for particle-free vacuum, low temperature vacuum and other related vacuum system are established and developed to support the SHINE project construction.

REFERENCES

[1] Z.Y. Zhu *et al.*, "SCLF: An 8-GeV CW SCRF Linac-Based X-Ray FEL Facility in Shanghai", in *Proc. FEL'17*, Santa Fe, NM, USA, Aug. 2017, pp. 182-184. doi:10.18429/JACoW-FEL2017-MOP055

[2] D. Reschke, "Cleanness Techniques", in *Proc. SRF'05*, Ithaca, NY, USA, July 2005, paper SUP03, pp. 71-77.

12th Int. Conf. Mech. Eng. Design Synchrotron Radiat. Equip. Instrum. MEDSI2023, Beijing, China JACoW Publishing
ISBN: 978-3-95450-250-9 ISSN: 2673-5520 doi:10.18429/JACoW-MEDSI2023-WEPPP047

INSTALLATION PROCESS EXPERIMENT OF HEPS STORAGE RING EQUIPMENT

C. H. Li†, Z. H. Wang, S. Lu, L. Dong, S. Yang, S. Y. Chen, Y. D. Xu, Y. F. Wu, F. S. Chen, M. Yang, L. Wu, G. Feng, Institute of High Energy Physics, Beijing, China

Abstract

HEPS is a new generation synchrotron radiation source under construction in China. In order to complete high-precision installation of the 1.4 km storage ring within a limited construction period, it is necessary to identify and solve potential issues in various aspects, including operation space, installation process, alignment scheme, and unit transportation, prior to the regular batch installation. Therefore, a full-process installation experiment was performed and the feasibility of relevant schemes are verified. Batch installation is currently in progress based on the experimental experience.

INTRODUCTION

The High Energy Photon Source (HEPS) is the fourth-generation synchrotron radiation source currently under construction in China, characterized by high energy and extremely low emittance. The circumference of the storage ring is approximately 1.4 km, and compact 7BA achromats is adopted [1], which brings lots of challenges to the installation. In order to complete high-precision installation within a very limited construction period, it is necessary to identify and solve potential issues in various aspects, including installation operation space, alignment installation process, pre-alignment precision, and transportation reliability, before the regular installation in batches.

The experiment object is a standard 7BA cell, as shown in Fig. 1, which includes 6 pre-alignment units, 5 BLG magnets, 1 ID beamline, and 1 BM beamline.

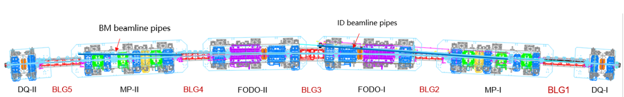

Figure 1: A standard 7BA cell.

The experiment was performed in a laboratory adjacent to HEPS. The pre-alignment was carried out in a thermostatic room, while other processes were conducted in the hall. The experiment lasted for approximately 4 months.

PRE-ALIGNMENT SCHEME

The magnet pre-alignment errors are required to be less than 30 μm, which accumulate from several processes such as measuring, magnet positioning, magnet opening/closing, and transportation. The magnet positioning deviation between magnets within a girder is required to be less than 10 μm, and much higher measuring accuracy and precise alignment mechanism of micron level are needed.

Measuring Accuracy

The laser tracker, which is the most popular instrument in accelerator alignment, cannot meet such high precision requirements directly. Therefore, a laser tracking interferometer system is developed and the measuring accuracy can be improved to 6 μm [2].

Based on multi-lateration measurement principle, four laser trackers are arranged in a specific layout, as shown in Fig. 2, to measure one target point simultaneously. Only distances are extracted from the measuring parameters, which is more accurate than the angles in the laser tracker measurement, for calculating the coordinates of the targets. Meanwhile, the target coordinate is displayed on the screen in real-time, and the magnet position can be adjusted precisely by operating the alignment mechanism.

Figure 2: Laser tracking interferometer system.

Pre-alignment Process

Before installation, wipe the mounting surface to ensure there are no debris, stickers, or other foreign objects. Ensure that the six support points of the girder body bear force evenly, and then assemble a group of magnets on this girder into a pre-alignment unit.

Basic pre-alignment procedure includes following steps:

1. Transport the unit into the thermostatic room for temperature stabilization. At least 4 hours are needed before measurements to eliminate the influence of environmental temperature on the equipment.
2. Level and tighten the girder on the plinth, and establish a coordinate system based on the girder as the alignment reference.
3. Measure the position of each magnet and fit it with the theoretical values to determine the adjustment amount for each magnet.
4. Select a magnet as the alignment reference, usually is the magnet located in the middle of the girder and with

† lichunhua@ihep.ac.cn

ISBN: 978-3-95450-250-9 ISSN: 2673-5520 doi:10.18429/JACoW-MEDSI2023-WEPPP047

a larger size, and adjust it firstly. Then the other magnets are properly aligned one by one. This method is helpful to reduce alignment errors.

5. Do an overall measurement to verify and evaluate the accuracy of the alignment and save the data if the requirements are met.

Magnets Position Adjusting

As shown in Fig. 3, wedge jack is used for the magnet adjustment in the vertical direction and the adjustment range is ±1 mm. Fine screw push-pull mechanism is used in the horizontal direction and the adjustment range is ±4 mm [3]. Both mechanisms are designed with high stiffness to guarantee the resolution of micron level. The magnet position deviation is reduced gradually through adjustment until to 0.01 mm.

It is important to make sure there is as less internal stress as possible after the tightening of the magnets, to keep the position unchanged in a long time. Therefore, in-place tightening technique [4] is proposed and tested, and the positional deviation during tightening can be controlled less than 0.01 mm with a torque of 130 N·m.

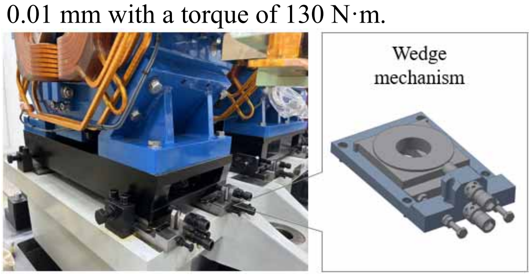

Figure 3: Magnet alignment mechanism.

Alignment of Sextupoles and Movers

In order to reduce the residual error of beam optics correction and improve the dynamic aperture, sextupole Mover is developed to do beam-based alignment online. Wedge mechanism is adopted in the Mover design, and two motors drive a couple of wedge plates by a certain algorithm to realize transverse and vertical motion. The moving accuracy is required to be less than 5 µm at the magnet center height, and the online moving range is ±0.3 mm [5]. Both the sextupole and the Mover should be aligned on the girder properly.

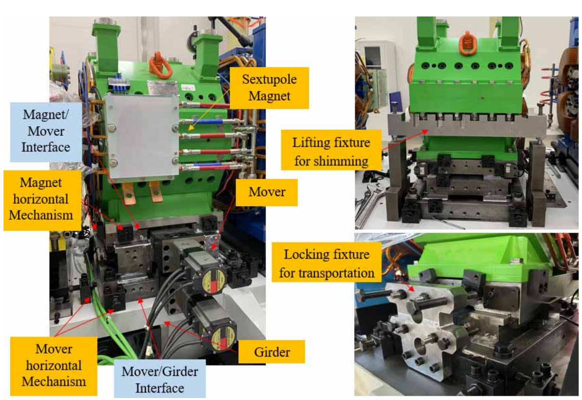

Figure 4: Installation of the sextupole and Mover.

Figure 4 shows the installation of the sextupole and the Mover. There are 3 Movers mounted on each MP girder, positioning errors and efficiency are both aspects of concern. According to the check results, the Mover can be fixed on the girder directly and shims are inserted in the interface of magnet and Mover using a special lifting fixture to compensate the flatness errors. Residual errors are eliminated by operating the Mover. A whole range motion of the Mover is tested to check the coupling errors in the non-motion directions.

The position stability of the Mover during the transportation is also tested [6], and the change of grating readings is about 10 µm. The solution is to lock the Mover slide using a fixture, record the grating readings before transportation and restore them after transportation

REPEATABILITY OF MAGNET OPENING AND CLOSING

The magnets will be opened to install the vacuum chambers after pre-alignment, and the magnet position error after reclosing should meet the alignment requirements. The repeatability error is required to be less than 0.01 mm, and the deviation from the theoretical value should be less than 0.021 mm. The magnets of two typical large units are tested, and one is the MP unit with 8 magnets and the other is FD unit with 5 magnets. All the magnets are designed with pins to obtain repeatability after the core opening/closing.

Table 1: Test Result of Magnet Opening/Closing

Unit Type	Test Times	Deviation/mm			Comparison Item
		DX	DY	DZ	
MP	1st	0.006	0.008	0.005	Before opening
		0.006	0.008	0.016	Theoretical value
FD	1st	0.017	0.009	0.017	Before opening
		0.018	0.012	0.019	Theoretical value
	2nd	0.006	0.003	0.004	1st opening
	3rd	0.006	0.003	0.004	2nd opening

Table 1 presents the result of the test, with DX and DY data being of utmost concern. For the MP unit, the magnet position repeatability and the deviation from the theoretical value are both less than 0.01 mm. As for the FD unit, the deviation from the theoretical value is less than 0.02 mm while the repeatability exceeds 0.01 mm at the first time. Therefore, two more tests are performed, and the position variation reduced a lot to 0.006 mm in the second time and keep stable in the third time, which meeting the error requirements of this stage.

The main contribution of the variation comes from the larger-sized magnets of ABF2/3 and BD1/2, and additional experiments are carried out on the two types of magnet. As shown in Fig. 5, dozens of targets are glued on the magnet

ISBN: 978-3-95450-250-9 ISSN: 2673-5520 doi:10.18429/JACoW-MEDSI2023-WEPPP047

for measuring, and the variation of the magnet shape before and after opening/closing can be monitored easily. According to the result, the shape of iron cores changes slightly and the coordinates of the target points changes accordingly. It is deduced that the internal stress generated during the assembly process have released during the magnet opening/closing process. This experience has been taken into account for reference in the batch installation, and relevant procedures have been developed accordingly.

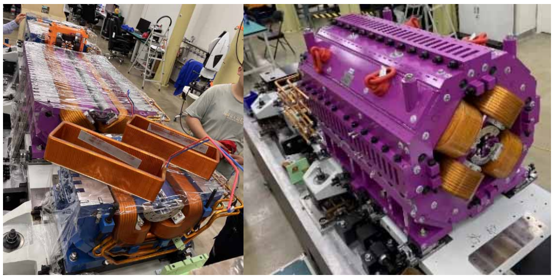

Figure 5: Opening/closing test on BD1/2.

TRANSPORTATION RELIABILITY

On the way to HEPS tunnel, the pre-alignment unit need to pass through a sinking channel. The magnet positions deviation after transportation is required to be less than 0.015 mm. Both MP unit and FD unit are tested. The transportation route is from alignment hall to the entrance of the HEPS tunnel. Figure 6 shows the transportation fixtures.

Several measures are taken to ensure minimal change in magnet positions in this process:

1. A self-levelling and vibration-reducing transport platform is designed specially to keep the magnet and girder level, which is particularly useful when the truck is going up or down slopes.
2. The 6 support points of the girder should maintain balanced force in the whole transportation process.
3. A constant speed of 10-20 km/h of the truck is secured.

According to the test result, as shown in Table 2, the magnet position variation after transportation is less than 0.01 mm, and the deviation from the theoretical value is less than 0.015 mm, better than the requirements of this stage.

Table 2: Test Result of Transportation

Unit Type	Deviation/mm			Comparison Item
	DX	DY	DZ	
MP	0.005	0.004	0.005	Before Transportation
	0.007	0.007	0.014	theoretical value
FD	0.006	0.006	0.011	Before Transportation
	0.01	0.009	0.007	Theoretical value

Self-levelling platform FD Unit lifted onto the truck

Figure 6: Transportation test.

MOCKUP EXPERIMENT

The alignment process in the tunnel has been simulated in the experiment hall on the 7BA mockup. The sequence is shown below:

1. 6 pre-alignment units and 5 Dipoles: Tightened on the plinth by non-stress method.
2. 12 BPMs: Aligned prio to the vacuum chambers, which request as less exposure time to the atmosphere as posssible, due to the NEG film.
3. 18 vacuum chambers: installation, alignment and vacuum seal proceed through a flow process. Same reason as above.

The operation space is checked in the whole process, including the magnet opening/closing, vacuum elements alignment, and vacuum connection, and special tools are used a lot in the critical places.

SUMMARY

A full-process installation experiment was performed and the feasibility of relevant schemes are verified:

1. The alignment accuracy meets the required specifications.
2. The repeatability of the magnet opening /closing better than 0.01 mm is achievable. The issues encountered during the process have been solved.
3. The magnet displacement during transportation is less than 0.015 mm, confirming the reliability of the transportation scheme.
4. The installation process in the tunnel has been tested and the operation space has been checked, with potential issues resolved.

Batch installation is currently in progress.

REFERENCES

[1] Y. Jiao *et al.*, “Modification and Optimization of the Storage Ring Lattice of the High Energy Photon Source”, *RDTM 4*, pp. 415–424, 2020. doi:10.1007/s41605-020-00189-7

[2] S. Lu *et al.*, “A laser tracker-based multilateration method for pre-alignment of High Energy Photon Source storage ring”, *Nucl. Instrum. Methods*, vol. 1045, p. 167533, 2023. doi:10.1016/j.nima.2022.167533

[3] C.H. Li *et al.*, “Overall design and installation of the HEPS storage ring magnet support system”, in *Proc. CWAA&M’23*, Yinchuan, NX, China, July 2023.

[4] C.H. Li *et al.*, “Design and test of support for HEPS magnets”. *RDTM 5*, pp. 95–101, 2021. doi:10.1007/s41605-020-00223-8

ISBN: 978-3-95450-250-9 ISSN: 2673-5520 doi:10.18429/JACoW-MEDSI2023-WEPPP047

[5] L. Wu *et al.*, “Design and test of the beam-based alignment sextupole experimental mover prototype for HEPS”, *RDTM 5,* pp. 570–575, 2021. doi:10.1007/s41605-021-00287-0

[6] L. Wu *et al.*, “Progress of HEPS sextupole mover”, in *Proc. CWAA&M’23*, Yinchuan, NX, China, 2023.

ISBN: 978-3-95450-250-9 ISSN: 2673-5520 doi:10.18429/JACoW-MEDSI2023-WEPPP049

DESIGN OF MULTIPLE EXPERIMENTAL MODELS FOR PINK SAXS STATION

Guang Mo†, Zhihong Li, Xueqing Xing, Zhongjun Chen, Yunpeng Liu, Ye Tian, Zhaoqiang Cui, Zhonghua Wu, Institute of High Energy Physics, Chinese Academy of Sciences, Beijing, China

Abstract

Pink small angle X-ray scattering station is dedicated to performing scattering related experiments. A classical in air planar undulator is adopted as the beam source. The fundamental radiation can be adjusted within 8-12 keV through altering the magnetic gaps. Monochromatic beam and pink beam can be switched through moving in and out of the monochromator. Three set diamond compound refractive lenses with different curvatures are employed to focus the 12 keV monochromatic beam to achieve different focusing modes. With the help of a flexible vacuum detector tube, varies experimental models could be carried out easily.

INTRODUCTION

Small angle X-ray scattering (SAXS) is a powerful technique for studying nano materials [1]. As for numerous scattering experiments, different experimental demands are proposed by users. For example, as monochromatic beam is not necessary for some SAXS measurements [2], they prefer higher beam flux to shorten exposure time and to carry out higher time resolved scattering experiments at the expense of sacrificing energy resolution and beam size. Conversely, some researchers hope to carry out fine experiments with higher energy resolution and small beam size. In order to accommodate these seemingly contradictory needs of diverse users, a muti-functional SAXS station is under construction at HEPS.

HEPS [3] (high energy photon source), which is a 6 GeV synchrotron radiation facility with low emittance, provide perfect conditions for meeting these requirements. The high flux pink beam, which is from the fundamental radiation of the undulator, will be used directly after reflected by a pure silicon reflector to perform high time-resolution experiments. Monochromatic beam, which is obtained by a horizontal double Si(111) crystal monochromator, also can be used alternately to perform high energy resolution experiments. With the help of flexible monochromator, focusing element and a SAXS tube, the main parameters of SAXS station can be adjusted conveniently, which are reflected in the following aspects. First, the pink beam and monochromatic beam can be switched through moving in and out a horizontal double crystal monochromator. Second, the incident beam energy can be altered through adjusting the gaps of undulator at the range of 8-12 keV with the help of a monochromator. Third, for the commonly used 12 keV monochromatic beam, four types of focusing modes can be changed through changing on-line diamond CRLs. Four, the different range of scattering angle can be altered easily by the help of a flexible tube. This design can meet the vast majority needs of users. The main specifications of the SAXS beamline is shown in Table 1.

The available experimental techniques include single SAXS, WAXS, USAXS, SAXS-CT, ASAXS and combined SAXS/WAXS/USAXS, etc. The measuring mode includes transmission and grazing incidence, static and dynamic (in situ, time resolved) measurements. The time resolution lies in microseconds to seconds based on different sample environments and detectors. Some sample environmental devices, including in-situ heating, in-situ growing, in-situ tension, will be equipped in our station.

Table 1: Main Specifications of the SAXS Beamline at HEPS

Pink beam	
Energy range	8-12 keV
Flux at sample	~10^{15} ph/s
Beam size @sample	500 µm × 500 µm
Energy resolution	1.5 %
Scattering angle	0.001°~50°
Monochromatic beam	
Energy range	8-30 keV
Flux at sample	~10^{13} ph/s
Beam size @sample	300 µm × 300 µm 14 µm × 6 µm;
Energy resolution	~2×10^{-4}

DESIGN

Overall Description

The basic idea of design, sketched in Fig. 1, is that the monochromator and the focusing devices (CRL) can be moved in and out of the beamline. Without monochromator and CRLs, the quasi monochromatic beam from the fundamental radiation of the undulator also can be directly collimated to measure the sample. A set of three-slits is used to reduce the scattering background, which are not drawn in the diagram.

We specify the beam source as the starting position (0 m). The front-end of the beamline is about 32 m long, which is mainly used to provide radiation protection and heat reduction to the downstream devices. The beamline starts from the front-end ratchet wall exit (32 m from the source) and ends at 49.9 m, which is located in the first optical

* Work supported by HEPS project.
† mog@ihep.ac.cn

ISBN: 978-3-95450-250-9 ISSN: 2673-5520 doi:10.18429/JACoW-MEDSI2023-WEPPP049

experimental hutch (FOE). The beamline's major function includes beam deflection, beam monochromatizing, beam focusing, collimation, monitoring, vacuum maintenance and bremsstrahlung stop. In the following, we only describe the main elements, including undulator, deflector, monochromator, CRLs and vacuum SAXS tube.

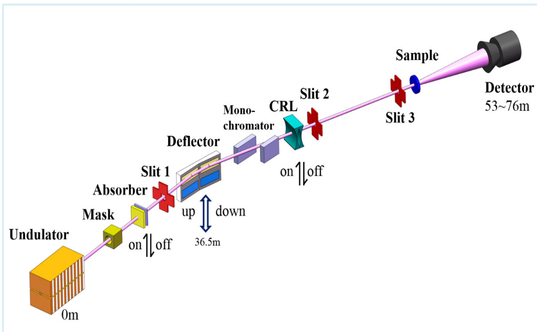

Figure 1: Main composition of pink SAXS beamline.

Insertion Device (Undulator)

In order to fully utilize the high energy and low emittance of HEPS, a typical planar in-air undulator (IAU25) undulator [4] is chosen as the light source, whose fundamental radiation could be directly used as the pink beam. The undulator has been optimized to provide fundamental radiation energy at the range of 8 ~ 12 keV with magnets gap of 11.29 ~ 17.40 mm for high flux application. The source spot has 43.7 μm × 17.5 μm FWHM size and 9.6 μrad × 9.1 μrad FWHM diverfence at 12 keV with 0.1% BW, which will be our commonly used energy in the future for users. The maximum angular flux density is 6.2E18 phs/s/mrad2/0.1% BW.

Deflector

To use the fundamental radiation of the source, the higher harmonics must to be suppressed. A horizontally deflecting system is installed firstly at the downstream of the source. The deflection system is employed to achieve the following functions: (1) Deflect the synchrotron radiation for deviation from the direct bremsstrahlung radiation. (2) Suppress the higher harmonic. (3) Reduce the thermal load for the downstream devices. In order to improve the beam stability and further suppress the higher harmonic, a set of twin separate flat single-crystal silicon mirrors (sketched in Fig. 1) are accepted. As the two mirrors are arranged with a fixed 5 mrad angle, the angle between incident beam and exit beam is fixed at 10 mrad, which is not changeable with the rotation. As the cut-off energy of pure silicon reflection is about 14 keV when the grazing angle is about 2.5 mrad, the higher harmonics from the 2nd will be suppressed efficiently. The specification of deflection double mirror is shown in Table 2.

Higher energy X-ray also be needed to measure some metal samples. In order to obtain X-ray beam higher than 12 keV, the metal Pt would be evaporated with a width of 5 mm on the upper side of the deflectors as showed in Fig. 1. At the grazing angle of 2.5 mrad, the cut-off energy of Pt reflection can be increased to 30 keV, which covers the 1st, 2nd and 3rd harmonics. The cut-off energy can be altered by vertically raising and lowering the deflection mirrors. Additionally, it should be noted that the monochromator must be used when the Pt film is employed as deflector.

Table 2: Specification of Deflection Double Mirror

Specification	Value
Mirror material	Sigle-crystal silicon
Reflective surface	Polished Si, Evaporated Pt
Dimension	$200 \times 50 \times 50$ mm^3
Surface error	≤ 0.3urad
Surface roughness	≤ 3Å
Angle between two mirrors	5 mrad

Monochromator

Following the deflecting system, a normal horizontal double-crystal Si(111) monochromator is equipped. The specification of monochromator is illustrated in Table 3. Pink beam and monochromatic beam can be switched through moving the first crystal in or out of the beam path. The working energy range is between 7 to 30 keV, which is corresponding to the cut-off energy of Pt reflection at the grazing angle of 2.5 mrad. The horizontal offset between the pink beam path and the monochromatic beam path is only 15 mm. Thus, the two different beam paths can be compatible in the same tube easily.

Table 3: Specification of Monochromator

Specification	Value
crystal	Si(111)
Energy range	7 ~ 30 keV
Deflecting direction	horizontal
Minimum energy step	0.1 eV
Exit offset	15 mm
Cooling method	liquid nitrogen

Compound Refractive Lenses (CRL)

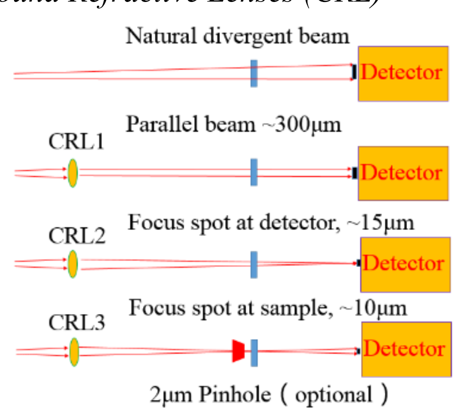

Figure 2: Four type focusing modes (only for the12 keV monochromatic beam).

ISBN: 978-3-95450-250-9 ISSN: 2673-5520 doi:10.18429/JACoW-MEDSI2023-WEPPP049

As for the commonly used 12 keV monochromatic X-ray, three single diamond CRLs are employed to obtain different focusing modes. The CRLs are mounted and controlled by a homemade tranfocator, which is placed at the downstream of monochromator. Without any CRL, we can use the natural divergent beam and large beam spot to carry out the normal SAXS measurements. The larger beam spot can improve the SAXS statistics. By using the first set CRL, we can obtain parallel beam with circle shape of about 300 μm diameter. As the divergence angle is basically zero, the parallel beam is conveniently for the functional extension. By using the second set CRL, the incident beam is focused at the detector (about 15 μm). Then we can obtain the best angle resolution with a smaller scattering angle and lower scattering background. By using the third set CRL, the beam can be focused at sample position with the size of about 10 μm × 6 μm. Then we can carry out some high spatial resolution experiments and use small sample holders, such as DAC, capillary cell, etc. To carry out higher spatial resolution SAXS measurements, a scatterless pinehole with pore size of 2 μm is being considered as future upgrade plan. The schematic diagram of focusing modes is shown as Fig. 2.

Vacuum SAXS Tube and Detectors

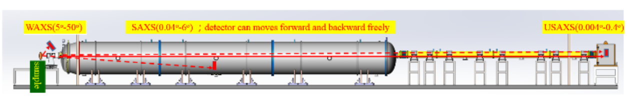

Figure3: The schematic diagram of the vacuum SAXS tube and the detectors.

A 23 m long versatile SAXS tube is shown in Fig. 3. In our station, the sample is fixed at the 53 m from the source. Three vacuums compatible Eiger2 detectors will be installed along the tube. The WAXS detector is suspended diagonally above the sample to collect about −5°~ 50° scattering signals. The SAXS detector, which is used to collect scattering angle between 0. 04° and 6°, is installed in the front large tube with a diameter of 1.5 m and a length of 14 m. The detector can move freely within the tube according to experimental requirements. The USAXS detector, which is used to collect 0.001°~ 0.1° scattering signals, is placed at the end of tube. The vacuum degree of the tube is less than 1.0 Pa. In addition to normal individual measurements, the three detectors can work simultaneously to collect the whole large angle range from 0.001° to 50°. Two kinds of beamstop used for transmission mode and grazing incidence mode respectively, are installed in front of the SAXS and USAXS detectors.

CONCLUSION

As a user facility, to meet the different demands is our goal of effort. Beside normal monochromatic SAXS experiments, we also achieve abnormal high photon flux to perform high time resolved scattering experiments at the expense of energy resolution on our station. The beam energy, photon flux, beam sizes and SDD (sample to detector distance) also can be altered conveniently according to the actual demands of users. Various experimental techniques, including SAXS, WAXS, USAXS, ASAXS, GiSAXS and combined SAXS/WAXS/USAXS, etc., can be performed on our station. In the near future, some home-made in-situ sample environmental devices will be equipped.

REFERENCES

[1] O. Glatter and O. Kratky, *Small Angle X-ray Scattering*, New York, USA, Academic Press, 1982.

[2] C. Riekel, P. Suortti, "Layout of a 4 m Double-Focusing Laboratory Camera for Small-Angle Scattering", *J. Appl. Crystallogr.*, vol. 24, pp. 549-554, 1991.

[3] http://english.ihep.cas.cn/doc/2639.html

[4] K. J. Kim, "Characteristics of synchrotron radiation", *AIP Conf. Proceedings*, vol. 184, issue 1, pp. 565-632, Apr. 1989.

ISBN: 978-3-95450-250-9 ISSN: 2673-5520 doi:10.18429/JACoW-MEDSI2023-WEPPP050

QUICK SCANNING CHANNEL-CUT CRYSTAL MONOCHROMATOR FOR MILLISECOND TIME RESOLUTION EXAFS AT HEPS

Yuanshu Lu, Hao Liang, Yunsheng Zhang, Zekuan Liu, Dashan Shen, Yang Yang, Shan Zhang, Zheng Sun, Institute of High Energy Physics, Chinese Academy of Sciences, Beijing, China

Abstract

The design and capabilities of a Quick scanning Channel-Cut monochromator (QCCM) for HEPS are presented. The quick scan and step scan are realized by a torque motor directly driven Bragg axis, controlled by a servo controller. This design allows easy and remote control of the oscillation frequency and angular range, providing comprehensive control of QXAFS measurements. The cryogenically cooled Si(311) and Si(111) crystals, which extends the energy range from 4.8 keV-45 keV. The dynamic analysis verifies the rationality of the mechanical structure design. The device was fabricated and tested, results show an oscillation frequency up to 50 Hz with a range of 0.8, and a resolution of 0.2 arcsecond in step scan mode. This device demonstrates the feasibility of large range quick scan and step scan by a single servo control system.

INTRODUCTION

An X-ray Absorption Spectroscopy (XAS) is a standard method at synchrotron radiation sources to study solid or liquid, crystalline and non-crystalline matter [1, 2]. The Quick scanning Extended X-ray Absorption Fine Structure (QEXAFS), reduces the scanning time of a single spectrum from 10 minutes to 10 milliseconds [3, 4, 5]. It has become one of the ideal methods for in situ investigations of the kinetics of chemical reactions. Highly optimized for general use and perfect compatibility with conventional XAFS beamline structures [6, 7].

High energy photon source (HEPS) is one of the world's lowest emissivity, highest brightness of the fourth generation of synchrotron radiation light source. The electron beam group emissivity of HEPS will be lower than 60 pm·rad, providing a very small light source size and extremely high brightness and other excellent performance, the excellent characteristics of synchrotron radiation light source makes the monochromator working conditions worse. We have constructed a dedicated beamline X-ray absorption spectroscopy stations (B8 beamline) at the HEPS. It is a high-performance hard X-ray beamline based on X-ray absorption spectroscopy and related derivative experimental methods. Target energy covering 4.8 keV-45 keV.

DESIGN OF THE MONOCHROMATOR

The QCCM, as shown in Fig. 1, contains: high precision rotating axes system, crystal components, vacuum chamber system and base adjustment system.

The High Precision Rotating Axes System

The high-precision rotating axes system, as shown in Fig. 2 relies on the torque motor (KEDE CNC, GTMH0360WS-50) to drive the rotation axes and the crystal components to rotate, the peak torque of the motor is 756 N m, the continuous torque is 516 N m, the stator is provided with a water-cooling channel, and the heat generated during the motor movement is taken away by circulating cooling water. The torque motor transmits the torque to the vacuum chamber through the magnetic seal unit (Rigakual). An RESM150 angle encoder system (Renishaw) is installed on the atmospheric side of the rotating axes system, and an RESA150 absolute angle encoders (Renishaw) is installed on the vacuum side, which are used for measuring the angle of the crystal during step scanning and quick scanning.

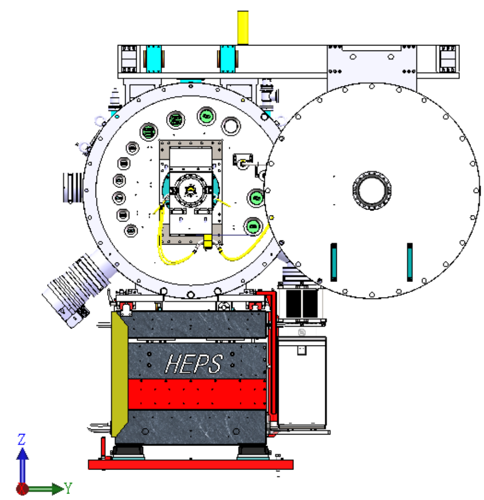

Figure 1: The show of QCCM.

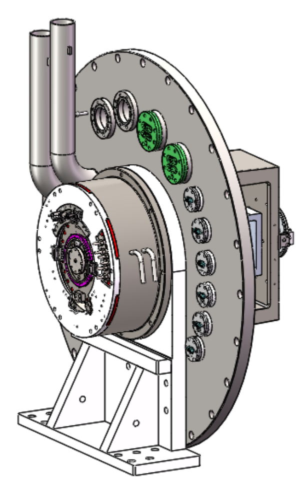

Figure 2: Diagram of rotating axes system.

ISBN: 978-3-95450-250-9 ISSN: 2673-5520 doi:10.18429/JACoW-MEDSI2023-WEPPP050

In order to verify the feasibility of the design scheme of the rotating axes, ANSYS was used to simulate the rotating deformation of the rotating axes under the worst working condition (50 Hz/10 ms), and a total of three cycles were simulated. As shown in Figs. 3 and 4, the simulation results show that the maximum deformation of the rotating axes is about 6 mm, which occurs at the bottom of the crystal support, and the deformation near the rotating center is the least.

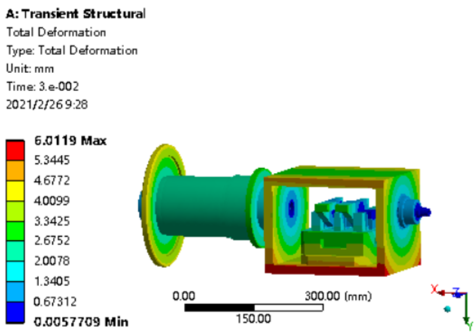

Figure 3: Dynamic simulation analysis.

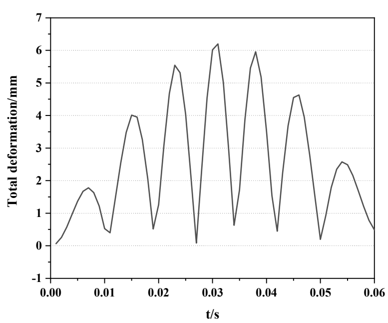

Figure 4: Deformation results of dynamic simulation.

On the basis of simulation analysis, the mode of the rotating axes system are about 339 Hz, as shown in Figs. 5 and 6, which has a high natural frequency.

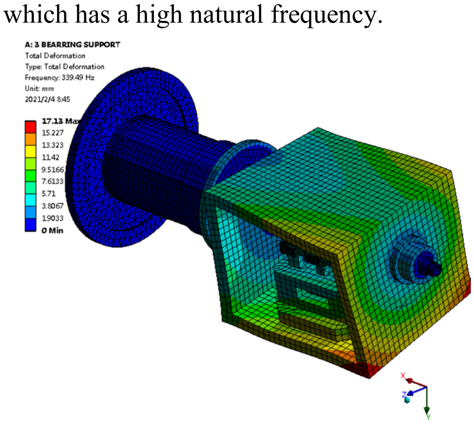

Figure 5: Modal analysis of rotating axes.

	Mode	Frequency [Hz]
1	1.	339.49
2	2.	342.59
3	3.	612.74
4	4.	720.77
5	5.	918.11
6	6.	1110.2

Figure 6: Results of modal analysis.

The Crystal Components

The crystal components are placed side-by-side by Si(111) and Si(311), and the Si(111) has a working energy range of 4.8 kev-23 keV and the Si(311) has a working energy range of 10 keV-45 keV, as shown in Fig. 7. By moving the crystal support mechanism to switch the crystal, so as to achieve the purpose of changing the energy range. At the same time, liquid nitrogen cooling is used to take away the heat generated on the crystal during the working process.

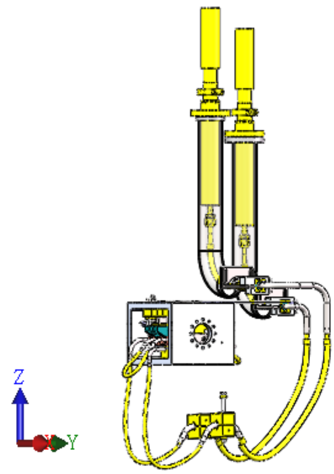

Figure 7: Diagram of crystal components.

The beam path is shown in Fig. 8. Since the distance h between the first crystal and the second crystal is a fixed value, the height H of the outgoing beam is related to the Bragg Angle, and the incident point of the outgoing beam on the second crystal also moves with the change of the Bragg Angle. By properly lengthening the length of the second crystal, the light leakage of the crystal is prevented.

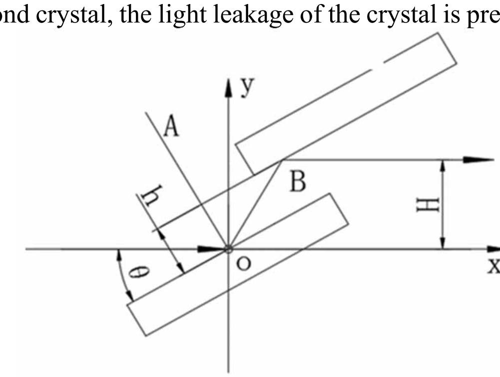

Figure 8: The crystal beam path.

The calculation formula of beam height is as follows:

$$H= oB\cdot\sin(2\theta) = h\cdot\sin(2\theta)/\sin\theta = 2\cdot h\cdot\cos\theta. \quad (1)$$

According to the requirements of the beamline for the working energy range of 4.8 keV-23 keV and 10 keV-45 keV, the working range of the Bragg Angle can be calculated as: Si(111): 4.93°-24.3°, Si(311): 4.83°-22.25°.

The size of the crystal is shown in Fig. 9. The two crystals are designed as mirror images of each other. The first crystal is chamfered to prevent from blocking the optical path.

ISBN: 978-3-95450-250-9 ISSN: 2673-5520 doi:10.18429/JACoW-MEDSI2023-WEPPP050

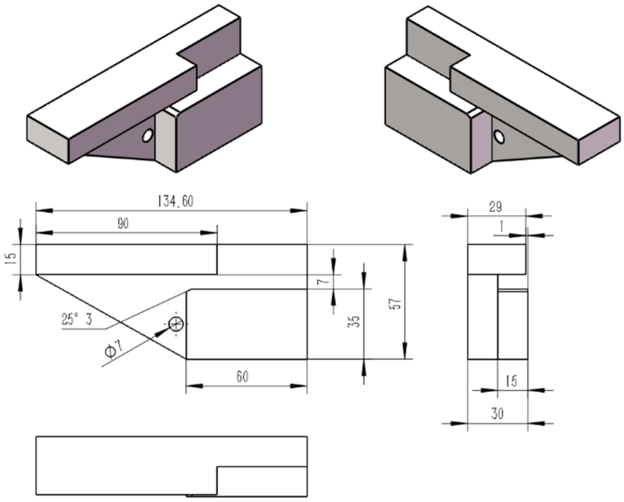

Figure 9: Crystal size (The Si(111) and Si(311)crystals are mirror images of each other).

The Base Adjustment System

The base adjustment system is shown in Fig. 10.

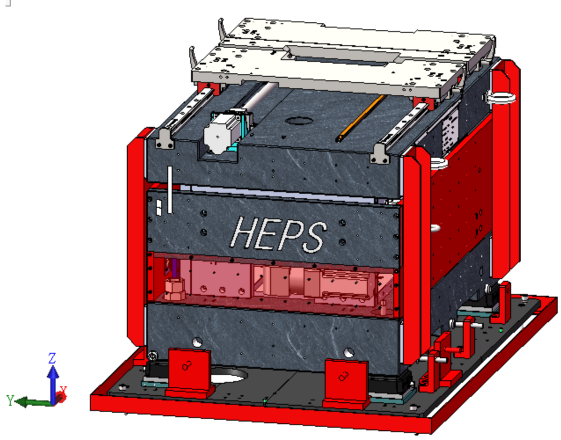

Figure 10: The base adjustment system.

The base has two wedge-shaped block assemblies, and the wedge block component is driven by the motor to realize the lifting in the Z direction and the rotation in the Y direction above the table. The X direction movement is completed by the stepping motor driving the roof.

SPORTS PERFORMANCE TEST

The QCCM has both quick scanning mode and step scanning mode. The test results are shown in Fig. 11. The maximum scanning frequency measured at the present stage is 50 Hz (100 spectra per second), and the coverage Angle range is 0.8°, which is better than the international indicators. The step scanning mode single step resolution is 0.2 arcseconds; offline test results of motion performance are shown as follows: scanning frequency 12.5 Hz (Angle range 4.2°), scanning frequency 25 Hz (Angle range 2.2°), scanning frequency 40 Hz (Angle range 1.2°), scanning frequency 50 Hz (Angle range 0.8°).

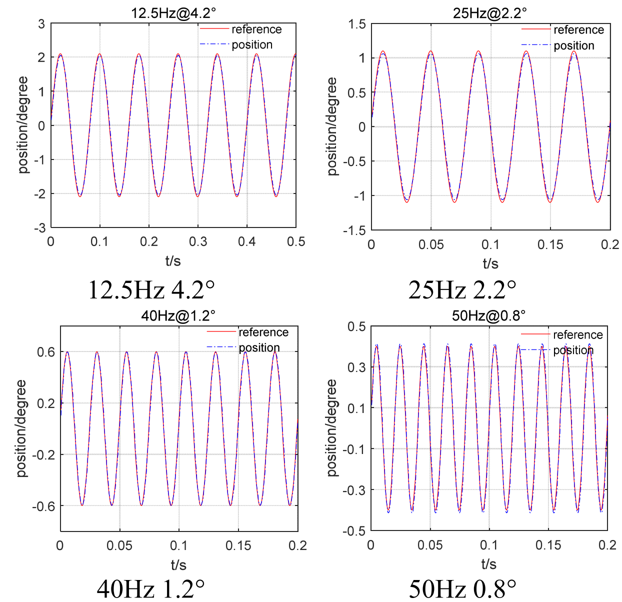

Figure 11: The different frequency motion performance test.

CONCLUSION

This paper mainly introduces the development process of HEPS B8 QCCM and the preliminary test of motion performance. As the first fast scanning monochromator developed by ourselves in China, its motion test results are higher than the existing international results. Please pay attention to the detailed test data in the subsequent article.

ACKOWLEDGEMENTS

This work was supported by the High Energy Photon Source (HEPS), a major national science and technology infrastructure in China.

REFERENCES

[1] P.A. Lee, P.H. Citrin, P. Eisenberger, and B.M. Kincaid,"Extended x-ray absorption fine structure, its strengths and limitations as a structural tool", *Rev. Mod. Phys.*, vol. 53, no. 4, p. 769, 1981. doi:10.1103/RevModPhys.53.769

[2] J.J. Rehr and R.C. Albers, "Theoretical approaches to x-ray absorption fine structure", *Rev. Mod. Phys.,* vol. 72, p. 621, 2000. doi:10.1103/RevModPhys.72.621

[3] O. Müller, D. Lützenkirchen-Hecht, and R. Frahm, "Quick scanning monochromator for millisecond in situ and in X-ray absorption spectroscopy", *Rev. Sci. Instrum.,* vol. 86, p. 093905, 2015. doi:10.1063/1.4929866

[4] E. Fonda, A. Rochet, M. Ribbens, L. Barthe, "The SAMBA quick-EXAFS monochromator: XAS with edge jumping", *J. Synchrotron Radiat.*, vol. 3, pp. 417-424, 2012. doi: 10.1107/S0909049512009703

[5] T. Nonaka, K. Dohmae, T. Araki, and Y. Hayashi, "Quick-scanning x-ray absorption spectroscopy system with a servo-motor-driven channel-cut monochromator with a temporal resolution of 10 ms", *Rev. Sci. Instrum.,* vol. 83, p. 083112, 2012. doi:10.1063/1.4746770

[6] Y. Nagai, K. Dohmae, Y. Ikeda, N. Takagi, T. Tanabe, N. Hara, G. Guilera, S. Pascarelli, M.A. Newton, I. Kuno,

ISBN: 978-3-95450-250-9 ISSN: 2673-5520 doi:10.18429/JACoW-MEDSI2023-WEPPP050

H. Jiang, H. Shinjoh, and S. Matsumoto, "In Situ Redispersion of Platinum Autoexhaust Catalysts: An On-Line Approach to Increasing Catalyst Lifetimes?", *Rev. Angew. Chem. Int. Ed. Engl.*, vol. 47(48), pp. 9303-9306, 2008. doi:10.1002/anie.200803126

[7] J. Stötzel, D. Lützenkirchen-Hecht, R. Frahm, C.V. Santilli, S.H. Pulcinelli, R. Kaminski, E. Fonda, F. Villain, and V. Briois, "QEXAFS and UV/Vis Simultaneous Monitoring of the TiO2-Nanoparticles Formation by Hydrolytic Sol-Gel Route", *J. Phys. Chem. C.*, vol. 114, no. 14, p. 6228, 2010. doi:10.1021/jp9105019

ISBN: 978-3-95450-250-9 ISSN: 2673-5520 doi:10.18429/JACoW-MEDSI2023-WEPPP051

THE DESIGN OF A 2 m LONG COPPER LIGHT EXTRACTION VESSEL AT DIAMOND LIGHT SOURCE FOR THE DIAMOND-II UPGRADE

V. Danielyan†, M.P. Cox, P. J. Vivian, R. Fielder, S. L. Hodbod, T. Lockwood
Diamond Light Source, Didcot, Oxfordshire, UK

Abstract

The design of a 2 m long light extraction copper vacuum vessel for Diamond-II (D-II) storage ring upgrade in Diamond Light Source (DLS) is described. Initially, an aluminium vessel with two discrete copper absorbers was considered, further studies have shown the concept was not capable of handling high heat loads making the aluminium vessel arrangement an unworkable solution. Therefore, it was decided to change the design concept from an aluminium vessel to a copper vessel. The main difference between two concepts is that the copper vessel has integrated absorbing surfaces instead of discrete absorbers. Due to the change, it was possible not only to reduce the power densities of the absorbing surfaces, but also it allows placing active cooling directly on the high heat loaded areas. These two factors contributed to a significant reduction of the peak temperatures. Synchrotron light raytracing, thermal analysis, vacuum performance, beam impedance, prototyping and next steps of the new copper vessel are also covered in this paper.

INTRODUCTION

The D-II Storage ring vacuum system comprises 48 arcs and 48 straights [1]. There are 4 main types of arc girder vessel strings: MS, SM, ML and LM girder vessel strings. The above-mentioned copper vessel is located on the upstream end of the LM girder vessel string, vessel 2 shown in Fig. 1. There are 6 LM Girders in the whole storage ring, which means 6 LM vessel 2 are required for various light extractions. The vessel is designed in a way that it covers all 6 cases, hence no special vessels are required. The most challenging case is the LM girder vessel 2 for I05 light extraction.

Figure 1: Diamond II LM girder vessel string.

The main challenges associated with the design of this vessel at that particular location are, firstly, the heat loads of I05 beamline upgrade involving the installation of a powerful and highly divergent APPLE-knot quasi-periodic (QP) insertion device (ID) [2]. Second aspect is the requirement of a homogeneous NEG (non-evaporable getter) coating on the complex internal geometry of the vessel. Detailed FEA analysis shows the peak temperature is reduced from 446°C to 71°C for the copper vessel as compared to the aluminium vessel discrete absorbers. The change from an aluminium vessel to a copper vessel will not only reduce the peak temperatures, thereby making it a workable solution according to DLS FEA criteria [3], but has the added benefits of improved vacuum performance, reduced beam impedance, reduced capital and operating cost, as well as reduced manufacturing risks due to splitting of vessels into three separate sub-vessels.

DESIGN AND PROTOTYPING

Figure 2 shows the design of both aluminium (a) and copper (b) versions of LM girder vessel 2. Many features of the original aluminium vessel design have been reused on the copper vessel, particularly regions of multipole magnets, downstream pumping, and crotch absorber section etc. Key differences between two vessel designs are listed in the Table 1. The copper vessel is comprised of 3 separate sub-vessels: vessel 2_a, _b, and _c, where vessel 2_b is the highest heat loaded section.

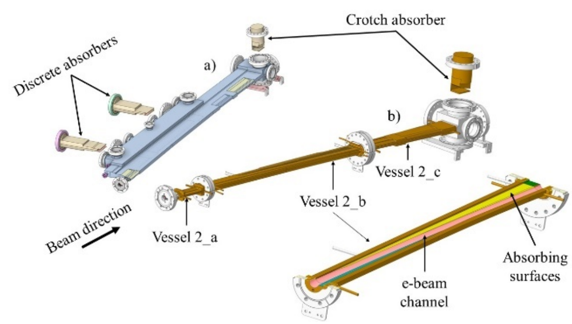

Figure 2: LM girder vessel 2 design versions: a) aluminium and b) copper.

Table 1: Design Differences Between Al. and Cu Vessels

Features	Al. Vessel	Cu Vessel
Antechamber	yes	no
Discrete absorbers	yes	no
Bimetallic flanges	yes	no
Int. Absorbing surfaces	no	yes
Water cooled	no	yes
NEG coated	no	yes
Manufacturing method	welded	brazed

There are two sets of beam position monitor (BPM) buttons at the entry and exit flanges. Vessel 2_a upstream flexible flange allows movements of +2 mm extension, -5 mm compression, and ±0.25 mm of lateral offsets. The design constraints are different for each sub-vessel (e.g. available space, power load etc.), and these factors are dictating the design of both internal and external geometries. Figure 3

† vahe.danielyan@diamond.ac.uk

ISBN: 978-3-95450-250-9 ISSN: 2673-5520 doi:10.18429/JACoW-MEDSI2023-WEPPP051

highlights cross-sectional views and the aperture dimensions in several critical locations of the vessel. The minimum height of the vessel was limited to 6 mm due to the NEG coating limitations. The prototype NEG coating experiments will prove whether the 6 mm aperture can be reduced up to 5 mm or not. Minimum wall thickness of the copper vessels is 1 mm, in a very localised areas, around multipole magnets regions. This approach has already been taken in other light sources [4].

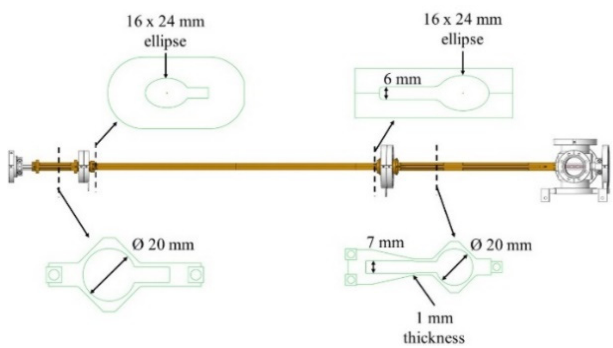

Figure 3: LM girder vessel 2 internal apertures.

The prototyping phase is divided into two directions: NEG trials and full prototype vessel manufacturing (NEG coated). It was decided to test the NEG coating on the trial assembly, firstly to ensure that the coating requirements on such a complex geometry is achievable, and secondly to define the minimum height of the vessel. NEG coating trials and full prototype vessel manufacturing is currently in progress.

RAYTRACING AND FEA

The long and wide shape of the copper vacuum vessel offers a much larger surface area for photon absorption than discrete absorbers and gives the possibility of placing cooling channels closer to the region of highest heat load. Figure 4 illustrates the simulation method.

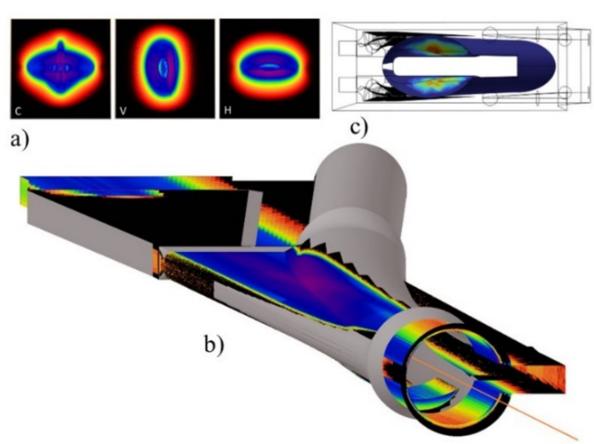

Figure 4: Simulation procedure: a) I05 APPLE-knot QP normal incident power density, polarisation in 3 modes (Synrad), b) Ray tracing onto the walls of the vacuum vessel, circular mode (Synrad), c) Projected wall power density in ANSYS.

First, Synrad is used to illuminate the vessel walls for each of the three modes (horizontal, vertical, and circular) of the APPLE-knot Quasi-periodic ID with a period of 140 mm and 10 eV minimum electron energy. The heat load is then mapped onto a FEA model and a conjugate heat transfer analysis is performed in COMSOL using turbulent flow in the cooling channels on the upper and lower sides of the vessel shown in Fig. 5. Several design iterations have been performed and the maximum vessel wall temperature for the circular mode is 71° for a total heat load of 7 kW and peak (absorbed) wall power density of 4 W/mm^2. Figure 6 shows maximum displacements and stresses due to atmospheric pressure loading of copper vessel around the thin-walled regions. Maximum 21 µm deflection and 16 MPa Von Mises stress was predicted in static structural FEA analysis.

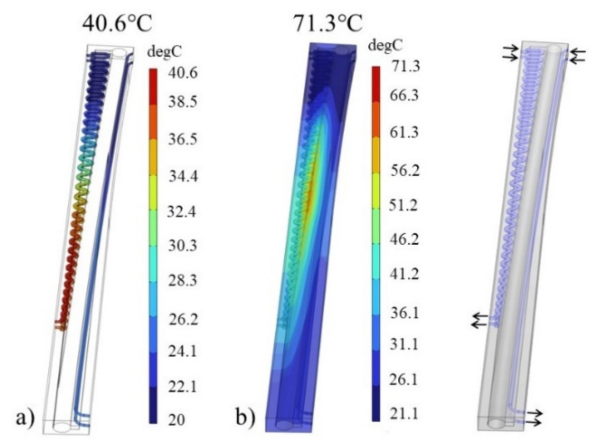

Figure 5: COMSOL simulations a) coolant temperature and b) vessel body temperature.

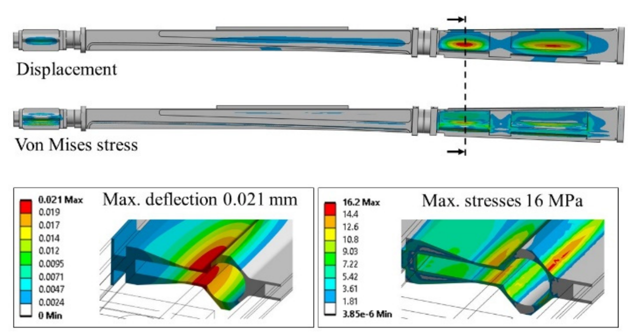

Figure 6: Maximum displacements and stresses of the copper vessel due to atmospheric pressure loading.

VACUUM SIMULATIONS

Monte-Carlo dynamic simulations were carried out for the two vessel designs using Synrad and Molflow [5]. Firstly, Synrad was used to model the synchrotron radiation photons incident on the vessel wall including reflections. Molflow was then used to calculate the pressure distribution along the electron beam path, taking into account photon stimulated desorption. This was carried out for the 4 main residual gases (CO, H_2, CO_2 and CH_4) and for a range of beam conditioning doses in Ampere.hours. Figure 7 shows the calculated pressure *vs.* distance curve along the

ISBN: 978-3-95450-250-9 ISSN: 2673-5520 doi:10.18429/JACoW-MEDSI2023-WEPPP051

entire machine cell. The pressure in LM vessel 2, between z = 400 and z = 600 cm along the electron beam path, is reduced from 10^{-8} mbar to 10^{-10} mbar after 100 A.h with an electron beam current of 300 mA. This compares with the design target of average pressure 10^{-9} mbar or lower under these conditions. This illustrates the beneficial reduction in pressure for the NEG-coated copper vessel compared with the uncoated Aluminium vessel.

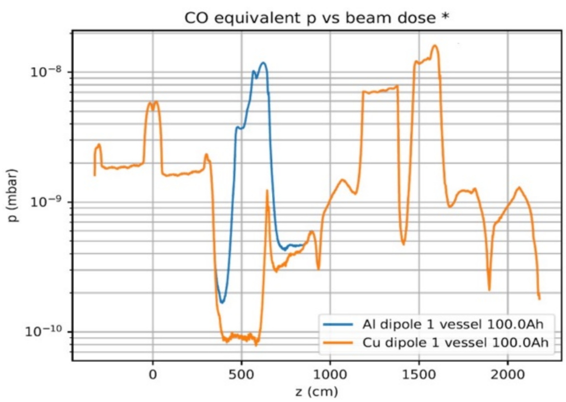

Figure 7: Calculated pressure vs. distance curve along the entire machine cell.

BEAM IMPEDANCE SIMULATIONS

Wakefields and impedance were calculated for the two vessel designs using CST Studio [6]. A bunch length of 1 mm and wake length of 300 mm were used for the simulations. A comparison of the real transverse and longitudinal impedances are shown in Fig. 8. The copper vessel has significantly reduced impedance, especially at low frequencies in both transverse planes. This is especially important in the horizontal, where the aluminium design for this vessel was one of the most significant contributors to the total storage ring impedance. A summary of loss and kick factors for the two designs is shown in Table 2. The horizontal kick factor is reduced by nearly a factor of 60 for the copper design. Reduction in the other planes is smaller, but still significant.

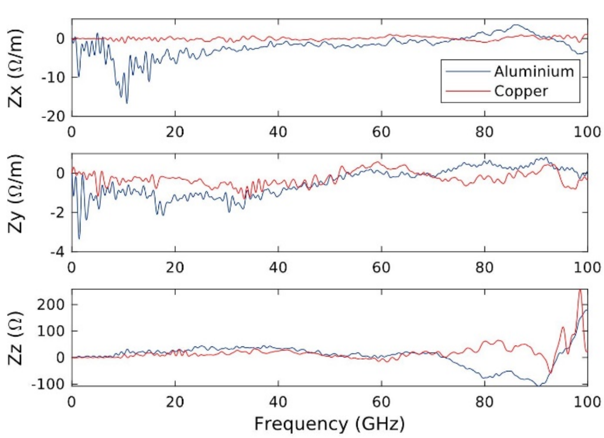

Figure 8: Comparison of real impedance for aluminium and copper vessel designs.

Table 2: Transverse Kick and Longitudinal Loss Factors Comparison for Two Designs

	kx V/pC/mm	ky V/pC/mm	kz V/pC
Aluminium	-0.1206	-0.0284	0.2378
Copper	-0.0021	-0.0063	0.0778

CONCLUSION

A workable solution of LM girder vessel 2 was developed for Diamond II storage ring, which is capable of handling the heat load of a new APPLE-knot insertion device. Peak temperatures of the copper vessel have been reduced from 446°C to 71°C compared to the previous concept. The beam impedance and average vacuum pressure around vessel 2 was significantly improved. NEG coating trails and the full prototyping vessel manufacturing has already been commenced. The intention is to implement the light extraction copper vacuum vessel of the LM girder onto the remaining MS, SM and ML girder designs. The intention is to implement the same concept of the copper vessel onto the MS, SM and ML girder designs.

REFERENCES

[1] Diamond-II Technical Design Report, Diamond Light Source, Didcot, UK, https://www.diamond.ac.uk/Diamond-II.html

[2] A. Ramezani Moghaddam, C. Cacho, and B. Singh, "Quasi-periodic Apple-knot undulator for Diamond Light Source", in *Proc. IPAC'23*, Venice, Italy, May 2023, pp. 1192-1195. doi:10.18429/JACoW-IPAC2023-MOPM093

[3] S. K. Sharma, "A Comparison of Front-End Design Requirements", in *Proc. MEDSI'20*, Chicago, USA, Jul. 2021, p. 53. doi:10.18429/JACoW-MEDSI2020-MOPB15

[4] R. Ganter *et al.*, "SLS 2.0 vacuum components design", in *Proc. IPAC'23*, Venice, Italy, May 2023, pp. 4301-4304. doi:10.18429/JACoW-IPAC2023-THPA147

[5] R. Kersevan and M. Ady, "Recent Developments of Monte-Carlo Codes Molflow+ and Synrad+", in *Proc. 10th Int. Particle Accelerator Conf. (IPAC'19)*, Melbourne, Australia, May 2019, pp. 1327-1330. doi:10.18429/JACoW-IPAC2019-TUPMP037

[6] CST Studio Suite, https://www.3ds.com/products-services/simulia/products/cst-studio-suite/

ISBN: 978-3-95450-250-9 ISSN: 2673-5520 doi:10.18429/JACoW-MEDSI2023-WEPPP054

VIBRATION ANALYSIS OF STORAGE RING GIRDER FOR THE KOREA 4GSR*

G. W. Hong †, H. G. Lee, T. Ha, H. S. Han
Pohang Accelerator Laboratory (PAL), Pohang, Republic of Korea

Abstract

Ensuring the mechanical stability of the girder for a 4th generation storage ring (4GSR) is crucial to provide a high-quality photon beam to users because the mechanical motion should be maintained at less than 10 % of the electron beam size which is expected to be sub-micrometer. One of the key roles of the girder is to provide structural rigidity and temperature stability while effectively suppressing vibrations from the ground during accelerator operation. The Korea 4GSR girder is being designed to have the first natural frequency above 50 Hz to minimize the effect of the ground vibration. In order to maintain better mechanical stability, it is necessary to conduct research not only on the natural vibration evaluation of the girder but also on external vibrations to the girder structure. In this paper, we introduce the result of the harmonic analysis of the girder structure using the finite element method.

INTRODUCTION

The Korea 4GSR girder system is designed to conform to a storage ring circumference of approximately 800 m to conform to stable accelerator design variables. Alignment mechanisms such as motor-driven cam moves, wedge jacks, and motor-driven wedge jacks are used in the case of circular synchrotron accelerator girder systems that are driven worldwide. The girder system for the PLS-II of the third-generation circular accelerator used an alignment mechanism through screw jacks to secure a wide driving range and mechanical rigidity [1]. The Korea 4GSR girder system was developed using a ball screw jack with improved moving accuracy and durability instead of the existing TM screw jack for the girder body adjustment. In addition, it was developed using a motor control drive and a displacement sensor for convenience in precise alignment of the accelerator [2]. This research explains the design concept of Korea 4GSR and structural design to secure rigidity [3], natural frequency evaluation [4], and structural stability due to random frequency [5] using Finite element analysis (FEA) to analyse mechanical characteristics.

Requirement for the Girder System

Beam physical requirements must be satisfied for the design of the Korea 4GSR girder system. In the global cases where upgrades from 3rd generation to 4th generation circular accelerators have been made, vibration characteristics of the ground and characteristics of the accelerator building should be reliably identified in order to build a successful synchrotron accelerator. Korea 4GSR should be operated stably for the external environment, and development that meets the following requirements should be carried out for the girder system.

- Electron beam height: 1.4 m.
- High flatness of girder top and low deformation for installation and operation of accelerators.
- Securing high primary resonant frequencies for limited conditions.
- Motor driven alignment mechanisms.
- Optimal girder design for free space in storage-ring tunnels.
- Securing mounting holes for installing various devices.
- Ensuring thermal stability.

The main parameters for developing the girder system of Korea 4GSR are as follows.

Table 1: Main Parameters for the Girder System [6]

Parameter	Value	
Number of cells	28	cells
Circumference	798.8	m
Beam height	1.4	m
Levelling range (Vertical)	± 10	mm
Lowest natural frequency	50	Hz
Adjustment method	Motorized (Vertical)	
Positioning accuracy	± 10	μm

Design Layout

The girder design is heavily influenced by the beam physics design and device configuration. There is a total of 28 cells at about 800 m around the storage ring, and the types are normal cells and high beta injection (HBI) cells, each cell was developed into five girders. The layout of the girder system is also composed of two types because the normal cell consists of symmetrical upstream and downstream based on the central bending section, and the HBI cell has a non-symmetric configuration [7]. There are three types of girder for installing the storage ring accelerator. All girder adjustment devices are designed in the same mechanism with 4 points motor-driven in the Y direction and 3 points in the X and Z directions being manually adjusted. For a normal cell, three girders based on the center of each cell are designed to be 4.8 m in the longitudinal direction, and the girders at both ends of the cell are designed to be 3.8 m. The HBI cell is designed with the three

* This research were supported in part by the Korean Government MSIT(Multipurpose Synchrotron Radiation Construction Project) and also supported by Pohang Accelerator Laboratory(PAL) (Republic of Korea). PAL is supported by MSIP and POSTECH.
† gwhong@postech.ac.kr

girders in the center of each cell at 4.8 m, the upstream direction girders at 3.4 m, and the downstream direction girders at 3.8 m long. Figure 1 shows a girder system that includes an electromagnet on the beam path.

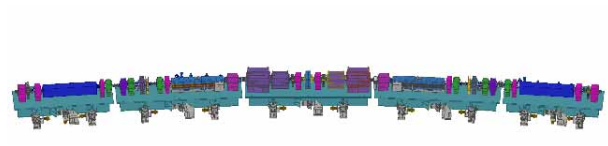

Figure 1: Design of the girder in the achromat.

METHODOLOGY

The center bending magnet girder model was used to analyse the overall mechanical stability. Mechanical characteristic analysis has consisted of a self-weight analysis of gravity, a natural frequency analysis of the girder structure itself, and a random frequency analysis of external vibrations. In order to obtain the FEA results, the analysis results were confirmed using the Ansys 2022. In addition, Vibration data of the Korea 4GSR site was obtained using an accelerometer of 10 V/g to acquire ground vibration data that could affect the accelerator. Figure 2 shows the comparison of the Korea 4GSR accelerator ground vibration measurement data and the vibration criteria (VC) [8] with the 1/3 octave rms value of the accelerator site.

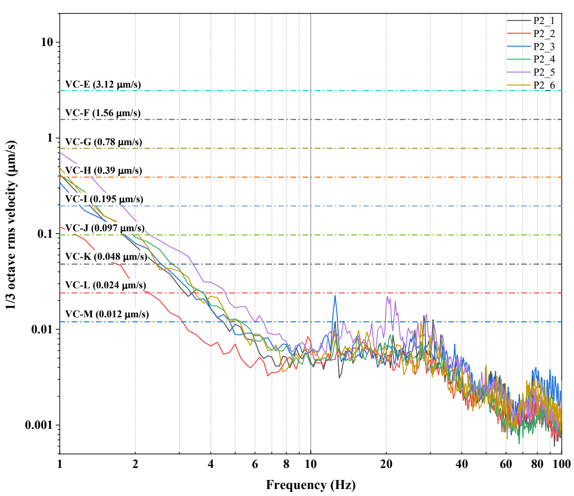

Figure 2: Comparison of the ground vibration and VC.

RESULT

Static Analysis

Static analysis to identify deformation due to gravity was evaluated for two cases: conditions by girder itself and a girder system including a vacuum chamber and a magnet. In order to proceed with the static analysis, the analysis was carried out, including the properties of the material constituting the girder system and the boundary conditions of the elements constituting the adjustment system. The results of the interpretation can be seen in detail in Fig. 3. The first case is the interpretation of the girder itself. As a result of this analysis, the maximum displacement of the girder system is 18.4 μm, and it can be confirmed that the maximum displacement occurs at the center point in the beam length direction, which is the center of gravity of the girder body. In the second case, an analysis was performed considering the weight such as a magnet and vacuum chamber on the top of the girder system. The maximum displacement from the origin of the girder design was confirmed to be 60.9 μm. It was confirmed that the maximum displacement point occurred at the end of the girder body and a displacement of 54 μm occurred on the girder top plate. The displacement of the girder endpoint is the result of not considering the center of gravity of the magnet and the appearance of the accelerating device, and detailed verification is required based on the prototype that is scheduled to be manufactured. The results of analysing the displacement amount and displacement point of the girder system through static analysis will enable the installation and operation of the circular synchrotron accelerator to a level that can be accurately measured and aligned with the girder system during the construction.

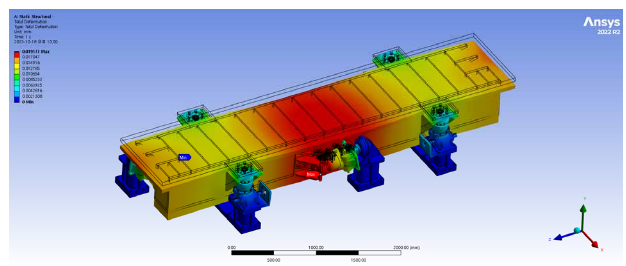

Figure 3: Deformation analysis of the girder system.

Modal Analysis

Displacement and vibration propagation of the storage ring girder system affect the trajectory of the accelerated beam, causing the performance of the circular accelerator to deteriorate. For ESRF-EBS, it aims to maintain the vibration stability of the mechanical system below 10 % of the electron beam size. Vibration stability through error study of beam physics will be presented in Korea 4GSR, and a system with rigidity should be secured while maintaining vibration stability caused by external vibration in the girder system for this purpose. Based on the existing girder components, the 4GSR girder system has been improved to secure mechanical rigidity and vibration suppression capabilities by utilizing the rib for reinforcing rigidity.

Considering the structure and material characteristics of the girder system, research should be conducted to study the dynamic characteristics of the girder system and to increase the 1st natural frequency inside the structure. The design of the girder vibration part was carried out through modal analysis based on linear vibration theory and finite element techniques. Analysing the dynamic characteristics of the girder can be used as basic data to avoid resonance and reduce displacement.

The modal analysis of the girder system confirmed that the 1st natural frequency was more than 58 Hz, which shows a higher natural frequency characteristic than the girder system design goal of 50 Hz. Evaluation of the natural frequency of the accelerator devices is an important

12th Int. Conf. Mech. Eng. Design Synchrotron Radiat. Equip. Instrum. MEDSI2023, Beijing, China JACoW Publishing
ISBN: 978-3-95450-250-9 ISSN: 2673-5520 doi:10.18429/JACoW-MEDSI2023-WEPPP054

factor in securing the stability of the beam. Since the amount of displacement amplified when high-frequency band resonance occurs in the accelerator is less than when resonance occurs at low frequencies, research on how to increase the natural frequency of the girder system and suppress external vibration should be conducted continuously. In particular, the natural frequency results are expected to be guidelines that can minimize the frequency effect of peripheral devices or facilities generated during beam operation as well as the external vibration.

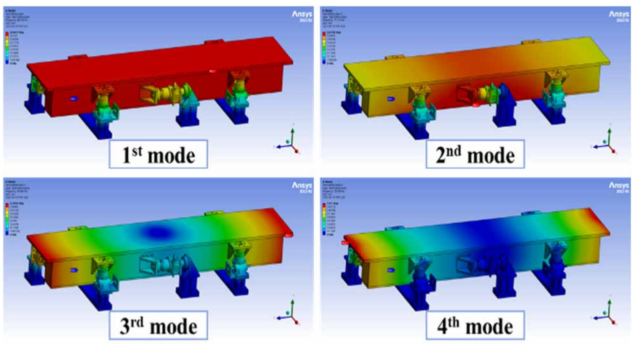

Figure 4: Modal analysis.

Table 2: Frequency of Difference Distortion Modes

Mode	Frequency [Hz]	Mechanical Property
1st	58.08	Transversal translation
2nd	71.17	Transversal + Roll
3rd	90.68	Translation beam Dir.
4th	122.96	Torsional

Random Vibration Analysis

In order to analyse the effect of the girder system on the ground vibration of the synchrotron accelerator site, ground vibration data was obtained by using an accelerometer of 10 V/g measuring level. The power spectral density (PSD) data of the ground measured as shown in Fig. 5 was confirmed to be at an appropriate level compared to the fourth-generation circular accelerator currently operating globally. The average displacement of RMS from 1 to 100 Hz was 2.7 to 12.8 nm through the ground vibration measuring. Civil engineering work is underway in the Korea 4GSR area and the data measured was considered to have been affected by variable environmental factors. It is expected that more reliable data can be obtained when the ground formation of the accelerator is completed.

When evaluating random vibration by applying external vibration variables to the center bending girder, the displacement of the top plate could be seen around 28 pm as shown in Fig. 6. In particular, a result value of a very low strain of 20 pm was calculated in the center of the girder top plate. This value is less than 10 % of the Korea 4GSR Beam size which can sufficiently function as a girder system.

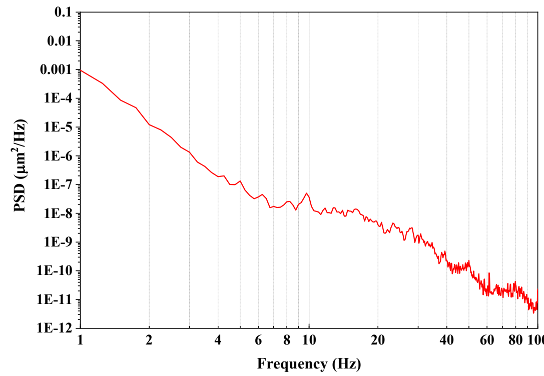

Figure 5: Ground vibration response.

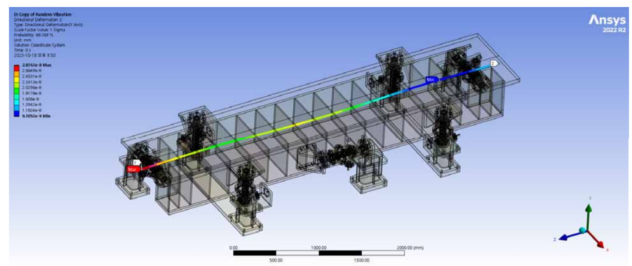

Figure 6: Random vibration analysis.

CONCLUSION

FEA for the girder system was performed to investigate the structural characteristics. The gravity analysis based on its own weight, the displacement of the girder itself was confirmed to be at the level of 18 µm and 54 µm when the magnet was included. In the natural frequency analysis, the first natural frequency was confirmed to be 58 Hz or more. The floor stability in all locations is remarkably well placed with respect to the common VC curves, with integrated displacement between 1 and 100 Hz below in the range from 2.7 to 12.8 nm RMS. The random vibration analysis results that can affect the beam operation were confirmed at 28 pm on the girder top plate which was confirmed that less than 10 % of the beam size would not affect the operation. Based on the results of this study, it is expected that more complete results will be derived by acquiring data through field experiments through measurement and prototypes in an improved environment for the development of the girder system.

REFERENCES

[1] H.G. Lee *et al.*, "Girder and support system for PLS-II project", in *Proc. IPAC'11*, San Sebastián, Spain, Sep 2011, pp. 1759-1761.

[2] Filippo Cianciosi *et al.*, "The girder system for the new ESRF storage ring", in *Proc. MEDSI'16*, Barcelona, Spain, Jul. 2016, pp. 147-151. doi:10.18429/JACoW-MEDSI2016-TUCA06

[3] S. Andresen, "Innovative and biologically inspired PETRA IV girder design", in *Proc. MEDSI'20,* Chicago, IL, USA, Jul. 2020, pp. 360-363. doi:10.18429/JACoW-MEDSI2020-THOB03

[4] Z. Liu, W.G. Jansma, J. Nudell, and C.A. Preissner, "Validation of APS-U magnet support design analysis and

ISBN: 978-3-95450-250-9 ISSN: 2673-5520 doi:10.18429/JACoW-MEDSI2023-WEPPP054

prediction", in *Proc. MEDSI'20*, Chicago, IL, USA, Jul 2020, pp. 89-92.
doi:10.18429/JACoW-MEDSI2020-MOPC16

[5] S. Sharma and C. Spataro, "Recent studies on the vibration response of NSLS-II girder support system", in *Proc. MEDSI'20*, Chicago, IL, USA, Jul. 2020, pp. 81-94.
doi:10.18429/JACoW-MEDSI2020-MOPC13

[6] J. Ko *et al.*, "Comparison of photon beam characteristics of Korea-4GSR with PLS-II", *Nucl. Instrum. Methods Phys. Res., Sect. A*, vol. 1021, no. 1, p.165941, Jul. 2022. doi:10.1016/j.nima.2021.165941

[7] J. Lee *et al.*, "Concurrent operation of round beam and flat beam in a low-emittance storage ring", *Nucl. Eng. Technol.,* vol. 55, no. 10, pp.3866-3873, Oct. 2023.
doi:10.1016/j.net.2023.07.002

[8] Vibration Criteria Standards, https://www.minusk.com/content/technology/vc_curves_minus_k_vibration_isolation.html, accessed on July 19, 2023.

ISBN: 978-3-95450-250-9 ISSN: 2673-5520 doi:10.18429/JACoW-MEDSI2023-WEPPP058

PERMANENT MAGNET IN SOLEIL II

A. Berlioux†, Y. Benyakhlef, C. Kitegi, F. Marteau, A. Mary, E. Raimon, M. Ribbens, K. Tavakoli
Synchrotron SOLEIL, Saint-Aubin, France

Abstract

Twenty years after SOLEIL Synchrotron was established, the facility needs to adapt to follow new scientific fields that have emerged since. The proposed new lattice for upgrading SOLEIL storage ring will reduce the horizontal emittance by a factor 50 to reach less than 100 pm·rad.

This new lattice presents significant challenges and requires compact magnets that provide strong gradients. As a result, PM (permanent magnet) technology is preferred over electromagnet (EM) technology whenever possible. All sextupoles and octupoles will be EM to ensure efficient optic correction. However, all dipoles, reverse bends and quadrupoles will be PM.

The replacement of aging infrastructure and the use of permanent magnets (PM) will lead to a noticeable reduction in SOLEIL's electric power consumption and environmental footprint.

SOLEIL II lattice consists of 116 dipoles with gradient and 354 PM quadrupoles which can also be used as reverse bends. All PM multipoles have been designed by SOLEIL's Mechanical Engineering Group in close collaboration with the Magnetic and Insertion Devices Group.

INTRODUCTION

Since its inception in 2008, SOLEIL has proudly represented the cutting-edge of French third-generation light sources. This facility harnesses an electron beam emittance of 4 nm·rad, fueled by an energy of 2.75 GeV, delivering intensity at 500 mA in a multibunch configuration [1].

Having achieved years of successful operation, SOLEIL embarked upon an ambitious project dedicated to advancing its capabilities. The project, known as SOLEIL II, aspires to reduce the horizontal emittance of the electron beam less down to 100 pm·rad at 2.75 GeV. Our mission is to design and construct a fourth-generation synchrotron light source while preserving the existing infrastructure, including 29 beamlines spanning from far-infrared to hard X-rays.

The lattice of the new storage ring consists of alternating 7BA and 4BA High Order Achromat type cells, including more than twelve hundred magnets. To achieve such challenge, magnet design compactness is a key parameter. Permanent Magnets (PM) technology offers us a great balance between space and magnetic strength. Dipoles, reverse-bends and quadrupoles have been designed with such technology. Table 1 list the main materials used.

Table 1: Main Materials

Class	Designation
Magnets	Sm_2Co_{17}
Iron	XC06 (or ARMCO)
	Permendur (Fe-Co)
	34CrMo4
Stainless Steel	316L (μ<1.01)
Aluminium	2017A T4
Mu-metal	$NiFe_{15}Mo_5$

DIPOLES

Within the SOLEIL II storage ring lattice, there are eight distinct categories of dipoles, including four normal short dipoles (DNC) and four normal long dipoles (DNL). Table 2 is listing their main characteristics [2].

Table 2: Main Dipoles Parameters

Dipole	Diamater (mm)	Deviation (mrad)	Mag. Length (mm)	On axis field (T)	Gradient (T/m)	Quantity
DNC1	23	42.22	460	0.921	-18.7	22
DNC2	23	40.09	460	0.874	-18.7	16
DNC3	23	41.85	460	0.912	-18.7	1
DNC4	23	48.43	460	1.061	-18.7	1
DNL1	19	68.86	940	0.593 1.2 0.593	-21.57 0 -21.57	58
DNL2	19	65.39	940	0.563 1.2 0.563	-21.57 0 -21.57	16
DNL3	19	69.02	940	0.593 1.2 0.593	-21.57 0 -21.57	1
DNL4	19	68.51	940	0.593 1.2 0.593	-21.57 0 -21.57	1

Short Dipoles

DNC are used at the upstream and the downstream of 7BA and 4BA cells [3]. Their poles are curved with a hyperbolic profile, adding a transverse gradient. Low carbon steel is used for all magnetics parts and an aluminium bloc enable the transmission of forces. Mu-metal plates are used as a magnetic shield. They are fixed on both sides of the dipole to prevent crosstalk with the very close magnets next to it. Figure 1 shows the actual 3D model of the DNC.

† anthony.berlioux@synchrotron-soleil.fr

ISBN: 978-3-95450-250-9 ISSN: 2673-5520 doi:10.18429/JACoW-MEDSI2023-WEPPP058

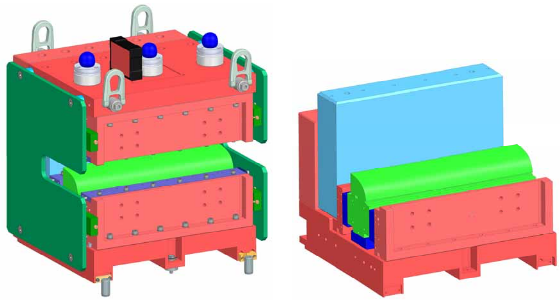

Figure 1: Short dipole 3D model.

Long Dipoles

Every DNL consists of three distinct sections: two identical end regions and a central segment. The end region poles have a straight design featuring a hyperbolic profile. In regular DNLs, the central segment generates a magnetic field of 1.2 T peak without any transverse gradient. Eight DNLs from this group will be used as superbends, with each one capable of producing a central magnetic field of either 1.7 T or 3 T peak. The overall gradient is adjusted mechanically, using floating poles. Low carbon steel is used for all magnetics parts. For 3T superbends dipoles, the central pole is made of permendur to support the magnetic field. Two aluminium blocs enable the transmission of forces. Mu-metal plates are also used as magnetic shield. Figure 2 shows the difference between 1.2 T and 3 T long dipoles.

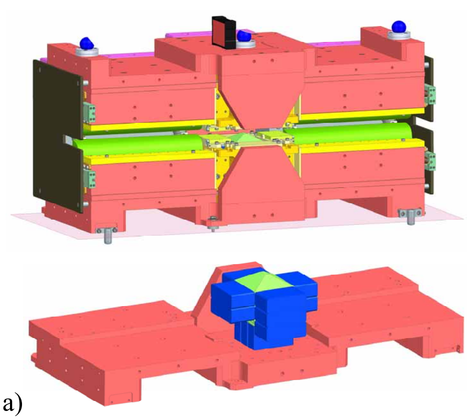

a)

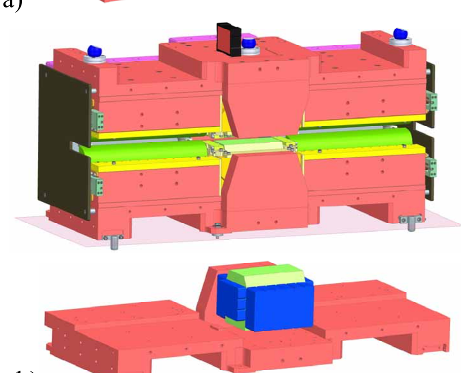

b)

Figure 2: a) 3 T superbend dipole b) 1.2 T standard dipole.

QUADRUPOLES AND REVERSE BENDS

We have opted for the geometry recommended by the ESRF [4] in the design of SOLEIL II quadrupoles and reverse-bends. This choice is based on its inherent simplicity, which still allows achieving a high gradient within a compact envelope. Moreover, it provides adequate off-axis space for the photon vacuum chamber.

SOLEIL II lattice include a total of 23 families of quadrupoles and reverse-bends, their primary parameters are detailed in Table 3 [3].

Table 3: Main Parameters of the Quadrupoles and Reverse Bends

Magnet type	Reverse Bend		Quadrupole	
Aperture	21	18	16	21
Angle (mrad)	-3.44 to -3.27	-0.81 to -0.77	0	
Length (mm)	136	119	54 to 94	146 to 216
Dipole field (T)	-0.232 to -0.22	-0.059 to -0.088	0	
Gradient (T/m)	82.97	103.69	112 to 127	87 to 90
quantity	152	40	150	12

In practice, our proposal entails the initial creation of a cluster of magnet families, ideally between 7 to 10 in number. This could be achieved by adjusting the thickness of the magnetic shunts located at the ends of the magnets. The precise distribution within the initial cluster will be decided at a later stage, following the finalization of the lattice configuration.

A first quadrupole prototype, showed in Fig. 3, was delivered in early 2021 with a profile intentionally remained unoptimized to highlight a specific signature during magnetic measurements. These measurements aimed to evaluate the precision of the manufacturing process and the results are rather encouraging.

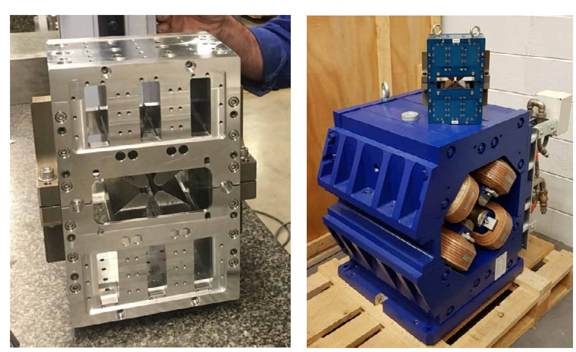

Figure 3: Empty prototype N01 (left) and on SOLEIL quadrupole (right).

A second prototype with a simplified mechanical design and an optimized profile will be delivered before the end of the year. Magnetic shunts are also implemented to control the gradient in orange in Fig. 4.

ISBN: 978-3-95450-250-9 ISSN: 2673-5520 doi:10.18429/JACoW-MEDSI2023-WEPPP058

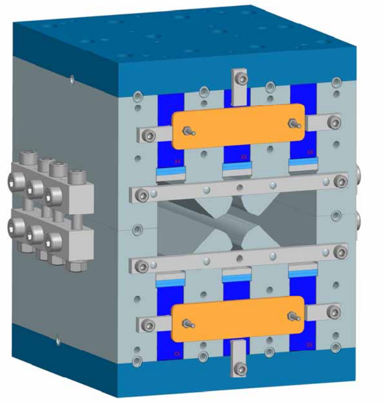

Figure 4: Quadrupole prototype N02 3D model.

TOOLING

Mechanical tooling has been developed internally, with the cooperation of the Magnetic and Insertion Devices Group, to facilitate the precise insertion of magnets inside the empty yoke. This equipment ensures a good integration, enhancing the efficiency and safety placement of the magnets.

For quadrupoles, two tooling are facing each other on the yoke, one pushing the magnets inside, the other one smoothly holding it with the help of springs. Figure 5 shows the inserting tooling on first quadrupole prototype.

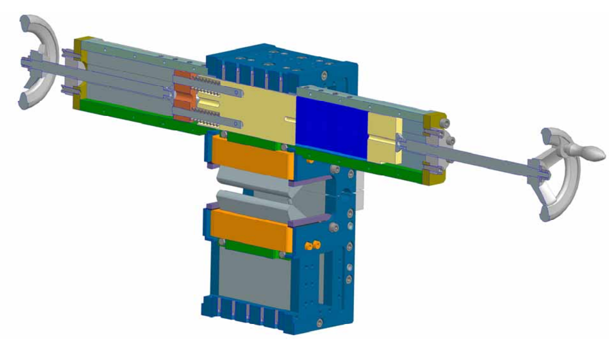

Figure 5: Inserting quadrupole N01 magnets tool.

For dipoles, the tooling is even more important because there are more steps to assemble all parts. The dipoles are in three parts, so we need to assemble all three parts apart before grouping them together. The procedure is as following:

1. Insert the magnets in low-field module and high-field yoke.
2. Insert low-field module on high-field yoke.
3. Adjust the position of floating poles and hyperbolic poles as the reference.
4. Group up upper yoke and lower yoke.

Figure 6 regroups all the steps of the previous procedure.

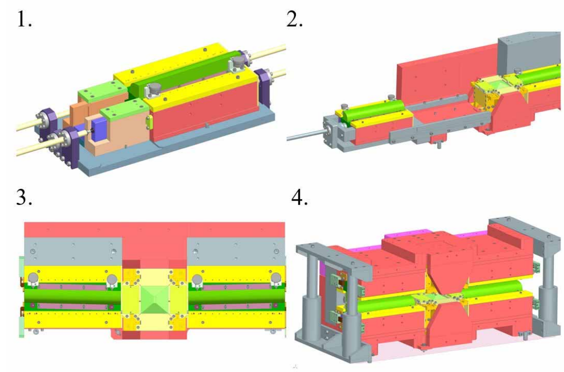

Figure 6: Assembling procedure for long dipoles.

Finally, to be able to lift and bake all the vacuum chambers ex situ, dipoles need to be extracted. A special tooling has been developed for long and short dipoles. The dimensions are not the same between those two dipoles, but the principle is the same. The goal is to raise the dipole without touching the vacuum chamber. The distance available is around 0.5 mm. Figure 7 shows the following sequences:

1. Dipole on the girder,
2. Assembly of the tool on the girder,
3. Lifting the dipole with the help of laser tracker,
4. Sliding the dipole following the flying height with the laser tacker.

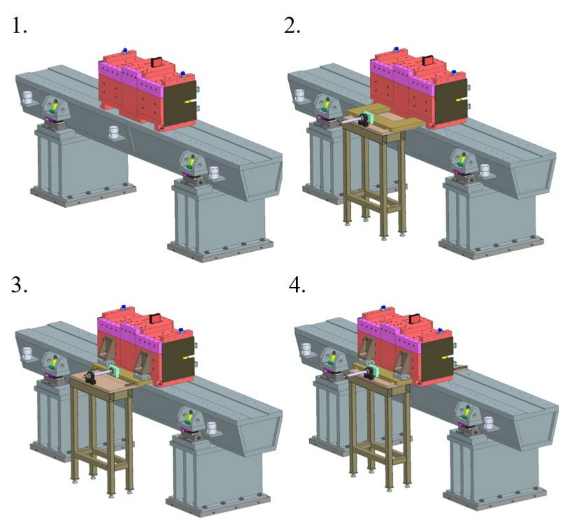

Figure 7: Extracting procedure for dipoles.

REFERENCES

[1] Synchrotron SOLEIL, `https://www.synchrotronsoleil.fr`

[2] C. Kitegi *et al.*, “Magnet design status of SOLEIL II”, in *Proc. MT28*, Aix-en-Provence, France, 10-15 Sep 2023, paper MT28-3PoA02-03.

[3] K. Tavakoli *et al.*, “Challenges and solutions for the mechanical design of SOLEIL II”, presented at MEDSI’23, Beijing, China, Nov. 2023, paper WEOBM01, this conference.

[4] P. N'gotta, G. Le Bec, and J. Chavanne., “Hybrid high gradient permanent magnet quadrupole”, *Phys. Rev. Accel. Beams*, vol. 19, p. 122401, Dec. 2016. `doi:10.1103/PhysRevAccelBeams.19.122401`

ISBN: 978-3-95450-250-9 ISSN: 2673-5520 doi:10.18429/JACoW-MEDSI2023-THOAM01

DEVELOPMENT AND QUALIFICATION OF MICROMETRE RESOLUTION MOTORIZED ACTUATORS FOR THE HIGH LUMINOSITY LARGE HADRON COLLIDER FULL REMOTE ALIGNMENT SYSTEM

M. Noir * [1], M.Sosin † [1], P.Biedrawa[2], S.Fargier[1], W.Jasonek[2]
[1]CERN, Geneva, Switzerland
[2]AGH, University of Science and Technology, Krakow, Poland

Abstract

In the framework of the High-Luminosity Large Hadron Collider project at CERN, a Full Remote Alignment System (FRAS) is under development, integrating a range of solutions for the remote positioning of accelerator components. An important component of FRAS is the motorized actuator allowing the remote adjustment of accelerator components with a micrometre resolution. These actuators need to fulfill multiple requirements to comply with safety rules, and be highly reliable and maintenance free as thus are located in a harsh environment.

The integration of the safety functions required for the FRAS was crucial, with the motorized actuators able to provide an absolute position monitoring of the available stroke, integrating electrical end-stops and having an embedded mechanical stop as a hardware safety layer. In addition, the design has been elaborated to allow a rapid, in-situ re-adjustment of the nominal stroke in order to cope with potential readjustment requirements, following long-term drifts caused by ground motion.

This paper describes the design approach, prototyping and qualification of these motorized actuators.

INTRODUCTION

The High-Luminosity-Large Hadron Collider (HL-LHC) project is an upgrade of the current LHC that aims to increase its integrated luminosity by a factor of 10. In order to achieve such a luminosity, components of the Long Straight Sections (LSS) will be replaced around the two major detectors (ATLAS and CMS), representing a major modification of 1.2 km of beam line [1, 2].

The increased luminosity will generate higher radiation levels in the LSS and prevent from an easy and safe access in the area. In order to reach the required physics performance, the LSS components will have to be aligned within +/- 0.3 mm (1 sigma) over a 450 m length. The alignment will be performed by the Full Remote Alignment System (FRAS) [3, 4]. It consists of a set of sensors and actuators allowing a micrometre position monitoring and remote adjustment of the accelerator components.

To perform their adjustment, the heaviest components, like magnets, will be installed on a set of 3 standardised jacks (each jack providing 2 degrees of freedom of adjustment). The following chapters describe the design, prototyping and qualification of the radial and vertical motorized adapters used for the accurate adjustment of each jack position.

SYSTEM CRITICALITY DUE TO REMOTE OPERATION

During the alignment operations in HL-LHC, the available stroke of the vacuum interconnection bellows linking adjacent components of the beam lines must be taken into account before a relative movement. As the FRAS will be operated remotely, a safety strategy has been implemented to protect the machine from unexpected relative movements that could lead to major failures. Two safety functions, representing the major challenges in the adapters design, have been assigned to the motorised adapters:

- They shall provide at anytime the absolute position of the adapter within its stroke, to control that the displacement at the level of the bellows is performed within the limits of ±2.5 mm.
- A mechanical end-stop shall block any motion if the nominal stroke of ±2.5 mm is exceeded. This additional feature represents a challenge regarding the developed force of the adapters (up to 17 500 kg).

MOTORISED ADAPTERS DESIGN

Vertical Position Adjustment

Each vertical adapter has been designed to withstand loads up to 17.5 T, to fit into small jack adapter volume (Figure 1). The compactness of the overall design was one of the major challenges which is why a quasi-hydraulic actuation solution has been selected. The main concept relies on the deformation of a polyurethane pastille in the actuator head. A pushing finger driven by a self-locking thread-nut system deforms radially the pastille taking the full chamber space and lifting the piston to adjust the jack position as per an hydraulic cylinder (see Figure 2). This system, already used today in the LHC, provides a micrometre position adjustment.

Radial Position Adjustment

For the radial actuation, the motion is performed by the jack mechanism itself, consisting of a screw-nut actuation system linked to a high-ratio worm gear (see Figure 1). Hence, the radial motorized adapter role is to provide a high resolution rotary motion and to measure it in an absolute way. The global stroke of the actuator to perform the ±2.5 mm final motion corresponds to 58 revolutions.

* michel.noir@cern.ch
† mateusz.sosin@cern.ch

ISBN: 978-3-95450-250-9 ISSN: 2673-5520 doi:10.18429/JACoW-MEDSI2023-THOAM01

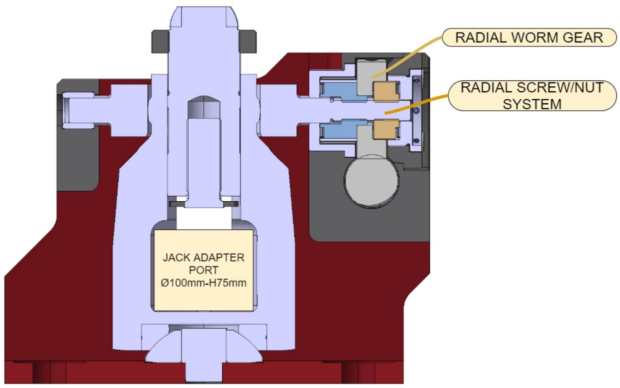

Figure 1: Cross-Section of the HL-LHC jack.

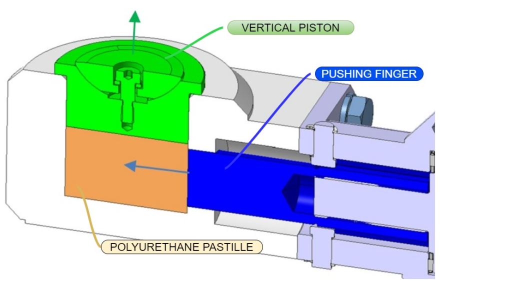

Figure 2: Vertical adapter head based on polyurethane pastille deformation.

Stroke Position Monitoring and Nominal Position Adjustment

Both adapters are designed to provide a jack head (see Figure 3) movement stroke of ±2.5 mm (either radially or vertically). This value shall not be exceeded under any circumstances. To do so, a stroke monitoring feedback loop is embedded in the design of each motorized adapter. Using an additional worm gear reduction constrained by a spring, each adapter is equipped with a "feedback axis" rotating by 360° for a full actuation stroke. This so called feedback axis (Figure 4) is equipped with a resolver operating in an absolute regime (one rotation matched to the full stroke of the jack) and electrical end-switches to prevent any over-stroke movements.

Even if the motorized adapter stroke has been limited for remote operation to prevent too important shifts, the situation where the stroke limits are reached might appear. Such situation caused for example by the floor motion, could lead to the necessity of modifying the nominal position of each motorized adapter.

Due to this additional constrain, the motorized adapters have been designed in a way, that the nominal position of the motorized stroke of ±2.5 mm can be manually adjusted within a higher range of ±5 mm. Hence, both actuators mechanisms allow for a quick and manual adjustment of their motorized range during technical stops if required (Figure 5).

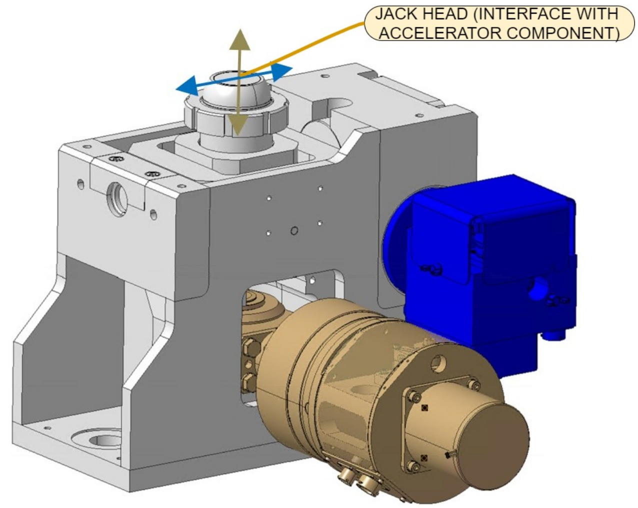

Figure 3: Jack equipped with radial and vertical motorized adapters.

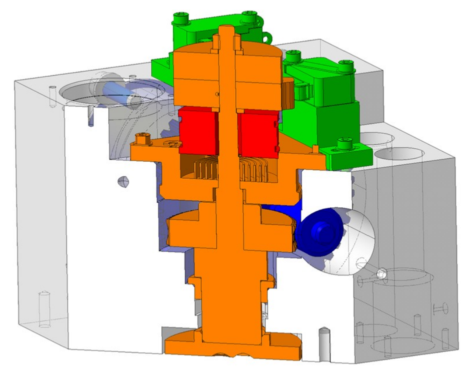

Figure 4: Stroke monitoring system with output axis [Blue], feedback axis [Orange], resolver [Red] and electrical End Switches [Green].

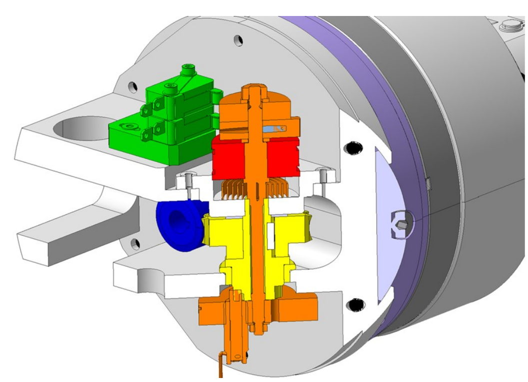

Figure 5: Stroke monitoring system with output axis [Blue], feedback axis [Orange], resolver [Red] and electrical End Switches [Green].

Mechanical End-Stop

In addition to the electrical end-stops (electrical end-switches) and the absolute stroke position monitoring, a mechanical end stop is included in both adapter designs. This additional protection layer need has been specified

ISBN: 978-3-95450-250-9 ISSN: 2673-5520 doi:10.18429/JACoW-MEDSI2023-THOAM01

in the FRAS Software Functional Specification [5]. The mechanical end-stop is the last protection barrier against over-stroke movement, in case of a failure of the motion interlock of the electrical end-switches. Unlike classic design, this mechanical end-stop has to be adjustable in case of a stroke-adjustment operation. Hence, the system is based on the feedback axis that contains a programming wheel. This wheel, after over-passing the electrical end-switches, triggers a mechanism that immediately locks the motor axis, preventing any motion of the input pinion linked to the stepper motor axis (Figure 6).

The use of a two-stages triggering system allows reducing the pressure on the feedback axis and consequently reducing the friction on the axis that could degrade the global system backlash.

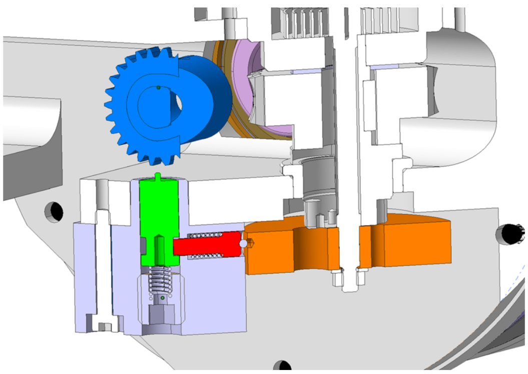

Figure 6: Mechanical end-stop and triggering system composed of programming wheel [Orange], primary axis [Red] and locking axis [Green].

QUALIFICATION TESTS

In order to verify the performances of the various safety functions, a series of qualification tests has been performed on both adapters. It has been decomposed by adapters functions in order to obtain a step by step validation.

Currently, a set of 2 radial and 3 vertical adapters passed the individual tests that are described in the next chapters. In the future, a real use case on a test magnet, equipped as for HL-LHC is foreseen.

Test Configuration

In order to measure the adapters performance, two tests configurations, adapted to both vertical and radial adapters, has been designed.

- On the Vertical adapter, the measurement is performed on the piston, called "pushing finger", that shall normally be in contact with the polyurethane pastille (see Figure 2). A micrometric dial gauge has been installed on this piston to compare the stepper motor steps, the resolver reading and the real displacement (see Figure 7).
- On the Radial adapter, the measurement is performed on the output shaft that is at the interface between adapter and HL-LHC Jack. A rotating encoder is used in that case to perform the position reading (see Figure 8).

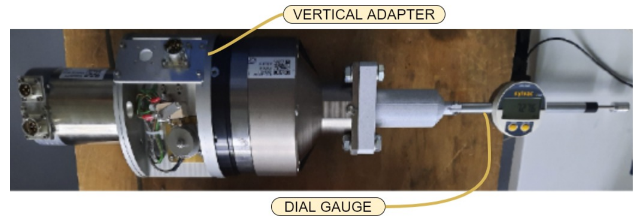

Figure 7: Vertical adapter in test configuration with a micrometric dial-gauge.

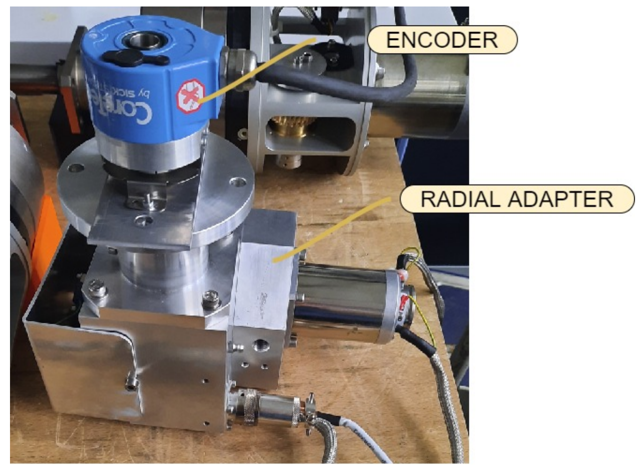

Figure 8: Radial adapter in test configuration with an absolute encoder on the output shaft.

Stroke Monitoring Parameters

Several stroke monitoring parameters have been determined by the tests conducted on the Vertical and Radial adapters:

- The repeatability of the system along the full stroke, reaching several times with the same orientation some referenced positions (based on motor step counting);
- The total system backlash has been computed over 50 cycles, going back and forward to the same position (by using as the reference the stepper motor steps measurements);
- The global position error value has been determined by comparison with the external measurement system (Figures 7 and 8).

Tests results are summarized in Tables 1 and 2 for both adapters. Note that all defect values are extrapolated to the jack head motion - see Figure 3. Consequently, the presented values are already affected by the reduction ratio between measurement point and jack head.

Mechanical End-Stop

The mechanical end-stop system has also been tested.

Before the machining of the adapter prototypes, a mockup containing only the programming wheel and the motor

Table 1: Position Parameters for the Vertical Adapter

PARAMETER	SPECIFICATION	RESULT
Total Stroke [mm]	5 ± 0.05	4.952
Repeatability [μm]	0.5	0.05
Backlash [μm]	1	0.02
Absolute position [μm]	20	6

Table 2: Position Parameters for the Radial Adapter

PARAMETER	SPECIFICATION	RESULT
Total Stroke [mm]	5 ± 0.05	4.971
Repeatability [μm]	0.5	0.05
Backlash [μm]	1	0.25
Absolute position [μm]	20	10

axis has been assembled (see Figure 9). In order to verify the reliability of the system, its triggering has been performed up to 75 times without any failures. It confirmed an instantaneous locking of the motor axis even with the stepper motor at full speed. In normal operation, the triggering of this safety system is treated as a critical issue, and would lead to the replacement or the inspection of the full adapter in order to perform a global system failure analysis.

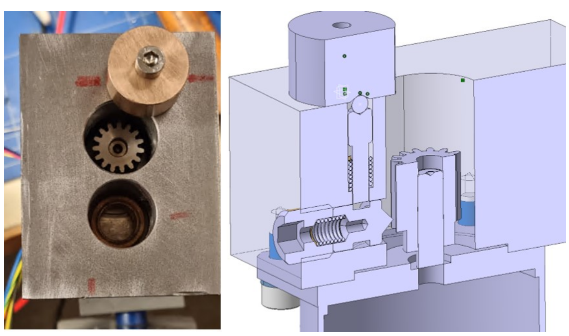

Figure 9: Mechanical end-stop triggering test configuration.

A set of tests on the final design has also been performed on both vertical and radial adapters to confirm the implementation of the design on the full assembly. Tested at nominal motor speed, both adapters showed an instantaneous stopping of the motion. This validates the additional safety layer performed by the mechanical stop. Moreover, only the motor pinion was slightly damaged by this test so the system can be reused in other designs even in applications where the actuation rate would be higher.

CONCLUSION

The individual tests of the vertical and radial motorized adapters have shown very good results with an accurate reading of the actuator position and an appropriate triggering of the safety functions.

Additional qualification steps must still be performed on the full magnet set-up, to crosscheck the operation of the motorized adapters and jacks supporting a real component. The aim of this step will be to check that adapters properties are still compliant under nominal load and that motorized adapters allow an accurate adjustment of the component, providing correct stroke measurements used for the bellows protection. As the design is now validated, the radial adapter concept will be extrapolated for the position adjustment of smaller accelerator components in the frame of the FRAS. In that case, a Universal Adjustment Platform (UAP) [6], already developed at CERN, will be motorised with the same type of actuator.

REFERENCES

[1] G. Apollinari, I. B. Alonso, O. Brüning, M. Lamont, and L. Rossi, "High-Luminosity Large Hadron Collider (HL-LHC): Preliminary Design Report", CERN, Geneva, Rep. CERN-2015-005, 2015. doi:10.5170/CERN-2015-005

[2] O. Aberle *et al.*, "High-luminosity large hadron collider (HL-LHC): Technical design report", CERN, Geneva, Rep. CERN-2020-010, 2020. doi:10.23731/CYRM-2020-0010

[3] A. Herty *et al.*, "HL-LHC Full Remote Alignment Study", in *Proc. IPAC'19*, Melbourne, Australia, May 2019, pp. 3716–3719. doi:10.18429/JACoW-IPAC2019-THPGW057

[4] P. Biedrawa *et al.*, "Full remote alignment system for the High-Luminosity Large Hadron Collider HL-LHC", CERN, Geneva, Tech. Rep. CERN-BE-2023-007, 2022.

[5] M. Sosin, "Full remote alignment system software - functional specification", CERN, Geneva, Rep. LHC-_-ES-0047, 2022.

[6] M. Sosin, T. Blaszczyk, A. Herty, J. Jaros, and H. M. Durand, "Design and Study of a 6 Degree-Of-Freedom Universal Adjustment Platform for HL-LHC Components", in *Proc. IPAC'19*, Melbourne, Australia, May 2019, pp. 3720–3722. doi:10.18429/JACoW-IPAC2019-THPGW058

ISBN: 978-3-95450-250-9 ISSN: 2673-5520 doi:10.18429/JACoW-MEDSI2023-THOAM02

SmarGon MCS2: AN ENHANCED MULTI-AXIS GONIOMETER WITH A NEW CONTROL SYSTEM

W. Glettig, D. Buntschu, E. Panepucci, M. Wang, Paul Scherrer Institute, Villigen PSI, Switzerland
A. Omelcenko, SmarAct GmbH, Oldenburg, Germany

Abstract

As an improvement on the commercially available SmarGon multi-axis goniometer (SmarAct GmbH), the Macromolecular Crystallography (MX) Group at the Paul Scherrer Institute (PSI) has been pursuing a further development of the system. In addition to suggesting mechanical improvements to SmarAct for improved ruggedness and reliability, PSI has developed a brand-new and flexible control system for better customization, reliability, and control. Calibration routines were implemented to reduce systematic errors, and the system has been tailored for practical beamline usage. SmarGon is a six degree-of-freedom positioning device, allowing positioning of a sample and orientation around any given point, with < 5 µm sphere of confusion diameter. It was purpose-built for protein-crystallography experiments but, as will be presented here, was also re-purposed for other applications. Two devices have been in continuous 24/7 use for two years at the MX Beamlines PXI & PXII at SLS.

INTRODUCTION

Initially developed based upon PSI's 6-axis-goniometer for protein crystallography PRIGo [1], SmarAct GmbH's SmarGon is a further developed and commercially available positioning device [2] allowing 4 mm translational XYZ motion and three angles of rotation ω: $[-\infty, +\infty]$, χ: $[0, 90°]$, φ: $[-\infty, +\infty]$ around any arbitrary point in space (Fig. 1). Positioning resolution is 1 nm and spheres of confusions are achievable of below 1 µm for ω, and well below 7 µm for χ & φ. [2]

Figure 1: SmarGon with a representation of the rotations ω: $[-\infty,+\infty]$, χ: $[0, 90°]$, φ: $[-\infty,+\infty]$.

SmarGon is used to position and orientate a sample with respect to the X-ray beam, and is one of the central components of a macromolecular crystallography (MX) beamline setup [3]. It was purpose built for MX experiments, but has also been used in other applications.

INITIAL RELIABILITY ISSUES

While offering advantages over the PRIGo Goniometer in terms of compactness and build simplicity, a big challenge in daily operation was to preserve SmarGon's reliability over extended periods of time. MX beamlines are often set up for high throughput and can process hundreds of samples a day. They are often controlled remotely, and now increasingly in unattended automatic operation [4]. In such cases, downtime must be avoided, and all systems must be as remotely monitorable and controllable as possible, without any need for physical human intervention.

The initial version of SmarGon posed problems: Due to its fine mechanical structure it was prone to mechanical damage caused by rough human manipulation during manual sample mounting, or unforeseen collisions during robotic sample mounting [5]. User-prepared samples can sometimes present unpredictable defects, leading to misgripped samples and ice-related slipping and sticking issues.

Another limitation was the inability to customise the control system for different modes of operation, like permitting flexible recovery in case of problems during remote access. Or in tweaking the calibration routine. Or modifying interfaces, to extend remote system diagnostics or to collect usage statistics.

Improvements both on the mechanical side as well as on the control side were strongly requested.

MECHANICAL IMPROVEMENTS

Over the initial design of the SmarAct goniometer, several simple mechanical improvements were implemented by SmarAct GmbH, primarily to increase robustness and reliability of the mechanism, and by improving processes for more repeatable assembly tolerances. These improvements are now standard in the latest SmarGon devices. Revisions to the pivot and ball joints were made and hard stops were added to prevent dislodging. Both during manual interaction and during robotic sample mounting, misaligned or mis-gripped samples can cause large forces on the goniometer, which can lead to plastic deformation of the mechanical structure. The design of a critical area of high stress, and the choices of materials were revised. Holding forces of the SmarAct piezo stick-slip positioners were taken into account, so that during a physical interaction the compliance in the structure would be in the sliders, and not as a plastic deformation of the structure.

ISBN: 978-3-95450-250-9 ISSN: 2673-5520 doi:10.18429/JACoW-MEDSI2023-THOAM02

SmarAct MCS2 CONTROLLER

SmarAct's initial controller architecture (Delta Tau PPMAC + SmarAct SDC2) proved to be rather cumbersome when customizing for reliable beamline operation. The decision was made to replace the old system with a new one, using SmarAct's state-of-the-art MCS2 controller. Main advantages included: 1) Use of distance coded reference marks, so (re-)referencing could be performed in less than two seconds, with minimal sample movement. 2) Higher resilience to knocks: MCS2 uses a higher encoder readout and interpolation frequency over previous versions (~8 kHz –> 50 kHz), and therefore it can sustain a 'faster' knock, in case of unintended collisions with the sample mounting robot system, so the loss of encoder counts is no longer an issue, and the encoder can be trusted.

Using MCS2 provides a robust foundation for the control of the individual positioners. But a high-level system is required for geometrical model calculation, trajectory generation and user interfacing, and for more complex operations like calibration and active correction.

ROS & SMARGOPOLO

MCS2 can be interfaced via USB or Ethernet. An API for Windows and Linux is provided by SmarAct. For more predictable latency, it was decided to do high-level control on a PC connected via USB.

ROS (Robot Operating System) [6] was selected as a framework for the high-level controller. ROS is an open-source set of software libraries and tools to build robot applications. It has widespread use in robotics research and has strong community support. ROS was installed on Ubuntu Linux 20.04 LTS on a moderately performing Desktop PC (HP Z240, i7, 8GB RAM, 256GB SSD). At the time of development, ROS 1 LTS version "Noetic Ninjemys" was widespread and therefore used. Today ROS2 exists, but has a significantly different system architecture, and porting requires significant refactoring of the code.

A ROS package named "smargopolo" was written to control SmarGon MCS2 (Fig. 2). Smargopolo follows a microservices architecture, with several independent modules (executables) processing parts of the control loop. Trajectory generation, geometrical models, active correction, device interfacing, user input parsing are all individual modules. The package provides a RESTful interface for user and beamline software control, and handles communication with the hardware (MCS2 & Aerotech).

Between modules, ROS offers a lightweight and fast publisher-subscriber communication protocol, ROS messages. This also allows introspection of a running system to observe system behaviour and detect faults.

ROS comes with visualisation tools for signal plotting, and for 3D visualisation. A 3D model of SmarGon was implemented, which can be driven from a running loop and used as a digital twin to test functionality during development. ROS also provides a tool to record streams (rosbag), where motion can be recorded, and later analysed or replayed.

Hardware interfacing can be done whenever there is a device driver/API available for Linux. For instance, ω rotation of SmarGon is controlled with an Aerotech A3200 controller. A fast and pragmatic way to get the absolute position from the Aerotech controller to smargopolo, was to get the Aerotech controller to convert its ω angle into to a sine and cosine signal on two free analog outputs on the controller, and to read this signal by two analogue inputs on a LabJack UE9 I/O card on smargopolo. The advantage of this is an absolute position readout, and no need for coordination if one of the devices needs to be restarted.

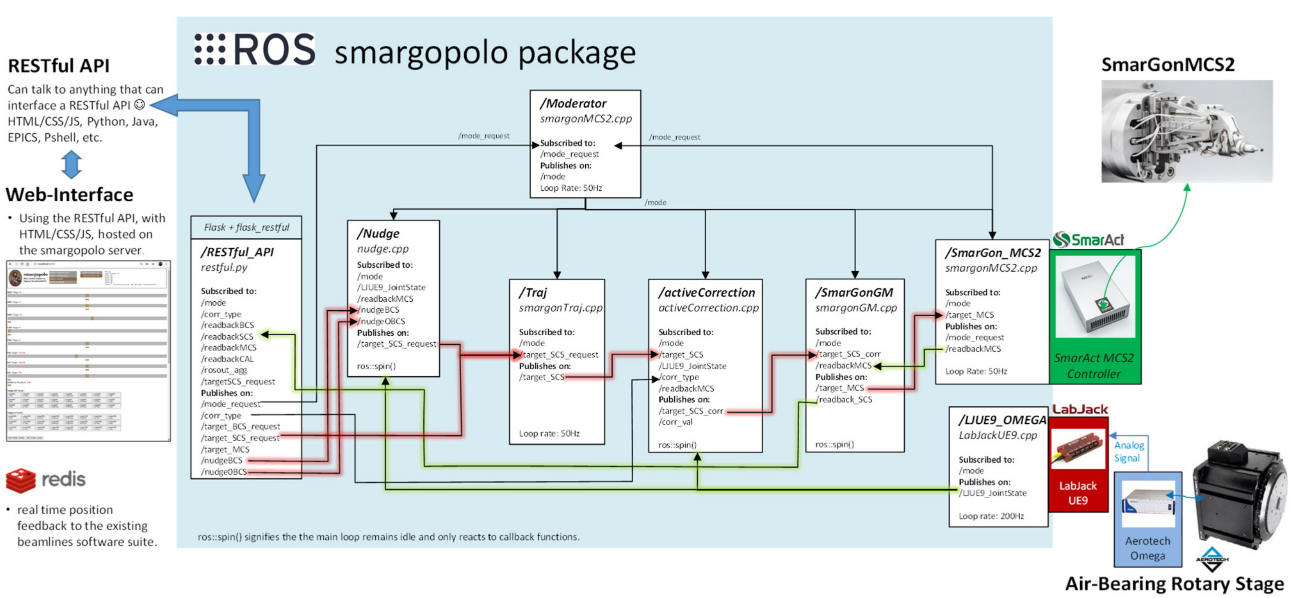

Figure 2: Smargopolo ROS package system architecture. Each box represents a module in the microservice architecture, and the lines represent message flow. Most modules are C/C++ compiled executables, /RESTful_API is a Python script. Red lines show the message flow in actuation direction, green lines show readback message flow.

ISBN: 978-3-95450-250-9 ISSN: 2673-5520 doi:10.18429/JACoW-MEDSI2023-THOAM02

Interfacing can be extended with flexiblity. ROS is bilingual and allows modules to be written in Python or in C/C++, depending on the required performance. The RESTful API was implemented in Python using flask & flask_restful. Utilising this API, a user friendly web-interface (HTML/CSS/JavaScript) was written, and is in frequent use. The beamline control software [7] interfaces the API from code written in Java & Python. The SLS beamline software suite also uses a redis database for real time status & position tracking of devices. There was no issue adding this into the Python code of smargopolo.

CALIBRATION

The conversion from user coordinates into motor coordinate is done with an inverse kinematics model (in the opposite direction, it's the direct kinematics model which transforms motor positions into user coordinates). While these geometrical models can be implemented with whatever complexity is required, it is often more efficient to model the geometry with easily verifiable lengths and angles, while making simplifications regarding orthogonality and parallelism. Non-linear effects, like gravitational sag, mounting and bearing inaccuracies, etc. are more difficult to model geometrically, and may vary even amongst devices of the same build.

The concept is to measure the remaining residual systemic error, and to actively correct for it in operation. We rely on the system's repeatability to improve accuracy.

In theory, for every point in the entire workspace, a correction vector must be known. For SmarGon this means, in 6 dimensional space (3 linear + 3 rotational coordinates) corrections in 6 dimensions need to be known.

In practice we can concentrate on a sub-portion of the workspace which is of high importance, and deduce the rest. This is driven by a time vs. performance trade-off of the calibration procedure. Re-calibration might be necessary if there was collision incident, or if a spare part has needed to be exchanged. In such cases, the calibration procedure must be swift, easy to perform and reliable, to be able to resume beamline operation quickly.

The workspace coordinates of main concern for the MX application are the ω and the χ (and φ) axes. Radial and axial runout of these rotations must be kept to minimum. Calibration routines were therefore focused on minimizing these runout errors. In MX, this performance metric is referred to as the sphere of confusion (SoC).

ω is used for every MX data acquisition run. The main contributing factor to runout error is gravitational sag of the mechanical structure. This is rather repeatable. Calibration typically reduces +/− 5 µm errors to +/− 1 µm.

The χ angle is primarily used to change orientation of the crystal. It has the largest run-out error, due to the translation-to-rotation linkage, where the geometrical model doesn't perfectly match with reality. Errors in the region of 30 µm have been observed. With calibration this can be reduced to < 7 µm for χ: [0, 90°], or < 5 um for the commonly used χ: [0, 40°].

φ is more rarely used, and for practical reasons is not calibrated.

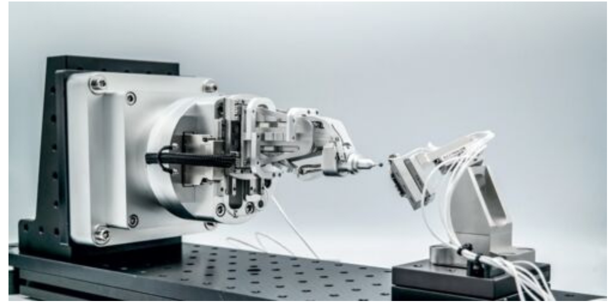

Figure 3: The calibration setup involves rotating a calibration sample, a sapphire sphere (D=2mm) around each of the rotation axes individually and measuring the runout in three dimensions (XYZ). This is negatively fed back into smargopolo as a translation.

In a practical calibration scene (Fig. 3), for ω, points (XYZ positioning errors) over the 360 range are collected every 0.1 degrees and averaged over 10 degrees. These are saved in a lookup table (LUT). χ can be stepped in increments of 10 degrees from 0 to 90, and at each step, a ω rotation is performed like above, and new points are added to the LUT.

This results LUT with 10*36 = 360 points, where for each point correction values in OX, OY & OZ directions are recorded.

In regular operation, this LUT serves as the basis for the active correction. Intermediate points are calculated with bilinear interpolation. With 360 points, this does not put much strain on the main control loop in smargopolo.

USER COORDINATES

SmarGon's coordinate system (SCS) (Fig. 4) corresponds to the coordinate system of PRIGo, where the X & Y axes rotate on the omega stage. The coordinates [OX, OY, OZ, CHI, PHI, OMEGA] describe position and orientation target of the sample. The vector [SHX, SHY, SHZ] describes a sample holder pin from the pin base to the centre of the crystal to be measured at the tip. Smargopolo continuously tries to fulfil the vector equation, so that the sample holder [SHX, SHY, SHZ] is orientated along [CHI, PHI, OMEGA], and positioned, so that the sample at the tip of the sample holder lies on the point [OX, OY, OZ].

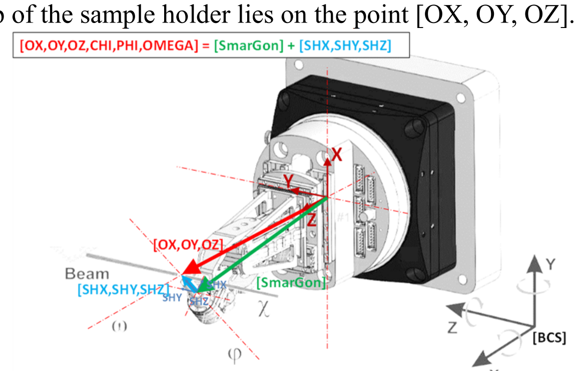

Figure 4: SmarGon's coordinate system (SCS) and vector equation that smargopolo constantly strives to fulfil. SCS rotates with ω, while the beamline coordinate system (BCS) does not.

ISBN: 978-3-95450-250-9 ISSN: 2673-5520 doi:10.18429/JACoW-MEDSI2023-THOAM02

SmarGon was designed for the following use case:

During installation of SmarGon at the beamline, technical staff calibrate it, so its rotation axes (ω, χ, φ) all intersect in one point (within tolerated runout errors). This intersection point is referred to as O in the SCS. O is set to lie on the ω axis (with OX & OY) at a given distance from the base (OZ = 190 mm).

Local beamline staff can then set up the beamline and translate the whole ω stage incl. SmarGon, so the ω axis intersects with the X-Ray at the given distance of 190 mm. O will then be in the centre of interest.

Now when users mount their samples, sample centring is done only via SHX, SHY & SHZ. Similar to a tool vector on an industrial robot, SH represents the Sample Holder vector, which will be different for every newly mounted sample. With SHX, SHY & SHZ, different parts of the sample can be brought into the centre of interest O. With the nudge function, relative motion along any given axis can be performed, so you can nudge the sample along the beamline axes (BCS), or along the axes of a viewing camera, to get it well centred.

Hence, when rotation around CHI, PHI & OMEGA is performed, the sample will stay in the point of interest O.

INTERFACING

Using the RESTful API, readback position can be called using the HTTP verb GET:

```
GET: smargopolo:3000/readbackSCS
```

A JSON object is returned, with the form:

{"SHX": 0.1, "SHY": 0.2, "SHZ": 18.3, "OMEGA": 90.0, "CHI": 20.0, "PHI": 5.0, "OX": -0.04, "OY": -0.18, "OZ": 189.30, seq": 765.0, "secs": 6543.0, "nsecs": 43210.0}

Setting a position can be done with the PUT verb:

```
PUT: smargopolo:3000/targetSCS?SHX=0.123&SHY=0.456
```

This will return the current set values as a JSON object.

There are also other commands for status readback, nudging (relative motion in BCS), referencing, and active correction. For practical use, a web-interface allows easy control of the system (Fig. 5). It uses the RESTful API.

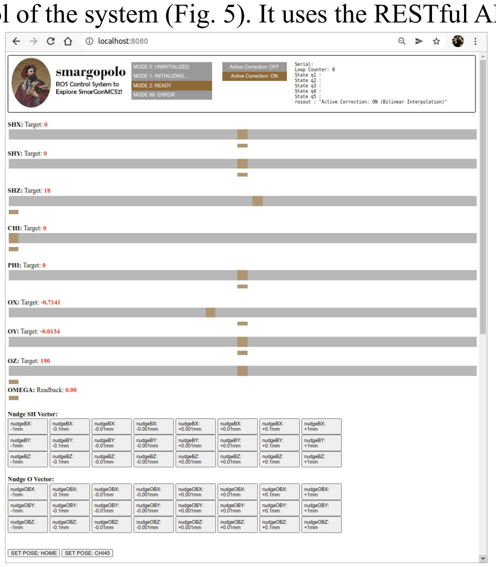

Figure 5: Smargopolo web-interface with double-sliders: the upper part is the move command, the thinner bar below is the current readback value. Nudge buttons below allow relative movement of SH & O in BCS.

APPLICATIONS OUTSIDE MX

A feature of SmarGon is that rotation around an arbitrary point can be performed, due to the use of a geometrical model in the control system. Compared to hexapod architectures, typically, larger rotation angles can be covered. Two rotations can even rotate indefinitely; ω: [−∞, +∞], χ: [0, 90°], φ: [−∞, +∞]. The system is also well adapted to orientation tasks where self-shadowing must be kept minimal.

An application outside the field of MX was for Small Angle Scattering Tensor Tomography (SAS-TT) experiments at the PXI beamline. A tomographic setup and multi-axis sample orientation was required. SmarGon could be re-purposed to allow orientation of the sample along axes commonly used in tomography experiments.

In another spontaneous setup for an experiment at beamline PXI, it was necessary to thread the 50 µm X-ray beam through a capillary of 100 µm inner diameter and 24 mm length. SmarGon was used to position the entrance of the capillary into the beam, and orientation could be scanned until the most intense signal could be detected.

CONCLUSION

With these improvements, SmarGon is now reliable enough to be constantly operated at all MX beamlines at SLS. Two devices have been in continuous 24/7 use for two years at beamlines PXI & PXII at SLS, with very satisfactory results. The replacement of PRIGo at PXIII, after 13 years of operation, is planned during the SLS 2.0 upgrade.

Thanks to the open platform, we are confident to be able to further optimise and adapt the design to accommodate emerging applications in the future.

ACKNOWLEDGEMENTS

The SLS MX Group would like to acknowledge the ongoing and fruitful collaboration between SLS and SmarAct GmbH.

REFERENCES

[1] S. Waltersperger *et al.*, "PRIGo: a new multi-axis goniometer for macromolecular crystallography," *J. Synchrotron Radiat.*, vol. 22, part 4, pp. 895-900, Jul. 2015. doi:10.1107/S1600577515005354

[2] SmarAct GmbH, http://www.smaract.com/en/smargon

[3] M. R. Fuchs *et al.*, "D3, the new diffractometer for the macromolecular crystallography beamlines of the Swiss Light Source," *J. Synchrotron Radiat.*, vol. 21, no. 2, pp. 340-351, 2014. doi:10.1107/S160057751400006X

[4] K. M. L. Smith *et al.*, "SDU – software for high-throughput automated data collection at the Swiss Light Source," *J. Synchrotron Radiat.*, vol. 30, part 3, pp. 538-545, May 2023. doi:10.1107/S1600577523002631

[5] I. Martiel *et al.*, "The TELL automatic sample changer for macromolecular crystallography," *J. Synchrotron Radiat.*, vol. 27, part 3, pp. 860-863, May 2020. doi:10.1107/S1600577520002416

ISBN: 978-3-95450-250-9 ISSN: 2673-5520 doi:10.18429/JACoW-MEDSI2023-THOAM02

[6] M. Quigley *et al.*, "ROS: an open-source Robot Operating System," *ICRA workshop on open source software*, vol. 3. no. 2, 2009.

[7] J. A. Wojdyla *et al.*, "DA+ data acquisition and analysis software at the Swiss Light Source macromolecular crystallography beamlines", *J. Synchrotron Radiat.*, vol. 25, part 1, pp. 293-303, Jan. 2018. doi:10.1107/S1600577517014503

ISBN: 978-3-95450-250-9 ISSN: 2673-5520 doi:10.18429/JACoW-MEDSI2023-THOAM04

OVERALL PROGRESS ON DEVELOPMENT OF X-RAY OPTICS MECHANICAL SYSTEMS AT HIGH ENERGY PHOTON SOURCE (HEPS)

Shanzhi Tang[†, 1], Jianye Wang, Weifan Sheng[1], Haihan Yu, Zhongrui Ren, ZinaOu, Ruzhen Xu, Ruiying Liao, Luhan Ma, Xiaohui Kuang, Hao Liang, Ming Li[1], Hanjie Qian, Yuhui Dong[‡, 1]
Institute of High Energy Physics, Chinese Academy of Sciences Beijing, China
[1]also at University of Chinese Academy of Sciences, School of Nuclear Science and technology, Beijing, China

Abstract

High Energy Photon Source (HEPS) regarded as a new 4th generation synchrotron radiation facility, is under construction in a virgin green field in Beijing, China. The X-ray optics/mirror mechanical systems (MMS) play an important role, which would be expected to be designed carefully and rigidly for the extremely stable performance requirement of HEPS. In addition, there are indeed big challenges due to so many types of mirror systems, such as white beam mirror (WBM), harmonic suppression mirror (HSM), combined deflecting mirror (CDM), bent mirror, Nano-KB, and the transfocator of Compound refractive lens (CRLs), etc. Therefore, overall progress on design and manufacture of the MMS is introduced, in which a promoting strategy and generic mirror mechanical system as a key technology is presented and developed for the project of HEPS. Furthermore, ultra-stable structure, multi-DOF precision positioning, Eutectic Gallium Indium (E-GaIn)-based vibration-decoupling water-cooling, clamping, and bending have always been prior designs and considerations.

INTRODUCTION

To meet the extreme requirement of 4th generation synchrotron radiation facility, many efforts and design considerations on the X-ray optics mechanical system are presented, such as an ultra stability mirror system or benches [1-7], a better mounting and water-cooling of mirror [8], and an improved bender [9].

HEPS is a new and under construction 4th generation synchrotron radiation facility. It has a 6 GeV storage ring with a circumference of 1360.4 m and a natural emittance of 34.2 pm [10]. The ground stability of vibration should be required to 25 nm @1~100 Hz. So, the stability of mechanical engineering design of synchrotron instrument and device becomes a critical important issue. Besides, there are 15 beamlines in Phase I of HEPS, which has so many types of mirror systems, such as white beam mirror (WBM), harmonic suppression mirror (HSM), combined deflecting mirror (CDM), bending mirror, Nano-KB, and the transfocator of Compound refractive lens (CRLs), etc. This bring out another big challenge. So, to deal with the problems, a promoting strategy is presented at HEPS. The steps as follows: firstly, a high-performance generic mirror mechanical systems (GMMS) is first proposed and developed. Secondly, GMMS-based variable mirror mechanical system or Transfocator will be designed and manufactured. Actually, GMMS would been also applied for the main mechanical system of Laue double bent crystal monochromator (LDBM). Finally, lots of specific mechanical designs in vacuum will be implemented, including bender, water cooling, support and clamping, and other custom-made mechanisms.

† tangsz@ihep.ac.cn and
‡ dongyh@ihep.ac.cn

OVERALL DESIGN STRATEGY

It is well known that base support, positioning, and clamping are the three common main functions of the mirror mechanical system (MMS), although the types of MMS are different. So, a high-performance MMS is presented and developed, which not only features ultra-stable, bust also has a high accuracy attitude adjustments and stress-free mirror mounting. More importantly, it is expected to be a generic MMS (GMMS) for a large number and variety mirrors at HEPS. Therefore, a strategy of GMMS is proposed as shown in Fig. 1. Moreover, a customized GMMS-based design scheme will be formed as shown in Fig. 2.

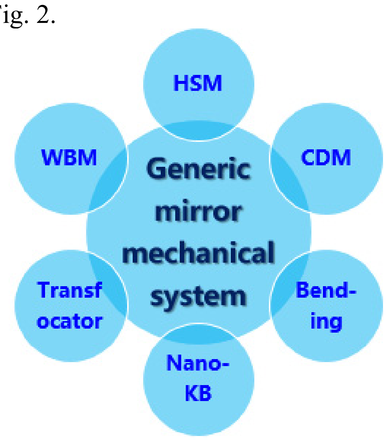

Figure 1: The promoting strategy of design for MMS.

Compared to the existed mirror mechanical systems, the vibration stability of ≤ 25 nrad rms@1-120 Hz and 5-DOF positioning-motorized are extracted as the main technical parameters of GMMS. And it must be compatible for horizontal reflection mirror and vertical reflection mirror as shown in Fig. 3. It is that the performance of yaw adjustment mechanism is equivalent to pitch. Be-

ISBN: 978-3-95450-250-9 ISSN: 2673-5520 doi:10.18429/JACoW-MEDSI2023-THOAM04

cause the yaw angle of the horizontal reflection layout is same to the pitch of the vertical for the same system. Correspondingly, the pitch of the horizontal is also same to the yaw of the vertical.

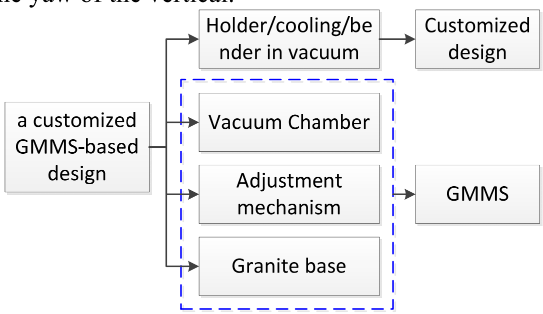

Figure 2: A customized GMMS-based design scheme.

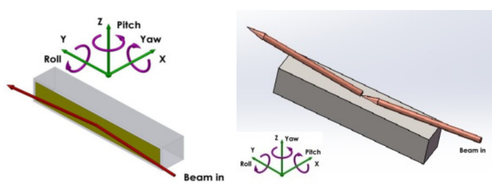

(a) (b)

Figure 3: Layouts of horizontal and vertical reflection mirrors. (a) Horizontal reflection. (b) Vertical reflection.

GMMS DESIGN

According to the standard coordinate system defined by HEPS beamlines as shown in Fig. 3, the main parameters of 5-DOF is shown in Table 1.

Table 1: Main Parameters of 5-DOF for GMMS

	Parameter	Resolution	Range	Type
1	Horiz.Translation (Tx)	≤ 1 µm	±10 mm	motorized
2	Vert. Translation (Tz)	≤ 1 µm	±10 mm	motorized
3	Horiz.angle (Rz)	≤ 0.1 µrad	±10 mrad	motorized
4	Vert.angle (Rx)	≤ 0.1 µrad	±10 mrad	motorized
5	Roll (Ry)	≤ 10 µrad	±17.5 mrad	motorized

To ensure adequate stiffness, the overall mechanical structure of GMMS based on the combination of a multi-layer granite adjustment mechanism and a double-disc flexure hinge angle mechanism is designed. As shown in Fig. 4, the multi-layer granite adjustment mechanism can provide 4-DOF with motorized type in air of Tx, Tz, Rx, and Ry. The granite wedges lift based on sine bar method are employed for adjustments of the height Tz and angle Rx instead of the traditional cantilever support structure. Self-locking is another key point used for each DOF to guarantee the static stiffness and stability. Besides, the simplified double-disc flexure hinge angle mechanism can realize the other degree of Rz with a PiezoMotor in vacuum. The monolithic flexure hinge is designed as shown in Fig. 5, which can be cut by slow wire processing. It has a higher stiffness than by assembling. By FEA-modal simulation, the mechanical structure has been optimized and many times iteration designed, which has an adequate 1st mode eigenfrequency, as shown in Fig. 6.

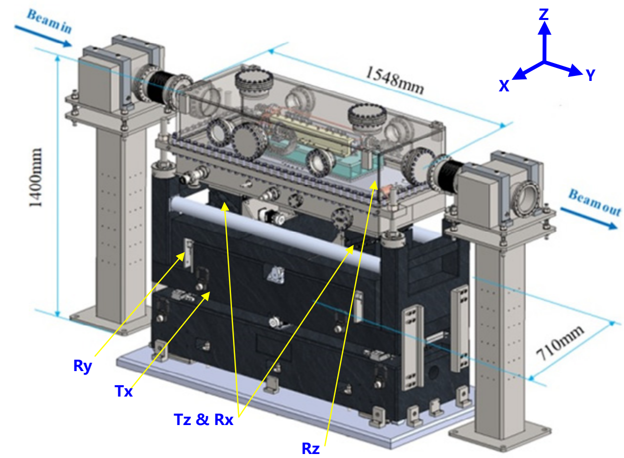

Figure 4: The overview of the typical design of GMMS.

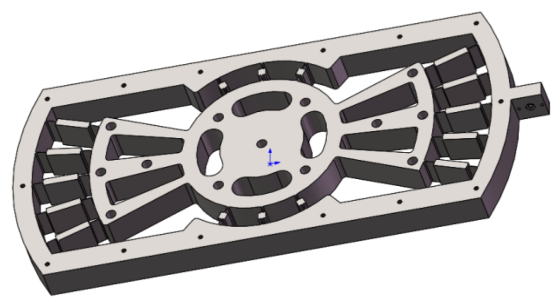

Figure 5: Monolithic flexure hinge.

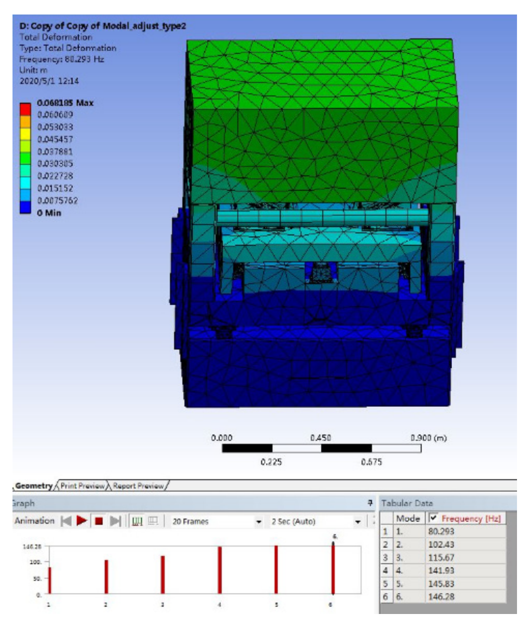

Figure 6: FEA-Modal simulation.

12th Int. Conf. Mech. Eng. Design Synchrotron Radiat. Equip. Instrum. MEDSI2023, Beijing, China JACoW Publishing
ISBN: 978-3-95450-250-9 ISSN: 2673-5520 doi:10.18429/JACoW-MEDSI2023-THOAM04

A CUSTOMIZED GMMS-BASED DESIGN

As is mentioned above, specified mechanical structure in vacuum need to be a customized GMMS-based designed, especially bender, watercooled & mounting assembly unit.

Firstly, independent four-shaft bending with gravity association design method is presented by Prof. Ming Li at HEPS. Based on the method, the high stiffness bender is customized designed, as shown in Fig. 7. It performs higher stiffness and stability than thin or leaf spring type bender although it takes up more space in the mirror ends.

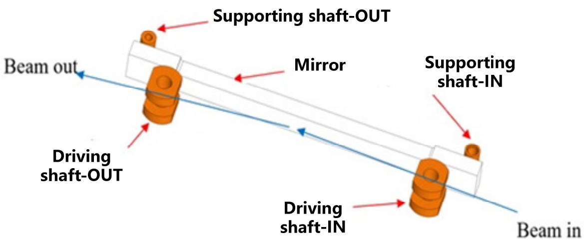

Figure 7: Principle diagram of an independent four-shaft bending.

Secondly, a bath watercooled structure filled eutectic Ga-In alloy is designed for the white beam mirror with non-bent or bent. It can overcome the problem caused by the vibration impact of fluid and the water pipes in the case of ensuring sufficient cooling capacity. As shown in Fig. 8, mirror slope error can be controlled based on geometrical optimized by FEA for different heat load or variety energy. Furthermore, In order to avoid corrosion effect between Eutectic Ga-In alloy and heat sink metal for X-ray optics cooling, a novel coating of tungsten (W) is presented and developed at HEPS [11].

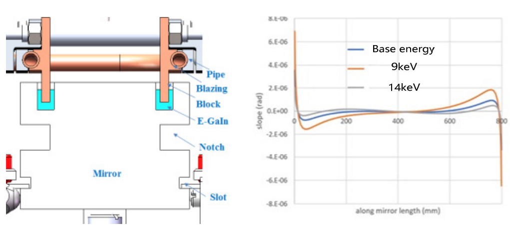

(a) (b)

Figure 8: Principle diagram of a bath watercooled structure filled eutectic Ga-In alloy. (a) Structure. (b) Thermal deformation controlled based on geometrical optimized by FEA.

Thirdly, the clamping and combination of double mirrors system, as a specified structure, has also considered and developed, which is usually need by CDM and HSM, as shown in Fig. 9. For the former, clamping and mechanical combination positioning need to be carefully considered. And for the latter, it is not only the mounting and fixing quasi-static structure of traditional parallel double mirrors, but also needs the kinetic design of the fixed exit height similar to the T-type compensation mechanism of monochromators, as shown in Fig. 9 (b).

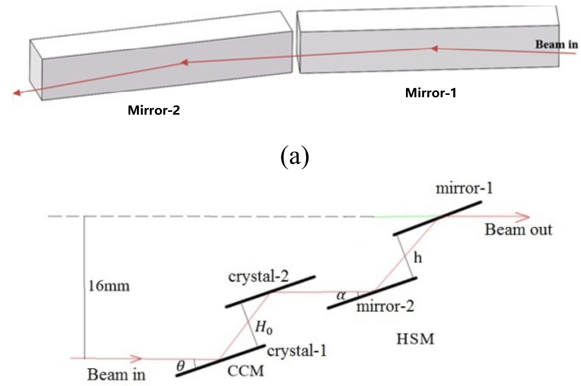

(b)

Figure 9: Principle diagram of the double mirrors system. (a) CDM. (b) Complicated HSM for the height compensation of the channel cut mono. (CCM) at B8-XAS beamline.

Finally, transfocator, a switch mechanism of CRLs regarded as an effective high energy X-ray component is developed. In traditional design, N sets of motors or actuators for the motion and state switch of the N arms in which each arm is as a stack filled CRLs. It looks bulky and inflexible when N becomes larger due to the series structure. To deal with this problem, a compact transfocator by the parallel driving structure is presented, as shown in Fig. 10. It just employs 2 sets for N arms, which has a simplified & stable structure and a longer work distance.

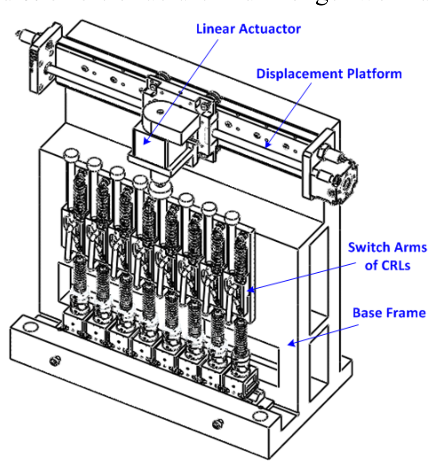

Figure 10: A compact transfocator.

Besides, an in-vacuum motion mechanism similar to the above HSM is designed for the LDBM of B1-EM beamline. This is so that the GMMS can also be applied here.

MANUFACTURE, ASSEMBLY, AND TEST

Now, the first GMMS, as the application of BE-WBM, has been manufactured and delivered in December 2022. It is not only a pure GMMS, but also has a customized watercooled mirror clamping. It is proved to be effective and feasible by assembly and test.

Than, the 9 sets of GMMS as first batch has been manufactured and delivered in July 2023. FAT passed

ISBN: 978-3-95450-250-9 ISSN: 2673-5520 doi:10.18429/JACoW-MEDSI2023-THOAM04

smoothly that indicates the design, manufacture, and assembly are mature and available, as shown in Fig. 11. And the next step is to finish manufacturing the second batch (10 sets) in the middle of next year.

Figure 11: FAT pictures of first batch of GMMS.

So, the GMMS can be evolved or directly applied for many kinds of mirrors, e. g. the white beam mirror (WBM) or WBM-bender, harmonic suppression mirror (HSM), combined deflecting mirror (CDM), bent mirror, Nano-KB, and the transfocator of Compound refractive lens (CRLs), etc. As shown in Table 2. There are the total 20 sets of GMMS and customized MMS. Therefore, the challenge will be derived from mirror installation and transportation which need many rigid and careful considerations.

Table 2: Beamlines Optics/Mirrors at HEPS Phase I

Beamline	**Optics/mirror**	**Quantity**
B1-EM	LDBM	1
B2-NAMI	WBM-bender Transfocator	2
B3-SDB	Transfocator	1
B5-HX-HERS	WBM	1
B6-HPB	Transfocator	1
B8-XAS	WBM-bender Bent mirror HSM	3
B9-LODISP	Transfocator 1 Transfocator 2	2
BA-MX	Transfocator	1
BB-pink-SAXS	CDM	1
BC-high-NESS	Bent mirror	1
BD-TEX	WBM-bender Bent mirror HSM	3
BE-TXM	WBM Bent mirror	2
BF-TB	Bent mirror-TF	1
	Total:	20

CONCLUSION

A promoting strategy of MMS is presented for the development of large quantity and variety type optomechanical systems. And the corresponding conclusions are as follows:

1) A customized GMMS-based design strategy has been implemented for beamlines at HEPS, in which generic and specific are both effectively considered.

2) Progress on GMMS manufacturing and assembling imply that an ultra-stable and 5-DOF mechanical system is achievable and fine so that the first batch has been already delivered.

3) The various mirror benders or clamping & water-cooling or special-mechanisms in vacuum are also smooth in process of design and fabrication.

REFERENCES

[1] T. Mairs, R. Baker, C. Clavel, *et al.*, “Upgrading beamline performance: ultra stable mirror developments at ESRF”, in *Diamond Light Source Proceedings,* vol. 1, no. MEDSI-6, UK, 2010. doi:10.1017/S2044820110000663

[2] R. Baker, R. Barrett, C. Clavel, *et al.*, “New generation mirror systems for the ESRF upgrade beamlines”, *J. Phys.Conf.,* vol. 425, p. 052015, 2013.

[3] R. R. Geraldes, G. V. Claudiano, L. M. Volpe, *et al.*, “The design of exactly-constrainted X-ray mirror systems for SIRIUS”, in *Proc. MEDSI’18,* Paris, France, Jun. 2018, pp.173-178. doi:10.18429/JACoW-MEDSI2018-WEOAMA04

[4] R. R. Geraldes, A. Sikorski, C. S. N. C. Bueno, *et al.*, “Granite benches for SIRIUS X-ray optical systems”, in *Proc. MEDSI’18*, Paris, France, Jun. 2018, pp. 361-364. doi:10.18429/JACoW-MEDSI2018-THPH12

[5] S. Bean, V. De Andrade, A. Deriy, *et al.*, “A new ultra-stable variable projection microscope for the APS upgrade of 32-ID”, in *Proc. MEDSI’20*, Chicago, USA, Jul. 2020, pp. 211-214. doi:10.18429/JACoW-MEDSI2020-TUPC15

[6] C. A. Preissner, S. J. Bean, M. Erdmann, *et al.*, “A family of high-stability granite stages for synchrotron appllication”, in *Proc. MEDSI’20*, Chicago, USA, Jul. 2020, pp. 341-344. doi:10.18429/JACoW-MEDSI2020-THOA01

[7] G. B. Z. L. Moreno, S. A. L. Luiz, A. C. Pinto, *et al.*, “Tolerance-budgeting for ultra-stable KB systems”, *J. Phys. Conf.*, vol. 2380, p. 012074, 2022. doi: 10.1088/1742-6596/2380/1/012074

[8] L. Zhang, R. Barrett, K. Friedrich, *et al.*, “Thermal distortion minimzation by geometry optimization for water-cooled white beam mirror or multilayer optics”, *J. Phys.Conf.*, vol. 425, p. 052029, 2013.

[9] Z. Qiao, J. Anto, L. Assoufid, *et al.*, “Surface twist characterization and compensation of anelliptically bent hard X-ray mirror”, in *Proc. MEDSI’20*, Chicago, USA, Jul. 2020, pp. 99-102. doi:10.18429/JACoW-MEDSI2020-TUOA01

[10] Y. Jiao, G. Xu, X. H. Cui, *et al.*, “The HEPS project”, *J. Synchrotron Radiat.*, vol. 25, pp. 1611-1618, 2018. doi:10.1107/ S1600577518012110

[11] Shanzhi Tang, Tian He, Haihan Yu, *et al.*, “A novel coating to avoid corrosion effect between eutectic gallium–indium alloy and heat sink metal for X-ray optics cooling”, *Rev. Sci. Instrum.*, vol. 93, no. 12, p. 123102, 2022. doi:org/10.1063/5.0127785

ISBN: 978-3-95450-250-9 ISSN: 2673-5520 doi:10.18429/JACoW-MEDSI2023-THOAM05

MODELING THE DISTURBANCES AND DYNAMICS OF THE NEW MICRO CT STATION FOR THE MOGNO BEAMLINE AT SIRIUS/LNLS

G. S. Baldon*, G. S. de Albuquerque†, F. Ferracioli, G. B. Z. L. Moreno, R. R. Geraldes
Brazilian Synchrotron Light Laboratory (LNLS), CNPEM, Campinas, Brazil

Abstract

At the 4th generation synchrotron laboratory Sirius at the Brazilian Synchrotron Light Laboratory (LNLS), MOGNO is a high energy imaging beamline, whose Nano-Computed Tomography (CT) station is already in operation. The beamline's 120 nm × 120 nm focus size, 3.1 mrad × 3.1 mrad beam divergence, and 9×10^{11} ph/s flux operated at 21.5 keV, 39.0 keV, and 67.7 keV energies, allow experiments with better temporal and spatial resolution than lower energy and lower stability light sources. To further utilize its potential, a new Micro-CT station is under development to perform experiments with 0.5 µm – 55 µm resolution, and up to 4 Hz sample rotation. To achieve this, a model of the disturbances affecting the station was developed, which comprised: i) the characterization and simulation of disturbances, such as rotation forces; and ii) the modeling of the dynamics of the microstation. The dynamic model was built with the in-house developed Dynamic Error Budgeting Tool, which uses dynamic substructuring to model 6 degrees of freedom rigid body systems. This work discusses the trade-offs between rotation-related parameters affecting the sample-to-optics stability and the experiment resolution in the frequency domain integrated up to 2.5 kHz.

INTRODUCTION

The MOGNO beamline [1] is the hard x-ray micro- and nano-computed tomography (CT) beamline at Sirius, the 4th generation synchrotron light source at the Brazilian Synchrotron Light Laboratory (LNLS). As illustrated in Fig. 1, the beam is generated at a dipole, passes through a slit, and is primarily focused in the horizontal plane with an elliptical mirror (M1). Next, the beam's focus size (120 nm×120 nm) and position, 3.1 mrad conical divergence, and energy (21.5 keV, 39.0 keV, and 67.7 keV), is finally achieved through a Kirkpatrick-Baez (KB) mirror system, with two stripes and multi-layer coating (Tungsten and Boron Carbide), which allows the beam to reach the sample with a photon flux of 9×10^{11} ph/s. The main detector of the beamline is a PiMega 135D [2], located 27 m away from the focus, which delivers a maximum frame rate of 2×10^3 fps with a 85 mm × 85 mm sensor consisting of a 1536 × 1536 pixel array.

The sample may be at one of the two experimental stations of the beamline: the nanostation, currently under commissioning; or at the microstation, now under construction, and whose error budget is the main subject of this work. Both take advantage of the high photon flux and high frame rate

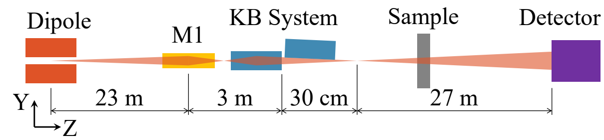

Figure 1: The MOGNO beamline layout. Approximate distances. Z is parallel to the beam, and Y is the vertical upwards.

of the detector to execute time-resolved CT scans, where they can be acquired periodically to observe transient phenomena in in-situ experiments, such as flow through porous media. The time resolution for the nanostation is limited at 5 s, and, for the microstation, at 0.5 s. Additionally, both stations were designed to allow high-throughput CT scans, where the samples are exchanged by a robot without the need of the researcher doing it manually, which greatly improves the speed of experiments with large batches.

The main difference between the stations is the resolution and field of view (FOV): the nanostation was designed to perform CT scans at higher resolution at the cost of smaller FOV and smaller sample sizes. Its sample stage allows movement on a 7 m-long granite rail along the beam direction, resulting in experiments that can range from 120 nm to 13 µm resolution and from 150 µm to 20 mm FOV; the microstation will have a 30 m-long rail, resulting in resolutions between 500 nm and 55 µm, and from 800 µm to 85 mm FOV.

In this work, the objective is the development of a model to analyze the disturbances and the error budget of the microstation. As source and detector stabilities have been designed to meet the more demanding requirements of the nanostation, the main source of error for the microstation is the vibration of the sample itself.

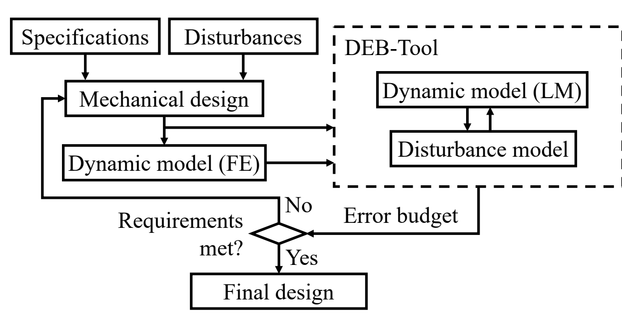

Figure 2: The specifications and disturbances are boundary conditions to the design, which is iterated to meet the requirement, attested through models. Here, FE means finite element, and LM means lumped mass. Adapted from [3].

* gabriel.baldon@lnls.br
† guilherme.sobral@lnls.br

ISBN: 978-3-95450-250-9 ISSN: 2673-5520 doi:10.18429/JACoW-MEDSI2023-THOAM05

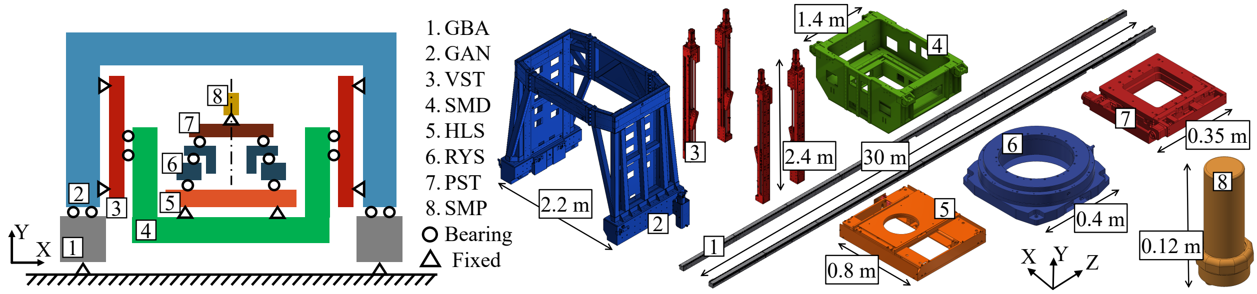

Figure 3: On the left is a schematic of the design of the microstation. And on the right are the detailed parts illustrated in the schematic.

METHODOLOGY

The methodology followed in this work can be summarized with the schematic shown in Fig. 2. This work starts with the mechanical design, which involves the conceptual and detailed design of the system. In this work, the detailed design is important for the disturbance models, as it provides crucial information about the geometry and inertia of system components, improving the fidelity of the model [3].

The dynamic model serves as an ideal representation of the system's dynamics. Two methods are employed for this purpose: finite element (FE) software ANSYS and a lumped mass (LM) approach using the in-house developed DEB-Tool (Dynamic Error Budgeting Tool). The FE-based models provide high accuracy results, but are computationally intensive. While LM models, which fundamentally represent rigid bodies, are much more efficient, and can generate results without the need of a detailed design, but require adjustments to account for flexibility.

At LNLS's beamline engineering teams, FE models are used discerningly. In most cases, an FE model of the complete system in impractical, so these are mostly used to model subsystems to feed information for the LM models. Here, the FE model serves as a high-fidelity reference, guiding adaptations to tune the LM model within DEB-Tool, which is the primary model for aiding the iterative design process.

The tuning of the LM model is done by dividing bodies into smaller parts to represent their flexibility, and is aided by looking at the mode shapes generated with the FE model. The results of such tuning are deemed good when the differences in eigenfrequency between the LM and the FE models are within 5 % for the first five eigenmodes.

Both FE models on ANSYS and the LM models on DEB-Tool can use power spectral density (PSD) curves as input to model disturbances, but in this work only DEB-Tool is used for vibration propagation. The input PSDs can be in terms of force, acceleration, velocity or displacement, and with a complete dynamic model, these inputs can return an output PSD on any node of the model. Here, the disturbances considered are two: the floor vibration, with a displacement PSD, and the rotating unbalance, with a force PSD.

Besides the vibration results from the dynamic model, the error budget includes the spindle error motion, which is how the rotational motion of the sample deviates from a perfect Ry spin. The total combination of these errors must be within a specified limit, and if this requirement is not met, design changes must be made. For the microstation, the limit depends on the resolution of the image, so the critical value is 500 nm peak-to-peak.

MECHANICAL DESIGN

Following the methodology described in the previous section, the microstation design was iteratively changed along the design phase. In its current stage, the station is divided into two gantries, one for sample positioning and the other for supporting auxiliary systems, e.g., the high-throughput module. This allows each gantry to be designed independently, focusing on their different requirements: stiffness, stability, and repeatability for the sample positioning gantry; and structural integrity for the other gantry. A simplified schematic of the sample positioning structure (focus of this work) and its detailed parts are shown in Fig. 3.

A 30 m-long granite base (GBA) coupled with two different mechanisms, granite airpads and linear guides, allows the movement of the microstation along the Z direction. Granite airpads offer repeatability when moving and high stiffness when static [4], and linear guides are used when transitioning between the 3 m-long granite beams that compose the GBA. The movement is actuated using a servo motor with a rack and pinion mechanism attached to the side of the base.

The gantry (GAN) is the trapezoidal steel frame structure that supports four vertical stages (VST) responsible for vertical sample movement, utilizing linear guides and independent servo motors for actuation.

The sample module (SMD) holds a stack of mechatronic stages for sample positioning and rotation, and it is kinematically mounted to the VST with canoe-balls [5]. The horizontal long stroke stage (HLS) provides a 300 mm range for sample positioning. Atop the HLS is the rotational stage (RST), a commercial item by Physik Instrumente (PI) with high precision air bearings, enabling infinite rotation and high-speed operation (up to 7 Hz).

A planar stage (PST) aligns the sample with the RST's rotation axis, offering a range of ±24 mm, allowing for high-resolution imaging of regions near the sample edge and enabling helical CT scans for noise reduction [6]. However, the PST introduces load unbalance on the RST, which is

ISBN: 978-3-95450-250-9 ISSN: 2673-5520 doi:10.18429/JACoW-MEDSI2023-THOAM05

addressed by an autobalancing system currently under development by MI-Partners, a Dutch precision engineering firm. The disturbances modeled here consider the microstation with and without the autobalancing system.

DYNAMIC MODEL

As described previously, the dynamic model is done here with two methods: FE and LM.

Finite Element Model

The finite element model was developed in ANSYS Mechanical. It uses the CAD model as input, with simplifications to the geometry, eliminating small holes, fillets, chamfers, and other features that do not affect structural performance but require a finer mesh. Contact between bodies is modeled with the contact stiffness function, and the stiffness values follow empirical data gathered at LNLS from previous projects.

Lumped Mass Model

In the CAD software the bodies are subdividing according to the results of the FE model. From that, the parameters for DEB-Tool, including position of disturbance sources, are automatically exported with Inventor Export Tool (IET), an in-house VBA script developed for this purpose. In DEB-Tool, each connection between bodies is modeled as an elastic support with proportional damping. Figure 4 shows the resulting LM model.

The stiffness of each elastic support is iteratively tuned to match the mode shapes of the FE model, and its initial values are either estimated analytically, or come from experimental data. The results of the modal analysis after this process can be found in Table 1, showing the eigenfrequencies found with each model (LM and FE), and the error between them.

DISTURBANCES

With the dynamic model in DEB-Tool in agreement with the FE model, the next step is to introduce the disturbances and estimate the output errors. The two disturbances modeled were the floor vibration and the rotational unbalance.

Table 1: Modal Analysis Results with FE and LM Models

Mode	Mode shape	f [Hz] LM	f [Hz] FE	Error [%]
1	Rz	26	25.9	-0.3
2	Rx	35.1	36.1	3
3	Rx	49	48.2	-2
4	Ry	53	54.2	2
5	Y	77	78	1

The floor vibration was measured in 6 degrees of freedom (DOF) using two Wilcoxon 731A seismic accelerometers. Each can measure acceleration in 1 DOF up to 450 Hz, with a peak of 0.5 g, and two of these combined can be used to measure ground rotational vibration. The measured signal is processed to find the displacement and given as input in DEB-Tool as PSD from 1 Hz to 450 Hz.

The rotational unbalance was modeled with a simple dynamic model, to find the amplitudes of reactions at the stage bearing (point O in Fig. 4(c)) in 6 DOF, given rotation speed ω, mass m_d, height of the center of gravity (COG) h_d, and unbalance distance u_d, as shown in Eq. (1). These amplitudes are then used as a multiplicative factor in DEB-Tool for a PSD of a unitary sine wave at the rotation frequency (Eq. (2)), since the forces will be a single sine with the same frequency as the rotation speed. In the case of using an autobalancing system, the specification is that it will have a mass of up to 70 Hz and will balance the system to 1 N amplitude residual force. To model this into the system, the same approach is used as before, only changing the unbalance distance to result in the 1 N amplitude (Eq. (3)).

$$\begin{cases} F_x = F_z = m_d\, u_d\, \omega^2 \\ M_x = M_z = \left(m_d\, u_d\, \omega^2\right) h + \left(m_d\, g\right) u_d \\ F_y = M_y = 0 \end{cases} \tag{1}$$

$$\mathrm{PSD}_{F_x,\omega} = F_x^2\, \mathrm{PSD}(\sin(\omega t)) \tag{2}$$

$$u_{d,auto} = m_d^{-1}\, \omega^{-2} \tag{3}$$

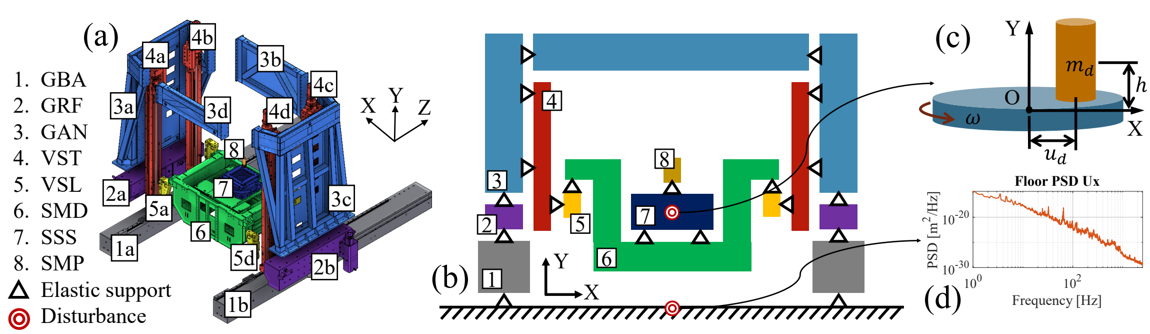

Figure 4: The 3D CAD model, in an exploded view, built in Autodesk Inventor used as input in IET (a). The lumped masses and connections used in DEB-Tool (b). And the modeled disturbances: a dynamic model for rotational unbalance (c), and the measured PSD for the floor vibration (d).

ISBN: 978-3-95450-250-9 ISSN: 2673-5520 doi:10.18429/JACoW-MEDSI2023-THOAM05

With the input PSD of the disturbances, DEB-Tool uses the dynamic model to output the displacement PSDs, cumulative power spectra (CPSs), or cumulative amplitude spectra (CASs) at any point of interest (POI) in the model. Here, the POI is the COG of the sample. The result is also divided by contribution: in this case, for each DOF, three curves are output, one for the contribution of the floor, one for the rotational unbalance, and one for the total displacement. Figure 5 shows the output CPS of the sample COG in the X direction with floor vibration and an unbalance of 15 mm of a 40 kg mass rotating at 2 Hz. The contribution of the unbalance to the final vibration is about 40 times larger than the contribution of the floor vibrations on the horizontal direction X, and about 1.5 times on the vertical direction Y.

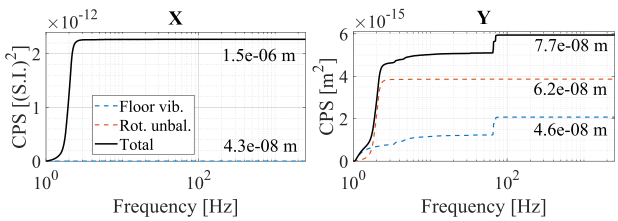

Figure 5: Resulting CPS of sample COG displacement in X (left) and Y (right) directions. The values at the end are the cumulative RMS displacements from each contribution, integrated up to 2.5 kHz.

ERROR BUDGET

Besides the error from the dynamics, the other error that needs to be considered for the microstation is the spindle error motion. Combined, they must total to less than the resolution of the image, which is 500 nm at most. In root mean squared (RMS) terms, the total error of the system must be less than 83 nm RMS on each direction of the image plane (X and Y).

The spindle error motion is a characteristic of the the rotation stage, and it is measured at a spindle error analyzer (SEA) [7]. The measurement is done with loading representative cases: no load at all, to measure the performance of the stage alone; 40 kg load, unbalanced to 20 mm, and rotating at 2 Hz representing the unbalanced system; and 70 kg load, balanced and rotating at 2 Hz, to represent the autobalancing system. The last two cases are the ones used in the error budget. The errors measured with the SEA are on X, Y, Z, Rx, and Rz directions, and these can be manipulated to find the translation of the sample COG, which is at a higher position than the metrology target used in the SEA.

The SEA measurements can be divided into two categories: synchronous (or repeatable) and asynchronous (or random). The synchronous error is the part of the error that repeats every rotation; it is mostly due to the bearing form errors, and can be compensated with metrology and calibration procedures. The asynchronous part is the part that is different every rotation, and can be modeled as random noise; this error can be compensated with in-situ metrology (that measure the spindle error during the tomography [8]), but not with calibration, as it is not repeatable.

Combining the errors, the error budget for the microstation can be analyzed, and its results are shown in Table 2. The bottom three rows show the combination of all the errors, linearly summed; "with calibration" removes the synchronous error from spindle error motion; and "with metrology" removes the synchronous and asynchronous errors. It is important to note that the calibration and the in-situ metrology would have errors of their own, but based on the stability of our SEA measurement system, that error would be of the order of 10 nm, which is much less than the synchronous error that it would be compensating.

Table 2: Error budget of the microstation. All values in nm RMS. For 500 nm resolution, the total error must be less than 83 nm RMS.

Source	W/o Auto.		W/ Auto.	
	X	Y	X	Y
Dynamics	1500	77	46	46
Spindle sync.	220	85	231	64
Spindle async.	25	27	26	17
Total	**1745**	**189**	**303**	**127**
W/ calibration	**1525**	**104**	**72**	**63**
W/ metrology	**1500**	**77**	**46**	**46**

From these results it can be concluded that the microstation will only be able to perform to its full specifications with the addition of the autobalancing system and at least some calibration. Otherwise, it will be limited to either lower resolutions, lower rotation speeds, or shorter unbalancing distances. Another possibility would be the addition of a metrology system between the floor and the sample, which would be able to compensate the dynamic vibration of the structure, but that seems to be a more expensive and less effective solution than the autobalancing system, as it would probably need high performance metrology at a long distance due to the geometry of the microstation.

CONCLUSION

The dynamics and the disturbances of the microstation have been modeled as a way to help the design process. Here, it was shown how this methodology led to the decision of an autobalancing system, and how the experiments will have to be limited while the autobalancing system is under development.

ACKNOWLEDGMENTS

The authors are grateful for all the support given by our fellow colleagues at LNLS, especially the MOGNO, PLL, OPT, MEP, and MArÉ groups; for the insights from the team at MI-Partners; and also for the funding provided by Petrobras, Equinor, and the Brazilian Ministry of Science, Technology and Innovation.

ISBN: 978-3-95450-250-9 ISSN: 2673-5520 doi:10.18429/JACoW-MEDSI2023-THOAM05

REFERENCES

[1] N. L. Archilha *et al.*, "MOGNO, the nano and microtomography beamline at Sirius, the Brazilian synchrotron light source", *J. Phys.: Conf. Ser.*, vol. 2380, p. 012123, 2022. doi:10.1088/1742-6596/2380/1/012123

[2] The Pimega 135D 2022, https://www.pitec.co/pimega-135d

[3] R. R. Geraldes *et al.*, "Predictive modeling through Dynamic Error Budgeting applied to the High-Dynamic Double-Crystal Monochromator for Sirius light source", *Precis. Eng.*, vol. 77, pp. 90–103, 2022. doi:10.1016/j.precisioneng.2022.04.009

[4] R. R. Geraldes *et al.*, "Granite Benches for Sirius X-ray Optical Systems", in *Proc. MEDSI'18*, Paris, France, Jun. 2018, pp. 361–364. doi:10.18429/JACoW-MEDSI2018-THPH12

[5] A. H. Slocum, "Kinematic couplings: A review of design principles and applications", *Int. J. Mach. Tools Manuf.*, vol. 50, no. 4, pp. 310–327, 2010. doi:10.1016/j.ijmachtools.2009.10.006

[6] D. M. Pelt and D. Y. Parkinson, "Ring artifact reduction in synchrotron x-ray tomography through helical acquisition", *Meas. Sci. Technol.*, vol. 29, p. 034002, 2018. doi:10.1088/1361-6501/aa9dd9

[7] E. R. Marsh, *Precision spindle metrology*. DEStech Publications, Inc., 2010.

[8] J. Zhao, "Method for correction of rotation errors in Micro-CT System", *Nucl. Instrum. Methods Phys. Res. A*, vol. 816, pp. 149–159, 2010. doi:10.1016/j.nima.2016.01.051

ISBN: 978-3-95450-250-9 ISSN: 2673-5520 doi:10.18429/JACoW-MEDSI2023-THOBM02

FIRST RESULTS OF A NEW HYDROSTATIC LEVELING SYSTEM ON TEST PROCEDURES AT SIRIUS

W. R. Heinrich†, G.R.S. Gama, G.J. Montagner, E. Teixeira, S.P. Oliveira
Setup Automação, Campinas, Brazil
R. B. Cardoso, L. R. Leão, S. R. Marques, R. T. Neuenschwander
LNLS/CNPEM, Campinas, Brazil

Abstract

The Hydrostatic Leveling System (HLS) is commonly employed in Structural Health Monitoring (SHM) to anticipate issues in large-scale structures. Particularly in structures like particle accelerators, it is used in high-precision alignment, where small differences in elevation such as terrestrial tides, could affect machine operation. This study outlines the development and evaluation of the first HLS based in Linear Variable Differential Transformer (LVDT) and were used to monitor the structure at LNLS/CNPEM, Brazil, from 2020 to 2023. A comparative analysis with a capacitance-based off-the-shelf HLS was executed, and experimental data analyzed through Fast Fourier Transform (FFT) confirmed the presence of tidal components in both HLS's data. Additionally, the correlation between level and temperature data was demonstrated by Pearson coefficient. The Setup-HLS device, developed with support from Brazilian national resources, exhibited accurate measurements in building tilt and diurnal and semi-diurnal Earth tide variations. Future researches include a calibration jig and an online verification system. This research provides a viable alternative to existing HLS systems.

INTRODUCTION

The Hydrostatic Leveling System (HLS) is a precision measurement and monitoring system designed to detect differences in elevation between points in the system, typically achieving submicrometric precision and repeatability on the order of microns. This is accomplished by measuring the fluid's height difference, usually water, contained in a recipient, and the inclination between two points in the system where two sensors are located. Various technique principles are employed in HLS systems, including fiber optic and interferometric methods [1], ultrasonic technologies [2], capacitance and dielectric measurements [3], as well as mechanical and optical approaches [4].

The system is applied in diverse fields such as monitoring sea levels, water reservoirs, groundwater, dams, seismic events, building foundations, tunnels, traffic of heavy vehicles, and alignment of particle beams in accelerators. Generally, HLS is widely used in Structural Health Monitoring (SHM) to predict potential structural issues in large-scale equipment and facilities.

During the development of this system, it is crucial to meticulously isolate specific phenomena and sources of uncertainty that may influence measurement results, including tidal forces. Tidal forces result from spatial gradients in the gravitational field strength originating from celestial bodies. This gravitational phenomenon induces the elongation of the body experiencing the tidal force along the axis aligned with the center of mass of the attracted body.

The consequences of tidal forces encompass various occurrences on Earth, such as ocean tides, earth's rotation, tidal heating, tidal locking and terrestrial tides (or solid-earth tides). Careful consideration of tidal forces is essential for accurate and reliable HLS measurements.

On Earth, the principal manifestation of this gravitational interaction arises from the Moon's and Sun's gravitational influences, leading to the periodic oscillation of the semidiurnal of terrestrial tide, with a typical amplitude of approximately 0.55 meters [5]. Moreover, terrestrial tides and localized gravitational field variations contribute to minute perturbations in particle accelerator systems, on the order of 1 millimeter, as evidenced by measurements conducted in Geneva at the Large Electron-Positron Collider (LEP). The standard model of electroweak interactions requires precise knowledge of the LEP beam energy with an accuracy of 20 ppm. However, small fluctuations, induced by tidal effects, resulted in a beam energy variation of approximately 120 ppm [6].

HLS has been employed to precisely measure the tidal effect, which has well known periods and frequency components, so detecting these frequencies in the results measured by the HLS is a step in the sensor validation.

This study introduces a novel and robust HLS, denoted as Setup-HLS, which represents a pioneering application of the Linear Variable Differential Transformer (LVDT). The device is capable to quantify terrestrial tidal influences on level variations at the micrometer scale and was used for testing and structural monitoring at the Laboratório Nacional de Luz Síncrotron (LNLS-CNPEM) in Campinas, São Paulo, Brazil, from the years 2020 to 2023 [7, 8].

DEVICE CONCEPT

The Setup-HLS system employed in this study is an innovative Brazilian HLS, funded by FAPESP/FINEP. It was specifically designed for implementation at the Sirius facility and achieved a Technology Readiness Level of 9 (TRL 9) during its development, indicating proven functionality in an operational environment [9]. The configuration of the Setup-HLS comprises a cylindrical enclosure made of anodized aluminum, housing instrumentation responsible for converting analog water

ISBN: 978-3-95450-250-9 ISSN: 2673-5520 doi:10.18429/JACoW-MEDSI2023-THOBM02

level signals into digital format. The analog signal originates from the core of the device, constructed from super permalloy and operated through a Linear Variable Differential Transformer (LVDT) system. The principal element in the core system configuration, including the LVDT, is shown in Fig. 1. The selection of materials and sensor configuration was motivated by their superior stability in the presence of high-frequency interference, resistance to temperature fluctuations, and cost-effectiveness compared to other alternatives.

The choice of acrylic as a material for the sensor housing and the use of LVDT as the working principle were aimed at mitigating the effect of temperature on sensor readings, in line with literature on HLS sensor design [10]. The shelter infrastructure includes a thermosensitive probe and a vibration transducer to accommodate the measuring rod's response to environmental conditions over an extended duration. The temperature transducer monitors laboratory temperature and assesses its influence on water level measurements. At the lower end of the apparatus, an opening is designated for water inflow, while an additional orifice is positioned at the upper end to facilitate the establishment of air pressure equilibrium.

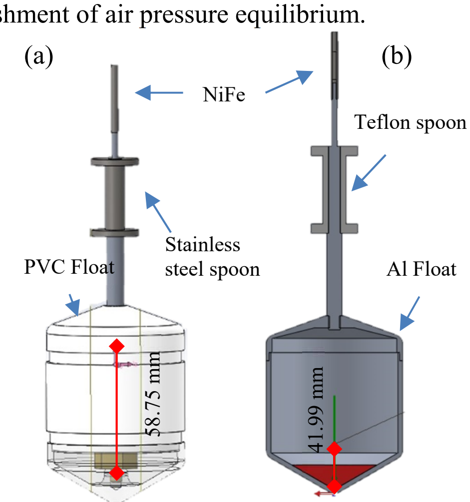

Figure 1: Float modification from (a) TRL5 to (b) TRL9.

As demonstrated in the next section, the tidal effect can be accurately measured when the friction between the steel spool and the housing does not impede the float's movement. Although the application of lubricant improved the situation, the gradual desiccation of the lubricant led to the cessation of the float's movement. To overcome this challenge, a PTFE spool was adopted as a replacement for the steel spool, as depicted in Fig. 1(b). Additionally, the vibration profile was altered to trigger more frequent movements, aiming to prevent friction-related issues.

Furthermore, an aluminum float was utilized to increase weight and lower the center of gravity, resulting in a more stable apparatus configuration. An analytical study was conducted to elevate the buoyancy center.

The device is equipped with a semiconductor electronic tilting system on the top of the cylinder, offering a resolution of 0.1° inclination. LED indicators, calibrated by three springs that hold the entire device body, facilitate the tilting system. The springs are connected to a stainless-steel ring that can be fixed in any location using screws.

These LEDs were employed for coarse calibration during the installation and commissioning of the beamlines at Sirius. A LabView software was developed and utilized for fine slope calibration, as well as for hydrostatic level and temperature measurements (in the laboratory) as a preliminary test.

Electronic communication is facilitated by a self-made circuit requiring a 24V power supply and utilizing RS-232 to transmit LVDT AD converted displacement and temperature data to the acquisition software. Three images of the Setup-HLS are provided in Fig. 2: (a) Setup-HLS without case protection, (b) PTFE spool and permalloy core, and (c) on-site. A subjective comparative analysis with other types of HLS is presented in Table 1.

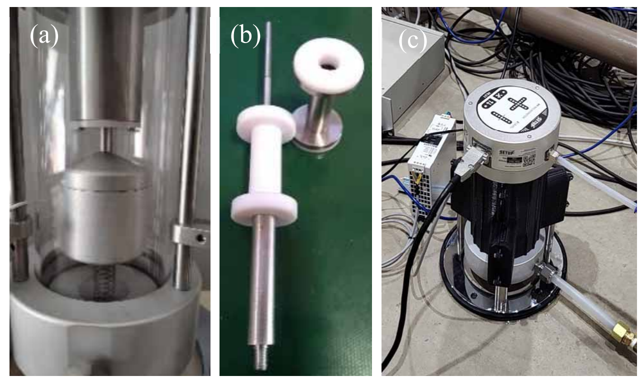

Figure 2: (a) Aluminum float, (b) PTFE spoon (c) Setup-HLS on the top Sirius ring accelerator's shell.

Table 1: Feature Comparison of Different Types of HLS

Features	Technique Principles*		
	F.O.I.	**U.T.**	**C.D.**
Resolution (S.N.)	10^{-12}m	10^{-5}m	10^{-6}m
Fluid dependence	No	Yes	Yes
Temperature influence	Free	+	++
Magnetic field influence	Free	Free	+
Eletric field influence	Free	+	+
Air humidity influence	Free	Free	+
Price (x EUR1000/point)	>160.0	>20.0	>8.0

*S.N.: Scientific Notation, F.O.I.: Fiber Optic and Interferometric, U.T.: Ultrasonic Technologies and C.D.: Capacitance and Dielectric.

It is observed that HLS Fiber Optic and Interferometric exhibits the highest resolution, no influences from other external variables, but comes at a higher cost. On the other hand, HLS Capacitance and Dielectric offers good resolution, compared to HLS Ultrasonic Technologies, but at a lower cost.

The Setup-HLS features resolution in the micrometer range. Additionally, the acrylic transparent coating allows for visual inspection and integration with computer vision using a microscopic lens for measurement validation. Moreover, the material exhibits a thermal expansion coefficient close to that of water (both ~68.0 µm/m-°C at 20.0 °C), nullifying the effect of temperature-induced

ISBN: 978-3-95450-250-9 ISSN: 2673-5520 doi:10.18429/JACoW-MEDSI2023-THOBM02

container shape modification, despite this, the new HLS does not depend on the type of fluid thus enabling the use of synthetic fluid that may have some advantage due to functional physicochemical characteristics. Their calibration relies solely on the interchangeability of the upper ogive of the devices, without affecting the operation of the HLS network. The device has a lower susceptibility to electric and magnetic fields compared to the Capacitance and Dielectric and no humidity influence. The temperature influence will be analyzed in the following section.

EXPERIMENTAL PROCEDURE

The Setup-HLS was securely anchored to the top of the concrete shielding of the accelerator at four evenly spaced points, each 90° apart around the circumference of the accelerator. To investigate the effects of tidal phenomena, a pre-installed pipeline developed by Sirius, containing a heterogeneous solution of water and air, was utilized. This pipeline was connected to a capacitance-based off-the-shelf HLS, which had previously been used to measure tidal effects. At Sirius, the capacitance-based HLS configuration comprises 20 devices operating continuously [11]. The Setup-HLS arrangement was meticulously linked to the capacitance-based HLS via the pipeline at four points.

Water levels were continuously measured by the Setup-HLS over three years, but for the purposes of this study, data from a one-week period were analyzed, encompassing measurements of both temperature and pipeline hydrostatic variation. The Setup-HLS recorded temperature and water variation every 756 seconds, while the capacitance-based HLS was configured to collect data at a more frequent interval of 31 seconds. The acquisition time was determined by the Sirius team managing the experiment. The resulting data has been collected and will be presented in the forthcoming section.

RESULTS AND DISCUSSION

In this section, we present the Setup-HLS dataset for the evaluation of hydrostatic leveling fluctuations and a comprehensive statistical analysis of the gathered data was executed, establishing correlations between the outcomes obtained from a commercially available capacitance-based HLS deployed concurrently at the same measurement site.

The Sirius accelerator facility is structured with 60 distinct circular structural axes, and the Setup-HLS sensor is positioned along four specific axes designated as 14, 29, 44, and 59. It is worth noting that the HLS on axis 59 encountered a mechanical locking issue, and the results obtained from this axis were excluded from the analysis.

The data depicted in Fig. 3 correspond to axes 14 and 29. Graph (a) illustrates a noticeable decreasing tendency in water level at the first axis, while graph (b) shows an increasing tendency in the level on the second axis, which is spaced 15 axes apart. This dataset, pertaining to level measurements, may indicate a building tilt.

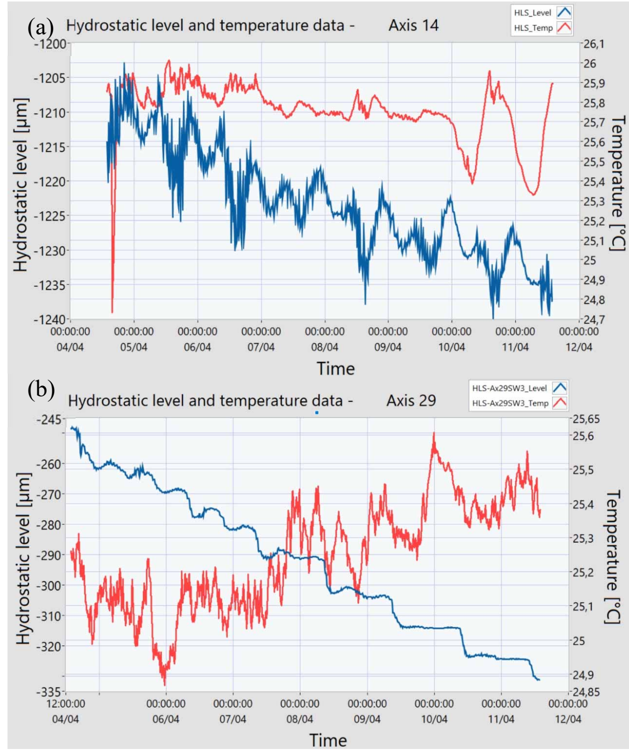

Figure 3: Graph presenting hydrostatic level (blue) and temperature measurements (red) for the period, from Setup-HLS (a) Axis 14, (b) Axis 29.

Based on these initial observations, software has been developed using LabVIEW to process measurement data for both sensors, Setup-HLS, and capacitance-based HLS. The software provides metrics to assess device performance linked to two goals: 1) The ability to detect real physical phenomena through hydrostatic level measurement; 2) Studying the interdependence between level measurement and temperature data.

A brief description of the calculations performed will be provided: For goal 1, a conspicuous oscillatory pattern with an estimated periodicity of approximately 12 hours can be observed in Fig. 3, representing the tidal effect. A Fast Fourier Transform (FFT) analysis was conducted on level measurement data for both devices installed on axis 14. This analysis allowed the identification of components of the terrestrial tide frequency. The absolute values of the four main FFT components and their frequencies were listed and can be seen in Table 1.

Components with frequencies corresponding to periods larger than 33.68 hours were ignored. As presented in [12], a model for Earth tides in the state of Sao Paulo is proposed, based on gravitometer measurements. The main diurnal and semidiurnal components identified are M2, S2, and K1, corresponding to tidal periods of 12h25m, 12h, and 23h56m, respectively [13]. As seen in Table 2, these main components are present in the results of the FFT analysis for both sensors, among the four most significant components found. It can be inferred from the frequency values for the components listed. It is noted that for Setup-HLS, the 23h56m component is slightly more significant than the 12h component.

ISBN: 978-3-95450-250-9 ISSN: 2673-5520 doi:10.18429/JACoW-MEDSI2023-THOBM02

Table 2: Main FFT Components for Level Measurement

Setup-HLS FFT components		Capacitance-based HLS FFT components	
Period (hours)	**Intensity** (mm)	**Period** (hours)	**Intensity** (mm)
24.06	24.68	24.00	17.39
12.03	22.50	12.00	26.06
16.84	13.10	12.92	10.96
12.96	12.96	11.20	7.20

For goal 2, level and temperature data were individually considered for each sensor, whether Setup-HLS or the capacitance-based HLS. Both level and temperature data were scaled to the [-1, +1] range and filtered using a 3rd-order Butterworth high-pass filter with a cutoff frequency equivalent to a 6.944-hour period. Pearson coefficient calculations were performed between the values in resulting data, and the results are listed in Table 3 for both Setup and capacitance-based sensors.

Table 3: Pearson Coefficient between Hydrostatic Level Measurement and Temperature Data for Both Sensors with 31-Second Interval

Location on Sirius	Level to Temperature – Pearson Coefficient	
	Setup-HLS	**Capacitance-based HLS**
Axis 14	0.42	0.43
Axis 29	0.37	0.84
Axis 44	0.61	0.91
Axis 59	0.03	0.45

As observed, higher absolute values for Pearson correlation between water level and temperature signals were noted in capacitance-based sensors compared to HLS Setup sensors, for both measured periods. As shown in [14] a simulation was developed in the same laboratory investigating the amplitude of thermal displacement on the concrete ring shield. These results point to displacement of up to 80 microns in radial direction at 1.5 degrees Celsius of temperature variation. Although the work did not provide enough information to estimate the final contribution to the vertical uncertainty displacement estimation, it demonstrates the need to evaluate HLS sensors in a calibration process that properly isolate the uncertainties components.

CONCLUSIONS

The Setup-HLS was able to accurately measure the effects of tides and building tilt over time, and probably will detect several geological factors with similar amplitude such as changes in the water table, seismic oscillations, earth quakes, etc. After 30 months of level/tilt monitoring it became apparent that there were challenges in isolating uncertainty components and system interferences to HLS measurements. These challenges included influences such as ambient temperature in the measurements, changes in the physical state and treatment of water within the container or even biological effects as the observed growth of algae in the hydrostatic channels. In this paper the strategy of isolating a known terrestrial tide periodic effects to compare the measurements between HLSs were successfully demonstrated. The complexity for isolating each uncertainties components at the submicron order of magnitude at the field, indicates that is recommended to periodically perform system calibration and reliability analysis for measurement repeatability, to verify sensor manufacture's declared specifications and proper system operation.

For future works, a calibration jig is currently been proposed in order to allow statistical analysis of measurement uncertainties and also to study the behavior of the HLS sensors; there is also a possibility for simple system verification using an online testing aiming to map unknown interferences over the time. In addition, interference of the electromagnetic field and concrete expansion influences to device measurements are a relevant field of study.

REFERENCES

[1] A. Herty *et al.*, "Hydrostatic Levelling Sensors Based on Extrinsic Fibre Fabry-Perot Interferometer Technology", in *Proc. 14th International Workshop on Accelerator Alignment*, Grenoble, France, Oct. 2016.

[2] H. J. Choi *et al.*, "Operation Status of HLS System Installed to Measure Ground Change of Large Scientific Equipment in Real Time", in *Proc. MEDSI'18*, Paris, France, Jun. 2018, pp. 245-248. doi:10.18429/JACoW-MEDSI2018-WEPH18

[3] T. Morishita and M. Ikegami. "The slow-ground-motion monitoring based on the hydrostatic leveling system in J-PARC linac", *Nucl. Instrum. Methods Phys. Res., Sect. A*, vol. 602, pp. 364-371, Apr. 2009. doi: 10.1016/j.nima.2009.01.152

[4] S. F. Xu, X. Y. He, P. Wang, W. Wang, and Q. Y. Yao, "Analysis of Tidal Effects on Measurement Accuracy of HLS", in *Proc. IPAC'13*, Shanghai, China, May 2013, paper WEPME027, pp. 2989-2991.

[5] G. Petit and B. Luzum, IERS Conventions (2010), http://www.iers.org/TN36/

[6] L. Arnaudon *et al.*, "Effects of terrestrial tides on the LEP beam energy", *Nucl. Instrum. Methods Phys. Res., Sect. A*, vol. 357, pp. 249-252, Apr. 1995. doi:10.1016/0168-9002(94)01526-0

[7] L. Liu *et al.*, "Sirius Commissioning Results and Operation Status", in *Proc. IPAC'21*, Campinas, Brazil, May 2021, pp. 13-18. doi:10.18429/JACoW-IPAC2021-MOXA03

[8] O Laboratório Nacional de Luz Síncrotron – LNLS, https://www.lnls.cnpem.br/sobre/, accessed on 16 October 2023.

[9] Final Report of the NASA Technology Readiness Assessment (TRA) Study Team, https://ntrs.nasa.gov/api/citations/20170005794/downloads/20170005794.pdf, accessed on 16 October 2023.

ISBN: 978-3-95450-250-9 ISSN: 2673-5520 doi:10.18429/JACoW-MEDSI2023-THOBM02

[10] S. Takeda, “Development of New Hydrostatic Levelling Equipment for Large Next Generation Accelerator”, in *Proc. EPAC'04*, Lucerne, Switzerland, Jul. 2004, paper WEPLT113, pp. 2113-2115.

[11] S. R. Marques *et al.*, “Improvements on Sirius Beam Stability”, in *Proc. IPAC'22*, Bangkok, Thailand, Jun. 2022, pp. 226-229. doi:10.18429/JACoW-IPAC2022-MOPOPT002

[12] D. Blitzkow *et al.*, “First Results Using the Microg LaCoste for Developping an Earth Tide Model in São Paulo”, in *Proc. Thirteenth International Congress of the Brazilian Geophysical Society*, Rio de Janeiro, Brazil, Aug. 2013. doi:10.1190/sbgf2013-372

[13] T. Hartmann and H. Wenzel. “The HW95 tidal potential catalogue”, *Geophys. Res. Lett.*, p. 22-24, Dec. 1995. doi:10.1029/95GL03324

[14] S. R. Marques *et al.*, “Improvements on Sirius Beam Stability”, in *Proc. IPAC'22*, Bangkok, Thailand, Jun. 2022, pp. 226-229. doi:10.18429/JACoW-IPAC2022-MOPOPT002

ISBN: 978-3-95450-250-9 ISSN: 2673-5520 doi:10.18429/JACoW-MEDSI2023-THOBM04

DEVELOPMENT OF A MIRROR CHAMBER FOR SHINE PROJECT

F. Liu†, T. Wu, S. He, H. Yuan, X. Zhang, Z. Wang, W. Li
Center for Transformative Science, ShanghaiTech University, Shanghai, China
L. Zhang, J. Chen, W. Zhu
Shanghai Advanced Research Institute, CAS, Shanghai, China

Abstract

A 5-DOF mirror chamber test system was developed to adjust offset mirror or distribution mirror for the SHINE project. Two linear guides were used for horizontal translation and coarse pitch adjustments. Three vertical gearboxes were used for height, roll and yaw adjustments. In the vacuum, a fine flexure structure was engineered for the fine pitch adjustment with a piezo actuator. To prevent the cooling vibrations, the cooling module was separately fixed and the heat from the mirror was conducted by Ga/In to the cooling blade. Pitch angular vibration were measured by several equipment under different conditions. Results showed that the pitch angular vibration was below 40 nrad above 1 Hz without active vibration control, and below 10 nrad with active vibration isolation system.

INTRODUCTION

Shanghai HIgh repetitioN rate XFEL and Extreme light facility (SHINE) started the ground breaking on 27th April, 2018. The whole facility is 3.1 km long installed in the tunnels about 29 meters underground. The whole facility was shown in Fig. 1. The first 1.5 kms were for the linac to accelerate the electron bunches up to 8 GeV, and generate X rays in the range between 0.4~25 keV within 3 beamlines. In the Near Experimental Hall (NEH) and Far Experimental Hall (FEH), 10 endstations were built in the first phase. As shown in Fig. 1, there was highway lying along the facility, and a river passing across the tunnel between Shaft 3 and Shaft 4, and a subway Line 13 running right above the tunnel between Shaft 4 and Shaft 5. To investigate the vibration transfer between the ground to the optics, a mirror chamber system was developed according to the requirements of M1 adjustments.

MIRROR CHAMBER SETUP

According to the requirements for the M1 adjustments, the specifications were listed in Table 1 and the schematic of the mirror chamber was shown in Fig. 2. The X translation was used to move the mirror in and out of the beam when necessary, the Z translation was intended to change the stripe of the mirror, however, considering the ground settlement of the tunnel, 100 mm adjustment range was designed. To make a stable and reliable chamber system, most of the adjustments were put outside the vacuum, and the vacuum chamber was supported separately.

The whole mirror chamber system was shown in Fig. 3, the base was made of two granites, in between were four air bearings, and two linear translations were installed in the two ends. When the translation move in the same direction, horizontal movement was realized, when they move in opposite directions, a pitch angle would appear (detailed in Fig. 4) [1]. For the vertical translation and the roll and yaw adjustment, since no fine adjustments were necessary, ordinary gearboxes were employed, however, the stiffness in the radial directions were carefully designed to meet pitch angle stabilities. And the contacts of the three kinematic supports were also optimized for better stability issues. To minimize the influence by water cooling, the mirror was cooled by a copper blade inserted in an Indium Galium eutectic bath on the mirror, and the cooling tubes were fixed to a separate support decoupled to the mirror holder as shown in Fig. 5. Considering the vertical translation when exchanging the stripes on the mirror, the water cooling movement was coupled to the vertical translation of the mirror holder by connecting the two gearboxes with a shaft.

Figure 1: Topview of the SHINE facility.

† liufang@shanghaitech.edu.cn

ISBN: 978-3-95450-250-9 ISSN: 2673-5520 doi:10.18429/JACoW-MEDSI2023-THOBM04

Table 1: Specifications of the Mirror Chamber System

Axis	Range	Resolution
Mirror X translation (in/out beam)	± 40 mm	2 µm
Mirror Z translation (High adjustment)	± 50 mm	5 µm
Pitch (coarse)	± 8 mrad	10 µrad
Pitch (fine)	± 70 µrad	5 nrad
Roll	± 1°	10 µrad**
Yaw	± 200 µrad	10 µrad
Z translation of Chamber (manual)	80 mm	0.1 mm
X translation of Chamber (manual)	± 30 mm	0.1 mm

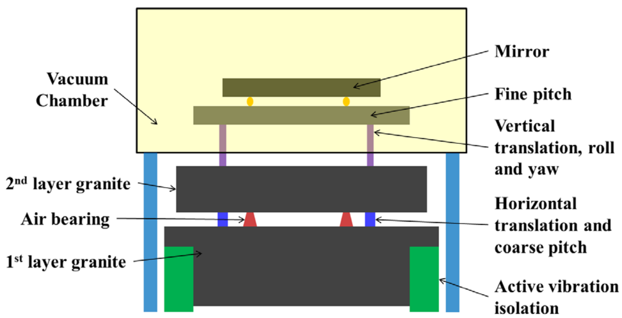

Figure 2: Schematic of the mirror chamber system.

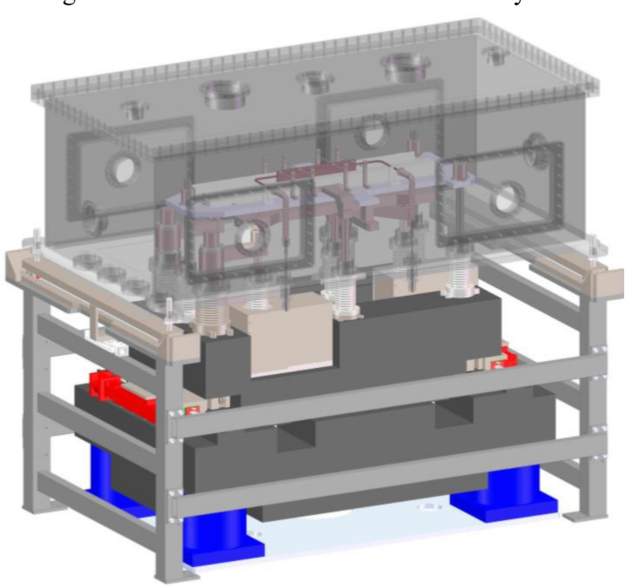
Figure 3: 3D model of the mirror chamber system.

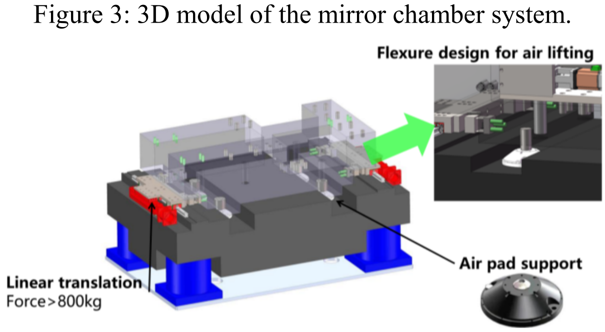

Figure 4: Model of coarse pitch and X-translation with air pad support.

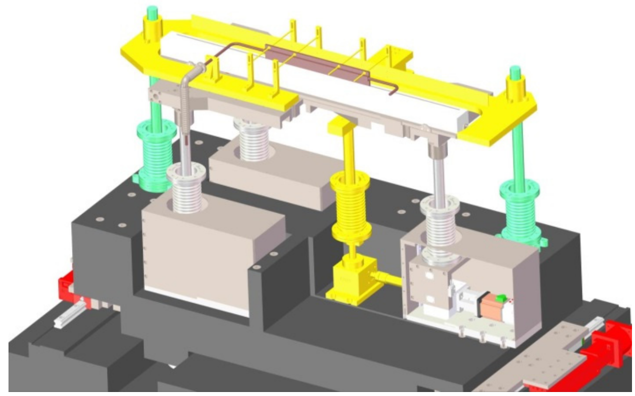
Figure 5: Mirror cooling was decoupled to the cooling blade, while the movement of the water cooling was coupled to the vertical translation of the mirror.

An active vibration isolation system (STACIS-III, TMC) using piezo compensation was chosen to isolate the ground vibrations, and hopefully to keep the same position relative to the ground below 2 Hz.

MEASUREMENT AND DISCUSSION

The real mirror chamber system without vacuum chamber was shown in Fig. 6. The movement of the coarse pitch and translation were measured by 5529A Dynamic Calibration System (Keysight) [2], the resolution of the fine pitch was measured by IDS3010 (attocube GmbH) [3], and the pitch angular vibrations of the mirror were measured in three ways as demonstrated in Fig. 7. The absolute angular velocity of pitch was measured by using two geophones (941B) [4] glued to the mirror dummy made of aluminium 800mm in distance as labelled in V1 and V2 in Fig. 7. The relative angle between the ground and the mirror was measure by 5529A, and the relative angle between the upper granite and mirror was measured by IDS3010.

As shown from Fig. 8 to Fig. 10, the resolution of X translation was better than 167 nm, coarse pitch angular resolution was 1.5 µrad and the range was over ±10 mrad. The fine pitch resolution was 5 nrad shown in Fig. 11.

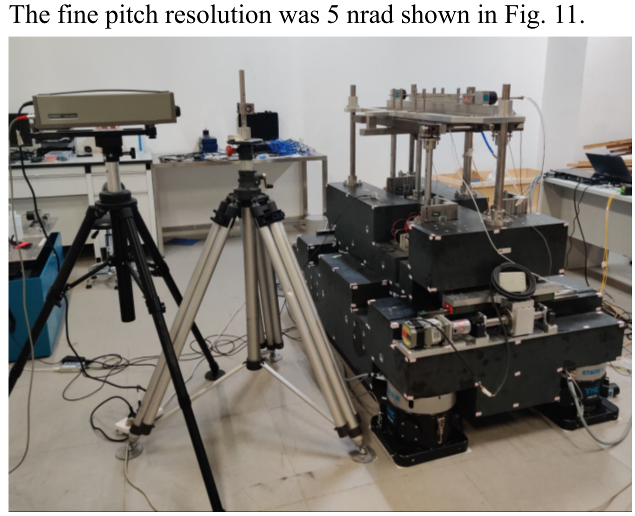
Figure 6: Mirror chamber system and the measurement set up.

ISBN: 978-3-95450-250-9 ISSN: 2673-5520 doi:10.18429/JACoW-MEDSI2023-THOBM04

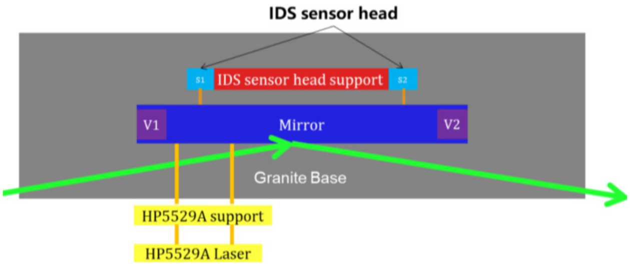

Figure 7: Measurement set up for pitch angle of the mirror.

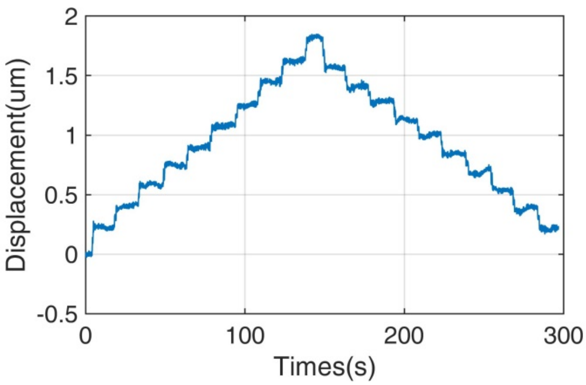

Figure 8: X translation was tested with each step of 167 nm when airpads were pressurized.

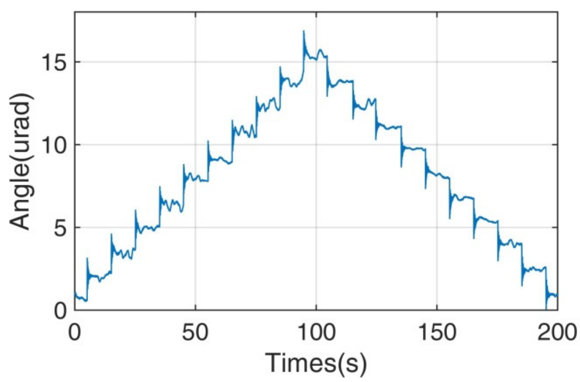

Figure 9: Coarse pitch was tested with each step of 1.5 μrad when airpads were pressurized.

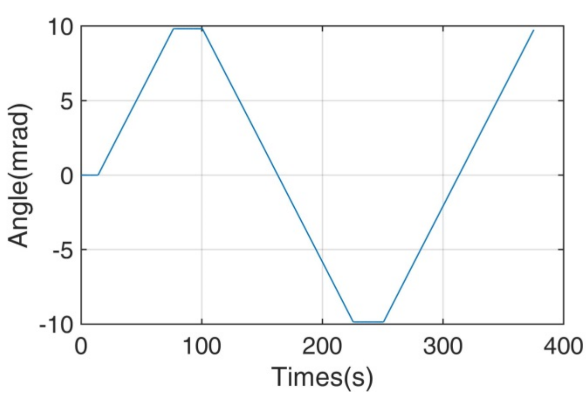

Figure 10: Coarse pitch range was moved from −10 mrad to 10 mrad.

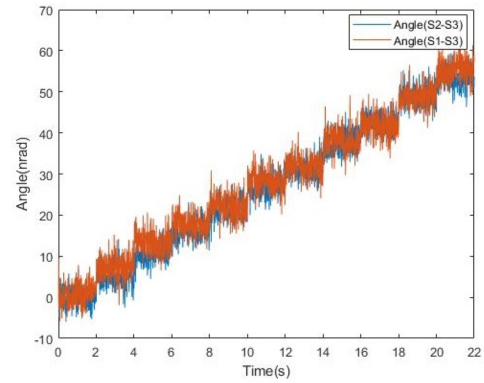

Figure 11: Fine pitch was tested with each step of 2 nm by the piezo, resulting about a 5 nrad resolution.

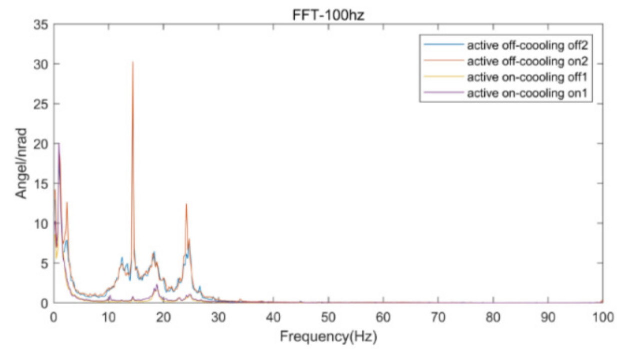

Figure 12: Absolute pitch vibration comparison with and without cooling when active vibration isolation system on and off in spectrum.

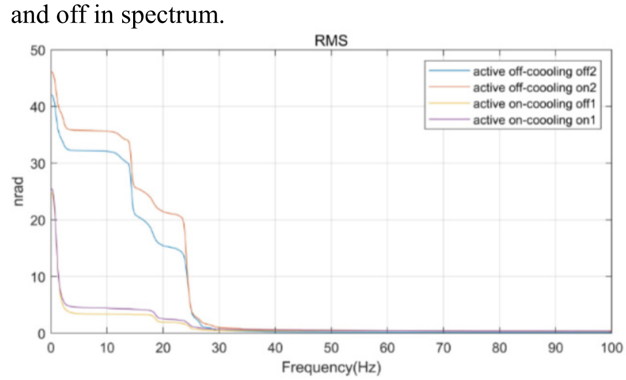

Figure 13: Absolute pitch vibration comparison with and without cooling when active vibration isolation system on and off in statistics.

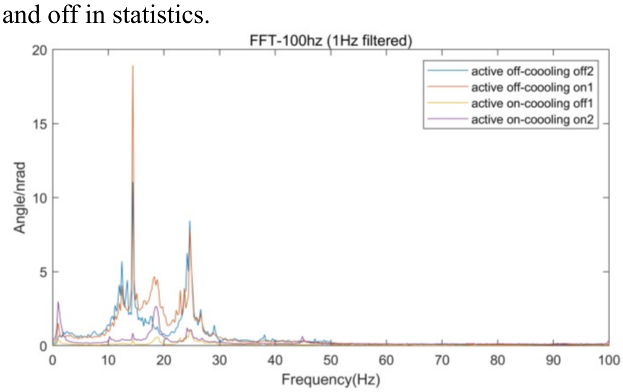

Figure 14: Pitch vibration comparison between mirror and granite with and without cooling when active vibration isolation system on and off in spectrum.

ISBN: 978-3-95450-250-9 ISSN: 2673-5520 doi:10.18429/JACoW-MEDSI2023-THOBM04

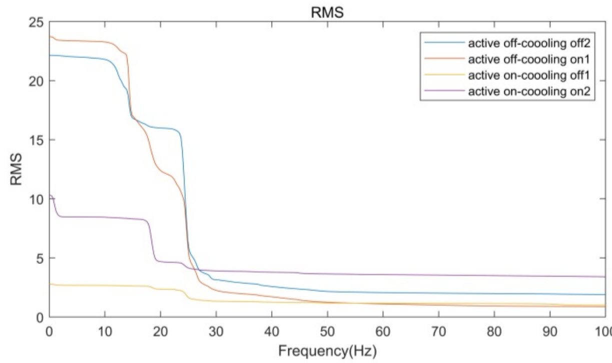

Figure 15: Pitch vibration comparison between mirror and granite with and without cooling when active vibration isolation system on and off in statistics.

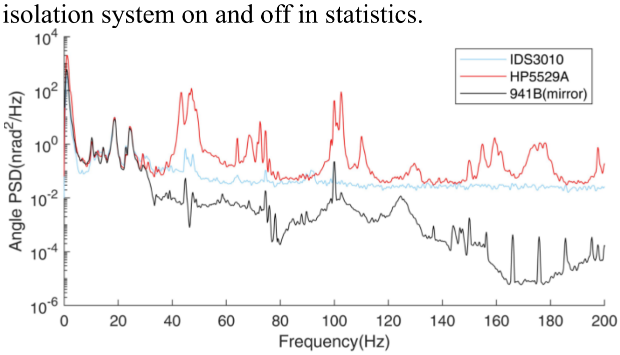

Figure 16: Spectrum comparison of pitch angle with different measurements when active vibration isolation was enabled and water cooling was functioning.

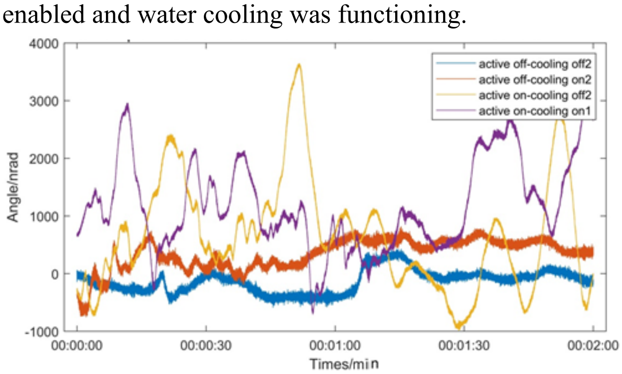

Figure 17: Waveform of pitch angle comparison between mirror and ground with and without cooling when active vibration isolation system on and off.

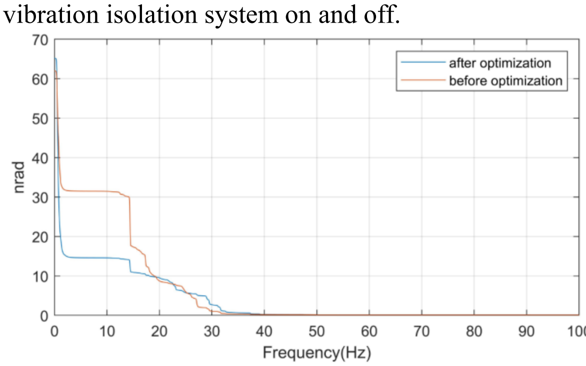

Figure 18: Comparison of stabilities with the optimization of the joints connecting to the pillars of the gearboxes.

Figure 12 to Fig. 15 showed the spectrum as well as the RMS vibrations measured by geophones and IDS with a 1Hz high pass filter applied to the data when the airpads were seated on the granite. Figures 12 and 13 showed that the absolute pitch vibration was about 40 nrad without active vibration isolation, the relative pitch angular vibration was about 25 nrad between mirror and the granite. Most of the vibration spectrums were below 30 Hz. When the active vibration isolation was enabled, the pitch vibration was below 10 nrad in both measurements. Figure 15 also indicated that the effect of water cooling was less than 8 nrad (water flow was 4 L/min) by comparing the data when active vibration isolation was enabled. Figure 16 showed the spectrum of the three measurements comparison when active vibration isolation was enabled and water cooling was on. By comparing the spectrums, it showed that in the range of 2-30 Hz, the spectrum were consistent by all three methods, which was also the main spectrums of the vibration. For HP5529A, spectrum above 40 Hz was higher than the other two methods, which was due to the vibration caused by the support itself. For the IDS, spectrums above 50 Hz were about the same, it was explained that this was the signal noise of the instrument. Figure 17 was the waveforms of the pitch angles in 2 minutes. When active vibration isolation was disabled, the width of the waveform were bigger than the width when active vibration isolation was active, which indicated that the active vibration isolation did improve the high frequency vibrations. However, there were another random slow motions up to 5 µrad were observed. The reason was not yet clear. Figure 18 indicated that the joints connections were also important, by optimization, stability was improved from 30 nrad to 15 nrad.

CONCLUSION

A 5-DOF high heat-load and high stability mirror chamber test system was developed to demonstrate the stability performance in the SHINE environment. Results showed that the stability was under 40 nrad with water cooling. By decoupling the cooling blade and the support, the effect by water cooling could be minimized to 8 nrad. By isolating the ground vibration with active vibration isolation system, the pitch angle vibration reduced to less than 10 nrad. By optimizing the joints of connecting to the pillars, vibration could be further improved.

REFERENCES

[1] F. Liu, Z. Liu and Y. Chen, “A two-dimensional high stability adjustment mechanism”, National Intellectual Property Bureau of China, 202111035778.2, Jul. 25, 2023.

[2] https://www.keysight.com/us/en/product/5529A/dynamic-calibration-system.html

[3] https://www.attocube.com/en/products/laser-displacement-sensor/displacement-measuring-interferometer

[4] http://www.topreascend.com/tprs-Products-7397129/

ISBN: 978-3-95450-250-9 ISSN: 2673-5520 doi:10.18429/JACoW-MEDSI2023-THPPP002

ANALYSIS OF HAZARDS IN A FLAMMABLE GAS EXPERIMENT AND DEVELOPMENT OF A TESTING REGIME FOR A POLYPROPYLENE VACUUM WINDOW

S. Bundrock, E.X. Li, D.M. Smith, B.E. Billinghurst
Canadian Light Source Inc., Saskatoon, Canada

Abstract

Far Infrared Spectroscopy (Far-IR) is a bend magnet infrared beamline at the Canadian Light Source. The beamline utilizes a gas cell loaded with experimental gas which light is bounced through and a spectrometer to measure the absorption of the gas. For an experiment at Far-IR utilizing methane and nitrogen at 100 K temperatures, issues with icing and inconsistent absorption gradients were noted at the Polymethylpentene Rigid Plastic (TPX™) window separating the cell filled with the flammable gas mixture from the vacuum of the spectrometer. The possibility of replacing the existing windows with new 50-micron thick polypropylene window was investigated. Material properties were not available for polypropylene at the operating temperature of the experiment. Due to the hazardous nature of the gas being held back a hazard analysis was carried out to identify potential risks and mitigations for the change. Additionally, with material properties unavailable, a testing regime was established to ensure the polypropylene could survive in the experimental environment. The experiment was successfully completed. using the modified window assemblies.

INTRODUCTION

The Far-IR beamline uses several different Fourier Transform Infrared Spectroscopy (FTIR) methods during operation. When a FTIR method is to be utilized with a gas the beamline is equipped with gas cells of a known light path length. Some experiments require the use of flammable or potentially hazardous gasses. For safe handling of these gasses the beamline is equipped with a hazardous gas exhaust system; an explosion proof vane pump is used for post-experiment gas removal into the dedicated exhaust system. Far-IR's 2 m gas cell has a volume of 300 L and includes a cold nitrogen gas cooling system used to maintain cell contents at cryogenic temperatures when required. The 2 m cell is separated from a Bruker© spectrometer by a pair of windows; several window materials can be used. One such material is Polymethylpentene Rigid Plastic (TPX™). The windows separate the rough vacuum of the spectrometer from the cell's experimental conditions while simultaneously allowing synchrotron light to pass through. The 2 m cell and Bruker© spectrometer can be seen in Fig. 1.

In one instance, complications with the TPX windows at cryogenic temperatures interfered with the collection of quality data. A proposed modification of the windows to address these complications introduced uncertainty as to whether the modified windows could survive the experimental operating conditions.

Figure 1: Far-IR 2m gas cell and Bruker© spectrometer.

BACKGROUND

Two primary issues arose with the 6.6 mm thick TPX windows during an experiment. This experiment used the 2 m cell with a 1 atm methane mixture at 100 K. Ice would form in-vacuum on the spectrometer side interfering with transmission through the windows. TPX has a temperature-dependant absorption spectrum and as the methane moved within the cell, the temperature of the windows would fluctuate. This fluctuation produced inconsistent experimental conditions and unrepeatable results. Therefore, alternate window solutions were investigated. A requirement for a new window material was transparency in the visible range as a laser is used to align optics prior to an experiment. The FAR-IR beamline staff proposed 50 µm polypropylene windows as they had been observed to have better absorption spectra in previous published work [1].

OBJECTIVES

1. Design a new window assembly to eliminate icing and minimize absorption problems.
2. Complete a hazard analysis of risks introduced by window modification.
3. Test if proposed polypropylene windows can safely withstand experimental conditions.

FINAL DESIGN AND CONSIDERATIONS

The new window assemblies featured numerous modifications from the original TPX window to address the issues observed. To address ice formation, a two-window design with internal vacuum break was adopted. This design is pictured in Fig. 2. The added vacuum gap minimized icing by reducing heat transfer from the methane, maintaining the spectrometer side window at a higher and more stable temperature. Creating a smaller vacuum space reduced the

ISBN: 978-3-95450-250-9 ISSN: 2673-5520 doi:10.18429/JACoW-MEDSI2023-THPPP002

amount of water available to freeze on the cell side window. A vacuum seal-off valve was added to the body of the assembly to allow this new vacuum space to be pumped down. A 3D printed cap was added to the valve to prevent movement in the event of window failure.

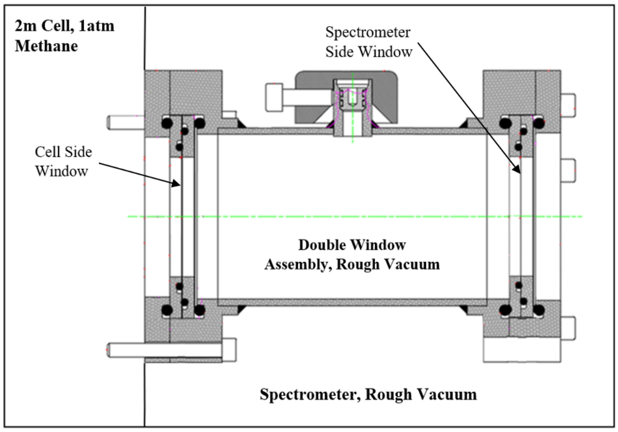

Figure 2: Double window assembly final design.

The variable absorption problem was addressed by switching the window material to polypropylene. Polypropylene has significantly lower absorption compared to TPX; any variations in the absorption due to temperature were negligible. The reduced thickness of the window had the added benefit of increasing the amount of light that reached the experimental sample. The new windows were clamped between two retaining plates. The retaining plates were designed to have the same thickness as the original TPX windows allowing for interchangeability during testing. O-rings around and within the retaining plates were used to form a vacuum seal in the double window assembly, and firmly secure components in place.

HAZARD ANALYSIS

The experiment utilized different mixtures of methane gas that would create a flammable mixture if mixed with air. Therefore, during the design process a hazard analysis was carried out to identify potential risks and their significance that would be introduced by the proposed modifications to the windows. The scope was limited to failure modes introduced through failure of the polypropylene windows.

Potential Failure Scenarios

Three scenarios were identified for gas release in the event of a window failure. The first scenario is window failure while the spectrometer scroll pumps were off. Experimental gas would be confined to the spectrometer and 2 m cell. The second scenario occurs if the spectrometer scroll pumps are left running, possibly due to human error. Experimental gas would be pumped from the spectrometer into the Far-IR hutch. The third scenario occurs if the spectrometer scroll pumps are left running and routed to vent into the beamlines hazardous gas system. Experimental gas would be pumped unregulated from the spectrometer into the hazardous gas system. This was a proposed modification to regular procedures to possibly eliminate the risk of scenario two. Typically, the spectrometer scroll pumps are not exhausted to the hazardous gas system.

Severity Analysis

The severity of the hazard for each potential scenario was analysed. For the analysis, a worst-case scenario of 100% methane in the 2 m cell was assumed. Severity was determined by investigating whether the scenario could possibly produce a flammable mixture and the potential damage ignition would cause.

In the first scenario the gas is contained to the 2 m cell and the spectrometer, eliminating the risk of the methane mixing with air. The mixture will remain 100% methane and be above the upper flammable limit [2]. Therefore, there is minimal hazard in the first scenario.

In the second scenario the methane would be released directly into the experimental hutch. If dispersed equally with the volume of air in the hutch, the 300 L of methane could form a mixture below the lower flammable limit [2]. However, as the methane mixes with the hutch air it could form a gas cloud capable of igniting. The result would be partial volume deflagration in the hutch. The potential damage from ignition was calculated using the methodology presented in *SFPE Handbook of Fire Protection Engineering 5th edition*. In this calculation the peak pressure of a fully stoichiometric mixture ignition is scaled by the mass of methane for the scenario in question over the mass of methane in a fully stoichiometric mixture. The peak pressure of 7.1 bar g for a methane ignition was taken from table 69.1 in *SFPE Handbook of Fire Protection Engineering* [3]. The mass of methane released from the 300 L 2 m cell was 0.5385 kg, significantly less than the 6.89 kg needed to fully mix with the 116310 L of the hutch.

$$P = (7.1bar\ g)\frac{0.5385kg}{6.89kg} = 55.38kPa$$

The result was a scaled peak pressure of 55.38 kPa. As per table 69.2 in the *SFPE Handbook of Fire Protection Engineering,* this corresponds to a “Near complete destruction of houses” [3]. This represents a significant hazard to human life and equipment for the given scenario.

For the third scenario, where methane is vented into the hazardous gas system via the spectrometer scroll pumps, the pumping rate of methane relative to the system flow rate must be determined. The hazardous gas system has a capacity of 23.6 L/s. Hazardous exhaust systems are typically designed to maintain gas levels below 25% of the lower flammable limit [4]. To achieve this, methane would have to be vented at a rate lower than 0.295 L/s. The two spectrometer scroll pumps each vent at a rate of 8.3 L/s for a total rate of 16.6 L/s [5]. This is significantly higher than the allowable rate; therefore, an explosive mixture like the second scenario could form in the system.

Mitigations

To minimize the risks related to a window failure, several mitigations for the identified hazards were developed. To prevent the occurrence of the second and third failure scenarios, the spectrometer scroll pumps must be verified to be off prior to and during the experiment. To mitigate the risk of a flammable mixture forming in the hazardous gas system the methane mixture must be diluted with nitrogen prior to removal from the cell and spectrometer. Finally, any pumping to remove methane shall be done by the 2 m cell's explosion proof vane pump.

MATERIAL TESTING REGIME

Due to the significance of the worst-case scenario in event of a failure, testing must be carried out on the polypropylene prior to use. Relevant material properties could not be found for polypropylene at the operating temperature of 100 K and to ensure the material would survive as a vacuum window, testing was required.

Failure Modes

Four failure modes for the new windows were highlighted as requiring testing. The first failure mode investigated is fatigue. The new windows would undergo two load cycles for each use. One cycle occurs as the window assemblies' internal vacuum space is pumped down, followed by unloading as the cell and spectrometer are pumped down. The second cycle occurs as the cell is loaded with the experimental gas. If the experiment is performed many times, it is reasonable to assume fatigue failure is a possibility. The second mode of failure is creep. This is a risk as the thin windows would be held under vacuum a load for the extent of the experiment. Each experimental measurement lasted several hours; however, the window would be held under load while the cell and methane were cooled in preparation. The total time the window would be held under vacuum is estimated at 24 hours. If the cell side window were to fail, the spectrometer side window would be subject to the third mode of failure; a sudden shock caused by the methane mixture rushing into the assembly's vacuum space. This would cause a sudden increase in pressure on the spectrometer side window. The final failure mode is a weakening of the window due to low experimental temperature.

Tests Developed

To address each mode of failure a test was developed to be carried out on the windows prior to use. To test fatigue, the assembly would be pumped down and then let up 15 times. Fifteen cycles were selected as it was significantly higher than the two cycles that a given window would experience and could still be completed in the time frame available before the experiment. To test creep, the assembly would be pumped down and held under vacuum for at least one week at room temperature. This value was selected as it was significantly longer than the 24 hours of the experiment while still being completable in the available time frame. To address the failure due to a shock, a test flange was created to hold vacuum behind one of the windows in the assembly. Failure would be manually induced on the opposite window. This test was carried out on both the TPX and polypropylene windows, as the TPX would be needed for the cold temperature testing. The potential failure at low temperature was addressed by completing an in-situ experiment using solely nitrogen in the 2 m cell and TPX as the spectrometer side window. TPX was used preventively as in the event of failure of the polypropylene window, TPX would be capable of surviving the experimental conditions.

Test Regime Construction

After identification of the required tests, a testing regime was developed. The fatigue and creep tests were carried out first as they represent the lowest stress situation; fatigue was tested first as it simulates a standard use case. Rupture tests were then carried out on the polypropylene and TPX windows, due to the requirement that they be capable of withstanding a shock during cold temperature in-situ testing. The windows were checked between each test for visual damage and pumped down to ensure they still held vacuum. Cold temperature was tested last as it exposed the window to nearly identical experimental conditions.

CONCLUSION

The hazard analysis identified that the worst-case scenario for failure represented a significant hazard. Mitigations were developed allowing for the experiment to proceed with the polypropylene windows. Material testing was needed due to the unknown properties of polypropylene and hazard significance. Material testing demonstrated that polypropylene windows could survive the operational conditions of the experiment. The new windows were used for the experiment after successfully passing testing.

Future Work/Limitations

The extent of the tests was limited to maintain a reasonable timeframe for completion. For example, the fatigue testing was limited to 15 cycles. This was deemed sufficient relative to the two cycles seen in the experiment. This necessitated the polypropylene windows be changed after each use. For reuse of the windows in the assembly a higher number of tests cycles would be needed. As a result of these limitations, the polypropylene window assembly was only approved for use in the experiment investigated.

ACKNOWLEDGEMENTS

Thanks to the following individuals for their contribution to the work: Dean Willenborg, Jeff Wetzel, Lawrence Pirness, Luke Robson, P.Eng., and Reg Aupperle.

REFERENCES

[1] E.H. Wishnow, A. Leung, and H.P. Gush, "Cryogenic multiple reflection absorption cell and Fourier transform spectrometer system for the far infrared", *Rev. Sci. Instrum.*, vol. 70, pp. 23-31, 1999. doi:10.1063.1.1149537

ISBN: 978-3-95450-250-9 ISSN: 2673-5520 doi:10.18429/JACoW-MEDSI2023-THPPP002

[2] A. Matei *et al.,* "Use of explosibility diagrams in potentially explosive atmospheres", *MATEC Web Conf.,* vol. 305, p. 00087, 2020. doi:10.1051/matecconf/202030500087

[3] *SFPE Handbook of Fire Protection Engineering*, M. Hurley (ed.), Society of Fire Protection Engineers, 2016. doi:10.1007/978-1-4939-2565-0

[4] *Industrial Ventilation: A Manual of Recommended Practice for Design*, ACGIH, 25th Edition, 2004.

[5] Agilent TriScroll 600, https://www.agilent.com/cs/library/datasheets/public/datasheet-scroll-pump-triscroll600-5994-2926en-agilent

ISBN: 978-3-95450-250-9 ISSN: 2673-5520 doi:10.18429/JACoW-MEDSI2023-THPPP003

FEM SIMULATIONS FOR A HIGH HEAT LOAD MIRROR

J. Seltmann†, H. Geraissate, M. Hoesch,
Deutsches Elektronen-Synchrotron DESY, Hamburg, Germany

Abstract

At the variable polarization XUV beamline P04 of PETRA III the first mirror is used to switch the beam between the two branches of the beamline. The heat load on this white beam mirror is dependent on the degree of polarization and the energy of the first harmonic of the synchrotron radiation. For this project the water cooled "notched" mirror approach by Khounsary, and Zhang et al., has been evaluated with FEM simulations. These show promising results for linear horizontal (LH) polarization in which the heat load profile is aligned with the mirror length. For linear vertical (LV) polarization the heat load is concentrated in the mirror centre, which violates the basic concept of the "notched" mirror design and therefore the simulation results indicate only poor performance. To compensate for this a secondary cooling loop has been implemented and will be shown to improve the performance for the LV case significantly. Additionally, a new design approach is evaluated to reduce the peak temperatures of the mirror, which otherwise ranged at 140-180 °C.

P04 VARIABLE POLARIZATION XUV BEAMLINE

Beamline P04 at the 6GeV storage ring PETRA-III is a XUV to soft x-ray facility in the range of 250-3000 eV. The 5 m long APPLE-II undulator allows to change polarization rapidly while achieving high brightness and coherence. The frontend consists of several apertures of which the smallest has a diameter of 4mm. A set of a vertical and a horizontal slit can be used to further reduce the footprint of the beam. The first set of optics at 35 m from the undulator is used to switch between the two branches of the beamline.

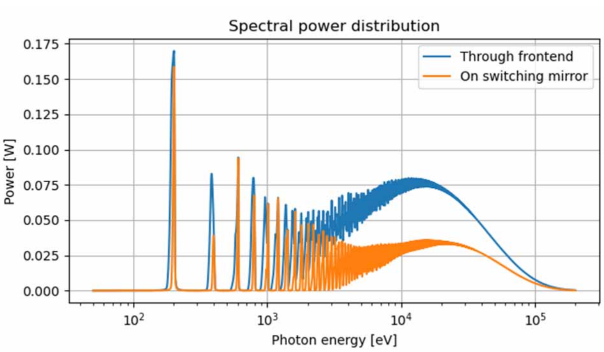

Figure 1: Spectral power distribution with open frontend apertures (blue) and on the mirror (yellow).

This switching mirror unit (SMU) consists of two mirrors facing each other, were one mirror at a time is used to reflect horizontally into its beamline branch at a grazing incidence of 0.8° [1].

HEAT LOAD CONSIDERATIONS

High K (up to K=7.1) operation of the undulator combined with the high electron energy of the storage ring results in high on-axis heat load due to higher harmonics contributions. Figure 1 shows the simulated spectral power distribution done with SPECTRA [2].

The high flexibility in terms of polarization of the APPLE-II undulator leads to different power distributions for each polarization setting, as the plots in Fig. 2 from OASYS-SRCalc show [3-4].

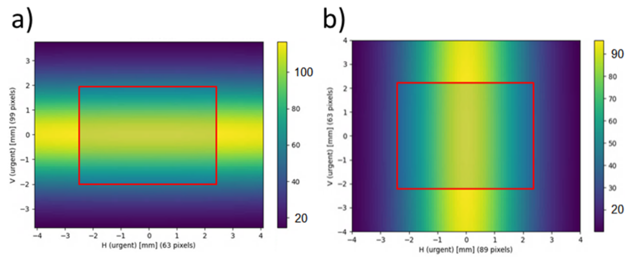

Figure 2: Power density [W/mm²] distribution with open frontend apertures for a) LH and b) LV polarized light. The footprint on the mirror is marked in red.

For LH polarization we expect the highest power on the mirror which will be distributed along the whole length of the mirror (400 mm). LV polarized light has lower absolute values but the power density is focussed in the centre of the mirror (Table 1).

Table 1: Polarization Cases

Polarization	**LH**	**LV**	**Circular**
Total power [kW]	3.90	3.21	0.6
Mirror power [kW]	2.1	1.5	0.3
Max. power den. [W/mm²]	1.66	1.30	0.13

Besides LH and LV polarization all other linear orientations are also possible but aren't broached by this study. The case of circular polarization is easier in terms of heat load considerations, since the higher harmonics are distributed radially and therefore easily cut by the frontend apertures.

NOTCHED MIRROR DESIGN

The water cooled "notched" mirror approach by Khounsary [5] and Zhang et al. [6] has been chosen instead of an internal cooling design as shown by Reininger et al. [7]. This design uses the bulk material of the mirror for stabilization, by cooling only on a small segment on the mirror sides, separated by a notch. By changing the depth of the notch, the profile of the mirror centreline can be shaped for a known heat load. This design favours a uniform heat load distribution along the mirror length, which is incompatible with varying heat loads at first.

† Joern.seltmann@desy.de

ISBN: 978-3-95450-250-9 ISSN: 2673-5520 doi:10.18429/JACoW-MEDSI2023-THPPP003

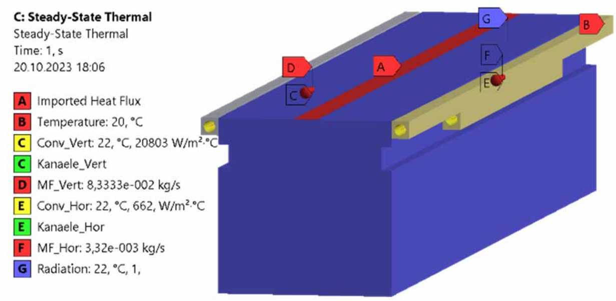

Figure 3: Boundary conditions for SST calculation in Ansys® on notched design.

To overcome this limitation, a second, shorter cooling loop was added, to be able to switch the cooling according to the expected heat load. An Ansys® simulation [8] using a "Steady-State Thermal" (SST) model, which simulates the temperature profile resulting from the beam footprint and the cooling scheme, was set up (Fig. 3). In this model the water is treated as beam like, to allow for the increasing temperature along the mirror length.

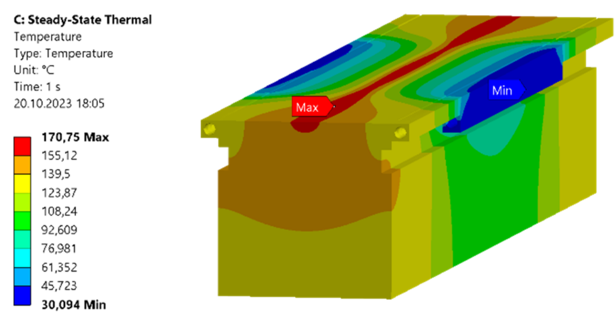

Figure 4: LV polarization on notched design result for SST calculation in Ansys®.

Figure 4 shows a result for LV polarization, where the second, shorter cooling lines take the bulk of the power from the mirror.

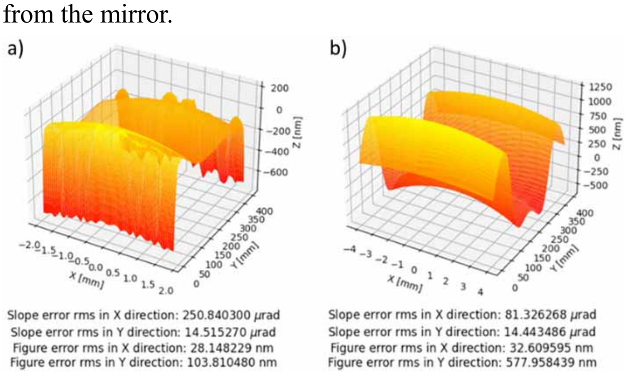

Figure 5: Resulting mirror surfaces for a) LH and b) LV polarization on the notched design.

The result of the SST model is forwarded to a "Static Structural" model in Ansys® to simulate the thermal deformation of the mirror (Fig. 5).

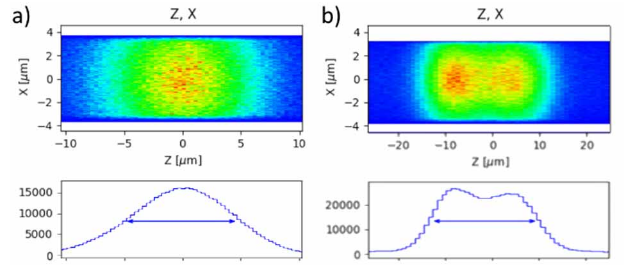

Figure 6: Resulting focus profiles for a) LH and b) LV polarization for notched design.

These are exported to OASYS-Shadow [9], to ray-trace the whole beamline without any deformations and with deformations on the switching mirror. Ray-tracing is done with a monochromatic beam close to undulator resonance of one million rays, which uses mostly the central region of the mirror. The resulting profiles of the beam focus make it easy to evaluate the changes inflicted by surface deformation, even for arbitrary surface profiles. In Fig. 6 the vertical (X) focus size is defined by the exit slit of the monochromator, while the horizontal (Z) size for a beamline with perfect optics should be about 9 μm (FWHM) and gaussian shaped. The LH case comes close, but the LV case has a second focus and double the width (Table 2). The peak to valley (P-V) height of the centreline is measured normal to the mirror surface in the 200 mm long region around the mirror centre.

Table 2: Results for Notched Design

Polarization	LH	LV
Max. temperature [°C]	163.8	170.8
P-V height of centreline [μm]	0.17	0.92
Focus width (FWHM) [μm]	9.81	23.4

DOUBLE BRACKET DESIGN

To reduce the overall temperature the cooling power had to increase, but with the position of the notch, there was very little room for improvement left. On a first try the upper "lips" of the mirror were extended to make space for one cooling bracket on top and a second below the lip on each side. This already reduced the temperature significantly, but the centreline profile now couldn't be influenced by the depth of the notch as before. The notches were removed and it was possible to use the height of the lips for the same purpose instead.

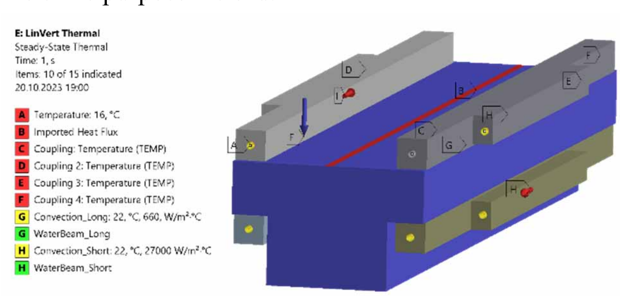

Figure 7: Boundary conditions for SST calculation in Ansys® on double bracket design.

The boundary conditions for the SST model are similar to Fig. 4, except that the upper water lines are coupled to their lower counterparts to even out the effects of increased water temperature and to minimize the number of individual water lines (Fig. 7). In Fig. 8 the temperature performance of this approach is obvious when compared to Fig. 4. In both cases the shorter cooling lines take the bulk of the power, but Fig. 8 shows a much better contained thermal profile.

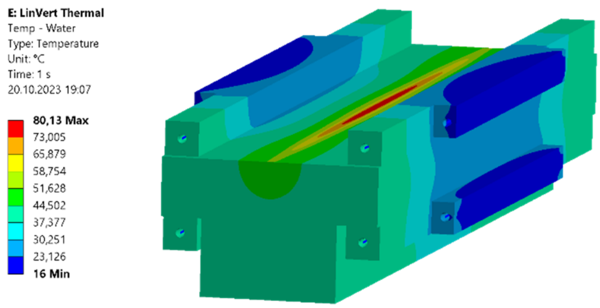

Figure 8: Result for SST calculation in Ansys® for LV polarization on double bracket design.

The resulting mirror profile for the LH polarization looks similar to the already good result of Fig. 5a), while the LV case has improved due to a relative broad and relative flat area in the mirror centre (Fig. 9).

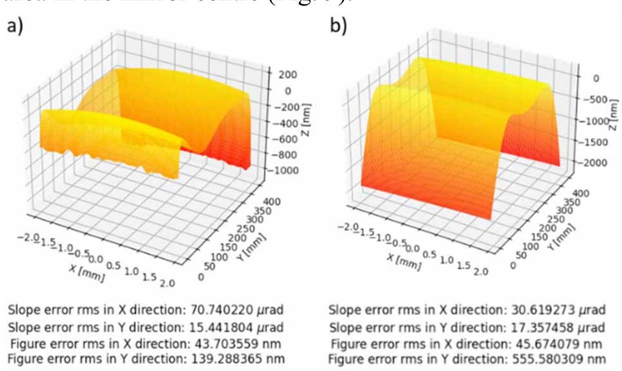

Figure 9: Resulting mirror surfaces for a) LH and b) LV polarization on the double bracket design.

The focus profile for the LH case repeats the performance from the notched design as expected (Fig. 10a)). For the LV case the horizontal FWHM could be improved to 15.5 µm (Table 3) and the profile is focussed to a single point (Fig. 10b)).

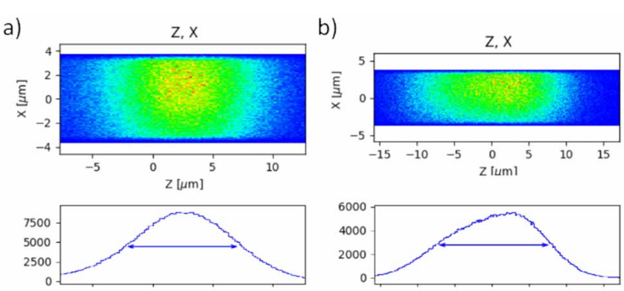

Figure 10: Resulting focus profiles for a) LH and b) LV polarization for double bracket design.

Table 3: Results for Double Bracket Design

Polarization	LH	LV
Max. temperature [°C]	88.76	80.13
P-V height of centreline [µm]	0.16	0.19
Focus width (FWHM) [µm]	9.66	15.52

CONCLUSION

The notched design shows good results in terms of thermal deformation and focus footprint for the LH case. With the second cooling line the LV polarization can be handled too. However, the temperature on the mirror surface is getting far too high, due to the smaller effective cooling area of the second cooling loop.

The double bracket design more than doubles the contact surface of the cooling lines which leads to strongly reduced maximum surface temperatures. This makes improvements for two thermal load cases much easier and improves the thermal deformations especially for the LV case.

REFERENCES

[1] J. Viefhaus *et al.*, “The Variable Polarization XUV Beamline P04 at PETRA III: Optics, mechanics and their performance”, *Nucl. Instrum. Methods Phys. Res. Sect. A*, vol. 710, pp. 151–154, May 2013. doi: 10.1016/j.nima.2012.10.110.

[2] T. Tanaka, “Major upgrade of the synchrotron radiation calculation code SPECTRA”, *J. Synchrotron Radiat.*, vol. 28, no. 4, pp. 1267–1272, Jul. 2021. doi: 10.1107/S1600577521004100.

[3] L. Rebuffi and M. Sanchez del Rio, “Interoperability and complementarity of simulation tools for beamline design in the OASYS environment”, in *Advances in Computational Methods for X-Ray Optics IV,* K. Sawhney and O. Chubar, Eds., San Diego, United States, 2017, p. 8. doi: 10.1117/12.2274232

[4] R. Reininger, “SRCalc”, 2001, unpublished.

[5] A.M. Khounsary, “Thermal management of next-generation contact-cooled synchrotron x-ray mirrors”, in *Proc. SPIE International Symposium on Optical Science, Engineering, and Instrumentation,* A. M. Khounsary, A.K. Freund, T. Ishikawa, G. Srajer, and J.C. Lang, Eds., Denver, CO, USA, Nov. 1999, p. 78. doi: 10.1117/12.370114.

[6] L. Zhang *et al.*, “Thermal distortion minimization by geometry optimization for water-cooled white beam mirror or multilayer optics”, *J. Phys. Conf. Ser.,* vol. 425, no. 5, p. 052029, Mar. 2013. doi: 10.1088/1742-6596/425/5/052029.

[7] R. Reininger, K. Kriesel, S.L. Hulbert, C. Sánchez-Hanke, and D.A. Arena, “A soft x-ray beamline capable of canceling the performance impairment due to power absorbed on its optical elements”, *Rev. Sci. Instrum.,* vol. 79, no. 3, p. 033108, Mar. 2008. doi:10.1063/1.2897587.

[8] Ansys® Mechanical Products, Release 22.2.

[9] L. Rebuffi and M. Sánchez del Río, “ShadowOui: a new visual environment for X-ray optics and synchrotron beamline simulations”, *J. Synchrotron Radiat.*, vol. 23, no. 6, pp. 1357–1367, Nov. 2016. doi: 10.1107/S1600577516013837.

ISBN: 978-3-95450-250-9 ISSN: 2673-5520 doi:10.18429/JACoW-MEDSI2023-THPPP005

DEVELOPMENT OF A VACUUM CHAMBER DISASSEMBLY AND ASSEMBLY HANDCART

X. J. Nie*, J. X. Chen, H. Y. He, L. Liu, R. H. Liu, C. J. Ning, G. Y. Wang, J. B. Yu, Y. J. Yu, J. S. Zhang, Institute of High Energy Physics (IHEP CSNS) China
also at Spallation Neutron Source, Dongguan, China
L. Kang, Institute of High Energy Physics (IHEP) Accelerator Center, Dongguan, China

Abstract

This paper developed a dedicated disassembly and assembly handcart for CSNS magnetic alloy cavity vacuum chamber. The optimal supporting section structure was determined by the use of ANSYS to analyze the strength of different sections. The stress situation of the handcart was improved by adding an extension rod at the end of the handcart. The installation position of the handcart was determined by the center position of the associated equipment. The development of the disassembly and assembly handcart structure was completed through structural optimization, disassembly and assembly process analysis, and positioning scheme design. The development of a handcart can improve the positioning accuracy of the vacuum chamber and prevent damage to the vacuum chamber during disassembly and assembly process.

INSTRUCTIONS

Magnetic alloy cavity is an important device for CSNS power increase. The length of its vacuum chamber is about 1.8 m with the weight of 75 kg. The vacuum chamber needs to pass through several cavities during the assembly-disassembly of it. And it is necessary to protect the insulating ceramics in the middle of the vacuum chamber. Meanwhile, just one small gap was left between the vacuum chamber and cavity to ensure the performance of the cavity. The smallest gap was only 3.5 mm. These factors make disassembly and assembly of the vacuum chamber very difficult and challenging. So, a dedicated handcart was developed for the disassembly and assembly of vacuum chamber.

OVERALL STRUCTURE DESIGN

The overall structure of the handcart is determined by the functions it is intended to achieve and working conditions [1]. First, the handcart is used to support the vacuum chamber steadily. And then it is required to smoothly move to the installation position of the vacuum chamber. To achieve the above functions, the overall handcart structure is designed as the following picture, which is composed of a base, support part, and guide part. The structure of the handcart is shown in Figure 1.

SUPPORT STRUCTURE DESIGN

The support beam is extended into the interior of the vacuum chamber during disassembly and assembly, supporting the weight of the vacuum chamber. Its strength and deformation need to be within a reasonable range. Based on the working condition of the support beam, it is determined that the force acting on the support beam is a cantilever structure. Several different cross-sectional shapes of support beams were selected for comparison. And the one with the best stress conditions was determined as the support beam. I-beams, rectangular tubes, and circular tubes were selected for comparison in usual materials. One end of the support beam was fixed and the load of the vacuum chamber was uniformly acted on the supporting surface [2]. The calculation results were shown in Table 1.

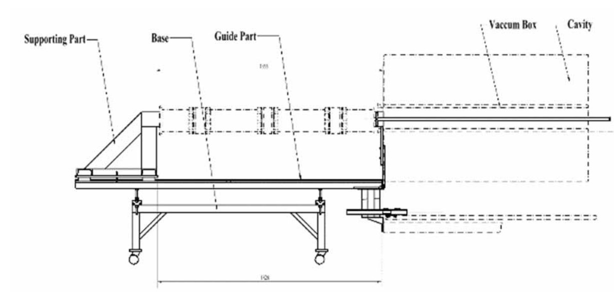

Figure 1: Overall structure of the handcart.

Table 1: Stress and Deformation for Support Beams with Different Cross-sectional Shapes

Cross-sectional shapes	Maximal stress [MPa]	Maximal deformation [mm]
I-beam	17.6	0.67
Rectangular	21.0	0.97
Circular	26.6	1.12

The distribution of stress and deformation on the supporting beams of each section is shown in Figure 2.

From above results, it can be concluded that under the same load, I-beam has the best stress state. And it can also be found that there is still significant deformation under cantilever structure for I-beam. If the cantilever structure can be eliminated, the stiffness of the support beam can be greatly improved. Figure 3 shows the stress and deformation distributions of the support beam under two fixed ends. The maximum deformation is only 0.02 mm, and the maximum stress is only 4.9 MPa.

* niexj@ihep.ac.cn

ISBN: 978-3-95450-250-9 ISSN: 2673-5520 doi:10.18429/JACoW-MEDSI2023-THPPP005

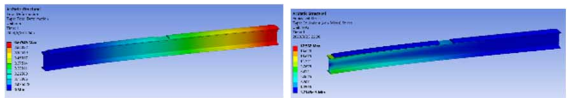

(a) Deformation for I-beam (b) Sress for I-beam

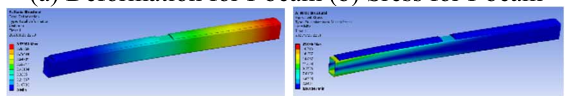

(c) Deformation for rectangular (d) Sress for rectangular

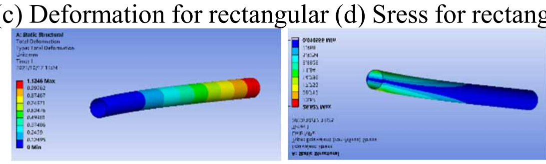

(e) Deformation for circular (f) Sress for circular

Figure 2: Distribution of deformation and stress for different sections.

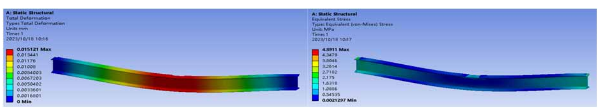

(a) Deformation (b) Sress

Figure 3: Distribution of deformation and stress for two fixed ends I-beam.

But it is quite difficult to fix the two ends of the support beam under actual working conditions. To improve the stress condition, two expansion rods are added to the side of the I-beam, which are extended during operation and supported by auxiliary support at the other end. And it is necessary to connect the support structure with other parts to form a complete handcart. Therefore, the final support structure was consisted of installation seat, support beam, and expansion rods, which was shown in Figure 4.

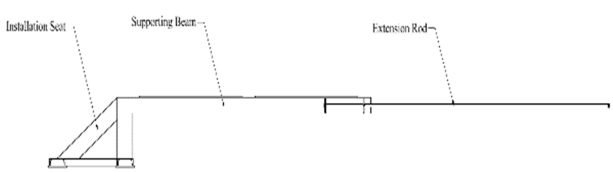

Figure 4: General drawing of support structure.

DESIGN OF POSITIONING AND GUIDING MECHANISM

When disassembling and assembling the vacuum chamber, the inner cylinder of the cavity has been aligned and adjusted in place, so it can be used as a reference to locate the handcart [3]. According to the structure of the cavity, a positioning mechanism is set up on the support surface of the cavity, and a circular sleeve is used for positioning. Since the position of the cavity has been adjusted, the center of the positioning sleeve is naturally parallel to the center of the cavity. To adjust the center of the positioning sleeve to the same vertical plane of the cavity, this positioning sleeve can be used to guide the direction of the handcart. To achieve directional guidance of the handcart, a positioning sleeve and two guide rails are set at the handcart end, and the handcart position is adjusted to be concentric with the positioning sleeve at the cavity end to achieve directional guidance of movement. The positioning guide mechanism is shown in Figure 5.

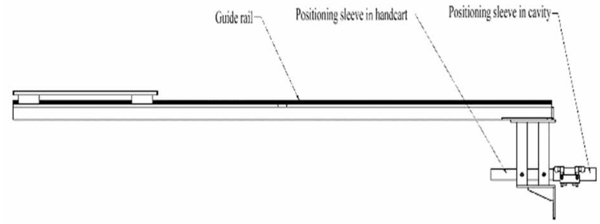

Figure 5: General drawing of positioning and guiding mechanism.

To ensure smooth installation, a gap fit is used between the two sleeves. Assuming the gap between the sleeves is Δ, the guiding length is L, and the movement distance is L_1, then the offset t generated from the entire movement can be calculated using Eq. (1).

$$t = L_1 \times \tan\left(\arctan\frac{\Delta}{L}\right) = \frac{L_1}{L}\Delta \qquad (1)$$

If the gap is designed as 0.5 mm and the guide length is 300 mm, the offset produced within the 1.8-meter range of motion is only 3 mm, which is less than the minimum gap between the cavity and the vacuum chamber. So, the positioning and guiding mechanism can meet the requirements.

BASE DESIGN

The base is directly placed on the ground to support, adjust and transport the handcart. The base is welded by profiles, which is easy to process with low cost and good strength. Four universal wheels are installed at the bottom of the base for easy transportation, and an adjustment mechanism is fixed at the top to adjust the position of the handcart. The overall structure of the base is shown in Figure 6.

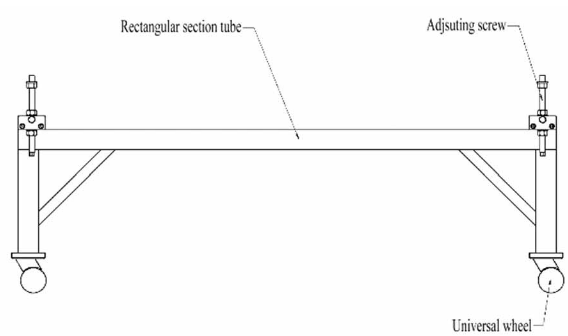

Figure 6: Overall drawing of the base.

SUMMARY

By analysing the disassembly and assembly conditions of the cavity vacuum chamber, the overall structure of the handcart was achieved. And ANSYS was used to analyse and compare the stress situation of support beams with different cross-sectional shapes, and the cross-sectional shape with the best stress conditions was selected as the support

ISBN: 978-3-95450-250-9 ISSN: 2673-5520 doi:10.18429/JACoW-MEDSI2023-THPPP005

beam. A positioning and guiding mechanism was designed for the handcart using the center of the cavity. An adjust and movable base has been designed for the handcart. The handcart can meet the disassembly and assembly requirements of the vacuum chamber in a long distance and small gap in the magnetic alloy cavity.

ACKNOWLEDGEMENTS

The authors would like to express their appreciation to all the colleagues who have contributed to this project.

REFERENCES

[1] K. Xie, Y. Zhang, L. Chen *et al.*, "Design and analysis of flexible support structure for low temperature infrared lens", *LASER & INFRARED*, vol. 53, no. 8, pp. 1260-1265, Aug. 2023. doi:10.3969/j.issn.1000-5078.2023.08.019

[2] Y. X. Yang and F. Xu, "Force simulation of roller shaft head welding based on ANSYS Workbench", *China Rubber/Plast. Technol. and Equip.*, vol. 49, no. 10, pp. 58-62. 2023. doi:10.13520/j.cnki.rpte.2023.10. 014

[3] J. Wang and X. Cui, "Design of a Precise Rotation-Driving Positioning Device for Aircraft Tires", *ENGINEERING & TEST*, vol. 63, no. 2, pp. 76-78. Jun. 2023. doi:10.3969j.issn.1674-3407.2023.02.024

ISBN: 978-3-95450-250-9 ISSN: 2673-5520 doi:10.18429/JACoW-MEDSI2023-THPPP007

OPTIMIZING INDIRECT COOLING OF A HIGH ACCURACY SURFACE PLANE MIRROR IN PLANE-GRATING MONOCHROMATOR*

Jie Chen#, Zimeng Wang, Xuewei Du, Minghao Lin, Qiuping Wang
NSRL, University of Science and Technology of China, Hefei, Anhui, P. R. China

Abstract

For the cooling of the plane mirror in VIA-PGMs (variable-included-angle plane-grating monochromators), the top-side indirect cooling based on water is preferred for its advantages, such as cheaper, easier to use, smart notches, etc, when compared to the internal cooling. But it also arises challenges to control the RMS residual slope error of the mirror, whose requirement is less than 100 nrad. This requirement is even hard to fulfill, when combined with 1) the asymmetry thermal deformation on the meridian of the footprint area during the energy scanning, 2) the high heat load deduced by the synchrotron light and 3) the no obvious effects of the classical optimizations, such as increasing footprint size, cooling efficiency or adding smart notches. An effective way was found after numerous attempts, which is to make the footprint area far from the mirror's edge to reduce the asymmetry of the thermal deformation except for leading to a longer mirror. This paper will illustrate how the asymmetry affects the mirror's residual slope error and then, focus on the relationship among the asymmetry of cooling and the distance to provide a reference for optical cooling.

INTRODUCTION

In recent years, numerous light sources are developing synchrotron facilities with higher brightness, smaller divergence angle and more stability. During the development, the researching of the optics cooling of the beamline has draw much attention for the crucial role to realize these goals. There are so many articles focus on the cooling art of the first mirror because it bears the highest heat load among all the optics in a beamline [1-5]. However, for some VIA-PGMs in the downstream of the first mirror, few report about the cooling of optics in the PGM was found. And the cooling of the VIA-PGM had become an issue in some synchrotron facilities with high brightness and ultra small divergence angle, not only for its thermal working condition and high accuracy surface requirement of the mirror but also for its different optimization of cooling, compared to first mirror. This article will briefly list the common optimizations for the cooling of first mirror as references; then, based on a high heat load mirror of a beamline of Hefei Advanced Light Facility (HALF) [6], the limitation of these optimization are introduced; and at last, the reason and resolution are provided.

* This work is supported by the Chinese Academy of Science (CAS) and the Anhui province government for key techniques R&D of Hefei Advanced Light Facility.
# jiechen9@ustc.edu.cn

OPTIMIZATIONS FOR INDIRECT COOLING OF THE FIRST MIRROR

For water cooling solutions, indirect cooling technology is still the first choice in design, when considering drawback of the internal cooling optical components, such as the long supply period, expensive, difficult to maintain, etc. [7]. Further, the indirect cooling has the capacity to utilize the reverse thermal moment, local heat compensation, etc to improve the slope error of thermal deformation. This part briefly introduces the common optimization method of the first mirror cooling of the beamline.

From 1996, Khounsary et al. adjusted the width of the cooling area and the bias and the depth of the notches on the side of the first deflection mirror to change the temperature distribution, which diminished the meridian slope error of the central part of the footprint (Fig. 1(a)) [1, 7, 8]. The principle of the two method are same. The bending of the mirror can be substantially reduced or reversed by a reverse thermal moment generated from the temperature difference between different uniform temperature region. And the notch has a more obvious effect because it makes the temperature difference between the uniform temperature region larger, and thus the expands the balanced thermal moment.

From 2013, Zhang Lin et al. reported the method on cooling length tuning to optimize the edge effect of the first mirror and upgrade it via heaters, as shown in Fig. 1(b) [4, 9]. At the two ends of the spot area, the heat flow reduced and became zero out of the area. This sharp change in heat flow leaded to a large slope error in these area, which named the edge effect on meridian. The effect also affected the inner zone of the spot area except for the edge area. Zhang's method made the cooling length shorter than the spot length, which can rise the temperature of the two end locations, to compensate the effect.

In 2016, Corey Hardin et al. reported a cooling method based on liquid metal bath and surface shape tuning technique for horizontal deflection mirrors. This method decoupled the effect of fluid induced vibration to optical components during cooling. As Fig. 1(c), although the optical element used unilateral cooling, the structure of the mirror still retains a symmetrical design [10].

In 2022, Wang Shaofeng and Gao Lidan et al. illustrated another cooling method for horizontal deflection mirror. Different from the design of Corey Hardin, this is a structure of unilateral cooling, notches and asymmetry to simplify the processing and assembly, as in Fig. 1(d) [11].

Beyond the mentioned above, the slope error of thermal deformation can also be decreased by improving the cool-

ISBN: 978-3-95450-250-9 ISSN: 2673-5520 doi:10.18429/JACoW-MEDSI2023-THPPP007

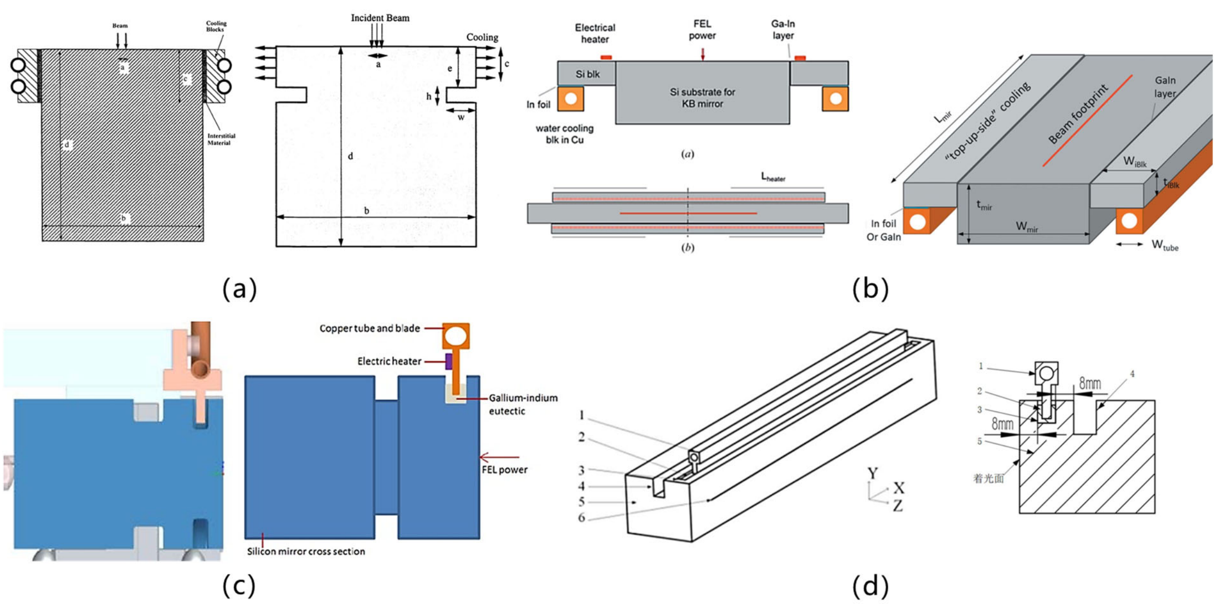

Figure 1: The optimizations for the first mirror of beamline.

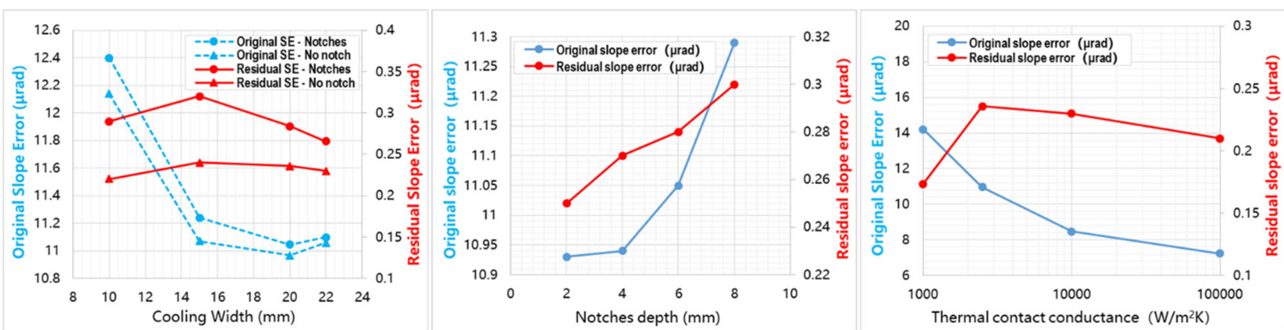

a) Influence of the cooling width and notches bias. (TCC = 2500W/m²K)

b) Influence of the notches' depth. (TCC = 2500W/m²K)

c) Influence of the contact thermal conductance. (No notch, Cooling width: 20mm)

Figure 2: Optimizations effects on the residual slope error in the meridian direction (Film coefficient = 3600 W/m^{2}K , *Thermal contact conductance, TCC).

ing efficiency via In-Ga which can reduce the defomation generated by clamp force [7, 12].

LIMITATIONS OF THESE OPTIMIZATIONS FOR PLANE MIRROR

The optimizing methods mentioned in section 2 focused on the first mirror of beamline, whose spot area featured with 1) the symmetry center of the heat load distribution coincides with the symmetry center of the cooling structure of the optical element in the meridian direction; 2) the length of the spot area are as long as the mirror; 3) the power density on the spot area are almost uniform in the meridian direction [7, 13]. However, for the plane mirror in the VIA-PGM (variable-included-angle plane-grating monochromators), the spot size on it are very short than the mirror and the spot's location are vary with the output energy of the PGM. Figure 3 pictured a plane mirror's 6σ power density of a beamline's PGM in HALF under the maximum heat load working condition. The meridian slope error of the 4σ area should be smaller than 200 nrad.

These optimizations mentioned were implemented and the corresponding results are shown in Fig. 2. From Figs. 2 (a) and (b), the limited improvement of the two methods can be witnessed, none of them can push the residual slope error down to 200 nrad. Figure 2(c) also tells a slight changing about thermal contact conductance, except for the 1000 W/m^{2}K condition whose margin is not enough and temperature rises to 71 ℃. The heat flow compensation cooling method is relative complex so that not discuss conducted here.

RESOLUTIONS FOR COOLING OF PLANE MIRROR

A core reason, that can be put after comparing the curve of deformation and fitted one ,is the asymmetry of thermal deformation in the meridian direction, which dues to the asymmetry cooling structure. This problem will become even worse under the maximum heat load working condition. The effective way to handle it is make the high heat load spot far from the edge of the plane mirror. Via parametric simulation, the balanced parameter can be easy found via curves shown in Fig. 4.

ISBN: 978-3-95450-250-9 ISSN: 2673-5520 doi:10.18429/JACoW-MEDSI2023-THPPP007

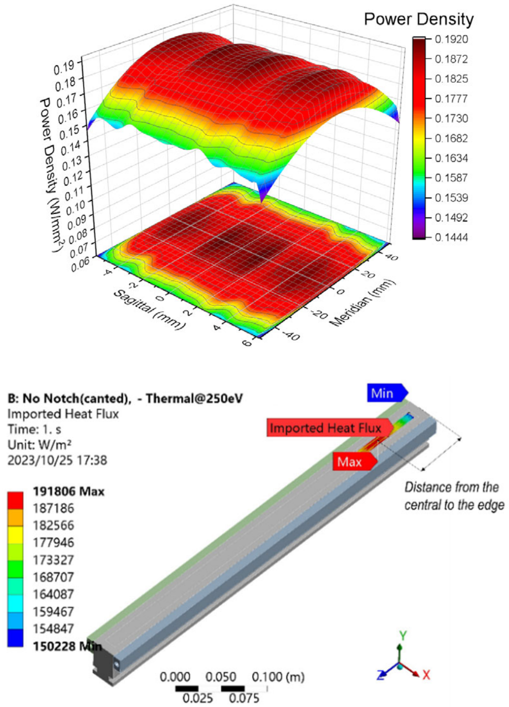

Figure 3: Power density under the maximum working condition (q''_{max}=0.192 W/mm^{2}K, P = 188.5 W) and the cooling structure utilized.

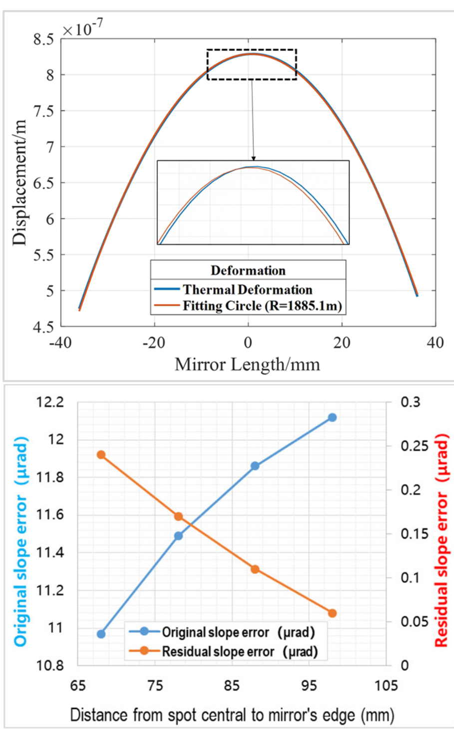

Figure 4: Distance effects on the residual slope error.

CONCLUSIONS

Careful considerations of the cooling of the plane mirror are demanded, whose optimizations are different from the first deflection mirror. In this part, design and analysis of a high heat load plane mirror's cooling of VIA-PGM were described. Combined with the optimizations targeted to the first mirror and symmetry improvement of the PM's cooling structure, the monochromator is expected to provide the required performance for heat load of up to 0.192 W/mm^2, 188.5 W on the mirror at the max heat load condition. But it is suitable for these monochromator who has a relative large space to do the implement.

ACKNOWLEDGMENTS

We wish to thank Gao Lidan, Jin Limin and Xu Zhongmin for their assistance and fruitful discussions.

REFERENCES

[1] A.M. Khounsary, "Thermal management of next-generation contact-cooled synchrotron x-ray mirrors". *SPIE*, vol. 3773, pp. 78–87, 1999. doi:10.1117/12.370114

[2] Z. Xu *et al.*, "Study on cooling for optical parts with high heat loads at the SSRF", *J. Phys. Conf. Ser.*, vol. 425, no. 5, p. 52011, 2013. doi:10.1088/1742-6596/425/5/052011

[3] L.-M. Jin *et al.*, "A numerical comparison between internal cooling and side cooling of the reflection mirror for Spatial and Spin (S^2) beam-line at SSRF", *Nucl. Instrum. Methods Phys. Res., Sect. A*, vol. 902: pp. 190–196, 2018. doi: 10.1016/j.nima.2018.06.015

[4] L. Zhang *et al.*, "Thermal distortion minimization by geometry optimization for water-cooled white beam mirror or multilayer optics", *J. Phys. Conf. Ser.*, vol. 425, p. 052029, 2013. doi:10.1088/1742-6596/425/5/052029

[5] G. Cutler *et al.*, "A cantilevered liquid-nitrogen-cooled silicon mirror for the Advanced Light Source Upgrade", *J. Synchrotron Radiat.*, vol. 27, no. 5, pp. 1131–1140, 2020. doi:10.1107/S1600577520008930

[6] Z. Sun, G. Feng, and X. Liu, "Construction of Hefei advanced light facility begins", *The Innovation*, vol. 4, no. 6, p. 100514, 2023. doi:10.1016/j.xinn.2023.100514

[7] A.M. Khounsary and W. Yun, "On optimal contact cooling of high-heat-load x-ray mirrors", *Rev. Sci. Instrum.*, vol. 67, pp. 3354–3354, 1996. doi:10.1063/1.1147402

[8] A. Khounsary *et al.*, "Performance of side-cooled high-heat-load mirrors", *Adv. Mirror Technol. Synchrotron X-Ray Laser Appl.*, vol. 3447. pp. 81-91. 1998. doi:10.1117/12.331120

[9] L. Zhang *et al.*, "Optimizing X-ray mirror thermal performance using matched profile cooling", *J. Synchrotron Radiat.*, vol. 22, no. 5, p. 1170–1181, 2015. doi:10.1107/S1600577515013090

[10] C.L. Hardin *et al.*, "Optimizing x-ray mirror thermal performance using variable length cooling for second generation FELs", *SPIE*, vol. 9965, p. 996505, 2016. doi:10.1117/12.2235825

[11] S. Wang *et al.*, "The invention relates to an asymmetrical slotted cooling structure suitable for horizontal reflector type mirrors", Patent Authority and 2022. Page 7.

[12] A. Crisol *et al.*, "The ALBA high-stability monochromator for VUV and soft X-rays", *J. Phys. Conf. Ser.*, vol. 2380, p. 12051, 2022. doi:10.1088/1742-6596/2380/1/012051

[13] A.M. Khounsary *et al.*, "Thermal contact resistance across a copper-silicon interface", *SPIE*, vol. 3151, pp. 45–51, 1997. doi:10.1117/12.294497

ISBN: 978-3-95450-250-9 ISSN: 2673-5520 doi:10.18429/JACoW-MEDSI2023-THPPP008

OPTIMIZATION OF THERMAL DEFORMATION OF A HORIZONTALLY DEFLECTING HIGH-HEAT-LOAD MIRROR BASED ON eInGa BATH COOLING *

Jie Chen#, Xuewei Du, Zimeng Wang, Minghao Lin, Qiuping Wang
NSRL, University of Science and Technology of China, Hefei, Anhui, P. R. China

Abstract

The synchrotron facilities are developing towards higher brightness, lower divergence, narrower pulse, higher stability, etc. Therefore, the requirements of the first mirror of the beamline, who bear high-heat-load, were also upgraded, and the performances of the mirror become affected easily by other factors, such as flow induced vibration, clamping force, etc. Indirect water cooling based on eInGa bath is regarded as an effective mean to solve these thorny problems in designing of the first mirror cooling. However, for the case a horizontal deflection mirror, the unilateral cooling method is usually adopted, resulting in some changes in the structure of the mirror. In this paper, a first mirror horizontally deflecting of Hefei Advanced Light Facility (HALF) are taken as an example to introduce the optimization method to achieve ultra-low slope error in the meridian direction. The results show that this optimization method provides a rapid design process to design the cooling scheme of the horizontally deflecting mirror based on the eInGa bath.

INTRODUCTION

In synchrotron facilities, the first mirror of the beamline has the advantages of substantially reducing the heat load of downstream optics, suppressing high order harmonics and radiation shielding [1]. The cooling method of the first mirror, depended on the heat load power density and total heat load on it, can adopt direct water cooling, indirect water cooling or liquid nitrogen indirect cooling schemes [2-5]. Since the power density on the first mirror has a good uniformity and symmetry in the meridian direction, an indirect water cooling, combined with the thermal deformation optimization method via passive reverse thermal moments, were developed [6, 7]. With the improvement of the brightness, stability and low divergence of the synchrotron light source, the surface shape requirement of the first mirror of the beamline has reduced to the order of hundreds nano-radian, which also leads challenges, such as the flow induced vibration caused by the coolant, the clamping deformation caused by the liquid cooled copper plates when cooling the mirror and the non- uniformity of the thermal conductance between contact blocks, etc. The indirect water-cooling scheme based on eInGa bath is regarded as an effective means to solve these problems [8, 9]. However, for the case that the first mirror is a horizontal deflection one, the optimization method is different because of the changes of cooling structure, such as: 1) the side of the mirror needs to be slotted for holding eInGa; 2) the cooling area changes from bilateral to unilateral. These factors will significantly affect the design and optimization of the mirror and its cooling structure. Taking a high-heat-load first mirror of the beamline of Hefei advanced light source (HALF) as an example, this paper introduces the optimization method to achieve the ultra-low meridian slope error in the meridian direction of the high heat load horizontally deflecting mirror.

THERMAL DEFORMATION OPTIMIZATION METHOD BASED ON eInGa BATH COOLING

The eInGa bath cooling method for the first mirror of the beam line has many advantages [8, 10]. First, the eInGa liquid metal has a very high and uniform heat transfer coefficient at the contact interface between components, up to 100,000 W/m^2K [10]. Although the thermal conductivity is only 28 W/m•K, it still turn out to be an excellent thermal interface material. Secondly, the viscosity of eInGa liquid alloy is very low, only 1.99×10^{-3} Pa•s, a factor of two greater than that of water [11], makes the vibration transfer ability extremely bad, which can effectively decouple the flow induced vibration transmitted from the water-cooled copper plate to the optical element. Third, the liquid metal can avoid the clamping force on the optics since no direct contact between the cooling mechanism and the mirror. However, the application of cooling based on the eInGa bath will also have some influences on the mirror body and the cooling structure.

Limitation

In the first mirror of vertical deflection, eInGa grooves can be applied on the top surface and near the edges of it [8]. This cooling topology is similar to the cooling efficiency of the double-sided clamping structure [12]. The difference is that since the insertion of the cooling structures in the mirror body, the depth of the notches will also increase, but the level of the reverse thermal moment on each side will not change much.

However, in the first mirror of horizontal deflection, the eInGa groove can only be applied on the top surface of the mirror, i.e., on one side of the incident plane, as shown in Fig. 1. This cooling structure is very different from the previous: 1) The cooling efficiency is reduced. As the cooling structure is changed to one side, the cooling efficiency is reduced by twice compared with the two-

* This work is supported by the Chinese Academy of Science (CAS) and the Anhui province government for key techniques R&D of Hefei Advanced Light Facility.
# jiechen9@ustc.edu.cn

12th Int. Conf. Mech. Eng. Design Synchrotron Radiat. Equip. Instrum. MEDSI2023, Beijing, China JACoW Publishing
ISBN: 978-3-95450-250-9 ISSN: 2673-5520 doi:10.18429/JACoW-MEDSI2023-THPPP008

side cooling, resulting in a further increase in the surface temperature of the mirror. 2) Deeper notch. Since the eInGa groove is cut into the side surface of the incident surface, the distance between the cooling area and the heating area is reduced. In this case, notch deeper than the depth of the groove is needed to adjust the stress by near the middle temperature isotherm between the hot and cold regions. 3) Thicker mirror body size. Limited by the process and reliability, there is a certain distance between the eInGa groove and the incident surface in the normal direction of it. The greater the distance, the smaller the reverse thermal moment. Thus, the increasing of the thickness of the mirror body is needed to generate a greater reverse thermal moment, and the reverse thermal moment is greater than twice the bilateral cooling.

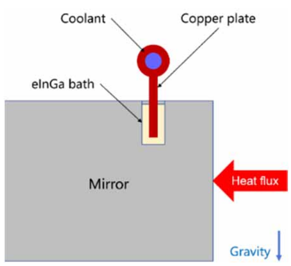

Figure 1: A horizontally deflecting mirror (silicon) based on eInGa bath and its cooling structure.

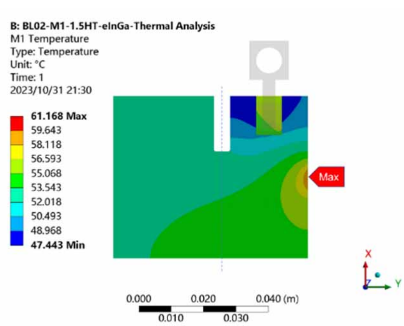

Figure 2: Temperature distribution on the cross section of the mirror. (The reverse bending thermal moment can only be formed between the uniform temperature zone (green) and the region with a lower temperature than it (bule). The thermal stress region pairs are as follows: 1) The bending thermal stress: the uniform temperature regions and the high temperature region (red); 2) The reverse bending thermal stress: the low temperature region and the uniform temperature region; 3) Lateral bending thermal stress: the high temperature region and the low temperature region.).

For the horizontally deflecting mirror, the optimization of the thermal deformation of the mirror should adopt an asymmetric structure rather than a symmetrical structure, that is, the notch is applied only on the top surface of the mirror. In this case, notch can achieve a greater depth to generate larger reverse thermal moment. On the other hand, for a bilateral notch structure, although the mirror can be widened to avoid the middle region of the mirror being too thin, the cooling efficiency may decrease and the footprint region's temperature may fly. The last but not least, there is a lack of thermal stress zone pairs in the bottom part of the mirror to balance the lateral bending and bowing of the mirror body which can be witnessed in Fig. 2. Therefore, the presence or absence of the notch in the bottom part of the mirror will not improve thermal deformation.

Optimizations for the Unilateral Cooling Based On eInGa Bath

After the limit factors of the first mirror for horizontal deflection being settled, the mirror and its cooling structure are basically determined, as shown in Fig. 3. For this module, the thermal deformation in the meridian direction of the incident surface can be treated as the superposition of three effects, namely, bowing, bumping and edge effect [12, 13]. The thermal deformation of the bowing and the bumping derives from the total heat load and power density distribution respectively. And the edge effect derives from the changes in heat load conditions and cooling efficiency at both ends of a spot, featured with a sharp thermal deformation change in this area.

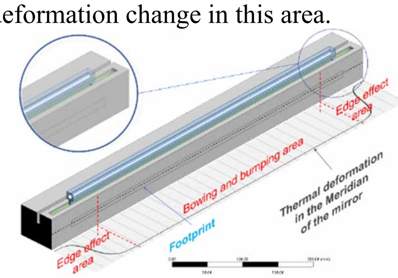

Figure 3: Horizontally deflecting mirror and its cooling structure（Usually, subject to the process, the wall thickness on each side of eInGa bath is ⩾8 mm, and the width of the bath is ⩾8 mm.)

For the first mirror, the distribution of heat load power density in the meridian direction is usually uniform. Taking a first mirror of a beamline of Hefei Advanced Light Facility as an example, its power density is shown in Fig. 4. According to the following calculation, the nonuniformity of its heat load in the meridian direction is 1.5 %, which represents a good uniformity.

$$\text{Nonuniformity}=\frac{\frac{1}{n}\sqrt{\sum_{1}^{n}(PowerDensity-\overline{PowerDensity})^2}}{\overline{PowerDensity}}\times 100\%$$

Therefore, the three effects of thermal deformation can be handled separately. In the meridian direction, a nearly complete compensation for a bowing deformation can be achieved by controlling the position and depth of notch [6, 12]. The bumping, a deformation relative small under conditions of uniform power density in the meridian direction, can also be optimized to some degreee in this process [14, 15]. For the edge effect, there are two ways to deal with it. One is to shorten the length of the cooling zone and reduce the cooling efficiency near the two ends of the spot. The other is over irradiation, which extrapolates the area affected by the edge effect away from the central region by making the spot size longer. Therefore,

ISBN: 978-3-95450-250-9 ISSN: 2673-5520 doi:10.18429/JACoW-MEDSI2023-THPPP008

for the first horizontally deflecting mirror based on eInGa bath cooling, the optimization work of meridian thermal deformation is decomposed into the optimization of the mirror body and the evaluation of the region affected by edge effects.

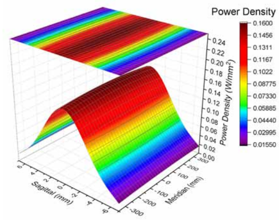

Figure 4: The power density distribution of the first horizontal deflection mirror ($q''_{max} = 0.16$ W/mm^2, $P = 618$ W).

For optimization of the bowing and the bumping thermal deformation of mirror, the thickness of the mirror needs to be determined first. According to the process parameters of the groove on a silicon mirror, and the width of notch who is about 5 mm, the distance between notch and the incident plane of the mirror is at least 24 mm. The balancing thermal moment with respect to the middle of the mirror's cross section (the dotted line in Fig. 2) essentially renders a meridian flat mirror (except at the end) [16] the total thickness of the mirror body should be thicker than double of (24.0+2.5) mm, for example, thickness =60 mm. Among them, the length of the cooling mechanism is equal to the length of the light spot, because, shorter than the spot size, two high temperature points will be generated on the incident surface, and longer than the light spot size will expand the influence area of the edge effect. In addition, the notch depth, when notch of a certain depth makes the meridian surface curvature at positive or negative transition points, can be regard as the optimal value. At this point, the size of the area affected by the edge effect is independent of the mirror length.

In the determination of the over irradiated region, to ensure that the slope error of the thermal deformation in the meridian direction of the central region meets the design requirements, the length of the over irradiated region should meet the following relationship:

$$(Over\ irradiation\ region) \geq (Central\ area) + 2\times(Edge\ effect)$$

When evaluating the influence length of the edge effect, a slope error limit should be specified, such as 100 nrad. Then, the notch depth was optimized to the transition point for the mirror's spot length equals to the length of concerned area of the mirror 500 mm. The meridian thermal deformation curve, slope error and RMS slope error were obtained, as shown in Fig. 5.a). Then, according to the RMS slope error curve and slope error limit, the length of the region beyond the limit is defined as the edge effect influence region, which is 29 mm. Finally, according to the above formula, the length of the over irradiation area of the mirror is determined to be 558mm. A FEA was implemeted by utilizing these parameters. As shown in Fig. 5 b, the original slope error RMS in the meridian of the area (500 mm) is 62 nrad, the residual slope error RMS is 59 nrad, and the fitting circle radius is about 4542.8 km.

CONCLUSIONS

The curve transition point of the meridian thermal deformation provide a judgement of the notch optimization for eInGa bath cooling. Combined with tuning of notch depth and evaluating of edge effect, a horizontally deflecting mirror can achieve a slope error of sub-hundred nano rad in meridian directon. In this paper, we illustrated the technological limitations of the first beam line mirror based on eInGa bath cooling, the principle and method of optimizing the shape error of the spot area of it and utilized the method to gain a cooling scheme featured with a sub-hundred nano rad origin slope error RMS in meridian.

ACKNOWLEDGMENTS

We wish to thank Gao Lidan, Tang Shanzhi, Jin Limin and Xu Zhongmin for their assistance and fruitful discussions.

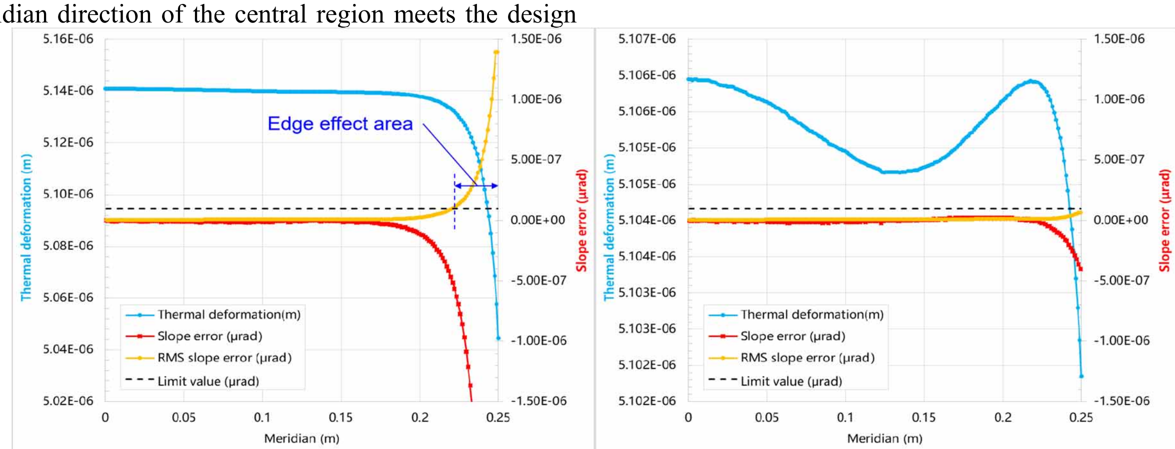

(a) (b)

Figure 5: (a) The thermal deformation, RMS slope error, etc of the mirror (Under condition of curvature transition point of meridian thermal deformation and 500 mm footprint length); (b) The optimized results of the meridian thermal deformation and slope error the mirror.

ISBN: 978-3-95450-250-9 ISSN: 2673-5520 doi:10.18429/JACoW-MEDSI2023-THPPP008

REFERENCES

[1] W. Yun *et al*., "Advantages of using a mirror as the first optical component for APS undulator beamlines", *Rev. Sci. Instrum.*, vol. 67, no. 9, pp. 3353-3354, 1996. doi:10.1063/1.1147398

[2] H. Oyanagi, Y. Kuwahara, and H. Yamaguchi, "A directly water-cooled silicon crystal for high power insertion devices", *Rev. Sci. Instrum*., vol. 66, no. 9, pp. 4482-4486, 1995. doi:10.1063/1.1145346

[3] A.M. Khounsary and W. Yun, "On optimal contact cooling of high - heat - load x - ray mirrors", *Rev. Sci. Instrum.*, vol. 67, no. 9, p. 3354, 1996. doi:10.1063/1.1147402

[4] L. Zhang *et al.,* "Thermal deformation of cryogenically cooled silicon crystals under intense X-ray beams: measurement and finite-element predictions of the surface shape", *J. Synchrotron Radiat.,* vol. 20, no. 4, pp. 567-580, 2013. doi:10.1107/s0909049513009436

[5] L. Zhang *et al.,* "The performance of a cryogenically cooled monochromator for an in-vacuum undulator beamline", *J. Synchrotron Radiat.,* vol. 10, no. 4, pp. 313-319. doi:10.1107/s0909049503012135

[6] A.M. Khounsary, "Thermal management of next-generation contact-cooled synchrotron x-ray mirrors", in *Proc. SPIE,* vol. 3773, 1999. doi:10.1117/12.370114

[7] L. Zhang *et al.*, "Optimizing X-ray mirror thermal performance using matched profile cooling", *J. Synchrotron Radiat.,* vol. 22, no. 5, pp. 1170-1181, 2015. doi:10.1107/S1600577515013090

[8] S. Wang *et al.,* "Highly efficient thermal deformation optimization method for smart - cut mirrors over the entire photon energy range", *J. Synchrotron Radiat.,* vol. 29, no. 5, 2022. doi:10.1107/s1600577522007160

[9] T. Li *et al.,* "A reliable FEA-based calculation approach of convective heat transfer coefficient for Steady-State Thermal analysis of X-ray water-cooled mirrors", *Nucl. Instrum. Methods Phys. Res., Sect. A,* vol. 1040, p. 167288, 2022. doi:10.1016/j.nima.2022.167288

[10] C.L. Hardin *et al.,* "Optimizing x-ray mirror thermal performance using variable length cooling for second generation FELs", in *Proc. SPIE*, vol. 9965, 2016. doi:10.1117/12.2235825

[11] M.D. Dickey *et al.,* "Eutectic Gallium-Indium (EGaIn): A Liquid Metal Alloy for the Formation of Stable Structures in Microchannels at Room Temperature", *Advanced Funct. Mater.*, vol. 18, no. 7, pp. 1097-1104, 2008. doi:10.1002/adfm.200701216

[12] L. Zhang *et al.,* "Thermal distortion minimization by geometry optimization for water-cooled white beam mirror or multilayer optics", *J. Phys. Conf. Ser.,* vol. 425, no. 5, pp. 52029-4, 2013. doi.10.1088/1742-6596/425/5/052029

[13] P. Brumund *et al.,* "Thermal optimization of a high-heat-load double-multilayer monochromator", *J. Synchrotron Radiat*., vol. 28, no. 5, pp. 1423-1436, 2021. doi:10.1107/S160057752100758X

[14] T.W. Tonnessen and S.E. Fisher, "Design and analysis of cooled optical components for synchrotron beamlines", in *Proc. SPIE 1740*, 1993. doi:10.1117/12.138710

[15] A.M. Khounsary *et al.*, "Contact-cooled U monochromators for high heat load x-ray beamlines", in *Proc. SPIE 2855*, 1996. doi:10.1117/12.259834

[16] A.M. Khounsary *et al.,* "Performance of an optimally contact-cooled high-heat-load mirror at the APS", in *Proc. SPIE, 3447,* 1998. doi:10.1117/12.331120

12th Int. Conf. Mech. Eng. Design Synchrotron Radiat. Equip. Instrum. MEDSI2023, Beijing, China JACoW Publishing
ISBN: 978-3-95450-250-9 ISSN: 2673-5520 doi:10.18429/JACoW-MEDSI2023-THPPP009

THE HEAT LOAD CALCULATION IN THE GRATING-BASED BEAMLINE AT HEFEI ADVANCED LIGHT FACILITY (HALF) *

Zimeng Wang†, Jie Chen, Xuewei Du, Qiuping Wang and Donglai Feng, National Synchrotron Radiation Laboratory, University of Science and Technology and China, Hefei, Anhui, China

Abstract

The light emitted by the 4th generation synchrotron radiation (SR) light source is more concentrated. Therefore, its heat load causes more severe thermal deformation on the beamline optics than the 3rd generation SR light source. The requirement on the optical element surface quality is also higher to achieve better spectral resolution, coherence preservation and focusing. The precise calculation of heat load on the optical elements is fundamental for the thermal analysis including cooling method and thermal deformation simulation. A heat load calculation code has been developed for SR beamline optics, which consists of SR source calculation module for precise power density distribution, mirror reflectivity module and grating efficiency module. Therefore, it can be applied to mirrors, crystals and gratings.

This code has been used to calculate the heat load of BL10 - the Test Beamline optics at Hefei Advanced Light Facility (HALF). The heat absorbed by the first three optical elements are precisely calculated, including a toroidal mirror, a plane mirror and a plane grating.

INTRODUCTION

To quantitatively calculate the heat load on the synchrotron radiation (SR) beamline optical elements, it is necessary to combine the angular distribution calculation of the source power density with the calculation of optical element transmission efficiency, including the reflectivity of the mirrors and the diffraction efficiency of the gratings. SRCalc [1, 2] is one of the software that calculates the optical elements. However, SRCalc only contains mirror and crystal heat load calculation. Currently, there is still no software available that enables the calculation of grating heat load. Therefore, in beamline design, the calculation of grating thermal load is often estimated.

The light source and efficiency calculation programs mentioned earlier have been completed. Therefore it is possible to achieve precise calculations of the heat load for all optical elements, including the gratings. This paper will take the Test Beamline (BL10) in Hefei Advanced Light Facility (HALF) [3] as an example of heat load calculation including mirrors and gratings.

* Work supported by the Chinese Academy of Science (CAS) and the Anhui province government for key techniques R&D of Hefei Advanced Light Facility.
† zimeng@ustc.edu.cn

HALF TEST BEAMLINE HEATLOAD CALCULATION

HALF is a 4th generation SR light source with the emittance of 73.2 pm•rad in both x and y directions. The storage ring energy is 2.2 GeV and the current is 350 mA. The Test Beamline (BL10) is an undulator-based beamline. The undulator consists of 98 periods with 40 mm as its period length.

The Test Beamline aims to use a grating monochromator with extra high spectral resolving power of 10^5@400 eV, ranging from 275 eV to 1500 eV in the first-version optical design. High-quality optical surface is required with overall slope error from 100 – 200 nrad (rms). In order to control the thermal-induced slope error, the precise heat load distribution absorbed by the optical elements should be calculated, which is fundamental for cooling system design and simulation. Here, the undulator source angular power density distribution up to 80th order is calculated.

Optical Design

The Test Beamline adopted the collimated SX-700 grating monochromator as shown in the Fig. 1. The toroidal mirror M_1 collimates the source light in the vertical direction and focus it onto the exit slit in the horizontal direction. The plane mirror (PM) reflects the incoming light from M_1 to the centre of plane grating GR. The light diffracted from GR is focused by the cylindrical mirror M_2 to the exit slit in the vertical direction. The grazing incident angle and M_1 and M_2 are 2°.The heat load of M_1, PM and GR will be calculated at 275 eV.

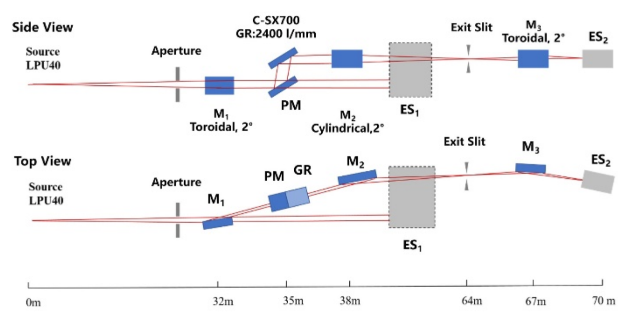

Figure 1: The beamline optical design.

Mirror Heat Load Calculation

The heat load of the mirrors is calculated by combining the source property and mirror reflectivity calculation. The spatial power density distribution can be calculated from the angular distribution of the source power density $\frac{d^2 P^n_{\sigma,\pi}}{d\varphi d\psi}$ [4]:

ISBN: 978-3-95450-250-9 ISSN: 2673-5520 doi:10.18429/JACoW-MEDSI2023-THPPP009

$$\left.\frac{d^2P^n_{\sigma,\pi}}{dxdy}\right|_{\mathrm{M_1}} = \sum_n \frac{d^2P^n_{\sigma,\pi}}{d\varphi d\psi} \times \frac{\sin\theta_{\mathrm{M_1}}}{r_1^2}$$

Here, $r_1 = 34$ m is the distance from source to M₁, $\theta_{\mathrm{M_1}} = 2^\circ$ is the grazing angle of M₁; n is the order of the undulator, σ and π indicate the light polarization. The photon energy of the n^{th} order at position (x, y) is $E_n(x, y)$. The mirror reflectivity at grazing angle θ for photon energy of $E_n(x, y)$ is $R_{\sigma,\pi}(\theta, E_n(x, y))$. Therefore, the reflected power density at (x, y) by M₁ can be calculated by:

$$\left.\frac{d^2P^n_{\sigma,\pi}}{dxdy}\right|_{\mathrm{M_1\_refl}} = \left.\frac{d^2P^n_{\pi,\sigma}}{dxdy}\right|_{\mathrm{M_1}} \times R_{\sigma,\pi}\left(\theta_{\mathrm{M_1}}, E_n(x, y)\right)$$

Here, M₁ reflects the light in the horizontal direction. Therefore, the σ-polarized light at source incidents on the M₁ as π-polarized light, which is same to the π-polarized light from source.

Deducted the reflected power density by M₁ from the incident power density to M₁, the absorbed power density can be calculated by the following equations. Figure 2 shows the calculation result of the M₁ heat load.

$$\left.\frac{d^2P^n_{\sigma,\pi}}{dxdy}\right|_{\mathrm{M_1\_absorb}} = \left.\frac{d^2P^n_{\sigma,\pi}}{dxdy}\right|_{\mathrm{M_1}} - \left.\frac{d^2P^n_{\sigma,\pi}}{dxdy}\right|_{\mathrm{M_1\_refl}}$$

$$\left.\frac{d^2P}{dxdy}\right|_{\mathrm{M_1\_absorb}} = \sum_{\sigma,\pi}\sum_{n=1}^{80} \left.\frac{d^2P^n_{\sigma,\pi}}{dxdy}\right|_{\mathrm{M_1\_absorb}}$$

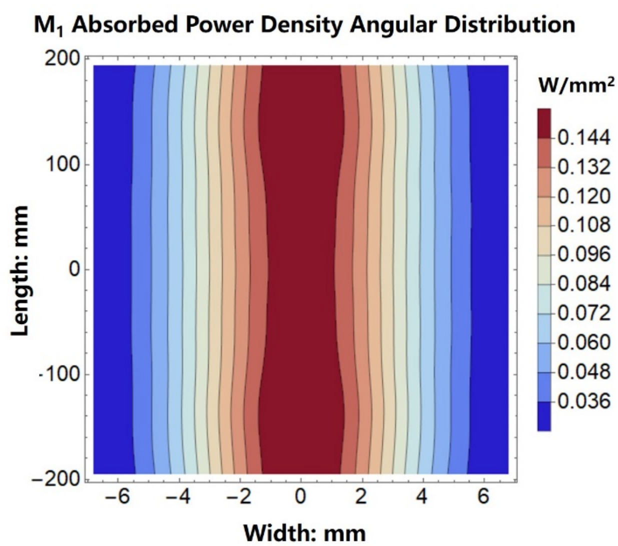

Figure 2: The heat load absorbed by the mirror M₁.

The reflected light by M₁ incidents on the plane mirror PM at grazing angle $\theta_{\mathrm{PM}} = 4.58^\circ$. PM is $r_{cm} = 3\ m$ away from M₁. The incident power density on PM can be calculated from the optical geometry:

$$\left.\frac{d^2P^n_{\pi,\sigma}}{dxdy}\right|_{\mathrm{PM}} = \left.\frac{d^2P^n_{\pi,\sigma}}{dxdy}\right|_{\mathrm{M_1\_refl}} \times \frac{\sin\theta_{\mathrm{PM}}}{\sin\theta_{\mathrm{M_1}}} \times \frac{r_{cm}}{r_{1t} - r_{cm}}$$

Here, $r_{1t} = 32$ m is the distance between M₁ and the exit slit. The reflected and absorbed power density by PM is calculated in the same way as M₁. Figure 3 shows the calculated heat load on PM:

$$\left.\frac{d^2P^n_{\sigma,\pi}}{dxdy}\right|_{\mathrm{PM\_refl}} = \left.\frac{d^2P^n_{\pi,\sigma}}{dxdy}\right|_{\mathrm{PM}} \times R_{\sigma,\pi}\left(\theta_{PM}, E_n(x, y)\right)$$

$$\left.\frac{d^2P}{dxdy}\right|_{\mathrm{PM\_absorb}} = \sum_{\sigma,\pi}\sum_{n=1}^{80}\left(\left.\frac{d^2P^n_{\pi,\sigma}}{dxdy}\right|_{\mathrm{PM}} - \left.\frac{d^2P^n_{\sigma,\pi}}{dxdy}\right|_{\mathrm{PM\_refl}}\right)$$

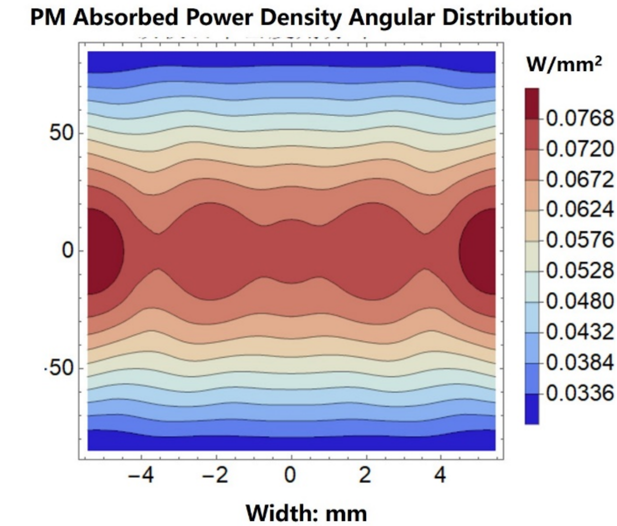

Figure 3: The heat load absorbed by the mirror PM.

Grating Heat Load Calculation

The reflected light from the plane mirror incident on the grating at an incident angle of $\alpha = 89.3^\circ$. The outgoing light from grating consists of the reflected light and the diffracted light. The absorbed power density distribution can be calculated.

$$\left.\frac{d^2P^n_{\sigma}}{dxdy}\right|_{\mathrm{gr}} = \left.\frac{d^2P^n_{\sigma,\pi}}{dxdy}\right|_{\mathrm{PM\_refl}} \times \frac{\cos\alpha}{\sin\theta_{\mathrm{PM}}}$$

$$\left.\frac{d^2P}{dxdy}\right|_{\mathrm{gr\_out}} = \sum_{\sigma,\pi}\sum_{n=1}^{80}\left[\sum_{m=1}^{3}\left.\frac{d^2P^n_{\sigma}}{dxdy}\right|_{\mathrm{gr}} \times Eff_{m,\sigma,\pi}(\alpha, E_n) + \left.\frac{d^2P^n_{\sigma,\pi}}{dxdy}\right|_{\mathrm{gr}} \times R_{\sigma,\pi}\left(\frac{\pi}{2} - \alpha, E_n\right)\right]$$

Here, $Eff_{m,\sigma,\pi}(\alpha, E_n(x, y))$ are the m^{th} order diffraction efficiencies [5] for photon energy $E_n(\mathrm{x}, \mathrm{y})$ at incident angle α with σ- and π-polarized light. For $m > 3$ order diffraction, the efficiency is close to zero. Therefore Only m = 1, 2, 3 diffraction orders are calculated. The absorbed power density by the grating can be calculated. Figure 4 shows the grating heat load.

$$\left.\frac{d^2P}{dxdy}\right|_{\mathrm{gr\_absrob}} = \left.\frac{d^2P}{dxdy}\right|_{\mathrm{gr}} - \left.\frac{d^2P}{dxdy}\right|_{\mathrm{gr\_out}}$$

ISBN: 978-3-95450-250-9 ISSN: 2673-5520 doi:10.18429/JACoW-MEDSI2023-THPPP009

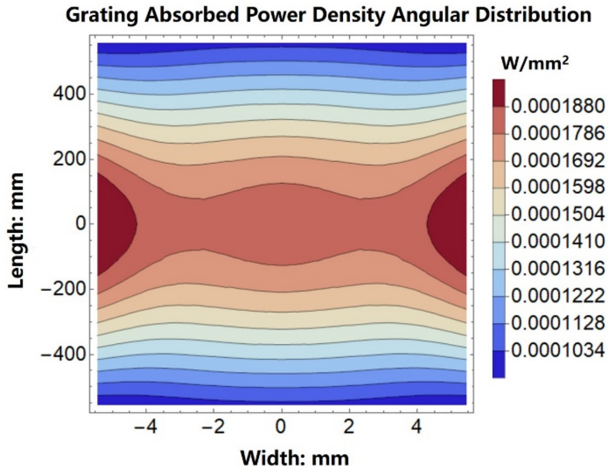

Figure 4: The heat load absorbed by the grating GR.

CONCLUSION

A heat load calculation method for SR beamline optics is introduced. The heat load distribution on mirror M_1, PM and grating Gr in BL10 Test Beamline were calculated. The mirror calculation results are matched with SRCalc. Therefore, heat load on all mirrors and gratings can be calculated precisely. Therefore, heat load on all mirrors and gratings can be calculated precisely.

ACKNOWLEDGEMENTS

This work is supported by the Chinese Academy of Science (CAS) and the Anhui province government for key techniques R&D of Hefei Advanced Light Facility.

REFERENCES

[1] R. Reininger, *SRCalc*, 2001, unpublished.

[2] L. Rebuffi, X. Shi, M. S. Rio and R. Reininger, "A ray-tracing algorithm for *ab initio* calculation of thermal load in undulator-based synchrotron beamlines", *J. Synchrotron Radiat.*, vol. 27, pp. 1108-1120, Sep. 2020.

[3] Z. Sun, G. Feng, X. Liu, "Construction of Hefei advanced light facility begins", *The Innovation*, vol. 4, issue 6, 100514, Sep. 2023.

[4] K-J. Kim, "Characteristic of Synchrotron Radiation", *AIP Conference Proceedings*, vol. 184, pp. 565-632, Apr. 1989.

[5] V. S. Valdes, W. R. McKinney and C. Palmer, "The differential method for grating efficiencies implemented in mathematica™", *Nucl. Instrum. Methods Phys. Res. Sect. A*, vol. 347, issues 1-3, pp. 216–219, Aug. 1994.

ISBN: 978-3-95450-250-9 ISSN: 2673-5520 doi:10.18429/JACoW-MEDSI2023-THPPP010

MECHANICAL ANALYSIS AND TESTS OF AUSTENITIC STAINLESS STEEL BOLTS FOR BEAMLINE FLANGE CONNECTION

T. T. Zhen, L. J. Lu†, S. Sun, R. B. Deng, F. Gao, H. X. Deng
Shanghai Advanced Research Institute, Chinese Academy of Sciences, Shanghai, China

Abstract

Cryogenic tests of 1.3 GHz superconducting accelerator cryomodule for the Shanghai Hard X-ray Free Electron Laser Installation Project (SHINE) are in progress. For better performance, a study of mechanical analysis and tests of austenitic stainless steel bolts for beamline flange connection has been done in preliminary work. In order to satisfy the residual magnetism and strength, high-strength austenitic stainless steel bolts are selected. For higher sealing performance, the torque coefficient is determined by compression test, the lower limit of yield of the bolts is obtained by tensile test, then the maximum torque applied to the bolts under real working conditions can be obtained according to the relationship between preload and torque. A finite element model is established to get the deformation curve of the gasket, and the measured results of gasket thickness are compared to ensure the reliability of the simulation. The deformation curve of the gasket is used to calculate the change of compression force under the temperature cycling load (cool down and warm-up). Finally, the results of residual magnetism show that the bolts have a negligible effect on magnetic field.

INTRODUCTION

1.3 GHz superconducting accelerator is characterized by extremely good vacuum condition [1-3]. Many of the flanges that are along the beamline immersed in the insulation vacuum. The connection construction is shown in Figure 1, which has to guarantee a reliable sealing performance both at room and cryogenic temperature, also after warm-up.

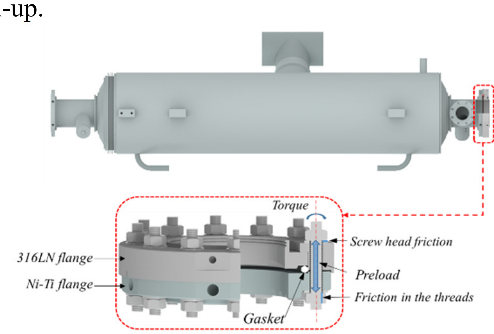

Figure 1: Beamline flange connection.

The mechanical properties, the applied torque, the preload changes with temperature of the bolts, etc., all affect sealing quality.

† lulj@sari.ac.cn

TENSILE TEST

For the requirement of the residual magnetism and higher fracture toughness at cryogenic temperature, 316LN high-strength bolts are selected. The mechanical properties of the bolts prepared by a domestic and a foreign company respectively have been tested at room temperature. The size [4] of the tensile samples is shown in Figure 2. Four samples are tested and the average value is used for discussion.

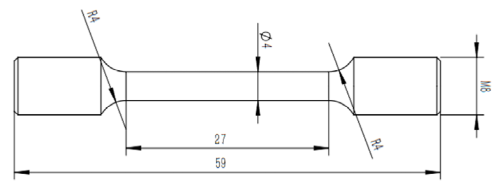

Figure 2: Sampling map.

All samples are tested for mechanical properties at room temperatures. The engineering stress-strain curves of some tensile samples are shown in Figure 3.

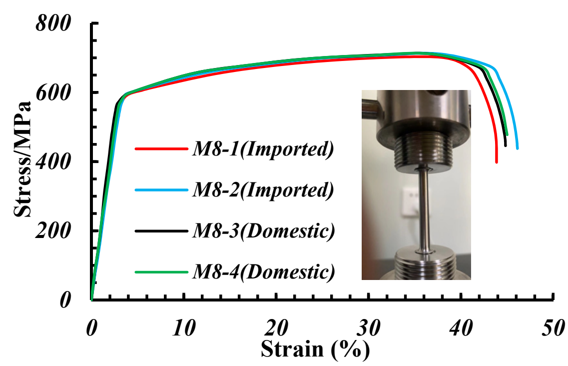

Figure 3: Engineering stress-strain curves of the samples.

The results including R_{el} (Lower limit of yield), UTS (Ultimate tensile strength) and EL (Elongation), are shown in Table 1. From Table 1, it can be seen that the average R_{el} of the bolts is 595 MPa, and the EL is greater than 40 %.

Table 1: Tensile Test Results at Room Temperature

Coding	R_{el} *MPa*	UTS *MPa*	EL *%*
Imported-1	598	711	44
Imported-2	596	710	46
Domestic-3	586	704	45
Domestic-4	603	712	45

ISBN: 978-3-95450-250-9 ISSN: 2673-5520 doi:10.18429/JACoW-MEDSI2023-THPPP010

MEASUREMENT OF TORQUE COEFFICIENT

Given the mechanical properties of the bolts, the torque coefficient is measured to determine the maximum torque that could be applied. A representation of the experimental apparatus is shown in Figure 4. A ring force sensor with a precision of 1% has been used for the compression test. The upper and lower flanges made by 316LN and niobium-titanium respectively are used to simulate the demountable connection.

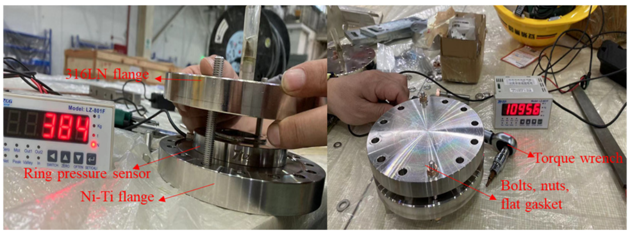

Figure 4: Presentation of the experimental apparatus.

According to the mechanical design manual:

$$T = FKd \quad (1)$$

$$K = \frac{d_2}{2d}\tan(\emptyset + \rho_v) + \frac{\mu}{3d} \times \frac{D_w^3 - d_0^3}{D_w^2 - d_0^2} \quad (2)$$

Where K is torque coefficient, F is clamp force, μ and $\boldsymbol{\rho_v}$ are friction factor, other parameters are bolt-related dimensions. Formula (2) shows when the bolt size is determined, K is effected by the friction coefficient, which can be measured by the compression test. Three sets of tests a carried out using the same batch of different M8 bolts with the same surface treatment. The test results are shown in Figure 5.

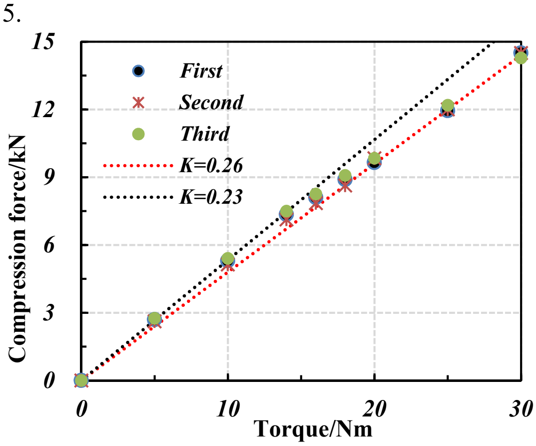

Figure 5: Relation between torque and compression force.

It can be seen that:

- Compression force and torque are basically linear. K spans a range from 0.23 to 0.26.
- K increases slightly with the torque, which may resulted by thread deformation.

Considering the combined effects of tension and torsion,

$$\frac{1.3F}{S} < \frac{R_{el}}{1.1} \quad (3)$$

Where S is stress cross section of the bolts, '1.1' is taken into account manual tightening torque deviation (The accuracy level of the torque wrench used is not lower than class 2 specified in JJG707-2003). So we got maximum torque:

$$T_{max} = 31.7 \text{ Nm}.$$

TEMPERATURE EFFECT ON COMPRESSION FORCE

Temperature change (cool down and warm-up) may induce additional deformations to the gasket and the bolts which may lead to leakage of the connection [5]. Therefore a finite element model has been developed to simulate the behaviour of the connection. The beamline connection simplified geometry is shown in Figure 6. The force-deformation curve is obtained by simulation shown in Figure 7.

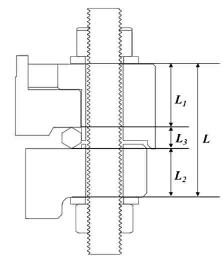

Figure 6: Simplified geometry of the beamline connection.

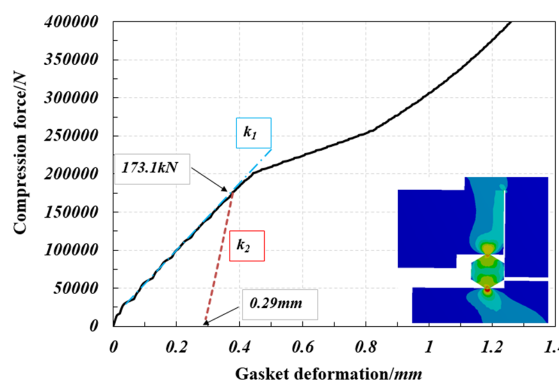

Figure 7: Force-deformation curve of the gasket.

A torque of 30 Nm is applied to each bolt to achieve a better sealing performance. According to Formula (1) and the torque coefficient measured in previous part, the compression force on the gasket is $F_c = Tn/Kd = 173.1$ kN.

When the compression force is completely released, the thickness of the gasket is reduced by 0.29 mm which is consistent with measurement shown in Figure 8.

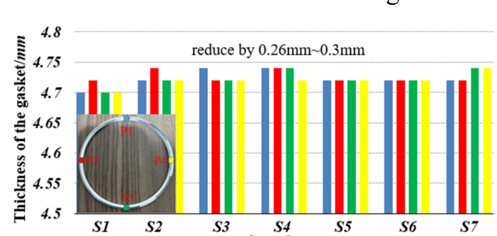

Figure 8: Thickness of the gaskets after applied 30 Nm.

In the cool down to the liquid helium temperature the difference of thermal elongation is

$$\Delta L_t = L\Delta T - L_1\Delta T_1 - L_2\Delta T - L_3\Delta T_3 = 0.00734 \text{ mm}$$

ISBN: 978-3-95450-250-9 ISSN: 2673-5520 doi:10.18429/JACoW-MEDSI2023-THPPP010

That means the gasket will be further compressed and the preload of the bolts will increase. By the deformation relation,

$$\frac{\Delta F}{k_1}+\frac{\Delta FL}{nES}=\Delta L_t,$$

$\Delta \boldsymbol{F}$ increases by 2890 N. That is the axial force of a single bolt increases 241 N. Judging from Formula (3), the bolt is still elastic deformation.

When it returns to room temperature, as

$$\frac{\Delta F}{k_2}+\frac{\Delta FL}{nES}=\Delta L_t,$$

the preload of a single bolt decreased by 1077 N, which is a small value compared to the initial preload of 14423 N.

In conclusion, it can be seen that the change of compression force caused by temperature change is small, and will not affect the sealing performance of the beamline flange connection.

RESIDUAL MAGNETISM TEST

The beamline flange connection should not affect the magnetic field, and the residual magnetism of bolts is required to be less than 0.5 Gs. For higher reliability, the tightening torque of the M8 bolt is set to 30 Nm, which is very close to the torque that may result in plastic deformation of the bolt. Taking into account the error of artificial tightening force and the temperature change, 5 M8 bolts are selected for the remanence detection in factory state and plastic deformation state. Conservatively, the tightening torque of the bolts even reach 50 Nm. Whether the bolt has plastic deformation is determined by the length of the bolt before and after the torque is applied as shown in Figure 9. The test results of residual magnetism are shown in Figure 10.

Figure 9: Length measurement.

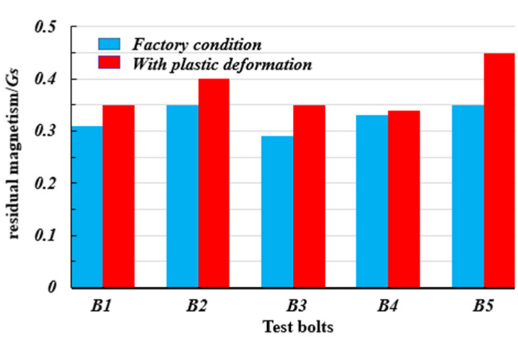

Figure 10: Residual magnetism of the bolts.

According to the results, when plastic deformation of the bolts occurs, the residual magnetism increases to a certain extent, but it still meets the requirement of less than 0.5 Gs.

CONCLUTIONS

A study on behaviours of the austenitic stainless steel bolts for 1.3 GHz superconducting cavities' beamline flange connection has been performed. The lower limit of yield and torque coefficient obtained by related tests are used to calculate maximum tightening torque. The results of finite element analysis, gasket thickness test and the change of compression force with temperature indicate that temperature cycle has little effect on the sealing performance of the beamline flange connection. The residual magnetism of the selected austenitic stainless steel bolts also meet the engineering requirement (less than 0.5 Gs). Subsequently, the allowable torque of bolts at the other connections can be determined in same way.

ACKNOWLEDGEMENTS

This work was supported by the CAS Project for Young Scientists in Basic Research (YSBR-042), the National Natural Science Foundation of China (12125508, 11935020), Program of Shanghai Academic/Technology Research Leader (21XD1404100), and Shanghai Pilot Program for Basic Research – Chinese Academy of Sciences, Shanghai Branch (JCYJ-SHFY-2021-010).

REFERENCES

[1] Z. Y. Zhu, Z. T. Zhao, D. Wang, *et al.*, "SCLF: an 8-GeV CW SCRF linac-based X-ray FEL facility in Shanghai", in *Proc. FEL'17*, Santa Fe, NM, USA, Aug. 2017, pp. 182-184. doi:10.18429/JACoW-FEL2017-MOP055

[2] Z. T. Zhao, C. Feng and K. Q. Zhang, "Two-stage EEHG for coherent hard X-ray generation based on a superconducting linac", *Nucl. Sci. Tech.*, vol. 28, no. 8, p. 117, 2017. doi: 10.1007/s41365-017-0258-z

[3] C. Feng and H. X. Deng, "Review of fully coherent free-electron lasers", *Nucl. Sci. Tech.*, vol. 29, no. 11, p. 160, 2018. doi: 10.1007/s41365-018-0490-1

[4] Weijun Wang, Chuanyi Zhao, Huan Jin, *et al.*, "Mechanical properties evaluation of ReBCO CICC jacket based on super-austenitic stainless steel for CFETR high-field magnet", *Nucl. Mater. Energy*, vol. 34, p. 101344, 2023. doi: 10.1016/j.nme.2022.101344

[5] https://jra-srf.desy.de/e86/e123/e126/e436/infoboxContent437/note-2006-002-SRF.pdf

ISBN: 978-3-95450-250-9 ISSN: 2673-5520 doi:10.18429/JACoW-MEDSI2023-THPPP012

SHAPE OPTIMIZATION DESIGN OF MONOCHROMATOR PRE-MIRROR IN FEL-1 AT S³FEL*

Zhongmin Xu†, Chuan Yang, Yinpeng Zhong, Weiqing Zhang[1]
Institute of Advanced Science Facilities, Shenzhen, China
[1]also at Dalian Institute of Chemical Physics, Chinese Academy of Sciences, Dalian, China

Abstract

For the monochromator pre-mirror in FEL-1 at S³FEL, the deformation induced by high heat load result in severe effects on the beam quality during its off-axis rotation. To meet the pre-mirror shape error requirement for X-ray coherent transport, an integration of passive cooling and active heating systems for thermal management of the monochromator pre-mirror has been proposed, developed, and modelled. An active heating system with multiple electric heaters is adopted to compensate for the pre-mirror shape further. Finally, using MHCKF model, the optimization of multiple heat fluxes generated by all electric heaters was accomplished. The results show that the thermal management using passive cooling and active heat schemes is effective to obtain high-precision surface shape for the pre-mirror.

INTRODUCTION

The Shenzhen Superconducting Soft X-ray Free Electron Laser (S³FEL) is a new light source under construction phase at Institute of Advanced Science Facilities (IASF), Shenzhen. S³FEL consists of 2.5 GeV CW superconducting linear accelerator and four initial undulator lines, aiming to generate X-rays between 40eV and 1 keV at rates up to 1 MHz [1]. According to the Maréchal Criteria [2], in order to meet the needs of FEL wavefront coherent transmission, the height error RMS of the pre-mirror mirror should be less than 0.9 nm and the slope error RMS should be less than 100 nrad, which are more stringent than those of the mirrors in synchrotron radiation facilities. Therefore, it is necessary to choose an appropriate shape control scheme.

PRE-MIRROR MODEL AND BOUNDARY CONDITIONS

The structure of the monochromator shown as Figure1 is different with that of LCLS-II, European XFEL [3]and SwissFEL. It consists of a front plane mirror and plane variable-line-spacing grating. During the course of the pre-mirror off-axis rotation, the spot centres of different wavelengths on the surface of are moving. Meanwhile, the pre-mirror will absorb high heat load, resulting in serious local bulging and bending deformation. If the traditional cooling methods are adopted, the mirror shape is unlikely to meet all of the working conditions.

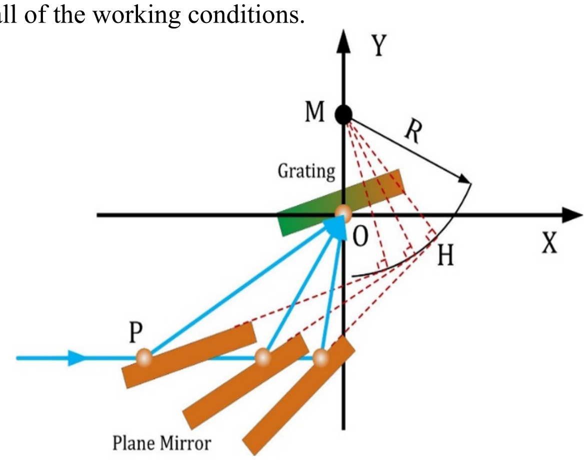

Figure 1: Structure of Grating monochromator in FEL-1.

Power density distributions of wavelength 1-3 nm absorbed by the pre-mirror in beamline FEL-1 are shown Figures. 2, 3 and 4. And the footprints information for three wavelengths are listed in Table 1. Footprint centre of 2 nm X-ray is located at the centre of pre-mirror, while those of other two wavelengths on either side. Though their maximum power density for each wavelength is not much different, the absorbed power of each wavelength is quite different.

Table 1: Footprints Information for Three Wavelengths

Wavelength	Length of Footprint	Absorbed Power
1 nm	150 mm	5.46 W
2 nm	174 mm	11.2 W
3 nm	200 mm	16.65 W

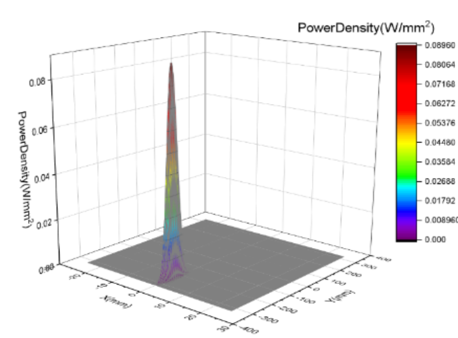

Figure 2: Power density distribution of wavelength 1 nm.

* Work supported by the National Natural Science Foundation of China (Grant No. 22288201) and Scientific Instrument Developing Project of the Chinese Academy of Sciences (Grant No. GJJSTD20190002)
† xuzhongmin@mail.iasf.ac.cn

ISBN: 978-3-95450-250-9 ISSN: 2673-5520 doi:10.18429/JACoW-MEDSI2023-THPPP012

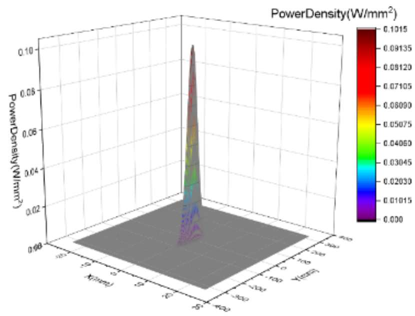

Figure 3: Power density distribution of wavelength 2 nm.

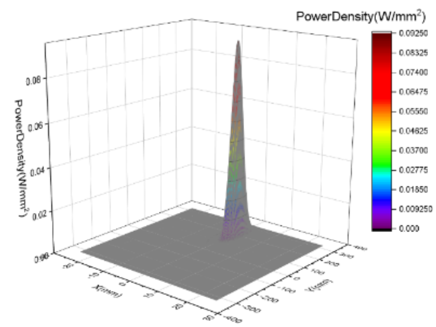

Figure 4: Power density distribution of wavelength 3 nm.

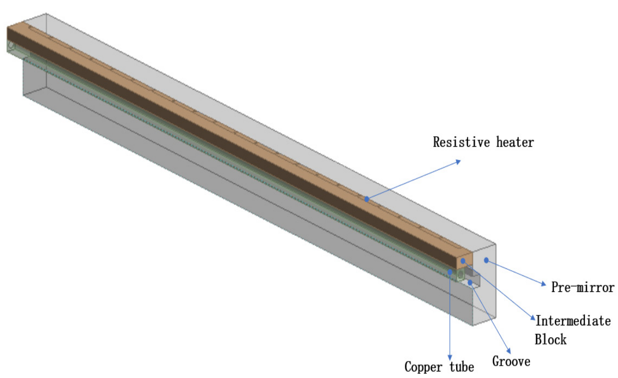

Figure 5: Pre-mirror and shape compensation system in FEL-1.

Table 2: Specifications for the Pre-mirror

Substrate	Silicon
Coating	B_4C
size (mm^3)	700×60×60
Effective size (mm^2)	700×30
Shape	Plane

According to REAL scheme proposed by Zhang [4], this paper establishes a 3D model and shape compensation system for the FEL-1 pre-mirror in Ansys Workbench. Considering the symmetry of the model and boundary conditions, only half of the model was used, as shown in Figure 5. As a plane mirror (grey part), its specifications are listed in Table 2. A groove is opened along the side of the mirror. while the copper tube is used to circulate cooling water. Its inner diameter of the tube is 6mm, and the applied heat transfer coefficient is 5E-3 W/mm²/°C. 21 electric heaters are attached to the intermediate block (made of silicon) for compensating the mirror shape. To simplify the model, all heaters have been omitted. Instead, 21 rectangles representing the positions of the heaters are drawn on the intermediate block, with each rectangle measuring 30 mm*5 mm, and a distance of 2 mm between two rectangles. The corresponding heat flux generated by each heater is applied equivalently on the rectangle.

MATHEMATICAL MODEL

In this case, the actual deformation of the pre-mirror is induced by processing, clamping, gravity and heat, etc. Taking the thermal compensation into account, the final deformation can be expressed by MHCKF model [5].

$$M(x)H + C(x) + K(x) = F(x) \tag{1}$$

where *M(x)* is the response function of the electric heaters; H is a series of the heat fluxes; *C(x)* is the mirror initial deformation caused by the processing, clamping, and gravity, etc.; *K(x)* is the deformation in the meridional direction caused by the X-ray power; *F(x)* represents the actual deformation generated by the three left terms.

In our case, it was found that the ideal form of *F(x)* is a straight line, and its intercept value in the Cartesian coordinate system is close to the maximum thermal deformation caused by X-rays. Therefore, *F(x)* can be written as follows.

$$F(x) = (max(K\ (x)) + \varepsilon)I \tag{2}$$

where $max(K\ (x))$ is the maximum deformation value of *K(x)*; ε is a perturbation term; *I* is a column vector of all 1s.

The least squares solution of H can be calculated using expression (3).

$$H \approx \left(M^T(\mathrm{x})M(\mathrm{x})\right)^{-1}M^T(\mathrm{x})(-C(x) - K(x) + (max(K\ (x)) + \varepsilon)I) \tag{3}$$

HEATERS RESPONSE FUNCTIONS (HRF)

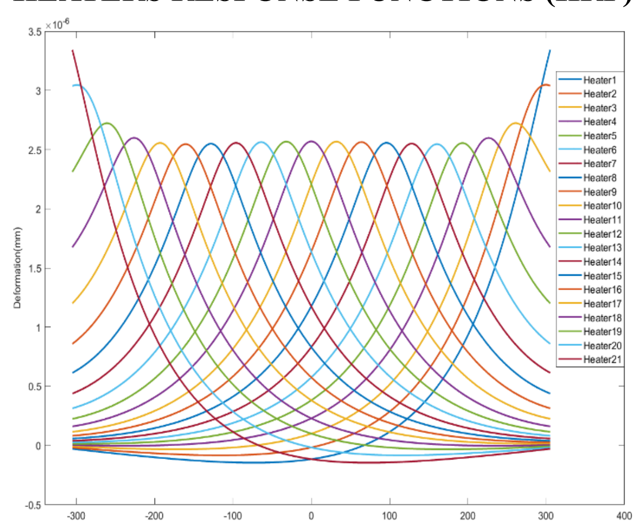

Figure 6: The deformation curves calculated by Ansys sequentially.

To obtain the response function of each heater shown in Figure 5, apply a heat flux of 0.001 W/mm² sequentially to each rectangle on the intermediate block using Ansys Workbench. After thermal analysis, all deformation curves

12th Int. Conf. Mech. Eng. Design Synchrotron Radiat. Equip. Instrum. MEDSI2023, Beijing, China JACoW Publishing
ISBN: 978-3-95450-250-9 ISSN: 2673-5520 doi:10.18429/JACoW-MEDSI2023-THPPP012

are shown in Figure 6. Finally, these deformations values are divided by 0.001 W/mm^2 to obtain the Heaters Response Functions (HRF) of the heaters.

OPTIMIZATION RESULTS

It is assumed that the initial deformation for the pre-mirror is negligible in this simulation, so that *C(x)* doesn't need to be considered. Thus, to solve H in expression (3), only perturbation term, ε, is unknown. Therefore, by continuously searching for ε, the heat flux values applied to all electric heaters can be found, shown as Figure 7.

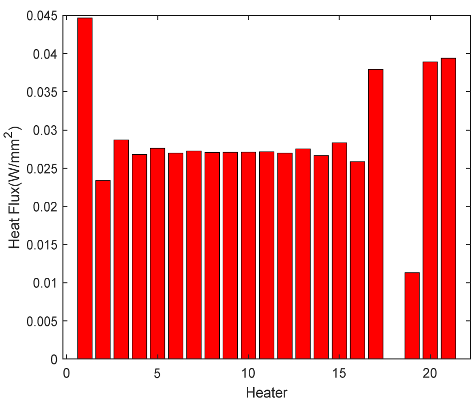

(a)

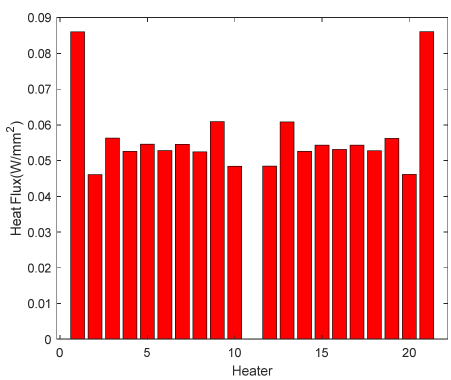

(b)

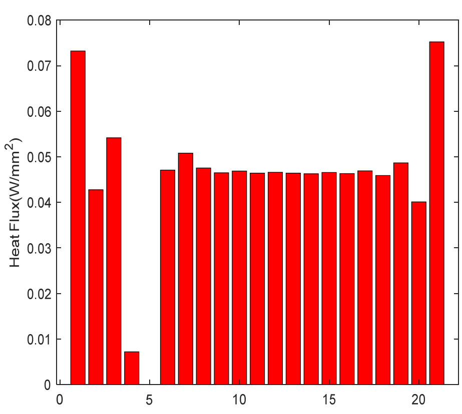

(c)

Figure 7: Heat Fluxes through optimization for (a) 1 nm X-ray; (b) 2 nm X-ray; (c) 3 nm X-ray.

Then, all heat fluxes are used as boundary conditions to evaluate the thermal, deformation, and surface shape results using finite element analysis software. From Table 3, both height and slope error RMS are much less than required.

Table 3: Shape Error for Three Wavelengths

Wavelength	Height error RMS	Slope error RMS
1 nm	0.29 nm	11.85 nrad
2 nm	0.31 nm	13.03 nrad
3 nm	0.27 nm	10.81 nrad

CONCLUSION

In this paper we only calculated the shape compensation at the left, middle, and right positions of the pre-mirror for three wavelengths. It can be seen that the shape compensation scheme using the electric heaters and the MHCKF model are effective for solving the pre-mirror shape problem caused by the moving X-ray. From this, it can be inferred that the pre-mirror shape can be compensated well during the course of X-ray footprint movement at any position on its surface.

ACKNOWLEDGEMENTS

The authors would like to thank the S^{3}FEL project team for all their efforts and support.

REFERENCES

[1] S^{3}FEL Project Team. S^{3}FEL Project Proposal Report, 2021, unpublished.

[2] A. Maréchal, M. Francon, *Diffraction, structure des images; influence de la coherence de la Lumiere*, Masson Paris, 1970.

[3] M. Altarelli, "The European X-ray Free-Electron Laser: toward an ultra-bright, high repetition-rate X-ray source", *High Power Laser Sci. Eng.*, vol. 3, pp. 1-7, 2015. doi:10.1017/hpl.2015.17

[4] Lin Zhang, Daniele Cocco, Nicholas Kelez, Daniel S. Morton, Venkat Srinivasan, Peter M. Stefan, "Optimizing X-ray mirror thermal performance using matched profile cooling", *J. Synchrotron Radiat.*, vol. 22, pp. 1170-1181, 2015. doi:10.1107/S1600577515013090

[5] Zhongmin Xu, Weiqing Zhang, Chuan Yang, Yinpeng Zhong, "Shape optimization design of the offset mirror in FEL-1 beamline at S^{3}FEL", *Sci. Rep.*, vol. 13, p.9653, 2023. doi:10.1038/s41598-023-36645-9

ISBN: 978-3-95450-250-9 ISSN: 2673-5520 doi:10.18429/JACoW-MEDSI2023-THPPP013

STUDIES ON THE INFLUENCES OF LONGITUDINAL GRADIENT BENDING MAGNET FABRICATION TOLERANCES ON THE FIELD QUALITY FOR SILF STORAGE RING

J. Zhu†, M. Zhang†, C. Wang, D. Liang, Y. Shi
Institute of Advanced Science Facilities, Shenzhen, China

Abstract

The advanced storage ring of 4th generation synchrotron radiation facility, known as the diffraction-limited storage ring (DLSR), is based on multi-bend achromat (MBA) lattices, which enables an emittance reduction of one to two orders of magnitude pushing beyond the radiation brightness and coherence reached by the 3rd generation storage ring. The longitudinal gradient bending (LGB) magnets, with multiple magnetic field stages in beam direction, are required in the DLSR to reduce the emittance. The permanent magnet based LGB magnets are selected for the Shenzhen Innovation Light-source Facility (SILF) due to the advantages of operation economy, compactness and stability compare to the electro-magnet. In this paper, the influences of typical LGB magnet fabrication tolerances on the field qualities are presented using a dedicated parameterized finite element (FE) model, including the poles height tolerances, the pole tip inclination (in different orientations).

INTRODUCTION

Benefit from supporting the cutting-edge researches in various disciplines and industry applications, such as physics, material, bioscience, medicine, electronics, chemistry, etc., the advanced storage ring of 4th generation synchrotron radiation facility based on multi-bend achromat (MBA) lattices (also known as the diffraction-limited storage ring, DLSR) is emphasized and constructed world widely, pushing beyond the radiation brightness and coherence attained by the 3rd generation storage ring [1]. In the Institute of Advanced Science Facilities (IASF, Shenzhen, China), a storage ring of this type in Shenzhen Innovation Light-source Facility (SILF) is proposed and under preliminary design [2]. The longitudinal gradient bending (LGB) magnets, with multiple field stages in beam line direction, are required in DLSR design to reduce the electron beam emittance. Concerning the advantages of operation economy, compactness and stability compare to the electro-magnet, the permanent magnet (PM) based LGB magnets are selected and designed for SILF storage ring.

Typical structure of the LGB magnet is shown in Fig. 1. Field of five stages is first designed by adjusting the PM block number, size and easy magnetization direction in each module. The pole profile is optimized to fulfill the field quality requirements in good field region, i.e. the homogeneity of the field in transverse direction and / or the integrated field in beam direction (denoted as TFH and IFH respectively). The C-shape design has an open access to the magnet gap which simplifies the beam pipe installation and field measurements. Sm_2Co_{17} is selected as the PM material, which has small temperature coefficient and good magnetic performance. The pole, yoke, shielding plates and field tuning bolts are made of soft iron DT4. The material of the bolts for the back yoke fixation is carbon steel. The Fe-Ni alloy with high temperature coefficient (grade 1J30) is introduced at the magnet opening side to compensate the field changes result from the temperature variations. The field tuning bolts provide an additional approach to actively adjust the fields afterwards.

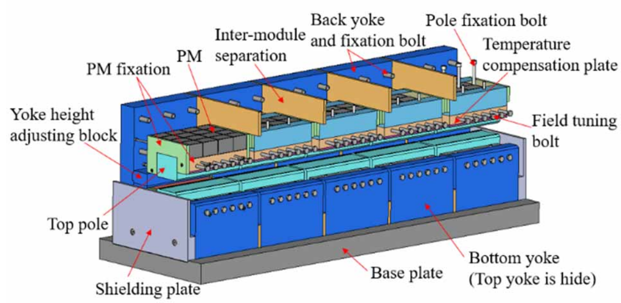

Figure 1: Typical structure of LGB magnet for SILF (5 modules assembled).

The five magnet modules have similar structures as shown in Fig. 1. Aluminium blocks fill the remain voids between the poles and yokes to support the PMs. The magnet modules are assembled separately at first and then combined as entire structure by bolting to the base plate and separated longitudinally by thin aluminium plates.

The fabrication and assembly tolerances of the LGB magnet will inevitably affect the final field quality, in order to conduct the LGB magnet manufacturing process in this regard, the influences of LGB magnet fabrication tolerances on the field quality are investigated using a dedicated parameterized finite element (FE) model, including the pole height tolerances, the pole tip inclination in transverse and longitudinal directions. The influences of the mesh sizes on field quality are firstly studied in order to find a compromise between the computation accuracy and efficiency with respect to the FE model size.

PARAMETERIZED FE MODEL

A parameterized FE model of the entire typical LGB magnet is firstly developed in Opera-3D®, however, the computation time turns out very long. We therefore reduce the model size to has only one module, i.e. the one for the highest field stage with the shielding plates at both ends, as shown in Fig. 2. The model size reduction is under the assumption that the relative change of the TFH / IFH results from a particular fabrication tolerance is the same for

† email address: zhujiawu@mail.iasf.ac.cn; zhangmiao@mail.iasf.ac.cn

ISBN: 978-3-95450-250-9 ISSN: 2673-5520 doi:10.18429/JACoW-MEDSI2023-THPPP013

single module and entire LGB magnet. The assumption is reasonable since the change of the field / integrated field is proportional to the field / integrated field itself. As a result, the influences on the entire LGB magnet TFH / IFH could be easily deduced from the study results of single module.

All the non-magnetic materials are excluded from the FE model. The defined parameters including all the geometry dimensions, mesh size of different parts, air field size, PMs number, the magnetic material properties, the pole height tolerances and the pole tip inclinations. The interested region in the magnetic gap and extended at the ends is modelled in special with refined mesh, and with as much as possible nodes aligned on the field extraction lines (to reduce the field interpolation errors).

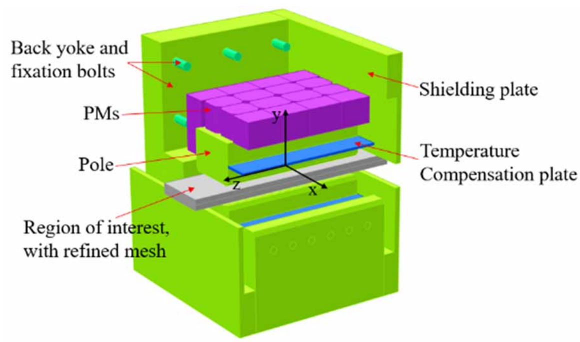

Figure 2: The parameterized FE model of single module in the typical LGB magnet.

INFLUENCES OF MESH SIZE ON FIELD QUALITY

In order to lowering the influences of mesh sizes and external air field size on the calculated field quality, a prior study is carried out to find the reasonable mesh sizes for different parts and the external air field size (ratios to the model sizes in x, y and z directions). The mesh sizes for magnetic materials, interested region in magnetic gap, external air field are defined for each run separately, as well as the external air field size. Table 1 lists the results of the studied cases. Following conclusions could be drawn from the studies:

- Further reduction of the mesh size at the interested region does not improve the accuracy significantly.
- The reduction of magnetic material mesh size reduces the TFH, and also increases the field at the middle plane of good field region (by ~10 Gauss, not listed in Table 1), but does not show strong relation to the IFH. It is reasonable since the refined mesh of magnetic materials reflects more accurately the material nonlinearity, and the integrated field is indirectly related to the fields of a certain region. However, the model size of element number is increased dramatically.
- The external air field size also affects the results of field homogeneity. Although the influences are not significant, the larger external air field is preferred to weaken the influences of the parallel magnetic flux conditions at the exterior surfaces.

INFLUENCES OF FABRICATION TOLERANCES ON FIELD QUALITY

The definition of three types of tolerances are illustrated in Fig. 3, each has separated values for top and bottom poles. If considering the coupling between different tolerances, the number of cases to be calculated will be tremendous. For example, if each tolerance has 10 different values, the number of total cases will be 10^6! In order to reduce the case number, we first verified that the field deviation ΔBy on the extraction points result from one specific tolerance is irrelevant to the values of other tolerances. The field deviation ΔBy is relative to the reference case, which has zero tolerances for all types. The extraction points are actually the points on the lines for field quality calculation, including the TFH and IFH. Moreover, taking the advantage of model symmetry (about the XZ plane), only the

Table 1: Studied Cases of the Influences of Mesh Sizes on Field Quality

Cases	Magnetic materials mesh size [mm]	Interested region mesh size [mm]	External air field size[1]	Air field mesh size [mm]	TFH[2] [$\times10^{-4}$]	IFH[3] [$\times10^{-4}$]
Case 1	3.0	1.0	4, 4, 4	20	2.05	2.10
Case 2	3.0	0.5	4, 4, 4	20	2.01	4.11
Case 3	2.0	1.0	4, 4, 4	20	1.35	1.84
Case 4	1.0	1.0	4, 4, 4	20	0.27	3.89
Case 5	2.0	1.0	3, 3, 3	20	1.06	3.29
Case 6	2.0	1.0	5, 5, 5	20	1.05	1.77
Case 7	1.0	1.0	4, 4, 4	15	0.30	3.79
Case 8	2.0	0.5	4, 4, 4	20	1.08	2.26
Case 9	2.0	1.0	6, 6, 6	20	1.04	2.93
Case 10	1.0	1.0	6, 6, 6	15	0.29	3.98

[1] Ratios to the model size in x, y and z directions.
[2] By along the line: $y = z = 0, -10 < x < 10\ mm$.
[3] By on the plane: $y = 0, -10 < x < 10\ mm, -131 < z < 131\ mm$.

ISBN: 978-3-95450-250-9 ISSN: 2673-5520 doi:10.18429/JACoW-MEDSI2023-THPPP013

tolerances for top pole are considered in the calculation, i.e. $dy1$, $d\theta1$ and $d\varphi1$, the left ones for bottom pole are considered as equal. The calculated tolerances for each type are:

- $dy1$ from 30 to -30 µm with the interval of 5 µm, including the reference case when $dy1$ is 0 µm;
- $d\theta1$ from 0.79 to -0.79 mrad with the interval of 0.1316 mrad;
- $d\varphi1$ from 0.966 to -0.966 mrad with the interval of 0.0966 mrad.

Therefore, there are totally 45 cases calculated, for each of them, the field deviation ΔBy is calculated and saved for the extraction points. The field By (on extraction points) for the different combinations of tolerances could be handled now by adding the corresponding field deviations (result from different tolerances), as well as the reference fields. In this way, the field homogeneity of all different combinations of tolerances could be calculated.

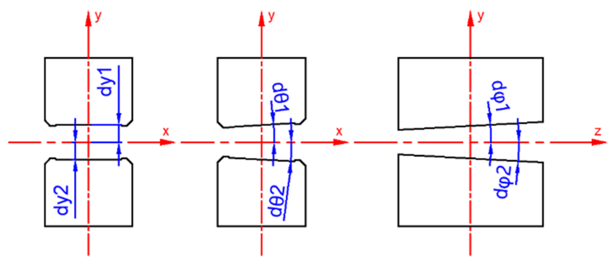

Figure 3: The defined pole tolerances for the field quality study.

In order to convert further the results into the desired requirements on the fabrication tolerances, we assume that the requirements of the same type of tolerance for both top and bottom poles are the same, i.e. the requirements for tolerances $dy1$ and $dy2$ are the same, etc. The three types of tolerance requirements are denoted as Ry, $R\theta$ and $R\varphi$. Since the corresponding field homogeneity are related to all Ry, $R\theta$ and $R\varphi$, we define all the possible combinations of these requirements. For each of the combinations, the result data are filtered and the worst homogeneities are found out as the corresponding requirements of field homogeneity. As an example, in case the tolerance requirement is defined as Ry =10 µm, $R\theta$ =0.2632 mrad, $R\varphi$=0.1932 mrad (all are positive values). The cases not satisfy the following conditions are filtered out:

- -10 µm $\leq dy1, dy2 \leq$ 10 µm,
- -0.2632 mrad $\leq d\theta1, d\theta2 \leq$ 0.2632 mrad,
- -0.1932 mrad $\leq d\varphi1, d\varphi2 \leq$ 0.1932 mrad.

Then, the worst field homogeneities are found as the corresponding requirements.

Table 2 lists the results of some of the tolerance requirements combinations. The change of field homogeneities relative to the reference case are also listed, which will be used when extend the results to the entire five modules LGB as explained at the beginning of Section 2. According to the results, following conclusions could be drawn:

- The TFH is more sensitive to $R\theta$ than other two types of tolerance requirements.
- The IFH is sensitive to all types of tolerance requirements, however, the dependence on $R\varphi$ becomes minor when beyond the first interval of 0.1 mrad. The reason is that the IFH shows strong nonlinearity to the tolerances.
- The combination of different tolerance requirements worsen the IFH, especially when both $R\theta$ and $R\varphi$ are existed.

Table 2: Study Results of Some of the Fabrication Tolerance Combinations

Ry [µm]	$R\theta$ [mrad]	$R\varphi$ [mrad]	TFH[1] [10^{-4}]	IFH[1] [10^{-4}]
0.0	0.0	0.0	1.04/0.0	2.9/0.0
5.0	0.0	0.0	1.08/0.04	3.67/0.77
10.0	0.0	0.0	1.08/0.04	5.17/2.27
0.0	0.13	0.0	1.3/0.26	4.16/1.26
0.0	0.26	0.0	1.83/0.79	5.32/2.42
0.0	0.0	0.1	0.6/0.07	3.26/1.81
0.0	0.0	0.2	0.65/0.12	3.26/1.81
5.0	0.13	0.0	0.7/0.17	4.07/2.62
0.0	0.13	0.1	0.75/0.22	5.36/3.91
5.0	0.0	0.1	0.61/0.08	4.89/3.44
5.0	0.13	0.1	0.77/0.24	6.77/5.32

CONCLUSION

To compromise between the computation accuracy and efficiency, the influence of mesh size on the field quality is firstly studied with a dedicated parameterized FE model for LGB magnet, and the mesh size of moderate model size and accuracy is selected. The influences of LGB fabrication tolerances on TFH and IFH are then studied. The tolerances including the pole tip height, and inclinations in transverse and longitudinal directions for both top and bottom poles. The situation of different combinations of these tolerances is considered under the assumption that the coupling among them is minor. Finally, the requirements (in terms of the worst field homogeneities) for different fabrication tolerance combinations are given, and the results indicate that the TFH is more sensitive to transverse inclination, while the IFH shows strong nonlinearity to all the tolerances.

REFERENCES

[1] Seunghwan Shin, "New era of synchrotron radiation: fourth-generation storage ring", *AAPPS Bull.*, vol. 31, no. 21, pp. 57-59, Aug. 2021. doi:10.1007/s43673-021-00021-4

[2] Tao He, Zhenbiao Sun, *et al.*, "Physics design of the Shenzhen innovation light source storage ring", *J. Instrum.*, vol. 18, p. P05037, May, 2023. doi: 10.1088/1748-0221/18/05/P05037

[1] homogeneity and the change of homogeneity relative to reference case.

ISBN: 978-3-95450-250-9 ISSN: 2673-5520 doi:10.18429/JACoW-MEDSI2023-THPPP014

A SPECIAL-SHAPED COPPER BLOCK COOLING METHOD FOR WHITE BEAM MIRRORS UNDER ULTRA-HIGH HEAT LOADS

J. Liu, X. Yan, H. Qin†, Institute of Advanced Science Facilities, Shenzhen, Guangdong, China

Abstract

In order to fulfil the more stringent requirements of optical figure accuracy for cooled X-Ray mirrors imposed to high heat loads, especially from advanced insertion devices in the diffraction limited storage rings (DLSR), investigations on the cooling system for white beam mirrors are conducted in this paper. A special-shaped copper block (SSCB) cooling method is proposed, using eutectic indium-gallium alloy as heat transfer medium. The SSCB cooling technology can keep a 550 mm-length mirror slope error of 0.2 μrad (RMS) under 230 W absorption heat power, showing great advantages in the accuracy and flexibility for thermal deformation minimization when compared with the traditional ones.

INTRODUCTION

The diffraction limited storage ring generates high-quality X-Ray with more collimated, brighter and coherent beams, showing novel technical superiority and greatly expanding the synchrotron radiation applications [1-3]. However this also poses a serious challenge on the cooling mechanism design of beamline optics [4-6]. How to efficiently carry away the heat on optical components, and achieve the very closely ideal mathematical surfaces (e.g. ellipsoids, paraboloids, etc.) is one of the key problems in the DLSR beamline transportation system [7, 8].

Various efficient cooling technologies have been developed to solve thermal release issues for water-cooled white beam mirror (WBM) [9-14], including top-side contact water cooling, In-Ga bath and water-cooling, mirror geometry optimization (smart notch structure), variable-length cooling, electric heater compensation, and so on. The top-side contact cooling scheme has been a routine way for most WBMs at third generation synchrotron radiation beamline. The design of the In-Ga bath and water-cooling copper blade is applied under more intense X-Ray beams due to better thermal conductivity, which can achieve sub-nano surface shape control combining with the notch structure and electric heater compensation method. However, the latter demands complicated mirror process, mounting, relatively high sensitivity power control algorithms and costs. How to achieve efficient thermal release and meet higher optical profile requirements, in practice, has become an urgent challenge.

In this article, a cooling scheme for WBMs called special-shaped copper block (SSCB) cooling, is presented. We describe the cooling model and optimize the cooling mechanism geometry by finite element analysis (FEA). It can achieve precise control on mirror surface optical profile by adjusting the layout of local thermal resistance of the mirror cooling mechanism. The quantitative correspondence between cooling mechanism, temperature distribution, and thermal deformation is studied by finite element methods.

OPTIMIZATION OF THE COOLING MECHANISM

The grazing-incidence X-Ray mirror can be considered as a one-dimensional mechanical beam. The thermal slope error of the mirror can be calculated from Eq. (1).

$$\theta(x) = -\frac{12}{WH^3}\int_0^x \frac{1}{E}\left[\int_{-H/2}^{H/2}\int_{-W/2}^{W/2} \alpha E T(x,y,z) z\,dy\,dz\right]dx \tag{1}$$

where W is the mirror width;
H is the mirror thickness;
α is the coefficient of thermal expansion;
E is the elastic modulus;
T(x, y, z) is the temperature-coordinate distribution.

The cross-section of a WBM imposed to an intense X-Ray beam can be divided into three parts, the central part and two parts at mirror ends. A half model with temperature distribution is shown in Fig.1 [15]. The central part is affected by illuminated beam, causing a tendency of convex warping owing to the upper hot and lower cool temperature distribution, based on Eq. (1). However, the situation is just on the opposite at both ends, since the top-side contact cooling generates a descent temperature gradient from lower to upper. As in Eq. (1), a negative value is obtained at the side parts, which offsets with the central one during the integration. The overall thermal deformation close to flat can be easily achieved along the beam footprint length, while hard to eliminate local fluctuations. It is obviously unreasonable to adopt a globally consistent cooling mechanism along the mirror length in order to minimize the thermal slope error.

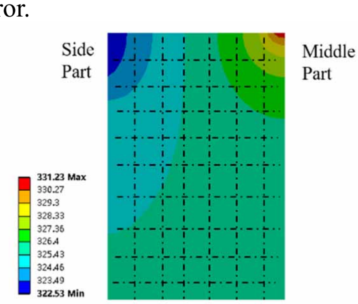

Figure 1: Half of the mirror cross-section

A cooling scheme of SSCB is proposed, which is expected to achieve thermal deformation control precisely by introducing grooves on the heat transfer path of the cooling blades properly. For the cooling mechanism with In-Ga eutectic alloy as heat transfer medium, the position of the heat

† qinhongliang@mail.iasf.ac.cn

ISBN: 978-3-95450-250-9 ISSN: 2673-5520 doi:10.18429/JACoW-MEDSI2023-THPPP014

transfer efficiency adjustment grooves should be set between the In-Ga bath and the coolant channel on the cooling copper block, as illuminated in Fig. 2.

By adjusting the matching degree between the groove parameters (e.g. the dimension, shape, position) and the absorption power density distribution, a precise control of the mirror surface temperature distribution can be achieved. It is expected to accomplish high-precision optical profile control, which will be verified by FEA simulations.

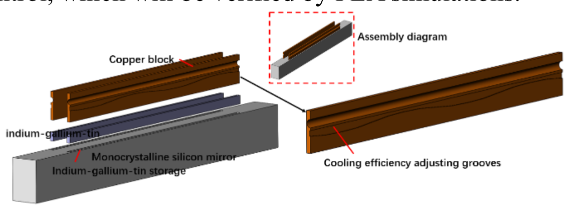

Figure 2: Schematic diagram of SSCB cooling structure.

SIMULATION AND DISCUSSION

FEA Modelling

The mirror substrate is made of monocrystalline silicon material, and the cooling mechanism is made from oxygen-free high-conductivity copper (OFHC). In-Ga eutectic alloy, in liquid state at room temperature, is selected as the interfacial heat exchange medium, and filled in two rectangular baths on the illumination surface of the mirror substrate symmetrically where the water-cooled copper blades immersed in. The material thermal-mechanical parameters are shown in Table 1.

Table 1: Material Parameters of the Cooling System

Material	OFHC	In-Ga alloy	Si
Density（kg/m^3）	8940	6350	2330
Elastic modulus (Gpa)	115	—	168
Poisson’s ratio	0.343	—	0.28
Yield strength (MPa)	340	—	—
Thermal conductivity (Wm-1°C-1)	391	28	148
CTE (°C-1, 25°C)	1.77×10^{-6}	—	2.5×10^{-6}

The mirror is 550 mm (length)×50 mm (width)×50mm (Height). In-Ga bath is 15 mm deep. The upper part of the copper blade is brazed with a water-cooling tube with an inner diameter of 8 mm. The lower part of the copper blade is immersed 10 mm in In-Ga.

Heat Load and Boundary Conditions

Considering an undulator light source, the incidence beam impinges on the mirror surface with a grazing incidence angle of 0.6°. The WBM (coated with Au) is located 30 m away from the light source, and the corresponding footprint is 4.5×430.5 mm^2 (width×length). The total absorbed heat power is about 230 W, and the maximum power density is 0.13 W/mm^2, as shown in Fig. 3. To remove the influence of edge effects of the thermal deformation, the central length of 366 mm is taken for mirror slope error evaluation.

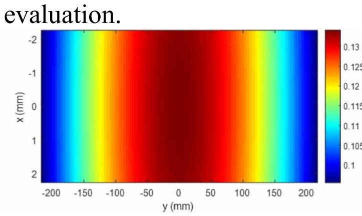

Figure 3: Absorption power density distribution.

The coolant flow rate is set to 1.5 L/min, corresponding to a flow velocity of about 0.5 m/s. The initial temperature of coolant (water) is 30 °C. It can be determined that the cooling system should be in the turbulent flow regime (Reynolds number is calculated to be 5000) [16]. The parameters applied in the simulation process are listed in Table 2.

Table 2: Heat Transfer Efficiency of the Cooling System

Heat transfer interface	Heat transfer efficiency W/(m·℃)
Water/Copper	3000
Copper/In-Ga	150000
Si/In-Ga	150000

The simply supported boundary conditions are imposed as Fig.4. Three translational degrees of freedom (XYZ) of point A are fixed. Limit the XZ and YZ translational degrees of freedom for the two points adjacent to A, i.e. point B and C, respectively. For point D, only one translational degree of freedom in the Z direction is fixed. In this way, reserving expansion space to ensure free thermal deformation of the mirror substrate.

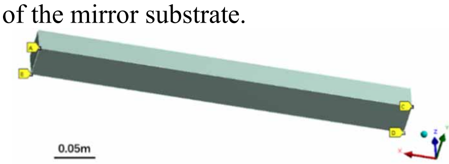

Figure 4: Diagram of the mirror fixing method.

Results

In this work, we firstly optimized the effective cooling length and the size of the mirror substrate. On this basis, a design of the SSCB cooling is applied, having two or three heat transfer efficiency adjustment grooves on each copper blade to minimize thermal slope error. The specific models involved are shown in Fig.5.

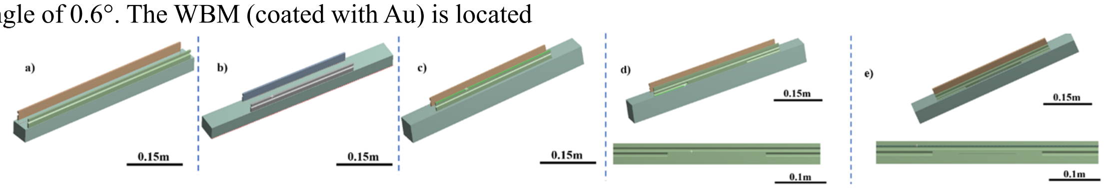

Figure 5: Specific models of the cooling scheme a) full-length cooling; b) optimized-length cooling; c) optimized mirror geometry; d) two grooves on the SSCB cooling; e) three grooves on the SSCB cooling.

ISBN: 978-3-95450-250-9 ISSN: 2673-5520 doi:10.18429/JACoW-MEDSI2023-THPPP014

The thermal deformation control abilities of the above cooling models (shown in Fig. 5) are compared by FEA, and the simulation results are shown in Fig.6. In the original scheme, the effective cooling length (i.e. length of the copper block) is close to that of the mirror. The temperature at the centre of the mirror optical surface is 319.7 K, obviously higher than the edges of 315.7 K, corresponding to a significant large convex profile with a high thermal slope error of 5.96 μrad (RMS). As the effective cooling length decreases, the temperature gap between the centre and the margin of the footprint area along the mirror length decreases and finally even turns into the opposite (centre temperature lower than the edges). The RMS thermal deformation of mirror profile gradually becomes smaller exhibiting a sinusoid-like curve (central convex and marginal concave) with cooling length decreasing, then transforms into much more concave shape in the central part. When the optimized cooling length is 310 mm (about 72% of the beam footprint length), the centre temperature is 323 K while the footprint edges are 328 K, and the slope error RMS reaches a small value of 0.74 μrad, much lower than the original scheme. To further improve thermal slope error, the mirror dimension should also be optimized. Reduce the width of the mirror substrate to 40 mm and expand the thickness to 60 mm. The dimension of the cooling copper block is also modified accordingly, whose optimized length is 370 mm. Finally, the footprint centre and edge temperature on mirror surface are 320 K and 320.8 K, respectively, being approximately uniform. The surface slope error RMS is as small as 0.60 μrad, which is improved furtherly. The SSCB cooling scheme has a cooling length of 400 mm, with both grooves setting symmetrically at close to the blade ends. The groove cross section is circular with a diameter of 8 mm and a length of 105 mm, respectively. Also, the temperature gap within the footprint is slightly greater than the former, appearing an obviously flatter profile in the middle of the footprint with the slope error of 0.41 μrad. These findings demonstrate that the method of adjusting local thermal resistance of the cooling mechanism has a strong capability in the WBM surface shape controlling. The smart grooves, to some extent, change the overall heat transfer efficiency relatively and homogenize surface temperature. The optimal slope error is achieved by cutting peaks and filling valleys in the sinusoid-like curve when setting the grooves at the right position, with regard to the concave shape region, with appropriate size. On the basis of the above, an additional groove is added in the middle of the blade to realize “secondary levelling” of the surface shape. By further optimization, the final solution was determined: the total length of the SSCB is 390 mm, the grooves on both ends is 99 mm long with the diameter of 8 mm; the groove in the middle is 100mm long by the diameter of 1mm. This cooling scheme achieves the local flatness within the mirror footprint area. The best slope error of the mirror has been reduced to 0.20 μrad, which is further reduced by more than 50%, compared to the two-groove SSCB cooling scheme.

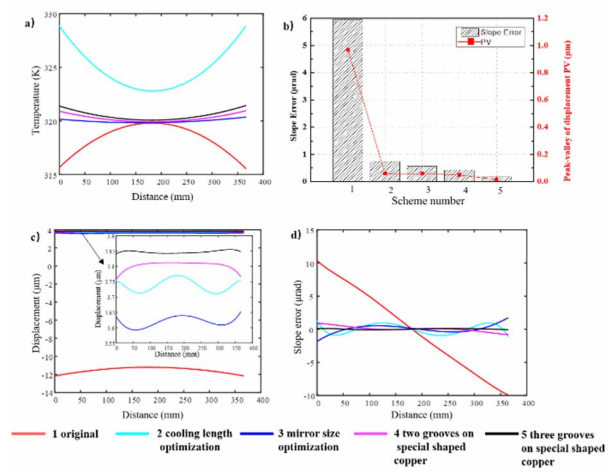

Figure 6: Simulation results of various cooling scheme a) Temperature distribution; b) Histogram of thermal displacement (P-V) and slope error (RMS); c) Thermal displacement curves; d) Thermal slope error

CONCLUSION

The finite element method is applied to explore the cooling mechanism of high-precision-profile white light mirrors. The effects of key parameters, such as effective cooling length, mirror dimension, and thermal resistance arrangement of the cooling mechanism, on the mirror temperature distribution and slope error under thermal load are studied. The specific conclusions are as follows.

The central part of the illuminated WBM is prone to thermal deformation accumulation. Longer effective cooling length corresponds to an obvious thermal bump, while a shorter one will lead to a significant concave profile. There is an optimal cooling length under a given heat distribution, which accounts for approximately 72% of the footprint length in this case.

The SSCB cooling technology can precisely adjust the thermal resistance layout on the heat transfer path by changing the shape of the heat transfer conducting grooves. Grooves at both cooling blade ends can realize a good adjustment on the mirror surface shape, making it flat and achieving a thermal slope of 0.41 μrad. On this basis, an extra groove in the blade centre can obtain "secondary levelling" effect, and after fine adjustment, the final thermal slope error of the mirror is reduced to 0.2 μrad. The variation of copper block shape has a further potential on WBM cooling, corresponding to various design routes, suitable for grazing incidence optics, and can achieve extremely high thermal surface accuracy.

REFERENCES

[1] F. Chen *et al.*, “Application of synchrotron radiation and other techniques in analysis of radioactive microparticles emitted from the Fukushima Daiichi Nuclear Power Plant accident-A review”, *J. Environ. Radioact.*, vol. 196, pp. 29-39, Jan. 2019. doi:10.1016/j.jenvrad.2018.10.013

ISBN: 978-3-95450-250-9 ISSN: 2673-5520 doi:10.18429/JACoW-MEDSI2023-THPPP014

[2] B. Heyden, "Shedding light on ore deposits: A review of synchrotron X-ray radiation use in ore geology research", *Ore Geol. Rev.*, vol. 117, p. 103328, Feb. 2020. doi:10.1016/j.oregeorev.2020.103328

[3] T. A. Ezquerra, M. C. Garcia-Gutierrez, A. Nogales, and A. J. Müller, "Introduction to the special issue on applications of synchrotron radiation in polymers science", *Eur. Polym. J.*, vol. 81 pp. 413-414, Aug. 2016. doi:10.1016/j.eurpolymj.2016.05.002

[4] D. A. Liakin, S. V. Barabin, A. Y. Orlov *et al.*, "Electrodes for beam position monitors for fourth generation synchrotron radiation source", *J. Surf. Investig.*, vol. 13, pp. 511-514. Jun. 2019. doi:10.1134/S1027451019030261

[5] L. Liu, R. T. Neuenschwander, and A. R. D. Rodrigues, "Synchrotron radiation sources in Brazil", *Philos. Trans. R. Soc. London, Ser. A*, vol. 377, no. 2147, p. 20180235, Jun. 2019. doi:10.1098/rsta.2018.0235

[6] E. L. Bright, C. Giacobbe, and J. P. Wright, "Beam heating from a fourth-generation synchrotron source", *J. Synchrotron Radiat.*, vol. 28, pp. 1377-1385, Sep. 2021. doi:10.1107/S160057752100669X

[7] D. H. Bilderback, A. K. Freund, G. S. Knapp, and D. M. Mills, "The historical development of cryogenically cooled monochromators for third-generation synchrotron radiation sources", *J. Synchrotron Radiat.*, vol. 7, pp. 53-60, Apr. 2000. doi:10.1107/S0909049500000650

[8] E. Esarey, P. Sprangle, and A. Ting, "Laser synchrotron radiation and beam cooling", presented at 17th international free electron laser conference, USA, 1995.

[9] A. Mhaisekar, M. J. Kazmierczak, and R. Banerjee, "Three-dimensional numerical analysis of convection and conduction cooling of spherical biocrystals with localized heating from synchrotron X-ray beams", *J. Synchrotron Radiat.*, vol. 12, no. 3, p. 318-28, May 2005. doi:10.1107/S0909049505003250

[10] J. Arthur, "Experience with microchannel and pin-post water cooling of silicon monochromator crystals", *Opt. Eng.*, vol. 34, pp. 441-444, Feb 1995. doi:10.1117/12.195395

[11] L. Jin *et al.*, "FEA-based structural optimization design of a side cooling collimating mirror at SSRF", *Nucl. Sci. Technol.*, vol. 28, pp. 1-6, Oct. 2017. doi:10.1007/S41365-017-0307-7

[12] S. Talwar and D. A. Markle, "Laser scanning apparatus and methods for thermal processing", United States Patent and No. US20040188396A1, Sep. 30, 2004.

[13] J. H. Underwood, P. J. Batson, H. R. Beguiristain, and E. M. Gullikson, "Elastic bending and water cooling strategies for producing high-quality synchrotron radiation mirrors in silicon", in *Proc. SPIE Int. Soc. Opt. Eng.*, vol. 3152, 1997. doi:10.1117/12.295550

[14] D. Cocco *et al.*, "Adaptive shape control of wavefront-preserving X-ray mirrors with active cooling and heating", *Opt. Express*, vol. 28, pp. 19242-19254, Jun 2020. doi:10.1364/OE.394310

[15] M. Mattenet and G. Marot, "Thermal deformations of a cooled x-ray mirror", *Opt. Photonics*, 1996. doi:10.1117/12.259831

[16] L. M. Jin *et al.*, "Thermal analysis of the first ultra-high heat-load front-end absorbers for the ultra-hard multi-functional X-ray beam-line at SSRF", *Nucl. Instrum. Methods Phys. Res., Sect. A*, vol. 989, p. 164955, Feb. 2021. doi:10.1016/j.nima.2020.164955

ISBN: 978-3-95450-250-9 ISSN: 2673-5520 doi:10.18429/JACoW-MEDSI2023-THPPP015

MECHANICAL DESIGN OF THE NOVEL PRECISE SECONDARY SOURCE SLITS

X. Yan, J. Liu, Z. Ji, Y. Gong, H. Qin†, Institution of Advanced Science Facilities, Shenzhen, China

Abstract

High-precision slits are extensively adopted in coherent or nano-focusing beamlines as the secondary source, which can accurately define or achieve a beam size at the micron or sub-micron scale, while maintaining high stability. This paper presents the design of a set of precise slits based on a flexure hinge mechanism, which enables a nano-scale resolution and a stroke of hundreds of microns simultaneously. The coarse or fine adjustment motion of each blade can be accomplished with or without a displacement amplification mechanism, which is driven by a piezo actuator. Furthermore, the kinematic and dynamics models are investigated through finite element analysis (FEA) and numerical analysis successively, yielding consistent results. The optimized slits system can provide a linear stroke of up to 400 μm with a resolution of 10 nm both in horizontal and vertical directions, whose first Eigen frequency is 130 Hz.

INTRODUCTION

As an important component of the beamline, the secondary source slit has the function of shaping the beam size and preventing scattering X-rays. With the increasing demands for smaller beam size in hard X-ray beamlines at diffraction-limited storage ring, the performance requirements for secondary source slits have become more challenging [1-2]. The aim of this work is thus the development of an innovative design of a large stroke compact slits system with nano scale beam shaping capability. The following sections will introduce design and analysis of the secondary source slits.

DESIGN OF THE SLITS

Specifications

Table 1: The Overall Specifications of Secondary Source Slits

Item	Specification
Vacuum	$\leq 10^{-9}$ mbar
Y/Z motion range	10 mm
Y/Z resolution	1 μm
Y/Z repeatability	± 2 μm
Parallelism between blades	≤ 0.2 μm
Range of rotary adjustment	± 0.5°
Slits blade motion range	−20 ~ 200 μm (H) −20 ~ 200 μm (V)
Slits resolution	0.01 μm
Slits repeatability	± 0.03 μm

† qinhongliang@mail.iasf.ac.cn

Mechanical Design

The overall slit system consists of five parts, including (1) the slit motion adjustment mechanism, (2) the chamber, (3) the vertical movement (Z direction), (4) the horizontal movement (Y direction) and (5) a marble support, as shown in Fig. 1 (see the specifications in Table 1).

The main mechanism containing slit motion and parallelism adjustment are integrated in a compatibility of ultra-high vacuum (UHV) chamber. There are two sets of slit motion adjustment components, positioned perpendicular to each other and slightly offset along the beam direction. These components enable horizontal and vertical slit openings, with each set comprising two translational mechanisms and one rotating mechanism. Figure 2 shows a motion adjustment assembly. One tungsten carbide blade is mounted on each translational mechanism, which is driven by a piezo actuator via a linear flexure hinge. Two translational mechanisms are symmetrically connected with the inner part of the flexible rotating mechanism, i.e. a circular flexible hinge, by which the pair of blades can be aligned to X-Ray beam accurately. The outer part of the rotating mechanism is fixed on the chamber bottom using silvered screws. Herein, there is a manual flexible hinge mechanism connected to one of the blades for parallelism alignment during installation.

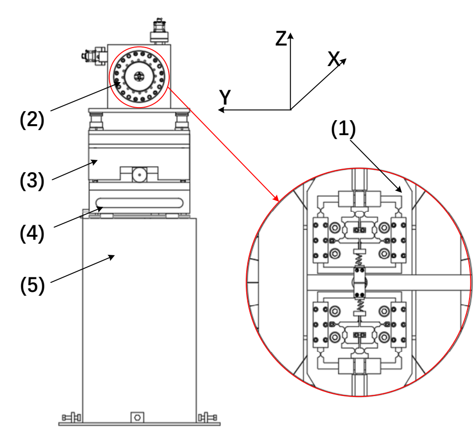

Figure 1: Schematic diagram of the secondary source slits.

There are two operation modes for the slit translational motion, corresponding to coarse or fine adjustment. (1) Displacement amplification mode. When the electromagnets are power-off, then the piezo actuator directly drives the hinge to accomplish the output displacement amplification. The blade fixed on the displacement output structure is connected to the hinge output end with a preload spring. (2) Non-displacement amplification mode. When the electromagnets are charged, it will clamp the rod fixed on the translational hinge input end, the blade is moved directly with the displacement output structure driven by the

ISBN: 978-3-95450-250-9 ISSN: 2673-5520 doi:10.18429/JACoW-MEDSI2023-THPPP015

piezo actuator, guiding by a pair of rails. The slit blade has a good output displacement response when the piezo actuator step scans with a step size of 10 nm.

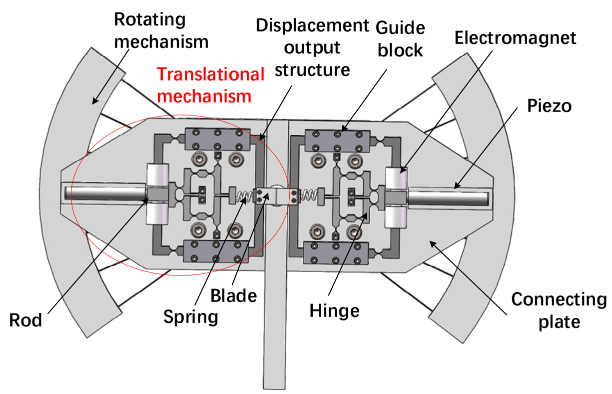

Figure 2: Motion adjustment mechanism.

The whole chamber is installed on two motorized stages, which have a motion stroke of 10 mm both in horizontal and vertical direction for alignment. A stable marble support is underneath the stages, isolating vibrations from the floor.

Analysis and Results

As illuminated in Fig. 3, the flexible hinge structure is the core of the slit displacement amplification mechanism. The working principle is described as follows.

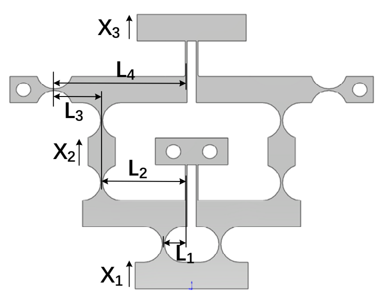

Figure 3: Two-stage lever-type flexure hinge mechanism.

The input displacement X_1 is driven by the piezo actuator, and the first-stage output displacement is X_2 with an amplification factor of L_2/L_1. Similarly, taking X_2 as the input displacement of the second lever-type hinge mechanism, the output displacement X_3 is obtained since the second amplification factor is L_4/L_3. Therefore, the total amplification ratio of the hinge mechanism is:

$$\frac{X_3}{X_1} = \frac{L_2}{L_1} \times \frac{L_4}{L_3}. \quad (1)$$

To meet the requirement for the secondary source slits, a comprehensive consideration of a linear stroke up to 200 µm, single nanometre resolution, and high stiffness are taken into account. The final amplification factor is 10 after optimizing the lever lengths. The static analysis of the translational mechanism is carried out by finite element method, and the maximum output displacements in two modes are 200 µm and 20 µm respectively while the input displacements varying from 1 to 20 µm, as shown in Fig. 4. Furthermore, analytical solutions are calculated. The relationship between input and output displacement of the translational mechanism in the two modes are depicted in Fig. 5. It can be seen that the finite element simulation results are in good consistent with the analytical ones, and the output-input displacement ratio is close to 10 in displacement amplification case. It is noteworthy that there is a slight deviation when the input displacement is greater than 14 µm, which may be due to the accumulated stress resulting from larger deformation. It is negligible because even the maximum deviation accounts for only 1 percent. In non-displacement amplification case, it works perfectly with a high resolution.

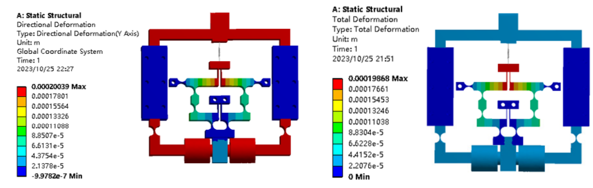

(a) (b)

Figure 4: Translational mechanism displacement with input displacement of 20 µm. (a) Displacement amplification mode (b) Non-displacement amplification mode.

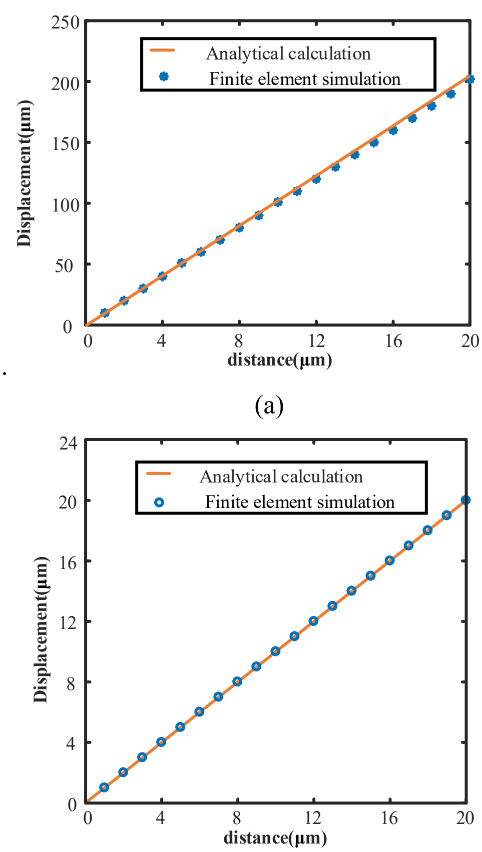

(a)

(b)

Figure 5: Input-output displacement curve of translational mechanism in two modes. (a) Displacement amplification mode. (b) Non-displacement amplification mode.

ISBN: 978-3-95450-250-9 ISSN: 2673-5520 doi:10.18429/JACoW-MEDSI2023-THPPP015

Considering the stress in the hinge as another determining factor, it is necessary to compromise the maximum stress below about 50 % of the yield strength of the material when the hinge deflects to the needed motion limit. QBe2 and 17-7PH stainless steel are chosen as the material of translational and rotating hinges respectively, and the equivalent stress results are shown in Fig. 6. Figure 6 (a) indicates that the maximum von Mises stress of translational hinges in non-displacement amplification case is 452.6 MPa while applying an input displacement of 20 μm. Figure 6 (b) indicates that the maximum von Mises stress of translational hinges in displacement amplification case is 452.1 MPa while applying an input displacement of 20 μm. Figure 6 (c) shows that the maximum von Mises stress of the rotating hinges is about a half of its yielding stress set as 171 MPa while applying a torque of 0.5 Nm. The maximum actuated rotary movement is about 0.55 degree.

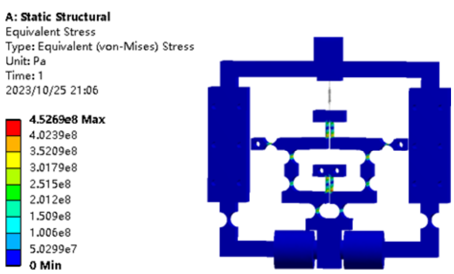

(a)

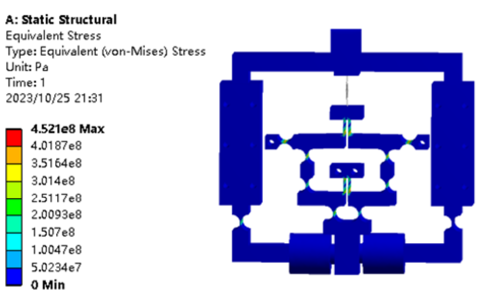

(b)

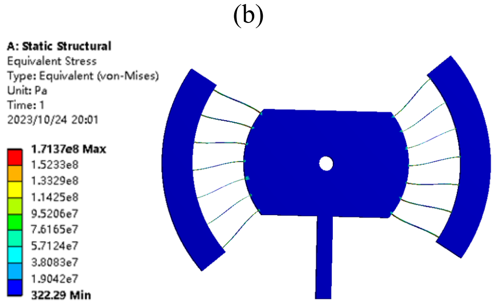

(c)

Figure 6: Maximum von Mises stress diagrams. (a) Translational mechanism in non-amplification mode. (b) Translational mechanism in amplification mode. (c) Rotating mechanism.

The first and second modal analysis results of the motion adjustment mechanism are shown in Fig. 7. It can be seen that the first natural frequency is 130 Hz. The overall structure has high stiffness and meets the stability requirements of precision instruments.

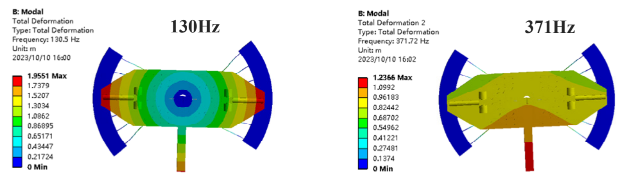

(a) (b)

Figure 7: The first two modal analysis results of motion adjustment mechanism. (a) First order modal shape. (b) Second order modal shape.

To achieve the main goal of maintaining a beam size between 5 - 10 μm in both the horizontal and vertical directions, the position drift of the secondary source slits should be less than 0.5 μm. The secondary source slit structure is made of marble support and invar alloy frame. If the ambient temperature fluctuates ± 0.1℃ within 24 h, it will lead to a drifting of up to 0.3 μm in the vertical direction (more severe than the horizontal one). Considering a relative worse condition, the disturbance of the ground vibration on the optical components is 0.4 μm. Thus the total error is 0.5 μm. Therefore, in order to ensure that the position instability of the secondary source slit less than 10 % of the beam size, the ambient temperature stability should be kept at least within ± 0.1℃.

CONCLUSION

A new high-precision secondary source slit is designed, which is characterized with a large opening size of 400 μm and single nano resolution. The first natural frequency of the optimized hinge mechanism has reached 130 Hz, which is of good stiffness. A slit prototype will be done based on the design in the near future.

REFERENCES

[1] Longlife Lee, Chien-Hung Chang, Liang-Jen Huang, *et al.*, "Design and Application of a Mono-beam Slit System at Taiwan Photon Source", *AIP Conference Proceedings*, vol. 2054, no. 1, p. 060054, 2019. doi:10.1063/1.5084685

[2] Hong-Yi Yan, Chien-Hung Chang, Chun-Yu Chen, *et al.*, "Mechanical Design of Secondary Source Slits for Hard X-ray Beam-lines at Taiwan Photon Source", in *Proc. MEDSI'16*, Barcelona, Spain, Sep. 2016, pp. 12-14. doi:10.18429/JACoW-MEDSI2016-MOPE05

ISBN: 978-3-95450-250-9 ISSN: 2673-5520 doi:10.18429/JACoW-MEDSI2023-THPPP016

NUMERICAL AND EXPERIMENTAL STUDIES TO EVALUATE THE CONSERVATIVE FACTOR OF THE CONVECTIVE HEAT TRANSFER COEFFICIENT APPLIED TO THE DESIGN OF COMPONENTS IN PARTICLE ACCELERATORS

M. Quispe†, J. J. Casas, C. Colldelram, M. Sanchez, ALBA-CELLS, Cerdanyola del Vallès, Spain
R. Capdevila, M. Rabasa, G. Raush, ESEIAAT, Terrassa, Spain
S. Grozavu, Universidad Politecnica de Madrid, Madrid, Spain
H. Bello, La Romanica, Barberà del Vallès, Sabadell, Spain

Abstract

The fluid boundary condition applied to the design of components in particle accelerators is calculated as a global variable through experimental correlations coming from the literature. This variable, defined as the convective heat transfer coefficient, is calculated using the conventional correlations of Dittus and Boelter (1930), Sieder and Tate (1936), Petukhov (1970), Gnielinski (1976), among others. Although the designs based on these correlations work properly, the hypothesis of the present study proposes that the effectiveness of these approximations is due to the existence of a significant and unknown conservative factor between the real phenomenon and the global variable. To quantify this conservative factor, this work presents research based on Computational Fluid Dynamics (CFD) and experimental studies. In particular, recent investigations carried out at ALBA confirm in a preliminary way our hypotheses for circular pipes under fully and non-fully developed flow conditions. The conclusions of this work indicate that we could dissipate the required heat with a flowrate lower than that obtained by applying the conventional experimental correlations.

INTRODUCTION

Nowadays, in particle accelerator engineering and in engineering in general, numerical simulations, such as FEA (Finite Element Analysis) and CFD (Computational Fluid Dynamics), are decisive to approve the viability of a proposed design. Although its importance is recognized, it is also known that the results of numerical simulations have a strong dependence on the precision and good approximation of other variables such as the geometric model, physical properties, boundary conditions, etc. In this context, the content of this work is oriented to the study of one of the boundary conditions commonly used in design: the convective heat transfer coefficient (h) for internal flow in cooling channels. In particular, at ALBA we are studying the conservative factors inherent in the "h" coefficient, currently obtained from experimental correlations reported in the literature. Our main working hypothesis considers the existence of a significant and not yet quantified conservative factor in the calculation of the "h" coefficient. The results of this study will be relevant for the design of the new components of ALBA II, our current project to become a fourth-generation accelerator. From the point of view of accelerator engineering, we will have the challenge of designing the new components for higher power densities, compared to ALBA I. In this new scenario, it will be important to know with a better precision the value of the "h" coefficient to avoid oversizing in the new designs.

For general engineering applications, the "h" coefficient is obtained from experimental correlations from the literature, reported by authors such as Dittus and Boelter (1930), Sieder and Tate (1936), Petukhov (1970), Gnielinski (1976) [1], among others. The design engineer must choose between those authors to obtain this coefficient, whose value is not unique depending on the selected experimental correlation. For example, for a hypothetical case of water at 23 ºC circulating in a pipe with an internal diameter of 10 mm and assuming a dissipation of 7 kW in the water, there is a difference of approximately 10 % between the values of "h" calculated with the correlations of Dittus – Boelter and Petukhov.

Another aspect to highlight of the "h" coefficient is the condition of its approximation: the experimental correlations have been formulated for thermal and hydraulic fully developed flow conditions. In real applications of particle accelerators, we rarely have fully developed flow, because the geometries are small in size, such as the cooling channels of mirrors, monochromators, front end masks, radiation absorbers, etc. These real geometries would increase the unknown conservative factor with respect to the case of fully developed flow, according to our hypothesis. On the other hand, from the point of view of the real phenomenon, conventional correlations assume homogeneity of the coefficient along the cooling channel, which is not true because this variable has local behaviour and its distribution is influenced by the geometry of the channel, by the flow conditions (especially for transient and turbulent cases), and by the temperature of the fluid.

In the same line of research, another variable to study is the approximation of the hydraulic diameter concept. In many applications we are forced to design cooling channels with non-circular cross sections. In these cases, the application of the hydraulic diameter concept suggested by conventional references introduces, in our opinion, a new conservative factor with respect to the case of a circular tube.

The investigations of this paper are based on CFD calculations, Heat Transfer (HT) simulations, and preliminary experimental studies in setups developed at ALBA. The HT simulation approximates the heat transfer in the fluid

†mquispe@cells.es

ISBN: 978-3-95450-250-9 ISSN: 2673-5520 doi:10.18429/JACoW-MEDSI2023-THPPP016

using the "*h*" coefficient, calculated through experimental correlations reported in the literature [1]. The HT and CFD cases have been carried out using the MECHANICAL and FLUENT modules of ANSYS WORKBENCH [2], respectively.

CIRCULAR CHANNELS: CFD STUDIES

Model Description

Two pipes with an internal diameter of 8 and 10 mm have been studied [3, 4], both 0.5 m lengths. The heat flux applied to the surface are assumed to be constant values of 80 and 12.55 kW/m^2, respectively (Fig. 1a). At the inlet, water at 23 ºC and a velocity range < 4 m/s are fixed.

O-grid structured mesh has been applied along all the wall boundaries inside the fluid, inflation layers has been introduced for a smooth transition of the mesh until reaching a $y+\approx 1$ [5] (Fig. 1b). Also, a grid convergence study of three levels of mesh refinement has been performed, implementing the convergence Python program provided as a part of the NASA Examining Spatial (Grid) Convergence tutorial [6]. The highest refinement has generated a mesh of around 2.5 million elements.

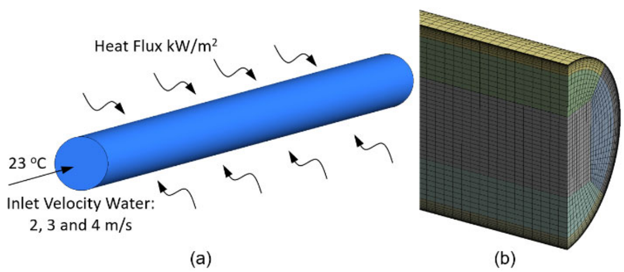

Figure 1: (a) Pipe simplified model, (b) Mesh detail.

A group of viscous models have been tested such as the $k-\omega$ Shear-Stress Transport (SST), $k-\omega$ Standard, the Realizable k-ε with Scalable Wall Functions (RKE ScWF), the Realizable k-ε with Enhanced Wall Treatment (RKE EWT) and the Transition SST [7]. The results have been compared with the Darcy–Weisbach equation for pressure drop and the Power-Law equation for the developed velocity profile, in order to select the most accurate. For this comparative study, according to studies carry out by [3] and [4], the authors agree on the better performance of the $k-\omega$ Shear-Stress Transport (SST) model.

For the studies, the Nusselt number $Nu = hD/k$ is computed, where D is the diameter of the channel and k the thermal conductivity of the fluid. The "*h*" coefficient is computed using the Newton's law of cooling $h = Q/(A(Tw\text{-}Tf))$, where Q is the heat transfer rate across the area A, Tw is the wall temperature and Tf the fluid bulk temperature. Tf is derived from the rate of flow of enthalpy divided by the rate of heat flux through a cross section, like defined in Neale's study [8], which can be calculated in ANSYS FLUENT as the Mass Flow Average of the temperature of a transversal area of the fluid.

Results

For the case of pipe internal diameter 8 mm, the results from Fig. 2 suggest that experimental benchmark coefficients are conservative. For instance, comparing CFD results with Dittus and Boelter's correlation, an increase between 12.6 and 13.8 % of the convective heat transfer coefficient has been found.

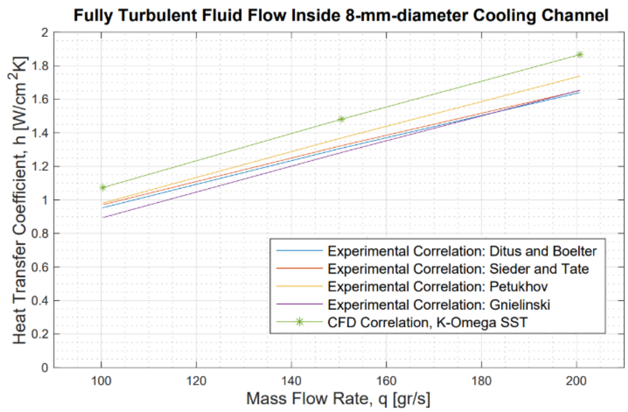

Figure 2: Experimental correlations of the "*h*" coefficients contrasted to the CFD values for circular channel flow 8 mm diameter.

For a pipe of 10 mm inner diameter, the different viscous models offer quite different results between themselves (Fig. 3). Compared with Dittus – Boelter, the average variation with the models are 25.9 %, 20.1 % and –3.4 % for the k-ω SST, RKE EWT and RKE ScWF, respectively. This last model deserves special attention for new studies, because its discrepancy is significant with respect to the other turbulence models.

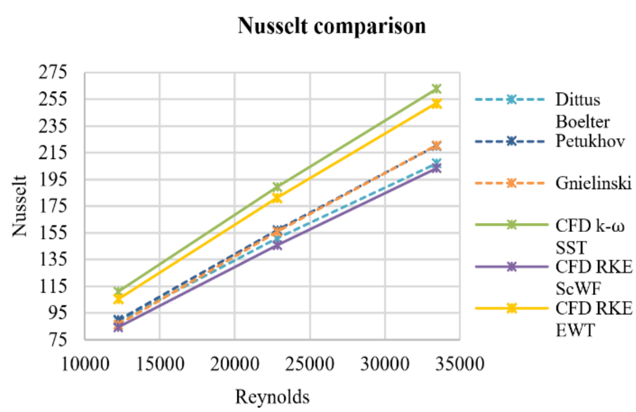

Figure 3: Comparison of Nusselt calculated by CFD to experimental correlations for channel 10 mm diameter.

The effect of the heat flux is also studied. The CFD Nusselt number (Nu CFD) is calculated based on the k-ω SST model, at 3 m/s inlet velocity and different heat fluxes. The results presented in Table 1 show that higher heat flux values the higher differences of the Nu CFD compared to the experimental correlations.

ISBN: 978-3-95450-250-9 ISSN: 2673-5520 doi:10.18429/JACoW-MEDSI2023-THPPP016

Table 1: Increase of Nu CFD (K-ω SST) for Different Heat Fluxes in Respect to Experimental Correlations

Heat Flux (W/m²)	ΔNu CFD - Dittus Boelter	ΔNu CFD - Petukhov	ΔNu CFD - Gnielinski
170000	29.38 %	22.07 %	21.70 %
125464	26.86 %	19.31 %	19.03 %
80000	24.23 %	17.20 %	17.00 %

MIRROR: CFD, HT, AND EXPERIMENTAL STUDIES

Model Description

This section presents numerical and experimental studies for non-fully developed flow conditions. The model reproduces a mirror with internal cooling channel. The geometry consists in an Al 6082 T6 block of 60×60×150 mm with a 10 mm diameter hole where the water flows through (Fig. 4 a). As boundary conditions, heat flux on the top surface (35.85 and 43.4 W) and fluid velocities of 1 and 2 m/s are imposed. For the experiment, heat flux is applied using two 65×11 mm heater foils (Fig. 4 b).

Three thermocouples type K are placed to measure surface temperature, as shown in Fig. 4b, and insulation is achieved using an aluminium foil layer underneath a fibre glass wool layer. The experimental setup used was developed at ALBA for hydraulic and thermal testing. It allows the user to regulate the flow rate and inlet temperature [9].

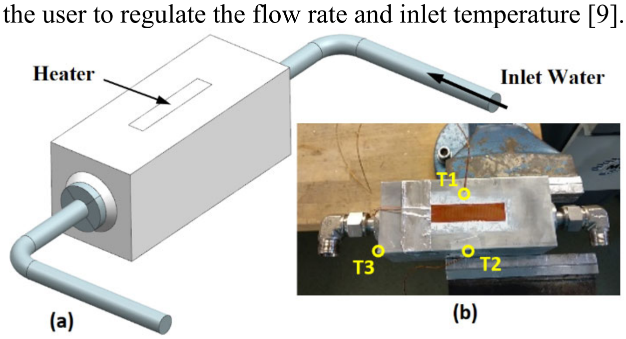

Figure 4: (a) Mirror simplified model, (b) Details of temperature sensors and heater for experiment.

For the CFD model, a mesh study is performed for three meshes (1.6M, 2.8M and 4M) with a $y+\approx 1$. HT simulations have also been carried out by applying the "*h*" coefficients, calculated at the average temperature of the fluid in the cooling channel.

Results

Figure 5 shows the results of three cases studied for different heat fluxes and inlet velocities. The temperature results applying the HT simulation are higher than the temperature results calculated with the CFD models described in the previous section. On the other hand, the results obtained with the RKE ScWF model are closer to the temperatures using the HT simulations. The results obtained with the RKE EWT and k-ω SST models show almost exactly the same temperature results, this behaviour is reproduced for all velocities and heat fluxes studied. The CFD results, applying the k-ω SST and RKE EWT models, are generally closer to the experimental results compared to the results obtained with the HT simulations.

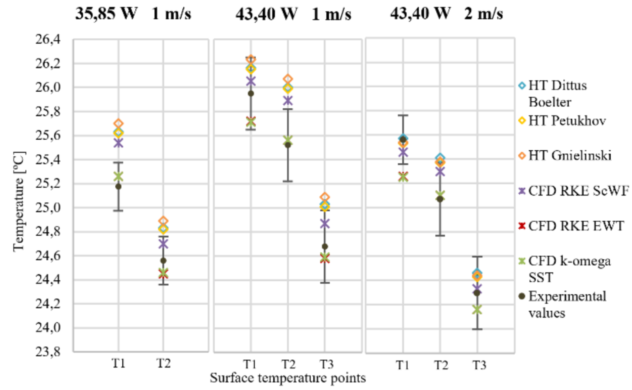

Figure 5: Results of numerical simulations and experimental studies for three study conditions.

Figure 6 shows the distributions of temperatures and velocities for the CFD model, considering the k-ω SST turbulence model, inlet velocity into the tube of 1 m/s and the value of the heat flux equals 43.4 Watts.

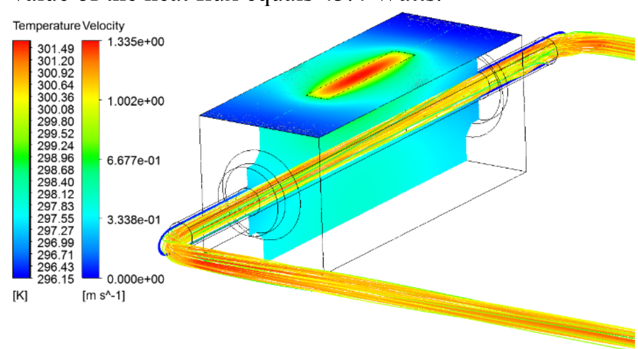

Figure 6: Velocity and temperature distributions for the case CFD k-ω SST, 43.4 W, and 1 m/s inlet.

CONCLUSIONS & FUTURE WORK

For the case of fully developed flow conditions in pipes with an internal diameter 8 mm, the CFD calculations (applying the k-ω SST viscous model) confirm the existence of an average conservative value of 14 % in the conventional convective heat transfer coefficient (taking as reference the Dittus and Boelter correlation). For the pipe of 10 mm diameter, average variations of 25.9 % and 20.1 % are obtained when the "*h*" coefficient (based on the Dittus and Boelter correlation) is compared with CFD calculations (based on the models of turbulence k-ω SST and RKE EWT, respectively). Then, this second diameter also confirms the existence of the conservative factor.

It has been found that the conservative factor is also affected by the heat flux condition: the conservative factor increases as the heat flux condition increases.

The experimental results for the proposed case also confirm the existence of the conservative value for non-fully developed flow conditions. However, to have a definitive conclusion, it is recommended to carry out similar experiments subject to higher heat fluxes.

ISBN: 978-3-95450-250-9 ISSN: 2673-5520 doi:10.18429/JACoW-MEDSI2023-THPPP016

REFERENCES

[1] W. M. Rohsenow, J. P. Hartnett, and Y. I. Cho, *Handbook of heat transfer*, McGraw-Hill Education, 1998. doi:10.1016/s0278-6125(99)90104-8

[2] ANSYS, https://www.ansys.com

[3] S. Grozavu *et al.*, "CFD Studies of the Convective Heat Transfer Coefficients and Pressure Drops in Geometries Applied to Water Cooling Channels of the Crotch Absorbers of ALBA Synchrotron Light Source", in *Proc. IPAC'22*, Bangkok, Thailand, Jun. 2022, pp. 2887-2890. doi:10.18429/JACoW-IPAC2022-THPOTK050

[4] M. Rabasa *et al.*, "CFD Studies and Experimental Validation of the Convective Heat Transfer Coefficient in Non-Fully Developed Flows Applied to Conventional Geometries Used in Particle Accelerators", in *Proc. IPAC'23*, Venice, Italy, May. 2023, pp. 4912-4915. doi:10.18429/JACoW-IPAC2023-THPM010

[5] SimScale CAE Forum, https://www.simscale.com/forum/t/what-is-y-yplus/82394

[6] NASA Examining Spatial (Grid) Convergence, https://www.grc.nasa.gov/www/wind/valid/tutorial/spatconv.html

[7] "Turbulence", in ANSYS FLUENT 12.0 Theory Guide, ANSYS Inc., 2009.

[8] A. Neale, D. Derome, B. Blocken, and J. Carmeliet, "CFD calculation of convective heat transfer coefficients and validation– Part I: Laminar flow", in *Proc. IEA Annex 41 working meeting*, Kyoto, Japan, Apr. 2006.

[9] M. Quispe, "Modular Setup for Thermal Hydraulic Measurements at ALBA Storage Ring", unpublished.

ISBN: 978-3-95450-250-9 ISSN: 2673-5520 doi:10.18429/JACoW-MEDSI2023-THPPP020

THE PRE-ALIGNMENT OF HIGH ENERGY PHOTON SOURCE STORAGE RING

Shang Lu†, Lan Dong, Jing Liang[1], Lingling Men, Tong Wang[1], Xiaolong Wang
Institute of High Energy Physics, Beijing, China
[1]also at Spallation Neutron Source Science Center, Dongguan, China

Abstract

In order to achieve 10 µm pre-alignment accuracy of storage ring in transverse and vertical, four laser trackers were used for set up a four-station µm measurement system. Experiment results show that the relative displacement measurement accuracy is better than 3 µm in 3-meter workpiece range, which can satisfy the real-time position feedback accuracy of the magnets in the process of ultra-high-precision pre-alignment. After two years of research and development, three pre-alignment standard workstations have been established. And the laser multilateration measurement method is adopted to the pre-alignment of the three, five and eight magnet girders in the storage ring of HEPS. Currently, 240 out of 288 girders have been pre-aligned after half a year of work.

INTRODUCTION

In order to improve the installation efficiency and accuracy of the storage ring for Chinese High Energy Photon Source (HEPS), each girder is usually pre-aligned in the laboratory, and then transported to the storage ring to participate in the tunnel alignment. Based on physical design of the accelerator, the standard deviation for the pre-alignment adjustment of magnets on one girder with respect to each other in transverse and vertical must below 10 µm.

In the particle accelerator field, laser tracker, such as the Leica AT930, is one of the most commonly used instruments for component fiducialization and alignment [1-3]. However due to the influence of the 15µm +6µm/m angle measurement accuracy, the three-dimensional coordinate measurement accuracy of the AT930 reaches 15µm +6µm/m. To improve its accuracy, numerous attempts have been made [2, 4]. However, these methods still cannot avoid the measurement of angle.

So, we build a four-station laser trackers multilateration measurement system for magnet pre-alignment. We first built a multilateration measurement system using four laser trackers. Then, the self-calibration of the system was completed by measuring more than 12 target points. Next, the front intersection is realized in combination with the Super-Cat's Eye, which realizes the real-time measurement of the coordinates of the magnet fiducial points. Finally, through careful adjustment, the pre-alignment of a girder with 8 magnets is completed, and the alignment standard deviation of transverse and vertical is within 6 µm.

† lushing@ihep.ac.cn

BASIC PRINCIPLE OF FOUR-STATION MULTILATERATION MEASUREMENT METHOD

The measurement principle of the multilateration measurement method mainly includes two parts: Self-calibration and Intersection measurement.

Self-calibration: The system parameters, that is, the coordinates of the four stations, are solved by measuring enough points.

Front intersection: Calculate the coordinates of the under-test point. After the system parameters are determined, four stations are used to measure the distance to the under-test point at the same time, and then the coordinate of the point can be calculated based on the distance.

There are four stations and n target point in the space, as shown in Fig. 1. Four stations were employed simultaneously to measure the distance to the target point. The center coordinate of the i-th station is $S_i = (X_i, Y_i, Z_i)$ $(= 1, 2, 3, 4)$ the coordinate of the j-th target point is $P_j = (X_j, Y_j, Z_j)$ $(j = 1, 2, 3, \ldots, n)$ the observed value between S_i and P_j is D_{ij}. The error equation group can be expressed as:

$$D_{ij} + v_{ij} = \sqrt{(X_i - x_j)^2 + (Y_i - y_j)^2 + (Z_i - z_j)^2} \quad (1)$$

where v_{ij} is the error corresponding to the observed value.

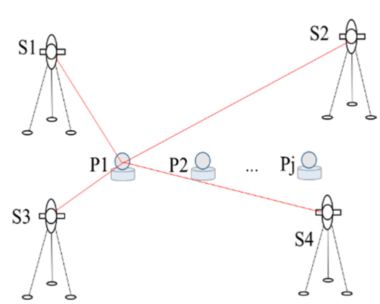

Figure 1: The principle of multilateration measurement method.

Expand Eq. (1) according to Taylor series and omit higher-order terms to obtain the error linear equation:

$$v_{ij} = f_{ij}\delta X_i + g_{ij}\delta Y_i + h_{ij}\delta Z_i - f_{ij}\delta x_i$$
$$-g_{ij}\delta y_i - h_{ij}\delta z_i - \left(D_{ij} - D_{ij}^0\right) \quad (2)$$

As the self-calibration process was completed, the coordinate of the four stations S_i $(i = 1, 2, 3, 4)$ and the target points P_j $(j = 1, 2, 3, \ldots, n)$ were obtained in one coordinate system [5]. Then assuming that the coordinate of under-test points is $W\ (X, Y, Z)$, the measurement distance between the four stations and under-test point W is L_i $(i =$

ISBN: 978-3-95450-250-9 ISSN: 2673-5520 doi:10.18429/JACoW-MEDSI2023-THPPP020

1,2,3,4). According to the principle of front intersection, the error equation for measurement distance is:

$$V_i + L_i = \sqrt{(X - X_i)^2 + (Y - Y_i)^2 + (Z - Z_i)^2} \quad (3)$$

Equation (3) is a nonlinear equation, by linearizing and calculating the total differential, the error equation can be written as:

$$V = A\delta X - l \quad (4)$$

By solving the Eq. 4 according to the principle of adjustment, the coordinates of the under-test point can be obtained.

CONSTRUCTION OF MEASUREMENT SYSTEM

According to measuring principle, a four-station laser trackers multiliteration measurement system (FLTMMS) for pre-alignment of HEPS storage ring was built in the laboratory as shown in Fig. 2. Four LeicaAT930 laser trackers were used, and the reflection target was Leica Red Ring Reflection (RRR, self-calibration measurement) or Super-Cat's Eye (SCE, front intersection).

In the self-calibration process, the RRR is used as the reflection target placed on the target point to ensure the self-calibration accuracy. However, during magnet pre-alignment adjustment, the coordinates of the magnet fiducial points need to be obtained in real time through intersection measurement, so four laser trackers must measure a point at the same time. This requires the SCE as a measurement target because its acceptance angle is large enough.

The four AT930 are mounted on support columns. All support columns are filled with sand to improve the stability of the instrument. 8 target points are placed around the four stations. 32 points are magnet fiducial points. The remaining 8 target points are home-point.

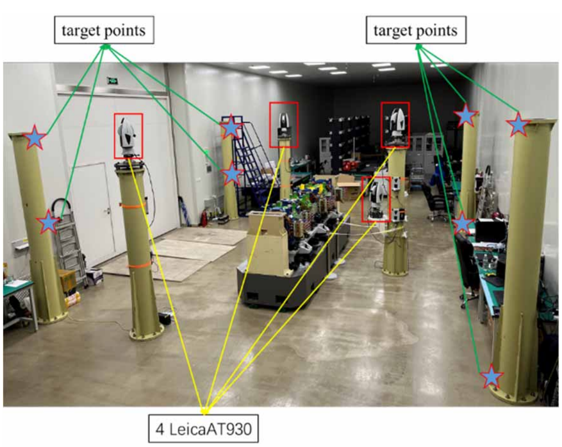

Figure 2: FLTMMS for pre-alignment of storage ring.

HIGH PRECISION PRE-ALIGNMENT WITH FLTMMS

The purpose of pre-alignment is to adjust the magnetic center of each magnet on the same girder to the theoretical position. The pre-alignment steps with FLTMMS are as follows:

First, self-calibration. In this step, the RRR is used as a reflection target. Four Leica AT930 trackers were used to measure more than 12 points (usually including 8 target points, 8 home points and 4 magnet fiducial points). Then, the system parameters are obtained through the adjustment solution.

Second, dynamic adjustment. The real-time deviation between the actual coordinate and the theoretical coordinate of the magnet fiducial points is obtained by front intersection. The adjustment process will stop when the deviation between the actual coordinate and the theoretical coordinate is less than 10 µm.

Third, locking. The magnet is firmly fixed on the girder by the locking mechanism after the dynamic adjustment process is complete. During the locking process, it is necessary to ensure that the deviation between the actual coordinate and the theoretical coordinate is within 10µm, so it is also necessary to use the SCE to monitor the magnet fiducial points in real time.

Finally, the pre-alignment of a girder with eight magnets was finished using the FLTMMS, the results are shown in Table 1. After pre-alignment, the *X* (transverse) direction deviation of the eight magnets is less than 10 µm, the *Y* (vertical) direction deviation is less than 14 µm. The standard deviations are less than 4 µm (transverse), 6 µm (vertical), respectively, which meets the accuracy requirements of HEPS pre-alignment.

Table 1: Results After Pre-Alignment

Fiducial Points	DX	DY	Fiducial Points	DX	DY
QD3F1	-0.001	0.009	SF1F1	0.005	0.010
QD3F2	-0.005	0.002	SF1F2	0.005	-0.011
QD3F3	-0.005	0.003	SF1F3	0.005	0.006
QD3F4	-0.001	-0.003	SF1F4	0.005	-0.004
SD2F1	0.001	0.001	ABF1F1	-0.010	0.001
SD2F2	-0.003	-0.014	ABF1F2	-0.002	0.004
SD2F3	-0.003	0.004	ABF1F3	-0.002	0.006
SD2F4	0.001	-0.011	ABF1F4	-0.010	0.006
OCT1F1	0.004	0.000	SD1F1	-0.002	-0.002
OCT1F2	0.000	-0.006	SD1F2	-0.001	-0.004
OCT1F3	0.000	0.007	SD1F3	-0.001	0.005
OCT1F4	0.004	0.007	SD1F4	-0.002	-0.006
QF2F1	0.000	0.004	QD2F1	-0.002	-0.002
QF2F2	0.008	0.006	QD2F2	0.002	0.002
QF2F3	0.008	-0.006	QD2F3	0.002	-0.002
QF2F4	0.000	-0.007	QD2F4	-0.002	-0.003
Standard Deviation	0.004	0.006			

CONCLUSION

In conclusion, a laser tracker-based multilateration method has been developed for the magnet pre-alignment

ISBN: 978-3-95450-250-9 ISSN: 2673-5520 doi:10.18429/JACoW-MEDSI2023-THPPP020

of HEPS storage ring. The multilateration system has been built in laboratory. It successfully achieved absolute position measurement accuracy of 7.1 μm and relative displacement measurement accuracy of 3 μm in a 4 m×1.2 m×1.5 m volume. After adjustment, a pre-alignment accuracy of 6 μm for HEPS magnets has been achieved. Currently, 240 out of 288 girders have been pre-aligned after half a year of work. The alignment accuracy of the multilateration system can still be improved by increasing the height difference of four stations. Furthermore, this laser tracker-based multi-lateration method can be applied to other high precision fields, for example, the field of industrial measurement.

REFERENCES

[1] H.W. Friedsam, "A new accelerator alignment concept using laser trackers", in *Proc. 4th Eur. Part. Conf.* London, UK,1994. pp. 2570-2572.

[2] B. Krause, A. Petrov, J. Prenting, M. Schloesser and K. Sinram, "Precise Alignment of Magnetic Quadrupole Axes for PETRA III", in *IEEE Trans. Appl. Supercond.*, vol. 18, no. 2, pp. 1641-1644, June 2008. doi: 10.1109/TASC.2008.922263.

[3] R. Junqueira Leão, C.R. Baldo, M.L. Collucci da Costa Reis, J.L. Alves Trabanco, "Engineering survey planning for the alignment of a particle accelerator: part II. Design of a reference network and measurement strategy", *Meas. Sci. Technol.*, vol. 29, pp. 034007, 2018. doi:10.1088/1361-6501/aa9dc3

[4] Z. Wang, T. Luo, W. Wang, Q. Huang, X. Li, "Fixing positions and orientations of laser trackers during bundle adjustment in multi-station measurements", *Meas. Sci. Technol.*, vol.32, p. 035017, 2020. doi:10.1088/1361-6501/abcd6b

[5] J. Zha, L. Li, L. Han, Y. Chen, "Four-station laser tracer-based geometric error measurement of rotary table", *Meas. Sci. Technol.*, vol. 31, p. 065008, 2020. doi:10.1088/1361-6501/ab64ab

ISBN: 978-3-95450-250-9 ISSN: 2673-5520 doi:10.18429/JACoW-MEDSI2023-THPPP023

DESIGN AND TEST OF A NEW CRYSTAL ASSEMBLY FOR A DOUBLE CRYSTAL MONOCHROMATOR*

Yang Yang[1], Hao Liang† [1,2], Dashan Shen[1], Zekuan Liu[1],Yunsheng Zhang[1], Shan Zhang[1], Yuanshu Lu[1], Lu Zhang[1]
[1]Institute of High Energy Physics, Beijing, P. R. China,
[2]University of Chinese Academy of Sciences, School of Physics, Beijing, P. R. China

Abstract

A vertical diffraction double crystal monochromator is a typical optical component in synchrotron radiation beamlines, its main requirements and characteristics are high angular adjustment resolution and stability. Due to the development of the 4th generation light sources, those requirements get even more challenging. This paper mainly introduces the design and test of a new crystal assembly design in a vertical diffraction double crystal-monochromator. The designed scheme has been fabricated. The surface slope error of the first both crystals was measured and below 0.1 μ rad RMS. The motion adjustment test of the second crystal module has been carried out under atmosphere, vacuum and cryocooled conditions, and the results are much better than required ones. The stability of the monochomator was measured, and results below 10 nrad RMS were observed under cooling conditions.

INTRODUCTION

HEPS is a 4th generation light source which employs multi-bend achromat lattices and aims to reach emittance as low as 60 pm•rad with a circumference of about 1360 m [1]. The vertical diffracting double crystal monochromator (VDCM) described in this paper will be serving the X-ray microscopic imaging line station of HEPS. The monochromator hosts 2 Si(111) crystal, covers an energy range of 5 keV to 15 keV. It works in fixed exit mode. The maximum heat load is 435 W, thus the monochromator is liquid nitrogen cooled. The relative pitch stability requirement is 100 nrad RMS. This paper mainly introduces the design and test of the crystal assembly of the monochromator. The crystal assembly includes 2 main sub-components, the first crystal component and the second crystal component. The first crystal component mainly includes the first crystal cooling and clamping, using micro-channel side cooling and flat plate clamping schemes. The second crystal component provides gap, coarse pitch and roll, fine pitch and roll for the second crystal. At the same time, the Angle monitoring system is designed (Fig. 1).

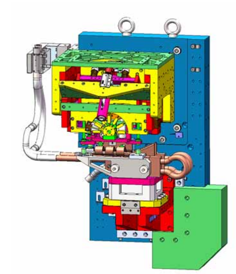

Figure 1: Crystal module design model.

The First Crystal Components

The first crystal component mainly includes the first crystal cooling and clamping component, crystal heat insulation component and crystal support structure.

Indirect cooling of the first crystal has been proven effective for high heat load monochromators around the world [2, 3]. Therefore, the crystal cooling in this scheme follows the microchannel edge cooling design, and the crystal clamping adopts the disc spring plate clamping mechanism. The two plates rely on the disc spring to provide compression force. Each disc spring is compressed by 0.2 mm, and six unilateral superpositions are used. The unilateral compression can be 1.2 mm, and the maximum force can be 814 N. The heat insulation of the crystal is designed with a machinable ceramic design, which is placed between the bottom of the crystal and the support structure. The heat leakage and mode analysis of the whole monocrystalline component are carried out. The overall heat leakage is 3.3 W, and the first-order angle direction mode is 312 Hz (Fig. 2).

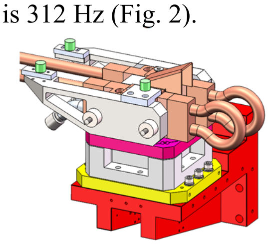

Figure 2: The first crystal components design model.

The design scheme was processed and assembled, and the crystal surface shape was measured (Fig. 3). The normal temperature result is less than 0.1 μrad, which meets the requirements of use.

* Work supported by all HEPS colleagues of monochromator
† yangyang@ihep.ac.cn and lianghao@ihep.ac.cn

ISBN: 978-3-95450-250-9 ISSN: 2673-5520 doi:10.18429/JACoW-MEDSI2023-THPPP023

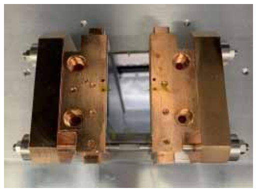

Figure 3: The first crystal clamping surface shape test.

The Second Crystal Components

The second crystal component mainly includes the clamping cooling structure of the second crystal and the angle adjustment mechanism of the second crystal (Fig. 4).

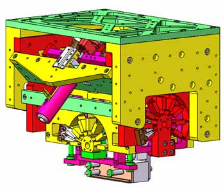

Figure 4: The second crystal components design model.

The cooling of the second crystal adopts mature copper foil cooling technology. The clamping of the second crystal mainly considers the deformation of the crystal under the action of gravity, using the Bessel point and the three-point support method. The finite element analysis results show that the surface shape of the central 30 mm area is 27.3 nrad RMS after removing the quadratic term. The scheme is processed and assembled, and the crystal surface shape is measured. The normal temperature result is less than 0.04 μrad, which meets the use requirements (Fig. 5).

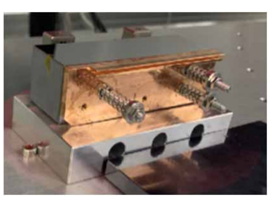

Figure 5: The second crystal clamping surface shape test.

The angle adjustment mechanism of the second crystal can realize the pitch and roll angle adjustment of the second crystal. The flexible hinge structure design of double-layer drive is mainly adopted. Through the top of two actuators [4, 5], the coarse and fine two-step adjustment of the angle can be realized. The resolution of the coarse adjustment actuator is 30 nm, and the fine adjustment actuators is 0.6 nm. At the same time, the spring preload structure is designed to provide preload and recovery force for the whole system. Two sets of angle monitoring systems are designed, one of which is a grating scale monitoring system, which is directly arranged at the installation position of the hinge end drive, and can realize the monitoring of the pitch and roll angle respectively. The other set is an interferometer monitoring system. The relative position monitoring is realized by a 3-point laser head mounted on the second crystal load plate and a corner cube mirror mounted on the first crystal assembly, and then the angle monitoring is calculated.

The scheme was processed and assembled, and the angular resolution and stroke test were carried out under the three environments of atmosphere, vacuum and vacuum low temperature. The test results showed that the motion range of the pitch and roll angle was more than 0.5°, the coarse adjustment resolution of the pitch and roll angle was less than 485 nrad (Fig. 6), and the fine adjustment resolution was less than 50 nrad, which is better than the use requirements (Fig. 7).

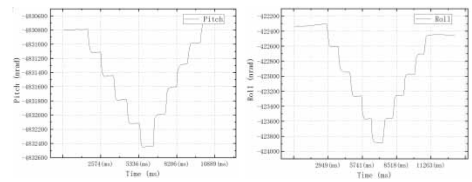

(a) (b)

Figure 6: Coarse adjustment resolution, pitch (a), roll (b).

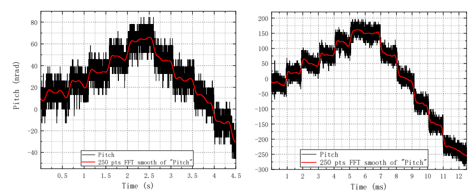

(a) (b)

Figure 7: Fine adjustment resolution, pitch (a), roll (b).

Global Stability Test

In the low temperature (17 Hz/2 L) vacuum environment, the overall stability test was carried out by using the interferometer angle monitoring system. The test results show that the pitch angle stability is about 10 nrad RMS, and the roll angle stability is about 28 nrad RMS (Fig. 8).

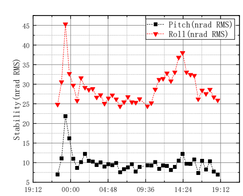

Figure 8: Angular stability result.

CONCLUSION

This paper mainly introduces the structure design and related test of a vertical diffraction monochromator crystal component. The test results show that the scheme has high stability and angle adjustment accuracy, has small crystal surface shape change, and the actual index is better than the parameter requirements. At the same time, the whole structure processing and assembly process is simple, easy to operate, and the vacuum adaptation degree is high. It can be identified as a preferred option and further tested in more detail.

ISBN: 978-3-95450-250-9 ISSN: 2673-5520 doi:10.18429/JACoW-MEDSI2023-THPPP023

ACKNOWLEDGEMENTS

We thank Weifan Sheng and Ming Li for their many suggestions on the design process, and Xiaobao Deng, Gang Li, Aiyu Zhou, Zongyang Yue, Rongli Cui, Dongni Zhang, and Lidan Gao for their support in testing.

We thank all HEPS colleagues for their support during the design, fabrication and testing.

This work was supported by the High Energy Photon Source (HEPS), a major national science and technology infrastructure in China.

REFERENCES

[1] Yi Jiao *et al.*, "Progress in the Design and Related Studies on the High Energy Photon Source", *Physics Procedia*, vol. 84, pp. 40-46, 2016. doi:10.1016/j.phpro.2016.11.008

[2] A. Chumakov *et al.*, "Performance of a silicon monochromator under high heat load", *J. Synchrotron Radiat.*, vol. 21, pp. 315-324, 2014. doi:10.1107/s1600577513033158

[3] A. Chumakov *et al.,* "Performance of a cryogenic silicon monochromator under extreme heat load", *J. Synchrotron Radiat.*, vol. 11, pp. 132-141, 2004. doi.10.1107/S0909049503026785

[4] https://www.newport.com.cn/

[5] https://www.pi.ws/

ISBN: 978-3-95450-250-9 ISSN: 2673-5520 doi:10.18429/JACoW-MEDSI2023-THPPP026

MOTORIZED UNIVERSAL ADJUSTMENT PLATFORM FOR MICROMETRIC ADJUSTMENT OF ACCELERATOR COMPONENTS

M. Noir * [1], M. Sosin † [1], D. Baillard[1], P. Biedrawa[2], A. Gothe[3], L. Gentini[1], W. Jasonek[2], François-Xavier Nuiry[1], V. Rude[1], P. Sarvade [1], R. Seidenbinder[1], K. Widuch[1]
[1]CERN, Geneva, Switzerland
[2]AGH, University of Science and Technology, Krakow, Poland
[3]Aarhus University, Faculty of Technical Sciences, Denmark

Abstract

In order to optimize alignment activities in a highly radioactive environment, the Geodetic Metrology Group at CERN has developed a standardized featuring 6 degree of freedom (DoF) Universal Adjustment Platform (UAP). After a first prototyping phase in 2021 with a manual UAP, the design has been consolidated and is now compatible with the installation of motorized actuators to form a remotely adjustable 5-6 DoF platform able to perform positioning with micrometre resolution. This paper presents the UAP and related motorized actuator development, elaborated in the frame of the High-Luminosity Large Hadron Collider project. The mechanical integration approach, design solutions, and test results are discussed.

INTRODUCTION

The CERN Large Hadron Collider (LHC) accelerator will soon be upgraded to operate at five times higher nominal luminosity to increase its potential for discoveries after 2029. In the frame of this project, named High-Luminosity-LHC (HL-LHC), nearly 1.2 km of beam components will be replaced [1, 2]. One of the key parameters to increase the integrated luminosity is the precise alignment of the accelerator components of the two high luminosity experiments in the Long Straight Sections (LSS). For the first time, a Full Remote Alignment System (FRAS), composed of a set of micrometre sensors and actuators, will be implemented on the HL-LHC components to determine continuously the position of the components and re-adjust them remotely if needed [3].

In the frame of this project, a Universal Alignment Platform (UAP), able to adjust lightweight accelerator components (up to 2000 kg) within 6 Degrees Of Freedom (DoF), has been developed by the Geodetic Metrology Group at CERN. This platform is an adaptive framework that will be used for several accelerator components such as collimators. It is based on in-house designed components, that can be scaled to the accelerator component according to its supporting points, available volume, etc. The concept of such a platform has been already presented in [4]. This paper focuses on the platform components characterization and details the proposed motorisation solution to perform remote adjustments in the frame of FRAS.

* michel.noir@cern.ch
† mateusz.sosin@cern.ch

6 DOF PLATFORM CONCEPT

The UAP platform is composed of the following elements (Figure 1):

- A lower interface plate (Blue) that is considered as fixed.
- A set of 6 micrometre actuators (Red) to perform adjustments in all DoF. The radial actuation is carried out by radial jigs while the vertical and longitudinal adjustments are performed by vertical jigs.
- Backlash-free joints (grey), with tailored length to remove any hyperstatism.
- A set of actuating shafts and supports (Orange), gathered at the front part of the platform for an easy access during the actuation of each jig.
- An upper plate (green) on which the accelerator component can be installed.

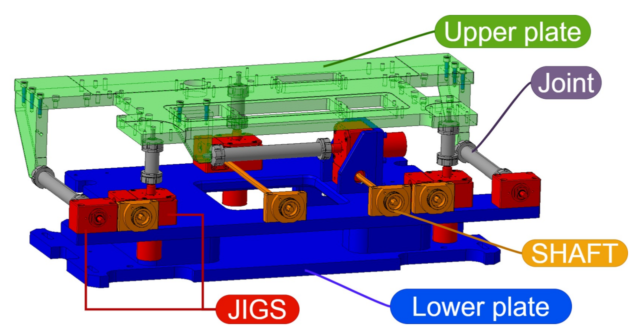

Figure 1: UAP Platform Composition.

Jigs, Joints and actuation shaft designs are now internally available at CERN and each user adapts the upper and lower plate to his needs. All these components are proposed for two models: a Light platform version (Safe Working Load - SWL- up to 300 kg) and a Heavy one (SWL up to 2000 kg). The application of this framework guarantees a common alignment procedure for all lightweight elements regardless the specificity of the supported component design. The first application has been developed in collaboration with the collimator team at CERN to validate the concept via 2 prototyping phases and obtain a robust design before serial production.

Based on this manual design, the paper presents the different steps of design and tests phases towards a motorized version compatible with the FRAS project.

ISBN: 978-3-95450-250-9 ISSN: 2673-5520 doi:10.18429/JACoW-MEDSI2023-THPPP026

INDIVIDUAL JIGS CHARACTERISATION

In order to obtain a preliminary estimation of the global behaviour of the platform , the mechanical parameters of a set of jigs (both radial and vertical) have been fully verified and characterised. This characterisation has been based on a sampling production corresponding to 3 complete UAP platforms. For each jig, the following parameters have been recorded for several positions distributed along the total jigs strokes (see Table 1):

- Maximal actuation torque over the full stroke without load on the output piston to check the smoothness of the actuation.
- 150 % Load test to check the structural viability of each jig with a monitoring of the necessary input torque.
- Input Jig Backlash - it represents the necessary rotation on the input shaft of a jig to get a detectable output motion (2 µm). The result is computed as a position defect on the output piston.
- Output Jig Backlash - it represents the output piston motion stroke when experiencing an alternated load of ±10 kg.

In order to record all these characteristics, a specific qualification bench coupled with an acquisition software has been designed to automatise most of the qualification steps and gather reliable results (see Figure 2). This bench will be used later to qualify the serial production and detect as soon as possible any potential manufacturing defects.

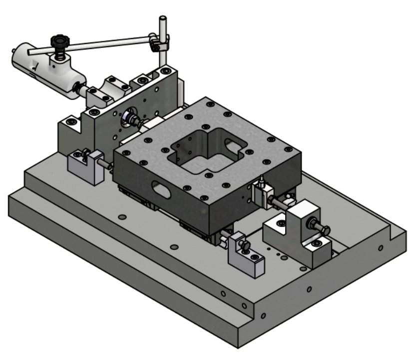

Figure 2: UAP Jig test bench overview.

Table 1: Mechanical Parameters - Vertical Jig

PARAMETER	TARGET	RESULT
Unloaded torque [N m]	<0.5	0.37
150 % Load torque [N m]	<8	6.7
Input Backlash [µm]	<15	13.3
Output Backlash [µm]	<5	3.4

MANUAL PLATFORM PERFORMANCES

Once the individual jigs were characterised, three complete UAP platforms have been assembled to support a set of three collimators. A series of tests, aiming to represent the different use-cases of the platform, have been conducted in a manual way before installing the motorized adapters (see Figure 3):

- Stability of the platform under external perturbation load : the platform position remains stable (< 20 µm displacement) when external forces of up to 100 kg are applied to the structure and then removed.
- Global stiffness behaviour - maximal displacements when 20 kg are applied longitudinally and radially to the structure are 240 µm along the Beam axis direction and 120 µm along the traversal axis.
- Single DoF adjustment - conducted to characterise the impact of one jig actuation on the other movements (parasitic motion of the platform).
- Position repeatability test : when the structure payload is removed and reinstalled, the payload position has been validated as repeatable (12 µm translation and 10 µrad rotation defect recorded)
- 3D Alignment - for a defect up to 10 mm, the alignment sequence requires only 3 iterations to reach an adjustment position scope of ±50 µm translation and ±100 µrad rotation.

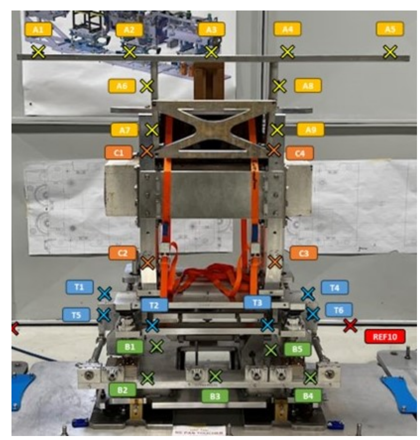

Figure 3: UAP Platform during test with a dummy collimator. Each cross represents a measurement target installed during the tests.

MOTORISED ADAPTERS CHARACTERISTICS AND IMPLEMENTATION

In order to be compatible with the FRAS, a motorized version of the UAP platform is necessary. The proposed concept, compatible with the standardisation philosophy of the UAP, is to develop a plug-in micrometre motorised adapter able to be connected directly to the manual version of the platform (Figure 4).

Based on the concept presented in [5] and the prototypes tested for the actuation of other equipment (see Figure 5), the design of two motorised adapters, dedicated to radial and vertical jigs, is currently in progress. These Micrometre resolution motorized adapters will be used to remotely actu-

ISBN: 978-3-95450-250-9 ISSN: 2673-5520 doi:10.18429/JACoW-MEDSI2023-THPPP026

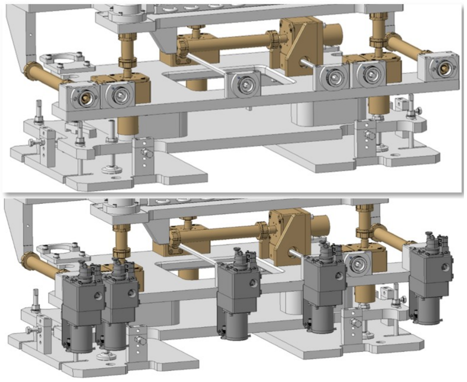

Figure 4: UAP Platform in manual and motorized versions.

ate the UAP platform. These actuators main characteristics are the following:

- Motorized actuation stroke at the jig level of ±2.5 mm.
- Possible readjustment of the motorized stroke within the JIG global stroke of ±15 mm.
- Absolute position monitoring at a micrometre level (20 µm maximal defect along the full stroke), provided by an embedded resolver in the adapter.
- Mechanical end-stop safety feature in order to prevent any displacement above the allowed stroke.

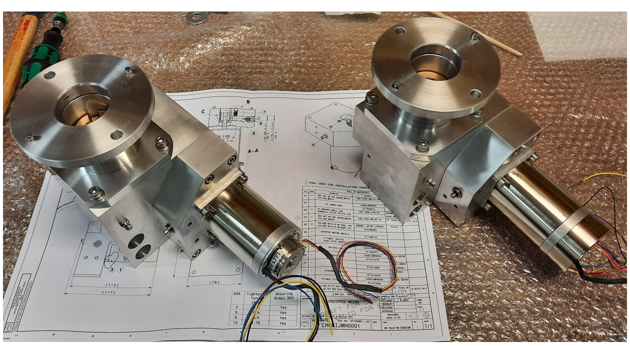

Figure 5: Motorized adapter overview.

Because vertical and radial jigs do not have the same gear ratio, an output stroke of ±2.5 mm on both jigs will represent, at the level of the actuator, a global stroke of 5 rev and 18.75 rev respectively for the radial and vertical adapters. Two different models of the same adapter design will then be provided in order to cope with the specificity of each type of jig.

CONCLUSION

In order to ease the design of a micrometre adjustment platform and to cope with the requirements of the FRAS Project, the Geodetic Metrology group at CERN, in close collaboration with UAP users, designed and tested the Universal Adjustment Platform and its standardized components. After two prototyping phases, the platform and its jigs are now fully successfully qualified and have been presented in this document.

The motorisation design of the platform is being finalized. It is based on already developed motorized adapters [5], allowing the remote and micrometre adjustment of the position of each jig. These adapters will be used as a plugin system able to transform a fully manual platform in a motorized version.

REFERENCES

[1] G. Apollinari, I. B. Alonso, O. Brüning, M. Lamont, and L. Rossi, "High-Luminosity Large Hadron Collider (HL-LHC): Preliminary Design Report", CERN, Geneva, Rep. CERN-2015-005, 2015. doi:10.5170/CERN-2015-005

[2] O. Aberle *et al.*, "High-luminosity large hadron collider (HL-LHC): Technical design report", CERN, Geneva, Rep. CERN-2020-010, 2020. doi:10.23731/CYRM-2020-0010

[3] A. Herty *et al.*, "HL-LHC Full Remote Alignment Study", in *Proc. IPAC'19*, Melbourne, Australia, May 2019, pp. 3716–3719. doi:10.18429/JACoW-IPAC2019-THPGW057

[4] M. Sosin, T. Blaszczyk, A. Herty, J. Jaros, and H. M. Durand, "Design and Study of a 6 Degree-Of-Freedom Universal Adjustment Platform for HL-LHC Components", in *Proc. IPAC'19*, Melbourne, Australia, May 2019, pp. 3720–3722. doi:10.18429/JACoW-IPAC2019-THPGW058

[5] M. Noir, M. Sosin, B. Piotr, and J. Wojciech, "Development and Qualification of Micrometric Resolution Motorized Actuators for the High Luminosity Large Hadron Collider Full Remote Alignment System", presented at MEDSI'23, Beijing, China, 2023, paper THOAM01, this conference.

ISBN: 978-3-95450-250-9 ISSN: 2673-5520 doi:10.18429/JACoW-MEDSI2023-THPPP028

DESIGN AND ANALYSIS OF CSNS-II PRIMARY STRIPPER FOIL

J. X. Chen[1], L. Kang[1], J. B. Yu[1], G. Y. Wang[1], L. Liu[1], Y. J. Yu[1], J. S. Zhang[1], J. Y. Zhang[1]
Institute of High Energy Physics, Chinese Academy of Sciences, Beijing, China
[1] also at Spallation Neutron Source Science Center, Dongguan, China

Abstract

Stripper foil is a key equipment for converting negative hydrogen ions into protons in the RCS injection zone of CSNS. The structure of the CSNS primary stripper foil adopts a rotating steel strip structure, and the maintenance time is long, requiring operators to carry out maintenance work in close proximity for a long time. The energy of CSNS-II injection beam has significantly increased from 80 MeV to 300 MeV, and the radiation dose in the injection area will also increase, making it impossible to maintain the equipment in close proximity for a long time. Therefore, it is necessary to redesign the primary stripper foil. This article will analyze the stripper efficiency and beam injection thermodynamics of CSNS-II stripper foil, carry out automatic foil store replacement structure design, motion analysis, and prototype testing, and envision remote maintenance solutions to achieve maintenance and repair of the stripper foil with minimal human intervention.

INTRODUCTION

Stripper foil is a key equipment for converting negative hydrogen ions into protons in a Spallation Neutron Source device. The CSNS stripper foil includes the primary stripper foil and the secondary stripper foil. The primary stripper foil adopts 100 μg/cm^2 diamond-like carbon film with a capacity of 22 pieces and a theoretical stripping efficiency of 99.7% [1-3]. The proton beam after being peeled off by the primary stripper foil enters the RCS for acceleration. The secondary stripper has a foil storage capacity of 1 piece with a 200 μg/cm^2 diamond-like carbon foil. A negative hydrogen ion absorption block is designed on the secondary stripper foil to absorb negative hydrogen ions that have not been stripped off through the primary stripper foil. The H_0 particles, after stripping one electron through the secondary stripper foil, are change into protons and extracted to the beam dump [4, 5]. The structure of the primary stripper foil of CSNS adopts a rotating steel strip structure, and the foils are uniformly distributed on the rotating steel strip. Each foil needs to be installed separately. At the same time, according to the radiation protection requirements of CSNS, the stripper foil does not consider radiation shielding and does not reserve installation space for radiation shielding. During the operation of the CSNS accelerator, the service life of the primary stripper foil is less than 1 month per piece, and the residual dose on the surface of the foil rack after operation can reach up to 2000 μSv/h, in addition, the operator needs to carry out maintenance work in close proximity for a long time. The secondary stripper foil structure is similar to the primary stripper foil structure, but there is no rotating steel strip structure. According to physical requirements, the CSNS-II stripper foil still adopts two sets of stripper foil devices, including one primary stripper foil and one secondary stripper foil, which have the same function as the CSNS stripper foil. However, due to the increase in radiation dose, it is impossible to maintain the equipment in close proximity. Therefore, a new overall foil store quick replacement mechanism must be adopted and a new maintenance plan must be redesigned.

ANALYSIS OF THE FOIL DURING BEAM INJECTION

According to the physical design scheme of the CSNS-II RCS injection zone, as shown in Fig. 1, the RCS injection beam energy is increased from 80 MeV to 300 MeV. After the injection energy of CSNS-II is increased to 300 MeV, according to the relationship between foil thickness and stripping efficiency shown in Fig. 2, in order to maintain a stripping efficiency of 99.7%, the thickness of the primary stripper foil needs to be increased to 260 μg/cm^2, and according to the size of the beam spot, the transverse size of the foil is required to be no less than 20 mm * 60 mm [4], and the material is HBC.

According to the analysis of beam injection into the stripper foil, when the injection energy is 300 MeV and the film thickness is 260 μg/cm^2, the number of repeated beam passes is 15, and the half axis size of the elliptical beam spot is 3 * 1.5 mm. Assuming that the beam spot is uniformly distributed within the central range, the rest is Gaussian distribution. The mathematical model of a Gaussian heat source is shown in formula (1).

$$D(x,y)=\frac{E_{\text{total}}}{2\pi\sigma_x\sigma_y}\exp\left(-\frac{x^2}{2\sigma_x^2}\right)\exp\left(-\frac{y^2}{2\sigma_y^2}\right) \tag{1}$$

Among them, E_{total} is the total energy deposited on the foil, and σ_x, σ_y are the radius of the major and minor axes of the elliptical Gaussian heat source. It is known that the injection point is 7 mm away from the edge of the foil. Therefore, the mathematical model of the Gaussian heat source is shown in formula (2).

$$D(x,y)=\frac{E_{\text{total}}}{2\pi\sigma_x\sigma_y}\exp\left(-\frac{(x-0.007)^2}{2\sigma_x^2}\right)\exp\left(-\frac{(y-0.007)^2}{2\sigma_y^2}\right) \tag{2}$$

12th Int. Conf. Mech. Eng. Design Synchrotron Radiat. Equip. Instrum. MEDSI2023, Beijing, China JACoW Publishing
ISBN: 978-3-95450-250-9 ISSN: 2673-5520 doi:10.18429/JACoW-MEDSI2023-THPPP028

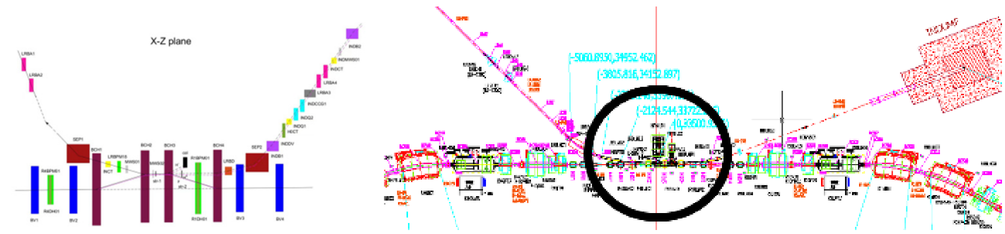

Figure 1: CSNS-II Injection Zone Layout.

Using ANSYS for simulation analysis, uniformly distributed power was loaded at the center, an elliptical Gaussian heat source was loaded at the periphery, and the temperatures of each sub step of the highest temperature node were obtained. The results are shown in Fig. 3. From the figure, it can be seen that after ten cycles, the temperature trend remained stable, with the highest temperature being 1483 K and the lowest temperature being 681 K. The temperature distribution is shown in Fig. 4, and the melting point of the carbon film is about 3800 K, so the temperature is within the range that the film can withstand.

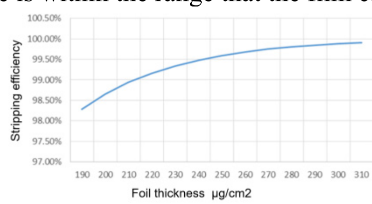

Figure 2: Stripping efficiency.

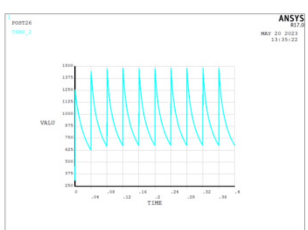

Figure 3: Temperature Curve of stripper foil.

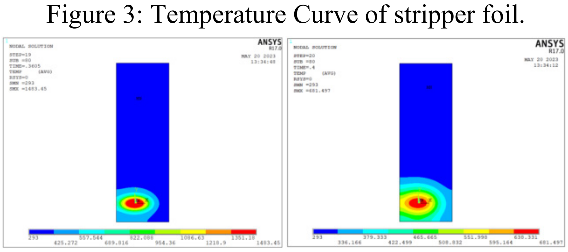

a The highest temperature b The lowest temperature

Figure 4: Distribution of the highest and lowest temperatures of the foil.

STRUCTURE SCHEME OF STRIPPER FOIL

Due to the high dose in the injection area and the high risk of personnel operating in close proximity, the CSNS-II stripper foil is planned to adopt an automatic replacement foil store structure and have remote maintenance capabilities, in order to complete the maintenance and repair of the stripper foil with minimal personnel intervention. At the same time, in order to reduce the overall radiation dose level in the injection area, it is necessary to extend the movement distance of the foil frame to provide installation and maintenance space for radiation protection shielding. The primary stripper foil needs to consider functions such as automatic replacement of the foil store, remote maintenance, and shielding. According to the frequency of use, the guiding mechanism should guide no less than 2000 times; The repeated positioning accuracy of the foil frame is ± 0.2 mm; During the movement of the foil frame, there is no detachment of the docking mechanism; The repeated positioning accuracy of the foil store is ± 0.05 mm.

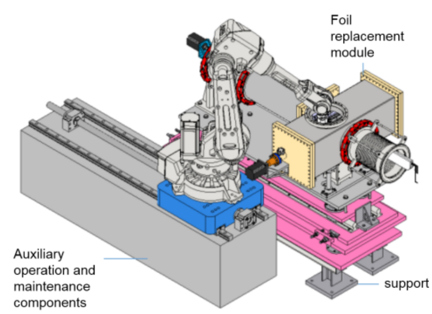

Figure 5: CSNS-II primary stripper foil.

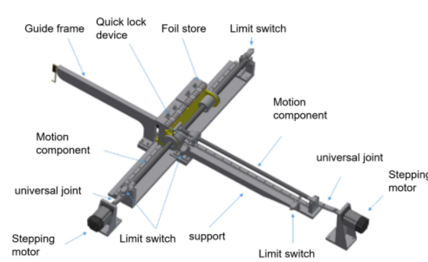

Figure 6: Internal structure of foil replacement module.

The primary stripper foil structure and foil replacement module are shown in Fig. 5, and the equipment mainly consists of foil replacement components, chassis components, and auxiliary operation and maintenance components. The foil replacement component is a key component for storing foils and achieving automatic foil replacement. In order to achieve rapid replacement of the stripper foil, a design scheme of an integral foil store was adopted. During maintenance, the maintenance of the stripper foil system can be completed by simply replacing the entire foil store, greatly reducing maintenance time and reducing residual radiation dose to personnel. Its internal structure is shown in Fig. 6, consisting of components such as foil frame guide, foil store components, guide rods, and support frames. The auxiliary operation

ISBN: 978-3-95450-250-9 ISSN: 2673-5520 doi:10.18429/JACoW-MEDSI2023-THPPP028

and maintenance component adopt a series robot for maintenance work. After the series robot takes out the entire foil store that needs to be replaced, the new foil store is loaded into the cavity of the foil replacement component. After evaluation, the foil replacement time is saved by more than 80% compared to the foil replacement time of the steel strip structure, effectively reducing the time for maintenance personnel to operate close range.

When replacing the foil, a high-precision automatic docking structure is used, which pushes the foil from the foil store to the working position through the docking between the guide rod and the slider; When the foil needs to be replaced, the slider is pulled back into the foil store through the guide rod, and then a new foil is switched to achieve the replacement of the foil. In order to achieve the overall replacement process of the foil store, the slider returned to the foil store needs to be locked to prevent it from sliding out. Therefore, a special mechanism needs to be set between the foil frame and the foil store to achieve self-locking functions. An asymmetric V-shaped plate spring is used to lock and open the slider. The force is shown in Figure 7. When the guide rod pushes the slider outward, it needs to overcome the locking force F of the leaf spring to push it out. When the guide rod pulls the slider back to the stripper foil, it needs to overcome the stopping force F of the leaf spring to retreat. The force situation of the leaf spring structure is shown in Fig. 7.

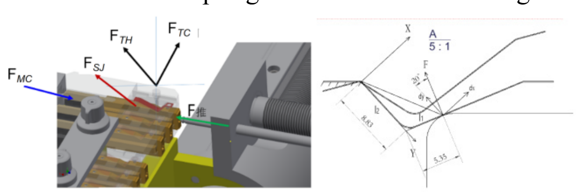

Figure 7: Force situation of self-locking structure.

E is known to be the elastic modulus of the material; I is the moment of inertia, $I = hb^3/12$, where b is the cross-sectional width and h is the cross-sectional thickness. According to the design parameters, $\theta = 20^{\circ}, L1 = 5.35, L2 = 8.8, h = 0.25\text{mm}$. It can be calculated that when the guide rod pulls the slider back to the foil store for self-locking $F_{TH} \approx 15.1N$, and when the guide rod inserts the slider for self-locking $F_{TC} \approx 6.28N$, it opens automatically. The actual measurement of the mechanism was carried out using a tension meter. When the guide rod is inserted into the slider for self-locking, its tension is 7.37 N, and when the guide rod exits the slider, its unlocking tension is 14.25 N, which has a small deviation from the calculated results.

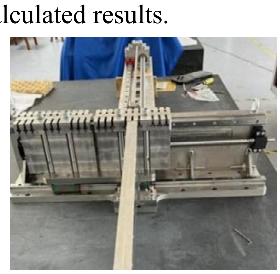

Figure 8: Prototype of stripper foil motion mechanism.

In order to verify the stability and motion accuracy of the structure, a set of experimental prototypes was developed, as shown in Fig. 8. Key parameters were tested, including reciprocating motion testing, repeated positioning accuracy testing, docking testing, and self-locking structure testing. After testing, the guiding mechanism has reciprocated more than 2000 times, and the repeated positioning accuracy is better than ± 0.1 mm. The lateral motion accuracy of the foil magazine is better than ± 0.007 mm.

CONCLUSION

The injection power of the CSNS-II primary stripper foil has been increased to 300 MeV, and the foil's thickness is 260 μg/cm^2. Using a combination of uniformly distributed and elliptical Gaussian analysis, the highest temperature on the foil is 1483 K, which is within the acceptable range of the foil. Due to the increase in injection power, the regional dose will increase. Adopting an overall foil storage structure design combined with the use of series robots for operation and maintenance work will effectively reduce maintenance time. Through the development and testing of the prototype, it has been proven that the structure has good stability and high motion accuracy, meeting the requirements for the foil system.

ACKNOWLEDGEMENT

The project is supported by the National Natural Science Foundation of China, No. 11975253.

REFERENCES

[1] Z. X. He, J. Qiu, C. H. Li, H. M. Qu and Y. Q. Zou, "Analysis of Thermal Effect for China Spallation Neutron Source Primary Stripper Foil (in Chinese)", *Atomic Energy Science and Technology*, vol. 47, no. 10, pp. 1867-1871. 2013. doi:10.7538/yzk.2013.47.10.1867

[2] Z. X. He, J. Qiu, C. H. Li, J. X. Chen, L. Kang, H. M. Qu and Y. Q. Zou, "Wrinkle analysis and mounting optimization of the primary stripper foil for CSNS (in Chinese)", *Chinese Physics C*, vol. 37, no. 10, pp. 85-90, 2013. doi:10.1088/1674-1137/37/10/107003

[3] Z. X. He, C. H. Li, H. M. Qu, G. L. Xu and Y. Q. Zou, "Design of primary stripper foil changer for CSNS/RCS (in Chinese)", *High Power Laser and Particle Beams*, vol. 24, no. 12, pp. 2885-2888, 2012. doi:10.3788/HPLPB20122412.2885

[4] J. X. Chen, J. X. Zheng, L. Kang, A. X. Wang, L. Liu, and X. J. Nie, "Design of the stripper foil system at a 7 MeV injection (in Chinese)", *High Power Laser and Particle Beams*, vol. 32, no. 08, pp. 93-97, 2020. doi:10.11884/HPLPB202032.200084

[5] J. X. Chen, J. B. Yu, L. Kang, J. X. Zheng, A. X. Wang, G. Y. Wang and X. J. Nie, "Stripper foil installation and aerodynamics analysis", *High Power Laser and Particle Beams*, vol. 30, no. 02, pp. 119-123, 2018. doi:10.11884/HPLPB201830.170114

ISBN: 978-3-95450-250-9 ISSN: 2673-5520 doi:10.18429/JACoW-MEDSI2023-THPPP029

TECHNOLOGIES CONCERNING METAL SEALS OF THE UHV SYSTEM FOR ACCELERATORS

H. Y. He, L. Liu, P. C. Wang, Y. S. Ma, B. Tan, Institute of High Energy Physics, Beijing, China

Abstract

Reviewed the domestic research on structural design and sealing function principle of the metal seals, wildly used in the Ultra High Vacuum (UHV) system for accelerators. Analysed and summarized the key technologies concerning the material, contact forms, machining process and test methods of sealing performance. The study will become the basis of designing, machining and quality measuring for the ultra-vacuum metal seals. It provided the foundation for generating seals standards to promote the development of vacuum technology application.

Introduction

V The metal sealing ring is a key sealing component of the accelerator ultra-high vacuum system, achieving a detachable metal to metal end face seal. Ultra-high vacuum systems such as the Beijing Positron and Negative Electron Storage Ring, Spallation Neutron Source, and High Energy Synchrotron Radiation Light Source in China have sealing rings that provide high-temperature degassing and baking at 300 °C, long-term radiation corrosion protection, and almost no penetration of small molecule gases during use. Traditional sealing rings cannot perform well under these harsh working conditions [1]. Metal sealing rings have been widely used in the field of ultra-high vacuum systems, and products with cross-sectional shapes such as O-shaped sealing rings, C-shaped sealing rings, and Δ knife edge sealing rings have reached the practical stage. The C-shaped sealing ring optimized from the basic O-ring, with the C-shaped opening facing towards atmospheric pressure, forms excellent self-sealing; At the same time, the Δ knife edge sealing ring utilizes the advantage of good plastic flow of soft metal to help compensate for the concave and convex gaps and scratches on the surface of the sealing end face, and prevent leakage [2]. At present, stable and reliable ultra-high vacuum metal sealing rings are mainly provided by foreign companies in fields such as accelerators, nuclear power, aerospace, and shipbuilding in China, such as GARLOCK in France and VAT in Switzerland. Due to technological lockdowns, domestic researchers can only obtain partial performance information about metal sealing rings through product manuals. The lack of systematic sealing theory and product standards has hindered the development of ultra-high vacuum metal sealing ring technology in China.

By analysing the research status of ultra-high vacuum metal sealing rings in China in recent decades, this paper summarizes the sealing contact forms, metal materials, and sealing leakage rate measurement methods, explores key issues of structural design optimization and material simulation, forming and processing methods, and sealing performance measurement technology, laying a foundation for establishing a theoretical system of ultra-high vacuum metal sealing rings and promoting engineering applications.

Classification of Metal Static Sealing Materials and Structures

Seals can be divided into two categories: static seals and dynamic seals. The main application of ultra-high vacuum metal sealing is the static sealing of detachable flange connected circular vacuum pipelines. Under external loads, the metal material undergoes plastic deformation and flow to compensate for the gap between the joint surfaces, making it smaller than the diameter of the gas molecules, forming an interface blockage and achieving effective sealing.

The materials and structures of metal sealing rings complement each other, and the research and optimization of materials and the development of finite element simulation analysis have driven the design and development of sealing ring structures. The working performance of metal sealing rings varies with changes in material, geometric shape, and wall thickness.

According to the sealing principle, the material of metal sealing rings is generally required to have certain compression deformation ability, strength, rigidity, rebound ability, and creep resistance. The earliest Baker Hughes Z seal, Caledyne CMTM seal, and Owen X-PAN seal designs used stainless steel, copper, and aluminum sealing rings, which generate radial rebound and expansion through cross-sectional compression. The sealing technology is widely used in industries such as motivation and petroleum. In recent years, with the increasing demand for scientific research and vacuum technology, sealing technology for covering soft metals with high compressive strength and tensile rate metals such as Inconel nickel alloy and Nimonic alloy has become one of the research hotspots. High strength and stiffness represent greater resistance to deformation, allowing for a more stable and reliable vacuum seal with the same sealing force. In addition, the basic requirements for ultra-high vacuum metal sealing rings are the gas release rate and permeability of the metal material. Choose materials with low adsorption, diffusion, and permeability to prevent interface cracks and isolated voids, which are more suitable for obtaining and cleaning extreme vacuum. In addition, the flange and flange locking chain in the accelerator ultra-high vacuum system are made of carbon steel materials such as stainless steel 316L with low magnetic permeability. Therefore, the working pressure of the metal sealing ring should be less than 98 MPa for high-pressure sealing [3].

ISBN: 978-3-95450-250-9 ISSN: 2673-5520 doi:10.18429/JACoW-MEDSI2023-THPPP029

According to the width of the sealing surface, metal sealing rings are mainly divided into three structural types: flat gasket seal, line seal, and lip seal. Ideally, the reliability of metal seals is independent of the width of the sealing surface. However, in practical situations, increasing the width of the sealing surface requires increasing the sealing pressure. With the improvement of mechanical processing capabilities, a large number of ultra-high vacuum systems in accelerators currently use line seals with small contact widths and lip shaped composite structures that utilize ambient atmospheric pressure to assist in self sealing [4]. The contact form of the sealing ring can also be divided into two basic contact forms based on the stiffness of the contact surface: rigid, soft, and flexible. One or two of the contact surfaces are treated as rigid bodies, and the other contact body with much smaller relative stiffness is used as deformable bodies, sacrificing the deformable body to provide plastic deformation blocked by the metal interface. Many ultra-high vacuum metal sealing rings and flange contact can be summarized as rigid flexible contact. Covering the surface of a high tensile strength metal matrix with well plastic flowing soft metal, the composite mechanical properties help block interface leakage and form a more effective ultra-high vacuum seal. At the same time, the sealing ring is usually used as a flexible body in contact alignment to achieve metal to metal sealing, which is more conducive to the replacement and maintenance of vacuum equipment.

Structural Design and Simulation Analysis of Ultra High Vacuum Metal Sealing Ring

Assuming that the sealing ring provides all plastic deformation to compensate for the concave and convex gaps on the joint surface, the final target parameters required for structural design are the sealing ring compression amount and interface contact stress. The core structural dimensions of the flange in the sealing structure include the inner diameter d1 of the sealing ring groove, the outer diameter d2 of the sealing ring groove, and the flange gap d3 (designed maximum compression); The core structural dimensions of the sealing ring are the inner diameter D1 of the sealing ring, the center diameter D2 of the sealing ring, and the height D3, as shown in Figure 1 (b). Generally, the inner diameter d1 of the sealing groove is calculated based on the size of the vacuum pipeline that needs to be sealed, and then the other dimensions above are designed.

The size relationship of the sealing ring structure can be summarized as follows:

$$\mathrm{L} = \mathrm{h} \times \mu \tag{1}$$

$$\mathrm{d1} = \mathrm{D}_2 - \mathrm{H}/2 - \mathrm{L}/2 - \mathrm{d}_0 \tag{2}$$

$$\mathrm{d2} = \mathrm{D}_2 + \mathrm{H}/2 + \mathrm{L}/2 + \mathrm{d}_0 \tag{3}$$

H is the longitudinal compression amount, which is between the minimum contact stress at the sealing interface and the failure of the sealing ring due to compression. μ Is the Poisson's ratio, and L is the lateral deformation of the sealing ring. D0 is the design margin, and it is required that when the longitudinal compression amount h is equal to the maximum design compression amount d3, the flange does not hinder deformation to prevent increasing the sealing pressure level [5].

Simulation analysis of sealing ring deformation belongs to large deformation contact analysis. As the compression amount h increases, μ It is no longer a constant. If the change curve of sealing ring material properties is not clear, it shall be determined by sample testing. Set the flange sealing contact surface as a discrete rigid body, set the large deformation material properties of the sealing ring, simulate and analyse the sealing ring structure according to the boundary conditions set in Figure 1 (a), obtain compression and contact stress values close to practical applications, and then complete the final optimization design of the sealing ring structure. Simulation analysis and structural design are not sequential and mutually guide optimization [6].

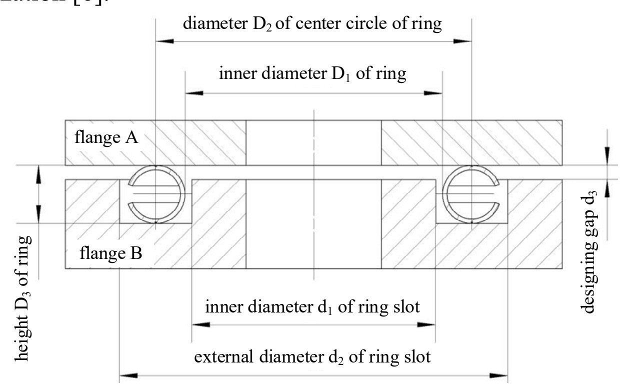

Figure 1: The force diagram of structure for c-section seals(a) and core dimensions of structure for c-section seals(b).

Helium Injection Leak Test and Result Analysis

Method for measuring the working performance of ultra-high vacuum metal sealing rings

In the accelerator ultra-high vacuum system, the plastic deformation during the sealing process is provided by the sealing ring, so the sealing ring is usually used once or several times. Therefore, the performance measurement objectives of ultra-high vacuum sealing ring tooling are the compression amount - line load, and line load - sealing leakage rate performance curves during one or several cycles of loading and unloading [7].

The comprehensive compression rebound test bench is commonly used to determine the compression amount linear load curve during the loading unloading cycle. At present, domestic manufacturers of comprehensive testing platforms include Ningbo Tiansheng Sealing Co., Ltd. and East China University of Science and Technology. Compress the sealing ring with a linear increase in load to obtain the loading curve between the compression amount and the line load, and then linearly reduce the load to obtain the unloading curve between the compression amount and the line load. During the loading unloading process, the sealing ring undergoes elastic stage, yield stage, strengthening

ISBN: 978-3-95450-250-9 ISSN: 2673-5520 doi:10.18429/JACoW-MEDSI2023-THPPP029

stage, and residual deformation stage during unloading [8]. Obtain the three important characteristic parameters of the maximum compression amount in the elastic stage, the line load of the maximum working compression amount, and the rebound amount after unloading from the curve, and be able to judge and predict the performance of the sealing ring in the special working environment.

The sealing structure composed of sealing rings, flanges, and flange chains is combined with a helium mass spectrometer leak detector to form a vacuum system, as shown in the schematic diagram in Figure 2. In the experiment, a comprehensive compression test bench can be used to apply dense sealing load, and in industrial practice, the working sealing pressure of the flange chain can be directly applied using a digital torque wrench [9]. During the loading unloading process of linear load variation, combined with the helium injection method to measure the sealing ring leakage rate value, the sealing ring linear load sealing leakage rate test curve is obtained, and the sealing performance data in operation is measured.

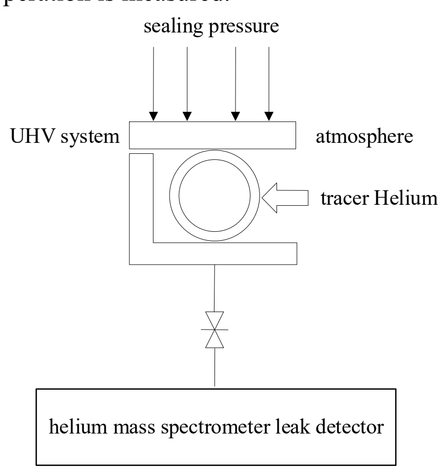

Figure 2: The sketch of testing the relationship curve of compress pressure leak rate.

REFERENCES

[1] Y. Liu *et al.*, "Failure Analysis on Rubber Sealing Structure of Mandrel Hanger and Improvement in Extreme Environment", *Engineering Failure Analysis*, vol. 125, pp. 1844-2002, 2021.

[2] H. L. Zhao, "Metal Sealing Performance of Subsea X-tree Wellhead Connector Sealer", *Chinese Journal of Mechanical Engineering*, vol. 28, pp. 649-656, 2015.

[3] X. J. Cui, R. Zhang, F. Han, *et al.*, "Finite element analysis and experimental research on metal to metal sealing components", *Petroleum Machinery*, vol. 42, pp. 107-115, 2014.

[4] C. Hou, H. L. Qin, W. S. Xiao, *et al.*, "Sealing Mechanism and Performance Analysis of Circular Metal Sealing Assembly", *Lubrication and Sealing*, vol. 39, pp. 34-39, 2014.

[5] W. C. Zhang, X. G. Li, S. J. Wei, *et al.*, "Simulation analysis and experimental verification of mechanical properties of metal O-rings", *Lubrication and Sealing*, vol. 8, pp. 8-12, 2014.

[6] Y. Fang, "Research on unloading rebound characteristics and calculation methods", *Journal of Water Resources and Building Engineering*, vol. 11, pp. 199-202, 2013.

[7] D. L. Zhu, S. X. Bai, "Experimental study on the rebound friction characteristics of fluororubber O-rings in reciprocating motion", *Lubrication and Sealing*, vol. 43, pp. 67-75, 2018.

[8] W. W. Yu, L. X. Cai, Y. M. Ye, *et al.*, "Research on the rebound characteristics of Inconel718 alloy O-ring", *Engineering Mechanics*, vol. 23, pp. 142-147, 2006.

[9] Q. D. Wang, X. B. Fang, L. J. Qian, *et al.*, "Design and Analysis of Automotive Leaf Springs Based on Virtual Prototyping Technology", *Journal of Mechanical Engineering*, vol. 37, pp. 63-66, 2001.

ISBN: 978-3-95450-250-9 ISSN: 2673-5520 doi:10.18429/JACoW-MEDSI2023-THPPP035

MECHANICAL SYSTEM OF THE U26 UNDULATOR PROTOTYPE FOR SHINE

S. W. Xiang, T. T. Zhen†, S. D. Zhou, Y. Y. Lei, J. Yang, W. Zhang, Z. Q. Jiang, R. B. Deng, H. X. Deng
Shanghai Advanced Research Institute, Chinese Academy of Sciences, Shanghai, China

Abstract

The Shanghai High repetition rate XFEL and Extreme light facility (SHINE) is under construction and aims at generating X-rays between 0.4 and 25 keV with three FEL beamlines at repetition rates of up to 1 MHz. The three undulator lines of the SHINE are referred to as the FEL-I, FEL-II, and FEL-III. Shanghai Synchrotron Radiation Facility (SSRF) will manufacture a total of 42 undulators (U26) with a period length of 26 mm for FEL-I and 22 undulators (U55) with a period length of 55 mm for FEL-II. Both the U26 and U55 are 4 m long and use a common mechanical system. By using the specially designed double lever compensation springs can eliminate different magnetic force on the drive units. A U26 prototype has been developed and tested at SSRF. This paper describes the mechanical system design, simulation and testing results of the U26 prototype, as well as its compatibility with U55.

INTRODUCTION

SHINE has three undulator lines [1-3], with FEL-I and FEL-II arranged side by side in the same tunnel, as shown in Fig. 1. Due to space limitations, the vacuum chamber needs to be installed and aligned on the undulator frame outside the tunnel. The width of the undulator is 1.1 m, and the transportation access space is 1.5 m to ensure that the undulator can be transported normally.

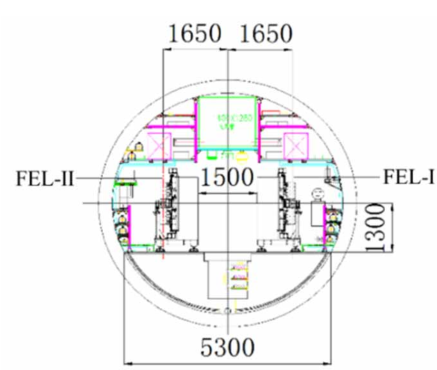

Figure 1: Cross section of the SHINE undulator tunnel.

MECHANICAL SYSTEM DESIGN

Considering that both U26 and U55 are 4 meters long, the mechanical system will be the same, but the magnetic structures will be different. The mechanical system is composed of a L-shape steel frame, girders, drive units, compensation springs, and alignment jacks, as illustrated in

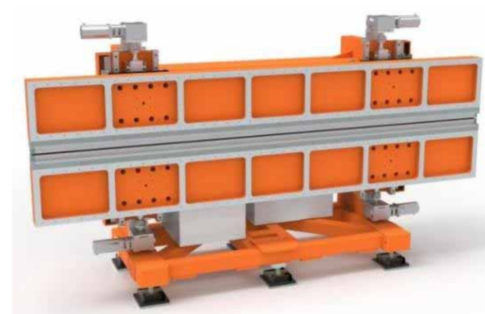

Figure 2: SHINE U26 prototype mechanical system.

Fig. 2. The function of the mechanical system is to support and drive the upper and lower girders with magnet structures to move symmetrically relative to the magnetic center. Mechanical tolerances are determined by FEL physics, and the main parameters of the mechanical system are listed in Table 1.

Table 1: Main Parameters of the Mechanical System

Parameter	Value	Unit
Maximum gap range	7-200	mm
Nominal gap range	7-14@U26 7-30@U55	mm
Maximum magnetic force	26@U26 65@U55	kN
Gap variation under maximum magnetic force	≤10@U26 ≤20@U55	µm
Gap drive repeatability	±1	µm
Taper range	±0.2	mm
Moving range of the magnetic center	±0.4	mm

The frame is a welded steel structure supported by a set of six jacks for leveling and alignment. The drive units adopt four motors to adjust the gap and the taper, and consists of motors, gearboxes, lead screws, linear guides, limit switches, hard stops, and encoders. In order to improve the rigidity of the girder, hardened and tempered 42CrMo forging are selected. The double lever compensation springs (DLCS) is composed of two sets of disc springs with different stiffness, as shown in Fig. 3. It is installed between the upper and lower support plates, which can eliminate the magnetic force on the drive units.

† email address: zhentt@sari.ac.cn

ISBN: 978-3-95450-250-9 ISSN: 2673-5520 doi:10.18429/JACoW-MEDSI2023-THPPP035

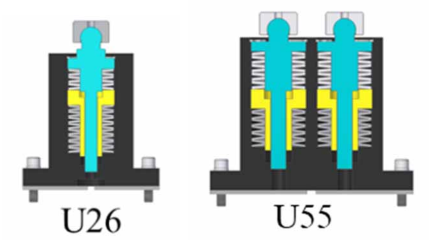

Figure 3: Double lever compensation springs.

GAP VARIATION ANALYSIS AND MEASURES

The upper and lower girders will deform under the magnetic force, resulting in the gap variation. The magnitude magnetic field. The results of gap variation measured by laser displacement meters are consistent with the Finite Element Analysis (FEA), as shown in Fig. 4. Under the magnetic force of 26 kN, the maximum gap variation of U26 is close to 8 µm as shown in Fig. 5. The phase anglemeasured is within 6°, which meets the physical requirements. Adjust the minimum gap of U26 to 4.6 mm, which can equivalent to simulating the maximum magnetic force 65 kN of U55. The maximum gap variation of U55 is close to 18 µm as shown in Fig. 6, which also meets the requirement in specification.

Figure 4: Gap variation measurement.

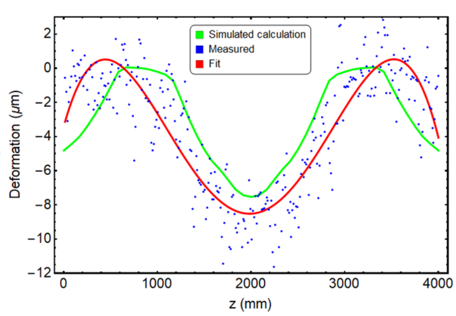

Figure 5: Maximum gap variation of U26.

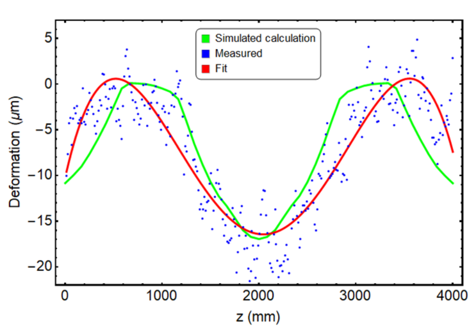

Figure 6: Maximum gap variation of U55.

SPRING CURVES MEASURED AND FATIGUE TEST

The compensation springs adopt the double lever structure, mainly used to eliminate the magnetic force on the drive units. The theoretical spring force curve is nonlinear and should as close as possible with the magnetic force curve. Actual spring force curves of U26 and U55 were measured by an electric servo testing machine, as shown in the Figs. 7 and 8. At the minimum gap of 7 mm, the spring force measured value of U26 is 28000 N, slightly higher than the theoretical value of 25000 N, with an error of 12%. At the minimum gap of 7 mm, the spring force measured value of U55 is 64700 N, slightly lower than the theoretical value of 65436 N, with an error of 1.2%. The results showed that measured curve basically coincide with the theoretical curve.

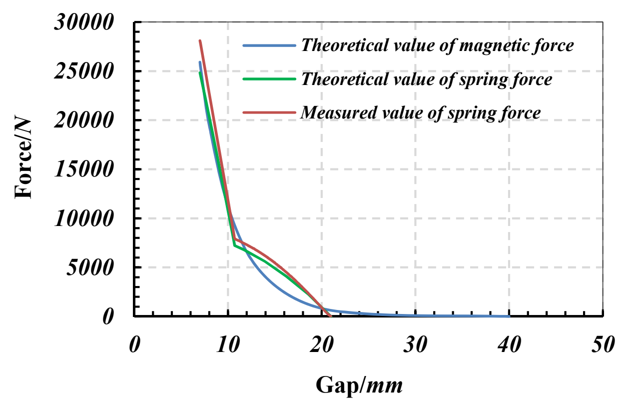

Figure 7: Magnetic and spring force curves of U26.

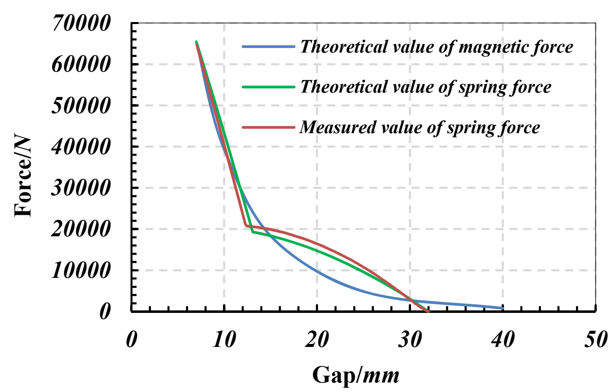

Figure 8: Magnetic and spring force curves of U55.

The long-term operation of compensation springs may cause significant changes in the spring force or structural fatigue damage due to friction, thereby affecting magnetic field stability. 5000 times fatigue tests were conducted on the compensation springs of U26 and U55 respectively. The results are shown in Figs. 9 and 10. It can be found that the movement is smooth, and the spring force curve basically coincides. Multiple movements lead to wear between the guide rod and the disc spring, resulting in a change in spring force of less than 7%, which can ignore the impact on magnetic field performance.

ISBN: 978-3-95450-250-9 ISSN: 2673-5520 doi:10.18429/JACoW-MEDSI2023-THPPP035

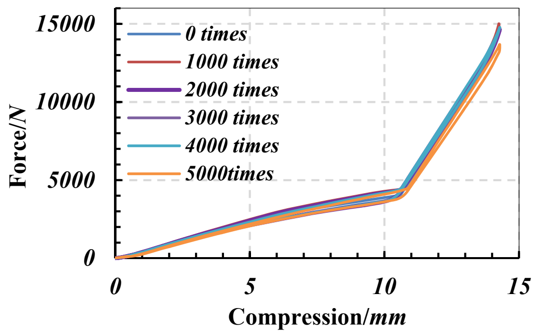

Figure 9: Spring fatigue test of U26.

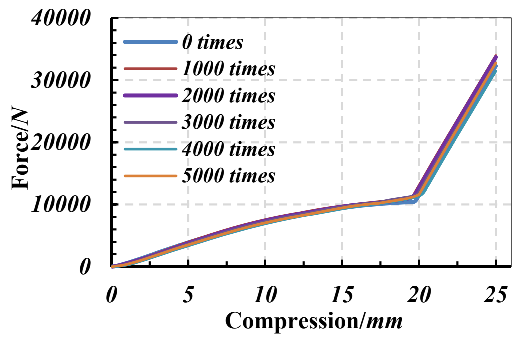

Figure 10: Spring fatigue test of U55.

The load reduction effect of the DLCS is ultimately verified by the control system reading the maximum output torque of the motor, as shown in Table 2. The results show that the magnetic force applied to the drive units has been eliminated by DLCS, and the output torque is mainly determined by gravity, friction, and inertial force.

Table 2: U26 Output Torque of the Motor (unit: nm)

Direction of motion	Position	without DLCS	with DLCS
7 mm→ 30 mm	upper girder 1	1.2	0.7
	upper girder 2	1.2	0.7
	lower girder 1	0.6	0.2
	lower girder 2	0.6	0.2
30 mm→ 7 mm	upper girder 1	0.5	0.35
	upper girder 2	0.5	0.35
	lower girder 1	0.9	0.9
	lower girder 2	0.75	0.75

LIFTING ANALYSIS AND TEST

All undulators will be tested in laboratory, to qualify their performance in the tunnel, it is necessary to ensure the structure does not occur irreversible deformation during lifting. The undulator adopts a three-point lifting method, with the lifting point located at the bottom of the frame and as close as possible to the three main support points of the undulator, which can effectively reduce the deformation caused during the process from standing to lifting, as shown in Fig. 11. Through finite element analysis, it is found that the maximum stress occurs at the front lifting point, which is 38 MPa much less than the yield strength of Q345. By measuring the magnetic field before and after lifting, the phase error variation caused by lifting is within a range of 1°, meeting the physical requirements, as shown in Fig. 12.

Figure 11: Lifting method and stress FEA results.

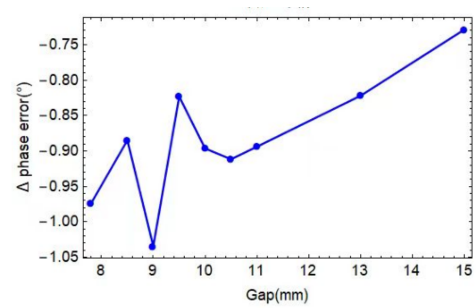

Figure 12: Phase error variation caused by lifting.

CONCLUTIONS

For the FEL-I at the SHINE a U26 prototype has been built and tested by SSRF, China. The measured performance parameters of the U26 prototype satisfy the technical requirements and are basically consistent with the design and simulation results. The mechanical system of U26 has been verified to be equally applicable to U55, which is beneficial for reducing equipment types and shortening research and development cycles.

ACKNOWLEDGEMENTS

This work was supported by the CAS Project for Young Scientists in Basic Research (YSBR-042), the National Natural Science Foundation of China (12125508, 11935020), Program of Shanghai Academic/Technology Research Leader (21XD1404100), and Shanghai Pilot Program for Basic Research – Chinese Academy of Sciences, Shanghai Branch (JCYJ-SHFY-2021-010).

REFERENCES

[1] Z. T. Zhao *et al.*, "SCLF: an 8-GeV CW SCRF linac-based X-ray FEL facility in Shanghai", *Proceedings of the FEL2017*. Santa Fe, NM, USA, 2017. doi:10.18429/JACOW-FEL2017-MOP055

[2] Z. T. Zhao, C. Feng, K. Q. Zhang, "Two-stage EEHG for coherent hard X-ray generation based on a superconducting linac", *Nucl. Sci. and Tech.,* vol. 28, p. 117, 2017. doi:10.1007/s41365-017-0258-z

[3] C. Feng, H. X. Deng, "Review of fully coherent free-electron lasers", *Nucl. Sci. and Tech.*,vol. 29, p.160, 2018. doi: 10.1007/s41365-018-0490-1

ISBN: 978-3-95450-250-9 ISSN: 2673-5520 doi:10.18429/JACoW-MEDSI2023-THPPP036

PROTOTYPE OF HIGH STABILITY MECHANICAL SUPPORT FOR SHINE PROJECT*

Rongbing Deng†, Fei Gao, Zhidi Lei, Xuefang Huang, Tingting Zhen, Haixiao Deng,
Shanghai Advanced Research Institute, Chinese Academy of Sciences, Shanghai, China

Abstract

Quadrupole stability of undulator segment is key to the beam performance in SHINE project. Vibration stability requirement of quadrupole is not larger than 200 nm displacement RMS between 1 and 100 Hz, but the field test of SHINE tunnel shows that the tunnel vibration during the day time is greater than 200 nm. In this paper, a mechanical support including a marble base and an active vibration reduction platform is sophisticated designed. Vibration stability of the key quadrupole fixed on this support is expected to be improved and the performances of the quadrupole meet the demands.

INTRODUCTION

Shanghai HIgh repetition rate XFEL aNd Extreme light facility (SHINE) is under construction. In undulator segment, the position of quadrupole is key to the beam performance. The position accuracy and stability of quadrupole are both nms. Quadrupole is supported by girder and girder is fixed to the ground. The high stability of mechanical support for quadrupole is important to assure the quality of the beam therefore. In SPring-8 [1], it is the cordierite ceramic support because ceramic has a low thermal expansion rate. In addition, sand is filled in the support to increase heat capacity to insure good stability. Support in SLAC [2] is a Mild Steel girder, which has sand inside and thermal insulation outside to ensure stability. In SHINE, the technical requirements of quadrupole are shown in Table 1.

Table 1: Technical Requirements of Quadrupole

Item	Value	Unit
Adjustment range of quadrupole center (H/V)	$\geq \pm 0.5$	mm
Adjustment step of quadrupole (H/V)	≤ 0.05	μm
Positioning accuracy of quadrupole (H/V)	$\leq \pm 0.1$	μm
Stability of Magnetic Center Vibration of Quadrupole (H/V, RMS, > 1 Hz)	≤ 0.20	μm

Acceptance requires that over 80 % of the total vibration measurement data (all day) meet the above stability requirement.

STRUCTURAL DESIGN

The overall mechanical support, as shown in Fig. 1, includes two parts: a marble base and an upper support. The marble base is fixed to the ground by grouting with steel plate. The thickness of grouting is not less than 40 mm and a raised plate below the marble used for adjusting the height displacement changes in the initial and later stages. The upper girder directly supports the beam equipment. The active vibration reduction platform plays an important role in dynamic vibration reduction and precise positioning. Adjustment range of the base is ± 10 mm both in vertical and horizontal direction. Adjustment range of the upper support is ± 10 mm in vertical direction and ± 5 mm in horizontal direction.

The active vibration reduction platform is fixed to the quadrupole base plate, and the seismometers are fixed on top of the marble to monitor the background vibration. Based on the vibration signal of seismometers, the piezoelectric motors in the active vibration reduction platform feedback adverse displacements to attenuate the vibration transmitted from the surrounding environment of the support platform to the quadrupole. The control cabinet is placed on the near undulator frame, as shown in the following figure.

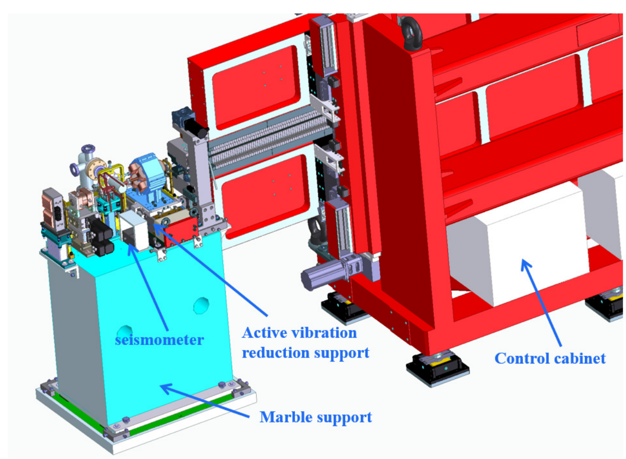

Figure 1: Mechanical support model.

The active vibration reduction platform is driven by piezoelectric motors, including 4 sets of vertical motors and 1 set of horizontal motors. A spring compensator is used to counteract gravity. A grating ruler is installed on the outer side to locate closed-loop feedback and facilitate the installation of lead plates for radiation protection. Considering a movement range of ± 0.5 mm, vertical and horizontal mechanical limits are designed internally, and vertical and

* This work was supported by the CAS Project for Young Scientists in Basic Research (YSBR-042), the National Natural Science Foundation of China (12125508, 11935020)
† dengrb@sari.ac.cn

ISBN: 978-3-95450-250-9 ISSN: 2673-5520 doi:10.18429/JACoW-MEDSI2023-THPPP036

horizontal electric shock switches are designed externally, as shown in Fig. 2, to facilitate precise adjustment of the protection range of the quadrupole according to the actual installation situation.

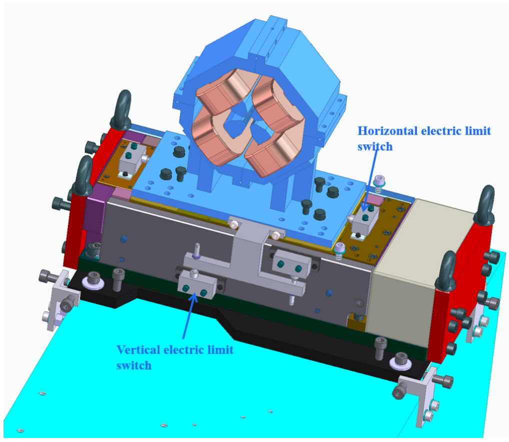

Figure 2: Limit switches in quadrupole support.

RESULTS

The quadrupole support is tested in lab at Shanghai Synchrotron Radiation Facility. Seismometers are placed on ground and top of dummy quadrupole at the same time. The contrasts of RMS value of vibration between ground and dummy quadrupole between 1 to 100 Hz are shown in Fig. 3 and Fig. 4. The vibration of dummy quadrupole is much less than ground vibration.

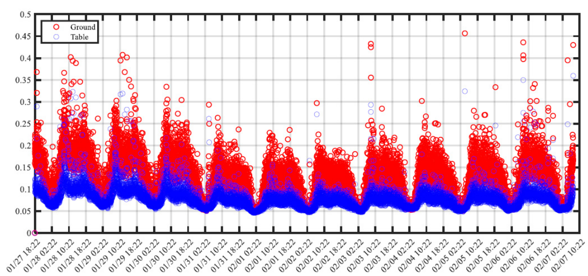

Figure 3: RMS contrasts between ground and dummy quadrupole in vertical direction.

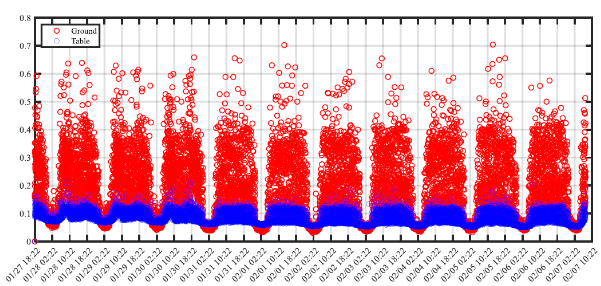

Figure 4: RMS contrasts between ground and dummy quadrupole in horizontal direction.

Capacitive Displacement Sensors are used to test the adjustment range, adjustment step and positioning accuracy of dummy quadrupole. The result of displacement step of dummy quadrupole as an example is shown in Fig. 5.

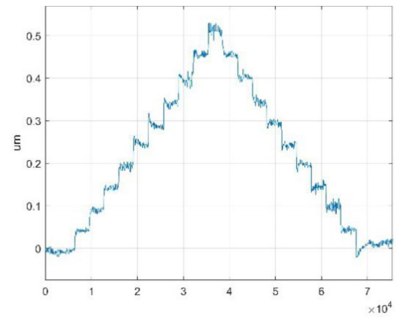

Figure 5: Adjustment step of dummy quadrupole.

CONCLUSIONS

An active vibration reduction platform fixed on a marble base is designed to meet SHINE requirements of precise positioning and high stability of quadruple. Prototype of the support works well and will be installed in tunnel of SHINE in the future.

REFERENCES

[1] T. Saeki, T. Shintake, *et al.*, "Development of A New Support-Stand with High Thermal Stability for the SCSS Project", in *Proc. APAC'04*, Gyeongju, Korea, Mar. 2004, paper MOP20003.

[2] M. White, J. Collins, P. Den Hartog, *et al.*, "Performance of Production Support and Motion Systems for the Linac Coherent Light Source Undulator System", in *Proc. PAC'09*, Vancouver, Canada, May 2009, paper WE5RFP063, pp. 2407-2409.

ISBN: 978-3-95450-250-9 ISSN: 2673-5520 doi:10.18429/JACoW-MEDSI2023-THPPP037

A MICRO-VIBRATION ACTIVE CONTROL METHOD BASED ON PIEZOELECTRIC CERAMIC ACTUATOR*

Z. Lei, R. Deng†, H. Deng
Shanghai Advanced Research Institute-Chinese Academy of Sciences, Shanghai, China

Abstract

In linear accelerator, ground vibration is transmitted to beam element (quadrupole magnet, etc.) through support, and then reflected to the influence of beam orbit or effective emittance. In order to reduce the influence of ground vibration on beam orbit stability, an active vibration isolation platform can be used. In this paper, an active vibration isolation system is proposed, which realizes the inverse dynamic process based on a nano-positioning platform and combines with a proportional controller to reduce the transmission of ground-based excitation to the beam element. The absolute vibration velocity signal obtained from the sensor is input to the controller as feedforward signal. The controller processes the input signal and then the output signal drives the piezoelectric ceramic actuator to generate displacement, realizing the active vibration control. The test results of the prototype show that the active vibration isolation system can achieve 50 % displacement attenuation, which indicates that the vibration control strategy has certain engineering application value in the construction of large accelerators.

INTRODUCTION

Shanghai High Repetition rate XFEL (X-ray Free Electron Laser) and Extreme light facility (SHINE) currently under construction is one of the most efficient and advanced free electron laser user installations in the world [1, 2]. It consists of a superconducting linac with an energy of 8GeV, three unshaker lines, three optical beam lines, and the first 10 experimental stations. The superconducting linear accelerator is composed of superconducting acceleration modules, each 1.3 GHz module is about 12 meters long, and mainly includes 8 TESLA type 9-cell superconducting cavities [3], couplers, tuners, BPM and superconducting quadrupole iron at one end. In order to achieve the submicron beam stability requirements of the superconducting linac and to suppress the cavity frequency deviation caused by mechanical vibration, the position jitter tolerance is generally not more than 10 % of the beam size [4]. In particular, engineering requires that the amplitude of some quadrupole magnet be less than 0.15 µm (1 Hz-100 Hz) perpendicular to the beam direction. SHINE facility is close to the Shanghai Synchrotron Radiation Facility (SSRF). The German Electron Synchrotron Institute has compared and analyzed the ground vibration of major light sources around the world, and the results show that the ground vibration level of the SSRF campus is significantly higher than that of other light sources [5]. Therefore, it is of practical significance for engineering construction to develop an active vibration isolation platform suitable for large accelerators.

DESIGN OF THE ACTIVE VIBRATION CONTROL STRATEGY

In order to reduce the influence of foundation vibration on quadrupole magnet, an active vibration isolation platform is used to reduce the transfer rate of displacement from foundation to magnet. In this paper, an active vibration isolation system is proposed, which realizes the inverse dynamic process based on a nano-positioning platform and combines with a proportional controller to reduce the transmission of ground-based excitation to the beam elements. The absolute vibration velocity signal obtained from the sensor is input to the controller as a feedforward signal. The controller processes the input signal and then the output signal drives the piezoelectric ceramic actuator to generate displacement to realize active vibration control.

EXPERIMENTAL RESULTS

For the evaluation of the proposed control strategy, the test bench shown in Fig. 1 is used. Ground broadband vibration act as excitation, and four piezoelectric actuator implements the described isolating strategy in the direction of gravity for damping the vibration in the upper mass M (260 kg).

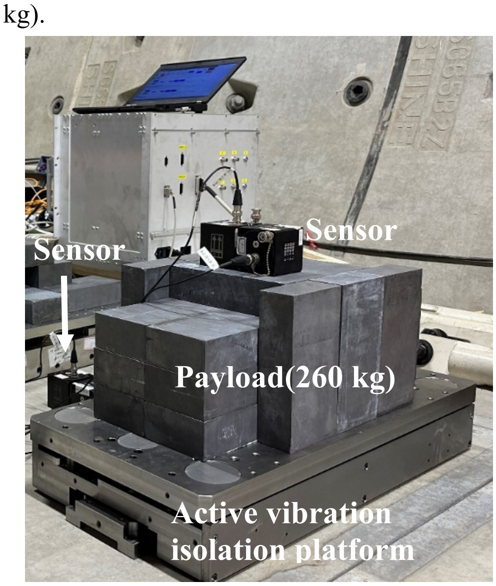

Figure 1: Test bench.

* Work supported by the CAS Project for Young Scientists in Basic Research (YSBR-042), the National Natural Science Foundation of China (12125508, 11935020), Program of Shanghai Academic/Technology Research Leader (21XD1404100), and Shanghai Pilot Program for Basic Research – Chinese Academy of Sciences, Shanghai Branch (JCYJ-SHFY-2021-010).
† dengrb@sari.ac.cn

ISBN: 978-3-95450-250-9 ISSN: 2673-5520 doi:10.18429/JACoW-MEDSI2023-THPPP037

Figure 2 shows the comparison of the displacement power spectral density obtained from ground and the surface of the payload when the active vibration control is on in a typical condition. The 1 Hz-100 Hz root-mean-square (RMS) value of displacement on the ground is 0.294 µm and on the payload is 0.128 µm, which means a displacement attenuation rate of 56 % is achieved.

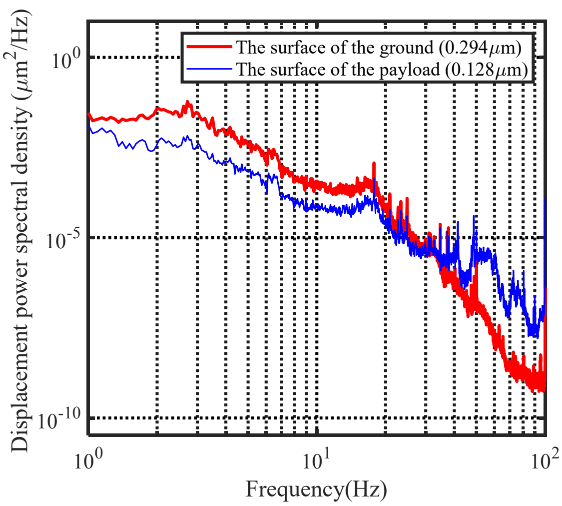

Figure 2: The comparison of the displacement power spectral density in the direction of gravity when the active vibration control is on.

Figure 3 shows the long-term test results of the active vibration isolation platform in the tunnel. As can be seen from the figure, displacement RMS obtained from the payload has a significant raise when the active vibration control turned off.

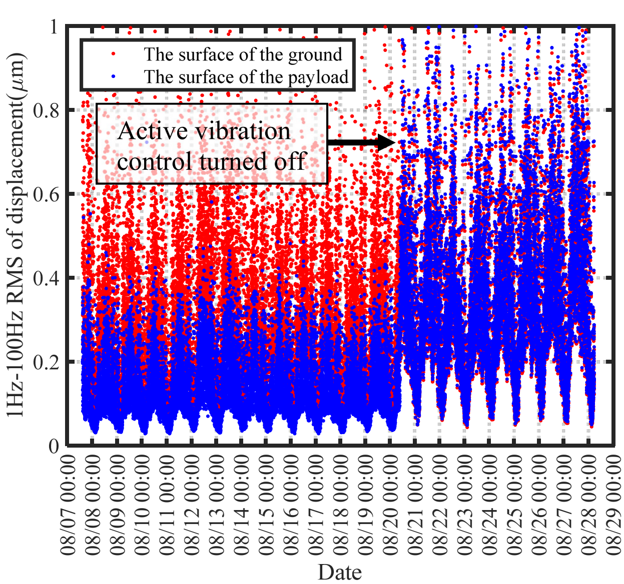

Figure 3: Long-term test results of displacement RMS.

Table 1 summarizes and compares the statistical results of the measured displacement RMS meeting the physical requirement (1 Hz-100 Hz displacement RMS less than 0.15 µm), and the statistical period is 48 consecutive hours from August 8 to August 9, 2023. As can be seen from the table, only 13.71 % of the time of the ground meets the physical requirement, which can be improved to 65.91 % after the active vibration control.

Table 1: Statistical Results of the Displacement RMS

	Less than 0.15µm percentage
Ground	13.71%
Payload	65.91%

CONCLUSION

Vibration control is a challenge for SHINE facility, and the active vibration isolation system proposed in this paper can achieve more than 50 % displacement attenuation in the actual broadband vibration environment, increasing the time to meet the physical requirement of some very demanding quadrupole magnet by 4.8 times.

REFERENCES

[1] Z. T. Zhao, C. Feng, K. Q. Zhang, “Two-stage EEHG for coherent hard X-ray generation based on a superconducting linac”, *Nucl. Sci. Tech.*, 2017, 28 (8), 117. doi:10.1007/s41365-017-0258-z

[2] C. Feng, H. X. Deng, “Review of fully coherent free-electron lasers”, *Nucl. Sci. Tech.*, 2018, 29 (11), 160. doi: 10.1007/s41365-018-0490-1

[3] J. J. Guo, Q. Gu, M. Zhang, *et al.*, “Power losses caused by longitudinal HOMs in 1.3-GHz cryomodule of SHINE”, *Nucl. Sci. Tech.*, 2019, 30 (7), 105. doi:10.1007/s41365-019-0628-9

[4] F. Yan, G. Xu, Z. Z. Wang, *et al.*, “Investigation of regulationplan for the vibration utility equipment of HEPS”, in *Proc. MEDSI'18*, Paris, France, Jun. 2018, pp.136-139. doi:10.18429/JACoW-MEDSI2018-TUPH41.

[5] W. Bialowons, R. Amirikas, A. Bertolini, *et al.*, “Measurement of ground motion in various sites”, in *Proc. EPAC'06*, Edinburgh, UK, Jun. 2006, paper MOPLS064, pp. 691-693.

ISBN: 978-3-95450-250-9 ISSN: 2673-5520 doi:10.18429/JACoW-MEDSI2023-THPPP038

GIRDERS FOR SOLEIL-II STORAGE RING

J. Da Silva Castro†, K. Tavakoli, S. Ducourtieux, Z. Fan, F. Lepage, A. Nadji
Synchrotron SOLEIL, Saint-Aubin, France

Abstract

After two decades since its establishment, the SOLEIL Synchrotron facility needs to adapt to follow new scientific fields that have emerged since. After the Conceptual Design Report (CDR) phase for the facility Upgrade, the SOLEIL teams have been working for several months on the Technical Design Report (TDR). The "SOLEIL Upgrade" project is called "SOLEIL II" and is divided into several sub-projects. Among these sub-projects, one concerns storage ring Girders that will support all magnets of the new Lattice. These 86 Girders, each one supported by 2 plinths, must ensure an excellent degree of vibration stability. Before obtaining a final design for these Girders, a significant amount of study work has already been carried out (design, finite elements simulations, sub-assembly prototyping, dynamic measurements, tests, etc.). To validate the concepts, a fully equipped prototype girder was launched into manufacturing. In this contribution the preliminary studies and the ongoing investigations on SOLEIL II girder design will be presented.

INTRODUCTION

SOLEIL [1] teams have been working for several months on its Technical Design Report of "SOLEIL II" project that aims to study and install an accelerator with new performances. One sub-project concerns girders of storage ring that will support the magnets of the new Lattice. These girders must make it possible to achieve an excellent degree of vibration and thermal stability, including adjustment precision, with acceptable manufacturing costs. The difficulty is to find the best compromise between the level of specifications and the costs to achieve them. Figure 1 shows the previous magnets supports and the current philosophy. That will constitute a substantial budget saving.

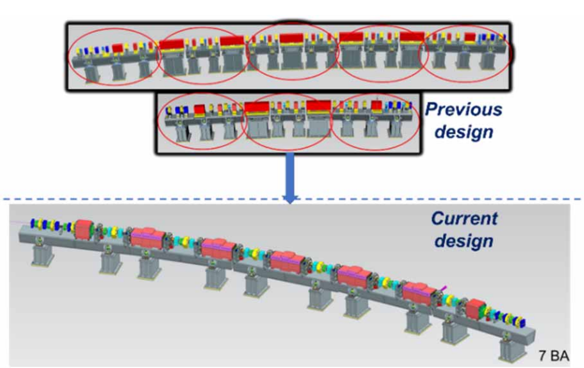

Figure 1: Previous and current magnets support situation (magnets in 7BA cell and 4BA cell of SOLEIL-II lattice.

† jose.dasilvacastro@synchrotron-soleil.fr

Previously girders were supported by 3 plinths. Currently girders are supported by 2 plinths. Now the target defined by accelerator physicists for the 1st modal frequency is ≈ 40 Hz. After few iterations, we came up on four girder length families, with two assembling configurations, single or double dipole [2]. The high density of multipoles is a real challenge in terms of components integrating on girders [3].

Table 1 allows to compare previous and current magnets supporting philosophies. At the cost of a reduction of the 1st modal frequency target, the number of supports and plinths has been drastically reduced.

Table 1: Previous and Current Supporting Situations

	Previous	**Current**
Girders Nb.	98	86
Long dipole plinths Nb.	76	0
Standard plinths Nb.	236	172
First modal frequency Hz.	70	40

GIRDERS AND PLINTHS INTERFACE

Figure 2 shows the design of girder and plinth interface that allows to adjust and lock girder position. Adjustment principle consists in, a preload first applied by spring washers. Then the girder is aligned with adjusting elements using Nivell wedge and Push and pull screws. Finally, girder is locked by the spring washers, loaded at 45000 N.

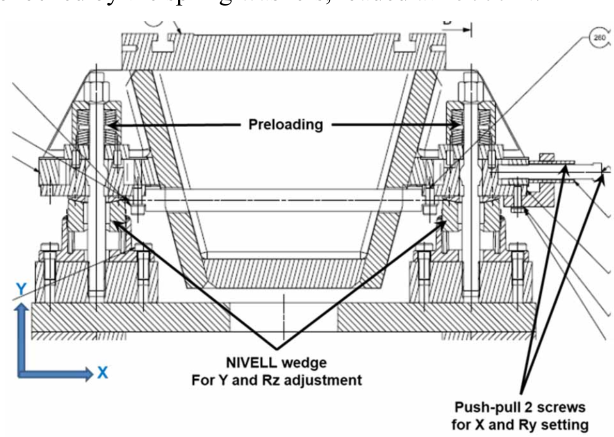

Figure 2: Girders positioning and locking system.

MODAL ANALYSIS

Current specification for the 1st modal frequency is 40 Hz minimum. FE simulations on both pessimistic configurations, regarding supported loads were carried out. In both case the 1st modal frequency is a transversal (X) bending mode of the plinths. Girder dynamic bending occurs from the 4th modal frequency at 105 Hz for single dipole

ISBN: 978-3-95450-250-9 ISSN: 2673-5520 doi:10.18429/JACoW-MEDSI2023-THPPP038

configuration and 94 Hz for double dipole configuration. First modal frequency is 49 Hz for single dipole configuration, and 45 Hz for double dipole configuration, more than 40 Hz. Figure 3 shows dimensions and masses of pessimistic configurations. Long dipole mass is 850 Kg. Other magnets masses are a few tens of kg each one.

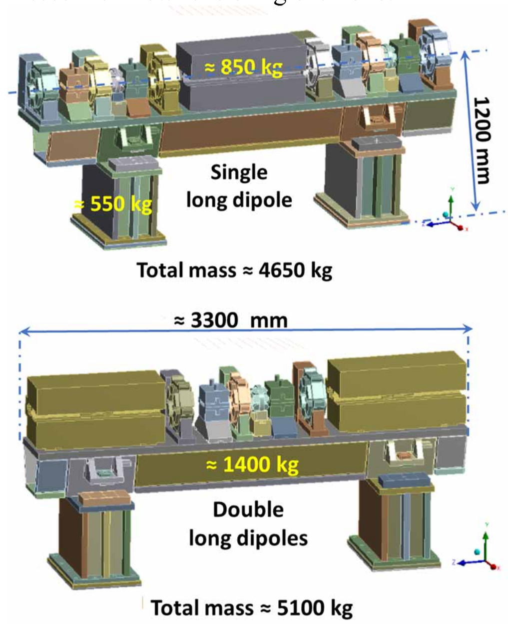

Figure 3: Both pessimistic configurations.

STATIC ANALYSIS

FE static analysis for both pessimistic configurations show a maximum displacement of the girder with single dipole of 0.025 mm. For the double dipole configuration, the maximum displacement of the girder is 0.03 mm.

In both case a maximum displacement of 0.01 mm can be reached with a compensation. It consists of machining the upper surface of girders (that supports magnets) at the same temperature conditions as the future tunnel and reproducing the same boundary conditions as the plinths. The future tunnel should be thermalized at 23 °C, compared to 21 °C currently, for economic reasons. An additional compensation consists in reproducing magnets load during machining of the upper surface. The theoretical maximum displacement could tend towards 0, with flatness tolerances close to 0.01 mm/m. This method would have a large impact on manufacturing cost and isn't currently justified.

FIRST PROTOTYPING AND TESTS

To validate design and check the FE simulation hypotheses mainly for modal analyses, we studied, provided, and installed a plinth prototype to carry out tests. Figure 4 shows the plinth in the testing area, manufactured by the company INGELIANCE, in France. Z defines the beam axis, Y the vertical axis, and X the transversal axis. A steel plate is grouted to the same concrete slab as current storage ring. Then the plinth is screwed onto this plate.

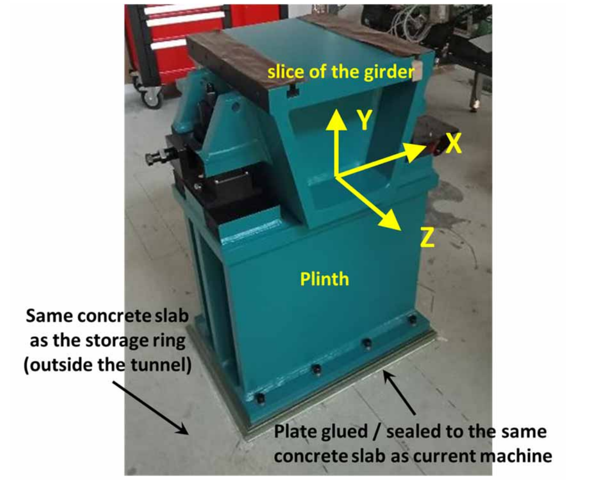

Figure 4: Plinth prototype in steel with a slice of girder.

In June 2022, vibration measurements were done. We observed eigen frequency in X and Z axis. In Y axis the plinth doesn't contribute much to the dynamic response. That will be controlled mostly by the flexibility of the girder (+3 m long) on its two plinths. On the Z axis we observed a bending mode at 55 Hz. On X axis we observed one twisting mode at 73 Hz and one bending mode at 99 Hz. From these values, we did an estimation of the bending frequency mode in X axis, for a loaded girder on two plinths. We considered a half of girder as shown on Fig. 5. 49 Hz is a value close to the results obtained in modal analysis. It's possibly an overestimated value because the flexibility of the plinth nor the lever arm of the magnets are considered. Still in X axis we extracted the displacement values of the ground and of the plinth. The estimated (transfer function) level of amplification for a loaded girder could be a difference of 15 nanometers between ground measurement and estimate values for a loaded girder.

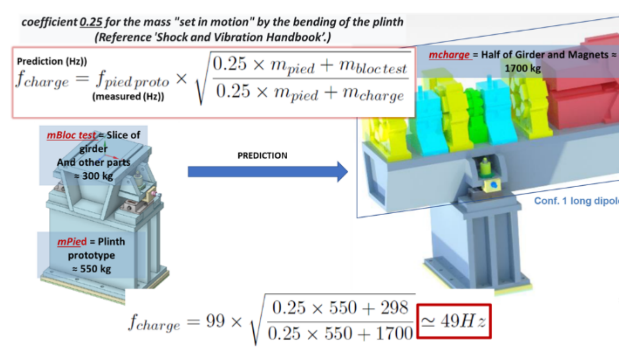

Figure 5: Prediction of bending frequency mode for a loaded girder with single dipole (X direction).

In June 2022, first alignment tests were carried out and showed that design seems to be a good basis for further studies. Adjustment under preload eliminates the problem of parasitic displacement. The fineness of fit is less than 1 µm in the Z-axis and a few µm in the other directions. Thermal stability also seems acceptable. In the area where the plinth prototype was installed, the temperatures varied between 23 °C and 23.5 °C, over 17 hours of measurements. Despite this, the thermal stability after adjustment

ISBN: 978-3-95450-250-9 ISSN: 2673-5520 doi:10.18429/JACoW-MEDSI2023-THPPP038

was a few µm. Thermal regulation in the storage ring tunnel will be +/- 0.1 °C, so better than in the tests area.

Thanks to these tests, the design of adjustment system was improved. As shown in Fig. 6, we replaced spring washers by specific springs (steinel.com) that allow more loading precision, avoiding mounting mistakes. We changed materials for sliding surfaces, using bronze. A spherical reference for Z positioning of girders was added.

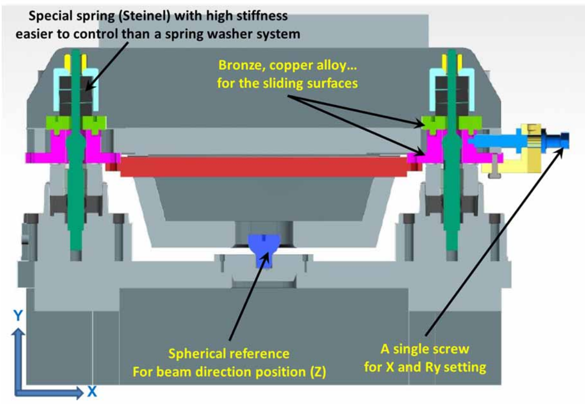

Figure 6: Design improvements.

GIRDER PROTOTYPE WITH DUMMY MAGNETS

With these encouraging results, thanks the plinth prototype, we decided to design and to provide a fully equipped girder prototype. The aim of this new prototype is to carry out as many full-scale tests and measurements as possible, for both pessimistic loading configurations. The goal is to validate the design and the processes. A single girder will allow to test both configurations alternately. Dummy magnets will have the same geometry, center of gravity and mass as the magnets currently being designed and/or prototyped.

Here is a non-exhaustive list of tests to carry out on girder prototype: alignment (precision and stability) tests; vibration stability and modal response measurements to estimate transfer functions and amplification levels; thermal stability measurements; loaded and not loaded girder deformation measurements; HLS system tests, study of motorization opportunity for installation procedure; impact studies of transporting of girder equipped on maintaining magnets alignment.

Figure 7 shows girder prototype and dummy magnets manufactured by NORTEMECANICA in Spain. Factory acceptance tests were done on October 17, 2023, with expected delivery at the end of October 2023. Installation is scheduled before the end of 2023. Tests and measurements will follow from the beginning of 2024.

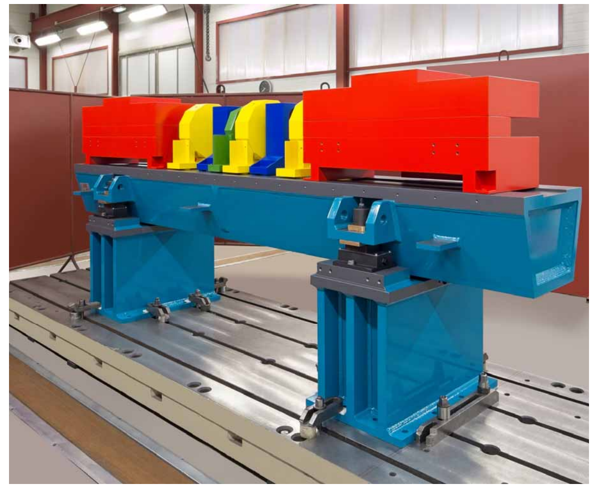

Figure 7: Manufacturing on progress.

CONCLUSION

Finding the best compromise between cost and performance is always a challenge. SOLEIL's upgrade lattice includes many distinctive zones, this fact increases the number of girder families. Some multipoles are quite narrow (~60 mm), these elements risk to have a lower natural frequency than the girders. The planning is very tight, lattice modifications can delay the design procedure. Factory and on-site acceptance tests will need to be rigorously followed and re-checked if needed because of very tight fabrication tolerances.

We continue the design procedure by carrying out integration studies of the girders in the tunnel of storage ring, considering front ends, building, interfacing with the magnets and with the vacuum chamber supports. We have also to think about logistics and installation process.

There is still a lot of work to be done to achieve our new research tool.

REFERENCES

[1] Synchrotron SOLEIL, `https://www.synchrotronsoleil.fr`

[2] J. Da Silva Castro *et al,* "Girder Design", presented at **M**achine **A**dvisory **C**ommittee, 14-16 November 2022.

[3] K. Tavakoli *et al*., "Challenges and solutions for the mechanical design of SOLEIL II", presented at MEDSI'23, Beijing, China, Nov 2023, paper WEOBM01, this conference.

ISBN: 978-3-95450-250-9 ISSN: 2673-5520 doi:10.18429/JACoW-MEDSI2023-THPPP040

THE GIRDER SYSTEM PROTOTYPE FOR ALBA II STORAGE RING

L. Ribó †, J. Boyer, N. Gonzalez, C. Colldelram, L. Nikitina, F. Perez
ALBA Synchrotron Light Source, Cerdanyola del Valles, Spain

Abstract

The main goal of the upgrade of ALBA Synchrotron Light Facility into ALBA II is the transformation of the current accelerator into a diffraction limited storage ring, which implies the reduction of the emittance by at least a factor of twenty. The upgrade will be executed before the end of the decade and will be profiting at maximum all existing ALBA infrastructures, in particular the building. The whole magnet layout of the lattice has to be supported with a sequence of girders for their positioning with respect to another located in an adjacent girder with an accuracy of 50 µm to ensure the functionality of the accelerator. Besides the girders must enable the remote repositioning the magnets against the overall deformation of the site while ensuring the vibrational stability of the components on top. Easiness of assembling and installation of the different subsystems of the machine on top of the girder has to be considered also as a design requirement, in order to minimize the installation time. Two prototypes are planned to be built next year in order to check its full functionality.

FROM ALBA TO ALBA II

ALBA current storage ring is composed by 264 magnets, which are distributed in 16 cells in an array of 2 girders of 6 meters for each cell. ALBA II proposed layout is composed by 592 magnets, in the same arc length as current ALBA storage ring [1], meaning that the compactness ratio has increased by a factor of 2 in the new projected storage ring with respect to the old one. In Fig. 1 is represented an overall distribution of one sector for the current and new storage ring, where the reduction of free space can be appreciated.

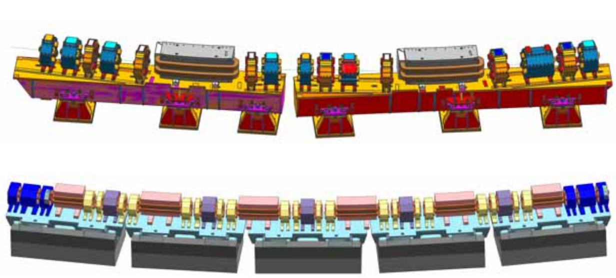

Figure 1: Current magnetic distribution of ALBA (top) and ALBA II cell layout (bottom).

As it can be seen on Table 1, the tolerances for positioning the girder will thus need to be tighter corresponding to a low emittance new machine, where the emmitance is reduced by a factor of 20 [2].

Table 1: Sizes Comparison

Dimension	ALBA	ALBA II
Compactness grade	49 %	80 %
Vacuum chamber size	28×56 mm	18 mm
Dynamic aperture	50 mm	6 mm
Beam Size	60 µm	5 µm

A NEW GIRDER DESIGN

In order to support the magnetic arrays, a new girder design is required. Taking into consideration the deformation of ALBA slab in the last 12 years, motorization for vertical positioning may be considered as a demand to be able to automatically compensate the small incremental vertical deformations and maintain electron beam stable in dynamic aperture.

The chosen strategy for conditioning the vacuum cell, will lead to a determinate vacuum section design, but according to the actual design status there are two possible layouts, which differ on the number and length of girders. That's why it is foreseen to prototype a girder design that will be fabricated in two different lengths, considering the ALBA II cell nowadays possible configurations. Apart from that, the girder design has to be modular enough in order to facilitate a full assembly outside the tunnel, together with the magnets and interfaces to minimize the installation time. In Table 2 the specifications for the girders prototype are summarized, in Fig. 2 the architecture and the main axes of movements are represented.

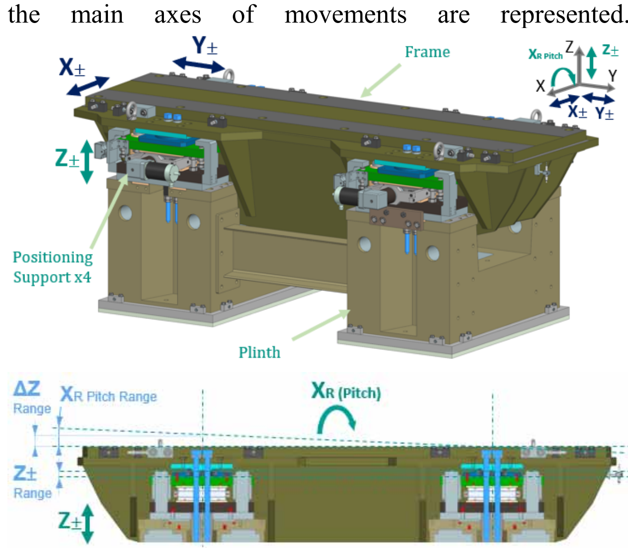

Figure 2: Motion axes and architecture.

† lribo@cells.es

12th Int. Conf. Mech. Eng. Design Synchrotron Radiat. Equip. Instrum. MEDSI2023, Beijing, China JACoW Publishing
ISBN: 978-3-95450-250-9 ISSN: 2673-5520 doi:10.18429/JACoW-MEDSI2023-THPPP040

Table 2: Prototype Specifications

Specification	Value	Comments
Length	2.6 m /4 m	Extreme possible lengths.
eBeam height	1400 mm	Girder interface height about 1 m, defined by magnet design.
Eigenmodes	> 50 Hz	By design.
XY adjustment Resolution	20 µm	Manual.
Z range manual	+/- 5 mm	Manual.
Z range motorized	+/- 1 mm	Value determinate by the final assembly architecture.
Z resolution	5 µm	Motorized axis.
Assembly weight	< 12 Tn	Considering magnet assembly.
Magnet positioning tolerance	50 µm	Considering magnets of consecutive girders.

DIMENSIONING AND ARCHITECTURE

As it is shown in Fig. 2, the girder is divided in 3 main parts. The plinth, acting as a support, the positioning system, which consists on the mechanics for the vertical and pitch positioning, and the frame, which is the moving part that supports the full arrange of magnets.

The plinth is designed to be screwed to a grinded steel plate which is epoxy-glued to the floor. This plinth will support the Z positioning system, together with the electrical interfaces. For the prototype it is still being considered whether the plinth will be steel welded or fabricated from a block of granite. After evaluation of the cost and performance, manufacturing strategy will be decided for the series production. Figure 3 shows a front view of the girder with dimensions of the most relevant magnets of the array.

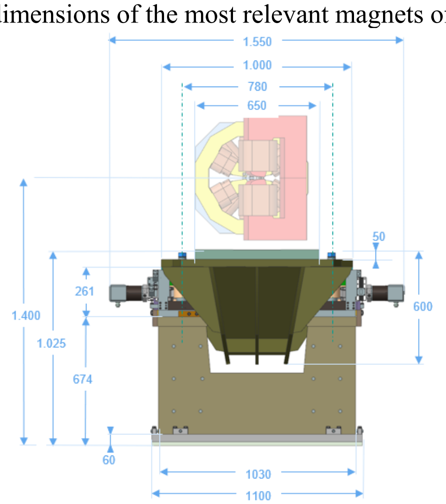

Figure 3: Front view and dimensioning.

THE MOTION SYSTEM

The motion system consists mainly on four actuators composed by motorized commercial wedge mounts, similar to the girder for the ESRF-EBS upgrade [3]. Wedge mounts are considered as the stiffest and coherent positioning system for such application, were tones of weight have to be positioned

The commercial wedge mount performs a precise vertical positioning but unguided, generating uncertainty in the horizontal position when it is actuated. That is why the system proposed is foreseen to be guided with a die press like system, where the top plate of the wedge is guided with respect to the bottom one with two linear bushings. Each actuator, composed by the motorized wedge and the guiding system, will include an absolute encoder and limit switches to control and limit its range.

Apart from that, in order to increase the rigidity of the system, a set of preloaded elastic elements are implemented. It is assumed a maximum reaction force of 40 kN in each actuator. This reaction force includes the weight of the magnetic array, the weight of the frame and the preload force that has been considered. This reaction force has been considered to calculate the input torque needed on the screw of the wedge mount to move the system. With that, the stepper motor and the reducer are sized.

In the next Fig. 4 the mentioned elements are shown as well as some selected references for the first prototype. A spherical contact as interface between the wedge mount and the top plate of the die press (in green) is foreseen.

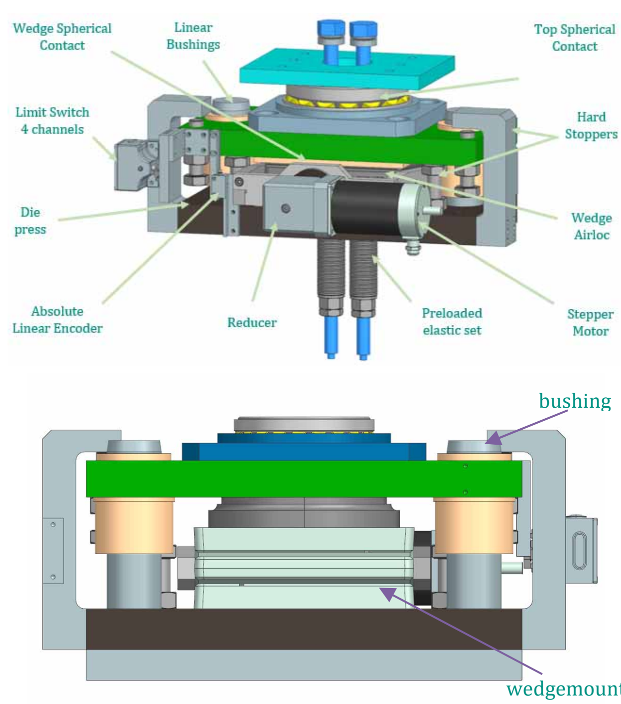

Figure 4: Positioning system detail. Top details of all the parts, bottom the wedge mount guided by the linear bushings is appreciated.

The girder frame is linked to the positioning system by means of spherical contacts (in Fig. 4 are represented as actuator top spherical contact). These will be axial roller conical bearings or precision spherical washers that will be interchangeable in order to test their performance. Three types of spherical contacts are foreseen to be evaluated in the prototype.

The wedge mount is able to be manually actuated by uncoupling the motor or acting on the second motor axis located in the back of the motor. This manual adjustment is needed to position and align the girder in a nominal position in height and pitch when being installed for first time in the machine.

THE FRAME

The frame will be manufactured by continuous welded steel and it has been optimized in shape and weight by FEA analysis in order to minimize deformations and maximize vibrational stability. The most optimal geometry found, based on welded plates is to distribute them in a triangular shape as it is shown in Fig. 5.

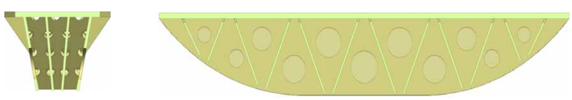

Figure 5: Shape of the optimized frame.

First eigenmodes and static deformation have been calculated by FEA, with the following boundary conditions: a fixation on the 4-frame supports and the inclusion of a model of the magnets as masses. When the frame shape was optimized, the full girder model with all the parts included in the model were simulated. The results of the FEA analysis are shown in Fig. 6.

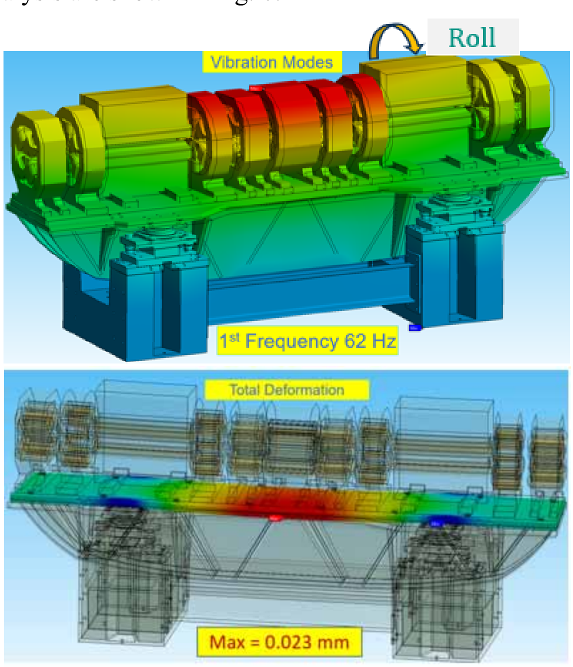

Figure 6: FEA results.

The horizontal alignment is foreseen to be implemented by a plate that will be adjusted in XY position on top of the frame by means of a push pull system with fine thread screws. Apart from that, it is foreseen a control of the relative position between girders by means of LVDT absolute encoders and limit switches. This is considered to be a need, as the stay clear area between the vacuum chamber and the yoke is very tight, and an interference can lead to stresses into in the vacuum pipe. The allowed range for this relative movement will have to be determined during the mock up phase, as it mainly depends on the design of the vacuum pipe.

TESTING OF THE PROTOTYPE

The objectives of developing this prototype are to evaluate the performance of the positioning system and the stability of an entire girder module, measuring ground vibration and vibrations induced by external excitation.

The prototype is designed in a modular way to be able to interchange spherical contacts, and leave sliding surfaces or impose mechanical restrictions between the plinths and the motion system, in order to evaluate the best performance of it. Assembly feasibility and easiness of transportation will also be evaluated as well for this prototype to learn from it and to optimize the assembly period of the full arrays of the new ALBA II machine.

ACKNOWLEGDEMENTS

The girder design team wants to acknowledge Filippo Cianciosi, Philippe Marion, Keihan Tavakoli, Jose Da Silva, Brad Mountford and Alejandro Crisol for the dedicated time on reviewing the design.

REFERENCES

[1] G. Benedetti, M. Carlà , U. Iriso, Z. Martí, and F. Perez, "Progress on the 6BA lattice for ALBA-II", in *Proc. IPAC'23*, Venice, Italy, May 2023, pp. 3098-3100. doi:10.18429/JACoW-IPAC2023-WEPL001

[2] F. Perez *et al.*, "ALBA II accelerator upgrade project status", in *Proc. IPAC'23*, Venice, Italy, May 2023, pp. 2582-2585. doi:10.18429/JACoW-IPAC2023-WEOGA1

[3] F. Cianciosi *et al.*, "The Girders System for the New ESRF Storage Ring", in *Proc. MEDSI'16*, Barcelona, Spain, Sep. 2016, pp. 147-151. doi:10.18429/JACoW-MEDSI2016-TUCA06

ISBN: 978-3-95450-250-9 ISSN: 2673-5520 doi:10.18429/JACoW-MEDSI2023-THPPP040

12th Int. Conf. Mech. Eng. Design Synchrotron Radiat. Equip. Instrum. MEDSI2023, Beijing, China JACoW Publishing
ISBN: 978-3-95450-250-9 ISSN: 2673-5520 doi:10.18429/JACoW-MEDSI2023-THPPP046

MECHANICAL DESIGN AND MANUFACTURE OF ELECTROMAGNETS IN HEPS STORAGE RING

L. Wu†, C. H. Li, S. Y. Chen, S. Yang, Y. D. Xu, Institute of High Energy Physics, Beijing, China

Abstract

The HEPS storage ring comprises 48 7BA (seven-bend achromat) cells. There are 37 independent magnets in every cell, of which 5 dipoles are permanent magnets and the rest of magnets are all electromagnets including quadrupoles, D-Q (dipole-quadrupole) combined magnets, sextupoles, octupoles and corrector magnets. These electromagnets with small aperture and high magnetic field gradient should achieve high machining and assembly precision. In October 2023, all storage ring electromagnets manufacturing have been completed. This paper mainly introduces the mechanical design, processing and assembly, and the manufacturing issues in the machining period.

INTRODUCTION

High Energy Photon Source (HEPS) is the first high-energy diffraction-limited storage ring light source in China which will be put into operation at the end of 2025. The electron beam energy of the storage ring accelerator is 6 GeV, which can provide 300 keV high-energy X-rays. HEPS storage ring comprises 48 7BA cells that are grouped in 24 super-periods, with a circumference of 1360.4 m and the natural emittance of 34.2 pm rad. Each 7BA cell has 37 independent magnets of various types and 22 sets of correction coils for generating correction fields. Table 1 shows the types and quantities of the magnets in one cell [1-2].

Table 1: Magnet Types and Quantities of One Cell

Magnet Type	Quantity per Cell	Quantity in Total
Longitudinal gradient dipole	5	240
D-Q combined magnet	6	288
Quadrupole	14	672
Sextupole	6	288
Octupole	2	96
Corrector	4	192
Independent magnet in total	37	1776

The longitudinal gradient dipoles adopt permanent magnet scheme, and the other magnets in HEPS storage ring are electromagnet. These electromagnets are characterized by high gradient, small aperture, high precision requirements and compact layout. The decrease of magnet aperture makes it difficult to manufacture and obtain high magnetic field precision. Compared with the usual medium or big aperture magnets, the high-order component of the magnetic field of the small-aperture magnet, especially the non-systematic magnetic field, is more sensitive to the machining and assembly accuracy of the pole. Starting from September 2019, on the basis of the research of HEPS-TF (Test Facility) magnet prototypes, the design, bidding and production of various types of magnets were officially launched, and by October 2023, all electromagnets were completed and delivered.

MECHANICAL DESIGN AND ASSEMBLY

Quadrupole and D-Q Combined Magnet

There are 20 quadrupoles and D-Q combined magnets per cell in the storage ring, for a total of 15 kinds. D-Q combined magnets are also quadrupoles in structure with their beam center deviates from the magnetic center at a certain distance during installation. In order to facilitate the installation of the magnet coil, they are designed as four part segmented poles.

According to the length and structure of the magnet, all quadrupoles are divided into three categories, including: Type I, type I+ (with correction coil), type II. And there are also three types of D-Q combined magnets: ABF1/4, ABF2/3 and BD1/2. The structures and main dimensions with the unit of millimeter are shown in Figure 1.

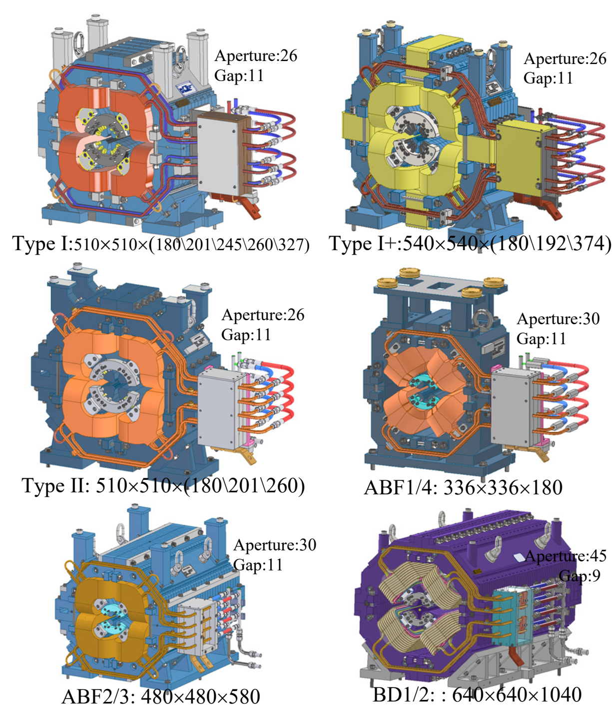

Figure 1: Structure of quadrupole, D-Q combined magnet.

† wulei@ihep.ac.cn

ISBN: 978-3-95450-250-9 ISSN: 2673-5520 doi:10.18429/JACoW-MEDSI2023-THPPP046

The magnet yoke of type I, type I+, ABF2/3 and BD1/2 is stacking laminations, which can reduce the manufacturing cost of the magnet and shorten the processing time. The laminations material is silicon steel sheet. According to the need of synchronous light extraction, type II quadrupoles are designed to process synchronous light extraction channels between the upper half and lower half yokes. The yoke of type II quadruple with the material of DT4 is processed by milling machine, and the magnetic pole is precision machining by EDM. 316L is used instead of ferromagnetic materials between the upper and lower yokes. The yoke of ABF1/4 use the same processing method for there are synchronous light extraction channel too.

Sextupole, Octupoles and Corrector

Every 7BA cell of HEPS storage ring has three kinds of sextupoles and a kind of octupoles: SD1/4， SF1/2, SD2/3 and OCT1/2. SD1/4 and SD2/3 are with correction coils.

The processing methods of sextuple and octupoles are milling and EDM (electrical discharge machining). They are divided into upper and lower yokes. All the poles of sextupoles and the middle two poles of octupoles are detachable. Figure 2 shows the structure of sextuple and octupole. Figure 3 is the corrector magnets with laminations yoke: FC1/2/3/4. The special structure is that the fixed plates at both ends of yoke is stainless steel with 5 mm thick.

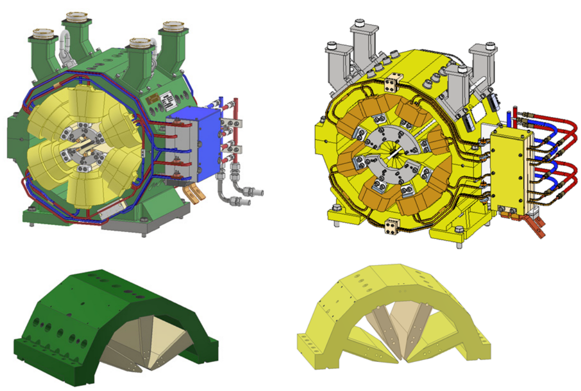

Figure 2: Structure of sextupole and octupole.

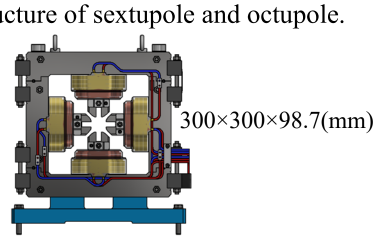

Figure 3: Structure of corrector.

The precision of pole space for the lamination assembly is better than 0.03 mm, and the precision of the magnet length is better than 0.25 mm. For the milling and EDM magnets, the precision of the pole space is better than 0.02 mm, and length error is less than 0.05 mm.

MAGNETIC FIELD QUALITY CONTROL MEASURES

The precision of mechanical manufacturing directly affects the magnetic field specifications. Magnets mainly controls the quality from the following aspects, including material, pole accuracy and repeatability accuracy.

Material

Maintain the consistency of the yoke material. The silicon steel sheet is punched after mechanical blending and magnetic blending. The plates of DT4 used in the same type of magnet are from the same furnace to ensure that the magnetic excitation performance of them are relatively consistent. The excitation performance of DT4 was tested and the magnetic performance annealing was carried out.

Pole Accuracy

The accuracy of the magnet pole face geometry, including the deviation of each point of the magnet pole face from the ideal position, the accuracy of the magnet aperture and the pole spacing meet the magnet tolerance (≤ 0.03 mm). For the lamination magnets, the punching accuracy and the stacking accuracy affect the pole face, so the effective measures are to improve the profile tolerance of the lamination (≤ 0.01 mm) and ensure that the straightness of the stacked laminations at the mating surfaces is smaller than 0.01 mm. Strictly control, monitor and maintain the positioning accuracy of the stacking mold. The mating surface between the yoke and the mold monitored at all times by a shim with a thickness of 0.02 mm. The laminations should be measured by Coordinate Measurement Machine, and it needs to be re-examined in batches. In addition, the magnet length error should be controlled smaller than ± 0.25 mm, the lamination coefficient should not be less than 98 %. For the machining magnets, milling and low speed wire EDM (electrical discharge machining) are adopted to process the pole. The tolerance is less than 0.02 mm, and the multi-poles of a single magnet are machined by one-time clamping to ensure the accuracy.

Repeatability Accuracy

The accuracy of the magnet aperture and pole space should meet the accuracy of ± 0.03 mm after split and reassembled at least three times because of the installation of vacuum chambers. The control measures are to reasonably arrange the cylindrical pins, use the pole clamps to fix the pole, control the bolt torque and bolting sequence. The specified torques on the assemble bolts is about 60N·m-80N·m. When the magnet is split, the mounting bolts are removed diagonally in order from the sides to the middle. And when the magnets are assembled, the bolts are tightened diagonally in order from the middle to the sides.

MAGNET DESIGN AND MANUFACTURING ISSUES

Filling Magnetic Material

In the prototype stage, under the design current, the magnetic field gradient of the lamination quadrupoles is lower than the design value, so the actual working currents is higher than the design current. After simulation analysis and discussion of physical and mechanical related personnel, the following improvement measures were carried out:

ISBN: 978-3-95450-250-9 ISSN: 2673-5520 doi:10.18429/JACoW-MEDSI2023-THPPP046

Reducing the gap between the long bolts of the pole and the stacked laminations (unilateral 0.05 mm); The nuts at both ends of the long blot, the fixing screws and dowels on the pole clamp were replaced by DT4 from stainless steel; A DT4 cap (Figure 4) is added outside the nuts; Magnetic annealing treatment is performed on the plates outside the laminations before processing. The final working current value is close to the design current.

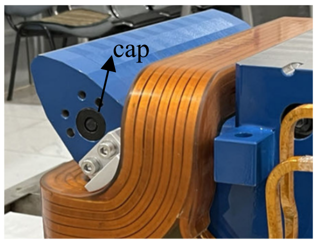

Figure 4: Cap outside the nut.

Optimize Welding Process

As the largest magnet in HEPS storage ring, BD1/2 is the most difficult to manufacture. When the BD1/2 prototype was developed, about 0.2 mm distortion of the pole mating surface in the stacking mold deformed after welding the fixed plate. Then, the welding process was optimized. As shown in the Fig. 5, the fillet weld is changed to downhand weld which is relatively easy to control, and the releasing stress groove is added correspondingly. The factory uses robot welding which can be more efficient and reduce deformation instead of manual welding. In addition, the stacking mold was improved to make the stress distribution more balanced.

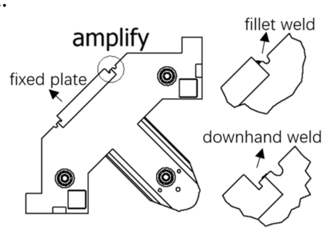

Figure 5: Optimize the welding process.

Dowel Installation

The dowel of the quadrupoles with correction coil which is shielded, should be paid attention to ensure positions. The dowel should be pre-installed before the installation of correction coil. After confirming the pole space meet the requirement, remove the upper half yoke and then install the correction coils.

Split Baseplates

Most of the magnets are supported by two split welded baseplates. During the processing, it was found that about 20 QF3/4 had a deviation of 1 ~ 2 mm in the mounting hole position for pre-drilling before welding the baseplates. The improvement measure is to confirm whether the position of mounting hole is correct when milling the bottom surface of the baseplates.

Temperature Switch

The temperature switch was a little far away from the pole in the initial design. In an accident during the sextuple magnetic measurement, the switch did not act immediately. After testing, the operating temperature of the switch is adjusted to 36 ± 3 °C, and three switches are added at the position close to the pole of sextupole. For D-Q combined magnets and quadrupoles, the operating temperature of the switch is adjusted to 43 ± 3 °C, and the installation position changed more close to the pole. Figure 6 shows the distribution of the switches in sextupole and quadrupole.

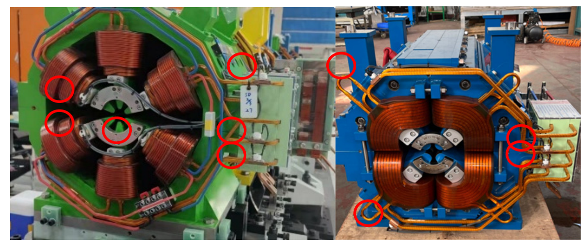

Figure 6: Switches in sextupole and quadrupole.

Magic Finger

The magic finger which is a fast and effective method of magnetic field harmonic compensation is designed on the pole to improve the high-order field component of the magnet. It is fixed by pole clamp, and its position can be adjusted in the magic finger groove. As a compensation method for magnetic field adjustment, the magic finger is only used as a remedial measure. Although the installation position of the magic finger is reserved on the pole of each magnet. Figure 7 is the magic fingers distribution. The physicists don't want to attach too much magic fingers on the poles. The manufacturer is required to meet the magnetic field specifications through high-precision processing and assembly. However, in the actual, some types of magnets can meet this requirement, such as QD2 and ABF2/3. However, there are also some magnets that need to use the magic finger to achieve the required specifications, such as QD7, QF5 and BD1/2. The number of magic fingers used per magnet is about 1-3. It was found that the qualified rate of lamination magnets is higher. The machining magnets may not be easy to achieve the required specifications only by processing due to the saturation of the magnetic properties of the yoke.

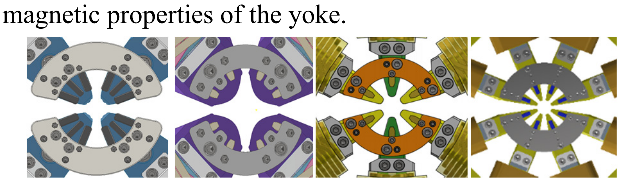

Figure 7: Distribution of magic fingers.

CONCLUSION

All the electromagnets manufacturing of HEPS storage ring have been completed. Magnetic measurement and installation are being carried out. Some experiences and lessons have been obtained in mechanical design and processing.

ISBN: 978-3-95450-250-9 ISSN: 2673-5520 doi:10.18429/JACoW-MEDSI2023-THPPP046

REFERENCES

[1] Y. Jiao *et al.*, "The HEPS project", *J. Synchrotron Radiat.*, vol. 25, pp. 1611-1618, 2018. doi:10.1107/S1600577518012110

[2] Y. Jiao, "Latest physics design of the HEPS accelerator", *Radiat. Detect. Technol. Methods*, vol. 4, p. 399, 2020. doi:10.1007/s41605-020-00212-x

ISBN: 978-3-95450-250-9 ISSN: 2673-5520 doi:10.18429/JACoW-MEDSI2023-THPPP047

NEG FILM DEVELOPMENT AND MASSIVE COATING PRODUCTION FOR HEPS*

Y. S. Ma†, F. Sun, T. Huang, Y. C. Yang, D. Z. Guo, H. Y. Dong, P. He
Institute of High Energy Physics, Beijing, China

Abstract

Massive production facilities of NEG coated vacuum chambers have been developed for HEPS in Huairou, Beijing, which based on the NEG coating prototypes of HEPS-TF. The facilities can achieve simultaneous coating of 16~20 vacuum chambers of HEPS including irregular shaped vacuum chambers. The pumping performance of the NEG coated vacuum chambers has been measured by test facilities. After heating at 200 °C for 24 hours, the highest pumping speed of H_2 is about 0.65 l/s·cm^2, and the highest capacity of CO is about 1.89×10^{-5} mbar·L/cm^2. The lifetime is more than 20 cycles of air exposure and re-activation. The pumping performance meets the design requirements of HEPS. Currently the NEG coated vacuum chambers are applied to the storage ring of HEPS.

Introduction

HEPS (High Energy Photon Source) was designed to be a fourth-generation synchrotron radiation light sources with the lowest emissivity and highest brightness in the world. One crucial technology is to coat non-evaporable getter (NEG) films on the inner wall of vacuum chambers of small aperture in order to meet ultra-high vacuum requirements.

The NEG coating is a deposition of a titanium, zirconium, vanadium alloy on the inner surface of the chamber, typically achieved through DC magnetron sputtering. The utilization of NEG coatings has been widespread in the fourth generation of light sources to meet the stringent vacuum requirements, primarily due to the low conductance of the vacuum chambers, like MAX-IV [1] and Sirius [2]. NEG coating have been massively empoyed in the straight sections of the LHC [3], approximately 6 km of vacuum chambers were coated with NEG film.

NEG Coating Development

A DC magnetron sputtering facility has been established at IHEP for the investigation of NEG coating since 2016, as depicted in Fig. 1 [4].

For achieving a uniform thickness distribution, the NEG coating chamber is equipped with a cathode made of twisted wires of high-purity (99.95 %) titanium (Ti), zirconium (Zr), and vanadium (V), each having a diameter of 1 mm. To maintain the proximity of the cathode wires to the chamber's axis, several ceramic spacers are strategically placed along the chamber's length, along with two adapters at the ends.

To create the necessary magnetic field, a solenoid with dimensions of 1500 mm in length and 280 mm in diameter is externally mounted on DT4. The ion pump is utilized to attain ultra-high vacuum (UHV), and the NEG bulk pump is employed to evacuate residual gases such as CO and H_2O to achieve UHV conditions.

The chambers are initially evacuated using a turbomolecular pump group, reaching a range of 10^{-9} mbar. They are then subjected to a 48-hour bake-out process at a temperature of 200°C, followed by a helium leak test to ensure their integrity before the coating process. A Residual Gas Analyzer (RGA) is utilized for monitoring residual gases during the coating process.

Prior to the coating process, thorough cleaning of the NEG-coated chamber with etching 50 µm and passivion is conducted to prevent any significant contamination or surface defects that may adversely affect the quality of the film.

During the coating process, krypton gas of high-purity (99.999 %) is used as the working gas, set at approximately 0.01 mbar. The chamber temperature is maintained at around 120 °C to facilitate the sputtering process.

Figure 1: Prototype of NEG coating facility.

Massive Coating Production for HEPS

Previously, high-quality NEG coating has been achieved by NEG coating prototypes. However, the circumference of the HEPS storage ring is approximately 1360.4 m, including about 1000 vacuum chambers to be coated. Therefore, massive production facilities has been developed to meet engineering requirements (see Fig. 2).

Except for the dipole-magnet vacuum chambers, which were made of 316L stainless steel, the other vacuum chambers in the storage ring were made of Cr-Zr-Cu alloy copper (C18150). To reduce the impedance of the stainless steel vacuum chambers, a 20 µm copper film has been coated on the inside. All of the Cr-Zr-Cu vacuum chambers, including those with a diameter of 22 mm, ante-chamber, and racetrack shape, with NEG coating is ongoing.

* Work supported by HEPS and HEPSTF
† mays@ihep.ac.cn

ISBN: 978-3-95450-250-9 ISSN: 2673-5520 doi:10.18429/JACoW-MEDSI2023-THPPP047

Figure 2: (a) Massive produce facilities of NEG coating, (b) Vacuum chambers were installed in parallel and series to massive coating.

The coating device A: Vacuum chambers are connected in parallel to 6 groups, each group of vacuum chambers length should be lower than 3.5 m, outer diameter is about 0.47 m.

The coating device B: Antechamber are connected in parallel to 4 groups, each group of vacuum chambers length should be lower than 1.5 m, due to its discharge difficulty.

Two setups of NEG coating have been built for vacuum chambers of HEPS at IHEP Lab. And a lot of test vacuum chambers have been coated, which shows that NEG film has good adhesion and thickness distribution.

Pumping Properties Evaluation

Given that the residual gases in the accelerator primarily consist of H_2 and CO (constituting approximately 99 %) and a smaller portion of Ar and CH_4, the pumping properties of H_2 and CO are of utmost importance when considering the NEG coating. To evaluate the performance of the NEG coating for accelerator applications, it is crucial to characterize its pumping speed and absorbing capacity.

The measurement of pumping speed and absorbing capacity is carried out using the transmission factor method, which was first introduced in NEG coating vacuum chambers by C. Benvenuti in 1999 [5]. The schematic diagram of the pumping speed measurement setup is depicted in Fig. 3. Following each activation cycle of the NEG coating, test gases are injected into the vacuum chamber using variable leak valves. The gases then pass through an orifice into the NEG coated pipe, where a significant portion of the gases is absorbed by the NEG coating. Two Residual Gas Analyzers (RGAs) are positioned at the ends of the pipe to monitor the pressure levels. By measuring the pressures P1 and P2 and calculating the ratio P2/P1, the sticking factor or pumping speed can be determined using mol-flow simulation.

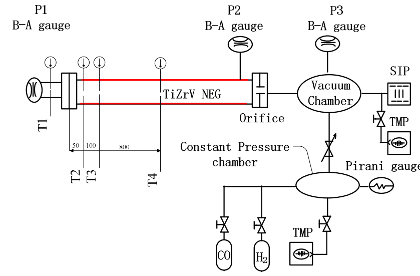

Figure 3: Schematic diagram of the pumping performance test facility.

The pumping speed of CO by the NEG coating is approximately 6-8 times higher than that of H_2, while the capacity of CO is much smaller than that of H_2. The pumping speed of H_2 and the capacity of CO are therefore considered to be more critical factors. Test results for the pumping speed of H_2 at different activation temperatures are presented in Fig. 4, and capacity of CO are presented in Fig. 5.The NEG coatings of TiZrV and TiZrVHf can be effectively activated at 160 °C. The pumping speed of H_2 increases as the activation temperature rises from 160 °C to 250 °C but decreases when the activation temperature exceeds 250 °C.

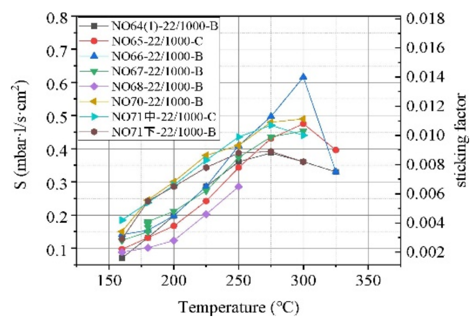

Figure 4: Pumping speed of NEG coating under different activation temperature.

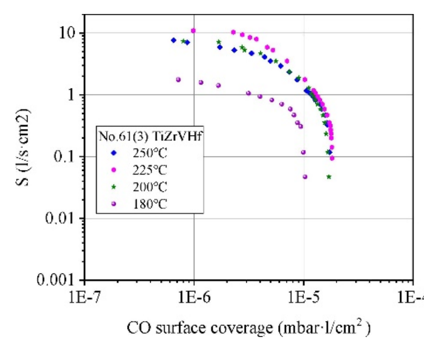

Figure 5: CO capacity of NEG coating under different activation temperature.

When all the absorption sites of the NEG coating are filled, its ability to pump gases diminishes. Molecules that contain oxygen atoms, such as H_2O, CO, O_2, etc., chemically adhere to the surface of the NEG coating, resulting in the formation of metallic oxides (M_xO_y). During the activation process, the metal oxides gradually decrease, and oxygen atoms diffuse into the bulk of the coating due to concentration gradients. This activation mechanism imposes limitations on the number of reactivation cycles that can be performed. Figure 6 presents the results regarding

ISBN: 978-3-95450-250-9 ISSN: 2673-5520 doi:10.18429/JACoW-MEDSI2023-THPPP047

the lifetime of a 1 µm thick NEG coating, highlighting its finite lifespan.

Massive produce of NEG coating presents a significant challenge, due the complex process and large number of vacuum chambers. Figure 2 shows the massive production facilities for HEPS, which is in Huairou, Beijing.

Due to impedance limitations of HEPS, it is crucial to adhere to a average thickness of 1um for the TiZrV NEG coating. However, this constraint imposes a limitation on the lifetime of the coating, allowing for fewer than 20 re-activation cycles.

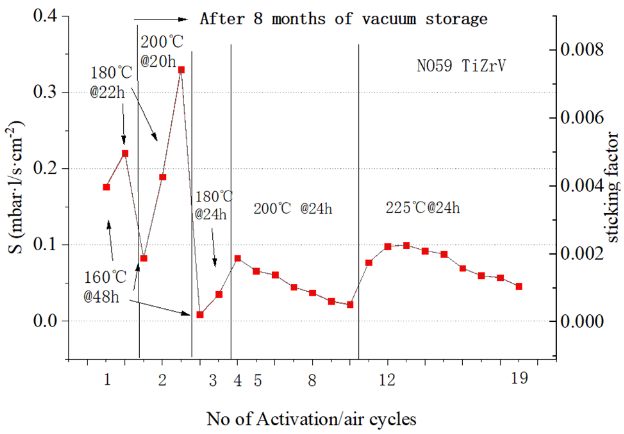

Figure 6: The lifetime of NEG coating of 1 µm thickness.

Thickness Distribution

To ensure a uniform distribution of thickness, one cathode is applied for round vacuum chambers with a 22 mm diameter. However, for ante-chambers and racetrack shape vacuum chambers, two cathodes are used as presented in Fig. 7.

Figure 7: Prototype of racetrack shape vacuum chamber, two cathodes were mounted along the axis direction.

The thickness distribution of the NEG coating along the axis of the vacuum chamber depends on factors such as the uniformity of plasma discharge pressure, magnetic field, and cathode position. Extensive experiments conducted in HEPS have demonstrated that achieving a distribution within ±30 % error is relatively straightforward.

CONCLUSION

As a fourth-generation synchrotron radiation light source, vacuum chambers with small apertures were employed for HEPS, making the performance of NEG coating is very crucial for its vacuum system. After years of development, the highly stability of the NEG coating has been achieved. Massive production of NEG coating is currently underway, and all vacuum chambers are expected to be completed within six months.

REFERENCES

[1] P.F. Tavares, E. Al-Dmour, A. Andersson, *et al.* "Commissioning and first-year operational results of the MAXIV 3 GeV ring ", *J. Synchrotron Radiat.*, vol. 25, pp. 1291-1316. doi:10.1107/S1600577518008111

[2] A.R.D. Rodrigues, J.F. Citadini, F.H. de Sá, R.H.A. Farias, et al., "Sirius Status Update", in *Proc. of IPAC2019*, Melbourne, Australia, May 2019, pp. 1381-1384. doi:10.18429/JACoW-IPAC2019-TUPGW003

[3] P. Chiggiato and P. Costa Pinto, "Ti–Zr–V non-evaporable getter films: From development to large scale production for the Large Hadron Collider", *Thin Solid Films*, vol. 512, pp. 382-388, 2006. doi:10.1016/j.tsf.2005.12.218

[4] Y. Ma, D.Z. Guo, P. He, B. Liu, and Y.C. Yang, "Preparation and Characterization of Non-Evaporable Ti-Zr-V Getter Films for HEPS", in *Proc. FLS'18*, Shanghai, China, Mar. 2018, pp. 125-127. doi:10.18429/JACoW-FLS2018-WEP2PT023

[5] C. Benvenuti, G. Canil, P. Chiggiato, *et al.*, "Surface cleaning efficiency measurements for UHV applications", *Vacuum*, vol. 53, pp. 317-320, 1999. doi:10.1016/S0042-207X(98)00364-9

ISBN: 978-3-95450-250-9 ISSN: 2673-5520 doi:10.18429/JACoW-MEDSI2023-THPPP049

REALIZATION OF A COMPACT APPLE X UNDULATOR*

L. Roslund†, K. Åhnberg, M. Al-Najdawi[1], L. Balbin, S. Benedictsson M. Ebbeni, M. Holz, H. Tarawneh, MaxIV Laboratory, Lund, Sweden
[1]also at SESAME, Allan, Jordan

Abstract

The APPLE X is a compact, elliptically polarizing undulator with a small round magnetic gap that provides full polarization control of synchrotron radiation at a lower cost and in less built-in space than comparable devices (Fig. 1). The APPLE X will be the source for MAX IV's potential future Soft X-ray Laser (SXL) Free Electron Laser (FEL). The mechanical design, finite element analysis optimization, assembly process, magnetic measurements, and shimming of a full-scale 2 m, 40 mm-period Samarium-Cobalt (SmCo) permanent magnet undulator are presented.

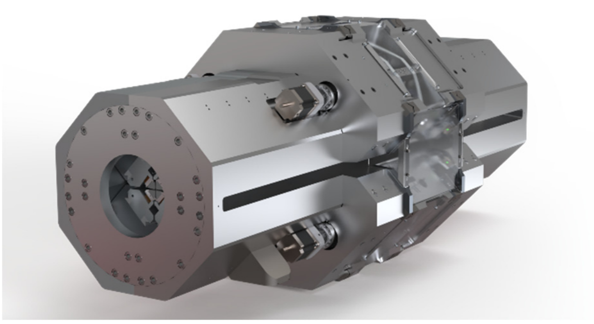

Figure 1: MAX IV APPLEX X prototype.

INTRODUCTION

A Soft X-ray Laser (SXL) beamline utilizing MAX IV Linear accelerator and the FEL technology is being designed at the MAX IV Laboratory and in collaboration between several Swedish Universities [1]. The baseline goal of the SXL beamline is to generate intense and short pulses in the range of 250 eV-1000 eV, and the conceptual design was reported in [2]. The set of features the undulator needs to fulfil includes being compact and light-weight, provide for independent gap- and phase adjustment, enable full polarization control, and K-value tuning via a radial gap operation. As a byproduct of the design, the undulator has the ability to create transverse field gradients as well as to neutralize its transverse field in a fixed-gap operation. An additional requirement is the ability to shim every individual magnet in the fully assembled undulator for magnetic fine-tuning. After a design review, in particular the shortening of the undulator length from 3 m to 2 m due to optimizations in the FEL design, prototyping of the APPLE X undulator is ongoing since late 2021 and has recently entered the assembly phase. The most recent key figures of the APPLE X undulator as it is being build are summarized in Table 1.

Table 1: Key Figures

Magnet Type	SmCo (B_r = 1.12 T)
Period Length	40 mm
Photon Energy	0.25-1 keV
Magnetic Gap Range	8.0-17.3 mm
Effective K range	3.9-1.51
Max. gap / min. eff. K	28 mm / 0.55
Undulator Magnetic Length	2 m
Weight	2800 kg

DESIGN

The main concept of the design is to handle the magnetic forces with an as tight and short mechanical circuit as possible. The reason being to reduce the lever arms and thus also the forces experienced by the structure of the device. Focus in the detailed design has therefore been to keep the size down on each step from magnet to keeper, shimming wedge, girder, motion wedge and strongback (Fig. 2).

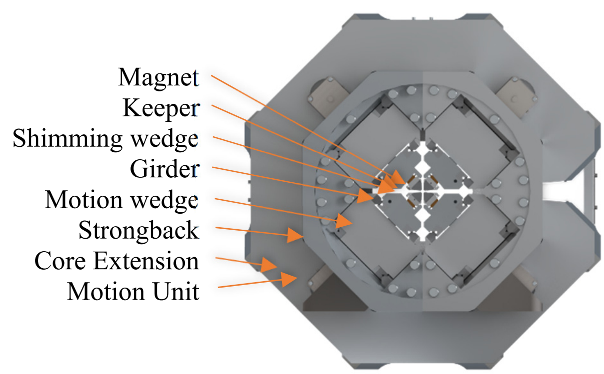

Figure 2: Outline of component stack

Nestled in through this is then the motion units (Fig. 3) one for each girder controlling radial motion and longitudinal motion on each individual girder. At first the design was a closed strongback in two half-moon parts forming a full circle around the inner parts, but due to a limitation in current magnetic measurement techniques the device is required to have a lateral opening on one side for access of a Hall-probe mounted on an arm moving along the device measuring the magnetic field. Initially the design was aiming at measurements being performed with a pulsed-wire system but will in the prototype accommodate a lateral opening for hall probe measurements and gives us the opportunity to commission a pulsed-wire system for magnetic measurements [3]. When successful, this new set-up will allow us to remove

* This project is co-funded by the MAX IV Laboratory and the European Union's Horizon 2020 research and innovation programme under grant agreement No 101004728 (LEAPS-INNOV)
† linus.roslund@maxiv.lu.se

ISBN: 978-3-95450-250-9 ISSN: 2673-5520 doi:10.18429/JACoW-MEDSI2023-THPPP049

the lateral opening in coming design reviews and thereby increase the structural integrity of the strongback. The lateral opening makes the device asymmetric and the strongback has become larger than the initial design but can possibly shrink again if the opening is removed in a future version. Actions to mitigate the deflection were introduced in the ends of the device where there was enough space for additional material in the form of stainless-steel rings. In the centre C-shaped external structures was introduced providing additional support and encapsule the motion units. These are referred to as core extension.

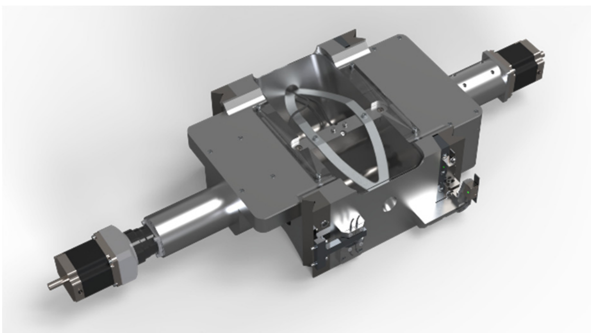

Figure 3: Motion Unit.

MATERIALS

The innermost parts were designed to be made of stainless-steel 316L to keep the strength up, the size down and the magnetic permeability close to 1.00. The strongback was due to its size and large cutouts designed to be made out of aluminium. The linear guides in the device are made out of tool steel 90MnCrV8 and provide additional stiffness to the parts but affects the magnetic field. This was simulated and the influence was determined to be low enough. During manufacturing the material Nitronic 50 was chosen as we had difficulty keeping the permeability low with 316L steel in the keepers. Initial test was promising but during mass production the permeability rose to as high values as 1.04. All keepers have due to this been annealed in vacuum oven and successfully been reduced to below 1.01.

It proved to be difficult to machine a 2 m long girder out of stainless steel that kept an overall straightness below 0.4mm. Due to delayed deliveries and failure to achieve the required tolerances and some errors in the machining of the girders new ones made of aluminium EN-AW 5083 was made which to a much higher degree fulfilled the required tolerances. In analysis additional deflection is estimated to be 5µm due to change of material.

MOTION

Each of the four girders holding an array of magnets can make radial and longitudinal motion. The longitudinal motion is supported by linear guides between the girder and the motion wedges. The longitudinal motion is performed by an arm extending through the strongback out to the motion unit where a roller screw adjust the position.

The radial motion is performed by the two motion wedges supported by linear guides to the strongback with an inclination of 1:10. The position of the wedges is adjusted in towards each other and away from each other to perform the radial move of the girder attached to them. With this configuration they provide additional support in the centre when the gap is smallest (Fig. 4). The motion is performed with arms extending out to the motion and a pair of roller screws connected with a gearbox to a single stepper motor. The motion unit moves radially together with the girder locked radially by the arms to girder and wedges. It is connected to the strongback by linear guides allowing the radial motion. Feedback of the radial position is also made at this interface between motion unit and strongback whilst longitudinal position is measured between the arm from the girder in respect to the motion unit.

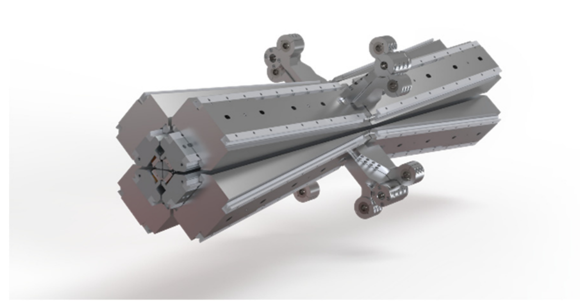

Figure 4: Motion wedges pulled together.

FEA

Static structural analysis has been made for the design looking at the deflection of the magnet arrays due to the forces they expose each other to. We have looked at three main cases. One with a strong pulling vertical force, one with a strong pulling horizontal force and one with a medium horizontal and vertical force (see Table 2).

Iterations of the analysis has been made to find a balance between the size and thickness of the girder keeping the lever arms short and then tuning the size of the strongback to an economical size where the performance is still within the required scope.

The deflection is worst for the first case where the vertical deflection of the magnet array is 32 µm concentrated in the centre of the device. It is on this case the focus of the analysis/design iterations has been (Fig. 5).

ISBN: 978-3-95450-250-9 ISSN: 2673-5520 doi:10.18429/JACoW-MEDSI2023-THPPP049

Table 2: Magnetic Forces per Girder

	Horizontal		
	Fx [kN]	Fy [kN]	Fz [kN]
Girder 1	1,1	0	-15,7
Girder 2	-1,1	0	-15,7
Girder 3	1,1	0	15,7
Girder 4	-1,1	0	15,7
	Circular		
	Fx [kN]	Fy [kN]	Fz [kN]
Girder 1	-7,5	0	-7,5
Girder 2	7,5	0	-7,5
Girder 3	-7,5	0	7,5
Girder 4	7,5	0	7,5
	Vertical		
	Fx [kN]	Fy [kN]	Fz [kN]
Girder 1	-15,6	0	1,1
Girder 2	15,6	0	1,1
Girder 3	-15,6	0	-1,1
Girder 4	15,6	0	-1,1

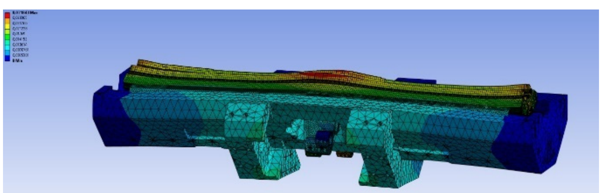

Figure 5: Deflection by magnetic forces.

The second case is very similar to the first case but have a slightly lower deflection due to that the strongback is stronger in this direction. The third case has medium radial forces. Between these cases we have low to medium longitudinal forces the deflection during these transfer cases is primarily dictated by the backlash of the motion unit which is expected to be low but have not been measured yet.

ASSEMBLY AND SHIMMING

The assembly of the device started slowly in the autumn of 2022 [4] and has due to delayed deliveries of the girders only recently passed the stage where all magnets has been mounted and received an initial magnetic shimming on the girders.

The assembly consists of three substages.

The motion units are mounted last on the finished device but is a self-contained unit with roller screws, gearbox and motors for radial and longitudinal motion. Four of these were assembled first as we awaited the delivery of the girders.

The girder is prepared with magnets mounted on keepers according to a sorting previously done. The nominal position of the magnets is first shimmed according to its physical position and then shimmed according to its magnetic position.

The strongbacks are prepared with motion wedges.

The final assembly is then performed by mating two girders in a jig sliding them into the strongback together as to avoid the alternating longitudinal forces between them. When both halves of the strongback are prepared the two are mated and then the C-shapes is slid in from each side. Last the motion units are attached and the device will receive a final tuning of the magnets as the field are now affected by the deflections of the total shape error and deflection. Since the shimming screws for the magnets are now embedded in the device a special couple of sticks has been developed which reach in to engage the screws in the small passages longitudinally present in the assembled device.

CONCLUSIONS

The design and analysis of the APPLE X undulator has been innovative and thorough. Manufacturing of the parts has been a rough experience with many delays but have at last been completed. The assembly of the APPLE X undulator is nearing completion. Initial shimming has been performed to a satisfactory level (Fig. 6). Tools and components have been manufactured assembled and tested. Ready for the final steps of the assembly which will take place in the end of 2023.

Figure 6: Shimmed girder.

REFERENCES

[1] S. Werin *et al.*, “The Soft X-Ray Laser Project at MAX IV”, in *Proc. 8th Int. Particle Accelerator Conf. (IPAC'17)*, Copenhagen, Denmark, May 2017, pp. 2760-2762. doi:10.18429/JACoW-IPAC2017-WEPAB077

[2] H. Tarawneh, P. N’gotta, L. Roslund, A. Thiel and K. Åhnberg, “Compact APPLE X for Future SXL FEL and 3 GeV Ring at MAX IV Laboratory”, in *Proc. IPAC'19*, Melbourne, Australia, May 2019, pp. 1833-1835. doi:10.18429/JACoW-IPAC2019-TUPRB072

[3] M. Ebbeni, M. Gehlot, M. Holz and H. Tarawneh, “A flexible approach on pulsed wire magnetic measurement method”, *Measurement*, vol. 199, p. 111438, 2022. doi:10.1016/j.measurement.2022.111438

[4] M. Holz, L. Balbin, M. Ebbeni, L. Roslund and H. Tarawneh, “Progress and challanges of the compact APPLE X undulator prototype at MAX IV”, in *Proc. IPAC’23*, Venice, Italy, May 2023, pp. 1233-1235. doi:10.18429/jacow-ipac2023-mopm110

ISBN: 978-3-95450-250-9 ISSN: 2673-5520 doi:10.18429/JACoW-MEDSI2023-THPPP050

OVERVIEW OF THE UNIFIED UNDULATOR SOLUTION FOR THE PolFEL PROJECT

J. Wiechecki†, National Synchrotron Radiation Centre SOLARIS, Kraków, Poland
P. Krawczyk, R. Nietubyć, National Centre for Nuclear Research, Otwock-Świerk, Poland
P. Romanowicz, D. Ziemiański, Cracow University of Technology, Kraków, Poland

Abstract

The PolFEL project, consisting of building a free electron laser, will be the first in Poland and one of the several sources in the world of coherent, tuneable electromagnetic radiation within the wide spectrum range from THz to VUV, emitted in pulses from femtoseconds to picoseconds, with high impulse power or high average power. The research infrastructure will include a free electron laser (FEL), a photocathode testing laboratory, end-stations, and laboratories necessary for the operation of the apparatus, and laboratories for users from the beamlines. The main FEL accelerator will consist of three independent branches, which will include chains of undulators adjusted to three different energy ranges: VUV, IR and THz. The main challenge was the unification of the final undulator solution, so that it could be applied to all three branches. The main goal of this approach was to save time, costs, human and material resources. The overview of issues and solutions related to the construction of undulators for the PolFEL project, and the challenges that had to be fulfilled to reach the final design, is presented in this publication.

PROJECT OVERVIEW

The PolFEL facility will be built at the National Centre for Nuclear Research in Otwock – Poland. The main goal of this infrastructure is to design, develop and build a free electron laser facility located in this part of Europe [1]. All activities will be supported by the largest research centres in Europe. This device will provide a wide wavelength range of electromagnetic radiation from 0.6 mm down to 60 nm. This will be possible since the linac will be split into three independent branches for different ranges: VUV, IR and THz.

Due to significant differences in the requirements towards the electron beam, which leads to the differences in geometry of the applied magnets, it is not possible to design a common solution for all three branches. However, to simplify the undulator design, increase safety, and reduce manufacturing and design costs it was assumed that the main frame for all undulators and drive systems would be unified.

BOUNDARY CONDITIONS

The PolFEL project requires three independent types of undulators with three different magnet configurations and quantities, as described in Table 1. This directly impacts the operating range of the undulators' girders and the forces acting on the i-beams. Each magnet must be settled on the girder within a certain position not exceeding the defined range of tolerances in the vertical direction and rotation.

On the other hand, each solution must be mechanically rigid, stable, and portable. The repeatability of the girder's movement and its position is the most critical factor that must be fulfilled to guarantee the stability of the electron beam. Furthermore, each undulator must have an opportunity to be aligned not only with the geological survey network but also to align its girders with the electron beam in real-time mode when the accelerator is fully operational.

Due to the huge amount of undulators that must be manufactured, each design must be reliable, simple, and cost-effective.

Table 1: Assumptions

Feature	VUV	THz	IR
Quantity	6	1	3
Period length [mm]	22	160	60
No. of effective periods per segment	73	8	25
Girder length [mm]	1644.5	1560	1605
Magnet material	$Nd_2Fe_{14}B$ $N_{45}UH$		
Magnet dimensions [mm] (W x H x L)	50/20 /5.5	100/100 /40	100/60 /15
Magnetic force acting on the beam in V direction [N]	300	4000	19000
Min / Max operational gap	8.5 / 13	100 / 200	22 / 60
Full open gap in [mm] where B=0 T	100	600	250
Vertical adjustment of the magnetic blocks [µm]	±100	±750	±450
Girders parallelism tolerance in z-axis (roll) [rad]	$<1.5\cdot10^{-3}$	$<1\cdot10^{-2}$	$<3.5\cdot10^{-3}$
Girders parallelism tolerance in x-axis (pitch) [rad]	$\pm5\cdot10^{-6}$	$\pm30\cdot10^{-6}$	$\pm15\cdot10^{-6}$
Girders parallelism tolerance in y-axis (yaw) [rad]	$\pm0.25\cdot10^{-3}$	$\pm0.5\cdot10^{-3}$	$\pm0.35\cdot10^{-3}$

CONSTRUCTION DETAILS

The high requirements put on each type of undulator forced an in-depth analysis. Many solutions have been taken into consideration [2-6], however, the most convenient and optimized idea was to unify the design of the undulators for all branches. This way, a common construction for all three devices has been designed, which

† jaroslaw.wiechecki@uj.edu.pl

ISBN: 978-3-95450-250-9 ISSN: 2673-5520 doi:10.18429/JACoW-MEDSI2023-THPPP050

required only minor modifications related to the magnet holders and jaws. The main goal of this approach was to identify the worst-case scenario, which means the most demanding working conditions with maximum force values. The final unified design took into consideration the largest gap openings (which are required in the THz device) and the highest acting loading (which were observed in the IR device) [7].

Main Support System

The main body of the undulator has a typical L-shaped frame that holds two movable girders with neodymium magnets (Fig. 1). Each of them is driven by two independent drive systems, consisting of servomotor, worm gear, and shaft with a nut attached to the girder. Four sets of rails with carriages placed on the side of the vertical beams are responsible for guiding both jaws with magnets in the vertical direction. The frame will be manufactured from standard S235JR construction steel grade, whereas two girders used as an undulator's jaws are made from aluminium. Elements that have direct contact with a strong magnetic field are made from stainless steel.

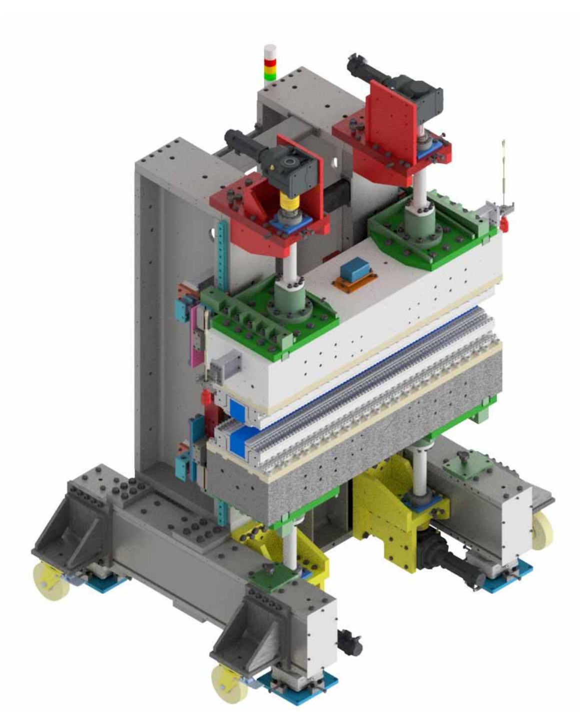

Figure 1: Undulator overview.

Four dismountable transportation wheels have been foreseen on the side planes of the frame, to facilitate movement in hard-to-reach areas. In its final position, each undulator will be placed on the alignment feet and anchored to the floor to protect against any unwanted movements.

The main supporting frame consists of two vertical pillars, settled on the horizontal H-shaped basis frame. Both pillars are shifted towards the centre of the construction due to the high demand for gap opening. This impacted the drive system's final location, which could not be placed in line with the vertical pillar and the horizontal perpendicular beam.

Magnet Keeper

The magnet keepers are the only elements that could not be fully unified. The wide range of forces, varying sizes of magnets, and various quantities of neodymium magnets impacted the design of the undulator. As presented in Table 1, there are many similarities between THz and IR magnets. Therefore, one common solution for both cases has been worked out based on the idea, that the single magnet block is placed in the centre of the aligning structure (Fig. 2). It is settled in the inner frame, which is susceptible to changes in position relative to the outer frame. Both collaborating elements are mutually positioned and fastened with four mounting screws, two of which also have an additional function to change the inner's frame and magnet position. The magnet block is secured at the top with additional handles (so-called fingers), which protect it against any unwanted movement under the influence of the interacting forces.

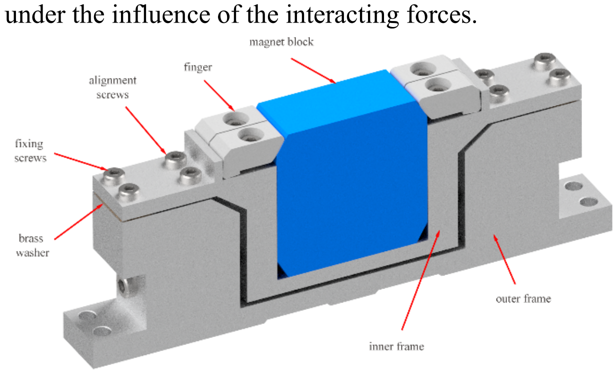

Figure 2: The concept of the magnet keeper (THz magnet keeper).

The positioning of the magnet block is done in two-stage sequence: rough adjustment by means of outer brass washers (located between inner and outer frames) and fine alignment using four inner mounting screws. Adjustment with the screws located closer to the magnet allows the magnet to tilt and adjust the vertical position within the small range. If the range is not sufficient, the height can be changed by exchanging the washer under the outer screw. This solution offers many possibilities and allows adjustments for both large and small ranges.

However, the above-presented solution cannot be implemented for a single VUV magnet due to its small dimensions. On the other hand, the promising possibilities offered by the THz magnet keeper have been observed in the experimental phase. Due to this fact, it was decided to keep the existing solution and modify the VUV magnets in such a way that they could be installed in a similar positioning system. The only modification that must be carried out is glueing two subsequent magnets to form a thick monolith. In this way, the functionality of the handles and the scope of their operation are being kept.

ISBN: 978-3-95450-250-9 ISSN: 2673-5520 doi:10.18429/JACoW-MEDSI2023-THPPP050

Magnet Grouping

Each magnet block, once placed inside its keeper, must be safely transported onto the girder, and fixed in the defined spot. The transportation of each magnet separately is associated with an increased risk of device damage and human injuries. Therefore, a single sub-assembly of the keeper is grouped into larger sets of three or five elements to facilitate assembly and increase installation safety and simplicity. Each block is fastened to an additional plate - an adapter, which is mounted in series onto the undulator jaws. Transport between the place of assembly and the final location will be carried out using a dedicated manipulator. This solution is applicable to all three types of undulators.

Drive System

The drive system is built out of four identical sets located at the top and bottom of the frame. Each pair is responsible for the vertical girder's movement. The single set includes a servomotor, worm drive, clutch, bearing and drive shaft with nut (Fig. 3).

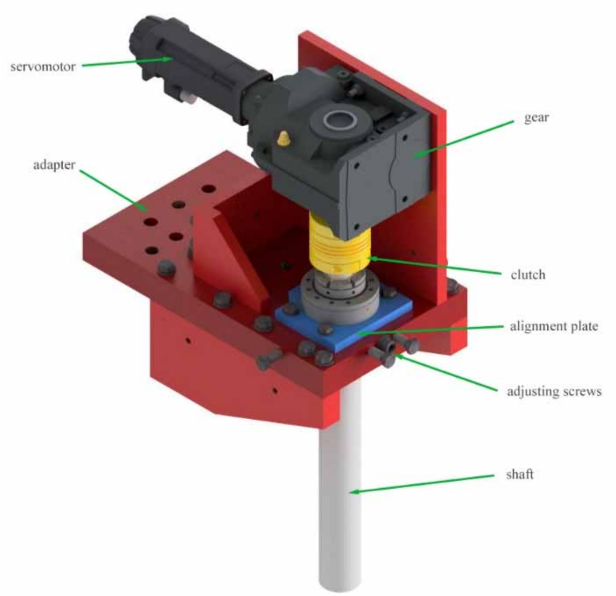

Figure 3: The layout of the drive system.

The sub-assembly will be settled on the adapter that allows position compensation in all 6 DOFs. For this purpose, an additional adjustable plate has been added that allows fine alignment of the screw position in the horizontal plane. The angular and vertical position compensation in small ranges can be modified using additional screws and washers. Through this solution, inaccuracies in manufacturing will be compensated and the lifetime of the drive system will be extended.

CONCLUSIONS

The PolFEL project turned out to be on many levels demanding and challenging project. Appropriate approach and planning of design work related to one of the most critical devices in the FEL infrastructure – the undulator, may contribute to the success of the entire project. Despite that work on undulators is still ongoing, a significant impact on cost reduction and timesaving can already be observed.

ACKNOWLEDGEMENTS

The authors would like to thank the undulator groups from Daresbury Laboratory and Paul Scherer Institute, for their support and constructive discussions.

REFERENCES

[1] G. Wrochna *et al.*, "On the PolFEL free electron laser project", *Synchrotron Radiat. Nat. Sci.*, vol. 8, pp. 1-7, Jul. 2009.

[2] E. Trakhtenberg *et al.*, "First prototype Undulator for LCLS Project – Mechanical Design and Prototype Lessons", in *Proc. 2nd Int. Workshop on Mech. Eng. Design of Synchrotron Radiation Equipment and Instrumentation Conf. (MEDSI02)*, Argonne, IL, USA, Sep. 2002, pp. 339-345.

[3] C. J. Milne *et al.*, "SwissFEL: The Swiss X-ray Free Electron Laser", *Applied Sciences,* vol. 7, July 2017. doi:10.3390/app7070720

[4] Berkeley lab, Engineering Division, https://engineering.lbl.gov/lcls-ii/

[5] LCLS-II Final Design Report, SLAC, CA, USA, Rep. LCLSII-1.1-DR-0251, 2015.

[6] J. Pflueger *et al.*, "Status of the undulator systems for the European X-Ray Free Electron Laser", in *Proc. 35th FEL Conf. (FEL2013)*, New York, NY, USA, 26-30 Aug. 2013, pp. 367-371.

[7] J. Wiechecki *et al.*, "Conceptual design of the THz undulator for the PolFEL project", in *Proc. FEL'22*, Trieste, Italy, 22-26 Aug. 2022, pp. 479-481. doi:10.18429/JACoW-FEL2022

ISBN: 978-3-95450-250-9 ISSN: 2673-5520 doi:10.18429/JACoW-MEDSI2023-THPPP052

DESIGN AND DEVELOPMENT OF COATED CHAMBER FOR IN-AIR INSERTION DEVICES

P.C. Wang*,[1], Y. Wang, University of Science and Technology of China,
National Synchrotron Radiation Laboratory, Hefei, China
L. Zhang†, J.M. Liu, X.Y. Sun, B.L. Zhu,
Y.S. Ma, S.M. Liu, B. Tan, Y.G. Wang, H.Y. Dong
Institute of High Energy Physics, Beijing, China
[1]also at Institute of High Energy Physics, Beijing, China

Abstract

The insertion devices (ID) is an important guarantee for further improving the performance of the light source and meeting the needs of different users. For in-air ID (undulator, wiggler, etc.), the magnetic structure is in the air, and there is a vacuum chamber in the middle of the magnetic structure to ensure the normal movement of the beam. In order to increase the magnetic field strength, the magnetic gap is generally relatively small. Factors such as small space, high precision, and low conductance all pose challenges to the design and processing of vacuum chamber. This paper introduces the development process of the vacuum chamber prototype of the coating type ID. Taking the application of the prototype in the HEPS project as an example, the simultaneous analysis and vacuum pressure distribution calculation are carried out, and the NEG coating scheme is proposed as an more economical means to obtain ultra-high vacuum. And the prototype NEG coating progress is introduced.

INTRODUCTION

The HEPS is a 6 GeV, green field light source, with the aim of generating X-ray synchrotron radiations with brightness of higher than 1×10^{22} ph/(s·mm^2·mrad^2· ‰BW) and photon energy of up to 300 keV at the designed beam current of 200 mA [1–5]. The ID is one of the important light-emitting components of the synchrotron radiations light source and meeting the application needs of different users [6, 7]. The main types of ID include in-air undulators/wiggler, in-vacuum undulators/wiggler, and polarization adjustable undulators. In-air IDs are usually used in applications where the photon energy is relatively low and the peak field strength is required for a line station that is not particularly high. The vacuum chamber is an important part of the ID, and its successful development is crucial. In order to obtain a vacuum chamber that meets the engineering needs, we carried out the vacuum chamber design, prototype development, NEG coating.

COATED CHAMBER FOR IN-AIR ID

Design Requirements and Layout

According to the layout of the linear section in the HEPS storage ring, specific requirements are proposed for the dimensions of the vacuum chamber along the Z-axis. This includes a distance of 5754 mm between BPMs at odd-numbered ends, which encompasses: 2 gate valves, 2 RF bellows, 2 transition vacuum chambers, and 2 front feeder coils with ID and their respective vacuum chambers. The experimental line stations necessitate a magnetic structure length of 5 m for these ID. Considering welding, installation space, and flange thickness requirements for the vacuum chambers, it is imperative that their Z-direction length exceeds 5 m.The layout of the 5 m in-air undulator (IAU) linear section is shown in Fig. 1.

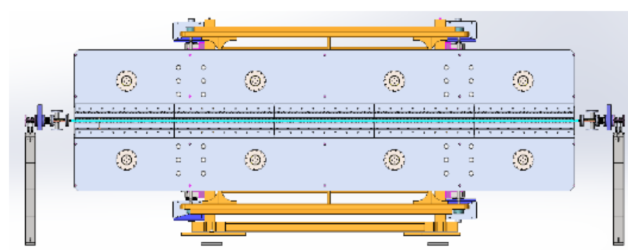

Figure 1: Layout of IAU.

According to the needs of the IAU, the parameters of the vacuum chamber can be proposed, as shown in Table 1.

Table 1: Parameters Vacuum Chamber

Parameter	Value
ID minimum gap in Y direction	11.0 mm
Straightness of vacuum chamber	±0.2 mm
Roughness of the inner surface	<Ra 0.8 µm
Thickness of vacuum chamber	9.3(±0.2) mm
Beam channel aperture size in Y direction	7.3(+0.05/-0.3) mm
Flatness of vacuum chamber	0.2 mm
Length of flange to flange	5376 mm
Cooling water velocity	<3 m/s
Static vacuum pressure	6.65×10^{-8} Pa
Dynamic vacuum pressure	1.33×10^{-7} Pa

Material Selection

Due to the characteristics of the undulator magnets, a vacuum chamber with narrow cross section (7.3 mm × 22 mm) and 5376 mm length is proposed. To achieve the necessary cross section geometry, mechanical strength, and vacuum

* wangpc@ihep.ac.cn
† zhanglei87@ihep.ac.cn

ISBN: 978-3-95450-250-9 ISSN: 2673-5520 doi:10.18429/JACoW-MEDSI2023-THPPP052

requirements, comparing the material properties of 6063-T5 and 6061-T6, 6061-T6 has higher strength and good corrosion resistance; 6063-T5 has better thermal conductivity, electrical conductivity, and extrusion performance. Therefore, after research and communication with the manufacturer, a custom 6063-T5 extruded aluminum profile was selected for the chamber prototype.

Synchrotron Radiation Power and Thermal Analysis

Aiming a safe performance for the chamber in accelerator environment under ultra-high vacuum, structural and thermal analysis were done using the software Ansys Mechanical.

After the synchronous light enters the vacuum chamber, it starts to hit the side wall of the vacuum chamber at 160 mm and continues to the outlet of the vacuum chamber, with a total power of about 391.7 W and cooling water on both sides. The support mode adopts a unilateral support mode, and a steel plate is installed on one side of the vacuum chamber to support the aluminum vacuum chamber. The steel plate is fixed on the slider and can slide along the Z direction; The support under the guide rail can adjust the height, pitch, etc.

Thermal simulation analysis of aluminum vacuum chamber was carried out. At the entrance of the vacuum chamber, the synchronous light power is large, and then the power gradually decreases with the increase of distance. The entrance is about 1 W/mm^2 and the exit is about 0.1 W/mm^2. The temperature is about 41.6 °C, which meets the requirements of use as shown in Fig. 2.

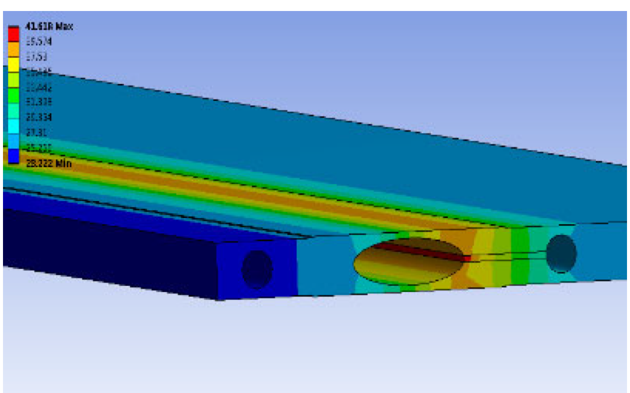

Figure 2: Thermal analysis of vacuum chamber.

The thermal-structural coupling analysis of the vacuum chamber was carried out. The stress of the coated vacuum chamber was 17.7 MPa, and the maximum displacement was 0.28 mm, which meet the usage requirement as shown in Fig. 3.

Pressure Distribution

Molflow software was used to calculate the pressure distribution. The outgassing data of 5×10^{-12} mbar·L/(s·cm^2) was selected. The dynamic gas output of the vacuum chamber by synchronous light was about 3.1×10^{-7} mbar·L/s, the

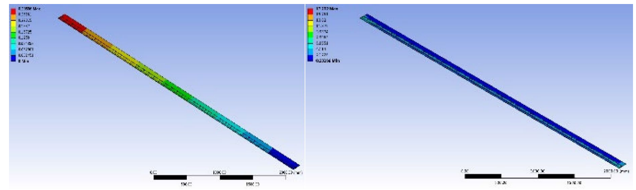

Figure 3: Structural analysis results.

suction adhesion coefficient of NEG film was 0.005, and the vacuum degree was about 5.8×10^{-8} Pa. The calculation results are shown in Fig. 4:

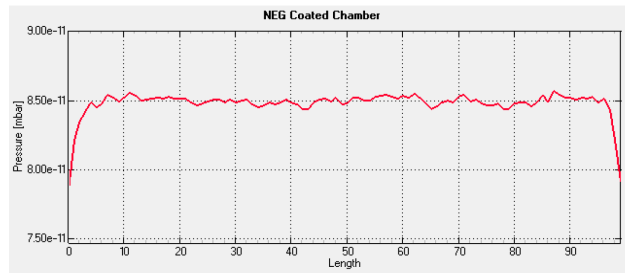

Figure 4: Vacuum pressure distribution.

PROTOTYPE MANUFACTURING

Aluminum tube is thermally extruded. The connection ports of cooling water channels and support plate are machined by numerical control machine tool. S.S.-Al transition plate are fabricated through explosion bonding in a domestic company. Ultrasonic flaw detection is used before the flange will be machined. Leak detection is carried out after the flange has been machined.

At the same time, the baking deformation measurement experiment is carried out, the stainless steel yoke plate is installed on the side of the vacuum chamber, and the yoke plate is fixed on the platform, and the aluminum vacuum chamber is in the suspended state. A plurality of heating plates (aluminum shell with heating wire inside) are uniformly distributed on the upper surface of the vacuum chamber, and a temperature sensor is placed next to it for temperature control, and the outside is covered with aluminum foil for heat preservation; Make a dial indicator in the middle position of the vacuum chamber and on the upper and lower surfaces of the elliptical hole to record the deformation data of the vacuum chamber. The test data show that the atmospheric pressure has no effect on the deformation of vacuum chamber after vacuuming. The main deformation is caused by thermal expansion at high temperature. However, the theoretical thickness of 9.3 mm and the expansion of 100 °C should be about 0.02 mm, which is much different from the actual result. After cooling from 180 °C to normal temperature, the deformation of the vacuum chamber is basically restored, and the shrinkage is 0.04 mm, which meets the needs of engineering use.The prototypes of aluminum vacuum chamber with a length of 5376 mm have been fabricated and tested, which meet the engineering requirements.

ISBN: 978-3-95450-250-9 ISSN: 2673-5520 doi:10.18429/JACoW-MEDSI2023-THPPP052

NEG COATING

The NEG coating scheme is proposed as an more economical means to obtain ultra-high vacuum.The prototype was coated aiming a film thickness of 1 µm. The cathode made from intertwisted 0.5 mm diameter Ti, Zr, V wires was submitted to a linear power density of 30 W/m, a magnetic field of 650 G and a vacuum pressure of 10 Pa. Cathode centering is critical for NEG coating of ID chamber. After NEG activation, the pressure was validated trough a measurement bench and the value of 3×10^{-8} Pa was achieved, as illustrated by Fig. 5. When the two angle valves of the two ion pump ports are closed, the vacuum is maintained only by the NEG film, and the vacuum degree can be maintained at 8×10^{-8} Pa. This shows that the NEG film coated on the inner wall of the in-air ID vacuum chamber has good performance.

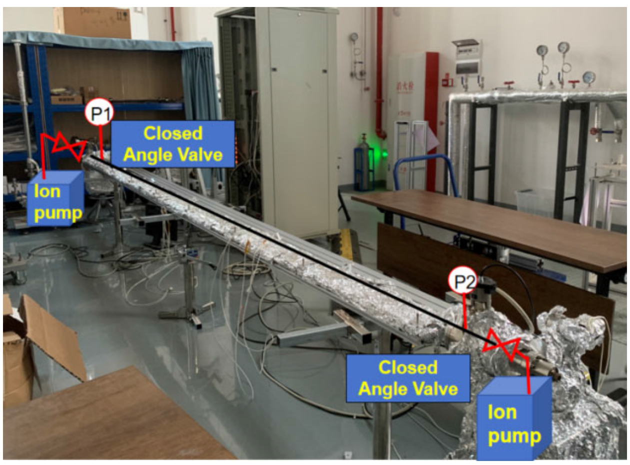

Figure 5: Ultimate pressure measurement bench.

CONCLUSION

The development process of the vacuum chamber prototype of the coating type ID was introduced. Taking the application of the prototype in the HEPS project as an example, the simultaneous light analysis and vacuum pressure distribution calculation were carried out. The prototypes of aluminum vacuum chamber with a length of 5376 mm have been fabricated and tested, which meet the engineering requirements. The NEG coating scheme is proposed and coated to obtain ultra-high vacuum. The vacuum is maintained only by the NEG film, and the vacuum degree can be maintained at 8×10^{-8} Pa. This shows that the NEG film coated on the inner wall of the insert vacuum chamber has good performance.

ACKNOWLEDGMENTS

The authors would like to thank KEYE Company in China for the machining of the chamber, vacuum group at CSNS in China for coating the NEG films.

REFERENCES

[1] Y. Jiao, "Latest physics design of the HEPS accelerator", *Radiat. Detect. Technol. Methods*, vol. 4, p. 399, 2020. doi:10.1007/s41605-020-00212-x

[2] Y.L. Zhao, H.F. Ji, X.H. Lu, *et al.*, "The high level applications for the HEPS Linac", *J. Instrum.*, vol. 18, p. P06014, 2023. doi:10.1088/1748-0221/18/06/P06014

[3] Y. Guo, N. Li, Y. Peng, *et al.*, "Study on the fringe field effects in HEPS booster", *Radiat. Detect. Technol. Methods*, vol. 7, pp. 382-386, 2023. doi:10.1007/s41605-023-00407-y

[4] C. Meng, N. Gan, D.Y. He, *et al.*, "Development Progress of HEPS LINAC", in *Proc. IPAC'22*, Bangkok, Thailand, Jun. 2022, pp. 2472-2475. doi:10.18429/JACoW-IPAC2022-THPOST016

[5] Y.Jiao, G. Xu, X.H. Cui, *et al.*, "The HEPS project", *J. Synchrotron Radiat.*, vol. 25, pp. 1611-1618, 2018. doi:10.1107/S1600577518012110

[6] H. Kitamura, "Recent trends of insertion-device technology for X-ray sources", *J. Synchrotron Radiat.*, vol. 7, pp. 121-130, 2000. doi:10.1107/S0909049500002983

[7] C.S. Hwang, J.C. Jan, C.S. Chang, *et al.*, "Development trends for insertion devices of future synchrotron light sources", *Phys. Rev. ST Accel. Beams*, vol. 14, p. 044801, 2011. doi:10.1103/PhysRevSTAB.14.044801

ISBN: 978-3-95450-250-9 ISSN: 2673-5520 doi:10.18429/JACoW-MEDSI2023-THPPP053

CLSI LINAC UPGRADE PROJECT

L.Lin, J. Campbell, S. Carriere, F. Le Pimpec, K. Wyatt
Canadian Light Source Inc., Saskatoon, Canada

Abstract

The Canadian Light Source Inc. (CLSI) is undertaking a significant Linear Accelerator (LINAC) injector Upgrade Project to enhance both the mechanical reliability and operational stability of Canada's primary research synchrotron facility. In late 2018, a critical gun failure led to a seven-month facility downtime. . This incident raised concerns that the original LINAC from 1980 continued to be a high risk to daily facility operations. Furthermore, several other mechanical systems within the facility, including cooling/heating water, HVAC, and certain aspects of the LINAC vacuum systems, have also aged, resulting in decreased reliability. The upgrade to the LINAC and its associated mechanical systems presents an opportunity to significantly improve the operational reliability of the entire facility.

INTRODUCTION

The CLSI's existing LINAC complex is based on a 1960s-era 2856 MHz RF, normal-conducting 250 MeV electron linear accelerator, capable of producing a 40 mA beam current. This accelerator is followed by an Energy Compression System (ECS) and a transfer line, which injects the beam into a Booster Ring, raising its energy to 2.9 GeV before the beam is injected into the Storage Ring. The LINAC operates in a multi-bunch mode at a rate of 1 Hz and can also work in a top-up mode, injecting a bunch train every few minutes. The existing LINAC is powered by a 220 kV DC thermionic electron source with bunching sections that achieve 13 MeV before injection into S-band traveling wave accelerating structures [1].

CLSI now requires a reliable, stable, and serviceable Injector, consisting of an electron source and a LINAC capable of generating a 250 MeV electron beam. This Injector should support a variable repetition rate ranging from 1 to 10 Hz. CLSI has acquired a "turnkey" Injector from Research Instrument GmbH (RI). This Injector will encompass various components, including the electron source, bunching sections, accelerator sections, RF plant, compression system, distribution system, vacuum systems, transport optics, diagnostics, control systems, and associated cooling/heating systems. The new Injector components are currently in the fabrication process, with a planned delivery date at CLSI in March 2024. User operations will resume after a 6-month downtime for installation and commissioning.

REQUIREMENTS

The new Injector, as shown in Fig. 1 [2], must meet the performance parameters outlined in Table 1 [1]. One of the key Injector characteristics is the requirement to remain operational even if one of the modulators feeding the RF structures fails. This feature will ensure continuous operation until the next maintenance period. The maximum repetition rate of the modulators and klystrons is set at 10 Hz.

Figure 1: The new injector.

Table 1: Injector Performance Parameters

Parameters	Values	Units
Accelerator Particles	electrons	n/a
Nominal Beam Energy	250	MeV
Minimum Beam Energy in any RF failure mode	180	MeV
Single Bunch Mode Beam charge in 500 MHz Bunch	1.5	nC
Single Bunch Mode Bunch Length 1 σ	1	ns
Multi Bunch Mode Beam charge per 500 MHz Bunch (adjustable)	>0.08	nC
Multi Bunch Mode Train Length, 5 to 70 bunches at 500 MHz (2 ns RF buckets)	10 to 140	ns
Center energy stability (pulse to pulse)	≤0.1	% (RMS)
Energy Spread	≤0.5	% (RMS)
Normalized Emittance (1s) (X or Y)	≤50	π mm·mrad
Injector Frequency adjustable to	3000.24 ± 0.030	MHz
Booster Synchrotron RF Frequency	500.04 ± 0.005	MHz
Injector Nominal Repetition rate	1	Hz
Modulators and Klystrons Repetition Rate	1 to 10	Hz
Pulse to pulse beam position variation (RMS)	0.2	mm
Pulse to pulse beam angle variation (RMS)	0.05	mrad

SCOPE

Research Instrument GmbH (RI) will provide a complete "turnkey" Injector. The Injector system will interface with several CLSI systems for which CLSI will be responsible, as illustrated in Fig. 2 [1].

As depicted in Fig. 2, there is a shared responsibility between RI and CLSI for both design and procurement. The hands-on installation and commissioning will be carried out by CLSI personnel under the guidance of RI's technical specialists.

PROJECT PLANNING

Project planning has been underway since late 2021. Through detailed schedule development, the project team, in coordination with RI, has established the "Dark Period" duration, set at six and a half months. The "Dark Period" has been divided into four major phases: dismantling of the existing injector, service integrations, installation, and

ISBN: 978-3-95450-250-9 ISSN: 2673-5520 doi:10.18429/JACoW-MEDSI2023-THPPP053

commissioning of the new injector. Prior to RI's arrival, CLSI will be responsible for dismantling all components and cable trays in the LINAC Hall, the adjacent hall, and modulator room. Additionally, all mechanical service upgrades are part of the Integration Phase. Installation and commissioning will be carried out by CLSI personnel, ranging from technical services to the accelerator physics group, under the leadership of RI specialists.

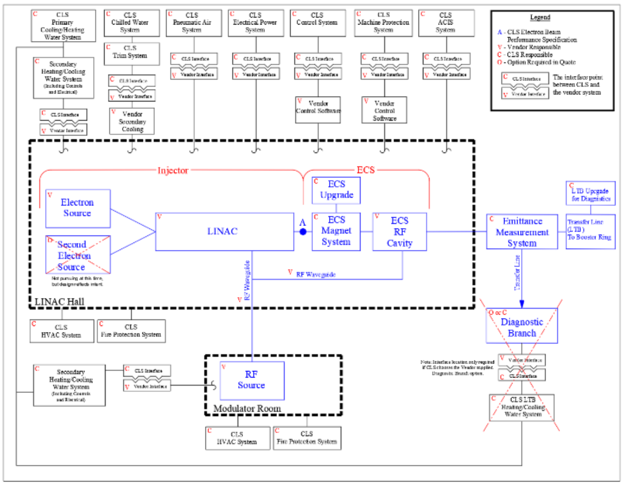

Figure 2: Scope of supply schematic of interfaces between RI and CLSI.

DESIGN

The primary design responsibility lies with RI as part of a "turnkey" project. CLSI's role has been to assist RI in the design of facility services to ensure seamless integration with existing systems and maximize cost-efficiency. A representation of the component and system design is depicted in Fig. 3 [2].

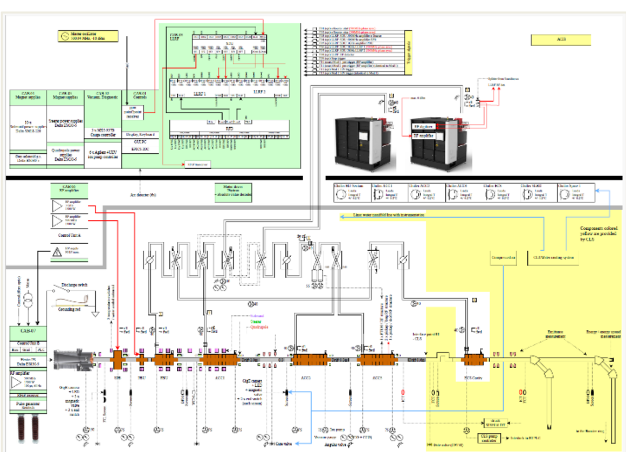

Figure 3: CLSI new injector block diagram.

Systems Designed by RI

RI's design incorporates the beam dynamics and lattice, the RF system in collaboration with CLSI for SLED [3] operation, and various RF structures, including the 3000.24 MHz ECS RF structure. This design also covers the related Mechanical, Electrical, and Control systems. RI has presented various design options in response to CLSI's requirements. One of these options use the SLED Technology. While this design is more intricate in terms of beam dynamics and synchronization for efficient acceleration, it offers the advantage of accommodating a 250 MeV LINAC in a more compact space, it reduces the number of required accelerating structures and RF modules (Klystron and solid-state modulator) to power them. These options alleviate the budgetary constraints and allow for the early procurement of critical spares, as recommended by RI.

RI's design also addresses the RF system. It features two solid-state modulators with klystrons for providing pulsed RF power to the 3 S-band traveling wave cavities. The power is distributed through a waveguide system. Fixed power splitters, adjustable amplitude shifters, and phase shifters are utilized to define the power level at each cavity. The odd frequency is driven by the need to synchronize the RF bucket of the storage ring at 500.04 MHz, which, although non-standard, closely aligns with the European 499.67 MHz (2998 MHz for S-band European).

CLSI Mechanical System Integration

The integration of the mechanical system has required close coordination and communication between CLSI and RI, as many of CLSI's systems are either closely adjacent to or directly interconnected with RI-supplied systems. Both parties have shared the CLSI facility's 3D models and survey coordinate system to facilitate communication and ensure seamless interface integration.

The new modulators will exist in the same room as the original modulators. As the LINAC is two floors below the modulator room level, CLS had to carefully define the envelopes of the floor tunnels between the modulator room and LINAC hall (for waveguide routing). Many of the RI supplied control cabinets will also exist in the modulator room and cable connections will run through these same floor tunnels, to the LINAC level.

Before RI arrives to oversee the installation, CLSI will carry out surveys, alignment, and grouting of accelerator floor stands. All accelerator structures and diagnostic sections are equipped with permanent magnetic survey nests, aiding in the alignment process. RI will provide CLSI with the fiducialization data for each section to ensure that each section is correctly positioned within the CLSI survey coordinate system.

The design of CLSI's mechanical services plays a crucial role in the project's integration. It has faced one of the most significant challenges in meeting the requirements of the New LINAC. RI initially proposed local air-cooled chillers for heating and cooling each RF structure. While this approach is straightforward in terms of design and control, it presented the challenge of requiring external air cooling. The existing Heating, Ventilation, and Air Conditioning (HVAC) system of the LINAC lacks the additional cooling capacity required. Currently, CLSI dose not have the budgetary flexibility to upgrade the HVAC system. The existing water service for the sections operates solely for heating purposes, rendering it unsuitable for reuse. RI initially

ISBN: 978-3-95450-250-9 ISSN: 2673-5520 doi:10.18429/JACoW-MEDSI2023-THPPP053

considered the chiller option to be the most cost-effective one, aligning with the project's schedule. Comprehensive evaluations were conducted on cooling and heating requirements, taking into account factors such as location, capacity, and the age of current systems. The design focus on maximizing the reuse of the current system to ensure cost efficiency. Given the substantial load that air-cooled systems would impose on the CLSI HVAC, the decision was made to shift to water-cooled chillers. To facilitate the operation of these water-cooled chillers, CLSI will renovate its chilled water system. The design of CLSI's mechanical services has been tailored to accommodate a 10 Hz repetition rate for future operation, requiring minimal modifications to the existing system, which currently operates at 1 Hz. Fig. 4 illustrates the Overall LINAC water system [4].

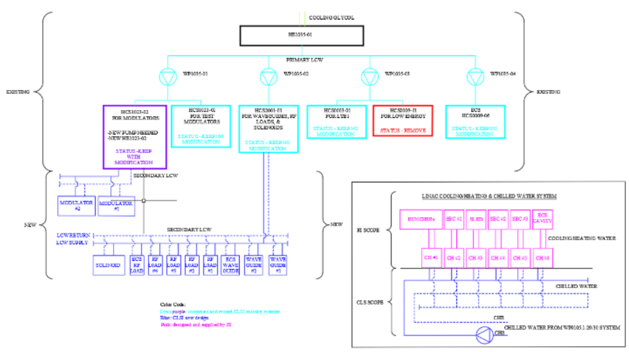

Figure 4: Overall LINAC water system diagram.

OUTCOMES

In December 2022, RI and CLSI reached an agreement on the overall design, and both institutions have either resolved or are finalizing details concerning the beam dynamics, vacuum systems, Low Level RF systems, controls and instrumentation, and machine protection systems. As an optional part of the project, RI is fabricating the ECS RF structure at the appropriate frequency and will supply the RF distribution waveguides. It was decided to retain the existing ECS system, as an insurance to guarantee the energy spread of the bunches for proper capture in the Booster ring. The energy spread, without the ECS, is theoretically expected to meet the specification in Table 1.

The design of mechanical service integration has effectively utilized current systems, including the LINAC primary cooling water system and the secondary cooling water for the modulator/klystron systems, with some necessary modifications. Substantial effort has been invested in the design of a chilled water system for the water-cooled chillers, considering the requirements of variable low flow and high-pressure applications.

The project's progress is proceeding smoothly, and it is adhering to the established timelines. The design is in the advanced stages of completion for both CLSI and RI. Procurements are currently in progress, with offsite fabrication in full swing from the RI side. The majority of the long lead procurements and manufacturing are on track to be completed by the end of 2023, with delivery to CLSI scheduled for early February 2024. Ceramics for the electron source, vacuum windows, and waveguides are critical path items and are expected to be delivered to CLSI in late February 2024.

CLSI successfully completed chilled water tie-in installations during the Fall 2023 outage, which has alleviated resource and schedule constraints during the "Dark Period". CLSI continues to work on the dismantling plan in conjunction with the installation and commissioning plans.

CONCLUSION

RI and the CLSI accelerator groups have reached a consensus on the injector's design, with operations initially planned at 1 Hz to align with operating licenses, with potential operation to 10 Hz later on. The design incorporates additional spacing to accommodate future needs and a second branch fed by a different electron source. These drift spaces could be harnessed in the future for adding more diagnostics to enable automation of operations and potentially extracting the beam for other applications, should the science division at CLSI require the use of electrons at different energies.

The mechanical service integration has efficiently leveraged current systems to achieve the most cost-effective solution. Chilled water system tie-ins were implemented during the Fall 2023 facility outage, saving time during the "Dark Period".

To date, the project remains on schedule and within budget. In the upcoming months, RI and CLSI will closely monitor the manufacturing and delivery of critical path items. The integrated schedule, jointly developed by RI and CLSI, instils confidence in CLSI that the established timelines can be met with the available internal CLSI resources.

ACKNOWLEDGEMENTS

The CLSI is funded by CFI, NSERC, NRC, CIHR, the Province of Saskatchewan, WED, and the University of Saskatchewan. The authors present this paper on behalf of the entire CLSI team encompassing CLSI engineering, Accelerator Operation Department, Control & Instrumentation and the Operation Technical Service. The authors express their appreciation for the exceptional teamwork between CLSI and Research Instruments.

REFERENCES

[1] CLSI, J. Campbell, 2022, "Technical Specification for a Linear Based Accelerator Injector", CLSI document# 1.8.27.1.Rev.4.

[2] RI, P. Biegun, 2022, "CLS LINAC Final Design Report", RI document# 6030-BP-15050-A.

[3] SLAC, Z. D. Farkas, "A Method of Doubling SLAC's Energy", 1973. https://s3.cern.ch/inspire-prod-files-0/068ed22dae5ba0bab8bcf19f9dcac092

[4] CLSI, 2023, "New LINAC Cooling/Heating Water Service Flow Diagram", CLSI drawing# LINAC\0296500.

ISBN: 978-3-95450-250-9 ISSN: 2673-5520 doi:10.18429/JACoW-MEDSI2023-FROAM01

DESIGN AND TESTING OF HEPS STORAGE RING MAGNET SUPPORT SYSTEM

Zihao Wang, Chunhua Li, Shu Yang, Lei Wu, Siyu Chen, Yuandi Xu, Shang Lu, Xiaoyang Liu, Minxian Li, Ningchuang Zhou, Haijing Wang
Institute of High Energy Physics, Chinese Academy of Sciences, Beijing, China

Abstract

Very low emittance of High Energy Photon Source (HEPS) demands high stability and adjusting performance of the magnet support. The alignment error between girders should be less than 50 µm. Based on that, the adjusting resolution of the girder are required to be less than 5 µm in both transverse and vertical directions. Besides, the natural frequency of magnet support system should be higher than 54 Hz to avoid the amplification of ground vibrations. To fulfill the requirements, during the development of the prototype, the structure was designed through topology optimization, static analysis, grouting experiments, dynamic stiffness test and modal analysis, and the rationality of the structure was verified through prototype experiments. During the tunnel installation, the performance of the magnet support system was again verified to be better than the design requirements through test work after installation.

INTRODUCTION

HEPS storage ring consists of 48 modified hybrid 7BA achromats. The circumference is 1360.4 m and each arc section is about 28 m. HEPS is designed with very low emittance of less than 60 pm·rad to provide much brighter synchrotron light. Precise positioning and stable supports of the magnets are required.

The alignment error between magnets on a girder should be less than 30 µm in horizontal and vertical direction, and that between girders should be less than 50 µm. Also, natural frequency of magnet support system should be higher than 54 Hz to decrease amplification of ground vibrations, which is very challenging. The requirements are listed in Tables 1 and 2 [1].

Table 1: Alignment Tolerance

Tolerances	Magnet to Magnet	Girder to Girder
Transverse	±0.03 mm	±0.05 mm
Vertical	±0.03 mm	±0.05 mm
Longitudinal	±0.15 mm	±0.2 mm
Pitch/yaw/roll	0.2 mrad	0.1 mrad

Table 2: Requirements for Support System

Parameter		Value
Resolution	Transverse	⩽ 5 µm
	Vertical	⩽ 5 µm
	Longitudinal	⩽ 15 µm
Natural frequency		⩾ 54 Hz

According to the layout of the magnets, there are 6 support units for the multipoles in each arc section, including 2 FODO modules, 2 MULTIPLET modules and 2 QDOUNLET modules, as shown in Fig. 1. The adjacent multipoles share one girder and are seated on the plinths through adjustable wedge mechanisms, while the 5 longitudinal dipoles are bridged between the plinths.

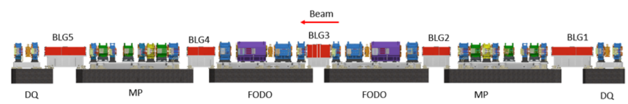

Figure 1: One arc section(1/48).

Stringent alignment accuracy requests high adjusting resolution of the girders. Table 2 shows the requirements. The resolution should be better than 5 µm in transverse and vertical directions and 15 µm in longitudinal direction.

DESIGN OF THE SUPPORT SYSTEM

The support system is designed as Fig. 2 shows. The girder should be capable of moving in 6 dimensions and the adjusting mechanisms are designed with 6 sets in vertical direction, 2 sets in transverse and 1 set in longitudinal direction. Each magnet is supported by a special adjusting mechanism to realize the three-direction adjustment, in which the sextupole is supported by the mover, which is able to realize the online adjustment.

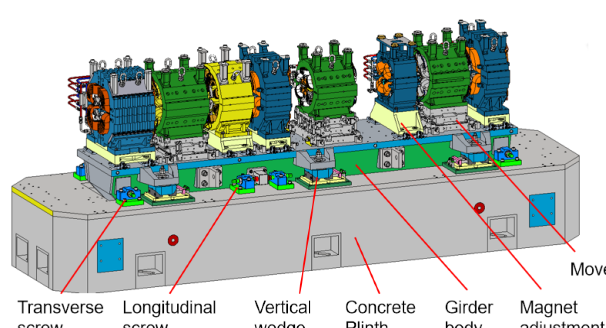

Figure 2: Support system.

Girder Body

After pre-simulation optimization [2], the effects of different structural parameters of the girder body on its deformation and natural frequency are analyzed, and the optimal stiffness is obtained by optimizing the shape of the cross-section and the distribution of the stiffeners. The structure of

ISBN: 978-3-95450-250-9 ISSN: 2673-5520 doi:10.18429/JACoW-MEDSI2023-FROAM01

the girder body is a six-point support box structure as shown in Fig. 3, and the material is HT350, which has higher structural damping, less residual internal stress, and more stable long-term dimensions.

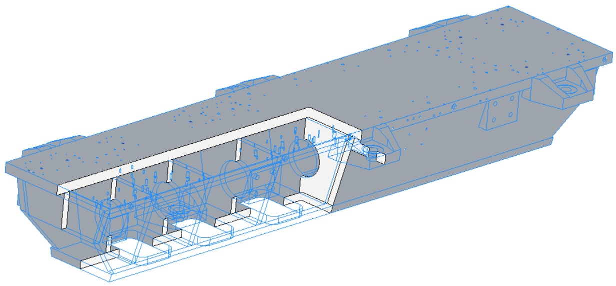

Figure 3: Girder body.

Plinth

With the advantages of good stability and low cost, concrete plinth is adopted by many synchrotron accelerators [3, 4]. The normal Elastic modulus of concrete is about 30 GPa, which is relative low to resist deformation. So high Elastic modulus recipe was developed and the sample achieved 53 GPa. The plinth is a reinforced concrete precast structure, which is designed to be groove shape to match the girder installation, as shown in Fig. 4.

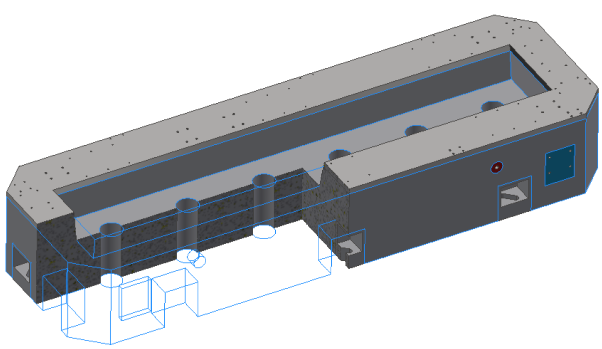

Figure 4: Plinth.

Support Components

In order to fulfill the pre-alignment and stability requirements, the support system is hierarchical adjusted of girder and magnets. High stiffness wedges are used as mechanisms for supporting and vertical motion, as shown in Fig. 5. The top surface of the wedge is equipped with a spherical disc to compensate for the angle change during alignment operation and keep contact of the interface. It is beneficial to guarantee the stiffness and avoid joint stress.

Sextupoles in the storage ring of HEPS will be adjusted based on beam trajectory. The mechanical design of a beam-based alignment sextupole mover should be developed. The motion accuracy of the mover should be better than 5 µm under 450 kg load of sextupoles. After preliminary prototype development, the structure of the mover was finalized as a 3-layer sliding wedge structure [5]. The movement range

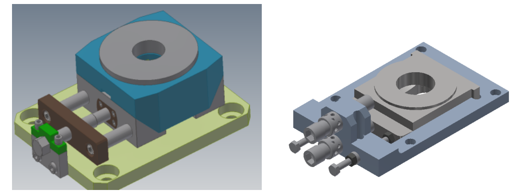

(a) Girder body adjustment (b) Magnet adjustment

Figure 5: Vertical adjustment.

is required to be ±0.3 mm in both horizontal direction and vertical direction.The yaw and roll should be less than 3”, and the pitch should be less than 2”. The horizontal displacement during vertical movement, which is called coupled error, should be less than 15 µm.

TEST OF THE SUPPORT SYSTEM

Plinth Grouting Experiment

In order to analyze the effect of foundation dimensions and grouting process on the natural frequency of the plinth, finite element simulation is used to compare and analyze the simulation and measured results for each working condition. The modal analysis module of finite element software is used to simulate the test results of different working conditions by taking the elastic foundation stiffness coefficient as the only variable. It should be added that: in the case of the same foundation, the size of the stiffness coefficient reflects more the influence of different connection method, in the case of the same connection method, the size of the stiffness coefficient reflects the influence of the foundation dimensions.

According to the experimental and simulation results of different working, the following conclusions are obtained: (1) with the same foundation and different connection methods, the epoxy secondary grouting results have higher stiffness coefficients and higher measured results, as shown in Fig. 6. (2) with the same epoxy secondary grouting method, different foundation dimensions, the area of the foundation and the thickness of the foundation have an effect on the stiffness coefficients, as shown in Fig. 7. (3) in the same foundation, the epoxy secondary grouting connection method has good repeatability, as shown in Fig. 8. Finally, the secondary

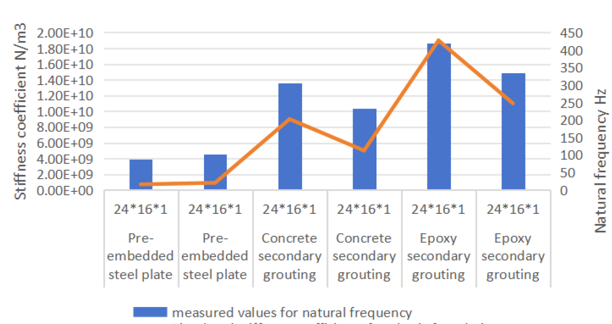

Figure 6: Same foundation dimensions and different connection methods.

ISBN: 978-3-95450-250-9 ISSN: 2673-5520 doi:10.18429/JACoW-MEDSI2023-FROAM01

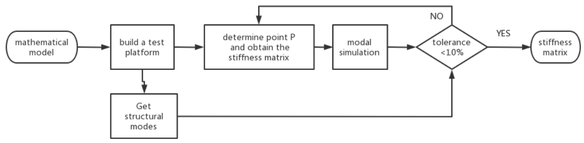

Figure 7: Flow chart.

$$\begin{bmatrix} m & & & & mR_{cp,z} & -mR_{cp,y} \\ & m & & -mR_{cp,z} & & mR_{cp,x} \\ & & m & mR_{cp,y} & -mR_{cp,x} & \\ & -mR_{cp,z} & mR_{cp,y} & I_{xx,p} & & \\ mR_{cp,z} & & -mR_{cp_x} & & I_{yy,p} & \\ -mR_{cp,y} & mR_{cp,x} & & & & I_{zz,p} \end{bmatrix} \begin{bmatrix} \ddot{x}_p \\ \ddot{y}_p \\ \ddot{z}_p \\ \ddot{\theta}_x \\ \ddot{\theta}_y \\ \ddot{\theta}_z \end{bmatrix} = \begin{bmatrix} K_{xx} & & & & & \\ & K_{yy} & & & & \\ & & K_{zz} & & & \\ & & & K_{\theta_x\theta_x} & & \\ & & & & K_{\theta_y\theta_y} & \\ & & & & & K_{\theta_z\theta_z} \end{bmatrix} \begin{bmatrix} x_p \\ y_p \\ z_p \\ \theta_x \\ \theta_y \\ \theta_z \end{bmatrix}$$

Figure 8: Stiffness matrix equation.

grouting method of epoxy-based grout was determined as the connection method between the storage ring plinth and the ground.

Modal Test

Free boundary constrained modal testing of the plinth, together with simulation is able to back-calculate the modulus of elasticity and thus assess the construction quality of the pedestal. The free boundary constraint modal design requirements for the plinth are shown in the Table 3.

Modal testing of grouted plinths is necessary during the bulk installation process to detect problematic plinths in time for timely treatment. The modal design requirements for grouted plinths are shown in the Table 3.

All the plinths are measured and the results fulfill the design requirements. The simulation and measurement results match well.

Support Components

The stiffness of the support components has an important influence on the stability of the support system, and the accuracy of its value determines the accuracy of the modal simulation results. Through the dynamic stiffness test, the stiffness matrix of the girder and magnet vertical adjustment mechanism is obtained, so as to get an accurate simulation model of the support system, which in turn provides conditions for the subsequent structural modification.

Test Method

Based upon rigid-body dynamics and frequency response function measurements, the method allows simultaneous determination of stiffness components in six coordinate directions (three translations, three rotations), resulting in a 6×6 stiffness matrix for the joint [6]. The accuracy of the stiffness matrix is then verified through finite element simulation by comparing the frequencies and vibrate shapes of the modal test and simulation results. The flowchart, formulas and test system are shown in Figs. 9 to 11.

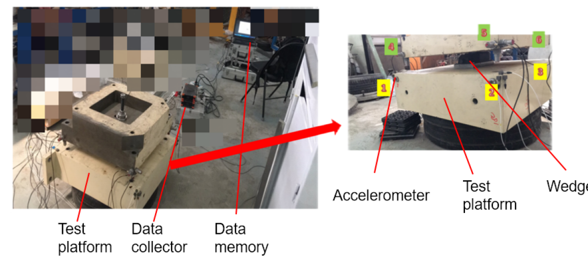

Figure 9: Test system.

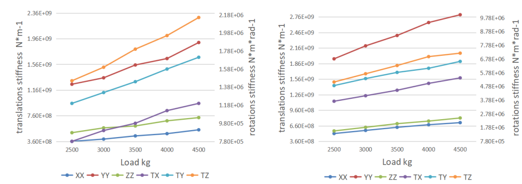

(a) Girder body adjustment (b) Magnet adjustment

Figure 10: Stiffness versus load curve.

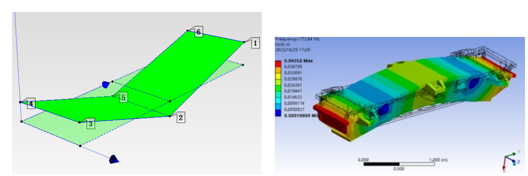

(a) measurement (b) simulation

Figure 11: Vibration shape.

Test Result

The stiffness matrices of the two adjusting mechanisms were tested separately and the results are shown in Fig. 12, where the values of the stiffness in each direction vary with the load.

Girder Body Modal Test

Girder body is a casting, and the material properties of each batch are different, so in the process of mass production, the free boundary condition modal test needs to be carried out on the girder body arriving from each batch. The results are consistent with the simulation results, as shown in Figs. 13 and 14. It fulfills the requirements of engineering use.

Motion Performance Test

Based on the installation requirements of the support unit, the motion performance test of the girder includes adjustment resolution, motion precision and locking offset [7]. As shown in Fig. 13, two dial gauges are fixed at each support points of the girder to monitor transverse (X), vertical (Y) and longitudinal (Z) offset. The dial gauges reading show that the girder can be operated by 1 µm per step in all three directions.

The motion precision of the girder is largely determined by the coupling of the motion. In the actual alignment process,

ISBN: 978-3-95450-250-9 ISSN: 2673-5520 doi:10.18429/JACoW-MEDSI2023-FROAM01

Table 3: Plinth Measurement Data

Type	No.	Free BC frequency Hz				Grouted frequency Hz
		design	Measured mean value	Measured max value	Measured min value	Measured mean value
MP	96	≥120	144	154	135	428 Hz
FODO	96	≥150	177	187	166	452 Hz
DQ	96	≥590	629	666	599	585 Hz

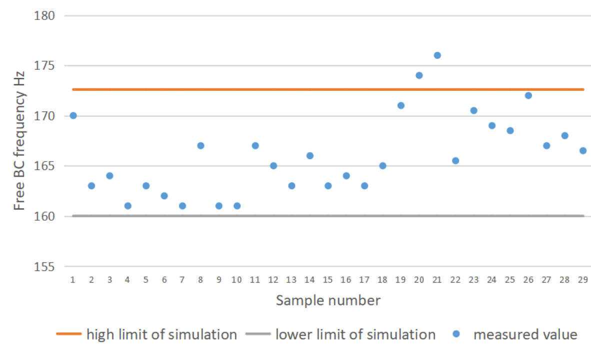

Figure 12: Free BC frequency measured value.

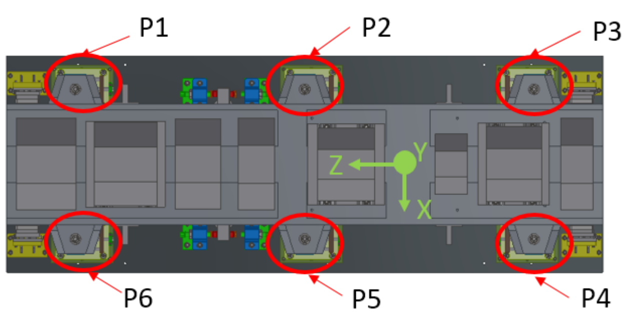

Figure 13: Schematic diagram of measuring point.

the vertical position is adjusted firstly, the coupling amount can be compensated in the subsequent horizontal adjustment. Therefore, the test mainly focuses on the motion coupling in horizontal adjustment.

In the test, 20 µm was used as the motion step, and the change of the dial gauges reading is recorded. The moving precision results are shown in Fig. 14. It can be seen that the moving errors of each measurement point in 3 directions are all less than 5 µm.

The motion coupling result in horizontal adjustment is shown in Figs. 13 to 14, and the position variation is less than 3 µm.

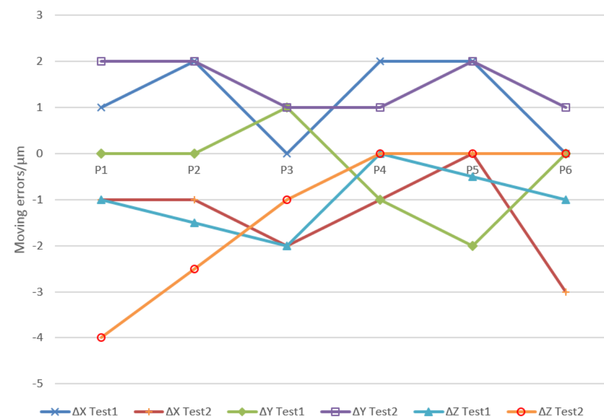

Figure 14: Motion precision test result.

Stability Testing

Modal testing was performed on the units after installation into the storage ring tunnel to measure their stability. Modal testing was completed for 204/288 units, results are shown in the Table 4, and the results were better than the design requirement of 54 Hz.

CONCLUSION

The requirements of HEPS storage ring magnet support are very challenging. The girder body and magnet hierarchical adjustment structure provides structural support for the realization of alignment accuracy, and high stiffness is a key concern of the structural design process. The plinth grouting experiment determines the engineering construction program of epoxy-based secondary grouting. The paired use of modal testing and simulation can obtain a more accurate value of the stiffness of the adjustment mechanism. The motion performance test results of the prototype provide a basis for the smooth implementation of the alignment process while verifying the adjustment performance of the support system. The support system test results of the tunnel show that the performance fulfill the design requirements.

Table 4: Support System Measurement Results

Typology	No. of tests	Measured mean value	Measured max value	Measured min value
MP	69	99.7 Hz	106 Hz	90 Hz
FODO	47	75.9 Hz	82 Hz	70 Hz
DQ	88	104.7 Hz	116 Hz	94 Hz

ISBN: 978-3-95450-250-9 ISSN: 2673-5520 doi:10.18429/JACoW-MEDSI2023-FROAM01

REFERENCES

[1] HEPS preliminary design report.

[2] C. H. Li *et al.*, “Design and Progress of Mechanical Support in HEPS”, in *Proc. IPAC'19*, Melbourne, Australia, May 2019, pp. 4180–4182. doi:10.18429/JACoW-IPAC2019-THPTS034

[3] Brian Norsk Jensen, “The MAX IV stability approach – From meters of clay to nanometers of optical stability”, in *2nd Swedish-German Workshop on X-Ray Optics*, Berlin, Germany, April 2015.

[4] J. T. Collins, H. Cease, S. J. Izzo, Z. Liu, J. Nudell, and C. A. Preissner, “Preliminary Design of the Magnet Support and Alignment Systems for the Aps-U Storage Ring”, in *Proc. MEDSI’16*, Barcelona, Spain, Sep. 2016, pp. 87–89. doi:10.18429/JACoW-MEDSI2016-MOPE34

[5] Lei Wu *et al.*, “Design and Test of the Beam-Based Alignment Sextupole Experimental Mover Prototype for HEPS”, *Radiat. Detect. Technol. Methods*, vol. 5, pp. 570–575, 2021. doi:10.1007/s41605-021-00287-0

[6] P. Becker *et al.*, “Using rigid-body dynamics to measure joint stiffness”, *Mech. Syst. Signal Process.*, vol. 13, no. 5, pp. 789–801, 1999. doi:10.1006/mssp.1999.1232

[7] Chunhua Li *et al.*, “Design and test of support for HEPS magnets”, *Radiat. Detect. Technol. Methods*, vol. 5, pp. 95–101, 2021. doi:10.1007/s41605-020-00223-8

ISBN: 978-3-95450-250-9 ISSN: 2673-5520 doi:10.18429/JACoW-MEDSI2023-FROAM02

VACUUM SYSTEM OF SPS-II: CHALLENGES OF CONVENTIONAL TECHNOLOGY IN THAILAND NEW GENERATION SYNCHROTRON LIGHT SOURCE*

T. Phimsen†, S. Boonsuya, S. Chitthaisong, P. Sunwong, S. Prawanta, S. Chaichuay, K. Sittisard, T. Pulampong, S. Srichan, N. Juntong, P. Sudmuang, P. Klysubun
Synchrotron Light Research Institute, Nakhon Ratchasima, Thailand

Abstract

Siam Photon Source II (SPS-II) is Thailand's first 4th generation synchrotron light source. It not only provides high-energy and high-brightness synchrotron radiation for both academic and industrial research after its completion, but it also strategically aims to strengthen the Thai industrial community during the design and construction period. The vacuum system is expected to play a crucial role in enhancing the country's manufacturing capability. Most of the main components in the system are planned to be domestically fabricated through technology transfer. Instead of using NEG coating technology, the vacuum system design of the SPS-II storage ring is based on conventional technology, leveraging the potential and expertise of the Thai industry. This paper reviews the challenges and adaptations made in the traditional design of the dense DTBA magnet lattice, considering magnet aperture limitations. The vacuum chambers and bending magnets have been modified to accommodate IR beamlines, which are included in the second-phase plan. The pressure profile of the vacuum system in the storage ring is evaluated, and the progress of the overall vacuum system of SPS-II is described.

INTRODUCTION

Siam Photon Source II (SPS-II) is Thailand's first 4th generation synchrotron light source, currently under design and prototype development [1]. One of the key systems of SPS-II is the vacuum system, which is responsible for maintaining the high-vacuum environment required for the operation of the particle accelerators and beamlines. Most of the main components in the system are planned to be domestically fabricated through technology transfer. This domestic production of the SPS-II vacuum system presents a significant opportunity to enhance local manufacturing capabilities. It is worth noting that, in 2022, the manufacturing sector accounted for more than 27 % of Thailand's GDP, according to data from the World Bank [2].

Compact lattice designs, similar to MBA lattices found worldwide, present limited space for vacuum components. The small gap between magnet poles limits chamber conductance and makes it difficult to evacuate outgassing, primarily from photon stimulated desorption (PSD). Non-Evaporable Getter (NEG) coating technology has been adopted by many light sources to overcome this limitation [3-5]. However, there are a few challenges associated with this technology that should be considered.

One issue to consider is the complexity of evenly and uniformly applying NEG coatings to intricate vacuum chambers. Complex geometries can make this application process challenging. Additionally, there is concern about the cost and complexity of replacing NEG coatings if they become contaminated or damaged, and the coatings' lifetimes.

Instead of relying on NEG coating technology, the vacuum system design for the SPS-II storage ring is based on conventional technology, harnessing the potential and expertise of the Thai industry. This strategic decision aims to strengthen the Thai industrial community during the design and construction phases.

After conducting parallel studies and development of prototypes for both SUS (stainless steel) and aluminum chambers, the decision to proceed with aluminum was made based on advice from RIKEN and NSRRC experts, as well as the constraints of a short research and development (R&D) period. The advantages of aluminum, including its lightweight nature, high strength-to-weight ratio, corrosion resistance, thermal conductivity, machinability, and cost-effectiveness, were key factors in selecting it as the material for further development.

VACUUM CHAMBER DESIGN

The lattice of the storage ring is the Double-Triple Bend Achromat (DTBA), which comprises 4 normal dipole magnets (BM), 2 combined-functions dipole magnets (DQ), 16 quadrupole magnets (QD, QF), 8 sextupole magnets, and 2 octupole magnets per cell as displayed in Fig. 1. The storage ring consists of 14 DTBA cells (23.393 m/cell), resulting in a total ring circumference of 327.502 m.

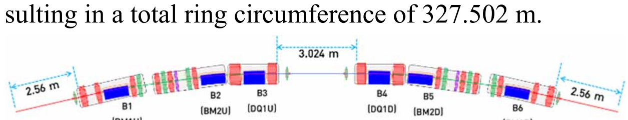

Figure 1: Schematic diagram of DTBA unit cell.

Each cell of the vacuum chamber can be divided into various sections: standard straight sections, middle straight sections, upstream arc section (including bending chambers PVCB-1 and PVCB-2), and downstream arc section (including bending chambers PVCB-3 and PVCB-4), as depicted in Fig. 2. The system has been designed to accommodate the use of three synchrotron radiation sources: two insertion devices (ID) located in the standard and middle straight sections, and the 5th bending magnet located in the downstream side of the cell.

* Work supported by Thailand's Science, Research, and Innovation Fund
† thanapong@slri.or.th

ISBN: 978-3-95450-250-9 ISSN: 2673-5520 doi:10.18429/JACoW-MEDSI2023-FROAM02

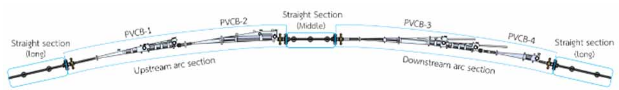

Figure 2: Schematic diagram of sectioned-vacuum chamber in DTBA unit cell.

Straight Section

Straight chamber will be manufactured using Al6063-T5 aluminum extrusion and will feature cooling channels along both sides. The cross-section of the beam duct will be elliptical in shape, with a vertical axis of 16 mm and a horizontal axis of 40 mm, matching the dimensions of the largest beam stay clear of the electron beam. This elliptical cross-section will be maintained consistently throughout the entire length of the beam duct. RF shield bellows will be installed on both side of the straight section to accommodate the thermal expansion during section baking-out (in the tunnel). The length measured from each yoke of the quadrupole magnets is 5.12 m for the standard straight section and 3.024 m for the middle straight section. However, these lengths need to accommodate the fast corrector chamber, BPM (Beam Position Monitor), gate-valve, and RF-shield bellow as well. As a result, the standard straight section or the middle straight section becomes shorter, limiting the available space for insertion devices. The available lengths of the standard straight section and middle straight section for insertion devices and relevant equipment are 4.1 m and 1.8 m, respectively.

Arc Section

Compared to NEG coated copper chamber, SPS-II bending chambers are very bulky. The chambers have been designed as triangular shape with long straight side of the chamber to be easier welded. Considering local manufacturing technology, the chamber has been designed as a two-different structure. It consists of straight parts made from Al6063-T5 aluminum extrusion and a Al6061-T6 bending part manufactured using CNC machining. The outside of the chamber will be machined to fit the shapes of poles and coils for the multipole magnets along the beam duct. Since the clearance between the chamber and the magnet is 1 mm typically, precise machining and positioning of the bending chamber are crucial to avoid any conflicts with nearby active components. The chambers have a minimum thickness of 1.6 mm due to the narrow space between magnet poles. To ensure sufficient structural strength, strategic thickening is applied to other sections outside the magnets, optimizing the overall thickness of the chamber. As a result, the maximum chamber's thickness, measured from top to bottom, is set at 80 mm.

Within the limited space between the magnets, photon absorbers and local pumps are strategically placed to take advantage of their effectiveness in localized pumping near the dominant PSD-outgas regime.

The entire upstream or downstream section will be baked in the laboratory before being transported and assembled in the tunnel. Consequently, a large RF-shield bellow is not required in this section. Instead, a single bellow will be installed between each chamber of each arc section to minimize stress and accommodate thermal expansion during operation.

The structural simulations were conducted using ANSYS software. The simulations focused on analysing deformation and safety factors of structure. Parameter setting for simulation consists of forces due to chamber weight itself, photon absorbers weight, atmospheric pressure, the weight of the pump, a thermal condition of 35 °C, and earth gravity of 9.8106 m/s^2. The selection of fixed and sliding supports have been made with careful consideration to ensure that the simulation results yield stress and deformation within acceptable tolerances.

The simulation results for all bending chambers demonstrate acceptable values with longitudinal deformation of less than 1 mm, vertical and horizontal deformation of less than 0.3 mm. The structural simulation results of all chambers indicate that the stress and safety factor of the simulation are within acceptable tolerances. Figures 3 and 4, as examples, show simulation results of stress and vertical deformation of PVCB-1, respectively.

It is important to highlight that this design approach results in a notably large magnet, which is already an exceptionally thin structure due to the compact lattice configuration. As a result, vibration becomes a more significant concern.

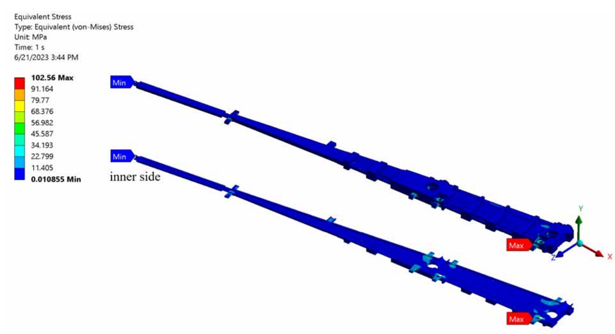

Figure 3: Stress of PVCB-1.

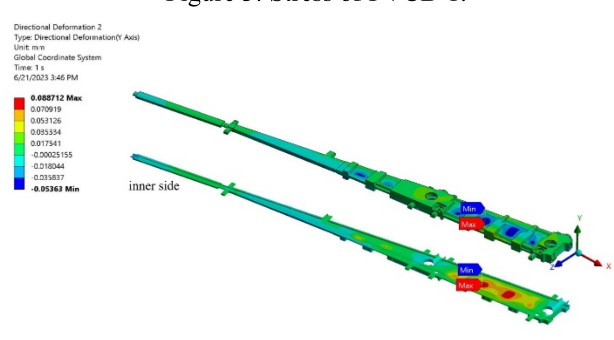

Figure 4: Vertical deformation of PVCB-1.

Bending Chamber for IR Extraction

Since Thailand is an agricultural country with biological diversity, an Infrared (IR) beamline is an important tool in this field of research. There is a plan to have two IR beamlines at SPS-II. However, due to concerns about beam instability and the complexity of designing IR extraction mirrors, the IR beamline has been placed as a second-phase project. Nevertheless, it is worth considering the design

ISBN: 978-3-95450-250-9 ISSN: 2673-5520 doi:10.18429/JACoW-MEDSI2023-FROAM02

and exploring the possibilities, especially for magnet and vacuum chamber design, before it is too late.

IR requires a large vertical opening angle; therefore, it is necessary to modify the magnets and vacuum chamber to meet this requirement. The sixth bending magnet in the cell has been selected for use as an IR source. Considering the space and vacuum system design, this region is quite independent from the others, making it easier to replace. Bending magnet for IR extraction has been designed with a larger gap than an ordinary dipole but still uses the same operating current [6].

The cross-section of the chamber must be enlarged to accommodate the required opening angles of ±20 mrad horizontally and ±12.5 mrad vertically. Following this expansion, it should gradually taper down to the standard shape with taper of 1/8 before passing through the magnet. This taper may introduce higher impedance, which should be considered in the impedance budget and studied further for its potential impact on instability.

PHOTON ABSORBERS

Different types of OFHC copper photon absorbers have been designed to accommodate various heat loads and heating power densities. These absorbers can be categorized based on the shape of the copper grove: flat, V-shape fin, triangular fin, and rectangular fin as shown in Fig. 5. The flat and V-shape fin absorber has two cooling water pipes, while the triangular fin and rectangular fin absorbers have four cooling water pipes, divided into two upper pipes and two lower pipes.

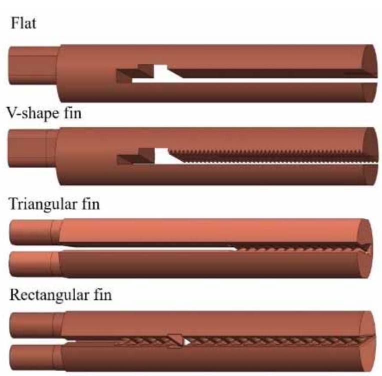

Figure 5: Type of OFHC copper photon absorber.

The simulations were conducted using ANSYS software by steady-state thermal and static structural modes. The simulations focused on analysing the deformation and safety factors of absorbers. For the simulation, the heat transfer coefficient (h) for the cooling water has been set to 10,000 W/mm². The ambient temperature and the inlet temperature of the cooling water are specified as 25 °C. Furthermore, the power of synchrotron radiation has been defined from the beam current of 600 mA which is two times higher than operation current target.

After conducting thermal and structural simulations on all seven OFHC absorbers, it has been determined that they all meet the tolerances. Among them, ABS-B4 in PVCB-4 comes closest to the limits, with absorber and water temperatures of 145.31 °C and 91.879 °C, respectively. The stress and safety factor for ABS-B4 are 99.137 MPa and 2.371, respectively. Figure 6 displays the temperature distribution of absorber ABS-B4. Although the simulation results for ABS-B4 show maximum values approaching the specified criteria's boundary, they remain within the tolerance range for OFHC. This highlights one of the advantages of conventional chamber design, which reduces power density by positioning absorbers as far from the radiation sources as possible.

Figure 6: The temperature distribution of ABS-B4.

PRELIMINARY STUDY OF PRESSURE PROFILE

The one-dimensional iteration method is a powerful tool for calculating pressure profiles in the vacuum system of a synchrotron storage ring. It relies on three essential factors: pumping speed (S), outgassing rates (Q), and conductance (C). The outgassing rate (Q) is determined based on the photon flux and the PSD yield, which is conservatively estimated at approximately 10^{-6} molecules per photon at a dose of 100Ah for this specific analysis. The pressure profile is described by the equation:

$$S_iP_i = Q_i+C_i(P_{i-1}-P_i)+C_i+1(P_{i+1}-P_i). \qquad (1)$$

In Eq. (1), "i-1," "i," and "i+1" represent the previous, current, and next mesh points in the system. This equation illustrates how the pressure at a specific point depends on various factors and the relationships between adjacent locations in the vacuum system, as shown in Fig. 7.

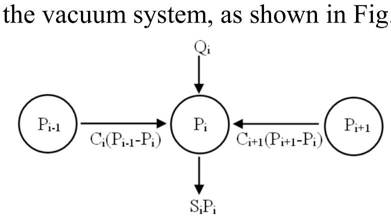

Figure 7: Layout of factors and the relationships between adjacent locations in calculation.

The conductance of a straight section is estimated to be 20 l/s, while bending chambers have a higher conductance of approximately 80 l/s. The calculation results show a very high average pressure of 4.66 x 10^{-9} mbar, which exceeds the tolerance. This is primarily due to limitations in conductance, as pressure profiles indicated in Fig. 8. High pressure is observed where there are no pumps especially at the beginning of the bending chamber.

ISBN: 978-3-95450-250-9 ISSN: 2673-5520 doi:10.18429/JACoW-MEDSI2023-FROAM02

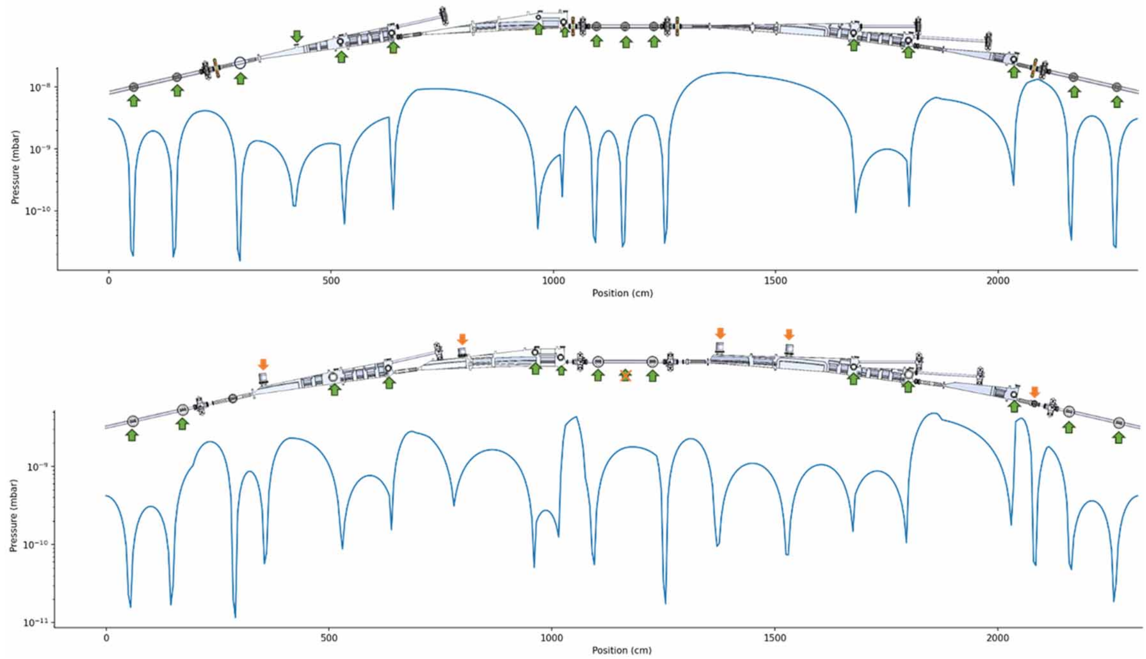

Figure 8: Pressure profile comparison of a single cell chamber between the original vacuum chamber design (top) and the improved design with additional pumps and conductance improvement (bottom). Green arrows indicate the location of the pumps along the cell, and the orange arrows indicate the additional pumps.

To address this, strategies for positioning photon absorbers and pumps to evacuate outgassing, primarily from PSD, have been explored. Additionally, the conductance of both bending chambers in the arc section and the dummy chamber in the straight section need to be improved. In this case, the antechamber size is increased, while the cross section of the dummy chamber in the straight section will be changed from an elliptical shape to a circular shape with an inner diameter of 40 mm. Figure 9 shows examples of improved cross-section design in the PVCB-4 case.

Figure 8 (bottom) shows an improved vacuum chamber layout featuring more pumps, resulting in an average pressure of 1.21 x 10^{-9} mbar, which is within tolerance. However, the structural and thermal properties of chambers and components need to be studied further, and the results should be confirmed using a Monte Carlo simulation program at the end. Besides, it is necessary to take an effort to reduce the dynamics outgassing as much as possible using oil-less machining technique and chemical cleaning.

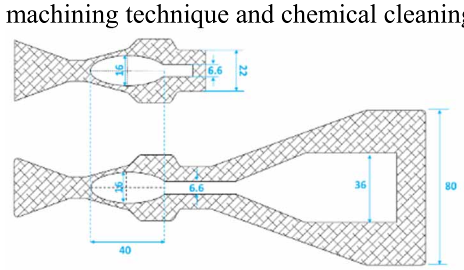

Figure 9: Comparison between cross section of bending chamber PVCB-4 before (top) and after (bottom) improving design.

DISCUSSION AND CONCLUSION

Conventional technology without NEG coating presents several challenges. First, finding adequate space for pumps, absorbers, and beam position monitors (BPMs) is very difficult. This can result in the sacrifice of straight section length, which in turn reduces the available space for insertion devices. Moreover, the bulky chambers require optimization of their thickness to achieve the best strength, necessitating more time and effort compared to using copper tubes. However, from the design perspective, the radiation synchrotron power density absorbed by absorbers is typically low. Therefore, photon absorbers made from oxygen-free high conductivity (OFHC) copper are sufficient to withstand the absorbed power.

The SPS-II project, which has received the Thai government's approval, will be situated within Rayong Province's Eastern Economic Corridor of Innovation (EECi). In line with Thailand's government development policy of fostering domestic manufacturing expertise, the project will prioritize local economic advantages by utilizing conventional vacuum technology.

Prototypes of vacuum chambers have been created to assess local manufacturing capabilities and pinpoint areas for improvement. High-precision machining, welding, and surface treatment techniques, such as oil-less machining and chemical cleaning, are the critical technologies that must be developed to meet the project's requirements. To prepare for the project, two welding technicians have received training, and a pilot plant has been constructed, which includes clean rooms for cleaning, welding, and assembly.

ISBN: 978-3-95450-250-9 ISSN: 2673-5520 doi:10.18429/JACoW-MEDSI2023-FROAM02

REFERENCES

[1] P. Klysubun *et al.*, "SPS-II: A 4th Generation Synchrotron Light Source in Southeast Asia", in *Proc. IPAC'22*, Bangkok, Thailand, Jun. 2022, pp. 764-768. doi:10.18429/JACoW-IPAC2022-MOOPLGD2

[2] https://data.worldbank.org/country/thailand

[3] M. J. Grabski *et al.*, "NEG Thin Film Coating Development for the MAX IV Vacuum System", in *Proc. IPAC'13*, Shanghai, China, May 2013, paper THPFI044, pp. 3385-3387.

[4] R. M. Seraphim *et al.*, "Vacuum System Design for the Sirius Storage Ring", in *Proc. IPAC'15*, Richmond, VA, USA, May 2015, pp. 2744-2746. doi:10.18429/JACoW-IPAC2015-WEPMA003

[5] C. Herbeaux, N. Béchu, and J.-M. Filhol, "Vacuum Conditioning of the SOLEIL Storage Ring with Extensive Use of NEG Coating", in *Proc. EPAC'08*, Genoa, Italy, Jun. 2008, paper THPP142, pp. 3696-3698.

[6] P. Sunwong *et al.*, "Design of dipole magnets for Siam Photon Source II", *J. Phys. Conf. Ser.* , vol. 2431, p. 012072, 2022. doi: 10.1088/1742-6596/2431/1/012072

ISBN: 978-3-95450-250-9 ISSN: 2673-5520 doi:10.18429/JACoW-MEDSI2023-FROAM04

STABILITY AND VIBRATION CONTROL FOR HIGH ENERGY PHOTON SOURCE IN CHINA

Fang Yan†, Guopin Lin, Gang Xu, Zhe Duan, Xiyang Huang, Daheng Ji, Yi Jiao, Yuanyuan Wei, Zihao Wang, Yunin Yang[1], Xiangyu Tan, Ping He, Weimin Pan
Key Laboratory of Particle Acceleration Physics and Technology, Institute of High Energy Physics, Chinese Academy of Sciences, Beijing, China
[1] also at China Agricultural university, Beijing, China

Abstract

The High Energy Photon Source (HEPS) is the first high-energy diffraction-limited storage ring (DLSR) light source to be built in China with natural emittance of few tens of picometer radian. Beam stability is critical for such an ultralow-emittance facility. Controlling and minimizing the vibration sources and their transmissions internally and externally of HEPS is an important issue for achieving the stability needed to operate the high brightest beams. In this presentation, we report the ground motion analytical model related with frequency, the designed site vibration specifications together with the careful consideration and basis. Also, the stable design concepts, passive and active ways to minimize effects on the stability of the photon beam and critical accelerator and beamline components caused by ambient ground motion sources and the actual control effect will be introduced in detail.

INTRODUCTION

The High Energy Photon Source (HEPS), is a fourth-generation photon source with designed natural emittance of 0.0342 nm.rad at 6 GeV, 200 mA beam current and a circumference of 1360.4 m [1]. The design sketch is shown in Fig. 1. HEPS storage ring consists of 48 modified hybrid 7 BAs with brilliance specification of 10^{22} photons/s/mm^2/mrad^2/0.1%BW [2]. With such an ultralow emittance design, HEPS has a very challenging beam stability requirement. The tolerance on the floor motion is required to keep beam fluctuation smaller than 10% of the RMS beam size and 10% of the beam divergence in the meanwhile with FOFB. According to the designed lattice, the RMS beam position and angular spread has to be smaller than 1 μm/0.2 μrad horizontal and 0.3 μm/0.1 μrad vertical respectively [3]. To fulfil such rigorous restrictions, special cares are mandatory in developing site vibration specifications, stable building design concepts, and passive and active ways to minimize effects on the stability of the photon beam and critical accelerator and beamline components caused by ambient ground motion sources.

This contribution presents the novel analytical ground motion model developed, the challenges faced, the effects obtained for the stability and vibration controlling of HEPS in China. The first section is a brief introduction of the project backgrounds. The second section presents the beam dynamics model developed. The detailed specifications

Figure 1: The design sketch of HEPS infrastructure in Beijing China.

established for controlling the vibrations together with the supporting reasons are introduced in the third section. The construction of all the infrastructure has been completed now. The actual stability status is presented in the fourth section. The last section is a summary.

BEAM DYNAMICS MODEL

Frequency Unrelated Model

The baseline lattice of the HEPS storage ring consists of 48 modified hybrid 7BAs, the schematic figure of each cell is shown in Fig. 2 [4]. Vibrations sources are usually difficult to be traced, whether it is microtremors or culture noises. Normally, vibrations are simulated as random noises (uncorrelated and unrelated with frequencies). Random vibrations are introduced into 14 quadrupoles and 6 dipole-quadrupole combination components (with corrector inside) of each cell. The components painted in blue are quadrupoles while the dipole-quadrupole combinations are painted partly in purple and partly in blue as shown in Fig. 2. Vibrations with displacement RMS integral of 25 nm (bare ground vibration level) with frequency of 1-100 Hz are introduced in. The vibration induced close orbit is recorded and the RMS orbit fluctuation and angular dispersion for each position are obtained. Then RMS orbit fluctuation and angular dispersion over RMS beam size and divergence at ID position with and without FOFB (Fast Orbit FeedBack) are plotted as shown in Fig. 3 and Fig. 4 respectively. From the simulations, we can see that, if 25 nm vibrations introduced in the lattice, the orbit and dispersion fluctuation can fulfil the 10% requirement with FOFB correction but not without FOFB.

† email address: yanfang@ihep.ac.cn

ISBN: 978-3-95450-250-9 ISSN: 2673-5520 doi:10.18429/JACoW-MEDSI2023-FROAM04

Figure 2: The schematic figure of each cell [4].

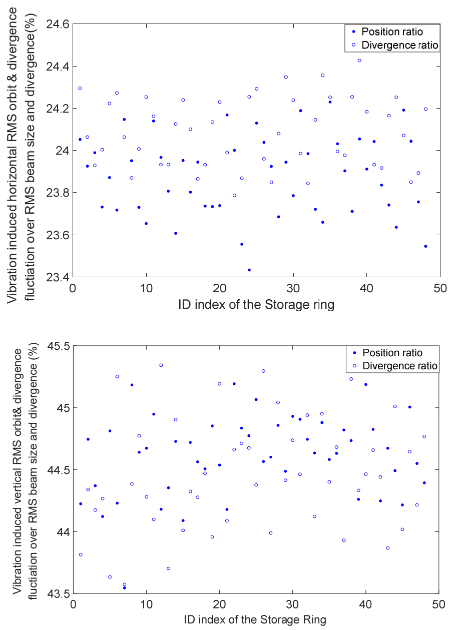

Figure 3: Vibrations (RMS: 25 nm) induced RMS orbit and divergence fluctuation over RMS beam size and divergence without FOFB at ID position horizontal (up) and vertically (down).

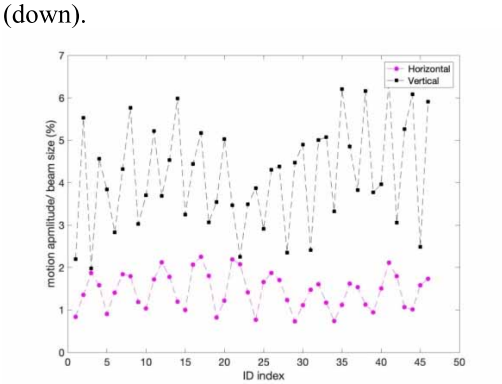

Figure 4: Vibrations (RMS: 25 nm) induced RMS orbit and divergence fluctuation over RMS beam size and divergence at ID position with FOFB.

Although the above-mentioned analysis approaches are widely used for ground motion simulations for many worldwide photo sources, the vibrations induced orbit and angular fluctuation are closely related with frequencies while vibration induced elements displacement are correlated with each other especially for vibration frequencies of few Hz. And also, vibration levels on ground are dominated mainly by noises with low frequencies. So that, ground motion analysis models related with frequency are quite essential.

Frequency Related Model

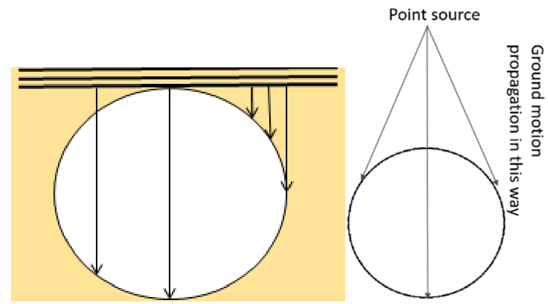

Figure 5: Plane wave model (left) and point wave model (right).

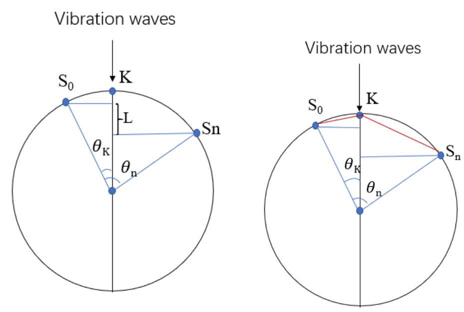

Figure 6: The relative displacement from vibration source to each element of the storage ring for plane wave model (left) and point wave model (right).

Vibrations on HEPS site can be classified into three categories: microtremors, culture noises and the motions from internal utility facilities. According to different vibration types, two different models can be used for ground motion analysis with frequency (to simplify the simulation, the storage ring can be treated as a circle). Microtremor propagates as a plane wave as shown in Fig. 5 (left: plane wave model), because it is normally transported from a long distance and the ground motion levels are almost the same everywhere at the site (the decay of the vibrations is not considered). For other noises from the last two categories (culture noises and internal motions), the source of the noises located nearby the photo source and propagate as a point source as shown in Fig. 5 (right: point source model). The decay of the vibrations along the propagation line cannot be neglected.

The vibrations at each position are superposition of a series oscillating waves with different frequencies. While beam transporting through each element of the lattice, all the vibrations induced by noises with different frequencies added up together, leading to fluctuations of the beam orbit at this element. The displacement on each element of the storage ring induced by noise with single frequency follows the formula as below:

$$X_f = A_f \times d(f,r) \times \cos(\omega t + \psi_f) \tag{1}$$

where, A_f is the vibration amplitude of each wave, ω is the angular frequency ($2\pi f$) while f is the vibration frequency. $d(f,r)$ is the decay formula related with f and the distance r from source to the element concerned. ψ_f is the initial phase of each vibration wave. So, the relative displacement

ISBN: 978-3-95450-250-9 ISSN: 2673-5520 doi:10.18429/JACoW-MEDSI2023-FROAM04

of each element on storage ring is mainly determined by the distance difference from vibration source to each element. And as shown in Fig. 6, the calculation of relative displacement between each element differs for different model, but they all satisfy a certain triangular relationship. To be noted, the relative displacement for each element from the vibration source is the same whether vibration sources located on the storage ring or outside. Using plane wave model (assuming noises in HEPS is mainly dominated by vibration sources far away), we can see from Fig. 7 that, if 25 nm vibrations introduced in the lattice, the orbit and dispersion fluctuation can fulfil the 10% requirement without FOFB.

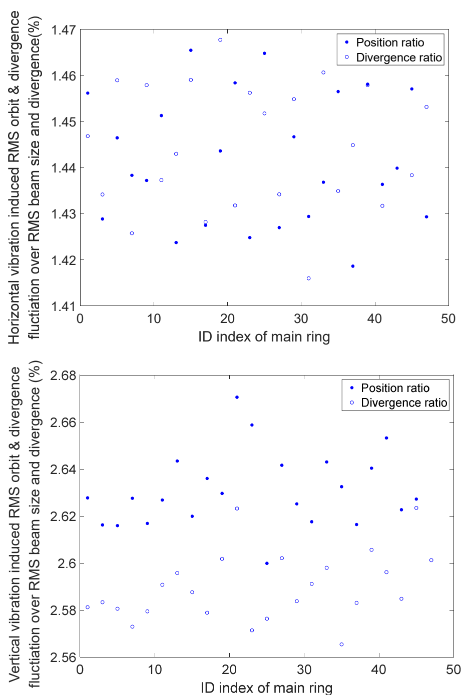

Figure 7: Vibrations (RMS: 25 nm) induced RMS orbit and divergence fluctuation over RMS beam size and divergence at ID position without FOFB under the simulation of frequency related models.

STABILITY SPECIFICATIONS

Although according to simulation results using the above-mentioned frequency related model, displacement RMS integral over 1-100 Hz of 25 nm introduced in the lattice can fulfil the 10% requirement without FOFB. We still take 25 nm as the specification on the slab of the storage ring to give some redundancy. And why we consider 1 Hz to be the lower limit of the specification, because that the betatron wavelength is comparable with ground motion waves with frequency of about 10-20 Hz, we take 1 Hz as the limitation to include one magnitude larger wavelength of vibrations in. The 100 Hz taken as the upper limit of the vibrations is because that the amplitudes of the vibrations are proportional to $1/f^2$, and there is not so much domination for vibrations above that.

To ensure fulfilling of the final vibration target on critical slabs, the 25 nm limitation is further decomposed to three specifications according to the propagation path of the motion waves:

1) Ambient motions caused by other vibration sources have to be smaller than 1 nm ($x/y/z$ direction).
2) No vibration amplification by the slab.
3) No vibration amplification by the base-girder-Magnet assembling, the eigen frequency of this assembling has to be kept bigger than 54 Hz except longitudinal plane.
4) No vibration amplification by the BPM girder, the eigen frequency of it has to be kept bigger than 54 Hz except longitudinal plane.

ACTUAL STABILITY CONTROL EFFECT ON HEPS

The construction of all the infrastructure has been completed now. We measured the amplification factor of the foundation comparing with the bare ground for vibrations frequency of 1-100 Hz using shaker. The shaker was placed on the ground with one seismometer on the ground and the other on the foundation (keep the same distance from shaker to the two sesemomers). As we can see from Fig. 8 that for the amplification factor of the slab, there are only few points are bigger than 1. The foundation is not amplified comparing with the ground if considering the whole integral from 1-100 Hz. The coherences of the ground are also tested on slab of HEPS storge ring, the reults shows (Fig. 9) that two sensors placed about hundred meters away have nicely coherence for vibration frequency of a few Hz.

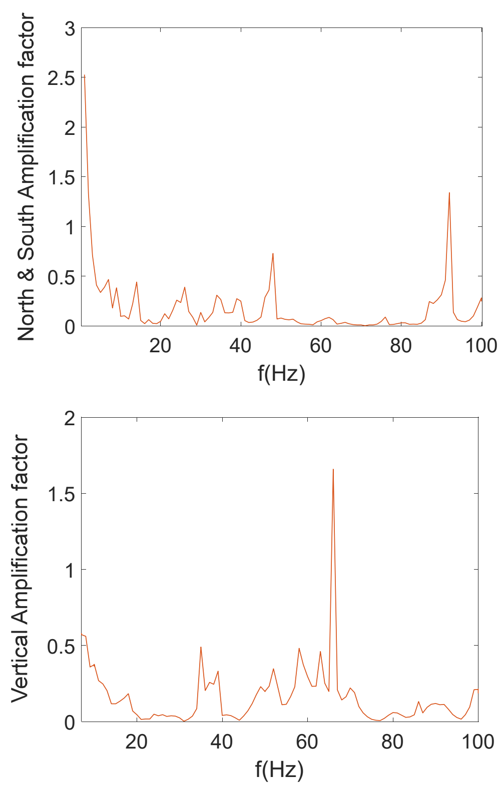

Figure 8: The horizontal (upper plot) and vertical (lower plot) amplification factor of HEPS foundation.

ISBN: 978-3-95450-250-9 ISSN: 2673-5520 doi:10.18429/JACoW-MEDSI2023-FROAM04

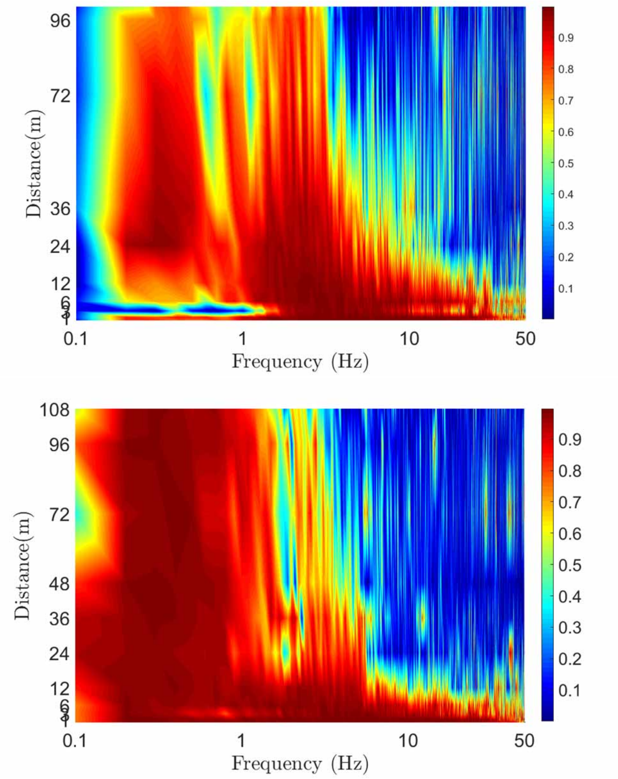

Figure 9: The horizontal (upper graph) and vertical (lower graph) coherence of ground motion as a function of distance between two sensors.

CONCLUSION

The green field motion on HEPS site are smaller than 25 nm (0.1 Hz frequency resolution/60 s average) in all three directions. Frequency related models are developed for vibration induced instability simulations. Ground motion specifications are established accordingly. 25 nm limit is further decomposed to three specifications according to the propagation path of the motion waves. Currently, the construction has been finished, all the magnet assembling installation is in process in the storage ring. According to the test, the foundation is not amplified comparing with the ground if considering the whole integral from 1-100 Hz. Two sensors placed about hundred meters away have nicely coherence for vibration frequency of a few Hz. The ground motions have not been amplified by the girder magnet assembling and BPM girder, at least for the prototypes. The vibration response of the sink tunnel doesn't show obvious differences from the regular slab.

REFERENCES

[1] Y. Jiao *et al.*, "Beam Dynamics Study in the HEPS Storage Ring", in *10th Int. Particle Accelerator Conf. IPAC2019*, Melbourne, Australia, May 2019. doi:10.18429/JACoW-IPAC2019-TUZPLS2

[2] Haisheng Xu *et. al*, "Equilibrium electron beam parameter of the high energy photo source", *Radiat. Detect. Technol. Methods*, vol. 7, pp. 279-287, 2023. doi:10.1007/s41605-022-00374

[3] Zhe Duan, "Estimation for the Orbit feedback Performance for HEPS", 10th GM2017 report, Beijing, China. Dec. 2017.

[4] Chunhua Li, "Update on mechanical engineering", IAC (International Advisory Committee) report, Beijing, China, Dec. 2019.

ISBN: 978-3-95450-250-9 ISSN: 2673-5520 doi:10.18429/JACoW-MEDSI2023

ISBN: 978-3-95450-250-9 ISSN: 2673-5520 doi:10.18429/JACoW-MEDSI2023

List of Authors

Bold papercodes indicate primary authors; ~~strike through/black~~ papercodes indicate **no submission received**

ISBN: 978-3-95450-250-9 ISSN: 2673-5520 doi:10.18429/JACoW-MEDSI2023

— E —

— F —

— G —

— H —

ISBN: 978-3-95450-250-9 ISSN: 2673-5520 doi:10.18429/JACoW-MEDSI2023

12th Int. Conf. Mech. Eng. Design Synchrotron Radiat. Equip. Instrum. MEDSI2023, Beijing, China JACoW Publishing
ISBN: 978-3-95450-250-9 ISSN: 2673-5520 doi:10.18429/JACoW-MEDSI2023

ISBN: 978-3-95450-250-9 ISSN: 2673-5520 doi:10.18429/JACoW-MEDSI2023

ISBN: 978-3-95450-250-9 ISSN: 2673-5520 doi:10.18429/JACoW-MEDSI2023

ISBN: 978-3-95450-250-9 ISSN: 2673-5520 doi:10.18429/JACoW-MEDSI2023

ISBN: 978-3-95450-250-9 ISSN: 2673-5520 doi:10.18429/JACoW-MEDSI2023

Institutes List

Aarhus University
Aarhus, Denmark
- Gothe, A.

AGH University of Science and Technology
Kraków, Poland
- Biedrawa, P.B.
- Jasonek, J.W.

ALBA-CELLS
Cerdanyola del Vallès, Spain
- Boyer, J.B.
- Carballedo, A.
- Casas, J.J.
- Colldelram, C.
- Crisol, A.
- Cuní, G.
- Frieiro, J.L.
- Garriga, D.
- González, N.
- Heinis, D.
- Juanhuix, J.
- Molas, B.
- Nicolàs, J.
- Nikitin, Y.
- Nikitina, L.
- Patera, A.P.
- Pérez, F.
- Quispe, M.
- Ribó, L.R.M.
- Sánchez, A.
- Sanchez, M.
- Šics, I.
- Traver Ramos, O.
- Valls Vidal, N.

ANL
Lemont, Illinois, USA
- Mittone, A.

AS - ANSTO
Clayton, Australia
- Afshar, N.
- de Jonge, M.D.
- Kewish, C.M.
- Lin, B.
- McKinlay, J.
- Morey, C.
- Porsa, S.
- Semeraro, M.
- Tan, Y.E.

AXILON AG
Huerth, Germany
- Andrianov, A.
- Diete, W.
- Schacht, A.
- Schweizer, I.
- Szillat, S.
- Venkataraman, C.
- Waterstradt, T.
- Wiesemann, U.

BNL
Upton, New York, USA
- Doom, L.
- Hetzel, C.
- Johanson, M.P.
- Kosciuk, B.N.
- Padrazo, D.
- Rank, J.
- Sharma, S.K.
- Todd, R.J.

BUAA
Beijing, People's Republic of China
- Li, Y.

CAU
Kiel, Germany
- Buck, J.
- Fu, X.R.
- Kalläne, M.
- Wu, W.
- Yan, L.

CERN
Meyrin, Switzerland
- Andreazza, W.
- Baillard, D.B.
- Bestmann, P.
- Biedrawa, P.B.
- Bursali, H.
- Chritin, N.S.
- Devauchelle, W.
- Fargier, S.F.
- Gentini, L.
- Harrison, A.
- Jasonek, J.W.
- Khatri, G.
- McLean, M.
- Noir, M.N.
- Nuiry, F.-X.
- Pasquino, C.
- Ramos Garcia, M.T.
- Rude, V.
- Sanda, F.
- Schwarz, P.
- Seidenbinder, R.
- Sosin, M.
- Storey, J.W.
- Veness, R.
- Vollenberg, W.
- Vollinger, C.
- Widuch, K.

CIAC
Changchun, People's Republic of China
- Han, Y.C.

ISBN: 978-3-95450-250-9 ISSN: 2673-5520 doi:10.18429/JACoW-MEDSI2023

CLS
Saskatoon, Saskatchewan, Canada
- Billinghurst, B.
- Bundrock, S.O.
- Campbell, J.N.
- Carriere, S.R.
- Le Pimpec, F.
- Li, X.E.
- Lin, L.X.
- Smith, D.M.
- Wyatt, K.D.

CNPEM
Campinas, SP, Brazil
- Ambrosio, C.
- Cardoso, R.B.
- Kuriyama, V.C.
- Leão, L.R.
- Marques, S.R.
- Martins, P.H.S.
- Passuelo, D.

Cosine Measurement Systems
Warmond, The Netherlands
- Barrière, N.
- Collon, M.J.
- Vacanti, G.

CUT
Kraków, Poland
- Romanowicz, P.R.
- Ziemiański, D.T.

DESY
Hamburg, Germany
- Biller, R.
- Buck, J.
- Chumakov, A.
- Dill, F.U.
- Geraissate, H.
- Hoesch, M.
- Huang, M.-J.
- Pfeffer, S.P.
- Rossnagel, R.K.
- Rubeck, J.R.
- Scholz, F.
- Schwartzkopf, M.
- Seltmann, J.
- Stoye, T.
- Welter, E.

DLS
Oxfordshire, United Kingdom
- Alcock, S.G.
- Beamish, S.A.
- Cheng, W.
- Cox, M.P.
- Crivelli, D.
- Danielyan, V.
- Duller, G.M.A.
- Farrelly, S.
- Fielder, R.T.
- Hodbod, S.L.
- Hudson, L.
- Hurlstone, M.L.
- Kelly, J.H.
- Liu, X.
- Lockwood, T.
- Magrath, D.L.
- Nagy, M.
- Olafsson, B.
- Patel, H.
- Vivian, P.J.
- Walters, A.C.

DNSC
Dongguan, People's Republic of China
- Liang, J.
- Liu, J.M.
- Liu, S.M.
- Sun, X.Y.
- Tan, B.
- Wang, P.C.
- Wang, T.

ESA-ESTEC
Noordwijk, The Netherlands
- Bavdaz, M.
- Ferreira, I.

ESEIAAT
Terrassa, Spain
- Capdevila, R.
- Rabasa, M.
- Raush, G.A.

ESRF
Grenoble, France
- Brochard, T.
- Brumund, P.
- Buisson, A.-L.
- Carceller, P.
- Cianciosi, F.
- Eybert, L.
- Maccarrone, C.
- Reyes-Herrera, J.
- Tafforeau, P.
- Van Vaerenbergh, P.
- White, S.M.

EuXFEL
Schenefeld, Germany
- Andersen, T.
- Ansaldi, G.
- Bartmann, A.
- Boesenberg, U.
- Carley, R.
- Deiter, C.
- Delitz, J.T.
- Doblas-Jimenez, D.G.
- Dommach, M.
- Göde, S.
- Grychtol, P.G.
- Hallmann, J.

ISBN: 978-3-95450-250-9 ISSN: 2673-5520 doi:10.18429/JACoW-MEDSI2023

- Izquierdo, M.
- Kohlstrunk, N.
- La Civita, D.
- Loureiro, D.
- Madsen, A.
- Mercurio, G.
- Möller, J.
- Molodtsov, S.
- Ohnesorge, O.J.
- Pudell, J.-E.
- Reich, A.R.
- Rodriguez-Fernandez, A.
- Scherz, A.
- Schmidt, A.
- Shayduk, R.A.
- Sinn, H.
- Sukharnikov, K.
- Teichmann, M.
- Tikhodeeva, T.E.
- Vannoni, M.
- Vardanyan, V.V.
- Wonhyuk, J.
- Yang, F.
- Zozulya, A.

Federal University of Uberlandia
Uberlândia, M.G., Brazil
- Lopes Ribeiro, A.

FMB Oxford
Oxford, United Kingdom
- Jane, E.R.
- Mateos, L.

HUBER Diffraktiontechnik GmbH&Co.KG
Rimsting, Germany
- Huber, N.
- Olea, G.
- Zeeb, J.

HZDR
Dresden, Germany
- Rehwald, M.

IAS
Wuhan City, People's Republic of China
- Chen, Y.
- Hao, X.R.
- He, J.H.
- Li, H.H.
- Li, H.
- Li, J.
- Liu, C.Y.
- Nie, Y.
- Wang, J.
- Wang, Y.
- Wei, G.
- Xiang, P.
- Xu, Y.
- Zhang, J.M.
- Zhang, Y.X.
- Zou, Y.

IASF
Shenzhen, Guangdong, People's Republic of China
- Gong, Y.J.
- Ji, Z.
- Liang, D.H.
- Liu, J.Y.
- Qin, H.
- Shi, Y.
- Wang, C.G.
- Xu, Z.M.
- Yan, X.X.
- Yang, C.
- Zhang, M.
- Zhang, W.Q.
- Zhong, Y.P.
- Zhu, J.

IEAP
Kiel, Germany
- Thiess, T.S.

IF-UFRGS
Porto Alegre, Brazil
- dos Santos, J.H.

IHEP
Beijing, People's Republic of China
- Bian, L.
- Chang, G.C.
- Chang, J.F.
- Chen, F.S.
- Chen, M.W.
- Chen, S.Y.
- Chen, Y.
- Chen, Z.J.
- Cheng, Y.S.
- Chu, S.Q.
- Cui, R.L.
- Cui, Z.Q.
- Dai, J.
- Deng, X.B.
- Diao, D.Z.
- Diao, Q.S.
- Dong, H.
- Dong, L.
- Dong, Y.H.
- Duan, Q.H.
- Duan, Z.
- Feng, G.
- Gao, L.
- Gao, Z.H.
- Gao, Z.Q.
- Guo, D.Z.
- Guo, L.
- Guo, Q.Y.
- Guo, Z.Y.
- Han, H.
- Han, J.
- Han, Q.
- He, H.Y.
- He, P.
- He, Q.L.

ISBN: 978-3-95450-250-9 ISSN: 2673-5520 doi:10.18429/JACoW-MEDSI2023

- He, T.
- Hong, Z.
- Hou, Q.
- Hu, H.
- Hu, Q.
- Hu, Y.
- Huang, X.Y.
- Ji, B.
- Ji, D.
- Jia, Q.J.
- Jia, X.
- Jiao, Y.
- Jin, S.X.
- Kang, L.
- Kuang, X.H.
- Li, C.H.
- Li, G.
- Li, M.X.
- Li, M.
- Li, Q.
- Li, Z.H.
- Li, Z.
- Lian, H.
- Liang, H.
- Liang, R.
- Liao, R.Y.
- Lin, G.P.
- Liu, F.
- Liu, L.
- Liu, P.
- Liu, S.H.
- Liu, S.
- Liu, W.C.
- Liu, Y.P.
- Liu, Y.
- Liu, Z.K.
- Lu, S.
- Lu, Y.S.
- Luo, P.
- Ma, L.H.
- Ma, Q.
- Ma, Y.S.
- Ma, Y.X.
- Men, L.L.
- Meng, F.
- Mo, G.
- Ou, Z.N.
- Pan, W.M.
- Qi, F.Z.
- Qian, H.
- Ren, Z.R.
- Shen, D.S.
- Sheng, W.F.
- Shi, H.
- Sun, F.
- Sun, H.
- Sun, Z.
- Tan, X.Y.
- Tan, Y.
- Tang, S.
- Tao, Y.
- Tian, Y.
- Wang, G.Y.
- Wang, H.Y.
- Wang, H.
- Wang, J.Y.
- Wang, J.
- Wang, L.F.
- Wang, S.F.
- Wang, X.H.
- Wang, X.L.
- Wang, X.
- Wang, Y.G.
- Wang, Z.H.
- Wei, Y.
- Wu, L.
- Wu, Y.F.
- Wu, Z.H.
- Xia, Y.H.
- Xing, X.
- Xu, G.
- Xu, R.Z.
- Xu, W.
- Xu, Y.D.
- Yan, F.
- Yang, F.F.
- Yang, F.G.
- Yang, J.L.
- Yang, M.
- Yang, S.
- Yang, Y.C.
- Yang, Y.
- Yin, C.X.
- Yu, H.H.
- Yu, J.B.
- Yue, S.P.
- Yue, Z.Y.
- Zeng, S.
- Zhang, B.B.
- Zhang, C.L.
- Zhang, C.R.
- Zhang, C.
- Zhang, D.N.
- Zhang, D.S.
- Zhang, G.K.
- Zhang, H.M.
- Zhang, H.Y.
- Zhang, J.C.
- Zhang, J.Y.
- Zhang, J.
- Zhang, L.Y.
- Zhang, L.
- Zhang, P.
- Zhang, Q.
- Zhang, S.
- Zhang, X.M.
- Zhang, X.W.
- Zhang, X.Y.
- Zhang, Y.J.
- Zhang, Y.S.
- Zhang, Z.B.
- Zheng, H.J.

ISBN: 978-3-95450-250-9 ISSN: 2673-5520 doi:10.18429/JACoW-MEDSI2023

ISBN: 978-3-95450-250-9 ISSN: 2673-5520 doi:10.18429/JACoW-MEDSI2023

- Rocha, T.M.
- Rodrigues, G.L.M.P.
- Saveri Silva, M.
- Silva Soares, T.R.
- Silva, D.R.
- Silva, G.H.
- Siqueira da Silva, M.H.
- Sotero, A.P.S.
- Sposito, U.R.
- Teixeira, V.C.
- Tolentino, H.C.N.
- Volpe, L.M.
- Wilendorf, W.H.
- Ynamassu, V.S.
- Zilli, V.B.

MAX IV Laboratory, Lund University
Lund, Sweden

- Al-Najdawi, M.A.
- Aurelius, O.
- Balbin, L.F.
- Benedictsson, S.M.
- Ebbeni, M.
- Felcsuti, G.
- González Fernández, J.B.
- Haghighat, V.H.
- Holz, M.
- Lidón-Simon, J.
- McDonald, S.A.
- Milas, M.
- Nygård, K.
- Roslund, L.K.
- Tarawneh, H.
- Ursby, T.
- Åhnberg, K.

MBI
Berlin, Germany

- Pfau, B.
- Schneider, M.

MI-Partners
Veldhoven, The Netherlands

- Faassen, R.
- Koorneef, L.
- Laro, D.
- Pancras, W.
- Princen, M.
- Ruijl, T.A.M.
- Wijnhoven, M.
- Wullms, P.

NCBJ
Świerk/Otwock, Poland

- Krawczyk, P.
- Nietubyc, R.

NSRC SOLARIS
Kraków, Poland

- Brzyski, M.
- Nowak, P.N.
- Piszak, M.
- Wiechecki, J.J.

PAL
Pohang, Republic of Korea

- Ha, T.
- Han, H.S.
- Hong, G.W.
- Hong, M.S.
- Jeong, D.
- Kim, B.J.
- Kim, S.H.
- Lee, H.-G.
- Lee, S.B.
- Na, D.H.
- Park, Y.J.

PALM Scientific
Naperville, Illinois, USA

- Antipov, S.P.

Peking University
Beijing, Haidian District, People's Republic of China

- Lei, J.

PSI
Villigen PSI, Switzerland

- Bugmann, B.S.
- Buntschu, D.
- Ganter, R.
- Glettig, W.
- Maeher, M.
- Panepucci, E.H.
- Rosenberg, C.
- Wang, M.
- Wang, X.
- Weber, A.

PTB
Berlin, Germany

- Cibic, L.
- Krumrey, M.
- Skroblin, D.

Rejected
–, Tanzania

- Li, Y.

SARI-CAS
Pudong, Shanghai, People's Republic of China

- Chen, J.H.
- Deng, H.X.
- Deng, R.
- Gao, F.
- Hua, W.Q.
- Huang, X.
- Jiang, Z.Q.
- Lei, Y.Y.
- Lei, Z.
- Li, Y.
- Liu, J.N.
- Liu, Y.F.
- Liu, Y.
- Lu, L.J.
- Sun, S.
- Tang, Q.

ISBN: 978-3-95450-250-9 ISSN: 2673-5520 doi:10.18429/JACoW-MEDSI2023

Tsukuba University
Ibaraki, Japan
- Sakurai, T.
- Uezono, N.

TUB
Beijing, People's Republic of China
- Luo, L.

UCAS
Beijing, People's Republic of China
- Tang, S.
- Yu, H.H.
- Zhang, J.Y.

Universidad Politecnica de Madrid, ETSI Aeronauticos
Madrid, Spain
- Grozavu, S.

University of Chinese Academy of Sciences
Beijing, People's Republic of China
- He, T.
- Li, M.
- Liu, W.C.
- Sheng, W.F.
- Tang, S.
- Yang, J.L.
- Yu, H.H.
- Zhang, X.M.

University of Tokyo
Kashiwa, Japan
- Ono, M.
- Yoshikawa, I.
- Yoshioka, K.

USTC
Hefei, Anhui, People's Republic of China
- Zhou, W.Y.

USTC/NSRL
Hefei, Anhui, People's Republic of China
- Bian, B.
- Chen, J.
- Du, J.
- Du, X.W.
- Feng, D.
- Jiang, S.K.
- Lin, M.H.
- Liu, Z.K.
- Ma, W.J.
- Peng, Y.
- Wang, A.X.
- Wang, P.C.
- Wang, Q.P.
- Wang, Y.
- Wang, Z.
- Wei, S.
- Xia, X.
- Xu, Z.L.
- Yuan, H.J.

Yokohama National University
Yokohama, Japan
- Ohno, S.

Yokohama National University, Graduate School of Engineering Science
Yokohama, Japan
- Sato, Y.